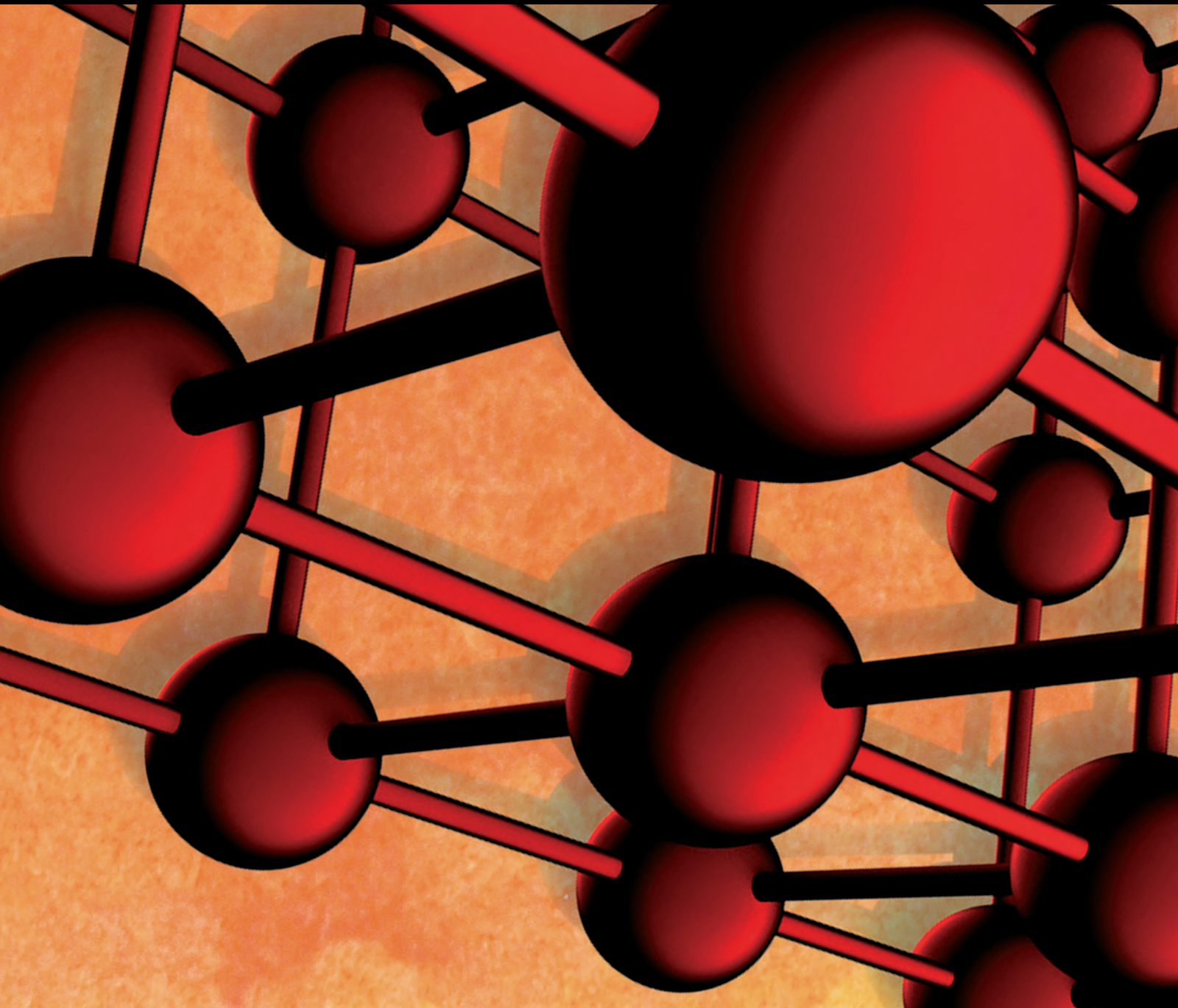


Advances in Materials Science and Engineering

Application of Materials in Agricultural Engineering

Lead Guest Editor: Palanivel Velmurugan

Guest Editors: Ponmurugan Karupiah and Velu Manikandan





Application of Materials in Agricultural Engineering

Advances in Materials Science and Engineering

Application of Materials in Agricultural Engineering

Lead Guest Editor: Palanivel Velmurugan


Guest Editors: Ponmurugan Karuppiah and Velu Manikandan



Copyright © 2024 Hindawi Limited. All rights reserved.

This is a special issue published in "Advances in Materials Science and Engineering." All articles are open access articles distributed under the Creative Commons Attribution License, which permits unrestricted use, distribution, and reproduction in any medium, provided the original work is properly cited.

Chief Editor































Amit Bandyopadhyay , USA

Associate Editors

Vamsi Balla , India
Mitun Das , USA
Sandip Harimkar, USA
Ravi Kumar , India
Peter Majewski , Australia
Enzo Martinelli , Italy
Luigi Nicolais , Italy
Carlos R. Rambo , Brazil
Michael J. Schütze , Germany
Kohji Tashiro , Japan
Zhonghua Yao , China
Dongdong Yuan , China
Wei Zhou , China

Academic Editors

Antonio Abate , Germany
Hany Abdo , Saudi Arabia
H.P.S. Abdul Khalil , Malaysia
Ismael Alejandro Aguayo Villarreal , Mexico
Sheraz Ahmad , Pakistan
Michael Aizenshtein, Israel
Jarir Aktaa, Germany
Bandar AlMangour, Saudi Arabia
Huaming An, China
Alicia Esther Ares , Argentina
Siva Avudaiappan , Chile
Habib Awais , Pakistan
NEERAJ KUMAR BHOI, India
Enrico Babilio , Italy
Renal Backov, France
M Bahubalendruni , India
Sudharsan Balasubramanian , India
Markus Bambach, Germany
Irene Bavasso , Italy
Stefano Bellucci , Italy
Brahim Benmokrane, Canada
Jean-Michel Bergheau , France
Guillaume Bernard-Granger, France
Giovanni Berselli, Italy
Patrice Berthod , France
Michele Bianchi , Italy
Hugo C. Biscaia , Portugal

Antonio Boccaccio, Italy
Mohamed Bououdina , Saudi Arabia
Gianlorenzo Bussetti , Italy
Antonio Caggiano , Germany
Marco Cannas , Italy
Qi Cao, China
Gianfranco Carotenuto , Italy
Paolo Andrea Carraro , Italy
Jose Cesar de Sa , Portugal
Wen-Shao Chang , United Kingdom
Qian Chen , China
Francisco Chinesta , France
Er-Yuan Chuang , Taiwan
Francesco Colangelo, Italy
María Criado , Spain
Enrique Cuan-Urquizo , Mexico
Lucas Da Silva , Portugal
Angela De Bonis , Italy
Abílio De Jesus , Portugal
José António Fonseca De Oliveira
Correia , Portugal
Ismail Demir , Turkey
Luigi Di Benedetto , Italy
Maria Laura Di Lorenzo, Italy
Marisa Di Sabatino, Norway
Luigi Di Sarno, Italy
Ana María Díez-Pascual , Spain
Guru P. Dinda , USA
Hongbiao Dong, China
Mingdong Dong , Denmark
Frederic Dumur , France
Stanislaw Dymek, Poland
Kaveh Edalati , Japan
Philip Eisenlohr , USA
Luis Evangelista , Norway
Michele Fedel , Italy
Francisco Javier Fernández Fernández , Spain
Spain
Isabel J. Ferrer , Spain
Massimo Fresta, Italy
Samia Gad , Egypt
Pasquale Gallo , Finland
Sharanabasava Ganachari, India
Santiago Garcia-Granda , Spain
Carlos Garcia-Mateo , Spain

Achraf Ghorbal , Tunisia
Georgios I. Giannopoulos , Greece
Ivan Giorgio , Italy
Andrea Grilli , Italy
Vincenzo Guarino , Italy
Daniel Guay, Canada
Jenő Gubicza , Hungary
Xuchun Gui , China
Benoit Guiffard , France
Zhixing Guo, China
Ivan Gutierrez-Urrutia , Japan
Weiwei Han , Republic of Korea
Simo-Pekka Hannula, Finland
A. M. Hassan , Egypt
Akbar Heidarzadeh, Iran
Yi Huang , United Kingdom
Joshua Ighalo, Nigeria
Saliha Ilican , Turkey
Md Mainul Islam , Australia
Ilia Ivanov , USA
Jijo James , India
Hafsa Jamshaid , Pakistan
Hom Kandel , USA
Kenji Kaneko, Japan
Rajesh Kannan A , Democratic People's
Republic of Korea
Mehran Khan , Hong Kong
Akihiko Kimura, Japan
Ling B. Kong , Singapore
Pramod Koshy, Australia
Hongchao Kou , China
Alexander Kromka, Czech Republic
Abhinay Kumar, India
Avvaru Praveen Kumar , Ethiopia
Sachin Kumar, India
Paweł Kłosowski , Poland
Wing-Fu Lai , Hong Kong
Luciano Lamberti, Italy
Fulvio Lavecchia , Italy
Laurent Lebrun , France
Joon-Hyung Lee , Republic of Korea
Cristina Leonelli, Italy
Chenggao Li , China
Rongrong Li , China
Yuanshi Li, Canada

Guang-xing Liang , China
Barbara Liguori , Italy
Jun Liu , China
Yunqi Liu, China
Rong Lu, China
Zhiping Luo , USA
Fernando Lusquiños , Spain
Himadri Majumder , India
Dimitrios E. Manolakos , Greece
Necmettin Maraşlı , Turkey
Alessandro Martucci , Italy
Roshan Mayadunne , Australia
Mamoun Medraj , Canada
Shazim A. Memon , Kazakhstan
Pratima Meshram , India
Mohsen Mhadhbi , Tunisia
Philippe Miele, France
Andrey E. Miroshnichenko, Australia
Ajay Kumar Mishra , South Africa
Hossein Moayedi , Vietnam
Dhanesh G. Mohan , United Kingdom
Sakar Mohan , India
Namdev More, USA
Tahir Muhmood , China
Faisal Mukhtar , Pakistan
Dr. Tauseef Munawar , Pakistan
Roger Narayan , USA
Saleem Nasir , Pakistan
Elango Natarajan, Malaysia
Rufino M. Navarro, Spain
Miguel Navarro-Cia , United Kingdom
Behzad Nematollahi , Australia
Peter Niemz, Switzerland
Hiroschi Noguchi, Japan
Dariusz Oleszak , Poland
Laurent Orgéas , France
Togay Ozbakkaloglu, United Kingdom
Marián Palcut , Slovakia
Davide Palumbo , Italy
Gianfranco Palumbo , Italy
Murlidhar Patel, India
Zbyšek Pavlík , Czech Republic
Alessandro Pegoretti , Italy
Gianluca Percoco , Italy
Andrea Petrella, Italy

Claudio Pettinari , Italy
Giorgio Pia , Italy
Candido Fabrizio Pirri, Italy
Marinos Pitsikalis , Greece
Alain Portavoce , France
Simon C. Potter, Canada
Ulrich Prah, Germany
Veena Ragupathi , India
Kawaljit Singh Randhawa , India
Baskaran Rangasamy , Zambia
Paulo Reis , Portugal
Hilda E. Reynel-Avila , Mexico
Yuri Ribakov , Israel
Aniello Riccio , Italy
Anna Richelli , Italy
Antonio Riveiro , Spain
Marco Rossi , Italy
Fernando Rubio-Marcos , Spain
Francesco Ruffino , Italy
Giuseppe Ruta , Italy
Sachin Salunkhe , India
P Sangeetha , India
Carlo Santulli, Italy
Fabrizio Sarasini , Italy
Senthil Kumaran Selvaraj , India
Raffaele Sepe , Italy
Aabid H Shalla, India
Poorva Sharma , China
Mercedes Solla, Spain
Tushar Sonar , Russia
Donato Sorgente , Italy
Charles C. Sorrell , Australia
Damien Soulat , France
Adolfo Speghini , Italy
Antonino Squillace , Italy
Koichi Sugimoto, Japan
Jirapornchai Suksaeree , Thailand
Baozhong Sun, China
Sam-Shajing Sun , USA
Xiaolong Sun, China
Yongding Tian , China
Hao Tong, China
Achim Trampert, Germany
Tomasz Trzepieciński , Poland
Kavimani V , India

Matjaz Valant , Slovenia
Mostafa Vamegh, Iran
Lijing Wang , Australia
Jörg M. K. Wiezorek , USA
Guosong Wu, China
Junhui Xiao , China
Guoqiang Xie , China
YASHPAL YASHPAL, India
Anil Singh Yadav , India
Yee-wen Yen, Taiwan
Hao Yi , China
Wenbin Yi, China
Tetsu Yonezawa, Japan
Hiroshi Yoshihara , Japan
Bin Yu , China
Rahadian Zainul , Indonesia
Lenka Zaji#c#kova# , Czech Republic
Zhigang Zang , China
Michele Zappalorto , Italy
Gang Zhang, Singapore
Jinghuai Zhang, China
Zengping Zhang, China
You Zhou , Japan
Robert Černý , Czech Republic

Contents

Retracted: Impact of Light and Temperature on Growth, Intracellular and Extracellular Pigment, and Lovastatin Yield by *Monascus ruber* in Synthetic Medium

Advances in Materials Science and Engineering
Retraction (1 page), Article ID 9819531, Volume 2024 (2024)

Retracted: Conversion of Aquaculture Waste into Biomedical Wealth: Chitin and Chitosan Journey

Advances in Materials Science and Engineering
Retraction (1 page), Article ID 9762327, Volume 2024 (2024)

Retracted: Using Depth Cameras for Recognition and Segmentation of Hand Gestures

Advances in Materials Science and Engineering
Retraction (1 page), Article ID 9896461, Volume 2023 (2023)

Retracted: Influence of Pore Structure Characteristics of Primary Coal on Coalbed Methane Adsorption

Advances in Materials Science and Engineering
Retraction (1 page), Article ID 9875192, Volume 2023 (2023)

Retracted: Experimental Study on the Principle of Oxygenation and Oxygenation Performance of Surface Blade Aerator

Advances in Materials Science and Engineering
Retraction (1 page), Article ID 9874841, Volume 2023 (2023)

Retracted: Study on Thermal Performance Measurement and Construction of Passive Exterior Wall with Low Energy: Teaching and Laboratory Building of Shandong Jianzhu University

Advances in Materials Science and Engineering
Retraction (1 page), Article ID 9870421, Volume 2023 (2023)

Retracted: Graphene: A Multifunctional Nanomaterial with Versatile Applications

Advances in Materials Science and Engineering
Retraction (1 page), Article ID 9860787, Volume 2023 (2023)

Retracted: Study of Mechanical Properties on Ferric Oxide Microparticles Reinforced with Polyethylene

Advances in Materials Science and Engineering
Retraction (1 page), Article ID 9857326, Volume 2023 (2023)

Retracted: Exhibition of Dielectric Property Based on Soil Class and Moisture Presence for Bengaluru District

Advances in Materials Science and Engineering
Retraction (1 page), Article ID 9851803, Volume 2023 (2023)

Retracted: Enhancement Modelling Based on Electrical Discharge Machining Successive Discharges

Advances in Materials Science and Engineering
Retraction (1 page), Article ID 9851560, Volume 2023 (2023)

Retracted: An Innovative Approach of N-Soft Quotient Topological Space

Advances in Materials Science and Engineering
Retraction (1 page), Article ID 9843835, Volume 2023 (2023)

Retracted: Mechanical Characterization of Biocomposites Reinforced with Untreated and 4% NaOH-Treated Sisal and Jute Fibres

Advances in Materials Science and Engineering
Retraction (1 page), Article ID 9838536, Volume 2023 (2023)

Retracted: Modeling and Optimization of MRR in Wire Electrical Discharge Machining of Silicon Particle-Reinforced AA6063 Composite

Advances in Materials Science and Engineering
Retraction (1 page), Article ID 9837546, Volume 2023 (2023)

Retracted: Development of Quality Information Management System for Alumina Ceramic Tube Manufacturing Process

Advances in Materials Science and Engineering
Retraction (1 page), Article ID 9836712, Volume 2023 (2023)

Retracted: Investigation of Mechanical and Physical Behaviours of Polyester Resin Matrix from Recycled Polyethylene Terephthalate with Bamboo Fibre

Advances in Materials Science and Engineering
Retraction (1 page), Article ID 9836015, Volume 2023 (2023)

Retracted: Implementation of TQM and the Integration of BIM in the Construction Management Sector in Saudi Arabia

Advances in Materials Science and Engineering
Retraction (1 page), Article ID 9835852, Volume 2023 (2023)

Retracted: Modeling and Analysis of Automotive Engine Crankshaft Made of Composite and Functionally Graded Materials

Advances in Materials Science and Engineering
Retraction (1 page), Article ID 9829137, Volume 2023 (2023)

Retracted: Optimization of Process Parameters for Friction Stir Welding of Different Aluminum Alloys AA2618 to AA5086 by Taguchi Method

Advances in Materials Science and Engineering
Retraction (1 page), Article ID 9821983, Volume 2023 (2023)

Retracted: The Impact of Family Sustainable Livelihood and Environmental Cognition on Herdsmen's Choice of Production Behavior

Advances in Materials Science and Engineering
Retraction (1 page), Article ID 9821589, Volume 2023 (2023)

Contents

Retracted: Investigation on Tensile Behaviour of Different Weld Joints through Taguchi Approach

Advances in Materials Science and Engineering
Retraction (1 page), Article ID 9818027, Volume 2023 (2023)

Retracted: Thermal Analysis of the Solar Dish Array Concentrator System

Advances in Materials Science and Engineering
Retraction (1 page), Article ID 9817086, Volume 2023 (2023)

Retracted: Effect of Using Modern Banking Services on Customer Inspiration: Statistical Analysis

Advances in Materials Science and Engineering
Retraction (1 page), Article ID 9812676, Volume 2023 (2023)

Retracted: Anti-Quorum Sensing in Pathogenic Microbes Using Plant-Based Bioactive Phytochemicals

Advances in Materials Science and Engineering
Retraction (1 page), Article ID 9805956, Volume 2023 (2023)

Retracted: Improved Chicken Reproduction and Yield of Improved Poultry from Titanium Dioxide (TiO₂) Nanoparticles Coated in Jimma Horro Area of Kellem Wollega Zone, Ethiopia

Advances in Materials Science and Engineering
Retraction (1 page), Article ID 9803190, Volume 2023 (2023)

Retracted: Optimization and Mechanical Properties of TiO₂ Reinforced AA 7150 Composites Using Response Surface Methodology

Advances in Materials Science and Engineering
Retraction (1 page), Article ID 9798651, Volume 2023 (2023)

Retracted: Deformation Analysis of Surrounding Rock of Deep Roadway by the Fluid Structure Coupling Model with MIDAS-GTS

Advances in Materials Science and Engineering
Retraction (1 page), Article ID 9798609, Volume 2023 (2023)

Retracted: Characterization and Parametric Optimization of EN-10149-2 Steel Welded Joints Made by MIG Welding

Advances in Materials Science and Engineering
Retraction (1 page), Article ID 9794234, Volume 2023 (2023)

Retracted: Thermal Conductivity of Thermally Insulated Concretes in a Nuclear Safety Vessel of Reactor Vault: Experimental Interpretation

Advances in Materials Science and Engineering
Retraction (1 page), Article ID 9793712, Volume 2023 (2023)

Retracted: HS-GC-IMS and ATR-FT-MIR Analysis Reveal the Differences in Volatile Compounds, Proteins, and Polyphenols of Royal Jelly

Advances in Materials Science and Engineering
Retraction (1 page), Article ID 9793648, Volume 2023 (2023)

Retracted: Antidandruff Activity of Polyherbal (*Murraya koenigii*, *Moringa oleifera*, and *Psidium guajava*) Extract against *Malassezia* Species: In Silico Studies

Advances in Materials Science and Engineering
Retraction (1 page), Article ID 9793538, Volume 2023 (2023)

Retracted: Ternary Complexation Process for New Spectrophotometric Assay of Levodopa using Ni(II) and 2,3-Diaminopyridine

Advances in Materials Science and Engineering
Retraction (1 page), Article ID 9793041, Volume 2023 (2023)

Retracted: Impact of BN and WC Particulate Reinforcements on Mechanical Properties and Damage Development of Al-2048 Metal Matrix Composites

Advances in Materials Science and Engineering
Retraction (1 page), Article ID 9792806, Volume 2023 (2023)

Retracted: Energy Efficient Utilization toward Rural Biomass Waste by Straw Biogas Engineering

Advances in Materials Science and Engineering
Retraction (1 page), Article ID 9787396, Volume 2023 (2023)

Retracted: Analysis of Pomegranate Dye Coated Titanium Nanotubes Anode for Solar Cell Application

Advances in Materials Science and Engineering
Retraction (1 page), Article ID 9787141, Volume 2023 (2023)

Retracted: Study on the Relationship between Conspicuous Need and Group Cultural Identity of Fashion Cultural Consumption

Advances in Materials Science and Engineering
Retraction (1 page), Article ID 9765360, Volume 2023 (2023)

Retracted: Application of Regression Analysis to Identify the Soil and Other Factors Affecting the Wheat Yield

Advances in Materials Science and Engineering
Retraction (1 page), Article ID 9759731, Volume 2023 (2023)

Retracted: Mechanics of Materials Natural Fibers Technology on Thermal Properties of Polymer

Advances in Materials Science and Engineering
Retraction (1 page), Article ID 9824791, Volume 2023 (2023)

Retracted: Using Convolutional Neural Networks for Segmentation of Multiple Sclerosis Lesions in 3D Magnetic Resonance Imaging

Advances in Materials Science and Engineering
Retraction (1 page), Article ID 9807562, Volume 2023 (2023)

Retracted: Dynamic Systems Enhanced by Electronic Circuits on 7D

Advances in Materials Science and Engineering
Retraction (1 page), Article ID 9782973, Volume 2023 (2023)

Contents



Retracted: Optimization of the Spark Plasma Sintering Process for High-Volume Fraction Tungsten Carbide/Al 2025 Composites

Advances in Materials Science and Engineering
Retraction (1 page), Article ID 9765143, Volume 2023 (2023)


Retracted: The Role of Gum Arabic for a Protective Kidney Dysfunction Induced Gentamicin on Diabetes Rats

Advances in Materials Science and Engineering
Retraction (1 page), Article ID 9757383, Volume 2023 (2023)


[Retracted] Impact of Light and Temperature on Growth, Intracellular and Extracellular Pigment, and Lovastatin Yield by *Monascus ruber* in Synthetic Medium

K. Suganya, A. Usha Raja Nanthini , Jayaraman Narenkumar, Subramani Abilaji, Aruliah Rajasekar, Subpiramaniyam Sivakumar, S. Prasath , Hesham S. Almoallim, and Tahani Awad Alahmadi
Research Article (6 pages), Article ID 2808733, Volume 2022 (2022)




[Retracted] Modeling and Optimization of MRR in Wire Electrical Discharge Machining of Silicon Particle-Reinforced AA6063 Composite

CR Mahesha, R. Suprabha, NPG Bhavani, Prashant Sunagar, Raja Ramesh, P. Balamurugan, Rajasekar Rajendran, and Anirudh Bhowmick 
Research Article (9 pages), Article ID 2594974, Volume 2022 (2022)

[Retracted] Optimization of the Spark Plasma Sintering Process for High-Volume Fraction Tungsten Carbide/Al 2025 Composites

C. R. Mahesha, Suprabha R, Chintada Polayya, Moti Lal Rinawa, T. Sakthi, Neha Munjal, Ishwarya Komalnu Raghavan , P. Ganeshan, and Chanakyan C
Research Article (7 pages), Article ID 6433716, Volume 2022 (2022)




[Retracted] Thermal Conductivity of Thermally Insulated Concretes in a Nuclear Safety Vessel of Reactor Vault: Experimental Interpretation


M. Anish , T. Arunkumar , J. Jayaprabakar, Sami Al Obaid, Saleh Alfarraj, M. M. Raj, and Assefa Belay 
Research Article (12 pages), Article ID 4493910, Volume 2022 (2022)


[Retracted] Influence of Pore Structure Characteristics of Primary Coal on Coalbed Methane Adsorption


Gang Liu 
Research Article (7 pages), Article ID 3087252, Volume 2022 (2022)





[Retracted] Exhibition of Dielectric Property Based on Soil Class and Moisture Presence for Bengaluru District


Sujit Kumar , N. Ahalya , Vikash Singh, Pravin P. Patil, A. V. Raghavendra Rao, A. Nirmala Jyothsna, P. Abhilash, Rupesh kushwah, and Sojan Palukaran Timothy 
Research Article (9 pages), Article ID 6807204, Volume 2022 (2022)



[Retracted] Study of Mechanical Properties on Ferric Oxide Microparticles Reinforced with Polyethylene
U. Tamilarasan, S. Dhanasekar, K. Raja Karthikeyan, T. S. Ramesh Babu, R. Gopinathan, V. G. Pratheep, P. Rajalakshmy, Ram Subbiah, and S. Praveen Kumar 
Research Article (7 pages), Article ID 3077301, Volume 2022 (2022)


[Retracted] Study on Thermal Performance Measurement and Construction of Passive Exterior Wall with Low Energy: Teaching and Laboratory Building of Shandong Jianzhu University
Yirui Lan  and Ran Zou
Research Article (11 pages), Article ID 3253085, Volume 2022 (2022)






[Retracted] Energy Efficient Utilization toward Rural Biomass Waste by Straw Biogas Engineering
Xiao Wang  and Dejie Zhao
Research Article (6 pages), Article ID 3338515, Volume 2022 (2022)

[Retracted] Antidandruff Activity of Polyherbal (*Murraya koenigii*, *Moringa oleifera*, and *Psidium guajava*) Extract against *Malassezia* Species: In Silico Studies
Akshata Sharma , Punniavan Sakthiselvan , V. Karthick , R. Subraja, T. Srinivasan, K. Amudha, and Shani T John 
Research Article (13 pages), Article ID 7373942, Volume 2022 (2022)

[Retracted] Optimization and Mechanical Properties of TiO₂ Reinforced AA 7150 Composites Using Response Surface Methodology
S V G V A Prasad, V. Kamalakar, J. Madhusudhanan, Puthalapattu Reddy Prasad, G. Adilakshmi, Nellore Manoj Kumar, Anitha Gopalan, Vinod Singh rajput, and Nagaraj Ashok 
Research Article (12 pages), Article ID 5779840, Volume 2022 (2022)

[Retracted] Impact of BN and WC Particulate Reinforcements on Mechanical Properties and Damage Development of Al-2048 Metal Matrix Composites
T. Sivakumar, Chikkappa Udagani, M. Sivaranjani, M. Sudhakar, Reem Mohammed Alharbi, Neveen Abdel-Raouf, Ibraheem Borie M. Ibraheem, Essam Nageh Sholkamy , Mahadeo A. Mahadik, and Simon Yishak 
Research Article (9 pages), Article ID 2286713, Volume 2022 (2022)

[Retracted] Investigation on Tensile Behaviour of Different Weld Joints through Taguchi Approach
Shoab Kamal, V. Parthiban, G. Puthilibai, M. Thirumal Azhagan, Neel Kamal, T. S. Senthil, and Simon Yishak 
Research Article (9 pages), Article ID 5258014, Volume 2022 (2022)

[Retracted] Application of Regression Analysis to Identify the Soil and Other Factors Affecting the Wheat Yield
Azhar Hayat , Muhammad Amin , Saima Afzal , Abdisalam Hassan Muse , Omer Mohamed Egeh , and Hafiz Saqib Hayat
Research Article (10 pages), Article ID 7793187, Volume 2022 (2022)

Contents


[Retracted] Analysis of Pomegranate Dye Coated Titanium Nanotubes Anode for Solar Cell Application

P. Thenmozhi, P. Sathya , S. Meyvel, and Subash Thanappan 
Research Article (7 pages), Article ID 3278255, Volume 2022 (2022)

[Retracted] Mechanical Characterization of Biocomposites Reinforced with Untreated and 4% NaOH-Treated Sisal and Jute Fibres

D. P. Archana , H. N. Jagannatha Reddy , and Basavaraju Paruti 
Research Article (11 pages), Article ID 7777904, Volume 2022 (2022)



[Retracted] Modeling and Analysis of Automotive Engine Crankshaft Made of Composite and Functionally Graded Materials

Saeed Asiri 
Research Article (15 pages), Article ID 4005368, Volume 2022 (2022)


[Retracted] The Role of Gum Arabic for a Protective Kidney Dysfunction Induced Gentamicin on Diabetes Rats

Garsa Ali Alshehry 
Research Article (8 pages), Article ID 8617445, Volume 2022 (2022)




[Retracted] Conversion of Aquaculture Waste into Biomedical Wealth: Chitin and Chitosan Journey

Jerrine Joseph, Kaari Manigundan, Mary Shamy Arokia Rajan, Manikkam Radhakrishnan, Venugopal Gopikrishnan, Subramanian Kumaran , Rajasekar Thirunavukkarasu, Wilson Aruni, and Velmurugan Shanmugam 
Review Article (12 pages), Article ID 2897179, Volume 2022 (2022)



[Retracted] Characterization and Parametric Optimization of EN-10149-2 Steel Welded Joints Made by MIG Welding

Kedir Beyene Behredin, Perumalla Janaki Ramulu , Beri Habtamu, Negash Besufekad, and Negash Tesfaye
Research Article (16 pages), Article ID 8276496, Volume 2022 (2022)

[Retracted] Using Convolutional Neural Networks for Segmentation of Multiple Sclerosis Lesions in 3D Magnetic Resonance Imaging

Abdulsattar Abdullah Hamad , Mustafa Musa Jaber, Mohammed Altaf Ahmed , Ghaida Muttashar Abdulsahib, Osamah Ibrahim Khalaf, and Zelalem Meraf 
Research Article (10 pages), Article ID 4905115, Volume 2022 (2022)

[Retracted] HS-GC-IMS and ATR-FT-MIR Analysis Reveal the Differences in Volatile Compounds, Proteins, and Polyphenols of Royal Jelly

Di Chen , Wenjing Lu, Qin Ye, Cen Zhang, Xiao Ge, and Chaogeng Xiao 
Research Article (8 pages), Article ID 3223558, Volume 2022 (2022)

[Retracted] The Impact of Family Sustainable Livelihood and Environmental Cognition on Herdsmen's Choice of Production Behavior

Qihang Wang  and Yinjia Miao


Research Article (9 pages), Article ID 4278331, Volume 2022 (2022)

[Retracted] An Innovative Approach of N-Soft Quotient Topological Space

G. Kabin Antony , M. Lellis Thivagar , B. Tamilarasan, and Mequanint Birhan 

Research Article (5 pages), Article ID 4627283, Volume 2022 (2022)

[Retracted] Study on the Relationship between Conspicuous Need and Group Cultural Identity of Fashion Cultural Consumption

Liang Zhao, Yunze Duan, Qiang Wang, Ke Zhou, Nailin Gu, Xiangzhong Li, and Jingyu Dai 

Research Article (9 pages), Article ID 3541548, Volume 2022 (2022)

[Retracted] Improved Chicken Reproduction and Yield of Improved Poultry from Titanium Dioxide (TiO₂) Nanoparticles Coated in Jimma Horro Area of Kellem Wollega Zone, Ethiopia

Soressa Shuma Abdisa, Jule Leta Tesfaye , Abel Saka , Abdisa Abraham, N. Nagaprasad , Lamessa Gudata, and Krishnaraj Ramaswamy 




Research Article (7 pages), Article ID 1984178, Volume 2022 (2022)

[Retracted] Experimental Study on the Principle of Oxygenation and Oxygenation Performance of Surface Blade Aerator

Pu Xing , Chen Yu, Kangkang Li, and Hui Wu

Research Article (14 pages), Article ID 3518833, Volume 2022 (2022)

[Retracted] Deformation Analysis of Surrounding Rock of Deep Roadway by the Fluid Structure Coupling Model with MIDAS-GTS

Jun Jiang , Zhengmeng Hou , Kepeng Hou, Yongfeng Lu , Huafen Sun, and Xiangdong Niu


Research Article (6 pages), Article ID 9945383, Volume 2022 (2022)

[Retracted] Development of Quality Information Management System for Alumina Ceramic Tube Manufacturing Process

Yulong Huang 

Research Article (13 pages), Article ID 5816221, Volume 2022 (2022)


[Retracted] Investigation of Mechanical and Physical Behaviours of Polyester Resin Matrix from Recycled Polyethylene Terephthalate with Bamboo Fibre

Nandagopal Kaliappan, Venkatesan Govindarajan, T CH Anil Kumar , R. Vishnu Kumar, S.

Muthukumar, Maqusood Ahamed , Mahadeo A. Mahadik, and Mebratu Markos 

Research Article (8 pages), Article ID 4233302, Volume 2022 (2022)



[Retracted] Effect of Using Modern Banking Services on Customer Inspiration: Statistical Analysis

Moqdad Ibrahim Jassem, Rafiduraida Abdul Rahman, and Abdelrahman Mohamed Ibrahim 


Research Article (6 pages), Article ID 7130559, Volume 2022 (2022)

Contents



[Retracted] Optimization of Process Parameters for Friction Stir Welding of Different Aluminum Alloys AA2618 to AA5086 by Taguchi Method

G. Sasikala, V. M. Jothiprakash, Bhasker Pant, R. Subalakshmi, M. Thirumal Azhagan, K. Arul , Wadi B. Alonazi, M. Karnan, and S. Praveen Kumar 
Research Article (9 pages), Article ID 3808605, Volume 2022 (2022)





[Retracted] Thermal Analysis of the Solar Dish Array Concentrator System

Yaseen H. Mahmood, R. Y. J. Al-Salih, Saif Amer Mahdi, and Abdelrahman Mohamed Ibrahim 
Research Article (8 pages), Article ID 1823630, Volume 2022 (2022)




[Retracted] Anti-Quorum Sensing in Pathogenic Microbes Using Plant-Based Bioactive Phytochemicals

Kumaran Subramanian, Harshni Selvaraj , Balakrishnan K, Pugazhvendan Sampath Renuga, Velmurugan S , and Wilson Aruni
Review Article (7 pages), Article ID 7532086, Volume 2022 (2022)






[Retracted] Ternary Complexation Process for New Spectrophotometric Assay of Levodopa using Ni(II) and 2,3-Diaminopyridine

Fadam Abdoon , Mustafa J. Bichan, Abdelrahman Mohamed Ibrahim , Alnoman Mundher Tayyeh, Medikundu Kishore , and Azam Abdelhakeem Khalid 
Research Article (8 pages), Article ID 4915162, Volume 2022 (2022)

[Retracted] Enhancement Modelling Based on Electrical Discharge Machining Successive Discharges

Farook Nehad Abed , V. Ramesh , Mohanad Fadhil Jwaid, Nidhi Agarwal, Deepika Koundal, and Abdelrahman Mohamed Ibrahim 
Research Article (7 pages), Article ID 8017375, Volume 2022 (2022)




[Retracted] Mechanics of Materials Natural Fibers Technology on Thermal Properties of Polymer

Malik Bader Alazzam , Fahima Hajjei , Ahmed S AlGhamdi , Sarra Ayouni , and Md Adnan Rahman 
Research Article (5 pages), Article ID 7774180, Volume 2022 (2022)






[Retracted] Implementation of TQM and the Integration of BIM in the Construction Management Sector in Saudi Arabia

Mohammad Abazid , Hüseyin Gökçekuş, and Tahir Çelik
Research Article (9 pages), Article ID 1232620, Volume 2021 (2021)







[Retracted] Graphene: A Multifunctional Nanomaterial with Versatile Applications

H. C. Ananda Murthy , Suresh Ghotekar , B. Vinay Kumar , and Arpita Roy 
Review Article (8 pages), Article ID 2418149, Volume 2021 (2021)

[Retracted] Using Depth Cameras for Recognition and Segmentation of Hand Gestures

Khalid Twarish Alhamazani , Jalawi Alshudukhi , Talal Saad Alharbi , Saud Aljaloud , and Zelalem Meraf 
Research Article (6 pages), Article ID 7100727, Volume 2021 (2021)

[Retracted] Dynamic Systems Enhanced by Electronic Circuits on 7D

Abdulsattar Abdullah Hamad , M. Lellis Thivagar , Malik Bader Alazzam , Fawaz Alassery ,
Muayyad Mahmood Khalil, V. Ramesh, Zelalem Meraf , and Vishal Kumar 
Research Article (11 pages), Article ID 8148772, Volume 2021 (2021)

Retraction

Retracted: Impact of Light and Temperature on Growth, Intracellular and Extracellular Pigment, and Lovastatin Yield by *Monascus ruber* in Synthetic Medium

Advances in Materials Science and Engineering

Received 8 January 2024; Accepted 8 January 2024; Published 9 January 2024

Copyright © 2024 Advances in Materials Science and Engineering. This is an open access article distributed under the Creative Commons Attribution License, which permits unrestricted use, distribution, and reproduction in any medium, provided the original work is properly cited.

This article has been retracted by Hindawi following an investigation undertaken by the publisher [1]. This investigation has uncovered evidence of one or more of the following indicators of systematic manipulation of the publication process:

- (1) Discrepancies in scope
- (2) Discrepancies in the description of the research reported
- (3) Discrepancies between the availability of data and the research described
- (4) Inappropriate citations
- (5) Incoherent, meaningless and/or irrelevant content included in the article
- (6) Manipulated or compromised peer review

The presence of these indicators undermines our confidence in the integrity of the article's content and we cannot, therefore, vouch for its reliability. Please note that this notice is intended solely to alert readers that the content of this article is unreliable. We have not investigated whether authors were aware of or involved in the systematic manipulation of the publication process.

Wiley and Hindawi regrets that the usual quality checks did not identify these issues before publication and have since put additional measures in place to safeguard research integrity.

We wish to credit our own Research Integrity and Research Publishing teams and anonymous and named external researchers and research integrity experts for contributing to this investigation.

The corresponding author, as the representative of all authors, has been given the opportunity to register their agreement or disagreement to this retraction. We have kept a record of any response received.

References

- [1] K. Suganya, A. Usha Raja Nanthini, J. Narenkumar et al., "Impact of Light and Temperature on Growth, Intracellular and Extracellular Pigment, and Lovastatin Yield by *Monascus ruber* in Synthetic Medium," *Advances in Materials Science and Engineering*, vol. 2022, Article ID 2808733, 6 pages, 2022.

Retraction

Retracted: Conversion of Aquaculture Waste into Biomedical Wealth: Chitin and Chitosan Journey

Advances in Materials Science and Engineering

Received 8 January 2024; Accepted 8 January 2024; Published 9 January 2024

Copyright © 2024 Advances in Materials Science and Engineering. This is an open access article distributed under the Creative Commons Attribution License, which permits unrestricted use, distribution, and reproduction in any medium, provided the original work is properly cited.

This article has been retracted by Hindawi following an investigation undertaken by the publisher [1]. This investigation has uncovered evidence of one or more of the following indicators of systematic manipulation of the publication process:

- (1) Discrepancies in scope
- (2) Discrepancies in the description of the research reported
- (3) Discrepancies between the availability of data and the research described
- (4) Inappropriate citations
- (5) Incoherent, meaningless and/or irrelevant content included in the article
- (6) Manipulated or compromised peer review

The presence of these indicators undermines our confidence in the integrity of the article's content and we cannot, therefore, vouch for its reliability. Please note that this notice is intended solely to alert readers that the content of this article is unreliable. We have not investigated whether authors were aware of or involved in the systematic manipulation of the publication process.

Wiley and Hindawi regrets that the usual quality checks did not identify these issues before publication and have since put additional measures in place to safeguard research integrity.

We wish to credit our own Research Integrity and Research Publishing teams and anonymous and named external researchers and research integrity experts for contributing to this investigation.

The corresponding author, as the representative of all authors, has been given the opportunity to register their agreement or disagreement to this retraction. We have kept a record of any response received.

References

- [1] J. Joseph, K. Manigundan, M. Shamy Arokia Rajan et al., "Conversion of Aquaculture Waste into Biomedical Wealth: Chitin and Chitosan Journey," *Advances in Materials Science and Engineering*, vol. 2022, Article ID 2897179, 12 pages, 2022.

Retraction

Retracted: Using Depth Cameras for Recognition and Segmentation of Hand Gestures

Advances in Materials Science and Engineering

Received 26 December 2023; Accepted 26 December 2023; Published 29 December 2023

Copyright © 2023 Advances in Materials Science and Engineering. This is an open access article distributed under the Creative Commons Attribution License, which permits unrestricted use, distribution, and reproduction in any medium, provided the original work is properly cited.

This article has been retracted by Hindawi, as publisher, following an investigation undertaken by the publisher [1]. This investigation has uncovered evidence of systematic manipulation of the publication and peer-review process. We cannot, therefore, vouch for the reliability or integrity of this article.

Please note that this notice is intended solely to alert readers that the peer-review process of this article has been compromised.

Wiley and Hindawi regret that the usual quality checks did not identify these issues before publication and have since put additional measures in place to safeguard research integrity.

We wish to credit our Research Integrity and Research Publishing teams and anonymous and named external researchers and research integrity experts for contributing to this investigation.

The corresponding author, as the representative of all authors, has been given the opportunity to register their agreement or disagreement to this retraction. We have kept a record of any response received.

References

- [1] K. T. Alhamazani, J. Alshudukhi, T. S. Alharbi, S. Aljaloud, and Z. Meraf, "Using Depth Cameras for Recognition and Segmentation of Hand Gestures," *Advances in Materials Science and Engineering*, vol. 2021, Article ID 7100727, 6 pages, 2021.

Retraction

Retracted: Influence of Pore Structure Characteristics of Primary Coal on Coalbed Methane Adsorption

Advances in Materials Science and Engineering

Received 26 December 2023; Accepted 26 December 2023; Published 29 December 2023

Copyright © 2023 Advances in Materials Science and Engineering. This is an open access article distributed under the Creative Commons Attribution License, which permits unrestricted use, distribution, and reproduction in any medium, provided the original work is properly cited.

This article has been retracted by Hindawi, as publisher, following an investigation undertaken by the publisher [1]. This investigation has uncovered evidence of systematic manipulation of the publication and peer-review process. We cannot, therefore, vouch for the reliability or integrity of this article.

Please note that this notice is intended solely to alert readers that the peer-review process of this article has been compromised.

Wiley and Hindawi regret that the usual quality checks did not identify these issues before publication and have since put additional measures in place to safeguard research integrity.

We wish to credit our Research Integrity and Research Publishing teams and anonymous and named external researchers and research integrity experts for contributing to this investigation.

The corresponding author, as the representative of all authors, has been given the opportunity to register their agreement or disagreement to this retraction. We have kept a record of any response received.

References

- [1] G. Liu, "Influence of Pore Structure Characteristics of Primary Coal on Coalbed Methane Adsorption," *Advances in Materials Science and Engineering*, vol. 2022, Article ID 3087252, 7 pages, 2022.

Retraction

Retracted: Experimental Study on the Principle of Oxygenation and Oxygenation Performance of Surface Blade Aerator

Advances in Materials Science and Engineering

Received 26 December 2023; Accepted 26 December 2023; Published 29 December 2023

Copyright © 2023 Advances in Materials Science and Engineering. This is an open access article distributed under the Creative Commons Attribution License, which permits unrestricted use, distribution, and reproduction in any medium, provided the original work is properly cited.

This article has been retracted by Hindawi, as publisher, following an investigation undertaken by the publisher [1]. This investigation has uncovered evidence of systematic manipulation of the publication and peer-review process. We cannot, therefore, vouch for the reliability or integrity of this article.

Please note that this notice is intended solely to alert readers that the peer-review process of this article has been compromised.

Wiley and Hindawi regret that the usual quality checks did not identify these issues before publication and have since put additional measures in place to safeguard research integrity.

We wish to credit our Research Integrity and Research Publishing teams and anonymous and named external researchers and research integrity experts for contributing to this investigation.

The corresponding author, as the representative of all authors, has been given the opportunity to register their agreement or disagreement to this retraction. We have kept a record of any response received.

References

- [1] P. Xing, C. Yu, K. Li, and H. Wu, "Experimental Study on the Principle of Oxygenation and Oxygenation Performance of Surface Blade Aerator," *Advances in Materials Science and Engineering*, vol. 2022, Article ID 3518833, 14 pages, 2022.

Retraction

Retracted: Study on Thermal Performance Measurement and Construction of Passive Exterior Wall with Low Energy: Teaching and Laboratory Building of Shandong Jianzhu University

Advances in Materials Science and Engineering

Received 26 December 2023; Accepted 26 December 2023; Published 29 December 2023

Copyright © 2023 Advances in Materials Science and Engineering. This is an open access article distributed under the Creative Commons Attribution License, which permits unrestricted use, distribution, and reproduction in any medium, provided the original work is properly cited.

This article has been retracted by Hindawi, as publisher, following an investigation undertaken by the publisher [1]. This investigation has uncovered evidence of systematic manipulation of the publication and peer-review process. We cannot, therefore, vouch for the reliability or integrity of this article.

Please note that this notice is intended solely to alert readers that the peer-review process of this article has been compromised.

Wiley and Hindawi regret that the usual quality checks did not identify these issues before publication and have since put additional measures in place to safeguard research integrity.

We wish to credit our Research Integrity and Research Publishing teams and anonymous and named external researchers and research integrity experts for contributing to this investigation.

The corresponding author, as the representative of all authors, has been given the opportunity to register their agreement or disagreement to this retraction. We have kept a record of any response received.

References

- [1] Y. Lan and R. Zou, "Study on Thermal Performance Measurement and Construction of Passive Exterior Wall with Low Energy: Teaching and Laboratory Building of Shandong Jianzhu University," *Advances in Materials Science and Engineering*, vol. 2022, Article ID 3253085, 11 pages, 2022.

Retraction

Retracted: Graphene: A Multifunctional Nanomaterial with Versatile Applications

Advances in Materials Science and Engineering

Received 26 December 2023; Accepted 26 December 2023; Published 29 December 2023

Copyright © 2023 Advances in Materials Science and Engineering. This is an open access article distributed under the Creative Commons Attribution License, which permits unrestricted use, distribution, and reproduction in any medium, provided the original work is properly cited.

This article has been retracted by Hindawi, as publisher, following an investigation undertaken by the publisher [1]. This investigation has uncovered evidence of systematic manipulation of the publication and peer-review process. We cannot, therefore, vouch for the reliability or integrity of this article.

Please note that this notice is intended solely to alert readers that the peer-review process of this article has been compromised.

Wiley and Hindawi regret that the usual quality checks did not identify these issues before publication and have since put additional measures in place to safeguard research integrity.

We wish to credit our Research Integrity and Research Publishing teams and anonymous and named external researchers and research integrity experts for contributing to this investigation.

The corresponding author, as the representative of all authors, has been given the opportunity to register their agreement or disagreement to this retraction. We have kept a record of any response received.

References

- [1] H. C. A. Murthy, S. Ghotekar, B. Vinay Kumar, and A. Roy, "Graphene: A Multifunctional Nanomaterial with Versatile Applications," *Advances in Materials Science and Engineering*, vol. 2021, Article ID 2418149, 8 pages, 2021.

Retraction

Retracted: Study of Mechanical Properties on Ferric Oxide Microparticles Reinforced with Polyethylene

Advances in Materials Science and Engineering

Received 26 December 2023; Accepted 26 December 2023; Published 29 December 2023

Copyright © 2023 Advances in Materials Science and Engineering. This is an open access article distributed under the Creative Commons Attribution License, which permits unrestricted use, distribution, and reproduction in any medium, provided the original work is properly cited.

This article has been retracted by Hindawi, as publisher, following an investigation undertaken by the publisher [1]. This investigation has uncovered evidence of systematic manipulation of the publication and peer-review process. We cannot, therefore, vouch for the reliability or integrity of this article.

Please note that this notice is intended solely to alert readers that the peer-review process of this article has been compromised.

Wiley and Hindawi regret that the usual quality checks did not identify these issues before publication and have since put additional measures in place to safeguard research integrity.

We wish to credit our Research Integrity and Research Publishing teams and anonymous and named external researchers and research integrity experts for contributing to this investigation.

The corresponding author, as the representative of all authors, has been given the opportunity to register their agreement or disagreement to this retraction. We have kept a record of any response received.

References

- [1] U. Tamilarasan, S. Dhanasekar, K. Raja Karthikeyan et al., "Study of Mechanical Properties on Ferric Oxide Microparticles Reinforced with Polyethylene," *Advances in Materials Science and Engineering*, vol. 2022, Article ID 3077301, 7 pages, 2022.

Retraction

Retracted: Exhibition of Dielectric Property Based on Soil Class and Moisture Presence for Bengaluru District

Advances in Materials Science and Engineering

Received 26 December 2023; Accepted 26 December 2023; Published 29 December 2023

Copyright © 2023 Advances in Materials Science and Engineering. This is an open access article distributed under the Creative Commons Attribution License, which permits unrestricted use, distribution, and reproduction in any medium, provided the original work is properly cited.

This article has been retracted by Hindawi, as publisher, following an investigation undertaken by the publisher [1]. This investigation has uncovered evidence of systematic manipulation of the publication and peer-review process. We cannot, therefore, vouch for the reliability or integrity of this article.

Please note that this notice is intended solely to alert readers that the peer-review process of this article has been compromised.

Wiley and Hindawi regret that the usual quality checks did not identify these issues before publication and have since put additional measures in place to safeguard research integrity.

We wish to credit our Research Integrity and Research Publishing teams and anonymous and named external researchers and research integrity experts for contributing to this investigation.

The corresponding author, as the representative of all authors, has been given the opportunity to register their agreement or disagreement to this retraction. We have kept a record of any response received.

References

- [1] S. Kumar, N. Ahalya, V. Singh et al., "Exhibition of Dielectric Property Based on Soil Class and Moisture Presence for Bengaluru District," *Advances in Materials Science and Engineering*, vol. 2022, Article ID 6807204, 9 pages, 2022.

Retraction

Retracted: Enhancement Modelling Based on Electrical Discharge Machining Successive Discharges

Advances in Materials Science and Engineering

Received 26 December 2023; Accepted 26 December 2023; Published 29 December 2023

Copyright © 2023 Advances in Materials Science and Engineering. This is an open access article distributed under the Creative Commons Attribution License, which permits unrestricted use, distribution, and reproduction in any medium, provided the original work is properly cited.

This article has been retracted by Hindawi, as publisher, following an investigation undertaken by the publisher [1]. This investigation has uncovered evidence of systematic manipulation of the publication and peer-review process. We cannot, therefore, vouch for the reliability or integrity of this article.

Please note that this notice is intended solely to alert readers that the peer-review process of this article has been compromised.

Wiley and Hindawi regret that the usual quality checks did not identify these issues before publication and have since put additional measures in place to safeguard research integrity.

We wish to credit our Research Integrity and Research Publishing teams and anonymous and named external researchers and research integrity experts for contributing to this investigation.

The corresponding author, as the representative of all authors, has been given the opportunity to register their agreement or disagreement to this retraction. We have kept a record of any response received.

References

- [1] F. N. Abed, V. Ramesh, M. Fadhil Jwaid, N. Agarwal, D. Koundal, and A. Mohamed Ibrahim, "Enhancement Modelling Based on Electrical Discharge Machining Successive Discharges," *Advances in Materials Science and Engineering*, vol. 2022, Article ID 8017375, 7 pages, 2022.

Retraction

Retracted: An Innovative Approach of N -Soft Quotient Topological Space

Advances in Materials Science and Engineering

Received 26 December 2023; Accepted 26 December 2023; Published 29 December 2023

Copyright © 2023 Advances in Materials Science and Engineering. This is an open access article distributed under the Creative Commons Attribution License, which permits unrestricted use, distribution, and reproduction in any medium, provided the original work is properly cited.

This article has been retracted by Hindawi, as publisher, following an investigation undertaken by the publisher [1]. This investigation has uncovered evidence of systematic manipulation of the publication and peer-review process. We cannot, therefore, vouch for the reliability or integrity of this article.

Please note that this notice is intended solely to alert readers that the peer-review process of this article has been compromised.

Wiley and Hindawi regret that the usual quality checks did not identify these issues before publication and have since put additional measures in place to safeguard research integrity.

We wish to credit our Research Integrity and Research Publishing teams and anonymous and named external researchers and research integrity experts for contributing to this investigation.

The corresponding author, as the representative of all authors, has been given the opportunity to register their agreement or disagreement to this retraction. We have kept a record of any response received.

References

- [1] G. K. Antony, M. Lellis Thivagar, B. Tamilarasan, and M. Birhan, "An Innovative Approach of N -Soft Quotient Topological Space," *Advances in Materials Science and Engineering*, vol. 2022, Article ID 4627283, 5 pages, 2022.

Retraction

Retracted: Mechanical Characterization of Biocomposites Reinforced with Untreated and 4% NaOH-Treated Sisal and Jute Fibres

Advances in Materials Science and Engineering

Received 26 December 2023; Accepted 26 December 2023; Published 29 December 2023

Copyright © 2023 Advances in Materials Science and Engineering. This is an open access article distributed under the Creative Commons Attribution License, which permits unrestricted use, distribution, and reproduction in any medium, provided the original work is properly cited.

This article has been retracted by Hindawi, as publisher, following an investigation undertaken by the publisher [1]. This investigation has uncovered evidence of systematic manipulation of the publication and peer-review process. We cannot, therefore, vouch for the reliability or integrity of this article.

Please note that this notice is intended solely to alert readers that the peer-review process of this article has been compromised.

Wiley and Hindawi regret that the usual quality checks did not identify these issues before publication and have since put additional measures in place to safeguard research integrity.

We wish to credit our Research Integrity and Research Publishing teams and anonymous and named external researchers and research integrity experts for contributing to this investigation.

The corresponding author, as the representative of all authors, has been given the opportunity to register their agreement or disagreement to this retraction. We have kept a record of any response received.

References

- [1] D. P. Archana, H. N. Jagannatha Reddy, and B. Paruti, "Mechanical Characterization of Biocomposites Reinforced with Untreated and 4% NaOH-Treated Sisal and Jute Fibres," *Advances in Materials Science and Engineering*, vol. 2022, Article ID 7777904, 11 pages, 2022.

Retraction

Retracted: Modeling and Optimization of MRR in Wire Electrical Discharge Machining of Silicon Particle-Reinforced AA6063 Composite

Advances in Materials Science and Engineering

Received 26 December 2023; Accepted 26 December 2023; Published 29 December 2023

Copyright © 2023 Advances in Materials Science and Engineering. This is an open access article distributed under the Creative Commons Attribution License, which permits unrestricted use, distribution, and reproduction in any medium, provided the original work is properly cited.

This article has been retracted by Hindawi, as publisher, following an investigation undertaken by the publisher [1]. This investigation has uncovered evidence of systematic manipulation of the publication and peer-review process. We cannot, therefore, vouch for the reliability or integrity of this article.

Please note that this notice is intended solely to alert readers that the peer-review process of this article has been compromised.

Wiley and Hindawi regret that the usual quality checks did not identify these issues before publication and have since put additional measures in place to safeguard research integrity.

We wish to credit our Research Integrity and Research Publishing teams and anonymous and named external researchers and research integrity experts for contributing to this investigation.

The corresponding author, as the representative of all authors, has been given the opportunity to register their agreement or disagreement to this retraction. We have kept a record of any response received.

References

- [1] C. Mahesha, R. Suprabha, N. Bhavani et al., "Modeling and Optimization of MRR in Wire Electrical Discharge Machining of Silicon Particle-Reinforced AA6063 Composite," *Advances in Materials Science and Engineering*, vol. 2022, Article ID 2594974, 9 pages, 2022.

Retraction

Retracted: Development of Quality Information Management System for Alumina Ceramic Tube Manufacturing Process

Advances in Materials Science and Engineering

Received 26 December 2023; Accepted 26 December 2023; Published 29 December 2023

Copyright © 2023 Advances in Materials Science and Engineering. This is an open access article distributed under the Creative Commons Attribution License, which permits unrestricted use, distribution, and reproduction in any medium, provided the original work is properly cited.

This article has been retracted by Hindawi, as publisher, following an investigation undertaken by the publisher [1]. This investigation has uncovered evidence of systematic manipulation of the publication and peer-review process. We cannot, therefore, vouch for the reliability or integrity of this article.

Please note that this notice is intended solely to alert readers that the peer-review process of this article has been compromised.

Wiley and Hindawi regret that the usual quality checks did not identify these issues before publication and have since put additional measures in place to safeguard research integrity.

We wish to credit our Research Integrity and Research Publishing teams and anonymous and named external researchers and research integrity experts for contributing to this investigation.

The corresponding author, as the representative of all authors, has been given the opportunity to register their agreement or disagreement to this retraction. We have kept a record of any response received.

References

- [1] Y. Huang, "Development of Quality Information Management System for Alumina Ceramic Tube Manufacturing Process," *Advances in Materials Science and Engineering*, vol. 2022, Article ID 5816221, 13 pages, 2022.

Retraction

Retracted: Investigation of Mechanical and Physical Behaviours of Polyester Resin Matrix from Recycled Polyethylene Terephthalate with Bamboo Fibre

Advances in Materials Science and Engineering

Received 26 December 2023; Accepted 26 December 2023; Published 29 December 2023

Copyright © 2023 Advances in Materials Science and Engineering. This is an open access article distributed under the Creative Commons Attribution License, which permits unrestricted use, distribution, and reproduction in any medium, provided the original work is properly cited.

This article has been retracted by Hindawi, as publisher, following an investigation undertaken by the publisher [1]. This investigation has uncovered evidence of systematic manipulation of the publication and peer-review process. We cannot, therefore, vouch for the reliability or integrity of this article.

Please note that this notice is intended solely to alert readers that the peer-review process of this article has been compromised.

Wiley and Hindawi regret that the usual quality checks did not identify these issues before publication and have since put additional measures in place to safeguard research integrity.

We wish to credit our Research Integrity and Research Publishing teams and anonymous and named external researchers and research integrity experts for contributing to this investigation.

The corresponding author, as the representative of all authors, has been given the opportunity to register their agreement or disagreement to this retraction. We have kept a record of any response received.

References

- [1] N. Kaliappan, V. Govindarajan, T. C. Anil Kumar et al., "Investigation of Mechanical and Physical Behaviours of Polyester Resin Matrix from Recycled Polyethylene Terephthalate with Bamboo Fibre," *Advances in Materials Science and Engineering*, vol. 2022, Article ID 4233302, 8 pages, 2022.

Retraction

Retracted: Implementation of TQM and the Integration of BIM in the Construction Management Sector in Saudi Arabia

Advances in Materials Science and Engineering

Received 26 December 2023; Accepted 26 December 2023; Published 29 December 2023

Copyright © 2023 Advances in Materials Science and Engineering. This is an open access article distributed under the Creative Commons Attribution License, which permits unrestricted use, distribution, and reproduction in any medium, provided the original work is properly cited.

This article has been retracted by Hindawi, as publisher, following an investigation undertaken by the publisher [1]. This investigation has uncovered evidence of systematic manipulation of the publication and peer-review process. We cannot, therefore, vouch for the reliability or integrity of this article.

Please note that this notice is intended solely to alert readers that the peer-review process of this article has been compromised.

Wiley and Hindawi regret that the usual quality checks did not identify these issues before publication and have since put additional measures in place to safeguard research integrity.

We wish to credit our Research Integrity and Research Publishing teams and anonymous and named external researchers and research integrity experts for contributing to this investigation.

The corresponding author, as the representative of all authors, has been given the opportunity to register their agreement or disagreement to this retraction. We have kept a record of any response received.

References

- [1] M. Abazid, H. Gökçekuş, and T. Çelik, "Implementation of TQM and the Integration of BIM in the Construction Management Sector in Saudi Arabia," *Advances in Materials Science and Engineering*, vol. 2021, Article ID 1232620, 9 pages, 2021.

Retraction

Retracted: Modeling and Analysis of Automotive Engine Crankshaft Made of Composite and Functionally Graded Materials

Advances in Materials Science and Engineering

Received 26 December 2023; Accepted 26 December 2023; Published 29 December 2023

Copyright © 2023 Advances in Materials Science and Engineering. This is an open access article distributed under the Creative Commons Attribution License, which permits unrestricted use, distribution, and reproduction in any medium, provided the original work is properly cited.

This article has been retracted by Hindawi, as publisher, following an investigation undertaken by the publisher [1]. This investigation has uncovered evidence of systematic manipulation of the publication and peer-review process. We cannot, therefore, vouch for the reliability or integrity of this article.

Please note that this notice is intended solely to alert readers that the peer-review process of this article has been compromised.

Wiley and Hindawi regret that the usual quality checks did not identify these issues before publication and have since put additional measures in place to safeguard research integrity.

We wish to credit our Research Integrity and Research Publishing teams and anonymous and named external researchers and research integrity experts for contributing to this investigation.

The corresponding author, as the representative of all authors, has been given the opportunity to register their agreement or disagreement to this retraction. We have kept a record of any response received.

References

- [1] S. Asiri, "Modeling and Analysis of Automotive Engine Crankshaft Made of Composite and Functionally Graded Materials," *Advances in Materials Science and Engineering*, vol. 2022, Article ID 4005368, 15 pages, 2022.

Retraction

Retracted: Optimization of Process Parameters for Friction Stir Welding of Different Aluminum Alloys AA2618 to AA5086 by Taguchi Method

Advances in Materials Science and Engineering

Received 26 December 2023; Accepted 26 December 2023; Published 29 December 2023

Copyright © 2023 Advances in Materials Science and Engineering. This is an open access article distributed under the Creative Commons Attribution License, which permits unrestricted use, distribution, and reproduction in any medium, provided the original work is properly cited.

This article has been retracted by Hindawi, as publisher, following an investigation undertaken by the publisher [1]. This investigation has uncovered evidence of systematic manipulation of the publication and peer-review process. We cannot, therefore, vouch for the reliability or integrity of this article.

Please note that this notice is intended solely to alert readers that the peer-review process of this article has been compromised.

Wiley and Hindawi regret that the usual quality checks did not identify these issues before publication and have since put additional measures in place to safeguard research integrity.

We wish to credit our Research Integrity and Research Publishing teams and anonymous and named external researchers and research integrity experts for contributing to this investigation.

The corresponding author, as the representative of all authors, has been given the opportunity to register their agreement or disagreement to this retraction. We have kept a record of any response received.

References

- [1] G. Sasikala, V. M. Jothiprakash, B. Pant et al., "Optimization of Process Parameters for Friction Stir Welding of Different Aluminum Alloys AA2618 to AA5086 by Taguchi Method," *Advances in Materials Science and Engineering*, vol. 2022, Article ID 3808605, 9 pages, 2022.

Retraction

Retracted: The Impact of Family Sustainable Livelihood and Environmental Cognition on Herdsmen's Choice of Production Behavior

Advances in Materials Science and Engineering

Received 26 December 2023; Accepted 26 December 2023; Published 29 December 2023

Copyright © 2023 Advances in Materials Science and Engineering. This is an open access article distributed under the Creative Commons Attribution License, which permits unrestricted use, distribution, and reproduction in any medium, provided the original work is properly cited.

This article has been retracted by Hindawi, as publisher, following an investigation undertaken by the publisher [1]. This investigation has uncovered evidence of systematic manipulation of the publication and peer-review process. We cannot, therefore, vouch for the reliability or integrity of this article.

Please note that this notice is intended solely to alert readers that the peer-review process of this article has been compromised.

Wiley and Hindawi regret that the usual quality checks did not identify these issues before publication and have since put additional measures in place to safeguard research integrity.

We wish to credit our Research Integrity and Research Publishing teams and anonymous and named external researchers and research integrity experts for contributing to this investigation.

The corresponding author, as the representative of all authors, has been given the opportunity to register their agreement or disagreement to this retraction. We have kept a record of any response received.

References

- [1] Q. Wang and Y. Miao, "The Impact of Family Sustainable Livelihood and Environmental Cognition on Herdsmen's Choice of Production Behavior," *Advances in Materials Science and Engineering*, vol. 2022, Article ID 4278331, 9 pages, 2022.

Retraction

Retracted: Investigation on Tensile Behaviour of Different Weld Joints through Taguchi Approach

Advances in Materials Science and Engineering

Received 26 December 2023; Accepted 26 December 2023; Published 29 December 2023

Copyright © 2023 Advances in Materials Science and Engineering. This is an open access article distributed under the Creative Commons Attribution License, which permits unrestricted use, distribution, and reproduction in any medium, provided the original work is properly cited.

This article has been retracted by Hindawi, as publisher, following an investigation undertaken by the publisher [1]. This investigation has uncovered evidence of systematic manipulation of the publication and peer-review process. We cannot, therefore, vouch for the reliability or integrity of this article.

Please note that this notice is intended solely to alert readers that the peer-review process of this article has been compromised.

Wiley and Hindawi regret that the usual quality checks did not identify these issues before publication and have since put additional measures in place to safeguard research integrity.

We wish to credit our Research Integrity and Research Publishing teams and anonymous and named external researchers and research integrity experts for contributing to this investigation.

The corresponding author, as the representative of all authors, has been given the opportunity to register their agreement or disagreement to this retraction. We have kept a record of any response received.

References

- [1] S. Kamal, V. Parthiban, G. Puthilibai et al., "Investigation on Tensile Behaviour of Different Weld Joints through Taguchi Approach," *Advances in Materials Science and Engineering*, vol. 2022, Article ID 5258014, 9 pages, 2022.

Retraction

Retracted: Thermal Analysis of the Solar Dish Array Concentrator System

Advances in Materials Science and Engineering

Received 26 December 2023; Accepted 26 December 2023; Published 29 December 2023

Copyright © 2023 Advances in Materials Science and Engineering. This is an open access article distributed under the Creative Commons Attribution License, which permits unrestricted use, distribution, and reproduction in any medium, provided the original work is properly cited.

This article has been retracted by Hindawi, as publisher, following an investigation undertaken by the publisher [1]. This investigation has uncovered evidence of systematic manipulation of the publication and peer-review process. We cannot, therefore, vouch for the reliability or integrity of this article.

Please note that this notice is intended solely to alert readers that the peer-review process of this article has been compromised.

Wiley and Hindawi regret that the usual quality checks did not identify these issues before publication and have since put additional measures in place to safeguard research integrity.

We wish to credit our Research Integrity and Research Publishing teams and anonymous and named external researchers and research integrity experts for contributing to this investigation.

The corresponding author, as the representative of all authors, has been given the opportunity to register their agreement or disagreement to this retraction. We have kept a record of any response received.

References

- [1] Y. H. Mahmood, R. Y. J. Al-Salih, S. Amer Mahdi, and A. Mohamed Ibrahim, "Thermal Analysis of the Solar Dish Array Concentrator System," *Advances in Materials Science and Engineering*, vol. 2022, Article ID 1823630, 8 pages, 2022.

Retraction

Retracted: Effect of Using Modern Banking Services on Customer Inspiration: Statistical Analysis

Advances in Materials Science and Engineering

Received 26 December 2023; Accepted 26 December 2023; Published 29 December 2023

Copyright © 2023 Advances in Materials Science and Engineering. This is an open access article distributed under the Creative Commons Attribution License, which permits unrestricted use, distribution, and reproduction in any medium, provided the original work is properly cited.

This article has been retracted by Hindawi, as publisher, following an investigation undertaken by the publisher [1]. This investigation has uncovered evidence of systematic manipulation of the publication and peer-review process. We cannot, therefore, vouch for the reliability or integrity of this article.

Please note that this notice is intended solely to alert readers that the peer-review process of this article has been compromised.

Wiley and Hindawi regret that the usual quality checks did not identify these issues before publication and have since put additional measures in place to safeguard research integrity.

We wish to credit our Research Integrity and Research Publishing teams and anonymous and named external researchers and research integrity experts for contributing to this investigation.

The corresponding author, as the representative of all authors, has been given the opportunity to register their agreement or disagreement to this retraction. We have kept a record of any response received.

References

- [1] M. I. Jassem, R. A. Rahman, and A. M. Ibrahim, "Effect of Using Modern Banking Services on Customer Inspiration: Statistical Analysis," *Advances in Materials Science and Engineering*, vol. 2022, Article ID 7130559, 6 pages, 2022.

Retraction

Retracted: Anti-Quorum Sensing in Pathogenic Microbes Using Plant-Based Bioactive Phytochemicals

Advances in Materials Science and Engineering

Received 26 December 2023; Accepted 26 December 2023; Published 29 December 2023

Copyright © 2023 Advances in Materials Science and Engineering. This is an open access article distributed under the Creative Commons Attribution License, which permits unrestricted use, distribution, and reproduction in any medium, provided the original work is properly cited.

This article has been retracted by Hindawi, as publisher, following an investigation undertaken by the publisher [1]. This investigation has uncovered evidence of systematic manipulation of the publication and peer-review process. We cannot, therefore, vouch for the reliability or integrity of this article.

Please note that this notice is intended solely to alert readers that the peer-review process of this article has been compromised.

Wiley and Hindawi regret that the usual quality checks did not identify these issues before publication and have since put additional measures in place to safeguard research integrity.

We wish to credit our Research Integrity and Research Publishing teams and anonymous and named external researchers and research integrity experts for contributing to this investigation.

The corresponding author, as the representative of all authors, has been given the opportunity to register their agreement or disagreement to this retraction. We have kept a record of any response received.

References

- [1] K. Subramanian, H. Selvaraj, B. K. P. Sampath Renuga, V. S. and W. Aruni, "Anti-Quorum Sensing in Pathogenic Microbes Using Plant-Based Bioactive Phytochemicals," *Advances in Materials Science and Engineering*, vol. 2022, Article ID 7532086, 7 pages, 2022.

Retraction

Retracted: Improved Chicken Reproduction and Yield of Improved Poultry from Titanium Dioxide (TiO₂) Nanoparticles Coated in Jimma Horro Area of Kellem Wollega Zone, Ethiopia

Advances in Materials Science and Engineering

Received 26 December 2023; Accepted 26 December 2023; Published 29 December 2023

Copyright © 2023 Advances in Materials Science and Engineering. This is an open access article distributed under the Creative Commons Attribution License, which permits unrestricted use, distribution, and reproduction in any medium, provided the original work is properly cited.

This article has been retracted by Hindawi, as publisher, following an investigation undertaken by the publisher [1]. This investigation has uncovered evidence of systematic manipulation of the publication and peer-review process. We cannot, therefore, vouch for the reliability or integrity of this article.

Please note that this notice is intended solely to alert readers that the peer-review process of this article has been compromised.

Wiley and Hindawi regret that the usual quality checks did not identify these issues before publication and have since put additional measures in place to safeguard research integrity.

We wish to credit our Research Integrity and Research Publishing teams and anonymous and named external researchers and research integrity experts for contributing to this investigation.

The corresponding author, as the representative of all authors, has been given the opportunity to register their agreement or disagreement to this retraction. We have kept a record of any response received.

References

- [1] S. Shuma Abdisa, J. Leta Tesfaye, A. Saka et al., “Improved Chicken Reproduction and Yield of Improved Poultry from Titanium Dioxide (TiO₂) Nanoparticles Coated in Jimma Horro Area of Kellem Wollega Zone, Ethiopia,” *Advances in Materials Science and Engineering*, vol. 2022, Article ID 1984178, 7 pages, 2022.

Retraction

Retracted: Optimization and Mechanical Properties of TiO₂ Reinforced AA 7150 Composites Using Response Surface Methodology

Advances in Materials Science and Engineering

Received 26 December 2023; Accepted 26 December 2023; Published 29 December 2023

Copyright © 2023 Advances in Materials Science and Engineering. This is an open access article distributed under the Creative Commons Attribution License, which permits unrestricted use, distribution, and reproduction in any medium, provided the original work is properly cited.

This article has been retracted by Hindawi, as publisher, following an investigation undertaken by the publisher [1]. This investigation has uncovered evidence of systematic manipulation of the publication and peer-review process. We cannot, therefore, vouch for the reliability or integrity of this article.

Please note that this notice is intended solely to alert readers that the peer-review process of this article has been compromised.

Wiley and Hindawi regret that the usual quality checks did not identify these issues before publication and have since put additional measures in place to safeguard research integrity.

We wish to credit our Research Integrity and Research Publishing teams and anonymous and named external researchers and research integrity experts for contributing to this investigation.

The corresponding author, as the representative of all authors, has been given the opportunity to register their agreement or disagreement to this retraction. We have kept a record of any response received.

References

- [1] S. V. G. V. A. Prasad, V. Kamalakar, J. Madhusudhanan et al., "Optimization and Mechanical Properties of TiO₂ Reinforced AA 7150 Composites Using Response Surface Methodology," *Advances in Materials Science and Engineering*, vol. 2022, Article ID 5779840, 12 pages, 2022.

Retraction

Retracted: Deformation Analysis of Surrounding Rock of Deep Roadway by the Fluid Structure Coupling Model with MIDAS-GTS

Advances in Materials Science and Engineering

Received 26 December 2023; Accepted 26 December 2023; Published 29 December 2023

Copyright © 2023 Advances in Materials Science and Engineering. This is an open access article distributed under the Creative Commons Attribution License, which permits unrestricted use, distribution, and reproduction in any medium, provided the original work is properly cited.

This article has been retracted by Hindawi, as publisher, following an investigation undertaken by the publisher [1]. This investigation has uncovered evidence of systematic manipulation of the publication and peer-review process. We cannot, therefore, vouch for the reliability or integrity of this article.

Please note that this notice is intended solely to alert readers that the peer-review process of this article has been compromised.

Wiley and Hindawi regret that the usual quality checks did not identify these issues before publication and have since put additional measures in place to safeguard research integrity.

We wish to credit our Research Integrity and Research Publishing teams and anonymous and named external researchers and research integrity experts for contributing to this investigation.

The corresponding author, as the representative of all authors, has been given the opportunity to register their agreement or disagreement to this retraction. We have kept a record of any response received.

References

- [1] J. Jiang, Z. Hou, K. Hou, Y. Lu, H. Sun, and X. Niu, "Deformation Analysis of Surrounding Rock of Deep Roadway by the Fluid Structure Coupling Model with MIDAS-GTS," *Advances in Materials Science and Engineering*, vol. 2022, Article ID 9945383, 6 pages, 2022.

Retraction

Retracted: Characterization and Parametric Optimization of EN-10149-2 Steel Welded Joints Made by MIG Welding

Advances in Materials Science and Engineering

Received 26 December 2023; Accepted 26 December 2023; Published 29 December 2023

Copyright © 2023 Advances in Materials Science and Engineering. This is an open access article distributed under the Creative Commons Attribution License, which permits unrestricted use, distribution, and reproduction in any medium, provided the original work is properly cited.

This article has been retracted by Hindawi, as publisher, following an investigation undertaken by the publisher [1]. This investigation has uncovered evidence of systematic manipulation of the publication and peer-review process. We cannot, therefore, vouch for the reliability or integrity of this article.

Please note that this notice is intended solely to alert readers that the peer-review process of this article has been compromised.

Wiley and Hindawi regret that the usual quality checks did not identify these issues before publication and have since put additional measures in place to safeguard research integrity.

We wish to credit our Research Integrity and Research Publishing teams and anonymous and named external researchers and research integrity experts for contributing to this investigation.

The corresponding author, as the representative of all authors, has been given the opportunity to register their agreement or disagreement to this retraction. We have kept a record of any response received.

References

- [1] K. B. Behredin, P. Janaki Ramulu, B. Habtamu, N. Besufekad, and N. Tesfaye, "Characterization and Parametric Optimization of EN-10149-2 Steel Welded Joints Made by MIG Welding," *Advances in Materials Science and Engineering*, vol. 2022, Article ID 8276496, 16 pages, 2022.

Retraction

Retracted: Thermal Conductivity of Thermally Insulated Concretes in a Nuclear Safety Vessel of Reactor Vault: Experimental Interpretation

Advances in Materials Science and Engineering

Received 26 December 2023; Accepted 26 December 2023; Published 29 December 2023

Copyright © 2023 Advances in Materials Science and Engineering. This is an open access article distributed under the Creative Commons Attribution License, which permits unrestricted use, distribution, and reproduction in any medium, provided the original work is properly cited.

This article has been retracted by Hindawi, as publisher, following an investigation undertaken by the publisher [1]. This investigation has uncovered evidence of systematic manipulation of the publication and peer-review process. We cannot, therefore, vouch for the reliability or integrity of this article.

Please note that this notice is intended solely to alert readers that the peer-review process of this article has been compromised.

Wiley and Hindawi regret that the usual quality checks did not identify these issues before publication and have since put additional measures in place to safeguard research integrity.

We wish to credit our Research Integrity and Research Publishing teams and anonymous and named external researchers and research integrity experts for contributing to this investigation.

The corresponding author, as the representative of all authors, has been given the opportunity to register their agreement or disagreement to this retraction. We have kept a record of any response received.

References

- [1] M. Anish, T. Arunkumar, J. Jayaprabakar et al., "Thermal Conductivity of Thermally Insulated Concretes in a Nuclear Safety Vessel of Reactor Vault: Experimental Interpretation," *Advances in Materials Science and Engineering*, vol. 2022, Article ID 4493910, 12 pages, 2022.

Retraction

Retracted: HS-GC-IMS and ATR-FT-MIR Analysis Reveal the Differences in Volatile Compounds, Proteins, and Polyphenols of Royal Jelly

Advances in Materials Science and Engineering

Received 26 December 2023; Accepted 26 December 2023; Published 29 December 2023

Copyright © 2023 Advances in Materials Science and Engineering. This is an open access article distributed under the Creative Commons Attribution License, which permits unrestricted use, distribution, and reproduction in any medium, provided the original work is properly cited.

This article has been retracted by Hindawi, as publisher, following an investigation undertaken by the publisher [1]. This investigation has uncovered evidence of systematic manipulation of the publication and peer-review process. We cannot, therefore, vouch for the reliability or integrity of this article.

Please note that this notice is intended solely to alert readers that the peer-review process of this article has been compromised.

Wiley and Hindawi regret that the usual quality checks did not identify these issues before publication and have since put additional measures in place to safeguard research integrity.

We wish to credit our Research Integrity and Research Publishing teams and anonymous and named external researchers and research integrity experts for contributing to this investigation.

The corresponding author, as the representative of all authors, has been given the opportunity to register their agreement or disagreement to this retraction. We have kept a record of any response received.

References

- [1] D. Chen, W. Lu, Q. Ye, C. Zhang, X. Ge, and C. Xiao, "HS-GC-IMS and ATR-FT-MIR Analysis Reveal the Differences in Volatile Compounds, Proteins, and Polyphenols of Royal Jelly," *Advances in Materials Science and Engineering*, vol. 2022, Article ID 3223558, 8 pages, 2022.

Retraction

Retracted: Antidandruff Activity of Polyherbal (*Murraya koenigii*, *Moringa oleifera*, and *Psidium guajava*) Extract against *Malassezia* Species: In Silico Studies

Advances in Materials Science and Engineering

Received 26 December 2023; Accepted 26 December 2023; Published 29 December 2023

Copyright © 2023 Advances in Materials Science and Engineering. This is an open access article distributed under the Creative Commons Attribution License, which permits unrestricted use, distribution, and reproduction in any medium, provided the original work is properly cited.

This article has been retracted by Hindawi, as publisher, following an investigation undertaken by the publisher [1]. This investigation has uncovered evidence of systematic manipulation of the publication and peer-review process. We cannot, therefore, vouch for the reliability or integrity of this article.

Please note that this notice is intended solely to alert readers that the peer-review process of this article has been compromised.

Wiley and Hindawi regret that the usual quality checks did not identify these issues before publication and have since put additional measures in place to safeguard research integrity.

We wish to credit our Research Integrity and Research Publishing teams and anonymous and named external researchers and research integrity experts for contributing to this investigation.

The corresponding author, as the representative of all authors, has been given the opportunity to register their agreement or disagreement to this retraction. We have kept a record of any response received.

References

- [1] A. Sharma, P. Sakthiselvan, V. Karthick et al., “Antidandruff Activity of Polyherbal (*Murraya koenigii*, *Moringa oleifera*, and *Psidium guajava*) Extract against *Malassezia* Species: In Silico Studies,” *Advances in Materials Science and Engineering*, vol. 2022, Article ID 7373942, 13 pages, 2022.

Retraction

Retracted: Ternary Complexation Process for New Spectrophotometric Assay of Levodopa using Ni(II) and 2,3-Diaminopyridine

Advances in Materials Science and Engineering

Received 26 December 2023; Accepted 26 December 2023; Published 29 December 2023

Copyright © 2023 Advances in Materials Science and Engineering. This is an open access article distributed under the Creative Commons Attribution License, which permits unrestricted use, distribution, and reproduction in any medium, provided the original work is properly cited.

This article has been retracted by Hindawi, as publisher, following an investigation undertaken by the publisher [1]. This investigation has uncovered evidence of systematic manipulation of the publication and peer-review process. We cannot, therefore, vouch for the reliability or integrity of this article.

Please note that this notice is intended solely to alert readers that the peer-review process of this article has been compromised.

Wiley and Hindawi regret that the usual quality checks did not identify these issues before publication and have since put additional measures in place to safeguard research integrity.

We wish to credit our Research Integrity and Research Publishing teams and anonymous and named external researchers and research integrity experts for contributing to this investigation.

The corresponding author, as the representative of all authors, has been given the opportunity to register their agreement or disagreement to this retraction. We have kept a record of any response received.

References

- [1] F. Abdoon, M. J. Bichan, A. Mohamed Ibrahim, A. Mundher Tayyeh, M. Kishore, and A. Abdelhakeem Khalid, "Ternary Complexation Process for New Spectrophotometric Assay of Levodopa using Ni(II) and 2,3-Diaminopyridine," *Advances in Materials Science and Engineering*, vol. 2022, Article ID 4915162, 8 pages, 2022.

Retraction

Retracted: Impact of BN and WC Particulate Reinforcements on Mechanical Properties and Damage Development of Al-2048 Metal Matrix Composites

Advances in Materials Science and Engineering

Received 26 December 2023; Accepted 26 December 2023; Published 29 December 2023

Copyright © 2023 Advances in Materials Science and Engineering. This is an open access article distributed under the Creative Commons Attribution License, which permits unrestricted use, distribution, and reproduction in any medium, provided the original work is properly cited.

This article has been retracted by Hindawi, as publisher, following an investigation undertaken by the publisher [1]. This investigation has uncovered evidence of systematic manipulation of the publication and peer-review process. We cannot, therefore, vouch for the reliability or integrity of this article.

Please note that this notice is intended solely to alert readers that the peer-review process of this article has been compromised.

Wiley and Hindawi regret that the usual quality checks did not identify these issues before publication and have since put additional measures in place to safeguard research integrity.

We wish to credit our Research Integrity and Research Publishing teams and anonymous and named external researchers and research integrity experts for contributing to this investigation.

The corresponding author, as the representative of all authors, has been given the opportunity to register their agreement or disagreement to this retraction. We have kept a record of any response received.

References

- [1] T. Sivakumar, C. Udagani, M. Sivaranjani et al., "Impact of BN and WC Particulate Reinforcements on Mechanical Properties and Damage Development of Al-2048 Metal Matrix Composites," *Advances in Materials Science and Engineering*, vol. 2022, Article ID 2286713, 9 pages, 2022.

Retraction

Retracted: Energy Efficient Utilization toward Rural Biomass Waste by Straw Biogas Engineering

Advances in Materials Science and Engineering

Received 26 December 2023; Accepted 26 December 2023; Published 29 December 2023

Copyright © 2023 Advances in Materials Science and Engineering. This is an open access article distributed under the Creative Commons Attribution License, which permits unrestricted use, distribution, and reproduction in any medium, provided the original work is properly cited.

This article has been retracted by Hindawi, as publisher, following an investigation undertaken by the publisher [1]. This investigation has uncovered evidence of systematic manipulation of the publication and peer-review process. We cannot, therefore, vouch for the reliability or integrity of this article.

Please note that this notice is intended solely to alert readers that the peer-review process of this article has been compromised.

Wiley and Hindawi regret that the usual quality checks did not identify these issues before publication and have since put additional measures in place to safeguard research integrity.

We wish to credit our Research Integrity and Research Publishing teams and anonymous and named external researchers and research integrity experts for contributing to this investigation.

The corresponding author, as the representative of all authors, has been given the opportunity to register their agreement or disagreement to this retraction. We have kept a record of any response received.

References

- [1] X. Wang and D. Zhao, "Energy Efficient Utilization toward Rural Biomass Waste by Straw Biogas Engineering," *Advances in Materials Science and Engineering*, vol. 2022, Article ID 3338515, 6 pages, 2022.

Retraction

Retracted: Analysis of Pomegranate Dye Coated Titanium Nanotubes Anode for Solar Cell Application

Advances in Materials Science and Engineering

Received 26 December 2023; Accepted 26 December 2023; Published 29 December 2023

Copyright © 2023 Advances in Materials Science and Engineering. This is an open access article distributed under the Creative Commons Attribution License, which permits unrestricted use, distribution, and reproduction in any medium, provided the original work is properly cited.

This article has been retracted by Hindawi, as publisher, following an investigation undertaken by the publisher [1]. This investigation has uncovered evidence of systematic manipulation of the publication and peer-review process. We cannot, therefore, vouch for the reliability or integrity of this article.

Please note that this notice is intended solely to alert readers that the peer-review process of this article has been compromised.

Wiley and Hindawi regret that the usual quality checks did not identify these issues before publication and have since put additional measures in place to safeguard research integrity.

We wish to credit our Research Integrity and Research Publishing teams and anonymous and named external researchers and research integrity experts for contributing to this investigation.

The corresponding author, as the representative of all authors, has been given the opportunity to register their agreement or disagreement to this retraction. We have kept a record of any response received.

References

- [1] P. Thenmozhi, P. Sathya, S. Meyvel, and S. Thanappan, "Analysis of Pomegranate Dye Coated Titanium Nanotubes Anode for Solar Cell Application," *Advances in Materials Science and Engineering*, vol. 2022, Article ID 3278255, 7 pages, 2022.

Retraction

Retracted: Study on the Relationship between Conspicuous Need and Group Cultural Identity of Fashion Cultural Consumption

Advances in Materials Science and Engineering

Received 26 December 2023; Accepted 26 December 2023; Published 29 December 2023

Copyright © 2023 Advances in Materials Science and Engineering. This is an open access article distributed under the Creative Commons Attribution License, which permits unrestricted use, distribution, and reproduction in any medium, provided the original work is properly cited.

This article has been retracted by Hindawi, as publisher, following an investigation undertaken by the publisher [1]. This investigation has uncovered evidence of systematic manipulation of the publication and peer-review process. We cannot, therefore, vouch for the reliability or integrity of this article.

Please note that this notice is intended solely to alert readers that the peer-review process of this article has been compromised.

Wiley and Hindawi regret that the usual quality checks did not identify these issues before publication and have since put additional measures in place to safeguard research integrity.

We wish to credit our Research Integrity and Research Publishing teams and anonymous and named external researchers and research integrity experts for contributing to this investigation.

The corresponding author, as the representative of all authors, has been given the opportunity to register their agreement or disagreement to this retraction. We have kept a record of any response received.

References

- [1] L. Zhao, Y. Duan, Q. Wang et al., "Study on the Relationship between Conspicuous Need and Group Cultural Identity of Fashion Cultural Consumption," *Advances in Materials Science and Engineering*, vol. 2022, Article ID 3541548, 9 pages, 2022.

Retraction

Retracted: Application of Regression Analysis to Identify the Soil and Other Factors Affecting the Wheat Yield

Advances in Materials Science and Engineering

Received 26 December 2023; Accepted 26 December 2023; Published 29 December 2023

Copyright © 2023 Advances in Materials Science and Engineering. This is an open access article distributed under the Creative Commons Attribution License, which permits unrestricted use, distribution, and reproduction in any medium, provided the original work is properly cited.

This article has been retracted by Hindawi, as publisher, following an investigation undertaken by the publisher [1]. This investigation has uncovered evidence of systematic manipulation of the publication and peer-review process. We cannot, therefore, vouch for the reliability or integrity of this article.

Please note that this notice is intended solely to alert readers that the peer-review process of this article has been compromised.

Wiley and Hindawi regret that the usual quality checks did not identify these issues before publication and have since put additional measures in place to safeguard research integrity.

We wish to credit our Research Integrity and Research Publishing teams and anonymous and named external researchers and research integrity experts for contributing to this investigation.

The corresponding author, as the representative of all authors, has been given the opportunity to register their agreement or disagreement to this retraction. We have kept a record of any response received.

References

- [1] A. Hayat, M. Amin, S. Afzal, A. H. Muse, O. M. Egeh, and H. S. Hayat, "Application of Regression Analysis to Identify the Soil and Other Factors Affecting the Wheat Yield," *Advances in Materials Science and Engineering*, vol. 2022, Article ID 7793187, 10 pages, 2022.

Retraction

Retracted: Mechanics of Materials Natural Fibers Technology on Thermal Properties of Polymer

Advances in Materials Science and Engineering

Received 31 October 2023; Accepted 31 October 2023; Published 1 November 2023

Copyright © 2023 Advances in Materials Science and Engineering. This is an open access article distributed under the Creative Commons Attribution License, which permits unrestricted use, distribution, and reproduction in any medium, provided the original work is properly cited.

This article has been retracted by Hindawi following an investigation undertaken by the publisher [1]. This investigation has uncovered evidence of one or more of the following indicators of systematic manipulation of the publication process:

- (1) Discrepancies in scope
- (2) Discrepancies in the description of the research reported
- (3) Discrepancies between the availability of data and the research described
- (4) Inappropriate citations
- (5) Incoherent, meaningless and/or irrelevant content included in the article
- (6) Peer-review manipulation

The presence of these indicators undermines our confidence in the integrity of the article's content and we cannot, therefore, vouch for its reliability. Please note that this notice is intended solely to alert readers that the content of this article is unreliable. We have not investigated whether authors were aware of or involved in the systematic manipulation of the publication process.

Wiley and Hindawi regrets that the usual quality checks did not identify these issues before publication and have since put additional measures in place to safeguard research integrity.

We wish to credit our own Research Integrity and Research Publishing teams and anonymous and named external researchers and research integrity experts for contributing to this investigation.

The corresponding author, as the representative of all authors, has been given the opportunity to register their agreement or disagreement to this retraction. We have kept a record of any response received.

References

- [1] M. B. Alazzam, F. Hajje, A. S. AlGhamdi, S. Ayouni, and M. A. Rahman, "Mechanics of Materials Natural Fibers Technology on Thermal Properties of Polymer," *Advances in Materials Science and Engineering*, vol. 2022, Article ID 7774180, 5 pages, 2022.

Retraction

Retracted: Using Convolutional Neural Networks for Segmentation of Multiple Sclerosis Lesions in 3D Magnetic Resonance Imaging

Advances in Materials Science and Engineering

Received 31 October 2023; Accepted 31 October 2023; Published 1 November 2023

Copyright © 2023 Advances in Materials Science and Engineering. This is an open access article distributed under the Creative Commons Attribution License, which permits unrestricted use, distribution, and reproduction in any medium, provided the original work is properly cited.

This article has been retracted by Hindawi following an investigation undertaken by the publisher [1]. This investigation has uncovered evidence of one or more of the following indicators of systematic manipulation of the publication process:

- (1) Discrepancies in scope
- (2) Discrepancies in the description of the research reported
- (3) Discrepancies between the availability of data and the research described
- (4) Inappropriate citations
- (5) Incoherent, meaningless and/or irrelevant content included in the article
- (6) Peer-review manipulation

The presence of these indicators undermines our confidence in the integrity of the article's content and we cannot, therefore, vouch for its reliability. Please note that this notice is intended solely to alert readers that the content of this article is unreliable. We have not investigated whether authors were aware of or involved in the systematic manipulation of the publication process.

Wiley and Hindawi regrets that the usual quality checks did not identify these issues before publication and have since put additional measures in place to safeguard research integrity.

We wish to credit our own Research Integrity and Research Publishing teams and anonymous and named external researchers and research integrity experts for contributing to this investigation.

The corresponding author, as the representative of all authors, has been given the opportunity to register their agreement or disagreement to this retraction. We have kept a record of any response received.

References

- [1] A. Abdullah Hamad, M. Musa Jaber, M. Altaf Ahmed, G. Muttashar Abdulsahib, O. Ibrahim Khalaf, and Z. Meraf, "Using Convolutional Neural Networks for Segmentation of Multiple Sclerosis Lesions in 3D Magnetic Resonance Imaging," *Advances in Materials Science and Engineering*, vol. 2022, Article ID 4905115, 10 pages, 2022.

Retraction

Retracted: Dynamic Systems Enhanced by Electronic Circuits on 7D

Advances in Materials Science and Engineering

Received 31 October 2023; Accepted 31 October 2023; Published 1 November 2023

Copyright © 2023 Advances in Materials Science and Engineering. This is an open access article distributed under the Creative Commons Attribution License, which permits unrestricted use, distribution, and reproduction in any medium, provided the original work is properly cited.

This article has been retracted by Hindawi following an investigation undertaken by the publisher [1]. This investigation has uncovered evidence of one or more of the following indicators of systematic manipulation of the publication process:

- (1) Discrepancies in scope
- (2) Discrepancies in the description of the research reported
- (3) Discrepancies between the availability of data and the research described
- (4) Inappropriate citations
- (5) Incoherent, meaningless and/or irrelevant content included in the article
- (6) Peer-review manipulation

The presence of these indicators undermines our confidence in the integrity of the article's content and we cannot, therefore, vouch for its reliability. Please note that this notice is intended solely to alert readers that the content of this article is unreliable. We have not investigated whether authors were aware of or involved in the systematic manipulation of the publication process.

Wiley and Hindawi regrets that the usual quality checks did not identify these issues before publication and have since put additional measures in place to safeguard research integrity.

We wish to credit our own Research Integrity and Research Publishing teams and anonymous and named external researchers and research integrity experts for contributing to this investigation.

The corresponding author, as the representative of all authors, has been given the opportunity to register their agreement or disagreement to this retraction. We have kept a record of any response received.

References

- [1] A. Abdullah Hamad, M. Lellis Thivagar, M. Bader Alazzam et al., "Dynamic Systems Enhanced by Electronic Circuits on 7D," *Advances in Materials Science and Engineering*, vol. 2021, Article ID 8148772, 11 pages, 2021.

Retraction

Retracted: Optimization of the Spark Plasma Sintering Process for High-Volume Fraction Tungsten Carbide/Al 2025 Composites

Advances in Materials Science and Engineering

Received 20 June 2023; Accepted 20 June 2023; Published 21 June 2023

Copyright © 2023 Advances in Materials Science and Engineering. This is an open access article distributed under the Creative Commons Attribution License, which permits unrestricted use, distribution, and reproduction in any medium, provided the original work is properly cited.

This article has been retracted by Hindawi following an investigation undertaken by the publisher [1]. This investigation has uncovered evidence of one or more of the following indicators of systematic manipulation of the publication process:

- (1) Discrepancies in scope
- (2) Discrepancies in the description of the research reported
- (3) Discrepancies between the availability of data and the research described
- (4) Inappropriate citations
- (5) Incoherent, meaningless and/or irrelevant content included in the article
- (6) Peer-review manipulation

The presence of these indicators undermines our confidence in the integrity of the article's content and we cannot, therefore, vouch for its reliability. Please note that this notice is intended solely to alert readers that the content of this article is unreliable. We have not investigated whether authors were aware of or involved in the systematic manipulation of the publication process.

Wiley and Hindawi regrets that the usual quality checks did not identify these issues before publication and have since put additional measures in place to safeguard research integrity.

We wish to credit our own Research Integrity and Research Publishing teams and anonymous and named external researchers and research integrity experts for contributing to this investigation.

The corresponding author, as the representative of all authors, has been given the opportunity to register their agreement or disagreement to this retraction. We have kept a record of any response received.

References

- [1] C. R. Mahesha, C. Polayya, M. L. Rinawa et al., "Optimization of the Spark Plasma Sintering Process for High-Volume Fraction Tungsten Carbide/Al 2025 Composites," *Advances in Materials Science and Engineering*, vol. 2022, Article ID 6433716, 7 pages, 2022.

Retraction

Retracted: The Role of Gum Arabic for a Protective Kidney Dysfunction Induced Gentamicin on Diabetes Rats

Advances in Materials Science and Engineering

Received 20 June 2023; Accepted 20 June 2023; Published 21 June 2023

Copyright © 2023 Advances in Materials Science and Engineering. This is an open access article distributed under the Creative Commons Attribution License, which permits unrestricted use, distribution, and reproduction in any medium, provided the original work is properly cited.

This article has been retracted by Hindawi following an investigation undertaken by the publisher [1]. This investigation has uncovered evidence of one or more of the following indicators of systematic manipulation of the publication process:

- (1) Discrepancies in scope
- (2) Discrepancies in the description of the research reported
- (3) Discrepancies between the availability of data and the research described
- (4) Inappropriate citations
- (5) Incoherent, meaningless and/or irrelevant content included in the article
- (6) Peer-review manipulation

The presence of these indicators undermines our confidence in the integrity of the article's content and we cannot, therefore, vouch for its reliability. Please note that this notice is intended solely to alert readers that the content of this article is unreliable. We have not investigated whether authors were aware of or involved in the systematic manipulation of the publication process.

Wiley and Hindawi regrets that the usual quality checks did not identify these issues before publication and have since put additional measures in place to safeguard research integrity.

We wish to credit our own Research Integrity and Research Publishing teams and anonymous and named external researchers and research integrity experts for contributing to this investigation.

The corresponding author, as the representative of all authors, has been given the opportunity to register their agreement or disagreement to this retraction. We have kept a record of any response received.

References

- [1] G. Ali Alshehry, "The Role of Gum Arabic for a Protective Kidney Dysfunction Induced Gentamicin on Diabetes Rats," *Advances in Materials Science and Engineering*, vol. 2022, Article ID 8617445, 8 pages, 2022.

Retraction

Retracted: Impact of Light and Temperature on Growth, Intracellular and Extracellular Pigment, and Lovastatin Yield by *Monascus ruber* in Synthetic Medium

Advances in Materials Science and Engineering

Received 8 January 2024; Accepted 8 January 2024; Published 9 January 2024

Copyright © 2024 Advances in Materials Science and Engineering. This is an open access article distributed under the Creative Commons Attribution License, which permits unrestricted use, distribution, and reproduction in any medium, provided the original work is properly cited.

This article has been retracted by Hindawi following an investigation undertaken by the publisher [1]. This investigation has uncovered evidence of one or more of the following indicators of systematic manipulation of the publication process:

- (1) Discrepancies in scope
- (2) Discrepancies in the description of the research reported
- (3) Discrepancies between the availability of data and the research described
- (4) Inappropriate citations
- (5) Incoherent, meaningless and/or irrelevant content included in the article
- (6) Manipulated or compromised peer review

The presence of these indicators undermines our confidence in the integrity of the article's content and we cannot, therefore, vouch for its reliability. Please note that this notice is intended solely to alert readers that the content of this article is unreliable. We have not investigated whether authors were aware of or involved in the systematic manipulation of the publication process.

Wiley and Hindawi regrets that the usual quality checks did not identify these issues before publication and have since put additional measures in place to safeguard research integrity.

We wish to credit our own Research Integrity and Research Publishing teams and anonymous and named external researchers and research integrity experts for contributing to this investigation.

The corresponding author, as the representative of all authors, has been given the opportunity to register their agreement or disagreement to this retraction. We have kept a record of any response received.

References

- [1] K. Suganya, A. Usha Raja Nanthini, J. Narenkumar et al., "Impact of Light and Temperature on Growth, Intracellular and Extracellular Pigment, and Lovastatin Yield by *Monascus ruber* in Synthetic Medium," *Advances in Materials Science and Engineering*, vol. 2022, Article ID 2808733, 6 pages, 2022.

Research Article

Impact of Light and Temperature on Growth, Intracellular and Extracellular Pigment, and Lovastatin Yield by *Monascus ruber* in Synthetic Medium

K. Suganya,¹ A. Usha Raja Nanthini ,¹ Jayaraman Narenkumar,^{2,3} Subramani Abilaji,² Aruliah Rajasekar,² Subpiramaniyam Sivakumar,⁴ S. Prasath ,⁵ Hesham S. Almoallim,⁶ and Tahani Awad Alahmadi⁷

¹Department of Biotechnology, Mother Teresa Women's University, Kodaikanal, Tamilnadu 624101, India

²Environmental Molecular Microbiology Research Laboratory, Department of Biotechnology, Thiruvalluvar University, Serkkadu, Vellore, Tamil Nadu 632115, India

³Centre for Materials Engineering and Regenerative Medicine, Bharath Institute of Higher Education and Research, Selaiyur, Chennai 600073, Tamil Nadu, India

⁴Department of Bioenvironmental Energy, College of Natural Resources and Life Science, Pusan National University, Miryang-Si, Gyeongsangnam-do 50463, Republic of Korea

⁵Department of Mechanical Engineering, College of Engineering and Technology, Mizan Tepi University, Mizan Tepi, Ethiopia

⁶Department of Oral and Maxillofacial Surgery, College of Dentistry, King Saud University, PO Box-60169, Riyadh-11545, Saudi Arabia

⁷Department of Pediatrics, College of Medicine and King Khalid University Hospital, King Saud University, Medical City, PO Box-2925, Riyadh 11461, Saudi Arabia

Correspondence should be addressed to A. Usha Raja Nanthini; biotechurn@gmail.com and S. Prasath; prasath@mtu.edu.et

Received 24 March 2022; Revised 21 April 2022; Accepted 1 June 2022; Published 5 July 2022

Academic Editor: Alicia E. Ares

Copyright © 2022 K. Suganya et al. This is an open access article distributed under the Creative Commons Attribution License, which permits unrestricted use, distribution, and reproduction in any medium, provided the original work is properly cited.

The development of alternate sources for the production of natural pigments has been targeted to overcome the utilization of artificial coloring, which is dangerous to human health and the environment. Dyes extracted from microbial sources are more important for beneficial food industry use, especially *Monascus* spp. produces several critical secondary metabolites such as lovastatin, γ -amino butyric acids, monascodilone, monascorubramine, monascin, ankaflavin, rubropunctatin, and citrinin. Lovastatin is a fungal polyketide that inhibits the rate-limiting enzymes HMG-CoA reductase, an essential precursor in cholesterol biosynthesis. The light source regulates fungi' growth, metabolism, and reproduction and is necessary for fungi' existence and distribution. The impact of different color lights (red, green, blue, yellow, and white, darkness) and different temperatures (27°C and 37°C) on extracellular and intracellular pigment yield, lovastatin production, and biomass of *Monascus ruber* was studied, and appropriate incubation temperature and time enhance the intracellular, extracellular pigment, and biomass production. However, when exposed to other color lights, fungus growth and pigment yield are significantly reduced in *Monascus ruber*. Then, fungi and pigment yield development is decreased when exposed to other color lights. It can be concluded that darkness influenced pigment production and biomass yield at both temperatures (27°C and 37°C). Similarly, the production of lovastatin and its concentration were analyzed by HPLC. The highest concentration of lovastatin was obtained at 27°C when exposed to red color light (302.6 mg/ml for extracellular fermentation broth) and (86.7 mg/ml for intracellular fermentation broth). At 37°C, the highest concentration of lovastatin was obtained from (571.5 mg/ml extracellular fermentation broth) when exposed to darkness and (170.4 mg/ml intracellular fermentation broth) exposed to red color light. Thus, the result provides the knowledge to enable us to explore the pigments and lovastatin yield for functional foods and large-scale industrial applications.

1. Introduction

Food additives have been widely used for improving food quality by the food industries. The most commonly used coloring agents are synthetic pigments having a lot of side effects, such as carcinogenic and mutagenic effects on the body. Because of the side effect of synthetic dyes, natural pigments and traditional pigments are becoming very popular nowadays. They are more reliable and safer. The standard coloring from the *Monascus* sp. is highly secure and rich in its nutrition and has a wide variety of applications in the food industries as food pigments and preservatives due to their light stability, temperature resistance, and acid-base change resistance and also has antioxidant, antibacterial, antiviral, and antitumor biological activities. The secondary metabolites produced by the *Monascus* sp are *Monacolin K* (Lovastatin), Citrinin, γ -aminobutyric acid, and dimeric acid [1, 2]. This Lovastatin is the most critical hypercholesterolemic compound used to lower blood cholesterol. Lovastatin inhibits the rate-limiting enzyme HMG-CoA reductase involved in cholesterol biosynthesis [3]. Light is the indeed source on Earth. It is essential to regulate the physiology of the organisms, including fungi [4]. So, many photoreceptors are present in the fungi, which receive and transduce the photon energy [5, 6]. For the growth phase of the fungus, the wavelength and intensity of electrical signals are related to light excitation, and it has been detected in *Phycomyces blakesleeianus* fungus [7]. In *A. nidulans*, condition induction is due to the response to other wavelengths of different lights [8, 9]. The growth of reproductive organs is light-dependent (i.e., boosting sexual development in the dark while stimulating asexual sporulation under illumination) [10]. In this study, the impact of incubation temperature and different color illuminations (blue, yellow, green, red, and white (uncovered)), dark on the production of pigment, biomass, and lovastatin by *Monascus ruber* have been investigated.

2. Materials and Methods

2.1. Microorganism. *Monascus ruber* (MTCC 1793) was obtained from MTCC, IMTECH Chandigarh, India. The culture was maintained at 4°C in potato dextrose agar (PDA) plates.

2.2. Fermentation by Liquid State. The fungal culture was cultivated in 100 ml of broth containing 1.4 g K_2HPO_4 , 30 g glucose, 0.5 g $MgSO_4 \cdot 7H_2O$, 1.0 g $(NH_4)_2SO_4$, 0.6 g KH_2PO_4 , 0.8 mg $ZnSO_4 \cdot 7H_2O$, 0.8 mg $NaMoO_4 \cdot 2H_2O$, 0.8 mg $FeCl_3 \cdot 6H_2O$, 0.4 mg $MnSO_4 \cdot 2H_2O$, and 0.08 mg $CuSO_4 \cdot 5H_2O$ in 1000 ml of distilled water in a conical flask. The pH of the broth was altered to 5.6 using 1 M HCl and 1 M NaOH before the sterilization process. The flasks were inoculated with the spore suspension and incubated at 27°C and 37°C for 7 days. The principle behind the augmented production of pigment and lovastatin by *M. ruber* is that the colored glass paper covered on the flask or light allows

unique color light spectrum to pass through the glass by controlling other color light spectrum [11].

2.3. Extracellular Pigment Estimation. 5 ml of solvent was taken per milliliter of fermented broth to estimate extracellular pigment. The samples were kept on a rotary shaker at 200 RPM for 1 hour and filtered through Whatman No. 1 filter paper. Ethanol extract is considered a control medium for pigment analysis. The analysis was carried out in Shimadzu UV-1800 Spectrophotometer at the wavelength of 350–600 nm 400 (yellow), 550 (pink), 520 (reddish-brown), and 540 (red), respectively. The pigment yield was measured in optical density units per gram, and the absorbance was converted to pigment units using the color value (CV) [12]:

$$\text{colour value} = \text{O.D} \times \text{dilution} \times \frac{\text{volume of extract}}{\text{amount of sample (ml)}} \quad (1)$$

2.4. Intracellular Pigment Estimation. 1 g of 7 days old mycelia mat was taken from fermented broth and washed with distilled water until it is clear. 5 ml of 90% ethanol and mycelia mat was added to a test tube and kept in a boiling water bath (30 minutes) for the pigment release. After that, it was filtered using (Whatman No. 1) filter paper and maintained on a rotary shaker at 200 RPM for 1 h. Optical density (OD) of the pigment extracted from the filtrate was measured in the same way as the extracellular pigment [12].

2.5. Estimation of Biomass. The fermented broth was filtered through (Whatman No. 1) filter paper, and the mycelial mat was washed twice with distilled water. Then, it was dried at 80°C in a hot air oven for the constant weight and measured as biomass [11].

2.6. Analysis of Lovastatin by HPLC. All the chemicals used were in analytical and HPLC grades for this analysis. The quantification of lovastatin was carried out in culture filtrate using HPLC (Shimadzu) using 250 × 4.6 mm C-18 column with a photodiode array (PDA) detector. The mobile phase acetonitrile/water (63:35 v/v), which was acidified with ortho-phosphoric acid at a concentration of 0.01 percent with a flow rate of 1 ml/min, was detected using UV at 238 nm. A 20 liter sample was put into the column for examination, with pure lovastatin serving as a reference [13, 14].

3. Results and Discussion

3.1. Effect of Lights on the Extraction of Extracellular Pigment. Environmental factors influence filamentous fungus development and metabolism because they help regulate cellular metabolism and optimize the production of particular biosynthetic products [15].

Table 1 shows how liquid fermentation was carried out under different lighting conditions, including blue (492–455 nm), green (577–492 nm), yellow (597–577 nm),

TABLE 1: Effect of an altered light source on extracellular pigment yield by *Monascus ruber* at 27°C and 37°C.

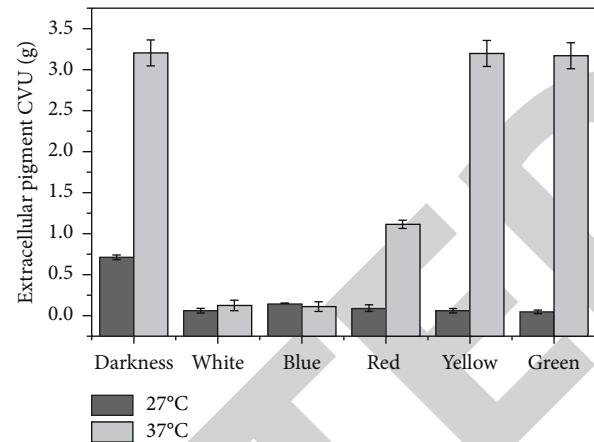
Extracellular pigment yield CVU (g)		
<i>Monascus ruber</i>		
Light	27°C	37°C
Darkness	0.716 ± 0.53	3.205 ± 0.01
White (unscreened)	0.067 ± 0.03	0.131 ± 0.01
Blue	0.155 ± 0.14	0.117 ± 0.00
Red	0.096 ± 0.07	1.115 ± 0.00
Yellow	0.070 ± 0.05	3.200 ± 0.00
Green	0.049 ± 0.01	3.172 ± 0.04

and red (780 622 nm), white (uncovered), and darkness. The absorption spectrum of different color light on extracellular broth indicates the changes in pigment level. At 27°C, the maximum pigment yield was obtained in darkness (0.716 ± 0.53 CVU/g), followed by blue (0.155 ± 0.14 CVU/g) and red (0.096 ± 0.07 CVU/g). A low yield of pigment was observed in white light (unscreened) (0.067 ± 0.03 CVU/g) and green (0.049 ± 0.01 CVU/g) light. An increase in pigment production was observed when incubated at 37°C in darkness (3.205 ± 0.01 CVU/g) followed by yellow (3.200 ± 0.00 CVU/g) and green (3.172 ± 0.04 CVU/g) light (Figure 1). A low yield of pigment production was noted in blue, red, and white (unexposed) light during fermentation. The effect of blue and red light on pigment creation and metabolism, growth, sexual, asexual development, pigment generation, and tropism in fungus has been examined [7, 15]. The concentration of secondary metabolites (GABA, red pigments, MONK, and citrinin) has also been found to vary depending on the color of light and the most resistant to sunlight [16].

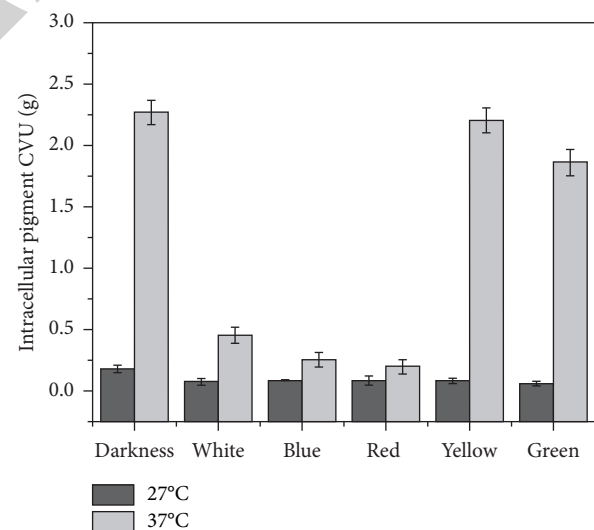
3.2. Effect of Lights on Intracellular Pigment Extraction. Production of intracellular pigment in the defined medium at 27°C and 37°C under darkness, white (unexposed), blue, red, yellow, and green exposure to light was observed and is given in Table 2.

At 27°C, a high level of pigment yield was observed in darkness (0.182 ± 0.05 CVU/g), blue (0.089 ± 0.05 CVU/g) light, and red (0.087 ± 0.09 CVU/g) light and the minimum yield was observed in green (0.060 ± 0.05 CVU/g) light, white (0.077 ± 0.05 CVU/g), and yellow (0.084 ± 0.04 CVU/g) light. At 37°C, the maximum pigment yield was observed in darkness (2.269 ± 1.82 CVU/g), yellow (2.205 ± 1.80 CVU/g), and green (1.860 ± 1.55 CVU/g) light (Figure 2). The minimum pigment yield was noted in red, white (unscreened), and blue light. Therefore, there is a drastic change in intracellular pigment production compared with extracellular at different temperatures. The result shows that the pigment production to varying temperatures by *Monascus ruber* is also correlated with light exposure.

3.3. Effect of Biomass Production. The effects of altered lights (blue, yellow, green, red, white (unexposed), and darkness) and different temperatures (27°C and 37°C) on the biomass production were observed by the dry biomass weight

FIGURE 1: Effect of an altered light source on extracellular pigment yield by *Monascus ruber* at 27°C and 37°C.TABLE 2: Effect of an altered light source on intracellular pigment yield by *Monascus ruber* at 27°C and 37°C.

Light	<i>Monascus ruber</i>	
	27°C	37°C
Darkness	0.182 ± 0.05	2.269 ± 1.82
White (unscreened)	0.077 ± 0.05	0.455 ± 0.13
Blue	0.089 ± 0.05	0.256 ± 0.12
Red	0.087 ± 0.09	0.201 ± 0.03
Yellow	0.084 ± 0.04	2.205 ± 1.80
Green	0.060 ± 0.05	1.860 ± 1.55

FIGURE 2: Effect of an altered light source on intracellular pigment yield by *Monascus ruber* at 27°C and 37°C.

(Figure 3). At 27°C, the increased biomass was obtained from the red (2.36 g/L) followed by blue (1.76 g/L), white (1.05 g/L), green (1.02 g/L), and black (1.62 g/L). The flask exposed to yellow light (0.7 g/L) produced meager biomass. At 37°C, the highly pigmented biomass was recovered from darkness (3.81 g/L), red (3.21 g/L), and green (2.54 g/L). The low biomass yield was recovered from blue (1.87 g/L) and yellow

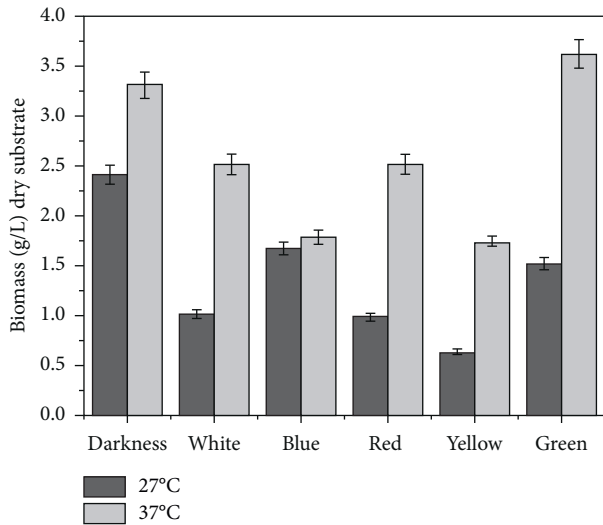


FIGURE 3: Effect of biomass production different wavelengths of light on *Monascus ruber*.

(1.8 g/L). It is due to photoreceptors conscious of darkness and light in the fungus [12]. This finding revealed that incubation in the dark was the most effective at generating biomass formation and intracellular and extracellular pigment output. There is light-sensing through phytochrome in *Aspergillus nidulans*, suggesting that a phytochrome-like mechanism could be active in those fungi [16]. Equally, enhanced biomass production was observed at 27°C and 37°C in red light and darkness. The yield of biomass is more in darkness than the red light.

4. Analysis of Lovastatin

4.1. Intracellular and Extracellular Production of Lovastatin. Pure lovastatin was used as a standard to quantify the amount of lovastatin present in *Monascus ruber*. The standard and extract of *Monascus ruber* lovastatin were eluted at a single peak with a retention time of 10.64 and 10.63, respectively. The effect of Intracellular lovastatin production, when exposed to different color lights incubated at 27°C and 37°C, was analyzed using HPLC. The maximum concentration of intracellular lovastatin was observed in blue color at 86.7 mg/ml at 27°C, followed by red color at 61.2 mg/ml. At 37°C, the maximum concentration was observed in red color at 170.4 mg/ml, followed by green color at 148.3 mg/ml (Figure 4 and Table 3). The effect of extracellular lovastatin production, when exposed to different color lights at 27°C and 37°C, was analyzed using HPLC (Table 4). A higher concentration of lovastatin was observed in red color at 14.20 mg/ml followed by blue color at 27°C. The increased concentration of lovastatin obtained in green color was 87.75 mg/ml, followed by white (unscreened) 48.17 mg/ml (Figure 5 and Table 4).

It is reported that the accumulation of monacolins (especially monacolin J) inhibited the biosynthesis of lovastatin. Therefore, there is a chance of collection of monacolin J in fermentation, and some of the lovastatin intermediates could absorb light at 238 nm in the

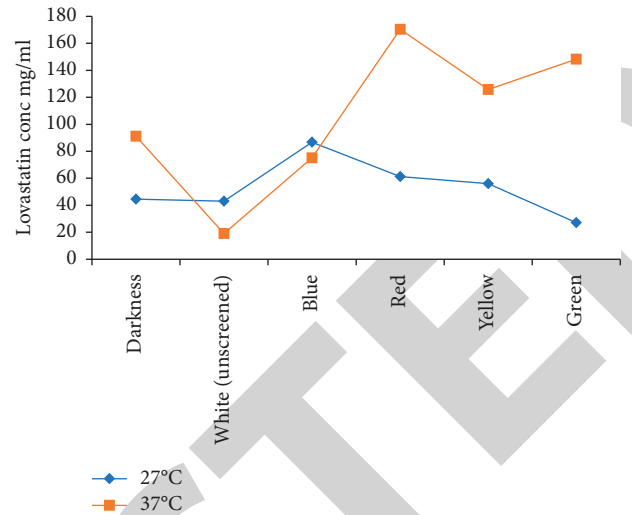


FIGURE 4: Intracellular lovastatin concentration (mg/ml) at 27°C and 37°C.

TABLE 3: Intracellular lovastatin concentrations (mg/ml) at 27°C and 37°C.

Sample name	Lovastatin (Conc. mg/ml)	
	27°C	37°C
Darkness	44.6	91.2
White (unscreened)	43.0	19.03
Blue	86.7	75.2
Red	61.2	170.4
Yellow	56.03	125.8
Green	27.15	148.3

TABLE 4: Extracellular lovastatin concentrations (mg/ml) at 27°C and 37°C.

Light	Lovastatin (Conc. mg/ml)	
	27°C	37°C
Darkness	215.4	571.5
White (unscreened)	119.5	102.6
Blue	225.1	57.8
Red	302.6	10.97
Yellow	230.1	88.7
Green	134.0	174.1

biosynthesis pathway [17]. The typical interference in the lovastatin also depends on diene groups in lovastatin [18, 19]. The excessive concentration of lovastatin produced might result from the dietary development of a complicated medium. Carboxymethylcellulose (CMC) on lovastatin synthesis in *A. terreus* PM3 restricted filamentous growth and pellet formation, stimulating lovastatin production [20]. Metal ion concentrations, such as Zn²⁺, Fe²⁺, Mg²⁺, Ca²⁺, Cu²⁺, and Mn²⁺, can alter cell biochemistry and affect metabolite production and cell development [21]. The present study reveals that the intracellular lovastatin production by *Monascus ruber* is higher when exposed to red light followed by green light at 37°C. Similarly, the extracellular lovastatin production is

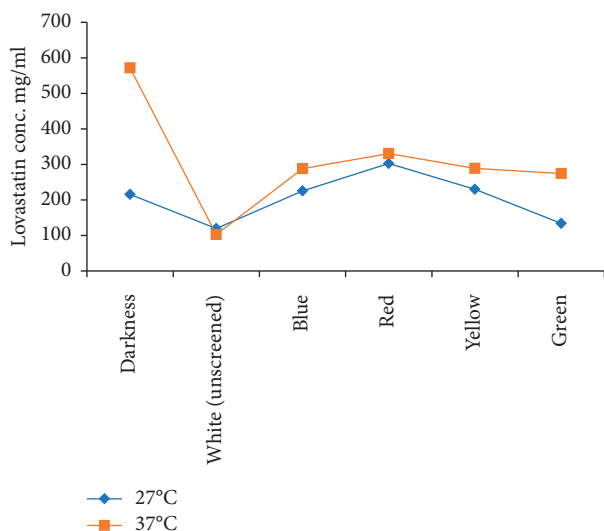


FIGURE 5: Extracellular lovastatin concentrations (mg/ml) at 27°C and 37°C.

higher in darkness, followed by a red light at 37°C. The results show that lovastatin production can be enhanced by red, green light, and dark and induced a high pigment and biomass production level.

5. Conclusion

The extracellular and intracellular pigment production, biomass yield, and lovastatin production of *Monascus ruber* with different color lights and temperatures were analyzed in the study. When incubated in the darkness, the maximum pigment yield at both 27°C and 37°C was obtained. The fungi grown under white (unscreened) light had significantly less potential, therefore postulating the existence of photoreceptors responsive to dark and light in the fungi. The biomass production in *Monascus ruber* was high when incubated in red light at both temperatures (27°C and 37°C). Therefore, the result shows that an initial biomass increase can be carried out under red light, and darkness can influence the pigment yield in temperatures (27°C and 37°C). Lovastatin, also known as monacolin *k*, is an inhibitor of cholesterol biosynthesis, produced by *Monascus* sp. as a secondary metabolite. HPLC was subject to estimate the extracellular, intracellular, and lovastatin production by *M. ruber* exposed to different light illumination and incubation time. The separation was done with a C-18 column, and the wavelength used for quantification was 238 nm with the diode array detector. This investigation of extracellular and intracellular lovastatin production in the fermentation broth showed a considerable variation. The highest concentration of lovastatin was obtained from the extracellular source when incubated under darkness and red color light at 37°C. Hence, this work reveals that incubating in the dark at 37°C is the best for lovastatin production. These results enable us to explore the pigments and lovastatin for functional foods and large-scale industrial applications.

Data Availability

The data used to support the findings of this study are included in the article. Should further data or information be required, these are available from the corresponding author upon request.

Conflicts of Interest

The authors declare that there are no conflicts of interest regarding the publication of this paper.

Acknowledgments

The authors are grateful to the Researchers Supporting Project Number TANSCHERGP/2019-20/TVU/HECP-0059, Tamil Nadu State Council for Higher Education-Research Grant Project, Tamilnadu, India. This project was supported by Researchers Supporting Project Number (RSP-2021/283) King Saud University, Riyadh, Saudi Arabia.

References

- [1] Y.-L. Lin, T.-H. Wang, M.-H. Lee, and N.-W. Su, "Biologically active components and nutraceuticals in the *Monascus*-fermented rice: a review," *Applied Microbiology and Biotechnology*, vol. 77, no. 5, pp. 965–973, 2008.
- [2] Y. Feng, Y. Shao, and F. Chen, "*Monascus* pigments," *Applied Microbiology and Biotechnology*, vol. 96, no. 6, pp. 1421–1440, 2012.
- [3] A. W. Alberts, J. Chen, G. Kuron et al., "Mevinolin: a highly potent competitive inhibitor of hydroxymethylglutaryl-coenzyme A reductase and a cholesterol-lowering agent," *Proceedings of the National Academy of Sciences*, vol. 77, no. 7, pp. 3957–3961, 1980.
- [4] A. Idnum and J. Heitman, "Light control growth and development via a conserved pathway in fungal kingdom," *PLoS Biology*, vol. 3, p. 95, 2005.
- [5] L. M. Corrochano, "Fungal photoreceptors: sensory molecules for fungal development and behaviour," *Photochemical and Photobiological Sciences*, vol. 6, pp. 725–736, 2008.
- [6] A. Herrera-Estrella and B. A. Horwitz, "Looking through the eyes of fungi: molecular genetics of photoreception," *Molecular Microbiology*, vol. 64, no. 1, pp. 5–15, 2007.
- [7] M. A. Mogus and J. J. Wolken, "Phycomyces: electrical response to light stimuli," *Plant Physiology*, vol. 53, no. 3, pp. 512–513, 1974.
- [8] L. N. Yager, H. O. Lee, D. L. Nagle, and J. E. Zimmerman, "Analysis of flu G mutations that affect light-dependent conidiation in *Aspergillus nidulans*," *Genetics*, vol. 149, pp. 177–1786, 1998.
- [9] A. M. Calvo, L. L. Hinze, H. W. Gardner, and N. P. Keller, "Sporogenic effect of polyunsaturated fatty acids on development of *Aspergillus* spp.," *Applied and Environmental Microbiology*, vol. 65, no. 8, pp. 3668–3673, 1999.
- [10] W. Rau and U. Mitzka-Schnabel, "Carotenoid synthesis in *Neurospora crassa*," *Methods in Enzymology*, vol. 110, pp. 253–267, 1985.
- [11] D. Rashmi and T. Padmavathi, "Exploring *Monascus sanguineus* as a potential natural source for pigment production," *International Research Journal of Biological Sciences*, vol. 2, no. 5, pp. 59–67, 2013.

Retraction

Retracted: Modeling and Optimization of MRR in Wire Electrical Discharge Machining of Silicon Particle-Reinforced AA6063 Composite

Advances in Materials Science and Engineering

Received 26 December 2023; Accepted 26 December 2023; Published 29 December 2023

Copyright © 2023 Advances in Materials Science and Engineering. This is an open access article distributed under the Creative Commons Attribution License, which permits unrestricted use, distribution, and reproduction in any medium, provided the original work is properly cited.

This article has been retracted by Hindawi, as publisher, following an investigation undertaken by the publisher [1]. This investigation has uncovered evidence of systematic manipulation of the publication and peer-review process. We cannot, therefore, vouch for the reliability or integrity of this article.

Please note that this notice is intended solely to alert readers that the peer-review process of this article has been compromised.

Wiley and Hindawi regret that the usual quality checks did not identify these issues before publication and have since put additional measures in place to safeguard research integrity.

We wish to credit our Research Integrity and Research Publishing teams and anonymous and named external researchers and research integrity experts for contributing to this investigation.


The corresponding author, as the representative of all authors, has been given the opportunity to register their agreement or disagreement to this retraction. We have kept a record of any response received.

References

- [1] C. Mahesha, R. Suprabha, N. Bhavani et al., "Modeling and Optimization of MRR in Wire Electrical Discharge Machining of Silicon Particle-Reinforced AA6063 Composite," *Advances in Materials Science and Engineering*, vol. 2022, Article ID 2594974, 9 pages, 2022.

Research Article

Modeling and Optimization of MRR in Wire Electrical Discharge Machining of Silicon Particle-Reinforced AA6063 Composite

CR Mahesha,¹ R. Suprabha,¹ NPG Bhavani,² Prashant Sunagar,³ Raja Ramesh,⁴ P. Balamurugan,⁵ Rajasekar Rajendran,⁶ and Anirudh Bhowmick⁷ 

¹Department of Industrial Engineering & Management, Dr. Ambedkar Institute of Technology, Bangalore, Karnataka 560056, India

²Department of Electronics and Communication Engineering, Saveetha School of Engineering, Saveetha Institute of Medical and Technical Sciences, Chennai, Tamil Nadu 602105, India

³Civil Engineering Department, M S Ramaiah Institute of Technology, Bengaluru, Karnataka 560054, India

⁴Department of Mechanical Engineering, Sri Vasavi Institute of Engineering and Technology, Nandamuru, Andhra Pradesh 521369, India

⁵Department of Mathematics, M.Kumarasamy College of Engineering, Karur, Tamil Nadu 639113, India

⁶Department of Automobile Engineering, Bharath Institute of Higher Education and Research, Chennai, Tamil Nadu 600073, India

⁷Faculty of Meteorology and Hydrology, Arba Minch Water Technology Institute, Arba Minch University, Ethiopia

Correspondence should be addressed to Anirudh Bhowmick; anirudh.bhowmick@amu.edu.et

Received 19 March 2022; Accepted 30 May 2022; Published 30 June 2022

Academic Editor: Palanivel Velmurugan

Copyright © 2022 CR Mahesha et al. This is an open access article distributed under the Creative Commons Attribution License, which permits unrestricted use, distribution, and reproduction in any medium, provided the original work is properly cited.

Improved properties can be found in aluminum alloys containing silicon carbide reinforcement particles. This work studies the machinability of Al 6063 reinforced with silicon carbide particles with wire electrical discharge machining. To attain a high material removal rate, wire EDM constraints such as current (I), pulse-on time (T_{on}), wire speed (W_s), voltage (I_v), and pulse-off time (T_{off}) can be adjusted with precision. Taguchi L16 orthogonal arrays are used to design the experiments and statistical methods are used to examine. These process characteristics had a significant impact on the overall rate of return, with a 28.2% impact on the MRR, 23.04% impact on the MRR, and 22.86% impact on the MRR. We achieved MRRs of 65.21 mg/min for samples containing 5% and 10% SiCp at optimal conditions, respectively. Linear regression was used to create the statistical model, which then used confirmation trials to verify its accuracy in predicting MRR (R -73.65%). The statistical model is used to estimate MRR based on various process parameter settings.

1. Introduction

Machining using EDM is an isolated phenomenon and removes material by repeatedly igniting a conductor and the workpiece in a dielectric liquid [1]. This fluid circulates to remove molten debris from the work area while it is being machined. You can use wire EDM to make complex forms out of conductive metals like aluminum, copper, brass, titanium, and other alloys [2]. While other technologies can produce thin walls with low surface roughness and short internal corner radii, wire EDM has the advantage of having

the least amount of burrs [3]. This approach's speed and economy are two additional perks. As a result of their low density, aluminum alloys are extensively employed in the transportation industry (aircraft, planes, and ships). Of the total, the transportation sector consumes 23%, followed by construction (25%), packing (8%) and engineering (11%), and electrical appliances (6%). This metal has a low density, high malleability, resistance to corrosion, and electrical conductivity [4, 5]. The aluminum 6000 series' superior mechanical and welding characteristics enable a wide range of goods, including aviation fittings and electrical

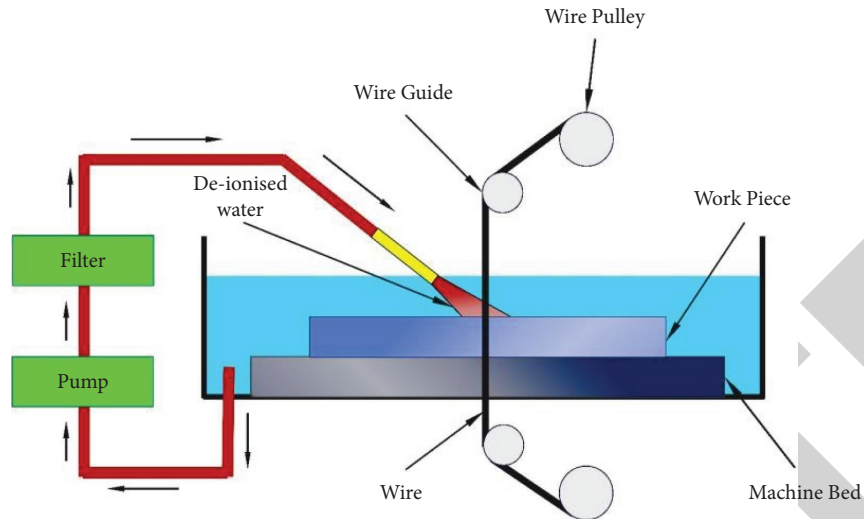


FIGURE 1: Schematic view of wire cut electrical discharge machine.

components and connections, camera lens mounting, and marine fits and accessories.

Alloying it with other substances like silicon carbide (SiC), aluminum oxide (Al_2O_3), magnesium oxide (MgO), water-glass (WC), silicon dioxide (SiO_2), or boron carbide (B_4C), etc, the inclusion of SiC and Al_2O_3 particles in an aluminum matrix enhanced yield strength (YS), ultimate tensile strength (UTS), elastic modulus (EM), and hardness (Hd), according to [6]'s research. Electrical conductivity was reduced by the addition of aluminum oxide, zirconium, cerium, and Mg. In comparison to the as-cast alloy, the age-hardened Al 6063-SiCp-reinforced composites demonstrated an increase in hardness of 120–145% [7]. Compared to high-temperature aging, lower-temperature aging demonstrated a significant improvement in wear resistance. Size reduction was achieved with the inclusion of grain refiners (Al-5Ti-1B), which also turned a long, coarse grain into a circular one with improved tensile and wear resistance. Strength/weight ratio, superior thermal stabilization, and abrasive resistance make SiCp a useful reinforcing particle [8, 9]. Al 6063 with SiCp had enhanced Young's modulus, strength, and toughness (500 nm). An investigation of Al MMC strengthened with silicon and Tungsten carbide was conducted by [10]. Load is transferred to the reinforcement through the robust interface among the matrix and strengthened composites. This procedure enhanced both elasticity and strength. References [11, 12] used continuous mechanical simulations to show that whiskers of Tungsten carbide and aluminum nitride strengthen Al composites. Figure 1 shows the schematic view of the wire cut electrical discharge machine.

The abrasive character of SiCp-reinforced aluminum alloys makes machining them challenging, which results in rapid tool wear and a poor surface finish [13]. Particle detachment and fracture in reinforced particles are what cause voids and cavities on the machined surface to appear. Nontraditional methods such as wire EDM (electrical discharge generated between the tool and workpiece) may be an option for removing metal from the workpiece [14, 15]. The

base metal is molten and vaporized by the spark gap's concentrated heat. The spark gap is filled with dielectric fluid, which is used to cool the machine as well as control the discharge of electricity. This procedure has a drawback in that it requires a workpiece that is electrically conducting [16–19]. Among the benefits of wire EDM are its ability to produce complicated profiles regardless of the workpiece's mechanical qualities and the fact that tools and workpieces do not come into direct touch during the machining process. Currently, wire EDM research trends are mostly focused on scientific research of application areas and optimization of processing variables [20]. For vehicle nozzles, turbine blade cooling holes, medicinal devices such as stents, microfluidic channels, and the fabrication of different micro-electromechanical devices, EDM has become increasingly popular in recent years. Polishing 3D printed parts with the wire EDM reduces surface roughness by roughly 80%, making it a useful tool for other applications as well [21]. The eradication of balling pits, voids, and porosity could be seen in the 3D printed SS316L material that had been polished with wire EDM. Because the long discharge time of the high ton produced roughness, the wire EDM polishing application of the low ton was promoted. Electrode wires are visible on the polished surface, accumulating in extremely small amounts [22].

Once it came to aluminum composites, [23] studied the effects of hot extrusion and heated treatment on reinforced SiCp size (0.7–13 μm). Smaller-sized SiCp and 0% particles were not significantly different in the surface quality after wire EDM. Both the kerf breadth and the electrode wear on the smaller-sized SiCp were greater than on test samples reinforced with larger particles [24, 25]. Moreover, the wire electrode was coated with matrix material during the milling process. Mixing MWCNTs into the dielectric fluid resulted in an increase in machining performance. Shape memory alloy nitinol wire EDM treated with MWCNTs (1 g/L) showed a 75.42% increase in MRR and a 19.15% decrease in SR. Additionally, it was determined that the recast layer's thickness

TABLE 1: Composition (%) of Al 6063.

Silicon	Iron	Copper	Magnesium	Manganese	Others	Aluminum
0.41	0.11	0.05	0.49	0.1	0.05	Remaining

had decreased significantly. Al413 - 9% composite was studied by [26] for its wire EDM machinability. The kerf-width and surface roughness were highly correlated with the machine's voltage, capacitance, and feed rate. Improving the supply enhanced the MRR during SiC/Al composite machining. Matrix SiCp content increases by 15%, whereas subsequent increases in SiC content increase the MRR in the opposite way [27]. The AA6025 composite was tested for its surface coarseness and material removal rate (silicon carbide: 10 wt% and aluminum oxide:10 wt.%) [28]. The conductive powder was shown to improve performance in the dielectric fluid by the researchers, according to their findings. This is because the conductive particles have diminished the dielectric fluid's strength and hence increased the spark gap. As a result of this phenomenon, the spark gap discharge remained more stable and higher during the ignition process. Researchers of [29, 30] used a 6%SiC/A356 surface to better understand EDM surface features. SiC/A359 is 30% and 10% SiC/Al359 is 30%. The harder the surface became, the denser the reinforced particles became. In EDM, copper electrodes transport a lot more metal than graphite electrodes. Researchers of [31–33] enhanced the wire EDM parameter settings to machine an Al 6063/cenosphere composite. In addition to increasing in size, the craters' surface wave smoothness also increased as I and T_{on} . Electrode wear is increased because of the composite's poor surface quality.

The weight percentage and volume percentage of reinforcing particles in the matrix influence the composite's mechanical properties. When reinforcing particles are consistently distributed throughout the material, the mechanical characteristics of composites improve [34]. Due to increased stress, reinforcing materials began forming aggregates that reduced their mechanical qualities. SiCp up to 10% was shown to boost tensile and hardness; however, after that point, these properties rapidly deteriorated. However, ductility decreased as the amount of SiCp in the alloy rose. More than 8% SiCp loading resulted in aggregated particles in the Al 6063 matrix when stir casting was performed on test samples. As a result, in this project, the weight fraction is capped at 8%. Traditional machining of Al-SiCp is plagued by pits, voids, microcracks, and cracked reinforcements on the cut surface. Wire EDM machining, for example, can get around these problems [35]. Wire EDM process constraints including T_{on} and T_{off} , W_s , and I_v are examined in this analysis in order to optimize these settings in order to maximize productivity in terms of the MRR. Fuzzy AHP-ARAS, genetic algorithms, and particle swarm optimization methods like the Grass-Hopper method and moth-flame are more appealing for experiments with large data sets; however, Taguchi and response surface approaches, as used in this study, are better instruments for optimization in small-scale experiments [36]. As a result, the Taguchi technique is used in this study to

TABLE 2: Wire electrical discharge machining process parameters and factors.

Factors	Code	1	2	3	4
I (A)	A	4	5	6	7
T_{on} (μ s)	B	25	35	45	55
T_{off} (μ s)	C	15	20	25	30
W_s (rpm)	D	180	360	720	1440
I_v (V)	E	90	100	-	-

optimize the MRR and build a regression model that reliably predicts the MRR.

2. Materials and Methods

Sample preparation, experimental setup, wire EDM processing parameters, and design of experiments are all covered in this part. The response parameter and optimization approach are also discussed.

2.1. Details of the Experiment and the Specimens. In this study, researchers in India employed a CNC 2-axis wire EDM manufactured by accord wire EDM. Mo wire with a width of 0.16 mm is employed to make the tool electrode. Soft water and gel make up the insulator. The regulator has a 0.001 mm resolution. Stir casting is employed to create the SiC particle-reinforced Al-6063 alloy. By mechanically stirring the molten metal, reinforcing particles (5 and 10% by weight) that have been preheated to 650°C are evenly distributed throughout the molten matrix, which is liquefied at 850°C. The molten metal is poured into a mold that has been preheated to 200 °C and allowed to cool to room temperature before being moved. Table 1 provides an overview of the Al 6063 composite's chemical makeup.

2.2. Design of Experiments. There is a numeral factor that affects the MRR of a wire EDM system including current and pulse duration, wire speed, and voltage. Variations in voltage and other parameters are made at two separate levels. Detailed parameters and factors for the wire EDM technique may be found in Table 2. Based on the results of the tests, these levels have been chosen. The L16 Taguchi orthogonal array is chosen since the experiments require a total of 13 degrees of freedom. Table 3 outlines the experiment's plan of action. There was a total of two experiments per condition. The thickness of the specimens and the dielectric fluid supply pressure remained persistent during the processing.

2.3. Dimension of Material Removal Rate. For a total of 20 mm, test specimens are put through wire EDM according to the procedure outlined in Table 2. (1) calculates MRR based on weight loss during machining for each experimental session. Digital mass stability is employed to determine the

TABLE 3: Design of Experiments and associated mean material removal rate.

Trial no.	Process parameters settings				Material removal rate		
	I	t_{on}	t_{off}	W_s	V	5%	10%
1	4	25	15	1440	90	0.382	0.315
2	4	35	20	720	90	0.412	0.402
3	4	45	25	360	100	0.375	0.376
4	4	55	30	180	100	0.198	0.196
5	5	25	20	360	100	0.495	0.484
6	5	35	15	180	100	0.456	0.442
7	5	45	30	1440	90	0.521	0.496
8	5	55	25	720	90	0.416	0.404
9	6	25	25	180	90	0.258	0.235
10	6	35	30	360	90	0.324	0.318
11	6	45	15	720	100	1.176	1.126
12	6	55	20	1440	100	1.019	0.945
13	7	25	30	720	100	0.712	0.622
14	7	35	25	1440	100	0.546	0.527
15	7	45	20	180	90	0.863	0.664
16	7	55	15	360	90	0.742	0.723

weightage of specimens before and after machining (w_i and w_f) (accuracy: 0.001 g). Five measurements were done for each sample to assure accuracy. The mean MRR of each testing for each sample with varying SiCp compositions is shown in Table 3. Figure 2 depicts cut surfaces of test materials machined under various circumstances.

$$MRR = \frac{w_i - w_f}{t} \text{ mg/s.} \quad (1)$$

2.4. Optimization of Material Removal Rate. An ANOVA technique was used to analyze wire EDM properties such as I , T_{on} and T_{off} , W_s , and V to assess their influence on material removal rate. With a 95% degree of confidence, the F-test is used to identify important process parameters. It is also possible to calculate the average MRR at several levels (Levels). The best conditions for a high MRR are determined for each of the study's process parameters based on the MRR levels that yield the highest MRR. Equations (2)–(5) are used to calculate the MRR under optimal conditions. Finally, regression analysis is used to construct a statistical model that can predict the MRR using regression coefficients.

$$n_{eff} = \frac{n}{1 + DF}, \quad (2)$$

$$T = \frac{\sum MRR}{n}, \quad (3)$$

$$MRR_{Optimum} = MRR[A_3 B_3 C_1 D_3 E_2] - 4 \times T, \quad (4)$$

$$\text{Confidence interval} = \pm \sqrt{F(\alpha, DF_{error}) \times \frac{MS_{error}}{n_{eff}}}. \quad (5)$$

2.5. Material Removal Theoretical Modeling. In wire EDM, the material is removed by a spark gap electric discharge. The

amount of spark energy generated through the sparking processing is calculated using (6). The quantity of heat generated by a spark is dependent on the spark's I , T_{on} , and I_v . Researchers employ the Gaussian heat input model to forecast the r_{sp} , despite the fact that other models exist. The axis of a spark has the highest heat intensity (qR) according to this model, and the heat flux related to this is represented by formula (7). The electric field among the electrode and workpiece ionizes the dielectric liquid, allowing electrons to flow freely. Eventually, a spark forms, which is hot enough to melt and evaporate the workpiece. The equation can be used to calculate the size of hemisphere craters created on the machined surface as an outcome of this phenomenon (8).

$$E_s = I_p \times I_v \times t_{on}, \quad (6)$$

$$q_f(R) = \frac{4.45 \times W_M \times I \times V}{\Pi \times (r_{sp})^2} \times e^{-4.5(R/r_{sp})^2}, \quad (7)$$

$$\Gamma = \frac{2}{3} \pi r^3. \quad (8)$$

3. Results and Discussion

3.1. Current and Wire Speed Have an Effect on MRR. As seen in Figure 2(a), MRR is influenced by the current. From 4 A to 6 A, the MRR rises significantly. At a current of 5 A, the highest material removal rate is 0.662 mg/s. The breakdown voltage and spark energy rise as the current increases from low to high values, as seen in (6). The high current melts and evaporates more material because of the higher. Other scholars have also found similar patterns. However, the MRR decreased slightly when the current was greater than 5 A. When there is not enough flushing from the molten pool, the recast layer forms on top of previously machined surfaces. During a discharge, debris dissolves from the dielectric fluid and degraded wire electrode particles are deposited as

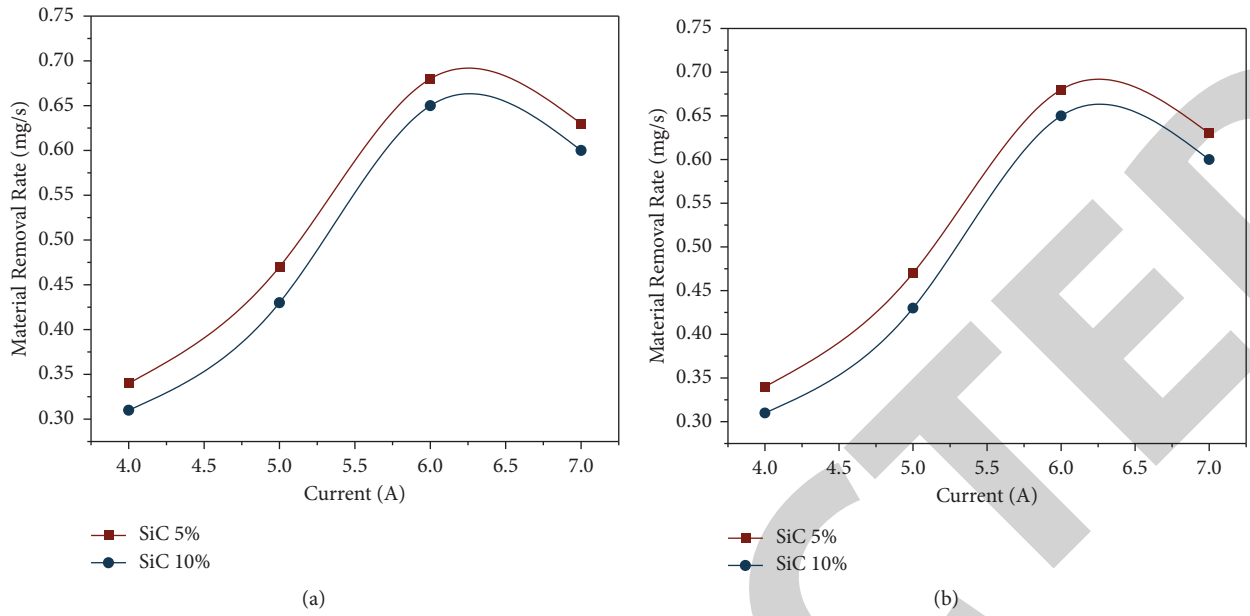


FIGURE 2: (a) Impact of I on material removal rate. (b) Impact of W_s on MRR.

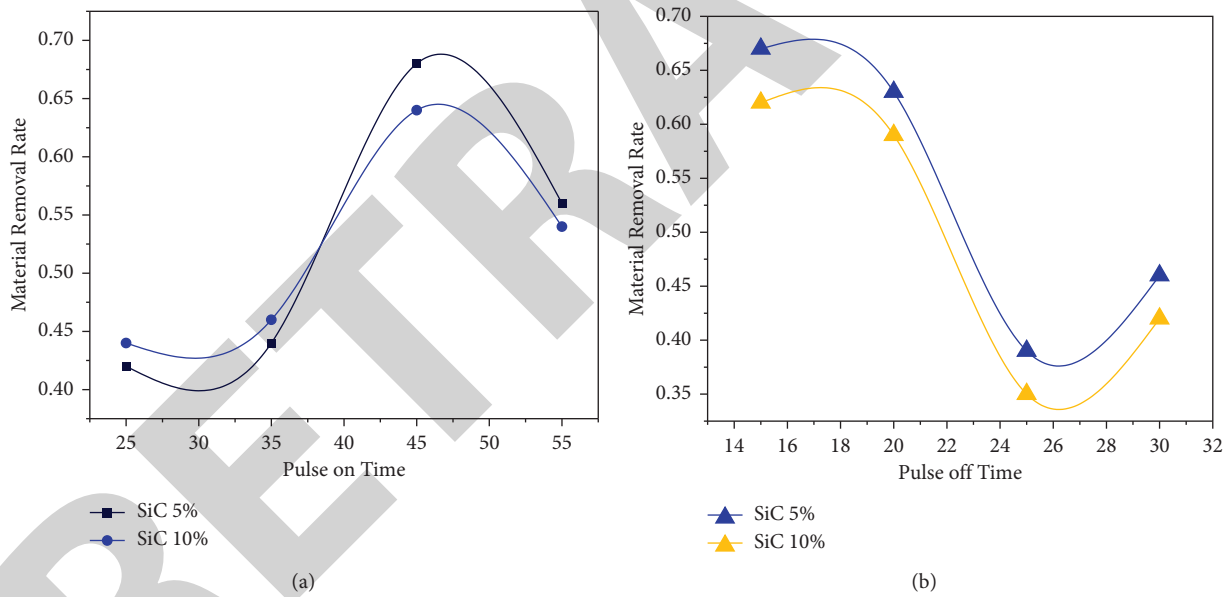


FIGURE 3: (a) Impact of t_{on} on material removal rate. (b) Impact of t_{off} on material removal rate.

the discharge energy increases to its maximum value. When current parameters are exceeded, the quick deposition of wreckage at the machining gap has a substantial effect on dielectric breakdown characteristics and material removal rate. As indicated in the image, wire speed has an impact on MRR, as illustrated in Figure 2(b). When the spool around which the electrode wire is coiled has a rotating speed of 180 to 1440 revolutions per minute, the MRR is indicated in Figure 2(b). The material removal rate rises from 0.382 mg/s to 0.664 mg/s when the spool rotation speed increases up to 720 revolutions per minute. When the spool's rotational speed was increased even further, the MRR was reduced by 10.52%. This is owing to the fact that when wire speed

increases, the quantity of spark energy obtainable for machining declines. Because of this, as wire speeds increase, the MRR falls.

3.2. *The Impact of Pulse-On Time (T_{on}) and Pulse-Off Time (T_{off}) on MRR.* MRR is affected by T_{on} and T_{off} times in Figure 3(a) and Figure 3(b). From 25 to 45s pulse-on time, the MRR was improved. Each spark's energy (E) is equal to $E = VI T_{on}$. As a result, larger craters are formed as a result of a longer pulse-on period. However, the MRR decreased from 0.685 mg/s to 0.582 mg/s when the pulse-on time exceeded 45 s. Longer cycles and lower spark frequencies, as shown in

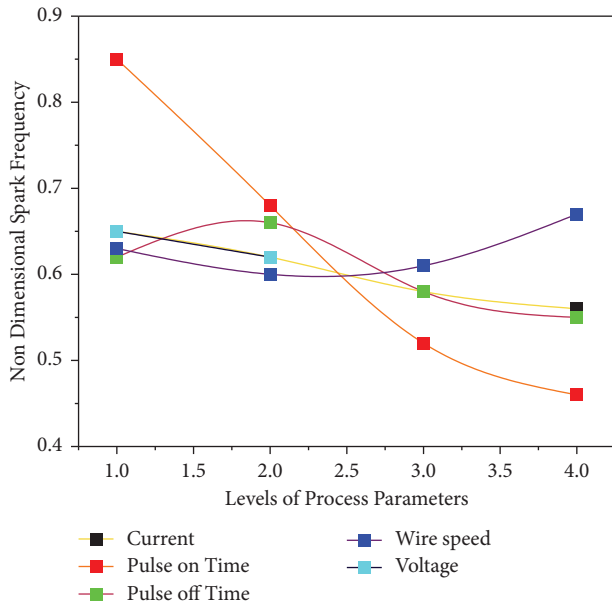


FIGURE 4: Spark frequency at variant levels.

Figure, may have resulted in the reforming of the molten pool surrounding the craters.

A consistent drop in MRR was seen as a result of increasing the pulse-off period from 15 seconds to 30 seconds, as depicted in Figure 4. During the pulse-off period, there is no sparking. As illustrated in Figure 4, growing the pulse time lengthens the cycle while decreasing the spark frequency. The MRR decreased as pulse-off time increased.

3.3. The Impact of Voltage on Material Removal Rate. The impact voltage on material removal rate is shown in Figure 5. MRR appears to be directly influenced by voltage. The MRR rises by 24.45% while the spark gap voltage rises from 90 V to 100 V. V , I , and T_{on} all affect the spark energy ($E = V I t_{on}$), as previously stated. As a result of the increased voltage, a larger volume of material was melted and vaporized, raising the MRR.

As an outcome of the electrical spark among the wire electrode and the substance, the dielectric fluid experiences an abrupt rise in pressure. The holes on the machined surface appear because of the increasing pressure on the molten pool. There are also a few globules of partly molten metal on the machined surfaces.

A few of the SiCp particles may be found on the cut surface of the cast layer, showing that they were relocated during the cutting process. This is because dielectric fluid is circulated during the machining process. To collect the heated reinforced molten particles, dielectric fluid is pumped over the machining surface. As the molten matrix pool hardens, these particles are fused to the machined surface. The majority of the crater looks to have a truncated sphere shape based on these photographs. Using a Gaussian heat distribution model, the predicted spark radius is in agreement with this result. There is an extended feature on the machined surface near the crater boundaries. There is a piece

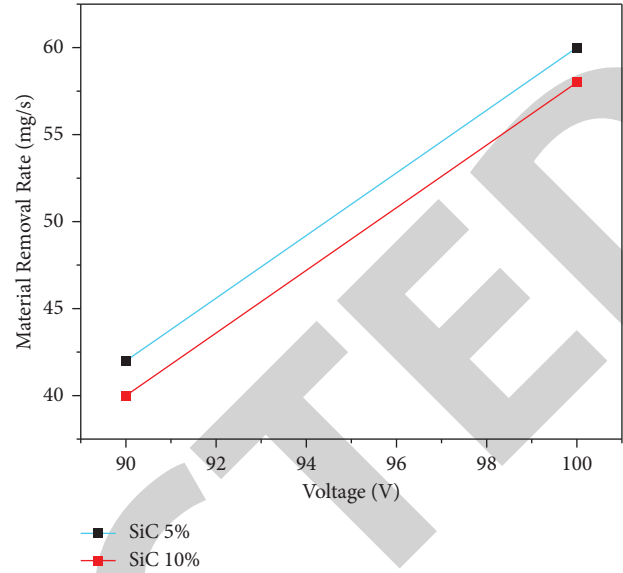


FIGURE 5: The impact voltage on material removal rate.

TABLE 4: ANOVA for material removal rate.

Source	Df	5% SiC			10% SiC		
		Seq SS	Adj MS	F	Seq SS	Adj MS	F
I	3	0.3140	0.1211	58.2	0.3156	0.1052	51.9
T_{on}	3	0.1862	0.0582	34.16	0.1862	0.0724	30.4
T_{off}	3	0.2416	0.0785	45.41	0.2621	0.08512	41.6
W_s	3	0.1440	0.0482	27.23	0.1543	0.0508	25.8
V	2	0.0812	0.0812	47.5	0.0856	0.0856	41.8
Residual error	2	0.0036	0.0019		0.3244	0.114	-
Total	16	0.9412	-	-	-	-	-

of the particle encased in the matrix material, making it more difficult to extract the reinforced SiCp. The spark gap exposes the remaining protruding portion to high temperatures. Sparks and traveling wire electrodes both have a significant impact on reinforced particles, causing shock waves and a mechanical moment. All the SiCp particles remain attached to the machined surface, and there is no evidence of debonding from the matrix. The quick cooling of molten metal and the segregation of alloying elements Mg, Si, etc. are largely responsible for the existence of blow holes. Blow holes are formed on a machined surface by a sparking process in the dielectric medium.

3.4. ANOVA of Material Removal Rate. Table 4 displays the outcomes of the Analysis of Variance for the MRR. Process characteristics that significantly affect MRR can be found utilizing the F-test on the Analysis of Variance data with a 95% confidence level. They have a considerable impact on MRR since their F-values are above critical values for the above variables. The percentage of each process parameter's contribution is also taken into consideration. Among the several factors influencing the rate of material removal, current accounted for the largest

TABLE 5: The mean material removal rate.

Level	I	T _{on}	T _{off}	W _s	V
5% SiC _p					
1	0.324	0.423	0.669	0.579	0.452
2	0.465	0.428	0.632	0.652	0.597
3	0.676	0.679	0.392	0.481	-
4	0.649	0.572	0.412	0.392	-
Delta	0.352	0.264	0.284	0.259	0.152
10% SiC _p					
1	0.322	0.412	0.652	0.385	0.441
2	0.456	0.419	0.619	0.472	0.582
3	0.652	0.662	0.382	0.631	-
4	0.639	0.531	0.416	0.561	-
Delta	0.341	0.251	0.267	0.251	0.152

TABLE 6: The predicted and experimental material removal rate (mg/min) at optimal conditions.

Trial No	5%			10%		
	Predicted MRR	Experimental MRR	Error (%)	Predicted MRR	Experimental MRR	Error (%)
1	71.4	68.4	5.80	68.3	63.4	7.12
2	71.3	67.3	6.70	68.4	62.6	8.01
3	71.4	67.5	4.60	68.4	64.8	6.21
4	71.4	67.4	7.0	68.4	62.4	8.15

share (28.2%), tracked by V (23.04%), T_{off} (22.84%), T_{on} (16.12%), and W_s (13.02%).

3.5. Optimum of Process Parameters. When using wire EDM to machine Al 6063-SiCp composite, the Taguchi approach is used to optimize machining parameters for maximum MRR. Table 5 displays the average MRR based on various process parameter configurations. There is a maximum MRR at settings A₃B₃C₁D₂E₂, i.e., I at level 3 (6 A), T_{on} at level 3 (45 s), T_{off} at level 1, W_s set to the level of 3, and voltage set to 100 V, as shown in the following table (level 2). For samples containing 5% and 10% SiCp, the anticipated MRR is 68.23 mg/min and 68.16 mg/min, respectively. Table 6 displays the findings of the confirmation trials, which were also carried out. Experiments have shown that MRR is consistent with the model's predictions. This table also shows the greatest change (delta) in MRR resulting from changes in the settings of a variety of processes. The processing factors are sorted in terms of current impact based on delta values: I, II, III, IV, and V are the pulse-off and pulse-on times, as well as the wire speed.

3.6. Regression Modeling of Material Removal Rate. In this area, we will go through the specifics of creating a statistical model that can be used to estimate MRR based on a variety of process parameter values. I, T_{on}, T_{off}, w_s, I_v, and the material removal rate are established by using a statistical model. The modeling takes into account the primary impact of these variables. As shown in (9), the regression model generated for samples with 5% and 10% SiCp can be expressed as (10). The equation has a 73.6% coefficient of determination (R²).

$$y = c + k_1 \times x_1 + k_2 \times x_2 + \dots + k_n \times x_n, \quad (9)$$

$$\begin{aligned} \text{Material Removal Rate} = & -1.20 + 0.114 \times I + 0.00685 \\ & \times t_{on} - 0.0194 \times t_{off} + 0.000135 \\ & \times w_s + 0.0142 \times I_v. \end{aligned} \quad (10)$$

The accurateness of forecasting material removal rate by regression model is evaluated by directing confirmation experiments up to the limits of operating factors, that is, $4 \leq I \leq 7$; $25 \leq t_{on} \leq 55$; $15 \leq t_{off} \leq 30$; $380 \leq w_s \leq 1440$; $90 \leq I_v \leq 100$. Test samples with a 5% and a 10% MRR have been found to have similar actual MRR values. There is a 4.45% minimal and a mean prediction error material removal rate, respectively. 2.19 standard deviations from the mean indicate a significant deviation. Table 6 depicts the predicted and experimental material removal rate (mg/min) at optimal conditions.

4. Conclusions

This analysis examined the impact of factors including I, t_{on}, t_{off}, w_s, I_v on processing of 5 wt% to 10 wt% SiC_p – Al 6063 alloys by wire electrical discharge machining. It is possible to increase the productivity of wire EDM companies by using the optimal settings to increase the MRR when working with these composites. Results have led to the following conclusions.

- (i) MRR was significantly influenced and rose by current, pulse-on time, pulse-off time, wire speed, and voltage but declined with rising pulse-off time and also wire speed over 720 rpm.

- (ii) The voltage (23.04%), pulse-on time (22.86%), pulse-off time (16.12%), and wire speed all contributed to MRR fluctuation to a lesser extent than the current (28.2%) wire speed (13.04%).
- (iii) The optimal setup which formed the greatest material removal rate (66.32 mg/min and 62.41mg/min for samples with 5% and 10% SiC_p) is current –6A, Pulse on time – 45 μ s, Pulse off time – 15 μ s, wire speed – 720rpm, and voltage-100 V.
- (iv) It is possible to estimate the MRR in wire EDM of Al 6063 with SiC, -p. up to 10 wt% within the operational range using the statistical model (mean, R²-73.65%).
($4A \leq I \leq 7A$; $25\mu s \leq t_{on} \leq 55\mu s$; $15\mu s \leq t_{off} \leq 30\mu s$; $380rpm \leq w_s \leq 1440rpm$; $90V \leq I_v \leq 100V$). The proposed regression model's MRR prediction error ranges from 4.45% to 20.46%.

Data Availability

The data used to support the findings of this study are included within the article. Further data or information are available from the corresponding author upon request.

Conflicts of Interest

The authors declare that there are no conflicts of interest regarding the publication of this paper.

Acknowledgments

The authors appreciate the support from Arba Minch University, Ethiopia, for the research and preparation of the manuscript. The authors thank Dr. Ambedkar Institute of Technology, M. S. Ramaiah Institute of Technology, and Sri Vasavi Institute of Engineering and Technology for providing assistance to complete this experimental work.

References

- [1] R. Ramesh, S. Suresh Kumar, D. Purushothaman, and N. T. Jeeva, "Performance study on copper coated tool using powder mixed EDM of monel 400," *Applied Mechanics and Materials*, vol. 766-767, pp. 600–605, 2015.
- [2] A. Perumal, C. Kailasanathan, B. Stalin et al., "Multiresponse optimization of wire electrical discharge machining parameters for Ti-6Al-2Sn-4Zr-2Mo (α - β) alloy using taguchi-grey relational approach," *Advances in Materials Science and Engineering*, vol. 2022, Article ID 690523, 13 pages, 2022.
- [3] M. A. Rahman, A. Ahmed, and M. Mia, "Trends in electrical discharge machining of Ti- and Ni-based superalloys: macro-micro-compound arc/spark/melt process," *Micro Electro-Fabrication*, Elsevier, vol. 2021, pp. 63–87, 2021.
- [4] J. Boban, A. Ahmed, M. A. Rahman, and M. Rahman, "Wire electrical discharge polishing of additive manufactured metallic components," *Procedia CIRP*, vol. 87, pp. 321–326, 2020.
- [5] V. Mohanavel and M. Ravichandran, "Influence of AlN particles on microstructure, mechanical and tribological behaviour in AA6351 aluminum alloy," *Materials Research Express*, vol. 6, no. 10, Article ID 1065, 2019.
- [6] R. Chaudhari, S. Khanna, J. Vora et al., "Experimental investigations and optimization of MWCNTs-mixed WEDM process parameters of nitinol shape memory alloy," *Journal of Materials Research and Technology*, vol. 15, pp. 2152–2169, 2021.
- [7] P. Sivaprakasam, P. Hariharan, and S. Gowri, "Optimization of micro-WEDM process of aluminum matrix composite (A413-B4C): a response surface approach," *Materials and Manufacturing Processes*, vol. 28, no. 12, pp. 1340–1347, 2013.
- [8] H. Hocheng, W. T. Lei, and H. S. Hsu, "Preliminary study of material removal in electrical-discharge machining of SiC/Al," *Journal of Materials Processing Technology*, vol. 63, no. 1–3, pp. 813–818, 1997.
- [9] B. Singh, J. Kumar, and S. Kumar, "Influences of process parameters on MRR improvement in simple and powder-mixed EDM of AA6061/10% SiC composite," *Materials and Manufacturing Processes*, vol. 30, no. 3, pp. 303–312, 2015.
- [10] A. Kumar Sharma, R. Bhandari, A. Aherwar, and C. Pinca-Bretotean, "A study of fabrication methods of aluminum based composites focused on stir casting process," *Materials Today Proceedings*, vol. 27, pp. 1608–1612, 2020.
- [11] V. Mohanavel, S. Suresh Kumar, V. Sivaraman, V. K. Girish, and M. Ravichandran, "Tungsten carbide particulate reinforced AA7050 aluminum alloy composites fabricated by liquid state processing," *AIP Conference Proceedings*, vol. 2283, Article ID 020087, 2020.
- [12] M. Ravichandran, V. Mohanavel, T. Sathish, P. Ganeshan, S. Suresh Kumar, and S. Ram, "Mechanical properties of AlN and molybdenum disulfide reinforced aluminium alloy matrix composites," *Journal of Physics: Conf. Ser.*, vol. 2027, Article ID 012010, 9 pages, 2021.
- [13] P. N. Singh, K. Raghukandan, M. Rathinasabapathi, and B. C. Pai, "Electric discharge machining of Al-10% SiCP as-cast metal matrix composites," *Journal of Materials Processing Technology*, vol. 155, pp. 1653–1657, 2004.
- [14] S. S. Habib, "Study of the parameters in electrical discharge machining through response surface methodology approach," *Applied Mathematical Modelling*, vol. 33, no. 12, pp. 4397–4407, 2009.
- [15] S. S. Agrawal and V. Yadava, "Modeling and prediction of material removal rate and surface roughness in surface-electrical discharge diamond grinding process of metal matrix composites," *Materials and Manufacturing Processes*, vol. 28, no. 4, pp. 381–389, 2013.
- [16] S. Singh and A. Bhardwaj, "Review to EDM by using water and powder-mixed dielectric fluid," *Journal of Minerals and Materials Characterization and Engineering*, vol. 10, no. 2, pp. 199–230, 2011.
- [17] S. S. Sidhu, A. Batish, and S. Kumar, "Study of surface properties in particulate-reinforced metal matrix composites (MMCs) using powder-mixed electrical discharge machining (EDM)," *Materials and Manufacturing Processes*, vol. 29, no. 1, pp. 46–52, 2014.
- [18] A. Dey, S. Debnath, and K. M. Pandey, "Optimization of electrical discharge machining process parameters for Al6061/cenosphere composite using grey-based hybrid approach," *Transactions of Nonferrous Metals Society of China*, vol. 27, no. 5, pp. 998–1010, 2017.
- [19] S. S. Kumar, M. Uthayakumar, S. T. Kumaran, and P. Parameswaran, "Electrical discharge machining of Al (6351)-SiC-B4C hybrid composite," *Materials and Manufacturing Processes*, vol. 29, no. 11–12, pp. 1395–1400, 2014.

Retraction

Retracted: Optimization of the Spark Plasma Sintering Process for High-Volume Fraction Tungsten Carbide/Al 2025 Composites

Advances in Materials Science and Engineering

Received 20 June 2023; Accepted 20 June 2023; Published 21 June 2023

Copyright © 2023 Advances in Materials Science and Engineering. This is an open access article distributed under the Creative Commons Attribution License, which permits unrestricted use, distribution, and reproduction in any medium, provided the original work is properly cited.

This article has been retracted by Hindawi following an investigation undertaken by the publisher [1]. This investigation has uncovered evidence of one or more of the following indicators of systematic manipulation of the publication process:

- (1) Discrepancies in scope
- (2) Discrepancies in the description of the research reported
- (3) Discrepancies between the availability of data and the research described
- (4) Inappropriate citations
- (5) Incoherent, meaningless and/or irrelevant content included in the article
- (6) Peer-review manipulation

The presence of these indicators undermines our confidence in the integrity of the article's content and we cannot, therefore, vouch for its reliability. Please note that this notice is intended solely to alert readers that the content of this article is unreliable. We have not investigated whether authors were aware of or involved in the systematic manipulation of the publication process.

Wiley and Hindawi regrets that the usual quality checks did not identify these issues before publication and have since put additional measures in place to safeguard research integrity.

We wish to credit our own Research Integrity and Research Publishing teams and anonymous and named external researchers and research integrity experts for contributing to this investigation.

The corresponding author, as the representative of all authors, has been given the opportunity to register their agreement or disagreement to this retraction. We have kept a record of any response received.

References

- [1] C. R. Mahesha, C. Polayya, M. L. Rinawa et al., "Optimization of the Spark Plasma Sintering Process for High-Volume Fraction Tungsten Carbide/Al 2025 Composites," *Advances in Materials Science and Engineering*, vol. 2022, Article ID 6433716, 7 pages, 2022.

Research Article

Optimization of the Spark Plasma Sintering Process for High-Volume Fraction Tungsten Carbide/Al 2025 Composites

C. R. Mahesha,¹ Suprabha R,¹ Chintada Polayya,² Moti Lal Rinawa,³ T. Sakthi,⁴ Neha Munjal,⁵ Ishwarya Komalnu Raghavan ,⁶ P. Ganeshan,⁷ and Chanakyan C⁸

¹Department of Industrial Engineering & Management, Dr. Ambedkar Institute of Technology, Bangalore, Karnataka 560056, India

²Department of Mechanical Engineering, Lendi Institute of Engineering and Technology, Vizianagaram, Andhra Pradesh 535005, India

³Department of Mechanical Engineering, Government Engineering College, Jhalawar, Rajasthan 326023, India

⁴Department of Mechanical Engineering, National Engineering College, Kovilpatti, Tamil Nadu 628503, India

⁵Department of Physics, Lovely Professional University, Phagwara, Punjab 144411, India

⁶Department of ElectroMechanical Engineering, Faculty of Manufacturing, Institute of Technology, Hawassa University, Hawassa, Ethiopia

⁷Department of Mechanical Engineering, Sri Eshwar College of Engineering, Coimbatore, Tamil Nadu 641202, India

⁸Department of Mechanical Engineering, Government College of Engineering, Thanjavur, Tamilnadu 613402, India

Correspondence should be addressed to Ishwarya Komalnu Raghavan; ishwarya138@hu.edu.et

Received 19 March 2022; Accepted 30 May 2022; Published 29 June 2022

Academic Editor: Palanivel Velmurugan

Copyright © 2022 C. R. Mahesha et al. This is an open access article distributed under the Creative Commons Attribution License, which permits unrestricted use, distribution, and reproduction in any medium, provided the original work is properly cited.

With an orthogonal experimental design, Spark plasma sintering method was used to create tungsten carbide with Al 2025 composites. Pressure, temperature, and hold time all had an influence on the mechanical characteristics of the composites. Pressure had the greatest effect on density and bending strength, followed by temperature and holding duration. After five minutes of sintering at 556°C under 40 MPa, a 50% tungsten carbide/Al 2025 composite material was produced, resulting in a density of 997.7 percent and a spectacular bending strength of 766.65 MPa. This study revealed the ability of high-volume fraction mixes to support huge loads.

1. Introduction

In addition to Si₃N₄, SiO₂, Al₂O₃, B₄C/Al, TiC, and WC, PAMCs have been researched, for their outstanding mechanical, chemical, and electrical qualities [1, 2]. As a result of their extraordinary dimensional stability, high specific modulus mixtures have developed more significantly in the aviation and microelectronics productions [3–5]. Squeeze or stir casting, pouring, power metallurgy, hot pressing, and pressure less infiltration have all been employed to create silicon carbide particle/2xxx aluminium composites [6, 7]. With these processes, it is difficult to limit pores, control bonding and reactivity between interfaces, and produce composite materials with huge volumes [8]. Experiment

failed to eradicate the holes that affect mechanical behavior to decline meaningfully due to high temperatures and lengthy vacuum hot pressing holding times. The tensile properties of hot-pressed tungsten carbide particles/2009 aluminium mixtures were examined by the authors [9] in this paper.

Spark plasma sintering seems to be a pressure-assisted pulsed-current method in which powders are put into an electrically conducting die and fused under pressure gradient. The Spark plasma sintering technique may be employed to produce composite materials with low porosity and good mechanical characteristics [10, 11]. This process has a greater heating rate than standard preparation methods, a lower preparation temperature, and quick

densification of the composite materials [12]. Improved interfacial bonding, cleaner surfaces, and smaller particle sizes are all advantages of SPS. To make 50 percent WC/6061Al composites, the authors in [13, 14] utilised Spark plasma sintering technology. Because of its 99.15 percent density and excellent interfacial attachment among the Al matrix and the tungsten carbide, it possessed a bending strength of 694 MPa. These composites were created by [15] using SPS to manufacture high-density 40 to 55 vol% tungsten carbide particles/pure aluminium composites with densities more than 99 percent [16, 17].

In Taguchi's multifactor orthogonal experimental design, the orthogonal array serves as the foundation [18–20]. It is easy to pick sample points that are equally dispersed across the whole factor test for optimum results in multifactor research. To further understand Spark plasma sintering preparation processing factors for TiB₂-silicon carbide ceramic materials, a total of four treatment variables at three orthogonal experimental design degrees were examined [21, 22]. Vickers hardness was determined to be 28.5 GPa at the ideal processing conditions for this composite. In addition to reducing the number of experiments, this method produces data that can be understood by everyone [23]. The impact of processing parameters on HfB₂, Al₂O₃, ZrB₂-based ceramics, and phenolic fibre has been widely explored in the literature using orthogonal experimental design [24, 25]. The manufacturing of 50 vol percent tungsten carbide/2025Al composites has not yet been reported by Spark plasma sintering through orthogonal experimental design. tungsten carbide/2025Al/SiC composites with large volume proportions of SiC were the focus of this research, and mechanical study was employed to explore the mechanical characteristics of the composite material [26–28]. It was feasible to compare the effects of various factors on the best sintering conditions for 50 vol percent tungsten carbide/2025Al composites using orthogonal experimental design (such as temperature, pressure, and holding time) [29]. In addition to high-volume fraction composite materials, this method's intelligence may be used to other high-volume proportion materials [30].

2. Materials and Methods

2.1. Materials. Tungsten carbide and 2025Al powders with particle sizes of 10 micron were employed as starting materials. Its chemical makeup is composed of Al and 4.7 percent Cu with the remainder being composed of 0.9 percent Mg, 0.6% iron, 0.6% silicon, and just 0.1% magnesium (mass fraction). Utilizing a 3:1 ball-to-powder weightage ratio in a zirconia tank, planetary ball mixing machine ran at 280 rpm for 2 hours to mix the tungsten carbide and 2025 Al particles. Particle fracture or Al flaking was not evident in either powder when comparing tungsten carbide with 2025Al powders. The combined powder was sintering in a graphite mould that had been precompressed at 10 MPa for 5 minutes with a Spark plasma sintering device. To assess the relative importance of various variables during SPS, an orthogonal table is created (Table 1). Although the infrared thermometer's lowest measurement

TABLE 1: The orthogonal experimental design's factors and levels.

Level	A	B	C
1	500	3	25
2	525	4	35
3	550	5	45

temperature was 100°C, the instrument reported 100°C when the mold's temperature fell below the required minimum.

2.2. Characterization and Evaluation. With the use of a universal testing apparatus, samples measuring 3 × 4 × 36 mm were tested for an average bending rate of 0.25 mm/min. An electronic analytical balance was employed to calculate the density of the composite. For the compactness and bending tests, a minimum of five samples were employed [31].

3. Results and Discussion

3.1. Analyzing Orthogonal Experiment. The L9 table was designated because of its orthogonal design and its three sintering temperatures, holding time, and pressure levels. Table 2 reveals the analysed results of the L9 orthogonal array. With K_{ij} ($i = 1, 2, 3$) and R as key factors, the orthogonal experiment is evaluated using the evaluation indices listed in Table 3. In order to compute R , which is the difference between highest and lowest values in relevant aspect column, K_{\max} and K_{\min} values are utilised. K_{ij} is the average of the test scores at the j^{th} grade level ($j = 1, 2, 3$). The best factor level will be determined by associating K values. The R value can indicate how much the K value varies.

WC/Al will function better if it has a larger density and flexural strength; consequently, the greatest K value should be used. It was determined that A2 (525°C), B1 (3 minutes), and C2 (35 MPa) were the best parameters for producing a dense composite (35 MPa). These are the best parameters for enhancing the bending strength. Various influences on the WC/2025Al composite are represented by the R value. Bending strength and density were most affected by the sintering pressure, surveyed by the holding duration and sintering pressure, in this study, $B < A < C$.

Orthogonal test analysis cannot predict inaccuracy in testing since it does not know how much each element has changed or whether there has been a random fluctuation in findings, in spite of its simplicity. This is a concern that is often overlooked in orthogonal studies. The test findings were subjected to an analysis of variance in order to address this issue. SPSS Statistics was used to conduct the experimental variance analyses.

The significance of each component was evaluated at the $P = 0.05$ level of consequence for each individual. To be deemed significant, the test index must have an effect on the P value of less than 0.05. A , B , and C can explain 85.4% of the density variation in table, which demonstrates that $R_2 = 0.854$. Temperature, time, and pressure may account for 88% of the density change during sintering according to

TABLE 2: Analyzing the results of the L9 orthogonal array.

S. No.	A	B	C	Density (g/cm ³)	Relative density (%)	Bending strength (MPa)
1	1	1	1	2.85	96.8	692.42 ± 25.52
2	1	2	2	2.90	98.4	738.12 ± 46.27
3	1	3	3	2.90	98.4	712.87 ± 82.52
4	2	1	3	2.89	98.8	759.25 ± 12.12
5	2	2	1	2.79	96.7	632.17 ± 20.04
6	2	3	2	2.91	99.1	767.75 ± 24.82
7	3	1	2	2.92	97.2	692.24 ± 56.72
8	3	2	3	2.99	99.4	710.26 ± 71.65
9	3	3	1	2.91	94.6	586.42 ± 9.72

TABLE 3: Calculation indices of the L9 orthogonal array.

Orthogonal array	A	B	C
<i>Density</i>			
K ₁₁	2.94	2.90	2.85
K ₁₂	2.91	2.90	2.92
K ₁₃	2.88	2.91	2.93
R	0.03	0.02	0.06
Level of optimum	A ₂	B ₃	C ₃
<i>Bending strength</i>			
K ₁₁	709.1	709.26	632.42
K ₁₂	716.12	692.42	732.87
K ₁₃	658.18	691.27	726.34
R	51.83	22.94	93.62
Level of optimum	A ₂	B ₁	C ₂

R₂ = 0.984%. F = 1.891; P = 0.346; P = 0.159; and F = 5.307; P = 0.159; bending strength was not changed by the sintering temperature. Sintering time F = 0.388; P = 0.721. An error of this magnitude (df = 2) and a low degree of freedom (df = 2) meant that the test was ineffective in distinguishing between variables of interest. ANOVA a higher sum of squares (SS) shows a bigger effect. C > A > B: density and bending strength were most strongly influenced by sintering pressure, whereas the holding time had the least impact.

Before a single index analysis approach is utilised to discover and optimise the complete scheme, the average weighting methodology is often employed to address multi-index orthogonal test concerns. The findings of the study are wrong since this method fails to take into account the differences and relative weights of the various indicators. As a result, the matrix approach was developed to quantify the degree to which each test aspect influences each directory and to swiftly establish the major and minor order of the components based on the weights. With this method, the issue of determining the best design for multi-index orthogonal tests is eliminated. The data are first organized into a three-tiered structural model. Experimentation index layer, component layer, and the flat layer make up the three layers (S). The formulas are given in equations (1)–(3), correspondingly, where $T_i = 1 / \sum_{j=1}^3 K_{ij}$ and $S_i = R_j / \sum_{i=1}^3 R_{ij}$.

$$M = \begin{pmatrix} K_{11} & 0 & 0 \\ K_{12} & 0 & 0 \\ K_{13} & 0 & 0 \\ 0 & K_{21} & 0 \\ 0 & K_{22} & 0 \\ 0 & K_{23} & 0 \\ 0 & 0 & K_{31} \\ 0 & 0 & K_{32} \\ 0 & 0 & K_{33} \end{pmatrix}, \quad (1)$$

$$T = \begin{pmatrix} T_1 & 0 & 0 \\ 0 & T_2 & 0 \\ 0 & 0 & T_3 \end{pmatrix}, \quad (2)$$

$$S^T = [S_1 \ S_2 \ S_3]. \quad (3)$$

According to equation, the weight matrix (k) which influences the assessment index is listed in the following equation:

$$k = MxTxS, \quad (4)$$

$$k^T = [k_1 \ k_2 \ k_3].$$

Density was the first sign of success in this endeavor. Equations (5)–(8) demonstrate that to compute the weight matrix (8),

$$M = \begin{pmatrix} 2.93 & 0 & 0 \\ 2.94 & 0 & 0 \\ 2.90 & 0 & 0 \\ 0 & 2.92 & 0 \\ 0 & 2.92 & 0 \\ 0 & 2.93 & 0 \\ 0 & 0 & 2.87 \\ 0 & 0 & 2.94 \\ 0 & 0 & 2.95 \end{pmatrix}, \quad (5)$$

$$T = \begin{pmatrix} \frac{1}{8.72} & 0 & 0 \\ 0 & \frac{1}{8.80} & 0 \\ 0 & 0 & \frac{1}{8.78} \end{pmatrix}, \quad (6)$$

$$S^T = \begin{bmatrix} 0.04 & 0.01 & 0.08 \\ 0.13 & 0.13 & 0.13 \end{bmatrix}, \quad (7)$$

$$k_D = MxTxS = \begin{bmatrix} 0.1034 \\ 0.1037 \\ 0.1023 \\ 0.0255 \\ 0.0255 \\ 0.0256 \\ 0.1006 \\ 0.2061 \\ 0.2068 \end{bmatrix}, \quad (8)$$

$$k_{BS} = \begin{bmatrix} 0.1069 \\ 0.1075 \\ 0.0990 \\ 0.0454 \\ 0.0439 \\ 0.0437 \\ 0.0949 \\ 0.1956 \\ 0.1940 \end{bmatrix}. \quad (9)$$

The weightage matrix of the five pointers that passed the OED test is the sum of $K-D$ and $K-BS$, assuming that the outcomes of these five indicators are of equal importance. The results of the computations may be seen in equation (1).

$$k = \frac{k_d + k_{bs}}{2} = \begin{bmatrix} 0.1052 \\ 0.1056 \\ 0.1007 \\ 0.0354 \\ 0.0347 \\ 0.0347 \\ 0.0977 \\ 0.2008 \\ 0.2004 \end{bmatrix} \quad (10)$$

$$= \begin{bmatrix} A_1 \\ A_2 \\ A_3 \\ B_1 \\ B_2 \\ B_3 \\ C_1 \\ C_2 \\ C_3 \end{bmatrix}.$$

Factor A1 is 0.1052, Factor A2 is 0.1056, and Factor A3 is 0.1007; A2 is the most significant factor in the test results. Using the same kind of analysis, B1 and C2 have the greatest weights. As a result, the ideal orthogonal test scheme is $A_2B_1C_2$, which means that the optimal WC/2025Al sintering process parameters are 550 C, 3 min of holding time, and 45 MPa of pressure. According to [32], TiN materials were synthesized at different temperatures in the radial direction of the specimen. Due to the high temperature at the material's centre, SPS can make Al matrix composites with electrically isolating reinforcing elements. Al will be expelled from the mould with a colossal number of holes after it is taken from the mould. Low speed (500 rpm) and zirconia as the grinding medium and container guaranteed that the particles remained in their original form and did not introduce any impurities into the environment.

High mechanical characteristics may be achieved by combining reinforcement with Al matrix in PAMCs at the right interfacial interface. High temperatures and pressures are commonly used in traditional techniques (such as extrusion and stirring casting) to make WC/Al composites; however, this is because the two materials have limited wettability. Brittle reactants like Al_4C_3 and $MgAl_2O_4$ are common because of this. Remarkably, the material properties, thermal conductivity, and resistance to abrasive corrosion are all affected by the hydrolysis of the flake-shaped Al_4C_3 . No other current methods for preventing the production of Al_4C_3 have a negative impact on densities (such as reducing processing temperatures and holding times) or performance (such as adding Mg or Si or doing a pre-oxidation treatment with WC). Low temperature, short-term preparation methods such as SPS have been described in the literature as being capable of producing more easily interfacial products-free composites, according to the literature.

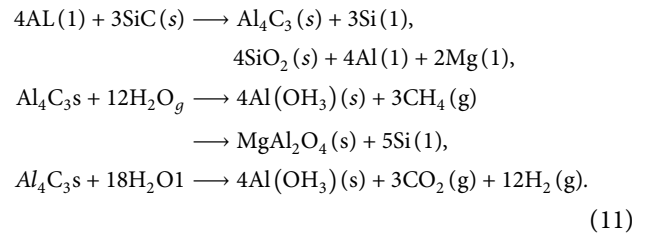


Figure 1 depicts WC/2025Al composites with variant SPS preparation circumstances. A summary of its entire behavior is seen in Table 2.

When heated to 525°C for five minutes under 35 MPa, the material had a bending strength of 766.65 Mega Pascal ($A_2B_3C_2$). Sintering at 550°C for 5 minutes under 30 MPa ($A_3B_3C_1$) reduced the mixture's bending strength (584.83 mpa) and elasticity ($A_3B_3C_1$) due to the material's large holes. WC/Al 2025 amalgamated density and contact configurations are affected by the sintering temperature, according to Yu and colleagues. Because of the alloy leakage, the density of the material reduced to around 96%, and the strength decreased from 367 to 211 MPa at 530°C. Figures 2(a) and 2(b) display density and bending strength values in the form of graph. After 2 minutes of holding time, the density of WC/Al 2025 went from

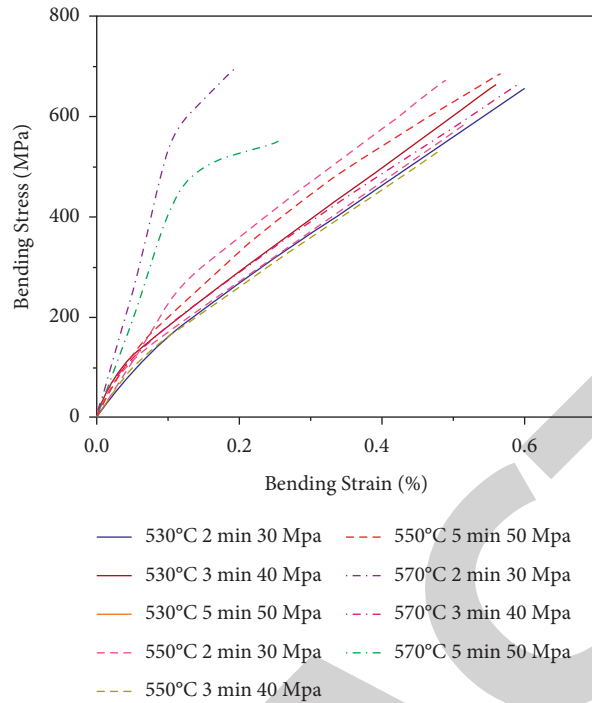


FIGURE 1: Bending curves of the 50 percent WC/Al 2025 composites made by Spark plasma sintering through variant conditions.

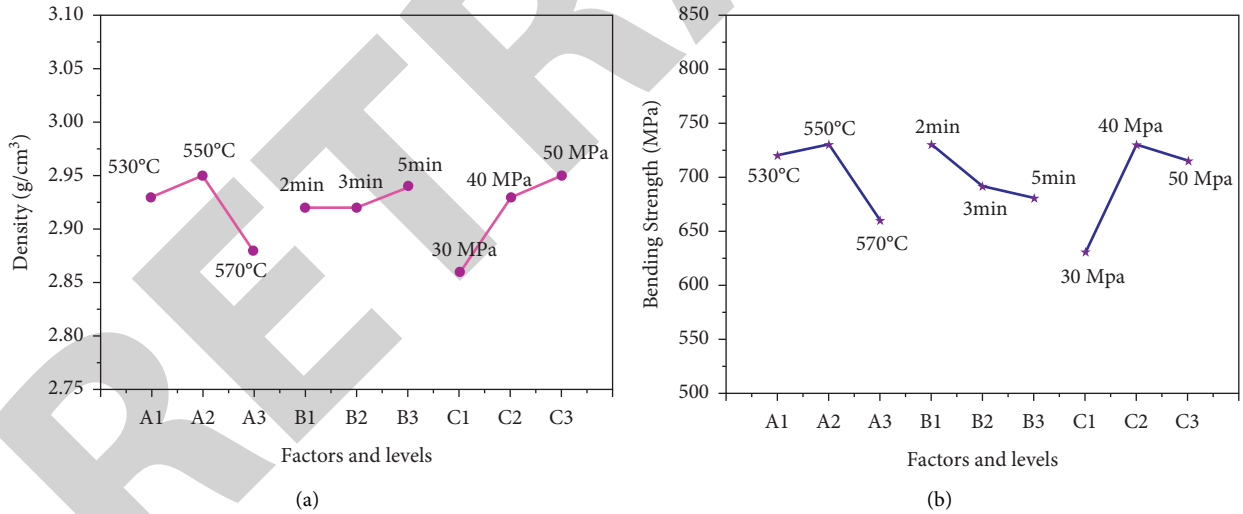


FIGURE 2: Impact factors of (a) density and (b) ending strength.

2.93 g/cm³ to 2.94 g/cm³, which may be ascribed to the molten Al filling the space between the WC and filling the larger holes, but not filling smaller ones. An increase in density of 2.90 g/cm³ occurred as the sintering temperature reached 570°C. Bending strength declined from 713.93 MPa to 692.45 MPa, a 3.2 percent drop, and the composites' density was 2.92 g/cm³ after two and three minutes of holding. However, holding for 5 minutes,

bending strength dropped to 692.45 Mega Pascal, while density raised to 2.95 g/cm³. The test's sensitivity might have been low due to the experiment's low degree of freedom and large error. A 40 MPa boost to the sintering pressure improves density by 0.34 percent but reduces bending strength by 0.80 percent. Figure 3 shows the comparison between WC/Al composite bending strength and temperature preparation.

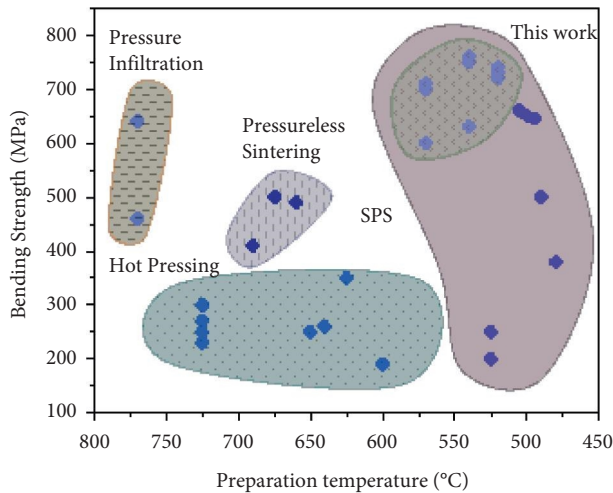


FIGURE 3: A comparison between WC/Al composite bending strength and temperature preparation.

4. Conclusions

A 50 vol% tungsten carbide/Al 2025 composite was made using Spark plasma sintering in this investigation. When performing visual, ANOVA, and matrix analyses, orthogonal experimental design was employed to find the best possible combination of each index. The following findings can be drawn from this investigation:

- (1) The sintering pressure, temperature, and holding time have most impact on SPS density and bending strength. Density and strength increase first when pressure and temperature rise.
- (2) On five minutes run at 525°C and 35 MPa produced a tungsten carbide/Al 2025 combination with a 99.7% density and 766.65 MPa bend strength. The developed composite material had no brittle interfacial products, the Al matrix was equally dispersed, and the interface was strongly bound. The tungsten carbide particles in the material shattered, allowing the particles to be drawn out, causing the material to fracture.

Data Availability

The data used to support the findings of this study are included within the article. Further data or information are available from the corresponding author upon request.

Conflicts of Interest

The authors declare that there are no conflicts of interest regarding the publication of this paper.

Acknowledgments

The authors appreciate the supports from Hawassa University, Ethiopia, for the research and preparation of the manuscript. The authors thank to Dr. Ambedkar Institute of Technology, Lendi Institute of Engineering and technology,

Government Engineering College for providing assistance to complete this experimental work.

References

- [1] V. Mohanavel, M. Ravichandran, M. M. Ravi Kumar, S. Suresh Kumar, S. Mahendran, and L. Yaswanth, "Nathan tribological and mechanical behaviour composites fabricated via compo casting, stir casting and in-situ casting an overview," *Journal of the Balkan Tribological Association*, vol. 25, no. 2, pp. 342–352, 2019.
- [2] N. Pourmohammadie Vafa, B. Nayebi, M. Shahedi Asl, M. Jaber Zamharir, and M. Ghassemi Kakroudi, "Reactive hot pressing of ZrB₂-based composites with changes in ZrO₂/SiC ratio and sintering conditions. Part II: mechanical behavior," *Ceramics International*, vol. 42, no. 2, pp. 2724–2733, 2016.
- [3] M. L. Bharathi, S. Adarsh Rag, L. Chitra, R. Mohammed Ashick, V. Tripathi, and S. Suresh Kumar, "Sami Al obaid, saleh alfarraj, mohanraj murugesan, ishwarya Komalnu raghavan, "investigation on wear characteristics of az91d/nanoalumina composites," *Journal of Nanomaterials*, vol. 2022, Article ID 2158516, 9 pages, 2022.
- [4] G. Wang, X. Ma, T. Hu, and D. Zhang, "Experimental and analytical study on factors influencing biomimetic undulating fin propulsion performance based on orthogonal experimental design," *Advanced Robotics*, vol. 27, no. 8, pp. 597–609, 2013.
- [5] V. Mohanavel, M. Ravichandran, S. Suresh Kumar, M. Melwin Jagadeesh Sridhar, S. Dineshkumar, and M. M. Pavithra, "Microstructural and tribological characterization of Al/EGG shell ash composites prepared by liquid metallurgy process," *Journal of the Balkan Tribological Association*, vol. 26, no. 2, pp. 319–326, 2020.
- [6] Z. Ahmadi, B. Nayebi, M. Shahedi Asl, I. Farahbakhsh, and Z. Balak, "Densification improvement of spark plasma sintered TiB₂-based composites with micron-, submicron- and nano-sized SiC particulates," *Ceramics International*, vol. 44, no. 10, pp. 11431–11437, 2018.
- [7] H. Yu, W. Wang, J. Liu, W. Tang, and Y. Wu, "Effect of porosity and interface structures on thermal and mechanical properties of WC/6061Al composites with high volume fraction of SiC," *Transactions of Nonferrous Metals Society of China*, vol. 29, no. 5, pp. 941–949, 2019.
- [8] H. Jiang, Z. Xu, Z. Xiu et al., "Effects of pulse conditions on microstructure and mechanical properties of Si₃N₄/6061Al composites prepared by spark plasma sintering (SPS)," *Journal of Alloys and Compounds*, vol. 763, pp. 822–834, 2018.
- [9] K. Chu, C. Jia, W. Tian, X. Liang, H. Chen, and H. Guo, "Thermal conductivity of spark plasma sintering consolidated SiCp/Al composites containing pores: numerical study and experimental validation," *Composites Part A: Applied Science and Manufacturing*, vol. 41, no. 1, pp. 161–167, 2010.
- [10] S. Meir, S. Kalabukhov, N. Froumin, M. P. Dariel, and N. Frage, "Synthesis and densification of transparent magnesium aluminate spinel by SPS processing," *Journal of the American Ceramic Society*, vol. 92, no. 2, pp. 358–364, 2009.
- [11] K. Mizuuchi, K. Inoue, Y. Agari, T. Nagaoka, and M. Sugioka, "Processing of Al/SiC composites in continuous solid-liquid co-existent state by SPS and their thermal properties," *Composites Part B: Engineering*, vol. 43, no. 4, pp. 2012–2912, 2012.

Retraction

Retracted: Thermal Conductivity of Thermally Insulated Concretes in a Nuclear Safety Vessel of Reactor Vault: Experimental Interpretation

Advances in Materials Science and Engineering

Received 26 December 2023; Accepted 26 December 2023; Published 29 December 2023

Copyright © 2023 Advances in Materials Science and Engineering. This is an open access article distributed under the Creative Commons Attribution License, which permits unrestricted use, distribution, and reproduction in any medium, provided the original work is properly cited.

This article has been retracted by Hindawi, as publisher, following an investigation undertaken by the publisher [1]. This investigation has uncovered evidence of systematic manipulation of the publication and peer-review process. We cannot, therefore, vouch for the reliability or integrity of this article.

Please note that this notice is intended solely to alert readers that the peer-review process of this article has been compromised.

Wiley and Hindawi regret that the usual quality checks did not identify these issues before publication and have since put additional measures in place to safeguard research integrity.

We wish to credit our Research Integrity and Research Publishing teams and anonymous and named external researchers and research integrity experts for contributing to this investigation.

The corresponding author, as the representative of all authors, has been given the opportunity to register their agreement or disagreement to this retraction. We have kept a record of any response received.

References

- [1] M. Anish, T. Arunkumar, J. Jayaprabakar et al., "Thermal Conductivity of Thermally Insulated Concretes in a Nuclear Safety Vessel of Reactor Vault: Experimental Interpretation," *Advances in Materials Science and Engineering*, vol. 2022, Article ID 4493910, 12 pages, 2022.

Research Article

Thermal Conductivity of Thermally Insulated Concretes in a Nuclear Safety Vessel of Reactor Vault: Experimental Interpretation

M. Anish ¹, T. Arunkumar ², J. Jayaprabakar,¹ Sami Al Obaid,³ Saleh Alfarraj,⁴ M. M. Raj,⁵ and Assefa Belay ⁶

¹School of Mechanical Engineering, Sathyabama Institute of Science and Technology, Chennai 600119, Tamilnadu, India

²Department of Mechanical Engineering, CMR Institute of Technology, Bengaluru 560037, Karnataka, India

³Department of Botany and Microbiology, College of Science, King Saud University, P.O. Box-2455, Riyadh-11451, Saudi Arabia

⁴Zoology Department, College of Science, King Saud University, Riyadh 11451, Saudi Arabia

⁵Department of Mechatronics Engineering, Seoul National University of Science and Technology, Seoul 01811, Republic of Korea

⁶Department of Mechanical Engineering, MizanTepi University, Tepi, Ethiopia

Correspondence should be addressed to Assefa Belay; assefa@mtu.edu.et

Received 6 March 2022; Accepted 3 May 2022; Published 21 June 2022

Academic Editor: Palanivel Velmurugan

Copyright © 2022 M. Anish et al. This is an open access article distributed under the Creative Commons Attribution License, which permits unrestricted use, distribution, and reproduction in any medium, provided the original work is properly cited.

Thermally insulated concretes are a type of alternative building material that helps improve thermal efficiency in nuclear reactor vault safety vessel applications. The experimental results of thermal conductivity values of lightweight concrete materials at various temperatures are presented in this paper. To minimize heat conduction in concrete, different lightweight aggregates and vermiculite are employed as coarse aggregate alternatives. Both linear and plane heat source approaches are used to calculate the thermal conductivity values of the specimens. The findings emphasize that increasing the proportion of lightweight particles in concrete may dramatically lower the thermal conductivity, with the kind of lightweight aggregates having a vital role in thermal insulation. The inclusion of micron-sized vermiculite decreases heat conductivity even further; however, the effect is less obvious than that of lightweight particles.

1. Introduction

Concrete is the major core material utilized in the building of the Nuclear Reactor Safety Vault, which acts as the last barrier against the reactor's high temperature heat waves and other fission products. Concrete's thermal conductivity is crucial for trapping heat and preventing it from dispersing into the surrounding environment. Because of their superior heat conductivity, thermally insulated concretes are chosen over standard concretes. This is performed by replacing coarse aggregates with appropriate lightweight aggregates. Pumice, coconut shell, and volcanic rock are the most common lightweight aggregates used in structural lightweight concretes. The addition of this LWA increases thermal insulation without compromising the mechanical

qualities of the concrete. Density, conductivity, and diffusivity all fall by 50% at 900°C when compared to room temperature values. The specific heat grows steadily until 500°C, then decreases from 7000°C to 900°C, and then increases over 900°C [1–3]. LWAs' porosity accounts for more moisture absorption than standard aggregates, impacting the thermal properties of structural concrete [3, 4]. The 28-day compressive strength of concrete estimated using the coconut shell aggregate is 19.1 N/mm², which is higher than the standard requirement for structural lightweight concrete [5]. The thermal conductivity of concrete varies from 2.01 to 2.95 W/m/K depending on the aggregate [6]. Normal concrete's thermal conductivity ranges from 2.194 W/m/K to 1.027 W/m/K at temperatures ranging from 20°C to 1100°C [7]. According to the research, traditional concrete thermal

conductivity varies from 0.6 to 3.3 W/m/K, whereas lightweight concretes vary from 0.4 to 1.89 W/m/k [8]. Although lightweight concretes are classed as aerated concretes and lightweight aggregate concretes (LWA), the latter has higher strength and density as well as poorer thermal conductivity, in addition to requiring a high energy production method [9]. When used as a fine aggregate, pumice dramatically inhibits heat conductivity by up to 40% [10]. The thermal conductivity of aggregate is substantially impacted by the value of aggregate loose unit weight and the volume of the aggregate matrix to the total volume ratio [11]. The incorporation of fly ash in a certain proportion with water in the mix design enhances the strength of the concrete while lowering heat conductivity [12]. At temperatures ranging from 0°C to 50°C, normal concretes have a thermal conductivity of 0.7–0.8 W/m-K, whereas lightweight concretes have a thermal conductivity of 0.5–0.6 W/m-K. Because LWAC may be used for partition or barrier walls due to its high thermal diffusivity and low unit weight, porosity is one of the major parameters that directly impacts its thermal conductivity [13]. According to DCT testing results, an increase in moisture content has an influence on the mechanical characteristics of concrete [14]. Concrete cracking drastically lowered thermal conductivity while maintaining the same specific heat capacity [15]. Both the inner vault, which holds the primary vessel, and the outer vault, which holds the safety vessel, are cylindrical structures. The vault's temperature is limited to 65 degrees Celsius, despite the fact that the main vessel may reach temperatures of up to 5000 degrees Celsius. Temperatures in the Reinforced Inner and Outer vaults range between 500°C and 550°C and 65°C and 90°C, respectively [16]. Coconut shell aggregate concrete is well-known for its excellent bonding strength and long-term durability without losing quality [17]. Because of the high porosity values, both thermal conductivity and tensile strength are reduced. The degree of damage to concrete varies depending on the weight, lowering thermal conductivity [18]. The thermal conductivity of LWAC has been determined to be proportional to the volume of LWA. Thermal conductivity is lowered by 7% when pumice replaces 25% of coarse aggregates, and by 20%, 28%, and 47% when 50%, 75%, and 100% pumice aggregates are used, respectively. Thermal conductivity reduces from 0.96 to 0.65 W/m K when 10% vermiculite is added and heated to 900°C. Mechanical strength and thermal conductivity increase [19]. Because the degree of strength depreciation is substantial at 400°C [20], concrete mechanical strength is directly proportional to the coarse aggregate. When 40% of the traditional aggregate is substituted with coconut shell, the concrete becomes lighter and the density is lowered by 7.5%. After 7 days, the strength of coconut shell concrete is significantly higher than that of control concrete. The water/cement ratio appeared to be affected by the amount of coconut shell utilized; as more cement was needed as the amount of coconut shell rose [21]. The k values of thermal insulating materials are tested in standard laboratory conditions. When a material is exposed to varying humidity and climatic conditions, its thermal performance changes dramatically [22]. Increasing the cement content without

TABLE 1: Physical properties of ordinary Portland cement and fly ash.

Properties	Cement	Fly ash
Sio ₂ (%)	20.0	61.0
Loss on ignition (%)	2.6	2.5
Specific gravity (g/cm ³)	3.15	2.18
Blain fineness (cm ² /g)	3350	3308

TABLE 2: Physical properties of normal aggregates.

Properties	Fine	Coarse
Source	Cleaned sea-sand	Ballast
Fineness modulus	2.83	6.84
Specific gravity	2.60	2.61
Dry bulk density	1480	1680

altering the workability of LWAC improves its resistance dramatically [23]. The purpose of this publication is to show how thermo-shielded structural concretes may be utilized in nuclear reactor safety vessels. The text is divided into two parts: Because of the use of lightweight aggregates and vermiculate, heat conductivity is reduced while strength is increased. Using a thermal needle probe in conjunction with the thermal moulding testing technique, thermal conductivity is evaluated. In addition, how this appropriate combination of concrete design will be improved in order to protect the nuclear safety vessel vault via the use of experimental analysis is also discussed.

2. Experiment

2.1. Primary Materials. Ordinary Portland cement, fly ash, GGBS (Ground Granulated Blast-furnace Slag), fine aggregate, coarse aggregates, and three lightweight coarse aggregates are the primary components [24]. Table 1 summarizes the characteristics of cement and fly ash. M40-sand that has been thoroughly washed and sieved is utilized as fine aggregates, whereas ballast is used as standard coarse aggregates as shown in Table 2. The fineness modulus of coarse aggregates is represented by an index value that indicates the average size of the particles included inside the coarse aggregate. It's estimated as part of the sieve analysis procedure, and it's done using conventional sieves. The value of fine aggregates may be calculated by adding together the cumulative percentage retained on each filter and dividing by 100. Pumice, volcanic rock, and crushed coconut shells are three diverse lightweight aggregates generated from various resources and procedures that are used as alternatives to typical coarse aggregates for enhancing thermal characteristics. Table 3 shows the physical parameters of lightweight aggregates. Micrometer-sized vermiculite is utilized as a substitute for aggregates. Vermiculite enhances thermal characteristics when combined with cement paste since it has a low thermal conductivity and density as shown in Table 4. The optical pictures of insulating LWA materials used for this study are shown in Figure 1.

TABLE 3: Mixture proportions.

Specimen	Cement (kg/m ³)	Fly ash (kg/m ³)	GGBS	Water (kg/m ³)	Aggregate			
					Fine (kg/m ³)	Coarse (kg/m ³)	Vermiculite (kg/m ³)	LWA (kg/m ³)
N0	350	0	0	150	818	1082	0	0
N5	280	52.5	17.5	150	777.1	1082	40.9	0
N10	280	52.5	17.5	150	736.2	1082	81.8	0
N20	280	52.5	17.5	150	654.4	1082	163.6	0
N30	280	52.5	17.5	150	572.6	1082	245.4	0
P0	280	52.5	17.5	150	818	898.06	0	183.94
P10	280	52.5	17.5	150	744.38	865.6	73.62	216.4
P20	280	52.5	17.5	150	728.02	843.96	89.98	238.04
P30	280	52.5	17.5	150	760.74	919.7	57.26	162.3
V0	280	52.5	17.5	150	818	865.6	0	216.4
V20	280	52.5	17.5	150	728.02	843.96	89.98	238.04
C0	280	52.5	17.5	150	818	865.6	0	216.4

TABLE 4: Properties of normal and lightweight coarse aggregates.

Properties	Normal	Pumice	Volcanic rock	Coconut shell
Raw material	Ballast	Volcanic	Volcanic	Coconut
Maximum size (mm)	20	20	15	12.5
Particle density (kg/m ³)	2500	300	710	650
Dry loose bulk density (kg/m ³)	1200	750	675	550
Shape type	Crushed	Crushed	Crushed	Flaky
Water absorption (%)	1	55	62	13.79



FIGURE 1: Images of lightweight aggregates. (a) Vermiculite. (b) Pumice. (c) Volcanic rock. (d) Coconut shell.

2.2. Tested Specimens. Table 3 shows 10 possible aggregate and vermiculite blends with varied mix patterns. The specimen name is abbreviated with a symbol, which is then followed by a number. The number indicates the volume % of vermiculite added (i.e., *N*: normal aggregate, *P*: pumice, *V*: volcanic rock, and *C*: coconut shell) and the symbol indicates the kind of aggregate (i.e., *N*: normal aggregate, *P*: pumice, *V*: volcanic rock, and *C*: coconut shell) (i.e., *N*: normal aggregate, *P*: pumice, *V*: volcanic rock, and *C*: coconut shell). Table 3 shows the mix design of *N0* for a structural insulated concrete used in a reactor with a compressive strength more than 27 MPa. The relative density and specific gravity of the components are considered when estimating the quantity of each item needed for a cubic metre of concrete. For example, the specimen is identified by the first letter of the primary ingredient, followed by the entire aggregate quantity of vermiculite to be replaced. The features and characteristics of normal and lightweight coarse aggregates are described in Tables 4 and 5, respectively.

TABLE 5: Specification of vermiculite.

Properties	Specifications
Composition	Phyllosilicates
Color	Light to dark brown
Density	160 kg/m ³
Crushed strength	0.56 mpa
Softening temperature	1200°C
Median diameter	50 μm
Bulk thermal conductivity	0.07 w/m/k

2.3. Making and Curing. For testing the compressive strength, a 150 mm × 150 mm × 150 mm cube is casted. A mold of size 300 mm × 300 mm × 300 mm is made to calculate the thermal conductivity. All cubes are de-moulded and cured in a tank at room temperature for 28 days (20 ± 3°C). Compressive strength, modulus of elasticity, density, and splitting tensile strength are measured after 28 days of curing. The thermal molds must be stored at room

temperature and 50% relative humidity for at least 14 days. Thermal conductivity is measured only after at least 28 days.

2.4. Measurement of Thermal Conductivity. The conventional approach for calculating thermal conductivity under adiabatic conditions is to measure the heat flux through the specimen, which requires a sophisticated experimental arrangement. In this work, three approaches are used: thermal needle probe method, thermal moulding method (one-dimensional and two-dimensional steady-state circumstances), and thermal moulding method (one-dimensional and two-dimensional steady-state conditions). Thermal conductivity is best measured under steady-state circumstances. The steady-state condition equation is as follows:

$$Q = k \cdot A \cdot t \frac{(T1 - T2)}{x} \quad (1)$$

2.5. Thermal Needle Probe method. Two needle probes are used to generate heat during the concrete mixing process. A thermal needle probe is used to assess thermal conductivity. The thermistor and heating wire are integrated in a stainless steel needle probe 90 mm long and 1.3 mm in diameter. At the centre, two needle probes are introduced, followed by concrete mixing and hardening. Heat is created radially from the probe by employing DC current. For 2 minutes, the temperature is recorded every 1 second. Using equation (2), the linear part of temperature evolution with time is used to calculate thermal conductivity k .

$$k = \frac{Q}{4\pi} \ln\left(\frac{\Delta t}{\Delta T}\right) \quad (2)$$

Q , applied heat energy. Δt , change in time. ΔT , change in temperature.

For each thermal probe, measurements are taken three times for two different input voltages (i.e., 10 and 15 V). Because the initial section of the temperature change is impacted by needle-concrete coupling, the conductivity is calculated from the linear portion temperature increment using a log time scale. The concrete mixes employed in this investigation comprise isotropic and homogenous components.

2.6. Thermal Molding Method. This method of heat transmission is preferred over the use of a thermal needle probe since the latter has a lower efficiency of heat transfer. Heating plates are used in this technique to transmit heat from the heating plate to the mould. In both one and two dimensions, the constant heat flow technique is utilized to calculate heat flow. In the one-dimensional heat flow method, just one heating plate is used, and the rest of the mould is completely insulated. When working with two-dimensional steady-state heat flow, two heating plates are placed on each side of the mould, opposing each other. The mould has been thermally insulated with asbestos sheeting in order to reduce the amount of heat lost. Figure 2 depicts the specimen layout as well as the thermocouple locations. A direct current is sent

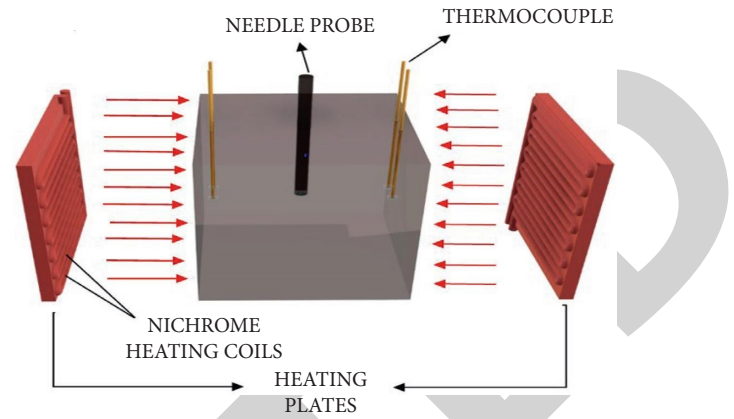


FIGURE 2: Thermal molding method: two-dimensional heat flow.

TABLE 6: Total volume fraction of vermiculite with respect to aggregates.

Notation	Volume of vermiculite (%)	
	Total aggregates	Coarse aggregates
5	4.8	15
10	9.7	28
20	19.6	51
30	29.5	78

TABLE 7: Specific heat of concrete specimens.

values (J/kg/k)	Material type
960	Concrete
920	Concrete
795	Normal weight concrete
921	Structural lightweight concrete
1000	Insulating lightweight concrete

via the heating plates, which generates heat as a result. The heating plate equipment is composed of Nichrome coils that are put into porcelain grooves and covered by asbestos material to prevent heat dissipation during the heating process. The direct current (DC) supply that powers the heating plate equipment is 3 kilowatts. The nine thermocouples are arranged in a consecutive manner to measure temperature every 10 seconds. The heat propagation through the mould is monitored by the four thermocouples that have been put into the mould until the steady-state condition has been attained. Thermal moulding outperforms needle probe because heat is transmitted throughout the specimen by delivering planar heat across the specimen. Two heating plates are supplied in order to ensure that heat propagation is homogenous on both sides of the heating element. Thermal property is assessed using Fourier's law equation (3), which takes into account the loss of heat due to the atmosphere, thereby meeting the principle of energy conservation. For example, the total volume percentage of vermiculite relative to aggregates and the specific heat of the concrete sample are shown in Tables 6 and 7.

$$\begin{aligned} \frac{dT}{dt} &= \alpha \frac{dT}{dx} - \lambda.T, \\ &= \frac{k}{\rho.c_p} \frac{dT}{dx} - \lambda.T^*, \end{aligned} \quad (3)$$

α -, thermal diffusivity [m²/s]. K , thermal conductivity [W/m/K]. c_p , specific heat [J/g/k]. ϕRgr -, density [kg/m³]. Heat loss coefficient, $\lambda = L / (dx.A.C_v.\rho)$ [1/S].

While the heat loss coefficient controls the steady-state temperature, the diffusivity monitors the rate of temperature rise. The change of temperature over time is analyzed using the finite difference approach, and equation (3) is amended. Thermal conductivity is measured using the specific heat and the density of the specimens, which are collected experimentally after 28 days of curing. According to Table 7, the average specific heat value for concrete is 890 J/kg/K. Thermal conductivity is calculated as a result. The heat loss coefficient and the projected thermal conductivity are independent, and they have no effect on temperature rise.

2.7. One-Dimensional Steady-State Condition. If the spatial distribution of temperatures in the conducting item does not change any more as the temperature difference driving the conduction remains constant, this form of conduction is said to be steady-state conduction. One-dimensional heat flow is applied when the heat energy flows along the coordinates normal to surface.

If k is a constant, then [4].

$$\frac{\partial T}{\partial x} + \frac{q}{k} = \frac{\rho c}{k} \frac{\partial T}{\partial t} = \frac{1}{\alpha} \frac{\partial T}{\partial t}, \quad (4)$$

$\partial T / \partial x$, longitudinal conduction. q , internal heat generation. $\partial T / \partial t$, thermal inertia. α , thermal diffusivity.

The concrete specimen is subjected to heat flow from just one side in this procedure, and the remaining sides are thermally insulated to decrease heat dispersion, as illustrated in Figure 3. Heat is applied to the concrete until a steady-state condition is reached. The temperature of the specimen is measured every two minutes for an hour. The temperature rise begins with the thermocouple closest to the heat source and continues in this manner. Temperature measurements are acquired by attaching thermocouples to the data logger system, and thermal conductivity is computed from the values using equation (4). Figure 4 shows the internal structure of the concrete vault.

3. Results and Discussion

From the prevailing effective factors, thermal needle probe and thermal molding methods are used to calculate thermal conductivity. The values from the one-dimensional steady-state method are analyzed with the recordings from the two methods to verify the experimental correctness. Results from the tested concrete specimen with various specifications are noted and further analyzed.

3.1. Effect of Lightweight Aggregates and Vermiculite. Figure 5 represents the thermal conductivity of normal concretes with varying amounts of vermiculite. A mean

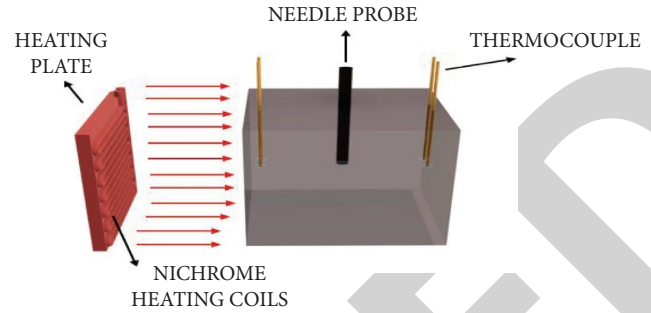


FIGURE 3: Thermal molding method: one-dimensional heat flow.

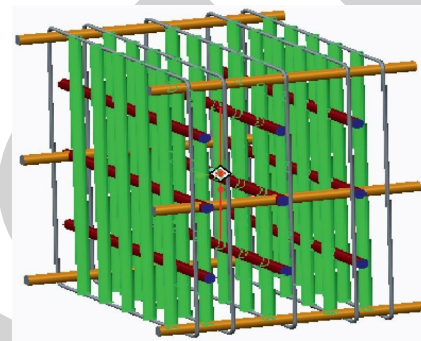


FIGURE 4: Internal structure of the concrete vault.

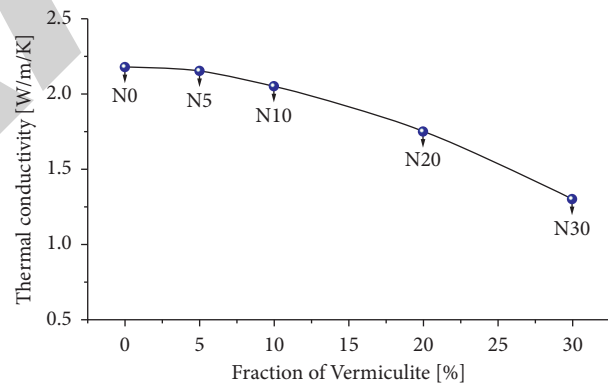


FIGURE 5: Thermal conductivity of normal concrete. On increasing the fraction of vermiculite, k decreases.

conductivity of 2.175 W/m/K is observed for concrete without addition of vermiculite. Thermal conductivity decreases to 1.30 W/m/K as the amount of vermiculite increases (accordingly the volume of coarse aggregate decreases), which is approximately 43% reduction at 30% of vermiculite (N30 specimen). To prevent the exclusion of coarse aggregates, addition of vermiculite is limited to not more than 30%.

Figure 6 depicts the thermal conductivity of pumice concrete specimens [P series] vs. normal aggregate concrete specimens. Pumice has a higher porosity and hence a superior heat conductivity. Vermiculite is added to the concrete mixture to produce mechanical fineness and strength. Furthermore, when the volume percentage of vermiculite is raised from 0 to 20%, the conductivity of the pumice concrete specimens drops to 30%.

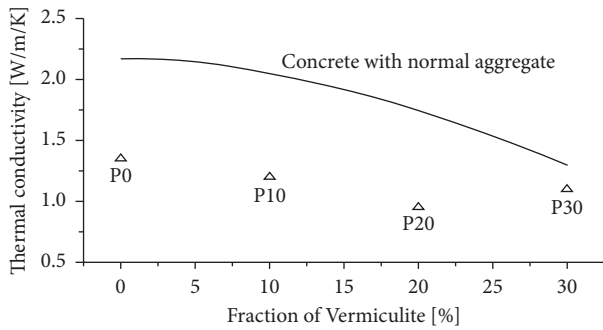


FIGURE 6: Thermal conductivity of concrete with pumice aggregates. Increase in vermiculite by 20% caused a 30% decrease in thermal conductivity, k .

Figure 7 compares the thermal conductivity of volcanic rock and coconut shell concretes to that of normal and pumice concretes. The solid line represents the heat conductivity of normal concrete as the vermiculite proportion increases. The dotted line is used to symbolize the same thing as the pumice (P series) concrete. The thermal conductivity of the volcanic rock concrete specimen V0 is 1.75 W/m/K. The thermal conductivity of the specimen was lowered to 1.5 W/m/K after the addition of 20% volume of vermiculite. Thermal conductivity decreases by 14% as vermiculite volume increases. Thermal conductivity values for C0 and V20 are comparable. However, vermiculite is not added to coconut shell concretes to ensure the fineness of the mechanical qualities. It is worth noting that pumice has the lowest heat conductivity. Pumice specimens with 20% vermiculite exhibit the lowest thermal conductivity.

The comparison between specimens without vermiculite and with 20% of vermiculite for four different aggregates specimens is shown in Figure 8. As justified earlier, adding 20% vermiculite, there is an effective improvement in reducing thermal conductivity in specimens with normal and pumice as coarse aggregates.

3.2. Effective Range of the Thermal Needle Probe Method.

The needle probe is inserted into the concrete specimen prior to hardening and provides radial heat into the specimen up to a certain reach. Because the needle probe is lodged inside the concrete specimen throughout the casting process, the recorded value at various temperature ranges reflects the material characteristics within the effective volume. The quantity of heat created by the probe is measured using thermocouples encased within the concrete specimen, and thermal conductivity is computed using equation (1). The main disadvantage of this approach is that the heat generated is not completely disseminated through the block; hence, the thermal moulding method is used.

3.3. Results from the Thermal Molding Method. The temperature change with time for four distinct specimens is depicted in Figure 9 using thermocouples within the specimen. The temperature difference between the specimen and the heating plate is represented by the red line. Based on

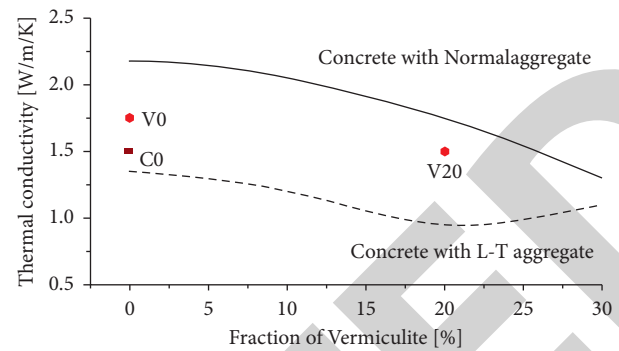


FIGURE 7: Thermal conductivity of coconut shell and volcanic rock concretes.

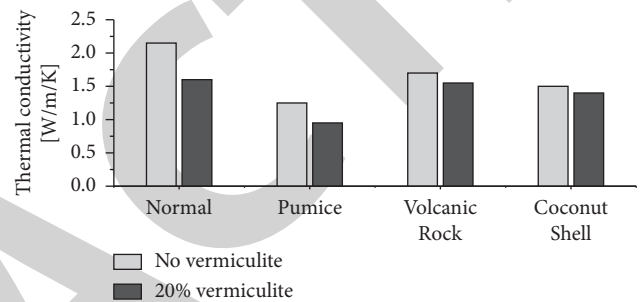


FIGURE 8: Thermal conductivity of concrete specimens with and without 20% vermiculite content.

the equation, experimental findings are represented by solid lines, while temperature is denoted by dotted lines (2). When the plate begins to heat, the temperature rises quickly and reaches 600 degrees Celsius. The temperature rises steadily from the first thermocouple to the heating plate. During transitory times, a lag is seen.

The temperature rises at each thermocouple in turn. Unless there is no heat loss, there is a coincidence between the thermocouple temperature and the asymptotic value at steady state. Despite insulating, temperature changes at steady state are observed owing to heat loss to the environment. The heat loss coefficient is sufficient to account for the temperature rise at four thermocouples over time. Thermal conductivity measured by thermal moulding and the needle probe techniques agrees well in Figure 10, demonstrating the importance of coarse particles and vermiculite. Low specific heat leads to poorer conductivity in the thermal moulding analysis because thermal conductivity has a reciprocal and linear connection. Table 8 highlights the specific heat values of several concrete materials, which range from 795 to 1000 J/kg/K. The temperature evolution throughout the transient period from the needle probe method may be used to calculate the specific heat value. Figures 11 and 12 show the density of specimens as a function of the percent of vermiculite used, as well as the compressive strength as a function of the fraction of vermiculite used.

3.4. Results from the One-Dimensional Heating Method.

The temperature readings by the thermocouples for the corresponding concrete specimens are plotted. Figure 13(a)

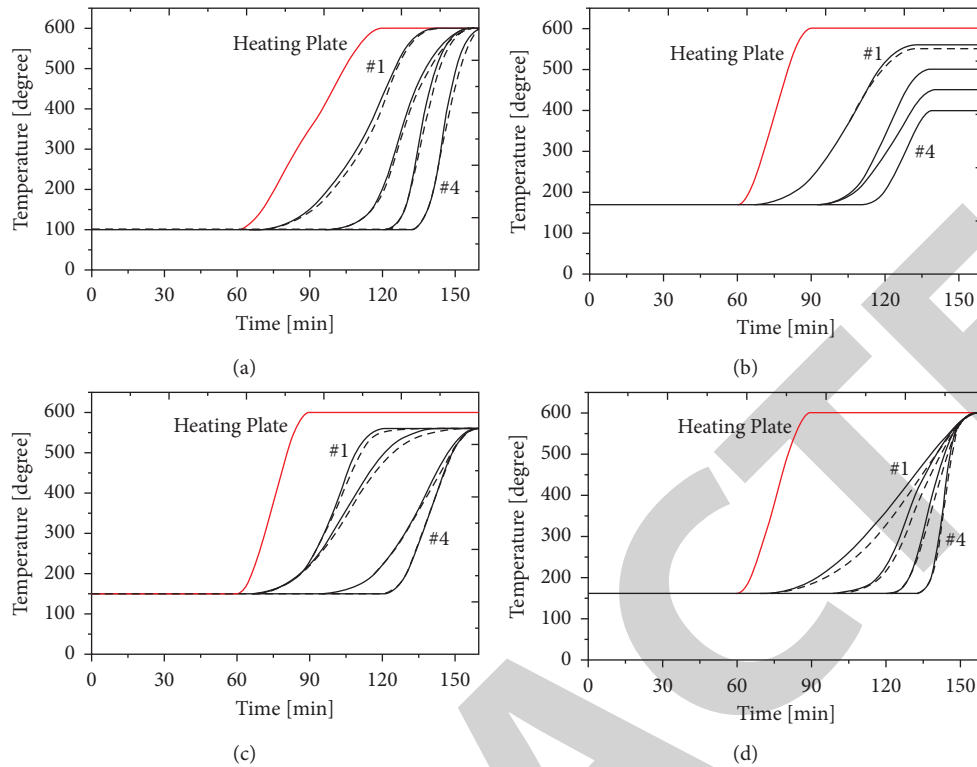


FIGURE 9: Temperature evolution of (a) N0, (b) N10, (c) N30, and (d) P20 specimens with time. Solid lines (experimental results) and dotted lines (evaluated temperature). Reddish colored line.

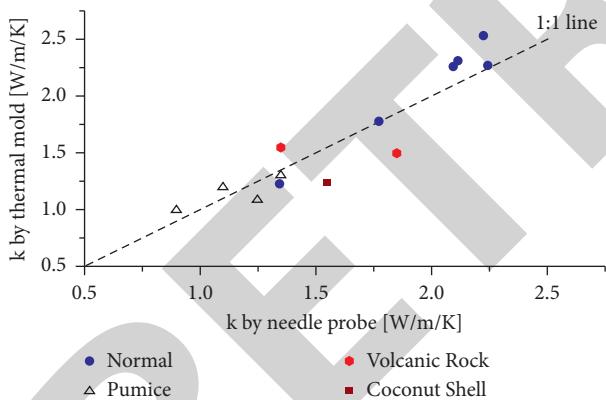


FIGURE 10: Thermal conductivity by the thermal needle probe and thermal molding methods.

shows the temperature readings by the thermocouples in normal aggregates specimens (*N* series). Each composition is designated by different symbols for better clarity. The thermocouples are denoted by *T* along with the number of their positions (*T*₁, *T*₂, etc.). When studied, it is noted that the N30 specimen shows low thermal conductivity among the other specimens in the *N* series when 30% fraction of vermiculite is added to the mixture. In Figure 13(b)), temperature recorded from the thermocouples from pumice concrete specimens is plotted. Among all the specimens, an efficient reduction in heat flow is demonstrated by the P20 specimen. Pumice acts as an excellent insulator at higher temperatures.

Figure 13(c)) shows the temperature values of the volcanic rock specimens V0 and V20. From the two specimens, V20 shows lower thermal conductivity than V0. Here, heat propagation is further reduced by the addition of vermiculite. Figure 13(d)) shows temperature depreciation throughout the C0 specimen recorded from the thermocouples. From the above figure, it is distinctive that among all the specimens, P20 specimen has the lowest thermal conductivity and hence provides better insulation than the rest.

3.5. *Applications of Thermo-Shielding Concretes.* Table 8 highlights the mechanical characteristics of hardened concrete after 28 days of curing. Normal concrete density fluctuates by around 15% from 2389 kg/m³ in N0 to 2023 kg/m³ in N30 when vermiculite is substituted up to 30%. According to Figure 10, the addition of vermiculite in volume has no significant effect on the density reduction in other LWAC. Except for the combination containing 30% vermiculite, all mixes achieve a 28-day cylindrical compressive strength of 28 MPa. The compressive strength of normal and LWAC concretes decreases significantly as the vermiculite replacement volume increases; however, the change in compressive strength and the density of coconut shell concretes is negligible. The modulus of elasticity and splitting tensile strength have comparable properties to density and compressive strength. The distribution and the size of LWAs have a significant impact on the mechanical characteristics of concrete. When applied to structural

TABLE 8: Mechanical properties at 25 days.

Specimen	Density (kg/m ³)	Compressive strength (MPa)	Modulus of elasticity (GPa)	Splitting tensile strength (MPa)
N0	2389	44.2	42.65	4.25
N5	2300	39.7	37.32	3.64
N10	2260	37.4	35.05	3.14
N20	2169	33.1	33.25	2.35
N30	2023	27.5	24.94	2.12
P0	1854	39.6	28.95	3.47
P10	1833	38.8	27.82	3.22
P20	1801	32.0	24.36	2.95
P30	1796	27.8	20.42	2.06
V0	1864	40.5	25.68	3.84
V20	1837	36.3	22.81	3.18
C0	1826	39.9	27.64	3.23

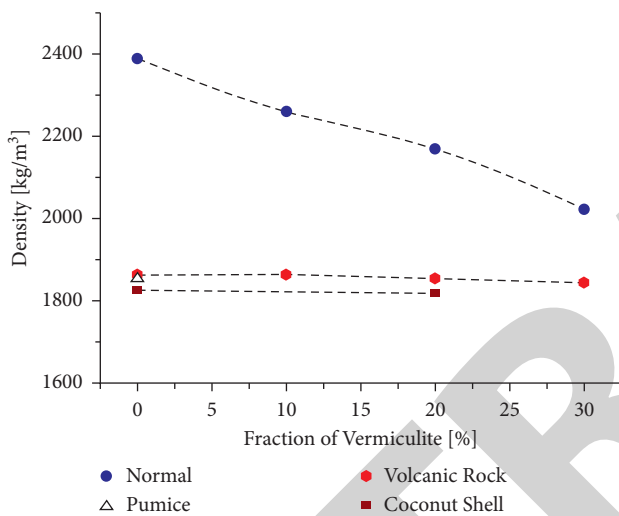


FIGURE 11: Density of specimens with a fraction of vermiculite.

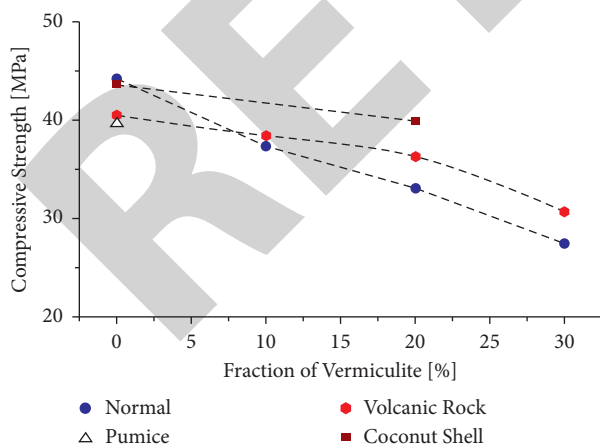


FIGURE 12: Compressive strength with a fraction of vermiculite.

elements such as the wall of a nuclear reactor safety vessel, the mechanical characteristics of insulated concrete with LWA and vermiculite meet the fundamental standard and code of building construction.

3.6. LWA Vermiculite Concrete. The RV model, as illustrated in Figure 14, is a scaled replica of a genuine RV in a nuclear reactor. It is built out of a cylindrical block of high strength concrete with a CS pipe running through the middle. The concrete block is 10 inches in diameter and 12 inches in length. The CS pipe has a diameter of 1 inch and a length of 18 inches. Both ends of the CS pipe are joined to a flange, which connects it to the external setup. The RV model is then attached to the external setup, which circulates the heat transfer fluid (water) at a higher temperature. The heat emitted by the water is collected by the tubes and conveyed through the concrete.

3.7. Fabrication of the RV Model. An appropriate mould made of LWA vermiculite is created in order to produce the cylindrical concrete block. The fundamental reason for this is because various building materials require varied amounts of time to set. Although the introduction of additives or admixtures changes the setting time of concrete, it is still required to ensure that the concrete maintains its right form. A PVC block with a diameter of 10" is utilized as the outer boundary, a CS pipe with a diameter of 1" passes through the middle of the PVC coupling, and a wooden board is used to close one of the apertures. Once the concrete has cured, the LWA vermiculite concrete mould is removed.

3.7.1. Experiment Procedure for the RV Model. The RV model is attached to the external setup by a flange, which is a square portion with mounting holes drilled in it. The CS pipe flowing through the RV model is likewise provided via a flange with the same size as the exterior configuration. An external setup interface gasket is supplied to prevent leaking at the RV. The reservoir is normally filled with the heat transfer fluid, which is water. With the assistance of an immersion heater, it is heated to a temperature of 60°C. The fluid flow rate is regulated and maintained at the desired level. Flow rate is determined with a flowmeter. As hot water circulates through the circuit, the concrete gradually warms up. Temperature measurements are recorded and tabulated every 5 minutes at each thermocouple. After a set period of time, the RV model reaches a steady state and there is no additional temperature growth.

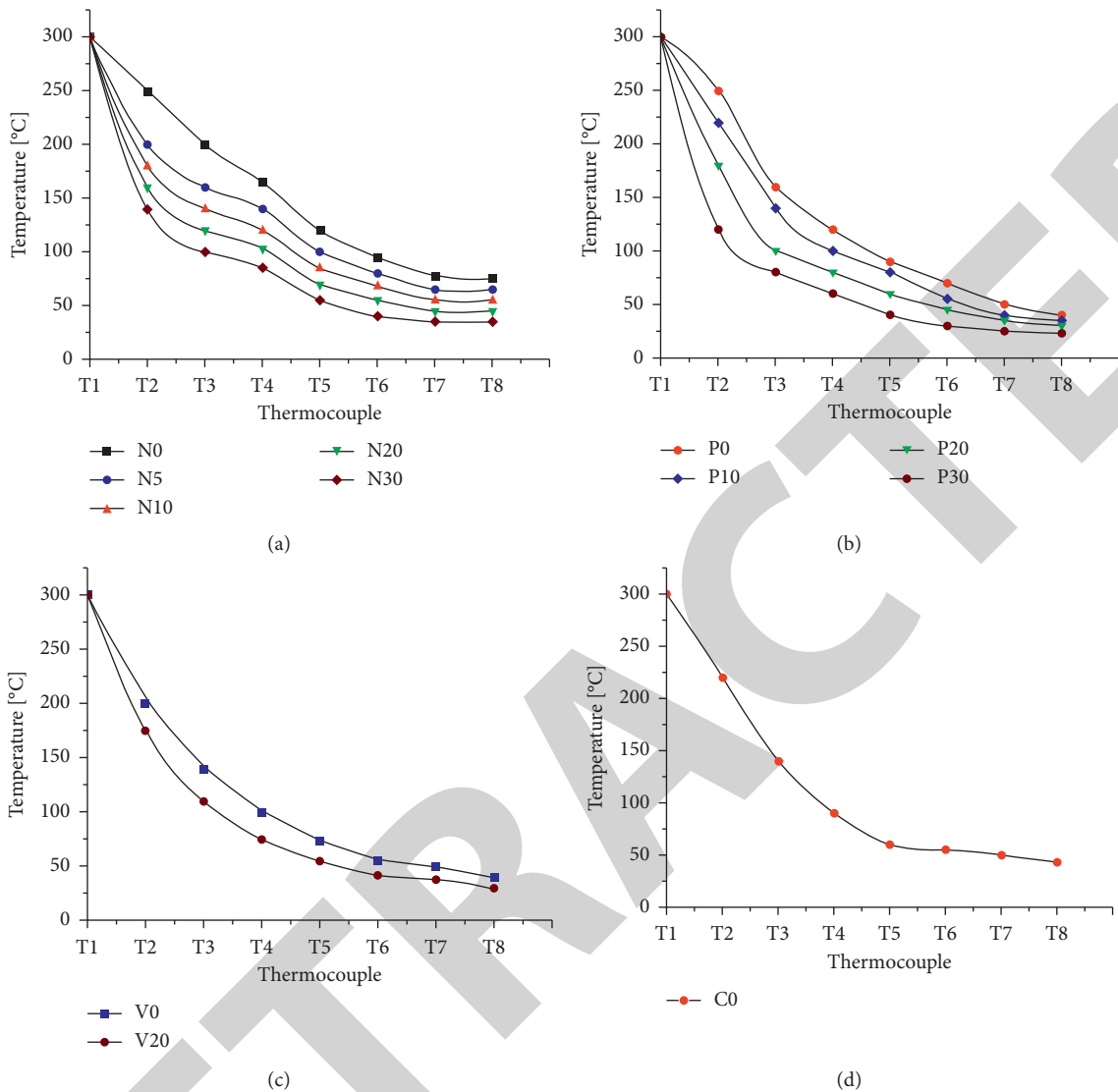


FIGURE 13: Temperatures across the thermocouples of (a) normal aggregates, (b) pumice aggregates, (c) volcanic rock, and (d) coconut shell aggregate specimens.

3.8. *Convective Heat Transfer through Pipe and Concrete Surface.* The photographs demonstrate the many steps of heat transmission from water to the concrete surface. Convective heat transfer from hot water to the pipe is seen in Figure 14. The average temperature of the water flowing through the pipe was determined to be 56°C, since heat is transferred from the water to the pipe surface as it runs. It can be observed that the pipe temperature at the intake is near to the water temperature, as indicated in red, and progressively decreases as they approach towards the exit, as shown in green. Heat from the pipe surface is transmitted to the outside surface of the RV model by convection as the exterior setup is exposed to the environment, as shown in Figure 15. Although conduction accounts for the majority of heat transmission through concrete, the action of air movement over the concrete surface also transmits heat. Because the region near the pipe absorbs heat faster than the outermost surface, the color variation ranges from orange at

the start to deep blue at the finish. The RV model is analyzed using ANSYS software to explore the heat transfer properties through the concrete material in detail. Because the project’s fundamental principle is heat transmission via conduction, the entire RV model is broken into minute nodes by meshing. The notion of meshing is the development of a grid across an entire model in order to analyze parameters such as temperature, heat flow, and temperature gradient at specified spots on the model known as nodes, and the results are obtained.

3.9. *ANSYS Thermal Gradient and Thermal Flux Vector Sum.* When the intake circumstances are supplied as input, this graphic displays the thermal gradient values along all three axes (x , y , and z) of the RV model. It is obvious that the temperature gradient values adjacent to the pipe are large, with a value of 702.18 W/m, and have a minimum value of

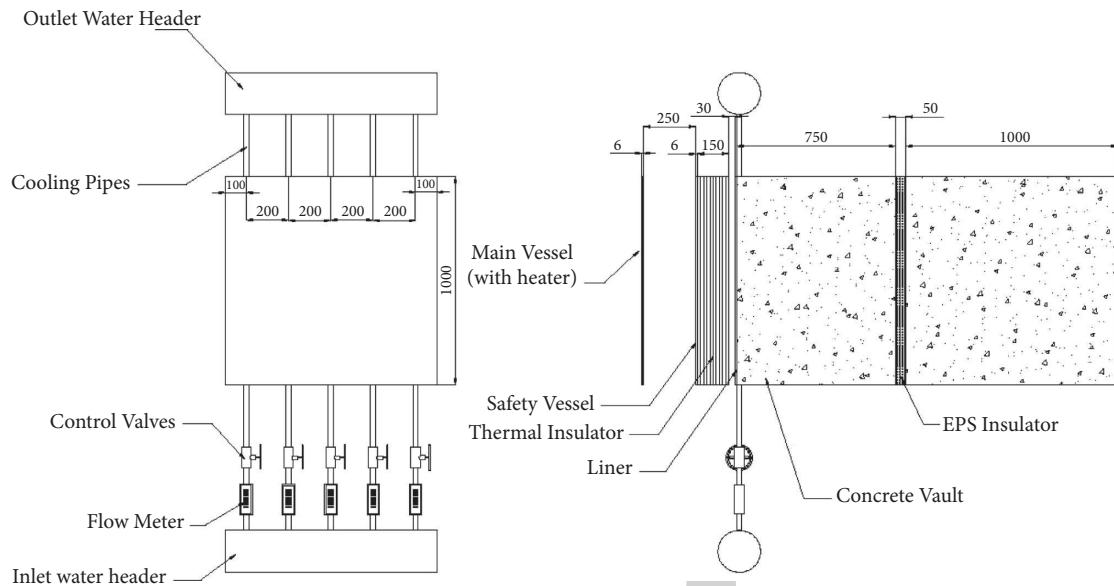


FIGURE 14: Concrete reactor vault.



FIGURE 15: Convective heat flow through the CS pipe and the concrete layer.

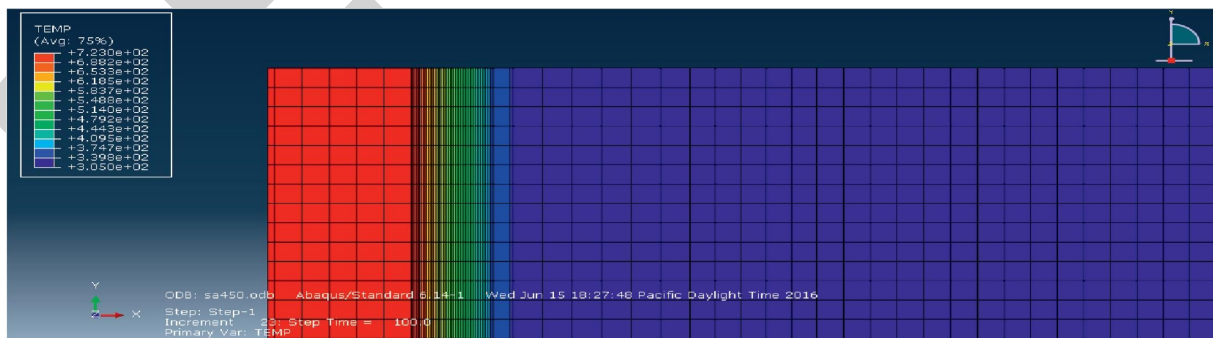


FIGURE 16: Showing thermal gradient for nodal solution.

75.98 W/m on the outside surface. As we go closer to the surface, the thermal gradient values become more similar to air conditions. Figure 16 depicts the results of the investigation into heat movement through the cylindrical concrete block as well as convection into the surrounding area. There

were nodes in the centre area and on the surface that had the largest heat flow, and there were nodes on the block that had the lowest heat flow, with the maximum value being 1098.93 W/m². x-axis heat flux for the nodal solution is negative, with a value of 1097.88 denoting the direction

opposed to the flow against the previously assumed direction, with a maximum value of 1098.93 W/m^2 in the centre and a value of -121.639 W/m^2 as it approaches the outside walls.

4. Conclusion

Experimentally determined thermal conductivity values for thermally insulated concretes with lightweight aggregates and vermiculite as substitute materials are investigated, and the findings are explained.

- (1) To validate the reliability of the estimated values in terms of application, results from the thermal needle probe technique and thermal moulding testing in one- and two-dimensional heat flow are experimented with.
- (2) The replacement of conventional aggregate with the LWAs effectively diminishes thermal conductivity subjected to the raw materials.
- (3) Coarse particles have a stronger impact than exfoliated vermiculite. In this investigation, pumice with a conductivity of 0.9 W/mK on 20–30% vermiculite was shown to be the most effective insulating addition.
- (4) To ensure mechanical soundness, the addition of vermiculite is restricted to not more than 20%. The quantitative value of the thermal conductivity evaluated at high temperatures becomes a vital factor to simulate and analyze the thermal behavior of the nuclear reactor safety vault built from these lightweight aggregate concretes.
- (5) The high strength concrete was cast according to the design mix. The experiment was carried out on the setup, calculations were done, and the values were validated using ANSYS software. Thermal conductivity (K) values for mild steel pipe and high strength concrete material were determined to be 53.3717 W/mK and 1.56503 W/mK , respectively, which were found to be consistent with theoretical values.
- (6) When the temperature of the main vessel (heater plate) is set at 100°C , the temperature difference between the inner (T49) and outer faces (T55) of the inner concrete vault is 3°C , which is less than the acceptable temperature difference. At 200°C , the temperature difference between the inner (T49) and outer faces (T55) of the inner concrete vault is 5°C , which is less than the acceptable temperature difference. At 300°C , the temperature difference between the inner (T49) and outer faces (T55) of the inner concrete vault is 7°C , which is less than the acceptable temperature difference. At 400°C , the temperature difference between the inner (T49) and outer faces (T55) of the inner concrete vault is 13°C , which is less than the acceptable temperature difference. At 500°C , the temperature difference between the inner (T49) and outer faces (T55) of the

inner concrete vault is 21°C , which is less than the acceptable temperature difference.

- (7) When the temperature of the main vessel (heater plate) was set to 57°C , the temperatures of the inner and outer faces of the inner concrete vault were 7°C (T49) and 4°C (T55), respectively, with a difference of 24°C , which was less than acceptable when using thermally insulated concretes with lightweight aggregates and vermiculite as alternate materials.
- (8) Thermal conductivity was found to be lower in plain concrete of grades N0, N5, and lightweight aggregates concrete, with conductivities of 1.65 W/mK , 1.59 W/mK , and 1.703 W/mK , respectively. This implies that the lightweight aggregates vermiculate concrete composition retains the heat energy transmitted by conduction from the pipe without letting it to distribute heat to the surrounding environment.

Data Availability

The data used to support the findings of this study are included within the article. Further data or information is available from the corresponding author upon request.

Conflicts of Interest

The authors declare that there are no conflicts of interest regarding the publication of this paper.

Acknowledgments

The authors thank MizanTepi University, Ethiopia, for providing help during the research and preparation of the manuscript. The authors thank the Sathyabama Institute of Science and Technology, CMR Institute of Technology, and Seoul National University of Science and Technology, for providing assistance to complete this work. This project was supported by Researchers Supporting Project number (RSP-2021/315) King Saud University, Riyadh, Saudi Arabia.

References

- [1] K. Y. Shin, S. B. Kim, J. H. Kim, M. Chung, and P. S. Jung, "Thermo-physical properties and transient heat transfer of concrete at elevated temperatures," *Nuclear Engineering and Design*, vol. 212, no. 1-3, pp. 233–241, 2002.
- [2] A. Saygılı and G. Baykal, "A new method for improving the thermal insulation properties of fly ash," *Energy and Buildings*, vol. 43, no. 11, pp. 3236–3242, 2011.
- [3] L. H. Nguyen, A. L. Beaucour, S. Ortola, and A. Noumowé, "Experimental study on the thermal properties of lightweight aggregate concretes at different moisture contents and ambient temperatures," *Construction and Building Materials*, vol. 151, pp. 720–731, 2017.
- [4] C. Tasdemir, O. Sengul, and M. A. au, "A comparative study on the thermal conductivities and mechanical properties of lightweight concretes," *Energy and Buildings*, vol. 151, pp. 469–475, 2017.
- [5] K. Gunasekaran and P. S. Kumar, "Lightweight concrete using coconut shells as aggregates," in *Proceedings of the*

Retraction

Retracted: Influence of Pore Structure Characteristics of Primary Coal on Coalbed Methane Adsorption

Advances in Materials Science and Engineering

Received 26 December 2023; Accepted 26 December 2023; Published 29 December 2023

Copyright © 2023 Advances in Materials Science and Engineering. This is an open access article distributed under the Creative Commons Attribution License, which permits unrestricted use, distribution, and reproduction in any medium, provided the original work is properly cited.

This article has been retracted by Hindawi, as publisher, following an investigation undertaken by the publisher [1]. This investigation has uncovered evidence of systematic manipulation of the publication and peer-review process. We cannot, therefore, vouch for the reliability or integrity of this article.

Please note that this notice is intended solely to alert readers that the peer-review process of this article has been compromised.

Wiley and Hindawi regret that the usual quality checks did not identify these issues before publication and have since put additional measures in place to safeguard research integrity.

We wish to credit our Research Integrity and Research Publishing teams and anonymous and named external researchers and research integrity experts for contributing to this investigation.

The corresponding author, as the representative of all authors, has been given the opportunity to register their agreement or disagreement to this retraction. We have kept a record of any response received.

References

- [1] G. Liu, "Influence of Pore Structure Characteristics of Primary Coal on Coalbed Methane Adsorption," *Advances in Materials Science and Engineering*, vol. 2022, Article ID 3087252, 7 pages, 2022.

Research Article

Influence of Pore Structure Characteristics of Primary Coal on Coalbed Methane Adsorption

Gang Liu 

College of Energy and Materials Engineering, Taiyuan University of Science and Technology, Taiyuan 030000, Shanxi, China

Correspondence should be addressed to Gang Liu; 202030070135@stu.tyust.edu.cn

Received 4 March 2022; Revised 14 April 2022; Accepted 9 May 2022; Published 14 June 2022

Academic Editor: Palanivel Velmurugan

Copyright © 2022 Gang Liu. This is an open access article distributed under the Creative Commons Attribution License, which permits unrestricted use, distribution, and reproduction in any medium, provided the original work is properly cited.

In order to better discuss the influence of pore structure characteristics of primary coal on coalbed methane adsorption, suburban coal and Zhaozhuang coal in Henan Province were systematically sampled. The analysis method of pore structure characteristics of primary coal is divided into shooting research and experimental analysis. Scanning electron microscope (SEM) was used to analyze the formation reason of coal micropores, pore shape, pore connectivity, pore size, and filling effect on coalbed methane adsorption. Experimental analysis is mainly based on CO₂ adsorption experiments to obtain specific surface, pore volume, and distribution of coal samples. The pore-specific surface area, pore volume, and adsorption-desorption curve of coal samples were obtained by ultralow-temperature N₂ adsorption experiment. Finally, the influence of pore structure characteristics of primary tectonic coal on coalbed methane adsorption was discussed by fusion of phase study and experimental analysis.

1. Introduction

Coal is a porous medium with two-way growth and development of pores. The pore structure of the surface layer of coal cultivation substrate is a reservoir for coalbed methane adsorption, and the penetrating pores inside it are also the primary safe channel for coalbed methane infiltration and spread. The characteristics of pore structure (area, pore size distribution, pore volume) have a very important regulatory effect on the cause, migration (adsorption, spread, infiltration) characteristics, and behavior of coalbed methane. It has a great guiding significance for the comprehensive utilization of coalbed methane and can reasonably ensure the safety factor of coalbed methane mining and discharge. At the same time, the structure of primary coal is the indication of initial chemical substances, accumulation, and conversion of coal and is the key initial characteristic of coal. Therefore, it is of great practical significance to discuss the pore structure characteristics of primary coal for coalbed methane adsorption.

2. Samples and Test Methods

2.1. Experimental Samples. The original coal sample system is taken from the coal mines in the suburbs of Henan Province and Zhaozhuang coal mine. Most coal seams still maintain the original ecological accumulation structure and structural characteristics, and their structures, formation, and endogenous gaps can generally be distinguished from each other. The macroscopic coal and rock types of coal are bright to semibright. The main components of macroscopic coal and rock are dominated by bright coal. Mirror coal accounts for a small part, and sometimes dark coal bands can be seen. The lamellar structure is obviously indigenous, most of which are horizontal layers, and sometimes, the wavy layer and the oblique layer can be seen with strip structure. The coal is hard to break. Fragmentation fracture is mostly shell, serrated, and staircase. Endogenous joints have good growth and development, excellent storage, and smooth and tidy joint surfaces and are dominated by shear joints [1].

2.2. Testing Method. In order to better obtain the pore structure characteristics of two kinds of primary coal samples, this study adopted scanning electron microscopy, CO₂ adsorption experiment, and ultralow-temperature N₂ adsorption experiment to explore. In the experiment, two kinds of coal samples were ground and broken, 32–60 meshes were selected, and 5–10 g were obtained, respectively.

2.2.1. SEM Experiment. VEGA3 LM tungsten filament scanning electron microscope was used in this test, which has high magnification and can observe the phase under 5 ~ 1000 k sight. High resolution means that pixels are clearer, objects are clearer, and particles are smaller; probe current range is 0.5 pA ~ 5 A, accelerating voltage range is 0.2 ~ 30 KV; the free working distance is 2 ~ 145 mm, which can complete the random transformation of the working distance, so as to observe the actual effect of primary coal micropores.

2.2.2. Low-Temperature N₂ Adsorption Test. Low-temperature N₂ adsorption experiment was carried out using the principle of physical adsorption and capillary condensation of nitrogen on a solid surface under saturated temperature standard. In this experiment, Autosorb-iQ analytical instrument from Conta, USA was used for testing at liquid nitrogen saturation temperature (77 K). The relative pressure during the experiment was 0–1. The N₂ isothermal adsorption–desorption curve, pore volume, and pore specific surface area value and distribution were obtained by changing the pressure.

2.2.3. CO₂ Adsorption Experiment. The CO₂ adsorption experiment is similar to the low-temperature N₂ adsorption principle, but because of the smaller CO₂ gas molecules and faster diffusion rate, it has higher saturation pressure at saturation temperature (273 K), which can be used to test micropores. Autosorb-iQ analytical instrument from Conta, USA was used for testing at liquid CO₂ saturation temperature (273). The relative pressure was 0–1, and the values and distribution of pore volume and pore specific surface area were obtained.

3. SEM Results and Analysis

3.1. Scanning Results. Through the analysis of coal samples in suburban Henan and Zhaozhuang mines, it is concluded that the homogeneity and integrity of primary structure coal samples are good. There are three types of micropores in coal (Figure 1 and 2), cell cavity pores (Figure 3 and 4), and mold pores (Figure 5 and 6).

Stomatal belongs to a metamorphic pore. In the coal-forming process, coal is subjected to metamorphism and formed by the “gas generation” and “gas accumulation” in the process [2–16]. Stomatals have a variety of shapes, and most of them are round, ellipsoid, and irregular. The pore distribution part presents large area directional production (Figure 1), or relatively concentrated production (Figure 2). The pore size is basically below 10 μm, and the sizes are

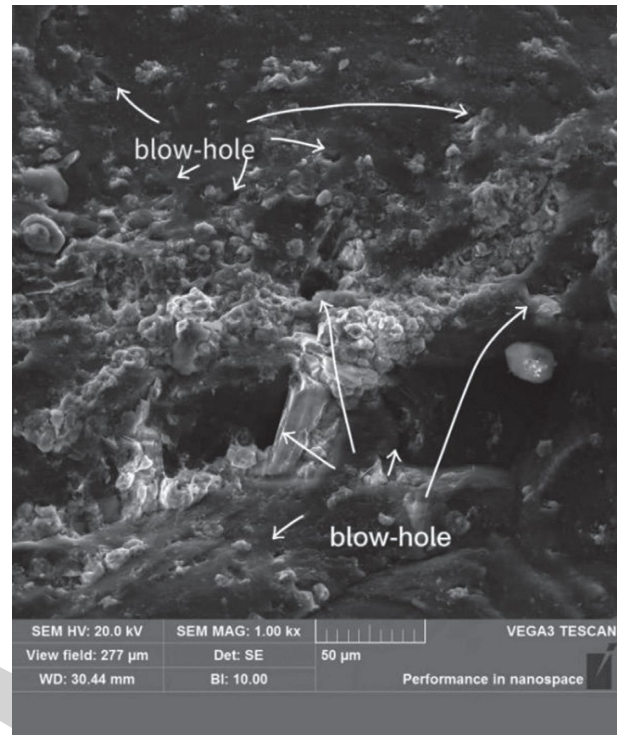


FIGURE 1: Directional generation of stomata.

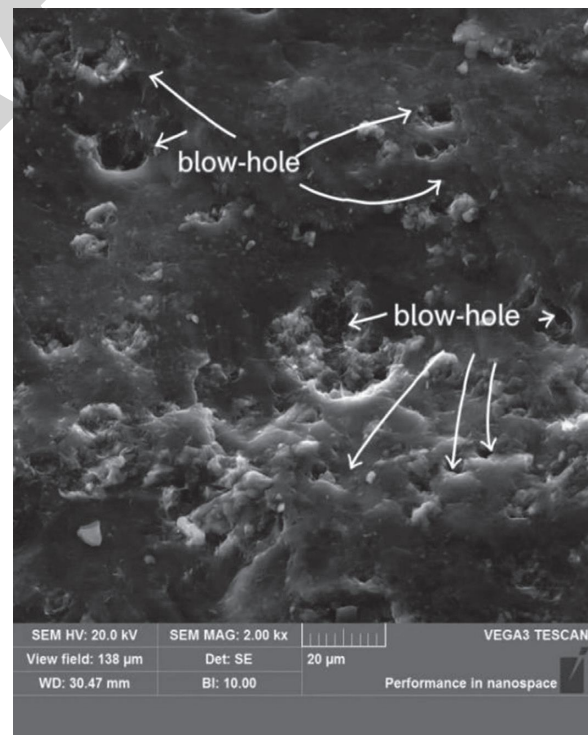


FIGURE 2: Relative concentration of stomata.

different. Pores are basically disconnected, and pores are often filled by granular, flake, and other clastic minerals.

Cavity pores are produced by the structural pores of the cells of coal-forming plants, belonging to the range of primary pores [2–17]. The pores basically exist in an isolated form, and

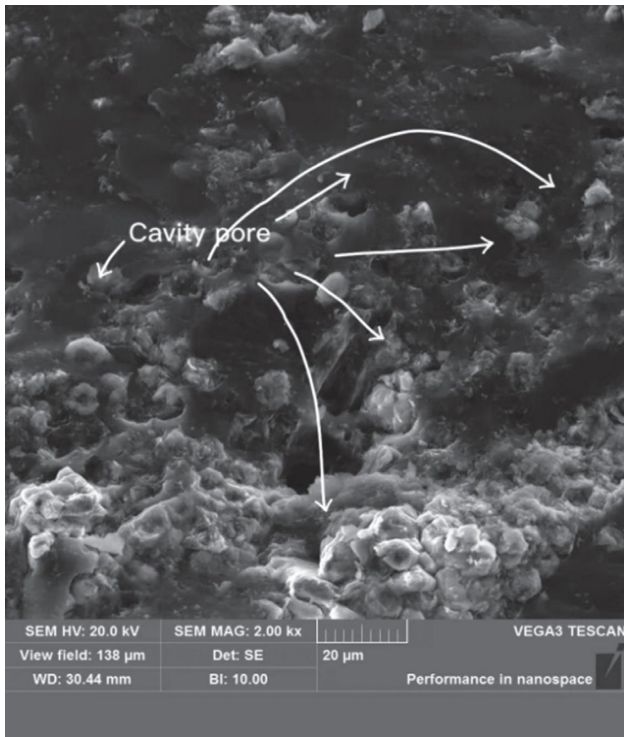


FIGURE 3: Detrital substances in cell cavity pores 1.

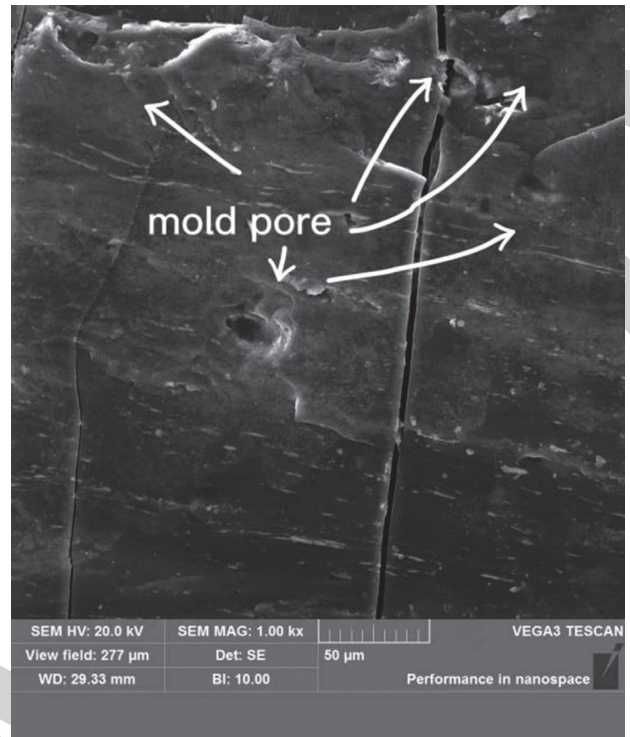


FIGURE 5: Complex form of mold hole 1.

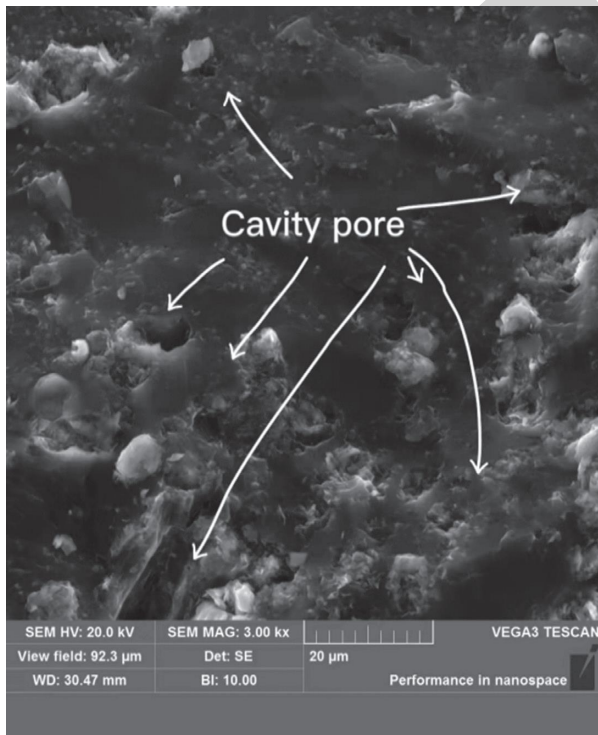


FIGURE 4: Detrital substances in cell cavity pores 2.

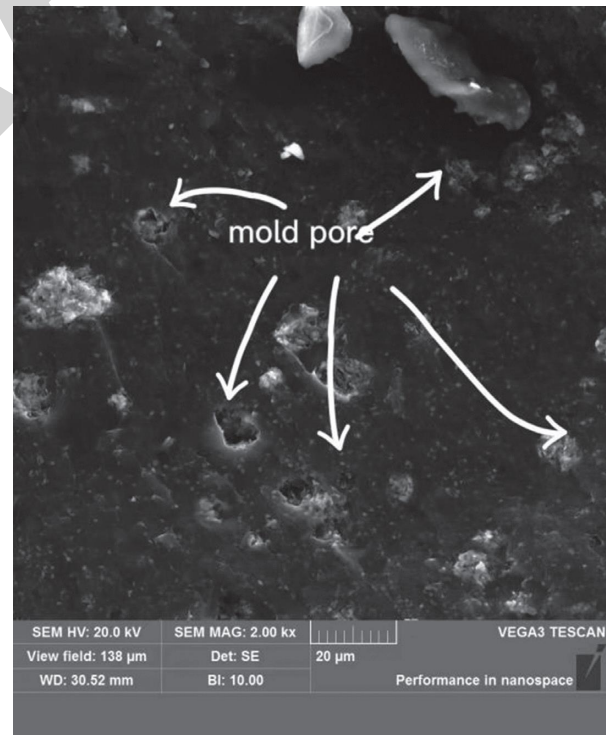


FIGURE 6: Complex form of mold hole 2.

most of the pores are subcircular. Some pores are deformed due to damage and eventually appear ellipsoid or a small number of irregular shapes. The pore size is different, and most of them are distributed between 1 and 10 μm . It is observed from the figure that most of the pores are independent and disconnected. It can

be clearly observed that the pores are filled with granular debris (Figures 3 and 4).

The mold hole belongs to a mineral hole. Due to the difference in the strength of minerals and soil organic matter in coal, some pits are formed due to the compressive stress

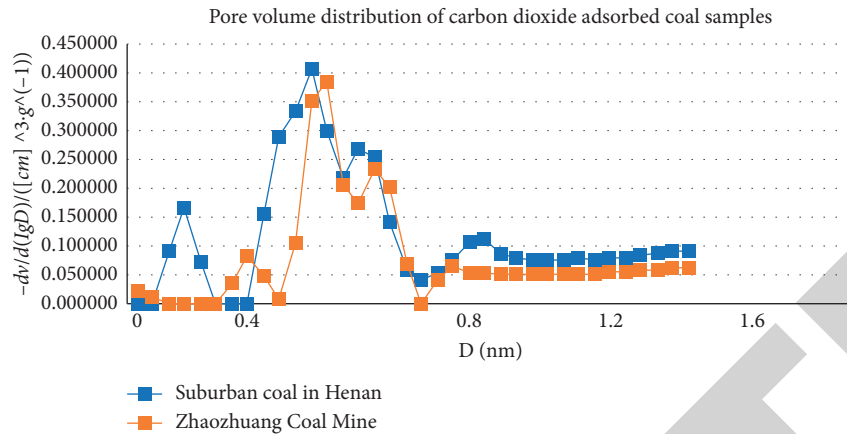


FIGURE 7: The pore volume distribution curve of carbon dioxide adsorption coal sample.

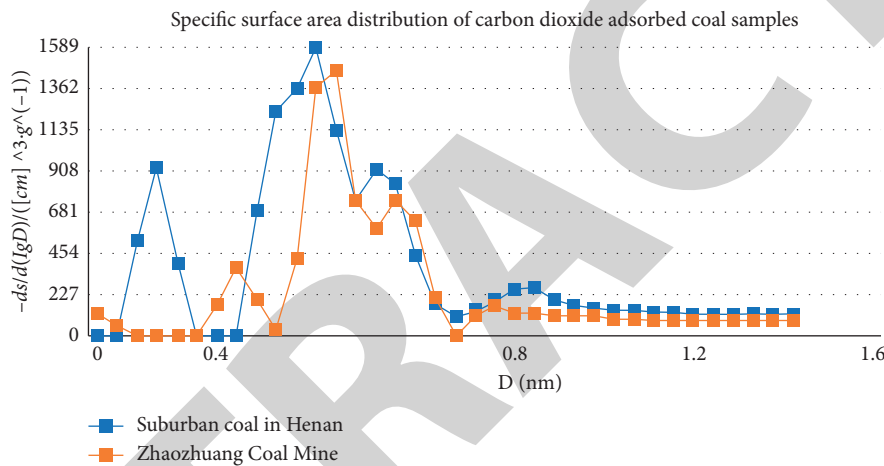


FIGURE 8: The specific surface area distribution curve of carbon dioxide adsorption coals.

during coal formation [2–18]. The shape of the mold hole is extremely complex and changeable, and the pores are not connected, which are called “dead holes” (Figures 5 and 6).

3.2. Result Analysis. IUPAC classification specification is selected. According to the classification method of pores defined by IUPAC, macropores are defined as (pore size more than 50 nm), mesopores are defined as (pore size 2–50 nm), and micropores are defined as (pore size less than 2 nm). The electron micrographs of two kinds of primary coal from suburban coal mines and Zhaochang coal mines in Henan Province are analyzed. The results show that the pores of primary coal are large and basically disconnected. Many studies have shown that micropores are the primary site for coalbed methane adsorption. The higher the connectivity between pores, the stronger the adsorption capacity of coalbed methane. Therefore, the adsorption capacity of primary coal for coalbed methane is weak, and the adsorption capacity is low.

4. Experimental Results and Analysis of CO₂ Adsorption

4.1. Experimental Results. Literature [19], through a large number of data analyses of three models (DFT, MC, and

TABLE 1: Numerical values of pore volume and specific surface area of coal samples 1.

Sample	$V/(\text{cm}^3 \cdot \text{g}^{-1})$	$S/(\text{m}^2 \cdot \text{g}^{-1})$
Suburban coal in Henan	0.083214	281.81
Zhaozhuang coal mine	0.055239	174.0

DA), finally concluded that the DFT model is applied to the CO₂ adsorption experiment to analyze the pore size distribution of micropores in coal is more accurate. In this paper, the adsorption data of CO₂ at low temperature were analyzed by the DFT model, and the pore volume, pore specific surface area, and distribution of the test samples were calculated (Figures 7 and 8, Table 1).

4.2. Result Analysis. The distribution density function of pore volume and pore specific surface area of primary coal samples, as a whole, increases with the increase of pore size, showing a fluctuation of “increase-decrease-increase-decrease”, and finally tends to be stable. The increase of the curves of the two coal samples reaches the maximum between 0.5 nm and 0.6 nm. After that, the pore volume distribution density function gradually decreases and tends to

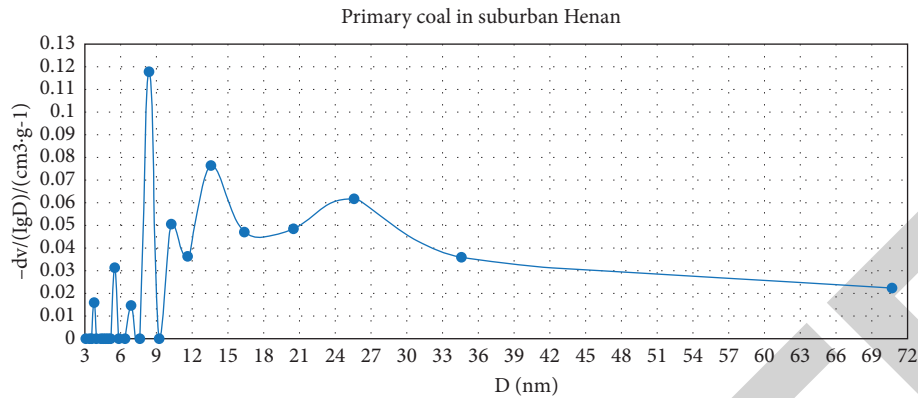


FIGURE 9: Distribution of pore volume of coal.

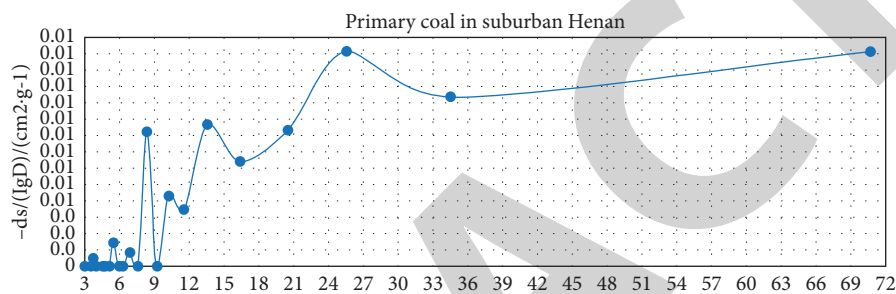


FIGURE 10: Distribution of pore specific surface area of coal.

be stable, indicating that the pore volume corresponding to the pore size of the test coal sample in the range of 0.5–0.6 nm is the largest, with the largest number of pores or the longest pore length. The pore specific surface area distribution of coal samples has a density function similar to the pore volume distribution. On the whole, the pore specific surface area distribution density function of coal samples increases first and then decreases with the increase of pore size, and the maximum increase is obtained at about 0.5 ~ 0.6 nm, followed by a small fluctuation, and finally tends to a very low value. The pore specific surface area corresponding to 0.5 ~ 0.6 nm is the largest. We believe that the dominant pore type of coal pore specific surface area is micropores. The larger the number of micropores, the larger the pore specific surface area of coal.

Combined with the data and distribution, the pore volume and specific surface area of the two coal samples are small, mainly concentrated in 0.5 ~ 0.6 nm. The adsorption of coalbed methane depends on the pore volume and pore specific surface area, and they are positively correlated [20]. The larger the pore volume and pore specific surface area, the stronger the adsorption. On the contrary, the smaller the adsorption capacity is.

5. Experimental Results and Analysis of Low-Temperature N₂ Adsorption

5.1. Experimental Results. In this paper, the test data were analyzed, and finally, the traditional BJH model was used to characterize the distribution of micropores and mesopores (Figures 9 and 10).

Reference [21] Chen Ping, Tang Xiuyi according to the adsorption curve and desorption loop shape, the pore morphology of coal is divided into three categories.

The L1 type one-end closed impermeable type (adsorption and desorption curves basically coincide) is mainly formed by the capillary condensation and evaporation pressure is basically the same, so the adsorption curve and desorption loop are basically the same.

The L2 open type (separation of adsorption and desorption curves) is mainly formed by the capillary condensation pressure lower than the pressure required for evaporation. There is a turning point at $P/P_0 = 0.5$, and the adsorption curve and desorption loop overlap at low pressure, while separation occurs at high pressure.

According to the adsorption curve and desorption loop shape in reference, the pore morphology of coal is divided into three categories. In the third category, according to the adsorption curve and desorption curve, a steep slope occurs at $P/P_0 = 0.5$, so it is called as slender bottle. The reason for the occurrence of the steep slope is the evaporation effect generated in the early desorption. Due to the different pressures required for evaporation and condensation, the separation of the curve is first caused, and then the liquid is quickly evaporated at $P/P_0 = 0.5$. Finally, the desorption curve is suddenly reduced and the steep slope is generated.

Based on this classification, this paper classifies and analyzes the morphological characteristics of coal pores according to the adsorption curves and desorption loops (Figure 10).

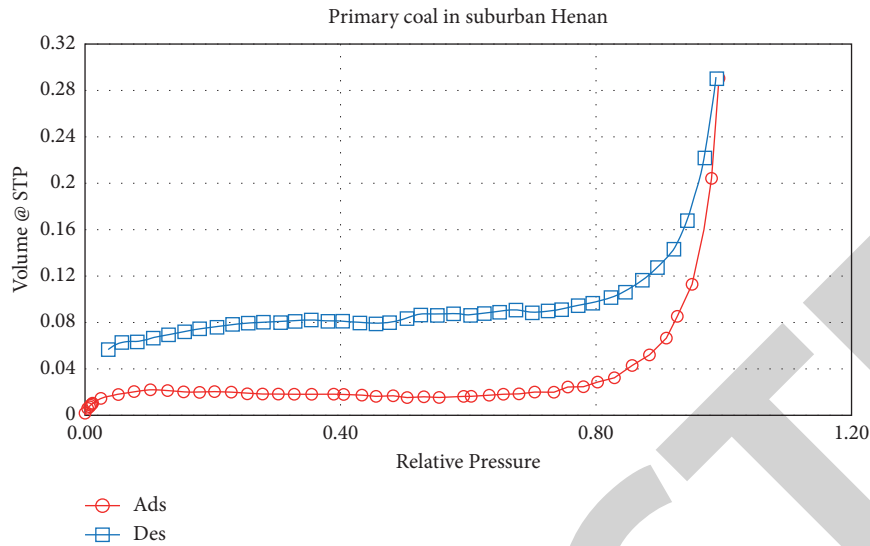


FIGURE 11: Adsorption and desorption curves of coal.

5.2. Result Analysis. From Figures 9 and 10, the pore volume and specific surface area are almost entirely distributed in the mesoporous phase (IUPAC).

Classification only a small part is distributed in the micropore stage. The number of micropores is very small, resulting in a very small proportion of pore volume and pore specific surface area to total pore volume and total pore specific surface area, and micropores are the primary site for coalbed methane adsorption, resulting in weak adsorption capacity and small intake of primary coal for coalbed methane [22].

By analyzing the adsorption and desorption curve of Figure 11, combined with classification, it is concluded that the adsorption and desorption curve of primary coal in suburban Henan belongs to the L1 type one-end closed impermeable type. Although this pore morphology structure may have good gas content, the permeability is general, which is not conducive to the adsorption of coalbed methane.

6. Conclusion

- (1) Through the analysis of the scanning electron microscope, it is concluded that the pores of primary structure coal are large, and there are three types of micropores: pores, cavity pores, and mold pores. The pores are mainly large pores and mesopores, with only a small amount of micropores, and the pores are basically disconnected. Micropores are the main sites for coalbed methane adsorption. The better the connectivity between pores, the stronger the adsorption capacity of coalbed methane. Therefore [2–4], the adsorption capacity of primary structure coal on coalbed methane is weak, and the adsorption capacity is low.
- (2) The results of CO₂ adsorption experiments show that the pore volume and specific surface area of the two coal samples are small, and the pore volume and specific surface area are determined by the number

of pores, so it can be seen that the distribution of micropores is very small, which is not conducive to the adsorption of coalbed methane.

- (3) According to the N₂ adsorption test at ultralow temperature, it is analyzed that the pore volume and specific surface area of primary coal are mostly dispersed in the mesoporous link, and only a small part is in the microporous plate link. The adsorption and desorption curve of primary coal in the suburbs of Henan Province belongs to the closed and impermeable type of L1 end, which is not conducive to the adsorption of coalbed methane.

In general, the pore structure characteristics of primary structure coal, such as pore specific surface area, pore morphology, pore size, and pore volume, are not conducive to the adsorption of coalbed methane.

Data Availability

No data were used to support this study.

Conflicts of Interest

The authors declare that there are no conflicts of interest regarding the publication of this article.

References

- [1] C. Yang, H. Chang, and X. Shao, "Study on micro-pore characteristics of structural coal in different coal bodies under scanning electron microscopy," *Coal Science and Technology*, vol. 47, no. 12, pp. 194–200, 2019.
- [2] H. Zhang, "Genetic types of coal pores and their research," *Journal of China Coal Society*, vol. 26, no. 1, pp. 40–44, 2001.
- [3] B. Howard, *Coal and Gas Outburst*, China Industrial Press, Beijing, China, 1966.
- [4] C. Liu, "Experimental study on coal hole structure characteristics," *Safety In Coal Mines*, vol. 21, no. 8, pp. 1–5, 1993.

Retraction

Retracted: Exhibition of Dielectric Property Based on Soil Class and Moisture Presence for Bengaluru District

Advances in Materials Science and Engineering

Received 26 December 2023; Accepted 26 December 2023; Published 29 December 2023

Copyright © 2023 Advances in Materials Science and Engineering. This is an open access article distributed under the Creative Commons Attribution License, which permits unrestricted use, distribution, and reproduction in any medium, provided the original work is properly cited.

This article has been retracted by Hindawi, as publisher, following an investigation undertaken by the publisher [1]. This investigation has uncovered evidence of systematic manipulation of the publication and peer-review process. We cannot, therefore, vouch for the reliability or integrity of this article.

Please note that this notice is intended solely to alert readers that the peer-review process of this article has been compromised.

Wiley and Hindawi regret that the usual quality checks did not identify these issues before publication and have since put additional measures in place to safeguard research integrity.

We wish to credit our Research Integrity and Research Publishing teams and anonymous and named external researchers and research integrity experts for contributing to this investigation.

The corresponding author, as the representative of all authors, has been given the opportunity to register their agreement or disagreement to this retraction. We have kept a record of any response received.

References

- [1] S. Kumar, N. Ahalya, V. Singh et al., "Exhibition of Dielectric Property Based on Soil Class and Moisture Presence for Bengaluru District," *Advances in Materials Science and Engineering*, vol. 2022, Article ID 6807204, 9 pages, 2022.

Research Article

Exhibition of Dielectric Property Based on Soil Class and Moisture Presence for Bengaluru District

Sujit Kumar ¹, N. Ahalya ², Vikash Singh,³ Pravin P. Patil,⁴ A. V. Raghavendra Rao,⁵ A. Nirmala Jyothsna,⁶ P. Abhilash,⁷ Rupesh kushwah,⁸ and Sojan Palukaran Timothy ⁹

¹Department of Electrical and Electronics Engineering, Jain (Deemed-To-Be-University), Bengaluru 560069, Karnataka, India

²Department of Biotechnology, MS Ramaiah Institute Technology, MSR Nagar, Bengaluru 560054, Karnataka, India

³Research Scholar, Department of Civil Engineering, Institute of Engineering and Technology, Lucknow 226021, Uttar Pradesh, India

⁴Department of Mechanical Engineering, Graphic Era Deemed to be University, Dehradun 248002, Uttarakhand, India

⁵Department of Chemical Engineering, B V Raju Institute of Technology, Narsapur 502313, Medak, Telangana, India

⁶Department of Physics, Ch. S. D. St. Theresa's College for Women (A), Eluru 534003, Andhra Pradesh, India

⁷Department of Civil Engineering, Annamacharya Institute of Technology and Sciences (Autonomous), Tirupati 517520, Andhra Pradesh, India

⁸Department of Chemistry, Government Shyam Sundar Agrawal PG College, Sihora 483225, Madhya Pradesh, India

⁹Faculty of Mechanical Engineering, Arba Minch Institute of Technology (AMIT) Arba Minch University, Arba Minch, Ethiopia

Correspondence should be addressed to Sojan Palukaran Timothy; sojan.palukaran@amu.edu.et

Received 5 March 2022; Accepted 19 April 2022; Published 12 June 2022

Academic Editor: Palanivel Velmurugan

Copyright © 2022 Sujit Kumar et al. This is an open access article distributed under the Creative Commons Attribution License, which permits unrestricted use, distribution, and reproduction in any medium, provided the original work is properly cited.

This research examined the dielectric characteristics of soils by utilizing four types of soil (clay-loam, loam, clay, and Frank) in a vector network analyzer (VNA) in the 600–8000 MHz microwave frequency range at ambient temperature ($25^{\circ}\text{C} \pm 3^{\circ}\text{C}$). In this experiment, three observations were performed on the basis of soil moisture contents (dry, 33%, 66%, and 100% field capacities (CC)). Both actual (dielectric constant) and fictional (loss factor) parts of the dielectric characteristics improved with increasing soil moisture; however, the responses were not linear. It was observed that dry soil dielectric characteristics were deficient when compared to wet soil. In conclusion, the dielectric behavior of soil mainly was resolute by the moisture in the soil. Frank soil had considerably lower dielectric characteristics, while the Jain University (JU) clay soil had a far more significant dielectric loss factor.

1. Introduction

There are different applications employed with microwave energy, as shown in Table 1, and there are results of soil treatment with a microwave also mentioned in Table 1. Its significant benefits include quick start-up time, accurate control, and volumetric warming [1].

It causes polar particles to rotate due to the oscillating electromagnetic field created when microwave radiation is also applied to the soil. The intermolecular friction generated by this causes the production of heat. To comprehend soil heating, it is necessary to comprehend the treatment of microwave soil [14].

To use a microwave, the material must absorb microwave energy and then used for heat. The complex permittivity, called the dielectric constant, reflects the materials' ability to store energy and the efficient manner in which they convert energy into heat, known as dielectric loss [2, 20, 25]. Dielectric loss factor (DLF) is dependent on microwave energy absorption. Soil is an intricate combination of water, minerals, ions, and vapors (mainly air), and many types of microorganisms and macroorganisms [26]. There are many ways of classifying soil, based on particle size [20]. Particle size is used to classify soils according to their proportion of sand, silt, and clay. Several scientific investigations have examined the dielectric characteristics of the soil. Particular

TABLE 1: Applications of microwave energy.

S. no.	Applications	References	Result of soil treatment with microwave	References
1	Food processing	[2–6]	Reduction of weed emergence	[7–11]
2	Textiles and leather processing	[1]	Increased carbon and nitrogen mineralization	[12]
3	Medical application	[13]		
4	Plasma	[15]		
5	Solvent-free chemistry	[16]		
6	Drying of wood	[17, 18]	Greater plant growth	[14]
7	Paper and cardboard	[19]		
8	Pest control	[20]		
9	Enhancing seed germination	[21, 22]		
10	Elimination of perilous waste from dirtied soil	[23, 24]		

studies focus on remotely sensed data, whereas others focus on soil heating [26–28]. However, it appears that there has been limited research on the engineering, technical, and health (ETH)-based microwave frequencies (895/916/923 MHz, 2460 MHz, and 5900 MHz). At high ETH frequencies, the dielectric property of soil becomes significant. Based on prior research (which found that moisture content has an enormous influence on dielectric characteristics [29], expected that moisture presence influence extreme impact over dielectric properties), the dielectric characteristics are fundamental because they influence moisture content directly [30–32]. In addition, the other variables that influence the dielectrics of soil are soil classification, as shown in Table 2, soil composition, and soil compactness.

There is an urgent requirement to examine soil dielectrics through ETH microwave frequencies since the dielectric behavior of most materials changes markedly with frequency.

Many disinfectants and seed deactivators use soil temperatures between 60°C and 120°C; however, microwave heating raises the temperature of hydrocarbon-contaminated soil to levels much higher than 200°C, as discovered by [23].

For a thorough examination of the dielectric characteristics of soil, knowing the consequence of soil organic matter on soil water holding capability should be considered. Studies show that soil organic matter concentrations contribute to warming during microwave treatment when starting at approximately 200°C [33]. The electrical conductivity of soil will also be affected by salinity since it influences the ability of soil to absorb electromagnetic energy through ion conduction. As a result, it impacts the loss factor of wet soil [34]. So, it follows that the primary concerns for soil dielectric property studies revolve around three parameters: frequency (600–8000 MHz), type of soil, and moisture present in the soil.

Different techniques are used for dielectric property measurements [35]. For frequencies between 50 and 100 MHz, the cavity resonator effectively works with trim loss materials. Free space analysis is helpful for significant, level, reedy, and shunt samples, and it can handle great frequencies (1 GHz–100 GHz) and temperatures over 373°C. Due to the nature of the lumped circuit approach, only frequencies below 100 MHz should be used. In contrast, because of the concern about loss, the distributed circuit

technique is often not suitable. The transmission line method is most suitable for liquids and solids, but not gases, because of their low permittivity in this frequency range of 20 to 100 GHz [35–37]. To conduct dielectric property testing, a closed-loop coaxial probe is sometimes used with food grains. This particular measuring instrument, a VNA, was often used with this kind of test [38–41]. Based on the soil characteristics, the most frequently used model was dielectric mixing [42]. The semiempirical model was suggested based on soil structure, moistness presence, unpackaged density, and temperature.

Extensive diversity of soil sorts, moistness levels, and frequencies is required to examine soil's dielectric characteristics and identify its heating pattern. To meet the goal of this study, the following tasks were completed: (i) assessed the frequency range (600–8000 MHz) for soil's dielectric properties and (ii) developed a multidynamic mixing model to predict soil dielectrics by combining different mathematical models, according to the results of Debye models.

2. Materials and Methods

2.1. Preparation of Soil Samples. Four soil types were utilized in this investigation to examine the dielectric characteristics of various types of the soil as in Table 1. Ramanagara, situated at 12.9°N, 77.2°E, served as the source for clay loam soil, while the other three soil types were gathered from Jain University in Bengaluru (JU) Karnataka, India: Magadi wheat field loamy soil (12.5°N, 75.2°E), clay soil from Kanakapura rice field (13.5°N, 80.4°E), and sugarcane field Frank soil (13.8°N, 81.4°E). The samples were allowed to dry for one week after collection. The aggregates were broken down to remove unwanted components such as dried roots, grasses, stones, and gravel preceding to be separated using a 1.5 mm soil filter, which results in a better assessment of the dielectric characteristics. To achieve an even distribution of nutrients, the different soils were carefully assorted by using the slicing technique.

2.2. Exploration of Soil Assets. Before they are sent to the laboratory for the complete analysis, samples are dried at 45°C for one day. Table 2 represents the data obtained after the experiment.

TABLE 2: Experimented data of soil assets.

Soil assets	Analytical method	Type of soil			
		Bangalore Clay loam	JU loamy Loam	JU clay Clay	JU frank Frank
Structure	Hydrometer and filter study				
Sand		48.0	58.2	49.6	84.8
Silt		15.1	24.9	18.2	7.2
Clay		35.6	21.1	33.1	6.7
Field capacity	Gravimetric	66	68	74	18
Organic carbon	Walkley and black	0.74	1.42	0.54	0.75
Electrical conductivity	Walkley and black	1.7	0.8	2.6	0.9
pH	1:5 CaCl ₂	7.6	5.8	7.3	5.4

2.3. *Preservation of Soil Dampness.* Four types of soil moisture (dry, 33%, 66%, and 100% CC) were maintained. To measure the volume of the soil field, a funnel was employed. The distilled water of 20 ml was then added to the soil to promote germination. A funnel was positioned in a cylinder of the correct volume and left overnight to measure the gravity water in the cylinder. The volume basis CC of the soil was calculated using the equation [43]. After drying, the soil samples were allowed to dry at 100°C for one day altogether. The other moisture content was reached by adding further deionized water to the soil and gently stirring it. To prevent water loss, all of the samples were stored in locked plastic bags at 3°C. Table 3 shows the particulars of the experiment attempting to find out all the variables of dielectric characteristics at once.

2.4. *Measurement of Soil Dielectrics.* A VNA (N5230 A PNA-L network analyzer) was used to quantify the complex permittivity as in Figure 1. To accurately evaluate the dielectric characteristics of materials, the network analyzer could determine frequencies from 10 to 50 GHz.

The primary portion of the analyzer was linked to an external computer, which in turn was connected to Agilent's related analytical software, which was implemented with an embedded algorithm for calculating permittivity characteristics. The network analyzer was calibrated using three standards before the test. The electrical short was created by a metal sheet that was placed below the probe. A set of standards, such as water or Teflon or ceramic, was used to validate the calibration (the test was conducted to ensure the calibration was correct). The dielectric characteristics of the experimental samples were then tested once they had acquired satisfactory values for the reference samples.

Different soil samples were examined in terms of their dielectric characteristics, with measurements spanning the frequency range of 600 to 8000 MHz. The frequency range used by industries, scientific and medical applications, and other expected usage frequencies, falls within this range. To increase the certainty of the statistics, samples were measured three times, with three replications of the process and three observations in each replication. The results from each replication were combined to give three averages, and this value was used for additional numerical examination. The integrity of the dimensions was protected by placing the soil sample in a 2.8 cm long ampule that had a diameter of 1.5 cm. Every experiment was performed at ambient temperature (25°C ± 3°C).

TABLE 3: Details of experiment.

Type of soil	Presence of moisture (CC) (%)	No. of samples observed
Clay loam	33	8
	66	8
	100	8
Loam	33	8
	66	8
	100	8
Clay	33	8
	66	8
	100	8
Loamy Frank	33	8
	66	8
	100	8

2.5. *Dispersion Deepness and Wavelength.* When it comes to dielectric materials, the two most significant factors are the dielectric constant and loss. Microwave treatment controls the warming design of a specific shape. Additional data acquired from the measurement of dielectric characteristics and the depth of the electromagnetic waves in the soil may include the wavelength of the waves [43, 44]. The electromagnetic power density starts decreasing from its surface value to a drop of 36.8% [2, 43].

2.6. *Analysis by Cole-Cole.* It is often required to conduct a curve-fitting analysis to get the observed complex permittivity. Debye relaxation model and dielectric relaxation time are often used in curve-fitting studies. The complex permittivity of a pure polar substance is given by Debye:

$$\varepsilon = \varepsilon_{\infty} + \frac{\delta_s - \delta_{\infty}}{1 + j\omega\tau} - j \frac{\sigma}{\omega\varepsilon_0} \quad (1)$$

The respective parameters are mentioned in [45]. The Debye equation cannot be simplified because all of the materials are not entirely polar. Consequently, it takes more time for the system to relax, and therefore, the Debye equation shown in (2) is not simplified [46]:

$$\varepsilon = \varepsilon_{\infty} + \frac{\varepsilon_s - \varepsilon_{\infty}}{(1 + j\omega\tau)^{1-\alpha}} - j \frac{\sigma}{\omega\varepsilon_0} \quad (2)$$

Real and fictional dielectric features may be divided into two components, as shown by Cole and Cole in (3) and (4) [46]:

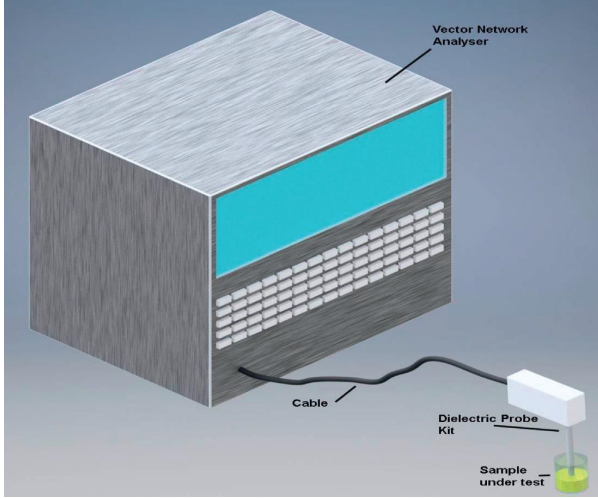


FIGURE 1: Representation of the vector network analyzer (VNA) (N5230A PNA-L) with the sample under test.

$$\epsilon' = \epsilon_{\infty} + \frac{(\epsilon_s - \epsilon_{\infty}) [1 + (w\tau)^{1-\alpha} \sin(\alpha\pi/2)]}{1 + 2(w\tau)^{1-\alpha} \sin(\alpha\pi/2) + (w\tau)^{2(1-\alpha)}}, \quad (3)$$

$$\epsilon'' = \frac{(\epsilon_s - \epsilon_{\infty})(w\tau)^{1-\alpha} \cos(\alpha\pi/2)}{1 + 2(w\tau)^{1-\alpha} \sin(\alpha\pi/2) + (w\tau)^{2(1-\alpha)}} + \frac{\sigma}{w\epsilon_0}. \quad (4)$$

Additionally, it is apparent that the dielectric characteristics of most ordinary ingredients, which include most vegetation, are connected to the moisture presence of the material, which may be either the extent of water in the substance or the percentage of water in the vegetation:

$$\epsilon(m) = \left[\epsilon_{\infty} + \frac{\epsilon_s - \epsilon_{\infty}}{(1 + jw\tau)^{1-\alpha}} - j \frac{\sigma}{w\epsilon_0} \right] \cdot F(m). \quad (5)$$

3. Results and Discussion

Figure 2 demonstrates dielectric characteristics of all soil samples at various frequencies and moisture content.

$$\epsilon' = \epsilon_{\infty} + \frac{(\epsilon_s - \epsilon_{\infty}) [1 + (w\tau)^{1-\alpha} \sin(\alpha\pi/2)]}{1 + 2(w\tau)^{1-\alpha} \sin(\alpha\pi/2) + (w\tau)^{2(1-\alpha)}} \cdot \text{erf}[-c(m - m_0)], \quad (7)$$

$$\epsilon'' = \frac{(\epsilon_s - \epsilon_{\infty})(w\tau)^{1-\alpha} \cos(\alpha\pi/2)}{1 + 2(w\tau)^{1-\alpha} \sin(\alpha\pi/2) + (w\tau)^{2(1-\alpha)}} + \frac{\sigma}{w\epsilon_0} \cdot \text{erf}[-c(m - m_0)]. \quad (8)$$

Figure 3 demonstrates how plot designs change with frequency and moisture content. Table 5 shows all the model equation's parameters for all soil types. JU Frank soil shows fit (r^2) of 0.964, whereas JU loam soil shows 0.995, signifying that the above models accurately represent the dielectric properties of these soils in which they vary by less than 0.2 percentage points over the assessment

The findings from this study are used to provide a representative sample of the dielectric characteristics of soil concerning frequency, soil type, and moisture, as shown in Table 4.

Dryness often increases as moisture is depleted, and this happens to both the actual (dielectric constant) and fictional (loss factor) properties of the dielectric (i.e., dry, 33%, 66%, and 100% CC).

Soil moisture is the primary determinant of soil dielectric characteristics since dry soil has a limited dielectric capacity. It was reported in [47, 48] that, with increased moisture content, the dielectric value also increases. Inversely related to their sand content and the moistness holding capability, therefore, the CC of soils is proportional to their water-binding capacity. Because of a significant amount of sand (84.8% (Table 2)), the JU loamy Frank's field capacity is lower than that of the other soils (48.0% to 58.2% (Table 2)).

When the frequency lowers, the JU clay soil's dielectric loss factor climbs significantly. The significant difference in ionic conductivity between these soils suggests that this may be linked to it (2.6 dS m^{-1} -Table 2). According to [46], the angular frequency (ω) is inversely proportional to ionic conductivity. Lower frequencies indicate it is more prominent; higher frequencies suggest it is smaller. When frequencies are lower, the dielectric loss factor in Bangalore soil is on the lower side, but when the moisture content is higher, the conductivity of the soil (1.7 dS- m^{-1}) is notable.

Most of the free water component has been leached away by gravity; thus, the remaining moisture is bound to water. The soil dielectric behavior was studied to establish an empirical formula for Debye [32].

Calculated best $F(m)$, which could represent the observed statistics, was

$$F(m) = \text{erf}[-c(m - m_0)]. \quad (6)$$

As a result, in this research, these soils' dielectric constant and loss factors are defined by modifying (5) and by replacing (6):

frequency range and moisture content range that were tested in this study.

What anticipated throughout this research was a more linear response to moisture content. The dielectric probe must be pressed down to establish excellent contact with the soil while making a measurement. Moisture inside soil makes the particles slide together, resulting in a higher bulk

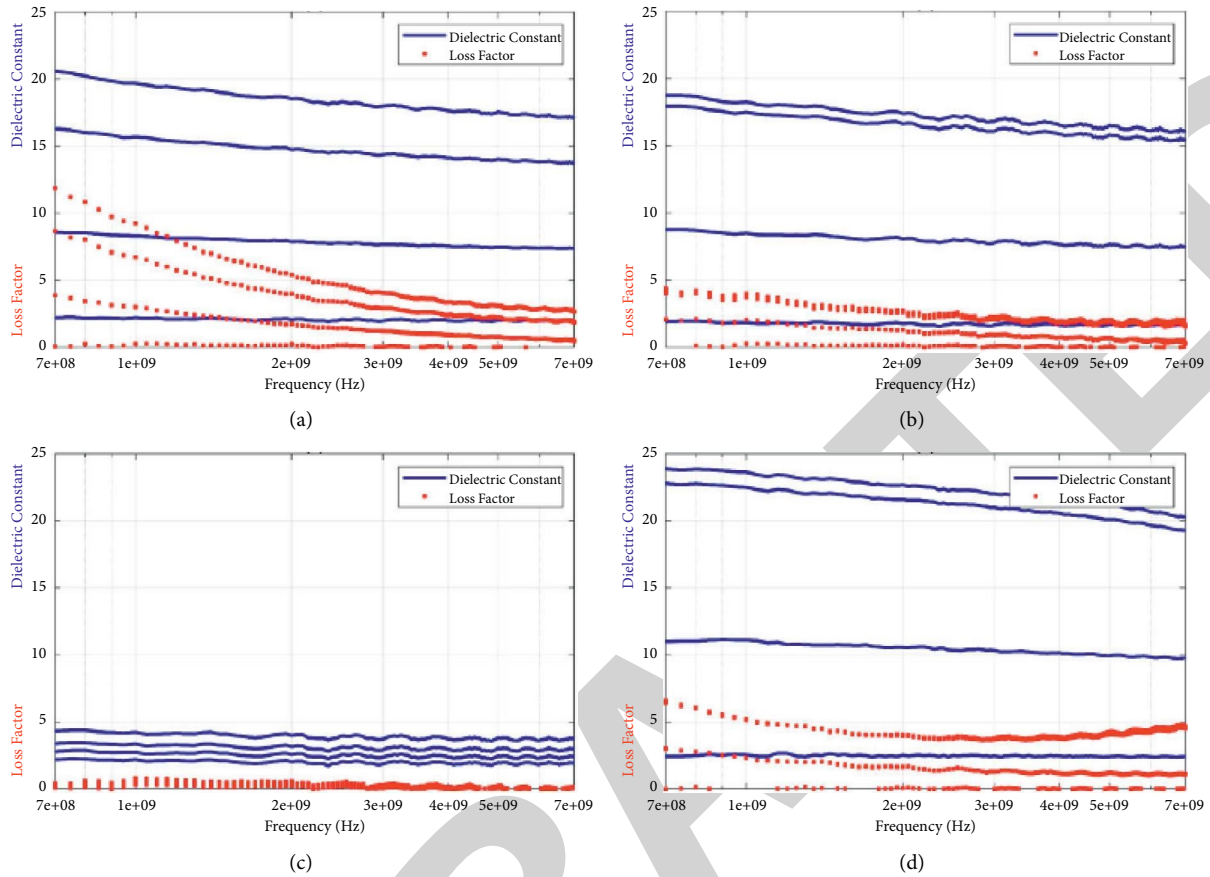


FIGURE 2: Four soil types were tested for their dielectric characteristics with respect to frequency and moisture presence: (a) JU clay, (b) JU loam, (c) JU frank, and (d) Bangalore clay loam.

TABLE 4: Information about soil moisture state, frequency, and type of soil in relation to dielectric data.

Type of soil	F (GHz)	Presence of moisture							
		Dry soil		33% CC		66% CC		100% CC	
		Real	Imaginary	Real	Imaginary	Real	Imaginary	Real	Imaginary
JU clay	0.8	2.204	0.059	8.478	3.712	16.301	8.658	20.621	11.760
	0.9	2.155	0.142	8.244	3.057	15.646	6.878	19.688	9.425
	1	2.214	0.262	8.214	3.001	15.594	6.700	19.685	9.215
	2	2.065	0.248	7.869	1.740	14.602	4.010	18.525	5.408
	2.54	1.998	0.147	7.771	1.432	14.513	3.418	18.215	4.652
	3	1.970	0.028	7.689	1.210	14.346	2.930	17.981	4.039
	4	1.999	0.001	7.549	0.909	14.111	2.306	17.621	3.346
	5	2.040	0.019	7.478	0.759	14.008	2.108	17.565	3.009
JU loam	5.95	2.019	0.119	7.426	0.621	13.842	1.968	17.354	2.817
	6	1.949	0.129	7.390	0.608	13.806	2.002	17.212	2.858
	7	2.004	0.197	7.385	0.501	13.720	1.868	17.054	2.612
	0.8	1.902	0.017	8.721	2.078	17.859	4.026	18.687	4.35
	0.9	1.835	0.140	8.425	1.858	17.401	3.546	18.184	3.859
	1	1.859	0.269	8.514	2.051	17.519	3.640	18.210	3.897
	2	1.782	0.205	8.041	1.200	16.539	2.578	17.304	2.718
	2.54	1.673	0.129	7.799	1.100	16.254	2.216	17.017	2.369
3	1.658	0.058	7.749	0.917	16.073	2.006	16.701	2.217	
4	1.659	0.012	7.642	0.705	15.843	1.725	16.531	1.928	
5	1.728	0.028	7.671	0.667	15.819	1.805	16.538	2.042	
5.95	1.682	0.075	7.515	0.450	15.501	1.611	16.222	1.738	
6	1.612	0.072	7.445	0.463	15.428	1.718	16.100	1.844	
7	1.676	0.148	7.457	0.292	15.354	1.460	15.879	1.658	

TABLE 4: Continued.

Type of soil	F (GHz)	Presence of moisture							
		Dry soil		33% CC		66% CC		100% CC	
		Real	Imaginary	Real	Imaginary	Real	Imaginary	Real	Imaginary
JU Frank	0.8	2.185	0.102	2.708	0.114	3.401	0.201	4.309	0.472
	0.9	2.121	0.140	2.268	0.312	3.249	0.316	4.159	0.544
	1	2.109	0.324	2.655	0.408	3.369	0.611	4.241	0.811
	2	2.016	0.249	2.547	0.376	3.152	0.439	4.001	0.526
	2.54	1.871	0.187	2.441	0.287	3.001	0.323	3.818	0.424
	3	1.847	0.057	2.363	0.127	2.915	0.175	3.721	0.255
	4	1.877	0.001	2.383	0.056	2.944	0.087	3.734	0.159
	5	1.989	0.072	2.471	0.146	3.035	0.163	3.815	0.218
	5.95	1.925	0.119	2.423	0.101	2.976	0.101	3.733	0.063
6	1.819	0.112	2.318	0.108	2.849	0.104	3.618	0.061	
7	1.912	0.215	2.419	0.224	2.950	0.230	3.738	0.217	
Bangalore clay loam	0.8	2.445	0.001	11.01	3.001	22.725	6.589	23.715	6.129
	0.9	2.531	0.012	11.12	2.521	22.625	5.428	23.724	5.328
	1	2.551	0.031	11.10	2.324	22.524	5.114	23.621	5.142
	2	2.537	0.092	10.45	1.623	21.432	3.927	22.582	4.024
	2.54	2.402	0.044	10.37	1.474	21.156	3.814	22.213	3.814
	3	2.490	0.009	10.34	1.325	21.012	3.780	22.008	3.798
	4	2.462	0.001	10.10	1.142	20.425	3.798	21.328	3.825
	5	2.426	0.052	9.935	1.273	20.012	4.001	21.168	4.250
	5.95	2.471	0.018	9.914	1.176	19.715	4.121	20.759	4.365
6	2.401	0.054	9.795	1.021	19.516	4.257	20.473	4.415	
7	2.421	0.039	9.780	1.119	19.173	4.498	20.195	4.625	

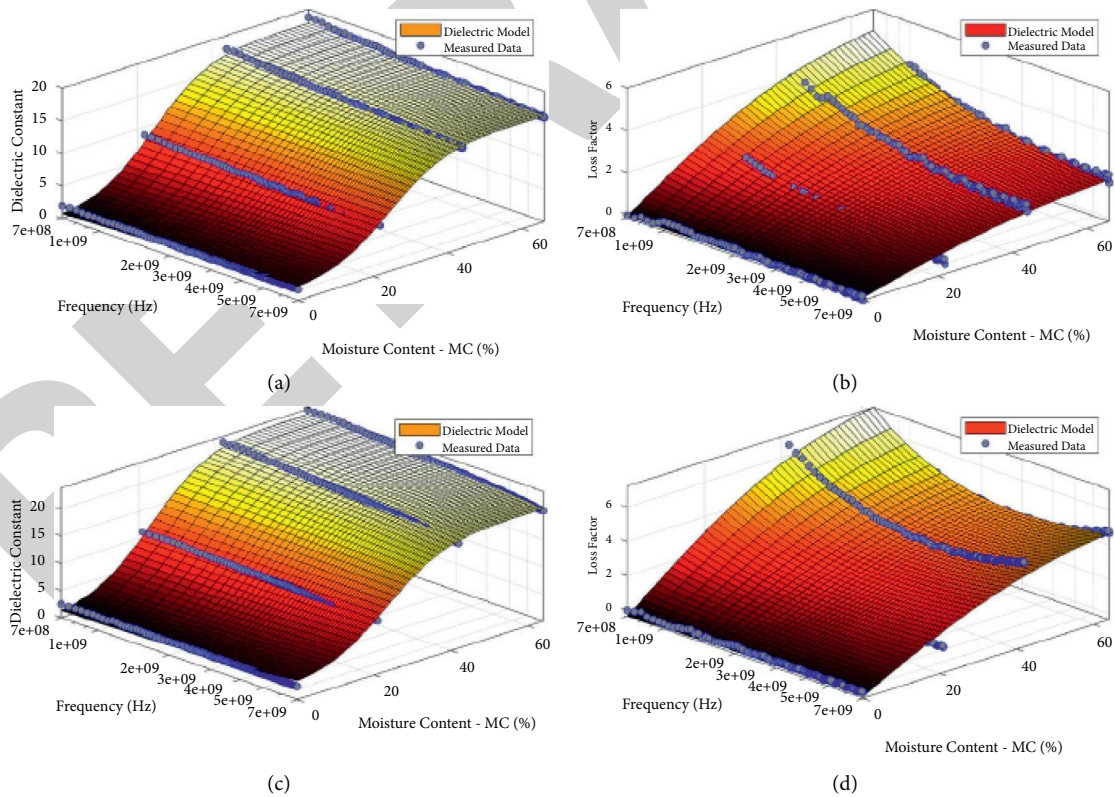


FIGURE 3: Comparisons between anticipated and observed dielectric characteristics for JU loam soil and Bangalore clay loam soil.

TABLE 5: List of all four soils investigated and their respective dielectric characteristics were simulated by the parameters utilized.

Parameter utilized	Types of soil			
	JU clay	JU loam	JU frank	Bangalore clay loam
Permittivity at high frequency, ϵ_{∞}	8.874	9.102	3.125	9.850
Static permittivity, ϵ_s	20.250	21.784	4.269	22.112
Alpha, α	0.202	0.652	0.000	0.211
C	2.452	5.102	7.622	6.230
m_0	0.256	0.236	0.117	0.241
r^2	0.993	0.995	0.964	0.995

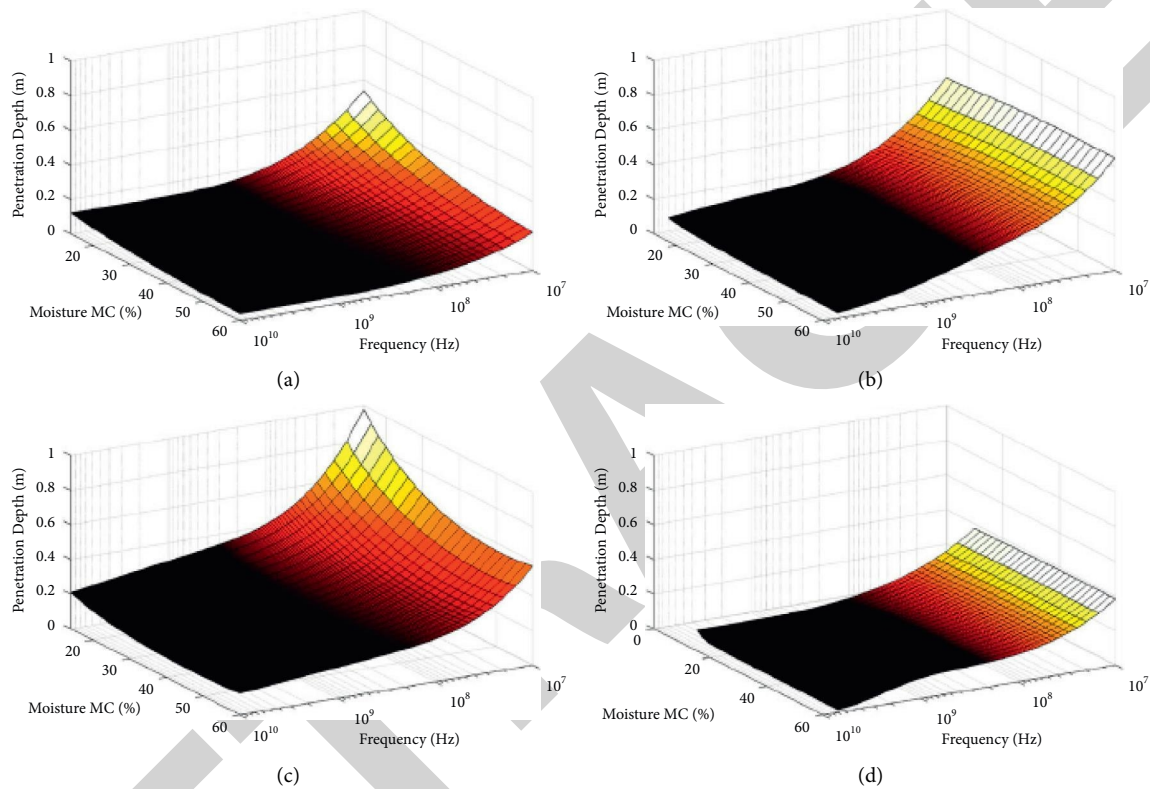


FIGURE 4: Various depths to which electromagnetic waves can penetrate in contrast to frequency and moisture content for (a) JU clay, (b) JU loam, (c) JU Frank, and (d) Bangalore clay loam soils.

density [49]. This will influence the dielectric characteristics. Optimal soil compaction occurs when the CC is 66%; as a result, the soil compaction measurements made when the test soil had 66% of its total capacity would have been greater than it should have been since the wet soil was under-compacted. It is feasible to calculate the dispersion deepness for electromagnetic waves in various soil types using models for dielectric characteristics, as shown in Figure 4.

Thus, dispersion deepness is related to frequency and moisture content, and as frequency drops, so does penetration. It is more difficult for low-frequency sound waves to reach the ground than for higher-frequency sound waves. Moreover, due to their dielectric characteristics, dry soils enable a greater penetration than wet soils because they have lower levels of electromagnetic field attenuation. While the image in Figure 4 shows soil texture impacts the depth of dispersion of electromagnetic energy, as JU Frank soil

(Figure 4(c)) pierces deeper with lower moisture content and a frequency of 107 Hz Bangalore clay loam at similar moisture and frequency.

4. Conclusion

The dielectric behavior of soil was observed by the presence of moisture in the soil. Frank soil had considerably lower dielectric characteristics, while the Jain University (JU) clay soil had a far more significant dielectric loss factor. Several models were created with different frequency and moisture content settings to examine the dielectric characteristics of soils. For the JU Frank soil, the best fit (r^2) diverges from 0.964 to 0.995 for JU loam soil. The findings shown above indicate that the models used to estimate the dielectric characteristics of these soils in this research were appropriate. To better understand how deep electromagnetic waves travel through soil, a new model was created that

models the dielectric characteristics of the soil. In both frequency and moisture content, dispersion falls. For very low frequencies, the depth of the soil penetrates deeper than higher frequencies. As it is the case with wet soils, dry soils too provide better soil dispersion.

Data Availability

The data used to support the findings of this study are included within the article. Further data or information are available from the corresponding author upon request.

Conflicts of Interest

The authors declare that there are no conflicts of interest regarding the publication of this paper.

Acknowledgments

The authors thank Space Applications Centre-Indian Space Research Organization (SAC-ISRO) Ahmedabad, India, for encouraging to work on soil moisture applications. The authors would like to thank Dr. G. Raju, Professor, JAIN (Deemed-to-be University), Bengaluru, for his constant support to complete this work successfully. Also, would like to acknowledge Dr. P. Pradeepa, EEE Department, Jain Deemed to be University, for the support and encouragement. The authors also appreciate the supports from Faculty of Mechanical Engineering, Arba Minch Institute of Technology (AMIT), Arba Minch University, Ethiopia, for the research and preparation of the manuscript.

References

- [1] K. G. Ayappa, H. T. Davis, G. Crapiste, E. A. Davis, and J. Gordon, "Microwave heating: an evaluation of power formulations," *Chemical Engineering Science*, vol. 46, no. 4, pp. 1005–1016, 1991.
- [2] A. C. Metaxas and R. J. Meredith, *Industrial Microwave Heating. IEE Power Engineering Series: 4*, c1983, Peregrinus on behalf of the Institution of Electrical Engineers, London, UK, 1983.
- [3] S. Chandrasekaran, S. Ramanathan, and T. Basak, "Microwave food processing-A review," *Food Research International*, vol. 52, no. 1, pp. 243–261, 2013.
- [4] M. Fazaeli, S. Yousefi, and Z. Emam-Djomeh, "Investigation on the effects of microwave and conventional heating methods on the phytochemicals of pomegranate (*Punica granatum* L.) and black mulberry juices," *Food Research International*, vol. 50, no. 2, pp. 568–573, 2013.
- [5] M. Benlloch-Tinoco, M. Igual, D. Rodrigo, and N. Martínez-Navarrete, "Comparison of microwaves and conventional thermal treatment on enzymes activity and antioxidant capacity of kiwifruit puree," *Innovative Food Science & Emerging Technologies*, vol. 19, pp. 166–172, 2013.
- [6] L. M. Ruiz-Ojeda and F. J. Peñas, "Comparison study of conventional hot-water and microwave blanching on quality of green beans," *Innovative Food Science & Emerging Technologies*, vol. 20, pp. 191–197, 2013.
- [7] M. Jamal, G. Brodie, and D. Gupta, "The effect of microwave soil treatment on rice production under field conditions," *American Society of Agricultural and Biological Engineers*, vol. 60, no. 2, pp. 517–525, 2017.
- [8] G. Brodie, S. Hamilton, and J. Woodworth, "An assessment of microwave soil pasteurization for killing seeds and weeds," *Plant Protection Quarterly*, vol. 22, no. 4, p. 143, 2007.
- [9] A. P. Cooper and G. Brodie, "The effect of microwave radiation and soil depth on soil pH, N, P, K, SO₄ and bacterial colonies," *Plant Protection Quarterly*, vol. 24, no. 2, pp. 67–70, 2009.
- [10] G. Brodie, C. Ryan, and C. Lancaster, "The effect of microwave radiation on prickly paddy melon (*Cucumis myriocarpus*)," *International Journal of Agronomy*, vol. 2012, pp. 1–10, Article ID 287608, 2012.
- [11] G. Graham Brodie and E. Eloise Hollins, "The effect of microwave treatment on ryegrass and wild radish plants and seeds," *Global journal of agricultural innovation, research & development*, vol. 2, no. 1, pp. 16–24, 2015.
- [12] E. Zagal, "Effects of microwave radiation on carbon and nitrogen mineralization in soil," *Soil Biology and Biochemistry*, vol. 21, no. 4, pp. 603–605, 1989.
- [13] E. J. Bond, X. Xu Li, S. C. Hagness, and B. D. Van Veen, "Microwave imaging via space-time beamforming for early detection of breast cancer," *IEEE Transactions on Antennas and Propagation*, vol. 51, no. 8, pp. 1690–1705, 2003.
- [14] G. Graham Brodie, "Derivation of a cropping system transfer function for weed management: Part 2 - microwave weed management," *Global journal of agricultural innovation, research & development*, vol. 3, no. 1, pp. 1–9, 2016.
- [15] P. P. Falciglia and F. G. A. Vagliasindi, "Techno-economic analysis of hydrocarbon-polluted soil treatment by using ex situ microwave heating: influence of soil texture and soil moisture on electric field penetration, operating conditions and energy costs," *Journal of Soils and Sediments*, vol. 16, no. 4, pp. 1330–1344, 2016.
- [16] A. Arrieta, D. Otaegui, A. Zubia et al., "Solvent-free thermal and microwave-assisted [3 + 2] cycloaddition: An experimental and theoretical study," *Journal of Organic Chemistry*, vol. 72, no. 12, pp. 4313–4322, 2007.
- [17] A. L. Antti and P. Perré, "A microwave applicator for on line wood drying: temperature and moisture distribution in wood," *Wood Science and Technology*, vol. 33, no. 2, pp. 123–138, 1999.
- [18] P. Zielonka and K. Dolowy, "Microwave drying of spruce: moisture content, temperature, and heat energy distribution," *Forest Products Journal*, vol. 6, p. 77, 1998.
- [19] A. M. Hasna, "Composite dielectric heating and drying: the computation process," *Lecture Notes in Engineering and Computer Science: Proceedings of the World Congress on Engineering*, vol. 2176pp. 679–686, London, 2009.
- [20] S. O. Nelson, "A review and assessment of microwave energy for soil treatment to control pests," *Transactions of the ASAE, Transaction American Society of Agricultural Engineers*, vol. 39, no. 1, pp. 281–289, 1996.
- [21] S. Nelson, L. A. T. Ballard, L. E. Stetson, and T. Buchwald, "Increasing legume seed germination by VHF and microwave dielectric heating," *Transactions of the American Society of Agricultural Engineers*, vol. 19, no. 2, pp. 369–371, 1976.
- [22] S. O. Nelson and L. E. Stetson, "Germination responses of selected plant species to RF electrical seed treatment," *Transactions of the ASAE*, vol. 28, no. 6, pp. 2051–2058, 1985.
- [23] P. P. Falciglia and F. G. A. Vagliasindi, "Remediation of hydrocarbon-contaminated soils by ex situ microwave treatment: technical, energy and economic considerations," *Environmental Technology*, vol. 35, no. 18, pp. 2280–2288, 2014.

Retraction

Retracted: Study of Mechanical Properties on Ferric Oxide Microparticles Reinforced with Polyethylene

Advances in Materials Science and Engineering

Received 26 December 2023; Accepted 26 December 2023; Published 29 December 2023

Copyright © 2023 Advances in Materials Science and Engineering. This is an open access article distributed under the Creative Commons Attribution License, which permits unrestricted use, distribution, and reproduction in any medium, provided the original work is properly cited.

This article has been retracted by Hindawi, as publisher, following an investigation undertaken by the publisher [1]. This investigation has uncovered evidence of systematic manipulation of the publication and peer-review process. We cannot, therefore, vouch for the reliability or integrity of this article.

Please note that this notice is intended solely to alert readers that the peer-review process of this article has been compromised.

Wiley and Hindawi regret that the usual quality checks did not identify these issues before publication and have since put additional measures in place to safeguard research integrity.

We wish to credit our Research Integrity and Research Publishing teams and anonymous and named external researchers and research integrity experts for contributing to this investigation.

The corresponding author, as the representative of all authors, has been given the opportunity to register their agreement or disagreement to this retraction. We have kept a record of any response received.

References

- [1] U. Tamilarasan, S. Dhanasekar, K. Raja Karthikeyan et al., "Study of Mechanical Properties on Ferric Oxide Microparticles Reinforced with Polyethylene," *Advances in Materials Science and Engineering*, vol. 2022, Article ID 3077301, 7 pages, 2022.

Research Article

Study of Mechanical Properties on Ferric Oxide Microparticles Reinforced with Polyethylene

**U. Tamilarasan,¹ S. Dhanasekar,² K. Raja Karthikeyan,³ T. S. Ramesh Babu,⁴
R. Gopinathan,⁵ V. G. Pratheep,⁶ P. Rajalakshmy,⁷ Ram Subbiah,⁸ and S. Praveen Kumar ⁹**

¹Department of Mechanical Engineering, Sri Sairam Engineering College, Chennai, Tamil Nadu 600044, India

²Centre for Excellence in Energy and Nano Technology, Department of Mechanical Engineering, S.A. Engineering College, Chennai-77, Tamilnadu, India

³Department of Mechanical Engineering, Panimalar Institute of Technology, Chennai, Tamil Nadu 600123, India

⁴Department of Civil Engineering, KG Reddy College of Engineering and Technology, Hyderabad, Telangana 500075, India

⁵Department of Mechatronics Engineering, Sri Krishna College of Engineering and Technology, Coimbatore, Tamil Nadu 641008, India

⁶Department of Mechatronics Engineering, Kongu Engineering College, Perundurai, Tamil Nadu 638060, India

⁷Department of Robotics Engineering, Karunya Institute of Technology and Sciences, Coimbatore, Tamil Nadu, India

⁸Department of Mechanical Engineering, Gokaraju Rangaraju Institute of Engineering and Technology, Hyderabad, Telangana 500090, India

⁹Department of Mechanical Engineering, Faculty of Mechanical Engineering, Arba Minch Institute of Technology (AMIT), Arba Minch University, Arba Minch, Ethiopia

Correspondence should be addressed to S. Praveen Kumar; praveen.kumar@amu.edu.et

Received 25 March 2022; Accepted 10 May 2022; Published 7 June 2022

Academic Editor: Palanivel Velmurugan

Copyright © 2022 U. Tamilarasan et al. This is an open access article distributed under the Creative Commons Attribution License, which permits unrestricted use, distribution, and reproduction in any medium, provided the original work is properly cited.

Polyethylene and ferric oxide microparticles were mixed in this work to generate a new polymer composite. Weight fraction and microparticle size were studied experimentally to discover how they influenced the tensile strength and Young's modulus. A response surface methodology was employed in the design of the research. The increased weight fraction of reinforcement results in the increase in Young's modulus and lowers the elongation percentage. As the microparticles expanded in size, so did their effect on the composite's mechanical characteristics. The tensile strength of specimens containing 20% ferric oxide and particle size of more than 91 μm was dropped by 18 percent due to the agglomeration of microparticles. The addition of 24% Fe_2O_3 microparticles smaller than 33 μm raised Young's modulus and tensile strength by 340 percent and 65 percent, respectively.

1. Introduction

A large amount of applications have taken advantage of the inherent properties of polyethylene (PE), including its high melting point, outstanding mechanical capabilities, less in density, corrosive resistance, and chemical resistance [1, 2]. With a wide range of applications, this thermoplastic material can be used to make pipes and fibres, make automotive parts, and produce aviation parts. Mechanical features such as Young's modulus and tensile strength keep material from being widely used in its current form [3]. Polymers can be

made to perform better by combining them with other polymers or by adding the appropriate reinforcements [4, 5]. The mechanical characteristics of polymers can be adjusted and enhanced by including diverse organic, inorganic, and mineral particles. Small amounts of fillers and the production of polymeric composites at the nano/microscale can considerably increase mechanical characteristics such as Young's modulus and tensile strength [6, 7]. However, filler collection and consequent inappropriate scattering in the polymer matrix are to blame for the composite material's poor mechanical characteristics [8]. Many researchers have

therefore been interested in improving polymer mechanical properties with numerous nano/microfillers such as carbon nanotubes, CaCO_3 , and ZnO .

The impact strength and Young's modulus were both raised to 68% after SiO_2 particles were incorporated into the PE polymer matrix [9, 10]. Young's modulus and tensile strength of polystyrene are significantly improved by mixing in titanium dioxide (TiO_2) particles. Young's modulus, tensile strength, and impact strength were all improved when clay nanoparticles were introduced to polyethylene (PE) at a weight concentration of roughly 1%. A more elastic and tensile polyethylene and PE mould with a TiO_2 stiff structure was shown to be more effective. Reinforced polymer composites' mechanical properties are influenced by a variety of parameters, including the size, shape, features, and distribution of the fillers inside the matrix. The authors in [11, 12] investigated the mechanical characteristics of a glass fibre reinforced polyethylene composite. The authors in [13] introduced polyethylene composites containing fine particles. According to their findings, the impact resistance of these composite materials is greatly improved by using these amplifiers.

Steel scrap with the best reinforcing characteristics is widely available, and this is one of the most common of those commodities [14–17]. In addition to environmental advantages such as low cost and great corrosive resistance, this material also has a high load capacity, making it a perfect reinforcement. Ferric oxide particles can improve the mechanical behavior of polymers because of their large surface area and energy and surface-to-volume ratio [18, 19]. This has resulted in the rise of Fe_2O_3 -reinforced polymer composites. The authors in [20] examined the mechanical behavior of epoxy reinforced with ferric oxide particles. An increase in tensile strength of 50% and fracture toughness of 106% was seen in their study. Researchers evaluated the epoxy matrix's mechanical properties in relation to ferric oxide-coated particles [21]. According to their observations in [22, 23], Young's modulus and toughness of epoxy resin increased from 300 MPa to 500 MPa when 3 wt. percent of ferric oxide is added.

Large-scale studies have found that ferric oxide particles have no effect on the mechanical behavior of polyethylene, one of the most broadly utilized polymers around the globe [24]. It was shown that incorporating ferric oxide particles into polyethylene can improve the material's mechanical qualities by conducting experimental tests. When analyzing the experimental data with response surface methods, tensile strength and Young's modulus are taken into account for the response [25–27]. Thus, our aim is to reinforce ferric oxide microparticles with polyethylene polymer tensile specimens made by melting and injecting the material in weight fractions of 6, 12, 18, and 24. The response surface methodology utilized to analyze the experiment's data made use of tensile strength and Young's modulus as variables.

2. Experimental Studies

2.1. Materials. It was found that polyethylene polymer with a melt flow and density of 906 kg/m^3 was used in the composite sector in this investigation. It was found that

ferric oxide particles can be found in five different sizes, ranging from $33 \mu\text{m}$ in diameter (grade A) to $125 \mu\text{m}$ in diameter (grade E), where μm is the average grain size. Using a twin-screw extruder by specifications of length = 580 mm, screw diameter = 18 mm, and $L/D = 45$, by melt blending process, the composites were made. The six heat zones of the extruder's temperature distribution were modified in accordance with the polyethylene material's melting temperature at 60, 90, 120, 150, 180, and 210 C inputs. According to Table 1, plastic injection equipment is used to generate various test samples with various weight % and sizes of ferric oxide particles after extrusion. With an inlet pressure of 90 bar and a cooling time of 65 seconds during molding, the device maintains a temperature range of 180–210 C. Standard injection molding was used to create samples for five various volume fractions of Fe_2O_3 particles (0, 6, 12, 18, and 24 percent wt.) and five distinct sizes.

The speed of the test was adjusted to 5 mm/min using the universal testing machine as shown in Figure 1. Until the sample failed, 1 ms of force-displacement data was recorded. Additionally, three trials were performed on each sample as shown in Figure 2 to ensure that there were no mistakes during the testing process. The response surface approach will be utilized to examine the data in this study, and Table 1 demonstrates the elements selected for this work and their range of differences in relation to research objectives.

3. Results

These are the outcomes of the experiments that were carried out for this investigation. Tests on different PE samples with different sizes and weight fractions of ferric oxide microparticles yield the results through direct tensile tests. The linear component of a stress-strain curve can be used to calculate a material's tensile strength by putting a lot of stress to it and then computing the elastic modulus. When doing ASTM tensile testing, pure PE20A and PE20E samples all fail. Using ferric oxide microparticles enhances strain variation and decreases the fracture strains of the specimens in general, as demonstrated by comparing the deformation of the specimens following the tensile test [28]. Polymer matrix microparticles embedded with ferric oxide microparticles boost the material's tensile strength under stress. Because of this, cracking can develop and spread more easily in a matrix that is under more tensile stress than it is under less stress. The polymer composite is tearing in a few places. These values increased to 2612 MPa and 38 MPa, respectively, when 24 weight percent of ferric oxide microparticles of grade A particle size was added to pure polyethylene, according to the data. Polyethylene terephthalate (PET) microparticles were employed to boost the modulus of the PE polymer by 300 percent and the material's strength by 60%. Ferric oxide particles can easily increase Young's modulus and tensile strength, according to these findings [29]. There was also an increase in tensile strength of 21.8 MPa when 20% grade E particles were added to the polyethylene. When compared to pure polyethylene, grade E microparticles raise Young's modulus by around 280 percent while decreasing tensile strength by about 18 percent and it

TABLE 1: Specimen specifications.

S. no.	Fe ₂ O ₃ wt.%	Grain size (μm)				
		33 μm (grade A)	33 to 61 μm (grade B)	62 to 68 μm (grade C)	68 to 92 μm (grade D)	92 to 125 μm (grade E)
1	6	PE6A	PE6B	PE6C	PE6D	PE6E
2	12	PE12A	PE12B	PE12C	PE12D	PE12E
3	18	PE18A	PE18B	PE18C	PE18D	PE18E
4	24	PE24A	PE24B	PE24C	PE24D	PE24E

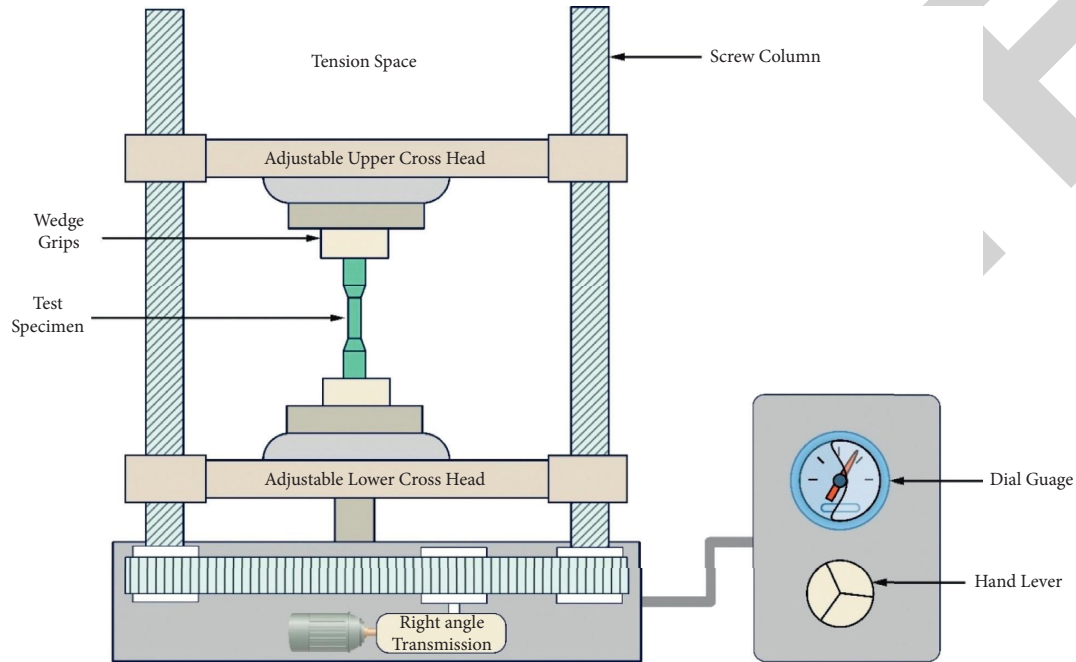


FIGURE 1: Universal testing machine.

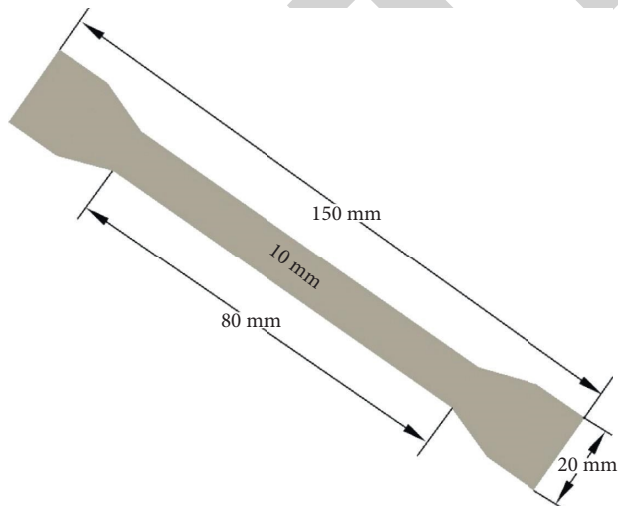


FIGURE 2: Specimen for tensile test.

matrix. According to the results of this study, using smaller microparticles improved polyethylene mechanical properties by increasing cohesiveness and decreasing particle aggregation.

These 20 polyethylene samples were reinforced with iron oxide microparticles of changing weight fraction and particle size [30]. There was a correlation between the amount and the size of reinforcement particles in the polymer matrix and an increase in Young's modulus as shown in the results of this research. Adding ferric oxide microparticles enhanced Young's modulus from 110 to 275 percent in comparison with pure polyethylene, based on weight fraction and microparticle size. The ratio of reinforcement to matrix modulus determines the composite material's elastic modulus. In order to enhance the modulus of a polyethylene/ferric oxide composite, the weight percentage of ferric oxide microparticles must be increased [31]. For specimens with a ferric oxide weight percentage of less than 12 percent, Young's modulus increases with increase in microparticle size in the experimental studies. Large microparticles have less impact on the composite material's Young's modulus if the polyethylene is reinforced with weight fraction larger than 12 weight percent. Particle agglomeration and a reduced bonding level between microparticles and matrix result in a lower modulus for greater percentages of ferric

is shown in Figure 3. There was also evidence of significant microparticle agglomerations, which resulted in stress concentration and crack initiation, leading to brittle material. In addition, the tensile strength decreases as a result of the weak connection between large microparticles and the

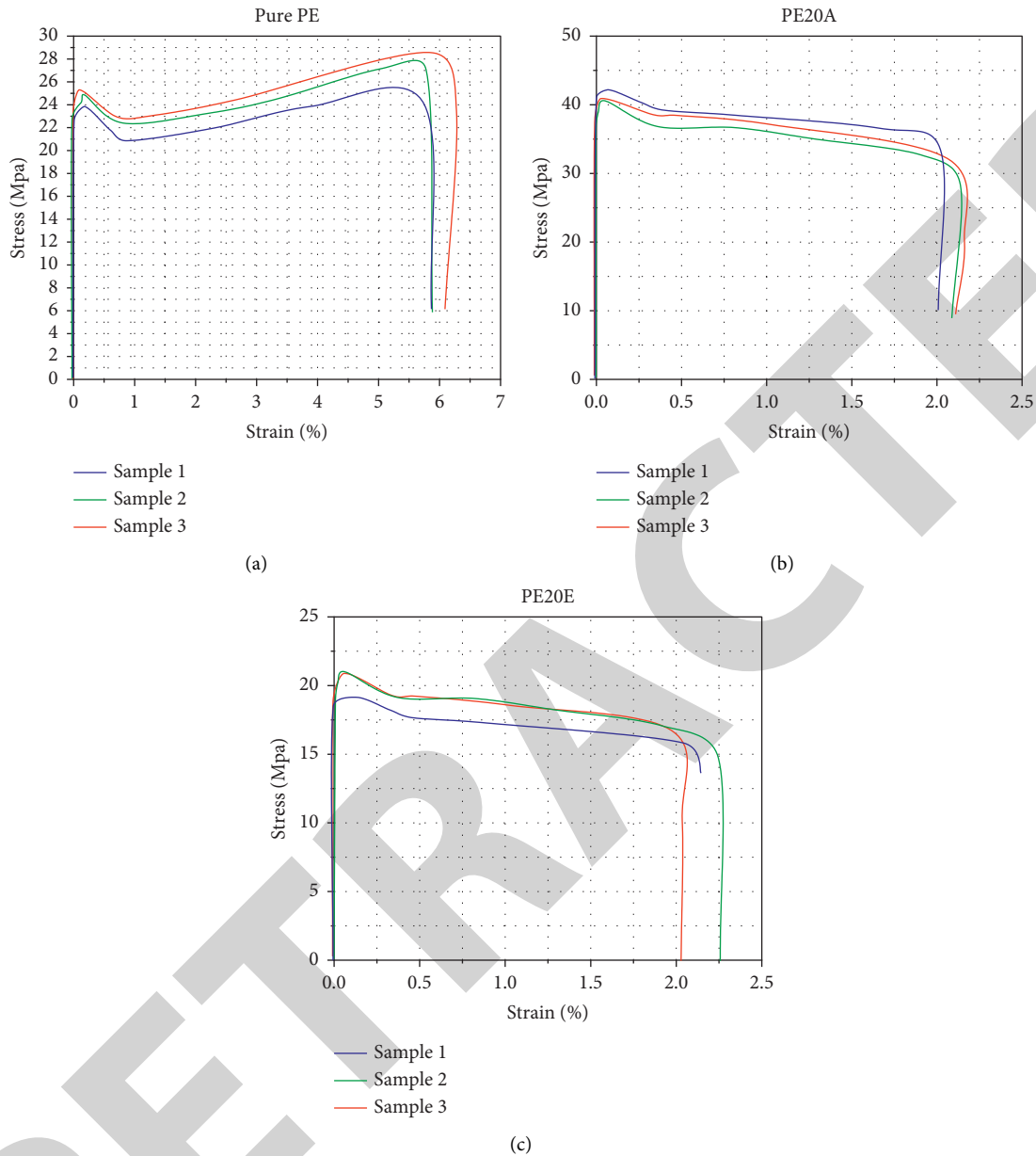


FIGURE 3: Stress-strain curve samples for (a) pure polyethylene, (b) polyethylene containing 20 wt percent of iron oxide with grade A particle size, and (c) polyethylene having 20 wt percent of iron oxide with grade E particle size.

oxide microparticles with big diameters (C and D grades) and it is seen in Figure 4.

PE enhanced with ferric oxide microparticles demonstrates increased tensile strength in Figure 5. The tensile strength of the polyethylene/ferric oxide composite is greatly affected by weight fraction and the microparticles used, and this behavior varies with particle size. The higher interfacial bonding between the polyethylene polymer and ferric oxide microparticles is also thought to lead to an increase in the sample's tensile strength and Young's modulus compared to the specimen. The polymer matrix/reinforcement particle interface is a key factor in determining the mechanical properties of polyethylene/ferric oxide composites at 24 wt percent [32]. For microparticle grade A, tensile strength is 60

percent more than that of polyethylene, making the composite more resistant to stress cracking than pure polyethylene. For microparticle grades B, C, and D, the tensile strength increased at first but later dropped when ferric oxide was added to polyethylene. The greater effective surface contact area between microparticles and matrix improves the tensile strength, which is highly dependent on stress transfer.

A method for increasing microparticle tensile strength involves transferring stress from the matrix to the microparticles. According to these findings, the polyethylene/ferric oxide composite with a tensile strength of 37.5 MPa, which contains 18 weight percent of grade B microparticles, has a tensile strength that is 70% higher than that of pure

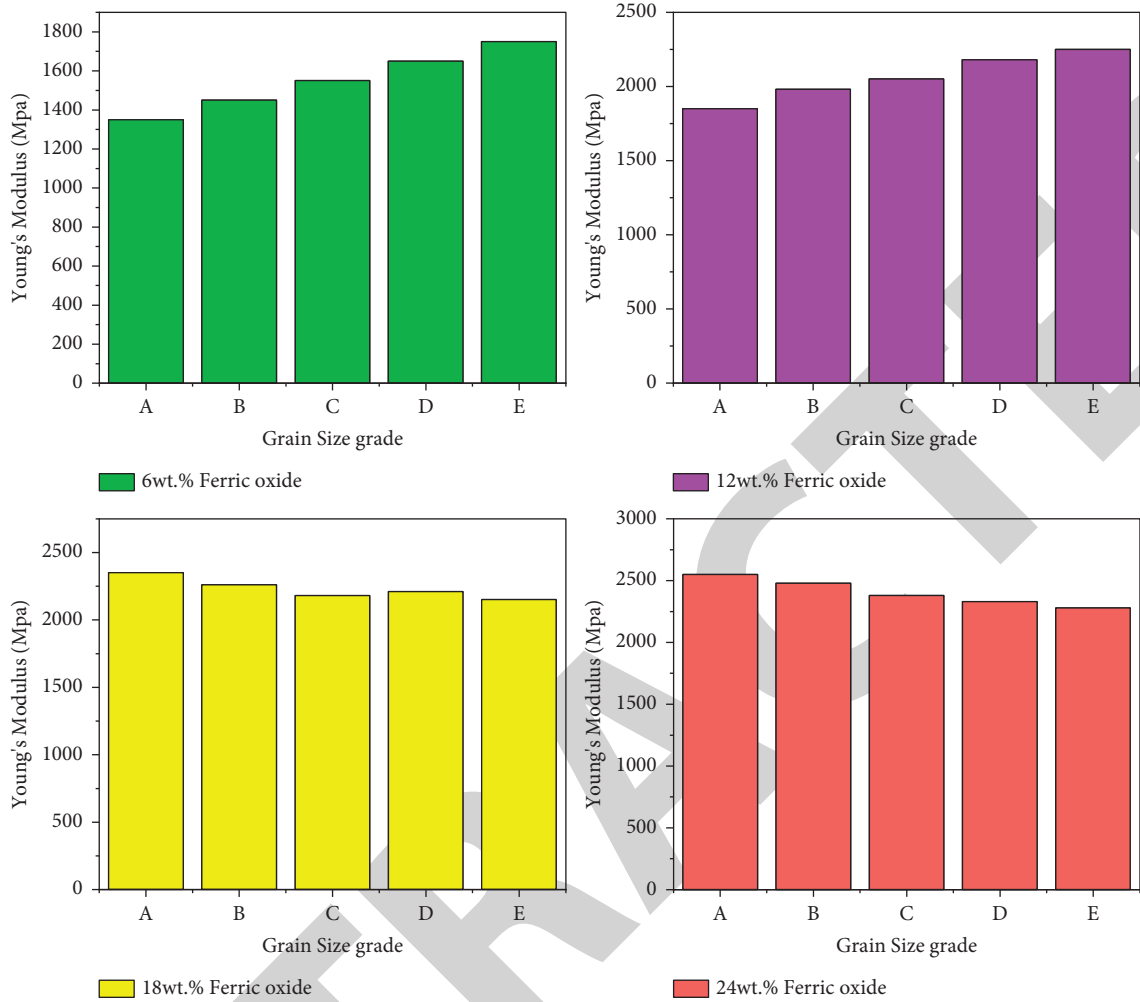


FIGURE 4: Effect of various weight fractions and ferric oxide particle size in Young's modulus of polyethylene/ferric oxide composites.

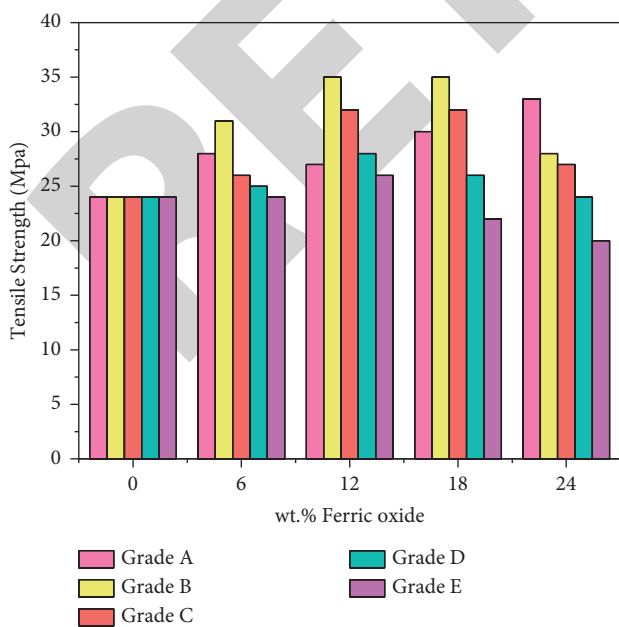


FIGURE 5: Impact of weight fractions and size of iron oxide particles on the tensile strength of polyethylene/ferric oxide composites.

polyethylene. Ferric oxide microparticles, which strengthen the matrix and deflect fracture propagation, are to blame for this increase in strength. The polyethylene/ferric oxide composite with increasing percentages of ferric oxide has weak regions that contribute to a decrease in the composite's strength. Ferric oxide agglomerations with enormous diameters are also observed at high levels of ferric oxide, weakening the matrix-particle connection even further. Due to the large stress concentrations, cracks may form in the vicinity of the agglomeration areas. The microcomposite's strength may decrease as the weight percentage and the size of the ferric oxide microparticles rise. The smallest rise in tensile strength is seen for microparticles of grade E. Although ferric oxide was used at a high percentage of 24 weight percent, the tensile strength of the microcomposite was 18 percent lower than that of pure polyethylene owing to agglomeration and reduced surface contact area [33]. Furthermore, the tensile strength and modulus of the polyethylene composites made in this study are comparable to those of specimens made in references with clay and aluminum hydroxide particles as reinforcement. RSM was utilized to decrease the number of tests and establish a measurable relationship between the mechanical parameters

TABLE 2: Statistical investigation and experimental information.

Model	SD	R ²
Linear	2.16	0.85
2F1	1.75	0.86
Quadratic	1.21	0.91
Cubic	0.62	0.95

of the composite as well as input factors (temperature and humidity) in this research. Some of the more accurate mathematical models for predicating mechanical qualities are provided in Table 2, which shows how well they perform.

According to statistical analysis, each parameter's relative relevance was estimated using a cubic model that had the lowest error. The response surface approach was used to construct surface curves for the PE/Fe₂O₃ composite with a standard deviation of 0.57. As a result, matrix and micro-particle bonding is highly stable in samples with more weight % of ferric oxide particles. The mechanical behavior of the composites has been greatly enhanced by the microparticles' ability to withstand the majority of the applied forces, and the results are shown in equations (1) and (2). The specimens containing microparticles with a diameter of 20 to 35 and a weight fraction of 15% to 20% had the highest tensile strength based on the results.

S and W denote microparticle size and weight fraction of ferric oxide microparticles. In the tensile strength equation, the microparticle size has the highest negative coefficient S. SW coefficient shows that increasing particle size and weight have a detrimental effect on tensile strength. This shows a negative contact among the size and weight fraction of particles. Agglomeration of microparticles occurs when the size and weight proportion of microparticles are simultaneously raised.

$$\begin{aligned} \text{Tensile Strength (MPa)} = & 27.62 - 9.30S + 3.91W - 5.01SW \\ & - 2.56S^2 - 3.54W^2 + 3.65S^3 \\ & - 0.77W^3 - 0.67SW^2. \end{aligned} \quad (1)$$

$$\begin{aligned} \text{Young's Modulus (MPa)} = & 1896.7 + 169.6S + 701.3W \\ & - 111SW - 5.6S^2 - 488.4W^2 \\ & - 32.7S^3 + 190.8W^3 \\ & - 216.8SW^2 + 1.8S^2W. \end{aligned} \quad (2)$$

4. Conclusion

This research was to examine the impact of microparticle size and volume % on polyethylene reinforcement.

- (i) When particles are dispersed, the strength and Young's modulus of the material increase dramatically by 100–260 percent depending on microparticle weight percentage and dimension.
- (ii) This process can manufacture PE/ferric oxide composites with more weight percent of microparticles

smaller than 62 μm to obtain composites with adequate mechanical characteristics for different technical applications.

- (iii) Using ferric oxide microparticles, polyethylene's force is efficiently transferred to their matrix. As well as bolstering the matrix and preventing cracks, the strong surface effect and the bond between ferric oxide microparticles and the matrix also play a role in this increased strength.
- (iv) For the PE/ferric oxide composite having 18 wt.% of microparticles of the size of $20 = a \leq 36 \mu\text{m}$ diameter, a 35 MPa value was achieved, which was approximately 75% greater than that of the pure PE material.

Data Availability

The data used to support the findings of this study are included within the article. Further data or information is available from the corresponding author upon request.

Conflicts of Interest

The authors declare that they have no conflicts of interest regarding the publication of this paper.

Acknowledgments

The authors appreciate the support from the Arba Minch University, Ethiopia, for providing help during the research and preparation of the manuscript. The authors appreciate the support from Sri Sairam Engineering College, Panimalar Institute of Technology, Sri Krishna College of Engineering and Technology, and S.A. Engineering College for their help in completing this work.

References

- [1] A. K. Singh, R. Bedi, and B. S. Kaith, "Composite materials based on recycled polyethylene terephthalate and their properties - a comprehensive review," *Composites Part B: Engineering*, vol. 219, Article ID 108928, 2021.
- [2] V. Mohanavel, S. Suresh Kumar, J. Vairamuthu, P. Ganeshan, and B. Nagaraja Ganesh, "Influence of stacking sequence and fiber content on the mechanical properties of natural and synthetic fibers reinforced penta-layered hybrid composites," *Journal of Natural Fibers*, vol. 2021, pp. 1–13, 2021.
- [3] M. R. Mansor, Z. Mustafa, S. H. S. M. Fadzullah, G. Omar, M. A. Salim, and M. Z. Akop, "Recent advances in polyethylene-based biocomposites," in *In Woodhead Publishing Series in Composites Science and Engineering, Natural Fibre Reinforced Vinyl Ester and Vinyl Polymer Composites*, S. M. Sapuan, H. Ismail, and E. S. Zainudin, Eds., Woodhead Publishing, Sawston, Cambridge, pp. 71–96, 2018.
- [4] G. Maruthupandian, R. Saravanan, S. Suresh Kumar, and B. G. Sivakumar, "A study on bamboo reinforced concrete slabs," *Journal of Chemical and Pharmaceutical Sciences*, vol. 9, no. 2, pp. 978–980, 2016.
- [5] A. H. A. Hoseini, M. Arjmand, U. Sundararaj, and M. Trifkovic, "Significance of interfacial interaction and agglomerates on electrical properties of polymer-carbon

Retraction

Retracted: Study on Thermal Performance Measurement and Construction of Passive Exterior Wall with Low Energy: Teaching and Laboratory Building of Shandong Jianzhu University

Advances in Materials Science and Engineering

Received 26 December 2023; Accepted 26 December 2023; Published 29 December 2023

Copyright © 2023 Advances in Materials Science and Engineering. This is an open access article distributed under the Creative Commons Attribution License, which permits unrestricted use, distribution, and reproduction in any medium, provided the original work is properly cited.

This article has been retracted by Hindawi, as publisher, following an investigation undertaken by the publisher [1]. This investigation has uncovered evidence of systematic manipulation of the publication and peer-review process. We cannot, therefore, vouch for the reliability or integrity of this article.

Please note that this notice is intended solely to alert readers that the peer-review process of this article has been compromised.

Wiley and Hindawi regret that the usual quality checks did not identify these issues before publication and have since put additional measures in place to safeguard research integrity.

We wish to credit our Research Integrity and Research Publishing teams and anonymous and named external researchers and research integrity experts for contributing to this investigation.

The corresponding author, as the representative of all authors, has been given the opportunity to register their agreement or disagreement to this retraction. We have kept a record of any response received.

References

- [1] Y. Lan and R. Zou, "Study on Thermal Performance Measurement and Construction of Passive Exterior Wall with Low Energy: Teaching and Laboratory Building of Shandong Jianzhu University," *Advances in Materials Science and Engineering*, vol. 2022, Article ID 3253085, 11 pages, 2022.

Research Article

Study on Thermal Performance Measurement and Construction of Passive Exterior Wall with Low Energy: Teaching and Laboratory Building of Shandong Jianzhu University

Yirui Lan ¹ and Ran Zou²

¹School of Architecture and Urban Planning, Shandong Jianzhu University, Jinan 250000, Shandong, China

²School of Management Engineering, Shandong Jianzhu University, Jinan 250000, Shandong, China

Correspondence should be addressed to Yirui Lan; lanyirui19@sdjzu.edu.cn

Received 22 March 2022; Revised 27 April 2022; Accepted 17 May 2022; Published 3 June 2022

Academic Editor: Palanivel Velmurugan

Copyright © 2022 Yirui Lan and Ran Zou. This is an open access article distributed under the Creative Commons Attribution License, which permits unrestricted use, distribution, and reproduction in any medium, provided the original work is properly cited.

It can provide theoretical support for the optimal design of low-energy walls by measuring the actual thermal conditions inside the walls of passive low-energy buildings and studying the rationality of the wall structure design. Taking the teaching and laboratory building of Shandong Jianzhu University as an example, this paper explores the method of using temperature and humidity sensor to measure the air temperature and humidity inside the wall to represent the solid temperature and humidity of the wall. Based on the measured data and calculation results, the rationality of the structure of the test external wall is analyzed from four aspects: the performance of insulation, the moisture drain performance of wall, the ability of preventing the penetration of the hot and humid air of the inner wall, and the waterproof performance of the outer wall. Results show that the external wall structure of polystyrene board (200 mm thick) for external insulation and thin plastering has good practical operation effect in three aspects of thermal insulation, internal moisture discharge, and external wall waterproof, which basically meets the design requirements of external wall of passive house in Germany. In terms of moisture protection of the inner wall, the inner wall of cement mortar (15 mm thick) may not be able to effectively prevent the infiltration of indoor hot and humid air. Thus, the insulation layer should be added into the external wall. In addition, the moisture inside the wall is obviously affected by the season. The drain performance of moisture inside the wall mainly occurs in the sweltering heat, and the drain direction is from the indoor side to the outdoor side. In the external insulation structure, there are two layers of graphite polystyrene plate (100 mm thick), and the insulation effect of polystyrene plate near the outdoor side is better than that near the indoor side. The combination of anticrack mortar (5 mm thick) and paint cannot completely prevent the infiltration of rainwater, but the infiltration of rainwater in the wall will be quickly discharged in a short time.

1. Introduction

With the popularization of German passive low-energy buildings in China, the energy-saving technology of high thermal insulation performance, no thermal bridge and high air tightness of exterior wall has been applied in domestic demonstration buildings. The exterior wall construction needs to meet two design goals in order to ensure the energy saving effect of the exterior wall with ultra-low-energy consumption. First, no thermal bridge is required, and the average heat transfer coefficient is less than or equal to

$0.15 \text{ W}/(\text{m}^2 \cdot \text{K})$ to effectively block the heat transfer path of the outer wall. This goal has always been the focus of domestic research on energy saving of building envelope. Second, it is necessary to reasonably design the water tightness and air permeability of the inside and outside of the wall to ensure that the inside of the wall is not affected by moisture [1, 2]. This goal has received little attention in academic research and engineering practice. And, today's buildings tend to be low energy and environmentally friendly, so more and more buildings will consider whether the building meets the requirements of low energy consumption.

This study provides a reference scheme for the construction of the external wall without carry and also provides a guarantee for the quality of the wall.

The research of the structure of low-energy insulation wall at home and abroad can be summarized as follows: (1) research institutions used energy consumption calculation software and thermal bridge simulation software to study the structural design of low energy consumption envelope structure and issued authoritative construction standards and Atlas. For example, PHI (Passive House Institute) in Germany has promulgated *Passive Energy Saving Transformation Standard and Passive House Institute Energy Saving Building Standard* [3]. The Center for Science, Technology, and Industrialization Development of the Ministry of Housing and Urban-Rural Development of the China has issued the Chinese Standard Atlas, namely, *Passive Low-Energy Buildings—Residential Buildings in Cold Regions* [4]. (2) The researchers used laboratory tests to study the thermal insulation and waterproof vapour insulation performance of building materials. European and American universities and research institutions have carried out a large number of thermal and wet physical property tests of materials. The Fraunhofer Institute of Building Physics in Germany has established a database of physical property parameters of building materials based on the accumulation of long-term test data [5]. Sun et al. studied and tested the thermal and wet physical property parameters of core components of external thermal insulation system, such as concrete, rock wool, EPS, adhesive, and plaster [6]. Yu carried out in-depth theoretical and experimental research on the thermal performance of wall building materials based on temperature and humidity [7]. (3) The researchers used numerical simulation to study the influence of wall construction practices or new building materials on wall moisture and heat performance. Jia simulated and analyzed the influence of polystyrene board and gap between them of composite insulation wall on the humid and hot state of the wall [8]. Chang et al. simulated the moisture and heat properties of cross-laminated wood and analyzed its moisture risk in 20 cities in South Korea [9]. Park et al. simulated the humidity and heat performance of walls using functional gypsum board (with porous materials and PCM added into the board) [10]. Havinga and Schellen simulated and analyzed the design factors affecting mold and condensation inside the wall during the energy-saving transformation of prefabricated buildings with internal thermal insulation [11]. (4) The temperature and humidity change inside the wall is measured to study the thermal performance of a component or a structural hierarchy of the wall quantitatively. Xue measured and compared the relative humidity changes of concrete base of EPS external insulation wall in Harbin at different time after completion and proposed that indoor and outdoor environment was the main factor affecting the humidity state of concrete layer [12]. Xia et al. measured the change of relative humidity in the base wall and insulation layer after the completion of two kinds of insulation walls in Harbin and pointed out that the increase of humidity would not affect the insulation performance of extruded polystyrene board [13, 14]. McClung et al. measured

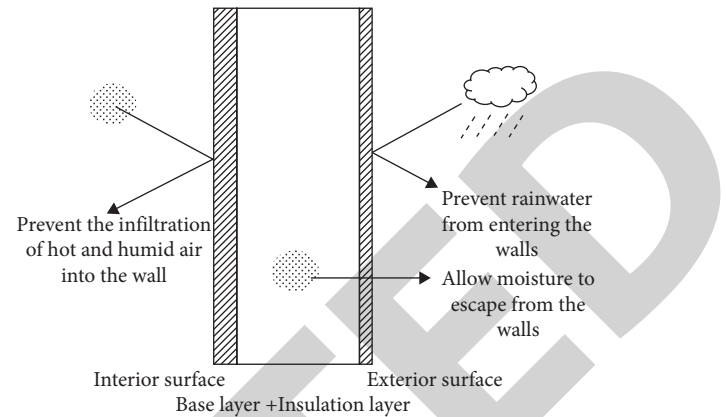


FIGURE 1: Design principles for water tightness and air permeability of low-energy exterior wall finishes.

the humidity and mold inside 16 kinds of walls composed of cross-laminate and analyzed the drying process of cross-laminate [15]. To sum up, the study of moisture and heat of building wall is the important and difficult point of the study of thermal insulation wall structure. The domestic construction field does not pay enough attention to the water vapor permeability coefficient of building materials and lacks long-term measurement and tracking of humidity and heat parameters of walls with high thermal insulation and low energy consumption. Thus, it is impossible to determine whether the completed exterior walls with low energy consumption can effectively reach the water vapor penetration and isolation requirements of the wall.

Therefore, taking the passive low-energy building demonstration project of Shandong Jianhua University as an example, this study used temperature and humidity sensors embedded in the wall to measure the temperature and humidity data at different locations in the external wall for a long time, in order to analyze the change rule of temperature and humidity inside the wall and to study the rationality of the wall construction, which can provide data support for the relevant researches. In addition, this study provides a reference scheme for the construction and inspection of building exterior walls.

2. Experimental Test of Thermal Performance

2.1. The Test Wall. In the design and construction process of passive low-energy buildings in China, the design principles should be followed as follows: the water vapor penetration resistance of the interior decorative layer is large, which prevents the indoor hot and humid air from penetrating into the wall in winter, while the high water tightness and low resistance of water vapor penetration of the exterior veneering layer prevent outdoor rainwater from entering into the wall and allow moisture to escape from the wall. The design principle of watertight and breathable design of low-energy exterior wall finishes is to reflect the performance of the exterior wall through the watertight and breathable condition of the exterior wall. The design principle of water tightness and air permeability of low-energy exterior wall finishes is shown in Figure 1.

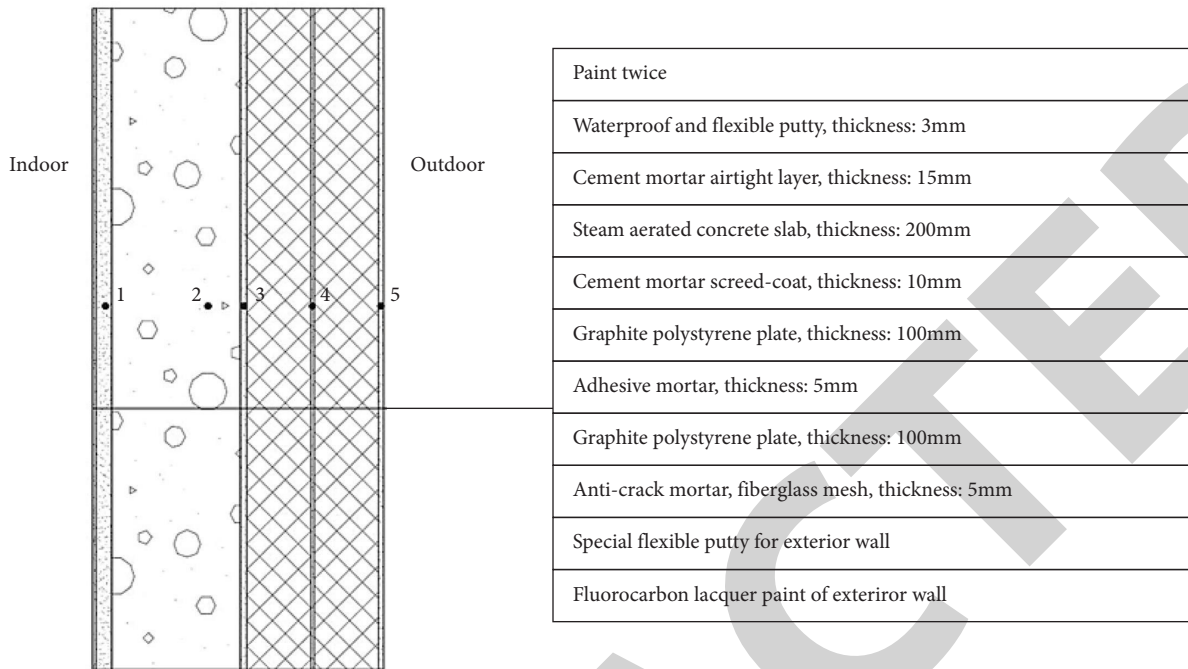


FIGURE 2: The structure of the test wall and the location of temperature and humidity measurement points in the wall. (1–5 represent the locations of temperature and humidity measurement points).

The Teaching and Laboratory Building of Shandong Jianzhu University, located in Jinan City, was completed in March 2017. It is a Sino-German cooperative demonstration project of passive low-energy buildings of the Ministry of Housing and Urban-Rural Development and the first batch of low-energy building demonstration project in Shandong Province. The main building has a total of 6 floors, with a total building height of 23.96 m and a total construction area of 9696.3 m². The exterior wall of the project was designed according to the principles shown in Figure 1, with a heat transfer coefficient of 0.14 W/(m²•K). The heat transfer coefficient K of the wall is the characteristic of the wall (including all structural levels) under stable heat transfer conditions, when the air on both sides of the wall. When the temperature difference is 1 K (1°C), the heat transferred through the unit square meter of wall area per unit time. The structural layers are shown in Figure 2, and the relevant physical properties of the building materials of the exterior wall are tested and shown in Table 1.

2.2. The Location of Measurement Points. The temperature and humidity sensors were located in three types of positions in this experiment according to the structural hierarchy of the test wall and the physical properties of the building materials. The first type is the position where the wall is in contact with the indoor and outdoor environment, such as points 1 and 5 shown in Figure 2. The second type is the position between two adjacent main structural layers, such as points 3 and 4 shown in Figure 2. The third type is the interior of building materials with high water vapor permeability coefficient, such as point 2 shown in Figure 2.

In this study, temperature and humidity sensors were placed inside the test wall of the building in the east, south,

west, and north directions, respectively, according to locations of the measurement points shown in Figure 2, and a total of 4 sets of temperature and humidity measuring equipment were prepared in order to collect related data.

2.3. Experiment Equipment. The experiment equipment adopts temperature and humidity integrated sensor (Visara HMP100) and plastic protective tube (19266HM). The shape and size of HMP100 and plastic protective tube are shown in Figure 3. Referring to “*Visala Structure Humidity Test Kit*,” the air temperature and humidity in the enclosed space inside the building component were measured to represent the temperature and humidity data of a test position inside the wall. HMP100 has two sensor elements: the temperature sensor (PT100) and the thin-film capacitive humidity sensor element, which is covered with a plastic filter (including a filter plastic grid and a filter membrane with a porosity of 0.2 μm, as shown in Figure 3(a)) to protect sensor components and filter dust. The plastic filter mainly filters the impurities generated during measurement. The above components constitute an effective test cavity to ensure the normal operation of the sensor. The temperature measurement range of the sensor is -40 to 80°C, and the relationship between temperature and accuracy is as follows: accuracy ±0.2°C (temperature in the range of 0–40°C) and accuracy ±0.4°C (temperature in the range of -40 to 0°C). The relative humidity measurement range of the sensor is 0–100%, and the relationship between temperature, relative humidity and accuracy is as follows: accuracy ±1.5% (temperature in the range of 0–40°C, humidity in the range of 0–90%) and accuracy ±3.0% (temperature in the range of -40 to 0°C, humidity in the range of 0–90%). In order to

TABLE 1: Physical property parameters of building materials for the test external wall.

ID	Structural layer	Heat conductivity coefficient ($\text{w}\cdot\text{m}^{-1}\cdot\text{K}^{-1}$)	Thickness (mm)	Water vapor penetration coefficient, μ ($\text{ng}\cdot\text{Pa}^{-1}\cdot\text{m}^{-1}\cdot\text{s}^{-1}$)	Sensor ID
1	Coating material of interior wall				
2	M7.5 cement mortar	0.93	15	5.8	1
3	Steam aerated concrete slab	0.146	200	27.7	2
4	M7.5 cement mortar	0.93	10	5.8	3
5	Graphite polystyrene plate	0.032	100	4.5	
6	Adhesive mortar	0.93	5	5.8	4
7	Graphite polystyrene plate	0.032	100	4.5	
8	Anticrack mortar	0.93	5	5.8	5
9	Fluorocarbon lacquer paint of exterior wall			0.1 mL*	

* According to the test method of JG/T210-2007 "Primer for Building Internal and External Walls," the water permeability test result of the alkali resistant sealing primer for the external wall coating of this project is 0.1 ml, and the water resistance test result is 96 h without abnormality. * Water vapor permeability coefficient refers to the water vapor partial pressure difference on both sides of a material with a thickness of 1 m under stable penetration conditions of 1 Pa, within 1 hour (the amount of water vapour that penetrates through an area of 1 square meter).

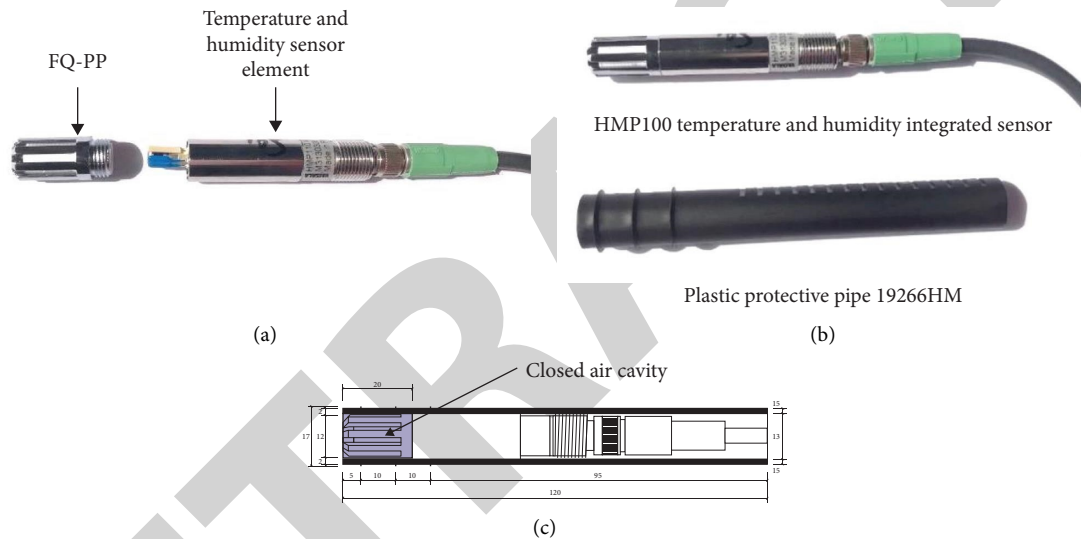


FIGURE 3: The shape and size of the temperature and humidity measurement equipment inside the wall. (a) FQ-PP (built-in filter membrane with $0.2\ \mu\text{m}$ pore), temperature, and humidity sensor element. (b) HMP100 temperature and humidity integrated sensor, plastic protective pipe 19266HM. (c) HMP100 temperature and humidity integrated sensor, plastic protective pipe 19266HM (after assembly).

measure the internal temperature and humidity of solid materials, Visala developed a plastic pipe 19266HM for the HMP100 sensor to protect it and seal the air inside the plastic filter to ensure that the sensor can measure the temperature and humidity of the test position inside the wall (Figure 3(c)).

2.4. The Installation Method of Experiment Equipment.

The size of the experiment equipment after assembly is large (diameter is 17 mm, and length is 120 mm). In this study, the thickness and construction technology of the wall structure layer are combined in the construction process, and two installation methods are used: (1) applied to the external wall base (point 2); (2) applied to exterior mortar layer (points 1, 3, 4, and 5).

- (1) Installation method for sensors inside autoclaved aerated concrete slabs (point 2, Figure 4)

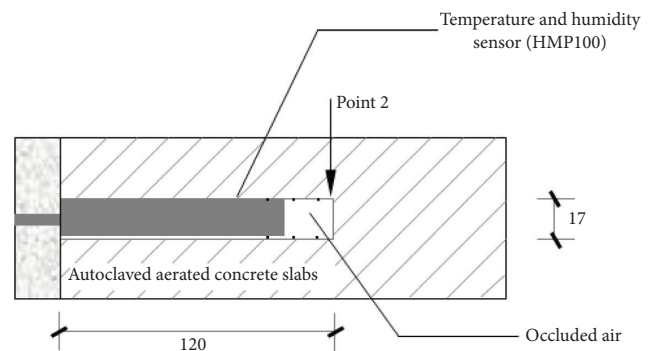


FIGURE 4: Installation method for sensors inside autoclaved aerated concrete slabs (/mm).

- ① After the autoclaved aerated concrete slabs are installed in place, a hole is drilled in the slabs from the inside to the outside perpendicular to the wall, with the diameter of 17 mm and the depth of 120 mm

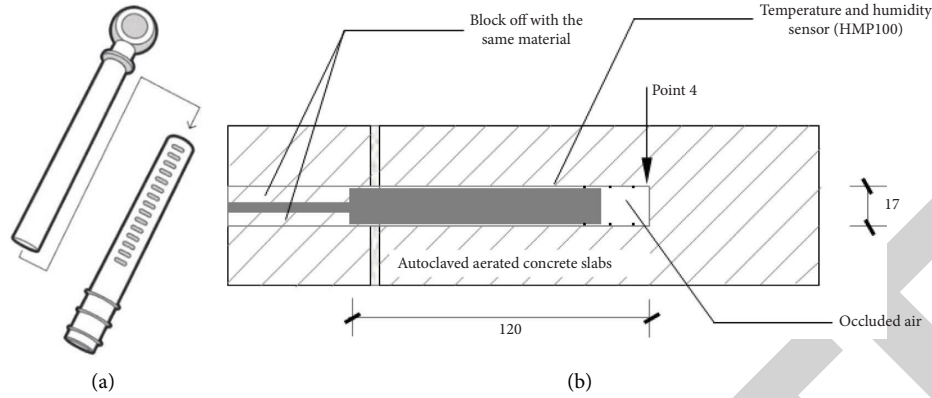


FIGURE 5: Installation method for sensors inside external wall mortar layer. (a) Embolize the long rubber into the plastic pipe. (b) Detailed construction drawing of sensor inside the mortar layer (/mm, point 4).

- ② Use a high-pressure dust blower to clean the inside of the hole
 - ③ Use a rubber hammer to knock the plastic pipe into the hole
 - ④ Inserted the HMP100 sensor into the plastic pipe, and then the construction of the airtight layer of the cement mortar of indoor side is carried out
- (2) Installation method for sensors inside external wall mortar layer (point 4, Figure 5)
- ① After the construction of the first graphite polystyrene plate on the left of point 4 is completed, a hole is drilled from the outside to the inside perpendicular to the wall with the diameter of 17 mm, and the depth runs through the first graphite polystyrene plate and the autoclaved aerated concrete strip.
 - ② Embolize the long rubber into the plastic pipe, and knock the plastic pipe into the hole with a rubber hammer. The bottom of the plastic casing is located at the interior side of the thickness range of the bonding mortar layer.
 - ③ The second layer of graphite polystyrene plate is constructed by the way of full adhesion. The long rubber plug can prevent the mortar from entering the plastic pipe. After the mortar solidifies, we can pull out the long rubber plug from the plastic pipe and clean the inside of the plastic pipe with a high-pressure dust gun.
 - ④ Insert the HMP100 sensor is into the plastic tube, and seal the hole with the same material.

The installation method for sensors located in the positions of points 1, 3, and 5 are the same as point 4.

2.5. Experiment Process. 20 temperature and humidity sensors were embedded inside the external wall in the east, south, west, and north directions with the installation methods above, and temperature and humidity sensors were installed in the indoor and outside of the wall, respectively. The temperature t and relative humidity φ of the indoor and

outside air of the wall and the wet air in the inner cavity of the wall were measured. The measured data were recorded every 30 min and then transmitted to the data platform through the network cable for storage. The whole test system has been running since February 2018. The embedded sensors in the east, south, and north external walls can work normally, while the embedded sensors in the west external wall failed to work normally.

3. Data Process

3.1. Calculation of Experimental Data. The state parameters of wet air include total pressure B , specific enthalpy H , moisture content d , temperature t , relative humidity φ , and water vapor partial pressure P_v . The state of wet air can be determined by three independent parameters including total pressure B , temperature t , and relative humidity φ . The temperature t of the wet air in the cavity measured by the sensor can be considered as the solid temperature of the wall at the location of the cavity. The material of the test wall is porous, and the cavity in the wall is connected with the atmosphere through the pores of the building's internal and external surface materials. Therefore, it is approximately considered that the total atmospheric pressure B in the cavity is unchanged and can be regarded as a constant 101.325 kPa.

The system can automatically record the temperature t_{ij} and relative humidity φ_{ij} of the air in the cavity at a certain time j at the test position i . According to the function relationship between the main parameters of wet air, the moisture content d_{ij} of the air in the cavity at a certain time j at the test position i can be calculated. The specific calculation formulas are as follows:

$$d_{ij} = 622 \frac{P_{vij}}{B - P_{vij}}, \quad (1)$$

$$P_{vij} = P_{v,b} \cdot \varphi_{ij},$$

where d_{ij} is the moisture content of test position i at a certain time j , and its unit is g/kg; P_{vij} is the partial pressure of water vapor at the test position i at a certain time j , and its unit is Pa; $P_{v,b}$ is the saturated water vapor pressure at the

temperature t_{ij} at the test position i at a certain time j , and its unit is Pa; and φ_{ij} is the relative humidity of test position i at a certain time j .

It should be noted that φ_{ij} and d_{ij} are the relative humidity and moisture content of the air in the cavity at test position i , rather than the humidity status of the solid wall at test position i . Therefore, the relative humidity and the moisture content of the air in the cavity obtained by the test system are used to represent the humidity status of the solid wall at the location of the cavity in this paper.

3.2. The Analysis Methods of Experimental Data. Based on the measured data and calculation results, the rationality of the structure of the test external wall is analyzed from four aspects: the performance of insulation, the moisture drain performance of wall, the ability of preventing the penetration of the hot and humid air of the inner wall, and the waterproof performance of the outer wall. The reason for the analysis from these four aspects is mainly because these four aspects cover all aspects of the outer wall:

- (1) The performance of insulation: in order to avoid the interference of direct sunlight, this experiment selects the measured temperature data of the north wall on the coldest and hottest day during the test period to analyze the thermal insulation performance of the wall.
- (2) The moisture drain performance of wall: the wall drains moisture outdoors in summer and absorbs moisture indoors in winter. In summer, the internal moisture is vaporized by sunlight and expelled. The annual measured humidity data inside the south-facing wall were selected to analyze the moisture drain performance of wall.
- (3) The ability of preventing the penetration of the hot and humid air of the inner wall: in winter, the indoor hot and humid air will permeate into the wall. The measured humidity data of the wall during the heating of the east, south and north walls were selected to analyze the moisture-proof performance of the inner wall surface.
- (4) The waterproof performance of the outer wall: the wind direction in Jinan city is changeable, and the east and southeast wind are the majority in the rainy season. Thus, the waterproof performance of the east wall and the outer wall is the most unfavorable. The measured humidity data of the east wall before and after the precipitation was selected to analyze the waterproof performance of the outer wall.

This study selected the whole year measured data from March 26, 2018, to March 26, 2019, for analysis. The working condition of one day between two precipitation periods from April 7, 2019, to April 13, 2019, can clearly reflect the waterproof performance of the outer wall surface. Therefore, the measured data in April 2019 was selected for the analysis of the waterproof performance of the outer wall surface.

3.2.1. The Performance of Insulation of Wall. The thermal insulation performance of the structural layer of outer wall can be approximately represented by the temperature difference between the test positions on both sides of the structural layer. The smaller the temperature difference is, the better the thermal insulation performance is. The temperature difference between test position i and $i + 1$ at a certain time j is calculated by

$$\Delta t_{(i+1)ij} = |t_{(i+1)j} - t_{ij}|, \quad (2)$$

where $\Delta t_{(i+1)ij}$ is the absolute value of the temperature difference between test position i and test position $i + 1$ at a certain time j , and the unit is °C; t_{ij} and $t_{(i+1)j}$ are the temperature values of test position i and test position $i + 1$ at a certain time j , and the unit is °C; i is the test position inside the wall, with values of 1, 3, 4, 5; j is the hour of the day, with values of 0, 1, 2, . . . , 23. The test wall is composed of thick aerated concrete slabs with the thickness of 200 mm, thick inner graphite polystyrene plate with the thickness of 100 mm, and thick outer graphite polystyrene plate with the thickness of 100 mm. In Figure 2, test positions 1, 3, 4, and 5 are, respectively, distributed on both sides of the structure layers. The thermal insulation performance of thick aerated concrete strip (200 mm), thick inner graphite polystyrene plate (100 mm), and thick outer graphite polystyrene plate (100 mm) can be characterized by Δt_{31j} , Δt_{43j} , and Δt_{54j} , respectively.

The steps of thermal insulation analysis of the wall are as follows:

- (1) Take the position of the test point as the abscissa and the internal temperature of the wall as the ordinate and draw the temperature points of test position 1, 3, 4, and 5 at time j on the coldest day during the test period. Then, connect the temperature points into a broken line. In the same way, draw the temperature polylines for 24 hours of the day.
- (2) Analyze the 24 temperature lines above and select the broken lines at some time when the temperature difference between inside (point 1) and outside (point 5) wall is large and the steady-state heat transfer approaches one dimension. Calculate Δt_{31j} , Δt_{43j} , and Δt_{54j} of those broken lines and calculate the average values ($\overline{\Delta t}_{31H}$, $\overline{\Delta t}_{43H}$, and $\overline{\Delta t}_{54H}$) as the evaluation basis of the heat preservation performance of the wall in winter.
- (3) The actual insulation effect of aerated concrete strip, inner graphite polystyrene plate, and outer graphite polystyrene plate was evaluated by comparing the relationship between the average values ($\overline{\Delta t}_{31H}$, $\overline{\Delta t}_{43H}$, and $\overline{\Delta t}_{54H}$) and the heat transfer coefficients (K_{31} , K_{43} , and K_{54}) of the corresponding structure layers.
- (4) The average values ($\overline{\Delta t}_{31H}$, $\overline{\Delta t}_{43H}$, and $\overline{\Delta t}_{54H}$) of the hottest days during the test period were calculated to evaluate the actual thermal insulation performance of the main structural layers in summer with the same method.

TABLE 2: The water vapor permeability resistance at the test location of the exterior wall.

Test location	Water vapor permeability resistance, H ($\text{Pa}\cdot\text{m}^2\cdot\text{s}\cdot\mu\text{g}^{-1}$)	
	Indoor side	Outdoor side
1	2.59	55.11
2	6.92	50.78
3	9.81	47.89
4	33.75	23.95
5	56.84	0.86

3.2.2. *The Moisture Drain Performance of Wall.* Calculate the water vapor permeability resistance of the indoor and outdoor side of the test location based on the thickness of the building structure layers, the position of temperature and humidity sensor, and the water vapor permeability coefficient μ of the building material. The calculation results are shown in Table 2.

In the process of exterior wall construction, the residual moisture is discharged to the indoor and outdoor, and it is difficult to discharge moisture at test position 2, 3, and 4. Therefore, the average daily moisture content \bar{d}_i of test position 2, 3, and 4 was calculated, respectively, in this study to evaluate the residual moisture drain performance inside the test wall. The calculation formula of the average moisture content is as follows:

$$\bar{d}_i = \frac{\sum_{j=0}^n d_{ij}}{24}, \quad (3)$$

where \bar{d}_i is the average daily moisture content at test position i , and the unit is g/kg, and d_{ij} is the moisture content at a certain time j in position i , the unit is g/kg.

3.2.3. *The Waterproof Performance of the Outer Wall.* Therefore, study the daily precipitation before and after the precipitation process and the average daily moisture content (\bar{d}_i) at test position 5, 4, and 3 during the period to analyze the effect of precipitation on the moisture content of the outdoor side and wall and evaluate the waterproof performance of the outer wall.

3.2.4. *The Ability of Preventing the Penetration of the Hot and Humid Air of the Inner Wall.* The indoor temperature and humidity of the building in winter are higher than the outdoor environment, and the water vapor flows to the outdoor through the envelope structure, which may result in the problem of moisture accumulation inside the wall. In order to ensure the durability and thermal insulation of materials, GB 50176-2016 “Code for Civil Building Thermal Design” stipulates that the increment of mass humidity of the insulation materials ($\Delta\omega$) shall not exceed a certain limit after a heating period. Thus, the moisture in the insulation materials can gradually distribute after the heating period, rather than accumulate inside year by year. The limits of $\Delta\omega$ are shown in Table 3.

TABLE 3: The allowed increment of mass humidity of the envelope insulation material during heating period.

Insulation material	The allowed increment of mass humidity [$\Delta\omega$] (%)
Porous concrete (foamed concrete, aerated concrete, etc.) ($\rho_0 = 500\sim 700 \text{ kg/m}^3$)	4
Model polystyrene foam	15

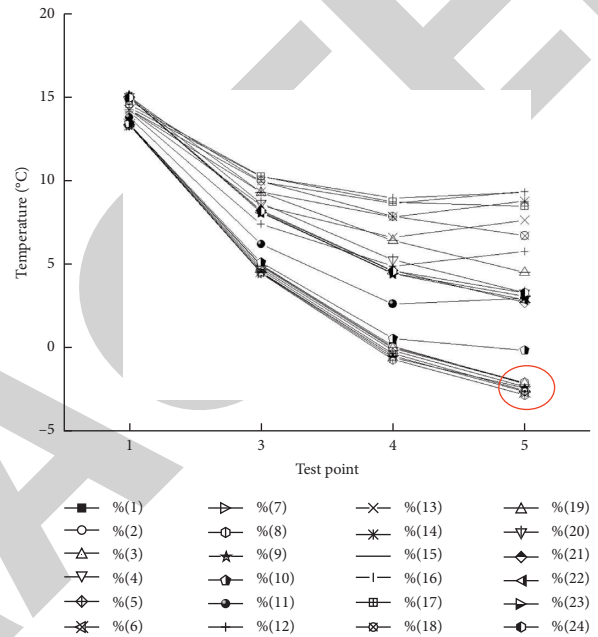


FIGURE 6: Temperature curve on the hour of the indoor side of the north-facing wall on January 13 (the coldest day during the test period).

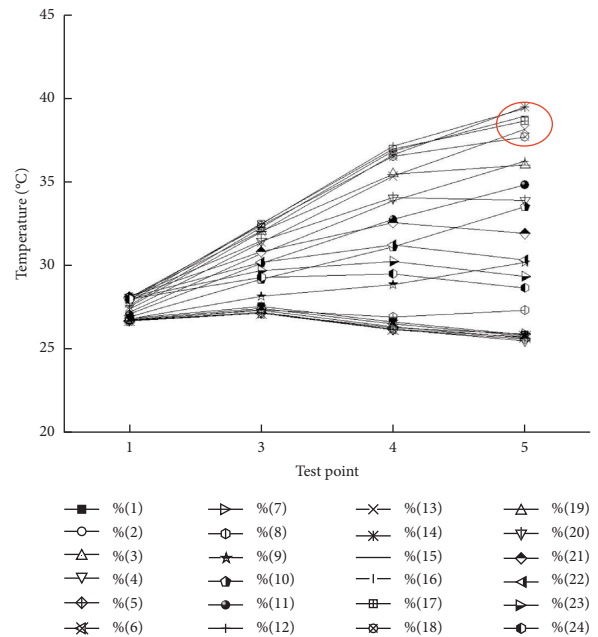


FIGURE 7: Temperature curve on the hour of the indoor side of the north-facing wall on July 11 (the hottest day during the test period).

TABLE 4: Thermal insulation performance of main structural layers of exterior wall.

Structural hierarchy	Test point	Thermal resistance, R ($\text{m}^2 \cdot \text{k} \cdot \text{w}^{-1}$)	Heat insulation performance, Δt_H ($^{\circ}\text{C}$)	Insulation performance, Δt_C ($^{\circ}\text{C}$)	Heat insulation performance of each unit of thermal resistance, $\Delta t_H/R$ ($^{\circ}\text{C}$)	Insulation performance of each unit of thermal resistance, $\Delta t_C/R$ ($^{\circ}\text{C}$)
Aerated concrete slabs	Point 1, 3	14.29	8.66	4.58	0.61	0.32
Inner graphite polystyrene plate	Point 3, 4	33.33	4.97	4.58	0.15	0.14
Outer graphite polystyrene plate	Point 4, 5	33.33	2.13	2.2	0.06	0.07

The increment of moisture content before and after the heating period can be represented by the increment of mass humidity of aerated concrete slabs and graphite polystyrene slabs inside the wall after the heating period. The calculation formula is shown as follows:

$$\Delta\omega_i = \frac{(\bar{d}_{iHE} - \bar{d}_{iHS})}{\bar{d}_{iHS}} \times 100\%, \quad (4)$$

where $\Delta\omega_i$ is the increment of mass humidity of material at test position i after the heating period; \bar{d}_{iHS} and \bar{d}_{iHE} are the average daily moisture content of test position i at the beginning and end of the heating period, respectively, and the unit is g/kg. The actual heating period in Jinan begins on November 15 each year and ends on March 15 of the following year. Thus, \bar{d}_{iHS} and \bar{d}_{iHE} are the average moisture content of test position i on November 15 of the current year and March 15 of the following year.

The necessary and sufficient condition to judge that the internal surface of the wall has good performance in preventing the infiltration of hot and humid air is $\Delta\omega_i \leq [\Delta\omega]$. Based on the judgment, the ability of preventing the penetration of the hot and humid air of the test inner wall can be evaluated.

4. Results

4.1. The Performance of Insulation of Wall. The coldest and hottest days of the year during the test period were January 13 and July 11, 2018. The temperature curves of the north-facing exterior wall on the hour are shown in Figures 6 and 7, respectively. It can be seen from Figure 6 that the temperature at different hours showed a trend of gradual decrease from indoor to outdoor (test point 1 to test point 5) in the coldest day of the year during the test period. During the coldest day, the temperature of the inner wall fluctuates in the range of 13.3~15.0 $^{\circ}\text{C}$, and the fluctuation range is obviously smaller than that of the outer wall (-2.8~9.3 $^{\circ}\text{C}$), which indicates that the wall has good thermal insulation performance on the coldest day and can keep the indoor temperature relatively stable without being affected by the outdoor cold air. At the same time, it can be seen from Figure 7 that the temperature at different hours from indoor to outdoor (test point 1 to test point 5) mostly showed a

gradually rising trend in the hottest day of the year during the test period. During the hottest day, the temperature of the inner wall fluctuates in the range of 26.7~28.1 $^{\circ}\text{C}$, and the fluctuation range is obviously smaller than that of the outer wall (25.5~39.5 $^{\circ}\text{C}$), which indicates that the inner wall has good thermal insulation performance and can keep the indoor temperature relatively stable without being affected by the outdoor warm air.

The points circled with red circle in Figure 6 shows the temperature values from 0 to 8 o'clock on January 13, and the points circled with red circle in Figure 7 shows the temperature values from 13 to 16 o'clock on July 11. During these two periods, the heat transfer inside the wall is close to one-dimensional steady heat transfer, and the average temperature difference of the main structural layers is shown in Table 4. The temperature difference between the two sides of the aerated concrete strip (200 mm) was significantly higher than that of the inner graphite polystyrene plate (100 mm) and the outer graphite polystyrene plate (100 mm), and the heat insulation performance of each unit of thermal resistance was 0.61 $^{\circ}\text{C}$, 0.15 $^{\circ}\text{C}$, and 0.06 $^{\circ}\text{C}$, respectively. The insulation performance was 0.32 $^{\circ}\text{C}$, 0.14 $^{\circ}\text{C}$, and 0.07 $^{\circ}\text{C}$, respectively, indicating that the thermal insulation performance of 100 mm graphite polystyrene plate in summer and winter was better than that of 200 mm aerated concrete strip slab with twice the thickness of it. At the same time, due to the complexity of the actual heat transfer process, the insulation performance of the graphite polystyrene plate with the same thickness applied on the inside and outside of the external wall is also different to some extent. As can be seen from Table 4, the insulation performance of the graphite polystyrene plate with the same thickness on the outside of the external wall is about 2 times better than that on the inside of the external wall.

4.2. The Moisture Drain Performance of Wall. The average daily moisture content in one year (from March 26, 2018 to March 26, 2019) of test point 2, 3, and 4 inside the east wall was calculated based on (3). The results are shown in Figure 8. The moisture content of steam pressurized concrete slab inside the east wall (test point 2) is the largest throughout the year; the moisture content of the inner graphite polystyrene plate (test point 3) is next, and the outer

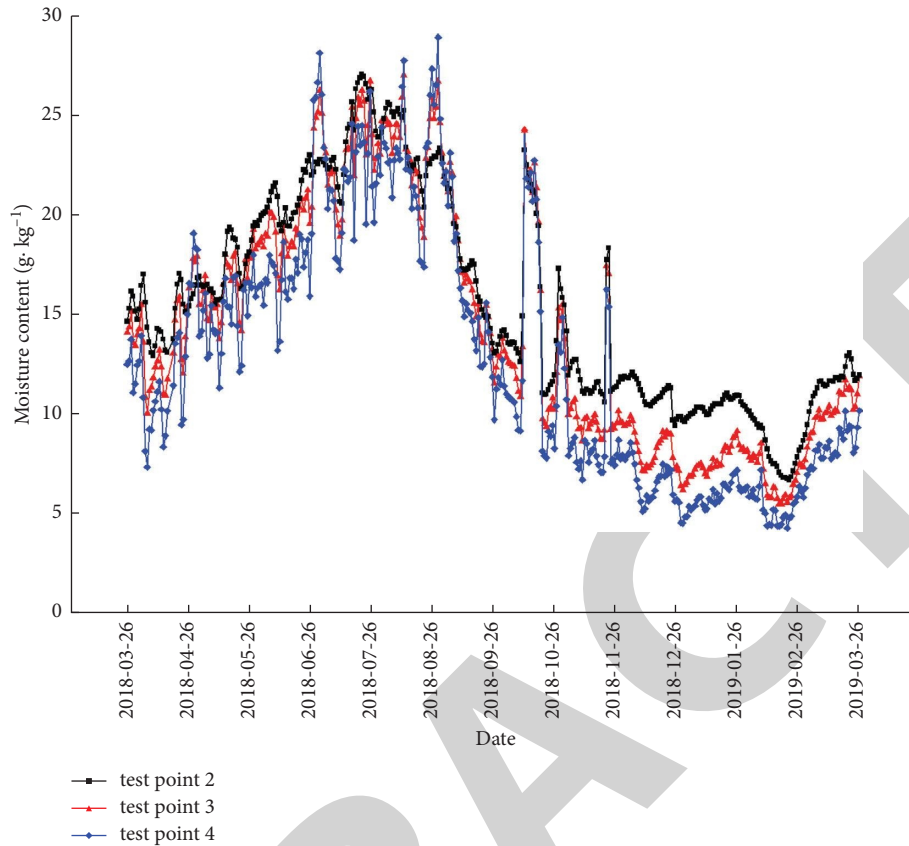


FIGURE 8: The curve of average daily moisture content inside the east wall.

graphite polystyrene plate is the smallest. In addition, the water vapor permeability resistance of test point 2 on the outdoor side is higher than test points 3 and 4 (see Table 2). It can be seen that the moisture inside the wall is mainly discharged to the outside wall.

The moisture content inside the east wall decreases in summer and autumn, especially from August to October with high temperature. On the contrary, the moisture content rises in spring and winter. The moisture content of test points 2, 3, and 4 inside the wall decreased little after one year, with a decrease of 18.4%, 15.6%, and 18.4%, respectively. In Figure 8, the moisture content of point A and B increased sharply during the test time. After investigation, it was found that points A and B were all in case of heavy rain, and the moisture content inside the wall was changed due to rainwater penetration.

4.3. *The Waterproof Performance of the Outer Wall.* There was significant precipitation on April 9 and April 11, 2019. The moisture content and precipitation at test points 3, 4, and 5 inside the east wall from April 7, 2019, to April 13 were selected to carry out waterproof analysis on the outer wall. The measured data are shown in Figure 9. It can be seen from Figure 9 that the precipitation on April 9 and 11 caused the moisture content of the outer wall (test point 5) to increase significantly on April 10 and 12, and the rainwater that penetrated into the outer wall was then discharged rapidly.

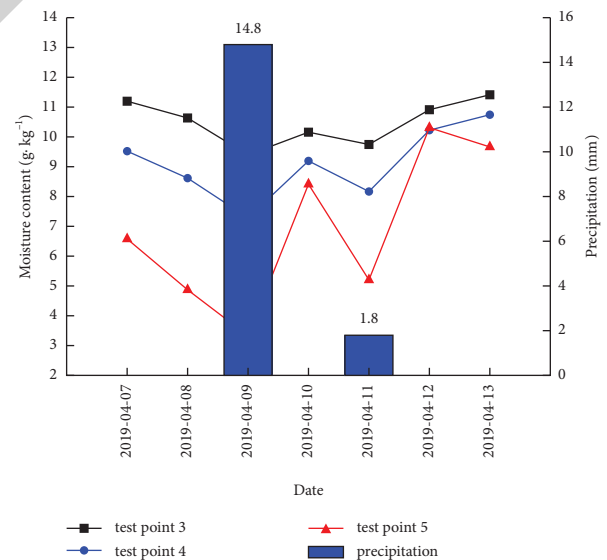


FIGURE 9: Average daily moisture content and precipitation inside the east wall.

The moisture content of the outer wall (test point 5) began to decrease on April 11 and 13. The moisture content of the graphite polystyrene plate (test position 4, 3) fluctuated in the same way as that of the outer surface of the external wall, but the fluctuation range was reduced. The measured data show that the outer surface of the external wall cannot

TABLE 5: Increment of mass humidity of insulation material inside the external wall after heating period.

Structural hierarchy	Test point	Heating period in 2018, $\Delta\omega_i$			The allowed increment of mass humidity [$\Delta\omega$](%)
		East wall	South wall	North wall	
Aerated concrete slabs	Point 2	6.43	14.9	1.99	4
Graphite polystyrene plate	Point 4	3.66	17.73	-2.39	15

completely prevent the infiltration of rainwater, but the influence time of rainwater on moisture content inside external wall is short since the rainwater that penetrates into the wall will be discharged quickly.

4.4. The Ability of Preventing the Penetration of the Hot and Humid Air of the Inner Wall. The heating period in winter in Jinan is from November 15 to March 15 of the next year. Therefore, the increments of mass humidity of building materials at the test point 2 and 4 of the east, south, and north exterior walls after the heating season in 2018 were calculated, respectively, based on (4). The calculation results are shown in Table 5. The increments of mass humidity of aerated concrete slabs on the east and south wall is 6.43% and 14.9%, respectively, after the heating season in 2018, exceeding the allowable increment of mass humidity of aerated concrete slabs by 4%. The increment of mass humidity of graphite polystyrene plate on the south wall is 17.73%, exceeding the allowable increment of mass humidity of graphite polystyrene plate by 15%. The infiltration of indoor hot and humid air in winter is not the only reason for the increase of moisture content inside the wall. Through the data analysis of one heating season, it can only be determined that the infiltration of indoor hot and humid air cannot be effectively prevented by the inner wall surface with the cement mortar airtight layer (15 mm) in this project. The exact conclusion needs the comprehensive comparative analysis of the data of multiple heating periods.

5. Conclusion

In this paper, the thermal performance of the exterior wall of the teaching and laboratory building of Shandong Jianzhu University was measured and the structural rationality was studied. The main conclusions are as follows:

- (1) The temperature and humidity sensors were used to continuously measure the temperature and humidity of the air inside the cavity of the wall, which can be used to represent the temperature and humidity of the solid wall at the position of the cavity. In order to ensure that the cavity data can accurately reflect the temperature and humidity of the wall, the installation design and construction process of the sensor must meet the requirements of air sealing of the cavity in the wall and accurate installation position of the sensor.
- (2) The external wall structure of polystyrene board (200 mm thick) for external insulation and thin plastering has good practical operation effect in three aspects of thermal insulation, internal moisture

discharge, and external wall waterproof, which basically meets the design requirements of external wall of passive house in Germany. In terms of moisture protection of the inner wall, the inner wall of cement mortar (15 mm thick) may not be able to effectively prevent the infiltration of indoor hot and humid air. Thus, the insulation layer should be added into the external wall.

- (3) The moisture inside the wall is obviously affected by the season. The moisture content increases in spring and winter and decreases in summer and autumn. The drain performance of moisture inside the wall mainly occurs in the sweltering heat, and the drain direction is from the indoor side to the outdoor side. In the external insulation structure, there are two layers of graphite polystyrene plate (100 mm thick), and the insulation effect of polystyrene plate near the outdoor side is better than that near the indoor side. The combination of anticrack mortar (5 mm thick) and paint cannot completely prevent the infiltration of rainwater, but the infiltration of rainwater in the wall will be quickly discharged in a short time.

The study only measured the temperature and humidity of the outer wall, but the performance of the outer wall is far more than these two parameters, so the next research can be done in the direction of other parameters.

Data Availability

No data were used to support this study.

Conflicts of Interest

The authors declare that there are no conflicts of interest regarding the publication of this article.

References

- [1] S. Xiong and X. Gao, "Application and technology of external thermal insulation system for passive ultra-low energy consumption building," *Construction Science and Technology*, vol. 11, pp. 56–60, 2018.
- [2] H. Künzel, H. M. Künzel, and K. Sedlbauer, "Long-term performance of external thermal insulation systems (ETICS)," *Acta Architectura*, vol. 5, no. 1, pp. 11–24, 2006.
- [3] German Institute of Passive House, *Standard for Passive Energy Saving Reconstruction and Standard for Passive*, 2015, https://passipedia.org/_media/picopen/cnuebersetzungneuer_kriterien2015.pdf.
- [4] 16J908-8, *Passive Low Energy Consumption Building -- Residential Building in Cold and Cold Regions*, China Planning Press, Beijing, China, 2017.

Retraction

Retracted: Energy Efficient Utilization toward Rural Biomass Waste by Straw Biogas Engineering

Advances in Materials Science and Engineering

Received 26 December 2023; Accepted 26 December 2023; Published 29 December 2023

Copyright © 2023 Advances in Materials Science and Engineering. This is an open access article distributed under the Creative Commons Attribution License, which permits unrestricted use, distribution, and reproduction in any medium, provided the original work is properly cited.

This article has been retracted by Hindawi, as publisher, following an investigation undertaken by the publisher [1]. This investigation has uncovered evidence of systematic manipulation of the publication and peer-review process. We cannot, therefore, vouch for the reliability or integrity of this article.

Please note that this notice is intended solely to alert readers that the peer-review process of this article has been compromised.

Wiley and Hindawi regret that the usual quality checks did not identify these issues before publication and have since put additional measures in place to safeguard research integrity.

We wish to credit our Research Integrity and Research Publishing teams and anonymous and named external researchers and research integrity experts for contributing to this investigation.

The corresponding author, as the representative of all authors, has been given the opportunity to register their agreement or disagreement to this retraction. We have kept a record of any response received.

References

- [1] X. Wang and D. Zhao, "Energy Efficient Utilization toward Rural Biomass Waste by Straw Biogas Engineering," *Advances in Materials Science and Engineering*, vol. 2022, Article ID 3338515, 6 pages, 2022.

Research Article

Energy Efficient Utilization toward Rural Biomass Waste by Straw Biogas Engineering

Xiao Wang ¹ and Dejie Zhao²

¹The New Material and Chemical Engineering Institute, Guang'an Vocational and Technical College, Guang'an 638000, Sichuan, China

²The People's Government of Daishi Town, Qianfeng, Guang'an 638000, Sichuan, China

Correspondence should be addressed to Xiao Wang; wangxiaoxiao077@163.com

Received 19 January 2022; Revised 16 February 2022; Accepted 22 February 2022; Published 1 June 2022

Academic Editor: Palanivel Velmurugan

Copyright © 2022 Xiao Wang and Dejie Zhao. This is an open access article distributed under the Creative Commons Attribution License, which permits unrestricted use, distribution, and reproduction in any medium, provided the original work is properly cited.

In this article, we summarize and analyze the constraints and technical difficulties of biogas plants in clusters, storage and transportation yards, pretreatment yards, and anaerobic fields. Combined with Tyre's own experience, several major techniques have been proposed. To guide and recommend the suitable technicians to decision makers, to acquire operation courses suitable for the general requirements of our biogas, and to promote the development of booth biogas seedlings in China, the use of environmental slam objects in a small and sufficient nonscale biogas program is formulated by the use of biogas funding alone. Current rating measures leverage the World Age Assessment (LCA) for the Integrated Booth Biogas Swing Type (typically 40,000 kWh) and Bio-Natural Gasoline Program (daily gasoline workload of 12,000 cubic curves). This is built upon the Environmental Impact Assessment and Analogy for Warships Both environmental stroke and sensitivity component analysis. These techniques include termination outlines, register analysis, dynamism drops for each performance stagecoach, and environmental issue calculations. According to the above summarization, when biogas dominates the family, the highest environmental emission becomes the biogas fermentation layer of the booth. Meanwhile, the most sympathetic substitute is the work cost of physical and chemical farting (mL g-ITS). The above two indicators denote the essence of biogas purification, and the choice of biogas purification technology. By evaluating the change in the impact of suppressing environmental emissions, the biogas substitute of scorpion charcoal has a remarkable improvement in the biogas equivalent of the charcoal-bright swing family. Comprehensive experimental results have demonstrated this conclusion.

1. Introduction

As a country dominated by agriculture, China has a large amount of agricultural straw and rich varieties. With the increment of grain output, the annual output of crop straw also increases year by year. The satisfaction of being proud of the importance of living on the street can be used effectively as a means of grandeur. On the contrary, if the application or negotiation cannot be completed, it will become a highlight of the resort. Also, the fiery heat exposed by a large number of booths can greatly adapt to publicity pollution and fire accidents. Therefore, after the "Eleventh Five-Year Plan," the appropriate use of booths has been highly praised by domestic scholars [1]. The straw biogas project can not only

solve the problem of excess straw in my country but also generate clean energy and solve the problem of increasing energy shortage. Therefore, it has been a hot topic of research and discussion nowadays. Although domestic research and promotion have been launched for many years, there are still many unresolved issues. Meanwhile, there are not many plans that have actually been put into practice. The biogas performance of anaerobic fermentation is perfect organic destruction utilization and fruit smart technology. It mainly includes assembly, storage and transfer, pretreatment, anaerobic fermentation, and biogas treatment [2, 3]. The technology has the characteristics of peace and stability, low energy consumption, no pollution, good ecology, and economic benefits. Therefore, it is widely applied in different

regions. Many related projects have been piloted and even put into production. In actual production, however, there are many bottlenecks in the application of this technology, such as straw collection, difficult storage and transportation, long fermentation time, low gas production rate, low utilization rate, and difficulty in straw pretreatment [4–6]. These problems hurt the development of biogas projects and have led to low investor enthusiasm and slow development of the industry. Based on years of working experience in the biogas industry, the authors summarize and analyze the key constraints and technical difficulties in each link of the straw biogas project. It also provides some comprehensive suggestions to some inspiration and thinking for the technicians in the biogas industry. We explore the biogas treatment route suitable for China's national conditions and promote the development of China's straw biogas project. The cost of straw collection and transportation is high, and the pertinence is poor. The cost of collection and transportation is high. The straws required to be handled in China are mainly dry yellow straws after grain harvesting. The collection process involves multiple steps. First, the straw is chopped down during harvest by using a hay rake or by hand. After stacking, they are bundled with semimechanized hydraulic devices and finally transported to the storage place by car. Therefore, high mechanical and labor costs have to be invested [7, 8]. Straw is low in density and light in texture, resulting in high unit transportation costs. Collection methods are poorly targeted and difficult to use. In order to reduce the transportation cost per unit mass, the straw should be compacted as much as possible to increase the stacking height. Also, when bundling, it is often bundled into high-density square bales or large round bales. Square bales are denser and easier to stack than the round bales. However, there are some problems in the usage of this high-density bales. First, the ventilation is poor, and the bales are prone to mold, which affects subsequent storage and anaerobic fermentation. Second, the straw needs to be broken before use, and the bales are very difficult to use. It is difficult to put it directly into the crusher, and it has to be disassembled before putting it in. Therefore, it is necessary to put in unpacking equipment and lifting machinery, which requires a large space and dust-proof measures. This will undoubtedly increase the cost and difficulty of straw processing. Even worse, it is difficult to store the straw. In practice, the production of straw is seasonal, and the biogas project needs to run all year round, requiring a large amount of straw to be stored for a long time. The moisture content of straw varies greatly, ranging from 10% to 50%. Practical experience has shown that straw with a moisture content of more than 5% is prone to mold when stacked, which affects the usage substantially. Processing stations require unpacking and drying. Straw with low moisture content can cause fires when stored intensively for long periods of time. In addition, if the moisture content of straw is too low, its processing difficulty will also increase. Because anaerobic bacteria can only use cellulose, no lighting can be used. During the drying processing of straw, as shown in Figure 1, cellulose will be more firmly wrapped by lignin, resulting in poor fermentation effect.

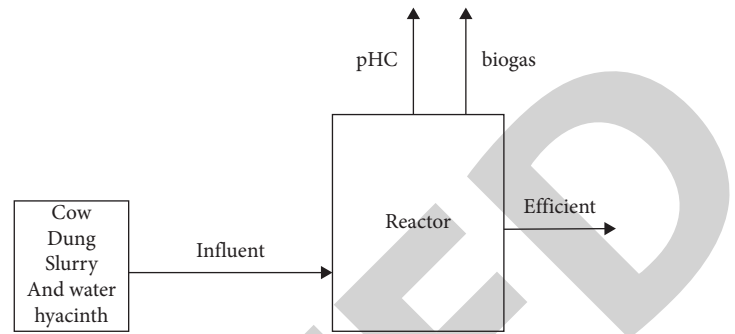


FIGURE 1: Production of biogas in our framework.

2. Related Work

Eustoma gas, also known as prairie gentian, belongs to the genus *Prairie gentian* of the Eustoma family. It is a one- or two-year herb [1]. It is native to North America and is often one of the most familiar symbols of the mug and pomegranate flower worldwide. [4–6]. Yunnan is one of the four provinces with the most matching human cream performance. In 2015, Yunnan's flower planting area was 75,100 hectares. Among them, pure cruciferous flowers are roses, eustoma, carnations, lilies, etc. Nonfading composition means the red split head 12,400 hectares. 8.69 billion castles account for more than 70% of the market part of the region. In the strong neglect bubble, *Eustoma* is a kind of dilemma that is rapidly improving in New York. The planting area is more than 400 hm², and *Gerbera* is excellent, suitable for the mayor of Yunnan to cut the head [5]. While dispelling obscene vineyards and scouring the happiness and teachings of the flower industry, how to effectively handle the flower stems has also become a key result faced by the mantle groups and sellers. In escort transportation, the custom of nonproductive blowing stations is mainly to operate directly or up the epigram and further use it as the fertilizer. A large number of stalls quickly point to lead to the unclean environment and heavily use grade and poor fertilizer capacity [6]. Therefore, adopting a proper, environmentally friendly, and qualified processing sequence is the key technique to arrange the worthless fake flower stalls. The use of *Eustoma* stems as bald head material to calculate options and power for biogas production through anaerobic fermentation. We expect to foresee a new distance where money uses worthless fake flower stems.

Coincidentally, in my rude situation, there are very few land-shared biogas to carry out full-scale biogas refinement and implementation. Also, there are poor and prominent trust and transformation of engineering projects, and the purpose and production of equipment and equipment do not even result. The straw biogas program has been improved, and many are permanently absent. Germany is a land that derives from the necessity of formerly biogas life [9–12]. It is not only an adult biogas production land but also a strong proof of rural biogas projects. Whether it is policies and regulations, fermentation products, or technical support, it is also one of the most important countries in the induction and practice of biogas engineering technology.

The charging system has been recognized as a wealth of experience [13]. Although the booth assembly method in our region is different from Germany, we can communicate in terms of engineering design and function. There are also some difficulties with inserting alien technology. First of all, the imported furniture is loose, the opening amount of the plan is huge, and the product is a hill. Accordingly, the entrance is often not enough to become the terminal suffering, suppressing the ecstasy of investors. Therefore, having a biogas subsidy is still one of the toilet elements disclosed by biogas. Second, technical problems are “unpleasant” tendencies. This claims that the introducer has obtained satisfactory technical support. A well-timed tier, which requires both a comprehensive analysis of the material and abyss of the technique. It adapts the technique to the characteristics of my rude booth. Excessive salinity content also inhibits protein composition. Therefore, the progress of the domestic use of the invented feces is worrying. The growth technology of saline-alkali deposits mainly includes three methods: drug growth, synthetic progress, and biological progress [6]. In the design of gardens and gardens, due to the limitation of funds and circumstances, the comprehensive method of physical promotion is adopted, which basically conforms to the characteristics of “moisturizing the taste and lightening the seasoning.” This mainly uses the second-hand drainage to ensure that the groundwater level is acceptable. We then downgrade and governance it. The drain should be slid in vigorously and skillfully to complete the get-away situation and barren land. The essence of the low-pollution constitution is the disclosure of national poverty [13–17]. Soil depletion is a major manifestation of the deteriorating laxative, analytical, and biological properties of the environment and country around Bedob. Immediately, in garden design, mixing and matching is the main habit to refute Zhuxian. A certain number of constitutional bases are incorporated to facilitate the real shares. The organized material in the substrate can be completely re-enacted with new compost, which creates an auspicious Earth. We can also constitute a mild but not quiet accumulation of land, which strongly condemns the problems of nutrient deficiencies and overstocking of Bedobium [18–20]. The combined hybrid system necessity is perfect in the project and can do both at the same time.

3. Proposed Method

Biomass Lingling production technology can be mainly divided into three categories. Figure 2 carries out the boundaries of the three token technologies, as shown in Figure 2. It shows the point to biomass for cremation/gasification impact family technologies. The calculation is as follows:

$$w_0 = \sum_{i=1}^T P_i. \quad (1)$$

Animation production life only counts biomass capital, such as animal husbandry, forestry downturn, or bleak towns. It can generate electricity quickly, or biomass can be gasified in a gasifier. The brisk government then drives the internal combustion cars or twisted turbines to generate

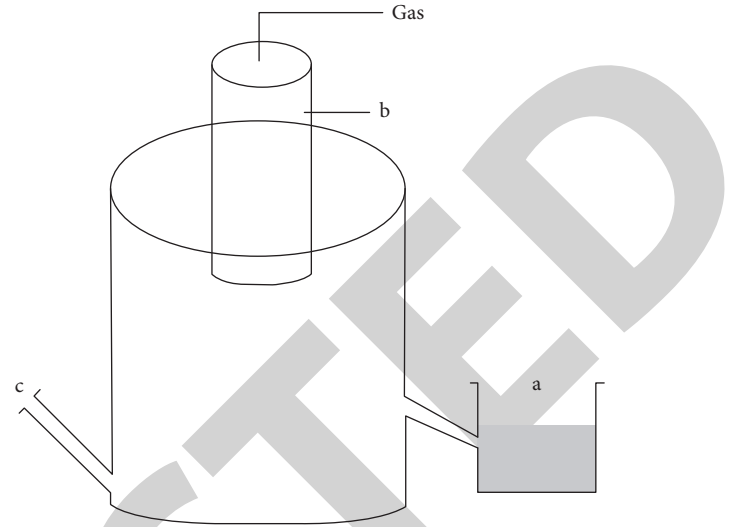


FIGURE 2: An illustration of our adopted token technology.

electricity. We suggest that the car differentiates the biomass-coupled rocking progeny technology. This is obtained by

$$u_0 = \frac{1}{w_i} \sum_{i=1}^T i \times P_i. \quad (2)$$

Their presumably good spirits come from artificial breezes like biomass and charcoal. Direct coincineration, intermediate coincineration, and matching coincineration techniques can be leveraged for spirits varieties [11]. It alludes to BECCS technology. By setting up the CCS-told furniture in biomass-backed impact technology, CO₂ emissions will be captured and stored to achieve zero or even carbon denial across the entire world calendar. At the meeting, the so-called biomass energy efficiency phantom technology has a relative firepower distribution in the power configuration of our district. As of 2018, China’s state-level biomass spiritual species accounted for 19.54 million kilowatts, of which state-level biomass accounted for 1.03% and Shenling accounted for 1.34% [12]. Among them, the stocks of the land planted and tree biomass dominant clan, wildfire spirit clan, and marsh God clan are 50%, 47%, and 3%, respectively. As the relevant biomass-dominated progeny just implemented mentioned above, mostly biomass-expressing-inflammatory buds, the conjugated sway family buds are still fully bounded, with only one demonstrated and demonstrated switch [21]. The above calculation is as follows:

$$w_i = \frac{1}{w_i} \sum_{i=t+1}^T P_i - HT(x) + c. \quad (3)$$

Biomass impact stocks and conjugate impact progeny techniques. They are pervasively used in developed countries such as Europe and the United States. The Biomass Eldar in Finland describes the descendants of 11% of the domination of the land. They build it as the largest area for humanity. This process can be calculated as

$$u_i = \frac{1}{w} (u - u(t)). \quad (4)$$

Many char-brilliant in the UK may have established illuminated government progeny near or in excess of 1000 MW under the provisions of conjugate breeding. The conjugate divinity varieties also recount a large part of the formation of biomass divinity in the US. This technique uses the crazy flaky ash and pitch charcoal are cobrilliant [21], i.e.,

$$g = w(t - ht(x)) + \sigma. \quad (5)$$

As serious as the BECCS technical harassment is, it is still in the post of interrogation and painting, pinned on wandering ranks. As of 2019 abortion, there are 8 BECCS examples in the manufacturer's remediation process, of which only 5 are evolving, with a perennial CO₂ retention of about 1.5 Mt [14]. Only some CCS units in China have been demonstrated and solved, and the cumulative supply of 2 million CO₂ types [14]. The maturity of all aspects of CCS technology and the increase in industrialization have also inhibited the follow-up appeal and promotion of BECCS technology. In summary, the general education direction of the three major indicators of biomass strength technology can be described as follows: biomass direct/gasification production > biomass blending force production > BECCS. The problem obedience effect is strong, BECCS > biomass direct chaos/gasification affects offspring > biomass chaos rules offspring, i.e.,

$$c = k\sqrt{(x_0 - x_1) + (u - t)}. \quad (6)$$

The technical arrangement can be described as follows: Biomass cofiring alcohol raw material > biomass mixing/gasification production > BECCS. Combined with the fire-carbon fracture trajectories of the force system under carbon indifference perception, all the three methods represent that the rocking technology of biomass life can play a considerable role. Upon rearranging the saplings, the quota of biomass burning/gasification technology can be increased, and the uniformity of regenerative ability Shengo products can be improved accordingly. The car brightness rules can be modified by biomass cocremation to gain a deeper understanding of the final difference. This may be the provision for decarbonization. This is obtained as follows:

$$\Delta_{\text{sum}} = -\frac{1}{2\pi\sigma^2} \left[1 - \frac{x^2 + y^2}{t^2} \right]. \quad (7)$$

In the future, the share of BECCS spirit descendant technologies could increase in a giant pane to ensure that the ruling sector enforces cyber cryptography and even offsets emissions. It includes technical practicality and personality. There are hundreds of designs of biomass divine species in China, but the application of conjugate divine nature formation technology is less, and only a few charcoal roasters have carried out biomass conjugate government production [15]. This is obtained as follows:

$$z = f(x, y) + tc(x). \quad (8)$$

Take Huadian International Shiliqian Power Plant Unit 5 as an example, it is the first unit in China to rapidly realize biomass blending metamorphism. The cofiring narrative

does not have problems such as carbonization and gnawing [13]. Guodian Changyuan Jingmen thermal power plant Unit 7 is the first privately owned 600 MW coal-fired midscale blending unit, under the strategy of enjoying general subsidies partially for the biopower offspring will affect profitability [13] is calculated as follows:

$$T(x) = z(x, y) + HT(x) - c. \quad (9)$$

Hubei Huadian Xiangyang Unit 6 takes the lead in using radiation and forest farms as nonpractical materials to indirectly coincinerate biomass-conjugated generating units. The safety and frugality of copper in the coincineration process can be experienced as indicative requirements [16]. There is still a fixed gap between the blending technology and the external state. On behalf of the company, char-illuminate in the UK has carried out the technological transformation of biomass-conjugation effect formation. This can obtain the proportion of biomass coincineration without retention ratio, which can be further leveraged in burning the reworked copper system from 2017. This technique uses 100% biomass Breeze. The Alholmens Kraft thermal power plant in Finland is the world's largest biomass cofiring cauldron, which can be used for charcoal cremation and has been operated stably for many years [15]. The calculation is as follows:

$$F(x) = z(x, y) + \int ht(x) + c. \quad (10)$$

The research, demystification, and presentation of the BECCS program have been a noticeable success in the United States and Canada. As a precedent, the industrial carbon capturing project in the US state of Illinois is typically the largest BECCS program and the only BECCS program among the 18 megascale CCSs of humanity. This scheme retains violent-harmless CO₂ ethanol produced from the narrative for storage in the proposed model with a prey dispersal rate of 1 Mt/a [14].

4. Experimental Results and Analysis

Compared to the cut-dried charcoal varieties, the biomass affects offspring to grow fresh and frugal pains. It is estimated that the adjustment cost of charcoal fire affecting offspring is 0.41 yuan/(kW·h). Also, the cause of the stall may be 0.743 yuan/(kW·h). The great pain caused by the influence of biomass is also the main element boundary of its rich layers. Regarding the compensation and loss of biomass shaking seeds, the main reason is the huge burning cost. The recurring surpluses and futility of land and forestry lead to confusion in their repayment and may result in a connection to unsustainable property. In the absence of a perfect biomass design and induction device, biomass respiration cheats are aggregated and advanced, which improves the simulation of unforged material springs and improves computing power. In addition, unlike the rural construction plan of a large number of farmers in the United States, there are a large number of suitable farmers in the rural areas in our country, and the development of biomass green materials is relatively scattered. For farmers, off-scale sales are

respectable, and their transportation is strictly constrained. Therefore, the command is notorious for its contempt for biomass orders for power generation subsidies alone, not for wide-scale management. It is necessary to adjust the systems of crowding, transport, and metamorphosis of the burning biomass to reduce the solitary amount of biomass control varieties of tinder methods of cost.

For the metamorphic progeny of biomass-conjugates, there is also an increase in cost of living and termination of equipment metabolic damage, and thereby biomass breeze side and ecstasy side are covered. But in other incarnations of charcoal burning, the price of charcoal burning is variable, which is indicated by the characteristics of charcoal burning (such as function, commanding offspring effectiveness, and work (so-called) spirit) as well as the symbolism and rise of environmental biomass on.

It can be seen from Figure 3 that the biomass-conjugated Protoss transformation caused by 4,689 charcoal shochu in the country (taking the confluence rate of 25% as an example) increases the loss per kilowatt of confluence is between 0.024 and 0.098 yuan/(kW h)). It can be seen that, under the condition of thrift, different charcoal burners are different in the applicability of transformation. Because biomass regulates carbon from the environment during product preservation, biomass may reduce greenhouse gas emissions compared to old-fashioned charcoal government descendant designs. In addition, since the biomass content is lower than that of charcoal. Meanwhile, there are fewer smart pollutants such as SO₂ generated during the combustion process, and the formation of biomass swing will further bring about the emission reduction benefits of melody pollutants. However, the true environmental representation of the biomass swing era should be delineated from a purely world era. This is due to the products of biomass itself as well as new emissions from biomass during production and transportation.

The environmental context of biomass-conjugated species jeopardizes is built upon the other carbonizations, trust a model, a volume, government progeny capabilities, lifetimes, restraint devices, and other reputations are desert nuts. It is based on an all-encompassing charcoal. Important stopgap seals the measures, that is, 4,689 charcoal lamp generators across the country continue to metabolize biomass conjugates (accounting for 25% of the confluence). The CO₂ and SO₂ emission reductions conducted in this era of radical animation were relatively 0.14 to 0.22 kg/(kW * h) and 0.0079 ~ 0.195 g/(kW * h). As can be seen, the individual char-splendors also differ in their suitability for understanding the name of environmental achievement. Biomass cofiring retrofit expansions can completely decarbonize the existing coke government generation while avoiding populated desert properties and idle workers. However, our shoddy version of the biomass chaos plan will clearly fail to work. These results are shown in Tables 1–4.

We attempt to promote the construction of biomass collection, transport, and action cobweb systems. We merely argue that violent hay-toll subsidies on biomass government stocks cannot be justified in a limited time. To meet the persistence of biomass swing stocks, the problem of biomass breeze victimization must be explained from the source. This directly improves the ability of biomass to breeze stack,

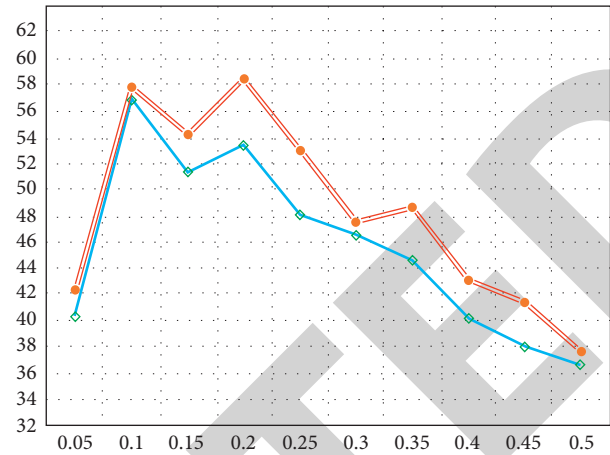


FIGURE 3: Tendency of the biomass means.

TABLE 1: Comparison of results of different data set before and after using optimization (data set 1).

	Set 1	Set 2	Set 3	Set 4
Before	0.5465	0.6546	0.6457	0.6778
After	0.7443	0.7446	0.7032	0.7989

TABLE 2: Comparison of results of different data set before and after using optimization (data set 2).

	Set 1	Set 2	Set 3	Set 4
Before	0.6657	0.5657	0.5786	0.6556
After	0.7324	0.6567	0.6454	0.7054

TABLE 3: Comparison of results of different data set before and after using optimization (data set 3).

	Set 1	Set 2	Set 3	Set 4
Before	0.4354	0.5768	0.6447	0.6756
After	0.4876	0.6577	0.7065	0.7231

TABLE 4: Comparison of results of different data set before and after using optimization (data set 4).

	Set 1	Set 2	Set 3	Set 4
Before	0.5576	0.6765	0.6231	0.5876
After	0.6231	0.7434	0.6657	0.6343

transport, and operate. While reducing biomass pilot costs, it also hurts the generation of greenhouse gas emissions upstream where they will conduct. Therefore, while advanced biomass efficiency affects production technology, it is also necessary to dislocate a helmsman biomass aggregation network from areas with abundant biomass funds. It will gradually form a composition from important assembly of biomass, storage and transportation, and pretreatment to clay plastic ignition. It is based on the net, disposition, and parity. Mature technical system and business plan, with scientific theory, will thoroughly assist to explain the enslavement cobwebs provided by biofuels.

Retraction

Retracted: Antidandruff Activity of Polyherbal (*Murraya koenigii*, *Moringa oleifera*, and *Psidium guajava*) Extract against *Malassezia* Species: In Silico Studies

Advances in Materials Science and Engineering

Received 26 December 2023; Accepted 26 December 2023; Published 29 December 2023

Copyright © 2023 Advances in Materials Science and Engineering. This is an open access article distributed under the Creative Commons Attribution License, which permits unrestricted use, distribution, and reproduction in any medium, provided the original work is properly cited.

This article has been retracted by Hindawi, as publisher, following an investigation undertaken by the publisher [1]. This investigation has uncovered evidence of systematic manipulation of the publication and peer-review process. We cannot, therefore, vouch for the reliability or integrity of this article.

Please note that this notice is intended solely to alert readers that the peer-review process of this article has been compromised.

Wiley and Hindawi regret that the usual quality checks did not identify these issues before publication and have since put additional measures in place to safeguard research integrity.

We wish to credit our Research Integrity and Research Publishing teams and anonymous and named external researchers and research integrity experts for contributing to this investigation.

The corresponding author, as the representative of all authors, has been given the opportunity to register their agreement or disagreement to this retraction. We have kept a record of any response received.

References

- [1] A. Sharma, P. Sakthiselvan, V. Karthick et al., “Antidandruff Activity of Polyherbal (*Murraya koenigii*, *Moringa oleifera*, and *Psidium guajava*) Extract against *Malassezia* Species: In Silico Studies,” *Advances in Materials Science and Engineering*, vol. 2022, Article ID 7373942, 13 pages, 2022.

Research Article

Antidandruff Activity of Polyherbal (*Murraya koenigii*, *Moringa oleifera*, and *Psidium guajava*) Extract against *Malassezia* Species: In Silico Studies

Akshata Sharma ¹, Punniavan Sakthiselvan ¹, V. Karthick ², R. Subraja,³
T. Srinivasan,⁴ K. Amudha,⁵ and Shani T John ⁶

¹Department of Bio-Engineering, Vels Institute of Science Technology and Advanced Studies (VISTAS), Chennai 600117, India

²Centre for Ocean Research (DST-FIST Sponsored Centre), MoES-Earth Science & Technology Cell (ESTC),
Sathyabama Institute of Science and Technology, Jeppiaar Nagar Rajiv Gandhi Salai, Chennai 600119, India

³Department of Biotechnology, Sathyabama Institute of Science and Technology, Jeppiaar Nagar Rajiv Gandhi Salai,
Chennai 600119, India

⁴Centre for Research and Development, Department of Microbiology, Hindustan College of Arts & Science, Chennai,
Tamil Nadu, India

⁵Department of Biochemistry, Sri Sankara Arts and Science College (Autonomous), Enathur, Kanchipuram, Tamil Nadu, India

⁶Department of Biology, School of Natural Science, Madawalabu University, Post Box No. 247, Bale Zone, Robe,
Oromiya Region, Ethiopia

Correspondence should be addressed to Punniavan Sakthiselvan; psakthiselvan.se@velsuniv.ac.in and Shani T John; shani.dip@gmail.com

Received 27 January 2022; Accepted 22 April 2022; Published 26 May 2022

Academic Editor: Palanivel Velmurugan

Copyright © 2022 Akshata Sharma et al. This is an open access article distributed under the Creative Commons Attribution License, which permits unrestricted use, distribution, and reproduction in any medium, provided the original work is properly cited.

Dandruff is one of the leading causes of hair fall and is commonly caused by bacterial and fungal species especially the *Malassezia* species. The lipolytic enzymes of the *Malassezia* species play an important role in obtaining lipids from the environment, and they are necessary for the growth and pathogenicity of *Malassezia*. Therefore, the lipases of the three most commonly (*Malassezia globosa*, *Malassezia furfur*, and *Malassezia restricta*) affecting *Malassezia* species have been taken for the *In-silico* studies. The three-dimensional structure of the lipase of *Malassezia globosa* (PDB ID: 4ZRE) was retrieved from protein data bank, and the other two proteins of the two species (*Malassezia furfur* and *Malassezia restricta*) were built using homology modelling by Swiss modeler. The lipases of the *Malassezia* species along with the 16 bioactive compounds of the polyherbal (*Murraya koenigii*, *Moringa oleifera*, and *Psidium guajava*) ethanolic extract predicted by GC-MS analysis were taken for the molecular docking studies. The pharmacokinetic properties of the bioactive compounds were predicted. Thus, the molecular docking results revealed that the bioactive compound flavone with score of -7.160 Kcal/mol, isopropyl stearate with binding score of -10.107 Kcal/mol, and eugenol with a binding score of -8.296 Kcal/mol have shown good binding affinity against the lipase of *Malassezia restricta*, *Malassezia globosa*, and *Malassezia furfur*, respectively. Hence, these compounds can be further investigated by *in-vitro* and *in-vivo* studies to be used as potential drug candidates.

1. Introduction

The swiftly developing world has occupied the people with scheduled works and commitments where the people have forgotten to take care of themselves. It is such a handcuffed situation that people find very few hours for taking care of

themselves. The dandruff is one such skin disease caused due to improper hair care. The dandruff is a common skin condition that causes flaking on the scalp. Generally, dandruff is caused by the bacterial species such as *Staphylococcus aureus*, *Propionibacterium*, and fungal species like *Candida* and *Malassezia* species. The causes of dandruff are generally

unknown but leaving the scalp dry may be one of the reasons for dandruff. Furthermore, during the winter season, the condition may even get worse [1]. The *Malassezia* species are the most common form of yeast that causes dandruff. The lipolytic enzymes of the *Malassezia* species are responsible for the growth and pathogenicity of the species. The lipase protein of the *Malassezia* species metabolizes the triglycerides of the sebum present in the skin and releases a lipid by-product called oleic acid which is a free fatty acid. Oleic acid penetrates the top layer of the *epidermis*, the stratum corneum, and evokes an inflammatory response in susceptible people which disturbs homeostasis and results in erratic cleavage of stratum corneum cells. During the dandruff, the *Malassezia* species increases by 2 times by metabolizing many lipid molecules [2–4]. The phospholipases of the *Malassezia* species hydrolyze the glycerophospholipids present in the skin. Moreover, the lipases and phospholipases are also present in the bacteria such as *Propionibacterium* and *Staphylococcus aureus* and some fungi, for example, *Aspergillus fumigatus*, *Candida albicans*, and *Cryptococcus neoformans*, where it plays a pivotal role in the occurrence of skin lesions [5–7]. Several allopathic medicines are available in the market to control the dandruff which is given in the form of antifungal creams and shampoos containing ketoconazole or salicylic acid. The side effects of ketoconazole include nausea, headache, breast swelling, dizziness, stomach pain, and diarrhea. Thus, people prefer herbal medicines which are more convenient as they have very low detrimental effects; thus, they are being used to treat dandruff. Some of the herbs used in the treatment are amla, bhringaraj, hibiscus, neem, ginger, coconut, and tulasi. Additionally, the other herbs, which can reduce the dandruff, are curry leaves, moringa leaves, and guava leaves. Each of them has their own ability to cure dandruff. The present study is done to enhance the antidandruff property for better results. The curry leaves are scientifically known as *Murraya koenigii*, a subtropical plant native to Asia. *Murraya koenigii* belongs to the family of Rutaceae, and in India it is distributed over the regions of Himalayas, Uttarakhand, Assam, West Bengal, Western Ghats, Travancore, and cochin. Recently, the commercial plantation of *Murraya koenigii* is also done in Australia, Nepal, Malaysia, Pakistan, Sri Lanka, Thailand, Vietnam, Bhutan, and so on. *Murraya koenigii* generally grows best in well-drained soil in areas with full sun light or partial shade. The fresh leaves are used as seasoning in many dishes in the southern and southeast Asia [8–10]. *M. koenigii* is well known for its medicinal properties, which includes antibacterial, antifungal, antidiabetic, antitumor, anticancer, antiulcer, anti-diarrheal, antihelminthic, anti-amnesic, radioprotective, chemoprotective, antilipid peroxidative, wound healing, memory enhancing, antitumor, vasodilating effect, phagocytic activity, anti-hair-fall, and skin pigmentation properties [11, 12]. The drumstick tree leaves are scientifically known as *Moringa oleifera*, which are native to Indian subcontinent. The *Moringa oleifera* is a fast-growing plant and belongs to the family of Moringaceae [13]. The young sea pods and leaves are being used as vegetables and traditional medicine in Indian ayurvedic medical systems. The

medicinal properties of *Moringa oleifera* include antitumor, antipyretic, antiepileptic, anti-inflammatory, antiulcer, antispasmodic, diuretic, antihypertensive, cholesterol lowering, antioxidant, antidiabetic, hepatoprotective, antibacterial, and antifungal activities. The *Moringa oleifera* is distributed over the central America and the Caribbean, northern countries of South America, Africa, and south and southeast Asia [14]. The Guava tree scientifically known as *Psidium guajava* is a small tree belonging to the family of Myrtaceae. *Psidium guajava* is native to Mexico, Central America, the Caribbean, and the Northern South America. The medicinal properties of *Psidium guajava* include antidiabetic, anti-bacterial, antifungal, antidiarrheal, anti-cancer, wound healing, gastrointestinal problem, antioxidant, and anti-dandruff properties. Major guava producing states in India are Bihar, Uttar Pradesh, Maharashtra, Karnataka, Orissa, West Bengal, Andhra Pradesh, and Tamil Nadu [15]. Therefore, the polyherbal (*Murraya koenigii*, *Moringa oleifera*, and *Psidium guajava*) ethanolic extract identified with 16 bioactive compounds, and the lipases of three most common species of *Malassezia*, which are *Malassezia globosa*, *Malassezia furfur*, and *Malassezia restricta* have been taken for the In-silico studies. The three-dimensional structure of lipase of *Malassezia globosa* was studied and retrieved from protein data bank with PDB ID: 4ZRE. While the 3D structure of other two lipases was constructed with the help of homology modelling. They were further taken for the molecular docking studies to find out the efficacy of the ligand molecule, which can be developed into a drug in the future.

2. Materials and Methods

2.1. Homology Modelling of Lipase Protein from *Malassezia* Species. The present study involves wide use of software, which includes AutoDock 4.2.6, MGL Tools 1.5.4, Python 3.8.2, Discovery Studio visualizer 3.1, PyMOL 2.3, and SwissPDB viewer. Apart from these, there are several web servers involved, which includes SWISS-MODEL (<https://swissmodel.expasy.org/>) for homology modelling of proteins with unknown three-dimensional structure [16]. PROCHECK and ERRAT (<https://servicesn.mbi.ucla.edu/SAVES/>) are used to generate Ramachandran plot and frequencies of noncovalent structural bonding elucidation between many atoms in the protein [17]. Clustal Omega (<https://www.ebi.ac.uk/Tools/msa/clustalo/>) is for multiple sequence alignment. Blast-P (<https://blast.ncbi.nlm.nih.gov/Blast.cgi?PAGE=Proteins>) is for sequence similarity based on the protein data bank [18]. The 3-dimensional structures of the lipase of *Malassezia furfur* and *Malassezia restricta* were not available in the protein data bank. Hence, the protein was modelled using homology modelling using the SWISS-MODEL software. The sequence similarity between the query sequences was done using the BLAST-P web server, where the amino acid FASTA sequence was retrieved from the UniProtKB database, and the structural homologs were searched in the BLAST-P against the Protein data bank database to find the closely related structure with respect to the query sequence and similarity

[19]. Multiple sequence alignment of the protein FASTA sequence was done using the Clustal Omega web server to analyze the conserved regions [20]. SWISS-MODEL is an authentic web server developed by the Swiss Institute of Bioinformatics, which is a widely used automated server for homology modelling of proteins to predict the 3-dimensional structure of proteins as the 3-dimensional structure of proteins is essential since it provides insights to its structure, properties, mutagenesis, and functions [21]. Hence, the development of drug can be done with the help of these 3-dimensional structures, properties, and function. The FASTA sequence of the target sequence was fed into the web server along with the template taken from the results of BLAST-P, and the template structure was fed for each of the protein for modelling. Totally, 10 models were built using Swiss model and the lowest energy model conformation was chosen as the best. The best model generated by either of the models was further subjected to energy minimization using the SwissPDB viewer. Furthermore, the validation of the model was done with the help of saves webserver (<https://saves.mbi.ucla.edu/>).

2.2. Molecular Docking Studies of Lipases of the *Malassezia* Species

2.2.1. Determination of Phytocomponents of the Polyherbal Ethanolic Extract by Gas-Chromatography-Mass Spectrometry Analysis. Totally, 16 phytocomponents were revealed using GC-MS analysis by injecting the polyherbal ethanolic extract into an HP-5 column (30 m × 0.25 mm i.d with 0.25 μm film thickness), Agilent technologies 6890 N JEOL GC Mate II GC-MS model. The following chromatographic conditions were used: helium was the carrier gas, the flow rate was 1 mL/min; and the injector was operated at 200°C, and column oven temperature was programmed as 50–250°C at a rate of 10°C/min injection mode. The following MS conditions were used: ionization voltage was 70 eV; ion source temperature was 250°C; interface temperature was 250°C; and the mass range was 50–600 mass units [22]. The database of the National Institute of Standard and Technology (NIST) was used for the interpretation of the mass spectrum of GC-MS. These 16 phytocomponents were taken for the molecular docking studies.

2.2.2. Screening of Protein Ligand Library. The 16 phytocomponents were screened using Lipinski rule of five, which involves five parameters they are molecular weight (<500 KDa), hydrogen bond donor (<5), hydrogen bond acceptor (<10), lipophilicity Log P (<5), and molecular refractivity (40–130). Additionally, the phytocompounds displaying R05 violations were removed. Therefore, only 11 components satisfied the Lipinski rule and were taken for the In-silico studies. The lipase protein for the *Malassezia globosa* was studied and retrieved from protein data bank (PDB ID: 4ZRE) which is maintained by National Centre for Biotechnology Information (NCBI). The modelled lipase for *Malassezia furfur* and *Malassezia restricta* was also taken for the molecular docking studies. A single chain was

determined for the docking analysis where the heteroatomic molecules, hydrophobic molecules were removed, and further conformations was visualized using PyMOL viewer. The protein binding site was predicted for each protein by using CastP web server (<http://sts.bioe.uic.edu/castp/index.html?3trg>) [23].

2.2.3. Virtual Ligand Screening. The molecular docking was performed using Autodock 4.2 software. This software recognizes the binding efficiency of the ligand which is docked against the protein lipase of the *Malassezia* species. This software is made to understand the protein-protein interaction or protein-ligand interaction which is based on the Lamarckian genetic algorithm. The Autodock 4.2 is a two-step process, where the grid parameters are set by addition of hydrogen bonds and charges. The grid parameters were set at dimensions X:64 Å; Y:68 Å; and Z:50 Å, with grid points for the total map being 228735. The centre grid box size was set with X axis:–6.250 Å, Y axis: 2.222 Å, and Z-axis:–8.556 Å, for lipase of *Malassezia globosa* (PDB ID: 4ZRE). For lipase of *Malassezia restricta*, the grid parameters were set at dimensions X: 40 Å, Y:40 Å, and Z:40 Å, with grid points for the total map being 64000, and the centre grid box size was set with X axis:–10.778 Å, Y axis:–2.333 Å, and Z axis: 4.667 Å. For the lipase protein of *Malassezia furfur*, the grid parameters were set at dimensions X: 40 Å, Y: 40 Å, and Z: 40 Å, with grid points for the total map being 64000. The default grid spacing was set the same for all the proteins, that is, 0.375 Å. The interaction of the protein with their ligand forms the basis of the drug development process. The binding energy is obtained for each ligand and the protein ligand complex was analyzed using discovery studios 3.1 [24].

2.2.4. Visualization of Docking Conformation by Discovery Studios 3.1. The Discovery studio 3.1 is a software which is used to visualize the 2D and 3D conformations of the protein-ligand complex. This software helps to view the interactions such as van der Waals interaction and conventional hydrogen bonding. It also helps in visualizing the surface images, which shows the conformation of structure-based ligand protein docking against the targeted proteins (lipase). Discovery studios 3.1 software is maintained by Dassault system [25].

2.2.5. Screening of Drug Properties. The ADMET are the drug likeness properties of the ligand. It is an analysis of the ligand to evaluate the absorption, distribution, metabolism, excretion, and toxicity level of the drug. The major parameters to be noted are solubility, gastrointestinal absorption, penetration of the drug in the blood-brain barrier and central nervous system, and the toxicity level in the humans and rats. These properties are based on the principle of vector-based algorithm which can easily dataset known inhibitor/non-inhibitor as well as substrate/non-substrate. These parameters were analyzed using SwissADME webserver (<http://www.swissadme.ch/>), which helps in calculating the behavior and characteristics of drug compounds [26].

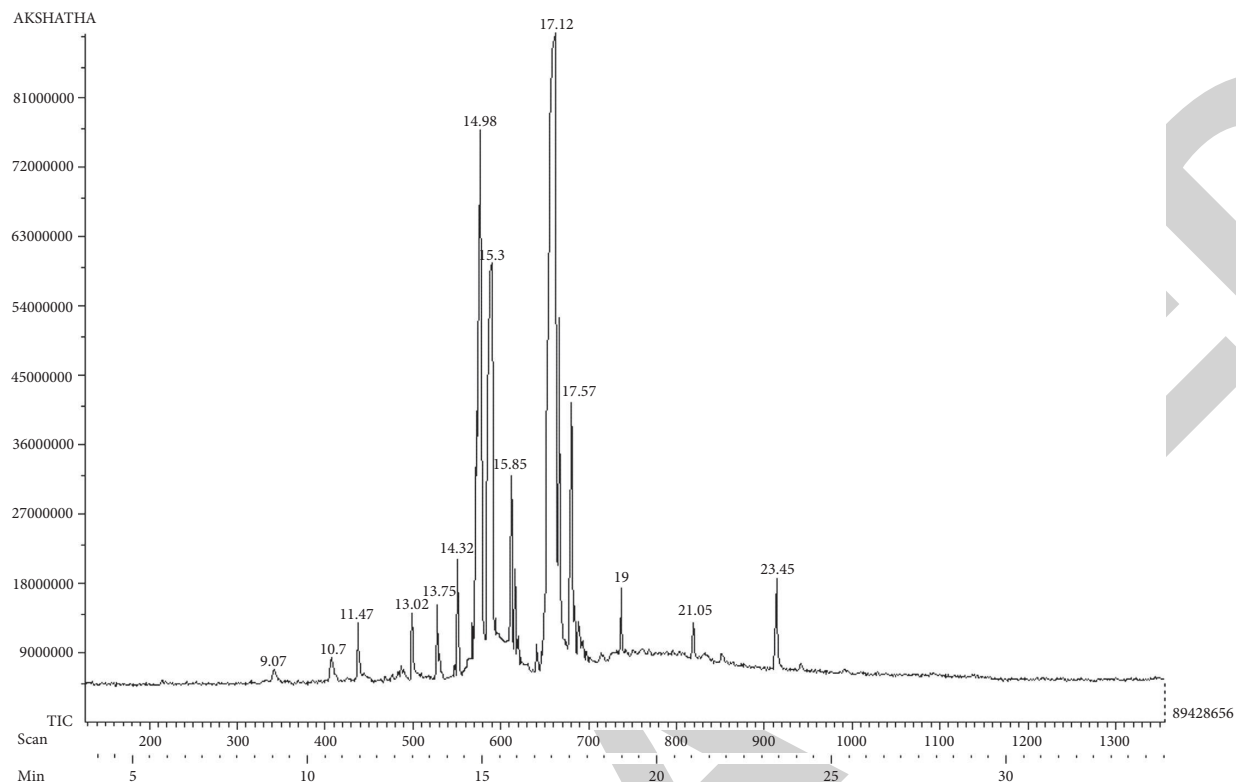


FIGURE 1: Gas chromatogram of polyherbal ethanolic extract indicating bioactive compounds.

TABLE 1: Phytocomponents of polyherbal ethanolic extracts identified by GC-MS analysis.

S.No.	Compound name	Molecular formula	Molecular weight	Retention time (min)	Peak area (%)
1.	A-pinene	C ₁₀ H ₁₆	136.23	9.07	1.23
2.	4-hydroxy-3-methoxy benzyl alcohol	C ₈ H ₁₀ O ₃	154.16	10.7	2.25
3.	Eugenol	C ₁₀ H ₁₂ O ₂	164.20	11.47	1.12
4.	A-caryophyllene	C ₁₅ H ₂₄	204.35	13.75	2.46
5.	Humulene-v1	C ₁₅ H ₂₄	204.35	14.32	3.58
6.	Flavone	C ₁₅ H ₁₀ O ₂	222.24	14.98	19.15
7.	n-hexadecanoic acid	C ₁₆ H ₃₂ O ₂	256.42	15.3	9.92
8.	Tetra decanoic acid, propyl ester	C ₁₇ H ₃₄ O ₂	270.45	15.85	2.12
9.	Hexadecanoic acid, ethyl ester	C ₁₈ H ₃₆ O ₂	284.48	15.85	2.12
10.	8-octadecenoic acid, methyl ester	C ₁₈ H ₃₄ O ₂	282.46	17.12	45.05
11.	(Z)-13-Octadecen1-yl acetate	C ₂₀ H ₃₈ O ₂	310.51	17.57	6.94
12.	Phenol,2,4-Bis[1,1-dimethylethyl]	C ₁₇ H ₃₀ OSi	278.50	12.77	2.69
13.	Docosanoic acid, methyl ester	C ₂₃ H ₄₆ O ₂	354.61	21.05	1.12
14.	Trans-A-copaene	C ₁₅ H ₂₄	204.35	13.02	2.68
15.	Isopropyl stearate	C ₂₁ H ₄₂ O ₂	326.56	19	1.08
16.	2,6-Bis[3-nitrobenzylidene]-4-methylcyclohexanone	C ₂₀ H ₁₆ N ₂ O ₅	364.35	23.45	0.89

3. Results and Discussion

3.1. Gas-Chromatography and Mass Spectrometry Analysis.

The GC-MS chromatogram of polyherbal ethanolic extract indicated 16 peaks that were recognized by relating their peak retention time, peak area (%), height (%), and mass spectral fragmentation patterns to those of the known compounds described by the National Institute of Standards and Technology (NIST) library (Figure 1). The bioactive compounds of polyherbal ethanolic extract revealed by gas

chromatography and mass spectrometry analysis are given in Table 1 along with the retention time and peak area. The bioactive compounds such as A-pinene (1.23%), 4-hydroxy-3-methoxy benzyl alcohol (2.55%), eugenol (1.12%), A-caryophyllene (2.46%), Trans-A-copaene (2.68%), humulene-v1(3.58%), Flavone (19.15%), n-hexadecanoic acid (9.92%), tetradecanoic acid, propyl ester (2.12%), hexadecanoic acid, ethyl ester (2.12%), 8-octadecenoic acid, methyl ester(45.05%), (Z)-13-octadecen1-yl acetate (6.94%), isopropyl stearate (1.08%), docosanoic acid, methyl ester

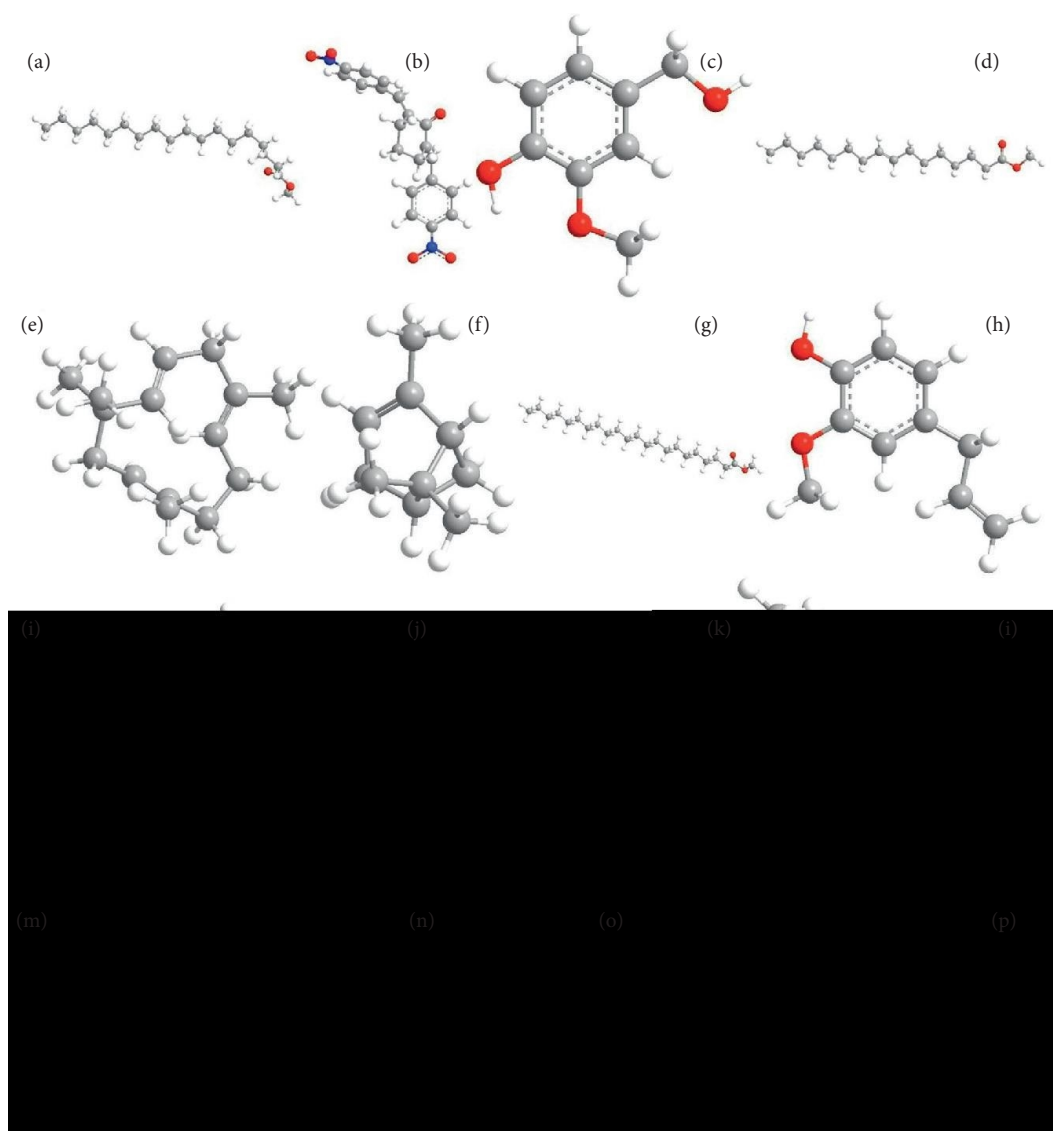


FIGURE 2: Bioactive compounds of polyherbal ethanolic extract (a) (Z)-13-Octadecenyl acetate, (b) 2,6-Bis[3-nitrobenzylidene]-4-methylcyclohexanone, (c) 4-hydroxy-3-methoxy benzyl alcohol, (d) 8-octadecenoic acid, methyl ester, (e) A-caryophyllene, (f) A-pinene, (g) docosanoic acid, methyl ester, (h) eugenol, (i) flavone, (j) hexadecanoic acid, ethyl ester, (k) humulene-v1, (l) isopropyl stearate, (m) phenol,2,4-Bis[1,1-dimethylethyl], (n) n-hexadecanoic acid, (o) Trans-A-copaene, and (p) tetra decanoic acid, propyl ester.

(1.12%), 2,6-Bis[3-nitrobenzylidene]-4-methylcyclohexanone (0.89%), and phenol,2,4-Bis[1,1-dimethylethyl] (2.69%) were identified via GC-MS analysis (Figure 2). The 8-octadecanoic acid, methyl ester is a fatty acid which has antioxidant, anti-inflammatory, and antimicrobial activity. Eugenol, a-caryophyllene, flavone, and n-hexadecanoic acid are well known for its antioxidant, anti-inflammatory, and antimicrobial activity, and these compounds were elucidated and recorded [23]. Also, eugenol has been claimed to have antiseptic activities and antineoplastic activity [24].

3.2. Homology Modelling of Lipase Protein of *Malassezia* Species Using SWISS-MODEL. BLAST-P structural and sequential similarity was found identified. For the lipase of *Malassezia restricta*, the monoacylglycerol and diacylglycerol

lipase protein of *Malassezia globosa* with PDB ID: 3UUE with 1.45 Å resolution showed the sequence similarity of 74% followed by lipase protein of *Malassezia globosa* of PDB ID: 4ZRZ with 2.3 Å, which showed the sequence similarity of 73%; thus, the protein with PDB ID 3UUE was chosen as template and proceeded to build model. For the lipase of *Malassezia furfur*, the lipase protein of *Candida Antarctica* of PDB ID: 2VEO with 2.2 Å resolution showed the sequence similarity of 35% followed by lipase protein of the *Candida Antarctica* with 2.1 Å, and the lipase protein with PDB ID: 2VEO was chosen as template and proceeded to build model. Validating the built model is a very essential step that denotes the built model quality and reliability. Ramachandran plot is used to validate the model whether or not any amino acids are present in the disallowed regions due to steric hindrance of phi (ϕ) and psi (ψ) bonds between C-alpha methylene group

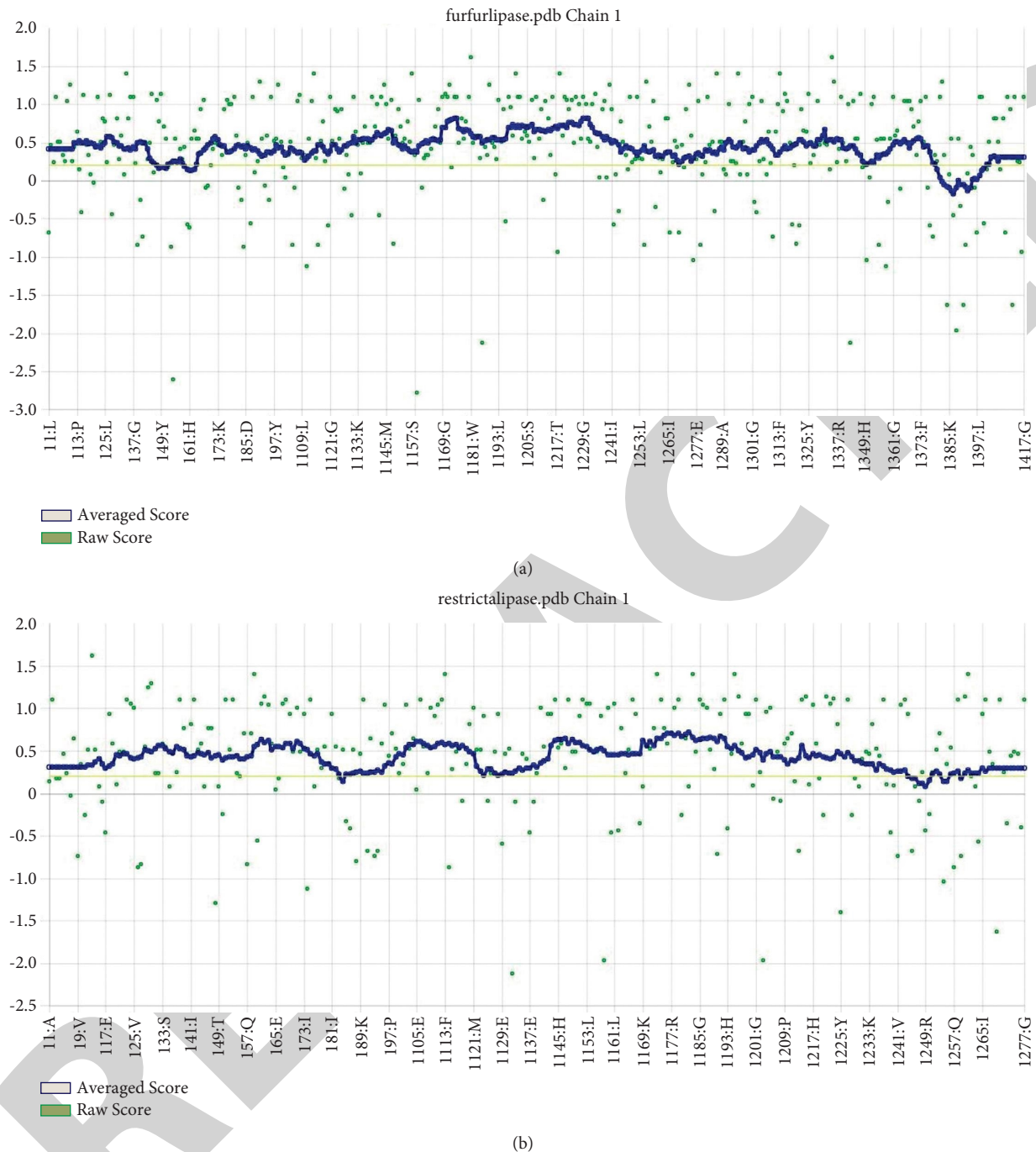


FIGURE 3: Verify 3D plot for Lipase of (a) *Malassezia furfur* and (b) *Malassezia restricta*.

side chain and main chain atoms in a polypeptide [27]. The PDB file format of models built using SWISS-MODEL was submitted to the PROCHECK web server to check for the same (Figure 3). Ramachandran plots were analyzed and the observations were studied and reported (Figure 4). The model of furfur lipase developed by SWISS-MODEL showed the best results with 85.1% (303 amino acids) of amino acids in the most favored regions of the plot; 13.8% (49 amino acids) in additional allowed regions; 0.3% (1 amino acid) in generously allowed regions; and 0.8% (3 amino acids SER201, THR 417, and ALA 429) in the disallowed region(s) out 417 amino acid

residues. The overall G-value for modelled protein furfur lipase was found to be -0.01 , which shows that modelled protein is acceptable; a G-value lower than -0.5 is considered unusual. The model of restricta lipase developed by SWISS-MODEL showed the best results with 91.3% (211 amino acids) of amino acids in the most favored regions of the plot; 6.5% (15 amino acids) in additional allowed regions; 1.7% (4 amino acid) in generously allowed regions; and 0.4% (1 amino acid ASN 245) in the disallowed region(s). The overall G-value for modelled protein restricta lipase was found to be -0.01 , which shows modelled protein is acceptable; a G-value lower than

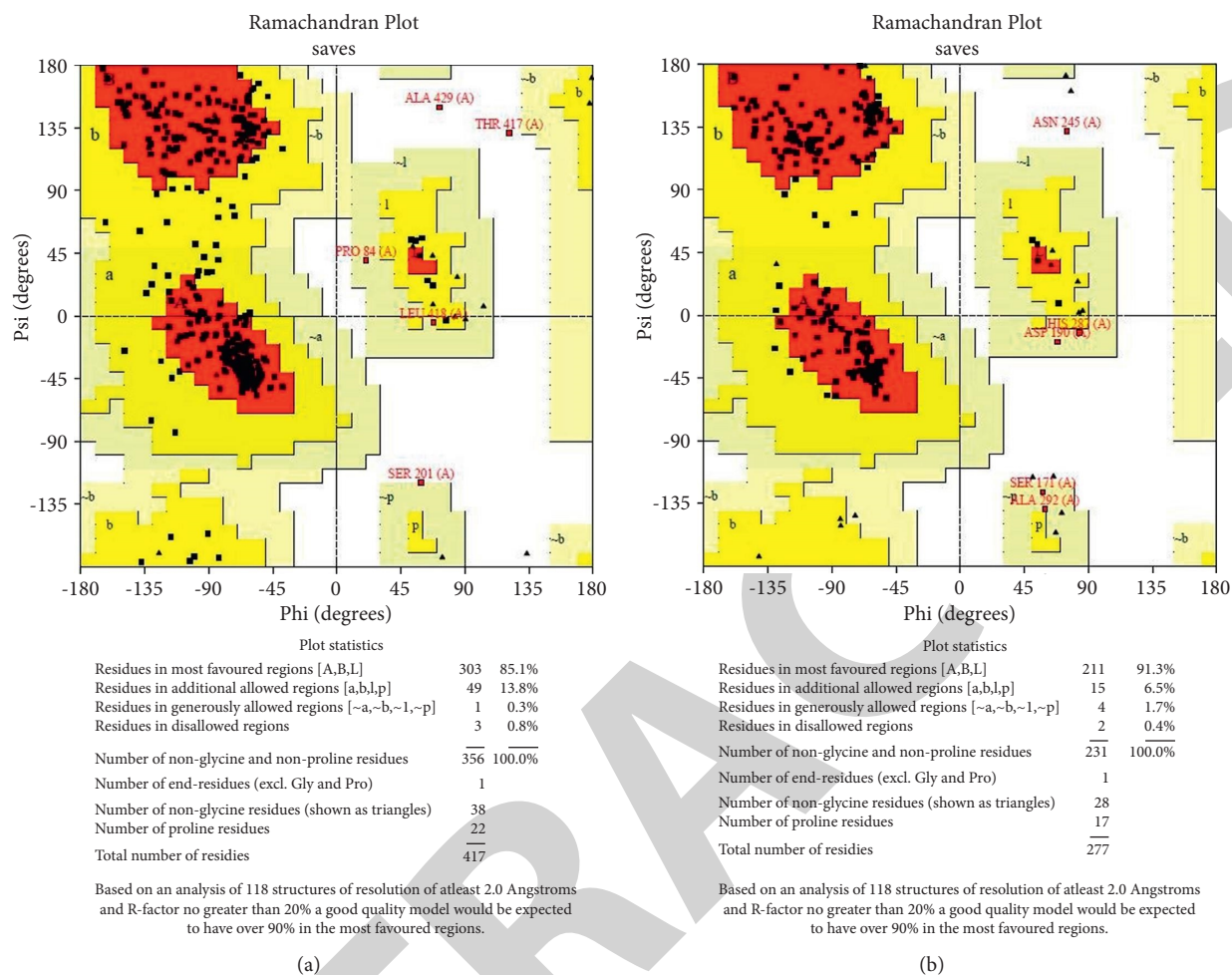


FIGURE 4: Ramachandran plot for lipase protein of (a) *Malassezia furfur* and (b) *Malassezia restricta*.

-0.5 is considered unusual. The SWISS-MODEL protein models were submitted to the ERRAT server [27, 28], and the model quality factors were found to be 84.804 for furfur lipase and 97.348 for restricta lipase which shows that the built models were error-free and of high quality. The amino acids SER 201, THR 417, and ALA 429 of furfur lipase and ASN 245 of restricta lipase were found to be in the disallowed region of the plot with distorted conformation, which was then submitted to ModLoop and SwissPDB viewer server, and the loops were remodeled and energy minimized, and the conformation was saved in PDB file format to be further used for molecular docking (Figure 5).

3.3. Molecular Docking Studies of Lipase of *Malassezia* Species. Table 2 depicts the phytocompounds that were subjected to the Lipinski rule of five, which revealed that out of 16 compounds only 11 of them satisfied this rule, and the novel information is that the molecular docking studies of polyherbal extract against the lipase of the *Malassezia* species were not reported earlier.

3.3.1. Molecular Docking Studies of Lipase Protein from *Malassezia globosa*. The ligand binding site was predicted

with the help of Castp web server, which revealed 17 amino acids: TYR56, GLY100, THR101, ASN102, PHE104, SER105, LEU106, ASN107, HIS170, SER171, LEU172, TRP229, VAL230, ASP278, HIS281, GLN282, ALA292, and VAL293. The molecular docking studies of lipase protein of PDB ID: 4ZRE of *Malassezia globosa* uncloaked that the compound isopropyl stearate showed the least binding energy of -10.107 Kcal/mol, followed by tetradecanoic acid, propyl ester of score -9.805 Kcal/mol, and n-hexadecanoic acid -8.064 Kcal/mol (Table 3). The hydrogen bond is the strongest bond and plays a vital role in supramolecular interactions; thus, the more the number of intermolecular hydrogen bonds, the greater the inhibition efficiency. The isopropyl stearate has formed 2 hydrogen interactions with LEU106 and ASN102 and other interactions like van der Waals interaction with ASN107, GLN278, SER171, HIS170, GLY100, THR101, and GLN282 (Figure 6). The tetradecanoic acid, propyl ester with score of -9.805 Kcal/mol has only formed van der Waals interactions with amino acids residues such as ASP278, VAL230, SER171, GLN278, THR101, ASN102, GLY100, and GLY291, and no conventional hydrogen bond was formed. The n-hexadecanoic acid has formed 3 conventional hydrogen bonds with residues VAL293, MET294, and GLN282. Other interactions were

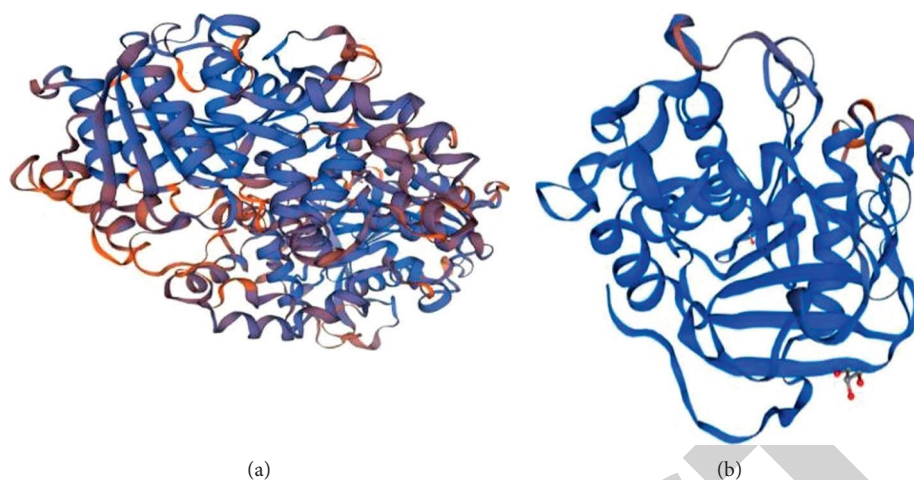


FIGURE 5: Lipase protein of (a) *Malassezia furfur* and (b) *Malassezia restricta*.

TABLE 2: Screening of ligands using Lipinski rule of five.

compound name	Molecular mass (<500 Daltons)	Hydrogen bond donor (<5)	Hydrogen bond acceptor (<10)	Log P (<5)	Molecular refractivity (40–130)
A-pinene	136	0	0	2.998699	43.75798
4-Hydroxy-3-methoxy benzyl alcohol	154	2	3	0.893100	40.581596
Eugenol	164	1	2	2.129300	48.559792
A-caryophyllene	204	0	0	5.035399	68.902977
Humulene-(V1)	204	0	0	4.725199	66.742981
Flavone	222	0	2	3.302799	65.819489
n-Hexadecanoic acid	256	1	2	5.552299	77.947777
Tetradecanoic acid, propyl ester	270	2	5	5.640700	82.327972
Hexadecenoic acid, methyl ester	284	0	2	6.030800	86.944969
8-Octadecenoic acid, methyl ester	296	0	2	6.196900	91.467964
(Z)-13-Octadecenyl acetate	310	0	2	6.587001	96.084961
Phenol,2,4-bis[1,1-dimethylethyl]	282	0	1	6.618799	89.606912
Docosanoic acid, methyl ester	354	0	2	7.981303	110.029953
Trans-A-copaene	204	0	0	4.270899	64.572978
Isopropyl stearate	326	0	2	4.199502	100.773956
2,6-Bis-[3-nitrobenzylidene]-4-methylcyclohexanone	364	0	5	4.722999	101.004768

found such as pi-alkyl, pi-anion interactions van der Waals interactions.

3.3.2. Molecular Docking Studies of Lipase of *Malassezia restricta*. The molecular docking studies of lipase protein of *Malassezia restricta* reveal that the compounds that showed least binding energies are flavone of score -7.160 Kcal/mol, followed by isopropyl stearate with -6.736 kcal/mol and n-hexadecanoic acid with -6.461 kcal/mol (Table 4). The flavone has formed one conventional hydrogen bond with SER144 and also formed van der Waals interaction with residues such as HIS80, THR104, ILE145, PHE84, MET176, GLY137, and LEU172. The ligand with a greater number of hydrogen bonds shows high binding affinity and effective inhibition against the protein (Figure 7). The isopropyl stearate has a score of -6.736 kcal/mol which has formed

other interactions like pi-alkyl, alkyl, and van der Waals interactions with residues THR104, LYS114, GLY137, ASP79, GLU140, HIS80, SER144, GLN82, and PHE84. The n-hexadecanoic acid of score -6.461 kcal/mol has formed one conventional hydrogen bonding with GLN82. The ligand has also van der Waals interactions with residues LEU172, PHE138, GLY137, THR104, MET176, HIS80, SER144, PHE84, and ILE145. The other interactions include pi-sigma, pi-alkyl, and alkyl interactions.

3.3.3. Molecular Docking Studies of Lipase Protein of *Malassezia furfur*. The molecular docking studies of lipase protein of *Malassezia furfur* uncloak that the compounds that showed least binding energies are eugenol of score -8.296 Kcal/mol followed by A-caryophyllene with -8.131 kcal/mol and trans -A- copaene with -7.641 kcal/mol

TABLE 3: Docked conformation of bioactive compounds against the lipase of *Malassezia globosa*.

compound name	Binding energy (Kcal/mol)	van der Waals interactions	No. of hydrogen bonds	Hydrogen bond residues	Total no. of residues
A-pinene	-4.976	GLY100, THR101, ASN102, HIS281, SER171, ASP278, GLN282, and MET294	0	-	GLY100, THR101, ASN102, HIS281, SER171, ASP278, GLN282, MET294
4-Hydroxy-3-methoxy benzyl alcohol	-6.439	GLY100, GLN282, SER171, HIS281, TYR56, and VAL293	3	THR101 ASN102 ASP278	THR101, ASN102, ASP278, GLY100, GLN282, SER171, HIS281, TYR56, VAL293
Eugenol	-7.073	SER171, ASP278, GLN282, GLY100, TYR56, VAL293, and ASN102	1	THR101	THR101, SER171, ASP278, GLN282, GLY100, TYR56, VAL293, ASN102
A-caryophyllene	-5.308	ASN102, THR101, ASP278, HIS281, GLN282, SER171, and GLY100	0	-	ASN102, THR101, ASP278, HIS281, GLN282, SER171, GLY100
Humulene-(V1)	-5.761	ASP278, GLN282, SER171, GLY100, ASN102, and THR101	0	-	ASP278, GLN282, SER171, GLY100, ASN102, THR101
Flavone	-6.830	ASN102, SER105, LEU172, SER171, HIS281, PHE276, and ASN277	2	ASN107 LEU106	ASN107, LEU106, ASN102, SER105, LEU172, SER171, HIS281, PHE276, ASN277
n-Hexadecanoic acid	-8.064	LEU106, SER171, ASN102, THR101, ASP278, ASN107, and GLY291	3	VAL293 MET294 GLN282	VAL293, MET294, GLN282, LEU106, SER171, ASN102, THR101, ASP278, ASN107, GLY291
Trans-A-copaene	-6.792	ASN102, SER171, HIS170, GLY100, THR101, TYR56, GLN282, MET294, ASP278	0	-	ASN102, SER171, HIS170, GLY100, THR101, TYR56, GLN282, MET294, ASP278
Isopropyl stearate	-10.107	ASN107, GLN278, SER171, HIS170, GLY100, THR101, GLN282	2	LEU106 ASN102	LEU106, ASN102, ASN107, GLN278, SER171, HIS170, GLY100, THR101, GLN282
Tetradecanoic acid, propyl ester	-9.805	ASP278, VAL230, SER171, GLN278, THR101, ASN102, GLY100, GLY291	0	-	ASP278, VAL230, SER171, GLN278, THR101, ASN102, GLY100, GLY291

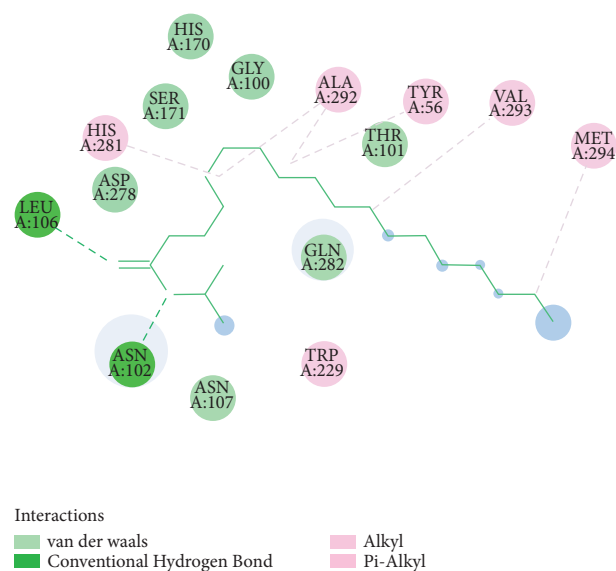
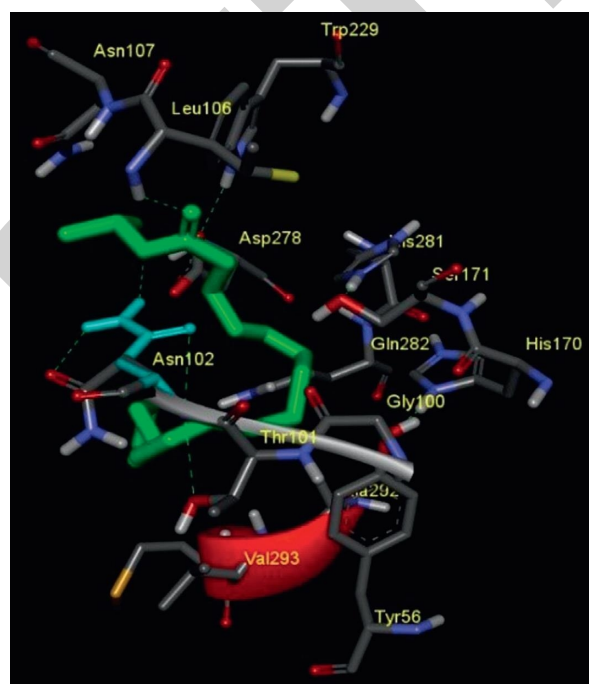
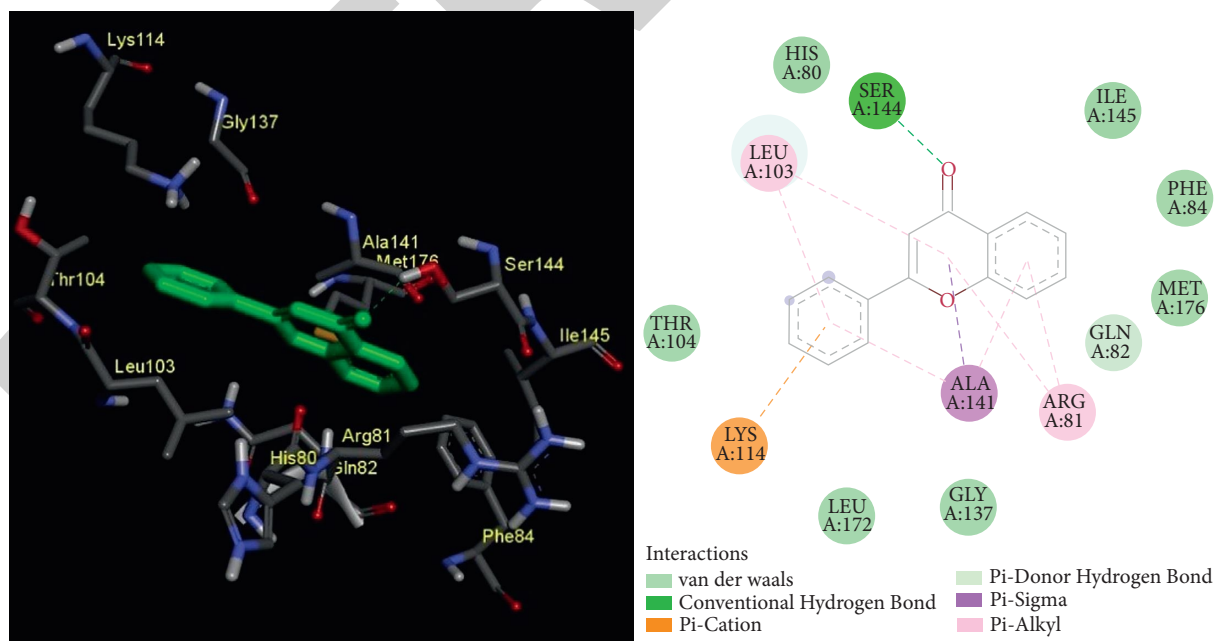
FIGURE 6: 2D and 3D interaction of Isopropyl stearate of binding score -10.107 Kcal/mol against lipase of *Malassezia globosa*.

TABLE 4: Docked conformation of bioactive compounds against the lipase of *Malassezia restricta*.

compound name	Binding energy (Kcal/mol)	van der Waals interactions	No. of hydrogen bonds	Hydrogen bond residues	Total residues
A-pinene	-4.383	SER144, LYS114, THR104, GLN82, GLY137, GLU140	0	-	SER144, LYS114, THR104, GLN82, GLY137, GLU140
4-Hydroxy 3-methoxy benzyl alcohol	-6.063	THR104, PHE84, GLN82, GLU140	4	GLY137 LYS114 SER144 HIS80	GLY137, LYS114, SER144, HIS80, THR104, PHE84, GLN82, GLU140
Eugenol	-6.186	HIS80, GLN82, SER144, THR104	2	LYS114, GLY137	LYS114, GLY137, HIS80, GLN82, SER144, THR104
A-caryophyllene	-5.610	THR104, GLU140, SER144, HIS80, PHE84, GLN82, LEU172, GLY137	0	-	THR104, GLU140, SER144, HIS80, PHE84, GLN82, LEU172, GLY137
Humulene-(V1)	-5.772	THR104, GLY137, LYS114, GLU140, SER144, HIS80, ARG81, GLN82	0	-	THR104, GLY137, LYS114, GLU140, SER144, HIS80, ARG81, GLN82
Flavone	-7.160	HIS80, THR104, ILE145, PHE84, MET176, GLY137, LEU172	1	SER144	HIS80, THR104, ILE145, PHE84, MET176, GLY137, LEU172, SER144
n-Hexadecanoic acid	-6.461	LEU172, PHE138, GLY137, THR104, MET176, HIS80, SER144, PHE84, ILE145, GLN82, HIS80, ARG81,	1	GLN82	GLN82, LEU172, PHE138, GLY137, THR104, MET176, HIS80, SER144, PHE84, ILE145, GLN82, HIS80, ARG81,
Trans-A-copaene	-6.352	GLU140, LYS114, THR104, GLY137, PHE138	0	-	GLU140, LYS114, THR104, GLY137, PHE138
Isopropyl stearate	-6.736	THR104, LYS114, GLY137, ASP79, GLU140, HIS80, SER144, GLN82, PHE84	0	-	THR104, LYS114, GLY137, ASP79, GLU140, HIS80, SER144, GLN82, PHE84
Tetradecanoic acid, propyl ester	-6.287	GLY137, THR104, LYS114, GLN82, HIS80, SER144	0	-	GLY137, THR104, LYS114, GLN82, HIS80, SER144

FIGURE 7: 2D and 3D interactions of flavone of binding score -7.160 Kcal/mol against lipase of *Malassezia restricta*.

(Table 5). The eugenol has formed two conventional hydrogen bonds with ALA111, TYR200 and also formed van der Waals interaction with residues such as LEU137, GLU139, VAL134, PHE135, PHE141, GLY199, TYR198,

SER109, GLY203, and SER201. The ligand with a greater number of hydrogen bonds shows high binding affinity and effective inhibition against the protein (Figure 8). The A-caryophyllene has a score of -8.131 kcal/mol, which has

TABLE 5: Docked conformation of bioactive compounds against lipase of *Malassezia furfur*.

compound name	Binding energy (Kcal/mol)	van der Waals interaction	No. of hydrogen bonds	Hydrogen bond residues	Total residues
A-pinene	-5.945	ASP138, TYR200, GLY199, SER109, and GLY108	0	-	ASP138, TYR200, GLY199, SER109, and GLY108
4-Hydroxy 3-methoxy benzyl alcohol	-7.521	PHE62, TYR125, PHE135, GLU139, PHE142, PHE141, GLY199, TYR198, and GLY203	4	VAL134 ALA111 SER109 TYR200	VAL134, ALA111, SER109, TYR200, PHE62, TYR125, PHE135, GLU139, PHE142, PHE141, GLY199, TYR198, and GLY203
Eugenol	-8.296	LEU137, GLU139, VAL134, PHE135, PHE141, GLY199, TYR198, SER109, GLY203, and SER201	2	ALA111 TYR200	LEU137, GLU139, VAL134, PHE135, PHE141, GLY199, TYR198, SER109, GLY203, SER201, ALA111, and TYR200
A-caryophyllene	-8.131	PHE62, GLU139, PHE135, ASP138, TYR125, VAL134, PHE141, GLY108, SER109, GLY199, GLY203, TYR200, and GLY386	0	-	PHE62, GLU139, PHE135, ASP138, TYR125, VAL134, PHE141, GLY108, SER109, GLY199, GLY203, TYR200, and GLY386
Humulene-V1	-7.501	SER109, GLU386, GLY203, VAL134, TYR125, GLU139, GLY199, and ASP138	0	-	SER109, GLU386, GLY203, VAL134, TYR125, GLU139, GLY199, and ASP138
Flavone	-5.875	TYR198, GLY199, TYR200, SER201, VAL110, VAL134, PHE135, GLU139, PHE62, and PHE141	0	-	TYR198, GLY199, TYR200, SER201, VAL110, VAL134, PHE135, GLU139, PHE62, and PHE141
n-Hexadecanoic acid	-5.824	TYR145, TYR125, PHE135, PHE62, GLU139, LEU137, ASP138, GLY203, GLY199, TYR200, and GLU386	1	SER109	SER109, TYR145, TYR125, PHE135, PHE62, GLU139, LEU137, ASP138, GLY203, GLY199, TYR200, and GLU386
Trans-A-copaene	-7.641	GLU386, TYR200, TYR198, GLY199, SER109, ALA111, ASP138, GLU139, VAL134, and PHE62	0	-	GLU386, TYR200, TYR198, GLY199, SER109, ALA111, ASP138, GLU139, VAL134, and PHE62
Isopropyl stearate	-2.321	SER201, GLY203, GLY199, GLY108, SER109, TYR125, PHE135, ASP138, GLU386, GLU139, and PHE62	0	-	SER201, GLY203, GLY199, GLY108, SER109, TYR125, PHE135, ASP138, GLU386, GLU139, and PHE62
Tetradecanoic acid, propyl ester	-1.483	GLY203, GLY199, GLY108, PHE141, VAL134, LEU137, PHE135, GLU139, ASP138, PHE62, TYR125, SER201, and GLU386	1	TYR200	TYR200, GLY203, GLY199, GLY108, PHE141, VAL134, LEU137, PHE135, GLU139, ASP138, PHE62, TYR125, SER201, and GLU386

formed other interactions like pi-alkyl, alkyl, and van der Waals interactions. The A-caryophyllene has no conventional hydrogen bonding. The Trans-A-copaene of score -7.641 kcal/mol has not formed any conventional hydrogen bonding with the protein but has formed van der Waals interactions with residues GLU386, TYR200, TYR198, GLY199, SER109, ALA111, ASP138, GLU139, VAL134, and PHE62. The other interactions include pi-sigma, pi-alkyl, and alkyl interactions.

3.3.4. Screening of Drug Properties. The drug properties (Supplementary Information) viz., absorption, distribution, metabolism, and excretion properties of the top five compounds with the best binding energies against the three proteins were reported. All the compounds showed very

good gastrointestinal absorption properties above 80%. None of the compounds were P-glycoprotein substrate except A-caryophyllene and flavone and inhibitors. The compounds also showed satisfactory blood-brain barrier and central nervous system permeability properties. The compounds were neither CYP2D6 substrate nor CYP2C9, CYP2D6, and CYP3A4 inhibitors. Compounds such as flavone, n-hexadecanoic acid, Trans-A-copaene, isopropyl stearate and tetradecanoic acid, and propyl ester were CYP3A4 substrates. The compounds flavone, Trans-A-copaene, isopropyl stearate and tetradecanoic acid, and propyl ester were CYP1A2 inhibitors, and flavone was the inhibitor of CYP2C19. None of the compounds reported AMES mutagenic property except eugenol and flavone. No compounds were hERG I inhibitor. The compounds were safe and were not hepatotoxic in nature. All compounds

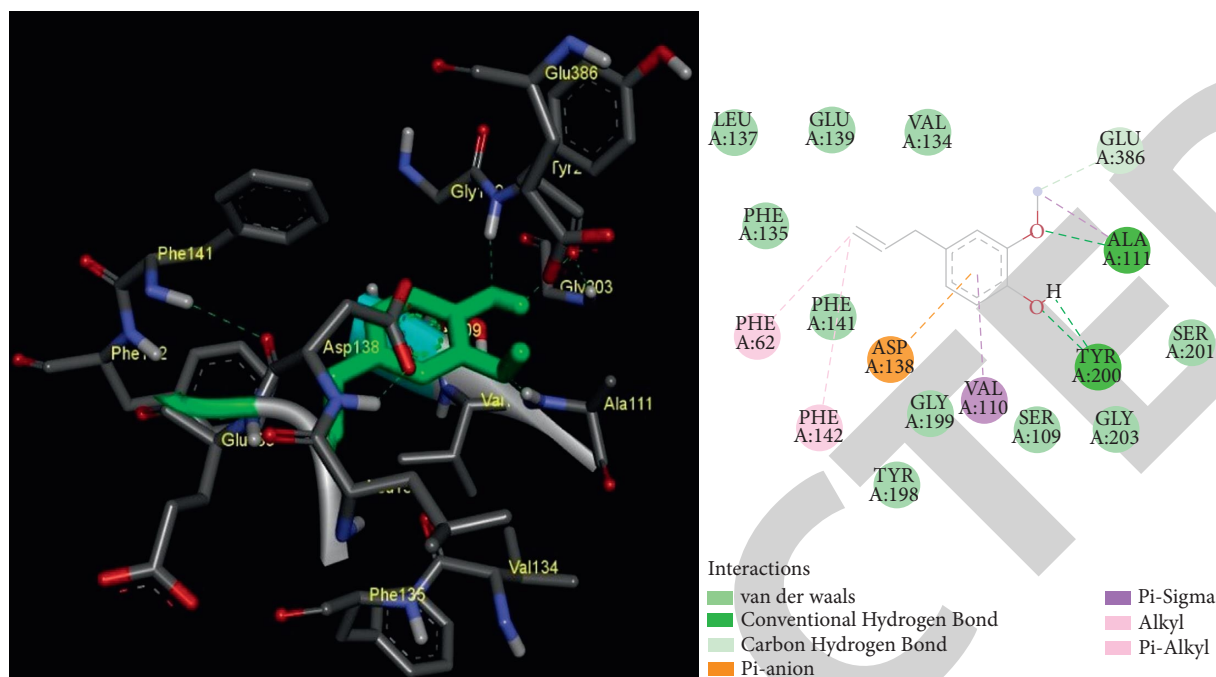


FIGURE 8: 2D and 3D interactions of eugenol of binding score -8.296 Kcal/mol against lipase of *Malassezia furfur*.

reported skin sensitisation property except α -pinene, 4-hydroxy-3-methoxy benzyl alcohol, flavone, and Trans- α -copaene.

4. Conclusion

Thus, the polyherbal ethanolic extract containing the components of *Murraya koenigii*, *Moringa oleifera*, and *Psidium guajava* reveals that the antidandruff property of the extract studied with the molecular docking has enhanced in an optimistic manner, where the 11 phytochemicals that satisfied the Lipinski rule have shown exceptional binding scores against the lipase. None of the compounds were reported as the carcinogen, cardiotoxic, and hepatotoxic. Therefore, the compounds were safe for consumptions. Hence, the lipase which is responsible for the growth and pathogenicity of the *Malassezia* species can be inhibited effectively by the polyherbal ethanolic extract. Further, these polyherbs can be used for hair care product preparation for its antidandruff property, which can be validated by In-vitro and In-vivo studies.

Data Availability

The data used to support the findings of the study can be obtained from the corresponding author upon request.

Conflicts of Interest

The authors declare that they have no conflicts of interest.

Supplementary Materials

The supplementary material contains 4 tables (Tables 6–9). Table 6 gives the information about absorption properties of

the polyherbal extract. Table 7 conveys the distribution property details of the polyherbal extract. Table 8 gives the information about the metabolism properties of the polyherbal extract. Table 9 conveys about the excretion and toxicity property of polyherbal extract. This information is discussed in Section 3.3.4, Screening of Drug Properties. (Supplementary Materials)

References

- [1] M. Narshana and P. Ravikumar, "An overview of dandruff and novel formulations as a treatment strategy," *IJPSR*, vol. 9, no. 2, pp. 417–431, 2018.
- [2] S. M. Rudramurthy, P. Honnavar, S. Dogra, P. P. Yegneswaran, S. Handa, and A. Chakrabarti, "Association of *Malassezia* species with dandruff," *The Indian journal of medical research*, vol. 139, no. 3, pp. 431–7, 2014.
- [3] Z. Xu, Z. Wang, C. Yuan et al., "Dandruff is associated with the conjoined interactions between host and microorganisms," *Scientific Reports*, vol. 65 pages, 2016.
- [4] C. Clavaud, R. Jourdain, A. Bar-Hen et al., "Dandruff is associated with disequilibrium in the proportion of the major bacterial and fungal populations colonizing the scalp," *PLoS One*, vol. 8, no. 3, Article ID e58203, 2013.
- [5] M. Shivaprakash, P. Honnavar, S. Dogra, P. Prakash, H. Sanjeev, and C. Arunaloake, "Association of *Malassezia* species with dandruff," *Indian Journal of Med Research*, vol. 139, no. 3, pp. 431–437, 2014.
- [6] T. O. Weerapongjuntachai, S. Y. Murayama, and S. Kajiwara, "The lipolytic enzymes activities of *Malassezia* species," *Medical Mycology*, vol. 47, no. 5, pp. 477–484, 2009.
- [7] W. Juntachai, T. Oura, S. Y. Murayama, and S. Kajiwara, "The lipolytic enzymes activities of *Malassezia* species," *Medical Mycology*, vol. 47, no. 5, pp. 477–484, 2009.
- [8] M. koenigii, *Curry Leaf Tree*, CABI, Wallingford, UK, 2018.

Retraction

Retracted: Optimization and Mechanical Properties of TiO₂ Reinforced AA 7150 Composites Using Response Surface Methodology

Advances in Materials Science and Engineering

Received 26 December 2023; Accepted 26 December 2023; Published 29 December 2023

Copyright © 2023 Advances in Materials Science and Engineering. This is an open access article distributed under the Creative Commons Attribution License, which permits unrestricted use, distribution, and reproduction in any medium, provided the original work is properly cited.

This article has been retracted by Hindawi, as publisher, following an investigation undertaken by the publisher [1]. This investigation has uncovered evidence of systematic manipulation of the publication and peer-review process. We cannot, therefore, vouch for the reliability or integrity of this article.

Please note that this notice is intended solely to alert readers that the peer-review process of this article has been compromised.

Wiley and Hindawi regret that the usual quality checks did not identify these issues before publication and have since put additional measures in place to safeguard research integrity.

We wish to credit our Research Integrity and Research Publishing teams and anonymous and named external researchers and research integrity experts for contributing to this investigation.


The corresponding author, as the representative of all authors, has been given the opportunity to register their agreement or disagreement to this retraction. We have kept a record of any response received.

References

- [1] S. V. G. V. A. Prasad, V. Kamalakar, J. Madhusudhanan et al., "Optimization and Mechanical Properties of TiO₂ Reinforced AA 7150 Composites Using Response Surface Methodology," *Advances in Materials Science and Engineering*, vol. 2022, Article ID 5779840, 12 pages, 2022.

Research Article

Optimization and Mechanical Properties of TiO₂ Reinforced AA 7150 Composites Using Response Surface Methodology

S V G V A Prasad,¹ V. Kamalakar,² J. Madhusudhanan,³ Puthalapattu Reddy Prasad,⁴ G. Adilakshmi,⁵ Nellore Manoj Kumar,⁶ Anitha Gopalan,⁷ Vinod Singh rajput,⁸ and Nagaraj Ashok ⁹

¹Department of Physics, Pithapur Rajah's Government Autonomous College, Kakinada 533001, Andhra Pradesh, India

²Department of Physics, Vel Tech Rangarajan Dr. Sagunthala R&D Institute of Science and Technology, Avadi, Chennai, Tamil Nadu, India

³Department of Biotechnology, Anand Institute of Higher Technology, Chennai 603103, TamilNadu, India

⁴Department of Chemistry, Institute of Aeronautical Engineering, Dundigal, Hyderabad 500043, Telangana, India

⁵Scienuvo R & D Services, Hyderabad 500038, Telangana, India

⁶Department of Physics, SCSVMV Deemed University, Enathur, Kanchipuram 631561, Tamil Nadu, India

⁷Department of Electronics and Communication Engineering, Saveetha School of Engineering, SIMATS, Chennai 602105, Tamilnadu, India

⁸Department of Mechanical Engineering, Nowgong Engineering College, Chhatarpur, Nowgong, Madhya Pradesh, India

⁹Faculty of Mechanical Engineering, Jimma Institute of Technology, Jimma University, Jimma, Ethiopia

Correspondence should be addressed to Nagaraj Ashok; nagaraj.ashok@ju.edu.et

Received 19 February 2022; Revised 13 April 2022; Accepted 21 April 2022; Published 25 May 2022

Academic Editor: Palanivel Velmurugan

Copyright © 2022 S v g v a Prasad et al. This is an open access article distributed under the Creative Commons Attribution License, which permits unrestricted use, distribution, and reproduction in any medium, provided the original work is properly cited.

The goal of this research is to increase the performance of AA 7150 reinforced with TiO₂ microparticles by optimizing the stir casting parameters. The response surface method's central composite design technique was used to optimize the three stir casting factors of stirring temperature (A), stirring speed (B), and stirring time (C). The ultimate tensile strength, hardness, impact strength, elastic modulus, and compressive strength were all tested. With the aid of analysis of variance, it was discovered that it had a substantial influence on the test samples' characteristics responses. 5 quadratic experiments were linked using factors' characteristics. At a level of 95% confidence, the models were found to be statistically important, and the variations were found to be less than 5%. The response surface was used to assess the parameter interaction profile. Each interaction's contour plots provided a range of stirring settings within which each property may be maximized.

1. Introduction

A typical practice in engineering is to strengthen an alloy matrix with ceramic particles [1]. The resulting materials are useful in an extensive range of fields. Numerous analyses have focused on the creation of high-performance composites due to the adaptability of alloy in modern engineering fields [2, 3]. The alloy and its composite have a higher strength-to-weight ratio than steel, making them better suited for lightweight and fuel-efficient applications in automobiles and airplanes. The 7000 family of aluminum

alloys includes Al 7150-T6, which has excellent mechanical qualities and may be employed in a extensive range of fields [4, 5]. Ceramic nano and microparticles, based ceramic particles, have been the focus of recent research aimed at enhancing alloy characteristics. As reinforcing particles in metal matrices, titanium-based particulates have a wide range of uses [6, 7]. For the Al 7150 matrix reinforced with SiC and TiC, stir casting was used to add 5% silicon carbide and 5% titanium carbide. With the incorporation of 5% silicon carbide and 5% titanium carbide, it was found that the YS, UTS, and IS were all the maximum [8]. With the help

of TiC, [9] reinforced Al 7150 at various percentages of 3, 4, 5, 6, or 7%. A seven weight percentage increase in particle concentration increased microhardness, YS, and UTS. The hardness and bending strength of Al 7150 were improved when 1.5, 3, 4.5, and 6 wt% of TiB₂ were injected into the alloy as observed by [10]. According to their research, the microstructure demonstrated a particle dispersion inside the matrix, increasing its characteristics. At particle dosages of 4, 8, and 12 wt%, titanium boride dispersion in Al 7150 matrix improved tensile strength and hardness, according to the research of [11, 12]. Even at 9 wt% TiC inclusion, the yield and tensile strength of Al 7150 were improved by TiC infusion. Adding titanium carbide at 3–7% of the aluminum alloy resulted in the same pattern. It was found that the microhardness, YS, and UTS of the stir cast product as particles increased [13–15].

At a concentration of 7%, the greatest increase in strength was observed. For Al 7150, titanium dioxide was used to boost compressive and tensile strength, with the maximum increase occurring at a titanium dioxide concentration of 15% weight. Reference [16] reinforced Al 6061 with titanium dioxide with an average particle size of 50 m. When the particle content was increased from 1 to 3 wt%, the hardness and ultimate tensile strength improved by 20.7, 52.6, and 66.7% and 31.6, 55.8, and 89.5%, respectively. The titanium dioxide particle-reinforced composite had better characteristics than the basic metal, corresponding to the analyses. Researchers [17, 18] developed TiO₂-AA 7150 composites with varied titanium dioxide particle concentrations of 5, 10, and 15% using the stir casting method. A 10% increase in the percentage of particles increased the mechanical parameters, tensile strength, flexural and compressive strengths, and hardness. The visualization technique has been used by [19, 20] to examine the impact of the stir casting factors on the supply of reinforcing materials. There is a significant improvement in mechanical qualities when the impeller is placed 40% away from the standard 45° blade angle. CFD models were used to examine the impact of vortex pressure, generated through stirring, on the MMC process [21].

Using Taguchi's experimental design, the researchers found that increasing the vortex height improved mechanical properties. Microstructural analysis [22] was also carried out in the study of the impact of stir casting factors on composite structural characteristics. According to the microstructural analysis, the reinforcing particles are uniformly dispersed, which leads to an increase in mechanical characteristics for the composites over time. The ideal stir casting factors for processing MMC have never been determined through RSM optimization, despite the fact that a variety of approaches have been used [23]. Previously studied influences on Al 7150's properties from variables such as stirring temperature, duration, and speed were not considered. Additionally, impeller rotation direction, blade angle, stirrer height, and reinforcement feed rate are all process variables [24, 25]. It is vital to figure out how these variables affect the microstructure so that you can optimize for alloy improvement under the best circumstances. A study conducted by [26, 27] shows that the UTS,

microhardness, IS, EM, and CS for Al 7150/10% weight microparticles of TiO₂ (mean size 13 mic) was best achieved at 10%, according to [28, 29] which found that 10% yielded the best performance for the microparticles. The purpose of this work is to investigate the mechanical properties of composites synthesized using a variety of parameters utilizing RSM.

2. Materials and Methods

2.1. Composite Preparation. This experiment made use of an aluminum alloy ingot, AA 7150-T6. Table 1 shows the spectrometer results for the chemical composition, whereas Table 2 lists the physical attributes. Crucible made of graphite was used for the stir casting procedure. The melt was warmed to 500°C for 10 minutes before TiO₂ microparticles of 13 microns were injected at a concentration of 10 weight%. The specimens were created in accordance with the central composite design plan based on the trial runs listed in Table 3 and Table 4. As reported by [15], the wettability of the matrix was increased by adding magnesium to the melt.

2.2. Testing Procedure. UTM equipment was employed to calculate the tensile strength (TS) of machined specimens 30 mm long and 5 mm in diameter (Instron 3369 Series). With a crosshead speed of 3.0 mm/min, ASTM E 8/E8M-2-compliant loads of 10,000 N were applied at a rate of 10⁻⁴ per second. The specimens were subjected to a 100 kN load at a cross-speed of 1 mm/min using universal testing equipment in accordance with ASTM E09-9. Each specimen was subjected to a Vickers microhardness test in accordance with ASTM E 384-17 utilizing a load of 10 N for ten seconds on its surface. Also, the high strain impact toughness of a specimen 10 × 10 mm² was studied by monitoring the absorbed energy until failure with a 300 N pendulum (ASTM E-23).

2.3. Experiment Design. The experimental procedure begins with the design of experiments utilizing the response surface methodology, which optimizes processing factors. Response surface methodology examines the relations among processing and responding factors. It is a routine trend to utilize the response surface methodology to model and analyze processes in which the rate is determined by multiple variables. A central composite design containing a level-three component was implemented using the Minitab 19 program. For each attribute evaluated, twenty experimental runs were undertaken, including six axial runs, eight factorial runs, and six repeats at the center point. The relationship between process factors and predicted responses was established using (1). The predicted response is denoted by Z , the intercept is denoted by A , the linear coefficient is denoted by B for first-order expressions, the quadratic coefficient is denoted by C for second-order expressions, the interaction coefficient is denoted by D , and the random error is denoted by E . The equation expresses the model of the first-order polynomial.

$$Z = A + BX_1 + CX_2 + C_n X_n + E. \quad (1)$$

TABLE 1: Composition of the alloy Al 7150 employed in the investigation.

Component	Zinc	Magnesium	Copper	Silicon	Iron	Titanium	Copper	Aluminium
Quantity (%)	8.2	2.9	0.15	0.2	0.2	0.1	0.22	Remaining

TABLE 2: Properties of aluminium 7150.

Properties	Ultimate tensile strength	Poisson ratio	Relative density
Aluminium 7150	607	0.33	2.84

TABLE 3: Factor levels in the experiment's design.

Factors	Levels		
	Low	Medium	High
(A)	550	650	750
(B)	450	550	650
(C)	10	15	20

TABLE 4: Experimental results, levels, and outputs.

Experimental run	Levels			Factors			Responses				
	A(°C)	B(rpm)	C(min)	A(°C)	B(rpm)	C(min)	YS	UTS	EM	El	IM
1	-1	-1	-1	550	450	10	501	581	82.6	8.76	4.21
2	0	0	-1.68	550	450	10	525	642	90.1	7.84	5.31
3	0	0	0	550	450	10	529	689	91.4	7.51	5.74
4	0	0	0	550	550	15	546	635	86.5	7.52	5.46
5	0	0	0	550	550	15	575	719	95.3	6.79	6.41
6	0	1.68	0	550	550	15	588	682	98.2	6.43	6.86
7	1	1	-1	550	650	20	522	600	79.4	7.82	4.86
8	-1	1	1	550	650	20	559	622	88.6	7.99	5.51
9	-1.68	0	0	550	650	20	574	637	92.1	6.62	5.90
10	1.68	0	0	650	450	15	530	634	87.3	8.55	5.17
11	0	0	0	650	450	15	558	715	92.3	7.24	5.86
12	1	-1	1	650	450	15	564	734	98.5	7.12	6.13
13	0	-1.68	0	650	550	20	579	672	92.6	8.08	5.78
14	-1	-1	1	650	550	20	601	745	96.5	7.34	6.84
15	0	0	0	650	550	20	629	771	102.3	6.09	7.15
16	1	1	1	650	650	10	561	628	86.7	8.47	5.00
17	0	0	1.68	650	650	10	582	665	91.2	7.12	5.66
18	-1	1	-1	650	650	10	618	692	93.2	6.83	6.16
19	1	-1	-1	750	450	20	524	600	84.5	8.17	4.24
20	0	0	0	750	450	20	531	657	86.8	6.94	4.87

Mean Square Error and RMS Deviation were used to assess the models' accuracy. These are anticipated benchmarks for the coefficient of correlation for forecast and adjusted data. It is recommended by [30] that the temperature range be in the range of 550 to 750°C, the duration be somewhere between 10 and 20 minutes, and the rotational speed be somewhere between 450 and 650 rpm.

3. Results and Discussion

3.1. ANOVA and Regression Models. Using Table 5, we can see that the P values for processing parameters are all lesser than 0.05, showing that these factors are significant because they affect the reaction size. The $A * A$ and $C * C$ squared interactions are technically important; however, the $B * B$ interaction is not. Similarly, A , B , and C parameters

TABLE 5: Analysis of variance for ultimate tensile Stress.

Source	Df	Seq SS	Contribution (%)	Adj SS	Adj MS	F value	P value
A	1	8276.2	37.12	8359.8	8359.4	229.45	0.000
B	1	2972.4	8.12	2972.1	2972.12	123.64	0.000
C	1	7908.5	28.24	7909.7	7909.5	234.51	0.000
A * A	1	4169.3	13.91	4175.7	4175.4	129.63	0.000
B * B	1	609.4	2.32	608.4	608.5	17.08	0.121
C * C	1	1828.6	5.98	1828.6	1828.5	134.24	0.000
A * B	1	459.4	1.71	472.3	472.5	13.12	0.056
A * C	1	8.9	0.04	10.2	10.3	0.27	0.627
B * C	1	69.8	0.25	69.4	69.7	1.89	0.178
Error	16	615.4	2.31	616.5	37.32		
Total	25	26917.9	100				

contribute 37.12, 8.12, and 28.24%, respectively, demonstrating that the components are relevant in decreasing

order of A, B, and C. The input variable is taken into account by the 2nd order polynomial function for UTS.

$$\begin{aligned} \text{Ultimate Tensile Strength} = & 229 + 6.15A + 0.4908B + 0.4657C + 0.1941A * A + 0.000405B * B + 0.002861C * C + 0.002286A * B \\ & + 0.00086A * C + 0.00081B * C. \end{aligned} \quad (2)$$

P values are less than 0.05 in Table 6, which indicates that the linear terms of Sintering temperature, speed, and time are important, accounting for 41.24%, 21.27%, and 30.15% of the total, respectively. As the input parameter changes, the hardness response of the features changes accordingly. It does not matter what the square terms A * A, B * B, C * C, or

A * B, A * C, or B * C mean. According to the linear terms, the temperature of the stirring is the most important, followed by the time of the stirring. Stirring speed had the least impact on any of the three variables. A 2nd order polynomial function for Hd is presented in

$$\begin{aligned} \text{Hardness} = & 186.7 + 50.5A + 0.4630B + 5.29C + 0.81A * A + 0.000189B * B + 0.0444C * C + 0.0260A * B \\ & + 0.557A * C + 0.00197B * C. \end{aligned} \quad (3)$$

Hardness is denoted by Hd, stirring temperature is denoted by A, stirring speed is denoted by B, and stirring time is denoted by C. ANOVA examination of the impact strength revealed a significant relationship between the response and the input factors. The squared relations A * A and C * C are not as substantial as the linear factors A, B, and C. Responses to A * B, A * C, and C * C are unaffected. A, B, and C each contribute 30.15%, 15.01%, and 27.14%;

therefore, A is the most important factor to consider and then comes the time of stirring, with the speed of stirring having the least impact. Table 7 shows ANOVA on IM.

At the 95% confidence and 5% significance levels, the elastic modulus's reaction to process variables is summarized in Table 8. It is clear from the plots that there is a significant correlation between the processing parameters A, B, and C in the linear model with P value.

$$\begin{aligned} \text{Impact Strength} = & 13.15 + 36.1A + 0.379B + 3.84C + 0.5A * A + 0.000156B * B + 0.0313C * C + 0.0165A * B \\ & + 0.368A * C + 0.00102B * C. \end{aligned} \quad (4)$$

A * A and C * C squared interactions had no effect on the answer; however, B * B has an effect. Statistically, the interfaces A * B and B * C are not significant, whereas A * C is. There is a 36.89% contribution from parameter A (stirring

temperature), followed by 18.12% from parameter B (stirring time) and 26.04% from parameter C (stirring speed). The input variable was incorporated into a second-order polynomial model.

TABLE 6: Analysis of variance on hardness.

Source	Df	Seq SS	Contribution (%)	Adj SS	Adj MS	F value	P value
A	1	8607.4	41.24	8601.8	8602.4	301.41	0.000
B	1	4668.1	21.27	4681.2	4682.1	235.14	0.000
C	1	6559.4	30.15	6571.3	6571.4	261.5	0.000
A * A	1	231.4	1.27	231.4	231.5	10.01	0.069
B * B	1	3.7	0.01	3.8	3.81	0.12	0.752
C * C	1	80.02	0.39	80.1	80.2	3.05	0.590
A * B	1	170.1	0.89	170.2	170.1	6.81	0.091
A * C	1	192.4	0.87	195.4	194.8	7.81	0.071
B * C	1	97.4	0.46	97.4	97.3	3.89	0.357
Error	53	369.1	3.45	26.4	26.5		
Total	62	20978.02	100				

TABLE 7: ANOVA on impact strength.

Source	Df	Seq SS	Contribution (%)	Adj SS	Adj MS	F value	P value
A	1	7971.2	30.15	7971.4	7971.6	218.7	0.000
B	1	4354.1	15.01	4835.3	4829.1	134.34	0.000
C	1	7274	27.14	8364.8	8364.8	235.54	0.000
A * A	1	4901.7	18.04	4904.4	4897.6	134.84	0.000
B * B	1	459.8	2.01	467.4	467.54	13.04	0.049
C * C	1	1169.3	5.34	1169.3	1169.4	33.16	0.000
A * B	1	69.7	0.27	69.4	69.5	0.27	0.594
A * C	1	608.4	2.35	609.4	609.54	6.48	0.079
B * C	1	10.1	0.04	10.2	10.26	17.94	0.864
Error	16	612.4	2.19	617.4	37.14	2.13	0.192
Total	25						

TABLE 8: Analysis of variance for elastic moduli.

Source	Df	Seq SS	Contribution (%)	Adj SS	Adj MS	F value	P value
A	1	7001.4	36.89	7001.5	7001.52	276.61	0.000
B	1	5254.5	18.12	5254.6	5254.62	204.14	0.000
C	1	5998.6	26.04	5998.61	5998.62	238.51	0.000
A * A	1	1.1	0.02	1.1	1.1	0.05	0.851
B * B	1	249.5	9.24	249.6	249.6	6.27	0.042
C * C	1	40.2	0.31	40.1	40.1	1.62	0.0227
A * B	1	69.4	0.39	69.4	69.3	2.79	0.112
A * C	1	186.2	5.84	186.3	186.4	4.39	0.026
B * C	1	27.2	0.22	27.3	27.2	2.05	0.321
Error	53	137.6	2.93	137.6	26.12		
Total	62	18965.6	100				

$$\text{Elastic Modulus} = 42.2 + 82.3A + 1.033B + 5.86C + 22.29A * A + 0.00571B * B + 0.0815C * C + 0.0184A * B + 0.643A * C + 0.00223B * C. \tag{5}$$

Elastic modulus (EM). A, B, and C have P values < 0.05, which indicates that they are substantial and contribute 38.14%, 7.24%, and 30.12% correspondingly to the composite's compressive strength response, as indicated in

Table 9. Correlations A * B, A * C, and B * C are irrelevant but the square terms A * A, B * B, and C * C are substantial. According to linear terms, the temperature of the stirring is the most important, followed by the time of the stirring.

TABLE 9: ANOVA on compressive strength.

Source	Df	Seq SS	Contribution (%)	Adj SS	Adj MS	F value	P value
A	1	70026	38.14	70026	70124	369.14	0.000
B	1	13541	7.24	13541	13542	70.08	0.000
C	1	59964	30.12	59964	59964.2	293.14	0.000
A * A	1	19245	9.97	19245	19245.4	99.41	0.000
B * B	1	1517	6.84	1517	1517.7	7.31	0.000
C * C	1	7669	5.14	7669	7669.2	40.12	0.009
A * B	1	749	0.39	749	749.8	4.01	0.091
A * C	1	1162	0.3	1162	1162.4	6.02	0.082
B * C	1	3174	1.29	3174	3174.4	15.81	0.063
Error	54	1049	0.57	10512	189.6		
Total	63	178096	100				

Stirring speed had the least impact on any of the three variables. The equation represents compressive strength (Pa).

$$\begin{aligned} \text{Compressive Strength} = & 80.9 + 133.8A + 3.018B + 24.38C + 18.81A * A + 0.00173B * B + 0.4381C * C + 0.055A * B \\ & + 1.361A * C + 0.0111B * C. \end{aligned} \quad (6)$$

3.2. Coefficient of Correlation for Mechanical Characteristics. Table 10 lists the correlation coefficients, R^2 (adj), R^2 (pred), and R^2 (the variance among R^2 (adj) and R^2 (pred)). If $R^2 = 98.41\%$ for UTS, then there is a strong correlation between the model and the dependent variable, with the model accounting for 98.41% of the observed variation. $R^2 = \text{Adj } R^2$ (adjustment) has a value of 97.61%, while $\text{Pred } R^2$ has a value of 94.42%. A credible model should have at least a 20% difference between the two regression coefficients because the difference between the two coefficients is at least 20% in the UTS. R^2 values of 95.04% for hardness, 96.29% for impact and elastic modulus, and 97.03% for compressive strength indicate that the model accurately characterizes the relationships by more than 90% of the variance. Elastic modulus, compressive strength, and hardness all have R^2 (%) values under 20%, indicating they meet the criteria for good correlation. There are so few variations from a straight line; it is safe to say that this model holds true for the vast majority of data. As can be seen in Figures 1(a)–1(e), where the dots are clustered along a line, the scatter plot of the residual data versus the fitted data shows that the data are heteroskedastic. A good model is one where the response residuals are evenly spread around the mean value.

3.3. Analysis of the Response Surface and Contour Plot. The greatest tensile strength can be achieved by plotting the response surface and contours. Temperature (T_m) and speed (Sp) of stirring have an impact on a composite's UTS. Two process parameters are plotted as a function of the other variable, and the model is shown as a graphical representation of this relationship. X and Y axes are used to plot input variables, and the Z axis is used for the response. Figure 2(a)

depicts the response surface for a continuous 15-minute period for the speed-temperature interaction. In contrast, at 550 rpm and 750°C, the maximum tensile strength response value dropped significantly. As a result, the final tensile strength is strongly influenced by the relationship between speed and temperature. Shifting a parabolic reflection profile with inflection points at 750°C and 550 revolutions per minute resulted in an inflection point pressure of 664 MPa. Using a 15-minute timer, Figure 2(b) shows how interaction temperature affects UTS. Temperature and pace have a significant impact on tensile strength. Part A's ideal strength range is between 600 and 640 MPa when temperature and speed are taken into account, which is between 721 and 841°C and 440–635 rpm.

The UTS of composites is affected by the relationship between stirring time (T) and speed (Sp). At a constant 650°C T_m , the relationship between stirring duration and speed can be shown in Figure 2(c). As the T and Sp grew beyond 500 rpm, a significant negative speed-temperature interaction occurred, consequential in a reduction in overall strength. As a result of the right speed and length of stirring, particles are more evenly dispersed in the melt. Speeds greater than 500 rpm resulted in turbulent churning that trapped gas and created blow holes, resulting in decreased tensile strength. There was a positive trend in the time and speed charts for both stirring speeds. Figure 2(d) displays the contour plot of the two variables, which are separated into portions by the boundary lines shown in the figure. As shown in Plot A, a churning speed of 462–555 rpm paired with an appropriate stirring period (between 20 and 22.5 minutes) can produce an ideal strength range of 660–675 MPa. This is the best part of the graph.

TABLE 10: Correlation coefficient.

Parameters	R ² (%)	R ² (Adj) (%)	R ² (Pred) (%)	γR ² (%)
UTS	98.41	97.61	94.42	<20
Hardness	95.04	94.81	92.86	<20
Impact strength	96.29	95.24	93.24	<20
Elastic modulus	97.03	96.41	94.86	<20
Compressive strength	98.42	97.42	95.16	<20

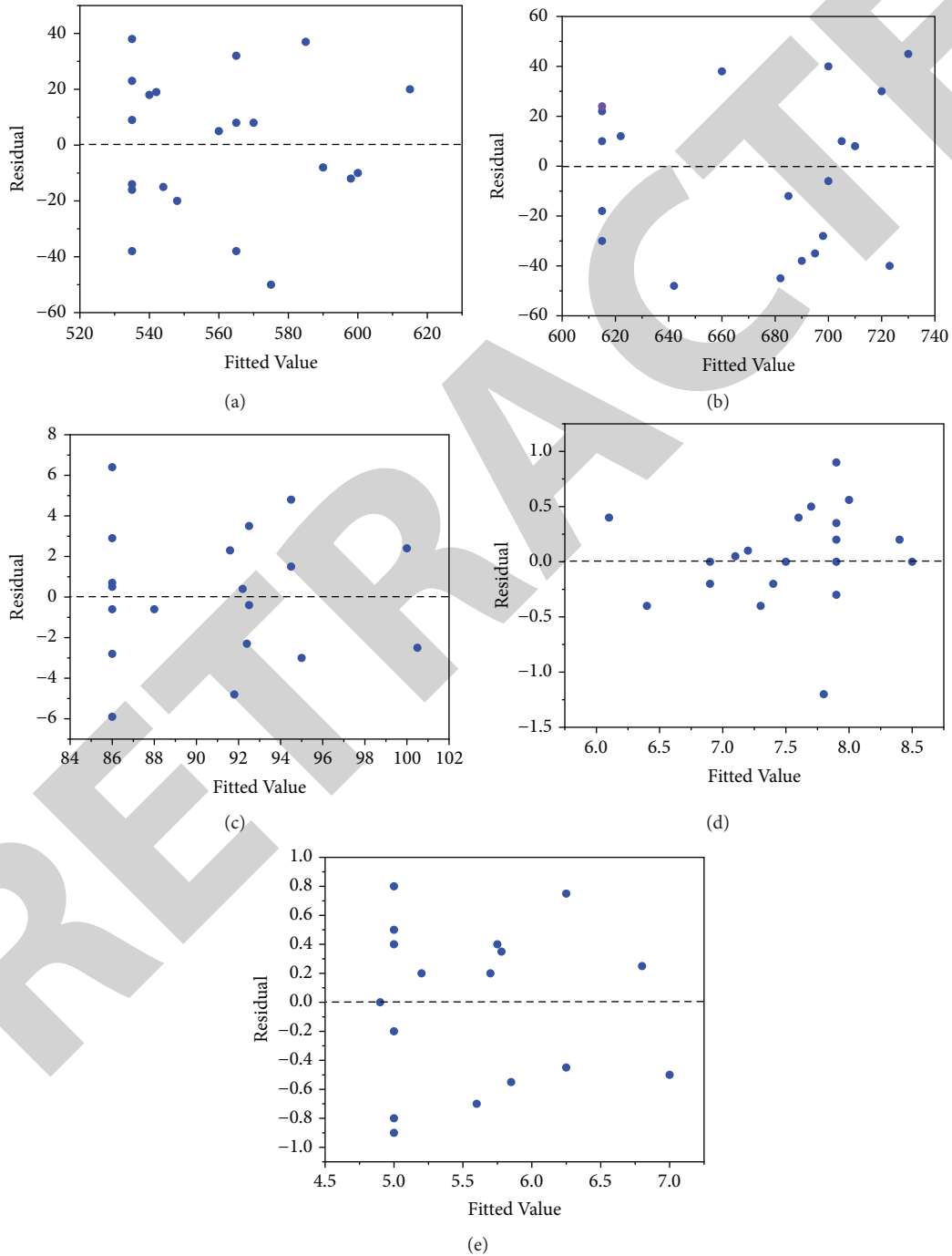


FIGURE 1: The residuals for responses are plotted using the normal probability distribution. (a) UTS, (b) H_d , (c) IS, (d) EM, and (e) CS.

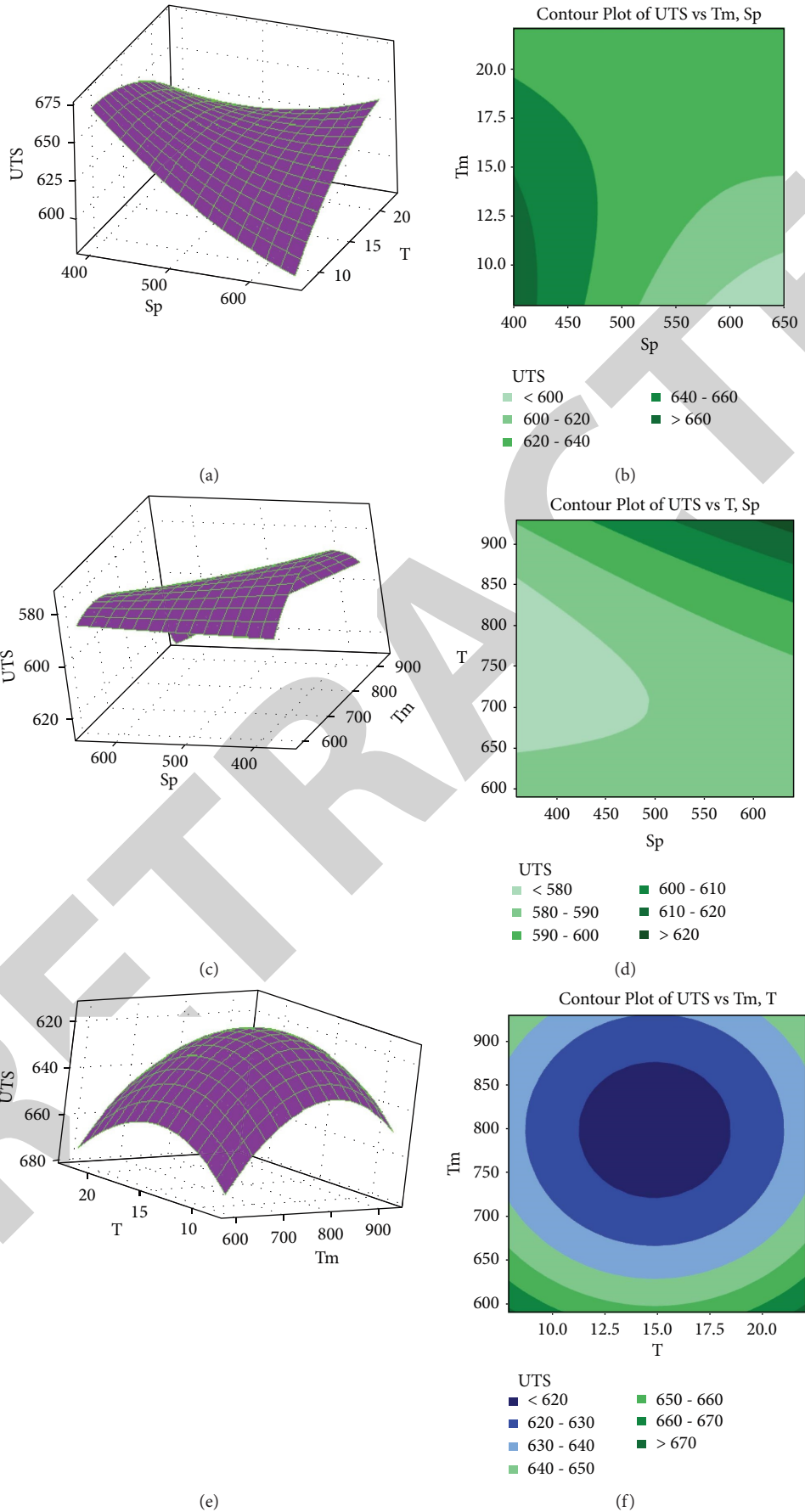


FIGURE 2: Reaction surface plots and contour plots for interactions show the effect of stirring constraint on the final TS of the generated mixtures. (a, b) Sp and Tm, (c, d) Sp and T, (e, f) Tm and T.

A composite's tensile strength is influenced by the temperature-stirring interaction (T) (T_m). When the temperature and time are properly controlled, the TS of the aluminum composite can be indicated in Figure 2(e). Increasing temperature and time both enhanced ultimate tensile strength; however, the temperature and time interaction cause a decrease in strength over 750°C. The temperature profile becomes parabolic at 750°C; however, the time profile shows a linear collaboration of positive gradients. The maximum strength of 665.8 MPa was achieved by combining the two parameters of 750°C and 22.5 minutes. Figure 2(f) depicts the relationship between ultimate tensile strength (T) and interaction time (T) and temperature (T). Boosting the amount of time and temperature had the desired effect of increasing strength. At 715–750°C and a length of 19.4–22.5 minutes, "A" determined the area of optimal strength that encompasses the value of 620–670 MPa.

Vickers microhardness of composite is affected by the interplay between stirring temperature (T_m) and speed (Sp). There was a gradual hardening of the material as the speed and temperature increased from –1 level. That the composite's hardness is influenced by the interaction between these two properties is evident from this. When speed and temperature were used as inputs, the concave profile shown in the picture was chosen. An interaction of 650 rpm and 835°C resulted in a maximum hardness of 119.2 HV. The picture also illustrates how the interaction affects the microhardness's response. Vickers microhardness of composites is affected by the interplay between stirring time (T) and stirring speed (Sp). The curve of Sp was concave, whereas the profile of stirring time was linear and positive, as depicted in the graph.

Stirring and temperature (T_m) time (T) affect the Vickers microhardness of a composite. Vickers microhardness of aluminum composite strengthened with TiO_2 ceramic microparticles at 500 rpm is shown to be impacted by the interplay of stirring duration and temperature. Hardness increased in lockstep with both temperature and elapsed time. This demonstrates that the composite's hardness is dependent on the interplay between these two variables. A concave temperature profile was shown whereas a linear one was shown for a time of 600 revolutions per minute at 835°C producing the maximum hardness of 119.2.

3.4. Impact Strength Response Surface and Contour Mapping.

The impact strength of the composite is affected by the interplay between stirring temperature (T_m) and speed (Sp). Impact strength increased with stirring speed, temperature, and speed; however, at 550 rpm stirring speed and 750°C temperature, impact strength decreased. As a result, the speed-temperature interaction pattern has a strong association with impact strength. With the ends facing down, the two experimental parameters shifted a parabolic profile.

Temperatures of 750°C and 550 rpm are the two sites of inflection, which provide a peak range of 5.27 J/m². At temperatures between 675°C and 842°C and speeds between 440 and 635 rpm, the interplay of temperature and speed

yielded a maximum strength of more than 5.0 MPa in Portion "A".

Speed and temperature had a substantial detrimental impact on strength when the rpm was greater than 500. With the proper speed and time of stirring, particles may be evenly dispersed in the melt. Turbulence, which causes gas entrapment and blowholes, reduces the strength of a mixture when it is stirred at more than 500 rpm. Stirrer speed increased linearly with a positive temporal gradient over time.

An impact composite's strength is influenced by the temperature-stirring time interaction (T) (T_m). Over 750°C, the temperature and time effect interacts in a negative way, resulting in an overall decrease in the impact strength. A 750°C inflection point marks the stirring temperature profile while stirring duration determines the positive gradient's linear interaction profile. When the two variables were merged, the energy output was 5.32 J/m² at 750°C and 22.5 minutes. The strength of the impact is affected by the contour plot of interaction duration against temperature. The impact strength was improved by increasing the time and temperature. At 725–785°C and 21.5–22.5 min, the portion labeled "A" found the spot for maximum strength, which is between 5.3 and 5.4 J/m². Figure 3 displays the reaction surface plot and contour plot for relations to show the impact strength of the generated composite as a result of stirring parameters. (a, b) Sp and T_m , (c, d) Sp and T , and (e, f) T_m and T .

Two elements were coupled to produce a parabolic interaction profile with inflection points at 750°C and 500 rpm, with the point of inflection reaching 95.5 GPa. Variations in temperature and speed interact with variable elastic moduli, and this graphic shows where those moduli are at different points in time. Thermal and mechanical interactions in Segment "A" result in a maximum strength range of about 94–96 MPa, which can be achieved by running the motor at temperatures between 780°C and 824°C and speeds between 475 and 580 rpm.

3.5. Mapping of Compressive Strength Using Response Surface and Contour Data.

The compressive strength of a composite is affected by the relationship between stirring temperature (T_m) and speed (Sp). Compressive strength increased over time as both speed and temperature increased. Because of this, the strong response is dependent on the interactions. The concave shape depicted in the image was the result of the two input factors speed and temperature. At 650 revolutions per minute and 820°C, the highest strength of 484.3 MPa was achieved.

The impact on composite compressive strength of the interplay between stirring time (T) and temperature (T_m) during stirring is as follows. For aluminum composites enhanced with TiO_2 ceramic microparticles generated at a persistent velocity of 550 revolutions per minute, the connection between stirring duration and the temperature was clearly visible. Thus, the interplay between the two parameters is critical to the composite's strength. It was apparent that the temperature had a parabolic profile with both edges facing down, whereas time had a linear profile that

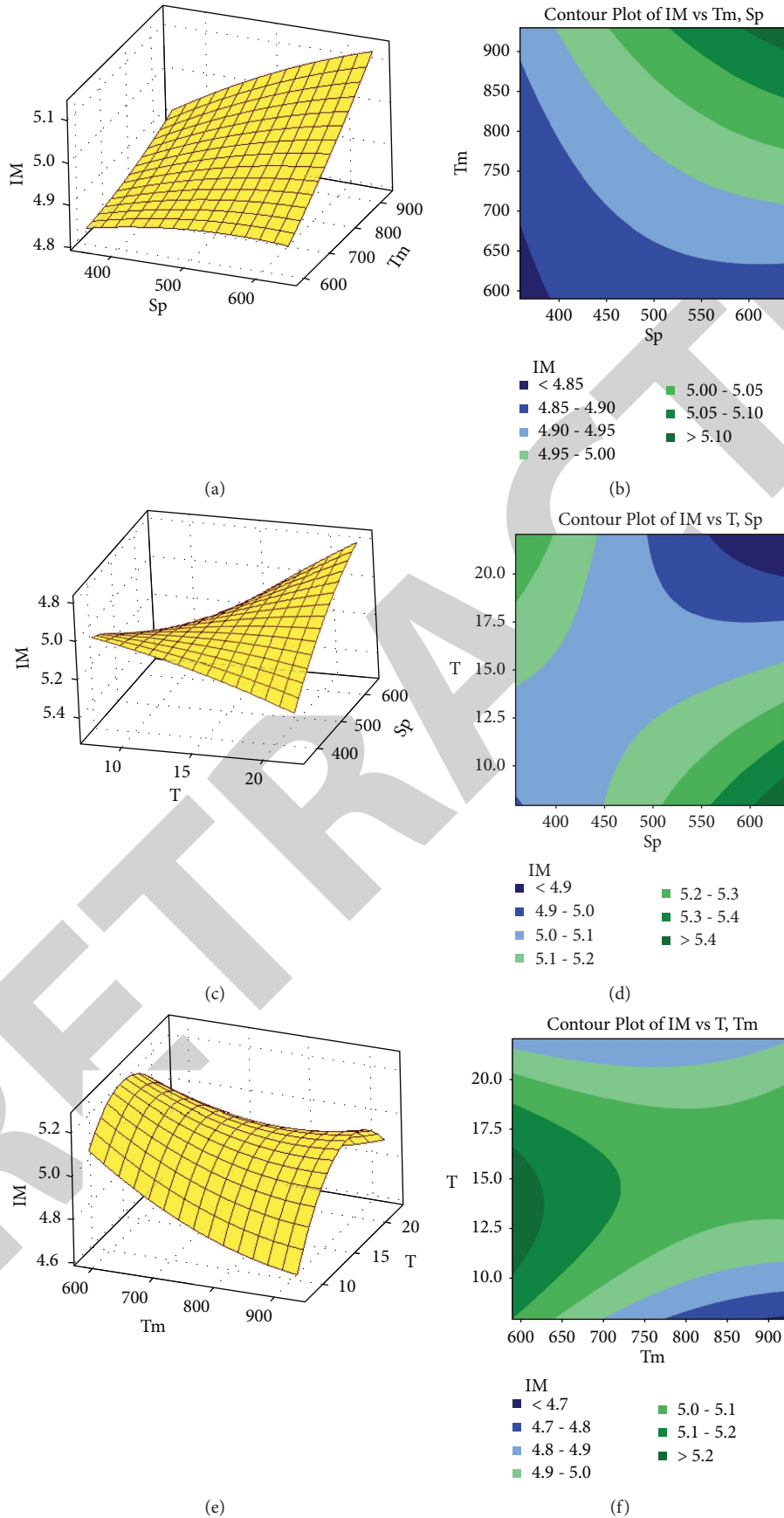


FIGURE 3: The reaction surface plot and contour plot for relations show the impact strength of the generated composite as a result of stirring parameters. (a, b) Sp and Tm, (c, d) Sp and T, and (e, f) Tm and T.

TABLE 11: The optimal parameters and outcomes. Overall, the desirability rating is 0.94.

	Optimal parameters		
	Temperature 780.1°C	Speed 568 rev/min	Time 23 minutes
	Predicted values	Experimental value	Deviation (%)
Compressive strength	496.8 Mpa	489.4 Mpa	1.51
Elastic modulus	98.2 GPa	101.5 GPa	2.82
Impact strength	5.4 kJ/m ²	5.67 kJ/m ²	4.38
Microhardness	120.4 HV	118.4 HV	1.98
Ultimate tensile strength	660.5 MPa	639.4 MPa	2.59

rose upward. At 650 rpm and 22.5 minutes, a maximum force of 486.8 MPa was achieved. Compressive strength is shown in the figure to be dependent on the collaboration.

3.6. Model Testing and Optimization. Minitab 19 was used to optimize the stirring temperature, speed, and time by means of the RSM. The tensile strength was increased by varying the independent variables from the lowest to the highest possible values. Optimization was performed at a 95% confidence level with no constraints, while the lesser and higher levels of all parameters were fixed. According to Table 11, optimum values for UTS, microhardness, IS, EM, and compressive strength (Table 11) were found. Stirring at 568 rpm, 780.1°C, and 23 minutes provides the optimum overall tensile strength. 568 rpm, 780.1°C, and 23 min were utilized to confirm the experimental run's speed, temperature, and time inputs. Table 11 shows the average results of the various experiments. Given that each property's variance is less than 5%, we can say with confidence that experimental results and anticipated results are good, proving that the model is accurate.

4. Conclusion

AA 7150/TiO₂ composites were created using the stir casting process by altering the method's three processing parameters. The UTS, hardness, IS, EM, and CS all behave differently depending on the interplay between these properties. The analysis of variance revealed that the stirring constraints had an effect on each characteristic; however, the chosen square interactions had a significant effect at a 95% confidence level. Over 94 percent of the data was adequately represented by the five models constructed for the statistically significant attributes as determined by the correlation coefficient. Reaction surfaces revealed a high dependence of each variable on the relationships between the processing parameters. When the temperature was less than 650 °C and the speed was less than 550 rpm, there was a favorable effect on the responses. Additionally, a stirring time of up to 30 minutes may be necessary to provide a uniform dispersion, which aids the reaction.

Data Availability

The data used to support the findings of this study are included within the article.

Conflicts of Interest

The authors declare that there are no conflicts of interest regarding the publication of this article.

Acknowledgments

The authors appreciate the support from Jimma Institute of Technology, Jimma University, Jimma, Ethiopia, for the research and preparation of the manuscript.

References

- [1] J. A. Jeffrey, S. S. Kumar, V. A. Roseline, A. L. Mary, and D. Santhosh, "Contriving and assessment of magnesium alloy composites augmented with boron carbide VIA liquid metallurgy route," *Materials Science Forum*, vol. 1048, pp. 3–8, 2022.
- [2] M. S. Kumar, S. R. Begum, C. I. Pruncu, and M. Shahedi Asl, "Role of homogeneous distribution of SiC reinforcement on the characteristics of stir casted Al-SiC composites," *Journal of Alloys and Compounds*, vol. 869, Article ID 159250, 2021.
- [3] V. Mohanavel, M. Ravichandran, S. Suresh Kumar, M. Melwin Jagadeesh Sridhar, S. Dineshkumar, and M. M. Pavithra, "Microstructural and tribological characterization of Al/EGG shell ash composites prepared by liquid metallurgy process," *Journal of the Balkan Tribological Association*, vol. 26, no. 2, pp. 319–326, 2020.
- [4] M. S. Kumar, C. I. Pruncu, P. Harikrishnan, S. R. Begum, and M. Vasumathi, "Experimental investigation of in-homogeneity in particle distribution during the processing of metal matrix composites," *Silicon*, vol. 14, pp. 629–641, 2021.
- [5] M. Saravana Kumar, S. R. Begum, and M. Vasumathi, "Influence of stir casting parameters on particle distribution in metal matrix composites using stir casting process," *Materials Research Express*, vol. 6, no. 10, Article ID 1065d4, 2019.
- [6] V. Mohanavel, S. S. Kumar, V. Sivaraman, V. K. Girish, and M. Ravichandran, "Tungsten carbide particulate reinforced AA7050 aluminum alloy composites fabricated by liquid state processing," *AIP Conference Proceedings*, vol. 2283, no. 1, Article ID 020087, 2020.
- [7] A. A. Adediran, A. A. Akinwande, O. A. Balogun, and B. J. Olorunfemi, "Optimization studies of stir casting parameters and mechanical properties of TiO₂ reinforced Al 7075 composite using response surface methodology," *Scientific Reports*, vol. 11, no. 1, pp. 19860–19920, 2021.
- [8] M. Tebaldini, C. Petrogalli, G. Donzella, and G. M. La Vecchia, "Estimation of fatigue limit of a A356-T6 automotive wheel in presence of defects," *Procedia Structural Integrity*, vol. 7, pp. 521–529, 2017.

Retraction

Retracted: Impact of BN and WC Particulate Reinforcements on Mechanical Properties and Damage Development of Al-2048 Metal Matrix Composites

Advances in Materials Science and Engineering

Received 26 December 2023; Accepted 26 December 2023; Published 29 December 2023

Copyright © 2023 Advances in Materials Science and Engineering. This is an open access article distributed under the Creative Commons Attribution License, which permits unrestricted use, distribution, and reproduction in any medium, provided the original work is properly cited.

This article has been retracted by Hindawi, as publisher, following an investigation undertaken by the publisher [1]. This investigation has uncovered evidence of systematic manipulation of the publication and peer-review process. We cannot, therefore, vouch for the reliability or integrity of this article.

Please note that this notice is intended solely to alert readers that the peer-review process of this article has been compromised.

Wiley and Hindawi regret that the usual quality checks did not identify these issues before publication and have since put additional measures in place to safeguard research integrity.

We wish to credit our Research Integrity and Research Publishing teams and anonymous and named external researchers and research integrity experts for contributing to this investigation.

The corresponding author, as the representative of all authors, has been given the opportunity to register their agreement or disagreement to this retraction. We have kept a record of any response received.

References

- [1] T. Sivakumar, C. Udagani, M. Sivaranjani et al., "Impact of BN and WC Particulate Reinforcements on Mechanical Properties and Damage Development of Al-2048 Metal Matrix Composites," *Advances in Materials Science and Engineering*, vol. 2022, Article ID 2286713, 9 pages, 2022.

Research Article

Impact of BN and WC Particulate Reinforcements on Mechanical Properties and Damage Development of Al-2048 Metal Matrix Composites

T. Sivakumar,¹ Chikkappa Udagani,² M. Sivaranjani,³ M. Sudhakar,⁴ Reem Mohammed Alharbi,⁵ Neveen Abdel-Raouf,^{6,7} Ibraheem Borie M. Ibraheem,⁷ Essam Nageh Sholkamy ,⁸ Mahadeo A. Mahadik,⁹ and Simon Yishak ¹⁰

¹Department of Mechanical Engineering, Malla Reddy College of Engineering & Technology, Maisammaguda 500100, Secunderabad, India

²Department of Physics, University College of Science Tumkur University, Tumakuru, Karnataka 572103, India

³Department of Civil Engineering, Sri Sai Ram Engineering College, Chennai, Tamil Nadu 600044, India

⁴Department of Mechanical Engineering, Sri Sai Ram Engineering College, Chennai, Tamil Nadu 600044, India

⁵Department of Biology, College of Science, University of Hafer Al-Baten, Hafer Al-Baten, Saudi Arabia

⁶Department of Biology, College of Science and Humanities in Al-Kharj, Prince Sattam Bin Abdulaziz University, Al-Kharj 11942, Saudi Arabia

⁷Department of Botany and Microbiology, Faculty of Science, Beni-Suef University, Beni-Suef 65211, Egypt

⁸Department of Botany and Microbiology, College of Science, King Saud University, Riyadh 11451, Saudi Arabia

⁹College of Environmental & Bioresource Sciences, Chonbuk National University, Iksan 570752, Republic of Korea

¹⁰College of Engineering and Argo-Industrial Technology, Sawla Campus, Arba Minch University, Arba Minch, Ethiopia

Correspondence should be addressed to Simon Yishak; simon.yishak@amu.edu.et

Received 25 December 2021; Accepted 11 March 2022; Published 16 May 2022

Academic Editor: Palanivel Velmurugan

Copyright © 2022 T. Sivakumar et al. This is an open access article distributed under the Creative Commons Attribution License, which permits unrestricted use, distribution, and reproduction in any medium, provided the original work is properly cited.

The primary goal of this work is to evaluate how BN and WC particles affect the mechanical properties and damage development behaviours of aluminum alloy-2048. Heat treatments for composites are also being investigated to improve mechanical properties. Tensile experiments reveal that BN particle reinforcement outperforms WC reinforcement in strength and flexibility for composites. T4 treatment, rather than traditional peak-aging treatment, is recommended for the composites (T6). The particle size distribution in 10v% WC/Al-2048 is the best in the three composites with the largest size of 16 μm and 80% of particles are from 6 to 10 μm . Tensile tests illustrate that 15v% BN/Al-2048 composite demonstrates a 9 and 14% rise in its ultimate tensile stress and 28 and 120% increases in its elongation. T4 heat treatment with an additional 0.6 percent prestrain can produce composites with the same UTS and 0.2 percent proof stress as T6 treatment, but the ultimate elongation below T4 treatment is over 100 percent more than that under T6 treatment. To make sense of the test results, an observation of the damage evolution behaviors of the reinforcing particles provides a concept that the composites' strength is primarily determined by the balance between the reinforcing particles sharing the load and creating strain discontinuity in the matrix. The fraction of broken particles in the 20v% WC/Al-2048 composite as a function of strain is much higher than that in the 15v% BN/Al-2048 composite. Because of their tolerance for substantial strain at the interface, maximum K1c, and moderate thermal extension, BN elements can share a lot of loads and provide more excellent reinforcement than WC particles in terms of composite strength and flexibility.

1. Introduction

MMCs are highly designed metals with greater durability, abrasion, and outstanding dampening properties, rendering them appropriate for a broad array of uses in mobility, gadgets, aircraft, and marine.

Aluminum alloy bonded with hyperparticles for increased strength and toughness. Aluminum composites provide a consumer with the benefits of lighter yet stable properties. Aluminum composites are a family of materials which have so far been effective at achieving the majority of the stringent standards in applications requiring low density, high stiffness, and intermediate tenacity. Particulate-reinforced metal matrix composites combine short compactness, increased toughness and stiffness, isotropic properties, and superior wear resistance [1]. Several composites, such as matrix alloy, preparation type, aged condition, capacity portion of reinforcements, element size, particle size distribution, type of reinforcement material, and the integration situation among matrix and particulate, could all have an impact on physical behavior [2, 3]. Many aluminum alloys, such as 2014, 7075, 6082, and 6061, reinforced with ceramic and ash particles have been investigated extensively [4, 5]. Al-2048 reinforced with ceramic particles has been developed to meet the requirement of some possible applications at high temperature, for instance, automotive brake callipers, conrods, and pistons, or supersonic aerospace airframe constructions [6–8]. The BN particle reinforced Al-2048 MMCs have also been the subject of a few studies. It is desirable to use spray deposition for 2048 alloy because it reduces the dispersions of iron and nickel [9]. This MMC has a lower potential cost as compared to high strength aluminum alloys. Because of the addition of the reinforcing ceramic phase, the tensile ductility and breaking toughness of PR-MMCs are far lower than those of their matrix alloys. As a result, many research efforts have been concerned with the analysis of the distortion and discontent methodology of PR-MMCs in terms of improving them explicitly for transportation sectors. [10–12].

Two kinds of particulate reinforcements, BN and WC, have been widely used in the development of PR-MMCs [13]. Many investigations on BN and WC particulate-reinforced MMCs are carried out independently so that the experimental results cannot be compared effectively due to the differences in the matrix alloys and in processing methods used by individual researchers [9]. Therefore, not much has been known about the effect of different type of reinforcing particles between BN and WC on the composite properties unfortunately. Paper [14] studied the difference between BN and WC particulate-reinforced Al-Cu alloys on the fortification types on the microstructure of the composites. The outcomes also showed that the occurrence of particulate fortification (both BN and WC with a mean size of $3\ \mu\text{m}$) in the Al alloy composite (AA2519) could not help in refining its toughness [15, 16]. Three Al-2048 matrix composites reinforced by particulate BN (with a median of $9\ \mu\text{m}$) and WC (with mean size of $8\ \mu\text{m}$ or $15\ \mu\text{m}$), respectively, were manufactured by a same spray forming process and by exactly same thermomechanical processes

afterwards in the present study [17–20]. The comparisons of mechanical properties and damage evolution behaviors during straining between the composites were investigated in order to have further understanding of the strengthening and failure mechanisms of the composites [9].

Although there have been some researchers reported in the literature about effects of reinforcing particles on the aging behaviors of the aluminum alloy matrix PR-MMCs, the T6 heat treatment which is the conventional heat treatment for aluminum alloys is popularly used for the composites in nearly all the studies and applications [21]. Heat treatments for the composites used in this study are also investigated to enhance their mechanical behaviour. The strengthening mechanisms in PR-MMCs are popularly believed in the micromechanical models [22]. These representations are concerted on the belongings of particulate fortification on solidification of the composite, i.e., the effects likewise increasing displacement thickness and resulting in fine scrap size. This conclusion is supported by numerous studies, which show that particulate reinforcement increases the strength of PR-MMCs with soft matrices but not with hard matrices. PR-MMCs' strength is largely determined by a balance between reinforcing particles sharing the load and creating strain discontinuities in their matrix, according to the cracking behaviour of reinforcing particles [23, 24]. This theory is used to explain the test results in this study, which show that hard matrix alloys are strengthened over their matrix alloys.

2. Materials and Experimental Procedure

This investigation made use of three PR-MMCs and an Al-2048 alloy. Boron nitride is a ceramic compound material that really has grown in popularity primarily because of its excellent heat conductivity, greasing properties, chemical inertness, mechanical strength, oxidation resistance, and nonwettability. BN/Al-2048 is a composite with a nominal 15% volume proportion of BN particle reinforcement. WC particle reinforced Al-2048 matrix composites with a volume fraction of 10% and 20% are referred to as 10v percent WC/Al-2048 and 20v percent WC/Al-2048. A spray-forming-deposition technique was used to create the tested materials. Ball grinding and sieving with a nominal grain size of $10\ \mu\text{m}$ were utilised for the production of commercial BN powder. An electrical melting technique and subsequent ball grinding and sieving result in WC powder with a nominal grain size of $10\ \mu\text{m}$, which is also available commercially. Chemical investigation identified the Al-2048 matrix as Al-2.5w% Cu-1.5w% Mg-1.1w% Ni-1.1w% Fe as its composition. To make bars with a diameter of $40 \times 100\ \text{mm}$, the ingots were heated to the temperature of 5100°C and then cooled by air (as extruded). A two-hour solution treatment at 530°C followed by machining into cylindrical tensile dumb-bell specimens with 5 mm diameter and 25 gauge length completed the procedure. As part of a study to see how particulate-reinforced Al-2048 composites age over time, they were aged at 200°C (peak-aged condition, T6) for 20 hours (BN and WC).

There was no additional use of artificial ageing for the others (T4). On the CSS servoelectric testing machine, the applied strain rate was $3.5 \times 10^{-5} \text{ Sec}^{-1}$ for all tensile tests. Structural characteristics of the materials were measured using extensometers and strain gauges of two different types during straining. An unloading/reloading process was used to generate a straight stress-strain line for higher measurement precision, while avoiding any damage to the reinforcements during the procedure. Using repeated unloading and reloading at room temperature, the elastic modulus of the composites was reduced during tensile straining as a means of assessing damage progression in the composites. Composite damage evolution during deformation cannot be studied by measuring the percentage of broken BN elements on the sectioned samples after several strains of tensile stress. The damage evolution in terms of the percentage of broken elements as a function of strain can then be investigated by the local fraction of broken particles matching the local actual strain in the necking area of a single tensile cracked specimen. Using a tensile test as shown in Figure 1, it is possible to determine the amount of plastic strain in the necked region. It was necessary to magnify tensile samples in order to correctly estimate their local diameters before conducting the tensile test. To measure the local diameter of the samples, the two broken halves of the specimens were aligned and adhered together with a very small drop of glue after the tensile test was completed for one second. Assuming that D_o and D , the diameters of the specimens, are known before and after the test, local true strain can be calculated using this formula: $T = -2\ln(D/D_o)$. Before polishing, broken samples are cut longitudinally along the stress axis using spark corrosion to stop additional mechanical mutilation.

3. Results and Discussion

3.1. Size Distribution of Reinforcing Particles. The observation of the composites after extrusion reveals that all three composites present rather good homogeneous reinforcement distribution. However, the size of reinforcing particles spreads a large range owing to the commercial ceramic powder made by low cost processes. 108 measurements dispersed frequently over the comprehensive sample surface of 60 mm^2 were selected to control the local reinforcement volume fraction and the particle geometry significance in these three composites. Each measured area is a $0.1 \times 0.083 \text{ mm}$ rectangle.

Figure 2 shows the distribution of the diameter of particulate reinforcement in the three tested composites in the as-extruded condition. The mean volume fractions in 15v% BN/Al-2048, 10v% WC/Al-2048, and 20v% WC/Al-2048 were measured as 15.8, 10.9, and 20.3%, respectively, which are close to the nominal specifications. The particle sizes in 15v% BN/Al-2048 are distributed in a large range up to $26 \mu\text{m}$, but size of 85% particles ranges from 6 to $14 \mu\text{m}$. The particle size distribution in 10v% WC/Al-2048 is the best in the three composites with largest size of $16 \mu\text{m}$ and particles of the size of 80% are from 6 to $10 \mu\text{m}$. Distribution of particle size in 20v% WC/Al-2048 is the poorest in three



FIGURE 1: Tensile testing setup.

composites with particle size up to $34 \mu\text{m}$ and 45% reinforcing particles are larger than $16 \mu\text{m}$. It is not surprising that distribution and size distribution of particulate reinforcements among the three examined composites are quite similar because of same processing, same matrix alloy, and same thermomechanical procedures. Therefore, the difference of mechanical properties caused by the differences in cluster and size distribution of reinforcement among the three tested composites would be small and has been neglected by this study. But, the mean particle size of 20v% WC/Al-2048 is quite different from the other two composites and its effect on the properties will be discussed later.

3.2. Composite Mechanical Qualities as an Effect of Heat Treatment. Mechanical characteristics of the materials tested at the room temperature under different heat treatments are listed. Every test datum comes from the average of at least two individual tests if the two tests yield a difference less than 3% between them; otherwise, a third test would be carried out. The results in the figures indicate that different heat treatments have little effect on elastic modulus for the composites, but can change the 0.2% proof stress of the mixtures dramatically. Conventional T6 treatment produces higher 0.2% proof stress but lower final elongation compared with the T4 heat treatment for both the matrix alloy and the composites. T4 treatment looks very interesting. Al-2048 matrix alloy has no effect of natural aging as the properties of the composite by natural aging for one week were tested. The tested data also show that the T4 heat treatment results in low UTS for Al-2048 matrix alloy compared with the T6 treatment. However, the T4 treatment for the composites makes their ultimate tensile strength (UTS) as high as T6 treatment. UTS and final elongation of the three composites under T4 and T6 treatments are shown in Figure 3.

Thus, the T4 treatment is better than the conventional T6 treatment for the composites. The T4 treatment does not look good if an application requires high 0.2% proof stress.

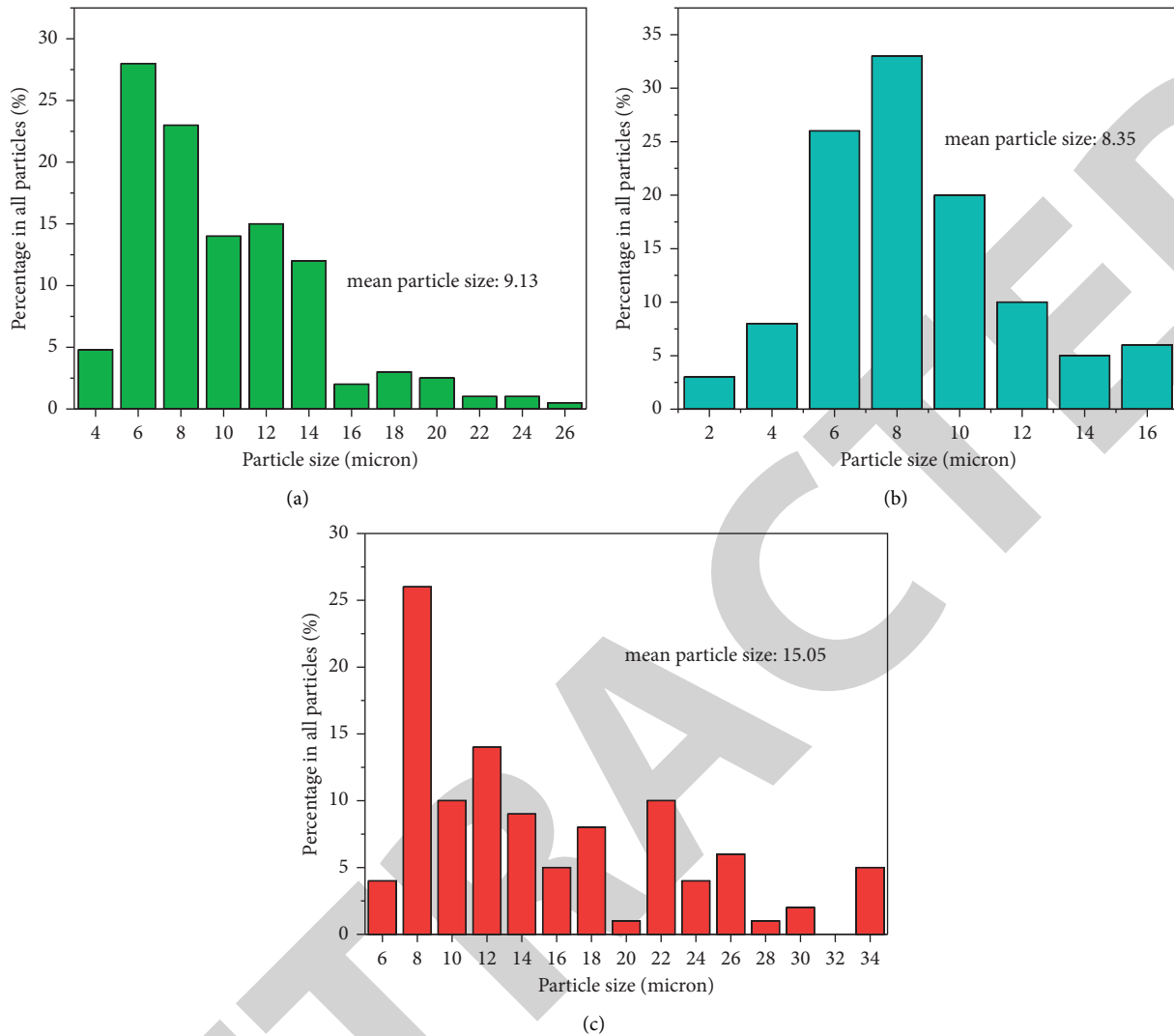


FIGURE 2: Size distribution of reinforcing particles in the composites: (a) 15v% BN/Al-2048, (b) 10v% WC/Al-2048, and (c) 20v% WC/Al-2048.

However, if composite in T4 state is given some prestrain, its 0.2% proof stress can be raised to a higher level. If the T4 composite is given a 0.6% prestrain, its subsequent 0.2% proof stress will be the same as the T6 composite; i.e., 0.8% proof stress of the T4 composite equals 0.2% proof stress of the T6 composite. The subsequent final elongation of the T4 composite should now be the tested elongation (8.24%) reduced by the prestrain of 0.6% which is still 124% larger than that of the T6 composite (3.4%). Therefore, T4 treatment in addition to a 0.6% prestrain is still the best treatment for the composites in the applications requiring a high yield strength. It can be concluded that the T4 heat treatment is more suitable for the composites than the regular T6 approach, though the T6 treatment is the best for the matrix alloy. The work hardening rate of a composite affects its 0.2 percent proof stress significantly, but with no effect on its UTS. The T6 heat treatment differs from the T4 treatment only in the fact that the T6 treatment produces precipitates in the matrices of the composites. It is the precipitates which strengthen the matrix of the composite, increase the work

hardening rate, and lead to high 0.2 percent proof stress of the composites. The precipitates also decrease ductility of the matrix and result in the low final elongation of the composites. The T4 and T6 heat treatments make no difference on UTS of the composites, which implies that it is the reinforcing particles which contribute to high UTS of the composites. Further discussions on strengthening mechanisms will be given in Section 3.5 to interpret the test results.

3.3. Influence of Reinforcement Type on Mechanical Behaviour of Composites. Though comparison of mechanical behaviour of the composites with different types of reinforcement leads to the same conclusions under both T4 and T6 treatments, only the composites under T4 treatment are selected to make the comparison because the study in last section suggests the T4 treatment being the best treatment for the composites. Stress-strain curves of three tested composites under T4 heat treatment are given in Figure 4 to compare the outcome of various types of reinforcements on

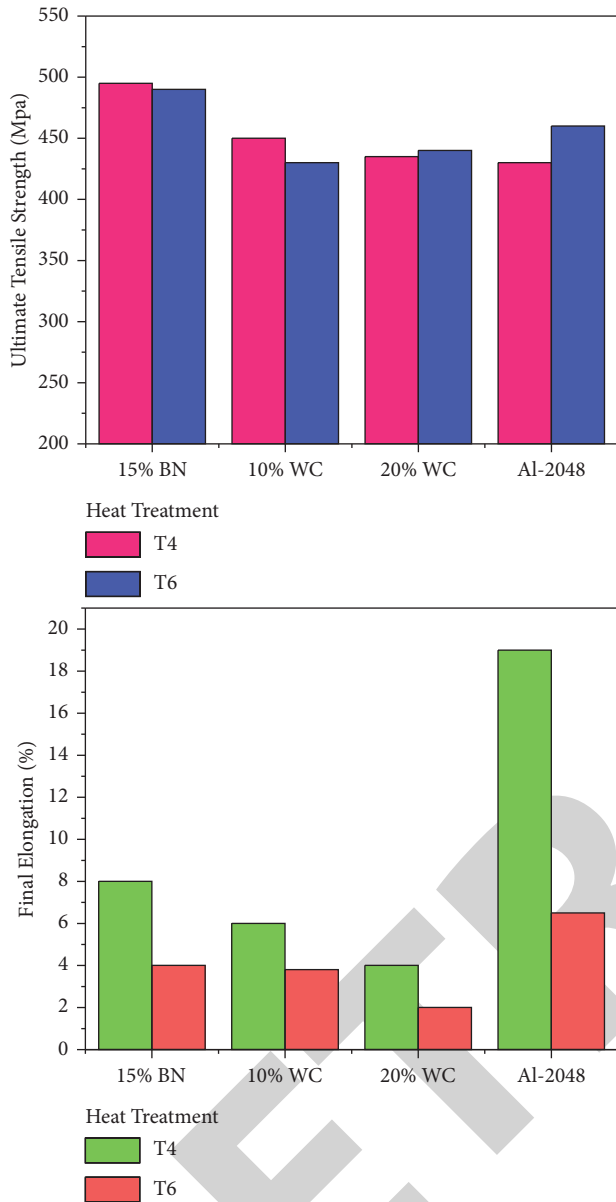


FIGURE 3: Comparison of UTS and final elongation of the composites with different heat treatments at the room temperature.

the tensile properties. It is shown that the 15v% BN/Al-2048 composite demonstrates 9 and 14% increases in UTS and 28 and 120% increases in final elongation over the 10 v and 20v % WC/Al-2048 composites, respectively. It is not easy to fabricate the composites with same volume fraction and same particle size of different reinforcements for theoretical study using industrial facilities, but convincing conclusions can still be deduced based on the above limited test results. It was reported that increasing particle size in a range from 8 μm to 30 μm can result in an increase in the strength of some PR-MMCs. More generally, reduction of the strength is not significantly affected by the particle size of reinforcement at the range of 10~20 μm for most matrix alloys at a volume fraction of reinforcement from 10% to 30%.

The UTS of 15v% BN/Al-2048 is 9% higher than that of 10v% WC/Al-2048 and 14% than 20v% WC/Al-2048, so it

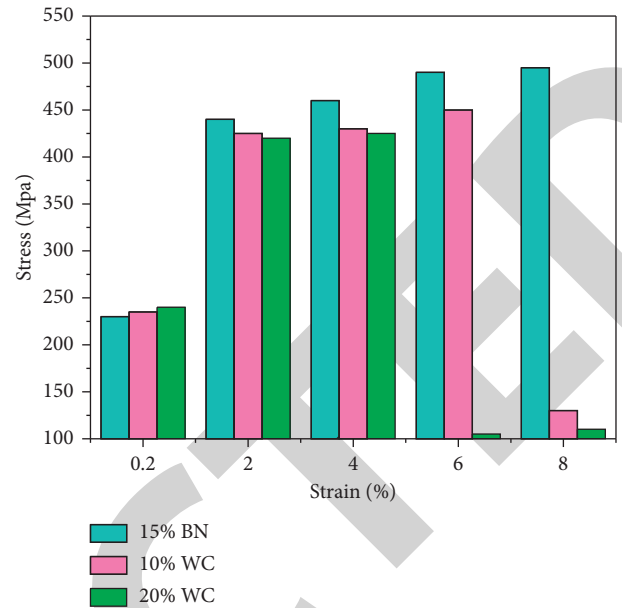


FIGURE 4: Stress-strain plots for all the three tested composites under T4 heat treatment.

can be seen that the BN particles have advantage over the WC particles in increasing strength of the composite, though it is neglected that the particle size is not the same among the three composites. It has been shown that ductility of a PR-MMC always decreases with increasing the volume fraction or/and the particle size. The volume fraction of reinforcement in 15v% BN/Al-2048 is higher than that in 10v% WC/Al-2048 and the average size of reinforcement in 15v% BN/Al-2048 is the about same as that in the latter. Nevertheless, 15v% BN/Al-2048 presents a much larger final elongation over that of 10v% WC/Al-2048. Therefore, it can be concluded that BN reinforcement has advantage of WC reinforcement in both strength and ductility for composite. This is a rather significant cognition. The reasons may rely on reinforcement fracture behavior during composite straining, i.e., the strengthening mechanisms which will be further discussed.

From the data, 20v% WC/Al-2048 shows the highest elastic modulus due to its highest volume fraction of reinforcements among the three composites. The modulus of elasticity of the 15v% BN/AA-2048 composite is only a little higher than that of the 10v% WC/Al-2048 composite. This indicates that BN particles have the same effect on elastic modulus as WC though WC shows a little better effect on stiffness of the composites than BN. The 20v% WC/Al-2048 with high volume fraction and larger element size of the reinforcement increases nothing in its UTS over 10v% WC/Al-2048, but loses nearly a half in its final elongation. This suggests that WC reinforcement is not good at increasing the strength of the Al-2048 alloy even with a 20% volume fraction and the severe ductility deterioration may affect the strength in turn.

3.4. *Damage Evolution of the Composites.* Broken reinforcing particles have almost not been found in all three composites after extrusion, and therefore, the effect of the damage

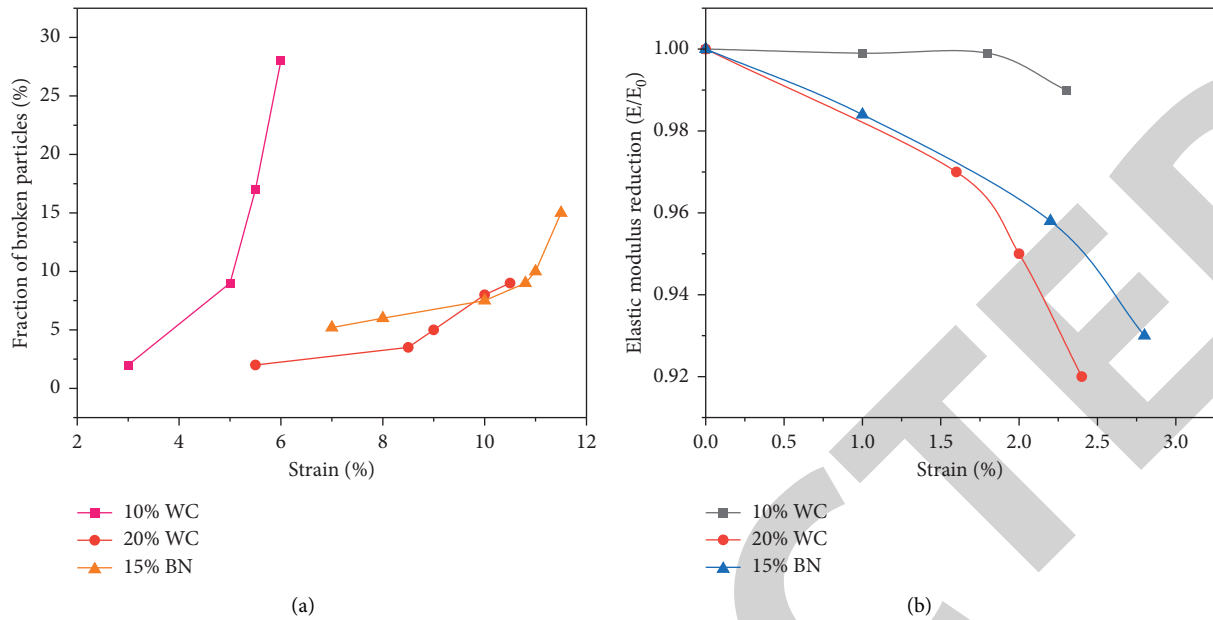


FIGURE 5: Damage evolution in the composites under T4 heat treatments during tensile straining shown by two ways: (a) by the fraction of broken elements as a function of tensile strains and (b) by elastic modulus reduction normalised by the modulus at zero strain during tensile straining.

particles which may occur during composite production on the subsequent damage evolution during mechanical testing of the AMCs has been neglected in this study. Damage evolution examinations were in agreement in only the composites under T4 heat treatment for the same reason that the T4 treatment is most suitable to the composites. The observation on longitudinal section of tensile fractured specimens beneath the fracture surface exposes that there are quite many reinforcing particles cracked in whole necking region, and the farther from the fracture surface, the fewer the cracked particles. The crack of the reinforcement is the only damage mode during deformation except a few shattered and micro voids at particle cluster which can be found just beneath fracture surface. The farther a position is from the fracture surface, the less the strain at that position. Particles cracking and plastic strain are shown to be linked by analysing at least 10 randomized observations across the material at the same strain. The three composites tested under the T4 treatment showed damage progression in the proportion of fractured particles as a function of tensile stresses. It can be seen that the numbers of broken reinforcements in all the three composites are increased with an increase in plastic strain. During tensile deformation, the elastic modulus decreases, allowing us to track the progression of the damage. Using the modulus at zero strain as a reference point, we calculated the modulus reduction data for all composites treated with the T4 treatment. For example, the percentage of broken particles in 10% WC/Al-2048 is lower than that in 15% BN/Al-2048 and 20% WC as a function of strain can be seen in Figure 5. This is consistent with the smallest reduction in E/E_0 of 10v% WC/Al-2048 during straining. It can also be seen that the rate of reduction in E/E_0 of 20v% WC/Al-2048 is faster than that of 15v% BN/Al-2048. The fraction of broken particles in the 20v%

WC/Al-2048 composite as a function of strain is much higher than that in the 15v% BN/Al-2048 composite. Therefore, the reduction in elastic modulus during straining as a damage parameter can be explained qualitatively by the increasing broken reinforcements.

3.5. Strengthening Mechanisms in the Composites. The micromechanical models consider that the increasing in strength of a composite comes only from the increasing in the strength of the matrix caused by the reinforcements; i.e., suppose that the stress in the reinforcements is always the same in the matrix. Our experimental results show that any of the three tested composites under the T4 treatment presents same UTS as under the T6 treatment. The only difference between a T4 composite and its T6 composite is the much softer matrix of the T4 composite. Thus, UTS of the T4 composite should be much lower than that of the T6 composite according to the micromechanical models. The continuum models such as shear lag theory and finite element numerical analysis would fail to explain the high UTS of the T4 composite too if constitutional law of the matrix alloy is used because UTS of the matrix alloy under the T4 treatment is much lower than T6 treatment.

Observation of reinforcements cracking behaviors after tensile fractured beneath fracture surface may reveal messages on the strengthening mechanisms in the composites. The fraction of broken particles is a function of strain in the 15v% BN/Al-2048 composite under the T4 and the T6 heat treatments, respectively, and the 10v% WC/Al-2048 composites. There are many reinforcing particles broken far away from the fracture surface, i.e., at very small strain. Strength of the BN or WC particles in the composites is at least over 1000 MPa and should be about 2000 MPa in

average and much higher than that of the matrix alloy. There exist many broken reinforcing particles far away from the fracture surface, indicating that the stress in the particles is much higher than in the matrix long before tensile fracture. A theory is suggested to interpret the test results that the particulate reinforcements contribute to the strength of a composite mainly by sharing a large part of the total load on the composite. The theory is based on the idea that the strengthening on the composites comes from the reinforcements themselves rather than their effects on increasing the strength of the matrix.

According to Eshelby's equivalent inclusion model, the stress in an elastic particle imbedded in an infinite plastic matrix, σ_p can be expressed by $\sigma_p = X\varepsilon$. And ε is defined as unrelaxed far field strain. In present case, ε can be defined as the accommodation strain which comes from the mismatch strain between the particle and the matrix during composite deformation. Therefore, the BN particles in the 15v% BN/Al-2048 composite under the T4 treatment should share a much larger quotient of the total load on the composite to compensate its soft matrix to result in the same UTS as the composite under the T6 treatment. The particles would share a large load provided a large accommodation strain be located at the interface between the particles and the matrix and at the matrix closely surrounding the particle. In fact, if all the particles in the composite sustain a load close to their strength, the UTS of the composite under the T4 treatment can be as high as 662 MPa according to the rule of mixtures which is much higher than the measured value of 491 MPa. The UTS of the composite is not so high because either the interface cannot accommodate a larger accommodation strain without debonding or the mismatch strain is relaxed plastically in the matrix failing to build up an accommodation strain around the particle large enough to transfer load.

Al-2048 reinforced by BN particles improves both strength and ductility over that reinforced by WC particles. It can be seen by comparing that there are much more broken reinforcing particles in the 15v% BN/Al-2048 composite than in the 10v% WC/Al-2048 composite after tensile test. This indicates that BN particles sustain a much larger load than WC particles in the view of statistics if stress distribution in the two composites is believed to be similar. The assumption is based on the results in the 15v% BN/Al-2048 curve which is very similar to the 10v% WC/Al-2048 curve. Therefore, UTS of the BN particulate-reinforced composite is higher than that of the WC reinforced composite with the same matrix, which implies that the BN interface has better ability to accommodate a large mismatch strain without debonding and strain relaxing than the WC interface. Moreover, fracture toughness K_{Ic} of BN values is typically $4 \text{ MPa m}^{1/2}$ whereas the typical value of WC is $2.5 \text{ MPa m}^{1/2}$ and better toughness of BN particles is another reason for the good reinforcing effects. Finally, lower coefficient of thermal expansion (CTE) of BN particles makes a larger difference in CTE from the Al-2048 matrix than WC particles which results in a higher dislocation density in the matrix around the BN particles. Dislocation network would make the bond between BN particles and the matrix stronger

and would help the load transfer. The high dislocation density increases the matrix strength and also helps to spread the tensile straining over whole composite which would result in high elongation in return.

However, it has to be explained by the above load transfer theory that there are more broken reinforcing particles in 20v% WC/Al-2048 than in 15v% BN/Al-2048. Meanwhile, UTS of 20v% WC/Al-2048 is much less than that of 15v% BN/Al-2048. That the 20v% WC/Al-2048 curve is very different from the 15v% BN/Al-2048 curve indicates a different stress distribution in the two composites during straining so that more broken particles in 20v% WC/Al-2048 do not mean higher load in the WC particles in average than in the BN particles. The broken particles in the 20v% WC/Al-2048 composite are mainly concentrated at the high strain region and there are nearly no broken particles at the low strains; i.e., there is no a platform on the curve. Many localized broken reinforcing particles at the final fracture stage in the 20v% WC/Al-2048 composite imply that the load in a WC particle can reach its strength to break it only at the position where the microvoids coalesce into a fracture surface. Therefore, the UTS of 20v% WC/Al-2048 would be still low without a high load in all the WC particles in average. Particulate reinforcement has a potential to share load but it also has disadvantage of making strain discontinuity in the matrix. The severe strain discontinuity in the matrix caused by the WC particles makes the 20v% WC/Al-2048 a very low final elongation, which means a premature fracture during tensile test. The premature fracture does not allow the matrix to produce a mismatch strain to the particles large enough to transfer a sufficient load from the matrix to all the particles. Therefore, the UTS of 20v% WC/Al-2048 is very low and in that case, the ductility rather than the strength of a matrix plays an important role in increasing the strength of a composite. This can also explain the fact in tested results which reveals that the UTS of the both composites reinforced by WC particles in the T6 condition is less than that of the matrix alloy in the T6 condition, but the UTS of 15v% BN/Al-2048 is higher than that of the matrix alloy.

Decreasing the size of the reinforcing particles can result in an increase in the strength of PR-MMCs in terms of dispersion strengthening. However, some researches have confirmed that the strength of PR-MMCs increases with increasing the reinforcement size when the size is larger than a specific value. This together with our experiments imply that the micromechanisms play an important role on the strengthening for small reinforcing particles in soft matrix, but the load transfer mechanism is the dominant factor for intermediate reinforcement size. On the other hand, the mismatch strain cannot be accommodated at the interface between the particles and the matrix when the reinforcement size is very large, and then, load transfer fails so that the strength of the composite decreases with increasing the size of reinforcement. The specific size values for the strengthening mechanism transformation vary according to different systems and can be calculated by load transfer models such as Eshelby approach and shear lag theory, which would result in the optimal reinforcement design.

4. Conclusions

- (1) Tensile tests show that 15v% BN/Al-2048 composite demonstrates 9 and 14% increases in its UTS and 28 and 120% increases in its elongation over the 10v and 20v% WC/Al-2048 composite, respectively. When it comes to the properties of PR-MMCs, BN reinforcement is superior to WC reinforcement. But BN particles present a slightly weak effect on increasing the elastic modulus of the composites than WC particles.
- (2) UTS of the composites reinforced by both BN and WC particles under T4 treatment are similar to those under T6 treatment, respectively. This difference in final elongation between T4 and T6 treatment is over 100%. T4 treatment is recommended instead of conventional peak-aging for composites (T6). Adding 0.6 percent prestrain to a T4 heat treatment increases the composites' 0.2 percent proof stress to a level comparable to T6 treatment.
- (3) All three tested composites show reinforcing particles damaging gradually during tensile straining. The elastic modulus of the composites has decreased due to the cracking of reinforcing particles.
- (4) Tensile test results of composites with different types of reinforcing particles and various heat treatments can only be interpreted by the theory that a composite's strength is primarily determined by the balance between reinforcing particles sharing the load and creating strain discontinuity of the matrix.
- (5) T4 heat treatment makes the composite more significant final elongation than T6 treatment due to the flexible and soft matrix in the T4 condition. Nevertheless, the strength of the composite in the T4 state with the soft matrix can be pretty high because of reinforcing particles sharing a more considerable quotient of total load, which requires a more considerable accommodation strain around the particles; meanwhile, the strain discontinuity is not as severe as to cause debonding.
- (6) They have a higher K_{1c}, lower thermal expansion, and a better ability to accommodate a considerable mismatch strain at the interfaces, making BN particles the best reinforcement over WC particles in strength and flexibility.

Data Availability

The data used to support the findings of this study are included within the article. Further data or information is available from the corresponding author upon request.

Conflicts of Interest

The authors declare that there are no conflicts of interest regarding the publication of this article.

Acknowledgments

The authors appreciate the supports from Arba Minch University, Ethiopia. The authors thank Sri Sai Ram Engineering College, Chennai; Malla Reddy College of Engineering & Technology, Chonbuk National University, for providing technical assistance to complete this work. This work also supported by the Deanship of Scientific Research, Prince Sattam bin Abdulaziz University, Al-Kharj, Saudi Arabia.

References

- [1] P. Garg, A. Jamwal, D. Kumar, K. Kumar, C. Mustansar, and P. Gupta, "Advance research progresses in aluminium matrix composites: manufacturing & applications," *Journal of Materials Research and Technology*, vol. 8, no. 5, pp. 4924–4939, 2019.
- [2] J. A. Jeffrey, S. S. Kumar, V. A. Roseline, A. L. Mary, and D. Santhosh, "Contriving and assessment of magnesium alloy composites augmented with boron carbide VIA liquid metallurgy route," *Materials Science Forum*, vol. 1048, pp. 3–8, 2022.
- [3] J. Ma, C. Fan, W. Chen et al., "Core-shell structure in situ reinforced aluminum matrix composites: microstructure, mechanical and tribological properties," *Journal of Alloys and Compounds*, vol. 901, Article ID 163613, 2022.
- [4] G. Fenta Aynalem, "Processing methods and mechanical properties of aluminium matrix composites," *Advances in Materials Science and Engineering*, vol. 2020, Article ID 3765791, 19 pages, 2020.
- [5] V. Mohanavel, M. Ravichandran, S. Suresh Kumar, M. Melwin Jagadeesh Sridhar, S. Dineshkumar, and M. M. Pavithra, "Microstructural and tribological characterization of Al/egg shell ash composites prepared by liquid metallurgy process," *Journal of the Balkan Tribological Association*, vol. 26, no. 2, pp. 319–326, 2020.
- [6] M. Kouzeli and A. Mortensen, "Size dependent strengthening in particle reinforced aluminium," *Acta Materialia*, vol. 50, no. 1, pp. 39–51, 2002.
- [7] B. X. Dong, Q. Li, Z. Wang et al., "Enhancing strength-ductility synergy and mechanisms of Al-based composites by size-tunable in-situ TiB₂ particles with specific spatial distribution," *Composites Part B: Engineering*, vol. 217, Article ID 108912, 2021.
- [8] J. Llorca, "An analysis of the influence of reinforcement fracture on the strength of discontinuously-reinforced metal-matrix composites," *Acta Metallurgica et Materialia*, vol. 43, no. 1, pp. 181–192, 1995.
- [9] J. J. Williams, Z. Flom, A. A. Amell, N. Chawla, X. Xiao, and F. De Carlo, "Damage evolution in SiC particle reinforced Al alloy matrix composites by X-ray synchrotron tomography," *Acta Materialia*, vol. 58, no. 18, pp. 6194–6205, 2010.
- [10] M. Antillon, P. Nautiyal, A. Loganathan, B. Boesl, and A. Agarwal, "Strengthening in boron nitride nanotube reinforced aluminum composites prepared by roll bonding," *Advanced Engineering Materials*, vol. 20, no. 8, Article ID 1800122, 2018.
- [11] J. Suthar and K. M. Patel, "Processing issues, machining, and applications of aluminum metal matrix composites," *Materials and Manufacturing Processes*, vol. 33, no. 5, pp. 499–527, 2018.
- [12] V. Mohanavel, Ashraff Ali, S. Prasath, T. Sathish, and M. Ravichandran, "Microstructural and tribological characteristics of AA6351/Si₃N₄ composites manufactured by stir

Retraction

Retracted: Investigation on Tensile Behaviour of Different Weld Joints through Taguchi Approach

Advances in Materials Science and Engineering

Received 26 December 2023; Accepted 26 December 2023; Published 29 December 2023

Copyright © 2023 Advances in Materials Science and Engineering. This is an open access article distributed under the Creative Commons Attribution License, which permits unrestricted use, distribution, and reproduction in any medium, provided the original work is properly cited.

This article has been retracted by Hindawi, as publisher, following an investigation undertaken by the publisher [1]. This investigation has uncovered evidence of systematic manipulation of the publication and peer-review process. We cannot, therefore, vouch for the reliability or integrity of this article.

Please note that this notice is intended solely to alert readers that the peer-review process of this article has been compromised.

Wiley and Hindawi regret that the usual quality checks did not identify these issues before publication and have since put additional measures in place to safeguard research integrity.

We wish to credit our Research Integrity and Research Publishing teams and anonymous and named external researchers and research integrity experts for contributing to this investigation.

The corresponding author, as the representative of all authors, has been given the opportunity to register their agreement or disagreement to this retraction. We have kept a record of any response received.

References

- [1] S. Kamal, V. Parthiban, G. Puthilibai et al., "Investigation on Tensile Behaviour of Different Weld Joints through Taguchi Approach," *Advances in Materials Science and Engineering*, vol. 2022, Article ID 5258014, 9 pages, 2022.

Research Article

Investigation on Tensile Behaviour of Different Weld Joints through Taguchi Approach

Shoab Kamal,¹ V. Parthiban,² G. Puthilibai,³ M. Thirumal Azhagan,⁴ Neel Kamal,⁵ T. S. Senthil,⁶ and Simon Yishak ⁷

¹Department of Electronics and Communication Engineering, MVJ College of Engineering, Bengaluru, Karnataka 560067, India

²Department of Mechanical Engineering, Agni College of Technology, Chennai, Tamil Nadu 600130, India

³Department of Chemistry, Sri Sairam Engineering College, Chennai, Tamil Nadu 600044, India

⁴Department of Production Technology, Madras Institute of Technology, Anna University, Chennai, Tamil Nadu 600044, India

⁵Department of Electrical and Electronics Engineering, Noida Institute of Engineering and Technology, Greater Noida, Uttar Pradesh 201306, India

⁶Department of Mechanical Engineering, Panimalar Engineering College, Chennai, Tamilnadu 600123, India

⁷College of Engineering and Argo-Industrial Technology, Sawla Campus, Arba Minch University, Arba Minch, Ethiopia

Correspondence should be addressed to Simon Yishak; simon.yishak@amu.edu.et

Received 13 March 2022; Revised 2 April 2022; Accepted 7 April 2022; Published 10 May 2022

Academic Editor: Palanivel Velmurugan

Copyright © 2022 Shoab Kamal et al. This is an open access article distributed under the Creative Commons Attribution License, which permits unrestricted use, distribution, and reproduction in any medium, provided the original work is properly cited.

Friction stir welding is a dependable method of joining metals and other materials. Relatively joint configuration-specific welding process parameters have not yet been tuned. This work is concerned with the Taguchi orthogonal arrays to perform an analysis of variance. In this study, FSW joint configurations of AA6262-T6 Al alloy, such as butt, lap, and T joints, were studied for optimization. An orthogonal array of welds was selected using the Taguchi method. After the welds were constructed, the ultimate tensile strength of each joint was examined for statistical optimization. The lack of parameter optimization studies for butt, lap, and T joints prompted this research to fill the void. As a result, each joint arrangement must be optimised for mechanical properties and a set of parameters must be developed.

1. Introduction

FSW has emerged as a potential replacement for traditional fusion welding techniques. Facing surfaces and the joining line, a spinning tool is introduced into the workpiece, generating a complicated stirring of the material in this solid-state joining procedure [1, 2]. New structural design concepts can be developed using FSW, a joining procedure with good reproducibility that has excellent promise in a variety of industries [3]. Welding aluminium, copper, and magnesium, as well as steel, titanium, and polymers, are important parts of this technology's exploration [4]. To mention a few, the high temperatures reached during the welding process result in FSW having no porous or fragmentation as well as low curvature and excellent mechanical qualities [5]. FSW does not require a shielding gas and it is

also environmentally friendly. It also prevents the flaws created during the metal's fusion and solidification processes. However, incorrectly calibrated process parameters can lead to product failure [6]. Failure to penetrate, fusion, cavities on the surface, and excessive flash and galling on the surface are some of the most prevalent faults related to FSW. To provide adequate process control for industrial use, it is still required to examine factor correlations and their impact on the combined structural rigidity [7, 8].

Figure 1 reveals the schematic diagram of the FSW approach. FSW optimization is the subject of several research works in the literature, most of which concentrate primarily on the butts. For the FSW process, there is a dearth of research into the right identifying the most efficient criteria for a system [9]. The most frequent joint arrangement is the butt joint because it distributes load well and is

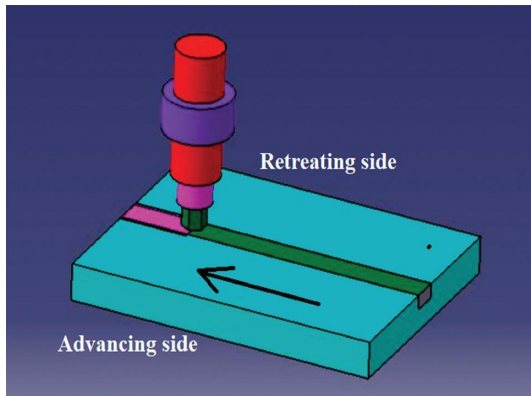


FIGURE 1: Schematic of FSW approach.

simple to set up. It is possible to find numerous examples of this joint arrangement being used in industry [10]. Resistance spot welding (RSW) has been replaced by other methods in the automobile sector. By avoiding the overlapping of two components, the weight of the joint is reduced. Many research works have been published as a result of the possible industrial use of FSW. Erbslöh et al. [11] explored the impact of welding conditions, whereas Acerra et al. [12] studied the mechanical and metallurgical qualities. Papadopoulos et al. [13] explored the production of faults on FSW butt joints of Al-Li alloy, while Zhang et al. [14] investigated the production of deviation occurs flaws. When the shape of the shoulder was analyzed, it was found that AA6262 FSW joints with scrolling or concave shoulders had better tensile properties than those with flat shoulders. A postweld heat treatment on AA6262 FSW joints improved the UTS and hardness, according to Yazdanian and Chen [15]. Using lower welding speeds also helped make this improvement more noticeable.

According to Dhas and Dhas [16], reveal an important geometry because they allow for improved thin skins' moment of inertia and toughness without adding a lot of bulk to the structure. Only a few research works have been done on FS welded T joints. Extruded AA6262-T6 aluminium alloy was tested for bending performance by Rajakumar and Balasubramanian [17]. The FS and MIG welded connections were evaluated. FSW-specific factors were also examined in the study. In cases where the radius of a fillet is to be circular, dissimilar joint studies were also conducted. Cui et al. [18] reported on an industrial case study of incompatible T-shaped pieces linked by FSW in the aerospace industry. The significance of shoulder configuration was also proven, as broader shoulders made it easier to weld accurately. Lap joints are extensively employed in mechanical structures, such as riveted connections or adhesive joints in aeronautical fuselages. The literature on FSW lap joint optimization is sparse. As Heidarzadeh et al. [19] have shown, FSW lap joints are an excellent alternative for riveted joints in primary aeronautical constructions due to their similar joint design. There are two crack-like unwelded areas at the overlap ends of lap joints. Hooking problem is the common name for this issue, which reduces the effective thickness of the sheet, with clear ramifications for the joint's

strength, as demonstrated by Lee et al. [20]. Probing length and welding speed were explored in [21] to see if they affected hooking phenomena. Longer probes did not result in stronger joints because of the amount of plastic agitated by a shorter probe length. Probe length and rotational speed were shown to be the two most important considerations.

Taguchi is the process optimization approach employed. The number of experiments can be reduced using design of experiment (DOE) procedures to save time and money. Taguchi is a frequently used DOE technique for optimizing the processing of materials. According to this method, complex systems can be easily analyzed and optimised using the orthogonal array (OA), fractional factorials that can be calculated via statistical analysis. Using ANOVA, The statistically significant correlation of the common UTS control factors was examined and verified the model's accuracy. The analysis of variance (ANOVA) approach is a standard technique used in association with the "Taguchi" process to validate the percentage contribution of each process parameter on the intended outputs. The use of Taguchi for the design of experiments to predict the mechanical properties of FSW has already been studied by several authors. On the other hand, this research focused primarily on improving the butt joint. In the investigations in references [22, 23], the welding and rotational speeds had a substantial impact on joint tensile strength. Taguchi can be utilized for this purpose. According to the study by Rajakumar and Balasubramanian [17], the Taguchi approach was used to optimise the FSW procedure for aluminium alloy joints. Welding parameters for AA6061 alloy were determined to be 1178 rpm, 115 mm/min, and 8.2 kN. The aim of this work is to make three possible joints of butt, lap, and T joint for AA6262-T6 that can be optimised for the tensile strength in the FSW process.

2. Experimental Works

Joints such butt, T, and double-pass overlap were employed for the welds, as depicted in Figure 2. For the welds on the butt and T joints, 3 mm thick aluminium alloy plates were employed; in contrast, 2 mm thick plates to create the lap joints were employed. The mechanical properties of the alloy utilized in this application are mentioned here. Probe penetration control was used to ensure that the welds were made in the correct rolling direction. Table 1 displays the factors used in the creation of each joint, along with a comparison of their values. Aspect and dimension (probe/shoulder ratio), determined by shoulder diameter fluctuation) were kept constant. Unlike butt joints, where a wide nugget (bigger joint surface) is the primary goal, lap joints are focused on minimizing or eliminating the hook defect, which has a significant impact on joint strength. The joint fillets and tunnel faults and bond defects must be avoided in T joints. There was no study conducted on the effect of the shoulder diameter on lap joints, thus it was kept at 15 millimetres. The distance between the two weld runs (weld beads) was evaluated as a parameter for this joint arrangement. An OA determining the optimal set of

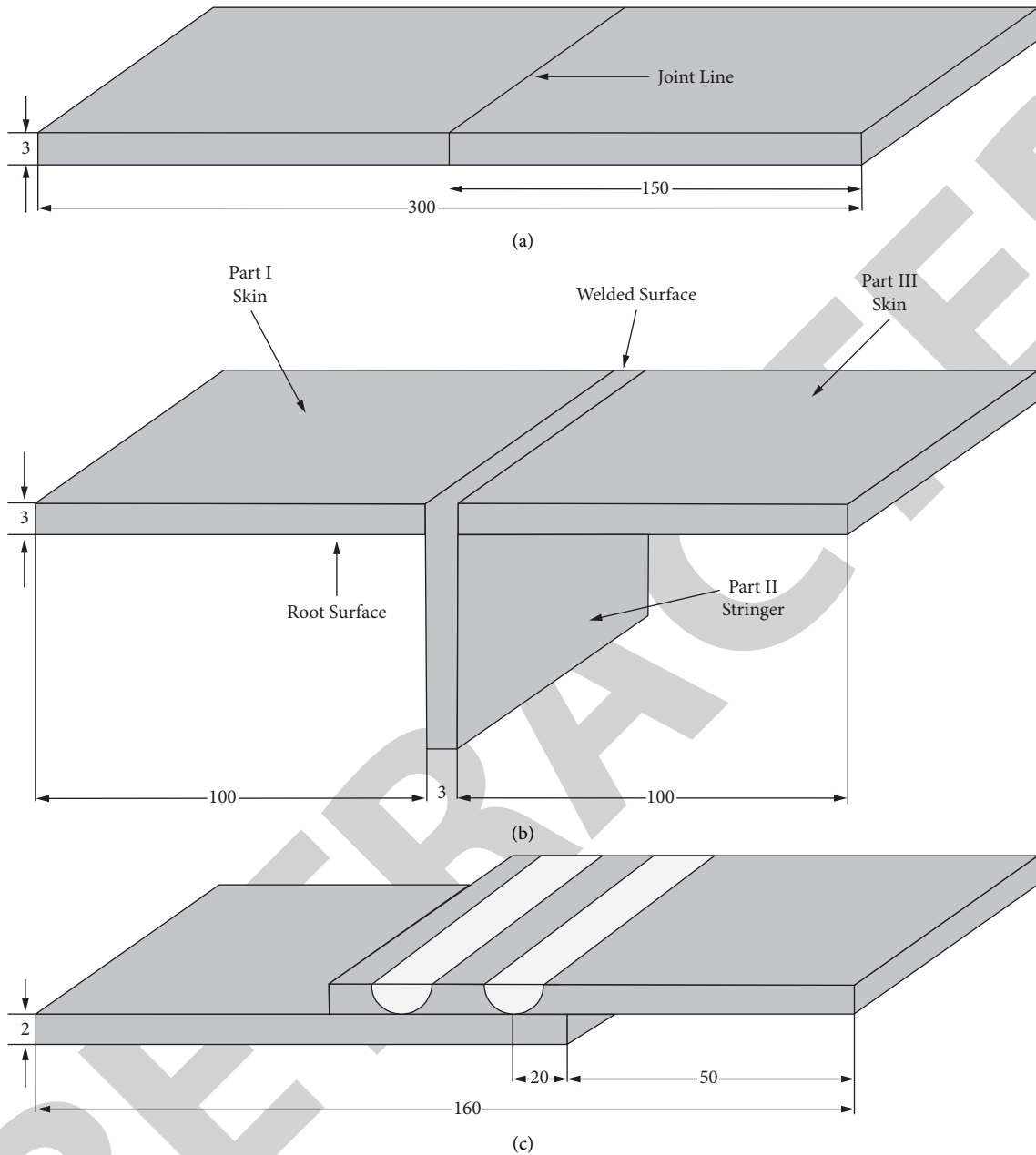


FIGURE 2: Joint configurations of (a) butt joint, (b) T joints, and (c) lap joints are employed.

variables was selected for each joint arrangement. Welded together were 27 butt and T joints and eight lap joints. After the welding process was completed, we performed tensile testing. Samples were machined transverse to the weld line in accordance with ASTM E8-M. Butt and T joints were constructed with a 60 and 12.5 mm-wide section length, respectively, to save space. Skins were loaded perpendicular to the stiffener in T joints with a 10 mm-high stiffener. The tensile specimens for lap joints have a diameter of 20 mm. Tensile testing was carried out at a cross-head speed of one millimeter per minute. For the purpose of performing an ANOVA with a 95% confidence interval, the UTS is used as the response data. As a result of a statistical study known as ANOVA, the impact of each parameter on the UTS was

quantified and the statistically significant difference and insignificance of several variables were determined.

Three parameters were also examined in relation to each other, as well. In all joint designs, we evaluated the impact of tool rotational speed on weld speed. For butt and T joints, there were two additional interactions that were influenced by tool rotating speed (D/d) and welding speed (S/d). Tool rotational speed and welding speed were taken into account while calculating lap joint penetration for lap joints. These analyses allowed us to identify the most important parameters and their interactions on the UTS, which was a significant accomplishment. Mean main effects and inter-parameter plots were used to determine the trend of each parameter's influence on the other parameters.

TABLE 1: Experimental design for each joint arrangement is planned out.

Orthogonal arrays Taguchi	Butt joint L27 (3 ¹³)			T joint L27 (3 ¹³)			Lap joints L8 (2 ⁷)	
	1	2	3	1	2	3	1	2
(A) Rotational speed (rpm)	725	1100	1600	520	1100	1600	830	1600
(B) Welding speed (mm/min)	206	300	380	79	220	400	82	310
(C) Tilt angle (°)	1	2	3	—	—	—	—	—
(D) Probe penetration (mm)	1.95	3.75	3.95	4.0	4.0	4.2	2.8	3.5
(E) Shoulder/probe ratio (D/d)	3.4	3.8	4.4	3.4	3.7	4.6	—	—
(F) Weld run distance (mm)							21	22

3. Results

3.1. Tensile Test Results. According to the OA that was chosen, the tensile outcomes are displayed in Table 2. In the test results, maximum weld joint efficiency was found to be 78% for butt welding, 60% for T joints, and 39% for lap joints.

3.2. ANOVA Analysis. Using a degree of confidence of 90%, ANOVA was conducted to examine the impact of each parameter/user-to-user communication. Analyses of important parameters (90 percent confidence level) yielded these percentages. As far as butt joints are concerned, the shoulder-to-probe diameter ratio appears to be the most important measure. There is a higher percentage contribution ($A * E, B * E$) for these interactions (A, E) in relation to the shoulder/probe diameter ratio; hence, the choice of welding or rotating speed depends on this ratio. The UTS was shown to be influenced primarily by the rotational speed of T joints. As a result, it has a higher percentage of influence on the shoulder/probe diameter ratio, indicating that the two are strongly linked. The welding and rotational rates have a significant impact on the UTS in lap joints, and it is shown in Figure 3.

3.3. Parameter Effect on Butt Joints. According to Figure 4, each parameter and its interactions are plotted in relation to UTS response for different joints. Rotor motion of 1100 rpm was discovered to improve the UTS of butt joints by analyzing the mean plot data. There is a considerable rise in UTS as the rotating speed increases from 735 to 1100 rpm. To get the finest joint mechanical qualities, we welded at a lower speed (206 mm/min). After studying welding speeds and rotational speeds, it was revealed that 1100 rpm with 300 mm/min led to an increase in UTS.

The best depth of probe penetration was found to be 3.75 mm (level 2). This can lead to considerable root deformation, or it can cause tool damage if a probe is too close to its rear plate, causing plastic deformation. Root defects might result from incomplete probe penetration. Because of the friction between the shoulder and the workpiece surface, a larger contact area is necessary to generate more heat in FSW. The usage of a bigger diameter ($D/d=3$) was also found to significantly decrease the UTS. However, as compared to the 15 mm diameter, the 12 mm diameter shoulder ($D/d=3.4$) has no significant impact on the UTS.

TABLE 2: The UTS of a material with different joints.

Trial run number	Ultimate tensile strength (MPa)		
	Butt	T	Lap
1	215	127	98
2	237	146	83
3	234	135	127
4	210	37	126
5	194	148	115
6	217	104	112
7	152	27	102
8	205	113	114
9	211	124	
10	241	162	
11	210	169	
12	238	109	
13	248	135	
14	208	131	
15	249	139	
16	147	131	
17	248	172	
18	251	141	
19	244	162	
20	235	110	
21	197	137	
22	191	141	
23	234	143	
24	174	163	
25	219	150	
26	221	149	
27	231	109	

There were noticeable improvements in joints when 1100 rpm and a 12-millimetre shoulder were combined. Larger shoulder sizes result in reduced UTS only when combined with faster welding speeds, as the two variables interact significantly. Shoulder diameter of 12 mm or 15 mm and probe penetration of 3.75 mm (90 percent plate thickness) should be used in butt welds to achieve high UTS.

3.4. T Joint Impact on Various Parameters. Each parameter and its interactions are plotted in Figure 4. Improved UTS was found to be most beneficial for T joints when rotated at 1100 revolutions per minute (rpm). The optimum joint mechanical qualities were found to be achieved by welding at a low speed. Although similar results were reported for the butt joint analysis, this is not entirely unexpected. It was found that while welding at 1100 rpm or even 1600 rpm, the

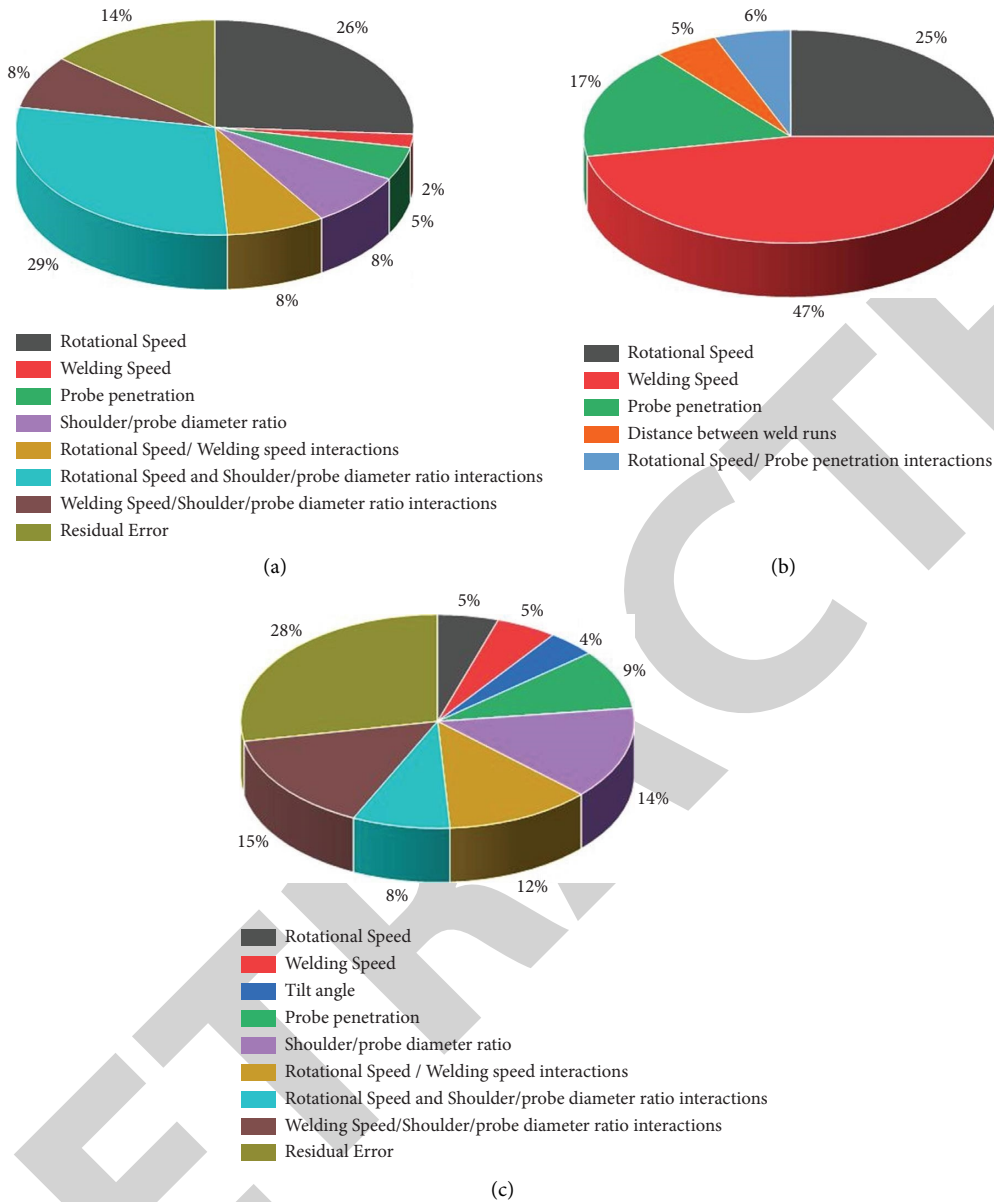


FIGURE 3: Percentage of the contribution of the significant parameters determined from ANOVA analysis for each joint configuration. (a) Butt joint. (b) T joint. (c) Lap joint.

UTS is not significantly affected by welding speed. The increased speed of welding has a clear negative effect on the process when the rotating speed is kept low.

With the average effect of the separate parameters, as well as the interactions between them, it is safe to say that using 1100 or 1600 rpm to weld T joints produces good UTS regardless of the speed used. The corners of T joints must be filled, and hence, the deformation in this place is helpful. Thus, a deeper probe penetration could result in better joints. In the mean plot, you can see this pattern. When comparing shoulder/probe diameter ratios (D/d), the average main effect analysis found that the 15 mm shoulder diameter ($D/d = 3.4$) can produce sound joints, just like butt joints. Smaller shoulder diameters ($D/d = 3.4$) and larger diameters ($D/d = 4.6$) have different compared to the intermediate diameter (15 mm; $D/d = 3.7$) in the T joint arrangement.

It was shown that only when smaller shoulders were used did the speed/shoulder/probe ratio combination have a significant impact on the UTS. Using modest welding speeds in this scenario ensures that the material is heated and mixed thoroughly, resulting in a better joint UTS. Low-diameter shoulders necessitate a high rotational speed, much like when utilizing larger shoulders. Speeds of 79 mm/min, 1100 rpm, 15 mm shoulder diameter ($D/d = 3.7$), and 4 mm probe penetration yield the best UTS in T joint welds (as a percentage of the plate thickness, it is around 130 percent).

3.5. *The Impact of Parameters on the Lap Joints.* The UTS response for lap joints is shown in Figure 5 in average main effect plots and their correlations. Using high rotating rates

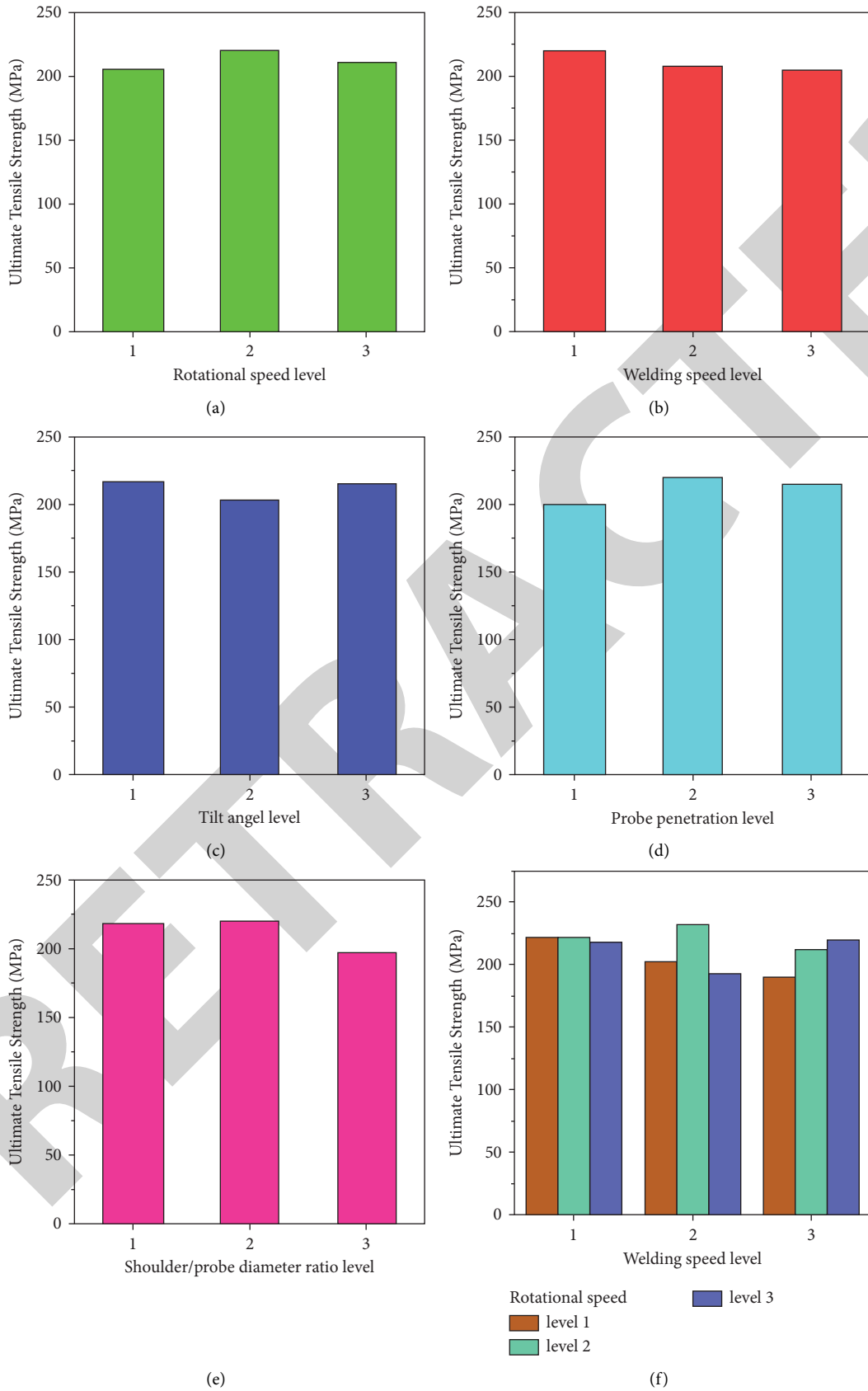


FIGURE 4: Continued.

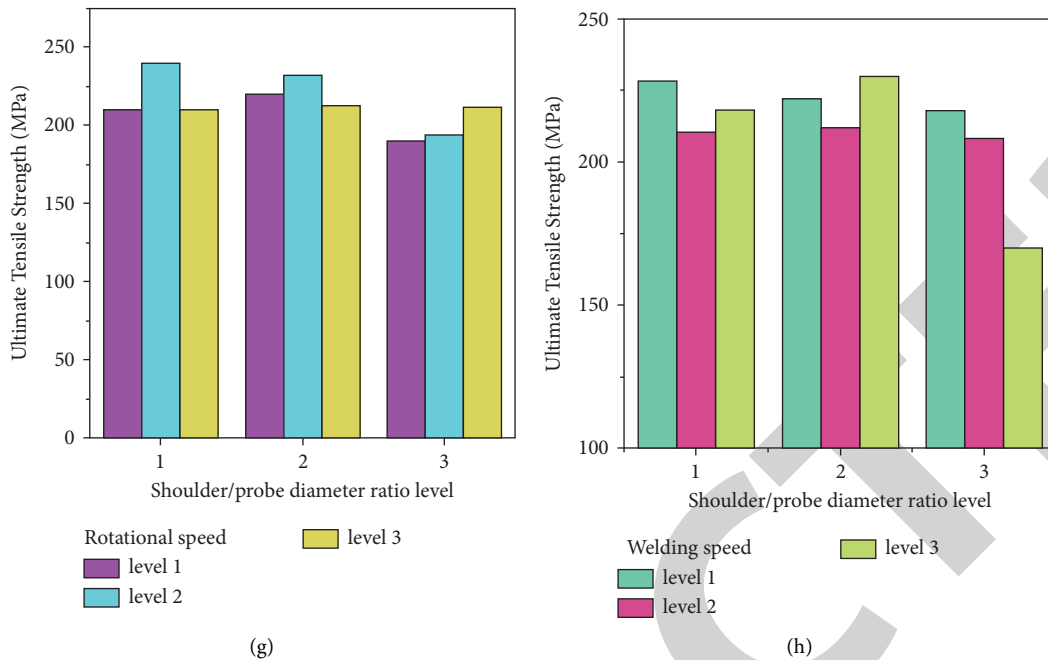


FIGURE 4: Ultimate tensile strength of different weld speeds and diameter ratios.

for lap joints has been proven to yield the greatest results (1600 rpm). Instead of the butt and T joints, welding speeds were found to be on the opposite end of the spectrum. Lap joints can be improved by using high welding speeds. Using the same welding speeds, the best characteristics were generated. It was only in lap joints that double weld runs were applied because of their tendency to form a hooking flaw on the retreating side. The lower UTS was seen when the distance between passes increased.

Neither of the characteristics had a significant impact on each other. Only the estimation of the interplay between rotational speed and probe penetration is of interest here. Only when a high penetration is used can the rotating speed have a major impact, requiring a high rotational speed. High probe penetration depths necessitate faster rotational speeds to agitate huge amounts of material. UTS can be increased by employing 1600 rpm, 3.5 mm probe penetration at 310 mm/min, according to this study (50 percent of plate thickness). In our experiments, we observed that the welding and rotational speeds had little effect each other. These settings were discovered to be the right quality: 1600 rpm and 310 mm/min.

4. Discussion

At weld, the shoulder's contact with the metal plate produces a lot of heat. The right combination of spinning and soldering rates is crucial in order to minimize heat input. Due to the greater friction surface, a big shoulder generates more heat. The time allotted for heating the material is determined by the welding speed. The use of high welding speeds may result in poor joint efficiency. It is also important to note that the rotating speed is directly linked to heat generation through friction; increasing the speed results in more

friction, which results in more heat being generated. Slower rotational rates might result in turbulence in the material flow, whereas higher speeds can cause higher temperatures. In both cases, joint mechanical characteristics may be compromised.

It is one of the most essential factors in determining the amount of heat that can be generated. There is a reason why the butt and T joint configurations have differing effects on the shoulder diameter. A diameter of 15 mm was found to be ideal for both types of joints. As for T joints, smaller diameters should be avoided, whereas larger dimensions should be prevented in butt joints. As opposed to T joints, which require the heat of three pieces, butt joints only need two. Consequently, in T joints, tiny shoulder diameters do not produce enough heat and are thus undesirable. In order to meet the joint fillets, forging activity is required; it takes more heat input to make FSW T joints. Large shoulder diameters are therefore advised.

Depending on the type of joint, heat and flux stirring needs can vary widely. The material must flow upwards in T and lap joints, while flux is required only in butt joints. It is dependent on the thermal conductivity and volume of heated material on how much heat is required for each joint design. The heating requirements in the mixing zone are the key difference between butt and T joint setups in terms of parameter values. Depending on the joint type, a good AA6262-T6 aluminium alloy flow is achievable by using rotating speeds ranging from 1100 to 1600 revolutions per minute and welding speeds ranging from 220 to 310 millimetres per minute as well as penetration of the probe and a shoulder of 15 mm. There are a number of variables that must be kept constant for these findings to hold up. For example, the tool geometry and joint configurations.

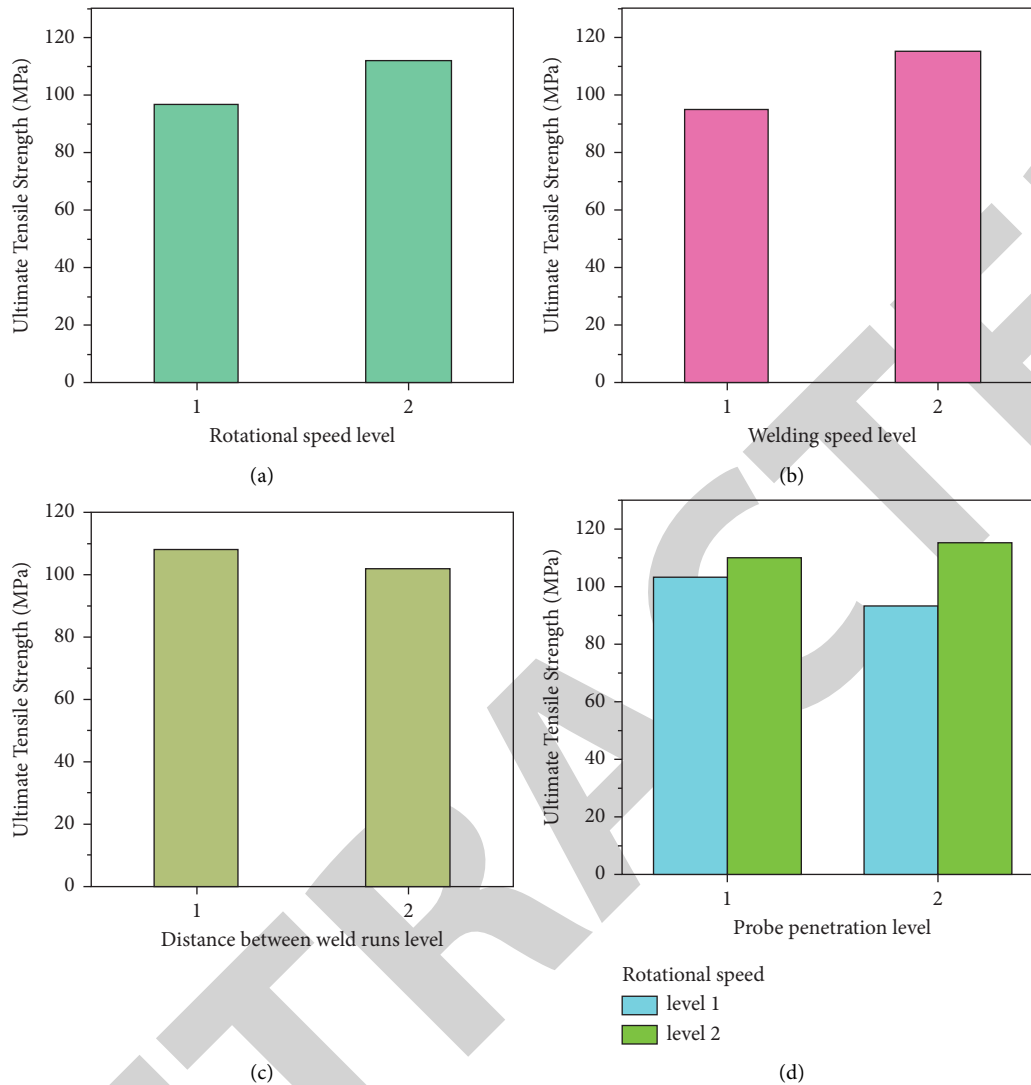


FIGURE 5: (a-d) Lap joint trend analysis of the mean main effect of the different parameters.

5. Conclusions

In three configurations, the Taguchi design of the experiment (DOE) was suitable for optimizing FSW aluminium welding joints. The contribution of each parameter was calculated, and the major and minor parameters were found. The influence on UTS was calculated using the mean main effects and interactions for each parameter. As far as welding parameters, the most critical factors are spindle speed, arc voltage, and shoulder diameters. Under these conditions, butt joints can reach the maximum UTS at 1100 rpm (300 millimetres per minute), 15-millimetre shoulder, and 3.75-millimetre probe penetration. Higher UTS can be achieved by welding T joints at rates ranging from 79 to 220 mm/min at a rotational speed of 1100 rpm, with a shoulder diameter of 15 mm and a penetration depth of 3.5 mm. 1600 rpm, 310 mm/min provides the best UTS in lap joints. Welding with different joint configurations requires varied parameter values to meet the area's thermal and material flow requirements.

Data Availability

The data used to support the findings of this study are included in the article. Should further data or information be required, these are available from the corresponding author upon request.

Conflicts of Interest

The authors declare that there are no conflicts of interest regarding the publication of this paper.

Acknowledgments

The authors thank Arba Minch University, Ethiopia, for the research and preparation of the manuscript to complete this work. The authors also thank the MVJ College of Engineering, Agni College of Technology, Madras Institute of Technology, Anna University, and Noida Institute of Engineering and Technology for the support in completing the work.

Retraction

Retracted: Application of Regression Analysis to Identify the Soil and Other Factors Affecting the Wheat Yield

Advances in Materials Science and Engineering

Received 26 December 2023; Accepted 26 December 2023; Published 29 December 2023

Copyright © 2023 Advances in Materials Science and Engineering. This is an open access article distributed under the Creative Commons Attribution License, which permits unrestricted use, distribution, and reproduction in any medium, provided the original work is properly cited.

This article has been retracted by Hindawi, as publisher, following an investigation undertaken by the publisher [1]. This investigation has uncovered evidence of systematic manipulation of the publication and peer-review process. We cannot, therefore, vouch for the reliability or integrity of this article.

Please note that this notice is intended solely to alert readers that the peer-review process of this article has been compromised.

Wiley and Hindawi regret that the usual quality checks did not identify these issues before publication and have since put additional measures in place to safeguard research integrity.

We wish to credit our Research Integrity and Research Publishing teams and anonymous and named external researchers and research integrity experts for contributing to this investigation.

The corresponding author, as the representative of all authors, has been given the opportunity to register their agreement or disagreement to this retraction. We have kept a record of any response received.

References

- [1] A. Hayat, M. Amin, S. Afzal, A. H. Muse, O. M. Egeh, and H. S. Hayat, "Application of Regression Analysis to Identify the Soil and Other Factors Affecting the Wheat Yield," *Advances in Materials Science and Engineering*, vol. 2022, Article ID 7793187, 10 pages, 2022.

Research Article

Application of Regression Analysis to Identify the Soil and Other Factors Affecting the Wheat Yield

Azhar Hayat ¹, Muhammad Amin ², Saima Afzal ¹, Abdisalam Hassan Muse ^{3,4},
Omer Mohamed Egeh ⁴ and Hafiz Saqib Hayat⁵

¹Department of Statistics, Bahauddin Zakariya University, Multan, Pakistan

²Department of Statistics, University of Sargodha, Sargodha, Pakistan

³Department of Statistics, Pan African University, Institute for Basic Sciences, Technology and Innovation, Nairobi, Kenya

⁴Department of Mathematics and Statistics, Amoud University, Borama, Somalia

⁵Department of Agronomy, Bahauddin Zakariya University, Multan, Pakistan

Correspondence should be addressed to Omer Mohamed Egeh; 1933@amoud.edu.so

Received 21 February 2022; Revised 12 April 2022; Accepted 19 April 2022; Published 10 May 2022

Academic Editor: Palanivel Velmurugan

Copyright © 2022 Azhar Hayat et al. This is an open access article distributed under the Creative Commons Attribution License, which permits unrestricted use, distribution, and reproduction in any medium, provided the original work is properly cited.

In farming and related fields, numerous connections exist that should be distinguished quantitatively. Several factors affect the various crop yields in different dimensions. These factors may have relation with farmer's practices or with quality of soil. In this study, our main focus is to explore the effect of soil and other factors on the wheat yield. Regression modeling plays an important role in the identification of such factors that greatly affect the crops yield. For reliable and valid results, one has to check the data for outliers and other critical results. In this study, we have fitted the regression models with and without satisfying some regression assumptions to determine the factors affecting yield of wheat. For analysis purposes, the required data were collected from the district Multan. It was observed that when the regression assumptions were satisfied, then coefficient of determination (R^2) was improved from 45% to 48%, R^2 (adjusted) was improved from 40% to 46%, and the standard error of the estimates was reduced from 2.772 to 2.649. These results indicate that the soil characteristics, such as saturation, electrical conductivity, organic matter, phosphorus, potassium, calcium carbonate, and micronutrients (zinc, copper, iron, manganese, and boron), are the significant factors for wheat yield. While among all other factors, urea, chemical coating of seed, use of compost, and previously sown crops are the significant factors for wheat yield.

1. Introduction

The agriculture sector plays a key role in the economy of Pakistan as it contributes 19.2% to gross domestic product (GDP) and 38.5% of the labor force is engaged in this sector [1]. It also has a major contribution to the foreign exchange earnings of the country and the development of other sectors. However, nowadays, Pakistan is facing the issues of water stress, pollution, and environmental degradation along with institutional and socio-economic problems; these issues have severely affected the agricultural productivity of the country. Consequently, there is a need for strong strategies and their implementation to improve productivity in the agriculture sector [2].

Wheat is the main food crop of Pakistan, and it dominates all crops in production. According to world population review (2022), Pakistan is ranked at seventh place among the highest wheat-producing countries in the world in terms of yield per acre, area, and production. The mean per capita consumption of wheat in Pakistan is about 125 kg per year and is about 60% of daily food for an average person [3].

The earnings of almost 80% of the farmers in Pakistan are dependent on wheat. It is grown at an area of 9 million hectares that is roughly 40% of the total cultivated land in the country. The wheat crop added about 8.7% to the total value of agriculture and contributes about 2.1% to the GDP [4]. Wheat is considered a staple crop for the countries in

temperate zones and is increasing in demand in the countries that are undergoing industrial and urban development. It is the main source of starch and energy, further it provides essential nutrients like vitamins, dietary fiber, and proteins, which are necessary for human growth [5]. That is why most researchers are strenuous to know factors that increase and decrease wheat production due to its high importance.

Worldwide, several analysts examined the impact of various factors on the yield of wheat. Barzegar et al. [6] investigated the impact of wheat straw, composted sugarcane residue on properties, and yield of wheat in Iran. They applied the split-plot design and found that organic materials increased wheat yield, aggregate stability, water retention, and decrease soil bulk density. Martre et al. [7] proposed mechanistic hypotheses for grain nitrogen accumulation in cereal. The four cultivars were tested in France. The proposed hypotheses were tested with the help of linear regression. It was found that under normal conditions, Arche and Rectal cultivars had the highest grain per year while Tamaro cultivar had the lowest grain per year. Plaut et al. [8] conducted experiments on Suneca and Batavia wheat varieties in Australia. A mechanistic model was developed and showed that kernel number was not affected by water deficit, but high temperature caused a significant reduction in both varieties. Water deficit and the high temperature were also found to increase the relative contribution of transported dry matter to kernels. Leilah and Al-Khateeb [9] explored the association between wheat yield and its components under drought conditions in Saudi Arabia. Multiple statistical techniques including correlation, linear regression, path analysis, factor analysis, cluster analysis, and principal components analysis were used and it was revealed that weight of grain, number of spikes per square meter, and biological yield had the most influence on wheat grain yield indicating that breeding material with these qualities can produce a high yield in drought conditions. Moriondo et al. [10] adapted the use of Normalized Difference Vegetation Index (NDVI) data obtained from the simulation model and satellite platforms for the estimation of wheat yield. This methodology was applied in two high wheat-yielding provinces of Italy. They found that the proposed methodology produced a better accuracy in the estimation of wheat yield. Khan et al. [11] studied the effect of zinc fertilizer at different levels on the yield of wheat in Multan, Pakistan. The difference among these treatments was compared using the least significant differences (LSD), polynomial curve fitting, and coefficient of determination, and it was found that application of 5 kg ha^{-2} of zinc sulphate gave the highest marginal rate of return as compared to other amounts of application of zinc sulphate. Whalley et al. [12] discussed the relation between soil strength and yield of wheat for two different soil types in England. They applied the factorial design and found that soil strength is a good predictor of crop yield irrespective of soil type, water status, and concluded that soil strength seemed to limit crop productivity. Abbas et al. [13] evaluated the influence of trace elements in nitrogen, phosphorus, and potassium absorption on wheat yield. With the help of randomized

complete block design (RCBD) and Duncan's multiple range test, they showed that limited use of iron increased wheat yield. If the application of iron was increased, the effect on the yield was insignificant or undesirable. Hassan et al. [14] conducted a study to find significant factors that were influencing the wheat yield in mixed cropping zones of Punjab. The data were collected from four different districts of Punjab. They applied the linear regression and found that seed rate, cost weedicide that was used, education of farmer, use of nitrogenous fertilizer, rotavator use, and sowing time are the significant factors for wheat yield. Gul et al. [15] explored the effect of foliar application of micronutrients on Ghazanive-98 variety of wheat in Peshawar, Pakistan. They applied the RCBD and found that foliar treatment of micronutrients affected the growth of the wheat variety without causing any effect on the time of growth.

Nadim et al. [16] evaluated the yield characteristics and physiology of the Gomal-8 variety of wheat for different levels of micronutrients in Dera Ismail Khan. With the help of RCBD, they found that the application of Boron produced a higher leaf area index while the application of copper produced a maximum number of tillers causing an increase in wheat yield. Rezaei and Hemati [17] studied the effect of soil properties on wheat yield in Iran. They applied the RCBD, and the results showed that a balanced percentage of sand, clay, and silt provide favorable conditions for the improvement of wheat yield. El-Lethy et al. [18] discussed the potassium impacts on wheat plants under saline conditions in Giza, Egypt. With the help of analysis of variance (ANOVA) and LSD, they concluded that the yield of wheat is decreased significantly in saline conditions, and potassium fertilizer reduces the undesirable effects of salinity. Alam and Salahin [19] conducted a series of experiments to study the effect of soil density and moisture retention on wheat yield in Bangladesh. They applied the multiple regression models and found that wheat yield almost doubled from lowest soil depth to highest soil depth. Muarya et al. [20] conducted a field experiment during the Rabi season in Kanpur to study the influence of potassium levels on wheat yield and growth. Using factorial RCBD, it was observed that the application of 80 kg ha^{-1} of potash (K_2O) produced the highest grain yield, straw yield, and biological yield compared to 0, 40, and 60 kg ha^{-1} application of K_2O . Limon-Ortega and Martinez-Cruz [21] studied the impact of nitrogen on wheat yield in Mexico. The data were analyzed through ANOVA. It was found that nitrogen sources impacted wheat yield and the number of spikes based on soil reaction while the fungicide spray had a positive influence on the wheat yield.

Ghadikolayi et al. [22] studied the influence of crop residue and nitrogen on wheat yield in Iran. They applied the RCBD and found that 135 kg/ha of nitrogen gave the highest soil organic matter (OM). It was also found that all of the residues used in the experiment reduced the yield of wheat but the reduction with the use of sunflower residue was lowest compared to other crop residue tested. Sarto et al. [23] investigated the effects of silicate application on soil chemical properties in Parana, Brazil. With the help of regression models and it was concluded that the calcium/magnesium silicate in acid clayey soil improves the yield of

wheat. However, the soil with pH higher than 5.3 and high silicon does not impact the grain yield of wheat.

Arshad et al. [24] conducted an experiment in Peshawar, Pakistan, to study the interactive impact of zinc and phosphorus on wheat. With the help of LSD test, it was found that 5 kg ha⁻¹ of zinc gave maximum straw yield, but 10 kg ha⁻¹ zinc significantly increased all other indicators of yield. As for phosphorus, 90 kg ha⁻¹ was observed to produce the best results. Mehmood et al. [25] studied the input factors that positively influence wheat production in Bahawalnagar, Punjab. The researchers used the linear regression and found that the sowing method, use of fertilizer, that is, nitrogen and phosphorus, variety of wheat, use of weedicides spray and irrigation mode have a significant effect on the wheat yield. Chairi et al. [26] conducted a study on the genetic gain in yield for durum wheat in three experiment stations in Spain. They considered the linear regression to determine variability in locations for absolute and relative genetic gain (AGG and RGG). The result of the analysis showed that the rate of genetic progress in durum wheat yield has been low in the past decade. Rajcic et al. [27] carried out tests on wheat plants in soil with low pH by applying nitrogen along with phosphorus and potassium fertilizers in Serbia. They applied correlation analysis and found that nitrogen had a significant impact on wheat yield and the treatments where the highest amount of nitrogen was applied with other combinations of phosphorus, and potassium had a high yield compared to the lower application of nitrogen. Polisetty and Paidipati [28] estimated the trends in the production of wheat using data from four states of India. The trend analysis was conducted using non-parametric methods including Pettitt's Standard Normal Homogeneity, Buishand's range test, and Mann Kendall test. The outcomes of the trend analysis showed that all states under consideration had an upwards trend and indicated an improvement in wheat production. Sial et al. [29] investigated the effect of waste-derived-biochars of milk tea and fruit peels on growth, yield, root traits, soil enzyme activity, and nutrient status of the wheat crop in Shaanxi, China. Eight treatments were analyzed with one-way ANOVA and it was found that plant height, dry weight of root and shoot, chlorophyll amount, grain yield significantly increased using the treatment of milk tea biochar and chemical fertilizer. Ashraf et al. [30] analyzed the input-output flow for wheat production to identify energy-efficient ways through data from Mailsi, Pakistan. It was found through multiple regression models that higher inputs, large fields, high fertilizer application, and tillage operation provided the highest energy outputs with high productivity and efficiency in energy. Zhou et al. [31] studied the relationship between the depth distribution of wheat roots and soil macroporosity in United Kingdom with six varieties of wheat. Two-way ANOVA was used, and it was determined that there was no significant difference in wheat genotypes, and the wheat root system was more affected by the soil macropore system. Recently, Hayat et al. [32] explored the effect of soil properties and other factors on the cotton yield of Pakistan. They observed that EC, pH, saturation, OM, P, Zn, Cu, Fe, and B are the significant factors for cotton yield. They also

found that fertilizer (Nitrophos, nitrogen, and urea), previously sown crops (wheat and corn), type of seed, chemical coating of seed, type of water, way of cultivation, and use of compost are also a significant factors for cotton yield.

As we have seen in the literature that worldwide, mostly researchers studied the effect of individual soil characteristic or two or other factors on the wheat yield separately. No one still studied the joint influence of soil characteristics and other factors on the wheat yield. So, in this study, our main focus is to explore the joint influence of these factors on the wheat yield. To explore the influence of these factors on the wheat yield, we will consider the linear regression model and will identify which factors contribute a significant role in the wheat yield. Moreover, we will also evaluate some of the regression assumptions to obtain the reliable results. These assumptions include no multicollinearity, constant error variance, no autocorrelation, no outlier, and influential observation [33, 34]. In this article, we have paid special attention to the regression model diagnostics and its impact on the wheat yield model for the identification of factors. Regression diagnostics include outliers and influential observations analysis which can affect the model estimates and predicted values. With the presence of these values, the fitted model results may indicate the significance of the factors which are playing no role in the response variables and vice versa.

2. Materials and Methods

The major food producing province of Pakistan is Punjab and is titled as "bread basket" to feed more than 220 million Pakistanis. Wheat is the main cereal crop produced in Punjab.

The investigation zone is in the bond that is made by five rivers of Punjab situated at 30.157 degrees North and 71.524 degrees South with an average elevation of 122 m above ocean level. The region as a zone of about 132.1 km square is partitioned into various tehsils. The normal temperature in the area fluctuates from 20°C to 45°C with normal precipitation of 175 mm a year. This demonstrates that a particular crop cannot be planned to cultivate in the soil for the entire year in the area because climate conditions change drastically. The conditions of this zone in winter are ideal for wheat production.

The population size is 2620 acres of this area, where one acre is taken as a single sampling unit. The sample was taken as 655 and computed using appropriate formula. Systematic random sampling technique was used to collect the soil samples. The sample was collected from every fourth acre using 4 as sampling interval.

It is necessary to maintain the specific concentrations of organic and inorganic matter in the soil for a good yield of crops. Five hundred grams soil was taken from each selected acre of land to measure the variables specified in Table 1. Then these samples were sent to laboratory of the Agriculture Department of Punjab under Agri-Smart project for the computations of the soil characteristics, where they used the several apparatus. The details of apparatus to measure variables related to soil characteristics are presented in

TABLE 1: Apparatus for measuring the soil characteristics

Sr. No	Variable	Apparatus
1	Saturation percentage	<ol style="list-style-type: none"> 1. Polythene sheets 2. Spade 3. Soil auger 4. Moisture boxes/cans 5. Balance 6. Oven 7. Ring stand 8. Funnel (glass or plastic) 9. Tubing (to attach to bottom of funnel) 10. Clamp (to secure tubing) 11. Filter paper (to line funnel) 12. Beakers (250 mL) 13. Graduated cylinder 14. Stirring rod (long)
2	Electrical conductivity	<ol style="list-style-type: none"> 1. Conductivity bridge 2. Vacuum filtration system
3	Power of hydrogen	<ol style="list-style-type: none"> 1. pH meter with combined electrode 2. Beakers: Preferably use polyethylene or TFE beakers 3. Mechanical stirrer, with inert plastic coating 4. Wash bottle, plastic
4	Organic matter	<ol style="list-style-type: none"> 1. Magnetic stirrer and teflon-coated magnetic stirring bar 2. Glassware and pipettes for dispensing and preparing reagents 3. Titration apparatus (burette)
5	Phosphorus	<ol style="list-style-type: none"> 1. Spectrophotometer or colorimeter 2. Standard laboratory glassware: beakers, volumetric flasks, pipettes, and funnels
6	Potassium	<ol style="list-style-type: none"> 1. Flame photometer with accessories 2. Beakers 3. Pipettes and volumetric flasks, as required for dilution and tests of interference effects
7	Calcium carbonate	<ol style="list-style-type: none"> 1. Hot plate 2. Burette 3. Erlenmeyer flask 4. Volumetric pipette
8	Zinc	<ol style="list-style-type: none"> 1. Atomic absorption spectrophotometer 2. Mechanical shaker, reciprocal
9	Copper	<ol style="list-style-type: none"> 1. Atomic absorption spectrophotometer 2. Mechanical shaker, reciprocal
10	Iron	<ol style="list-style-type: none"> 1. Atomic absorption spectrophotometer 2. Mechanical shaker, reciprocal
11	Manganese	<ol style="list-style-type: none"> 1. Atomic absorption spectrophotometer 2. Mechanical shaker, reciprocal
12	Boron	<ol style="list-style-type: none"> 1. Porcelain crucibles 2. Spectrophotometer 3. Polypropylene test tubes

Table 1. The factors estimated for each sample of soil attributes incorporate OM, phosphorous (P), potassium (K), and calcium carbonate (CC). The significant micronutrients in the soil that were estimated from each sample include zinc (Zn), copper (Cu), iron (Fe), manganese (Mn), and boron (B).

The information related to the utilization of fertilizer, such as DAP, potash, urea, Nitrophos, and nitrogen manures in the land per section of land is also collected from the farmers. The data about the recurrence of pesticides and water systems and strategy for the water system, that is, tubewell water or trench water were gathered. The information about the crop sown before wheat, seed type, that is, coated

or uncoated, the technique for cultivating, that is, penetrating or drilling sowing strategy, and utilization of fertilizer in the land were also collected. Further details and descriptions about these factors are given in Table 2.

3. Results

Descriptive analysis of all considered variables is given in Table 3. The descriptive statistics include average, standard deviation, coefficient of variation, maximum, minimum, range skewness, and Kurtosis. The average wheat yield in this area is found to be 41.87 mund/acre with a standard deviation of 3.66. The average saturation is 37.75% which

TABLE 2: Description of wheat yield and its associated factors.

Name of variable	Notation	Nature of variable	Unit of variable
Saturation (%)	—	Continuous	—
Electrical conductivity (dsm-1)	EC	Continuous	—
pH	—	Continuous	—
Organic matter (%)	OM	Continuous	—
Phosphorus	P	Continuous	Ppm
Potassium	K	Continuous	Ppm
Calcium carbonate (%)	CC	Continuous	—
Zinc	Zn	Continuous	Ppm
Copper	Cu	Continuous	Ppm
Iron	Fe	Continuous	Ppm
Manganese	Mn	Continuous	Ppm
Boron	B	Continuous	Ppm
Nitrophos	—	Discrete (frequency)	50 kg per acer
Nitrogen	—	Discrete (frequency)	50 kg per acer
DAP	—	Discrete (frequency)	50 kg per acer
Potash	—	Discrete (frequency)	50 kg per acer
Urea	—	Discrete (frequency)	50 kg per acer
Last crop	—	Discrete (frequency)	—
Water frequency	—	Discrete (frequency)	—
Pesticide frequency	—	Discrete (frequency)	—
Chemical coating of seed	—	Categorical	—
Type of water	—	Categorical	—
Way of cultivation	—	Categorical	—
Usage of compost	—	Categorical	—
Wheat yield per acre	—	Continuous	Munds

Note: Ppm = “parts per million”.

TABLE 3: Descriptive statistics of the consider characteristics.

Variables	Average	SD	CV	Minimum	Maximum	Range	Skewness	Kurtosis
Wheat yield	41.87	3.66	0.09	29.00	50.00	21.00	-1.41	-2.00
Saturation (%)	37.75	3.82	0.10	21.00	45.00	24.00	-4.81	-1.98
EC (dsm-1)	4.24	3.97	0.94	0.20	22.00	21.80	22.18	25.53
pH	8.26	0.29	0.03	7.20	9.00	1.80	-1.13	-2.66
Org. M. (%)	0.55	0.15	0.27	0.12	1.09	0.97	3.73	1.51
Phosphorus (ppm)	8.20	3.26	0.40	1.40	23.50	22.10	13.90	14.43
Potassium (ppm)	176.10	74.81	0.42	78	380.00	302	1.081	-0.058
CC (%)	6.36	1.43	0.23	2.80	13.20	10.40	5.37	6.84
Zinc (ppm)	0.78	0.22	0.28	0.10	1.00	0.90	-12.34	0.86
Copper (ppm)	0.18	0.02	0.11	0.05	0.32	0.27	-10.10	59.30
Iron (ppm)	4.08	0.68	0.17	0.42	4.93	4.51	-25.64	36.10
Manganese(ppm)	0.89	0.15	0.17	0.07	1.87	1.80	-20.26	51.24
Boron (ppm)	0.46	0.01	0.03	0.39	0.49	0.10	-6.93	2.83
Nitrophos	0.41	0.58	1.41	0.00	2.00	2.00	11.16	0.78
Nitrogen	0.51	0.71	1.40	0.00	3.00	3.00	11.97	1.68
DAP	1.01	0.50	0.50	0.00	3.00	3.00	1.65	8.23
Potash	0.31	0.49	1.60	0.00	2.00	2.00	12.42	1.08
Urea	1.92	0.68	0.35	0.00	4.00	4.00	0.14	3.37
Water frequency	3.40	0.70	0.21	2.00	5.00	3.00	1.61	-0.81
Pesticide frequency	1.93	0.82	0.43	1.00	6.00	5.00	7.32	2.54

means that the soil of this area is loam which indicated that this soil is suitable for wheat. The average value of EC is 4.24 dS/m depicting that there is slight saline soil which is a favorite for wheat. The average pH of the soil is 8.26 indicating that it is difficult for the plant to obtain phosphorus from the soil. The average amount of OM in the soil is 0.55%, which shows that there is a lack of organic components in the soil. The average amount of phosphorus in the soil is

8.20 ppm which is normal. The average amount of potassium in the soil is 176.10 ppm which is good for the soil to be called fertile. The average zinc is about 0.78 ppm in the soil indicating an intermediate amount of the nutrient. The average copper in the soil was found to be 0.18 ppm, which is a satisfactory amount for the fertility of the soil. The average iron in the soil is 4.08. This indicates the soil's high fertility. The manganese in the soil on average is 0.89 ppm which is a

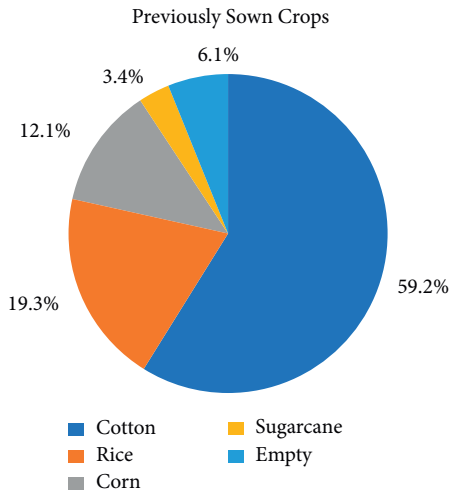


FIGURE 1: Pie chart for previously sown crops.

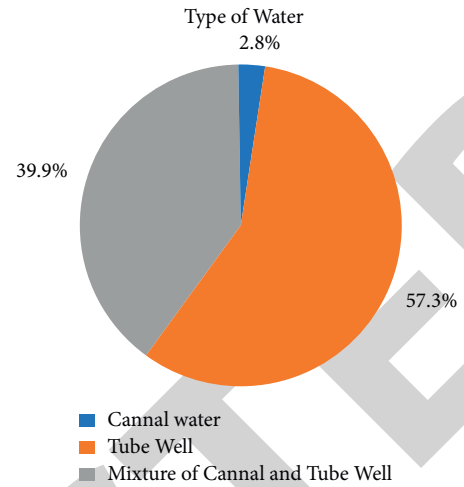


FIGURE 3: Pie chart for the type of water.

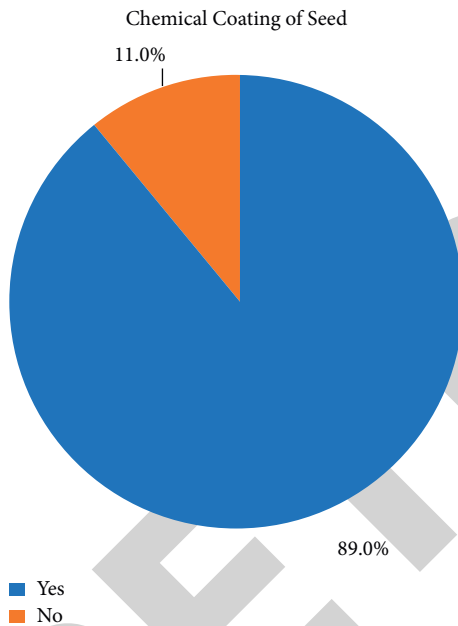


FIGURE 2: Pie chart for chemical coating of a seed.

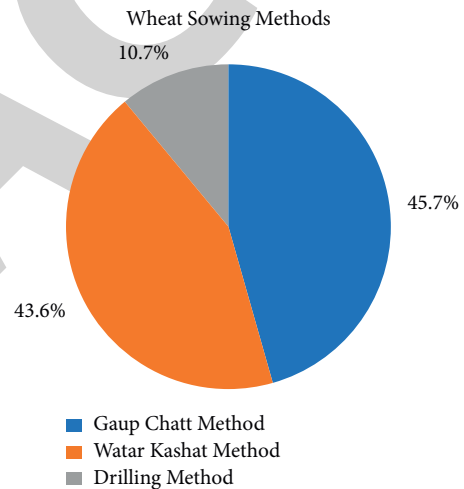


FIGURE 4: Pie chart for wheat sowing methods.

good amount for the fertility of the soil. Finally, the average amount of boron in the soil is 0.46 ppm indicating enough nutrients in the soil. The skewness of most data distribution was positive, and the highest values of the skewness coefficients were EC and phosphorus. Visconti et al. [33] studying soil saturation extracts in Spain, also found higher positive skewness for the soil potassium and attributed this to the fact that fertilizers may have been applied at a higher concentration at some locations. Negative skewness was observed in some factors such as iron (ppm), manganese (ppm), and zinc (ppm).

The summary of some qualitative factors is shown in Figures 1 to 5. Figure 1 shows that cotton was the most common previously sown crop as compared to other crops. From Figure 2, we have found that most of the seeds were chemically coated. Figure 3 displays that most farmers use

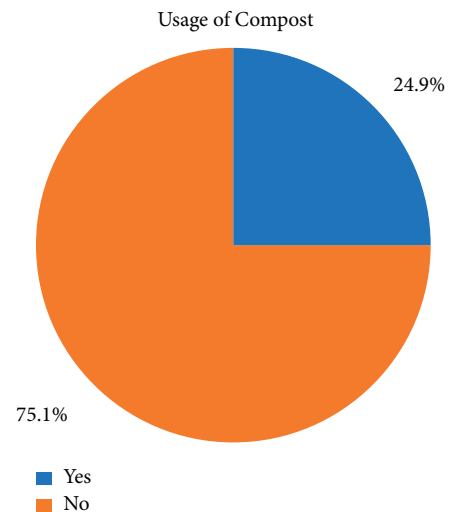


FIGURE 5: Pie chart for using compost.

TABLE 4: Regression analysis with and without outlier.

Term	Full data				After deleting outliers			
	Beta	SE	<i>T</i>	<i>P</i> value	Beta	SE	<i>T</i>	<i>P</i> value
Constant	69.350	6.2800	11.04	0.0000	68.420	6.0800	11.26	0.0000
Saturation (%)	-0.154	0.0335	-4.59	0.0000	-0.145	0.0324	-4.46	0.0000
EC (dsm-1)	0.072	0.0297	2.44	0.0150	0.080	0.0288	2.76	0.0060
pH	2.345	0.4440	5.28	0.0000	2.340	0.4330	5.41	0.0000
Org. M. (%)	1.454	0.7920	1.83	0.0670	1.862	0.7730	2.41	0.0160
Phosphorus (ppm)	-0.263	0.0388	-6.78	0.0000	-0.285	0.0375	-7.6	0.0000
Potassium (ppm)	-0.010	0.0019	-5.18	0.0000	-0.008	0.0019	-4.33	0.0000
CC (%)	-0.494	0.0829	-5.96	0.0000	-0.558	0.0804	-6.93	0.0000
Zinc (ppm)	-4.740	0.5950	-7.97	0.0000	-4.892	0.5810	-8.43	0.0000
Copper (ppm)	-10.740	5.7700	-1.86	0.0630	-11.500	5.6600	-2.03	0.0430
Iron (ppm)	-0.337	0.1670	-2.02	0.0440	-0.357	0.1610	-2.22	0.0270
Manganese (ppm)	-2.137	0.7890	-2.71	0.0070	-1.936	0.7580	-2.55	0.0110
Boron (ppm)	-55.210	9.2800	-5.95	0.0000	-52.210	8.9500	-5.83	0.0000
Nitrophos	0.092	0.2110	0.44	0.6610	0.001	0.2020	0.01	0.9950
Nitrogen	0.140	0.1690	0.83	0.4070	0.069	0.1640	0.42	0.6730
DAP	-0.117	0.2430	-0.48	0.6310	-0.188	0.2360	-0.8	0.4250
Potash	-0.052	0.2360	-0.22	0.8270	0.036	0.2300	0.16	0.8750
Urea	0.298	0.1750	1.70	0.0900	0.525	0.1970	2.66	0.0080
Water frequency	-0.171	0.1680	-1.01	0.3110	-0.277	0.1630	-1.7	0.0900
Pesticide frequency	0.139	0.1360	1.02	0.3080	0.279	0.1430	1.96	0.0510
Last crop								
Rice	0.785	0.2940	2.67	0.0080	0.713	0.2840	2.51	0.0120
Corn	0.299	0.3680	0.81	0.4170	0.493	0.3590	1.37	0.1700
Sugarcane	0.840	0.6280	1.34	0.1820	0.791	0.6010	1.32	0.1890
Empty	0.591	0.4760	1.24	0.2150	0.542	0.4560	1.19	0.2350
Seed chemical coating								
No	-1.031	0.3700	-2.79	0.0050	-0.959	0.3580	-2.68	0.0080
Water type								
Tube well	-0.172	0.6960	-0.25	0.8040	-0.054	0.6660	-0.08	0.9360
Both (tube well and canal water)	-0.350	0.7000	-0.50	0.6170	-0.229	0.6690	-0.34	0.7320
Way of cultivation								
Water kashat method	0.009	0.2410	0.04	0.9700	0.003	0.2340	0.01	0.9900
Drilling method	0.369	0.3940	0.94	0.3490	0.308	0.3830	0.8	0.4230
Compost use								
No	-1.218	0.2570	-4.74	0.0000	-1.167	0.2470	-4.72	0.0000

F (P value) = 17.75 (0.0000), S = 2.772, R^2 = 45.24%, R^2 (adj) = 40%

F (P value) = 19.59 (0.0000), S = 2.649, R^2 = 48.38%, R^2 (adj) = 45.91%

tube-well water in their wheat fields. Figure 4 indicates that most of the farmers use Gaup Chatt sowing method to grow wheat in this area. From Figure 5, we have found that most farmers did not use compost in their fields before sowing wheat.

After the analysis of descriptive statistics, the next step was to identify the contribution of significant variables by fitting a linear regression model to the data of the soil chemical and other characteristics which influence the wheat yield. The results obtained from the linear regression model on full data showed that R^2 of the fitted model explained 45.24% of the variability in wheat yield per acre due to the considered soil and other characteristics. The results of the F -test given in Table 4 show that considered variables contribute a 45.24% role in the wheat yield per acre. The adjusted R -squared statistic, which is a more suitable safeguard, used for not overfitting of the regression model with multiple factors, was 40%. The role of the individual factors

in the wheat yield was also explored. To determine the contribution of variables and identification of most significant variables, we use the t -test, and the results are reported in Table 4. It can be seen that saturation (%), EC, pH, phosphorus, potassium, CC, zinc, iron, manganese, and boron were found to be statistically significant factors at a 5% level of significance. Of these factors, zinc was found to be the most significant factor for wheat yield (see t values and its associated p values). The t value on absolute for this factor is larger than the t values of the other considered factors, and it is already indicated in the literature that zinc contributes a significant role in various crop yields [35–38]. The second-most important factor is soil phosphorous, which contributes a significant role to increase or decrease the wheat yield per acre. The factor previously sown crops (rice), chemical coating of seed (no), and use of compost (no) are statistically significant factors that are increasing the wheat yield. The nutrients organic matter and copper respectively are not play

TABLE 5: Residual analysis for the regression based on full data.

Observation number	Wheat yield	Fit	Resid	Std resid
27	38	43.32	-5.32	-2.01
82	36	41.308	-5.308	-2.02
135	38	43.36	-5.36	-2.05
153	35	40.494	-5.494	-2.06
213	47	41.73	5.27	2.01
302	47	41.454	5.546	2.03
315	37	42.057	-5.057	-2.02
319	36	41.725	-5.725	-2.11
366	35	40.427	-5.427	-2.01
368	38	43.278	-5.278	-2.01
370	38	43.521	-5.521	-2.05
388	36	41.558	-5.558	-2.09
477	50	44.39	5.61	2.07
506	37	42.438	-5.438	-2.0
517	35	40.519	-5.519	-2.03
533	38	43.473	-5.473	-2.08
614	38	43.517	-5.517	-2.05
617	36	41.291	-5.291	-2.03

a significant role in the growth of wheat yield. As well as the impact of some fertilizers namely Nitrophos, nitrogen, DAP, potash, and urea are not beneficial to some extent as compared to the factors discussed earlier.

The regression results are reliable if there is no outlier in the residual. Checking the presence and identification of outliers is the next step. For this purpose, we used standardized residuals. The evaluation of these residuals is given in Table 5. Table 5 indicates that the observation number 27, 82, 135, 153, 213, 302, 315, 319, 366, 368, 370, 388, 477, 506, 517, 533, 614, 617 are identified as outlier.

After identification of these outliers, the output showed the results of a linear regression model to describe the relationship between wheat yield per acre and 13 independents (qualitative and quantitative) variables. Since the p value of the F -test in Table 4 is less than 0.05, there was a statistically significant relationship between the wheat yield and associated factors with the exclusion of substantial values observations. The R^2 indicated that the model as fitted explained 48.38% of the variability in wheat yield per acre. The adjusted R -squared statistic, which was more suitable for comparing models with different numbers of independent variables, was 45.91%. The standard error of the estimate showed the standard deviation of the residuals to be 2.649 which was smaller as compared to model fitted variability with full data. Now we explore the role of the individual factors in the wheat yield. It can be seen from Table 4 that saturation (%), EC, pH, organic matter, phosphorus, potassium, CC, zinc, copper, iron, manganese, boron, and urea were found to be statistically significant factors at a 5% level of significance. One more thing is noted, the role of organic matter, copper, and urea was hidden in the full data set due to the outliers, but after removing the outliers, they are statistically contributing a significant role in the wheat yield.

Now we discuss the effect of farmer-related factors on wheat yield. One factor that is previously sown crop where several crops were indicated. Of these previously sown crops, rice was the most significant as compared to other previously

sown crops which increases the wheat yield. Other previously sown crops also increases wheat yield but not significantly. The second-most important farmer-related factor is chemical coating of the wheat seed which also contributes a significant role in the wheat yield. From Table 4, we observed that the wheat yield of the chemical coating seed was maximum as compared to the wheat yield where the seed is not chemical coated. The use of compost also increases wheat yield. Results indicate that the wheat yield of the land was higher where compost was used than where it was not used. In the similar way, we also study the impact of some fertilizers namely urea, Nitrophos, nitrogen, DAP, and potash on the wheat yield. Table 4 results show that urea fertilizer has a direct influence on the wheat yield while other types of fertilizers are not beneficial to some extent of this land area. Furthermore, water frequency has negative impact on wheat yield, which means that this crop need small water frequency. If we increase the water frequency, then wheat yield may be decreased. Pesticide frequency also has a direct impact on wheat yield. This indicated that several times use of pesticides increases the wheat yield.

After removing all outliers, the results of the fitted model as shown in Table 4 were entirely different as compared to the results of the model fitted to the full data model. On comparing the fitted models as given in Table 4, significant results satisfying the regression assumption outliers were found. It was found that the R^2 and adj R^2 (Adjusted) are increased from (45.24% to 48.38%) and (40% to 45.91%), respectively (Table 4). The standard error of the estimates decreased from (2.772 to 2.649) and indicated better results with satisfying regression assumptions.

4. Discussion

All previous studies for the wheat yield model did not give any attention to regression assumptions and all these factors simultaneously. This study focused on the effect of outliers on the regression analysis to identify the factors which affects the wheat yield. Here, we also studied the effect of outliers on the regression assumptions. We have seen that outliers have strongly affected the model estimates. Also, it can be observed that insignificant factors have turned out to be significant after deleting all these outlying values. After considering the regression assumptions, the significant role of organic matter, copper, and urea from fertilizers can be observed. These variables were insignificant when regression assumptions were not satisfied. These results coincide with previous studies [35–42].

The outliers may also be the cause of multicollinearity, heteroscedasticity, and autocorrelation. It is also observed that after deleting outlying observations, the multicollinearity, heteroscedasticity, autocorrelation, and error variance were reduced substantially. Based on our results, it is found that saturation (%), EC, pH, phosphorus, potassium, CC, zinc, iron, manganese, boron, chemical coating of seed, previously sown crops are the significant factors to change the wheat yield. Based on these results, it may be suggested that in all agriculture-related fields, the

identification and exclusion of outliers is a crucial step for obtaining better results of regression analysis.

5. Conclusion, Limitations, and Future Research

There are various factors which affect the crops yields. These factors include soil characteristics and farmer-related characteristics. As our interest is to identify the soil and other factors which influence the wheat yield. Also identify which one factor(s) are most critical to increase wheat yield which can be helpful for farmer. For the identification of such factors, we considered the regression analysis with the evaluation of outliers. When we ignore the presence of outlier, then the role of some important factors is found to be statistically insignificant. When we consider the outlier and exclude from the data, then these insignificant factors now indicate the significant role in the wheat yield. From the results, we found that saturation (%), EC, pH, phosphorus, potassium, CC, zinc, iron, manganese, boron, chemical coating of seed, and previously sown crops are the significant factors to change the wheat yields. Of these significant factors, more important six factors with order of importance are zinc, phosphorous, CC, pH, boron, and saturation.

This study considered some factors related to wheat yield, there may be other factors which may be related to wheat yield. These factors may be seed variety, land type, bushels, and so on. As our interest was mainly on soil characteristics and some other additional factors, we are unable to collect the information about these factors. This study can also be extended for other crops, such as maize, rice, and others to identify soil related factors and influence on yield. Moreover, such analysis can also be consider by considering some other regression models such as generalized linear models, nonlinear models, and nonparametric regression model.

Data Availability

The data used to support the findings of this study are included within the article.

Conflicts of Interest

The authors declare that they have no conflicts of interest.

References

- [1] Government of Pakistan, "Pakistan Economic Survey 2020-21. Finance Division," 2021, https://www.finance.gov.pk/survey/chapters_21/PES_2020_21.pdf.
- [2] M. Aslam, "Agricultural productivity current scenario, constraints and future prospects in Pakistan," *Sarhad Journal of Agriculture*, vol. 32, no. 4, pp. 289–303, 2016.
- [3] A. Azam and M. Shafique, "Agriculture in Pakistan and its impact on economy. A review," *International Journal of Advanced Science and Technology*, vol. 103, pp. 47–60, 2017.
- [4] Government of Pakistan, "Pakistan Economic Survey 2019-20. Finance Division," 2020, http://www.finance.gov.pk/survey/chapter_20/PES_2019_20.pdf.
- [5] P. R. Shewry and S. J. Hey, "The contribution of wheat to human diet and health," *Food and Energy Security*, vol. 4, no. 3, pp. 178–202, 2015.
- [6] A. R. Barzegar, A. Yousefi, and A. Daryashenas, "The effect of addition of different amounts and types of organic materials on soil physical properties and yield of wheat," *Plant and Soil*, vol. 247, no. 2, pp. 295–301, 2002.
- [7] P. Martre, J. R. Porter, P. D. Jamieson, and E. Tribou, "Modeling grain nitrogen accumulation and protein composition to understand the sink/source regulations of nitrogen remobilization for wheat," *Plant Physiology*, vol. 133, no. 4, pp. 1959–1967, 2003.
- [8] Z. Plaut, B. J. Butow, C. S. Blumenthal, and C. W. Wrigley, "Transport of dry matter into developing wheat kernels and its contribution to grain yield under post-anthesis water deficit and elevated temperature," *Field Crops Research*, vol. 86, no. 2-3, pp. 185–198, 2004.
- [9] A. A. Leilah and S. A. Al-Khateeb, "Statistical analysis of wheat yield under drought conditions," *Journal of Arid Environments*, vol. 61, no. 3, pp. 483–496, 2005.
- [10] M. Moriondo, F. Maselli, and M. Bindi, "A simple model of regional wheat yield based on NDVI data," *European Journal of Agronomy*, vol. 26, no. 3, pp. 266–274, 2007.
- [11] M. A. Khan, M. P. Fuller, and F. S. Baloch, "Effect of soil applied zinc sulphate on wheat (*Triticum aestivum* L.) grown on a calcareous soil in Pakistan," *Cereal Research Communications*, vol. 36, no. 4, pp. 571–582, 2008.
- [12] W. R. Whalley, C. W. Watts, A. S. Gregory, S. J. Mooney, L. J. Clark, and A. P. Whitmore, "The effect of soil strength on the yield of wheat," *Plant and Soil*, vol. 306, no. 1-2, pp. 237–247, 2008.
- [13] G. Abbas, M. Q. Khan, M. J. Khan, F. Hussain, and I. Hussain, "Effect of iron on the growth and yield contributing parameters of wheat (*Triticum aestivum* L.)," *The Journal of Animal and Plant Sciences*, vol. 19, no. 3, pp. 135–139, 2009.
- [14] I. Hassan, M. B. Chattha, T. H. Chattha, and M. A. Ali, "Factors affecting wheat yield: a case study of mixed cropping zone of Punjab," *Journal of Agricultural Research*, vol. 48, no. 3, pp. 403–408, 2010.
- [15] H. Gul, A. Said, B. Saeed, F. Mohammad, and I. Ahmad, "Effect of foliar application of nitrogen, potassium and zinc on wheat growth," *ARPN Journal of Agricultural and Biological Science*, vol. 6, no. 4, pp. 56–59, 2011.
- [16] M. A. Nadim, I. U. Awan, M. S. Baloch et al., "Effect of micronutrients on growth and yield of wheat," *Pakistan Journal of Agricultural Sciences*, vol. 48, no. 3, pp. 191–196, 2011.
- [17] M. Rezaei and Z. Hemati, "Reaction of wheat yield to soil physical and chemical Characteristics in Arak Fields," *World Applied Sciences Journal*, vol. 20, no. 8, pp. 1183–1187, 2012.
- [18] S. R. El-Lethy, M. T. Abdelhamid, and F. Reda, "Effect of potassium application on wheat (*Triticum aestivum* L.) cultivars grown under salinity stress," *World Applied Sciences Journal*, vol. 26, no. 7, pp. 840–850, 2013.
- [19] M. K. Alam and N. Salahin, "Changes in soil physical properties and crop productivity as influenced by different tillage depths and cropping patterns," *Bangladesh Journal of Agricultural Research*, vol. 38, no. 2, pp. 289–299, 2013.
- [20] P. Maurya, V. Kumar, K. K. Maurya, N. Kumawat, R. Kumar, and M. P. Yadav, "Effect of potassium application on growth

Retraction

Retracted: Analysis of Pomegranate Dye Coated Titanium Nanotubes Anode for Solar Cell Application

Advances in Materials Science and Engineering

Received 26 December 2023; Accepted 26 December 2023; Published 29 December 2023

Copyright © 2023 Advances in Materials Science and Engineering. This is an open access article distributed under the Creative Commons Attribution License, which permits unrestricted use, distribution, and reproduction in any medium, provided the original work is properly cited.

This article has been retracted by Hindawi, as publisher, following an investigation undertaken by the publisher [1]. This investigation has uncovered evidence of systematic manipulation of the publication and peer-review process. We cannot, therefore, vouch for the reliability or integrity of this article.

Please note that this notice is intended solely to alert readers that the peer-review process of this article has been compromised.

Wiley and Hindawi regret that the usual quality checks did not identify these issues before publication and have since put additional measures in place to safeguard research integrity.

We wish to credit our Research Integrity and Research Publishing teams and anonymous and named external researchers and research integrity experts for contributing to this investigation.

The corresponding author, as the representative of all authors, has been given the opportunity to register their agreement or disagreement to this retraction. We have kept a record of any response received.

References

- [1] P. Thenmozhi, P. Sathya, S. Meyvel, and S. Thanappan, "Analysis of Pomegranate Dye Coated Titanium Nanotubes Anode for Solar Cell Application," *Advances in Materials Science and Engineering*, vol. 2022, Article ID 3278255, 7 pages, 2022.

Research Article

Analysis of Pomegranate Dye Coated Titanium Nanotubes Anode for Solar Cell Application

P. Thenmozhi,¹ P. Sathya ,² S. Meyvel,³ and Subash Thanappan ⁴

¹Department of Physics, Government Arts College for Women, Salem 636008, Tamil Nadu, India

²Department of Physics, Salem Sowdeswari College, Salem 636010, Tamil Nadu, India

³Department of Physics, Chikkaiah Naicker College, Erode 638004, Tamil Nadu, India

⁴Department of Civil Engineering, Ambo University, Ambo, Ethiopia

Correspondence should be addressed to P. Sathya; sathyameyvel@gmail.com

Received 2 January 2022; Accepted 14 March 2022; Published 6 May 2022

Academic Editor: Palanivel Velmurugan

Copyright © 2022 P. Thenmozhi et al. This is an open access article distributed under the Creative Commons Attribution License, which permits unrestricted use, distribution, and reproduction in any medium, provided the original work is properly cited.

The titanium nanotube array is termed as titanium nanotubes anode (TNTA). Initially, four samples of TNTA were synthesized using electrochemical anodization method. The titanium nanotube arrays (TNAs) were fixed as anode for dye-sensitized solar cell application. The execution of dye-sensitized solar cells (DSSCs) is found on natural dyes removed out from natural materials. Then, pomegranate dye was exclusively prepared and coated on TNTA samples. These are very affordable and inexpensive and are abundantly available in India. The dye coated TNTAs were distinguished using UV-viewable spectrophotometer and SEM test for their spectral effects. The natural dye showed a wide-ranging absorption performance peak between 300 and 574 nm for the second sample and 300–572 nm for third sample. Their solar absorption property was studied.

1. Introduction

Gratzel's Dye-Sensitized Solar Cell (DSSC) emerged in 1991 [1] and came to notice because of its eco-friendly and low manufacturing cost. ADSSC consists of a nanocrystalline semiconductor permable anode soaked with dye, cathode, and an electrolytic solution of iodide and tri-iodide ions, respectively. Sensitizing dyes of DSSC absorb light from solar energy and convert it into electrical energy. Plenty of synthesized organic dyes and metal complexes are used as sensitizers. In spite of high relative efficiency, utilization of valuable material like ruthenium (Ru) complexes makes pitfall of DSSC. Also, its manufacturing cost is high due to the utilization of deficient noble materials. Reports prove that organic dyes are 9.85% efficient and low cost. Low yield and complicated synthesis are the major problem associated with natural dyes. However, it is easy to extract natural dyes from flowers, leaves, and fruits. Because of its low cost, nontoxic, and retro gradations nature, natural dyes have emerged a topic of interest. Till now, several natural dyes like carotene, chlorophyll and so on are used in DSSC as sensitizers.

DSSCs are based on the photo sensitization created by dyes on broad band-gap mesoporous oxide of metal semiconductors; this is because of the dye inclusion value of part of light spectrum noticed [2, 3]. The sensitized dye plays a major role in absorption of sunlight and converting the same into electrical energy. Fabricated metal complexes and various organic dyes like porphyrins [4], phthalocyanines [5, 6], platinum complexes [7], and fluorescent [8] are utilised as sensitizer.

Ru-based complexes sensitizers are extensively used in DSSC application due to their superior efficiency and long lasting nature. However, they also have several disadvantages like high cost, complex extraction methods, and ready to degrade with water [9]. The use of natural pigments as sensitizer is exciting due to its economical impact and environmental concern [10, 11]. Natural dye pigments extracted from vegetables and fruits [12–14] such as anthocyanins and chlorophyll are utilised as natural sensitizers in DSSCs.

About 0.66% transformation efficiency is obtained by utilising natural red Sicilian orange juice dye as sensitizer

[14]. Natural dye sensitizer attained maximum efficiency of 0.70% [15]. Rose Bengal dye produced a maximum efficiency of 2.09% [16]. Coumarin natural dye produced a maximum efficiency of 7.6% [17–20]. This work focuses on the accomplishment of pomegranate natural dye removed out from pomegranate fruit which has been reported as it is inexpensive and abundantly available in India [21]. The achievement of DSSC mainly depends on the dye. The dye must have the essential characteristic like powerful absorption in the visible light spectrum, bear an appropriate fitment of the chemical group, and establish electrons over the semiconductor surface [22–24].

2. Materials and Method

2.1. Electrochemical Anodization Method. In this work, the samples of vertically oriented titanium nanotubes anode (TNTA) have been synthesized by the electrochemical anodization process. In this work, all four samples of size $10 \times 10 \text{ mm}^2$ were used. Mixture of ethylene glycol is used as anodising electrolyte. DI water and NH_4F salt at different proportions. Anodization was performed at different four DC voltages. The experiments were performed at slightly above the room temperature under magnetic agitation. During the characterization, surface morphology and absorbent power of the four samples were studied by HRSEM, and UV-Visible Spectroscopy.

2.2. Preparation of Natural Pomegranate Dye. The sweet pomegranate used in this study was obtained from 7-year-old sweet pomegranate tree grown in India. The samples of pomegranates were collected from a natural source at random. During the 2018 growing seasons, they were harvested. 2 kg of fresh pomegranate was used to coat the single sample, and dye solution weighing 20 g was removed out from 150 ml of DI water at 36°C . This process has taken about 20 minutes. DI water is mixed with pomegranate and introduced into an ultrasonic cleaning machine for 20 minutes at 37 Hz frequency for dye removal under Degass mode. Finally, the solvents are agitated in a centrifugal machine at 250 rpm for 30 minutes.

Solid impurities were removed to obtain a clear dye solution. Pomegranate natural dye has been applied as sensitizers for four TNTA samples. Pomegranate natural dye had been removed out using DI water from the pomegranate fruit. Dye had been applied for TNTA samples and tested characterization of TNTA samples. With the intention of the fine-tuning of this research work, natural dyes are suitable alternative photo sensitizers for titanium nanotubes anode. Natural dyes are an environmental friendly and low cost. Figure 1 shows the pomegranate and pomegranate dye.

All the four samples of titanium nanotubes anode were soaked in pomegranate dye for 12 hours and dried in dark place. Pomegranate dye coated all the four TNTA samples characterizations have been analyzed by using SEM test and UV-Visible Spectroscopy test.

Finally, the UV-Visible Spectroscopy test values of the pomegranate dye coated titanium nanotubes anode

samples were examined. The natural dyes have enhanced the photon energy absorbing capacity of titanium nanotubes anode samples, and it was confirmed from the UV-Visible Spectroscopy results. The natural dye will enhance the solar radiation absorption capability of the titanium nanotubes anode (TNTA) samples. Also, natural dyes will increase the electron flow in the dye-sensitized solar cell. It would enhance the dye-sensitized solar cell (DSSC) execution. Hence, the second sample and the third sample are the best samples, and it would be suitable for solar cell applications.

3. Result and Discussion

3.1. HRSEM Study of TNTA Samples. The high resolution scanning electron microscopy (HRSEM) had recorded the top view images and the cross section images of the four titanium nanotubes anode samples. The HRSEM top view image confirms the formation of titanium nanotubes anode (TNTA) samples, fabricated at 60 V, 75 V, 40–20 V, and 50–25 V. Figures 2 and 3 exhibit the titanium nanotubes.

3.2. SEM Study of Pomegranate Dye Coated TNTA Samples. The scanning electron microscopy (SEM) had recorded the top view images of the pomegranate dye coated four titanium nanotubes anode samples. The SEM top view image confirms the deposition of pomegranate dye uniformly on the titanium nanotubes anode (TNTA) samples, fabricated at 60 V, 75 V, 40–20 V, and 50–25 V. Figures 4 and 5 exhibit the dye coated on the TNTA samples.

3.3. UV Measurements Study of TNTA. UV-Viewable spectrophotometer was utilised to evaluate the absorbance of removed out natural dyes and sensitized photo electrodes. Ultraviolet-visible spectrophotometer device inspected the contact of light radiation with titanium nanotubes anode (TNTA) thin foil in the ultraviolet (200–400 nm) and visible (400–800 nm) range value.

UV-Viewable spectrophotometry is the commonly employed methods in the solar cell research analysis. It includes measuring the amount of ultraviolet or viewable radiation captivated by a titanium nanotubes anode (TNTA) thin foil samples. The device which recorded the ratio of the intensity of two beams of light in the UV-Viewable region area is known as ultraviolet-visible spectrophotometer device.

The absorption spectrum value of the pomegranate dye was noted to know its light absorption performance of the titanium nanotubes anode (TNTA) samples. Figure 6 shows the UV pattern of first TNTA sample with pomegranate dye. The natural dye showed a wide-ranging absorption performance peak value between 300 and 570 nm. The maximum absorption performance value is 570 nm.

The absorption spectrum value of the pomegranate dye was noted to know its light absorption performance of the titanium nanotubes anode sample. Figure 7 shows the UV pattern of second TNTA sample with

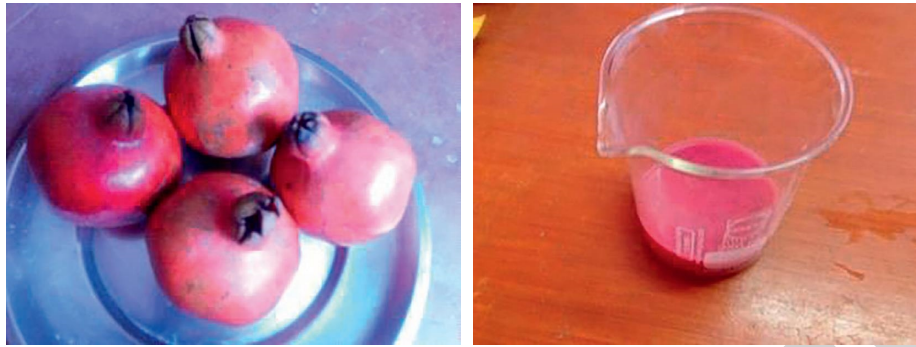


FIGURE 1: Sweet pomegranate and pomegranate dye.

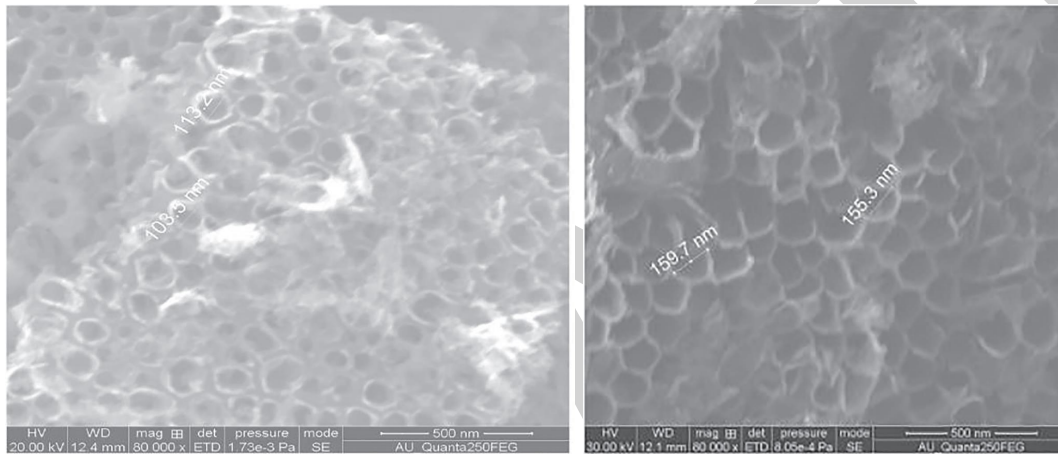


FIGURE 2: HRSEM top view of TNTA fabricated at 60 V and 75 V.

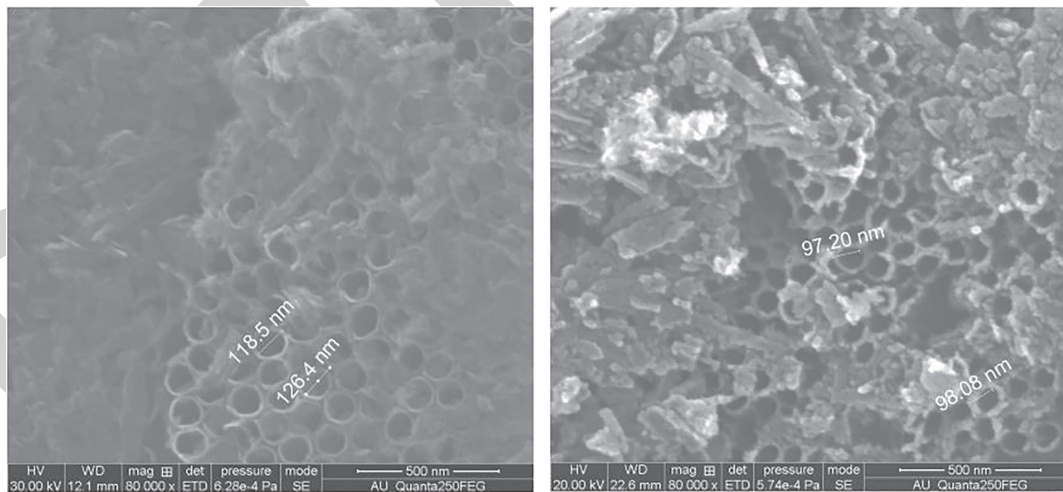


FIGURE 3: HRSEM top view of TNTA fabricated at 40–20 V and 50–25 V.

pomegranate dye. The natural dye showed a wide-ranging absorption performance peak value between 300 and 574 nm. The maximum absorption performance value is 574 nm.

The absorption spectrum value of the pomegranate dye was noted to know its light absorption performance of the titanium nanotubes anode sample. Figure 8 shows

the UV pattern of third TNTA sample with pomegranate dye. The natural dye showed a wide-ranging absorption performance peak value between 300 and 572 nm. The maximum absorption performance value is 572 nm.

The absorption spectrum value of the pomegranate dye was noted to know its light absorption performance of the titanium nanotubes anode fourth sample. Figure 9

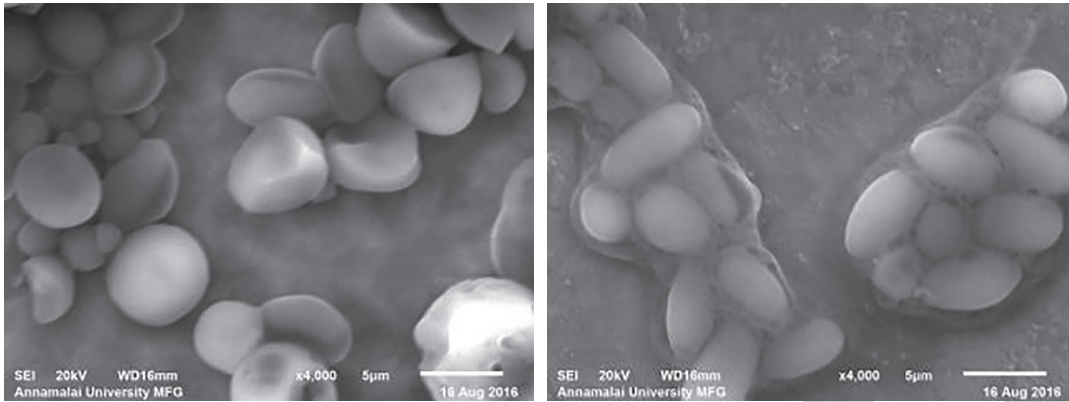


FIGURE 4: SEM image of 60 V and 75 V TNTA with pomegranate dye.

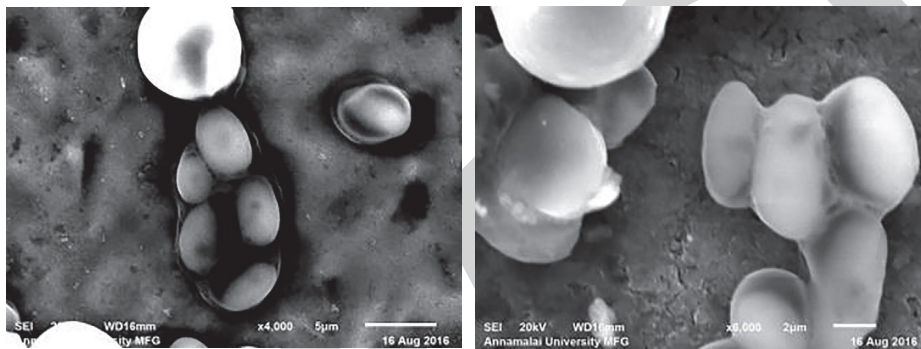


FIGURE 5: SEM image of 40–20 V and 50–25 V TNTA with pomegranate dye.

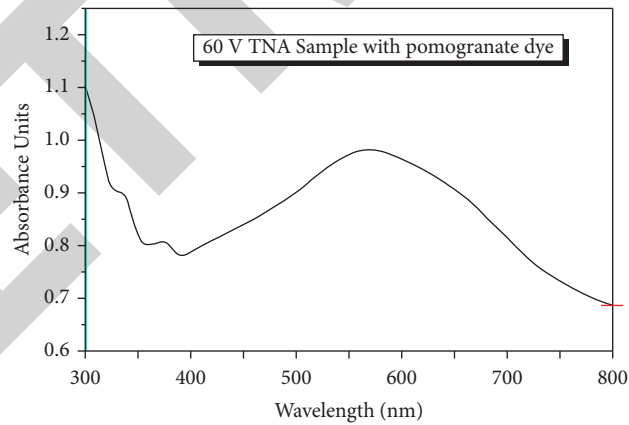


FIGURE 6: UV pattern of TNTA sample fabricated at 60 V with pomegranate dye.

shows the UV pattern of fourth TNTA sample with pomegranate dye. The natural dye showed a wide-ranging absorption performance peak value between 300 and

543 nm. The maximum absorption performance value is 543 nm. Table 1 shows the absorbance data of removed out dye from the pomegranate fruit using DI water.

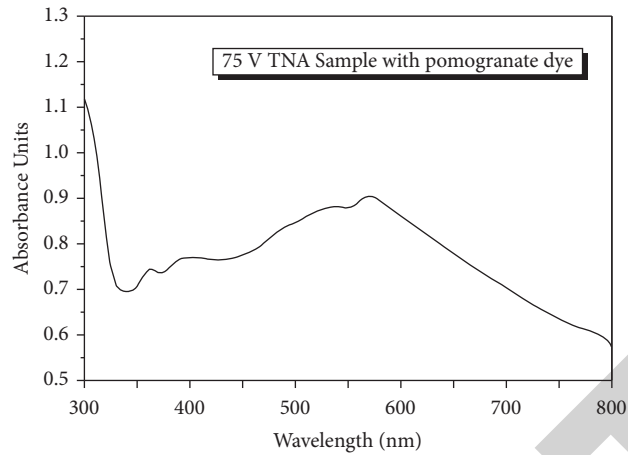


FIGURE 7: UV pattern of TNA sample fabricated at 75 V with pomegranate dye.

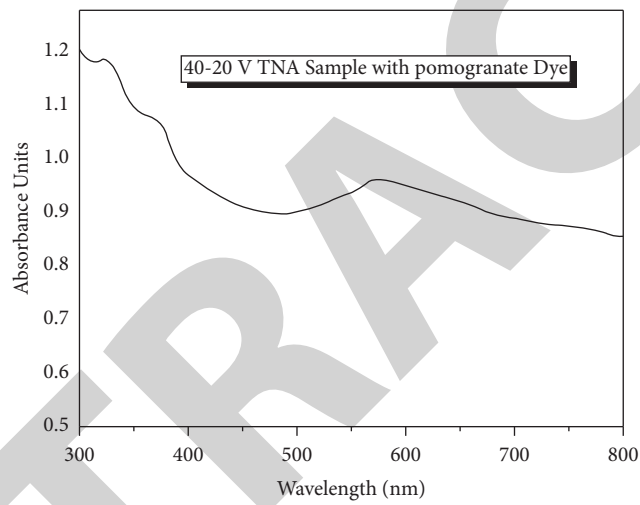


FIGURE 8: UV pattern of TNA sample fabricated at 40-20 V with pomegranate dye.

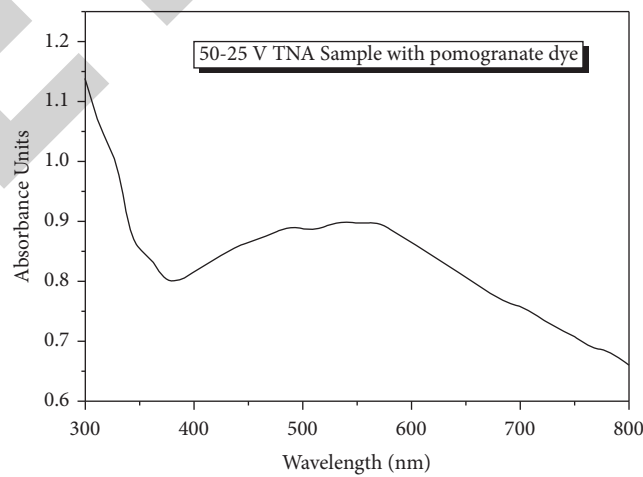


FIGURE 9: UV pattern of TNA sample fabricated at 50-25 V with pomegranate dye.

TABLE 1: Absorbance of pomegranate dye.

Sl. No.	Description	DC volt (V)	Visible light absorption range of sample with pomegranate dye
1	Sample 1	60	300 nm to 570 nm
2	Sample 2	75	300 nm to 574 nm
3	Sample 3	40–20	300 nm to 572 nm
4	Sample 4	50–25	300 nm to 543 nm

4. Conclusion

The natural dyes have enhanced the photon energy absorbing capacity of titanium nanotubes anode samples, and it was confirmed from the above UV-Visible Spectroscopy results. The UV-Spectroscopy test values of the natural dyes coated titanium nanotubes anode (TNTA) samples were examined. The natural dye showed a wide-ranging absorption performance peak between 300 and 574 nm for the second sample. The maximum absorption performance value is 574 nm. The natural dye showed a wide-ranging absorption performance peak between 300 and 572 nm for the third sample. The maximum absorption performance value is 572 nm. The natural dye will enhance the solar radiation absorption capability of the titanium nanotubes anode (TNTA) samples. Also, natural dyes will increase the electron flow in the dye-sensitized solar cell. It would enhance the dye-sensitized solar cell (DSSC) execution. Hence, the second sample and the third sample are the best samples, and it would be suitable for solar cell applications.

Data Availability

The data used to support the findings of this study are included within the article. Further data or information are available from the corresponding author upon request.

Conflicts of Interest

The authors declare that there are no conflicts of interest regarding the publication of this article.

References

- [1] B. O'Regan and M. Grätzel, "A low-cost, high-efficiency solar cell based on dye-sensitized colloidal TiO₂ films," *Nature*, vol. 353, no. 6346, pp. 737–740, 1991.
- [2] M. Rajeshwaran, P. Ganeshan, and K. Raja, "Optimization and biodiesel production from prosopis julifera oil with high free fatty acids," *Journal of Applied Fluid Mechanics*, vol. 11, no. 1, pp. 257–270, 2018.
- [3] N. M. Gómez-Ortiz, I. A. Vázquez-Maldonado, A. R. Pérez-Espadas, G. J. Mena-Rejón, J. A. Azamar-Barrios, and G. Oskam, "Dye-sensitized solar cells with natural dyes removed out from a chiote seeds, Solar Energy Mater," *Solar Cells*, vol. 94, pp. 40–44, 2010.
- [4] I. J. I. P. Kumar, K. Lingadurai, K. Raja, and P. Ganeshan, "Performance and emission characteristics of diesel-soybean methyl ester blends using variable piston geometry in direct injection compression ignition engine," *Asian Journal of Research in Social Sciences and Humanities*, vol. 7, no. 2, pp. 208–227, 2017.
- [5] K. Raja, V. S. Chandra Sekar, V. Vignesh Kumar, T. Ramkumar, and P. Ganeshan, "Microstructure characterization and performance evaluation on AA7075 metal matrix composites using RSM technique," *Arabian Journal for Science and Engineering*, vol. 45, no. 11, pp. 9481–9495, 2020.
- [6] M. D. K. Nazeeruddin, R. Humphry-Baker, M. Grätzel et al., "Efficient near-IR sensitization of nanocrystalline TiO₂ films by zinc and aluminum phthalocyanines," *Journal of Porphyrins and Phthalocyanines*, vol. 3, pp. 230–237, 1999.
- [7] G. Radhaboy, M. Pugazhavadivu, P. Ganeshan, and K. Raja, "Influence of kinetic parameters on Calotropis procera by TGA under pyrolytic conditions," *Energy Sources, Part A: Recovery, Utilization, and Environmental Effects*, vol. 1677812, pp. 1–14, 2019.
- [8] J. He, A. Hagfeldt, S.-E. Lindquist et al., "Phthalocyanine-sensitized nanostructured TiO₂ electrodes prepared by a novel anchoring method," *Langmuir*, vol. 17, no. 9, pp. 2743–2747, 2001.
- [9] A. Islam, H. Sugihara, K. Hara et al., "Dye sensitization of nanocrystalline titanium dioxide with square planar platinum(II) dd complexes," *Inorganic Chemistry*, vol. 40, no. 21, pp. 5371–5380, 2001.
- [10] J. M. Rehm, G. L. McLendon, Y. Nagasawa, K. Yoshihara, J. Moser, and M. Grätzel, "Femtosecond electron-transfer dynamics at a sensitizing dye-semiconductor (TiO₂) i," *Journal of Physical Chemistry*, vol. 100, no. 23, pp. 9577–9578, 1996.
- [11] D. Zhang, S. M. Lanier, J. A. Downing, J. L. Avent, J. Lum, and J. L. McHale, "Betalain pigments for dye-sensitized solar cells," *Journal of Photochemistry and Photobiology A: Chemistry*, vol. 195, no. 1, pp. 72–80, 2008.
- [12] A. Kay and M. Graetzel, "Artificial photosynthesis. 1. Photosensitization of titania solar cells with chlorophyll derivatives and related natural porphyrins," *Journal of Physical Chemistry*, vol. 97, no. 23, pp. 6272–6277, 1993.
- [13] M. K. Nazeeruddin, A. Kay, I. Rodicio et al., "Conversion of light to electricity by cis-X2bis(2,2'-bipyridyl-4,4'-dicarboxylate)ruthenium(II) charge-transfer sensitizers (X = Cl-, Br-, I-, CN-, and SCN-) on nanocrystalline titanium dioxide electrodes," *Journal of the American Chemical Society*, vol. 115, no. 14, pp. 6382–6390, 1993.
- [14] G. Calogero, G. Di Marco, S. Cazzanti et al., "Efficient dye-sensitized solar cells using red turnip and purple wild Sicilian prickly pear fruits," *International Journal of Molecular Sciences*, vol. 11, no. 1, pp. 254–267, 2010.
- [15] I. J. Isaac Premkumar, P. P. Ganeshan, S. Sudhagar, K. Raja, S. Senthil Kumaran, and V. S. Chandra Sekar, "An investigation on Piston structural analysis related with experimental cylinder pressures using different biodiesel blend ratios," *Materials Today Proceedings*, vol. 22, no. 4, pp. 2255–2265, 2020.
- [16] G. Calogero and G. D. Marco, "Red Sicilian orange and purple eggplant fruits as natural sensitizers for dye-sensitized solar cells," *Solar Energy Materials and Solar Cells*, vol. 92, no. 11, pp. 1341–1346, 2008.

Retraction

Retracted: Mechanical Characterization of Biocomposites Reinforced with Untreated and 4% NaOH-Treated Sisal and Jute Fibres

Advances in Materials Science and Engineering

Received 26 December 2023; Accepted 26 December 2023; Published 29 December 2023

Copyright © 2023 Advances in Materials Science and Engineering. This is an open access article distributed under the Creative Commons Attribution License, which permits unrestricted use, distribution, and reproduction in any medium, provided the original work is properly cited.

This article has been retracted by Hindawi, as publisher, following an investigation undertaken by the publisher [1]. This investigation has uncovered evidence of systematic manipulation of the publication and peer-review process. We cannot, therefore, vouch for the reliability or integrity of this article.

Please note that this notice is intended solely to alert readers that the peer-review process of this article has been compromised.

Wiley and Hindawi regret that the usual quality checks did not identify these issues before publication and have since put additional measures in place to safeguard research integrity.

We wish to credit our Research Integrity and Research Publishing teams and anonymous and named external researchers and research integrity experts for contributing to this investigation.

The corresponding author, as the representative of all authors, has been given the opportunity to register their agreement or disagreement to this retraction. We have kept a record of any response received.

References

- [1] D. P. Archana, H. N. Jagannatha Reddy, and B. Paruti, “Mechanical Characterization of Biocomposites Reinforced with Untreated and 4% NaOH-Treated Sisal and Jute Fibres,” *Advances in Materials Science and Engineering*, vol. 2022, Article ID 7777904, 11 pages, 2022.

Research Article

Mechanical Characterization of Biocomposites Reinforced with Untreated and 4% NaOH-Treated Sisal and Jute Fibres

D. P. Archana ¹, H. N. Jagannatha Reddy ¹ and Basavaraju Paruti ²

¹Department of Civil Engineering, Bangalore Institute of Technology, Bengaluru 560004, India

²Department of Hydraulics and Water Resource Engineering, HHOT Campus, Ambo University, Ambo, Ethiopia

Correspondence should be addressed to D. P. Archana; archana3190@gmail.com and Basavaraju Paruti; basavaraj.paruti@ambou.edu.et

Received 23 March 2022; Accepted 21 April 2022; Published 6 May 2022

Academic Editor: Palanivel Velmurugan

Copyright © 2022 D. P. Archana et al. This is an open access article distributed under the Creative Commons Attribution License, which permits unrestricted use, distribution, and reproduction in any medium, provided the original work is properly cited.

Composites reinforced with natural fibres have gained popularity compared to synthetic fibre-reinforced polymer composites due to their environmental sustainability, despite their reduced stiffness and load-bearing capability. In this work, the biocomposites reinforced with sisal and jute fibres which are made by hand layup technique were investigated for mechanical and water absorption characteristics. The effect of a 4 percent NaOH treatment concentration on the aforementioned properties was investigated. The specimens' tensile and flexural broken surfaces were morphologically characterized to investigate microstructural failures. The experimental results show that, compared to untreated fibre-reinforced composites, the biocomposites reinforced with 4 percent NaOH-treated fibre exhibit higher tensile, flexural, and impact strengths, as well reduced water absorption rate. These composites are aimed to be used for strengthening existing civil structures as a retrofitting element.

1. Introduction

Fibre-based composites have been widely investigated from the past many years, and a thorough study into their features and characteristics has permitted their use in a variety of engineering fields [1]. Apart from the major benefits of biocomposites, they also have some drawbacks, such as high moisture absorption, less strength than synthetic composites, incompatibility with fibres and matrices, limitation in processing temperature, quality variability, and less durability. Physical and chemical treatment of fibre is a viable method for overcoming the aforementioned drawbacks [1]. Natural fibre-reinforced composite (NFRC) materials are attracting a lot of attention right now because of its light weight, long life cycle, biodegradability, low cost, and excellent mechanical qualities [2]. These composites are more environmental friendly than synthetic fibre, with lower toxicity, pollution, and recyclability. NFRCs are preferred over synthetic fibre-reinforced composites for current applications because of the aforementioned economic and environmental benefits [3]. NFRCs have been shown to be a good alternative for synthetic fibre-based polymer composites and are used in a variety of

advanced applications in engineering [4]. Due to the intrinsic features of natural fibre, researchers are confronted with various hurdles in the development and implementation of NFRCs. The main challenges include fibre quality, water absorption capacity, thermal stability, and incompatibility in polymer matrices. In view of sustainability, eco-friendliness, and economic standpoint, Khalid et al [2] examined some of the major breakthroughs related to NFRCs. It also involves several chemical treatment processes, as well as the hybridization with synthetic fibres of NFs, which is a highly efficient means of increasing the mechanical characteristics of NFRCs. Vignesh et al [4] used a compression moulding process to make natural fibre polymeric composites with varied weight percents and then examined their properties. Increases in fibre weight percent resulted in improved properties, and the material was able to endure temperatures of up to 84°C in a heat deflection test. Supian et al [5] looked into the characteristics of hybrid composites that might be used for non-structural and semistructural purposes. Das et al [6] pointed out that the stacking sequence and fibre hybridization had a substantial impact on the hybrid laminates' mechanical and thermo-mechanical characteristics. M. Glavind [7] conducted

a research that endeavors promoting technology for achieving sustainability in the field of civil construction. They have focused on materials for replacement of cement, manufacturing of concrete structures and their life cycle, utilization, as well as on the concrete demolition and recycling choices. Upcoming trends and issues related to construction materials which are sustainable in nature were also discussed. According to Vilaplana et al [8], the goal of sustainable development in product design and materials could only be achieved through the crop growth sustainability integration, extraction of raw material, synthetic fibre replacement and modification procedure, methods of product manufacturing and material processing, service life application, and appropriate management of waste materials. Madurwar et al [9] found that the diverse agro-waste-based composite materials were comparatively cheaper construction materials, were light in weight and durable, have reduced thermal conductivity, and were eco-friendly, based on many works of literature offered in their study. As a result, the research, which focused on the use of agro-waste, was extremely useful for developing countries. P. Kandachar [10] conducted a thorough investigation into the significance of natural fibre in achieving the goal of social sustainability, concluding that these raw materials had the potential to contribute to the social sustainability of people in developing countries like India through appropriate policy matter measures and design approaches in a scientific manner. The usage of natural fibre based fabrics, according to Cristaldi et al [11], has significant environmental and cost benefits. The study also stated that the use of natural fibre mats, as well as their hybridization with various textiles and different layouts, as well as various manufacturing techniques, should all be investigated and developed in order to capture all of the benefits associated with natural fibre utilization. Sapuan et al [12] tested woven banana fibre composites of various geometries for tensile and flexural properties and found them to be very stable. A. C. Milanese et al [13] investigated woven sisal fibre in polyurethane and phenolic matrices individually. Untreated woven sisal fibres were employed, and they were compression moulded after being thermally treated at 60°C for 72 hours to produce composites. Investigations to determine the effect of moisture content on the mechanical behaviour of sisal fibres have been considered. Sisal/phenolic composites exhibited a higher tensile strength than the sisal/polyurethane composites, according to the findings. Ratna Prasad et al [14] tested jowar fibre-reinforced polymer composites for their properties. Because jowar composites exhibited good strength and rigidity, for light-weight applications, they can be used as an alternative to sisal and bamboo fibre. Munikenche Gowda et al [15] found that jute as a reinforcing material has better qualities such as nonhazardous to health, nontoxic, eco-friendly, less cost, and easy availability compared to conventional fibre such as glass and Kevlar. Jute fibre composites also outperformed numerous wood composites and some polymers in terms of strength. Present research revealed that the strength of NFRPs can be improved by the fibre treatment [16–21]. Ray et al [22] did a study and found that treating jute fibre with 5% of NaOH at room temperature for varied periods of time improved their characteristics overall. According

to A. Stocchi et al [23], alkali-treated jute fabric composites under stress for 4 hours showed a considerable improvement in stiffness. The research found that alkali-treated jute cloth composites had the highest strength values, regardless of the treatment period. Jawaid et al [24] stated that improvement in tensile and flexural properties of hybrid composites can be improved by incorporating woven jute fibres in pure oil palm. Fung et al [25] found that adding 10 wt. % sisal fibres to polypropylene matrix found increased tensile strength by roughly 10%, thus highlighting the potential of sisal fibres. But, when the composites were reinforced with sisal fibre that had been treated with high silane concentrations, Herrera-Franco et al [26] in their investigation found that the tensile strength of the composites has not improved to the considerable extent. Barreto et al [27] noticed that treating sisal fibre with NaOH solution has improved thermal stability in comparison with its raw form. Archana et al [28] reviewed various natural fibres owing to their structural and mechanical properties and described their potential for strengthening of existing structures. Hota et al [29] presented a comprehensive analysis of materials for civil engineering structures and innovation. They have focused on the sustainability and durability of civil structures. The work revealed that FRP composite materials are used for civil structures with regard to energy-efficient modular structures. The work highlights the processing methods and characterization of natural FRP composites. Archana et al [30] have studied the properties of biodegradable composites to suit the strengthening of the existing structure. They noticed that heat-treated fibre-reinforced composites have resulted in better properties than the untreated fibre composites. Based on their performance under tests, they were concluded that natural fibre-reinforced polymer composites can be used as a substitute for artificial fibre-reinforced polymer composites. Archana et al. [31] showed experimentally that jute NFRC system can be used for posttensioned beam strengthening in the civil application, and it can be a better choice for replacing artificial fibre composites. Sen et al [32] studied the efficacy of jute FRP composite for retrofitting of existing beams, and they have compared it with the artificial fibre systems such as carbon and glass FRP. Results were witnessed that jute FRP could provide good results under shear behaviour. Sen et al. [33] investigated the RC beams strengthened with natural and artificial FRP systems. Natural sisal FRP demonstrated noticeable performance in comparison with artificial glass and carbon FRP under flexural strengthening. This paper elucidates the significance and applicability of NFRCs such as sisal and jute fibre-reinforced polymer composites, which helps the researchers for future research works.

2. Materials and Methods

2.1. Preparation of Composites. Here, in this research work, two natural fibres mats are considered, namely Agave sisalana and Corchorus olitorius fibres, procured from Extraweave Pvt. Ltd., Kerala. Agave sisalana fibre is extracted from plant leaves, and Corchorus olitorius fibre is extracted from the stem of the matured plant. Figures 1(a) and 1(b) show the Agave sisalana fibre and Corchorus olitorius fibre extraction process. For

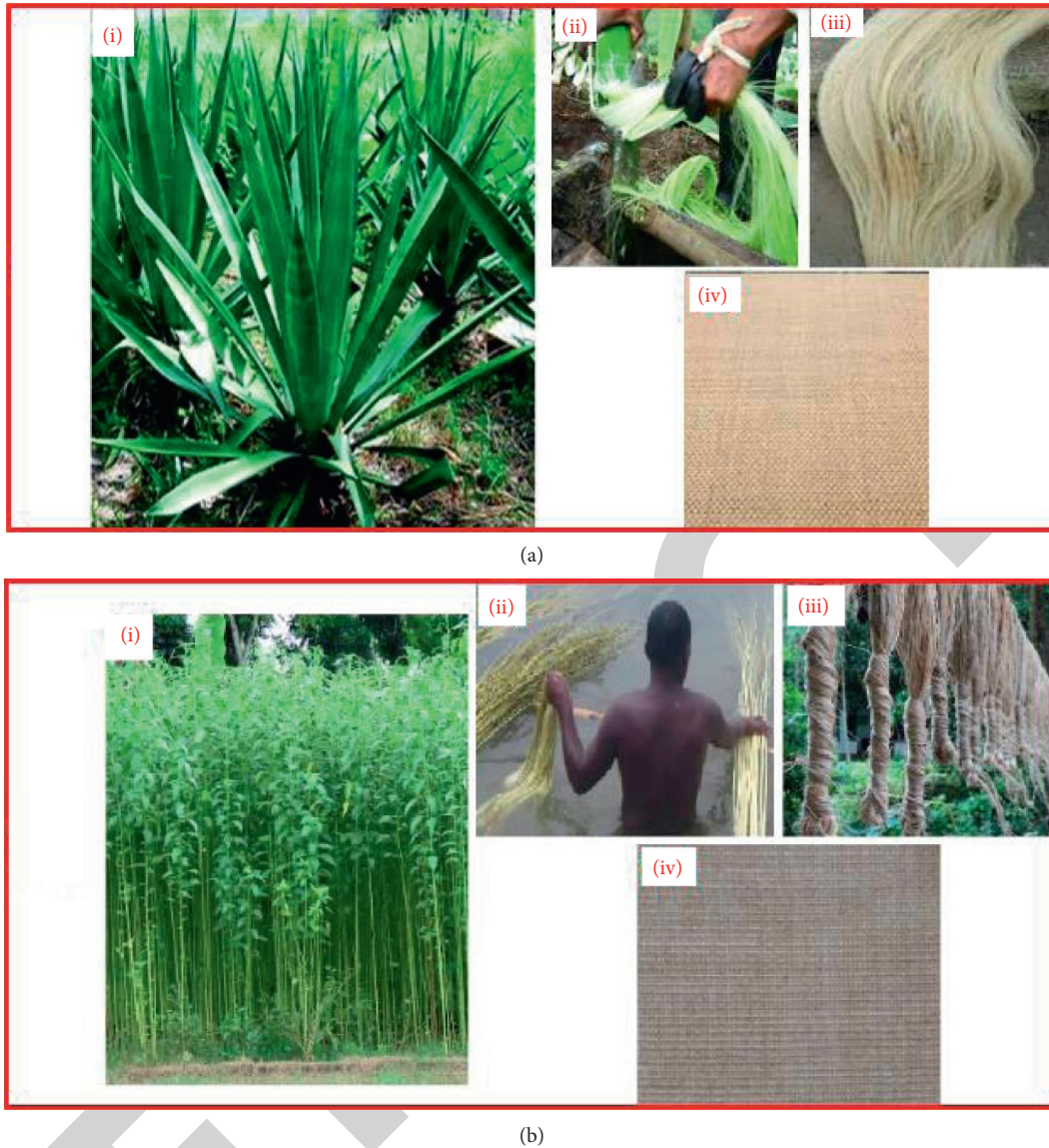


FIGURE 1: Fibre extraction process. (a) Extraction of sisal fibre, (i) sisal plant, (ii) fibre extraction process, (iii) a bundle of fibre, and (vi) fibre mat used in the study. (b) Extraction of Jute fibre, (i) jute plant, (ii) fibre extraction process, (iii) a bundle of fibre, and (vi) fibre mat used in the study.

composite fabrication, diglycidyl ether bisphenol A (LAPOX L12) epoxy resin was used along with the hardener triethylene tetra amine (TETA), procured with M/s Yuje Enterprises, Bengaluru, India. For the fabrication of composites, hand layup technique was used. Before manufacturing, the fibre mats were alkali treated with 4% NaOH solution [28], following standard procedure. A wooden mould coated with the releasing agent of $300 \times 150 \times 3.5$ mm size was used. The required quantity of resin and hardener was mixed. This mixture is poured into the mold where the fibre mat is placed. The mould setup is allowed for infiltration during which matrix is infiltrated into the fibre. The entrapped air was removed using a roller. Thereafter, a pressure of 0.2616 Kg/cm^2 was applied. The mould is allowed for 24 hours at room temperature undisturbed for curing. Figure 2 shows the process of composite preparation. Figure 3 demonstrates the methodology adopted for the work.

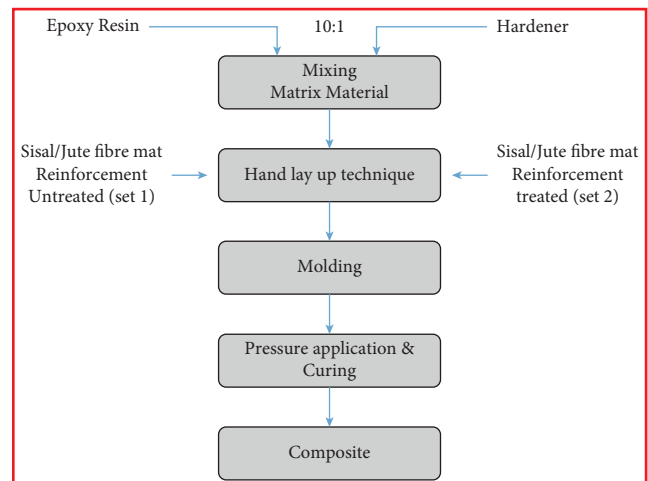


FIGURE 2: Flowchart of Composite preparation.

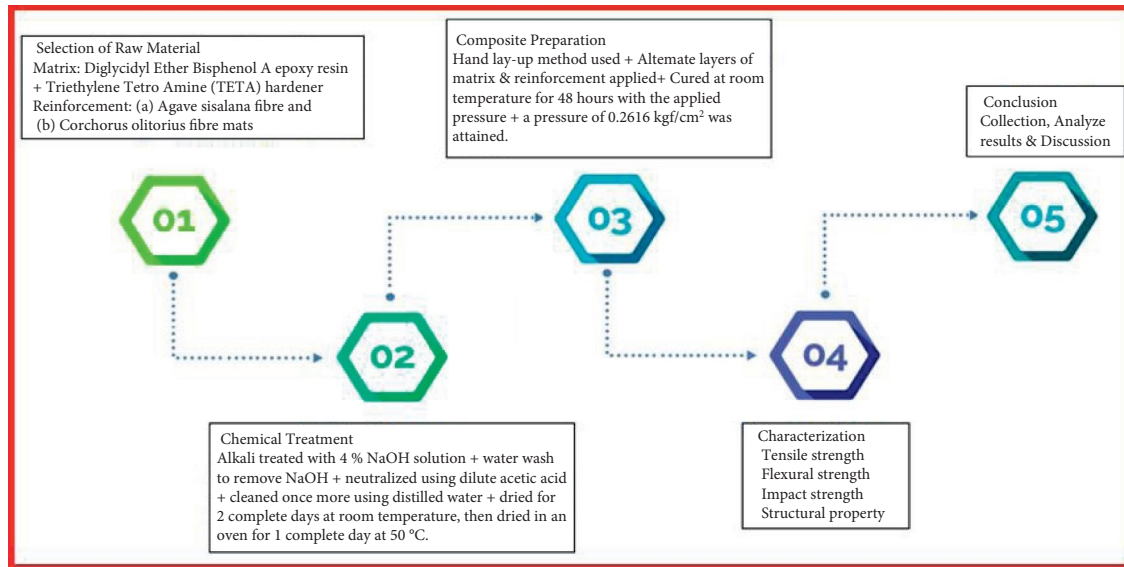


FIGURE 3: Methodology adopted for the work.

2.2. Surface Treatment of Fibre. In past, researchers have considered various chemical treatments to treat the natural fibres, and their effect on associated properties was studied [16, 34]. In this chemical treatment, hydroxyl groups (OH) react with chemical agents. In this study, cellulose fibres are treated with alkali (NaOH). Alkali removes hemicellulose lignin partially and also wax and other impurities. The concentration of NaOH and soaking time are used as a measure of effectiveness based on the effect they create. Figure 4 describes the preparation, treatment, and testing of prepared NFRCs.

2.3. Characterizations

2.3.1. Mechanical Tests. The tensile test was performed using the universal testing machine (make: Kalpak Instruments and Controls, Pune, Model: KIC-2-1000-C, 100 kN capacity), as shown in Figure 5, at a 2 mm/min cross-head speed and a 50 mm gauge length, as per ISO 527-4:1997(E) Part-4. The flexural test was carried out as per ISO 14125:1998 standard with the help of a three-point bending rig at a 2 mm/min cross-head speed and a 50 mm gauge length. The impact test was carried out as per ISO 18039 using an Izod impact machine, demonstrated in Figure 6. Specimen dimensions are shown in Figure 7. All the above-mentioned tests were conducted at room temperature. In each combination, three samples were tested, and average values were taken.

2.3.2. Water Absorption Test. The water absorption test was carried out as per the ASTM D570 standard. The specimen was weighed in a dried condition using a digital scale (mass m_1) before being immersed in water in a beaker. After withdrawing the sample from the water for 12 hours, it was weighed (mass m_2). The percent water absorption was calculated. For this purpose, difference in weight between samples before and after immersion in water was considered. The % absorption is given according to

$$(\%) \text{absorption} = \left(\frac{W_2 - W_1}{W_1} \right) * 100, \quad (1)$$

where W_2 refers to the weight of the specimen in grams after it has been removed from the water, while W_1 refers to the weight of the specimen before it has been soaked in water. Using mass balance testing, the weight of the specimen was estimated with a precision of 0.0001 g.

2.3.3. Electron Microscopy. The failure mechanism and microstructure of the prepared composites were analyzed using a Vega 3 Tescan which is a scanning electron microscope. Images were acquired with an SEM at a voltage of 26 kV at a working distance of 30 to 40 mm. To study the fracture morphology, samples were cut from the broken end of the composite surface.

3. Results and Discussion

3.1. Water Absorption Behaviour. From the present research work, it is seen that water uptake in lignocellulose fibre-based composites can be minimized by chemically treating the fibres to improve bonding between the hydrophilic lignocellulose fibres and the hydrophobic matrix system. Water intake of 4% NaOH-treated FRCs was found to be lower than that of the untreated FRCs. This demonstrated that the 4% NaOH-treated fibres exhibit better interfacial adhesion with the epoxy matrix.

3.2. Effect of Chemical Treatment on Tensile Strength. Figure 8(a) shows the effect of surface treatment with 4% concentration of NaOH solution of sisal and jute fibres on the tensile strength of composites. For the proportions evaluated in the study, treated fibre-reinforced composites show a higher value of tensile strength compared to untreated fibre-reinforced composites for both fibres, which

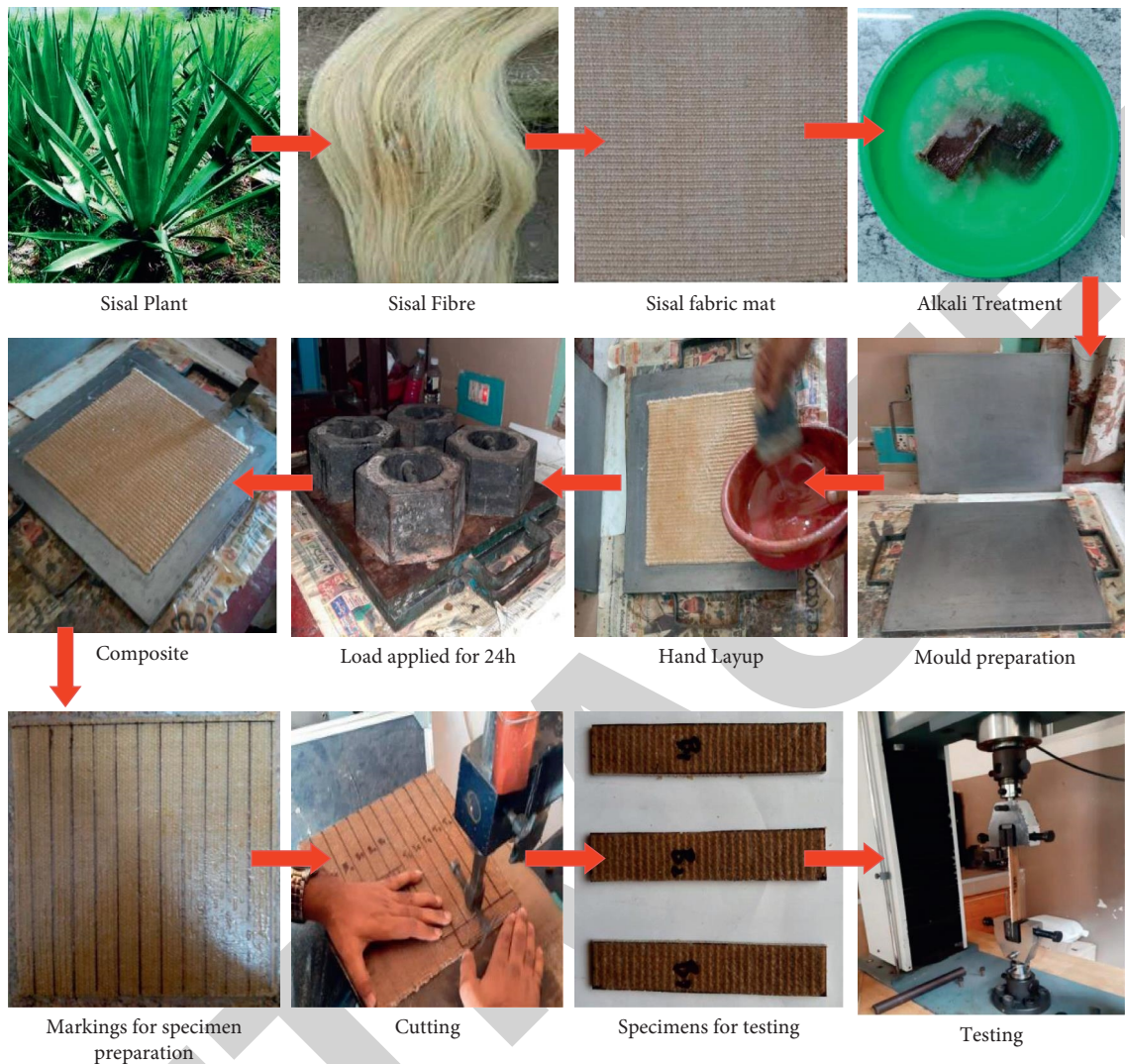


FIGURE 4: Preparation and testing of sisal fibre-reinforced composites.

was about 28 and 23 percent greater than the untreated composite reinforced with respective fibre. This demonstrates that the fibres that had been treated with NaOH exhibited greater epoxy matrix interfacial adhesion. Improved adhesion between the fibre and the matrix enhances stress distribution, increases load-carrying capacity, and improves tensile strength of the composites. Removal of hemicellulose and lignin from the fibre surface caused by treatment with alkali resulted in the formation of micropores on the fibre surface.

3.3. Effect of Chemical Treatment on Flexural Strength.

The sisal and jute fibres were treated with a 4 percent concentration of NaOH solution which improves the flexural characteristics of the SNFRC and JNFRC, and the results are presented in Figure 8(b). The flexural strengths of sisal and jute fabric-reinforced composites treated with 4% NaOH were found to be higher, about 10 and 13 percent greater than the untreated composite reinforced with

respective fibre. This could be because the fibres and epoxy matrix have better interfacial adhesion.

3.4. Effect of Chemical Treatment on Impact Strength.

The material's impact strength determines how well it absorbs energy under high impact loads. The impact strength of composites depends on fibre reinforcement, filler-matrix interface, void presence, filler influence, and testing conditions. Figure 8(c) illustrates the effect of treatment on the impact strength of untreated and also 4 percent NaOH-treated SFRC and JFRC, respectively. It observed that, like the tensile and flexural characteristics, the impact strength of treated fibre-reinforced composites improved significantly. The impact strength of the composites reinforced with 4% NaOH-treated sisal and jute fibres was 1.69 J/mm^2 and 1.28 J/mm^2 , respectively, which was 6.39 and 14 percent greater than the untreated composite reinforced with respective fibre. Due to the existence of microfractures in the interfacial region, the incorporation of untreated fibres in the epoxy



FIGURE 5: (a) Universal testing machine used for the tensile and flexural test (Make: Kalpak Instruments and Controls, Pune, Model: KIC-2-1000-C with the capacity of 100 kN). (b) Tensile test arrangement. (c) Bending test arrangement.



FIGURE 6: (a) Impact testing machine. (b) Izod test arrangement.

matrix led to poor interfacial adhesion, resulting in reduced mechanical characteristics [35]. When the material is loaded, the microcracks act as a failure mechanism, which causes the failure of composites completely. Furthermore, the impact behaviour of composites is largely determined by fibre

pullout [36]. Due to strong interfacial adhesion between the fibre and matrix, the 4 percent of NaOH-treated composites show reduced fibre pullout, resulting in higher impact strength. Properties of prepared composites measured in the laboratory are tabulated in Table 1.

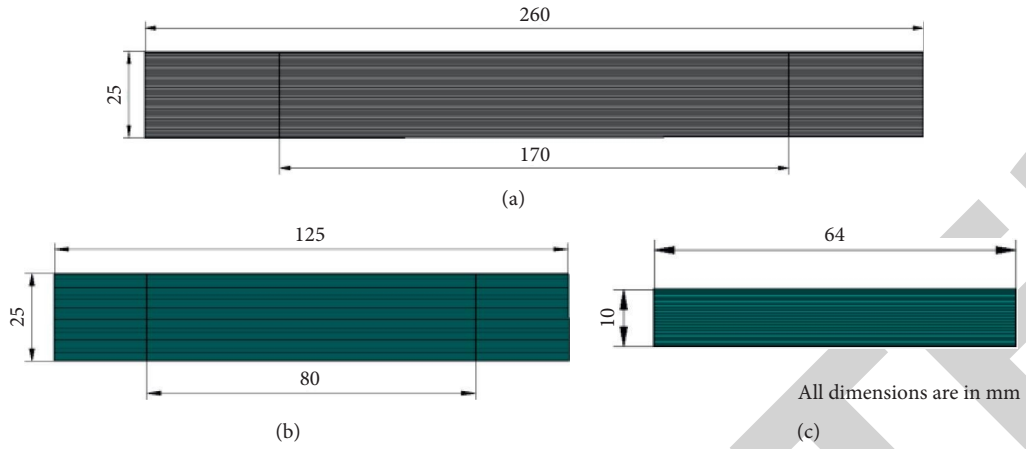


FIGURE 7: Specimen dimensions as per standards. (a) Tensile test specimen. (b) Flexural test specimen. (c) Impact test specimen.

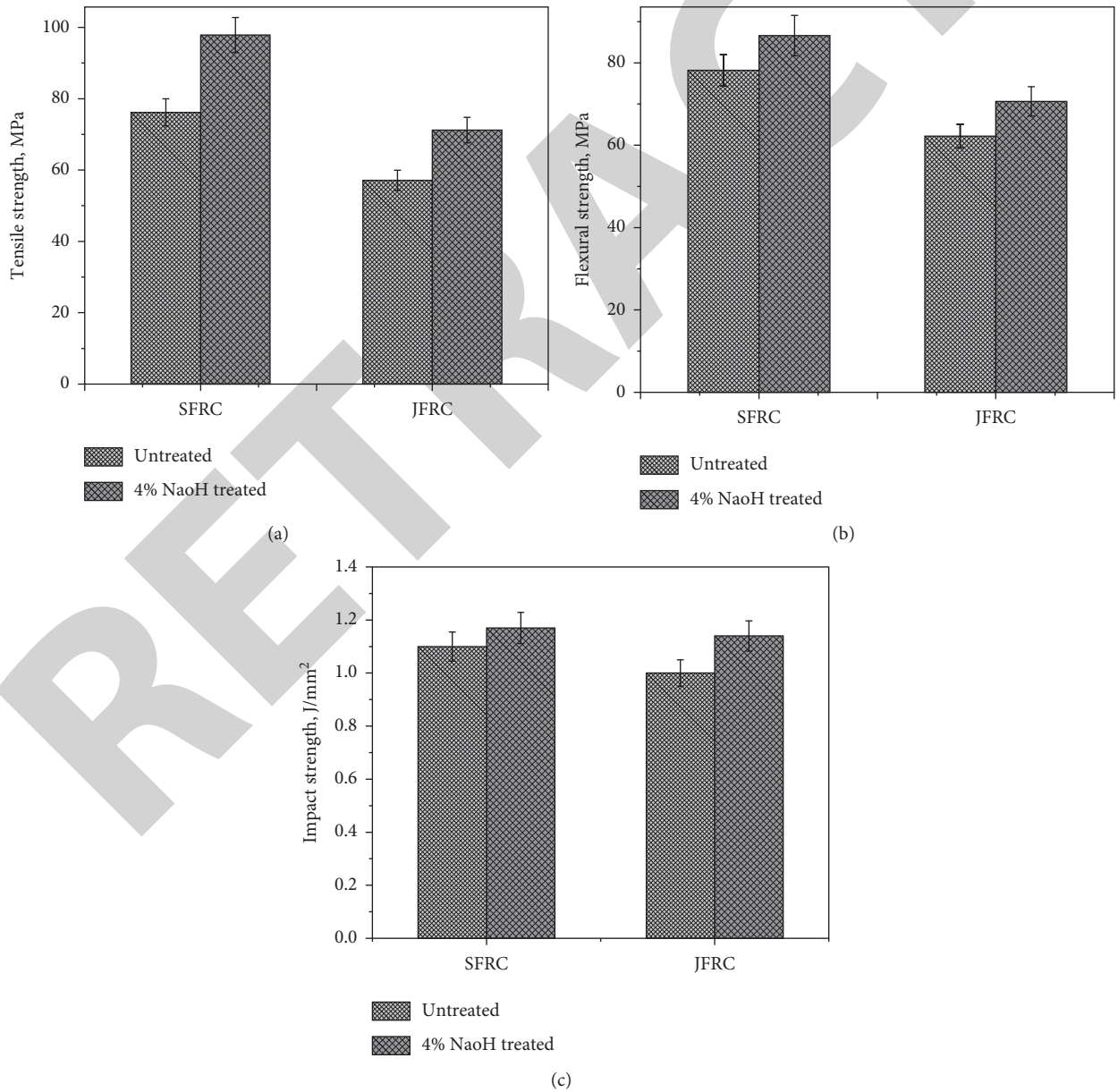


FIGURE 8: Characteristics of SFRC and JFRC. (a) Tensile strength. (b) Flexural strength. (c) Impact strength.

TABLE. 1: Properties of fabricated composites.

Composite	Tensile strength (MPa)		Flexural strength (MPa)		Impact strength (J/mm ²)	
	Untreated	4% NaoH treated	Untreated	4% NaoH treated	Untreated	4% NaoH treated
SNFRC	76.14	97.88	78.19	86.64	1.1	1.17
JNFRC	57.12	71.21	62.22	70.65	1.0	1.14

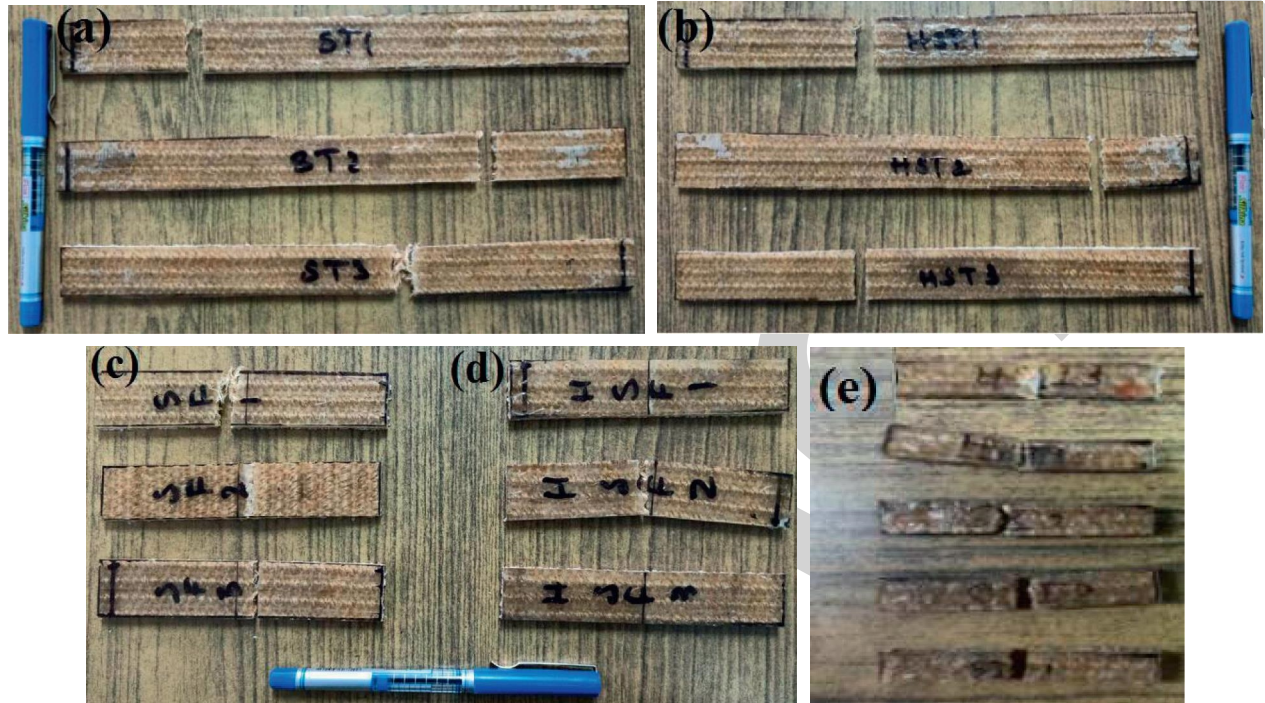


FIGURE 9: Sisal fabric-reinforced composites. (a) Untreated-fractured tensile specimens. (b) Heat-treated-fractured tensile specimens. (c) Untreated-fractured flexure specimens. (d) Heat-treated-fractured specimens undergo flexural failure. (e) Impact test fractured specimens.

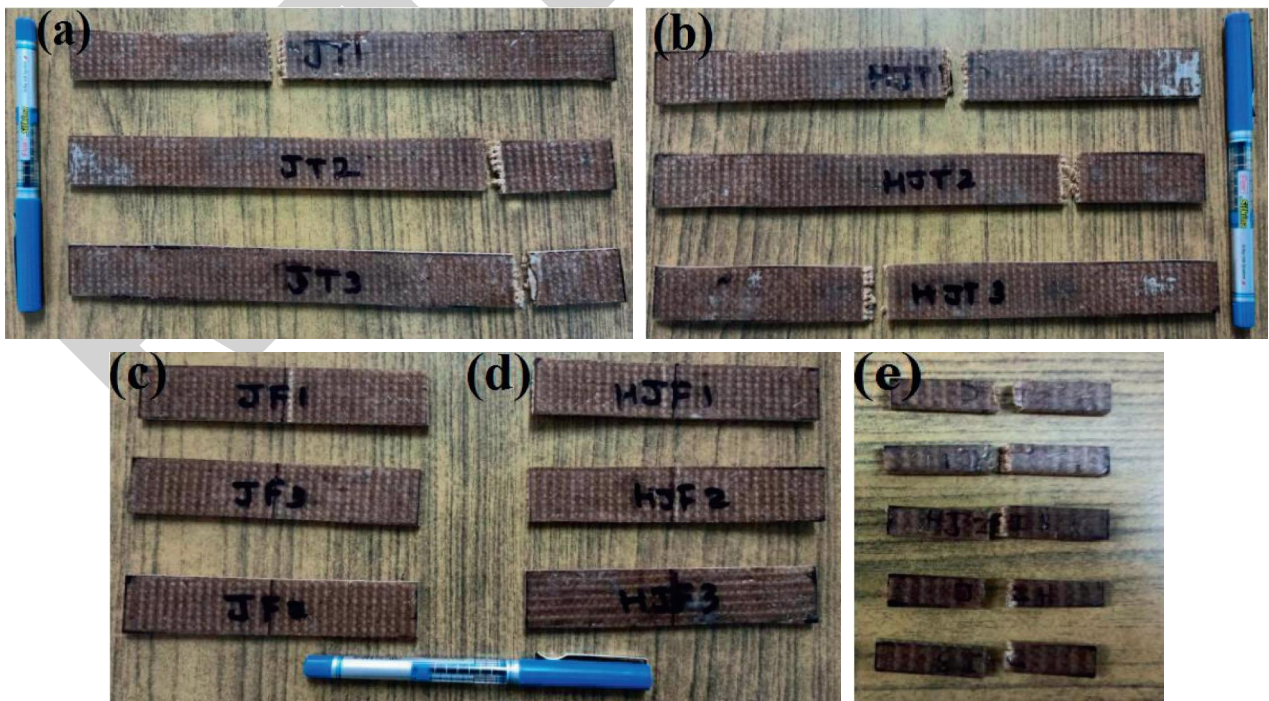


FIGURE 10: Jute fabric-reinforced composites. (a) Untreated-fractured tensile specimens. (b) Heat-treated-fractured tensile specimens. (c) Untreated-fractured flexure specimens. (d) Heat-treated-fractured specimens undergo flexural failure. (e) Impact test fractured specimens.

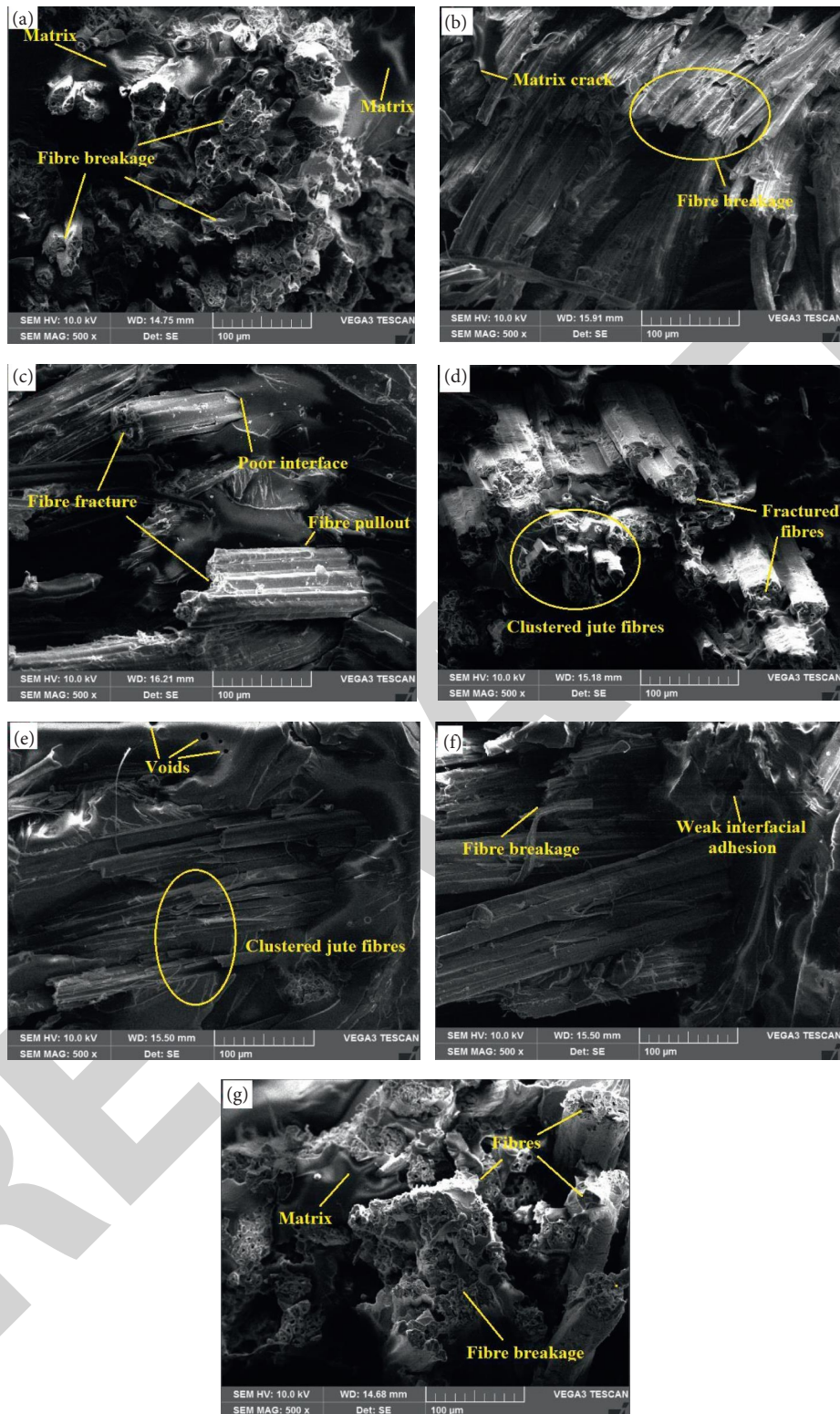


FIGURE 11: Fracture surfaces of tensile and flexural test specimens. (a) Sisal-untreated tensile. (b) Jute-untreated flexural. (c) Sisal 4% NaOH-treated tensile. (d) Jute 4% NaOH-treated tensile. (e, f) Jute 4% NaOH-treated flexural. (g) Sisal 4% NaOH-treated flexural.

3.5. *Scanning Electron Microscope (SEM) Analysis.* SEM images of tensile and flexural-tested specimens (shown in Figures 9 and 10) were taken to investigate tensile failure in composites. They were used to study the interfacial

characteristics, fractured specimen interior structure, and the development of internal cracks. The fracture surface appearance of the modified sisal and jute fibre-reinforced composites is shown in Figure 11. Because of the weak bonding between

the matrix and the fibre in fracture surfaces, fibre pullout may be seen in micrographs. The alkali treatment improves, somewhat, the bonding between fibre and the matrix. The pullout of fibres leaves just a few holes, owing to poor compatibility between the hydrophilicity of the untreated fibre and the hydrophobicity of the matrix [37]. After the modification, the holes are reduced, and more number of fibre breaks are appeared, indicating that the composite has a good interface. This modification procedure is particularly effective since an alkali and heat treatment may help the composite material develop a good interface [38].

4. Conclusions

The hand layup approach was used to effectively fabricate natural fibre-reinforced polymer composites (SNFRC and JNFRC), and the tensile, flexural, impact, and water absorption characteristics were examined. In the research, the influence of NaOH treatment on the above properties was investigated, and the following findings were obtained.

- (i) Composites with 4% NaOH-treated sisal and jute fibre reinforcement had better mechanical properties such as tensile, flexural, and impact characteristics which is because of improved adhesion between the fibre and matrix interface.
- (ii) The morphological analysis demonstrated that using treated fibre-reinforced composite systems increased the bonding and resulted in superior mechanical properties.
- (iii) In both SNFRP and JNFRP cases, the treated fibre-reinforced composites demonstrated decreased water absorption rates due to improved hydrophobicity of the composites compared with untreated fibres.

From the present work, it can be concluded that the sisal and jute fibre treated with 4% NaOH are the best reinforcements for the development of epoxy-based matrix composites. These composites may be used in both domestic and industrial applications for low and medium loads.

Data Availability

The data used to support the findings of this study are included within the article.

Conflicts of Interest

The authors declare that they have no conflicts of interest.

References

- [1] S. Sekar, V. Shanmugam, S. Kumar et al., "Effects of water absorption on the mechanical properties of hybrid natural fibre/phenol formaldehyde composites," *Scientific Reports*, vol. 11, 2021.
- [2] M. Y. Khalid, A. Rashid, and Z. U. Arif, W. Ahmed and H. Arshad, "Natural fiber reinforced composites: sustainable materials for emerging applications," *Results in Engineering*, vol. 11, p. 100263, 2021.
- [3] D. K. Rajak, D. D. Pagar, P. L. Menezes, and E. Linul, "Fiber-reinforced polymer composites: manufacturing, properties, and applications," *Polymers*, vol. 11, no. 10, p. 1667, 2019.
- [4] V. Vignesh, A. N. Balaji, N. Nagaprasad, M. R. Sanjay, A. Khan, and A. M. Asiri, G. M. Ashraf and S. Siengchin, "Indian mallow fiber reinforced polyester composites: mechanical and thermal properties," *Journal of Materials Research and Technology*, vol. 11, pp. 274–284, 2021.
- [5] A. B. M. Supian, M. Jawaid, B. Rashid et al., "Mechanical and physical performance of date palm/bamboo fibre reinforced epoxy hybrid composites," *Journal of Materials Research and Technology*, vol. 15, pp. 1330–1341, 2021.
- [6] S. C. Das, D. Paul, S. A. Grammatikos et al., "Effect of stacking sequence on the performance of hybrid natural/synthetic fiber reinforced polymer composite laminates," *Composite Structures*, vol. 276, p. 114525, 2021.
- [7] M. Glavind, "Sustainability of cement, concrete and cement replacement materials in construction," *Sustainability of Construction Materials*, Woodhead Publishing Limited, Cambridge, UK, 2009.
- [8] F. Vilaplana, E. Stromberg, and S. Karlsson, "Environmental and resource aspects of sustainable biocomposites," *Polymer Degradation and Stability*, vol. 95, no. 11, pp. 2147–2161, 2010.
- [9] M. V. Madurwar, R. V. Ralegaonkar, and S. A. Mandavane, "Application of agro-waste for sustainable construction materials: a review," *Construction and Building Materials*, vol. 38, pp. 872–878, 2013.
- [10] P. Kandachar, "Materials and social sustainability," *Materials Experience*, Delft University of Technology, Book Chapter, 2014.
- [11] G. Cristaldi, Alberta Latteri, Giuseppe Recca and Gianluca Cicala, *Composites Based on Natural Fibre Fabrics, Woven Fabric Engineering*, InTech, Sciyo, Book Chapter, 2010.
- [12] S. M. Sapuan, A. Leenie, M. Harimi, and Y. K. Beng, "Mechanical properties of woven banana fibre reinforced epoxy composites," *Materials & Design*, vol. 27, no. 8, pp. 689–693, 2006.
- [13] A. C. Milanese, M. O. H. Cioffi, and H. J. C. Voorwald, "Mechanical behavior of natural fiber composites," *Procedia Engineering*, vol. 10, pp. 2022–2027, 2011.
- [14] A. V. Ratna Prasad and K. Mohana Rao, "Mechanical properties of natural fibre reinforced polyester composites: jowar, sisal and bamboo," *Materials & Design*, vol. 32, no. 8-9, pp. 4658–4663, 2011.
- [15] T. Munikenche Gowda, A. C. B. Naidu, and R. Chhaya, "Some mechanical properties of untreated jute fabric-reinforced polyester composites," *Composites Part A: Applied Science and Manufacturing*, vol. 30, no. 3, pp. 277–284, 1999.
- [16] M. M. Kabir, H. Wang, K. T. Lau, and F. Cardona, "Chemical treatments on plant-based natural fibre reinforced polymer composites: An overview," *Composites Part B: Engineering*, vol. 43, no. 7, pp. 2883–2892, 2012.
- [17] F. Sarasini, J. Tirillo, C. Sergi, M. C. Seghini, L. Cozzarini, and N. Graupner, "Effect of basalt fibre hybridisation and sizing removal on mechanical and thermal properties of hemp fibre reinforced HDPE composites," *Composite Structures*, vol. 188, pp. 394–406, 2018.
- [18] J. Bessa, J. Matos, C. Mota et al., "Influence of surface treatments on the mechanical properties of fibre reinforced thermoplastic composites," *Procedia Engineering*, vol. 200, pp. 465–471, 2017.
- [19] V. Fiore, T. Scalici, and A. Valenza, "Effect of sodium bicarbonate treatment on mechanical properties of flax-

Retraction

Retracted: Modeling and Analysis of Automotive Engine Crankshaft Made of Composite and Functionally Graded Materials

Advances in Materials Science and Engineering

Received 26 December 2023; Accepted 26 December 2023; Published 29 December 2023

Copyright © 2023 Advances in Materials Science and Engineering. This is an open access article distributed under the Creative Commons Attribution License, which permits unrestricted use, distribution, and reproduction in any medium, provided the original work is properly cited.

This article has been retracted by Hindawi, as publisher, following an investigation undertaken by the publisher [1]. This investigation has uncovered evidence of systematic manipulation of the publication and peer-review process. We cannot, therefore, vouch for the reliability or integrity of this article.

Please note that this notice is intended solely to alert readers that the peer-review process of this article has been compromised.

Wiley and Hindawi regret that the usual quality checks did not identify these issues before publication and have since put additional measures in place to safeguard research integrity.

We wish to credit our Research Integrity and Research Publishing teams and anonymous and named external researchers and research integrity experts for contributing to this investigation.

The corresponding author, as the representative of all authors, has been given the opportunity to register their agreement or disagreement to this retraction. We have kept a record of any response received.

References

- [1] S. Asiri, "Modeling and Analysis of Automotive Engine Crankshaft Made of Composite and Functionally Graded Materials," *Advances in Materials Science and Engineering*, vol. 2022, Article ID 4005368, 15 pages, 2022.

Research Article

Modeling and Analysis of Automotive Engine Crankshaft Made of Composite and Functionally Graded Materials

Saeed Asiri 

Faculty of Engineering, King Abdulaziz University Department of Mechanical Engineering, Jeddah 80204, Saudi Arabia

Correspondence should be addressed to Saeed Asiri; sasiri@kau.edu.sa

Received 16 March 2022; Revised 5 April 2022; Accepted 11 April 2022; Published 28 April 2022

Academic Editor: Palanivel Velmurugan

Copyright © 2022 Saeed Asiri. This is an open access article distributed under the Creative Commons Attribution License, which permits unrestricted use, distribution, and reproduction in any medium, provided the original work is properly cited.

With the consistent advancement and technical improvisation in the automobile industry, the researchers are working on the material optimization techniques to select and utilize the materials effective in power transmission. It is well known that power transmission systems in the mechanical industries and, namely, in automotive machineries, require a durable material with proper properties to ensure the optimum operational conditions during power transmission. The material utilized in the driving shaft must have a proper endurance and considerable yielding limit that means they have that ability to sustain the fatigue in the power transmission elements. The method of study is that engine shafts are a major part of the automobiles and the production of these shafts is an important requirement for the resistance against bending and torsion. The torsion and bending resisting moments are important before selecting the material. As a result, selecting the optimal material and surface treatment procedure to offer the highest performance for the shaft is crucial. Wear resistance and corrosion resistance are the two most important factors to consider when selecting a material for a surface. This paper is able to show the effect of materials of the crankshaft on those two elements. The research discusses the shafts of three different types of materials: homogeneous, composite, and functionally graded materials (FGM). For the optimum performance of the vehicle engine shaft, FGM is the ideal material to consider. It has been shown that the performance of crankshaft was improved in case of FGM. Based on the results of the modal and harmonic analysis, it is concluded that FGM crankshaft would offer the best durability and show optimum performance when compared with the other two material crankshafts investigated in this study.

1. Introduction

The automobile industry requires proper selection of materials for the power transmission. The main aim of selecting the suitable materials is to increase the effectiveness of the bending and torsion resistance. Functionally graded materials (FGM) provide varying quality grades with the dimensions. Functionally graded materials (FGMs) have turned into the object of public consideration for different application fields [1–3]. FGMs have the properties of the two unrefined substances, which are combined as one, and the part dispersion is evaluated consistently. For instance, one of the FGMs delivered utilizing the properties of metallic perseverance with an appreciable advantage of endurance limit. It can utilize functionally graded materials (FGM) as a material to endure the stresses. The creators have proposed

another creation technique utilizing a strategy bringing about a mechanical partition of solids and fluids and they have prevailed about delivering thick squares of FGMs utilizing this technique. Moderate cover of the limit layers through persistent degree utilizing filtration refined useful degree of FGMs. This research article focuses on choosing the optimum material for an engine shaft and the surface treatment method. Shafts are always designed in a circular shape, which is due to the distribution of stress in the shaft towards the radius which can make them to be in a solid or hollow shape. When rust poses a severe danger to the shaft's longevity, stainless steel is the material that is most likely to hold up the longest. 440C stainless steel and 316 stainless steels are the two most prevalent stainless-steel grades used to make linear shafts (2021) (MiSUMi Mech Lab). The parameters for choosing a material for an engine shaft are

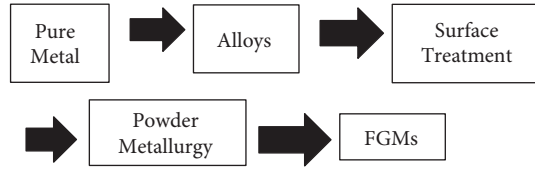


FIGURE 1: FGM production process.

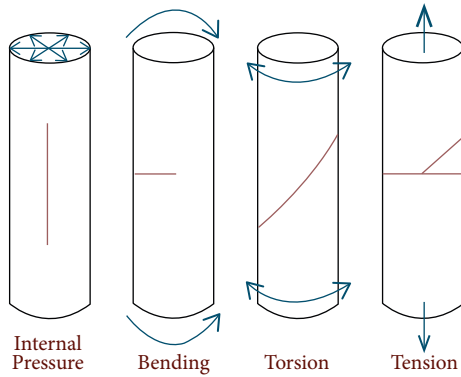


FIGURE 2: Fracture planes caused by general fatigue forces.

TABLE 1: Geometrical dimensions of the crankshaft.

S no.	Description	Values
1	Crankshaft length (mm)	589
2	Crankshaft height (mm)	160
3	Crank pin length (mm)	38
4	Crank pin diameter (mm)	27
5	Diameter of shaft (mm)	72
6	Maximum pressure	100 MPa
7	Fixed support	Both ends of the shaft

entirely dependent on the application. There are several predefined factors to consider when choosing a shaft's material, such as the strength factor, shaft stiffness, and the shaft's capacity to go through several heat treatment methods [1].

Although there are some common features that must be present in the material from which the shaft is manufactured, they are as follows:

- (i) High strength
- (ii) Simplicity to manufacture so that the production process is as painless as possible
- (iii) It must have strong heat treatment qualities so that the shaft can resist harsh operating conditions

Steel is one of the materials of choice for the manufacturing of shafts in normal operation. It has a considerable amount of strength and can handle most operating circumstances. Because it is inexpensive, it is favored over a variety of more expensive materials. A functional graded material (FGM) is a sort of amalgamated form

TABLE 2: Properties for carbon composite.

Properties	Values
Density (kg/m^3)	4500
Elastic modulus (GPa)	0.85
Poisson's ratio	0.499
Shear modulus (GPa)	0.284

TABLE 3: Mechanical and physical properties of the FGM (316 steel + Al_2O_3).

Property	Value
Density (kg/m^3)	$8000(1 - r/r_0) + 3800(r/r_0)$
Young's modulus (Pa)	$1.93 \times 10^{11}(1 - r/r_0) + 3.204 \times 10^{11}(r/r_0)$
Poisson's ratio	$0.27(1 - r/r_0) + 0.26(r/r_0)$
Shear modulus	$78 \times 10^9(1 - r/r_0) + 127.14 \times 10^9(r/r_0)$

TABLE 4: Mechanical and physical properties of Al_2O_3 .

Property	Value
Density (kg/m^3)	3800
Young's modulus (GPa)	320.4
Poisson's ratio	0.26
Compressive yield strength (MPa)	400
Shear modulus	127.14 GPa

TABLE 5: Physical properties for stainless steel 316

Property	Value
Mass density (kg/m^3)	8000
Young's modulus (GPa)	193
Poisson's ratio	0.27
Shear modulus (GPa)	78

created by combining two or more different types of materials. A compositional gradient is projected onto the mixture of specifications of FGM. As a result, it exhibits diverse qualities depending on the situation [2, 3]. The production technique for functionally graded materials has been mentioned in Figure 1.

A large portion of FGMs is molecule supported FGMs and their arrangements rely upon position. The particle reinforced FGMs, which contain particles (ceramics) in the framework (metal), the grid, will be exposed to plastic deformation; particles will have a loose bond that will eventually break [3]. The heat resistance of the functionally graded materials is appreciable in the major conduct of utility for the power transmission purposes. In the past many investigations of FGMs, a perceptible mixture of metals has taken on to ensure the desirable material properties [4].

This paper is about the production of composite materials in the manufacturing aspect of functionally graded materials (FGM). The requirement for innovative materials

TABLE 6: Material properties of FGM (316 steel + Al_2O_3).

Layers	1	2	3	4	5	6	7	8
Radial coordinate (mm)	0	10	20	30	40	50	60	70
Mass density (kg/m^3)	8000	7475	6950	6425	5900	5375	4850	4325
Young's modulus (GPa)	193	208.9	224.8	240.8	256.7	272.6	288.5	304.5
Poisson's ratio	0.27	0.269	0.2675	0.266	0.265	0.2638	0.2625	0.2613

TABLE 7: Modal analysis results of stainless-steel crankshaft.

Modes	Frequency	Deformation (mm)
1	329.31	9.35
2	751.29	19.13
3	962.65	12.496
4	1737.5	15.33
5	2346.4	17.17

TABLE 8: Modal analysis results of carbon composite crankshaft.

Modes	Frequency	Deformation (mm)
1	318.41	12.386
2	742.33	25.288
3	931.12	16.88
4	1669.8	19.51
5	2244.5	21.835

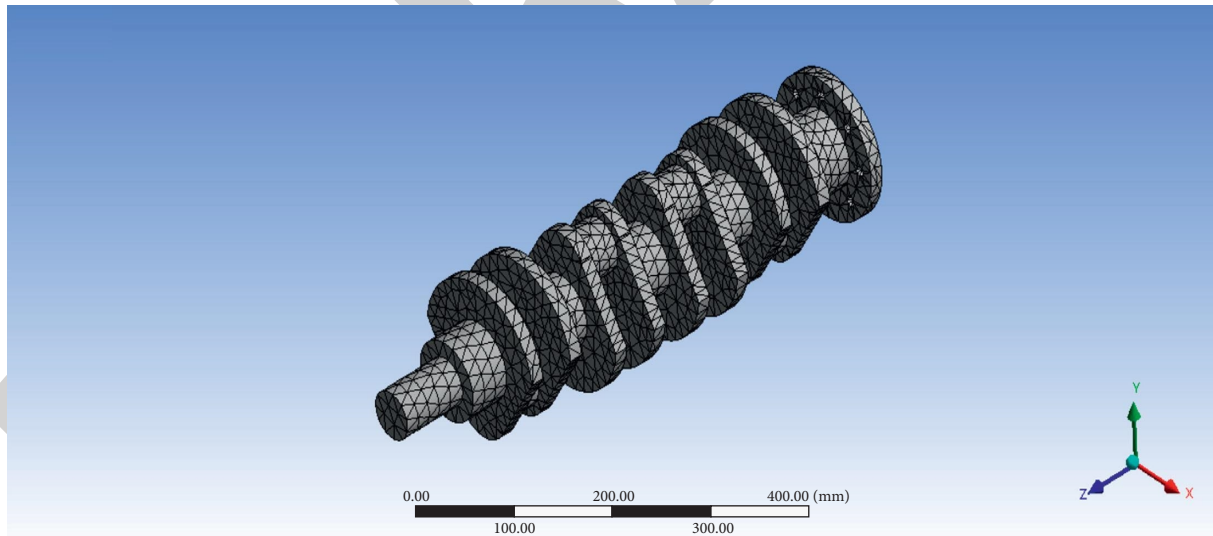


FIGURE 3: 3D model of a meshed crankshaft created in ANSYS software.

with exact properties has brought about the slow adjustment of materials from their essential states (solid) to composites. Current advances in designing and the handling of materials have prompted another class of reviewed complex materials called practically evaluated materials (FGMs). This article takes a gander at the best handling innovations and uses of the high level, great items created in FGMs. It additionally features about the future exploration scope in FGMs [5].

In this paper, the evaluative methods on functionally graded materials (FGM) have been performed to study the effectiveness of using FGM in engine shafts. An outline has been uncovered on the improvement of functionally graded materials (FGM), their ideas, their properties, and their primary assembling steps [6]. This potential implies that the originator is not generally restricted to a scope of existing homogeneous materials, albeit many investigations have

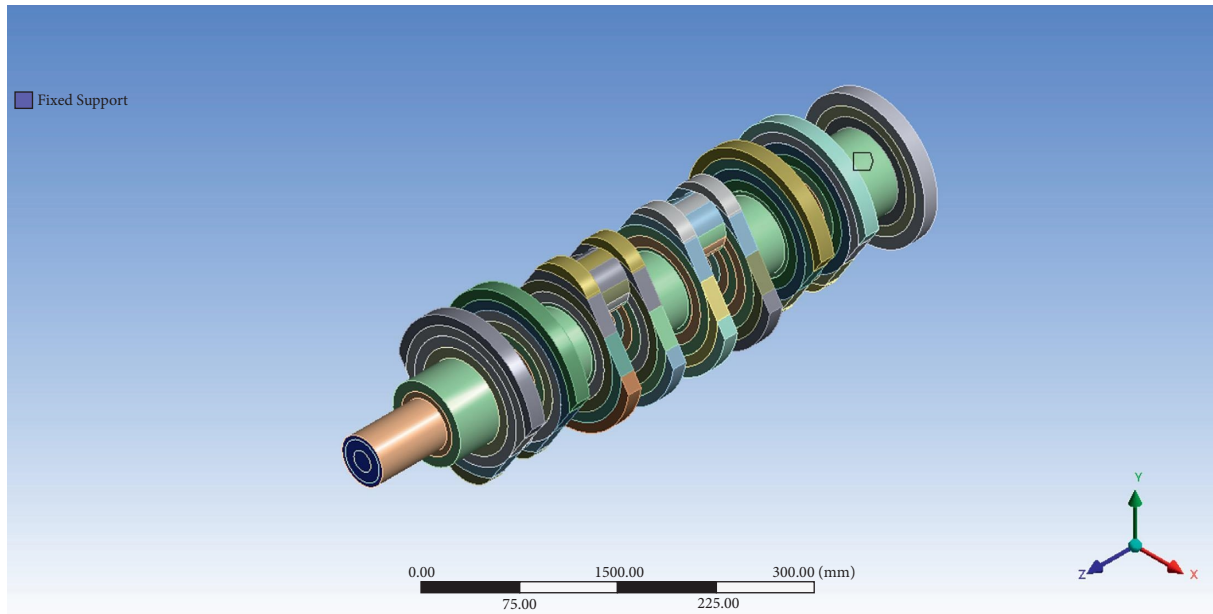


FIGURE 4: Engine shaft (FGM).

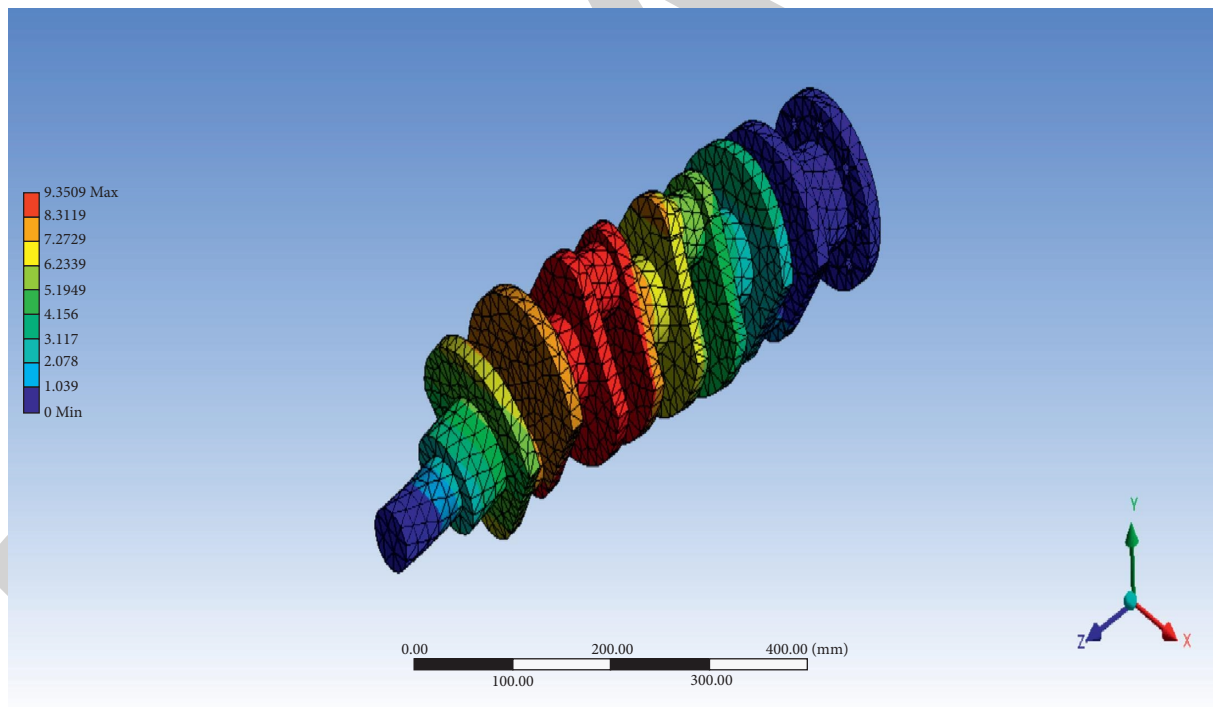


FIGURE 5: Deformation of stainless-steel crankshaft at the first mode of vibration.

zeroed in on the examination of this material, engineers and different experts occupied with the plan cycle with functionally graded materials FGM. Utilization of the functionally graded materials FGM is by all accounts quite possibly the best materials in the acknowledgment of the maintainable advancement in the business [7].

The research entails finding the ideal material that will show optimum performance and would be able to avoid

failure as much as possible. To plan, it is necessary to first understand the significant failures that occur over the life span of a crankshaft. When calculating the likelihood of a shaft failing, it is necessary to consider the types of loads that it is subjected to during its operation. One of the most encountered forms of load is rotational, which causes the shaft to twist and flex, potentially losing its stiffness and causing the system to collapse.

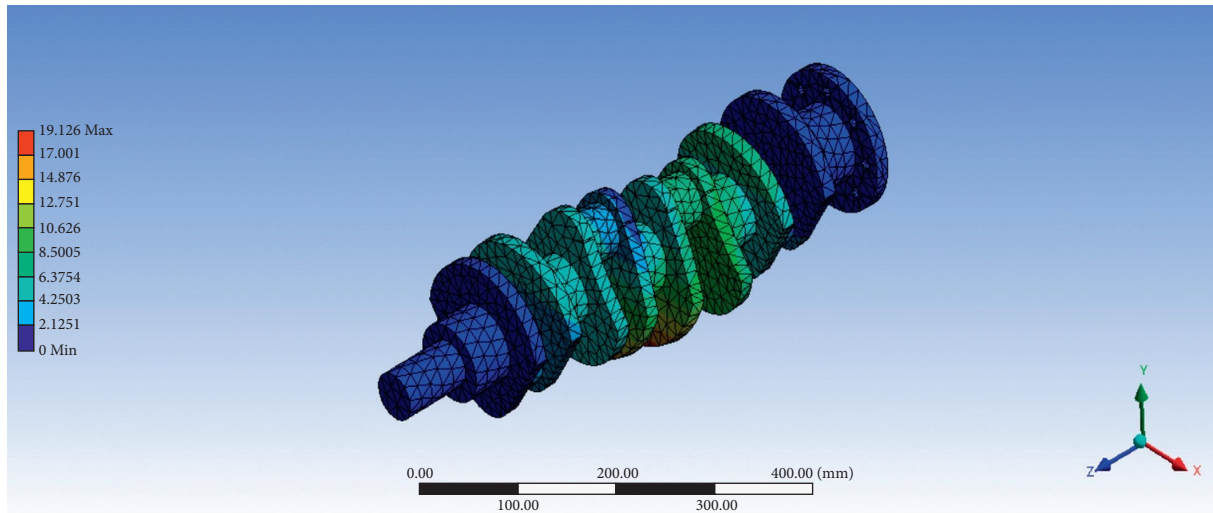


FIGURE 6: Deformation of stainless-steel crankshaft at the second mode of vibration.

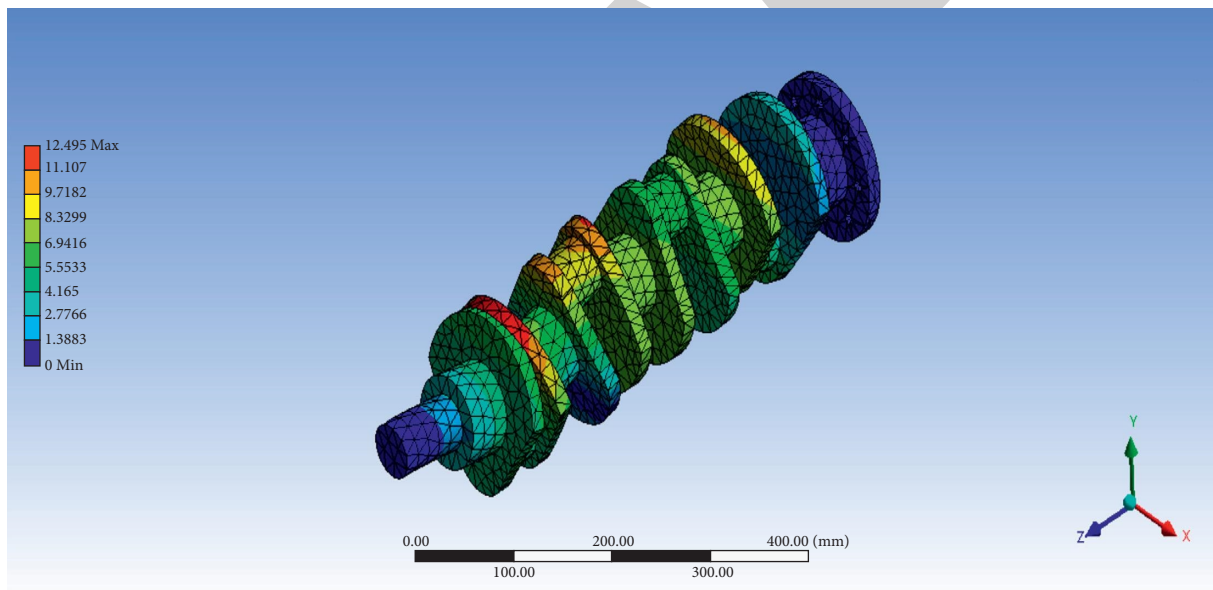


FIGURE 7: Deformation of stainless-steel crankshaft at the third mode of vibration.

Other weights acting on the crankshaft could be as a result of location of loading. For example, in underwater systems, the shaft may corrode because of the presence and influence of water beneath it. As a result, going prepared for these unique situations is a must. Figure 2 depicts a cylinder and how various forces operate on it to induce deformation. Repetitive loading cycles induce fatigue failure. It is a startling truth, but the forces that generate plastic deformation are larger than the forces that cause fatigue failure. Corrosion-resistant characteristics and the ease with which it resists erosion are two significant factors to consider when evaluating for a part's strength, as they indicate how much endurance and reliability it can rely on. Let us talk about fatigue planes and the process that causes our engine shaft to

break due to fatigue failure. In the uncommon event of a fatigue failure, a thorough examination of the break planes is required to devise a preventative strategy. Torsion is something it can resist. The objective is to have a shaft with enough torsional strength to sustain the torque applied to it [8].

2. Methodology

2.1. Finite Element Modeling and Simulation. Using ANSYS Workbench 2021, this research aims to perform the numerical simulations of engine crankshaft made of 316 stainless steel, carbon composite, and FGM material to reveal the material with optimum performance. The

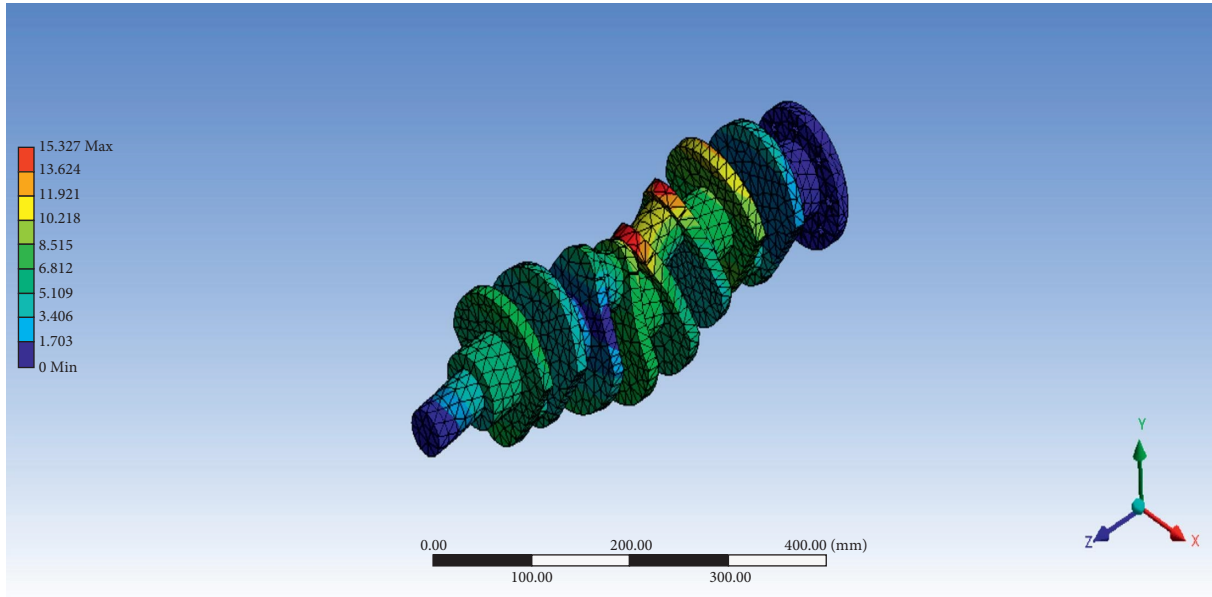


FIGURE 8: Deformation of stainless-steel crankshaft at the fourth mode of vibration.

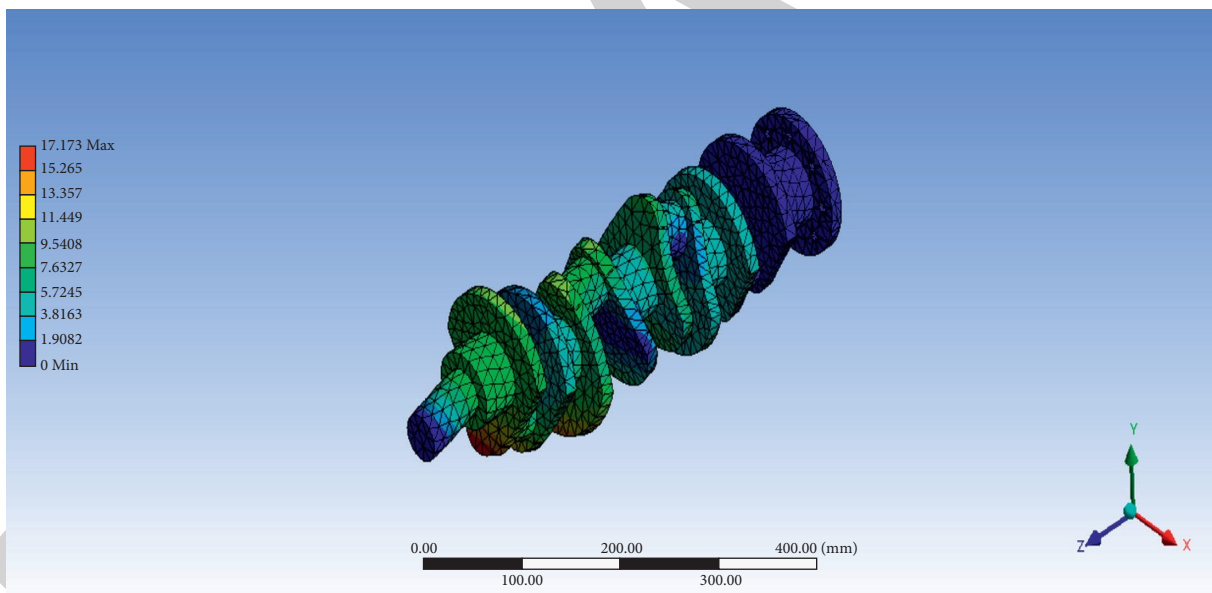


FIGURE 9: Deformation of stainless-steel crankshaft at the sixth mode of vibration.

harmonic analysis and response spectrum will be performed on the shafts to investigate the behavior of the shaft under the action of the loading, which produces frequencies that are unique to each material. Such frequencies are known as the fundamental or natural frequencies of vibrations, and when it coincides with the frequency response of vibration, there will be resonance, which if attained, can lead to the cause of fracture development within the surface [9].

For the purpose of this work, the geometrical dimension and physical properties of the 316 stainless and carbon composites and FGM to be used for the analysis are all presented in Tables 1 to 8. Also, presented in Figures 3 and 4

is the 3D model of the meshed crankshaft in ANSYS workbench.

2.2. *Engine Shaft (316 Steel + Al₂O₃) FGM Modeling.* The effective material properties of FGMs can be mathematically modeled as [10, 11]

$$P_{eff}(T, \xi) = P_m(T)V_m(\xi) + P_c(T)(1 - V_m(\xi)), \quad (1)$$

where P_{eff} is the effective material property of FGM; P_m is the temperature-dependent properties of the metal; P_c is the temperature-dependent properties of the ceramic; and V_m is

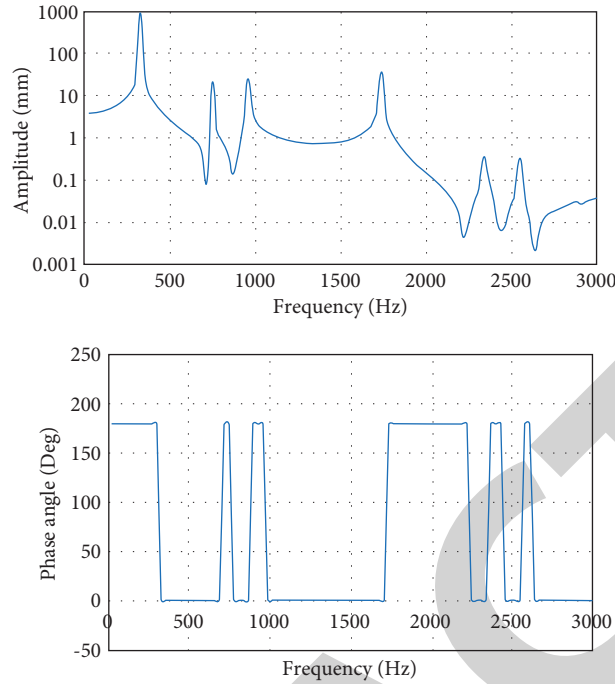


FIGURE 10: Frequency response diagram of stainless-steel crankshaft.

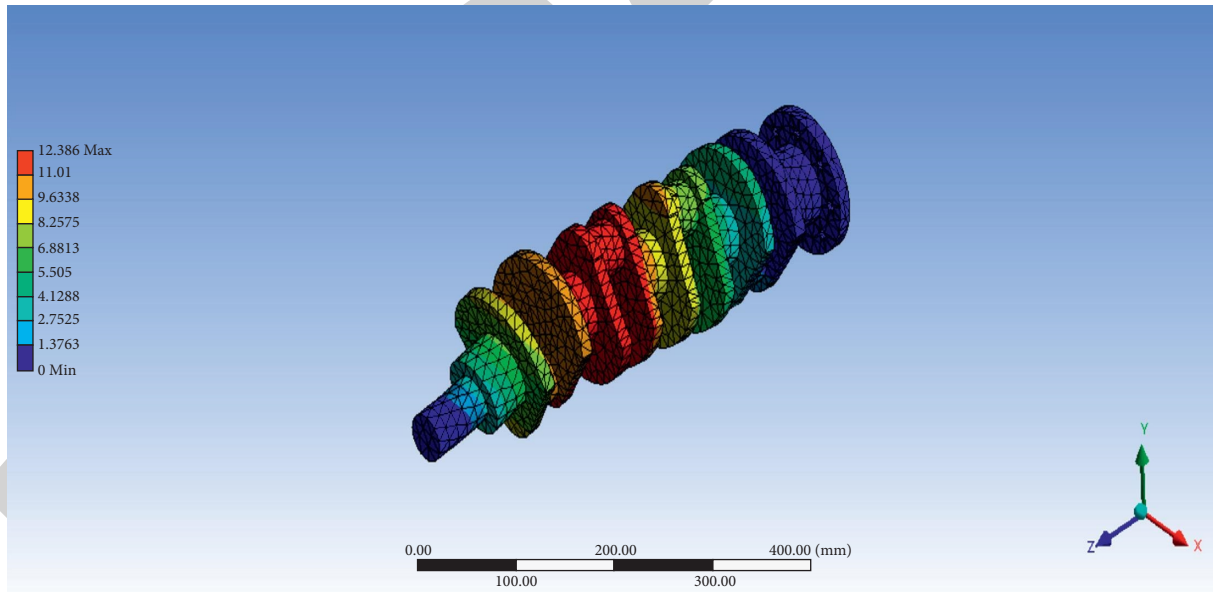


FIGURE 11: Deformation of carbon fiber composite crankshaft at the first mode of vibration.

the volume fraction of the metal constituent of the FGM. Additionally, a simple power-law exponent of the volume fraction distribution is used to express the amount of metal in FGMs [12]. The expression of an axisymmetric cylinder for the volume fraction of ceramic V_c is

$$V_c = \left(\frac{r - r_i}{r_o - r_i} \right)^n, \quad (2)$$

where r_o is the cylinder outer radius; r_i is the cylinder inner radius, r is the radial coordinate ($r_i \leq r \leq r_o$), and n is the index of power-law. In this way, the preceding distribution, the material of the shaft gradually changes from ceramic-rich in the outer surface to metal-rich in the inner surface [13, 14]. In this paper, it was considered a power-law index (n) equivalent to 1. As a result, the grading relations for the mechanical and physical properties of the FGM compound developed from stainless steel in addition with aluminum

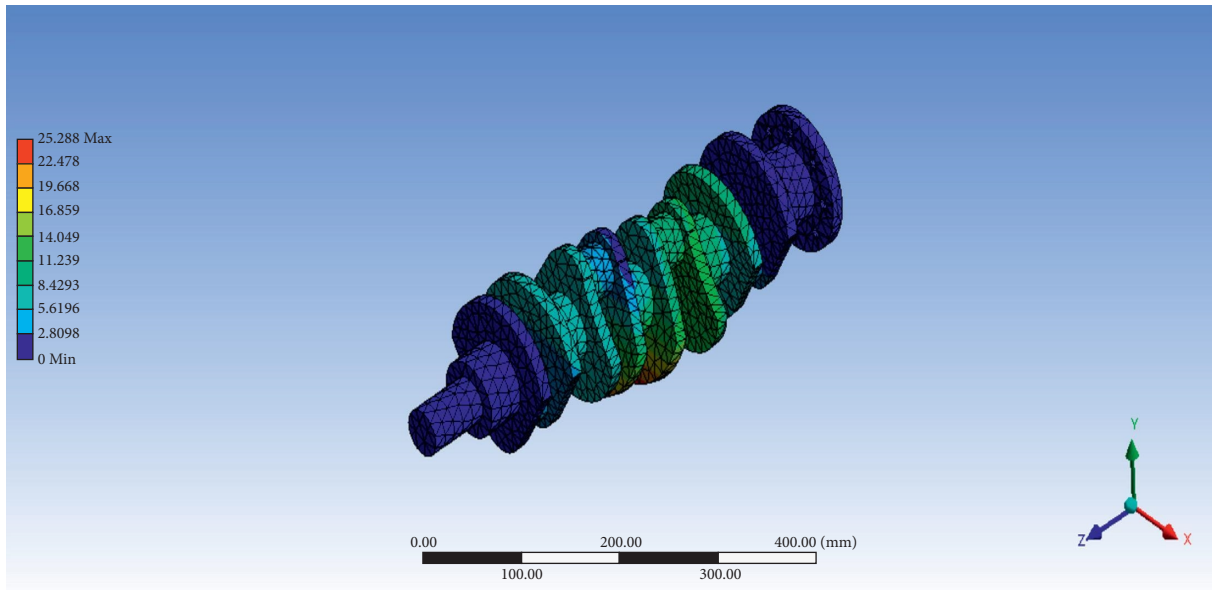


FIGURE 12: Deformation of carbon fiber composite crankshaft at the second mode of vibration.

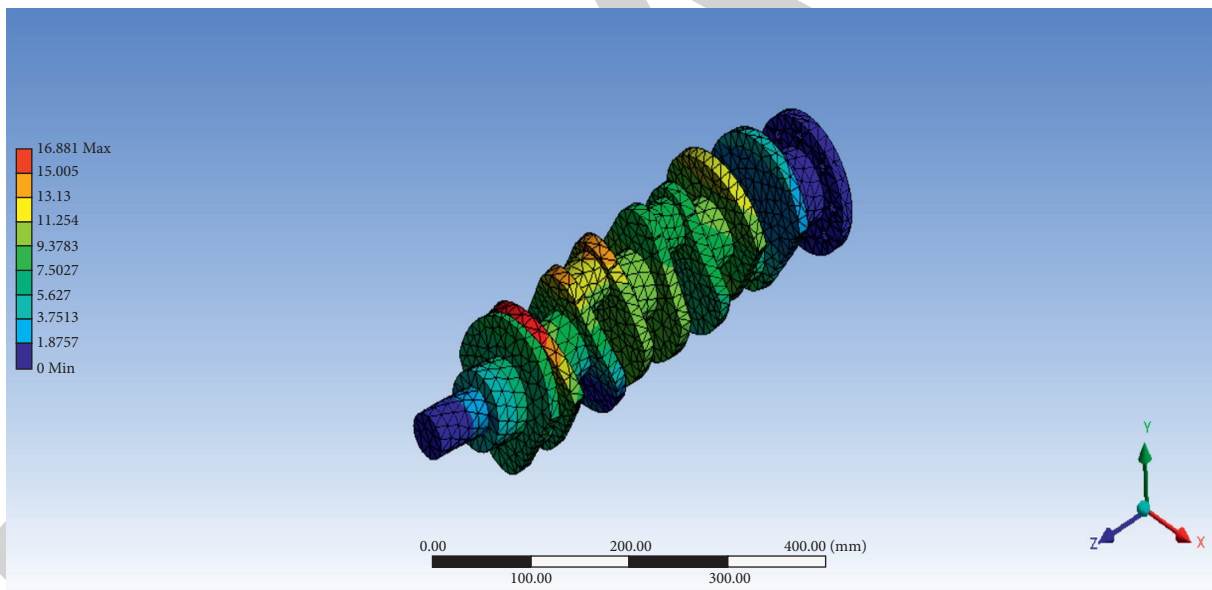


FIGURE 13: Deformation of carbon fiber composite crankshaft at the third mode of vibration.

oxide (Al_2O_3) and considering equations (1) and (2) are defined and presented in Tables 3 to 6

3. Results and Discussion

3.1. Engine Shaft (Stainless Steel). Stainless steel is an appreciable material for the low torque and power transmission shafts. The following are some essential properties of the engine's selected material [15]

Due to its corrosion resistance, high strength, and capacity to resist fracture, stainless steel is the suitable material

to be selected [16]. As a result, it is an excellent choice for working in hostile environments. The set of simulated results from the modal or free vibrations analysis and harmonic analysis or forced vibrations analysis of the stainless-steel crankshaft in ANSYS are presented in Figures 5 to 9 and Table 7. Finally, Figure 10 depicts the frequency response diagram of the engine shaft during vibrations.

The frequency acquired from the mode shapes in ANSYS is represented graphically in Figures 5 to 9. The possible maximum vibrational intensity that will be experienced by the crankshaft is determined by the natural frequencies of

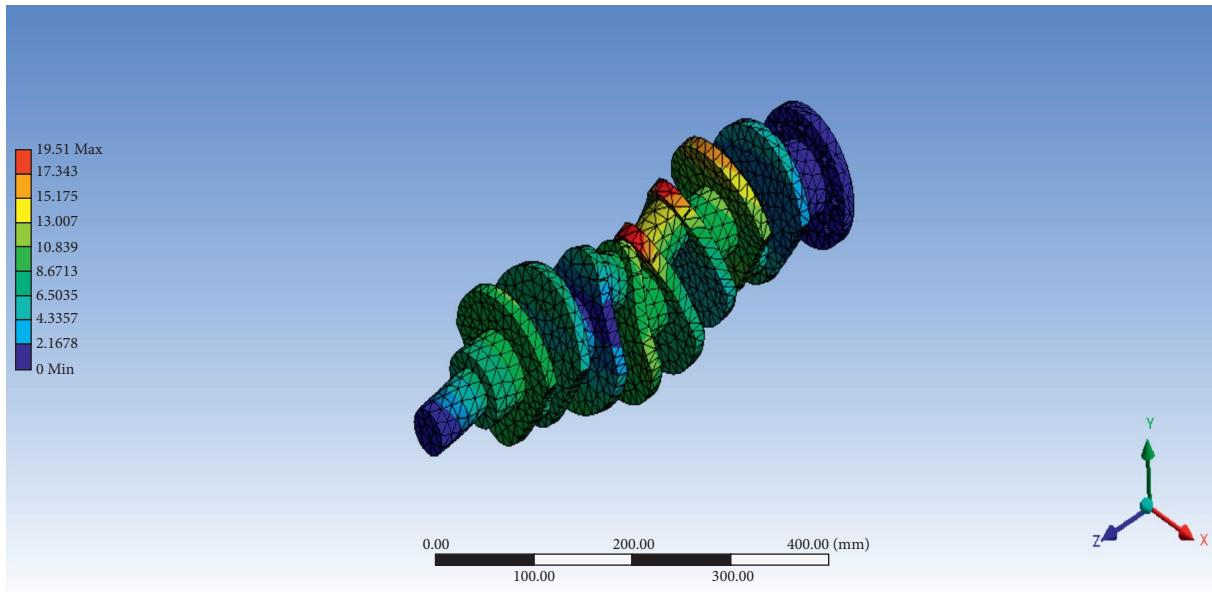


FIGURE 14: Deformation of carbon fiber composite crankshaft at the fourth mode of vibration.

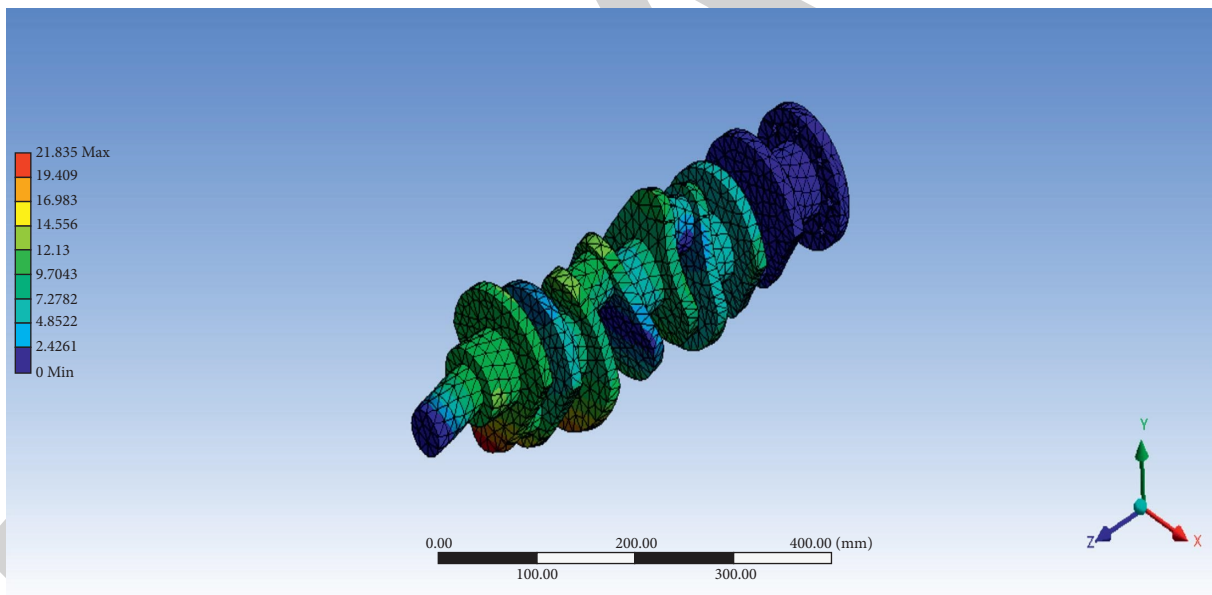


FIGURE 15: Deformation of carbon fiber composite crankshaft at the fifth mode of vibration.

vibration. In contrast to the minimum, both factors, as well as the number of cycles, have a significant impact in determining the overall deformation. The natural frequencies and vibrational deformation for the three scenarios will then be compared to determine which material shows the best performance for the engine shaft [17, 18].

3.2. Engine Shaft (Carbon Fiber Composite). In this section, we have presented the results of modal and harmonic analysis of the crankshaft made with carbon fiber composite;

we will look at whether the material is the best for our engine shaft development. Various tests are undertaken on the three models created in the chase, and the conclusions are expressed later [19, 20]. Carbon composite is known for its stiffness, and it will be compared with other materials in this study.

Figures 11 to 16 present the results of modal and harmonic analysis for the carbon composite crankshaft.

While Figures 11 to 15 present deformations at each mode of vibration for the carbon composite crankshaft, the natural frequencies for carbon fiber are shown in Table 8.

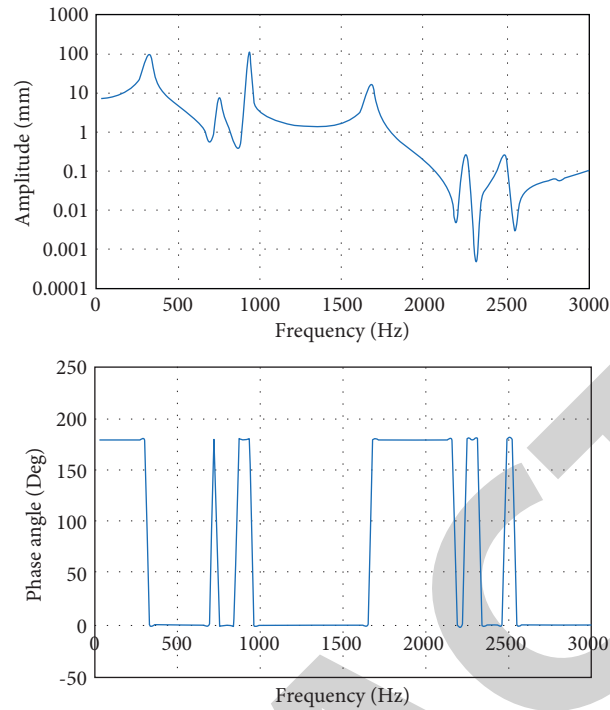


FIGURE 16: Frequency response diagram of carbon composite crankshaft.

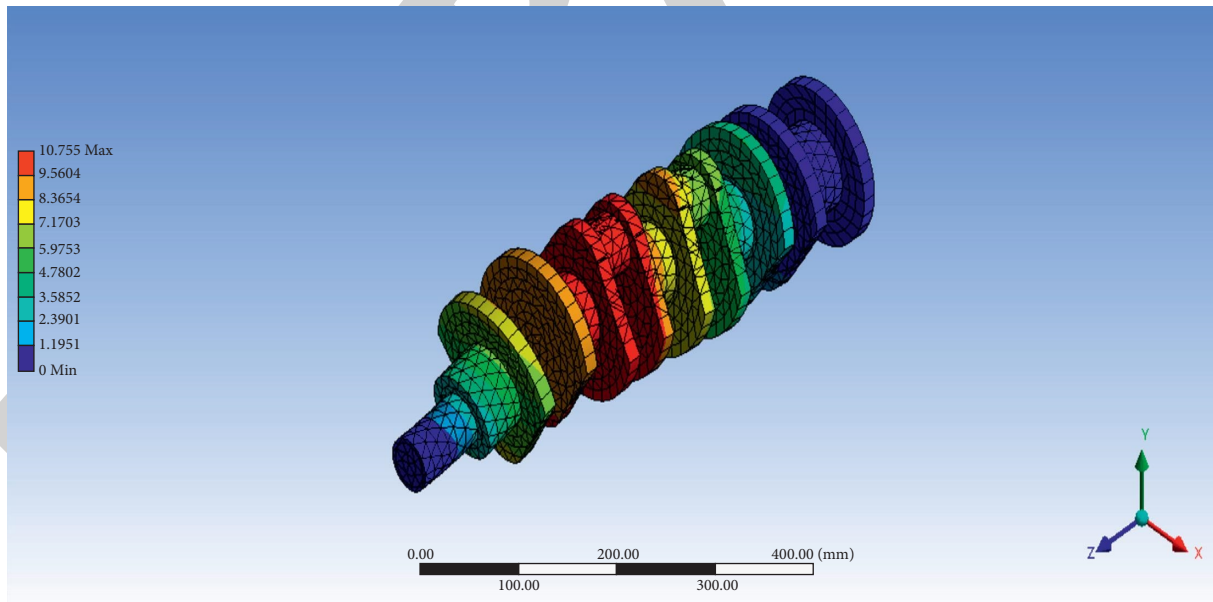


FIGURE 17: Deformation of FGM crankshaft at the first mode of vibration.

The system response of carbon fiber in frequency domain has been determined using ANSYS shown in Figure 16. The system behavior of the shafts in steady-state reactions will be explored further down [21, 22]. It entails determining how well a thing performs when it is subjected to loads.

3.3. Engine Shaft (FGM). Figures 17 to 21 present the overall deformation of a functionally graded material engine shaft (FGM) during the first five modes of vibration. The overall deformation data from ANSYS show a colored depiction of the stress concentrations in the body. It provides information about the component's most susceptible part. The

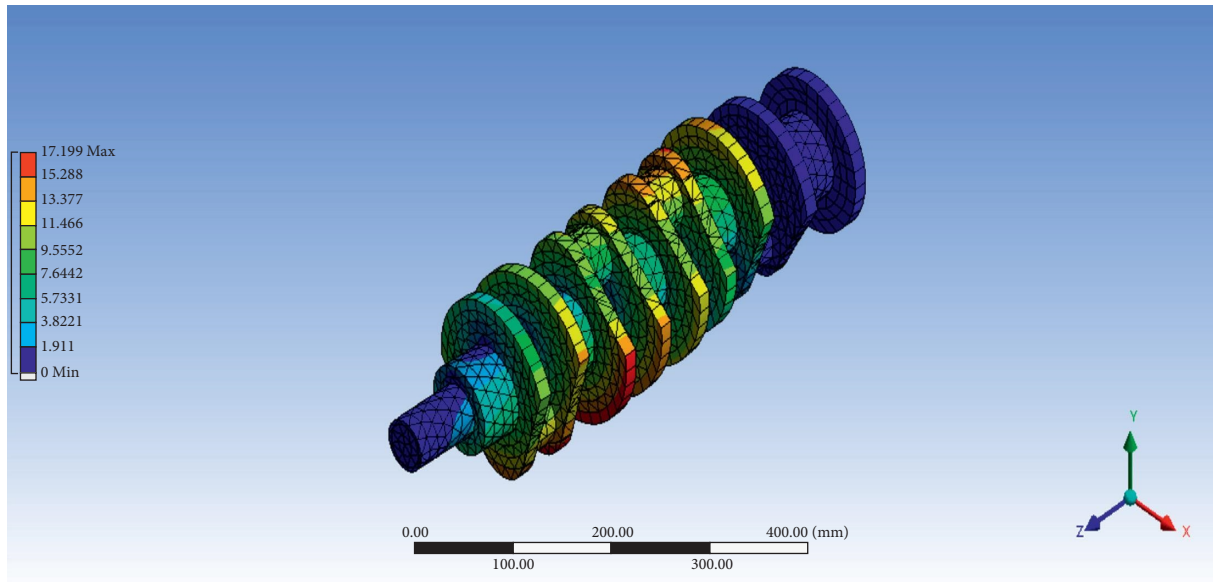


FIGURE 18: Deformation of FGM crankshaft at the second mode of vibration.

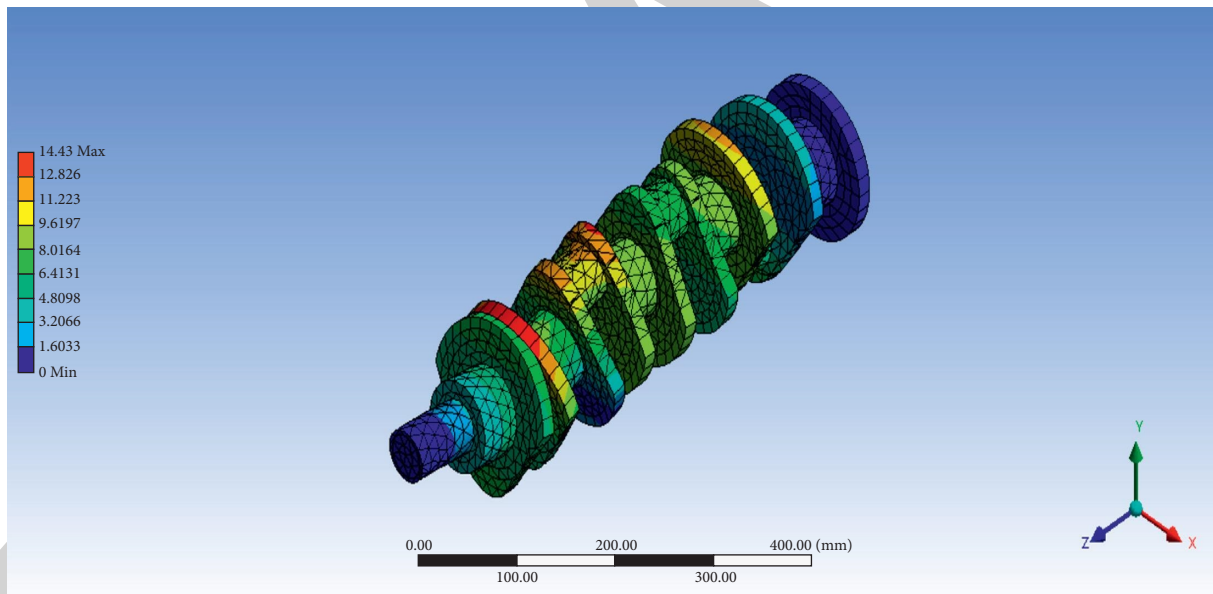


FIGURE 19: Deformation of FGM crankshaft at the third mode of vibration.

results are tabularized in Table 9 for more clarity. It can be observed that the deformation varies approximately sinusoidally as it increases and decreases interchangeably. In this scenario, stress concentration is largely towards the diameters' margins, resulting in a fatigue failure near the shaft's circumferential boundary [23, 24].

Figures 22 and 23 show the graph of comparisons of the frequency response and natural frequencies from the modal analysis results of the 316 steel, composite, and FGM crankshaft. Considering the amplitude of vibration as shown in Figure 23, the composite crankshaft suffers the highest

deformation while on the average, FGM and 316 steel crankshaft suffers almost the same level of deformation. Also, as shown in Figure 24, the FGM crankshaft clearly possesses the far-highest natural frequencies during the first five modes of vibrations followed by 316 steel crankshaft. Such materials like FGM with high values of natural frequencies would certainly offer durability and optimum performance under loading. Going by this analysis, FGM has shown the best performance due to its highest set of natural frequencies and low deformations. This is a very important selection criterion in the design of engine crankshaft.

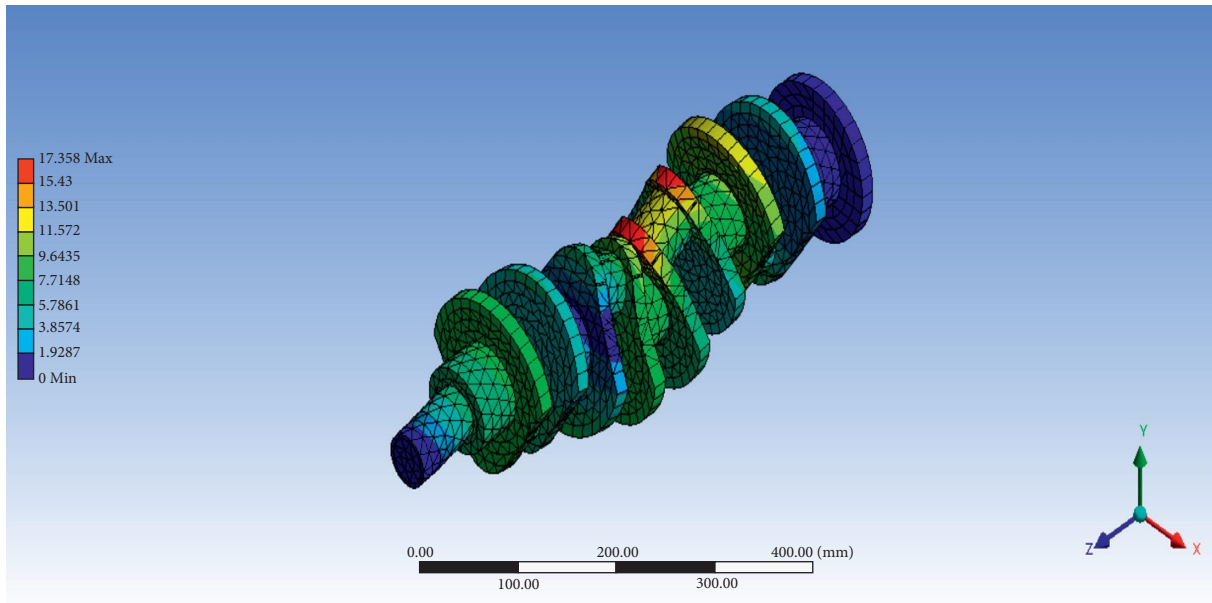


FIGURE 20: Deformation of FGM crankshaft at the fourth mode of vibration.

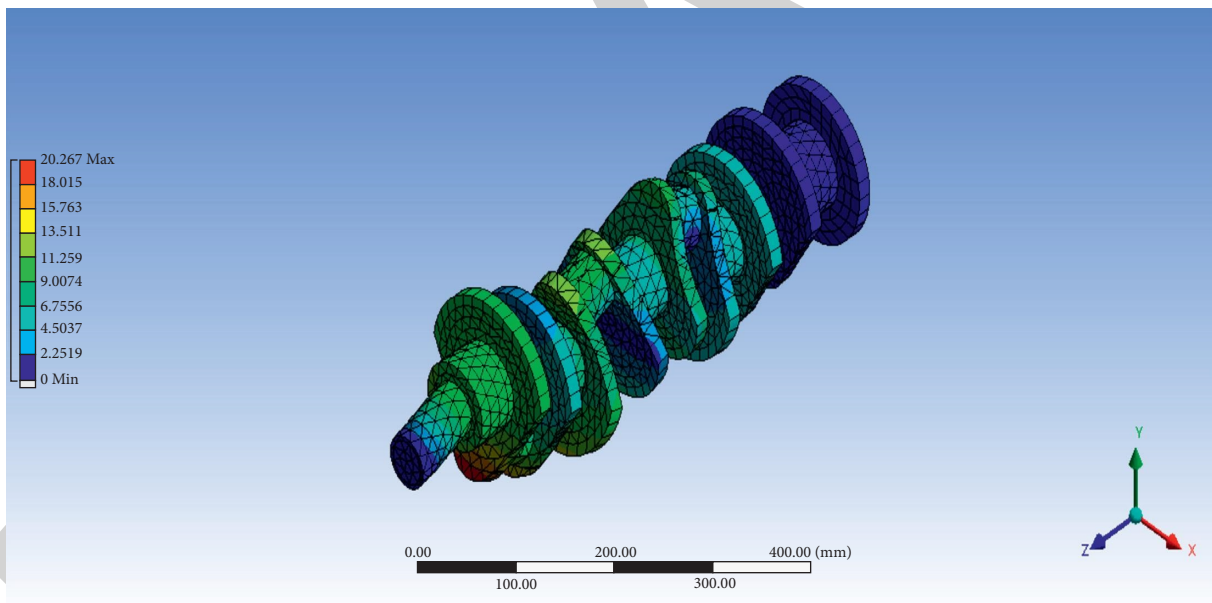


FIGURE 21: Deformation of FGM crankshaft at the fifth mode of vibration.

TABLE 9: Modal analysis results of FGM crankshaft.

Modes	Frequency	Deformation (mm)
1	432.26	10.755
2	943.56	17.199
3	1234.8	14.43
4	2208.9	17.358
5	2943.5	20.267

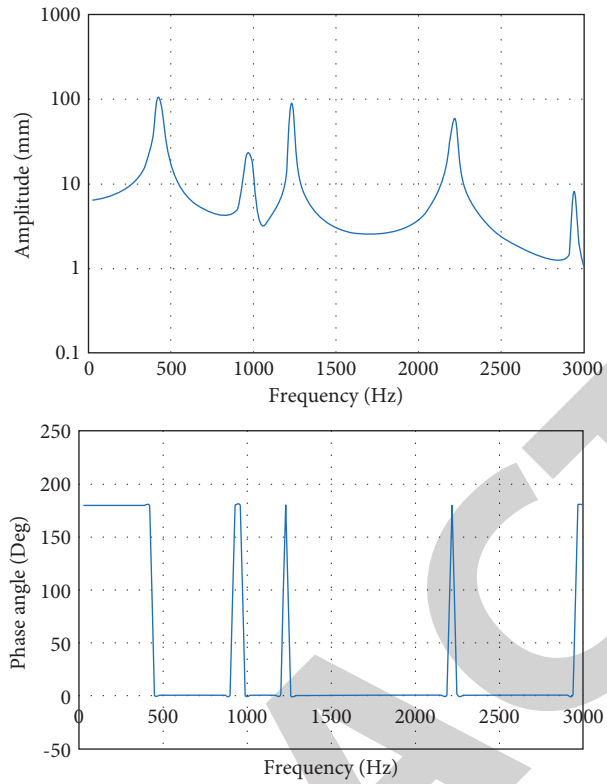


FIGURE 22: Frequency response of FGM crankshaft at the fifth mode of vibration.

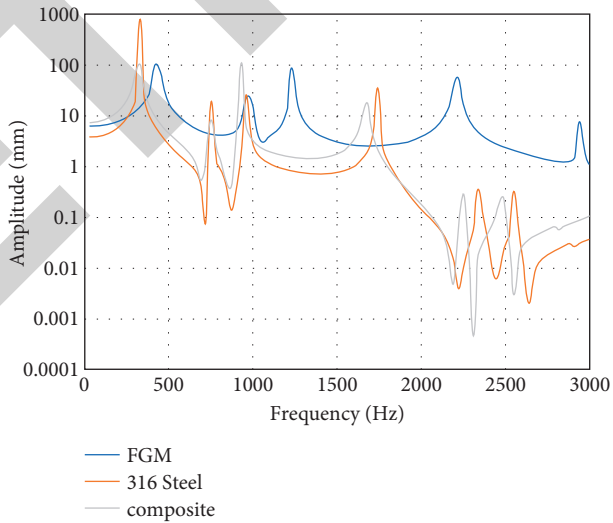


FIGURE 23: Frequency response diagram of the 316 steel, composite, and FGM crankshaft.

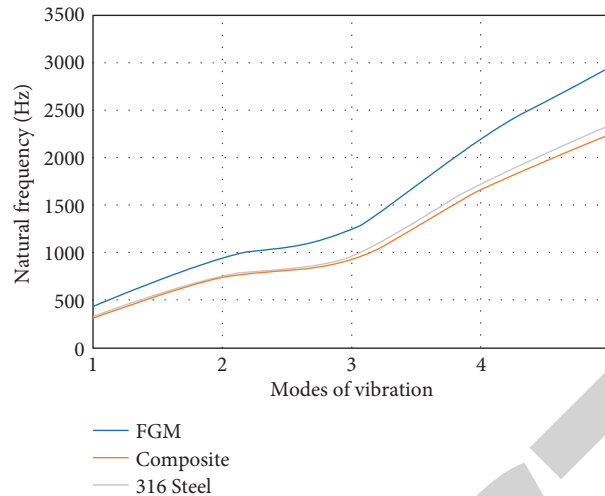


FIGURE 24: Natural frequencies of the 316 steel, composite, and FGM crankshaft.

4. Conclusion

Functionally graded materials (FGM's) are the appreciable and distinctive types of materials that have different properties based on the varying dimensions of the materials. In this study, we have investigated the use of stainless steel, a composite, and a FGM in the design of crankshaft. The finite element model of the crankshaft was created using ANSYS to perform modal and harmonic analysis to visualize how the system behaves in real-world conditions. The ultimate objective is to guarantee that the shaft functions properly and that the component's life is extended. The contribution of study is to show that performance of stainless-steel crankshaft would be improved when it is functionally graded into a new material. Based on the results of the modal and harmonic analysis, it is concluded that FGM crankshaft would offer the best durability and show optimum performance when compared with the other two material crankshafts investigated in this study. It is recommended that more research works should be carried out on the modal and harmonic analysis of engine crankshaft using many more conventional and functionally graded material (FGM) types as this aspect is of great engineering importance [25, 26].

Data Availability

The data used to support the findings of this study are included within the article.

Conflicts of Interest

The author declares no conflicts of interest.

References

- [1] S. Efendi and Andoko, "Design and simulation of cracks in A four-cylinder engine crankshaft using finite element method," *IOP Conference Series: Materials Science and Engineering*, vol. 494, no. 1, Article ID 012004, 2019.
- [2] B. Kieback, A. Neubrand, and H. Riedel, "Processing techniques for functionally graded materials," *Materials Science and Engineering A*, vol. 362, no. 1-2, pp. 81-106, 2003.
- [3] Y. Miyamoto, W. A. Kaysner, B. H. Rabin, A. Kawasaki, and R. G. Ford, "Functionally graded materials: design, processing and applications," *Springer Science & Business Media*, vol. 5, 2013.
- [4] Y. M. Shabana, "Elasto-Plastic thermal stresses in functionally graded materials considering microstructure effects," *Current Advances in Mechanical Design and Production VII*, vol. 7, pp. 223-231, 2015.
- [5] S. Das and S. T. K. Das, "Functionally grade composite material production," *Encyclopedia of Materials: Composites*, vol. 2, pp. 798-803, 2021.
- [6] F. Erdogan, "Fracture mechanics of functionally graded materials," *Composites Engineering*, vol. 5, no. 7, pp. 1-5, 1995.
- [7] M. B. Alazzam, F. Hajje, A. S. AlGhamdi, S. Ayouni, and M. A. Rahman, "Mechanics of materials natural fibers technology on thermal properties of polymer," *Advances in Materials Science and Engineering*, vol. 2022, Article ID 7774180, 2022.
- [8] A. H. Mostefa, S. Merdac, and N. Mahmoudi, "An overview of functionally graded materials «FGM», in *Proceedings of the Third International Symposium on Materials and Sustainable*, Boumerdes, Algeria, November 2018.
- [9] R. Ben Yedder, "Heat transfer by natural convection in composite trombe wall solar collector," Edited by J. T. Beard and H. C. Heuritt, Eds., in *Proceedings of the ASME, Solar Energy Technology*, vol. 8, San Francisco, 1989.
- [10] R. A. E. Mahamood and E.T. Akinlabi, "Laser-metal deposition of functionally graded, Ti6Al4V/TiC," *Mater. Des.* vol. 84, pp. 402-410, 2016.
- [11] M. B. Alazzam, N. Tayyib, S. Z. Alshawwa, and M. Ahmed, "Nursing care systematization with case-based reasoning and artificial intelligence," *Journal of Healthcare Engineering*, vol. 2022, Article ID 1959371, 2022.
- [12] V. Birman and L. W. Byrd, "Modeling and analysis of functionally," *graded materials and structures*, vol. 60, 2007.
- [13] R. J. Cochran and R. E. Hogan, "Benchmark Problem," in *Proceeding of the of the 1995 ASME Cong., Comparison of Computational Results for Natural Convection in a Square Enclosure, with Variable Viscosity*, pp. 1112-1117, Iuquerque, NM, and Livermore, CA, November 1995.

Retraction

Retracted: The Role of Gum Arabic for a Protective Kidney Dysfunction Induced Gentamicin on Diabetes Rats

Advances in Materials Science and Engineering

Received 20 June 2023; Accepted 20 June 2023; Published 21 June 2023

Copyright © 2023 Advances in Materials Science and Engineering. This is an open access article distributed under the Creative Commons Attribution License, which permits unrestricted use, distribution, and reproduction in any medium, provided the original work is properly cited.

This article has been retracted by Hindawi following an investigation undertaken by the publisher [1]. This investigation has uncovered evidence of one or more of the following indicators of systematic manipulation of the publication process:

- (1) Discrepancies in scope
- (2) Discrepancies in the description of the research reported
- (3) Discrepancies between the availability of data and the research described
- (4) Inappropriate citations
- (5) Incoherent, meaningless and/or irrelevant content included in the article
- (6) Peer-review manipulation

The presence of these indicators undermines our confidence in the integrity of the article's content and we cannot, therefore, vouch for its reliability. Please note that this notice is intended solely to alert readers that the content of this article is unreliable. We have not investigated whether authors were aware of or involved in the systematic manipulation of the publication process.

Wiley and Hindawi regrets that the usual quality checks did not identify these issues before publication and have since put additional measures in place to safeguard research integrity.

We wish to credit our own Research Integrity and Research Publishing teams and anonymous and named external researchers and research integrity experts for contributing to this investigation.

The corresponding author, as the representative of all authors, has been given the opportunity to register their agreement or disagreement to this retraction. We have kept a record of any response received.

References

- [1] G. Ali Alshehry, "The Role of Gum Arabic for a Protective Kidney Dysfunction Induced Gentamicin on Diabetes Rats," *Advances in Materials Science and Engineering*, vol. 2022, Article ID 8617445, 8 pages, 2022.

Research Article

The Role of Gum Arabic for a Protective Kidney Dysfunction Induced Gentamicin on Diabetes Rats

Garsa Ali Alshehry 

Food Science and Nutrition Department, Collage of Science-Taif University, Taif, Saudi Arabia

Correspondence should be addressed to Garsa Ali Alshehry; garsa.a@tu.edu.sa

Received 3 March 2022; Revised 14 March 2022; Accepted 21 March 2022; Published 23 April 2022

Academic Editor: Palanivel Velmurugan

Copyright © 2022 Garsa Ali Alshehry. This is an open access article distributed under the Creative Commons Attribution License, which permits unrestricted use, distribution, and reproduction in any medium, provided the original work is properly cited.

The target of this study was to estimate Gum Arabic for total phenols and flavonoids. In addition to antioxidant activities, estimate gum Arabic for total phenols and flavonoids. In addition to antioxidant activities, the problem of studying the potential effect of experimental diabetes kidney failure induced by gentamicin and the effect of taking gum Arabic. The results were observed to increase the content of phenols and total flavonoids. The method of study was that diabetic rats groups were fed on a basal diet, and intake of drinking water separately at concentrations of 5, 10, 15, and 20 g gum Arabic dissolved in 100 ml of water/day indicated that the lipid profile gradually decreased in triglycerides from group (1) was 128.30 mg/dL to group (4) was 77.53, total cholesterol-lowering from 163.18 mg/dL to 111.19 mg/dL, LDL reducing from 101.61 mg/dL to 37.83 mg/dL, VLDL lessening from 25.73 mg/dL to 15.51 mg/dL, and glucose reduced from 192.52 mg/dL to 111.24 mg/dL. and glucose became less from 192.52 mg/dL to 111.24 mg/dL. The kidney functions indicated to creatinine, urea, uric acid, blood urea nitrogen, and bilirubin were decreased from 1.34, 0.95, 2.24, 45.61, and 0.66 mg/dl in group (1) to 0.78, 29.84, 2.12, 16.25, and 018 mg/dL in group (4), respectively, when taking Gum Arabic. Furthermore, in the treatment group with Gum Arabic at different doses, the results could be noticed that sodium and calcium were gradually increased, and there was gradual reduction in potassium, phosphor, and magnesium. The results found that the treatment with GA had lowered the effects of gentamicin and streptozotocin, as evidenced by improvement of the lipids profile, kidney function, some minerals in serum, and antioxidant enzyme in kidney tissue, which may be referred to as its content of antioxidant active ingredients. Therefore, it is recommended that Gum Arabic is a beneficial dietary tool in reducing the advancement of chronic kidney disease in diabetic rats.

1. Introduction

Diabetic kidney disease (DKD), previously known as diabetic nephropathy, is a popular complication of diabetes and about 20–40% of diabetic patients have this condition [1] due to damage to kidney function. This complication is caused to significant microvascular alternatives due to high glucose in the blood, elevated lipid profile, and oxidative stress [2].

Diabetes mellitus (DM) is a metabolic disease that causes increased glucose in the bloodstream, which could be due to more complications, including kidney failure [3]. This is a much-intended result treatment but is very expensive due to the cost of obtaining the donor's kidneys [4].

The basics of chronic kidney disease and exacerbated conditions, which include inflammation, oxidative stress, cell death, and lineaments, are consistently seen in humans and rats [5]. There are other main diseases like tumor necrosis agents and oxidative enzymes and oxidative stress leading to influences in rats' kidney failure [6, 7].

Gum acacia (GA) is a soluble dietary fiber, and the benefit of GA has been confirmed in humans with kidney failure, and more experimental studies have assured the beneficial effects of GA in kidney failure [8]. The benefit of GA has been confirmed in rats with diabetic kidney failure and in diabetes rats [9].

Gum Arabic (GA) is globally used in the diet and pharmaceutical industries. Therefore, it has become clear that GA has an antioxidant effect. [10]. Gum Arabic contains

excellent emulsifying characteristics and reduced viscosity; these characteristics are used globally mostly in food industries and soft drinks as a stabilizer [11].

Gum Arabic contains hydrophilic carbohydrates and hydrophobic protein, which adsorbs on the oil droplets while keeping the hydrophilic carbohydrate flocculation and aggregation particles through electrostatic for vacuum repulsion in food additives [12, 13].

The authors of [14, 15] studied antioxidant assays for the detection of total phenolic compounds (TPCs) and the selection of appropriate and inexpensive methods for determining antioxidant capacity in Gum Arabic (GA) samples. The results revealed that the Folin-Ciocalteu Index (FCI) and copper-reduced antioxidant capacity (CUPRAC) are closely related to ferric antioxidant capacity (FRAP). Therefore, these methods are successful in their ability to determine GA antioxidant activity. Thus, GA is mostly known as less acidic that can be obtained from proper methods to detect antioxidant capacity. The research contribution was conducted to study gum Arabic as a dietary intake on kidney failure in diabetic rats.

2. Materials and Methods

2.1. Materials. Gum Arabic (*Acacia Senegal* L.) and kits were purchased from Sigma-Aldrich Corp., St. Louis, MO, USA. 48 adult male Wistar rats weighing 180–200 g were obtained from a pharmacy college at King Saud University. Animals were fed on a basic diet for a week; it consisted of cornstarch 60%, casein 20%, corn oil 10%, salt mixture 4%, vitamin mixture 1%, and cellulose 5% according to [16].

Gum Arabic goes into solution water at 10% w/v and is given to rats as drinking water. The drinking daily intake for every rat in the separately different groups has doses of about 5, 10, 15, and 20 g/kg body weight rat/day.

2.2. Methods

2.2.1. Extraction of Antioxidant. The quantitative content of phenols and flavonoids as well as the antioxidant activity of Gum Arabic were estimated. Use solvents were methanol, ethanol, and acetone 70% according to [17].

2.2.2. Determination of Phenols and Flavonoids Content. The phenol content was measured according to [18] with Folin-Ciocalteu reagent and then measured at 760 nm and calculated as mg Gallic acid equivalents/100 g sample.

The total flavonoid content was determined according to [19] and then measured at 510 nm and calculated as mg quercetin equivalent/100 g dry weight.

2.2.3. DPPH Assay. The antioxidant activity was measured according to [20] and then measured at 515 nm and calculated as mg Trolox/100 g sample.

2.2.4. Cupric Ion Reducing Antioxidant Capacity (CUPRAC) Assay. The CUPRAC was determined according to [21]. It was recorded at 450 nm wavelength and mg Trolox/100 g of the sample.

2.2.5. FRAP Assay. Ferric Reducing-Antioxidant Power (FRAP) was assayed according to [22] and then measured at 593 nm and calculated as mg Trolox/100 g of the sample.

2.3. Nutritional Experiments. Forty-eight rats were divided into two groups: the first group (8 rats) was named the negative group, fed on the basic diet for six weeks. The residual forty rats were injected with gentamicin to induce kidney failure according to [23]. Then, the same rats were injected with streptozotocin into their leg muscles (5 mg/100 g rat) to stimulate diabetes according to [15, 24]. After that, the injected rats were re-divided into five groups, with the diabetic kidney rats positive group fed on the basic diet. The four treatment groups were fed on a basic diet and the daily intake of drinking water was measured for each group separately at concentrations of 5, 10, 15, and 20 g from Gum Arabic dissolved in 100 ml water per day.

The blood samples were collected at the end of the experiment and centrifuged to obtain sera and kept at -20°C for analysis. The levels of serum glucose, total cholesterol, and triglycerides were determined according to [25–27], respectively. High, low, and very-low-density lipoprotein cholesterol in serum was estimated by [28–30]. Kidney functions such as serum creatinine, urea, uric acid, and blood urea nitrogen (BUN) concentrations were estimated by [31–34], respectively. Moreover, total bilirubin was assessed according to [35].

Sodium (Na) and potassium (K), calcium (Ca), phosphorus (P), and manganese (Mn) were determined in serum calorimetrically according to [36].

The kidney sample was taken, and malondialdehyde (MDA), superoxide dismutase (SOD), and catalase (CAT) were determined by [37–39].

2.4. Statistical Analysis. The results were presented for analysis of variances, and Duncan's multiple range tests at the ($P \leq 0.05$) level were used to compare the means. The analysis was carried out using the ANOVA procedure of the Statistical Analysis System [40].

3. Results and Discussion

3.1. Total Phenolic, Flavonoid, and Antioxidant Activity Extracted from Gum Arabic. The quantitative determination of phenols and flavonoids content extracted from 70% different solvents (methanol, ethanol, and acetone) at Gum Arabic and the finding are tabulated in Table 1. The results showed that in 70% methanol, the highest extracted phenols and flavonoids content were 55.28 mg GAE/100g, and 40.35 mg QE/100g dry weight. Furthermore, total phenolic content in 70% from ethanol and acetone were 30.67 and 8.58 mg GAE/100 g, in addition,

TABLE 1: Effect of the various solvents on total phenolic, flavonoid, and antioxidant activity extracted from Gum Arabic.

Antioxidant content and activity	Solvent extraction of Gum Arabic		
	Methanol	Ethanol	Acetone
Total phenolic acids mg GAE/100 g of dry weight	55.28 ± 1.25	30.67 ± 0.81	8.58 ± 0.04
Total flavonoid mg QE/100 g dry weight	40.35 ± 1.12	27.38 ± 0.46	5.89 ± 0.03
DPPH mg Trolox/100 g of dry weight	30.68 ± 0.98	25.91 ± 0.38	11.58 ± 0.07
CUPRAC mg Trolox/100 g of dry weight	35.18 ± 0.84	22.39 ± 0.17	9.87 ± 0.06
FRAP mg Trolox/100 g of dry weight	32.28 ± 0.76	28.23 ± 0.52	10.38 ± 0.05

Values expressed are means ± SD of three replicate.

and total flavonoids were 27.38 and 5.89 mg QE/100 g dry weight, respectively. The result was agreed with those findings reported in literature methods which recorded that methanol was also chosen for apricots to determine total antioxidant capacity [41, 42]. Phenols are important to antioxidant activity due to chelating redox-active metal ions, disrupting lipid-free radical chains, and inhibiting transformations of hydroperoxide into reactive oxygen [43].

The table shows that the antioxidant activities as DPPH, OUPRAC, and FRAP were the highest in 70% methanol with 30.68, 35.18, and 32.28 mg Trolox/100 g of dry weight, respectively, extracted from Gum Arabic. In addition, the activities extracted from Gum Arabic from ethanol and acetone were 25.91, 22.39, and 28.23 mg Trolox/100 g in ethanol followed by 70% acetone which were 11.58, 9.87, and 10.38 mg Trolox/100 g of dry weight, respectively. Furthermore, the authors of [44] found a relationship between phenolic content and FRAP. Moreover, the authors of [45] indicated that the phenolic content was linked with ABTS activity. Therefore, it could be noticed that the significant content of phenolic acids as a reducing agent may be due to an electron donation. The authors of [6] found the DPPH capacity for scavenged free radicals independently. Therefore, plant extracts had phenolic content that readily donated a hydrogen atom to DPPH to give DPPH-H, considered as required to be done mechanism of antioxidants.

3.2. Serum Lipid Profile Assay in Different in Rats Diabetic Kidney Failure. Results from Table 2 and Figure 1 show that the lipid profile of control group diabetic kidney failure rats was the highest in triglycerides. Total cholesterol, LDL, VLDL, and glucose were 146.38, 180.38, 122.73, 29.28, and 220.39 mg/dL, respectively. Meanwhile, HDL cholesterol was the lowest in the control group rats with diabetic kidney failure was 25.19 mg/dL, and the highest in the control healthy rats group (50.59 mg/dL), compared with the different treatment groups at various doses with Gum Arabic.

The results from different diabetic kidney rats groups fed on a basal diet and that had daily intake of drinking water separately at concentrations of 5, 10, 15, and 20 g Gum Arabic dissolved in 100 ml water/day indicated that the lipids profile were gradually decreased. Therefore, it could be noticed that the triglycerides decreased from group (1) at 128.30 mg/dL to group (4) at 77.53, total cholesterol-

lowering from 163.18 mg/dL to 111.19 mg/dL, LDL reducing from 101.61 mg/dL to 37.83 mg/dL, VLDL lessening from 25.73 mg/dL to 15.51 mg/dL, and glucose was become less from 192.52 mg/dL to 111.24 mg/dL, respectively. Gum Arabic had contained dietary fiber and is utilized to treat chronic kidney disease patients [46] and relieve chronic renal failure in rats [47].

The first pathway indicates that Gum Arabic elevated the excretion of the bile salts in the feces, which may be due to the liver consuming the cholesterol and lowering body fat along with blood cholesterol. Moreover, GA in a diet for rats is responsible for cholesterol formation and overexpresses genes involved in lipid oxidation in rats. Furthermore, the authors of [50–52] reported that overexpression of the fasting-induced lipid factor gene in Gum Arabic-fed mice stimulates lipolysis and reduces fat accumulation in their bodies.

3.3. Serum Kidney Assay in Rats' Diabetic Kidney Failure.

Serum creatinine, urea, uric acid, blood urea nitrogen, and bilirubin were determined in different rats' group diabetic kidney failure, and the results are shown in Table 3 and Figure 2. Diabetic kidney failure rats' positive group was the highest in the kidney functions by 1.35, 110.67, 2.28, 55.43, and 0.82 mg/dL, respectively. This complication is due to significant microvascular changes due to hyperglycemia, hyperlipidemia, and oxidative stress [1]. The diabetic rats in different groups treated with various doses from Gum Arabic were improved to nearly equal control rats' healthy group. The results indicated that the creatinine, urea, uric acid, blood urea nitrogen, and bilirubin were decreased from 1.34, 0.95, 2.24, 45.61, and 0.66 mg/dl in group (1) to 0.78, 29.84, 2.12, 16.25, and 0.18 mg/dL in group (4), respectively. Furthermore, the preventative influence of Gum Arabic on kidney function was also certain to considerably lowering kidney functions concentrations in diabetic kidney failure patients [53]. Gum Arabic has been reported to have a direct antioxidant influence. The kidneys are protected from the kidney failure influence of gentamicin, which is a recognized reason for kidney damage through elevated oxidative stress mechanisms [54].

The authors of [55] noted that Gum Arabic treatment is effective with lowering uric acid, bilirubin, and anti-inflammatory influences, causing that Gum Arabic is a possible treatment supplement, useful in kidney failure and cardiovascular diseases, and it has no side effect when consumed for a long time.

TABLE 2: Serum lipid profile assay in different study groups.

Groups treatment	Triglycerides mg/dL	T. cholesterol mg/dL	LDL mg/dL	HDL mg/dL	VLDL mg/dL	Glucose mg/dL
Control negative	75.25 ^c ± 5.57	110.69 ^c ± 12.49	36.82 ^c ± 1.98	50.59 ^a ± 2.76	15.05 ^c ± 0.17	110.26 ^c ± 12.17
Control positive	146.38 ^a ± 13.26	180.38 ^a ± 14.16	122.73 ^a ± 12.76	25.19 ^e ± 1.16	29.28 ^a ± 0.21	220.39 ^a ± 14.16
Group (1)	128.3 ^b ± 12.14	163.18 ^b ± 13.58	101.61 ^b ± 10.37	31.17 ^d ± 1.24	25.73 ^b ± 0.18	192.82 ^b ± 13.28
Group (2)	111.88 ^c ± 9.59	146.16 ^c ± 14.31	80.46 ^c ± 7.05	37.22 ^c ± 1.36	22.38 ^c ± 0.19	156.76 ^c ± 14.15
Group (3)	95.06 ^d ± 8.91	128.78 ^d ± 12.79	59.78 ^d ± 4.86	43.69 ^b ± 2.38	19.12 ^d ± 0.23	138.53 ^d ± 12.46
Group (4)	77.53 ^e ± 5.12	111.19 ^e ± 13.45	37.83 ^e ± 2.53	49.76 ^a ± 1.42	15.51 ^e ± 0.15	111.24 ^e ± 11.49

Values are mean and SD ($n=8$); where: Mean values in the same with the letter are significantly different at 0.05 levels.

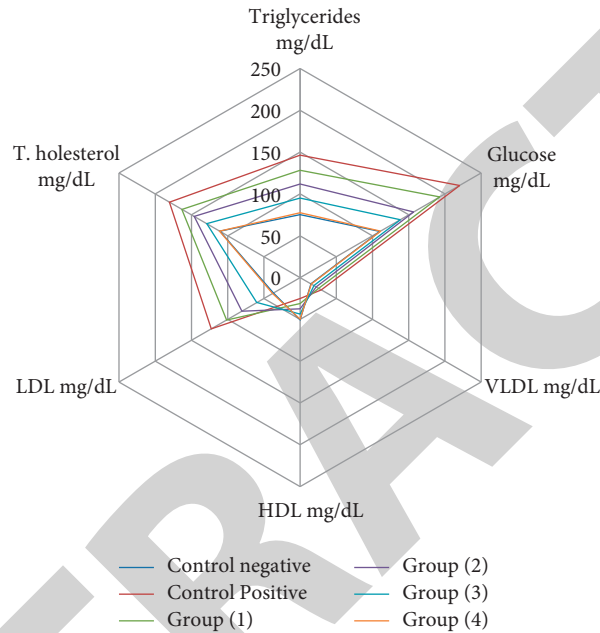


FIGURE 1: Serum lipid profile assay in different study groups.

TABLE 3: Serum kidney assay in different study groups.

Groups treatment	Creatinine mg/dL	Urea mg/dL	Uric acid mg/dL	BUN mg/dL	Bilirubin mg/dL
Control negative	0.72 ^c ± 0.01	30.54 ^e ± 0.24	2.11 ^e ± 0.01	15.76 ^e ± 0.28	0.15 ^e ± 0.01
Control positive	1.53 ^a ± 0.03	110.67 ^a ± 3.07	2.28 ^a ± 0.03	55.43 ^a ± 0.79	0.82 ^a ± 0.04
Group (1)	1.34 ^b ± 0.04	95.64 ^b ± 2.13	2.24 ^b ± 0.04	45.61 ^b ± 0.82	0.66 ^b ± 0.05
Group (2)	1.15 ^c ± 0.02	70.49 ^c ± 1.27	2.20 ^c ± 0.06	35.74 ^c ± 0.46	0.51 ^c ± 0.03
Group (3)	0.98 ^d ± 0.01	51.24 ^d ± 0.25	2.16 ^d ± 0.05	26.18 ^d ± 0.37	0.35 ^d ± 0.02
Group (4)	0.78 ^e ± 0.01	29.84 ^e ± 0.29	2.12 ^e ± 0.01	16.25 ^e ± 0.24	0.18 ^e ± 0.01

BUN: blood urea nitrogen. Values are mean and SD ($n=8$), where mean values in the same with the letter are significantly different at 0.05 levels.

3.4. Some Minerals on Serum in Rats Diabetic Kidney Failure.

Results in Table 4 and Figure 3 observed that diabetic kidney rats had the lowest sodium and calcium levels (105.36mmol/L and 5.76 mg/dL) and the highest potassium, phosphor, and magnesium levels (18.51mmol/L, 8.34mg/dL, and 3.15mg/dL). The authors of [56] showed a significant increase in calcium and sodium ratio as well as a lowering phosphorous and potassium ratio in patients taking the GA for six months. Excess serum phosphorous is a risk agent of death for patients' chronic renal failure (CRF). The authors of [55, 57] found that chronic kidney disease can lead to elevations in circulating magnesium

that can cause heart diseases and can decrease the secretion of parathyroid hormone that causes hypocalcaemia and sodium, which causes arrhythmias out of its influence on the potential heart cell membrane [58]. Hyponatremia can be referred mainly to elevate sodium loss due to inhibition of kidney reabsorption of sodium. Magnesium increases in serum due to lowering urine excretion of magnesium out of the kidneys that are not working satisfactorily [59].

Furthermore, in the treatment rats group with Gum Arabic at different doses, the results could be noticed that sodium and calcium were gradually increased from

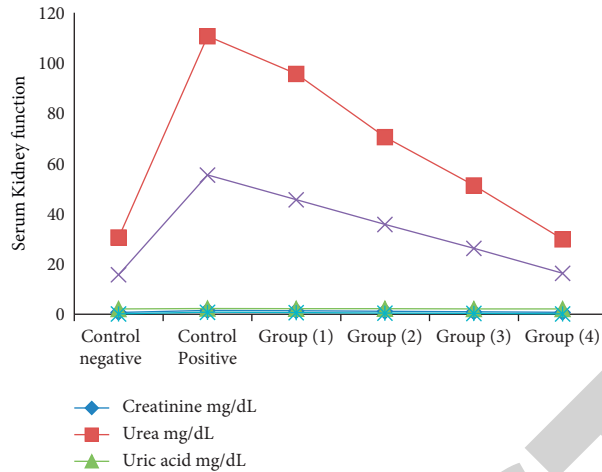


FIGURE 2: Serum kidney assay in different study groups.

TABLE 4: Effect of Gum Arabic and some minerals on serum in rats diabetic kidney failure.

Groups treatment	Sodium m mol/L	Potassium m mol/L	Phosphorus mg/dL	Calcium mg/dL	Magnesium mg/dL
Control negative	130.17 ^a ± 4.29	18.51 ^a ± 0.49	4.51 ^e ± 0.15	10.29 ^a ± 0.38	1.79 ^e ± 0.01
Control positive	105.36 ^c ± 2.64	9.82 ^c ± 0.08	8.34 ^a ± 0.24	5.76 ^c ± 0.04	3.15 ^a ± 0.04
Group (1)	111.56 ^d ± 3.17	11.98 ^d ± 0.15	7.42 ^b ± 0.17	6.89 ^d ± 0.03	2.83 ^b ± 0.07
Group (2)	117.43 ^c ± 2.69	14.12 ^c ± 0.18	6.51 ^c ± 0.16	7.94 ^c ± 0.07	2.53 ^c ± 0.09
Group (3)	123.15 ^b ± 3.17	16.71 ^b ± 0.36	5.56 ^d ± 0.09	9.06 ^b ± 0.12	2.19 ^d ± 0.08
Group (4)	129.86 ^a ± 1.68	18.49 ^a ± 0.48	4.62 ^e ± 0.07	10.16 ^a ± 0.15	1.82 ^e ± 0.02

Values are mean and SD ($n = 8$), where mean values in the same with the letter are significantly different at 0.05 levels.

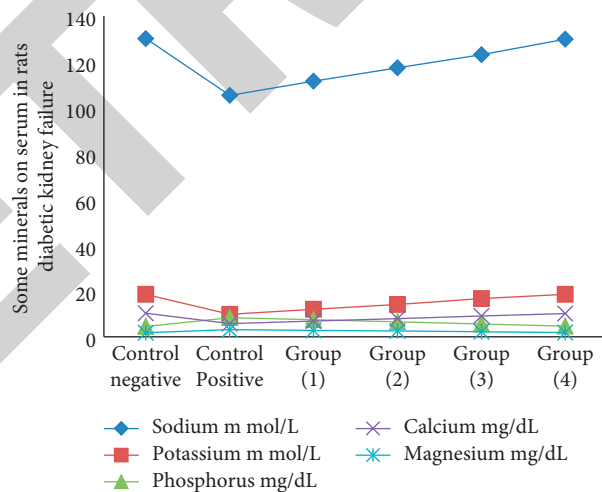


FIGURE 3: Effect of Gum Arabic and some minerals on serum in rats' diabetic kidney failure.

111.56 mmol/L and 6.89 mg/dL to 129.86 mmol/L and 10.16 mg/dl, respectively. The high calcium content in GA led to a considerably elevated calcium level [46]. A reduction in plasma phosphate ratio leads to an elevation in the ratio of ionized calcium in the plasma and therefore nullifies hyperparathyroidism, the major pathophysiological factor in advanced kidney disease [60]. Intake GA which contained calcium has been reducing blood pressure, activating calcium-receptors, in addition, subsequent inhibition of

sodium, potassium, and chloride transport to the outer layer [61].

3.5. Malondialdehyde, superoxide dismutase, and catalase in kidney tissues rats. Over the years, it has begun to be clear that elevated oxidative stress may lead the development of a great number of diseases and disease-attached complications [62].

TABLE 5: Oxidative enzymes in the kidney tissues of rats in different groups.

Groups treatment	MDA nmol/g tissue	SOD U/g tissue	CAT (K unit/g)
Control negative	220.15 ^e ± 7.28	1543.48 ^a ± 50.68	3.12 ^a ± 0.03
Control positive	340.59 ^a ± 10.35	851.35 ^e ± 20.18	1.43 ^e ± 0.01
Group (1)	310.70 ^b ± 11.19	1024.37 ^d ± 30.48	1.85 ^d ± 0.02
Group (2)	280.58 ^c ± 7.95	1197.26 ^c ± 25.79	2.26 ^c ± 0.03
Group (3)	250.71 ^d ± 8.36	1370.39 ^b ± 30.79	2.68 ^b ± 0.05
Group (4)	221.12 ^e ± 6.73	1540.23 ^a ± 55.17	3.09 ^a ± 0.07

Values are mean and SD ($n=8$), where mean values in the same with the letter are significantly different at 0.05 levels.

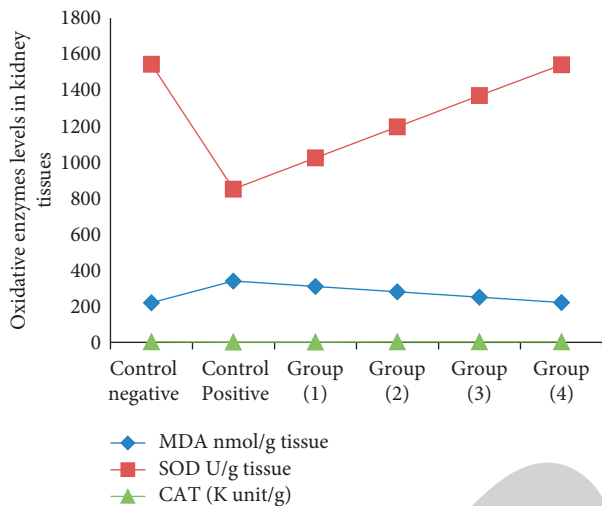


FIGURE 4: Oxidative enzymes in kidney tissues of rats in different groups.

The increased MDA level combined with decreased glutathione (GSH) in diabetic mice refers that peroxidation may be included in the progress of diabetes complications [63] due to free radical damage [64]. Meanwhile, when taking the different fats group various doses, the MDA was decreased from 310.70 to 221.12 nmol/g tissue; this may be the MDA decrease when the rats' group increases doses from gum Arabic. Administration of Gum Arabic considerably reduced MDA levels, which indicates that the Gum Arabic therapy may be caused by the high activity of antioxidants. Elevated oxidative stress has been reported in diabetic rats as an aid development of complications in diabetes [65].

Moreover, Gum Arabic contained high amounts from total phenolic and flavonoids. In addition, it had the highest antioxidant activity and dietary fiber, which reducing the oxidative enzymes as superoxide dismutase (SOD), and catalase (CAT) in rats' diabetic kidney failure when taken Gum Arabic. The results reported that when rats' different groups diabetic kidney failure took high doses of Gum Arabic, the SOD and CAT were improved and increased to 1540.23 U/g and 3.09k unit/g, respectively. The authors of [9] found that the activity of oxidative enzymes was considerably elevated in the Gum Arabic group than in diabetic groups and the control groups. Furthermore, to prohibit damage from oxygen-free radicals, tissues have developed an antioxidant defense system that includes nonenzymatic antioxidants and enzymatic activities such as the dissociation of the superoxide anion

(O⁻²) into H₂O₂, GSH-Px, and CAT and both detoxification of H₂O₂ and the conversion of lipid hydroperoxides into nontoxic alcohols [66].

Oxidative stress can produce significant interrelated imbalances in cellular metabolism and the destruction of cells by lipid peroxidation. Lipid peroxidation has attracted a lot of attention due to its connection with a number of abnormal physiological processes [67].

4. Conclusion

Gum Arabic contains rich amounts of phenols and flavonoids; in addition, it was found that Gum Arabic had the highest antioxidant activity. The rats' diabetic kidney failure was fed on a basal diet, and the daily intake of drinking water for each group separately at concentrations of 5, 10, 15, and 20 g Gum Arabic dissolved in 100 ml water per day. The results observed that the rats' diabetic kidney failure, when taken high doses from Gum Arabic, as well as the lipid profile, kidney functions, some minerals in serum, and antioxidant enzymes in the kidney, were improved. This may be because the Gum Arabic is safe, edible, and protective against diabetic and kidney damage.

Data Availability

The data used to support the findings of this study are included within the article.

Conflicts of Interest

The author declares that there are no conflicts of interest.

References

- [1] O. Gheith, N. Farouk, N. Nampoory, M. A. Halim, and T. Al-Otaibi, "Diabetic kidney disease: worldwide difference of prevalence and risk factors," *Journal of nephro pharmacology*, vol. 5, no. 1, pp. 49–56, 2016.
- [2] W. T. Cade, "Diabetes-related microvascular and macrovascular diseases in the physical therapy setting," *Physical Therapy*, vol. 88, no. 11, pp. 1322–1335, 2008.
- [3] V. M. Hass, "Updated management of chronic kidney disease in patients with diabetes," *Journal of the American Academy of Physician Assistants*, vol. 27, no. 6, pp. 17–22, 2014.
- [4] H. J. Jeon, T. Y. Koo, M. Han et al., "Outcomes of dialysis and the transplantation options for patients with diabetic end-stage renal disease in Korea," *Clinical Transplantation*, vol. 30, no. 5, pp. 534–544, 2016.
- [5] B. H. Ali, L. Cahliková, L. Opletal et al., "Effect of aqueous extract and anthocyanins of calyces of *Hibiscus sabdariffa*

- (Malvaceae) in rats with adenine-induced chronic kidney disease,” *Journal of Pharmacy and Pharmacology*, vol. 69, no. 9, pp. 1219–1229, 2017.
- [6] A. Dua, S. Vats, V. Singh, and R. Mahajan, “Protection of biomolecules against *in vitro* oxidative damage by the antioxidants from methanolic extract of *Trigonella foenum-graecum* seeds,” *International Journal of Pharma Sciences and Research*, vol. 4, pp. 3080–3086, 2013.
- [7] A. Abdullah Hamad, M. Lellis Thivagar, M. Bader Alazzam et al., “Dynamic systems enhanced by electronic circuits on 7D,” *Advances in Materials Science and Engineering*, vol. 2021, Article ID 148772, 11 pages, 2021.
- [8] S. Elamin, M. J. Alkhwaja, A. Y. Bukhamsin et al., “Gum Arabic reduces C-reactive protein in chronic kidney disease patients without affecting urea or indoxyl sulfate levels,” *International journal of nephrology*, vol. 2017, no. 3, Article ID 9501470, 6 pages, 2017.
- [9] A. A. Ahmed, J. S. Fedail, H. H. Musa, A. A. Kamboh, A. Z. Sifaldin, and T. H. Musa, “Gum Arabic extracts protect against hepatic oxidative stress in alloxan induced diabetes in rats,” *Pathophysiology*, vol. 22, no. 4, pp. 189–194, 2015.
- [10] L. Kaddam, I. Fadl-Elmula, O. A. Eisawi et al., “Gum Arabic as novel anti-oxidant agent in sickle cell anemia, phase II trial,” *BMC hematology*, vol. 17, no. 4, p. 4, 2017.
- [11] E. Dauqan and A. Abdullah, “Utilization of Gum Arabic for industries and human health,” *American Journal of Applied Sciences*, vol. 10, no. 10, pp. 1270–1279, 2013.
- [12] J. K. Lelon, I. O. Jumba, J. K. Keter, C. Wekesa, and F. D. O. Oduor, “Assessment of physical properties of gum Arabic from *Acacia Senegal* varieties in Baringo District, Kenya,” *African Journal of Plant Science*, vol. 4, pp. 95–98, 2010.
- [13] M. Bader Alazzam, H. Mansour, M. M. Hammam et al., “Machine learning of medical applications involving complicated proteins and genetic measurements,” *Computational Intelligence and Neuroscience*, vol. 2021, Article ID 1094054, 6 pages, 2021.
- [14] M. B. Alazzam, F. Hajje, A. S. AlGhamdi, S. Ayouni, and M. A. Rahman, “Mechanics of materials natural fibers technology on thermal properties of polymer,” *Advances in Materials Science and Engineering*, vol. 2022, Article ID 7774180, 5 pages, 2022.
- [15] M. E. S. Mirghania, A. A. M. Elnoura, N. A. Kabbashia, M. Z. Alama, K. H. Musa, and A. Abdullah, “Determination of antioxidant activity of gum Arabic: an exudation from two different locations,” *ScienceAsia*, vol. 44, pp. 179–186, 2018.
- [16] AOAC, *Official Methods of Analysis of Association of Official Chemists*, AOAC, Washington, D.C., USA, 18th edition, 2010.
- [17] A. A. Soares, C. G. M. de Souza, F. M. Daniel, G. P. Ferrari, S. M. G. da Costa, and R. M. Peralta, “Antioxidant activity and total phenolic content of *Agaricus brasiliensis* (*Agaricus blazei* Murril) in two stages of maturity,” *Food Chemistry*, vol. 112, no. 4, pp. 775–781, 2009.
- [18] A. Qawasmeh, H. K. Obied, A. Raman, and W. Wheatley, “Influence of fungal endophyte infection on phenolic content and antioxidant activity in grasses: interaction between *Lolium perenne* and different strains of *Neotyphodium lolii*,” *Journal of Agricultural and Food Chemistry*, vol. 60, no. 13, pp. 3381–3388, 2012.
- [19] A. Eghdami and F. Sadeghi, “Determination of total phenolic and flavonoids contents in methanolic and aqueous extract of *Achillea millefolium*,” *Journal of Organic Chemistry*, vol. 2, pp. 81–84, 2010.
- [20] K. H. Musa, A. Abdullah, B. Kuswandi, and M. A. Hidayat, “A novel high throughput method based on the DPPH dry reagent array for determination of antioxidant activity,” *Food Chemistry*, vol. 141, no. 4, pp. 4102–4106, 2013.
- [21] R. Apak, K. Güçlü, M. Özyürek, and S. E. Çelik, “Mechanism of antioxidant capacity assays and the CUPRAC (cupric ion reducing antioxidant capacity) assay,” *Microchimica Acta*, vol. 160, no. 4, pp. 413–419, 2008.
- [22] D. Huang, B. Ou, and R. L. Prior, “The chemistry behind antioxidant capacity assays,” *Journal of Agricultural and Food Chemistry*, vol. 53, no. 6, pp. 1841–1856, 2005.
- [23] E. O. Farombi and M. Ekor, “Curcumin attenuates gentamicin-induced renal oxidative damage in rats,” *Food and Chemical Toxicology*, vol. 44, no. 9, pp. 1443–1448, 2006.
- [24] Z. Mader, “Effect of brown rice and soybean dietary fiber on the control, glucose and lipid metabolism in diabetic rats,” *Am. M. J. Clin. Nutr.* vol. 38, no. 3, pp. 388–393, 1983.
- [25] N. W. Tietz, *Text Book of Clinical Chemistry*, Saunders, W. B. Co., London, England, 1986.
- [26] C. C. Allain, L. S. Poon, C. S. G. Chan, W. Richmond, and P. C. Fu, “Enzymatic determination of total serum cholesterol,” *Clinical Chemistry*, vol. 20, no. 4, pp. 470–475, 1974.
- [27] P. Fossati and L. Prencipe, “Serum triglycerides determined colorimetrically with an enzyme that produces hydrogen peroxide,” *Clinical Chemistry*, vol. 28, no. 10, pp. 2077–2080, 1982.
- [28] M. Burstein, “HDL Cholesterol determination after separation of high density lipoprotein,” *Lipids Res*, vol. 11, pp. 583–589, 1970.
- [29] J. C. Fruchart, “LDL Cholesterol determination after separation of low density lipoprotein,” *Rev. Fr. Des Laboratoire*, vol. 103, pp. 7–17, 1982.
- [30] R. Lee and D. Nieman, *Nutritional Assessment*, Mosby, Missouri, USA, 2nd edition, 1996.
- [31] L. D. Bowers and E. T. Wong, “Kinetic serum creatinine assays. II. A critical evaluation and review,” *Clinical Chemistry*, vol. 26, no. 5, pp. 555–561, 1980.
- [32] A. C. Burtis and T. Ashwood, *Textbook of Clinical Chemistry. 3rd Ed.*, AACCW. B. Saunders Co., London, England, 1999.
- [33] M. Jelikić-Stankov, P. Djurdjević, and D. Stankov, “Determination of uric acid in human serum by an enzymatic method using N-methyl-N-(4-aminophenyl)-3-methoxyaniline reagent,” *Journal of the Serbian Chemical Society*, vol. 68, no. 8–9, pp. 691–698, 2003.
- [34] R. L. Rouse, S. R. Stewart, K. L. Thompson, and J. Zhang, “Kidney injury biomarkers in hypertensive, diabetic, and nephropathy rat models treated with contrast media,” *Toxicologic Pathology*, vol. 41, no. 4, pp. 662–680, 2013.
- [35] F. Vinchi, S. Gastaldi, L. Silengo, F. Altruda, and E. Tolosano, “Hemopexin prevents endothelial damage and liver congestion in a mouse model of heme overload,” *American Journal Of Pathology*, vol. 173, no. 1, pp. 289–299, 2008.
- [36] R. J. Henry, M. D. Hagerstown, *Clinical Chemist. Principles and Techniques*, Hareer Row, American Chemical Society, Washington, BC, USA, 2nd edition, 1974.
- [37] W. Wasowich, J. Neve, and A. Peretz, “Optimized steps in fluorometric determination of thiobarbituric acid-revive substances in serum: importance of extraction Ph and influence of sample preservation and storage,” *Clinical Chemistry*, vol. 39, pp. 2522–2526, 1993.
- [38] Y. Sun, L. W. Oberley, and Y. Li, “A simple method for clinical assay of superoxide dismutase,” *Clinical Chemistry*, vol. 34, no. 3, pp. 497–500, 1988.

Retraction

Retracted: Conversion of Aquaculture Waste into Biomedical Wealth: Chitin and Chitosan Journey

Advances in Materials Science and Engineering

Received 8 January 2024; Accepted 8 January 2024; Published 9 January 2024

Copyright © 2024 Advances in Materials Science and Engineering. This is an open access article distributed under the Creative Commons Attribution License, which permits unrestricted use, distribution, and reproduction in any medium, provided the original work is properly cited.

This article has been retracted by Hindawi following an investigation undertaken by the publisher [1]. This investigation has uncovered evidence of one or more of the following indicators of systematic manipulation of the publication process:

- (1) Discrepancies in scope
- (2) Discrepancies in the description of the research reported
- (3) Discrepancies between the availability of data and the research described
- (4) Inappropriate citations
- (5) Incoherent, meaningless and/or irrelevant content included in the article
- (6) Manipulated or compromised peer review

The presence of these indicators undermines our confidence in the integrity of the article's content and we cannot, therefore, vouch for its reliability. Please note that this notice is intended solely to alert readers that the content of this article is unreliable. We have not investigated whether authors were aware of or involved in the systematic manipulation of the publication process.

Wiley and Hindawi regrets that the usual quality checks did not identify these issues before publication and have since put additional measures in place to safeguard research integrity.

We wish to credit our own Research Integrity and Research Publishing teams and anonymous and named external researchers and research integrity experts for contributing to this investigation.

The corresponding author, as the representative of all authors, has been given the opportunity to register their agreement or disagreement to this retraction. We have kept a record of any response received.

References

- [1] J. Joseph, K. Manigundan, M. Shamy Arokia Rajan et al., "Conversion of Aquaculture Waste into Biomedical Wealth: Chitin and Chitosan Journey," *Advances in Materials Science and Engineering*, vol. 2022, Article ID 2897179, 12 pages, 2022.

Review Article

Conversion of Aquaculture Waste into Biomedical Wealth: Chitin and Chitosan Journey

Jerrine Joseph,¹ Kaari Manigundan,¹ Mary Shamy Arokia Rajan,¹ Manikkam Radhakrishnan,¹ Venugopal Gopikrishnan,¹ Subramanian Kumaran ¹, Rajasekar Thirunavukkarasu,¹ Wilson Aruni,^{2,3} and Velmurugan Shanmugam ⁴

¹Centre for Drug Discovery and Development, Col. Dr. Jeppiaar Research Park, Sathyabama Institute of Science and Technology, Chennai 600119, Tamil Nadu, India

²Musculoskeletal Disease Research Laboratory US Department of Veteran Affairs, Loma Linda, CA, USA

³Amity University, Mumbai, Maharashtra, India

⁴Department of Biology, School of Natural Science, Madawalabu University, Oromia Region, Ethiopia

Correspondence should be addressed to Subramanian Kumaran; kumarans.cddd@sathyabama.ac.in and Velmurugan Shanmugam; velkas.cas@gmail.com

Received 10 November 2021; Accepted 18 March 2022; Published 22 April 2022

Academic Editor: Alicia E. Ares

Copyright © 2022 Jerrine Joseph et al. This is an open access article distributed under the Creative Commons Attribution License, which permits unrestricted use, distribution, and reproduction in any medium, provided the original work is properly cited.

Biowaste originating from aquaculture sector represents a potential feedstock to produce value-added substances and materials like chitin and chitosan. They are the long chain polymers of N-acetylglucosamine polymers with huge industrial and biomedical significance. Chitin has long been recognized as a useful biomaterial for drug delivery and neurological therapy. Similarly, chitosan oligosaccharide, a short chain polymer derived from chitin/chitosan, has been identified for its potential biomedical applications, including antibacterial, anti-inflammatory, and anti-Alzheimer action. Chitosan nanoparticles are also used extensively in biomedical applications. Here we have critically summarized various methods for the extraction of chitin, chitosan, and chitooligosaccharides and chitosan nanoparticle preparation and their diverse biomedical applications.

1. Introduction

Aquaculture is the world's most prominent, high-growth agribusiness enterprise. It caters to the elite needs and consumer satisfaction. Aquatic organisms make up more than 150 billion USD per year in the market. Similarly, in last 20 years, the shrimp production went up to 3 million tons in every year. This scenario is made feasible by increasing shrimp production through high stocking density and the use of high-quality protein feeds [1]. Aquaculture derived byproducts are mixed with items produced in industrial processing that are commercially important. In particular the chitin and chitosan source are epitomized by the exoskeleton [2]. Aquaculture waste materials are the abundant source of chitin [3]. The freshwater aquaculture contains fish

pens, fish cages, and ponds on a smaller scale in rice paddies. The brackish water is commonly carried out in coastal fish ponds. The rafts, stakes, and ropes are used in marine culture to hold a fish cage of mollusks and seaweeds. The disposal of large quantities of environmentally harmful effluents uneaten feed and feces such as fish waste, natural pigments (usually incorporated into feeds), disinfectants and chemotherapeutants, collagen, and chitosan has resulted in an increase in negative environmental impacts [4].

Chitin and its derivatives, which are a significant aquaculture waste, are increasingly being recognized as imperative biopolymers [5, 6]. They are used by aquatic inhabitants as nourishing material. The biological uses of chitin and its derivatives in the realm of therapeutics are vast, notably those related to anti-inflammatory,

antioxidant, antibacterial, immunity-enhancing, and anticancer effects and drug transport [6, 7]. As a result of its biological importance, this review focuses on the biomedically valuable products of chitin, chitosan, and its derivatives.

2. Chitin

Chitin (Figure 1(a)) is a primary polysaccharide found in crab shells and their byproducts. In nature, they are cationic polysaccharides linked to glycosaminoglycans. (1,4)-N-acetyl-D-glucosamine is the molecular name for it, and it appears in three polymorphic forms: α -chitins. This is due to extraordinarily strong hydrogen interactions between adjacent chains' amide groups and carbonyl groups. Deacetylated chitosan is a linear polysaccharide composed of randomly dispersed β -(1-4)-linked D-glucosamine and N-acetyl-D-glucosamine with varying degrees of deacetylation (DD; 40–99%) and molecular weight (MW) [8, 9]. Their degree of deacetylation is one of the most important factors influencing both its chemical and biological properties [9–11]. It has the ability to chelate different metal ions because of their neutral or negatively charged hydroxyl groups of D-glucosamine, GlcN residues, and amino groups [12, 13].

Furthermore, alkali concentration, polymer chemical form, chitin type and polymorphism type, chitin particle size, heterogeneous or homogeneous N-deacetylation, single or multiple procedures, atmosphere, and incubation duration have all been demonstrated to alter chitin and its deacetylated chitosan characteristics. All these traits, as well as its excellent mechanical properties, biocompatibility, and biodegradability, open the door to a wide range of applications [14, 15].

2.1. Extraction of Chitin. Chitin is found in crustaceans and shellfish as part of a complex protein network onto which calcium carbonate deposits to form the hard shell. Chitin separation from shellfish necessitates deproteinization and demineralization of two primary constituents: proteins and inorganic calcium carbonate. Over the years, many techniques for preparing pure chitin have been developed and employed; however, no standard approach has been accepted universally. Chemical or enzymatic treatments might be used for both deproteinization and demineralization.

2.1.1. Chemical Method

(1) Chemical Deproteinization. This is done in a heterogeneous manner with chemicals that depolymerize the biopolymer as well. Chemical approaches were used to begin the deproteinization process. A variety of chemicals have been attempted as deproteinization reagents, including NaOH, Na_2CO_3 , NaHCO_3 , KOH, K_2CO_3 , $\text{Ca}(\text{OH})_2$, Na_2SO_3 , NaHSO_3 , CaHSO_3 , Na_3PO_4 , and Na_2S . NaOH is the chosen reagent, which can be employed in concentrations ranging from 0.125 to 5.0 M, at various temperatures (up to 160°C) and for various treatment periods (from few minutes up to few days). In addition to deproteinization, NaOH causes partial

deacetylation of chitin as well as hydrolysis of the biopolymer, lowering the molecular weight of the biopolymer [16].

(2) Chemical Demineralization. Acid treatment with HCl, HNO_3 , H_2SO_4 , and CH_3COOH is the most common method for removing the minerals and calcium carbonate from chitin. Demineralization is simple to accomplish since it entails the breakdown of calcium carbonate into water-soluble calcium salts while also releasing carbon dioxide. The degree of mineralization of each shell, extraction duration, temperature, particle size, acid content, and solute/solvent ratio are all factors that influence these treatments. Calcium chloride is dependent on the acid content since it takes two molecules of HCl to convert one molecule of calcium carbonate into calcium chloride [17, 18].

Acid intake should be equal to, or even more than, the stoichiometric quantity of minerals in order to achieve a full reaction. Because the heterogeneity of the material makes it difficult to extract all minerals, a greater volume or more concentrated acid solution is required. Acidimetric titration may be used to evaluate it. The consumption of acid is correlated with the advancement of pH toward neutrality, but the persistence of acidity in the medium indicates that the reaction is complete. Demineralization has historically been achieved at room temperature with dilute HCl at various concentrations (up to 10% w/v), 90 percent formic acid, and 22% HCl, respectively [19].

2.1.2. Biological Method. Chitin extraction necessitates the use of proteases, which can be found in plants, bacteria, and animals. Proteases such as alcalase, pepsin, papain, pancreatin, devolvase, and trypsin remove proteins from crustacean shells while reducing deacetylation and depolymerization during chitin separation. This treatment can be used after or before the solid material's demineralization phase, which changes the accessibility of the reactant. Both pure and coarsely extracted proteases are used in the deproteinization process. Crude proteases, on the other hand, are not only economically cheaper but also more efficient due to the presence of coexisting proteases [20].

(1) Biological Deproteinization. Bacterial proteases have been found to be useful in the deproteinization process in numerous investigations. One example is the enzymatic deproteinization of previously demineralized shrimp waste to produce chitin and a nutrient-dense protein hydrolysate. Alcalase, a serine endopeptidase derived from *Bacillus licheniformis*, was used for deproteinization because of its selectivity for terminal hydrophobic amino acids, which results in nonbitter hydrolysate and allows for simple regulation of the degree of hydrolysis. Alcalase was employed for chitin, protein hydrolysate, and astaxanthin recovery [21]. The residual protein concentration of chitin separated by enzymatic deproteinization was considerably greater than that of chitin isolated by alkali treatment [22]. Shrimp shell deproteinization has recently used alkaline crude proteases from a variety of fish and marine invertebrates. Younes et al., 2014, investigated the use of crustacean feces as both a

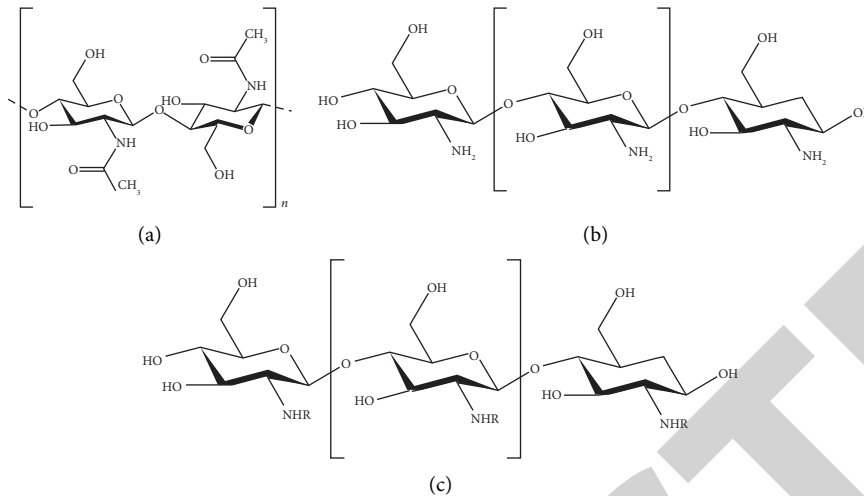


FIGURE 1: Structure of chitin (a), chitosan (b), and COS (c).

substrate and a source of proteases. For shrimp waste deproteinization, alkaline proteases are utilized from the red scorpion fish *Scorpaena scrofa* [23].

(2) *Nonenzymatic Process*. Deproteinization *via* fermentation, which can be done by endogenous microorganisms (also known as autofermentation) or by introducing chosen strains of microorganisms, can reduce the expense of employing enzymes. This method can use single-stage fermentation, two-stage fermentation, cofermentation, or sequential fermentation. For the fermentation of crustacean shells, a variety of microbial species have been proposed. Lactic acid fermentation and non-lactic-acid fermentation are the two types of fermentation that can be used [24].

- (1) *Lactic Acid Fermentation*. To ferment crustacean shells, inoculum generated from lactic acid and protease producing *Lactobacillus* sp. can be utilized. Lactic acid is formed when glucose is converted to alcohol, resulting in a lower pH in the silage, which inhibits the growth of spoilage bacteria. Calcium lactate precipitates when lactic acid reacts with calcium carbonate. The number of species and inoculum, carbon supply and concentration, starting pH and pH variation throughout fermentation, temperature, and fermentation length are all factors that influence the success of lactic acid fermentation [25–27].
- (2) *Non-Lactic-Acid Fermentation* For crustacean shell fermentation without lactic acid, bacteria (*Bacillus* sp., *Pseudomonas* sp.) and fungus (*Aspergillus* sp.) were employed. Ghorbel-Bellaaj et al. [28] tested 6 proteolytic *Bacillus* sp. (*B. pumilus* A1, *B. mojavensis* A21, *B. licheniformis* RP1, *B. cereus* SV1, *B. amyloliquefaciens* An6, and *B. subtilis* A26) on fermentation of shrimp waste. The highest degree of deproteinization was achieved with *B. cereus* SV1. *B. subtilis* was employed to ferment shrimp shells in jaggery broth, eliminating 84 percent of the proteins and 72 percent of the minerals [29]. The

fermentation process and hence deproteinization and demineralization efficiency are influenced by a variety of variables. Ghorbel-Bellaaj et al. [30] used a Plackett-Burman factorial design to investigate the important parameters influencing fermentation efficacy using *P. aeruginosa* A2. Shrimp shell concentration, glucose concentration, inoculum size, and incubation length were found to alter deproteinization and demineralization degrees [30].

3. Chitosan

Chitosan is a common term for a group of polymers formed by different degrees of chitin deacetylation. Figure 1(b) depicts the structure of chitosan. In reality, the degree of acetylation distinguishes chitin and chitosan, indicating the balance between the two types of residues (Figure 2). To convert chitin to chitosan, enzyme preparations or a chemical method are used [31, 32]. Chemical techniques are widely utilized in the commercial manufacturing of chitosan due to its low cost and adaptability for large scale production [33]. Because of its positive charges (NH_3^+) at pH (pH 6.5), chitosan is insoluble in neutral and acidic environment, which is one of its benefits.

Alkali deacetylation is used more frequently because glycosidic connections are particularly susceptible to acid [33]. N-Deacetylation of chitin can be accomplished in two ways: heterogeneously or homogeneously [34, 35]. In the heterogeneous method, chitin is treated for a few hours with a hot concentrated NaOH solution, and chitosan is produced as an insoluble residue that is deacetylated up to 85% to 99%. The homogeneous approach, which involves dispersion of chitin in concentrated NaOH (30 g NaOH/45 g H_2O /3 g Chitin) at 25°C for 3 hours or longer and then dissolving it in crushed ice at 0°C, is used to make alkali chitin.

The solubility of chitosan can be measured not only by the number of 2-acetamido-2-deoxy-D-glucose units in the molecule, but also by the distribution of N-acetyl groups [36]. According to Aiba [37], deacetylation reactions in heterogeneous conditions result in an uneven distribution of

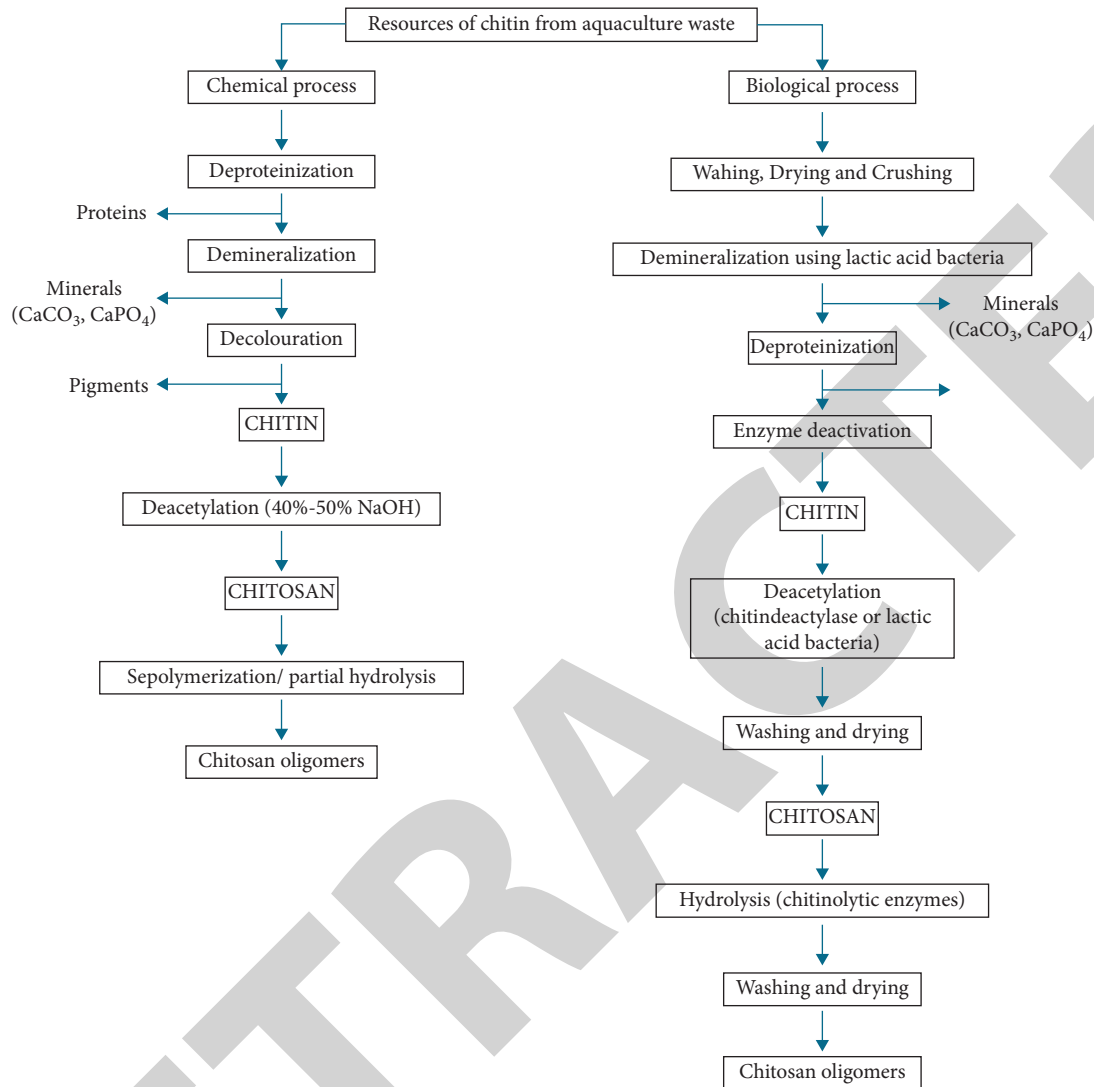


FIGURE 2: Flowchart of chemical and biological processes for chitin, chitosan, and COS.

N-acetyl-D-glucosamine and D-glucosamine residues, as well as some blockwise acetyl group distribution along polymeric chains. As a result, solubility and degree of chitosan aggregation in aqueous solutions may differ, leading to variances in average characteristics. Changes in DA, acetyl group distribution throughout chains, MW, and viscosity in solution may also be caused by differences in chitosan manufacturing [38]. In actuality, a number of factors in the deacetylation process might affect the characteristics of the finished chitosan [39]. Temperature and processing time have a significant impact on the DA and MW of chitosan, according to Rege and Block [40].

3.1. Extraction of Chitosan

3.1.1. Chemical Deacetylation. In industrial applications, the chemical conversion of chitin to chitosan, which is the most difficult and costly step, has been done with 50 percent NaOH at high temperatures. Chitin deacetylase performs this step-in nature at lower temperatures and a neutral pH

[41]. In N-acetyl-D-glucosamine residues of chitin, the enzyme hydrolyzes the linking between the acetyl group and the amine group. Chitin oligosaccharides are bioconverted into chitosan oligosaccharides and vice versa. DY-9 chitin deacetylase from *Absidia corymbifera* was found to be active against water-soluble chitin (WSCT-50), glycol chitin, chitosan (DD 71–88%), and chitin oligosaccharides [42, 43]. Chitin oligosaccharides were a suitable substrate because of their solubility, which improved the CDA's availability and accessibility. Size affects the rate of deacetylation of (GlcNAc) 2–6, as longer lengths result in higher rate activity. These data indicate that chitin solubilization is a limiting factor in CDA-mediated enzymatic chitin to chitosan bioconversion.

3.1.2. Enzymatic Method. Chitin deacetylases convert chitin to chitosan in a manner that is controlled and nondegradable and results in chitosan that is fresh and well defined [44]. Chitosan oligomers, in particular, are made using this method. Chitin deacetylase catalyzes the hydrolysis of

N-acetamido links in chitin to produce chitosan. Glycoproteins called chitin deacetylases are released into the periplasmic or culture media. Furthermore, all enzymes have a strong selectivity for β -(1,4)-linked N-acetyl-D-glucosamine polymers and are thermally stable at their optimal temperature (50°C). It is worth mentioning that acetate (a deacetylation product) has no effect on the chitin deacetylases produced by *C. lindemuthianum* and *A. nidulans*, making them suitable for biotechnological applications [45–47].

The impact of chitin deacetylase, isolated from the fungus *M. rouxii*, on the chitosan synthesis was examined using chitin as a substrate (in both its crystalline and amorphous form) [48]. The enzyme is inefficient on insoluble chitins because the degree of deacetylation stays low. As a result, it appears that pretreatment of chitin substrates prior to enzyme addition is necessary to increase the accessibility of the acetyl groups to the enzyme and therefore the deacetylation yield. Experiments with partially deacetylated water-soluble chitosan's and *M. rouxii* chitin deacetylase were carried out under controlled conditions to achieve this goal. The enzyme may deacetylate chitosan up to 97% under certain conditions (deacetylation from an initial chitosan with DA = 0.32 and a number-average degree of polymerization of 30) [49].

3.2. Chitosan Nanoparticles. The addition of a polyanion, such as tripolyphosphate, to a chitosan solution under continuous stirring can produce nanoparticles. Ionotropic gelation, microemulsion, emulsification solvent diffusion, and emulsion-based solvent evaporation are the most common ways for creating chitosan-based nanoparticles. Drugs are trapped inside the polymeric matrix through electrostatic contact, hydrogen bonding, and hydrophobic interactions, among other mechanisms. With or without a stabilizing agent like poloxamer, a positively charged chitosan solution is dissolved in acetic acid or any other negatively charged polyanionic solution. Nanoparticles are easily formed as a result of the complexation of positive and negative charged species during mechanical stirring at room temperature, resulting in the separation of chitosan into spherical particles of varied sizes and surface charges [50].

4. Chitin Oligosaccharides

Chitoooligosaccharides (COS), also called chitosan oligomers, contain oligomers of β -1, 4-linked 2-amino-2-deoxy-d-glucopyranose and 2-acetamido-2-deoxy-d-glucopyranose in Figure 1(c). It is produced by partial hydrolysis of chitosan and has a wide range of uses in the food and pharmaceutical industries due to its nontoxic nature. Anticoagulation, antioxidation, inflammatory resistance, immunological stimulation, antibacterial, antitumor, and other biological activities are among its numerous biological uses [51–53].

4.1. Extraction of Chitin Oligosaccharides. Chitin oligosaccharides can be made through enzyme hydrolysis, physical procedures, or chemical processes. Chitosanases and

nonspecific enzymes such as cellulase, lysozyme, lipase, protease, amylase, and others were used for enzymatic hydrolysis [54]. Acid hydrolysis and hydrogen peroxide oxidation were straightforward chemical procedures to use, but their detrimental environmental impact limited their use. Physical techniques, such as ultrasonic treatment, ultraviolet radiation, and microwave therapy, have a lower cost and produce easier-to-purify goods than the other two methods. The transglycosylation process of glycolytic enzymes such as chitinase, chitosanase, and other glycosidases produced chitin oligosaccharides. Using a transglycosylation reaction, it was discovered that chitinase isolated from *Trichoderma reesei* KDR-11 transforms (GlcNAc) 4 to (GlcNAc) 2 (55.7%) and (GlcNAc) (39.6%) [55]. COS with DP 4–12 were successfully generated using a lysozyme-catalyzed transglycosylation reaction with N,N',N''-tri (monochloro) acetylchitotriose and N,N',N''-tri-acetylchitotriose as substrates, followed by a base-catalyzed removal technique to remove the N-monochloroacetyl groups [56, 57].

5. Biological or Biomedical Applications of Chitin and Its Derivatives

The chitin and chitosan or chitosan derivatives have recently been reported to several biological applications such as antimicrobial, anti-inflammatory activity, anticancer, wound-dressing and healing activity, drug delivery, vaccine adjuvant, tissue engineering, etc. Figure 3 shows a review of the potential applications and side effects of chitin, chitosan, and COS.

5.1. Antimicrobial Activity. Chitin has no antibacterial properties in general [58], despite the fact that chitosan and chitosan-derived compounds from various sources can potentially inhibit a wide range of pathogens. Furthermore, numerous studies have shown that chitosan oligosaccharide has been shown to have antibacterial action against *Staphylococcus aureus* [59], *Cryptosporidium parvum* [60], *Candida auris* [61], and *Ceratocystis fimbriata* in several investigations [62]. Similarly, chitosan oligosaccharide silver and gold nanoparticles exhibited potential antibacterial properties [63–65] (Table 1).

5.2. Anti-Inflammatory Activity. Inflammation is a critical human body defensive mechanism against infections, injuries, and poisons. The ability of chitosan, chitin, and chitosan oligosaccharide to inhibit and induce inflammation makes them useful anti-inflammatory agents. It has been shown that chitin, for example, promotes inflammation in obese people's peripheral blood mononuclear cells [76]. In an experimental atopic dermatitis mouse model, chitin nanofibril was used to suppress NF- κ B to reduce skin inflammation [77]. In DSS-induced colitis, chitosan improved intestinal barrier function by boosting the expression of tight junction proteins such claudin-1, occludin, and ZO-1 [78]. Furthermore, chitosan oligosaccharide inhibited NF- κ B downstream targets like COX-2

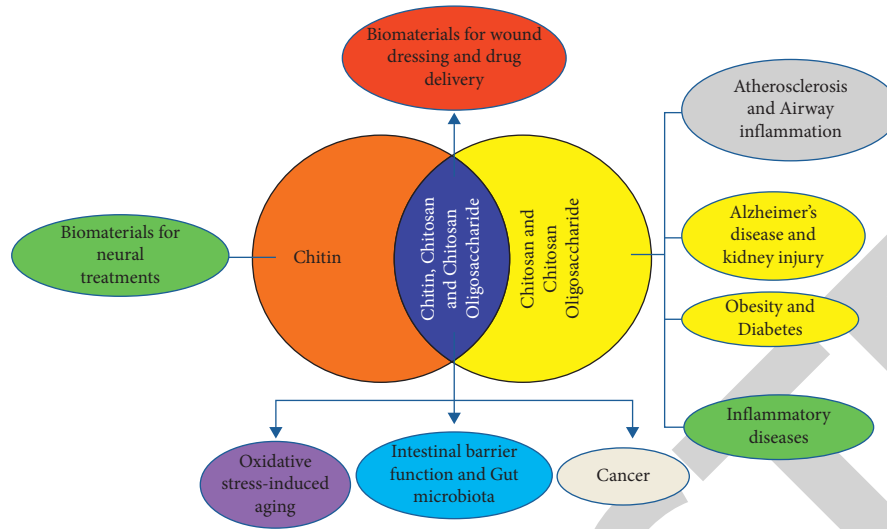


FIGURE 3: Biomedical applications of chitin, chitosan, and COS.

TABLE 1: Antimicrobial activity of chitosan or chitosan-based commercial products.

Product	Antimicrobial activity	MIC	References
Pentafluoropropionyl-chitosan	<i>S. aureus</i> , <i>S. sanguinis</i> , <i>S. epidermidis</i> , <i>B. subtilis</i> , <i>E. coli</i> , <i>P. aeruginosa</i> , and <i>S. enterica</i>	256, 128, 128, 128, >512, >512 and >512 µg/ml	[66]
2,3,4,5,6-Pentafluorobenzyl-chitosan	<i>S. aureus</i> , <i>S. sanguinis</i> , <i>S. epidermidis</i> , <i>B. subtilis</i> , <i>E. coli</i> , <i>P. aeruginosa</i> , and <i>S. enterica</i>	512, 128, 128, 128, >512, >512 and >512 µg/ml	[66]
Pentadecafluorooctanoyl-chitosan	<i>S. aureus</i> , <i>S. sanguinis</i> , <i>S. epidermidis</i> , <i>B. subtilis</i> , <i>E. coli</i> , <i>P. aeruginosa</i> , and <i>S. enterica</i>	512, 256, 256, 256, >512, >512 and >512 µg/ml	[66]
Pentafluoropropionyl-HTCC	<i>S. aureus</i> , <i>B. subtilis</i> , <i>S. epidermidis</i> , <i>S. sanguinis</i> , <i>E. coli</i> , <i>P. aeruginosa</i> , and <i>S. enterica</i>	256, 128, 256, 128, 512, 128, 512	[66]
2,3,4,5,6-Pentafluorobenzyl-HTCC	<i>S. aureus</i> , <i>B. subtilis</i> , <i>S. epidermidis</i> , <i>S. sanguinis</i> , <i>E. coli</i> , <i>P. aeruginosa</i> , and <i>S. enterica</i>	128, 64, 512, 128, 512, 128 and 256 µg/ml	[66]
Pentadecafluorooctanoyl-HTCC	<i>S. aureus</i> , <i>B. subtilis</i> , <i>S. epidermidis</i> , <i>S. sanguinis</i> , <i>E. coli</i> , <i>P. aeruginosa</i> , and <i>S. enterica</i>	256, 128, 512, 128, 512, 128 and 256 µg/ml	[66]
Carboxymethyl chitosan	<i>E. coli</i> and <i>S. aureus</i>	0.05 and 0.1 µg/ml	[67]
Quaternized chitosan	<i>E. coli</i> and <i>S. aureus</i>	0.0125 and 0.025 µg/ml	[67]
Quaternized carboxymethyl chitosan	<i>E. coli</i> and <i>S. aureus</i>	0.00625 and 0.0125 µg/ml	[67]
Chitosan	<i>E. coli</i> , <i>F. oxysporum</i> , <i>B. cinerea</i> , and <i>D. sorokiniana</i>	20, 100, 10, and 10 ppm	[68]
Chitosan	<i>X. campestris</i>	500 ppm	[69]
Chitosan	<i>S. enterica</i>	2000 ppm	[70]
Chitosan	<i>P. aeruginosa</i> , <i>A. hydrophila</i> , <i>S. dysenteriae</i> , <i>A. fumigates</i> , and <i>C. albicans</i>	>200, 1000, >200, >2000, and 500 ppm	[71]
Chitosan	<i>E. aerogenes</i>	250 ppm	[72]
Chitosan	<i>B. cereus</i> and <i>L. brevis</i>	1000 and 1000 ppm	[73]
Chitosan	<i>M. canis</i> and <i>T. mentagrophytes</i>	1100, 2200 ppm	[74]
Chitosan oligosaccharide (10 kDa)	<i>Propionibacterium acnes</i>	32–64 µg/mL	[75]

and upstream targets like TLR-4 in lipopolysaccharide-induced inflammation in intestinal epithelial cells [79]. Furthermore, through downregulating IL-4, IL-5, and IL-13 and upregulating IFN, chitosan oligosaccharide protects sensitized mice from shrimp tropomyosin-induced food allergy [80]. Chitosan oligosaccharide also lowered liver IL-1 levels, reducing inflammatory reactions caused by heat stress [81].

5.3. Anticancer. Chitin, chitosan, and their derivatives have anticancer efficacy in a variety of cancer cells. They serve as a vehicle for the delivery of anticancer drugs as well. Previous studies stated that chitin suppressed cancer cells by inhibiting the mediators chitinase-3 like protein-1 (CHI3L1) and vascular endothelial growth factor C (VEGF-C) [82, 83]. Silver and poly-L-lactic acid encapsulated chitin nanoparticles also exhibited potential anticancer action in MCF7

breast cancer cell line [84]. Similarly, chitosan was also found to inhibit human melanoma cell lines such as SKMEL38, RPMI7951, and A375 significantly [85]. It also demonstrated anticancer potential in human cancers such as human ovarian cancer, breast cancer, and cervical carcinoma [86]. When chitosan was combined with additional compounds like carboxymethyl chitosan and chitosan selenate, it had a huge cytotoxic impact on cancer cell lines [87].

5.4. Wound-Dressing and Healing Activity. Chitin has been utilized as a tissue adhesive and as a key component of biomaterials for wound healing and tissue repair [88]. Chitin and chitin-based compounds, such as diacetyl chitin, chitin hydrogel, and chitin-amphiphilic ion, improved wound healing effectiveness [89–91]. Similarly, the wound healing ability of chitin nanoparticles/nanofibers was studied in diabetic induced rats [92, 93]. Furthermore, chitin nanofibrils are used as biomaterial for bleeding purposes which are significantly better than commercially available products [94]. Chitosan and chitosan oligosaccharide/chitoooligosaccharide, on the other hand, are used for wound healing. Infectious animal models were treated with chitosan/chitosan oligosaccharide nanoparticles to see whether they could heal [95–97]. The wound healing ability of chitosan-based materials such as chitosan-polyurethane hydrogel, chitosan-curcumin complex, quaternary ammonium chitosan nanoparticles, and carboxymethyl chitosan with alginate was investigated using a diabetic rat model [98, 99].

5.5. Drug Delivery. In recent years, chitosan has shown to be an excellent carrier for variety of active substances [100]. Because of its biocompatibility, biodegradability, bioabsorption, and pH sensitivity, low-molecular-weight chitosan is utilized as a drug carrier for anticancer chemotherapy and other treatments [101]. Furthermore, the transport of proteins/peptides, growth hormones, antibiotics, anticancer, and anti-inflammatory medicines is considerably more effective using chitosan/chitosan-based materials or nanoparticles. Other research has been directed to treat diseases such as depression, schizophrenia, migraine, brain tumors, general anxiety disorder, epilepsy, pain, viral and bacterial infections, and so on [102].

Doxorubicin, an anticancer medication, can be encapsulated with chitosan nanoparticles to decrease adverse effects and enhance absorption and survival time [103]. Chitosan nanoparticles, for example, are utilized as a drug carrier for anticancer medicines that inhibit the activity of human colorectal adenocarcinoma, lung cancer, and prostate-3 cancer cell lines. Antimicrobial and antioxidant activities of chitosan nanoparticles are encapsulated with the antibiotic gentamicin. With the release of chitosan nanoparticles against pneumonia, antibiotics are more effective while reducing their toxicity [104].

5.6. Tissue Engineering. The tissue engineering is developed as a key field of regenerative medicine, with the potential to overcome some of the drawbacks of traditional replacement

treatments that rely on pure synthetic materials. The development of hybrid materials resulting from the integration of cells into 3D porous scaffolds or hydrogels is one of the most prevalent ideas connected with tissue engineering research. In three dimensions, the scaffold material plays an important role in cell anchoring, proliferation, and tissue development. The material should be able to construct porous scaffold structures, with porosity properties tailored to the application. A recent study highlighted chitosan and its derivatives as potential scaffold materials since they are predicted to dissolve when new tissue forms, reducing inflammation responses and hazardous breakdown products [105–107].

A CMC/HA composite was used for bone regeneration since chitin and its derivatives have been demonstrated to speed up the release of cell growth factor during wound healing. The effects of a CMC/HA composite on bone healing in cell lines and animals were investigated [108]. The nanofibers made from a water-soluble carboxymethyl chitin CMC/PVA scaffold may promote cell adhesion/attachment and proliferation, implying that these scaffolds could be beneficial in tissue engineering [109]. Another form of nanofibers produced from N-CECS/PVA acted as a bio-composite nanofiber and showed substantial cellular adhesion and proliferation, making it useful as a wound dressing for skin regeneration [110].

In another study, Liu et al. [111] employed chitosan hydrogel as a scaffold for chondrocytes to repair articular cartilage abnormalities. They created the hydrogels by combining chitosan with sodium glycerophosphate (GP) and hydroxyethyl cellulose (HEC) and discovered that both in vivo and in vitro methods produced good outcomes. They came to the conclusion that this hydrogel may promote matrix buildup and could be used to repair articular cartilage abnormalities in the future [111]. Zhang et al. [112] developed and studied a calcium phosphate chitosan composite as a scaffold for bone tissue engineering, and the mechanical property of the ceramic phase was shown to be improved by matrix reinforcement without altering the osteoblast phenotype.

A 3D porous scaffold made of gelatin chitosan nanobioglass was created for bone tissue engineering. The scaffold produced in this example had around 80% porosity, greater compressive strength, proliferation, adhesion, and the capacity to transform into artificial bone grafts quickly [113, 114]. The nano-TiO₂-chitosan artificial skin with collagen proved to be a promising artificial skin substitute, demonstrating nano-unique TiO₂'s bactericidal action and chitosan's immune-enhancing impact [115]. Chitosan derived from sponges and composed with sodium alginate has been shown to be effective in skin tissue engineering [116]. A lyophilized glutaraldehyde crosslinked chitosan extracted from a sponge used for blood hemostasis performed similarly. Chitosan served as a mechanical barrier to blood, forcing it to rapidly coagulate [117].

5.7. Gene Therapy. Gene therapy is a type of medication delivery in which the cellular machinery is manipulated to achieve a therapeutic effect [118]. Mao et al. [119] looked at

the variables that influence siRNA and DNA delivery and transfection effectiveness. PEGylation has been found to improve biocompatibility and stability of siRNA loaded complexes, and chitosan derivatives are also utilized for therapeutic gene delivery to the brain [120].

Despite the flexibility of chitosan, nanoparticles have become the preferred treatment for a range of neurological illnesses: glioblastoma, medulloblastoma, Parkinson's disease, and Alzheimer's disease [121]. This method of treatment has been utilized to treat viral infections like HIV-infected brain. The search for less invasive procedures has recently driven the development of new formulations for nose-to-brain gene transfer. The search for less invasive procedures has recently driven the development of new formulations for nose-to-brain gene transfer. Rassu et al. [122], for example, created chitosan-coated solid lipid nanoparticles containing BACE1 siRNA for intranasal use in the treatment of Alzheimer's disease. This opens the door to further research into developing an effective combination of NAG-loaded CSNPs as a fish feed to boost growth and immune response in commercial aquaculture production [123].

6. Conclusion and Future Perspectives

Chitin, chitosan, and COS may be utilized as nanodelivery system carrier materials and have a wide range of biomedical applications, including drug delivery, antimicrobial agents, and wound healing. Researchers should also investigate novel applications for chitin, chitosan, and COS as well as animal trials to learn more about their human-related consequences. However, more measures must be taken to increase the safety and effectiveness of chitin in biological applications. These materials, which are made from aquaculture waste, are gaining popularity and have a wide range of applications. However, while developing chitin/chitosan-based goods for applications in many sectors for human benefit, we must consider environmental protection and green manufacturing.

COS has been used to treat a variety of human illnesses and pathological situations, as opposed to chitin or chitosan. Low-molecular-weight chitosan oligosaccharide with >90% deacetylation suppresses inflammatory responses by boosting anti-inflammatory pathways. Chitosan oligosaccharide also possesses antioxidative and anticancer properties. Interestingly, chitosan oligosaccharide, as a prebiotic for gut microbiota, modifies gut microbiota, reducing systemic illnesses, including atherosclerosis. The degree of deacetylation and polymerization determines the biological effects of these compounds, which remains a problem in the development of chitosan oligosaccharide as a useful dietary supplement. More research is needed to uncover the exact molecular/cellular processes of these polymers' biological impacts, particularly the function of their prebiotic effect and direct influence on disease-specific cells or therapeutic targets.

Data Availability

All data used to support the findings of this study are included within the article.

Conflicts of Interest

The authors have no conflicts of interest to declare.

Acknowledgments

The authors are grateful thanks to Department of Biology, School of Natural Science, Madawalabu University, Oromia Region, Ethiopia. The authors would like to thank the Management of Sathyabama Institute of Science and Technology, Chennai, India, for their help and cooperation.

References

- [1] B. T. Iber and N. A. Kasan, "Recent advances in Shrimp aquaculture wastewater management," *Heliyon*, vol. 7, no. 11, Article ID e08283, 2021.
- [2] J. Vázquez, P. Ramos, J. Mirón, J. Valcarcel, C. Sotelo, and R. Pérez-Martín, "Production of chitin from *Penaeus vannamei* by-products to pilot plant scale using a combination of enzymatic and chemical processes and subsequent optimization of the chemical production of chitosan by response surface methodology," *Marine Drugs*, vol. 15, no. 6, p. 180, 2017.
- [3] N. Suryawanshi and J. S. Eswari, "Shrimp shell waste as a potential raw material for biorefinery—a revisit," *Biomass Conversion and Biorefinery*, pp. 2190–6823, 2021.
- [4] R. L. Naylor, R. W. Hardy, A. H. Buschmann et al., "A 20-year retrospective review of global aquaculture," *Nature*, vol. 591, no. 7851, pp. 551–563, 2021.
- [5] F. Lionetto and C. Esposito Corcione, "Recent applications of biopolymers derived from fish industry waste in food packaging," *Polymers*, vol. 13, no. 14, p. 2337, 2021.
- [6] M. Muthu, J. Gopal, S. Chun, A. J. P. Devadoss, N. Hasan, and I. Sivanesan, "Crustacean waste-derived chitosan: antioxidant properties and future perspective," *Antioxidants*, vol. 10, no. 2, p. 228, 2021.
- [7] L. G. Confederat, C. G. Tuchilus, M. Dragan, M. Sha'at, and O. M. Dragostin, "Preparation and antimicrobial activity of chitosan and its derivatives: a concise review," *Molecules*, vol. 26, no. 12, p. 3694, 2021.
- [8] N. Mati-Baouche, P.-H. Elchinger, H. De Baynast, G. Pierre, C. Delattre, and P. Michaud, "Chitosan as an adhesive," *European Polymer Journal*, vol. 60, pp. 198–212, 2014.
- [9] B. K. Park and M.-M. Kim, "Applications of chitin and its derivatives in biological medicine," *International Journal of Molecular Sciences*, vol. 11, no. 12, pp. 5152–5164, 2010.
- [10] M. S. Benhabiles, R. Salah, H. Lounici, N. Drouiche, M. F. A. Goosen, and N. Mameri, "Antibacterial activity of chitin, chitosan and its oligomers prepared from shrimp shell waste," *Food Hydrocolloids*, vol. 29, no. 1, pp. 48–56, 2012.
- [11] A. Wassila, L. Adour, and A. Amrane, "Chitin extraction from crustacean shells using biological methods," *Food Technology and Biotechnology*, vol. 51, pp. 12–25, 2013.
- [12] S. Bijay, Y. Choi, T. Akaike, and C. Cho, *Marine Materials, Gene Delivery*, Chennai, India, 2015.
- [13] M. Dash, F. Chiellini, R. M. Ottenbrite, and E. Chiellini, "Chitosan—a versatile semi-synthetic polymer in biomedical applications," *Progress in Polymer Science*, vol. 36, no. 8, pp. 981–1014, 2011.
- [14] I. Aranaz, M. Mengibar, R. Harris et al., "Functional characterization of chitin and chitosan," *Current Chemical Biology*, vol. 3, no. 2, pp. 203–230, 2009.

- [15] I. Kardas, M. Struszczyk, M. Kucharska, L. A. M. van den Broek, J. E. G. van Dam, and D. Ciecchańska, *Chitin and Chitosan as Functional Biopolymers for Industrial Applications*, Springer, New York, NY, USA, 2013.
- [16] I. Younes and M. Rinaudo, "Chitin and chitosan preparation from marine sources. Structure, properties and applications," *Marine Drugs*, vol. 13, no. 3, pp. 1133–1174, 2015.
- [17] E. L. Johnson and Q. P. Peniston, "Utilization of shellfish waste for chitin and chitosan production," in *Chemistry & Biochemistry of Marine Food Products*, R. E. Martin, G. J. Flick, C. E. Hebard, and D. R. Ward, Eds., AVI Publishing Co., Westport, CT, USA, 1982.
- [18] F. Shahidi and J. Synowiecki, "Isolation and characterization of nutrients and value-added products from snow crab (*Chionoecetes opilio*) and shrimp (*Pandalus borealis*) processing discards," *Journal of Agricultural and Food Chemistry*, vol. 39, no. 8, pp. 1527–1532, 1991.
- [19] A. Tolaimate, J. Desbrieres, M. Rhazi, and A. Alagui, "Contribution to the preparation of chitins and chitosans with controlled physico-chemical properties," *Polymer*, vol. 44, no. 26, pp. 7939–7952, 2003.
- [20] J. Pal, H. O. Verma, V. K. Munka, S. K. Maurya, D. Roy, and J. Kumar, "Biological method of chitin extraction from shrimp waste an eco-friendly low cost Technology and its advanced application," *International Journal of Fisheries and Aquatic Studies*, vol. 1, pp. 104–107, 2014.
- [21] A. Gildberg and E. Stenberg, "A new process for advanced utilisation of shrimp waste," *Process Biochemistry*, vol. 36, no. 8-9, pp. 809–812, 2001.
- [22] L. Manni, O. Ghorbel-Bellaaj, K. Jellouli, I. Younes, and M. Nasri, "Extraction and characterization of chitin, chitosan, and protein hydrolysates prepared from shrimp waste by treatment with crude protease from *Bacillus cereus* SV1," *Applied Biochemistry and Biotechnology*, vol. 162, no. 2, pp. 345–357, 2010.
- [23] I. Younes, O. Ghorbel-Bellaaj, M. Chaabouni et al., "Use of a fractional factorial design to study the effects of experimental factors on the chitin deacetylation," *International Journal of Biological Macromolecules*, vol. 70, pp. 385–390, 2014.
- [24] W. Arbia, L. Arbia, L. Adour, and A. Amrane, "Chitin extraction from crustacean shells using biological methods-a review," *Food Technology and Biotechnology*, vol. 51, pp. 12–25, 2013.
- [25] K. Prameela, C. Murali Mohan, P. V. Smitha, and K. P. J. Hemablatha, "Bioremediation of shrimp biowaste by using natural probiotic for chitin and carotenoid production an alternative method to hazardous chemical method," *International Journal of Applied Biology and Pharmaceutical Technology*, vol. 1, pp. 903–910, 2010.
- [26] M. S. Rao, J. Muñoz, and W. F. Stevens, "Critical factors in chitin production by fermentation of shrimp biowaste," *Applied Microbiology and Biotechnology*, vol. 54, no. 6, pp. 808–813, 2000.
- [27] K.-T. Oh, Y.-J. Kim, V. N. Nguyen, W.-J. Jung, and R.-D. Park, "Demineralization of crab shell waste by *Pseudomonas aeruginosa* F722," *Process Biochemistry*, vol. 42, no. 7, pp. 1069–1074, 2007.
- [28] O. Ghorbel-Bellaaj, I. Younes, H. Maâlej, S. Hajji, and M. Nasri, "Chitin extraction from shrimp shell waste using *Bacillus* bacteria," *International Journal of Biological Macromolecules*, vol. 51, no. 5, pp. 1196–1201, 2012.
- [29] T. K. Sini, S. Santhosh, and P. T. Mathew, "Study on the production of chitin and chitosan from shrimp shell by using *Bacillus subtilis* fermentation," *Carbohydrate Research*, vol. 342, no. 16, pp. 2423–2429, 2007.
- [30] O. Ghorbel-Bellaaj, K. Jellouli, I. Younes, L. Manni, M. Ouled Salem, and M. Nasri, "A solvent-stable metalloprotease produced by *Pseudomonas aeruginosa* A2 grown on shrimp shell waste and its application in chitin extraction," *Applied Biochemistry and Biotechnology*, vol. 164, no. 4, pp. 410–425, 2011.
- [31] D. Kafetzopoulos, A. Martinou, and V. Bouriotis, "Bio-conversion of chitin to chitosan: purification and characterization of chitin deacetylase from *Mucor rouxii*," *Proceedings of the National Academy of Sciences*, vol. 90, no. 7, pp. 2564–2568, 1993.
- [32] K. Kurita, T. Sannan, and Y. Iwakura, "Studies on chitin, 4: evidence for formation of block and random copolymers of N-acetyl-D-glucosamine and D-glucosamine by hetero- and homogeneous hydrolyses," *Makromolekulare Chemie*, vol. 178, no. 12, pp. 3197–3202, 1977.
- [33] H. K. No and S. P. Meyers, "Preparation and characterization of chitin and chitosan-A review," *Journal of Aquatic Food Product Technology*, vol. 4, no. 2, pp. 27–52, 1995.
- [34] K. L. B. Chang, G. Tsai, J. Lee, and W.-R. Fu, "Heterogeneous N-deacetylation of chitin in alkaline solution," *Carbohydrate Research*, vol. 303, no. 3, pp. 327–332, 1997.
- [35] T. Sannan, K. Kurita, and Y. Iwakura, "Studies on chitin, 2. Effect of deacetylation on solubility," *Makromolekulare Chemie*, vol. 177, no. 12, pp. 3589–3600, 1976.
- [36] M. Rinaudo and A. Domard, *Chitin and Chitosan*, G. Skajak-Braek, T. Anthonsen, and P. Sanford, Eds., Elsevier Applied Sciences, London, UK, 1989.
- [37] S.-i. Aiba, "Studies on chitosan: 4. Lysozymic hydrolysis of partially N-acetylated chitosans," *International Journal of Biological Macromolecules*, vol. 14, no. 4, pp. 225–228, 1992.
- [38] J. Berger, M. Reist, A. Chenite, O. Felt-Baeyens, J. M. Mayer, and R. Gurny, "Pseudo-thermosetting chitosan hydrogels for biomedical application," *International Journal of Pharmaceutics*, vol. 288, no. 2, pp. 197–206, 2005.
- [39] Q. Li, E. T. Dunn, E. W. Grandmaison, and M. F. A. Goosen, "Applications and properties of chitosan," *Journal of Bioactive and Compatible Polymers*, vol. 7, no. 4, pp. 370–397, 1992.
- [40] P. R. Rege and L. H. Block, "Chitosan processing: influence of process parameters during acidic and alkaline hydrolysis and effect of the processing sequence on the resultant chitosan's properties," *Carbohydrate Research*, vol. 321, no. 3-4, pp. 235–245, 1999.
- [41] Y. Zhao, R.-D. Park, and R. A. A. Muzzarelli, "Chitin deacetylases: properties and applications," *Marine Drugs*, vol. 8, no. 1, pp. 24–46, 2010.
- [42] Y. Zhao, Y. J. Kim, K. T. Oh, V. N. Nguyen, and R. D. Park, "Production and characterization of extracellular chitin deacetylase from *absidia corymbifera* DY-9," *Journal of the Korean Society for Applied Biological Chemistry*, vol. 53, no. 2, pp. 119–126, 2010.
- [43] Y. Zhao, W. T. Ju, G. H. Jo, W. J. Jung, and R. D. Park, "Perspectives of chitin deacetylase research," in *Biotechnology of Biopolymers*, M. Elnashar, Ed., InTech, Rijeka, Croatia, 2011.
- [44] I. Tsigos, A. Martinou, D. Kafetzopoulos, and V. Bouriotis, "Chitin deacetylases: new, versatile tools in biotechnology," *Trends in Biotechnology*, vol. 18, no. 7, pp. 305–312, 2000.
- [45] C. Alfonso, O. M. Nuero, F. Santamaria, and F. Reyes, "Purification of a heat-stable chitin deacetylase from

- Aspergillus nidulans and its role in cell wall degradation," *Current Microbiology*, vol. 30, no. 1, pp. 49–54, 1995.
- [46] I. Tsigos and V. Bouriotis, "Purification and characterization of chitin deacetylase from *Colletotrichum lindemuthianum*," *Journal of Biological Chemistry*, vol. 270, no. 44, pp. 26286–26291, 1995.
- [47] K. Tokuyasu, M. Ohnishi-Kameyama, and K. Hayashi, "Purification and characterization of extracellular chitin deacetylase from *Colletotrichum lindemuthianum*," *Bioscience, Biotechnology, and Biochemistry*, vol. 60, no. 10, pp. 1598–1603, 1996.
- [48] X.-D. Gao, T. Katsumoto, and K. Onodera, "Purification and characterization of chitin deacetylase from *absidia coerulea*," *Journal of Biochemistry*, vol. 117, no. 2, pp. 257–263, 1995.
- [49] A. Martinou, V. Bouriotis, B. T. Stokke, and K. M. Vårum, "Mode of action of chitin deacetylase from *Mucor rouxii* on partially N-acetylated chitosans," *Carbohydrate Research*, vol. 311, no. 1-2, pp. 71–78, 1998.
- [50] A. Alishahi, A. Mirvaghefi, M. R. Tehrani et al., "Chitosan nanoparticle to carry vitamin C through the gastrointestinal tract and induce the non-specific immunity system of rainbow trout (*Oncorhynchus mykiss*)," *Carbohydrate Polymers*, vol. 86, no. 1, pp. 142–146, 2011.
- [51] C. Muanprasat and V. Chatsudthipong, "Chitosan oligosaccharide: biological activities and potential therapeutic applications," *Pharmacology & Therapeutics*, vol. 170, pp. 80–97, 2017.
- [52] P. Zou, X. Yang, J. Wang et al., "Advances in characterisation and biological activities of chitosan and chitosan oligosaccharides," *Food Chemistry*, vol. 190, pp. 1174–1181, 2016.
- [53] F. Liaqat and R. Eltem, "Chitooligosaccharides and their biological activities: a comprehensive review," *Carbohydrate Polymers*, vol. 184, pp. 243–259, 2018.
- [54] N. Miguez, P. Kidibule, P. Santos-Moriano, A. O. Ballesteros, M. Fernandez-Lobato, and F. J. Plou, "Enzymatic synthesis and characterization of different families of chitooligosaccharides and their bioactive properties," *Applied Sciences*, vol. 11, no. 7, p. 3212, 2021.
- [55] T. Usui, H. Matsui, and K. Isobe, "Enzymic synthesis of useful chito-oligosaccharides utilizing transglycosylation by chitinolytic enzymes in a buffer containing ammonium sulfate," *Carbohydrate Research*, vol. 203, no. 1, pp. 65–77, 1990.
- [56] P. B. McElroy, A. Sri Hari, B. J. Day, and M. Patel, "Post-translational agcl," *Journal of Biological Chemistry*, vol. 292, no. 13, pp. 5532–5545, 2017.
- [57] W.-J. Jung and R.-D. Park, "Bioproduction of chitooligosaccharides: present and perspectives," *Marine Drugs*, vol. 12, no. 11, pp. 5328–5356, 2014.
- [58] W. Tachaboonyakiat, E. Sukpaiboon, and O. Pinyakong, "Development of an antibacterial chitin betainate wound dressing," *Polymer Journal*, vol. 46, no. 8, pp. 505–510, 2014.
- [59] F. Khan, J.-W. Lee, D. T. N. Pham, and Y.-M. Kim, "Chitooligosaccharides as antibacterial, antibiofilm, anti-hemolytic and anti-virulence agent against *Staphylococcus aureus*," *Current Pharmaceutical Biotechnology*, vol. 20, no. 14, pp. 1223–1233, 2019.
- [60] S. A. Ahmed, H. S. El-Mahallawy, and P. Karanis, "Inhibitory activity of chitosan nanoparticles against *Cryptosporidium parvum* oocysts," *Parasitology Research*, vol. 118, no. 7, pp. 2053–2063, 2019.
- [61] M. Mammeri, A. Chevillot, M. Thomas et al., "Efficacy of chitosan, a natural polysaccharide, against *Cryptosporidium parvum* in vitro and in vivo in neonatal mice," *Experimental Parasitology*, vol. 194, pp. 1–8, 2018.
- [62] L. S. Arias, M. C. Butcher, B. Short et al., "Chitosan ameliorates *Candida auris* virulence in a *Galleria mellonella* infection model," *Antimicrobial Agents and Chemotherapy*, vol. 64, 2020.
- [63] J. Zhang, W. Tan, Q. Li, F. Dong, and Z. Guo, "Synthesis and characterization of N,N,N-trimethyl-O-(ureidopyridinium) acetyl chitosan derivatives with antioxidant and antifungal activities," *Marine Drugs*, vol. 18, no. 3, p. 163, 2020.
- [64] L. Mei, Z. Xu, Y. Shi et al., "Multivalent and synergistic chitosan oligosaccharide-Ag nanocomposites for therapy of bacterial infection," *Scientific Reports*, vol. 10, no. 1, Article ID 10011, 2020.
- [65] F. Khan, J. W. Lee, P. Manivasagan, D. T. N. Pham, J. Oh, and Y. M. Kim, "Synthesis and characterization of chitosan oligosaccharide-capped gold nanoparticles as an effective antibiofilm drug against the *Pseudomonas aeruginosa* PAO1," *Microbial Pathogenesis*, vol. 135, Article ID 103623, 2019.
- [66] Z. E. D. Cele, A. M. Somboro, D. G. Amoako, L. F. Ndlandla, and M. O. Balogun, "Fluorinated quaternary chitosan derivatives: synthesis, characterization, antibacterial activity, and killing kinetics," *ACS Omega*, vol. 5, no. 46, pp. 29657–29666, 2020.
- [67] L. Sun, Y. Du, L. Fan, X. Chen, and J. Yang, "Preparation, characterization and antimicrobial activity of quaternized carboxymethyl chitosan and application as pulp-cap," *Polymer*, vol. 47, no. 6, pp. 1796–1804, 2006.
- [68] X. Fei Liu, Y. Lin Guan, D. Zhi Yang, Z. Li, and K. De Yao, "Antibacterial action of chitosan and carboxymethylated chitosan," *Journal of Applied Polymer Science*, vol. 79, no. 7, pp. 1324–1335, 2000.
- [69] K. Kurita, "Chitin and chitosan: functional biopolymers from marine crustaceans," *Marine Biotechnology*, vol. 8, no. 3, pp. 203–226, 2006.
- [70] H. Barzegar, A. Karbassi, J. Jamalian, and M. Aminlari, "Investigation of the possible use of chitosan as a natural preservative in mayonnaise sauce," *Journal of Science & Technology of Agriculture & Natural Resources*, vol. 43, p. 12, 2008.
- [71] G.-J. Tsai, W.-H. Su, H.-C. Chen, and C.-L. Pan, "Antimicrobial activity of shrimp chitin and chitosan from different treatments and applications of fish preservation," *Fisheries Science*, vol. 68, no. 1, pp. 170–177, 2002.
- [72] F. Devlieghere, A. Vermeulen, and J. Debevere, "Chitosan: antimicrobial activity, interactions with food components and applicability as a coating on fruit and vegetables," *Food Microbiology*, vol. 21, no. 6, pp. 703–714, 2004.
- [73] H. No, N. Y. Park, S. H. Lee, and S. P. Meyers, "Antibacterial activity of chitosans and chitosan oligomers with different molecular weights," *International Journal of Food Microbiology*, vol. 74, no. 1-2, pp. 65–72, 2002.
- [74] A. Balicka-Ramisz, A. Wojtasz-Pająk, B. Pilarczyk, A. Ramisz, and Ł. Laurans, "Antibacterial and antifungal activity of chitosan," in *Proceedings XII International Congress of Animal Hygiene*, A. Kryński and R. Wrzesień, Eds., Warsaw, Poland, 2005.
- [75] J.-H. Kim, D. Yu, S.-H. Eom et al., "Synergistic antibacterial effects of chitosan-caffeic acid conjugate against antibiotic-resistant acne-related bacteria," *Marine Drugs*, vol. 15, no. 6, p. 167, 2017.

- [76] C.-J. Huang, K. N. Beasley, E. O. Acevedo et al., "Chitin enhances obese inflammation ex vivo," *Human Immunology*, vol. 75, no. 1, pp. 41–46, 2014.
- [77] R. Izumi, K. Azuma, H. Izawa et al., "Chitin nanofibrils suppress skin inflammation in atopic dermatitis-like skin lesions in NC/Nga mice," *Carbohydrate Polymers*, vol. 146, pp. 320–327, 2016.
- [78] J. Wang, C. Zhang, C. Guo, and X. Li, "Chitosan ameliorates DSS-induced ulcerative colitis mice by enhancing intestinal barrier function and improving microflora," *International Journal of Molecular Sciences*, vol. 20, no. 22, p. 5751, 2019.
- [79] L. Shi, B. Fang, Y. Yong et al., "Chitosan oligosaccharide-mediated attenuation of LPS-induced inflammation in IPEC-J2 cells is related to the TLR4/NF- κ B signaling pathway," *Carbohydrate Polymers*, vol. 219, pp. 269–279, 2019.
- [80] T. Jiang, H. Ji, L. Zhang, Y. Wang, and H. Zhou, "Chitosan oligosaccharide exerts anti-allergic effect against shrimp tropomyosin-induced food allergy by affecting Th1 and Th2 cytokines," *International Archives of Allergy and Immunology*, vol. 180, no. 1, pp. 10–16, 2019.
- [81] R. Lan, S. Li, Q. Chang, and Z. Zhao, "Chitosan oligosaccharides protect sprague dawley rats from cyclic heat stress by attenuation of oxidative and inflammation stress," *Animals*, vol. 9, no. 12, p. 1074, 2019.
- [82] S. Libreros, R. Garcia-Areas, Y. Shibata, R. Carrio, M. Torroella-Kouri, and V. Iragavarapu-Charyulu, "Induction of proinflammatory mediators by CHI3L1 is reduced by chitin treatment: decreased tumor metastasis in a breast cancer model," *International Journal of Cancer*, vol. 131, no. 2, pp. 377–386, 2012.
- [83] S. Libreros, R. Garcia-Areas, and V. Iragavarapu-Charyulu, "CHI3L1 plays a role in cancer through enhanced production of pro-inflammatory/pro-tumorigenic and angiogenic factors," *Immunologic Research*, vol. 57, no. 1-3, pp. 99–105, 2013.
- [84] D. Solairaj, P. Rameshthangam, and G. Arunachalam, "Anticancer activity of silver and copper embedded chitin nanocomposites against human breast cancer (MCF-7) cells," *International Journal of Biological Macromolecules*, vol. 105, pp. 608–619, 2017.
- [85] L. Gibot, S. Chabaud, S. Bouhout, S. Bolduc, F. A. Auger, and V. J. Moulin, "Anticancer properties of chitosan on human melanoma are cell line dependent," *International Journal of Biological Macromolecules*, vol. 72, pp. 370–379, 2015.
- [86] Z. Abedian, A. A. Moghadamnia, E. Zabihi et al., "Anticancer properties of chitosan against osteosarcoma, breast cancer and cervical cancer cell lines," *Caspian Journal of Internal Medicine*, vol. 10, no. 4, pp. 439–446, 2019.
- [87] Z. Jiang, B. Han, H. Li, Y. Yang, and W. Liu, "Carboxymethyl chitosan represses tumor angiogenesis in vitro and in vivo," *Carbohydrate Polymers*, vol. 129, pp. 1–8, 2015.
- [88] M. Nakajima, K. Atsumi, K. Kifune, K. Miura, and H. Kanamaru, "Chitin is an effective material for sutures," *Japanese Journal of Surgery*, vol. 16, no. 6, pp. 418–424, 1986.
- [89] C. Klinger, S. Żółtowska-Aksamitowska, M. Wysokowski et al., "Express method for isolation of ready-to-use 3D chitin scaffolds from aplysina archeri (aplysineidae: verongiida) demosponge," *Marine Drugs*, vol. 17, no. 2, p. 131, 2019.
- [90] K. Shao, B. Han, J. Gao et al., "Fabrication and feasibility study of an absorbable diacetyl chitin surgical suture for wound healing," *Journal of Biomedical Materials Research Part B: Applied Biomaterials*, vol. 104, no. 1, pp. 116–125, 2016.
- [91] J. N. I. Balitaan, C.-D. Hsiao, J.-M. Yeh, and K. S. Santiago, "Innovation inspired by nature: b," *International Journal of Biological Macromolecules*, vol. 162, pp. 723–736, 2020.
- [92] F.-C. Chao, M.-H. Wu, L.-C. Chen et al., "Preparation and characterization of chemically TEMPO-oxidized and mechanically disintegrated sacchachitin nanofibers (SCNF) for enhanced diabetic wound healing," *Carbohydrate Polymers*, vol. 229, Article ID 115507, 2020.
- [93] M. Kuwabara, Y. Sato, M. Ishihara et al., "Healing of pseudomonas aeruginosa-infected wounds in diabetic db/db mice by weakly acidic hypochlorous acid cleansing and silver nanoparticle/chitin-nanofiber sheet covering," *Wound Medicine*, vol. 28, 2020.
- [94] E. N. Maevskaia, A. S. Shabunin, E. N. Dresvyanina et al., "Influence of the introduced chitin nanofibrils on biomedical properties of chitosan-based materials," *Nanomaterials*, vol. 10, no. 5, p. 945, 2020.
- [95] Z.-W. Li, C.-W. Li, Q. Wang et al., "The cellular and molecular mechanisms underlying silver nanoparticle/chitosan oligosaccharide/poly(vinyl alcohol) nanofiber-mediated wound healing," *Journal of Biomedical Nanotechnology*, vol. 13, no. 1, pp. 17–34, 2017.
- [96] C. W. Li, Q. Wang, J. Li et al., "Silver nanoparticles/chitosan oligosaccharide/poly(vinyl alcohol) nanofiber promotes wound healing by activating TGF β 1/Smad signaling pathway," *International Journal of Nanomedicine*, vol. 11, pp. 373–386, 2016.
- [97] A. Cifuentes, V. Gómez-Gil, M. A. Ortega et al., "Chitosan hydrogels functionalized with either unfractionated heparin or bemiparin improve diabetic wound healing," *Biomedicine & Pharmacotherapy*, vol. 129, Article ID 110498, 2020.
- [98] J. Natarajan, B. K. R. Sanapalli, M. Bano, S. K. Singh, M. Gulati, and V. V. S. R. Karri, "Nanostructured lipid carriers of pioglitazone loaded collagen/chitosan composite scaffold for diabetic wound healing," *Advances in Wound Care*, vol. 8, no. 10, pp. 499–513, 2019.
- [99] C. Viezzer, R. Mazzuca, D. C. Machado, M. M. de Camargo Forte, and J. L. Gómez Ribelles, "A new waterborne chitosan-based polyurethane hydrogel as a vehicle to transplant bone marrow mesenchymal cells improved wound healing of ulcers in a diabetic rat model," *Carbohydrate Polymers*, vol. 231, Article ID 115734, 2020.
- [100] D. Zhao, S. Yu, B. Sun, S. Gao, S. Guo, and K. Zhao, "Biomedical applications of chitosan and its derivative nanoparticles," *Polymers*, vol. 10, no. 4, p. 462, 2018.
- [101] M. N. V. Ravi Kumar, "A review of chitin and chitosan applications," *Reactive and Functional Polymers*, vol. 46, no. 1, pp. 1–27, 2000.
- [102] D. D. Ojeda-Hernández, A. A. Canales-Aguirre, J. Matias-Guiu, U. Gomez-Pinedo, and J. C. Mateos-Díaz, "Potential of chitosan and its derivatives for biomedical applications in the central nervous system," *Frontiers in Bioengineering and Biotechnology*, vol. 8, p. 389, 2020.
- [103] S. Mitra, U. Gaur, P. C. Ghosh, and A. N. Maitra, "Tumour targeted delivery of encapsulated dextran-doxorubicin conjugate using chitosan nanoparticles as carrier," *Journal of Controlled Release*, vol. 74, no. 1-3, pp. 317–323, 2001.
- [104] Y.-C. Huang, R.-Y. Li, J.-Y. Chen, and J.-K. Chen, "Biphasic release of gentamicin from chitosan/fucoidan nanoparticles for pulmonary delivery," *Carbohydrate Polymers*, vol. 138, pp. 114–122, 2016.
- [105] A. Di Martino, M. Sittinger, and M. V. Risbud, "Chitosan: a versatile biopolymer for orthopaedic tissue-engineering," *Biomaterials*, vol. 26, no. 30, pp. 5983–5990, 2005.

Retraction

Retracted: Characterization and Parametric Optimization of EN-10149-2 Steel Welded Joints Made by MIG Welding

Advances in Materials Science and Engineering

Received 26 December 2023; Accepted 26 December 2023; Published 29 December 2023

Copyright © 2023 Advances in Materials Science and Engineering. This is an open access article distributed under the Creative Commons Attribution License, which permits unrestricted use, distribution, and reproduction in any medium, provided the original work is properly cited.

This article has been retracted by Hindawi, as publisher, following an investigation undertaken by the publisher [1]. This investigation has uncovered evidence of systematic manipulation of the publication and peer-review process. We cannot, therefore, vouch for the reliability or integrity of this article.

Please note that this notice is intended solely to alert readers that the peer-review process of this article has been compromised.

Wiley and Hindawi regret that the usual quality checks did not identify these issues before publication and have since put additional measures in place to safeguard research integrity.

We wish to credit our Research Integrity and Research Publishing teams and anonymous and named external researchers and research integrity experts for contributing to this investigation.

The corresponding author, as the representative of all authors, has been given the opportunity to register their agreement or disagreement to this retraction. We have kept a record of any response received.

References

- [1] K. B. Behredin, P. Janaki Ramulu, B. Habtamu, N. Besufekad, and N. Tesfaye, "Characterization and Parametric Optimization of EN-10149-2 Steel Welded Joints Made by MIG Welding," *Advances in Materials Science and Engineering*, vol. 2022, Article ID 8276496, 16 pages, 2022.

Research Article

Characterization and Parametric Optimization of EN-10149-2 Steel Welded Joints Made by MIG Welding

Kedir Beyene Behredin,¹ Perumalla Janaki Ramulu ,² Beri Habtamu,¹ Negash Besufekad,³ and Negash Tesfaye¹

¹Department of Mechanical Engineering, School of Mechanical, Chemical and Materials Engineering, Adama Science and Technology University, Adama, Ethiopia

²Department of Mechanical Engineering & CoE for Advanced Manufacturing Engineering, School of Mechanical, Chemical and Materials Engineering, Adama Science and Technology University, Adama, Ethiopia

³Department of Mechanical Engineering, Defence University College of Engineering, Bishoftu, Ethiopia

Correspondence should be addressed to Perumalla Janaki Ramulu; perumalla.janaki@astu.edu.et

Received 19 January 2022; Revised 3 March 2022; Accepted 29 March 2022; Published 22 April 2022

Academic Editor: Palanivel Velmurugan

Copyright © 2022 Kedir Beyene Behredin et al. This is an open access article distributed under the Creative Commons Attribution License, which permits unrestricted use, distribution, and reproduction in any medium, provided the original work is properly cited.

Advanced high strength steels (AHSS) are multiphase steels that contain various concentrations of ferrite, bainite, martensite, and retained austenite phases. The unique physical characteristics of AHSS present some challenges to welding and bonding processes. AHSS have tendency to change microstructure and mechanical properties by any welding process like other steels. Based on the significant applications in various industries, the experimental works are carried out on one of AHSS materials, EN-10149-2 S700MC, with thickness of 2 mm steel sheet metal by MIG welding process parameters such as current, voltage, and welding speed. For all combinations of process parameters, the butt joints are fabricated. The butt joints are inspected through different nondestructive testing for defects detection. All the defect-free joints are characterized through microstructure (at different zones of joint), hardness, and tensile tests. From the obtained mechanical test results, the process parameters are optimized through design of experiment techniques (DoE). The analysis from DoE method is used to identify which parameter is the most significant among all parameters. Confirmatory test is also done by taking the optimal parameters and the result shows that the improvement of the response variables is acceptable and also shows that the method that is used for optimization was valid.

1. Introduction

Metal Inert Gas (MIG) welding is one of the extensively used joining processes in manufacturing industries. The input parameters of MIG welding play a significant role in determining the quality of welded joints. Weld geometry directly affects the complexity of weld schedules and thereby the construction and manufacturing costs of steel structures and mechanical devices get affected. The weld quality is depending on the process parameters, hence the selection of the best parameters to be known for optimum results. Earlier, in most of the research, the considered MIG parameters were welding current, arc voltage, and welding speed. These parameters affect the weld characteristics

remarkably. Because they can be varied over a large range, they are considered the primary adjustments in any welding operation. During the MIG welding process, the electrode melts within the arc and becomes deposited as filler material. The shielding gas that is used prevents atmospheric contamination from atmospheric contamination and protects the weld during solidification. The shielding gas also assists with stabilizing the arc which provides a smooth transfer of metal from the weld wire to the molten weld pool. Based on the literature on MIG welding process, parameters effect on weld quality and optimization impact on various materials are described as Sathiyaraj et al. [1] optimized the gas metal arc welding (GMAW) process input parameters considering the multiple output variables (bead width (BW), bead height

(BH), and depth of penetration (DP)) for 904L SASS sheet. For optimization, grey-based Taguchi approach was used and the experiment designed, L27 orthogonal array. The predicted bead profiles had better DP and lower BH and BW. It was found that the optimized setting values are improving the response values by 10 percent. Katherasan et al. [2] optimized the process parameters (wire feed rate (F), voltage (V), welding speed (S), and torch angle (A)) in order to obtain the optimum bead geometry (bead width (W), reinforcement (R), and depth of penetration (P)), considering the ranges of the process parameters using evolutionary algorithms, namely, genetic algorithm (GA) and simulated annealing (SA) algorithm. Pipavat et al. [3] presented the influence of MIG welding parameters like welding current, welding voltage, and welding speed on mechanical properties like tensile strength and hardness on austenitic stainless steel AISI 316. Experiments based on Taguchi technique were carried out to obtain the data. An orthogonal array and analysis of variance (ANOVA) employed and investigated the welding characteristics of AISI 316 material and optimized the welding parameters. Kumar et al. [4] investigated the influence of shielding gas composition of gas metal arc welding (GMAW) and gas tungsten arc welding (GTAW) on the mechanical properties of austenitic stainless steel 316L with 3 and 6 mm thick plates. Optimization of shielding gas mixtures, current intensities, flow rates, and welding speed is required to automate the process and to improve the overall efficiency of the weld process. The obtained results proved that the tensile strength, hardness, and impact strength were higher for GTAW weld specimens compared to GMAW weld specimens. Kalita and Barua [5] investigated the effect of MIG welding process parameters on C20 carbon steel as parent metal and ER70S-4 electrode such as welding current, voltage, and shielding gas flow rate on tensile strength. An experiment was designed using Taguchi's orthogonal array L9, three levels each. The selected levels for welding current were 170 A, 200 A, and 230 A, for voltage they were 20 V, 25 V, and 30 V, and for shielding gas flow rate (CO_2) they were 8 lit/min, 12 lit/min, and 16 lit/min. The experiments were conducted using TORNADO MIG 400 welding machine with three repetitions. The optimal set of process parameters for optimal tensile strength (475.87 N/mm^2) was found to be as follows: 200 A welding current, 30 V welding voltage, and 8 lit/min gas flow rate. The effect of shielding gas flow rate was found to be insignificant and was kept at the most economic level (8 lit/min).

Narwadkar and Bhosle [6] optimized controllable MIG input parameters such as current, voltage, and gas flow rate by using the Taguchi method for butt welded Fe410WA. Angular distortion was minimized by optimizing the input parameters. An orthogonal array of nine trials was considered for the design of the experiment. After measuring the distortion angle, observed readings were verified by using ANOVA and it was found that the " p " values were less than 0.05. Theoretical calculations were done to optimize the process parameters to achieve the minimum distortion angle. A confirmation test was taken for validation purposes and to confirm the result. Ghosh et al. [7] identified an

optimal parametric combination of MIG welding for quality of weld of austenitic stainless steel AISI 316L by adopting Taguchi technique. An orthogonal array, S/N ratio, and ANOVA were employed, the welding characteristics of material were studied, and the welding parameters were optimized. The parameters like effect of current, gas flow rate, and nozzle to plate distance on quality of weld were studied through experiment and analyses. The result computed the contribution from each parameter, and optimized parameters were identified for maximum tensile strength and percentage elongation. Mvola and Kah [8] examined the effects of shielding gas mixtures and their components, presented a cross-comparison of shielding effects in fusion welding, and suggested guidelines for adaptive controllability of shielding gas in advanced adaptive fusion welding of both ferrous metals (i.e., carbon steels, stainless steels, and high-strength steels) and nonferrous metals (i.e., aluminium and its alloys, nickel and its alloys, and copper and its alloys).

Kalacska et al. [9] investigated the weldability of different advanced high strength steels (AHSS). The welding parameters were successfully optimized for butt welded joints. The joints were investigated by visual examination, tensile testing, and quantitative metallography and hardness measurements. Govinda Rao et al. [10] proposed the vibratory weld treatment during welding to enhance the flexural and impact strength of weldments. It was found that the mechanical properties showed nonlinear behavior with the chosen input parameters. An efficient neural network based prediction tool was developed to approximate the mechanical properties of weldments without performing the experiments, outputting values predicted for the given input values. Rizvi [11] optimized different welding process parameters which affect the weldability of stainless steel (AISI) 304H through Taguchi techniques by L9 orthogonal array and also studied the fracture mode characterization. Analysis of variance (ANOVA) and signal-to-noise ratio (SNR) were applied to determine the effect of welding current, wire feed speed, and gas flow rate on mechanical, microstructure properties of SS304H. Ultimate tensile strength, toughness, microhardness, and mode of fracture were examined and it was observed from results that welding voltage has a major impact, whereas gas flow rate has minor impact on ultimate tensile strength of the welded joints. Optimum process parameters were found to be 23 V, 350 IPM travel speed of wire, and 15 l/min gas flow rate for tensile strength and mode of fracture was ductile fracture for tensile test specimen. Odiaka et al. [12] reviewed on the improvement of weld integrity involved parametric optimization of MIG welding process. Some suggestions in terms of postweld heat treatment, pulsed current, hybrid welding, and vibratory welding were discovered to be alternative means of improving weld integrity. The use of reinforcing powders was also discovered, and it was suggested that the quality of MIG welded steel joints improved by using titanium alloy powder as weld joint reinforcement. Alagarsamy and Kumar [13] optimized the gas metal arc welding parameters on the impact strength, hardness, and flexural strength of dissimilar weld joints of SS316L and AISI D2 steels by using Taguchi based grey relational method. The experiments were planned

as per Taguchi L8 orthogonal array by considering four input parameters: current, voltage, speed, and root gap. The experimental results showed that the maximum impact strength of 4.36 J/mm², maximum hardness of 49.5 HRC, and maximum flexural strength of 583.3 MPa were obtained for the weld joints fabricated under the optimum welding conditions of current of 80 amps, voltage of 15 volt, speed of 45 cm/min, and root gap of 2.0 mm. The most significant parameter on multiple output response is the root gap. The contribution of root gap was 54.64% and followed by 20.26% and 11.94% of welding speed and voltage, respectively. Guizani et al. [14] optimized the mechanical brush finishing of MIG welded joints on AISI316L thin steel sheet. The experimental design methodology of the Taguchi design (L9) and the analysis of variance (ANOVA) with an objective function of microhardness in brushed layers was used. The effects showed the major influence of the depression and the number of passes on the magnitude of hardening of the brushed layers in the various zones of the weld. Gejendhiran et al. [15] focused on the effect of process welding parameters of GMAW and GTAW process for acquiring greater mechanical properties of weld plates of thin gauge mild steel and stainless. The shielding gas, weld voltage, and current were chosen as process parameters to acquire greater welding effectiveness and efficiency. The mechanical properties are ultimate tensile strength, toughness, and hardness of the weldment. After completion of the experimental work, the S/N ratio and mean S/N ratio were evaluated and optimum values of each parameters were evaluated through the Taguchi method. Subsequently, the significant coefficient for each input factor of the mechanical properties was evaluated by using ANOVA and prediction on the mechanical properties evaluated by using regression analysis. 15 mm IS2062 mild steel was welded by GMAW with the shielding gas mixtures of pure (100%) CO₂, Ar+20% CO₂, and Ar+10% O₂. The tensile strength optimum value was provided by the shielding gas mixture Ar+20% CO₂ and also it gives the optimum value for toughness. The higher hardness value was obtained by pure (100%) CO₂ with respect to other shielding gas mixtures. Baskoro et al. [16] investigated the GMAW parameters for welding of A36 mild steel to get the minimum of distortion. The type of welded joint used was square groove T-joint fillet weld with filler wire ER70S-6. The welding current and the welding speed were selected as input parameters, while the response used was longitudinal bending distortion and angular distortion. L9 Taguchi's orthogonal array was applied. The minimum conditions were determined using S/N ratio with a quality character of the smaller the better. The results show that the welding current of 170A and the welding speed of 4.0 mm/s were obtained as the minimum of longitudinal bending distortion and angular distortion. Based on analysis of variance, the welding current was a parameter that greatly affects the longitudinal bending distortion with the percentage contribution of 64.36%, while angular distortion was strongly influenced by welding speed parameter with the percentage contribution of 53.38%.

Kumar and Gandhinathan [17] reviewed the effects of welding current, voltage, gas flow rate, welding speed, and

gas pressure on mechanical properties like tensile strength and percentage of elongation of MIG welded joints of AISI 1018 mild/low carbon steel plates. Optimization was done and found optimum welding conditions to maximize tensile strength and percentage elongation of welded joints. From the study, it was found that when the welding current, voltage, and gas flow rate increase, the tensile strength decreases, but when welding speed increases, the tensile strength also increases for AISI 1018 steel weld joint. AISI 1018 is nonhardenable ductile steel belonging to low carbon steel categories. Rout et al. [18] proposed fuzzy-regression-particle swarm optimization (PSO) based hybrid optimization approach for getting maximum weld quality in terms of weld strength and bead depth of penetration. The predicted weld quality or the multiperformance characteristic index (MPCI) values in terms of combined weld strength and bead geometry found to be highly correlated with the weld process parameters. Radhakrishnan et al. [19] observed that the variation of mechanical properties depends on tensile strength in the MIG welding, for which parameters like arc voltage, welding speed, and current were considered and experimental analysis was carried out. The percentage influence of the welding characteristics on the tensile strength was also found using ANOVA method. The optimum welding framework combinations were obtained by using the analysis of S/N ratio.

In the literature survey of welding parameters on the conventional MIG welding machines like welding current, welding voltage, welding speed, arc length, angle of welding, air gap, and welding position, stick length, shielding gas, work piece material weldability, which affects the desired output like strength, hardness, and microstructure for different materials like mild steel, carbon steel, and aluminum alloys were studied. However, the optimization of welding parameters and characterization of AHSS steel sheets material welded by MIG welding process are not studied. Therefore, it is vital to study the optimization and characterization of welding parameters for AHSS of EN-10149-2 S700MC with thickness of 2 mm.

The difficulties in welding operation of AHSS of EN-10149-2 S700MC with thickness of 2 mm steel sheet metal on MIG welding process and how to overcome those challenges by selecting optimal welding parameters are discussed as follows:

- (1) Identifying significant factors (welding current, welding voltage, and welding speed) that affect the surface quality of MIG welding process for AHSS of EN-10149-2 S700MC with thickness of 2 mm.
- (2) Scientifically recommending the optimum welding process parameters for MIG welding process for AHSS of EN-10149-2 S700MC steel sheet metal material.

2. Experimental Methodology

2.1. Base Material. The experimental works were carried out on AHSS of EN-10149-2 S700MC with thickness of 2 mm steel sheet metal butt welded joints by different MIG welding

process parameters. An advanced high strength AHSS of EN-10149-2 S700MC steel sheet metal chemical composition is shown in Table 1.

2.2. MIG Welding Machine. Metal Inert Gas (MIG) welding embraces a group of arc welding processes in which a continuous electrode (the wire) is fed by powered feed rolls (wire feeder) into the weld pool.

MIG welding is usually carried out with a handheld gun as a semiautomatic process. The MIG process was suited to a variety of job requirements by choosing the correct shielding gas, electrode (wire) size, and welding parameters. Telwin MIG-MAG made machine was used with the filler material of ER70S. The chemical composition of the ER70S filler material is indicated in Table 2. The fixed or preselected welding variables were electrode type (ER 70S-6), electrode size (0.8 mm diameter), type of current (DC), and so forth, which were set before the actual welding.

The primary welding variables that were considered in this research include welding current (I), arc voltage (V), and travel speed (S). Secondary adjustable variables considered were work angle and the travel angle of the electrode.

2.3. Metallurgical Microscope. The microstructure of the specimen was observed by using metallurgical microscope (model: Huvitz HRM-300 series; magnification: 50x, 100x, 200x, 500x, and 1000x; scanning area: 104×102 mm; illumination system: 12 V, 1000 W halogen lamp). All samples were seen at 100x magnification. The microstructures of welded samples were captured at different zones like base metal, weld zone, thermomechanical zone, and heat-affected zone.

2.4. Microhardness Testing. The Vickers hardness model HVS 50 testing machine with a square base diamond pyramid as the indenter was used. The included angle of the pyramid was 136° between opposite faces subjected to a test force between 1 gf and 100 kgf. The area of the sloping surfaces of the indentation was calculated. The Vickers hardness is the quotient obtained by dividing the kgf load by the square mm area of indentation.

2.5. Universal Tensile Testing Machine. Universal tensile testing machine was used to measure the tensile strength of the weld joint. Properties are usually determined by doing tensile test. For the test results, yield stress, tensile strength, percentage elongation on gauge length, and percentage reduction in area were extracted. The test was carried out using Bairoe computer controlled electrohydraulic universal testing machine (model HUT-600) with cross head speed of 1 mm/min. The tests were measured three times for each sample and the average was taken.

2.6. Specimen Preparation

2.6.1. Welding Specimen. The sample of advanced high strength steel EN-10149-2 as a base metal was taken and

prepared to the required dimensions of 300 mm length, 90 mm width, and 2 mm thickness used as the workpiece. These specimens were prepared with a V-shaped groove with the root face, and the root gaps were 15° , 1 mm, and 0.9 mm, respectively. Thereafter, 27 pairs of specimens with constant groove angle and root face were prepared. To make a butt joint, two sheets were tacked at the two ends along the width, with a constant root gap of 0.9 mm. Copper coated mild steel wire with diameter of 0.8 mm was used in the experiment as the electrode. The wire was fed through the welding gun by a roller drive system. The shielding gas used was a mixture of 98% argon and 2% CO_2 , supplied in a regulated manner at a constant flow rate and at a constant pressure.

In this work, horizontal (PA/1G) welding position was used to join the sample. The welding joint was done at root opening of 0.8 mm and at a bevel angle of 10° and groove angle of 15° .

2.6.2. Tensile Specimen. Tensile samples were prepared in standard form (dog bone) with the following dimensions: total length of 300 mm, gauge length of 100 mm, grip length of 90 mm, thickness of 2 mm, and width of 20 mm, as shown in Figure 1 schematically with dimensions; for every experiment three test samples were reputed.

2.7. Optimization of Process Parameters. MINITAB 18 tool was used to analyze data for optimization. Taguchi method was used as a special design of orthogonal arrays to study the entire parameter space with only a small number of experiments to analyze the effect of welding parameters on mechanical property of EN-10149-2 AHSS.

Taguchi method was used to determine the minimum number of experiments to be conducted in the overall experiments based on the below equation.

$$N = L^P, \quad (1)$$

where N is the number of experiments to be conducted, P is the number of parameters, and L is the number of levels.

Before selecting the particular orthogonal array (OA), it is necessary to set the number of controlled parameters and the number of levels for these parameters. The estimation of the selected parameters level was done by doing weld bead joint geometry. In the present work, there were three variables (welding current, welding voltage, and welding travel speed) and three levels for each parameter as described in Table 3.

According to full factorial design; a total of 27 experiments were required to optimize the parameters. Taguchi experimental design suggests L9 orthogonal array, where 9 experiments are sufficient to optimize the parameters. This setup allows the testing of all three variables without having to run 27 (3^3) experiments as shown in Table 4.

Signal-to-noise (S/N) ratio technique was used for prediction of optimum results. The S/N ratio takes both the mean and the variability into account. Analysis of Variance (ANOVA) was also implemented to investigate which

TABLE 1: Chemical composition of base metal (S700MC).

C	Si	Mn	P	S	Al	Nb	V	Ti	Cu	Cr	Ni	Mo	B	Zr
0.056	0.18	1.78	0.01	0.003	0.038	0.06	0.01	0.116	0.011	0.04	0.03	0.005	0.0004	0.003

TABLE 2: Chemical composition of filler electrode ER70S.

Grade	C	Si	Mn	Cr	Ni	Mo	V	Ti	Al	Zr	P	S	Cu
ER70S	0.05	0.55	11.15	0.04	0.15	0.005	0.008	0.10	0.10	0.07	0.012	0.006	0.010

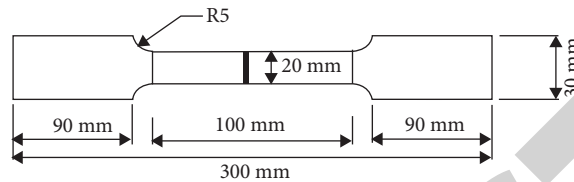


FIGURE 1: Sample for tensile test.

TABLE 3: Process parameters and their levels.

S. no	Process parameter	Unit	Levels		
			Level 1	Level 1	Level 1
1	Current (I)	A	60	65	70
2	Voltage (V)	V	16	17	18
3	Welding speed (S)	mm/s	2	4	6

TABLE 4: Orthogonal arrays for number of experiments.

Experimental runs	Experimental variables		
	Current (A)	Voltage (V)	Speed (mm/s)
1	60	16	2
2	60	17	4
3	60	18	6
4	65	16	4
5	65	17	6
6	65	18	2
7	70	16	6
8	70	17	2
9	70	18	4

welding process parameter significantly affects the quality characteristics. Taguchi recommended a logarithmic transformation of mean square deviation (S/N ratio) for the analysis of results. ANOVA separates the overall variation from the average S/N ratio into contribution by each of the parameters and the errors.

3. Results and Discussion

Experimental study was conducted to evaluate the effect of welding parameters, namely, welding current, welding voltage, and welding speed, on the welding material property of tensile strength, hardness, and microstructure of base material, fusion zone, and heat-affected zone. The results for each experiment are discussed in this section. Design of

experiment techniques is used to identify the optimum welding parameters and to identify the most influential parameters.

3.1. Microstructural Analysis

3.1.1. Microstructure of Parent Material. Microstructural study of weld joint includes analysis of solidified molten zone, heat-affected zone (HAZ), and parent material region. Figure 2 shows the microstructure of EN-10149-2 S700MC steel; this sample contains 60% area fraction ferrite and 40% area fraction martensite. The structure of these steels is a soft ferrite phase in which the martensitic islands are scattered; by increasing the amount of martensite in the structure, the strength is raised. Ferrite is a soft phase with lower yield

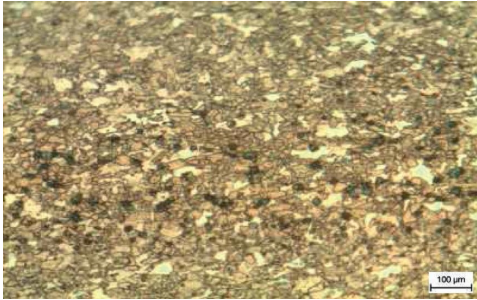


FIGURE 2: Microstructure of parent material (at 100x).

strength and more ductility. To have high strength and acceptable formability, the number of phases is essential. The behavior of these two-phase steels depends on the volume fraction of phases, morphology, grain size, and the carbon content.

3.1.2. Microstructure of Weld Zone. The weld metal microstructure of fusion welded joints is greatly influenced by the chemical composition of filler metal and the heat input ($V \times I \times t$) of the process. Since welding involves high temperature, the diffusion of atoms is better promoted. A transition zone gets formed along the fusion boundary which is chemically discrete compared to both base metals (mostly in concentration) shown in Figure 3. The inter-metallic compounds that form also play a significant role in affecting the tensile strength of the material; that is why the tensile strength of the welded part is increased.

3.1.3. Microstructure of Heat-Affected Zone. The rate of solidification is different compared to the technique followed during the fabrication of the base metal. This results in a significant change in the size of the grains in the HAZ-fusion boundary (coarser grains are observed along the fusion boundary) indicated in Figure 4. However, lower heat input leads to fast cooling rate, which results in fine microstructure.

3.2. Hardness Analysis of Weld Zone. The hardness measurement values in the weld zone are tabulated in Table 5. The S/N ratio has been calculated using MINITAB 18 for each single number of experiments and is recorded in Table 5.

3.2.1. Response Table for Hardness of Welded Zone. As in Table 6, for S/N ratios, the larger the better.

Table 7 shows means for hardness of WZ.

In this experimental analysis, the voltage has the greatest influence on the signal-to-noise ratio, followed by current and speed. According to Taguchi's experimental principle, the S/N ratio must be larger. In this work, the level averages in the response table show that the greater S/N ratio and the mean are when the current, voltage, and speed were 70 A, 18 V, and 6 mm/s, respectively, as shown in Figures 5 and 6. Tables 6 and 7 show the average of each of the response

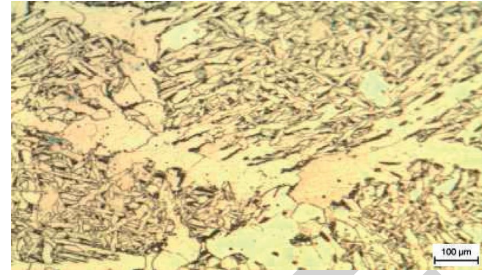


FIGURE 3: Microstructural analysis of WZ (100x).

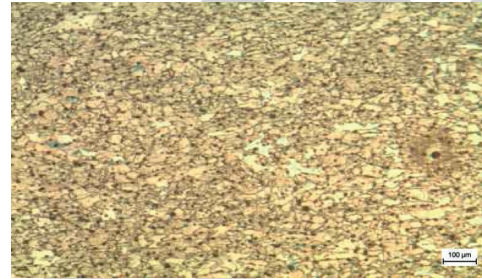


FIGURE 4: Microstructure analysis of HAZ (100x).

characteristics (S/N ratio, mean) for each level of every variable. The tables contain the rank of each variable according to the delta statistics reading which compares the relative magnitude of each variables effect.

The S/N ratio allows us to quantify the size of the applied or controlled signal relative to fluctuations that are outside experimental control, or, in other words, it is a statistical method used to evaluate the ratio of mean of the required value to the standard deviation from the expected value. As shown in Table 6, the S/N of the optimum value of each parameter is almost similar, which means that each parameter in the welding process has equal chance to bring the performance change. The adequacy of the model has been investigated by the examination of residuals. From the normal probability plot, it is found that the residuals fall on a straight line; it implies that the errors are distributed normally. The plot of residual versus predicted/fitted surface roughness values reveals that there is no obvious pattern and unusual structure shown in Figures 7 and 8. This implies that the proposed model is adequate and there is no reason to suspect any violation of the independence or constant variance assumption.

3.2.2. Analysis of Variance (ANOVA) of Hardness for Weld Zone. In order to determine the significance of each variable, it is necessary to know the critical "F" value and compare this critical "F" value with the calculated "F" value. If the calculated "F" value is greater or equal to the critical "F" value which is obtained from 0.05 significance level, then the variable is significant. However, if it is less than critical value, the parameter is nonsignificant. The critical value can be obtained by using degree of freedom of each parameter and degree of freedom of the error from 0.05 significance

TABLE 5: Hardness of welded zone reading and S/N ratio.

S. no.	Welding current	Welding voltage	Welding speed	Hardness of weld zone	SNRA1	MEAN1
1	60	16	2	135	42.6067	135
2	60	17	4	152	43.6369	152
3	60	18	6	155	43.8066	155
4	65	16	4	140	42.9226	140
5	65	17	6	153	43.6938	153
6	65	18	2	150	43.5218	150
7	70	16	6	150	43.5218	150
8	70	17	2	158	43.9731	158
9	70	18	4	163	44.2438	163

TABLE 6: Response table for signal-to-noise ratio for hardness of WZ.

Level	Current	Voltage	Speed
1	43.35	43.02	43.37
2	43.38	43.77	43.60
3	43.91	43.86	43.67
Delta	0.56	0.84	0.31
Rank	2	1	3

TABLE 7: Response table for means for hardness of WZ.

Level	Current	Voltage	Speed
1	147.3	141.7	147.7
2	147.7	154.3	151.7
3	157.0	156.0	152.7
Delta	9.7	14.3	5.0
Rank	2	1	3

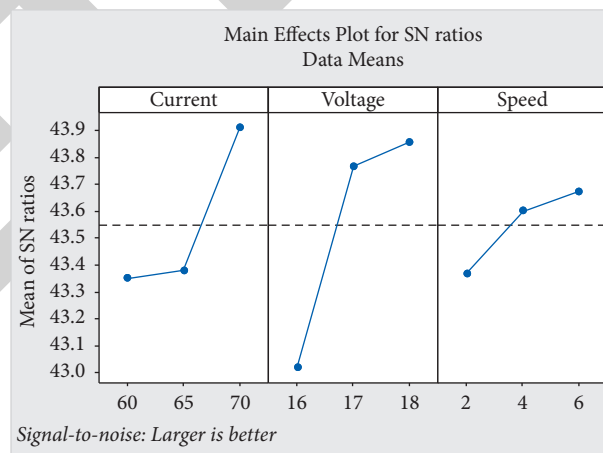


FIGURE 5: Main effect plot for S/N of hardness of welded zone.

level. Based on this, the critical value is " F_{cr} " ($0.05, 2, 8$) = 4.46 is noted which is lesser than " F " value shown in Table 8.

In statistical hypothesis testing, a result has statistical significance when it is very unlikely to have occurred given the null hypothesis. More precisely, a study's defined significance level, α , is the probability of the study rejecting the null hypothesis, given that it was true and the p value of a

result, p , is the probability of obtaining a result at least as extreme, given that the null hypothesis was true. The result is statistically significant, by the standards of the study, when $p < \alpha$.

The effect of the significant feature can be determined according to " F " and " p " values, which is explained as follows.

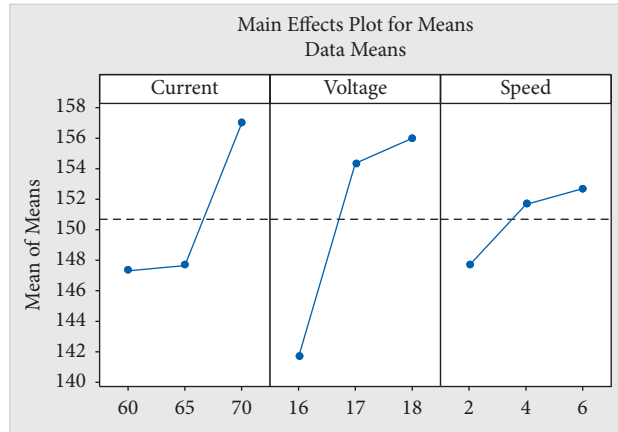


FIGURE 6: Main effects plot for means of welded zone.

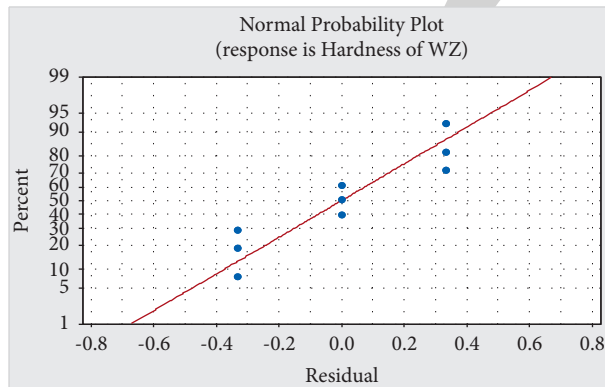


FIGURE 7: Normal probability plot of residual for hardness of weld zone.

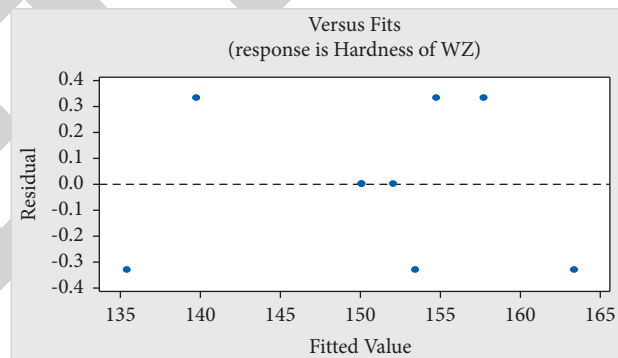


FIGURE 8: Plot of residual versus fitted hardness of weld zone values.

TABLE 8: General linear model of hardness of weld zone versus current, voltage, and speed for ANOVA.

Source	DF	Seq. SS	Percent of contribution (%)	Adj. SS	Adj. MS	F-value	p value	Significance
Current	2	180.667	30.52	180.667	90.333	271.00	0.004	
Voltage	2	368.667	62.27	368.667	184.333	553.00	0.002	
Speed	2	42.000	7.09	42.000	21.000	63.00	0.016	
Error	2	0.667	0.11	0.667	0.333			
Total	8	592.000	100.00					

Table 8 shows that the parameters current and voltage have “ p ” value less than 0.05% which means those variables have significant influence on the hardness of weld zone of the weld sample using GMAW process. When arranging their numerical value voltage has a greater influence with “ p ” and “ f ” values of 0.002 and 553, followed by current, 0.004 and 271, and speed, 0.016 and 63.

Also percentage contribution is one way to know the influence of each parameter on the hardness of weld zone. Parameter with high percentage of contribution has high power to change the performance of the system. In this case, voltage with 62.27%, current with 30.52%, and speed with 7.07% have a rank of 1 to 3, respectively, by their percentage of influence. Total allowable error = $(0.667/592) \times 100\% = 0.11\%$

3.3. Hardness Analysis of Heat-Affected Zone. Hardness of heat-affected zone (HAZ) was recorded after the sample was measured using the hardness testing machine and the result of each experiment reading has been recorded and on the base of this reading of the signal-to-noise ratio for each sample was calculated as shown in Table 9.

As shown in Table 9, for the S/N ratio of each experiment, the larger the better. On the basis of these results, the S/N ratio has been calculated separately for every single number of experiments. The heat input at the weld zone is greater than that of HAZ during welding; the welding process and welding technique both influence the energy input, which is used to make a weld. The higher the energy input is, the slower the cooling rate is. Increasing heat input tends to soften the weld zone, and its hardness level is reduced.

3.3.1. Response Table for Heat-Affected Zone. Table 10 Shows that, for S/N ratios, the larger the better.

Table 11 shows the means.

Tables 10 and 11 show the average of each of the response characteristics (S/N ratio, means) for each level of every variable. The table contains the rank of each variable according to the delta statistics reading, which compares the relative magnitude of each variables effect. The S/N ratio allows us to quantify the size of the applied or controlled signal relative to fluctuations that are outside experimental control. As shown in Table 10, the S/N of the optimum value of each parameter is almost similar, which means that each parameter in the welding process has equal chance to bring the performance change, or they have similar significance for the change.

3.3.2. Analysis of Variance (ANOVA) for HAZ. The critical value is obtained by using degree of freedom of each parameter and degree of freedom of the error from 0.05 significance level, as shown in Table 12. Based on this principle “ F_{cr} ” (0.05, 2, 8) = 4.46 critical values, which is less than the “ F ” value in Table 12. The numerical value voltage has the greatest influence with “ p ” and “ f ” values of 1708 and 0.001, followed by current with “ p ” and “ f ” values of 703 and 0.001

and speed with “ p ” and “ f ” values of 199 and 0.005, respectively. In this case, voltage with 65.42%, current with 26.92%, and speed with 7.62% have a rank of 1 to 3, respectively, by their percentage of influence. Total allowable error = $(0.222/580.22) * 100 = 0.04\%$

3.4. Parent Metal Hardness. The average hardness number of the sample is 158.70. Table 13 shows the trials of test for samples. The data were taken on all the samples.

3.5. Tensile Test Analysis. After doing tensile testing operation on prepared samples as shown in Figure 9, the results of the tensile strength on different combination of parameters data are recorded and organized to calculate the S/N ratio of each sample. The input experimental values are measured using universal tensile testing machine.

The signal-to-noise ratio was measured using MINITAB 18 software as shown in Table 14.

From Table 14, for the S/N ratio of each experiment, the larger the better. By using this formula or the software, the results of tensile strength on different set of combination of parameters are shown in Table 14. On the basis of these results, the S/N ratio has been calculated separately for every single number of experiments.

3.5.1. Response Table for Tensile Strength. Table 15 shows the average of each of the response characteristics (S/N ratio, means) for each level of every variable. Table 15 contains the rank of each variable according to the delta statistics reading, which compares the relative magnitude of each variables effect.

In this experimental analysis, the voltage has the greatest influence on the signal-to-noise ratio and means analysis followed by current and speed. The level averages in Tables 15 and 16 show that the S/N ratio and mean are high when voltage, current, and speed, are at 18 volt, 65 A, and 4 mm/sec, respectively, as shown in Figures 10 and 11.

Therefore these values are the proper or optimum welding variables based on which maximum tensile strength was achieved.

3.5.2. Analysis of Variance (ANOVA) for Tensile Strength. The critical F_{cr} value can be obtained by using degree of freedom of each parameter and degree of freedom of the error from 0.05 significance level, as shown in Table 17. Based on this principle F_{cr} (0.05, 2, 8) = 4.46.

As shown in Table 17, all factors have p value less than 0.05% which means the variables have their own influence on the tensile strength of the weld sample using GMAW process. However, their numerical value is different. When we arrange their values, voltage, current, and speed have p and f values of 1843 and 0.001, 291 and 0.003, and 79 and 0.012, respectively. From this, it was obvious that voltage followed by current and speed have significant effect on tensile strength on welded sample of EN-10149-2 S700MC sheet metal with 2 mm thickness. Also percentage contribution is one way to know the influence of each parameter on the response. Parameter with

TABLE 9: Hardness of HAZ reading and S/N ratio.

S. no.	Current	Voltage	Speed	Hardness of HAZ	SNRA1	MEAN1
1	60	16	2	129	42.2118	129
2	60	17	4	146	43.2871	146
3	60	18	6	149	43.4637	149
4	65	16	4	134	42.5421	134
5	65	17	6	147	43.3463	147
6	65	18	2	144	43.1672	144
7	70	16	6	143	43.1067	143
8	70	17	2	151	43.5795	151
9	70	18	4	157	43.9180	157

TABLE 10: Response table for signal-to-noise ratio of the hardness of HAZ.

Level	Current	Voltage	Speed
1	42.99	42.62	42.99
2	43.02	43.40	43.25
3	43.53	43.52	43.31
Delta	0.55	0.90	0.32
Rank	2	1	3

TABLE 11: Response table for S/N ratio of the hardness of HAZ.

Level	Current	Voltage	Speed
1	141.3	135.3	141.3
2	141.7	148.0	145.7
3	150.3	150.0	146.3
Delta	9.0	14.7	5.0
Rank	2	1	3

TABLE 12: General linear model of hardness of HAZ ANOVA table.

Source	DF	Seq. SS	Percent of contribution (%)	Adj. SS	Adj. MS	F-value	p value	Significance
Current	2	156.222	26.92	156.222	78.111	703.00	0.001	Significant
Voltage	2	379.556	65.42	379.556	189.778	1708.00	0.001	Significant
Speed	2	44.222	7.62	44.222	22.111	199.00	0.005	Significant
Error	2	0.222	0.04	0.222	0.111			
Total	8	580.222	100.00					

TABLE 13: Vickers hardness test value.

Sample	Parent metal			Average value
	Trial 1	Trial 2	Trial 3	
Sample no. 1	166	153	159	159
Sample no. 2	168	160	170	166
Sample no. 3	165	150	156	157
Sample no. 4	140	155	158	151
Sample no. 5	150	154	162	155
Sample no. 6	155	168	170	164
Sample no. 7	171	166	154.3	164
Sample no. 8	158	157	146.3	154
Sample no. 9	166	158	149.1	158
Average value	160	158	158	158.70

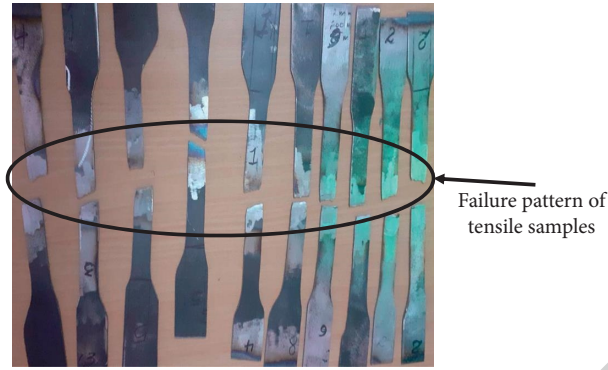


FIGURE 9: Tensile tested samples.

TABLE 14: Tensile strength reading and signal-to-noise ratio.

S. no.	Current (A)	Voltage (V)	Speed (mm/s)	Tensile strength (MPa)	S/N ratio	MEAN1
1	60	16	2	745	57.4431	745
2	60	17	4	762	57.6391	762
3	60	18	6	775	57.7860	775
4	65	16	4	762	57.6391	762
5	65	17	6	768	57.7072	768
6	65	18	2	785	57.8974	785
7	70	16	6	750	57.5012	750
8	70	17	2	759	57.6048	759
9	70	18	4	782	57.8641	782

TABLE 15: Response table for S/N ratio of tensile strength (the larger the better).

Level	Current	Voltage	Speed
1	57.62	57.53	57.65
2	57.75	57.65	57.71
3	57.66	57.85	57.66
Delta	0.13	0.32	0.07
Rank	2	1	3

TABLE 16: Response table for means of tensile strength.

Level	Current	Voltage	Speed
1	760.7	752.3	763.0
2	771.7	763.0	768.7
3	763.7	780.7	764.3
Delta	11.0	28.3	5.7
Rank	2	1	3

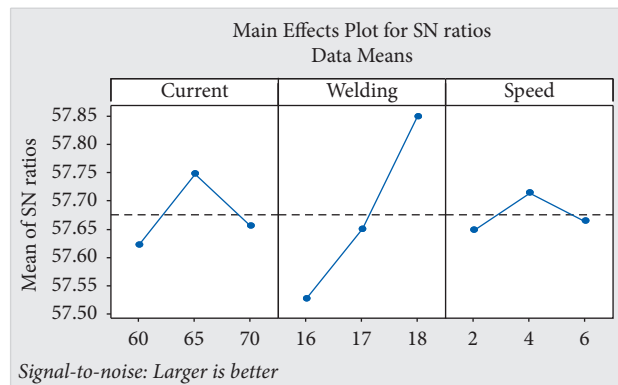


FIGURE 10: Main effects plot for S/N of tensile strength.

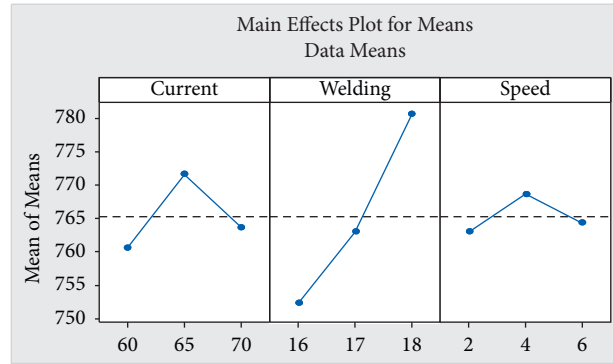


FIGURE 11: Main effects plot for means of tensile strength.

TABLE 17: General linear model of tensile strength versus current, voltage, and speed.

Source	DF	Seq. SS	Contribution (%)	Adj. SS	Adj. MS	F-value	p value	Significance
Current	2	194.00	13.14	194.00	97.000	291.00	0.003	Significant
Voltage	2	1228.67	83.24	1228.67	614.333	1843.00	0.001	Significant
Speed	2	52.67	3.57	52.67	26.333	79.00	0.012	Significant
Error	2	0.67	0.05	0.67	0.333			
Total	8	1476.00	100.00					

high percentage of contribution has high power to change the performance of the system. So voltage with 83.24% %, current with 13.14%, and speed with 3.57% have a rank of 1 to 3, respectively, by their percentage of influence. Total error = $(0.67/1476) * 100 = 0.05\%$

3.6. Taguchi Parameter Optimization Formula for Confirmatory Test

$$P_{opt} = X + (C - X) + (V - X) + (S - X), \quad (2)$$

where P_{opt} is optimal condition, X is the overall mean of S/N data, C is mean of S/N data for welding current at optimal level, V is mean of S/N data for welding voltage at optimal level, and S is mean of S/N data for welding travel speed at optimal level.

3.6.1. Parameter Optimization of Hardness of Weld Zone.

$$\begin{aligned}
 P_{opt} &= (X + (I3 - X) + (V3 - X) + (S3 - X)), \\
 P_{opt} &= (43.54 + (43.54 - 43.54) + (43.55 - 43.54) + (43.54 - 43.54)), \\
 P_{opt} &= 43.55.
 \end{aligned} \quad (3)$$

Predicted performance of WZ hardness is as follows:

The optimal condition for maximum hardness of weld zone was obtained using MINITAB 18 software.

From Table 3, the following data are taken:

The optimum working parameters are I3, V3, and S3 (i.e., current at I3 = 70A, voltage at V3 = 18 V, and speed at S3 = 6 mm/s).

X is the overall mean of S/N data = 43.54.

I1 is mean of S/N data for welding current at level 1 = 43.54.

V1 is mean of S/N data for welding voltage at level 1 = 43.55.

S3 is mean of S/N data for welding travel speed at level 3 = 43.54.

Then the optimal condition for hardness of WZ is as follows:

$$\begin{aligned}
 y^2_{\text{opt cond}} &= 10^{(\text{Popt}/10)}, \\
 y^2_{\text{opt cond}} &= 10^{(43.55/10)}, \\
 y^2_{\text{opt cond}} &= 10^{(4.355)}, \\
 y^2_{\text{opt cond}} &= 22646.44, \\
 y &= \sqrt{22646.44}, \\
 &= 150.48 \text{ VHN}.
 \end{aligned} \tag{4}$$

Therefore the optimal value for weld zone hardness is 150.48 VHN.

From this, the researchers conclude that the optimal value of weld zone hardness at parameters of current at 70 A, voltage at 18 V, and speed at 6 mm/s is **150 VHN**.

$$\begin{aligned}
 P_{\text{opt}} &= (X + (I3 - X) + (V3 - X) + (S3 - X)), \\
 P_{\text{opt}} &= (43.18 + (43.18 - 43.18) + (43.18 - 43.18) + (43.18 - 43.18)), \\
 P_{\text{opt}} &= 43.18.
 \end{aligned} \tag{5}$$

Predicted performance of hardness of HAZ is as follows:

$$\begin{aligned}
 y^2_{\text{opt cond}} &= 10^{(\text{Popt}/10)}, \\
 y^2_{\text{opt cond}} &= 10^{(43.18/10)}, \\
 y^2_{\text{opt cond}} &= 10^{(4.318)}, \\
 y^2_{\text{opt cond}} &= 20796.96, \\
 y &= \sqrt{20796.96}, \\
 &= 144.21 \text{ VHN}.
 \end{aligned} \tag{7}$$

Therefore the optimal value for HAZ hardness is 144.21 VHN.

From this, the researchers conclude that the optimal value of HAZ hardness at parameters of current at 70 A, voltage at 18 V, and speed at 6 mm/s is **144 VHN**.

3.6.3. Taguchi Parameter Optimization Formula for Tensile Strength. The optimal condition for maximum tensile strength was obtained as follows:

Current at I2 = 65 A, voltage at V3 = 18 V, and speed at S2 = 4 mm/s.

X is the overall mean of S/N data = 57.6757.

I2 is mean of S/N data for welding current at level 2 = 57.6766.

V3 is mean of S/N data for welding voltage at level 3 = 57.6766.

S2 is mean of S/N data for welding travel speed at level 3 = 57.6633.

3.6.2. Parameter Optimization of Hardness of HAZ. The optimal condition for maximum hardness of HAZ was obtained as follows:

Current at I3 = 70 A, voltage at V3 = 18 V, and speed at S3 = 6 mm/s.

X is the overall mean of S/N data = 43.18.

I1 is mean of S/N data for welding current at level 1 = 43.18.

V1 is mean of S/N data for welding voltage at level 1 = 43.18.

S3 is mean of S/N data for welding travel speed at level 3 = 43.18.

Then the optimal condition for hardness of HAZ is as follows:

Then the optimal condition for tensile strength is as follows:

$$\begin{aligned}
 P_{\text{opt}} &= (X + (I3 - X) + (V3 - X) + (S3 - X)), \\
 P_{\text{opt}} &= \left(\begin{array}{l} 57.6757 + (57.6766 - 57.6757) \\ + (57.6766 - 57.6757) \\ + (57.6733 - 57.6757) \end{array} \right), \\
 P_{\text{opt}} &= 57.6751.
 \end{aligned} \tag{8}$$

Predicted performance of tensile strength is as follows:

$$\begin{aligned}
 y^2_{\text{opt cond}} &= 10^{(\text{popt}/10)}, \\
 y^2_{\text{opt cond}} &= 10^{(57.6751/10)}, \\
 y^2_{\text{opt cond}} &= 10^{(5.76751/10)}, \\
 y^2_{\text{opt cond}} &= 10^{(5.76751)}, \\
 y^2_{\text{opt cond}} &= 585477.21, \\
 y &= \sqrt{585477.21}, \\
 &= 765.16 \text{ MPa}.
 \end{aligned} \tag{9}$$

Therefore the optimal value for tensile strength is 765.16 MPa.

From this, the researchers conclude that the optimal value for tensile strength at parameters of current at 65 A, voltage at 18 V, and speed at 4 mm/s is **765 MPa**.

3.6.4. Confidence Interval versus Confidence Level. Confidence interval is a range of values that are expected to include an unknown population parameter based on the experiment sample, and confidence level is how likely the

TABLE 18: Compression between actual (experimental value) and theoretical (expected value) values of tensile strength, hardness of weld zone, and hardness of HAZ.

Optimum parametric condition obtained by Taguchi method	Maximum tensile strength obtained by confirmatory test	Prediction for parametric optimization by Taguchi method	% error
Current 65 A Voltage 18 V Speed 4 mm/s	765 MPa	780 MPa	0.5%
Optimum parametric condition obtained by Taguchi method	Maximum hardness of weld zone obtained by confirmatory test	Prediction for parametric optimization by Taguchi method	% error
Current 70 A Voltage 18 V Speed 6 mm/s	150 HVN	157.38 HVN	0.38%
Optimum parametric condition obtained by Taguchi method	Maximum hardness of HAZ obtained by confirmatory test	Prediction for parametric optimization by Taguchi method	% error
Current 70 A Voltage 18 V Speed 6 S	144 HVN	144.57 HVN	0.57%

value will fall within the experiment confidence interval. Interval is a range but confidence level is a percentage. In this work, 95% confidence level was used. Probability for 95% (0.95) confidence interval is calculated as

$$\text{Probability} = \frac{\text{Confidence interval} + \text{Alpha}}{2}, \quad (10)$$

where Alpha is just a shorter word for level of significance. Alpha is the complement of confidence level.

$$\text{Alpha} = 1 - \text{confidence level}. \quad (11)$$

For 95% confidence level, $\text{Alpha} = 1 - 0.95 = 0.05$.

$$\text{Probability} = \text{Confidence interval} + \frac{\text{Alpha}}{2}, \quad (12)$$

Probability is $(0.95 + 0.05/2) = 0.9750$. z value = 1.96, for the probability 0.9750, with 95% confidence interval.

Margin of Error (E) is calculated as follows:

$$\text{Margin of Error } (E) = \text{Standard error} \times Z, \quad (13)$$

$$\text{But Standard error} = \frac{\text{Standard deviation}}{\text{Square root sample size}}. \quad (14)$$

Standard deviation can be calculated using the following formula:

$$SD = \sqrt{\sum_{i=1}^n \frac{(\text{Reading } i - \text{Average})^2}{n - 1}}, \quad (15)$$

where n is the number of experiments.

Average of the sample can be calculated as

$$\sum_{i=1}^n \frac{(x_1 + x_2 + \dots + x_n)}{n}. \quad (16)$$

Using equation (13), averages for hardness of weld zone, hardness of heat-affected zone, and tensile strength were, 150 VHN, 144 VHN, and 765 MPa, respectively.

By using equation (15), standard deviations for tensile strength, hardness of weld zone, and hardness of heat-affected zone were 23.12, 37.89, and 41.92, respectively.

Standard error was calculated using

$$\text{Error} = \frac{SD}{\sqrt{n}}, \quad (17)$$

where Error is standard error; SD is standard deviation; n is the number of experiments.

Using equation (6), standard errors for tensile strength, hardness of weld zone, and hardness of heat-affected zone were obtained as 7.70, 12.33, and 13.97, respectively.

$$\text{Margin of error} = \text{standard error} * Z. \quad (18)$$

Margins of Error (E) for tensile strength, hardness of weld zone, and hardness of heat-affected zone are 15.08, 7.16, and 8.37, respectively.

Then confidence interval can be calculated as

$$\text{Predicted value} \pm E. \quad (19)$$

For hardness of welded zone, we have the following:

Upper interval = predicted value + $E = 150 + 7.16 = 157.16$ VHN.

Lower interval = predicted value - $E = 150 - 7.16 = 142.84$ VHN.

For hardness of HAZ zone, we have the following:

Upper interval = predicted value $E = 144 + 8.37 = 152.37$ VHN.

Lower interval = predicted value - $E = 144 - 8.37 = 135.63$ VHN.

For tensile strength, we have the following:

Upper interval = predicted value + $E = 765 \text{ MPa} + 15.08 = 780.08 \text{ MPa}$.

Lower interval = predicted value - $E = 765 \text{ MPa} - 15.08 = 744.02 \text{ MPa}$.

3.7. Confirmatory Test. After the experiment has been done and the optimal level of welding process parameters has been selected, the final step is to predict and verify the improvement of the performance characteristics using the optimum level of the welding process parameters. The purpose of confirmation of experiment is to verify the optimum conditions so as to reduce the variation. Therefore confirmation experiment is conducted by using the levels of optimal setting parameters. This experimental combination of parameters resulted in substantial reduction in variation of performance characteristics and shows the factors or parameters and levels chosen from the experiment do provide the desired results. This is done by welding the same base metal by using the same material and selected optimal welding parameters. In this study, the experiment has been done three times and the final result was recorded from the average of them. If the predicted and the observed values are close to each other, then the used model is adequate for describing the effect of parameters on quality characteristics, and if there is a large difference in observed values and predicted values, then the used model is not adequate. Table 18 shows the comparison between actual (experimental value) and theoretical (expected value) values of tensile strength, hardness of weld zone, and hardness of HAZ, in which the % error is indicated.

4. Conclusions

This research has described the use of Taguchi method statistical techniques ANOVA and S/N ratio for analyzing and optimizing the effect of welding parameters on the mechanical properties of AHSS of EN-10149-2 S700MC with thickness of 2 mm structural steel with MIG process. The process was performed using a specific set of controllable variables, voltage, current, and welding speed, for the response variables of tensile strength and hardness microstructure of weld joint.

The study found that the controlled factors had significant influence on the response variables. The orders of the significant effect on the response variable were determined according to their percentage contribution. The result shows

the comparison between the experimental and the theoretical values of the tensile strength and the hardness of weld zone.

Optimization is done for increasing the tensile strength, hardness of weld zone, and hardness of HAZ. The tensile strength was increased from 765 MPa to 780 MPa with a minimum error of 0.5%. The hardness of weld zone has been increased from 150 VHN to 157 VHN and the hardness of HAZ increased from 145.1 VHN to 166.47 VHN. Increasing the hardness of weld zone and HAZ means increasing the resistivity of plastic deformation of welded joint and the opposite is true.

The confirmatory test was done by taking the optimal parameters and the result shows that the improvement of the response variables is acceptable and also shows that the method that was used for optimization is valid. The contribution of the parameters on the change of tensile strength, hardness of weld zone, and hardness of heat-affected zone has been explained in terms of percentage. The parameter with higher percentage has a great contribution to the change and the parameter with low percentage has low contribution to the performance change. Based on this principle, for tensile strength, voltage, current, and speed have 83.24%, 13.14%, and 3.57% percentage contributions, respectively.

For hardness of weld zone, voltage, current, and speed have 62.27%, 30.52%, and 7.07% percentage contributions, respectively. For hardness of heat-affected zone, current, voltage, and speed have 51.69%, 16.16%, and 16.10% percentage contributions for the change. The main scientific finding of this work is as follows: using optimum MIG welding process parameters, it is possible to weld AHSS of EN-10149-2 S700MC with thickness of 2 mm and to get defect-free high-quality weld joint with maximum required mechanical and microstructural property.

Data Availability

The data were extracted from the MIG welding process on advanced steel material and made for M.S. thesis. The entire thesis is available in the university database.

Disclosure

This work was submitted as M.S. thesis on "Characterization and Parametric Optimization of EN-10149-2 Steel Welded Joints Made by MIG Welding."

Conflicts of Interest

The authors declare that they have no conflicts of interest.

Acknowledgments

The authors are thankful to Adama Science and Technology University (ASTU) for providing necessary accessories to perform this work and submitting the study as MSc thesis.

Retraction

Retracted: Using Convolutional Neural Networks for Segmentation of Multiple Sclerosis Lesions in 3D Magnetic Resonance Imaging

Advances in Materials Science and Engineering

Received 31 October 2023; Accepted 31 October 2023; Published 1 November 2023

Copyright © 2023 Advances in Materials Science and Engineering. This is an open access article distributed under the Creative Commons Attribution License, which permits unrestricted use, distribution, and reproduction in any medium, provided the original work is properly cited.

This article has been retracted by Hindawi following an investigation undertaken by the publisher [1]. This investigation has uncovered evidence of one or more of the following indicators of systematic manipulation of the publication process:

- (1) Discrepancies in scope
- (2) Discrepancies in the description of the research reported
- (3) Discrepancies between the availability of data and the research described
- (4) Inappropriate citations
- (5) Incoherent, meaningless and/or irrelevant content included in the article
- (6) Peer-review manipulation

The presence of these indicators undermines our confidence in the integrity of the article's content and we cannot, therefore, vouch for its reliability. Please note that this notice is intended solely to alert readers that the content of this article is unreliable. We have not investigated whether authors were aware of or involved in the systematic manipulation of the publication process.

Wiley and Hindawi regrets that the usual quality checks did not identify these issues before publication and have since put additional measures in place to safeguard research integrity.

We wish to credit our own Research Integrity and Research Publishing teams and anonymous and named external researchers and research integrity experts for contributing to this investigation.

The corresponding author, as the representative of all authors, has been given the opportunity to register their agreement or disagreement to this retraction. We have kept a record of any response received.

References

- [1] A. Abdullah Hamad, M. Musa Jaber, M. Altaf Ahmed, G. Muttashar Abdulsahib, O. Ibrahim Khalaf, and Z. Meraf, "Using Convolutional Neural Networks for Segmentation of Multiple Sclerosis Lesions in 3D Magnetic Resonance Imaging," *Advances in Materials Science and Engineering*, vol. 2022, Article ID 4905115, 10 pages, 2022.

Research Article

Using Convolutional Neural Networks for Segmentation of Multiple Sclerosis Lesions in 3D Magnetic Resonance Imaging

Abdulsattar Abdullah Hamad ^{1,2} Mustafa Musa Jaber,^{3,4} Mohammed Altaf Ahmed ⁵, Ghaida Muttashar Abdulsahib,⁶ Osamah Ibrahim Khalaf,⁷ and Zelalem Meraf ⁸

¹Department of Medical Laboratory Techniques, Dijlah University College, Baghdad 10021, Iraq

²Department of Medical Laboratory Techniques, Al-Turath University College, Baghdad 10021, Iraq

³Department of Medical Instruments Engineering Techniques, Dijlah University College, Baghdad 10021, Iraq

⁴Department of Medical Instruments Engineering Techniques, Al-Farahidi University, Baghdad 10021, Iraq

⁵Department of Computer Engineering, College of Computer Engineering & Sciences, Prince Sattam Bin Abdulaziz University, Al-Kharj 11942, Saudi Arabia

⁶Department of Computer Engineering, University of Technology, Baghdad, Iraq

⁷Al-Nahrain Nanorenewable Energy Research Center, Al-Nahrain University, Baghdad, Iraq

⁸Department of Statistics, Injibara University, Injibara, Ethiopia

Correspondence should be addressed to Zelalem Meraf; zelalemmeraf@inu.edu.et

Received 27 February 2022; Revised 31 March 2022; Accepted 6 April 2022; Published 22 April 2022

Academic Editor: Palanivel Velmurugan

Copyright © 2022 Abdulsattar Abdullah Hamad et al. This is an open access article distributed under the Creative Commons Attribution License, which permits unrestricted use, distribution, and reproduction in any medium, provided the original work is properly cited.

Magnetic Resonance Imaging to detect its lesions is used to diagnose multiple sclerosis. Experts usually perform this detection process manually, but there is interest in automating it to speed up the diagnosis and monitoring of this disease. A variety of automatic image segmentation methods have been proposed to quickly detect these lesions. A Gaussian Mixture Model is first constructed to identify outliers in each image. Then, using a set of rules based on expert knowledge of multiple sclerosis lesions, those outliers of the model that do not match the lesions' characteristics are discarded. Furthermore, segmented lesions usually correspond to gray matter-rich brain regions. In some cases, false positives can be detected, but the rules used cannot eliminate all errors without jeopardizing the segmentation's quality. The second method involves training a convolutional neural network (CNN) that can segment lesions based on a set of training images. This technique can learn a set of filters that, when applied to small sections of an image called "patches," produce a set of characteristics that can be used to classify each voxel of the image as a lesion or healthy tissue. On the other hand, the results show that the networks are capable of producing results in the worked database comparable to those produced by the algorithms in the literature.

1. Introduction

Magnetic resonance imaging (MRI) is a medical imaging technique that allows obtaining images of different parts of the body, such as the brain, heart, or spine, helping diagnose various pathologies that may be affecting a patient [1]. This technique has many advantages over other brain scanning techniques, including the use of nonionizing radiation and the generation of images with a high degree of contrast

between the different types of tissues present in the brain (cerebrospinal fluid, white and gray matter), which makes it an excellent support for diagnosing diseases that affect the central nervous system [2], such as epilepsy and dementia.

Among these diseases is multiple sclerosis, a chronic disease that causes damage to the central nervous system, characterized by the appearance of regions of inflammation and demyelination of neurons, which result in a progressive loss of the patient's motor, sensory, and cognitive abilities

affected. Through MRI, it is possible to detect the regions affected by this disease and make a diagnosis based on the number and size of the lesions detected [3].

This task is generally performed by an expert medical professional or semiautomatically, using computational image segmentation techniques [4], which require parameter adjustment by the expert. This approach tends to present difficulties and disadvantages, such as high variability in the results issued by different experts. Due to this, the medical community's interest arises in developing automatic segmentation techniques to reduce the time required to identify damaged regions in the brain. There are many challenges in automatic segmentation problems, and their use in practice is quite limited due to the difficulty of correctly validating the predictions made by these tools. In this memory, the effectiveness of different segmentation methods for this type of image will be studied, proposing the use of convolutional neural networks for the segmentation of lesions and comparing them with traditional segmentation methods, analyzing the advantages and disadvantages that each of these methods they bring into practice [5].

This work aims to present different techniques of the literature in the area of image segmentation. Then, the implementation of these and their comparison in terms of performance and effectiveness in the segmentation problem of magnetic resonance images will be carried out. To validate results, the set of Boston Children's Hospital (BCH) training images of the MS Lesion Segmentation Challenge will be used [6], which consists of 10 images in T1, T2, and FLAIR modalities of different patients, accompanied by the segmentation of an expert. Because the segmentation of the test set is not publicly accessible, for supervised learning algorithms, in this case, convolutional neural networks, the set of images will be divided into a training subset, from which the model will be trained of convolutional networks, and a test set, with which the ability of the model to segment lesions in a new image correctly will be tested. This process will be performed five times per technique and an average of the performance measurements will be obtained. The current study aims to experimentally evaluate the performance of convolutional neural networks applied to the problem of automatic segmentation of multiple sclerosis (MS) lesions in multimodal magnetic resonance imaging, comparing it with other literary techniques.

2. Methodology

The proposed solution to the problem of segmentation of multiple sclerosis lesions in magnetic resonance images consists of implementing and evaluating two different methods applied in the literature to the problem. The dataset with which the proposal will be validated corresponds to the database of training images used in the multiple sclerosis lesion segmentation challenge organized by the Medical Image Computing and Computer-Assisted Intervention Society [7]. This database is available to the public and comprises magnetic resonance images of twenty different patients in 3 different modalities: T_1 -Weighted, T_2 -

Weighted, and T_2 -Fluid Attenuated Inversion Recovery (FLAIR), with their respective masks of segmented lesions. Ten of these images in their 3 modalities, with their respective segmentations, were provided by the University of North Carolina (UNC). The other ten were provided by Children's Hospital Boston (BCH).

The modalities of each image of the data set are coregistered, that is, the voxels of each image correspond to the same spatial coordinate of the brain. However, they lack a greater preprocessing, for which a preprocessing stage is necessary before the analysis application of segmentation algorithms to obtain good results.

Once the images have been preprocessed, two literature segmentation algorithms will be implemented. Once state of the art was evaluated, it was decided to implement a technique based on the Gaussian Mixture Models [8] based on the search for outliers in the model and the use of rules to eliminate false positives from the segmentation. On the other hand, the implementation of a convolutional neural network was chosen to segment lesions [9]. This method has become very popular in the literature in recent years.

To compare the effectiveness of both methods, the Sensitivity (True Positive Rate) and Precision (Positive Predictive Value) metrics will be used, which are given by

$$\begin{aligned} \text{TPR} &= \frac{TP}{TP + FN}, \\ \text{PPV} &= \frac{TP}{TP + FP}, \end{aligned} \quad (1)$$

where TP is the number of true positives from segmentation (correctly labeled lesions), FP is the number of false positives from segmentation (healthy regions that were labeled as lesions by segmentation), and FN is the number of false negatives from segmentation (lesions that were labeled as healthy tissue). Each of these measurements is quantified at the voxel level. Sensitivity represents the percentage of the correctly segmented lesion, while Precision measures the percentage of hits concerning the segmented region. A high Sensitivity indicates that most of the lesion voxels are correctly segmented. In contrast, a low Sensitivity indicates that lesions are not being detected or only a tiny portion of them are being detected. On the other hand, a high Precision indicates that a tiny percentage of the voxels segmented as lesions correspond to healthy tissue. In contrast, a low Precision indicates that the percentage of healthy tissue segmented as lesions is very high due to a large number of false positives. Finally, the Sorensen Dice similarity (DSC) [10] coefficient will be used, a standard metric used in the literature that allows determining the level of overlap between the obtained segmentation and the segmentation provided by an expert, which is given by the harmonic mean between the two metrics.

$$\begin{aligned} \text{DSC} &= \frac{2}{1/\text{TPR} + 1/\text{PPV}}, \\ &= \frac{2TP}{2TP + FP + FN}. \end{aligned} \quad (2)$$

3. Construction and Implementation of the Solution

3.1. Preprocessing. To obtain good results in the segmentation algorithms, it was necessary to perform a preprocessing stage to eliminate image noise and other irregularities present.

3.1.1. Bias Field Correction. MRI images fall victim to a signal that corrupts image quality known as the bias field. This signal is the product of inhomogeneities in the magnetic field used to obtain these images, and its presence results in blurred sectors in the image, adding noise to the intensity values of the image, which negatively affects the quality of the results obtained by algorithms of image processing and segmentation since these disturbances corrupt the distribution of intensities of the different objects and regions that appear in the image. To correct this signal, the N4ITK algorithm was used.

The N4ITK algorithm consists of a modification of the N3 algorithm (nonparametric nonuniformity normalization) that seeks to resolve some algorithm's shortcomings [11]. Given an image, the algorithm models the bias field as a function that multiplies the image without corruption as

$$v(x) = u(x)f(x) + n(x), \quad (3)$$

where $v(x)$ is the original image; $u(x)$ is the image without corruption; $f(x)$ is the bias field; $n(x)$ is the noise (assumed to be independent Gaussian noise).

Using the notation $\hat{u} = \log u$, the previous equation applying logarithm is of the form:

$$\hat{v}(x) = \hat{u}(x) + \hat{f}(x). \quad (4)$$

From this point, the image without corruption is iteratively estimated by

$$\begin{aligned} \hat{u}^n &= \hat{u}^{n-1} - \hat{f}_r^n, \\ &= \hat{u}^{n-1} - S^* \{ \hat{u}^{n-1} - E[\hat{u} | \hat{u}^{n-1}] \}, \end{aligned} \quad (5)$$

where $S^*\{\bullet\}$ is an approximation by B-Splines of the bias field residual between the n th and $n-1$ th iterations. Details of this implementation can be found in [11].

3.1.2. Skull Stripping. To avoid involving the voxels of the images corresponding to the background and the skull, the skull stripping task was performed to obtain a binary mask that only included those voxels corresponding to brain tissues [12]. For this task, BrainSuite software was used. The skull stripping task was performed using the BSE (Brain Surface Extractor) algorithm. Parameter selection was performed manually for each image until an appropriate mask was obtained that did not include skull voxels. The parameters that produced satisfactory results for each of the images in the BCH database were seen in Figure 1 and Table 1.

3.2. Gaussian Mixture Models (GMM). As in Karimian and Jafari [13] paper, the first method chosen for segmentation is modeling the intensities of the three types of brain tissue using 3-component Gaussian Mixture Models. The segmentation will be done by looking for outliers in the model using the truncated maximum likelihood estimator of the GMM, then applying a set of rules to eliminate false positives.

The algorithm proposed by Lee and Song [14] is dependent on several parameters, including the GMM's percentage of outliers and the thresholds used to eliminate them. To choose these parameters, we vary the percentage of outliers in the model h between $\{0; 0.2; 0.3; 0.4; 0.5\}$. Then, the Mahalanobis distance, T2 image intensity, and FLAIR image intensity thresholds were varied for each model. The Mahalanobis distance ranged from 0.4 to two. The parameters chosen correspond to the highest DSC combination.

A problem that was observed when adjusting the GMMs for the different images in the database is that the intensity distributions for white matter in the T2 and FLAIR images varied a lot between the different images, for which the use of a threshold single fixed for T2 and FLAIR images did not produce good results in segmentation. To solve this problem, an idea similar to that proposed in Jansen [15] of using thresholds based on parameters of the obtained model was taken. In this way, the regions of hyperintensity in the white matter of the T2 and FLAIR images are selected by the thresholds μ_{WM} , $T2 + kT2 \cdot \sigma_{WM}$, $T2$ and μ_{WM} , $FLAIR + kFLAIR \cdot \sigma_{WM}$, $FLAIR$, where μ_{WM} , i is the mean of the white matter intensities in the image in modality i , σ_{WM} , i is the standard deviation of the white matter intensities in the image in modality i , and $kT2$ and $kFLAIR$ are 2 constants associated with the threshold of their respective image. These last 2 parameters replace the fixed threshold defined by Karimian and Jafari and were made to vary in the range of values $\{0, 1, 2\}$. Finally, hypointensity in the T1 image, defined by the negative threshold μ_{WM} , $T1 - kT1 \cdot \sigma_{WM}$, $T1$, was also added to the set of rules. The parameter $kT1$ was varied in the same range as $kT2$ and $kFLAIR$.

Another issue with the method described in the paper is that most predicted lesions were located at the outer edge of the white matter, near the cortical gray matter. The solution proposed by Zhao et al. [16] is to apply a mask obtained from the morphological erosion operation to the white matter mask, allowing the elimination of nearby voxels from the lesion candidates. The internal holes of the white matter mask were filled before applying the erosion mask. The chosen erosion filter was $6 \times 6 \times 6$. A 3×3 erosion filter was applied to each slice of their set of images, whose resolution was half that of the images with which they worked, which is why the filter size was initially set to $6 \times 6 \times 6$. These voxels were segmented as a lesion and their final size was set to $9 \times 9 \times 9$, see Table 2.

The initial segmentation to obtain the estimators of the initial parameters of the model was performed on the T1 image using the K -means algorithm.



FIGURE 1: Original FLAIR image, image after applying bias field correction, and image after applying skull stripping.

TABLE 1: Parameters used in the BCH.

Image	Edge constant	Erosion size
BCH01	0.7	2
BCH02	0.7	2
BCH03	0.7	2
BCH04	0.9	2
BCH05	0.6	3
BCH06	0.7	3
BCH07	0.7	2
BCH08	0.7	3
BCH09	0.7	3
BCH10	0.7	3

TABLE 2: Parameters of means obtained for the white matter.

Image no.	$\mu_{WM, T2}$	$\mu_{FLAIR, T2}$
BCH01	77.89	73.7
BCH02	37.76	62.18
BCH03	38.08	80.85
BCH04	46.4	100.96
BCH05	45.26	63.65
BCH06	50.01	61.64
BCH07	53.88	59.78
BCH08	43.88	60.7
BCH09	58.38	57.84
BCH10	58.33	56.88

3.2.1. K-Means Algorithm. The K -means algorithm is an unsupervised learning algorithm commonly applied in clustering tasks. Given a set of points $X = \{x_1, x_2, \dots, x_n\}$ and a parameter k , corresponding to a positive integer, the algorithm is initialized by choosing k random points c_1, c_2, \dots, c_k within the same domain of X known as centroids. Then, for each point within the set X , the distance between x_i and each of the centroids c_j is calculated (commonly, the Euclidean distance is used) and the point x_i is assigned to the cluster corresponding to the closest centroid. Finally, the centroids are calculated again as

$$C_j = \frac{1}{n_j} \sum_{x_i \in C_j} x_i, \quad (6)$$

where C_j is the cluster containing the previously closest points to C_j and n_j is the number of points in the cluster C_j . These 2 steps are repeated iteratively until the cluster

assignment for each point does not change from one iteration to the next.

This algorithm applies to the image segmentation task. Given the set of pixels of a grayscale image, the points to be grouped correspond to the intensities of the pixels. In contrast, the centroids correspond to different intensity values in the range $[0, 255]$. As a result, the K -means algorithm performs a grouping of pixels with similar intensity values. The K -means algorithm has been used to perform the segmentation of different brain tissues in magnetic resonance images [17].

The K -means algorithm was used to perform a preliminary segmentation of the brain in the 3 different types of tissue based on the intensity of the pixels in the T1 image, obtaining, from lower to higher intensity, labels for the pixels corresponding to cerebrospinal fluid, spinal fluid, and gray and white matter.

3.3. Convolutional Neural Networks (CNNs). Second, the first Birenbaum architecture [18] is used to train a convolutional network using a subsampling of FLAIR image patches. Instead of a longitudinal MRI, the paper's SISTP (Single Image, Single TimePoint) architecture was used. In addition to the proposed architecture, an architecture without the Max pooling layer following the convolution layers was tested to compare performance. Both architectures tested 2 input types: 1 axial image and 1 image for each view type (axial, sagittal, and coronal). Each slice was obtained with a resolution of 0.5 mm and a distance of 1 mm between each slice. The intermediate values were interpolated during the registration process to obtain the final image with a resolution of 0.5 mm. It is then passed to a dense network of 16 neurons followed by the Softmax layer, which concatenates the 48 feature vectors obtained after the first dense layer of each image.

The implementation of the network was carried out using Keras [19], a library written in Python for the management and construction of neural networks in a modular way, using the Tensorflow library [20] as a backend.

In Figure 2, candidate voxels were chosen based on preliminary white matter segmentation from the T1 image using the K -means algorithm. This white matter mask replaced the segmentation obtained from registering an Atlas to a T1 image. $WM, FLAIR + k_{FLAIR} \cdot WM, FLAIR$ was

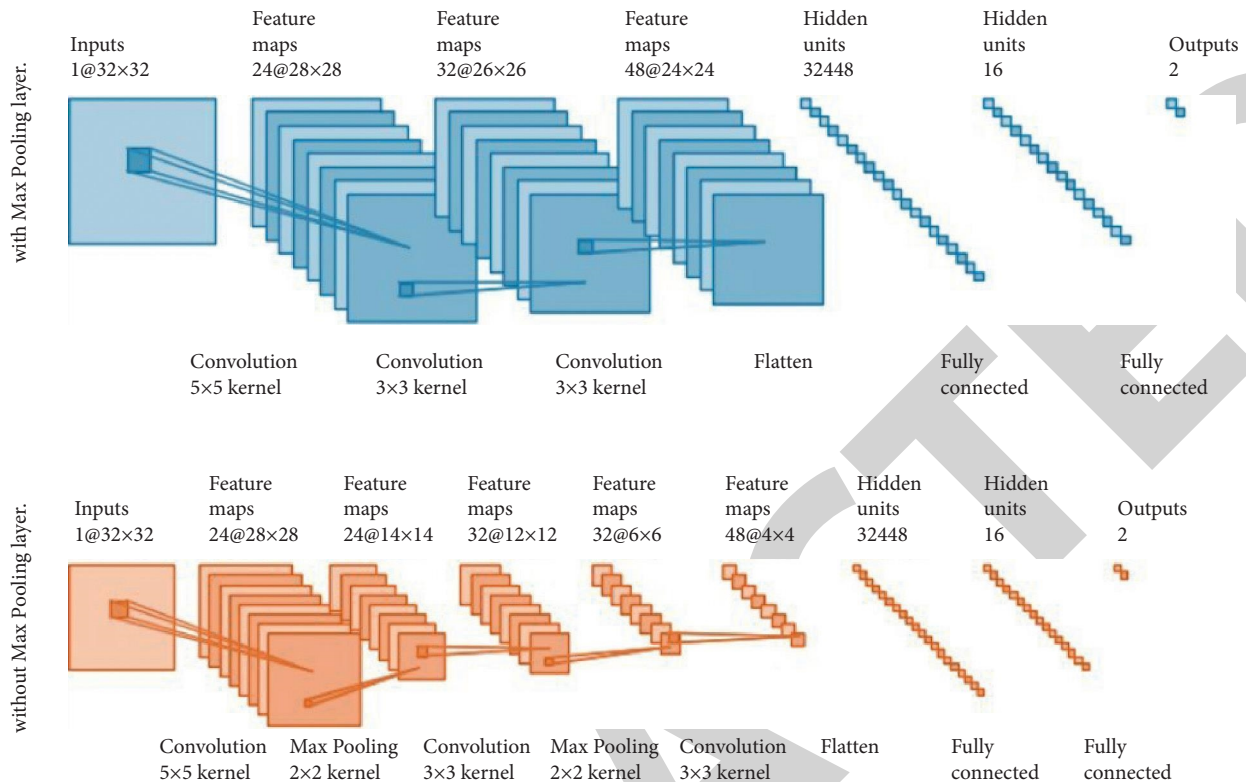


FIGURE 2: Architecture for 1 implemented input of the CNN with and without Max pooling layer.

used to define the threshold parameter for the FLAIR image [21]. The parameter was set to match the proportion of candidate voxels in Birenbaum et al. The final number of candidates for the network was 1,242,109 voxels ($k_{FLAIR} = 2$), which is close to the percentage reported in Birenbaum's paper, who claims that candidate sampling reduced network computations by 97.5 percent [20]. This subsampling leaves out a percentage of the image voxels corresponding to lesions. In addition to patch sampling, a loss function that penalized false negatives for lesions addressed the class imbalance issue. The weight parameter of this loss function was set at 20% for all trained networks based on the percentage of injuries observed in the training set. We will use leave-one-out cross-validation to evaluate the network's results. The network's model is then applied to the untrained image, yielding model evaluation metrics for that image. This is done for every image in the training set. Finally, the obtained model's evaluation metrics are averaged.

4. Results and Discussion

The results of the selection of parameters for the GMM are presented in the following graph (3), detailing the average DSC obtained for each parameter throughout all the images in the database. The best combination of parameters found, with respect to the DSC obtained, was $h = 0.2$; $d_{min} = 0.4$; $k_{T2} = 0$, and $k_{FLAIR} = 1$.

A larger area of the brain is considered a candidate for injury, so the number of true positives increases. There is a segmentation of more false positives, only a fraction of

which are eliminated by the false positive reduction rules. The h parameter also has the issue of losing information in the GMM due to training with fewer voxels, resulting in poor initial segmentation results. The elimination rule for voxels near the gray matter border reduced the number of false positives because many of the outliers detected in the model were in this region and were not filtered by the lesion selection rules. Figure 3 compares the Positive Predictive Value before and after applying this rule; see Figure 4.

Because the original papers from which the implemented techniques came used different databases to validate his experiments, the results obtained by other techniques were investigated in the public database of the MS Lesion Segmentation Challenge. Overall, the results show a high PPV for most of the techniques used, with relatively precise segmentation of multiple sclerosis lesions. The tradeoff is that the TPR obtained was generally low compared to the state-of-the-art techniques. As for the GMM segmentation, this is due to applying a set of rules that filter out false positives and in some cases remove voxels that corresponded to injuries. The low number of true positives in convolutional networks is due to subsampling used to reduce network training times. The main advantage of GMM is the speed of segmentation. The average time required to segment each image was 538.61 15.47 seconds, including reading the file and applying the EM algorithm to the model. Across all test cases, the EM algorithm took 27.96 3.04 seconds per iteration. Convolutional networks performed better on average, with similarity coefficients of 0.33 and 0.29 for 1-view networks and 0.34 and 0.26 for multiview networks, comparable to

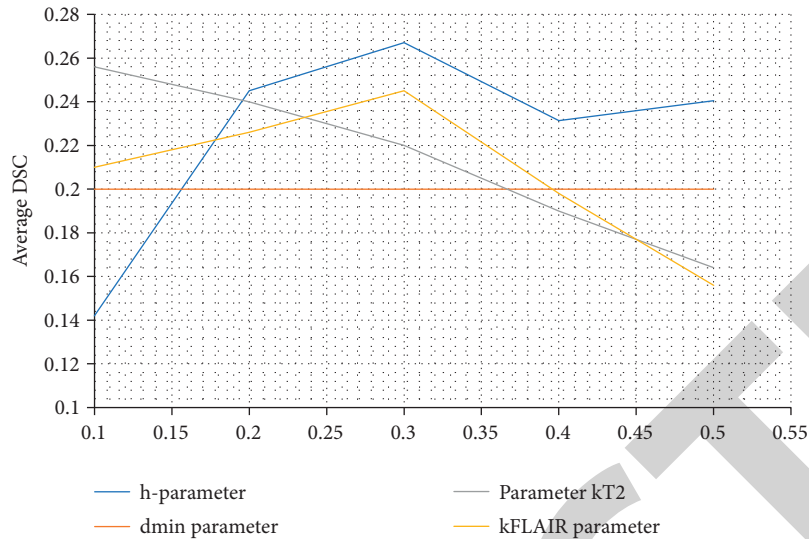


FIGURE 3: The results of the selection of parameters for the GMM.

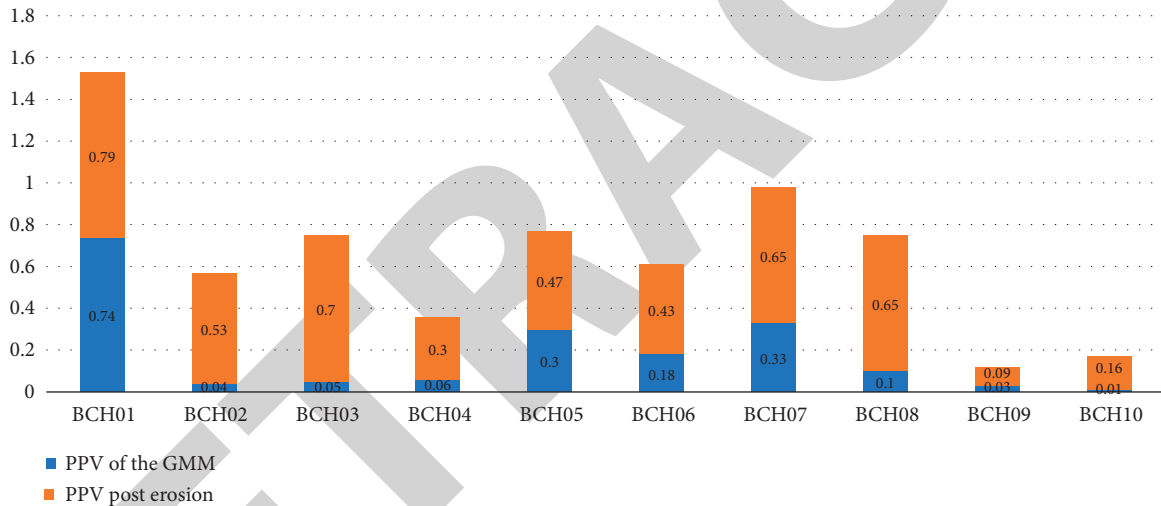


FIGURE 4: Comparison of PPV before and after application of erosion to the white matter mask.

most results in the state of the art. The network's average performance was better without the Max pooling layer in terms of results quality. The network underestimates the size of lesions (which explains the low TPR) and simply fails to identify some injuries when the Max pooling layer is added. The number of lesions detected, that is, those for which at least one voxel was classified as a lesion, was as follows.

In Figure 5, the network with the Max pooling layer was able to detect only a subset of the lesions that the network without it could detect. The only exception to this was image BCH08, in which the network with Max pooling for the axial view managed to find 2 lesions that were not detected by the other network; however, these successes could be classified as noise simply by looking at the results of the segmentation because they appear only in 1 or 2 slices of the image and cover a very small region.

In addition, in these images, it can be seen that the segmented regions corresponding to a lesion are not

necessarily contiguous, and multiple segmented lesions may appear that correspond to a single lesion see Table 3.

It can be seen that the number of regions that are segmented by the CNN is quite large, which is observed in the results as a large number of small-sized regions that appear in the segmentation around larger regions (usually well-defined lesions) classified), regions around the lateral ventricles of the brain and at the outer edges of the white matter, on the border with the gray matter. An alternative, studied later, to mitigate this discrepancy problem consists of performing a postprocessing stage in which morphological operations are applied to the segmentation mask, improving its quality.

Another problem observed with the segmentation of networks is the dependence on the initial selection of candidates. Although much of the white matter approximation using K -means yielded good results, there are some cases in which the hypointense areas in the white matter were classified as another type of tissue.

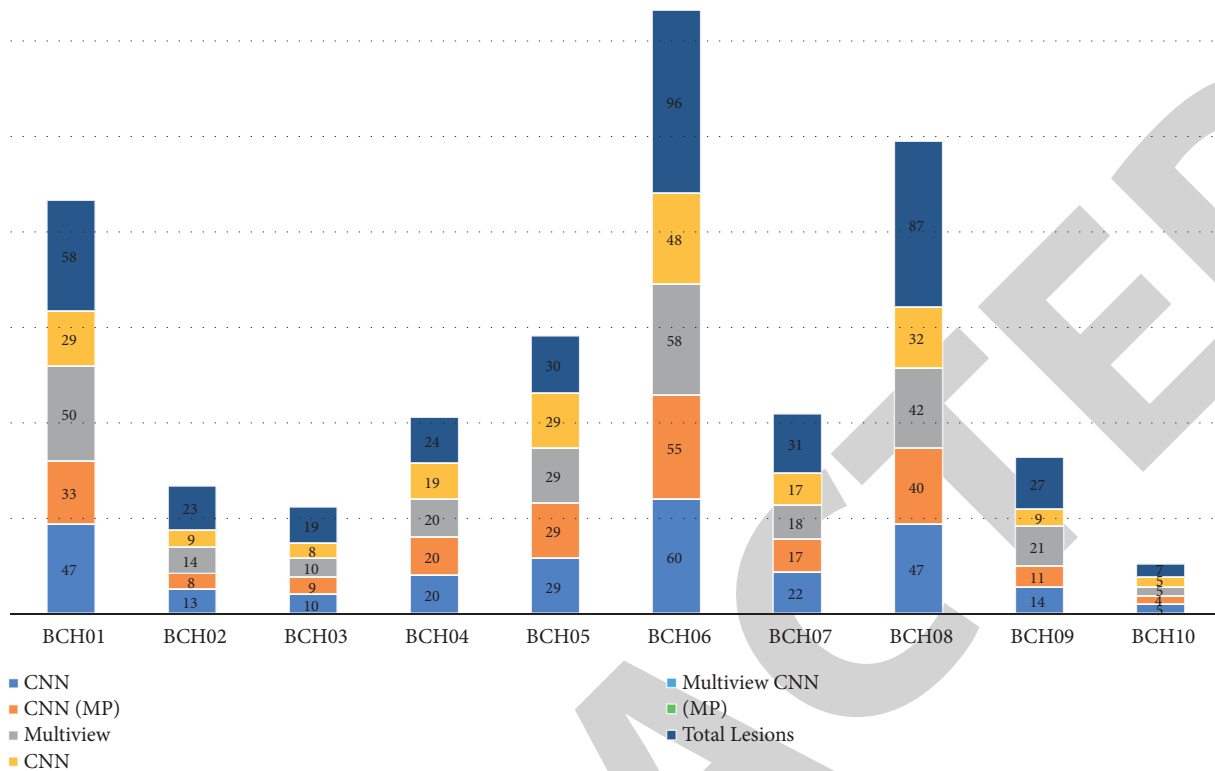


FIGURE 5: Number of segmented lesions.

TABLE 3: Number of segmented regions.

Image	CNN		CNN (max pooling)		Multiview CNN		Multiview CNN (MP)	
	No. of regions	Size >6	No. of regions	Size >6	No. of regions	Size >6	No. of regions	Size >6
BCH01	716	173	401	111	536	128	519	115
BCH02	197	57	148	40	414	103	491	122
BCH03	482	120	434	111	465	112	197	54
BCH04	1708	280	2084	300	1374	217	826	162
BCH05	1218	237	693	150	907	187	399	92
BCH06	670	165	512	149	599	156	352	115
BCH07	511	108	405	97	370	86	397	100
BCH08	545	129	465	117	420	104	384	86
BCH09	358	75	386	95	626	124	160	40
BCH10	159	38	133	32	309	80	60	20

In this case, the GMM segmentation is more accurate because it considers all tissue types when determining injury candidates. Although the GMM, like *K*-means, failed to segment white matter, all voxels were considered in the selection of outliers allowing better detection of lesions, not just those predicted to be white matter. One of the benefits of using the Max pooling layer is the reduced training time. The Max pooling layer reduced the feature map size, reducing the network training time by approximately 3. The results of multiview networks were not recorded due to the lengthy training time on the CPU (in hours, minutes, and seconds of execution). The GPU (Graphic Processing Units) reduces the training time. The time required to train the networks, even on the GPU, exceeds the average time required to obtain results from the GMM, which was approximately 9 minutes per image. This time includes file reading,

algorithm execution, and segmentation generation. Unlike convolutional networks, which can take days to train on the CPU, the GMM algorithm can be executed on the CPU without compromising execution time; see Figure 6.

4.1. Postprocessing. To improve the quality of the segmentation, morphological operations were applied to the obtained segmentations. The operation performed consists of a closure, which consists of applying a dilation filter followed by applying an erosion filter. The size of this filter was set at 5×5 to connect those regions that are close to each other but not enough to join regions that are not related to each other.

The results obtained after applying this filter, in addition to the percentage change observed for each metric, are found in Table 4.

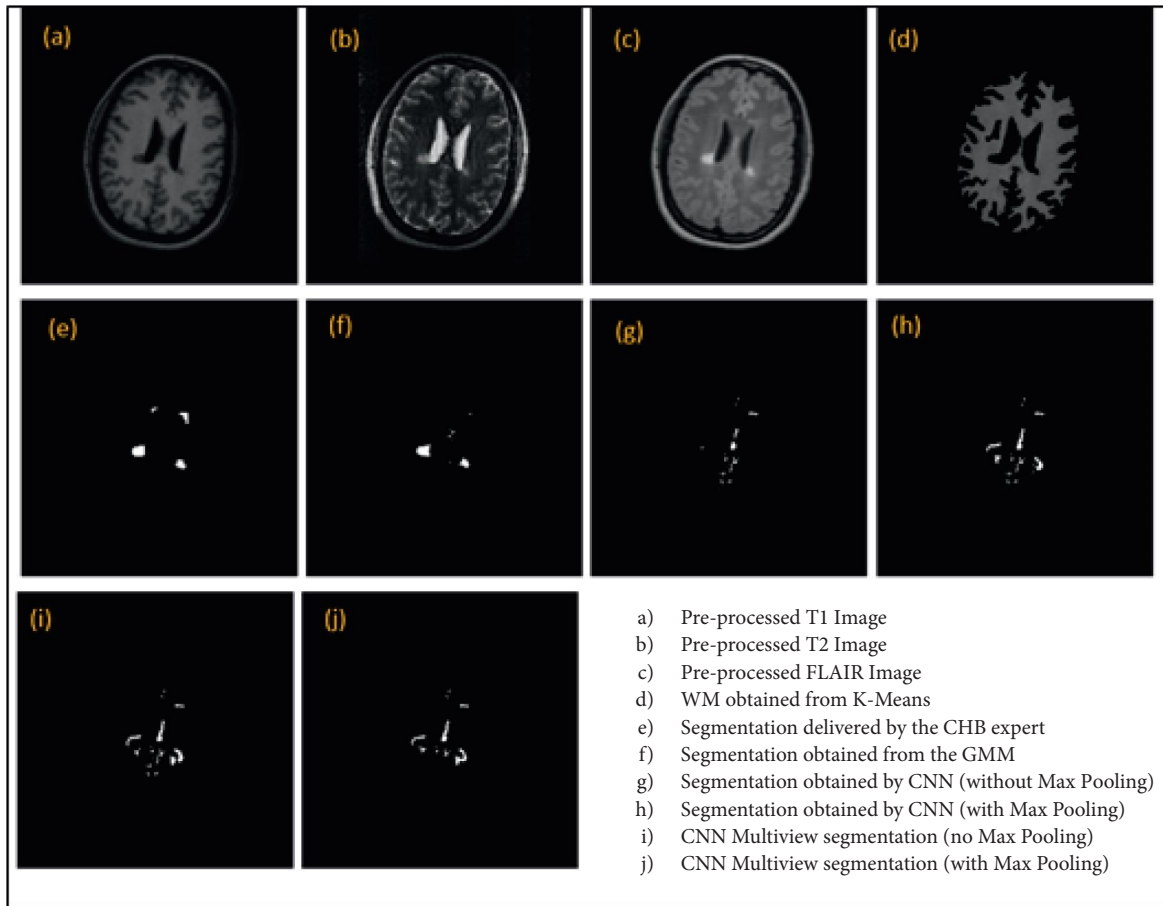


FIGURE 6: Example of an image in which the automatic segmentation of WM fails. (a) Preprocessed T1 image. (b) Preprocessed T2 image. (c) Preprocessed FLAIR image. (d) WM obtained from K-means. (e) Segmentation delivered by the CHB expert. (f) Segmentation obtained from the GMM. (g) Segmentation obtained by CNN (without max pooling). (h) Segmentation obtained by CNN (with Max pooling). (i) CNN multiview segmentation (no Max pooling). (j) CNN multiview segmentation (with Max pooling).

TABLE 4: Postprocessing results.

Image no.	GMM			CNN			CNN (Max pooling)			Multiview CNN			Multiview CNN (MP)		
	TPR	PPV	DSC	TPR	PPV	DSC	TPR	PPV	DSC	TPR	PPV	DSC	TPR	PPV	DSC
BCH01	0.46	0.8	0.59	0.58	0.57	0.57	0.33	0.6	0.42	0.55	0.59	0.57	0.32	0.64	0.32
BCH02	0.14	0.53	0.23	0.43	0.61	0.5	0.19	0.79	0.3	0.46	0.56	0.5	0.26	0.55	0.35
BCH03	0.2	0.69	0.3	0.39	0.47	0.43	0.35	0.49	0.41	0.4	0.46	0.43	0.25	0.65	0.36
BCH04	0.44	0.26	0.33	0.16	0.11	0.13	0.38	0.16	0.23	0.32	0.18	0.23	0.34	0.29	0.32
BCH05	0.2	0.63	0.3	0.25	0.21	0.23	0.26	0.26	0.26	0.25	0.23	0.24	0.23	0.32	0.26
BCH06	0.12	0.41	0.19	0.3	0.58	0.39	0.27	0.62	0.37	0.29	0.6	0.39	0.24	0.66	0.35
BCH07	0.34	0.62	0.44	0.37	0.69	0.48	0.32	0.73	0.44	0.36	0.73	0.48	0.28	0.77	0.41
BCH08	0.27	0.59	0.37	0.42	0.77	0.55	0.31	0.77	0.44	0.41	0.78	0.55	0.26	0.77	0.39
BCH09	0.04	0.07	0.05	0.24	0.53	0.33	0.3	0.53	0.3	0.3	0.42	0.35	0.11	0.61	0.19
BCH10	0.02	0.12	0.04	0.09	0.72	0.16	0.07	0.61	0.12	0.13	0.61	0.23	0.04	0.79	0.07
Average	0.22	0.47	0.28	0.32	0.53	0.38	0.28	0.56	0.33	0.35	0.52	0.40	0.23	0.61	0.30

The quality of segmentation improved significantly for all methods. That is because using morphological closure helped to alleviate one of the main issues with segmentations, which was an underestimation of the lesions' size, which was often mistaken for multiple isolated regions. The dilation filter joins adjacent regions by closing. After applying the erosion filter, unconnected regions return to their

original state, while connected regions stay connected for the most part.

In Figure 7, this filter also solves the problem of small holes appearing in some segmentation regions. This problem was most commonly seen in neural networks, where initial candidate selection was left out of the segmentation voxels that were largely surrounded by others chosen as candidates.

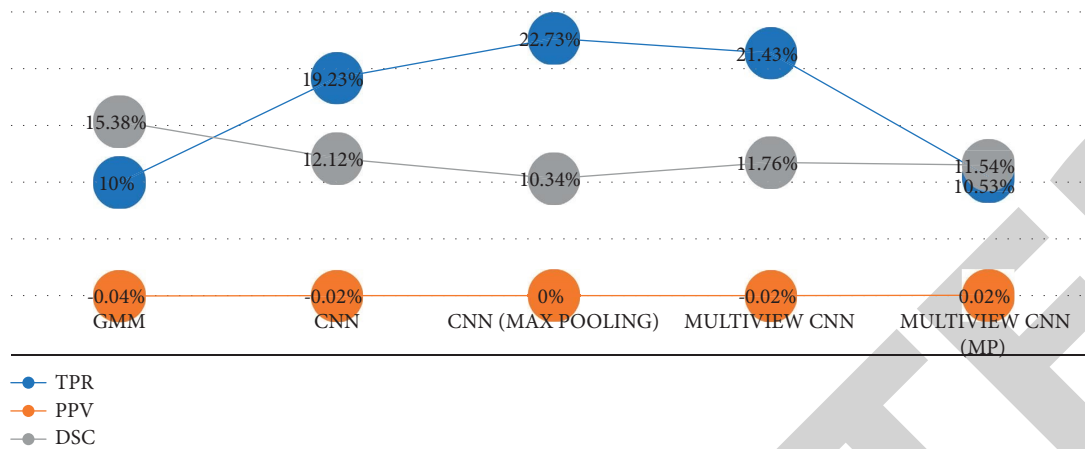


FIGURE 7: Changes in the metrics after the application of postprocessing.

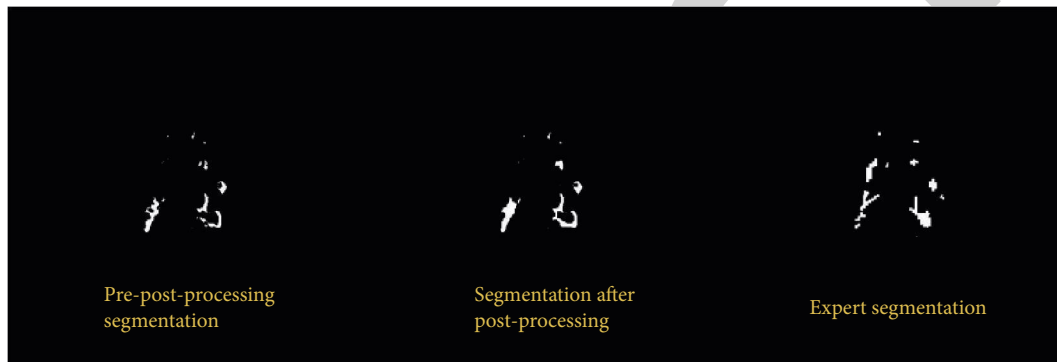


FIGURE 8: Example of the benefits of the closing filter.

In Figure 8, It should be noted that this filter increases the number of false positives in the segmentation since it allows those regions corresponding to false positives to connect in a similar way to lesions. However, given the improvement observed in the TPR and DSC metrics, it can be said that the advantages of applying the filter outweigh its disadvantages, especially since the filter attacks the weaknesses observed in the techniques, which were able to obtain a segmentation with a low percentage of both false positives and hits to lesions.

5. Conclusions

For the MS Lesion Segmentation training database, two alternative methodologies of the state of the art were implemented, along with minor changes. Based on outlier detection using GMM and segmentation using convolutional neural networks, these algorithms had not been tested in this database and had no performance records. Both approaches achieve precise segmentation of MS lesions with good PPV. The fundamental issue with both approaches was the poor average TPR. Convolutional neural networks performed the best, successfully classifying multiple sclerosis lesions from the first set of candidates. It is worth noting that the number of photos used to create these segmentations was rather small, around 1.5% of all possible patches. In this regard, the poor TPR seen due to the small number of

patches utilized and the issues observed in automatic matter segmentation may be improved by changing the patch selection for this technique. However, segmentation produced by detecting GMM outliers has several advantages over CNN. CNN's estimate is partially based on the initial injury candidate selection. Using solely white matter voxel-centered patches presents issues if the white matter segmentation has faults due to picture abnormalities. The GMM could not detect this issue because these abnormalities tend to show as outliers. Due to the minimal number of parameters in the GMM, the EM algorithm executes quickly, allowing for rapid segmentation of lesions. Using the GPU reduces the training time of CNNs to a level comparable to the time necessary to acquire a segmentation using the GMM in the CPU. Finally, applying a closure filter to the segmentation findings improved them significantly, alleviating underestimating the lesion size reported in both techniques.

6. Recommendation

Using the suggested methodologies, the segmentation quality can be improved in the state of the art for the database. A contiguous region for a single lesion is not always attainable because the approach does not employ information about the voxel's immediate surroundings, which causes segmentation issues. Instead, the GMM might

Retraction

Retracted: HS-GC-IMS and ATR-FT-MIR Analysis Reveal the Differences in Volatile Compounds, Proteins, and Polyphenols of Royal Jelly

Advances in Materials Science and Engineering

Received 26 December 2023; Accepted 26 December 2023; Published 29 December 2023

Copyright © 2023 Advances in Materials Science and Engineering. This is an open access article distributed under the Creative Commons Attribution License, which permits unrestricted use, distribution, and reproduction in any medium, provided the original work is properly cited.

This article has been retracted by Hindawi, as publisher, following an investigation undertaken by the publisher [1]. This investigation has uncovered evidence of systematic manipulation of the publication and peer-review process. We cannot, therefore, vouch for the reliability or integrity of this article.

Please note that this notice is intended solely to alert readers that the peer-review process of this article has been compromised.

Wiley and Hindawi regret that the usual quality checks did not identify these issues before publication and have since put additional measures in place to safeguard research integrity.

We wish to credit our Research Integrity and Research Publishing teams and anonymous and named external researchers and research integrity experts for contributing to this investigation.

The corresponding author, as the representative of all authors, has been given the opportunity to register their agreement or disagreement to this retraction. We have kept a record of any response received.

References

- [1] D. Chen, W. Lu, Q. Ye, C. Zhang, X. Ge, and C. Xiao, "HS-GC-IMS and ATR-FT-MIR Analysis Reveal the Differences in Volatile Compounds, Proteins, and Polyphenols of Royal Jelly," *Advances in Materials Science and Engineering*, vol. 2022, Article ID 3223558, 8 pages, 2022.

Research Article

HS-GC-IMS and ATR-FT-MIR Analysis Reveal the Differences in Volatile Compounds, Proteins, and Polyphenols of Royal Jelly

Di Chen ¹, Wenjing Lu,¹ Qin Ye,¹ Cen Zhang,¹ Xiao Ge,² and Chaogeng Xiao ¹

¹Institute of Food Science, Zhejiang Academy of Agricultural Sciences, Hangzhou 310021, Zhejiang, China

²Hangzhou Kang Li Food Co.,Ltd., Hangzhou 311401, Zhejiang, China

Correspondence should be addressed to Di Chen; cd0sindy@zju.edu.cn and Chaogeng Xiao; xiaochaogeng@163.com

Received 11 February 2022; Revised 15 March 2022; Accepted 23 March 2022; Published 15 April 2022

Academic Editor: Palanivel Velmurugan

Copyright © 2022 Di Chen et al. This is an open access article distributed under the Creative Commons Attribution License, which permits unrestricted use, distribution, and reproduction in any medium, provided the original work is properly cited.

Royal jelly (RJ) produced by honeybees (*Apis mellifera*) is a traditional functional food and usually suffers adverse impacts from heat exposure during collection and transportation. Based on the gas chromatography, the change to volatile compounds in RJ was screened by ion mobility spectrometry. Chemical characteristics were analyzed by infrared spectroscopy combined with a diamond ATR. The results showed that the flavor can be distinguished using HS-GC-IMS based on principal component analysis and 26 compounds, including esters, aldehydes, and ketone, were identified as the differential volatile compounds in RJ. Spectroscopy results suggested that the specific bands were related to the proteins and polyphenols, which were verified by electrophoresis and the Folin-Ciocalteu method. Water-soluble proteins were decreased by 13.11%, and polyphenols contents were decreased by 25.72% compared with the control. Thus, the combination of ATR-FT-MIR and volatile compound analysis can help to identify the quality of RJ quickly and sensitively from the aspect of flavor and chemical characteristics. Our study gives a meaningful suggestion for the analytic strategy of RJ quality.

1. Introduction

Royal jelly (RJ) represented a traditional food with broad bioactivity. This white-yellowish gelatinous-viscous substance was the main food of bee larvae and queen bees with a special flavor [1–3]. Nearly 100 tons of royal jelly were exported to Europe and Japan every year. RJ was secreted by the salivary glands of a specific honeybee [4]. It has numerous functional properties, including antioxidative activity, immune regulation, antibacterial activity, and antitumor activity, as well as insulin-like activity [5, 6]. These bioactive of RJ were largely dependent on its freshness and chemical composition characteristics. However, improper storage will lead to the degradation of the RJ flavor and have a great impact on its chemical composition [7–10]. So, analyzing the changes of favor and chemical characteristics is important to detect the RJ freshness and ensure its quality.

The flavor is a useful index in determining whether the quality of RJ is acceptable on the spot. The variation of flavor composition is essential for the freshness evaluation of RJ, as

well as its quality. It was reported that RJ harvested at 48 h contained more unique volatile compositions compared to the samples harvested at 72 h [11]. In addition, the flavor was also related to the quality of RJ commercial products. With the increasing emphasis on rapid detection of RJ quality, flavor characteristics analysis becomes critically important. Therefore, clarifying the flavor characteristics change is the key to the detection of RJ quality and ultimately satisfies collection preferences. Headspace extraction has been broadly applied in the analysis of volatile constituents. Moreover, volatile compounds of RJ have been evaluated under low temperature and room temperature storage, and 25 different compounds were found [12, 13]. However, some flavor compounds can only be detected by a certain method, and different flavor compounds may be extracted by different detection method as the complexity of foodstuffs. Up to now, less information is available on the characteristic of the RJ flavor by using ion mobility spectrometry.

Ion mobility spectrometry combined with GC is feasible and useful in analyzing flavor and figuring out specific

volatile compounds in recent years, which is rapid, sensitive, and simple. It can establish fingerprints at the ppb level in real time for detected samples according to the characterization of drift time and GC retention [14, 15]. It also investigates unbiased information and screens specific makers through nontarget analysis from a large amount of data. Therefore, ion mobility spectrometry combined with GC has been broadly applied in flavor analysis, drug study, and security detection [16]. As a new food resource, rapid detection of high quality RJ has drawn more and more attention. ATR-FT-MIR was another technique for rapid detection. Our study aimed to analyse the variation of flavor and chemical characteristics of RJ during the process of storage. Principal component analysis was performed on the flavor data which was acquired by the ion mobility spectrometry combined with GC. Verification of chemical characteristics changes was carried out based on the ATR-FT-MIR data. Integration of the two techniques may provide a new supplementary analytical strategy for the quality control of RJ.

2. Materials and Methods

2.1. Materials. RJ was obtained from the same colony of *Apis mellifera*. L at the Hangzhou Kangli Food, Co., Ltd, Zhejiang, China. The latitude and longitude are 120.2 E and 30.3 N. The same colony of *Apis mellifera* RJ was acute frozen and then placed at -80°C until analysis. Afterward, the RJ samples obtained from the same batch were prepared at different storage conditions based on the experiment. BSA was received from Beyotime Co. Ltd (Hangzhou, China). Last but not least, Folin-Ciocalteu was received from Zeheng Biological Technology Co. Ltd. (Hangzhou, China).

2.2. Ion Mobility Spectrometry Combined with GC Analysis. Flavor analysis was conducted with a FlavourSpec® flavor analyzer (GAS, Dortmund, Germany). The capillary column (ID: 0.53 mm) was applied in the GC. Ion mobility spectrometry combined with GC analysis was performed according to the literature with minor modifications [17]. RJ was placed in a plastic tube and adjusted for 15 min at 50°C . The incubation speed is set at 500 rpm. Headspace samples of 500 μL were automatically injected at 85°C . Carrier gas N_2 flows for 2 min at a rate of 0.002 L/m, and then, the flow of carrier gas changed to 0.01 L/m in the following 8 min, then changed to 0.1 L/m (10–20 min), and finally reached 0.15 L/m (20–30 min). Volatile constituents were departed by the column at 60°C , and the temperature of IMS was set at 45°C . RI and drift time were used to identify volatile constituents.

2.3. ATR-FT-MIR Spectroscopy. RJ samples were analyzed by a VERTEX70 attenuated total reflection midinfrared spectrometer (Bruker, USA) coupled with a diamond ATR accessory. Spectra data were acquired with scans of 24 and a resolution level of 4 cm^{-1} . The medium infrared spectra signal of the sample was detected in the region of $400\text{--}4000\text{ cm}^{-1}$ for five replicates. Approximately 0.05 g of RJ was transferred to the ATR diamond that was cleaned

with ethanol (75%). Background air spectrum was applied to each RJ sample spectra. Spectral data were analyzed by the OPUS version 6.5 (Agilent, USA) and the origin version 8.5.

2.4. Detection of Water-Soluble Protein and Total Polyphenol Content (TPC)

2.4.1. Determinations of Major Royal Jelly Proteins. Major royal jelly proteins (MRJPs) were extracted with PBS solution for 24 h at 4°C as previously described by Chen [18]. The extract of MRJPs was obtained by centrifuging (Eppendorf, Germany) at 12,000 rpm for 30 min under 4°C . SDS-PAGE was used to separate proteins that were present in MRJPs, and concentrations of MRJP (major royal jelly protein) 1 and MRJP3 were determined by Image J.

2.4.2. Determinations of Water-Soluble Proteins. The water-soluble proteins' content in RJ was determined using BSA as a standard. 50 μL of RJ diluted in distilled water was mixed with 250 μL of Coomassie light blue solution. After being cultured in the little light circumstances for 30 min, the light absorption value was taken at 595 nm. A standard curve was acquired by detecting the absorbance gradient of the BSA solution [19].

2.4.3. Determinations of Total Polyphenol Content (TPC). Total polyphenol content was detected using the literature method with some minor revisions [20]. Undiluted Folin-Ciocalteu reagent (1 mL) was added to an equal volume 10 mg/mL RJ solution, and then, 1 minute later, 5 mL of 1 M aqueous Na_2CO_3 was added. Finally, about 3 mL of purified water was added to the reaction system, making the volume up to 10 mL. The control contained all the reaction reagents except RJ. After being cultured at 25°C for 1 h, the light absorption value was determined at 760 nm. Polyphenol content was presented as protocatechuic acid (PCA) equivalents (mg PCA/g) based on the PCA calibration curve, and the values were presented as means of triplicate analyzes.

2.5. Statistical Analysis. IMS data were processed with vocal processing software, including an ion mobility spectrometry combined with a GC analysis library, a dynamic PCA plug-in, gallery plug-in, and reporter plug-in, which were used to analyze samples from different perspectives. Analysis of variance was performed in SPSS 18.0 (SPSS, USA), and p value of <0.05 was regarded as a statistically significant difference between groups. The results were presented as the mean \pm sd.

3. Results

3.1. Chemical Characterization by HS-GC-IMS. The 3D topographic of RJ sample is shown in Figure 1 according to the normalized reaction ion peak position and the ion drift time. Our study demonstrated that the volatile substances of 28°C stored RJ were well separated from the samples at frozen conditions (-20°C), as shown in the top three-dimension

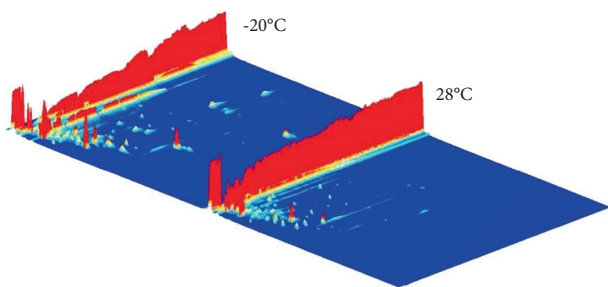


FIGURE 1: Three-dimensional topographic of the volatile components of RJ stored at -20°C and 28°C , respectively.

plot graphic. Most flavor components signal peaks were found in the RIP relative of 1.0–2.0 and the measurement run time of 1000–100 s. Many peaks were decreased at 28°C storage while some peaks were enhanced. In particular, many small peaks appeared during the measurement run time of 200–400 s and RIP relative of 1.0–1.5, indicating the formation of little other substances in 28°C stored RJ. The qualitative and quantitative results are shown in Figure 2. HS-GS-IMS have detected 45 signal peaks and 31 compounds were identified (Table 1). Volatile compounds of RJ samples were ketones, esters, aldehydes, alcohols, and others according to the identified components.

Fingerprint showed the effects of storage conditions on the variation of volatile compounds (Figure 3). A great deal of flavor contents of ethyl acetate, heptanal, 2-pentanone, 2-nonanone (D), ethyl octanoate (D), ethyl octanoate (M), 2-nonanone (M), ethyl hexanoate (M), 3-methyl-1-butanol, 2-heptanone (D), ethyl hexanoate (D), 2-heptanone (M), 2-propanol, butyl acetate (D), butyl acetate (M), n-Nonanal, ethanol, 6-methyl-5-heptene-2-one, benzaldehyde (D), and benzaldehyde (M) were relatively low in RJ at 28°C for 30 days (R2), indicating the loss of these volatile compounds were affected by the temperature, which might be the result of the action of enzymes or thermal decomposition during ambient temperature storage. On the contrary, 3-methylbutanol, 2-methylbutanal, furfural (D), furfural (M), 2-butanone, and 2-methylpropanoic acid were obviously enhanced in RJ at 28°C for 30 days compared to the frozen samples (R1). Volatile organic compounds in the differential model exhibited an obvious difference, and total volatile organic matter content was decreased in the process of ambient temperature storage (Figure S1).

As illustrated in Figure 4, the principal component analysis showed that RJ at the different storage conditions could be well separated. Ninety six percent of PC-1 and 2% of PC-2 explained 98% of the total variance, indicating that they could explain the main flavor characteristic. The PC-1 value decreased in the following order: $R1 < R2$. The close distance between samples means small differences, while the far distance means significant differences. Thus, the samples have great differences in flavor, and the regions of each group of RJ samples can be clearly separated.

3.2. Spectroscopy Characterization by ATR-FT-MIR. The average ATR-FT-MIR spectrum of the RJ samples gives molecular vibrations affected by ambient temperature

storage (Figure 5). Stretching vibration of O-H of protein-glycoconjugate covalent bond could raise a strong band at 3268 cm^{-1} . Spectral features related to stretching vibrations interaction of protein-glycoconjugate covalent bond for both O-H and C-O are also characterized in spectral of $3700\text{--}3200\text{ cm}^{-1}$ and $1260\text{--}1000\text{ cm}^{-1}$ (with max absorption at 1059 cm^{-1}).

The most prominent absorption with broadband at 1636 cm^{-1} that refer to the vibration of H-O-H deformation and carbonyl group stretching of proteins was shown in the fingerprint region. Protein's thalidomide I band characteristic absorption peak was located at $1600\text{--}1700\text{ cm}^{-1}$. Thus, signal at 1636 cm^{-1} is arising from the stretching vibrations of the carbonyl group of backbone conformation of the proteins in RJ. As shown in Figure 5(a), the band at 1546 cm^{-1} (thalidomide II bands $1500\text{--}1600\text{ cm}^{-1}$) occurs because of the C-N stretching vibrations and N-H deformation vibration. The reduced interaction between protein molecules causes the band to move. Absorption occurring at 1238 cm^{-1} and 1059 cm^{-1} is arising from stretching vibrations of a carbonyl group in the carbohydrates.

In Figure 5, differences of band positions and intensities represent unique spectral patterns of the samples, indicating significant differences of the composition. Variations in protein content (at 3268 , 1636 , 1546 , and 1059 cm^{-1}) present in RJ were distinguished significantly between analyzed samples, and the differences were mainly related to the protein, polyphenols, and flavonoid, as their corresponding spectral in the fingerprint ($1800\text{--}800\text{ cm}^{-1}$) are the prominent variation. RJ under 28°C storage reflect unique spectral features in the fingerprint region represented by the protein-glycoconjugate band at 1059 cm^{-1} due to the relatively low protein content, while frozen samples showed higher protein content (absorption maximum at 3268 and 1059 cm^{-1}).

3.3. Verification of Chemical Changes. Content of MRJP1 with 57 kDa in RJ stored at 28°C was significantly lower than those stored at -20°C , as shown in Figure 6(a) ($p < 0.01$). In addition, a similar phenomenon also was observed on MRJP3 (Figure 6(b) and Figure S2). Major royal jelly proteins were significantly decreased once the storage time was beyond 20 days of whatever stored at 28°C or 4°C . Figures 6(c) and 6(d) show that the content of water-soluble proteins and phenolic was significantly reduced by 13.11% and 25.72% at 28°C compared to -20°C for 30 days ($p < 0.05$). However, no significant difference was observed within 20 days ($p > 0.05$), indicating these bioactive constituents were also affected by the storage time except temperature.

4. Discussion

It is not a simple task to analyze all the flavor compounds with one simple method as the complexity of foodstuffs and the techniques are not sensitive enough [21–23]. So, as a rapid, simple, and sensitive analytical technique, HS-GC-IMS with high resolution was used in this study to

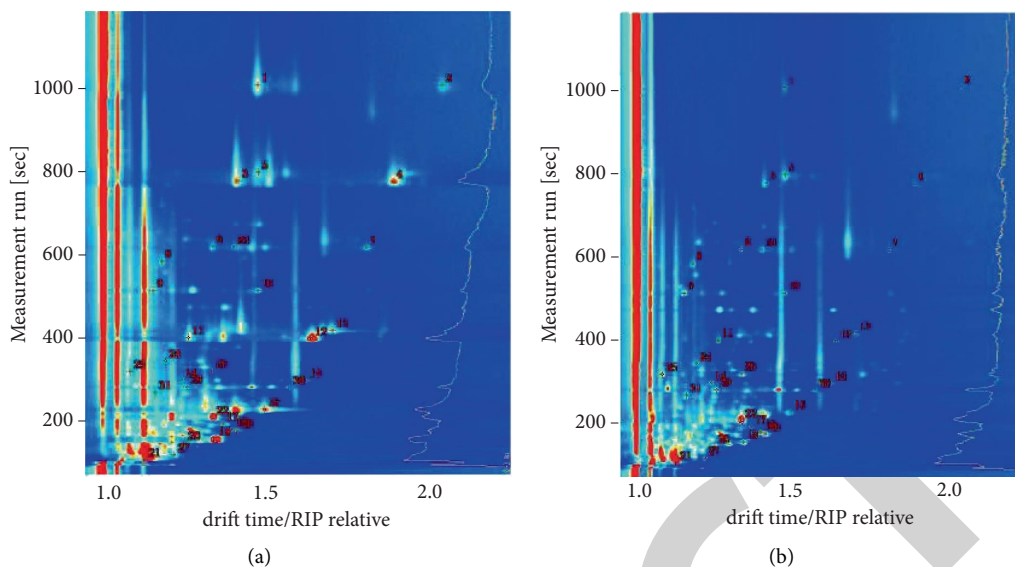


FIGURE 2: (a) Topographic plots for the selected markers obtained from the RJ stored at -20°C ; (b) topographic plots for the selected markers obtained from the RJ stored at 28°C .

TABLE 1: Identified compounds in the RJ samples.

Count	Compounds	Formula	MW	RI ¹	Rt ² (sec)	Dt ³ [a.u.]
1	^M Ethyl octanoate	C ₁₀ H ₂₀ O ₂	172.3	1191.1	1004.104	1.47491
2	^D Ethyl octanoate	C ₁₀ H ₂₀ O ₂	172.3	1191.1	1004.104	2.03767
3	^M 2-Nonanone	C ₉ H ₁₈ O	142.2	1095.4	774.036	1.41594
4	^D 2-Nonanone	C ₉ H ₁₈ O	142.2	1094.9	773.086	1.88863
5	n-Nonanal	C ₉ H ₁₈ O	142.2	1105.0	794.446	1.47735
6	^M Ethyl hexanoate	C ₈ H ₁₆ O ₂	144.2	1011.9	616.878	1.33869
7	^D Ethyl hexanoate	C ₈ H ₁₆ O ₂	144.2	1010.0	613.73	1.80745
8	6-Methyl-5-hepten-2-one	C ₈ H ₁₄ O	126.2	991.8	580.858	1.18144
9	^M Benzaldehyde	C ₇ H ₆ O	106.1	958.1	510.22	1.15428
10	^D Benzaldehyde	C ₇ H ₆ O	106.1	958.1	510.22	1.47476
11	^M 2-Heptanone	C ₇ H ₁₄ O	114.2	893.1	397.332	1.26379
12	^D 2-Heptanone	C ₇ H ₁₄ O	114.2	891.2	394.587	1.63893
13	^M Heptanal	C ₇ H ₁₄ O	114.2	904.2	414.718	1.70347
14	^D Butyl acetate	C ₆ H ₁₂ O ₂	116.2	808.6	294.658	1.24175
15	Butyl acetate	C ₆ H ₁₂ O ₂	116.2	808.4	294.449	1.62353
16	3-Methyl-1-butanol	C ₅ H ₁₂ O	88.1	732.7	223.668	1.49573
17	2-Pentanone	C ₅ H ₁₀ O	86.1	687.9	189.844	1.36792
18	2-Methylbutanal	C ₅ H ₁₀ O	86.1	661.3	176.725	1.39861
19	Ethyl acetate	C ₄ H ₈ O ₂	88.1	606.6	152.515	1.34292
20	2-Butanone	C ₄ H ₈ O	72.1	582.5	142.964	1.25243
21	Ethanol	C ₂ H ₆ O	46.1	459.1	102.541	1.12992
22	Acetoin	C ₄ H ₈ O ₂	88.1	709.5	205.377	1.33875
23	Octanal	C ₈ H ₁₆ O	128.2	1010.9	615.241	1.40095
24	(E)-2-Hexenal	C ₆ H ₁₀ O	98.1	850.0	341.129	1.1931
25	^M Furfural	C ₅ H ₄ O ₂	96.1	828.2	315.769	1.08536
26	^D Furfural	C ₅ H ₄ O ₂	96.1	829.0	316.723	1.33648
27	2-Propanol	C ₃ H ₈ O	60.1	502.7	115.311	1.22015
28	3-Methylbutanal	C ₅ H ₁₀ O	86.1	650.9	171.863	1.41264
29	^M Hexanal	C ₆ H ₁₂ O	100.2	791.9	277.685	1.25762
30	^D Hexanal	C ₆ H ₁₂ O	100.2	791.0	276.876	1.57128
31	2-Methylpropanoic acid	C ₄ H ₈ O ₂	88.1	778.4	264.561	1.16176

¹, retention index; ², retention time in the capillary column; ³, drift time; ^M, monomer; ^D, dimer.

assess the flavor changes and provide a supplementary analytical method for distinguishing RJ [24]. In the present study, RJ stored at -20°C contained a large

number of acid, ester, aldehyde, and ketone compounds, and flavor compounds were gradually decomposed during the 28°C storage. Thus, the overall content of

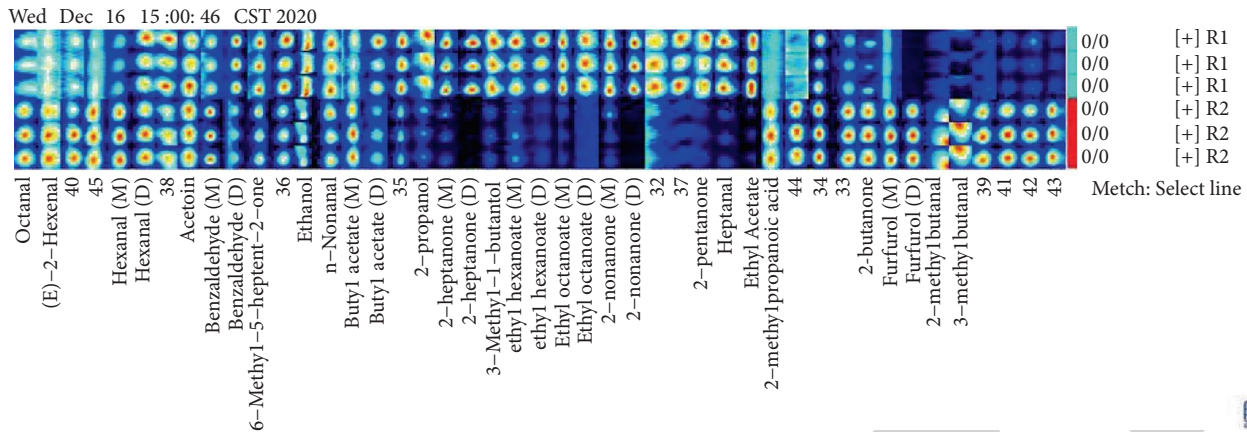


FIGURE 3: Gallery plot of the differential signal affected by the temperature. R1 refers to samples at -20°C . R2 refers to samples at 28°C . The darker the color, the higher the content of volatile organic compounds.

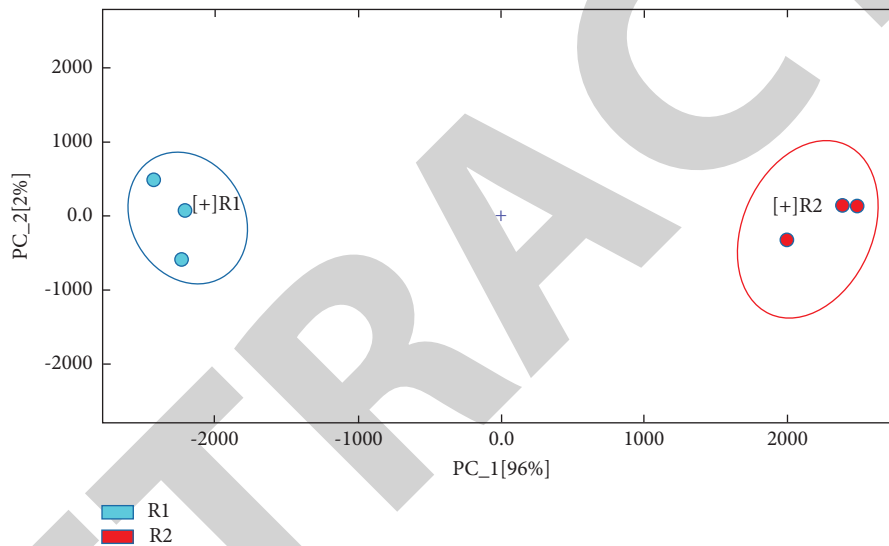


FIGURE 4: Principal component analysis for royal jelly samples at -20°C and 28°C based on the volatile compounds' intensity.

flavor compounds in frozen RJ was much higher than those stored at 28°C , similar to the reported literature that RJ of low temperature, and keeps the composition of volatile compounds unchanged [12]. The HS-GC-IMS results showed that the ambient temperature storage led to the decrease and formation of some flavor substances in RJ, exhibiting great effects on the composition of volatile constituents. However, special attention should be paid to discrepancies of the volatile compound between literature and the obtained data in this study, as previous studies using GS-MS have shown that 28°C storage make d-ethyl acetate increase twice. The differential methods for RJ collection and preparation can cause these discrepancies, as described above, as the analysis of volatile organic compounds is influenced by both extraction and detection techniques [12, 25]. In addition, as different plants also affect the flavor composition of benzoic acid methyl ester, acetic acid, octanoic acid, and hexanoic acid [13], RJ samples harvested from different plants should be studied in the future.

FTIR spectroscopy with ATR is able to accurately reflect the secondary structure information of the protein by the spectral absorption band of Amide-I and Amide-II at 1547 cm^{-1} with highly specific signals [26]. The relative spectra intensity of the typical bands of RJ stored at 28°C was decreased compared to the frozen samples. Moreover, temperature caused the amide-I band to move, which was similar with the reports of [27]. Furthermore, analysis of phenolic compounds of RJ is also important to the quality evaluation [28]. ATR-FT-MIR used in the present study can reflect the variation of polyphenol, which was verified by the total polyphenol analysis. These results were similar with the result of Zhao et al. that RJ phenol contents are decreased obviously at room temperature [12, 13]. So, FTIR with ATR in the present study can reflect the variation of proteins and polyphenols and is suitable to monitor chemical changes of RJ during the process of storage [29].

Based on the ATR-FT-MIR results, verification analysis of water-soluble proteins and the total polyphenol content was then carried out. Ambient temperature caused

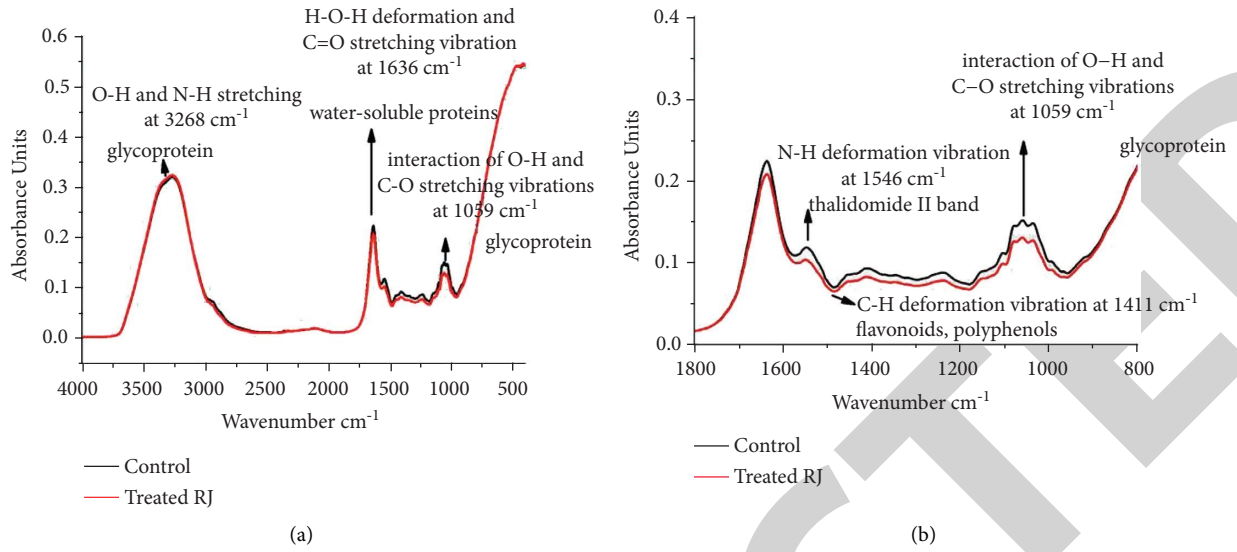


FIGURE 5: (a) Effects of ambient temperature (28°C) on the characteristic of the average middle infrared spectrum of the RJ samples (4000–500 cm⁻¹); (b) effects of ambient temperature (28°C) on the characteristic of average middle infrared spectrum located in the fingerprint region (1800–800 cm⁻¹).

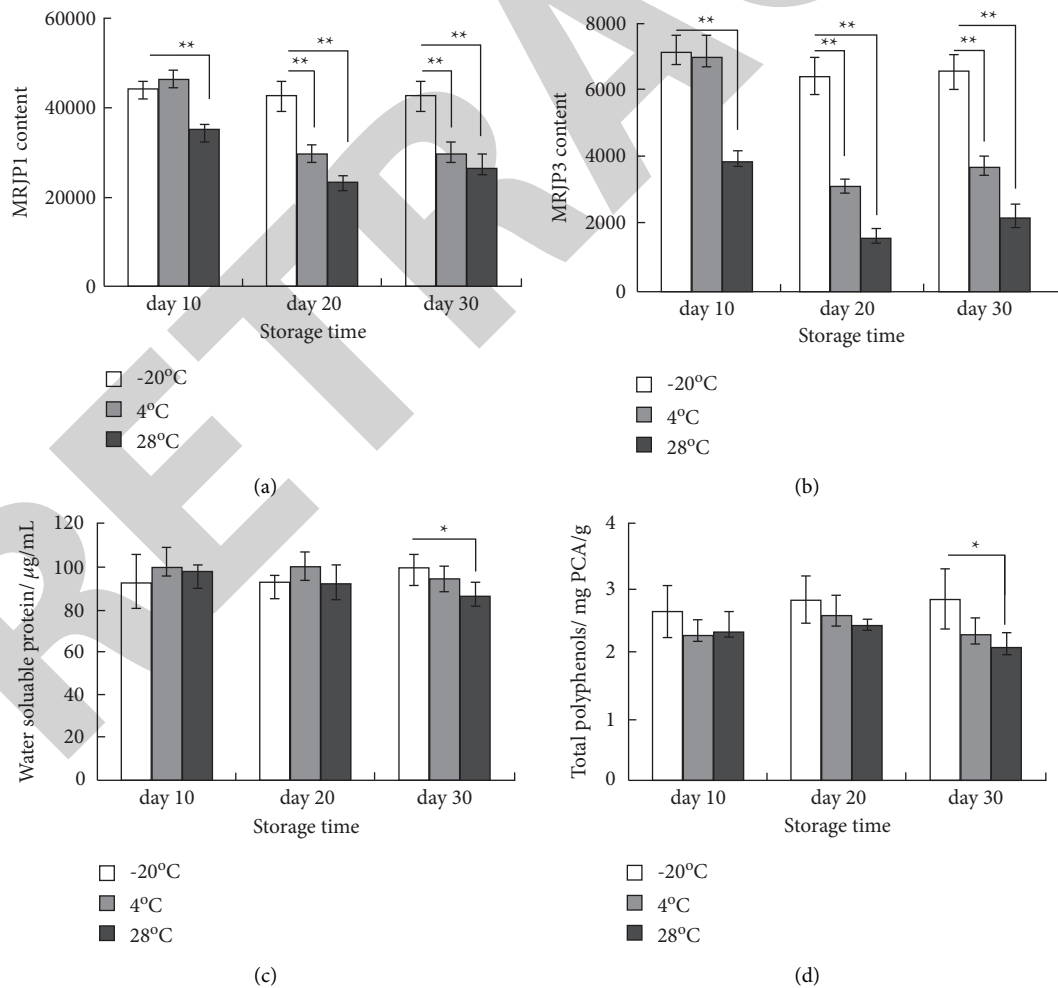


FIGURE 6: (a) Effect of temperature on the MRJP1; (b) effect of temperature on the contents of MRJP3; (c) effect of temperature on the contents of water-soluble protein; (d) effect of temperature on the contents of total polyphenols. *means statistical difference level for $p < 0.05$ and **means statistical difference level for $p < 0.01$ when compared to samples stored at -20°C.

the significantly reduction of the content of water-soluble proteins. MRJPs were important bioactivity constituents of RJ [30–32]; it can affect the biological function in bee larvae and determine the freshness and quality of RJ. So, it was usually used as a freshness marker for RJ [33]. Interestingly, the SDS-PAGE result showed that MRJP1, which consists about half of water-soluble proteins, was decreased significantly after ambient storage, indicating this protein makes an important attribution to this vibration in the ATR-FT-MIR spectrum (Figure 5 and Figure S2). However, the decrease of MRJP1 may be caused by molecules aggregation rather than degradation, as reported by Qao et al. [34].

Notably, China produces more than 4,000 tons of RJ annually and is the largest producer of RJ globally [34, 35]. In order to analyze the quality and freshness, there is a strong desire to develop sensitive and rapid methods to investigate the chemical composition variation of RJ [36]. Flavor and characteristic of the ATR-FT-MIR spectrum were important indicators to make sure the high quality of produced RJ [28]. Integration of the two techniques presented in this study could effectively distinguish the samples and was a potential new analytical strategy for the quality control of RJ.

5. Conclusions

In this study, HS-GC-IMS combined with ATR-FT-MIR were performed to assess the variation to volatile and heat sensitive compounds in RJ. The volatile compound fingerprints were constructed and a total of 31 differential compounds affected by the temperature were identified. The main flavor compounds in RJ were attributed to esters, aldehydes, and ketones based on HS-GC-IMS. PCA results indicate that the samples at different temperatures can be well separated. Verification of the ATR-FT-MIR results indicated that the temperature had more impact on the change of proteins and polyphenols compared to storage time. As a reliable analytical tool, HS-GC-IMS combined with ATR-FT-MIR is able to screen the quality of RJ quickly and sensitively from the aspects of flavor and chemical characteristics. Our study can give a meaningful suggestion for the analytic strategy of RJ quality.

Data Availability

No data were used to support this study.

Conflicts of Interest

All authors of this article declare that they have no conflicts of interest.

Acknowledgments

We would like to thank the laboratory colleagues for their advice and the financial support from the Zhejiang Province Key Research and Development Project, (Grant no. 2018C02051).

Supplementary Materials

Figure S1: GS-IMS Spectra of Volatile Organic Compounds Difference comparison in different RJ samples. Figure S2: SDS-PAGE analysis of MRJPs (A). M refers to Marker and 1–9 represent RJ stored at -20°C (day 10, 20, 30), 4°C (day 10, 20, 30), and 28°C (day 10, 20, 30), respectively. (*Supplementary Materials*)

References

- [1] M. Martinello and F. Mutinelli, "Antioxidant activity in bee products: a review," *Antioxidants*, vol. 10, no. 1, p. 71, 2021.
- [2] A. Buttstedt, R. F. A. Moritz, and S. Erler, "Origin and function of the major royal jelly proteins of the honeybee (*Apis mellifera*) as members of the yellow gene family," *Biological Reviews*, vol. 89, no. 2, pp. 255–269, 2014.
- [3] L. Shen, W. Zhang, F. Jin et al., "Expression of recombinant AccMRJP1 protein from royal jelly of Chinese honeybee in *Pichia pastoris* and its proliferation activity in an insect cell line," *Journal of Agricultural and Food Chemistry*, vol. 58, no. 16, pp. 9190–9197, 2010.
- [4] A. Ramanathan, A. J. Nair, and V. S. Sugunan, "A review on royal jelly proteins and peptides," *Journal of Functional Foods*, vol. 44, pp. 255–264, 2018.
- [5] N. Ab Hamid, A. B. Abu Bakar, A. A. Mat Zain et al., "Composition of royal jelly (RJ) and its anti-androgenic effect on reproductive parameters in a polycystic ovarian syndrome (PCOS) animal model," *Antioxidants*, vol. 9, no. 6, p. 499, 2020.
- [6] A. Hadi, A. Najafgholizadeh, E. Aydenlu et al., "Royal jelly is an effective and relatively safe alternative approach to bloodlipid modulation: a meta-analysis," *Journal of Functional Food*, vol. 41, pp. 202–209, 2018.
- [7] M. Kamakura, T. Fukuda, M. Fukushima, and M. Yonekura, "Storage-dependent degradation of 57-kDa protein in royal jelly: a possible marker for freshness," *Bioscience Biotechnology and Biochemistry*, vol. 65, pp. 277–284, 2001.
- [8] L.-r. Shen, Y.-r. Wang, L. Zhai et al., "Determination of royal jelly freshness by ELISA with a highly specific anti-apalbumin 1, major royal jelly protein 1 antibody," *Journal of Zhejiang University - Science B*, vol. 16, no. 2, pp. 155–166, 2015.
- [9] S. Tamura, S. Amano, T. Kono et al., "Molecular characteristics and physiological functions of major royal jelly protein 1 oligomer," *Proteomics*, vol. 9, no. 24, pp. 5534–5543, 2009.
- [10] A. Maghsoudlou, A. S. Mahoonak, H. Mohebodini, and F. Toldra, "Royal jelly: chemistry, storage and bioactivities," *Journal of Apicultural Science*, vol. 63, no. 1, pp. 17–40, 2019.
- [11] Y. H. Guo, L. B. Zhou, Q. Z. Pan, and L. Z. Zhang, "Effect of different harvesting times on the yield and composition of royal jelly," *Acta Agriculturae Universitatis*, vol. 37, pp. 120–125, 2015.
- [12] V. A. Isidorov, S. Bakier, and I. Grzech, "Gas chromatographic-mass spectrometric investigation of volatile and extractable compounds of crude royal jelly," *Journal of Chromatography B*, vol. 885–886, pp. 109–116, 2012.
- [13] Y.-z. Zhao, Z.-g. Li, W.-l. Tian, X.-m. Fang, S.-k. Su, and W.-j. Peng, "Differential volatile organic compounds in royal jelly associated with different nectar plants," *Journal of Integrative Agriculture*, vol. 15, no. 5, pp. 1157–1165, 2016.
- [14] M. Li, H. Du, and S. Lin, "Flavor changes of tricholoma matsutake singer under different processing conditions by using HS-GC-IMS," *Foods*, vol. 10, no. 3, p. 531, 2021.

Retraction

Retracted: The Impact of Family Sustainable Livelihood and Environmental Cognition on Herdsmen's Choice of Production Behavior

Advances in Materials Science and Engineering

Received 26 December 2023; Accepted 26 December 2023; Published 29 December 2023

Copyright © 2023 Advances in Materials Science and Engineering. This is an open access article distributed under the Creative Commons Attribution License, which permits unrestricted use, distribution, and reproduction in any medium, provided the original work is properly cited.

This article has been retracted by Hindawi, as publisher, following an investigation undertaken by the publisher [1]. This investigation has uncovered evidence of systematic manipulation of the publication and peer-review process. We cannot, therefore, vouch for the reliability or integrity of this article.

Please note that this notice is intended solely to alert readers that the peer-review process of this article has been compromised.

Wiley and Hindawi regret that the usual quality checks did not identify these issues before publication and have since put additional measures in place to safeguard research integrity.

We wish to credit our Research Integrity and Research Publishing teams and anonymous and named external researchers and research integrity experts for contributing to this investigation.

The corresponding author, as the representative of all authors, has been given the opportunity to register their agreement or disagreement to this retraction. We have kept a record of any response received.

References

- [1] Q. Wang and Y. Miao, "The Impact of Family Sustainable Livelihood and Environmental Cognition on Herdsmen's Choice of Production Behavior," *Advances in Materials Science and Engineering*, vol. 2022, Article ID 4278331, 9 pages, 2022.

Research Article

The Impact of Family Sustainable Livelihood and Environmental Cognition on Herdsmen's Choice of Production Behavior

Qihang Wang  and **Yinjia Miao**

Chongqing College of Electronic Engineering, Chongqing 401331, China

Correspondence should be addressed to Qihang Wang; 200624018@cqcet.edu.cn

Received 23 February 2022; Revised 22 March 2022; Accepted 31 March 2022; Published 13 April 2022

Academic Editor: Palanivel Velmurugan

Copyright © 2022 Qihang Wang and Yinjia Miao. This is an open access article distributed under the Creative Commons Attribution License, which permits unrestricted use, distribution, and reproduction in any medium, provided the original work is properly cited.

This study analyzed the influence of sustainable livelihood and environmental cognition on herdsmen's production behaviors on basis of logistic model. The consequences illustrated that the social capital followed by material capital, financial capital, and human capital has the greatest impact on herdsmen's production behaviors, but the natural capital played a vital role in promoting herdsmen's choice of raising breeding scale. The area and quality of grassland in herdsman families' sustainable livelihood could encourage herdsmen to increase breeding scale, while the quantity of livestock, structure of house, the number of labor, the level of education, the status of health, and the income of families could promote herdsmen to restrain the breeding scale. The cognition of policy and ecological environment also had a significant positive effect on herdsmen restraining breeding scale.

1. Preface

China is rich in natural grassland area, accounting for 41.7% of the territory area. However, the grassland degradation had become a serious environmental and ecological problem because of the nature and human. As the most vital users and producers, the herdsmen's breeding scale is a significant factor affecting grassland ecology [1, 2]. Sun et al. [3] indicated that the conflict between their growing livelihood demands and reasonable breeding quantity of grassland was the main reason of enlarging breeding scale. Sun et al. [4] showed that herdsmen had protection awareness, but the government could not realize the influence of breeding scale changing on herdsmen's lives comprehensively which could destroy protection of grassland resources by the governmental policy. The sustainable developed breeding policy should be formulated by combining the reality of local herdsman families' livelihood capital and improve herdsmen's settlement level, expand income channels, and standardize cooperatives' operation via accelerating the grassland circulation, so as to control the breeding scale and maintain the grassland ecological resources [3]. In the process of grassland protection, government should enhance

the participation of herdsmen, strengthen the publicity of grassland degradation and related policy content, expand the ways of herdsmen to increase their income, and then strengthen the living standards of herdsmen groups [3, 5]. Ding et al. [6] studied the Grassland Ecological Subsidy Policy and Livestock Reduction Behavior, and Wu et al. [7] used logit model to analyze the impact of livelihood strategies. In summary, although the existing literature researched herdsmen's breeding behaviors from the perspective of livelihood capital could provide reference for herdsmen's production behaviors, there is still room for further research. Most of the academic researches on Herdsmen's production behavior were focused on government policies and herdsmen's livelihood factors, but the consideration of internal factors, namely, herdsmen's environmental cognition, was rarely involved. In this study, the herdsmen in Wuchuan and Qinglong areas of Guizhou Province were taken as the research objects, and the production behavior of herdsmen's animal husbandry is discussed from two aspects of environmental cognition and family livelihood, which provides reference value for the government to improve the grassland policy and promote the sustainable development of grassland ecology.

2. Theoretical Research and Research Hypothesis

2.1. Concept Definition. In the 1980s, “sustainable livelihood” was first proposed. Zhang et al. [8] analyzed the research process of “sustainable livelihood” in China based on bibliometric method and believed that, among a large number of sustainable livelihood analysis systems, the sustainable livelihood framework constructed by DFID was the most widely used in the research field of China. The sustainable livelihood capitals of herdsman families mentioned in this article mainly include five different forms of capital (material capital, natural capital, human capital, social capital, and financial capital).

In the field of environmental psychology, environmental cognition is an important cornerstone of adapting to the environment and acting on the environment. It is a way for individuals to distinguish the environment, what impression the environment forms in their minds, and how this impression affects the individual acting on the environment. Environmental behavior is an important dimension of environmental cognition, which includes four dimensions: “environmental knowledge, environmental values, environmental protection attitude and environmental protection behavior” [9]. On the contrary, “Environmental cognition and environmental behavior are two independent concepts, and there is no contained relationship” [10]. This study illustrates that the production behavior of herdsman was closely related to the change of grassland ecological environment, and the cognitive level of grassland ecological environment was an important subconscious dominant factor of herdsman’s breeding behavior. Wang et al. [11] elucidated that the research of environmental cognition should be considered from three dimensions of policy environment, ecological environment, and economic environment. Because the economic environment was included in the family livelihood capital, it was no longer considered again here.

2.2. Livelihood Capital and Herdsman’s Production Behavior. Natural capital is the stock of natural resources, which is the basis of herdsman’s survival and development. When there are abundant natural resources, herdsman will lack the motivation to broaden their livelihood strategies and are more likely to expand their breeding scale. For example, Su Fang et al. (2009) pointed out that farmers with more natural resource capital tend to regard agricultural income as a key livelihood strategy. For example, Sun et al. [12] pointed out that farmers with more natural resource capital tended to regard agricultural income as a key livelihood strategy. Herdsman’s livelihood was highly dependent on natural resources, and extremely rich natural resources could meet the basic demands of herdsman’s husbandry, so that herdsman usually would not consider other ways of livelihood [13]. On this basis, the following assumptions were made in this study:

H1: when other factors are controlled, the more abundant the herdsman’s natural capital is, the more

likely the herdsman is to choose to improve the production behavior of breeding scale.

Human capital is the general term of knowledge, skills, and health status and is the basis of all livelihood activities. When the human capital of herdsman is more abundant, they are more likely to try other livelihood strategies and reduce the scale of breeding. For example, Wu et al. [14] elucidated that, for young herdsman, it was necessary to strictly implement compulsory education and encourage them to carry out higher education. For the students in pastoral areas, the tuition fees should be reduced appropriately, and the same environment as urban students should be provided, so as to lay a solid foundation for their diversified livelihood strategies in the future. According to the specific situation of the poor farmers, we should actively develop training and strengthen the skill of the labor force. For the labor force who continues to carry out agricultural activities, we should strengthen the skill training in agriculture, such as the cultivation technology of mountain fungi, goats, and cattle. For migrant workers, it was necessary to strengthen employment training in labor export and expand the livelihood channels of poor households [15]. On this basis, the following assumptions were made in this study:

H2: when other factors are controlled, the richer the human capital of herdsman is, the more likely they are to choose to reduce the scale of production.

Social capital is the social resources that herdsman could use to serve their livelihood. The richer the social resources are, the more opportunities and information they could obtain. Financial capital and social resources provided strong support and guarantee for herdsman to develop diversified livelihood activities [13]. The long-term stable trust relationship could strengthen their awareness of grassland protection and promote their common willingness of protecting grassland and reducing the scale of breeding [16]. Based on this, the following assumptions were proposed in this study:

H3: when other factors control, the richer the social capital of herdsman is, the more likely they are to choose to reduce the scale of production.

Material capital is the essential means of production for herdsman maintaining their livelihood. When the material capital is abundant, the family’s livelihood burden would be kept at a low level, and then the scale of livestock would be reduced. For example, Xie et al. [16] pointed out that the herdsman families with relatively large breeding scale, who would initiatively reduce the quantity of livestock and had less economic losses, were more likely to reduce the animal husbandry scale. Based on this, the following assumptions were proposed in this study:

H4: when other factors are controlled, the richer the material capital of herdsman is, the more likely the herdsman are to choose to reduce the production behavior of breeding scale.

Financial capital is the synthesis of all cash and cashable funds in the process of production and consumption. The higher the family income was, the larger the proportion of mutton sheep breeding was, and the lower the possibility of expanding the breeding scale was [3]. The gradual increase of herdsman's family's economic income represented the enhancement of their livelihood level, and the burden of enhancing their livelihood level through traditional animal husbandry would become smaller [17]. According to this, the following assumptions were proposed in this study:

H5: when controlling other factors, the richer the herdsmen's financial capital is, the more likely they are to choose to reduce the scale of production.

2.3. Environmental Cognition and Production Behavior. There was a natural basis for the subject who utilizes resources, but it was more restricted by the society (the group norms, value orientation, cultural tradition, and other aspects). The cognitive differences of the resource utilization theme on social policies and different types of geographical environment had more or less influence on their behavior patterns [11]. In the process of policy cognition, the more herdsmen understood the grassland reward and subsidy policy, the higher their satisfaction with the policy is and the lower the possibility of broadening the breeding scale is. In the ecological cognition, the more fully herdsmen understood the ecological environment of the nearby grassland, the less they would expand the breeding scale [17]. On this basis, the following assumptions are proposed in this study:

H6: when other factors are controlled, the higher the level of environmental cognition is, the more likely the herdsmen are to choose the production behavior of reducing the breeding scale.

3. Description of Data Source and Variable

3.1. Data Source. The data of this study came from the field survey conducted in Wuchuan County and Qinglong County of Guizhou Province from October 2019 to March 2021. The reason why the two places were chosen for the study was that they were the southern modern grassland ecological animal husbandry demonstration counties vigorously built by Guizhou Province. The two local governments had been sticking to the bottom line of ecological development, focusing on the poverty alleviation of industry, strengthening the quality of livestock and poultry products and farmers' benefit, changing the mode of industrial development, and fully promoting the healthy and rapid development of ecological animal husbandry. In this study, 434 households were investigated, including 273

households in Wuchuan County, accounting for 62.9%, and 161 households in Qinglong County, accounting for 37.1%. A total of 434 questionnaires were sent out, of which 384 were valid, with an effective rate of 88.48%.

3.2. Description of Variable

3.2.1. Explained Variables. This study used the statistical method on the change of breeding scale [17] for reference and utilized the change rate of breeding scale to express the breeding scale changes (Breed), recording "a" equal to the number of mutton sheep in 2018 minus the number of mutton sheep in 2017. When "a" was less than -0.2, it showed that the breeding scale had been reduced a lot and assigned 5; when $-0.2 \leq "a" < -0.05$, it represented that the breeding scale had been reduced a little and assigned 4; when $-0.05 \leq "a" < 0$, it showed that the breeding scale had not been changed and assigned 3, and so on.

3.2.2. Explanatory Variables. This study carried out analysis from five different dimensions: material capital, natural capital, human capital, social capital, and financial capital. From the perspective of human capital (Human), the health status, average level of education, and the number of family labor force were selected as the measurement indicators [15]. From the perspective of natural capital (Natural), grassland quality and grassland area were selected as the main measurement indicators [16]. From the perspective of material capital (Mat), the number of mutton sheep, household appliances, housing structure, and the numbers of scientific and technological products were selected as a measure [18]. In terms of social capital (Social), the social network relationship, village cadre experience, and cooperative participation were selected as reference. In terms of financial capital (Finan), this study selected total family income and credit capital as the measure [15, 19].

3.2.3. Control Variables. From the perspective of policy cognition (Policy), it referred to the policy cognition researches [20, 21], covering herdsmen's familiarity with reward and subsidy policies and their satisfaction with relevant policies. For ecological environment cognition (Env), it referred to the definition of environmental cognition researches [22], covering grassland ecological change cognition, and grassland degradation cognition of herdsmen is shown in Table 1.

3.2.4. Empirical Model. The empirical model used in the study is as follows:

$$\text{Breed} = a_0 + a_1 * \text{Human} + a_2 * \text{Natural} + a_3 * \text{Mat} + a_4 * \text{Social} + a_5 * \text{Finan} + \varepsilon, \quad (1)$$

$$\text{Breed} = a_0 + a_1 * \text{Human} + a_2 * \text{Natural} + a_3 * \text{Mat} + a_4 * \text{Social} + a_5 * \text{Finan} + a_6 * \text{Policy} + a_7 * \text{Env} + \varepsilon. \quad (2)$$

TABLE 1: Meaning of relevant variables and statistical results.

Variables	Variable definition and assignment	Mean value	Variance
Change of breeding scale	had been reduced a lot = 5 had been reduced a little = 4 had not been changed = 3 had been increased some = 2 had been increased a lot = 1	2.63	1.37
Gender of interviewee	Male = 1, female = 0	0.39	0.46
Age of interviewee	Age of interviewee	36.58	12.21
Health status of interviewees	“Excellent” = 5 “Good” = 4 “Average” = 3 “Bad” = 2 “Worse” = 1 “Incapacity to work” = 0	1.83	0.91
Education level of the interviewee	“College degree or above” = 5 “High school education” = 4 “Junior high school education” = 3 “Primary school education” = 2 “Illiteracy” = 1	2.09	1.14
Number of family labor force	Number of family labor force	2.52	0.93
Total household income in 2018	(Total household income in 2018 – mean value)/mean value	0.00	0.76
Credit situation	Access to credit: access to loans from commercial banks, rural credit cooperatives, and other organizations	0.12	0.28
Grassland area	Yes = 1; No = 0	4.38	3.76
Grassland quality	Family owned grassland area Excellent = 5 Good = 4 Average = 3 Bad = 2 Worse = 1	1.67	0.95
Number of mutton sheep	Total number of domestic mutton sheep in 2018	108.34	94.52
Housing structure	Soil mixing = 1 Wood mixing = 2 Brick = 3 One floor frame structure = 4 Two floors frame structure = 5	2.26	1.01
Number of household appliances and technology products	One type = 1 Two types = 2 Three types = 3 Four types = 4 Over five types = 5	2.45	2.12
Relationship with relatives and friends	Worse = 1 Bad = 2 General = 3 Good = 4 Very close = 5	3.21	3.48
Experience of village cadres	Yes = 1 No = 0	0.06	0.16
Cooperative participation	Yes = 1 No = 0	0.12	0.41
Policy cognition	Very familiar with the bonus and subsidy policy = 5 Quite understanding = 4 General understanding = 3 Quite not understanding = 2 Have no idea = 1 Satisfaction with grassland subsidy policy, very satisfied = 5 Relatively satisfied = 4 Generally satisfied = 3 Relatively dissatisfied = 2 Disappointed = 1	3.18	2.27
		3.09	1.58

TABLE 1: Continued.

Variables	Variable definition and assignment	Mean value	Variance
Cognition of ecological environment	Fences make the breeding less transferred and make the grassland under great ecological pressure Very disagree = 1 Less agree = 2 Average = 3 Quite agree = 4 Very agree = 5	3.31	2.19

3.3. *Description of Sample.* The basic information of herdsmen is shown in Table 2 via the statistical analysis of 384 limited samples. In the 384 limited samples, the proportion of female samples is relatively large, reaching 66.66%, which might because women were the main labor force of family breeding. From the perspective of herdsmen's age characteristics, about 68% of herdsmen are mainly 30–50 years old, indicating that the family breeding was mainly for middle-aged and young people. In terms of the education level of herdsmen, herdsmen's educational level was generally low. There are more than half of herdsmen with primary school culture and below, while only 95 herdsmen have the culture of high school and above. In terms of the number of mutton sheep breeding, more than half of the herdsmen's families have the number of mutton sheep concentrated in 100–300, accounting for 57.55%. According to the statistics of family income in 2018, the proportion of income in 50000–70000 yuan is the highest, accounting for 40.36%.

4. Process of Empirical Analysis

4.1. *Research Methods.* In this study, 384 valid questionnaires were collected and analyzed by SPSS 23.0, and the impact of material capital, natural capital, human capital, social capital, financial capital, environmental cognition, and relevant measurement indexes on herdsmen's production activities was analyzed by using Stata 14.0 mathematical statistics software and logistic model.

4.2. Empirical Analysis

4.2.1. *Impact of Sustainable Livelihood Capital on Herdsmen's Production Behaviors.* In order to verify the rationality of the hypothesis, the logistic model was used to implement regression analysis of the human capital, social capital, material capital, natural capital, and financial capital in the sustainable livelihood of herdsmen's families, so as to test the impact of various herdsmen families' livelihood capital on herdsmen production behaviors. The regression analysis results are shown in Table 3.

According to the regression results in Table 3, it can be seen that all the sustainable livelihood capital of the family has passed the significance test, which showed that the sustainable livelihood of the family did have an important impact on the production behavior of mutton sheep. It preliminarily verified the previous research's hypothesis and

illustrated that the natural capital variable in the sustainable livelihood had a positive correlation with the improvement of the breeding scale of herdsmen. Meanwhile, the finance capital, social capital, material capital, and human capital all had a positive correlation with limiting herdsmen's breeding scale. The social capital variable of livelihood capital could have the most vital impact on herdsmen's breeding scale output, followed by material capital, while the natural capital had the least impact on herdsmen's breeding scale.

4.2.2. *Regression Analysis of the Sustainable Livelihood of Herdsmen's Families and Environmental Cognitive Level on Herdsmen's Production Behaviors.* The impact of livelihood capital on herdsmen's production behaviors can be seen in Table 3. Next, we utilized Stata 14.0 software to incorporate the environmental cognition of control variables into the model for regression analysis, and the analysis results are shown in Table 4. Model 1 did not include the environmental cognition level of control variables into the analysis results, while model 2 was the results after the environmental cognition level had been included. According to the regression results in Table 4, comparing the results of model 2 with those of model 1, it is obvious that the goodness of fit, logarithmic likelihood, and chi-square values of model 2 are all better than those of model 1, so it is necessary to analyze the regression results of model 2.

- (1) In terms of natural capital, grassland area had a significant positive effect on herdsmen's production behavior of raising breeding scale, and the effect of grassland quality on herdsmen's production behavior had not been verified. The reason for this might be that the size of grassland area was a vital factor affecting the grassland's bearing capacity. If the larger the grassland area owned by herdsmen is, the greater the bearing capacity of their grassland would be, herdsmen might be willing to increase the number of breeding, and the willingness to increase the scale of breeding would become stronger. Because the quality of their own grassland was not compared with other factors through the comparative analysis, there was no clear judgment on the quality of the grassland, so the influence of the quality of the grassland on the production behavior of the herdsmen is not significant, so H1 had been partially verified.

TABLE 2: Basic characteristics of samples.

Characteristics	Sample characteristics classification	Numbers	Proportion (%)
Gender of respondents	Male	128	33.33
	Female	256	66.66
Age of respondents	Less than 30 years old	31	27.12
	30–40 years old	116	30.20
	40–50 years old	145	37.76
	50–60 years old	69	17.97
	Over 60 years old	23	5.99
Education level of respondents	Illiteracy	51	13.28
	Primary school	144	37.50
	Junior high school	94	24.48
	High school	64	16.67
Scale of breeding (number of mutton sheep)	College degree or above	31	8.07
	Less than 100	56	14.58
	100–200	117	30.47
	200–300	104	27.08
	300–400	75	42.45
Family income in 2018	More than 400	32	13.28
	Less than ¥ 1000	11	2.86
	¥ 10000–30000	34	8.85
	¥ 30000–50000	132	34.38
	¥ 50000–70000	155	40.36
	More than ¥ 70000	52	13.54

TABLE 3: The regression results of the sustainable livelihood capital of the family to the scale of breeding.

Variables	Coefficient	Odds ratio	Standard deviation	Z value
Natural capital	2.1625***	11.2943	10.1674	3.21
Human capital	3.0125**	14.6521	13.3692	2.26
Physical capital	3.2618***	24.1203	23.4670	3.25
Financial capital	2.3243***	12.8739	11.5218	2.71
Social capital	3.3267***	27.1824	25.6429	3.39
Constant terms	8.673***	0.0011	0.0011	4.98
Logarithm likelihood value		-232.1246		
Chi-square value		61.2051***		
Pseudo R ²		0.1531		
Sample size		384		

Note. *, **, *** indicate that they have passed the significance test at the statistical level of 10%, 5%, and 1%, respectively.

(2) In terms of human capital, all indicators of human capital had passed the verification, and the number of labor force, education level, and health status had a significant positive impact on herdsmen's choice to reduce breeding scale. The reason might be that the richer the herdsmen's family labor force was, the higher their education level was, the better their health status was, the more herdsmen choose to go out to work in cities, the more optimistic their income would be, and the lower their dependence on the income from animal husbandry would become. In addition, with the deterioration of grassland ecological environment and the continuous reduction of the income from animal husbandry in recent years, herdsmen with rich human capital may choose to restrain the breeding scale in production decision

making so as to reduce their excessive dependence on animal husbandry income so as to improve their living standards by seeking other livelihood channels; thus H2 had been fully verified.

(3) In terms of social capital, cooperative participation, village cadres experience, and social network relationship had significant positive effects on herdsmen's production behavior of reducing breeding scale. Perhaps it was because herdsmen had established close relationship networks with their relatives and friends after years of production activities. These networks could help herdsmen capture market, policy, environment, and other information related to animal husbandry timely and accurately, thus establishing a long-term and stable trust relationship. It was easy to form a common willingness of control breeding scale for protecting grassland and improving ecology. If the herdsman was a village cadre, his production behavior in animal husbandry would play a demonstration role for other herdsmen, especially when he chose to restrain the scale of animal husbandry and reduce the dependence of animal husbandry income. The cooperative members could realize the exchange and sharing of information and resources, and the production behavior of members would be affected by the unified planning, management, and production of cooperatives. And H3 had been fully verified.

(4) In terms of material capital, the number of mutton sheep and housing structure had a significant positive impact on herdsmen's production behavior of reducing breeding scale among the indicators of material capital. The reason might be that the

TABLE 4: Regression results of livelihood capital and environmental cognition measurement indexes on Herdsmen's production behavior.

Variables	Model 1		Model 2		
	Coefficient	OR value	Coefficient	OR value	
Natural capital	Grassland area	0.1241****	0.8524	0.1218**	0.8463
	Grassland quality	0.2672	0.7328	0.2581	0.7134
Physical capital	Quantity of mutton sheep	0.0031***	1.0032	0.0027***	1.003
	Housing structure	0.3216***	1.0035	0.3209***	1.0032
Human capital	Number of household appliances and technology products	-0.0124	0.8946	-0.01232	0.8938
	Number of family labor force	0.3074***	1.2989	0.3185***	1.2996
	Average level of education	0.0618**	1.0639	0.0671**	1.0712
Social capital	Health status	0.0214*	1.0213	0.0219*	1.0239
	Experience of village cadres	0.2689***	0.9241	0.2516***	0.9048
	Cooperative participation	0.3217***	1.3041	0.3025***	1.2897
Financial capital	Social network relationship	0.2864***	1.1431	0.2691***	1.0956
	Family income in 2018	0.1542***	1.2463	0.0857***	1.0925
Control variable	Credit situation	-0.0328	0.8955	0.0249	0.9141
	Policy cognition			0.2416**	1.2861
	Cognition of ecological environment			0.3512***	1.4276
Constant term					-2.4618***
Log likelihood value					-224.1568
Chi-square value					87.9700***
Pseudo R2					0.1681
Sample size					384

Note. *, **, *** indicate that they have passed the significance test at the statistical level of 10%, 5%, and 1%, respectively.

grassland ecology had been deteriorating in recent years, in which the overgrazing of herdsmen was the main cause of grassland degradation. If the number of mutton sheep was relatively large, the possibility of overgrazing would be greater, so the production behavior of reducing the scale of breeding would be actively chosen and the housing structure of herdsmen could fully reflect them. If the housing conditions were good, the livelihood level was good. This kind of situation might be due to the fact that herdsmen's families did not need to rely solely on breeding to obtain the corresponding economic income, and their income channels were diversified, so they would choose to reduce the production behavior of breeding scale, so H4 had been partially verified.

- (5) In terms of financial capital, it was found that only the total household income had passed the test, and other measurement indicators had not been verified, through the analysis of regression results. After analysis, it might be that the level of family income was a direct reflection of herdsmen's livelihood. Herdsmen with higher total family income meant that the less likely they were to over rely on traditional farming, the less likely their farming income would have an impact on the level of family livelihood, so the more likely they were to choose to reduce the number of farms. In addition, herdsmen with higher family income were more willing to enjoy high quality life and excellent grassland ecology, so as to reduce the number of livestock, increase the grassland ecological quality, and improve the quality of life, which was partially verified by H5.

- (6) In terms of environmental cognition level, the policy cognition and ecological environment cognition were used as control variables to analyze in model 2. The results showed that policy cognition and ecological environment cognition had significant positive effects on herdsmen's inhibition of breeding scale. On the one hand, it might be that the scale of mutton sheep breeding had been kept at a relatively high level in recent years. With the full implementation of relevant national award and subsidy policies, the livelihood pressure of herdsmen had been greatly relieved. In addition, the regulatory function of government agencies had resulted in the reduction of the scale of mutton sheep breeding. On the other hand, it might be affected by the national development strategy. At present, the state had made great efforts to build ecological civilization and increase environmental protection. The level of grassland ecological cognition of herdsmen had been significantly improved. The herdsmen with higher ecological cognition had stronger willingness to promote grassland restoration by restraining the scale of breeding, so H5 had been fully verified.

5. Conclusion

Based on the data of 384 herdsmen in Wuchuan and Qinglong of Guizhou Province, this study made an empirical analysis of the impact of environmental awareness and sustainable livelihood capital on Herdsmen's farming activities and finally drew the following conclusions:

- (1) Among the factors influencing herdsmen's choice of production behavior, social capital played the most important role in promoting herdsmen's choice of

reducing the number and scale of breeding and then human capital, material capital, and financial capital, but natural capital had a certain role in promoting herdsmen's production behavior of expanding the scale of breeding.

- (2) Among all kinds of measurement indicators involved in livelihood capital, cooperatives, village cadres, housing structure, livestock breeding scale, the number of labor force, health status, education level, and family income all had significant roles in promoting herdsmen's choice to inhibit the production behavior of breeding scale. The grassland area and grassland quality of natural capital could improve herdsmen's breeding scale remarkably.
- (3) The environmental cognition of herdsmen had significant positive effect on the scale of inhibition. In the measurement indicators of environmental cognition, policy cognition, and ecological environment cognition had vital positive effects on Herdsmen's choice to reduce the breeding scale, so the impact of herdsmen's environmental cognition level on their choice of production behavior could not be ignored.

Based on the above conclusions and discussions, we believe that we should solve the problem of single livelihood of herdsmen, strengthen the publicity and protection of environmental protection knowledge, build a perfect ecological compensation mechanism, let herdsmen share the external benefits of ecological protection, and encourage herdsmen to actively participate in the response of ecological protection behavior.

In addition, this study also has the following limitations, which need to be improved in the future. First, the research data in this paper belong to cross-sectional survey data, which can not dynamically track the research samples and continuously observe the production behavior of herdsmen. Second, this study mainly focuses on the impact of sustainable livelihoods on herdsmen production behavior, but the external institutional environment may also have an important impact, such as business environment and market development degree, which need to be discussed in the future

Data Availability

The data that support the findings of this study are available from the corresponding author upon reasonable request.

Conflicts of Interest

The authors declared no potential conflicts of interest with respect to the research, authorship, and/or publication of this article.

References

- [1] L. Li and H. Guo, "The impact of business relationships on safe production behavior by farmers: evidence from China," *Agribusiness*, vol. 35, no. 1, pp. 84–96, 2019.
- [2] Q. Zhang, Y. Zhao, and F. Y. Li, "Optimal herdsmen household management modes in a typical steppe region of Inner Mongolia, China," *Journal of Cleaner Production*, vol. 231, pp. 1–9, 2019.
- [3] Q. Sun, B. Li, and Z. Sun, "The influence of the difference of cooperative environmental cognition and family endowment on the scale of mutton sheep breeding," *Journal of Chinese animal husbandry*, vol. 54, no. 04, pp. 137–142, 2018.
- [4] Q. Sun, Z. Sun, and T. Liu, "An empirical analysis on the cognition and behavior of herdsmen's grassland ecological protection -- Based on the empirical analysis of 75 natural villages in Tibet," *Journal of Resources and Environment in Arid Area*, vol. 28, no. 08, pp. 26–31, 2014.
- [5] J. Jaitner, N. Corr, and L. Dempfle, "Ownership pattern and management practices of cattle herds in the Gambia: implications for a breeding programme," *Tropical Animal Health and Production*, vol. 35, no. 2, pp. 179–187, 2003.
- [6] W. Ding, S. O. Jimoh, and X. Hou, "Grassland ecological subsidy policy and livestock reduction behavior: a case study of herdsmen in northern China," *Rangeland Ecology & Management*, vol. 81, no. 03, pp. 78–85, 2022.
- [7] Y. Wu, R. Su, L. Xu, Z. Yang, and M. Wang, "Study on the relationship between herdsmen's livelihood capital and Livelihood Strategy-a case study of Xilinhot City and xiwuzhumuqin banner, Inner Mongolia," *Journal of Agro-technical Economics*, vol. 26, pp. 71–77, 2017.
- [8] C. Zhang, Y. Fang, and X. Chen, "Research progress of sustainable livelihood in China based on Bibliometrics," *Advances in Earth Science*, vol. 33, no. 09, pp. 969–982, 2018.
- [9] F. Cui and G. Tang, *Environmental Sociology*, Beijing Normal University Press, Beijing, 2010.
- [10] J. Wang, *Imagination of Environmental Sociology*, Kaili International Consulting Co., Ltd, Taipei, 2004.
- [11] X. Wang, C. Zhao, and H. Zhang, "Environmental cognitive differences and behavioral preferences of farmers and herdsmen in the area of returning grazing land to grassland," *Journal of Yellow River*, vol. 37, no. 4, pp. 94–97, 2015.
- [12] F. Sun, X. Pu, Z. Xu, and L. Wang, "Study on the relationship between livelihood capital and livelihood strategy-- take ganzhou district of zhangye city as an example," *Journal of China Population, Resources and Environment*, vol. 19, no. 06, pp. 119–125, 2009.
- [13] Y. Wang, S. Pan, T. Lu et al., "The impact of livelihood capital on the livelihood activities of herdsmen in the eastern margin of the Qinghai Tibet Plateau and regional differences," *Journal of Resources Science*, vol. 36, no. 10, pp. 2157–2165, 2014.
- [14] Y. Wu, R. Su, L. Xu, Z. Yang, and M. Wang, "A study on the relationship between livelihood capital and livelihood strategy of herdsmen--Take Xilinhot City and xiwuzhumuqin banner in Inner Mongolia as examples," *Journal of Agrotechnical*, no. 07, pp. 71–77, 2007.
- [15] R. He, G. Li, Y. Liu, L. Li, and F. Fang, "Research on analysis method and application of targeted poverty alleviation based on sustainable livelihood-- Taking Liangshan Yi Autonomous Prefecture of Sichuan Province as an example," *Journal of Progress in Geography*, vol. 36, no. 02, pp. 182–192, 2017.
- [16] X. Xie, M. Zhao, and Y. Cai, "Analysis of the influence of livelihood capital on Herdsmen's willingness to reduce livestock-- Micro demonstration based on 372 herdsmen in Inner Mongolia," *Journal of Arid Land Resources & Environment*, vol. 33, no. 06, pp. 55–62, 2019.
- [17] Q. Sun, J. Qiao, and B. Li, "Study on the behavior selection of herdsmen's breeding under the background of ecological

Retraction

Retracted: An Innovative Approach of N -Soft Quotient Topological Space

Advances in Materials Science and Engineering

Received 26 December 2023; Accepted 26 December 2023; Published 29 December 2023

Copyright © 2023 Advances in Materials Science and Engineering. This is an open access article distributed under the Creative Commons Attribution License, which permits unrestricted use, distribution, and reproduction in any medium, provided the original work is properly cited.

This article has been retracted by Hindawi, as publisher, following an investigation undertaken by the publisher [1]. This investigation has uncovered evidence of systematic manipulation of the publication and peer-review process. We cannot, therefore, vouch for the reliability or integrity of this article.

Please note that this notice is intended solely to alert readers that the peer-review process of this article has been compromised.

Wiley and Hindawi regret that the usual quality checks did not identify these issues before publication and have since put additional measures in place to safeguard research integrity.

We wish to credit our Research Integrity and Research Publishing teams and anonymous and named external researchers and research integrity experts for contributing to this investigation.



The corresponding author, as the representative of all authors, has been given the opportunity to register their agreement or disagreement to this retraction. We have kept a record of any response received.

References

- [1] G. K. Antony, M. Lellis Thivagar, B. Tamilarasan, and M. Birhan, "An Innovative Approach of N -Soft Quotient Topological Space," *Advances in Materials Science and Engineering*, vol. 2022, Article ID 4627283, 5 pages, 2022.

Research Article

An Innovative Approach of N -Soft Quotient Topological Space

G. Kabin Antony ¹, M. Lellis Thivagar ¹, B. Tamilarasan,¹ and Mequanint Birhan ²

¹School of Mathematics, Madurai Kamaraj University, Madurai 625021, Tamil Nadu, India

²Department of Mechanical Engineering, Mizan-Tepi University, Tepi, Ethiopia

Correspondence should be addressed to Mequanint Birhan; mequanint@mtu.edu.et

Received 28 February 2022; Revised 15 March 2022; Accepted 22 March 2022; Published 12 April 2022

Academic Editor: Palanivel Velmurugan

Copyright © 2022 G. Kabin Antony et al. This is an open access article distributed under the Creative Commons Attribution License, which permits unrestricted use, distribution, and reproduction in any medium, provided the original work is properly cited.

In the many approaches to soft set theory, the theory of N -soft topological space is a key component of studying topology. The notions of soft mapping in N -soft topological space as well as a novel notion of N -soft continuous mapping, N -soft quotient mapping, and N -soft quotient topology are discussed in this article. We also look at some of its traits and outcomes. It will give the foundation for real-world applications in this subject.

1. Introduction

The theory of soft sets was initiated in 1999, by Molodtsov [1], as a tool of mathematics to deal with uncertainties of problems with incomplete information in many fields like medical sciences, engineering, economics, physics, computer science, and so on. Later, many researchers established the basic structure of the soft set theory. In 2011, Shabir and Naz [2] and Cagman et al. [3] independently initiated the concepts of soft topological spaces, and they defined their basic notions and properties. We study the Cagman method to develop the theory of soft topological space.

Recently, in 2016, Thivagar et al. [4] introduced and established the theory of N -topological space from the geometric existence of topological space. Also, they derived various forms of quotient topology from quotient mappings [5]; in particular, they defined α -quotient mappings, strongly α -quotient mappings, and α^* -quotient mappings between topological spaces. Many researchers established the basic study of quotient topology [6–8].

Later, we expand the idea of soft topological space to N -soft topological space and investigate their fundamental features using appropriate examples. We investigate the concepts of N -soft continuous mapping and N -soft quotient mapping in N -soft topological space in this research. N -soft quotient mapping is also used to

create the notions of N -soft quotient topology. In addition, we look at the characterization of the N -soft continuous and N -soft quotient mappings. Finally, we apply these ideas to N -soft topology's probable attributes.

2. Preliminaries

Now we would like to present some basic notions of soft set theory, soft image, soft inverse image, N -soft topology, and N -soft topological subspace.

Definition 1 (see [1]). A soft set F_A on the universe U is defined by the set of ordered pairs $F_A = \{(x, f(x)) : x \in E, f_A(x) \in P(U)\}$, where $f_A: E \rightarrow P(U)$ such that $f_A(x) = \phi$ if $x \in A$. Here, f_A is called an approximation function of the soft set F_A . The value of $f_A(x)$ may be arbitrary. Some of them may be empty, and some may have nonempty intersection. The set of all soft sets over U will be denoted by $S(U)$.

Definition 2 (see [3]). Let $F_A \in S(U)$. The soft power set of F_A is defined by $\tilde{P}(F_A) = \{F_{A_i} : F_{A_i} \subseteq F_A, i \in I \subseteq \mathbb{N}\}$, and its cardinality is defined by $|\tilde{P}(F_A)| = 2^{\sum_{x \in E} |f_A(x)|}$ where $|f_A(x)|$ is the cardinality of $f_A(x)$.

Definition 3. Let $F_A \in S(U)$, $\tilde{\tau}_1, \tilde{\tau}_2, \dots, \tilde{\tau}_N$ be N -arbitrary soft topologies defined on F_A and the collection $N_{\tilde{\tau}}$ be defined by

$$N_{\tilde{\tau}} = \left\{ \tilde{S} \subseteq F_A : \tilde{S} = \left(\bigcup_{i=1}^n \widetilde{F_{A_i}} \right) \widetilde{\bigcup_{i=1}^n F_{B_i}}, \quad F_{A_i}, F_{B_i} \in \tilde{\tau}_i \right\}, \quad (1)$$

satisfying the following axioms:

- (i) $F_\phi, F_A \in N_{\tilde{\tau}}$.
- (ii) $\bigcup_{i=1}^{\infty} \tilde{S}_i \in N_{\tilde{\tau}}$ for all $S_i \in N_{\tilde{\tau}}$.
- (iii) $\bigcap_{i=1}^n \tilde{S}_i \in N_{\tilde{\tau}}$ for all $S_i \in N_{\tilde{\tau}}$.

Then, the pair $(F_A, N_{\tilde{\tau}})$ is called a N -soft topological space on F_A , denoted by $N_{\tilde{\tau}_f}$. The elements of the collection $N_{\tilde{\tau}}$ are known as N -soft open sets on F_A and the complement of N -soft open on F_A is known as N -soft closed sets.

Definition 4. Let $(F_A, N_{\tilde{\tau}})$ be a N -soft topological space and $G_B \subseteq F_A$. Then, the collection $N_{\tilde{\tau}} = \{H \cap G_B : H \in N_{\tilde{\tau}}\}$ is called a N -soft subspace topological space on G_B and $(G_B, N_{\tilde{\tau}})$ or $N_{\tilde{\tau}_g}$ is called a N -soft topological subspace of $(F_A, N_{\tilde{\tau}})$.

Definition 5 (see [9]). Let (X, E) and (Y, E') be soft classes. Let $u: X \rightarrow Y$ and $p: E \rightarrow E'$ be mappings. Then, a mapping $f: (X, E) \rightarrow (Y, E')$ is defined as follows: for a soft set (F, A) in (X, E) , $(f(F, A), B)$, $B = p(A) \subseteq E'$, is a soft set (Y, E') given by

$$f(F, A)(\beta) = \begin{cases} u\left(\bigcup_{\alpha \in p^{-1}(\beta) \cap A} F(\alpha)\right) & \text{if } p^{-1}(\beta) \cap A \neq \phi, \\ \phi, & \text{otherwise} \end{cases}, \quad (2)$$

for $\beta \in B \subseteq E'$. $(f(F, A), B)$ is called a soft image of a soft set (F, A) .

Definition 6 (see [9]). Let (X, E) and (Y, E') be mappings from a soft class (X, E) to another soft class (Y, E') and (G, C) be a soft set in soft class (Y, E') , where $C \subseteq E'$. Let $u: X \rightarrow Y$ and $p: E \rightarrow E'$ be mappings. Then, $(f^{-1}(G, C), D)$, $D = p^{-1}(C)$, is a soft set in the soft class (X, E) , defined as

$$f^{-1}(G, C)(\alpha) = \begin{cases} u^{-1}(G(p(\alpha))), & \text{if } p(\alpha) \in C \\ \phi, & \text{otherwise} \end{cases}, \quad (3)$$

for $\alpha \in D \subseteq E$. $(f^{-1}(G, C), D)$ is called a soft inverse image of (G, C) . Hereafter we shall write $(f^{-1}(G, C), E)$ as $f^{-1}(G, C)$.

3. N-Soft Continuous and N-Soft Quotient Mappings

In this section, we define the notion of N -soft continuous and N -soft quotient mappings and their characterization.

Definition 7. Let (F_X, E) and (F_Y, K) be soft sets on U and V , respectively. A mapping $f: (F_X, N_{\tilde{\tau}}, E) \rightarrow (F_Y, N_{\tilde{\sigma}}, K)$ is said to be N -soft mapping if $(F_X, N_{\tilde{\tau}}, E)$ and $(F_Y, N_{\tilde{\sigma}}, K)$ are N -soft topological spaces, and $u: U \rightarrow V$ and $v: E \rightarrow K$ are mappings.

Throughout this work, we represent the space $(F_X, N_{\tilde{\tau}}, E)$ as $\tilde{\mathfrak{F}}_X$ and the space $(F_Y, N_{\tilde{\sigma}}, K)$ as $\tilde{\mathfrak{F}}_Y$.

Definition 8. A soft mapping $f: \tilde{\mathfrak{F}}_X \rightarrow \tilde{\mathfrak{F}}_Y$ is said to be N -soft continuous if the inverse image of every N -soft open of $\tilde{\mathfrak{F}}_Y$ is N -soft open in $\tilde{\mathfrak{F}}_X$.

Example 1. Let the universe $U = \{w_1, w_2, w_3, w_4, w_5, w_6\}$ and the parameters $E = \{x_1, x_2, x_3, x_4\}$. Let $X = \{x_2, x_3, x_4\} \subseteq E$ and $F_X = \{(x_2, \{w_1, w_3\}), (x_3, \{w_5\}), (x_4, \{w_2, w_6\})\}$. Then, all the soft subsets of F_X are

$$\begin{aligned} F_{X_1} &= \{(x_2, \{w_1\})\}, \\ F_{X_2} &= \{(x_2, \{w_3\})\}, \\ F_{X_3} &= \{(x_2, \{w_1, w_3\})\}, \\ F_{X_4} &= \{(x_3, \{w_5\})\}, \\ F_{X_5} &= \{(x_2, \{w_1\}), (x_3, \{w_5\})\}, \\ F_{X_6} &= \{(x_2, \{w_3\}), (x_3, \{w_5\})\}, \\ F_{X_7} &= \{(x_2, \{w_1, w_3\}), (x_3, \{w_5\})\}, \\ F_{X_8} &= \{(x_4, \{w_2\})\}, \\ F_{X_9} &= \{(x_4, \{w_6\})\}, \\ F_{X_{10}} &= \{(x_4, \{w_2, w_6\})\}, \\ F_{X_{11}} &= \{(x_2, \{w_1\}), (x_4, \{w_2\})\}, \\ F_{X_{12}} &= \{(x_2, \{w_3\}), (x_4, \{w_2\})\}, \\ F_{X_{13}} &= \{(x_2, \{w_1, w_3\}), (x_4, \{w_2\})\}, \\ F_{X_{14}} &= \{(x_3, \{w_5\}), (x_4, \{w_2\})\}, \\ F_{X_{15}} &= \{(x_2, \{w_1\}), (x_3, \{w_5\}), (x_4, \{w_2\})\}, \\ F_{X_{16}} &= \{(x_2, \{w_3\}), (x_3, \{w_5\}), (x_4, \{w_2\})\}, \\ F_{X_{17}} &= \{(x_2, \{w_1, w_3\}), (x_3, \{w_5\}), (x_4, \{w_2\})\}, \\ F_{X_{18}} &= \{(x_2, \{w_1\}), (x_4, \{w_6\})\}, \\ F_{X_{19}} &= \{(x_2, \{w_3\}), (x_4, \{w_6\})\}, \\ F_{X_{20}} &= \{(x_2, \{w_1, w_3\}), (x_4, \{w_6\})\}, \\ F_{X_{21}} &= \{(x_3, \{w_5\}), (x_4, \{w_6\})\}, \\ F_{X_{22}} &= \{(x_2, \{w_1\}), (x_3, \{w_5\}), (x_4, \{w_6\})\}, \\ F_{X_{23}} &= \{(x_2, \{w_3\}), (x_3, \{w_5\}), (x_4, \{w_6\})\}, \\ F_{X_{24}} &= \{(x_2, \{w_1, w_3\}), (x_3, \{w_5\}), (x_4, \{w_6\})\}, \\ F_{X_{25}} &= \{(x_2, \{w_1\}), (x_4, \{w_2, w_6\})\}, \\ F_{X_{26}} &= \{(x_2, \{w_3\}), (x_4, \{w_2, w_6\})\}, \\ F_{X_{27}} &= \{(x_2, \{w_1, w_3\}), (x_4, \{w_2, w_6\})\}, \\ F_{X_{28}} &= \{(x_3, \{w_5\}), (x_4, \{w_2, w_6\})\}, \\ F_{X_{29}} &= \{(x_2, \{w_1\}), (x_3, \{w_5\}), (x_4, \{w_2, w_6\})\}, \\ F_{X_{30}} &= \{(x_2, \{w_3\}), (x_3, \{w_5\}), (x_4, \{w_2, w_6\})\}, \\ F_{X_{31}} &= F_X, \\ F_{X_{32}} &= \phi. \end{aligned} \quad (4)$$

Let $\tilde{\tau}_1 = \{\phi, F_X, F_{X_3}, F_{X_7}\}$ and $\tilde{\tau}_2 = \{\phi, F_X, F_{X_4}, F_{X_7}\}$ be two soft topologies. Then, $2\tilde{\tau} = \{\phi, F_X, F_{X_3}, F_{X_4}, F_{X_7}\}$ is a bi-soft topology on F_X .

Let another universe $V = \{h_1, h_2, h_3, h_4, h_5\}$ and the parameters $K = \{x'_1, x'_2, x'_3, x'_4\}$. Let $Y = \{x'_1, x'_2, x'_4\} \subseteq K$ and $F_Y = \{(x'_2, \{h_1\}), (x'_4, \{h_3, h_4\})\}$.

Then, all the soft subsets of F_Y are

$$\begin{aligned}
 F_{Y_1} &= \{(x'_1, \{h_2\})\}, \\
 F_{Y_2} &= \{(x'_2, \{h_1\})\}, \\
 F_{Y_3} &= \{(x'_1, \{h_2\}), (x'_2, \{h_1\})\}, \\
 F_{Y_4} &= \{(x'_4, \{h_3\})\}, \\
 F_{Y_5} &= \{(x'_4, \{h_4\})\}, \\
 F_{Y_6} &= \{(x'_4, \{h_3, h_4\})\}, \\
 F_{Y_7} &= \{(x'_1, \{h_2\}), (x'_4, \{h_3\})\}, \\
 F_{Y_8} &= \{(x'_1, \{h_2\}), (x'_4, \{h_4\})\}, \\
 F_{Y_9} &= \{(x'_2, \{h_1\}), (x'_4, \{h_3\})\}, \\
 F_{Y_{10}} &= \{(x'_2, \{h_1\}), (x'_4, \{h_4\})\}, \\
 F_{Y_{11}} &= \{(x'_1, \{h_2\}), (x'_4, \{h_3, h_4\})\}, \\
 F_{Y_{12}} &= \{(x'_1, \{h_2\}), (x'_4, \{h_3, h_4\})\}, \\
 F_{Y_{13}} &= \{(x'_1, \{h_2\}), (x'_2, \{h_1\}), (x'_4, \{h_3\})\}, \\
 F_{Y_{14}} &= \{(x'_1, \{h_2\}), (x'_2, \{h_1\}), (x'_4, \{h_4\})\}, \\
 F_{Y_{15}} &= F_Y, \\
 F_{Y_{16}} &= \phi.
 \end{aligned} \tag{5}$$

Let $\tilde{\sigma}_1 = \{\phi, F_Y, F_{Y_2}, F_{Y_{12}}\}$ and $\tilde{\sigma}_2 = \{\phi, F_Y, F_{Y_6}, F_{Y_{11}}\}$ be two soft topologies. Then, $2\tilde{\sigma} = \{\phi, F_Y, F_{Y_2}, F_{Y_6}, F_{Y_{11}}, F_{Y_{12}}\}$ is a bi-soft topology on F_Y .

Define mappings $u: U \rightarrow V$ and $v: E \rightarrow K$. $u(w_1) = \{h_1\}, u(w_2) = \{h_4\}, u(w_3) = \{h_1\}, u(w_4) = \{h_3\}, u(w_5) = \{h_2\}, u(w_6) = \{h_3\}$ and $v(x_1) = \{x'_3\}, v(x_2) = \{x'_2\}, v(x_3) = \{x'_1\}, v(x_4) = \{x'_3\}$. The bi-soft inverse image is $f^{-1}(F_Y, Y)x_2 = u^{-1}(F_Y(P(x_2))) = u^{-1}(F_Y(x'_2)) = u^{-1}(\{h_1\}) = \{w_1, w_3\}$, $f^{-1}(F_Y, Y)x_3 = u^{-1}(F_Y(x'_1)) = \{w_5\}$, where $D = p^{-1}(Y) = \{x_2, x_3\}$, and thus we have that bi-soft inverse image $f^{-1}(F_Y, Y)D = \{(x_2, \{w_1, w_3\}), (x_3, \{w_5\})\}$ is bi-soft open. Hence, the given soft mapping is bi-soft continuous mapping.

Definition 9. Let $\tilde{\mathfrak{F}}_X$ and $\tilde{\mathfrak{F}}_Y$ be N -soft topological spaces and let $f: F_X \rightarrow F_Y$ be a surjective map. Then, f is said to be a N -soft quotient map if a N -soft subset A of $\tilde{\mathfrak{F}}_Y$ is N -soft open if and only if $f^{-1}(A)$ is N -soft open in $\tilde{\mathfrak{F}}_X$.

Example 2. Consider the soft set of F_X and F_Y from Example 1. Let $\tilde{\tau}_1 = \{\phi, F_X, F_{X_3}, F_{X_{27}}\}$, $\tilde{\tau}_2 = \{\phi, F_X, F_{X_4}, F_{X_{28}}\}$, and $\tilde{\tau}_3 = \{\phi, F_X, F_{X_4}, F_{X_{10}}, F_{X_{28}}\}$ be three soft topologies. Then, $3\tilde{\tau} = \{\phi, F_X, F_{X_3}, F_{X_4}, F_{X_{10}}, F_{X_{27}}, F_{X_{28}}\}$ is a tri-soft topology on F_X and let $\tilde{\sigma}_1 = \{\phi, F_X, F_{Y_1}, F_{Y_{11}}\}$, $\tilde{\sigma}_2 = \{\phi, F_X, F_{Y_2}, F_{Y_{12}}\}$, and $\tilde{\sigma}_3 = \{\phi, F_X, F_{Y_6}, F_{Y_{12}}\}$ be three

soft topologies. Then, $3\tilde{\sigma} = \{\phi, F_X, F_{Y_2}, F_{Y_6}, F_{Y_{11}}, F_{Y_{12}}\}$ is a tri-soft topology on F_Y .

Define mappings $u: U \rightarrow V$ and $v: E \rightarrow K$. $u(w_1) = \{h_2\}, u(w_2) = \{h_3\}, u(w_3) = \{h_2\}, u(w_4) = \{h_5\}, u(w_5) = \{h_1\}, u(w_6) = \{h_4\}$ and $v(x_1) = \{x'_3\}, v(x_2) = \{x'_1\}, v(x_3) = \{x'_2\}, v(x_4) = \{x'_4\}$. The tri-soft inverse image is $f^{-1}(F_Y, Y)x_2 = u^{-1}(F_Y(x'_1)) = u^{-1}(\{h_2\}) = \{w_1, w_3\}$, $f^{-1}(F_Y, Y)x_3 = u^{-1}(F_Y(x'_2)) = u^{-1}(\{h_1\}) = \{w_5\}$, $f^{-1}(F_Y, Y)x_4 = u^{-1}(F_Y(x'_4)) = u^{-1}(\{h_3, h_4\}) = \{w_2, w_6\}$ where $D = p^{-1}(Y) = \{x_2, x_3, x_4\}$, and thus we have that tri-soft inverse image $f^{-1}(F_Y, Y)D = \{(x_2, \{w_1, w_3\}), (x_3, \{w_5\}), (x_4, \{w_2, w_6\})\}$ is tri-soft open and the tri-soft image is $f((F_X, X)x'_1) = u(\bigcup F(x_2)) = u(w_1, w_3) = \{h_2\}$, $f((F_X, X)x'_2) = u(\bigcup F(x_3)) = u(w_5) = \{h_1\}$, $f((F_X, X)x'_4) = u(\bigcup F(x_4)) = u(w_2, w_6) = \{h_3, h_4\}$ where $B = P(X) = \{x'_1, x'_2, x'_4\}$. Thus, the tri-soft image $f((F_X, X)D) = \{(x'_1, \{h_2\}), (x'_2, \{h_1\}), (x'_4, \{h_3, h_4\})\}$ is also a tri-soft open. So, the given soft mapping is tri-soft quotient mapping.

Theorem 1. Let $f: \tilde{\mathfrak{F}}_X \rightarrow \tilde{\mathfrak{F}}_Y$ be a relation preserving, N -quotient map. Then, the map $f^*: (F_X/R, N_{\tilde{\tau}}^-, E) \rightarrow (F_Y/R', N_{\tilde{\sigma}}^-, K)$ given by $f^*(A) = |f(A)|$ for every $A \in F_X/R$ is also a quotient map.

Proof. The N -soft quotient topology $N_{\tilde{\tau}}^-$ on F_X/R is given by $N_{\tilde{\tau}}^- = \{U \subseteq F_X/R: p^{-1}(U) \in N_{\tilde{\tau}}\}$ where $p: F_X \rightarrow F_X/R$ is the project mapping. Similarly, the N -soft quotient topology $N_{\tilde{\sigma}}^-$ on F_Y/R' is given by $N_{\tilde{\sigma}}^- = \{V \subseteq F_Y/R': q^{-1}(V) \in N_{\tilde{\sigma}}\}$ where $q: F_Y \rightarrow F_Y/R'$ is the projection mapping. Since f is relation preserving and N -soft continuous, f^* is N -soft continuous. That is, whenever a soft subset $U \subseteq F_Y/R'$ is N -soft open, $(f^*)^{-1}(U)$ is N -soft open in F_X/R . If $U \subseteq F_Y/R'$ such that $(f^*)^{-1}(U)$ is N -soft open in F_X/R ; then, $p^{-1}((f^*)^{-1}(U))$ is N -soft open in F_X . That is, $(f^*)^{-1}(U)$ is N -soft open in F_X . $(q \circ f)^{-1}(U)$ is N -soft open in F_X . That is, $f^{-1}(q^{-1}(U))$ is N -soft open in F_X and $q^{-1} \subseteq F_Y$. Therefore, $q^{-1}(U)$ is N -soft open $(F_Y, N_{\tilde{\sigma}}^-)$, since f is a N -soft quotient mapping. That is, $q^{-1}(U) \in N_{\tilde{\sigma}}^-$, and hence $U \in N_{\tilde{\sigma}}^-$. That is, U is N -soft open in F_Y/R' . Thus, a soft subset U is N -soft open in F_Y/R' if and only if $(f^*)^{-1}(U)$ is N -soft open in F_X/R . Therefore, f^* is a N -soft quotient map. \square

Theorem 2. Let $p: F_X \rightarrow F_Y$ be a N -soft quotient map; let A be a soft subspace of F_X , that is, N -saturated with respect to p ; let $q: A \rightarrow p(A)$ be the map obtained by restricting p .

- (i) If A is either a N -soft open map or a N -soft closed map, then q is a N -soft quotient map.
- (ii) If p is either a N -soft open map or a N -soft closed map, then q is a N -soft quotient map.

Proof

- (i) We shall prove the following:

- (a) $q^{-1}(V) = p^{-1}$ if $V \subseteq p(A)$.
- (b) $p(U \cap A) = p(U) \cap p(A)$ if $U \subseteq F_X$.

To prove (i) of (a), first let us assume that $V \widetilde{\subset} P(A)$ and A is N -saturated, $p^{-1}(V) \widetilde{\subset} A$. It implies that both $p^{-1}(V)$ and $q^{-1}(V)$ equal all points of A that are mapped by p into V . To examine the second equation, we observe that for any two soft subsets U and \widetilde{A} of F_X , we have the inclusion $p(U \widetilde{\cap} A) \widetilde{\subset} p(U) \widetilde{\cap} p(A)$. To verify the contrary, suppose $y = p(u) = p(a)$, for $u \in U$ and $a \in A$. Since A is N -saturated, A contains $p^{-1}(p(a))$, so that $A \widetilde{\subset} U$. Then, $y = p(u)$, where $u \in U \widetilde{\cap} A$.

To prove (i) of (b), let us suppose A is N -soft open or p is N -soft open. Given the soft subset V of $p(A)$, we assume that $q^{-1}(V)$ is N -soft open in A and show that V is N -soft open in $p(A)$. Suppose first that A is N -soft open. Since $q^{-1}(V)$ is N -soft open in A and A is N -soft open in F_X , the soft set $q^{-1}(V)$ is N -soft open in F_X . Since $q^{-1}(V) = p^{-1}(V)$, the latter set is N -soft open in F_X , so that V is N -soft open in F_Y because p is a N -soft quotient map. In particular, V is N -soft open in $p(A)$. Now suppose p is N -soft open. Since $q^{-1}(V) = p^{-1}(V)$ and $q^{-1}(V)$ is N -soft open in A , we have $p^{-1}(V) = U \widetilde{\cap} A$ for some soft set U , N -soft open in F_X (F_X be a soft set on the universe U). Now, $p(p^{-1}(V)) = V$ because p is surjective; then, $V = p(p^{-1}(V)) = p(U \widetilde{\cap} A) = p(U) \widetilde{\cap} p(A)$. The soft set $p(U)$ is N -soft open in F_Y because p is an N -soft open map; hence, V is N -soft open in $p(A)$.

- (ii) When A or p is N -soft closed, this may be demonstrated by substituting N -soft open with N -soft closed in step (i) of the proof (b). \square

4. N -Soft Quotient Topology

Here, we discuss the concept of N -soft quotient topological space from N -soft quotient mapping and their properties along with N -soft continuous mapping.

Definition 10. Let $\widetilde{\mathfrak{F}}_X$ be a N -soft quotient topological space. Let F_Y be a nonempty soft set and $f: F_X \rightarrow F_Y$ be a surjective map. Then, defined $N_\sigma = \{G \widetilde{\subset} F_Y: f^{-1}(G) \text{ is open in } N_\tau\}$ is a N -soft topology on F_Y relative to which f is a N -soft quotient topology on F_Y induced by f .

Definition 11. Let $\widetilde{\mathfrak{F}}_X$ be a N -soft topology and R be an equivalence relation on F_X . Let $P: F_X \rightarrow F_X/R: P(x) = [x] \forall x \in F_X$; then, the family F_X/R with N -soft quotient topology is called N -soft quotient space.

Remark 1. N -soft quotient topology for F_X/R is the strongest N -soft topology for which P is continuous, and this N -soft topology is given by $N_{\tau_p} = \{H \in F_X/R\}$; then, $P^{-1}(H) \in N_\tau$.

Theorem 3. Let $\widetilde{\mathfrak{F}}_X$ be a N -soft topological space and let F_Y be a nonempty soft set. Let $f: F_X \rightarrow F_Y$ be a N -soft quotient map. Then, the N -soft quotient topology F_X on F_Y induced by f is a N -soft topology.

Proof. We shall verify each of the three conditions for a topology:

- (i) The soft set $f^{-1}(\phi) = \phi$, which is N_τ -soft open in F_X . $f^{-1}(F_Y) = F_X$, which is N_τ -soft open in F_X . So, ϕ and F_Y are N_τ -soft open in the N -soft quotient topology.
- (ii) Suppose each of the soft sets in the collection $\{G_\beta\}_{\beta \in B}$ is N_τ -soft open in the N -soft quotient topology on F_Y . Then, $f^{-1}(\bigcup (G_\beta)) = \bigcup f^{-1}(G_\beta)$, which is a union of N_τ -soft open sets in F_X , and therefore it is N_τ -soft open in F_X . Thus, $\bigcup (G_\beta)$ is N_τ -soft open in the N -soft quotient topology, which implies that the arbitrary union of N_τ -soft open sets in the N -soft quotient topology is a N_τ -soft open set in the N -soft quotient topology.
- (iii) Suppose each of the soft sets G_i , $i = 1, 2, \dots, n$, is N_τ -soft open in the N -soft quotient topology on F_Y . Then, $f^{-1}(\bigcap G_i) = \bigcap f^{-1}(G_i)$, which is a finite intersection of N_τ -soft open sets in F_X , and therefore it is N_τ -soft open in F_X . Hence, $\bigcap G_i$ is N_τ -soft open in the N -soft quotient topology, and it follows that the finite intersection of open sets in the N -soft quotient topology is N_τ -soft open set. Hence, the N -soft quotient topology is a topology on F_Y . \square

Theorem 4. If f is a N -soft continuous and N -soft open mapping of a N -soft topological space $\widetilde{\mathfrak{F}}_X$ onto a N -soft topological space $\widetilde{\mathfrak{F}}_Y$, then N_σ must be the N -soft quotient topology for F_Y .

Proof. Let N_{τ_f} denote the N -soft quotient topology for F_Y . Since the N -soft quotient topology is the largest for which f is N -soft continuous, $N_\sigma \widetilde{\subset} N_{\tau_f}$. Again let $H \in N_{\tau_f}$; then, $f^{-1}(H) \in N_\tau$. Since f is N -soft open, it follows that $f[f^{-1}(H)] \in N_\sigma$, i.e., $H \in N_\sigma$ (since f is onto). Thus, $H \in N_{\tau_f} \Rightarrow H \in N_\sigma$, i.e., $N_{\tau_f} \widetilde{\subset} N_\sigma$. Hence, $N_\sigma = N_{\tau_f}$, the N -soft quotient topology on F_Y . \square

Theorem 5. Let f be a N -soft continuous mapping of a N -soft topological space F_X onto a N -soft topological space F_Y and let F_Y have a N -soft quotient topology. Then, a mapping g from F_Y onto a space N_τ is N -soft continuous if and only if the composite mapping $g \circ f$ is N -soft continuous.

Proof. Assume the mapping $g: F_Y \rightarrow N_\tau$ to be N -soft continuous. The soft mapping $f: F_X \rightarrow F_Y$ is N -soft continuous, and since the composite of N -soft continuous mapping is composite, $g \circ f$ is N -soft continuous as well. Conversely, let $g \circ f$ be N -soft continuous and let H be a N -soft open subset of N_τ . Then, $(g \circ f)^{-1}(H) = (f^{-1} \circ g^{-1})(H) = f^{-1}[g^{-1}(H)]$, which is N -soft open in F_X because of the N -soft continuity of $g \circ f$. By Definition 8, it follows that $g^{-1}(H)$ is a N -soft open subset of F_Y . Hence, g is N -soft continuous. \square

Retraction

Retracted: Study on the Relationship between Conspicuous Need and Group Cultural Identity of Fashion Cultural Consumption

Advances in Materials Science and Engineering

Received 26 December 2023; Accepted 26 December 2023; Published 29 December 2023

Copyright © 2023 Advances in Materials Science and Engineering. This is an open access article distributed under the Creative Commons Attribution License, which permits unrestricted use, distribution, and reproduction in any medium, provided the original work is properly cited.

This article has been retracted by Hindawi, as publisher, following an investigation undertaken by the publisher [1]. This investigation has uncovered evidence of systematic manipulation of the publication and peer-review process. We cannot, therefore, vouch for the reliability or integrity of this article.

Please note that this notice is intended solely to alert readers that the peer-review process of this article has been compromised.

Wiley and Hindawi regret that the usual quality checks did not identify these issues before publication and have since put additional measures in place to safeguard research integrity.

We wish to credit our Research Integrity and Research Publishing teams and anonymous and named external researchers and research integrity experts for contributing to this investigation.

The corresponding author, as the representative of all authors, has been given the opportunity to register their agreement or disagreement to this retraction. We have kept a record of any response received.

References

- [1] L. Zhao, Y. Duan, Q. Wang et al., "Study on the Relationship between Conspicuous Need and Group Cultural Identity of Fashion Cultural Consumption," *Advances in Materials Science and Engineering*, vol. 2022, Article ID 3541548, 9 pages, 2022.

Research Article

Study on the Relationship between Conspicuous Need and Group Cultural Identity of Fashion Cultural Consumption

Liang Zhao,¹ Yunze Duan,² Qiang Wang,³ Ke Zhou,⁴ Nailin Gu,⁵ Xiangzhong Li,¹ and Jingyu Dai ⁶

¹College of Humanities, Han-Liang Cultural Research Center, Shangqiu Normal University, Shangqiu 476000, Henan, China

²School of Communication, Shangqiu Normal University, Shangqiu 476000, Henan, China

³College of Foreign Languages and Tourism, Liming Vocational University, Quanzhou 362000, Fujian, China

⁴China Private Education Museum, Yellow River Institute of Science and Technology, Zhengzhou 450000, Henan, China

⁵School of Management, Suqian University, Suqian 223700, Jiangsu, China

⁶College of Art Design and Media, Sanda University, Shanghai 201209, China

Correspondence should be addressed to Jingyu Dai; yjdai@sandau.edu.cn

Received 17 February 2022; Revised 1 March 2022; Accepted 7 March 2022; Published 27 March 2022

Academic Editor: Palanivel Velmurugan

Copyright © 2022 Liang Zhao et al. This is an open access article distributed under the Creative Commons Attribution License, which permits unrestricted use, distribution, and reproduction in any medium, provided the original work is properly cited.

The consumption of sports and leisure apparel has distinct historical characteristics. It is linked to social fashion and fashion trends, which is an internal expression of college students' perceptions of sports connotation, aesthetic taste, and community affiliation. Furthermore, it serves as a vital link and conduit for college students' perceptions of sports fashion. This research includes fieldwork in a sportswear briefing and a thorough interview with 15 interviewees. This research builds an analytical framework for the relationship between sports, leisure clothes, and college students' consumption behavior based on the conspicuous consumption theory. This article examines the relationship and influence between college students' consumption behavior and sports and leisure clothing consumption in three categories of community affiliation, perceived value, and consumption behavior. According to the findings, college students' consuming activity shows off their affluence to a certain extent. But, at its core, college students' consumption is about understanding society and constructing their self-image. As a result, it reflects the changing value orientation of today's Chinese college students' purchasing habits. According to the research, it shows the importance of sports leisure apparel consuming behavior is rooted not only in the clothing but also in community identity.

1. Introduction

Sports clothing culture is a branch of sports culture. Sports clothing can be divided into professional sports clothing, leisure sports clothing, and sports leisure clothing. The characteristics of sports and leisure clothing are as follows: comfortable for daily leisure sports, simple and convenient for daily life leisure fitness and design, etc. It is found that sports account for 73.3% of leisure activities and sports leisure is becoming more and more popular in the current leisure industry. In recent years, sports and fitness have continued to become the most respected fashion trend in many countries and even in the world. The emergence of sports as a way of leisure is the product of social civilization.

It promotes the development of related industries, produces related consumption forms, and cultivates the development of related disciplines. As an important part of the relevant industrial chain, the garment industry has huge market potential.

China's fully open three-child policy will effectively promote the growth of the sportswear market. According to Euromonitor, a market research company, China's sportswear market will surpass the luxury market by 2022 and have a double-digit growth per year until 280.8 billion yuan. In the same period, the luxury market will only grow by single digits until 192.4 billion yuan per year. In contrast, the size of the European sportswear market will reach US \$64 billion by 2020. The group of college students in China continues to

expand with university enrollment expansion. By 2021, the number of college students has exceeded 40 million. The retail industry for college students is emerging one after another, and the fixed groups also provide many opportunities for the development of sportswear. On the other hand, the consumption power of college students is stable, and the market share has exceeded 200 billion yuan. Therefore, most of the development of Chinese national clothing brands are inseparable from the communication of college students. As a huge consumer group, college students are rising rapidly. Their preferences, psychological personality, consumption habits, and characteristics will affect the trend and development of our times.

2. Literature Review

Sports is an increasingly remarkable activity with the development of human civilization, abundant substance, and spirit development [1]. Clothing is the product of behavior development through dress, shoes, hats, and self-dress. Since its birth, sports and leisure clothing is a kind of interpersonal communication, nonverbal message transmission symbol, which has a special significance [2, 3]. Sports and leisure clothing is the art carrier that organically integrates sports and leisure culture with clothing culture, which has practicability and fashion.

The concept of “sportswear” first appeared in the eighteenth century. The industrial revolution promoted the development of the western economy. As a result, the aristocracy was richer and had more time and money to spend on sports, so they paid more and more attention to sports. The rise of sports promoted the generation and development of sports clothing. In 1711, Queen Anne built the racecourse, so hunting and racing became adventurous sports. At the time, the social class regarded such activities are participated by the upper class. This prompted Westerners to ritualize sports events and treat sports venues as social occasion [4]. During this period, “sportswear” was a single functional garment created for upper-class popular sports. These sports include tennis, golf, cycling, swimming, skating, yachts, and hunting. At the beginning of the nineteenth century, Western societies experienced a golden age of great development and prosperity of competitive and outdoor sports [5]. In the late nineteenth century, with the further development and innovation of industry, more and more dangerous athletic activities were also included in sports. In the West, special attention was paid to the credibility of the contestants because participants were mainly aristocracies. The noble gentleman style is popular in the west, which has an extremely sacred position in the hearts of the British [6].

Fashion media earlier noticed the birth of a new fashion, and they created an elegant title “Audience Sports Style” in 1928 [7]. In the 1930s, the clothing industry officially named it “Sportswear” and produced the clothing in great amounts as a new category of fashion. Entering the twentieth century, images of female gymnasts training in black cotton satin or navy serge knickers are forever fixed in historical moments. After the twenty-first century, sportswear has some changes because the organizing committee gradually reduced the

body cover rate of sportswear from 39% in the 1960s to 31% at the end of the 1970s. By the 1980s, the bikini made the body cover rate of sportswear reduce to 9% [8]. Therefore, it gave a wide space for fashion design and a large number of designers responded. American Ingenuity: Sportswear 1930–1970, published by the Metropolitan Museum of Art [7], holds that sports suits, “mix-and-match” style, large pockets, and sportswear referencing from men’s clothing have the original contribution on clothing culture and fashion culture.

After examining female costume in mid- and late nineteenth century, Vanbren noted that the wife’s costume is like a display window, through which husband’s authority and wealth can be reflected [9]. Veblen, who found connections between sportswear and upper society, proposed in 1899 that people could deliver the signal of property and consumers would build self-concepts (e.g., focus on opinions and reactions) from the relationship. Based on this social drive, buying luxury goods for displaying to others is known as conspicuous consumer [9].

Since then, conspicuous consumption has become another way of expression of luxury consumption. When special luxury goods are branded as “show status” and “isolate class” [10], scholars believe that the biggest reason for consumers to buy luxury goods is to show off [11]. But then some scholars questioned the conformity, uniqueness, and ostentation of luxury consumption, [12], which once again appeared in academia. Some scholars try to divide consumers into two types: shower and follower [13]. They argue that conspicuous consumption has three obvious characteristics, namely, “visibility,” “wealth,” and “status proof” [14]. Consumers with a low sense of power will tend to consume [15] based on the psychology of conspicuous consumption. College students are the typical group [16] with a low sense of power, who are more likely to have consumption behavior based on conspicuous consumption psychology. O’Cass and McEwen, researchers of the theory believe that consumers prefer to gain prestige from products and brands representing status. However, conspicuous consumption focuses on the visual display of products or using products in public”.

3. Research and Design

3.1. Root Theoretical Research Method. Glaser and Strauss pioneered the root theory, which is a way of building theory. It usually requires constant abstraction from the original empirical material to build the way [17]. It not only maintains a close connection with the fresh original data but also can reflect the abstract degree of the theory. Therefore, it is an effective research strategy and analysis program. Glaser notes that the root theory is to study abstract problems and their processes and focuses on social process analysis [18]. Glaser and Strauss’s theory derived the following versions: Glaser’s classical root theory, the programmed root theory of Strauss and Corbin, and Charmaz’s constructivism root theory. Classical root theory is based on objectivism epistemology and focuses on conducting study and discovering theory from the perspective of positivism. But the

programmed root theory tends to build theory. The constructivism root theory is based on the development of constructivism, and the researchers believe that local people also constitute the theory and improve its development.

By using the root theory, the purpose of this paper is to construct the theory of sports and leisure clothing consumption based on the objectivism epistemology and the college students' cases of sports and leisure clothing consumption. So the programmed root theory is adopted. It will directly start from practical observation by using the root theory and collect the consumption-related data of college students' sports and leisure clothing for continuously analyzing and comparing. Then it will incorporate new genera and conceptualized themes into the theory until the theory saturation is reached and build the theoretical framework of consumption motivation on the basis of the connections between these concepts.

3.2. Data Collection and Analysis. This study tries to collect firsthand data by using methods such as the observation method, interview method, and conference method and supplements secondhand data by using various data such as field observation. During the process of data collection, the researchers paid great attention to the triangular cross verification, whose purpose is to improve the reliability and validity of the overall analysis.

Among them, the observation method is to investigate links before or after blockchain fashion enterprise managers. The research team participates in shopping as consumers to experience different blockchain fashion products consumption and record each field observation and participation observation in the form of a written memorandum. The observation before the interview promotes the in-depth interview of the respondents, and the observation after the interview repeatedly compares the interview content and supplements the research data.

The consumption motivation and scenes of college students are complex and changeable. This study adopts a theoretical sampling method, including open sampling, relationship and differential sampling, and distinguished sampling. There are 30 respondents including sports and related majors and nonsports college students. Ensure that respondents can put forward their own views and opinions under the background of sports and leisure clothing consumption.

The snowball sampling method is more suitable in this study; when investigating different college students, let them introduce their professional situation first. The study was continuously analyzed and interviewed until the data are constantly repeated. When no new genera and dimensions are generated, the information saturation is reached; data collection was terminated.

The interview method, based on the in-depth interview, pays attention to the quality of the interview, so we need to explore the data of the research interview in detail and in depth. Based on this, the researcher team conducted more-to-one interviews as the basis of the interview. In terms of the interview content, the outline of the formal interview needs to

be constantly modified for different objects, and the outline is only targeted. The conspicuous consumption in this study is a very obscure and sensitive topic. So we need to give the interviewees thinking space according to the specific interview dialogue, which is conducive to deep and real expression.

The interview mainly centered on the following problems: (1) the connotation of sports and leisure clothing, including its contents and characteristics; (2) the background of sports and leisure clothing consumption, which can be explained by specific cases; and (3) the current existing problems of China's sports and leisure clothing brands, and the domestic and external causes of these problems. Second, the research team conducted research on college students of different majors from May 2021 to July 2021, and each interview is about 0.5 to 1 hour. Mostly, group discussion is used, and the duration of the group meeting is 1 to 2 hours. After the interview, the sound recording will be written, and the text will be delivered to the interviewees for confirmation after being modified. We need to pay attention to maintaining communication with the team members to ensure the effectiveness of each interview. More than 60,000 documents were compiled and coded using the root theory. Basic information of the interview is shown in Table 1.

4. Study of the Encoding Process

4.1. Open Encoding. Open coding requires researchers to adhere to the original data and code the data information word by word, sentence by sentence, or paragraph by paragraph. The data is continuously compared, kneaded, and recombined with the conceptualized and categorized categories in the coding analysis. It can be taken in two steps.

The first step is pasting labels on the sorted data and preliminary conceptualization. The concept is selected from the interviewed contents or academic literature or created, which can fully reflect the essential connotation of the data. This paper used the recommended gerund in the open coding, such as "lack of female design elements," and further data collection "what are female design elements? Why do you think it lacks?" The second is to classify and refine the concept drawn and classify repeated concepts, similar concepts, or concepts reflecting similar events. A higher, deeper abstract concept is produced to contain the initial concepts and form a category, such as "community attention" and "enlarge friends circle." This paper will use the original data, concepts, and categories to continuously explore the relationship between categories. Through open coding, this study obtained 66 concepts and 8 categories, as shown in Table 2.

4.2. Code. Open encoding is an abstract and generalized way and can reveal the truth behind the information. But the relationship between information still needs specific research and comparison after classification. Among them, the purpose of spindle coding is to find the main category, so as to successfully seek the connection between the concept with its relationship. Through spindle coding, the study analyzes four main categories, namely, construction evolution,

TABLE 1: The basic information of interviewees.

Item	Property	Total number	Percentage (%)	Coding of interview record
Gender	Male	15	50	M
	Female	15	50	F
Major	Sports major	20	67	S
	Nonsports major	10	33	N
Educational level	Below undergraduate	5	17	
	Undergraduate	20	67	
	Postgraduate or above	5	17	

TABLE 2: Examples of conceptualization and categorization of open coding.

Interview data	Initial conceptualization	Conceptualization	Categorization
<p>I think there are more and more sports and leisure clothing. China's sports and leisure clothing market is very new but mature. It is growing with the development of Chinese brand retail (a1). My parents, brothers, and sisters also like sports and leisure brands (a2). My parents prefer me to wear sports and leisure clothes compared to JK dresses. There are many famous sports and leisure brands, such as Vans × Liberaiders cobranded hoodie, which has a certain collection value. I will not wear it every day, but it can be used as a collection (a3), which makes me feel happy when I am in a bad mood. It makes me happier than luxury bags.</p> <p>At present, there are many very good sports and leisure brands in domestic. I would prefer to support Chinese goods (a4), such as HongXing Erke and Li Ning. These brands make me feel proud (a5) and have high-cost performance (a6).</p> <p>If I see my friends in the fashion cycle wear sports and leisure clothes, even if I don't like the clothes, I would immediately want to have them (a7). Although I will not buy the same color, I will consider similar styles of the same type and brand. This would make me look fashionable (a8) and bring a common topic with my friends (a9). If the price for sports and leisure clothes that I like very much is beyond my range, I would consider advancing living expenses from my parents or borrowing money from friends. Because many of them are often limited and are not available if I miss the season (a10).</p>	(a1) Sports and leisure brand market grows continuously with the development of the retail market	(A1) The market evolution and development of sports and leisure clothing in China (a1, a4)	(AA1) Evolution and development
	(a2) The consumption of sports and leisure brands is often supported by the families	(A2) Cost value (a3, a6, a10)	(AA2) Perception of value (A2, A3)
	(a3) Sports and leisure brands have a collection value	(A3) Emotional value (a5, a8)	(AA3) Community identity (A4, A5)
	(a4) Domestic sports brands have a certain consumer market	(A4) Relatives and friends agreement (a2, a7)	
	(a5) The consumption of domestic sports and leisure brands brings people pride	(A5) Social status improvement (A9)	
	(a6) The cost performance of sports and leisure brand consumption will also affect the consumption behavior		
	(a7) The consumption of sports and leisure clothing has a certain imitation effect		
	(a8) The consumption of sports and leisure brands enhances people's confidence		
	(a9) Sports and leisure brands are conducive to socializing expansion.		
	(a10) The consumption of sports and leisure clothing sometimes exceeds people's consumption power		

perceived value, community identification, and consumption behavior of sports and leisure clothing. The connotation is confirmed by the main category, as shown in Table 3.

Through interviews and spindle coding, the categories and their relationships are shown in Figure 1. Among them,

the selective coding is used due to its integration of data, living category, and relationship theory. Then the core content of the theory is sorted out through the relationship line in Figure 1, and the framework of the theory is gradually developed. Finally, the relationship between college

TABLE 3: The main category and corresponding categories.

The main category	Corresponding categories	The connotation of categories
Construction evolution (CE)	Evolution	Sports and leisure clothing market constantly evolves and develops along with the development of sports and fitness
Perceived value (PE)	Perceived emotional value (PEV)	In the process of consumption, college students feel positive feedback such as pleasure, happiness, and pride
	Perceived cost value (PCV)	College students feel the balance of cost performance in the process of consumption
	Product evaluation (PE)	In the process of use, college students feel the function of the product itself and also the positive feedback evaluation of the product, which is roughly consistent with the evaluation of friends
Community identification (CI)	National consciousness (NC)	When college students buy Chinese goods, it will bring pride, which is consistent with the pride of friends
	Community leaders (CL)	Positive reviews of the product are given by community leaders, which will cause the imitation effect
Consumption behavior of sports and leisure clothing	Interpersonal interaction (II)	After college students' consumption, the "visibility" of products increases more interpersonal interaction
	Self-image (SI)	After college students' consumption, the "visibility" of products helps improve their self-image

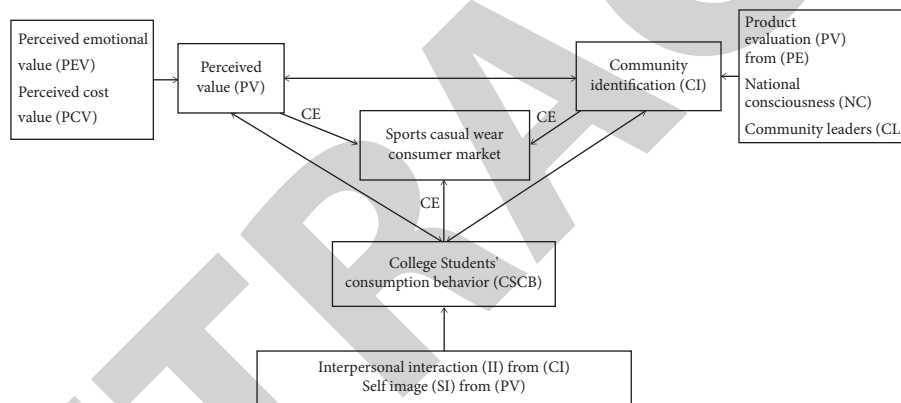


FIGURE 1: Model and selective coding processes.

students' consumption behavior in sports and leisure brands is sorted out.

The storyline of the main category: sports and leisure clothing consumption market consists of three dimensions of perceived value, community identification, and consumption behavior of sports and leisure clothing. Among them, perceived value is the basis. Sports and leisure clothing includes two perceptions, namely, emotional value (beauty and pride) and cost (cost performance). Community identification is the core environment formed by the sports and leisure clothing consumption market. The opinion of community leaders, personal consumption evaluation, and national consciousness are three intermediary variables of community identification. Consumption behavior is the last link of cultivating the formation of sports and leisure clothing consumption market and is based on interpersonal interaction and self-image. The above three dimensions constitute a dynamic relationship under the sports and leisure clothing consumption market, which revolves around consumption behavior.

5. Research Results

5.1. Sports and Leisure Clothing Consumption and Community Identification for College Students. From a psychological perspective, there is a "mirror relationship" between reality and imagination. It means that the subject recognizes some kind of visual image and views this image as an ideal pursuit for consumption imitation [19]. This subjective recognition will make members produce "community participation" and "community pressure" two reactions, and the former makes members tend to retain membership, recommend to others, and actively participate in group activities [20]. College students are a typical community and are more susceptible to this factor. Interviewee FN06 mentioned:

My friend Xiao L is rich, beautiful, and fashionable. Her clothes are not deliberately naked but always fill with the youth breath. She has prestige among friends, and I love her. She always pays attention to fashion news at home and abroad and keeps up with the latest style of sports and leisure clothes. Moreover, she is also familiar with the history of

those brands. When we meet, she will talk about the trend, and we always listen with relish. I used to know nothing about the trend. To join her party and have common topics with her, I also started to buy sports and leisure clothes and also imitate her consumption (FN06-PV-II-CI).

FN06 comes from a wealthy family in Shanghai and has her own car in college. She looks very youthful and beautiful in Y3 new coproducts of Adidas with Sanyo and coconut running shoes. Her friend FN07 wears a similar style as she wears. FN07's clothes have no international brand trademark but are more colorful. F07 is a college student from a small town. She went to college by taking the physical education exam and majored in physical education. Her family was not rich and can't afford luxury goods, so she chooses similar styles of sports and leisure clothes.

They and I are friends. We often go out, sing, and have dinner, so the style of clothes cannot be fully different. Although I don't have much money, I brush my credit card and pay for a credit card by teaching kids to play balls. Wearing similar clothes allows me to join their group, so the hard work is worthy. I won't be treated differently because my clothes are imitations. Sometimes, I wear cheap Chinese brands; they will mimic my clothes (FN07-PV-II-CI).

Sportswear first appeared as a style of clothing and gradually began to form a specific culture, that is, the huge consumption layer brought by people who love sports. Among them, young people's recognition of national culture often evolves with the improvement of the country and its national consciousness. About this point, respondent MS05's assistant teacher, a graduate student and national secondary athlete, expressed his views on the consumption of sports and leisure clothing.

We used to wear professional sportswear during training, mainly because the previous sports and leisure clothes were too ugly. Now, sports and leisure clothes have more kinds and are cheap, some of which are more comfortable than professional sportswear. So, in class, I will choose sports and leisure clothes. On the one hand, it has high-cost performance. On the other hand, it can also narrow the distance between me and students and let me look younger. I observe students wear a lot of kinds of clothes, especially when a star endorsed a national brand (e.g., Olympic champion Gong Lijiao endorses Xtep) or a news induced the consumption of a national brand (e.g., HongXing Erke donates for Henan); these news will particularly increase the enthusiasm of students to buy (MF09-CBCB).

The consumption of sports and leisure clothing is closely related to community identification, and this association will view the evaluation of the product itself and the opinions of community leaders as active variables. And national consciousness is viewed as an important intermediary variable. It can be seen that the marketing of sports and leisure clothing should be rooted in the community culture of college students and follow up the current affairs for experiential marketing publicity.

5.2. Consumption and Perceived Value of College Students' Sports and Leisure Clothing. Sports and leisure clothing is

closely related to physical sports, which means the conflict, attempt, reconciliation, and balance between sports and fabric. This relationship surpasses other relationships and forms a new popularity and aesthetic. This aesthetic experience is closely linked to consumer perception. The "perceived emotional value" contains four aspects, namely, pleasure, stimulation, novelty, and relaxation [21]. In the theoretical framework of perceived value, "perceived cost value" has an obvious influence on college students. Zuo Wenjin concluded that consumption contains the actual cost and risk perception. Perceived cost value refers to the benefits that consumers enjoy when buying sports and leisure clothing. It is also the perceived actual cost of goods and a psychological relationship.

In my opinion, the functional difference between sports and leisure clothing and professional sportswear is not very obvious, but the difference between prices is very big. My major is table tennis, and our professional sportswear has functions such as sweat evaporation from the skin and keeping warm. But its price is higher. So cleaning every day will accelerate depreciation, which will put pressure on me. I usually wear professional sportswear when I go out to compete. In daily classes and training, I will wear sports and leisure clothes bought in Taobao. The price is very cheap, so I don't have the pressure. My teacher doesn't comment on my dress, and as for the training effect, "good mood, good training" (MS05-PVC-PEV).

In the interview, we found that most girls would follow the trend and wear a similar style of sportswear. In addition, we found that many professional athletes will also wear sports and leisure clothes in training. Walking in the sports venues on campus, I found that most professional athletes also wear sports and leisure clothes when training. With the development of times, the trend changes rapidly. Consumers' demands for the function of sportswear are also in change. Consumers often have higher requirements for cost performance and hope that sports and leisure clothes can achieve the same functions as professional sportswear. Only in this way can help them daily exercise more comfortably. We hope it can have the advantages of "killing birds with one stone," such as controlling the moisture absorption to a certain extent, adjusting temperature, resisting the tensile and friction, and preventing from wind and rain. Therefore, the difference between professional sportswear and sports and leisure clothes began to get smaller and smaller, which is also a manifestation of the mass production and standardized production relationship under the market economy. In addition, the relationship between consumption and the perceived value of sports and leisure clothing continues to increase. For example, respondent MS07 said that sports and leisure clothes made him more relaxed than professional sportswear.

My height does not get the advantage and my sports performance can only reach above average. In the future, I may not be able to become a professional athlete, which often makes me in a bad mood at school. At first, I wear loose clothes and raised shoes just to cover up my shortcomings. But then I found that my dress was often the object of imitation, which brought me confidence. Now, I start to

consider using my sports knowledge to work in sports and leisure clothing sales after graduation (MS07-PEV).

The study of perceived value has been fully developed in psychology and sociology. For the retailer, perceived value is the result that they must pursue. The basic perception and psychological activities of customers also induce psychological activities of other consumption.

Even if their perception is sometimes greatly different from the actual situation, it may have positive or negative deviance, but it does not hinder that perception has guidance [22] for customer's behavior. Customer perception value theory provides a certain new chance for the improvement of core competitiveness. By studying college students' perceived value of sports and leisure clothing, it can be found that emotional value and cost value are often important internal driving forces for college students, which will even influence product evaluation in community identification.

5.3. Sports and Leisure Clothing Consumption and Conspicuous Consumption Behavior of College Students. Luxury consumption motivated by external factors may lead to more public consumption and conspicuous consumption [23]. Consumers who have primarily external consumption motivation pay more attention to the "visibility" [24] of the product than those who have mainly internal consumption motivation. "Visibility" characteristics include LOGO in sports and leisure clothing, fashionable styles, and classic patterns. With a strong "visibility," it is more likely to induce college students to conduct conspicuous consumption. Many students in the interview expressed similar ideas.

I am very yearning for the high-grade luxury goods in sports and leisure brands, such as limited edition shoes of Converse, presale coats, and dad shoes of Nike. Although I cannot afford these consumption, I sometimes buy secondhand and high imitation products to maintain a delicate image in the circle of friends. If it is a secondhand product, I will choose that with an obvious logo. After all, the secondhand product is not cheap. If it is a high imitation product, I will choose an unusual style to avoid producing embarrassment for wearing the same outfit (MS09-PV).

Conspicuous consumption is a very common psychological phenomenon in the growth of college students. American costume psychologist Mary Linhorn believes that clothing is the second layer of skin, which can mark people's social attributes such as skin color. The claim that clothing has a close relationship to human psychology has a high degree of recognition [25]. In an era when sports and leisure clothing did not rise, college students were keener on conspicuous consumption through mobile phones, computers, and other ways. The difference is that the change of the era has quietly changed the demand and motivation for sports and leisure clothes. In contemporary times, mobile phones and computers have been popularized, so the psychological implication of famous brands of sports and leisure clothes can arouse more resonance of college students.

I will subjectively think that students dressed in famous brands of sports and leisure clothes are rich. Although I don't know the brand culture, I will envy them wearing the

common logo. Some people may wear high imitation luxury goods, but I will also subconsciously think that it is authentic because of lack of professional discrimination ability. And I tend to think that people with high status should also wear luxury sportswear, which is a symbol of identity (FN11-PV).

The self-definition theory is proposed by Georg Simmel in 1890, which is based on the special perspective of social psychology. She believes that society has different symbols, which have a psychological implication on people's identity and status. People in the upper class wear sports and leisure clothing for horse riding, archery, sword, and other sports, which is to show class characteristics of wealthy and leisurely pace and also to show their identities. The clothing fabrics and sewing skills of clothes they wear on social occasions are the external display of rights, which is silent but shocking and conforms to the expression of the upper class. Sportswear can be said to be basically self-acquired roles, namely, helping players obtain roles through sportswear [26, 27]. Therefore, sportswear naturally is a symbol and conspicuous characteristic hidden behind the subconscious of consumers. With the change of times, it still has deep meaning between it and consumers' consumption behavior.

6. Conclusion

The design of sports and leisure clothing is the concentrated embodiment of leisure and fashion. The current design integrates more and more trend elements, younger, fashionable, and trendy. People pay more attention to the fashion sense of sportswear in their choice of sportswear.

The development of fashionable sportswear combines comfort and fashion. And most of the prices are moderate, so college students have the strongest demand for them. Moreover, by strengthening the role of perceived value, sports and leisure clothing can bring more objective improvement to college students' community recognition. On the surface, college students' consumption of sports and leisure clothing is invested in the product itself. The cost of sports and leisure clothing is often lower than that of other categories of clothing, but this does not hinder its advantages of high-cost performance, loose, and comfortable and is more suitable for the majority of college students. On the other hand, the consumption of college students also affects urban white-collar workers, especially those middle-aged and young people who are eager to look younger. They will obtain the emotional value of a product from the consumption of sportswear, so as to form the construction of self-image [28–40].

Data Availability

The data underlying the results presented in the study are available within the manuscript.

Disclosure

The content of the manuscript has not been published or submitted for publication elsewhere.

Conflicts of Interest

There are no potential conflicts of interest in our paper.

Authors' Contributions

The authors have seen the manuscript and approved to submit it.

Acknowledgments

Doctoral Research Project of Shangqiu Normal University: A study on the relationship between hotel salary equity, job engagement and organizational commitment of the new generation of employees.

References

- [1] PwC Sports Industry, "The 2020 PwC sports industry survey report [EB/OL]," 2020, <http://www.199it.com/archives/986128.html>.
- [2] H. Ulrich ombrecht, *Beauty of Sports: Cheer for the Human Body [M]*, Lin Mincai, Translation, Shanghai People's Press House, Shanghai, 2008.
- [3] C. Breward and D. Gilbert, *Fashion's World Cities [M]*, pp. 109–117, BERG, 2006.
- [4] T. D. Scales, *Difference between Men and Women Re-garding Decision-Making Styles for Sport Apparel [M]*, Indiana University of Pennsylvania, Indiana, 2017.
- [5] M. P. Catriona, *More than Mere Amusement&Working Class Women's Leisure in England,1750-1914 [M]*, Northeastern University Press, Boston, Mass, 2001.
- [6] E. Weber and H. Van Mullem, "Gender bod ynorms, and sports apparel advertisements [J]," *Journal of Kinesiology&Wellness*, vol. 9, pp. 21–27, 2020.
- [7] P. C. Warner, "The americanization of fashion: sportswear,the movies and the 1930s [A]," in *Twentieth-century American fashion [C]*, L. Welters and P. A. Cunningham, Eds., Berg, 2005.
- [8] Baidu, "Naked nude [EB/OL]," 2012, <http://baike.baidu.com/view/1095384.htm>,2012-07-19.
- [9] B. Van, *Free Class Theory [M].Cai Received 100*, Translation, The Commercial Press, Beijing, 1964.
- [10] D. Dubois, D. D. Rucker, and A. D. Galinsky, "Super size me: product size as a signal of status," *Journal of Consumer Research*, vol. 38, no. 6, pp. 1047–1062, 2012.
- [11] T. Veblen, *The Theory of the Leisure Class*, Penguin, New York, NY, 1899.
- [12] H. Leibenstein, "Bandwagon, snob, and veblen effects in the theory of consumers' demand," *Quarterly Journal of Economics*, vol. 64, no. 2, pp. 183–207, 1950.
- [13] G. Corneo and O. Jeanne, "Snobs, bandwagons, and the origin of social customs in consumer behavior," *Journal of Economic Behavior & Organization*, vol. 32, no. 3, pp. 333–347, 1997.
- [14] A. O'Cass and H. McEwen, "Exploring consumer satus and conspicuous consumption [J]," *Journal of Consumer Behaviour*, vol. 4, no. 1, pp. 25–39, 2004.
- [15] D. Dubois, D. D. Rucker, and A. D. Galinsky, "Super size me: product size as a signal of status," *Journal of Consumer Research*, vol. 38, no. 6, pp. 1047–1062, 2012.
- [16] C. Shi, B. Wang, M. Yan, and L. Zhang, "ERM ASS," in *Proceedings of the 2019 2nd International Conference on Education Reform, Management and Applied Social Science*, 2019, ERM ASS.
- [17] D. C North and W. Zhang, *Empirical Studies in Institutional Change [M]*, pp. 267–292, Economic Science Press, Beijing, 2003.
- [18] A. H. N. Mak, K. K. F. Wong, and R. C. Y. Chang, "Critical issues affecting the service quality and professionalism of the tour guides in Hong Kong and Macau," *Tourism Management*, vol. 32, no. 6, pp. 1442–1452, 2011.
- [19] E Roudinesco and B. T. Bray, *Jacques Lacan [M]*, Columbia University Press, Collumbia, 1997.
- [20] R Algesheimer, P Dholakia, and A Herrmann, "The social influence of brand community: evidence from European car clubs [J]," *Journal of Marketing*, vol. 69, no. 4, pp. 19–34, 2005.
- [21] J. C. Sweeney and G. N. Soutar, "Consumer perceived value: the development of A multiple item scale," *Journal of Retailing*, vol. 77, no. 2, pp. 203–220, 2001.
- [22] J. N. Sheth, B. I. Newman, and B. L. Gross, "Why we buy what we buy: a theory of consumption values," *Journal of Business Research*, vol. 22, no. 2, pp. 159–170, 1991.
- [23] J. K. Eastman and K. L. Eastman, "Conceptualizing a model of status consumption theory: an exploration of the antecedents and consequences of the motivation to consume for status," *Marketing Management Journal*, vol. 25, no. 1, p. 1e15, 2015.
- [24] J. L. Nueno and J. A. Quelch, "The mass marketing of luxury," *Business Horizons*, vol. 41, no. 6, p. 61e88, 1998.
- [25] M. Lin Horn, *Clothing: Man's Second Skin*, Shanghai People's Press, Shanghai, 1991.
- [26] D. Best, "The aesthetic in sport," *British Journal of Aesthetics*, vol. 14, no. 3, pp. 197–213, 1974.
- [27] M. Matthew, "Sport,artandtheaesthetic [EB/OL]," 2011, <http://www.sjsu.edu/faculty/masucci/sport,%20Art,%20%20the%20Aesthetic.pdf>.
- [28] A. Cavicchi and C. Santini, "Brunellopoli: a wine scandal under the tuscan sun," *Tourism Review International*, vol. 15, no. 3, pp. 253–267, 2011.
- [29] B. K. Lee, "Audience-oriented approach to crisis communication," *Communication Research*, vol. 31, no. 5, pp. 600–618, 2004.
- [30] J. Breitsohl and B. Garrod, "Assessing tourists' cognitive, emotional and behavioural reactions to an unethical destination incident," *Tourism Management*, vol. 54, pp. 209–220, 2016.
- [31] C. K. Dimitriou, "The quest for a practical approach to morality and the tourism industry," *Journal of Hospitality and Tourism Management*, vol. 31, pp. 45–51, 2017.
- [32] M. Yong and Yu Gui-Shen, "The tendency of vicissitude and development of costume in athletic sports [J]," *Science Information*, vol. 17, no. 09, pp. 151–152, 2007.
- [33] F. forecast, "China's sportswear market will surpass the luxury market in 2020," *The Light & Textile Industries of Fujian*, vol. 8, no. 8, p. 28, 2016.
- [34] H. U. Gumbrecht, *The beauty of Sports: Cheering for the Human Body [M]*, Shanghai People's publishing house, Translated by Lin Mingcai. Shanghai, 2008.
- [35] M. Horne, *Clothing: Human Second Skin [M]*, Shanghai People's publishing house, Shanghai, Translated by Le Jing-hong, Yang Zhiliang, 1991.
- [36] R. Glenn Richey and C. W. Autry, "Assessing interfirm collaboration/technology investment tradeoffs," *International Journal of Logistics Management*, vol. 20, no. 1, pp. 30–56, 2009.

Retraction

Retracted: Improved Chicken Reproduction and Yield of Improved Poultry from Titanium Dioxide (TiO₂) Nanoparticles Coated in Jimma Horro Area of Kellem Wollega Zone, Ethiopia

Advances in Materials Science and Engineering

Received 26 December 2023; Accepted 26 December 2023; Published 29 December 2023

Copyright © 2023 Advances in Materials Science and Engineering. This is an open access article distributed under the Creative Commons Attribution License, which permits unrestricted use, distribution, and reproduction in any medium, provided the original work is properly cited.

This article has been retracted by Hindawi, as publisher, following an investigation undertaken by the publisher [1]. This investigation has uncovered evidence of systematic manipulation of the publication and peer-review process. We cannot, therefore, vouch for the reliability or integrity of this article.

Please note that this notice is intended solely to alert readers that the peer-review process of this article has been compromised.

Wiley and Hindawi regret that the usual quality checks did not identify these issues before publication and have since put additional measures in place to safeguard research integrity.

We wish to credit our Research Integrity and Research Publishing teams and anonymous and named external researchers and research integrity experts for contributing to this investigation.

The corresponding author, as the representative of all authors, has been given the opportunity to register their agreement or disagreement to this retraction. We have kept a record of any response received.

References

- [1] S. Shuma Abdisa, J. Leta Tesfaye, A. Saka et al., “Improved Chicken Reproduction and Yield of Improved Poultry from Titanium Dioxide (TiO₂) Nanoparticles Coated in Jimma Horro Area of Kellem Wollega Zone, Ethiopia,” *Advances in Materials Science and Engineering*, vol. 2022, Article ID 1984178, 7 pages, 2022.

Research Article

Improved Chicken Reproduction and Yield of Improved Poultry from Titanium Dioxide (TiO₂) Nanoparticles Coated in Jimma Horro Area of Kellem Wollega Zone, Ethiopia

Soressa Shuma Abdisa,¹ Jule Leta Tesfaye ,^{2,3} Abel Saka ,² Abdisa Abraham,⁴ N. Nagaprasad ,⁵ Lamessa Gudata,² and Krishnaraj Ramaswamy ^{3,6}

¹Department of Animal Science, College of Agriculture and Veterinary Medicine, Dambi Dollo University, Dembi Dolo, Ethiopia

²Dambi Dollo University, College of Natural and Computational Science, Department of Physics, Dembi Dolo, Ethiopia

³Centre for Excellence-Indigenous Knowledge, Innovative Technology Transfer and Entrepreneurship, Dambi Dollo University, Dembi Dolo, Ethiopia

⁴Department of Natural Resource Management, College of Agriculture and Veterinary Medicine, Dambi Dollo University, Dembi Dolo, Ethiopia

⁵Department of Mechanical Engineering, ULTRA College of Engineering and Technology, Madurai 625104, Tamilnadu, India

⁶Department of Mechanical Engineering, College of Engineering and Technology, Dambi Dollo University, Dembi Dolo, Ethiopia

Correspondence should be addressed to Krishnaraj Ramaswamy; prof.dr.krishnaraj@dadu.edu.et

Received 12 November 2021; Revised 11 January 2022; Accepted 17 February 2022; Published 18 March 2022

Academic Editor: Palanivel Velmurugan

Copyright © 2022 Soressa Shuma Abdisa et al. This is an open access article distributed under the Creative Commons Attribution License, which permits unrestricted use, distribution, and reproduction in any medium, provided the original work is properly cited.

Current work was accompanied in Kellem Wollega Zones Jima Horro District, Western Ethiopia, to evaluate the reproduction and productive performances of titanium dioxide (TiO₂) nanoparticles' coated poultry. In the existence of sunlight as well as moistness, the titanium dioxide rusts and abolishes microorganisms (bacteria). The covering has been confirmed to decrease bacterial development. Once covered, the superficial remainders self-sanitized as it elongated as there is sufficient sunlight to galvanize the photocatalytic outcome. The middling poultry group scope per family was 12.04 heads. The overall middling time at first of local and improved chicken egg laying was 6.9 and six months, respectively. The overall hatchability and mortality were 82.3 and 41.1, respectively. The lowest chick mortality (39.8) was observed in Tribe Kebele (highland), and the highest clutches per year (2.96) were observed compared to other Kebeles (mid-altitude and low land). Poultry reproductivity is little, so diverse development approaches must be familiarized. The application of TiO₂ nanoparticles in agriculture is a promising method in increasing fine and improved products.

1. Introduction

Agriculture is the backbone of the Ethiopian economy, where the sector contributes about 42.3% to the total gross domestic product (GDP) [1]. The livestock sector as an integral part of agriculture contributes about 40% of agricultural GDP and a quarter (26.4%) of national GDP [2]. In terms of number, Ethiopia has the largest livestock population in Africa, and it is home to 56.71 million cattle, 29.33 million sheep, 29.11 million

goats, 2.03 million horses, 7.43 million donkeys, 0.4 million mules, 1.16 million camels, and 56.8 million chicken [3]. Chicken is the largest group of livestock species contributing about 33% of all animal protein consumed in the world [4].

A huge livestock population in general and chicken, in particular, could be expected to increase its contribution to the total agricultural output as well as to improve the living standards of smallholder farmers [5]. This is mainly due to their small size, fast reproduction, low labour, low energy,

and low initial capital requirement and less detrimental impact on the environment compared to other livestock [6].

Of the total chicken reared in Ethiopia, about 99% comprises indigenous, and only about 1% are exotic breeds of chicken. In Ethiopia, about 99% of the total national chicken products (eggs and meat) are contributed by indigenous chickens kept under the village management system, while the remaining 1% is obtained from an exotic breed of chickens kept under intensive management [7]. This might be a function of poor management and lack of awareness.

Nanotechnology is a new, advanced, and interdisciplinary systematic methodology that contains scheming, growth, and solicitation of ingredients and expedients at a molecular plane in nanometre measure at slightest one facet arrays in extent from 1–100 nanometres [8]. It is a wide-ranging continuum developing arena of knowledge that has bright claims which is straightforward and functional disciplines. It will authorize no arena untouched by its appealing systematic claims, and the agronomy segment is no exclusion. The applications of the nanoparticle are explained in Figure 1.

Household people all over the country in broad and emerging states in specific exercise poultry for multiuse practices' counting: as the basis of revenue and capitals to confirm foodstuff safety, traditional and community morals such as ceremonial, expense, and representation, donations to powerful public links, and basis of financial enabling for females [9]. Poultry households in America use bactericidal coverings (coating) to moderate the deliberation of food-borne pathogens in connection with the poultry during fabrication. Green Earth Nano Science Inc., a Canadian company (GENSCC), has established a self-sanitizing photo-catalyst covering (coated) for application in poultry houses [10]. This coating integrates nanoparticle of titanium dioxide (TiO_2). The inimitable photocatalytic characteristics of the nanoparticle of titanium dioxide (TiO_2) are galvanized when the covering is unprotected to likely or ultraviolet (UV) sunlight. In the existence of sunlight as well as moistness, the titanium dioxide rusts and abolishes microorganisms (bacteria). The covering has been confirmed to decrease bacterial development. Once covered, the superficial remainders self-sanitizing as elongated as there is sufficient sunlight to galvanize the photocatalytic outcome. The covering is appropriate by the Canadian-Food-Inspection-Agency (CFIA). In Denmark, the Chicken, as well as Hen Contamination Program, is investigating nano-coatings for self-cleaning and decontamination [11]. The even superficial at the nanoscale makes washing and decontamination more operative. Lastly, Danish researchers are also investigating coatings incorporating nanosilver, which does not need ultraviolet (UV) sunlight for galvanization. The ions from nanosilver preclude the growth of biofilms [12].

In Ethiopia, poultry shows vital parts in the living of supply defied people. Agreeing to poultry manufacture has traditional and financial profits, particularly, in the pastoral societies [13]. The poultry coverage of the country was at an expected 56.87 million, of which 95.86% are indigenous

types, 2.79% are cross types, and 1.35% are exotic types (Central Statistical Agency of Ethiopia) [14]. The old-style/community poultry manufacture method is the main method accomplished by nearly all pastoral families [15] and covers more than 90% of the whole poultry meat and egg manufactured in Ethiopia [16]. Investigation rumours from diverse parts of the country showed that the indigenous poultry types have little manufacture [17]. Amid the modern line of scientific novelties in the arena of agronomy, nanotechnology inhabits an illustrious location in remodelling agronomy and nutrition fabrication to fulfil the difficulties in an effective and expensive way.

This investigation was piloted to speak the ensuing aims to assess production yield of local coated with molten titanium dioxide (TiO_2) nanoparticles' poultry and identify major hatchability and mortality of poultry in Jimma Horro District.

2. Materials and Methods

2.1. Description of Study Areas. The survey was shown from November 2018 to December 2019 in three nominated farmer families of Oromia National Regional State. The assessment was conducted at Jimma Horro districts in Kellem Wallega Zone, Oromia National Regional State, Ethiopia. The altitude of the district ranges is between 1400 and 1800 meters above sea level, with average annual minimum and maximum temperature of 18°C and 27°C , respectively, while the annual rainfall ranges from 700 to 1000 mm (Ethiopian Digital Elevation Model, 2018). In the study area, livestock and crop farming are the major economic activity of the district. The livestock resource of the study district comprises 66267 cattle, 19421 sheep, 13647 goats, 257 horses, 6809 mules, 9873 donkeys, and 68401 chickens (Jimma Horro Livestock office 2021). Map of the study locations is indicated in Figure 2. The areas were selected because there are many farmers who practice traditional chicken production. Jimma Horro Woreda is one of the 11 woredas of Kellem Wollega zone of Oromia Regional State, located at a distance of about 665 km west of Addis Ababa. The planters in the part exercise diversified husbandry. The total human person of the woreda is around 56403, of which 50% is indicated to be male (Ethiopian Digital Elevation Model 2021).

2.2. Sampling Procedures and Cross-Sectional Survey. The three peasant associations were objectively nominated created on the availability and accessibility of improved titanium dioxide nanoparticle coated poultry ecotypes.

2.3. Data Collection. In this investigation, both secondary and primary data were used to generate qualitative and quantitative information. The questionnaire was translated into Afaan Oromo. It was pre-tested before administration, and some re-arrangement and corrections were made in accordance with respondents' perceptions. Information gathered through questionnaires is socio-economic characteristics of the respondents such as sex, age, education

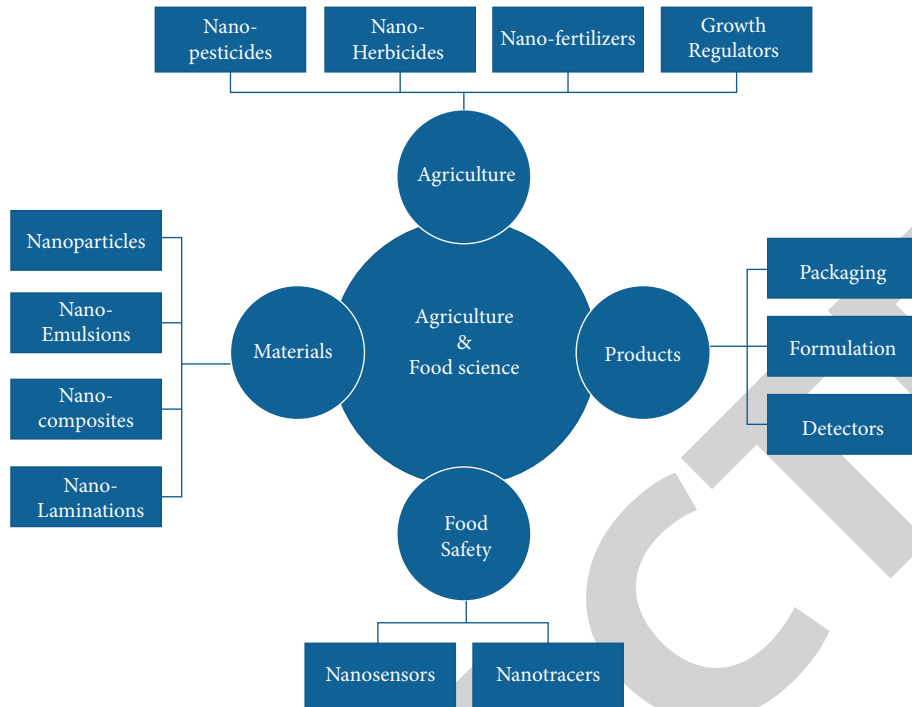


FIGURE 1: A graphic expression of bids of nanotechnology in agro-food division.

level, household size, livestock possession, the socio-economic benefit of chicken production and major production of egg and meat, and constraints, reproductive performances such as age at first egg, the purpose of keeping chicken, feed, and feeding situations, such as major feed sources, supplementation, and water source, and major diseases of chicken in the areas.

To collect primary information household survey, interviews, with focused groups and key informants, and personal observation were undertaken. The secondary data relevant to this study were collected from published and unpublished sources, Jimma Horro Agriculture and Rural Development Office. Prior to the actual survey, information was gathered through an informal survey based on which the information was obtained from secondary data and informal survey, and a semistructured questionnaire was developed. Both qualitative and quantitative data were interpreted by descriptive statistics. The analyzed data were organized in the form of a table, using percentage, rank, and average.

2.4. Data Analysis. The outcome of calm figures was studied by investigation of alteration (ANOVA) resulting from the SAS 2008. Statistics organized over survey, opinion, and discussion were considered by graphic numbers (SPSS version 20).

3. Results and Discussion

3.1. Features of Respondents. Family characteristics of respondents around study areas are illustrated in Table 1. Of the interviewed households, about 72.1% and 27.9% were males and females, respectively. About 93.3% were married, and the remaining 2.4%, 2.4%, and 1.8% were single,

divorced, and widowed, respectively. Education plays a great role in transferring technology to farmers and initiating their willingness to adopt technologies. Higher percentages of respondents in the study areas were educated (elementary to high school and college) and while only 23.6% were illiterate. The presence of educated farmers in the study district could be an opportunity in the management of chicken and other livestock production.

In relation to their livelihood, popular of the defendants (91.5%) were farmers. The common of the plotted families drop in age below 60% years old; performance that the prolific work essential for care, selling, and organization of poultry manufacture was leading in the household. The average household size was 6.16 ± 0.2 , 5.76 ± 0.3 , and 5.87 ± 0.2 for Tibe, Ilu Kitaye, and Nunu *kebeles*, respectively, whereas the overall family sizes per household of the study areas were 5.9 ± 0.2 ranging from 1–11 persons. Figure 2 illustrates the historical representation of variables and level/types of respondents.

3.2. UV Analysis of Titanium Dioxide (TiO_2) Nanoparticle. UV/visible studies show that the energy band gap decreases with increasing pH values of TiO_2 NPs corresponding to the redshift of the optical absorption edge [18]. This is due to an increase in pH value and lowering of interatomic spacing. It is noteworthy here that values of energy band gap obtained are lower as compared to energy bandgap 3.1 eV for pure anatase, 3 for rutile phase, and the data reported for the mixed-phase TiO_2 nanopowders exhibiting as a capable candidate for self-cleaning application [19]. UV-Vis characterization of TiO_2 coated poultry for improved chicken production is depicted in Figure 3.

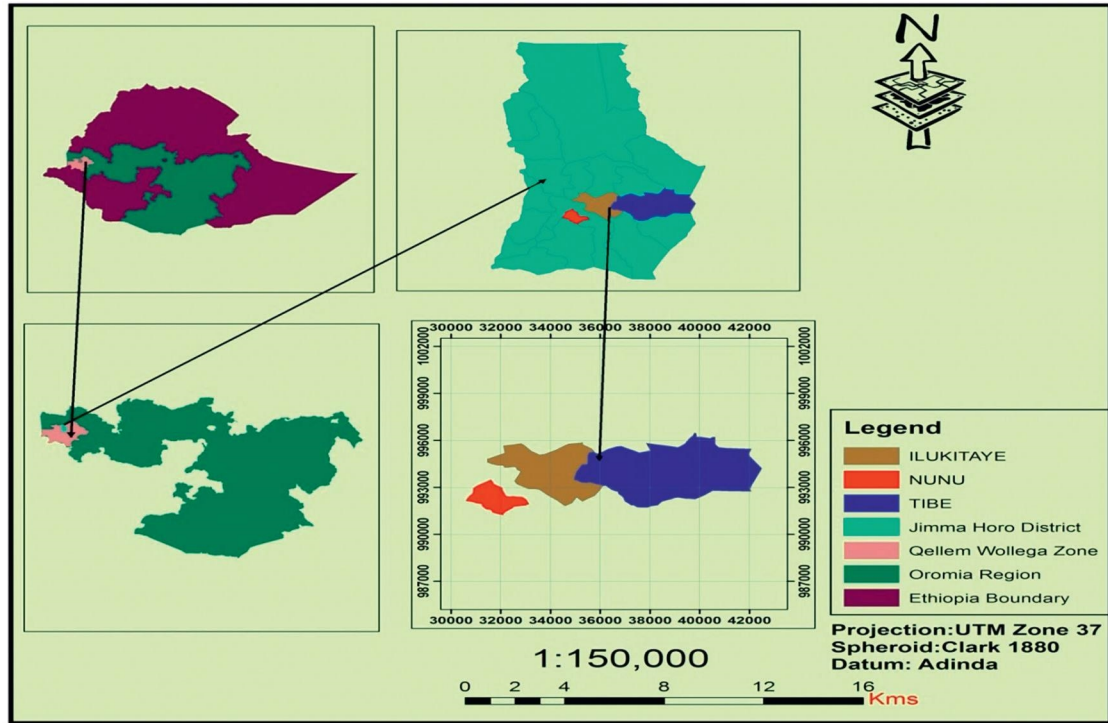


FIGURE 2: Map of study area (survey parts).

TABLE 1: Demographic features of defendants in the survey parts.

Variables	Kebeles			Total (N = 165)%
	Tibe (N = 55)%	Ilu kitaye (N = 55)%	Nunu (N = 55)%	
Gender of defendant				
Male	67.3	75.5	74.5	72.1
Female	32.7	24.5	25.4	27.9
Marital status				
Single	0	1.8	5.5	2.4
Married	100	96.4	83.6	93.3
Divorced	0	1.8	5.5	2.4
Widowed	0	0	5.5	1.83
Educational level				
Uneducated	18.2	25.5	27.3	23.6
Read and write	45.5	31	23.6	33.3
Elementary	20	30.9	14.5	21.8
High school	12.7	12.7	21.8	15.8
Technical vocation	3.6	0	12.7	5.5
Chief job				
Farmers	90.1	96.4	89.1	91.53
Traders	5.5	2.5	0	2.66
Depend on mining activity	0.8	1.1	0	0.63
Fisher men	0	0	0	0
Government worker	3.6	0	11.9	5.16
Age of households				
> 60 years	7.00	7.00	8	7
Between 35 and 60 years	63.70	58.80	59.64	60.71
Between 19 and 34 years	29	34.00	32.00	32
Average family size/household (mean ± SE)	6.16 ± 0.266	5.76 ± 0.308	5.87 ± 0.229	5.93 ± 0.167
Age of respondents	45 ± 0.984	43.13 ± 0.778	42.64 ± 0.676	43.59 ± 0.479

N, number of respondents; %, percent; SE, standard error.

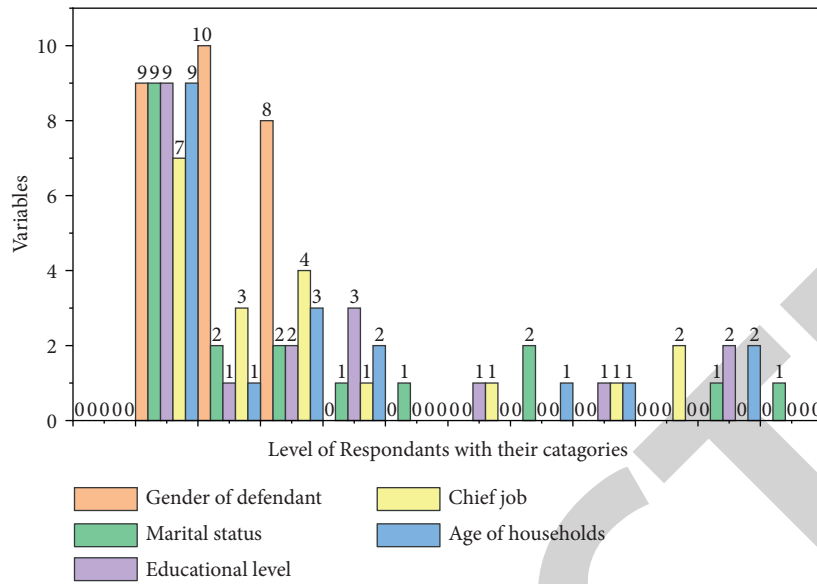


FIGURE 3: Historical representation of variables and level/types of respondents.

TABLE 2: Reproduction and manufacturing yields of the titanium dioxide nanoparticle coated improved poultry.

Parameter	Tibe (55)	Ilu kitaye (55)	Nunu (55)	Total		P value
	Mean ± SE	Mean ± SE	Mean ± SE	Mean	Range	
Egg produced from exotic per year	232 ± 0.5 ^a	230.1 ± 0.59 ^b	232.3 ± 0.59 ^c	225.2	220–250	0.001
Egg laid per hen per clutch	42.35 ± 0.2 ^a	42.27 ± 0.2 ^a	40.18 ± 0.29 ^b	41.60	37–47	0.001
Age at 1 st egg (exotic)	5.94 ± 0.0 ^b	6.4 ± 0.8 ^a	6.21 ± 0.06 ^a	6.00	5–7	0.001
Age at slaughtering (exotic)	4.76 ± 0.1 ^b	5 ± 0.086 ^{ba}	5.02 ± 0.07 ^a	5.01	4–6	0.003

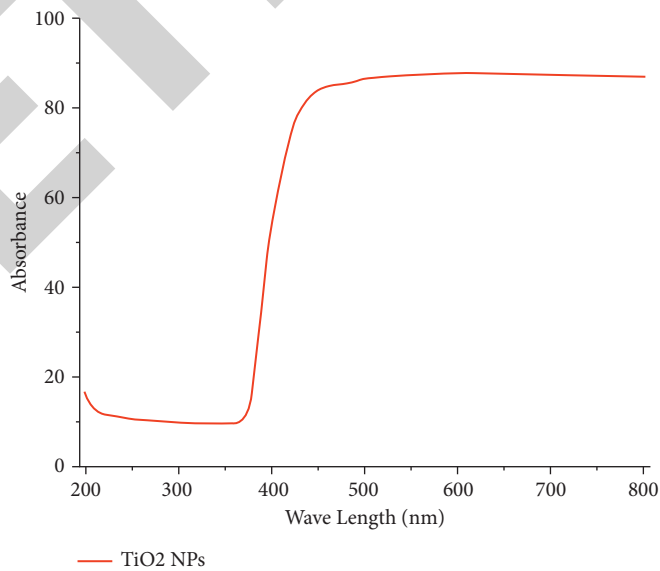


FIGURE 4: UV-Vis characterization of TiO₂ coated poultry for improved chicken production.

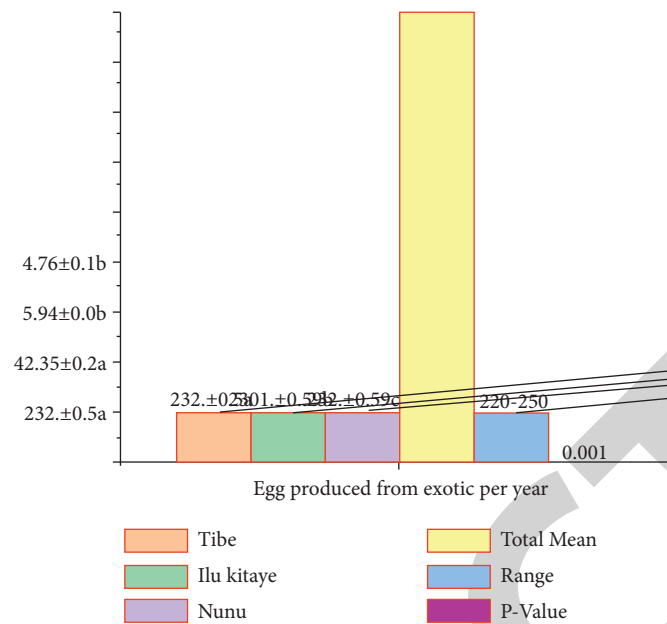


FIGURE 5: Historical representation of result analyzed for three kebele.

4. Reproduction Performance of Improved Chicken from Coated and Conventional Techniques of Poultry

4.1. Age of First Egg. The current survey shows the total muddling period at the first egg of improved chicken was six months, reaching from 5–7 months with significant variance ($P < 0.05$) between peasant associations (Table 2). The average at first egg (183 days) for improved chicken was extended than that described for the saleable chicken ranches. Figure 4 shows the historical representation of the result analyzed for three Kebele. Historical representation of result analyzed for three Kebele is depicted in Figure 5.

The average age at slaughter heaviness of 1.5kg of the improved broiler chicken of the Jimma Horro District was accomplished at around five months. There were differences among the diverse *Peasant associations* in age at slaughter heaviness of the improved broiler chicken ($P < 0.05$). The age at a slaughter weight of improved poultry in Tibe (highland) *kebele* was originated to be significantly advanced ($P < 0.05$) than Nunu (lowland) *Kebele* and Ilu Kitaye (mid-altitude). Comparing the three *kebeles*, *Tibe kebele* (highland) had the best performance. This might be a function of management in Tibe keble and was good compared to the other two *kebeles*.

4.2. Egg Manufacture Performance of Improved Chicken. The middling number of improved chicken eggs per clutch survey part is 41.6. There was significant variance ($P < 0.005$) among the three *Kebeles* (agro-ecologies) in the yield of the improved poultry as measured by the middling number of eggs per clutch. Poultry from Tibe (highland) and Ilu kitaye (mid-altitude) *kebeles* had significantly advanced ($P < 0.005$) middling amount of eggs/clutch than chicken of Nunu (low land) *kebele*.

The general mean yearly egg manufacture of improved chicken was 229.2 ranging from 220–250 seeds. This rate is minor than the rate described for improved breeds of Ethiopia, which harvest around 250 eggs per year per hen under village supervision situations [20]. The major difference in yearly egg manufacture of Tibe *kebele* (highland) is maybe related to the great egg manufacture per clutch noted in the *kebele*, which are the occupation of managing.

5. Conclusions

The results of the present study show that village-improved chicken plays a significant role in the livelihood of the farming community of Jimma Horro District. It serves as a source of income and as an affordable source of animal protein, and chickens are also used in many social and cultural or religious ceremonies. The majority (51%) of the respondents were keeping chicken for sale, while 20% and 14% were keeping chicken for eggs and meat for household consumption, respectively. The most dominant improved chicken production system in the study area was an extensive subsistence system which is based on scavenging and seasonal supplementary feeding of homegrown grains and household food refusals. In this study, the obtained result is that the average group scope per family of the Jimma Horro District was 12.04 poultry, and the importance is greater than the general middling. The middling titanium dioxide (TiO_2) nanoparticle-coated poultry group scope per family was 12.04 heads. The overall averaging time at first of local and improved chicken egg laying was 6.9 and six months separately. The overall hatchability and mortality were 82.3 and 41.1, respectively. The lowest chick mortality (39.8) was observed in Tibe *Kebele* (highland), and the highest clutches per year (2.96) were observed compared to other *Kebeles* (mid-altitude and low land). TiO_2 nanoparticle-coated poultry reproductivity is little, so diverse development

Retraction

Retracted: Experimental Study on the Principle of Oxygenation and Oxygenation Performance of Surface Blade Aerator

Advances in Materials Science and Engineering

Received 26 December 2023; Accepted 26 December 2023; Published 29 December 2023

Copyright © 2023 Advances in Materials Science and Engineering. This is an open access article distributed under the Creative Commons Attribution License, which permits unrestricted use, distribution, and reproduction in any medium, provided the original work is properly cited.

This article has been retracted by Hindawi, as publisher, following an investigation undertaken by the publisher [1]. This investigation has uncovered evidence of systematic manipulation of the publication and peer-review process. We cannot, therefore, vouch for the reliability or integrity of this article.

Please note that this notice is intended solely to alert readers that the peer-review process of this article has been compromised.

Wiley and Hindawi regret that the usual quality checks did not identify these issues before publication and have since put additional measures in place to safeguard research integrity.

We wish to credit our Research Integrity and Research Publishing teams and anonymous and named external researchers and research integrity experts for contributing to this investigation.

The corresponding author, as the representative of all authors, has been given the opportunity to register their agreement or disagreement to this retraction. We have kept a record of any response received.

References

- [1] P. Xing, C. Yu, K. Li, and H. Wu, "Experimental Study on the Principle of Oxygenation and Oxygenation Performance of Surface Blade Aerator," *Advances in Materials Science and Engineering*, vol. 2022, Article ID 3518833, 14 pages, 2022.

Research Article

Experimental Study on the Principle of Oxygenation and Oxygenation Performance of Surface Blade Aerator

Pu Xing , **Chen Yu**, **Kangkang Li**, and **Hui Wu**

Nanchang Hangkong University, 696 Fenghe South Avenue, Nanchang, China

Correspondence should be addressed to Pu Xing; xingpu@nchu.edu.cn

Received 29 December 2021; Revised 4 February 2022; Accepted 14 February 2022; Published 16 March 2022

Academic Editor: Palanivel Velmurugan

Copyright © 2022 Pu Xing et al. This is an open access article distributed under the Creative Commons Attribution License, which permits unrestricted use, distribution, and reproduction in any medium, provided the original work is properly cited.

In this article, the principle of aeration of aerator is analyzed through CFD simulation analysis and high-speed camera observation of aerator blades. Firstly, the flow field of oxidation ditch under the influence of a new curved blade aerator is simulated and analyzed. Then, the oxygenation performance of aerator under different operating parameters, that is different immersion depth and speed, is experimentally studied, and the structural optimization design of blade is carried out. Finally, the best parameters affecting oxygenation dynamic efficiency are obtained by fitting the experimental data, which provides a reference for the further optimization design of the aerator.

1. Introduction

The shortage of water resources and water pollution are worldwide problems. The discharge of wastewater remains high, and the water environment needs to be improved urgently. As a highly competitive secondary biological treatment technology in urban sewage and industrial wastewater treatment, oxidation ditch treatment process has the characteristics of simple process, good effluent quality, and easy stability of sludge [1] and has been widely used all over the world [2]. As the main equipment in the oxygen aeration link in the oxidation ditch [3], the aerator determines the treatment efficiency, energy consumption, and stability of the oxidation ditch, especially suitable for Carousel oxidation ditch [4]. The inverted umbrella aerator has the advantages of simple structure, strong oxygenation capacity, and high power efficiency [5], which is widely used in the surface aeration link of sewage treatment plant.

At present, there is a contradiction between oxygen charging, flow pushing, and energy consumption in the work of inverted umbrella aerator. The blade installation angle, blade number and blade design of inverted umbrella aerator, the rotating speed of aerator, and the immersion depth of impeller all have a certain impact on the

oxygenation performance. Scholars at home and abroad have also conducted a series of studies on these factors [6–8].

Wang Jiaquan [9] simulated the working conditions and oxygenation performance of various inverted umbrella aerators and analyzed the effects of blade installation angle, blade number, and blade shape on oxygenation capacity. Liu Jiawei [10] built an inverted umbrella aerator test-bed to analyze the flow characteristics of the internal flow field of the oxidation ditch under different motion parameters. The response surface method model was established to optimize the performance of the aerator. C Beatriz combined different rotating speeds, immersion depth, and blade angle and obtained the equation for estimating the performance of aerator through dimensional analysis [11]. Wei Wenli used RNG $k-\epsilon$ turbulence model in CFD software and multi-reference system method are used to analyze the distribution characteristics of overall gas content distribution rate and flow field characteristics in the stirred tank [12]. Wang Y studied the oxygenation performance of aerator under different rotating speed, immersion depth, and liquid level [13]. Dong L found that at the same speed, the oxygen charging speed of oxidation ditch will slow down with the increase of operation time [14]. Ming J studied the performance of aerators with different blade shapes [15].

Different from the straight plate blades of the traditional inverted umbrella aerator, Xing Pu and others studied and designed an aerator with curved blades, and the blade profile is designed according to the law of logarithmic helix [16, 17]. Through the finite element analysis of the aerator blade, and according to the real flow field, a series of optimization of the aerator blade is carried out to make it have better oxidation and aeration performance.

2. Mathematical Simulation Experiment

2.1. Modeling and Meshing. First of all, using SOLIDWORKS software to model the aeration wheel and oxidation ditch, the aerator impeller has a maximum diameter of 90 mm, the height is 25 mm, the number of blades is 6, the blade inclination angle is 70° , and the middle opening diameter is 50 mm. Curve blades are controlled by a trolling helix, which is built by the software's equation-driven curve, as shown in equation (1), and then the blade is generated by scanning, as shown in Figure 1.

$$\begin{cases} x(\theta) = r \cdot e^{\theta/\tan \beta} \cdot \cos \theta \\ y(\theta) = r \cdot e^{\theta/\tan \beta} \cdot \sin \theta \end{cases} \quad (1)$$

where r is the initial polar diameter, θ is the spiral rotation angle, and β is the helix angle.

After the construction of the aerator impeller model is completed, the working area of the aerator needs to be established, and this simulation uses the oxidation ditch model during the experiment. After modeling, the model is assembled, as shown in Figure 2, which is 1000 mm long and 800 mm wide. Then the origin of the coordinate system is placed at the center of the surface on the aerator impeller, which is 300 mm away from the bottom of the barrel.

The processed model is then imported into ANSYS, the grid is divided using the fluent meshing feature, and the maximum mesh size of the stationary domain is set to 7 mm, rotating the domain. The maximum mesh size is set to 4 mm. The final generated total number of grids is 2.71million, the three rotating domain grids are 40,000, the mass is 0.5 or more. The number of static domain grids is 2.59 million, with a mass of more than 0.8, which meets the grid quality requirements required for calculation. A grid-dividing diagram of the rotation and stationary fields is shown in Figure 3.

2.2. Numerical Simulation Analysis. The flow situation in the oxidation ditch is more complex; it takes a certain amount of time from the start of the aerator to the stable state of the oxidation ditch flow field, and the distribution of the flow field is very different at different times before the stabilization of the same channel, so the flow field is analyzed after the oxidation ditch is selected to reach a stable state. To facilitate the description of the various areas in the oxidation ditch, three aerator impellers are named with four ramps, as shown in Figure 4. In the vertical direction, the oxidation ditch flow field is divided into upper, middle, and lower layers. Four runs and three impellers were named, and the

walls of each channel was placed on and off the walls to distinguish them.

In order to analyze the flow field in the oxidation ditch, the simulation results are processed by CDF-post software, and the velocity cloud map, flow map, and turbulent kinetic energy cloud map at different locations in the flow field are made.

Figure 5 shows turbulent kinetic energy cloud maps of impellers 2 and 3 in the oxidation ditch at the XZ cross section, and Figure 6 shows velocity flow clouds at the impeller sections 2 and 3, where 6(a) shows impeller 2.

As can be seen from the two 6(a) diagrams, areas with high turbulence energy (the yellow and red areas in the figure) are distributed near the free liquid surface. According to the two-film theory, the membrane of the two phases of the turbulent local gas fluid becomes thinner and is conducive to the transfer of oxygen. Figure 6(a) have two red areas in the area: one around the blades, the outermost and fastest line of the aerator impeller, the largest relative speed of liquid to air, and the higher intensity of turbulent kinetic energy. The other is where the liquid collides with the wall. From Figure 6(b), it can be seen that the dense flow area is concentrated at the gas-liquid interface near the wall of the oxidation ditch, and there is a circulation vortex in the upper and lower phases of the gas liquid at the wall. Liquids have a higher speed when moving towards the wall, and it will take with the air on the surface and will move upward when it is close to the wall, while the negative pressure generated by blade rotation will cause the air above the impeller to move downwards, so the air above the surface near the wall will produce circulation. Some liquids are hit at the wall and move upward along the wall before falling into the water under the action of gravity, the liquid falling into the water will collide with the liquid moving towards the wall, will form bubbles and vortexes, and the water curtain generated by the water leap will also hit the surface of the water near the wall to form bubbles, so there is strong turbulent motion near the wall. Figure 6 is blade 2, and the left side of the blade is the right side of the wall of the channel; hence the liquid on the left will collide with the wall and the liquid on the right will fall into the flow way, so in Figure 5(a) turbulent kinetic energy distributions are different on the left and right, and there is no significant air circulation in the upper right in Figure 6(a).

Figure 7 are three-dimensional flow maps of the oxidation ditch at different angles when the inflow field reaches a stable state. Figure 8 are velocity cloud maps and velocity maps within oxide ditches at different depths (XY sections) when the flow field is stable, H is the distance of the liquid surface from the bottom of the pool, the aerator impellers move clockwise, the blue area in the figure has the lowest flow rate, the red area has the highest flow rate, and the direction of liquid flow in the oxidation ditch is shown by the black arrow in the figure.

As can be seen from Figure 7(a), the flow field near the blade has the highest speed, and the liquid leaves the impeller at a velocity perpendicular to the direction of the blade. The liquid pushed by blade 1 enters the a and b channels, and as can be seen from Figures 7 and 8(a), the distance between the

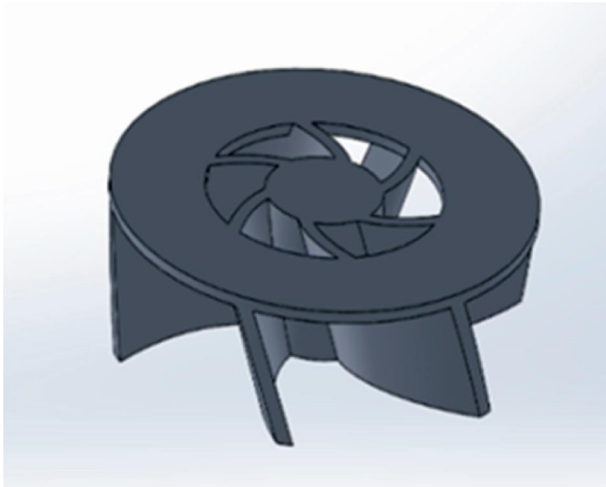


FIGURE 1: Impeller 3D model.

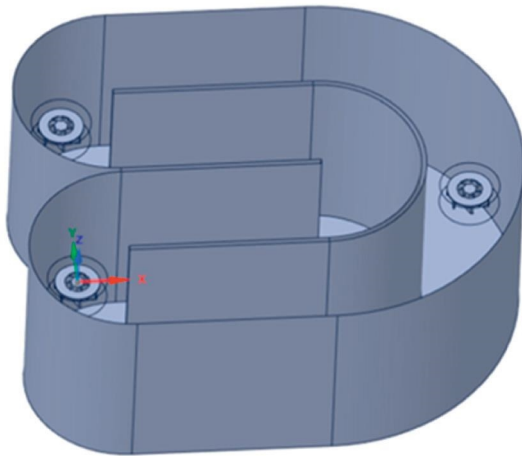


FIGURE 2: 3D model of the oxide ditch.

speed and the line in the b-runway is significantly greater than a, so the b-channel is the main push area of blade 1. Then the main push flow areas of blades 2 and 3 are *d* and *a*, respectively.

The liquid pushed by blades 2 and 3 meets on the right side of the *d*-flow channel, the liquid pushed by blades 1 and 3 meets on the lower left side of the *a*-channel, and the velocity direction changes after the two liquids meet, and the vector map at different depths shows that the liquid flows below its nearest impeller after the intersection. As can be seen from Figure 8(b)–8(d), the fast flow rate of liquid in the mid-flow field is mainly concentrated on the wall of the main push flow area, and the flow rate area gradually away from the corresponding aerator impeller as the depth increases. As can be seen in five images except Figure 8(a), the liquid velocity below the blade is generally moving towards the blade.

Channel *b* is the main push area of blade 1, the direction of liquid velocity is different at different depths, in the stratosphere layer, Figure 8(a) and 8(b), the velocity direction to the right, after contact with the wall at the end of

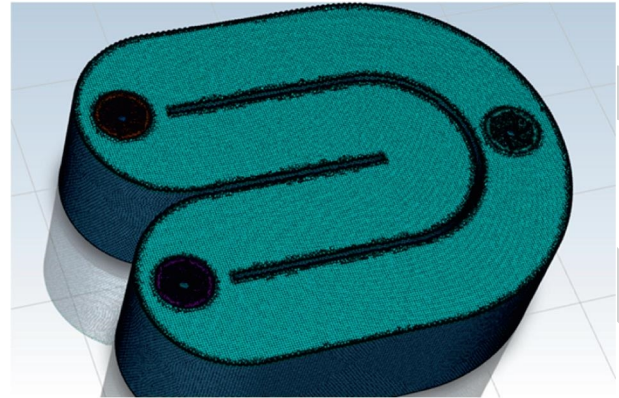


FIGURE 3: Grid division diagram.

the flow way, will flow along the wall facing the flow channel *c*; In Figure 8(c) and 8(d), the velocity of the high-flow area near the wall is directed to the right, but after touching the wall at the end of the flow way, the velocity is divided into two parts: one part continues to flow along the wall towards the flow channel *c*, and the other part flows back to the lower wall flow way of channel *b*. In the lower level of the flow field, in Figure 8(e) and 8(f), the flow rate of the liquid is mainly to the left, as opposed to the upper flow field. As can be seen from Figure 7, (a) circulation phenomenon occurs in runway *b* on a vertical cross section. The flow of channel *d* at different depths is similar to that of flow way *b*, and there is also a circulation in the vertical direction.

The flow at blade 3 is different from that of the other two blades, the main push flow area is the ring flow channel and the *a*-flow channel, the blade-driven liquid will flow down the outer runoff wall of the ring into the *a*-runway. After entering the *a*-channel, the high-speed area is mainly concentrated at the lower wall of the *a*-flow channel, and with the increase of depth, the position of high-flow rate gradually moves to the left, and the flow rate near the wall above the channel is lower. At the upper level of the flow field, the liquid speed is to the left, but there is a low-flow rate zone on the left side of the wall on the *a*-stream, where the liquid will produce a return flow in Figure 8(a). In the middle and lower layers of the *a*-flow channel, the flow rate gap between the upper and lower walls is large, and a circulation is generated between the high-flow zone and the low-flow zone, and the position of the circulation gradually moves to the right with the increase of depth.

The *c*-flow channel is the lowest speed area in the entire oxidation ditch flow field, and the liquid pushed by blade 1 will enter the *c*-flow along the circular wall at the corner, creating a circulation horizontally in the lower right-hand area of the middle of the *c*-flow.

Most of the liquid pushed by blades 7 and 1 enters the *b*-flow channel and creates a vertical circulation in the main push flow area, while the remaining push flow fluid flows downwards after hitting the wall, entering under the impeller and forming a small circulation near the impeller. The flow field near blade 2 is similar to blade 1. The liquid pushed upward by blades 2 and 3 meets at the junction of the *d*-runway and the ring runway, and the two fluids move

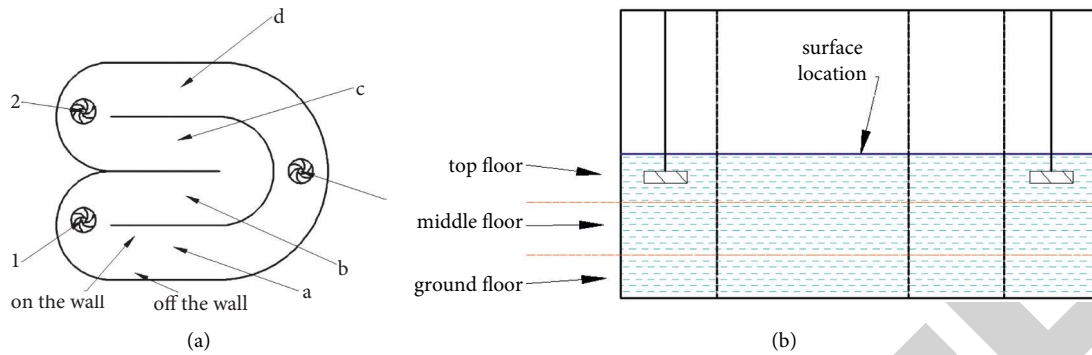


FIGURE 4: The name of the flow field and the flow channel.

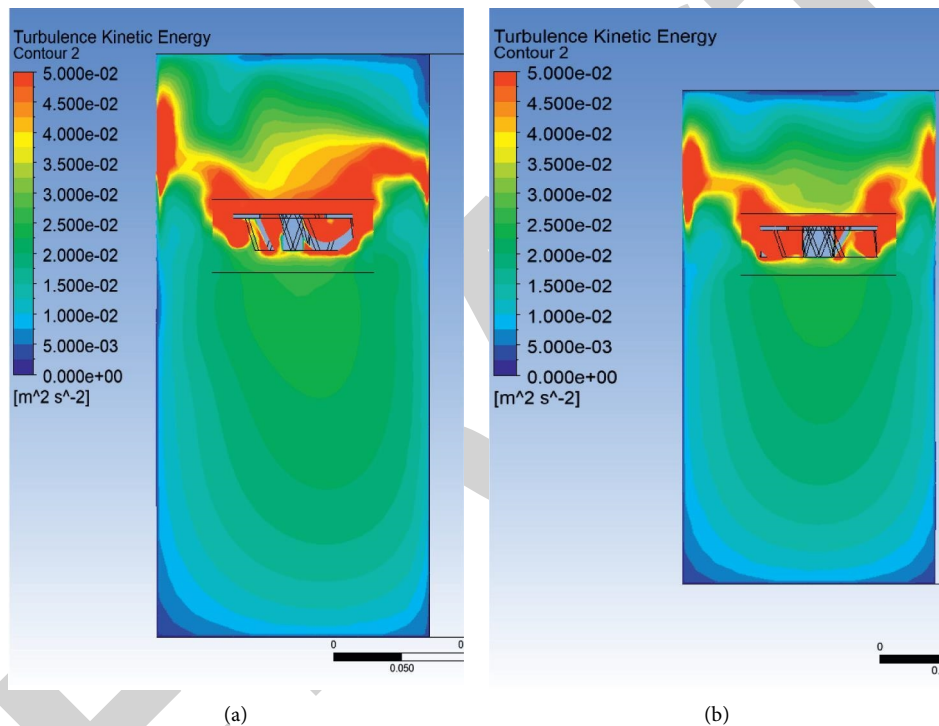


FIGURE 5: Turbulent kinetic energy cloud map.

below blade 3 after the encounter, some of which flows towards the impeller to form a circulation. The liquid pushed down by blade 3 enters the a-runway along the curved wall and eventually moves under blade 1. At the same time, there will be spiral circulation near the wall of the a-channel.

Figure 9 is a turbulent kinetic energy cloud map at different depths when the inflow field of the oxidation ditch is stable. As you can see from Figure 9, places with high turbulence energy (red and yellow areas in the figure) are concentrated around the blades, with low turbulence intensity in each runway. In the figure, H is the position of the section, the bottom of the pool H-0 mm, and the surface of the impeller is 300 mm from the bottom of the oxidation ditch, that is in the position of H-300 mm.

Figure 9(a) is light blue directly above the aerator impeller, where turbulence intensity is low, and there is a green area on the periphery with a high turbulence intensity. The fluid here is in a state where it is thrown out of the impeller and moves upward towards the slope, and is exposed to the wall by a drop in gravity. Liquids have a high-flow rate and are constantly in contact with air. The thrown liquid moves towards the wall layer by layer in a wave shape, which will produce vortices of different sizes. When the air contacts, the waves will be drawn into the air and enter the water to form bubbles. Part of the liquid generated by the hydraulic jump will also fall into the water here, and the impact when entering the water surface will draw in part of the air, resulting in high turbulence intensity. There are several red areas near the wall where the

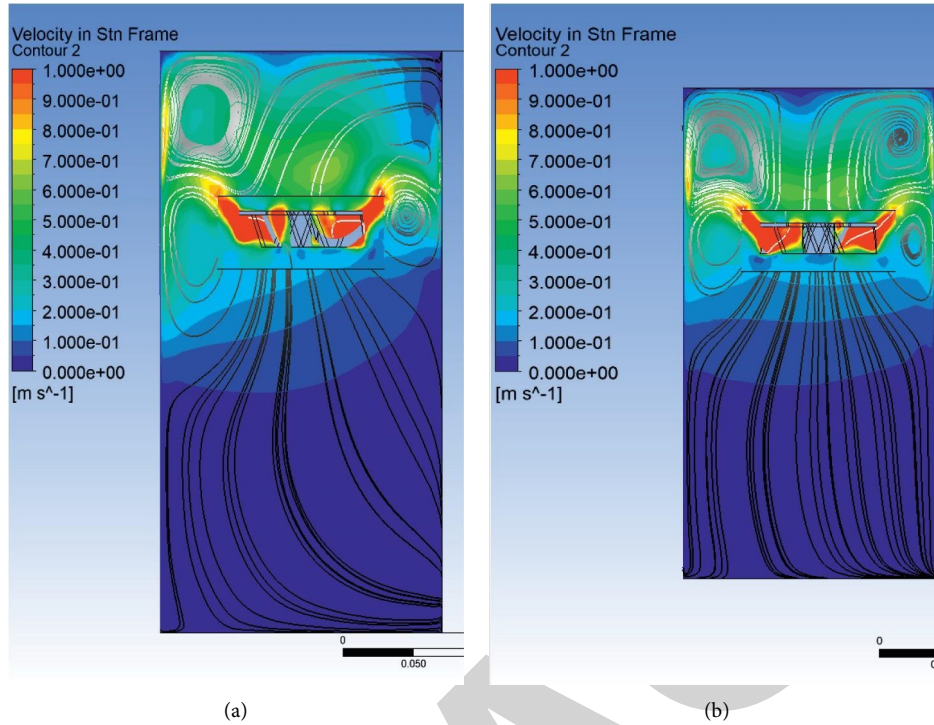


FIGURE 6: Speed stream cloud map.

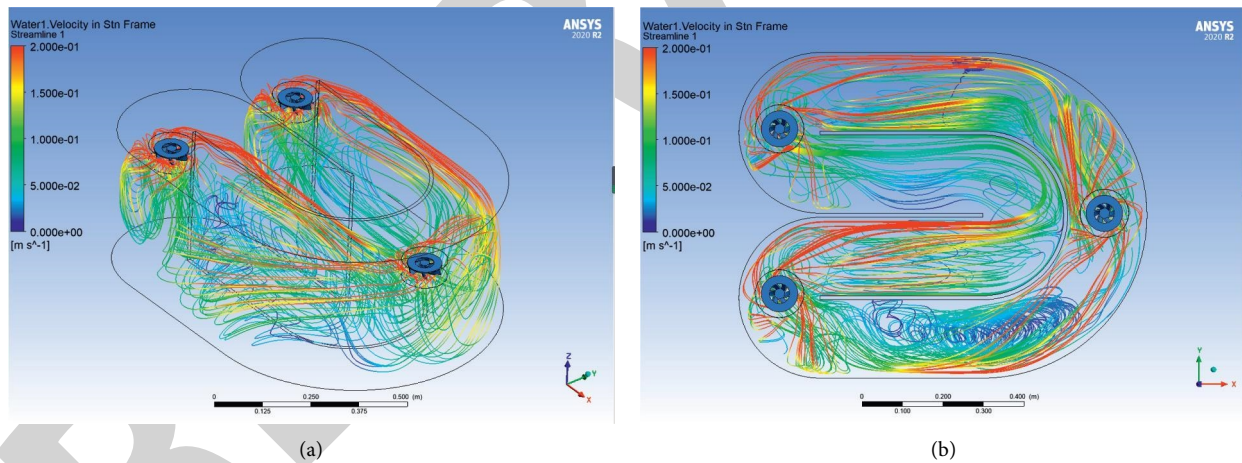


FIGURE 7: Flow charts at different angles.

liquid forms bubbles and moves downwards under the influence of gravity and push currents, where the flow of the liquid changes and has strong turbulent energy. The middle position is a concave structure produced by the high-speed rotation of the aerator impeller, from which air enters near the impeller, with no contact with the liquid surface and low turbulence. At Figure 9(b), the middle area is still a blue low-turbulent kinetic energy region, with a yellow-green ring-shaped high turbulent kinetic energy region on the periphery, and the rest a blue area with general turbulent kinetic energy. The liquid flies out of the yellow-green ring area under the push of the blade, giving it a high turbulence energy. The outer area of the green ring is

below the surface of the water, has no contact with the air, and the turbulence intensity is low.

For the upper and lower parts of the impeller, the area near the blade is the red area with high turbulent energy, and the rest is the cyan area with a certain turbulent kinetic energy (Figures 9(c) and 9(d)). The fluid in the red area with high turbulent kinetic energy is in direct contact with the blade, and the blade continues to work on the liquid. There are a large number of air bag behind the blade, and the relative velocity between the side and tail of the air bag is very fast, accompanied by a large number of bubbles and vortices, which have strong turbulent kinetic energy. The liquid moves upward in the push flow, causing the overall flow rate of the upper part of the blade

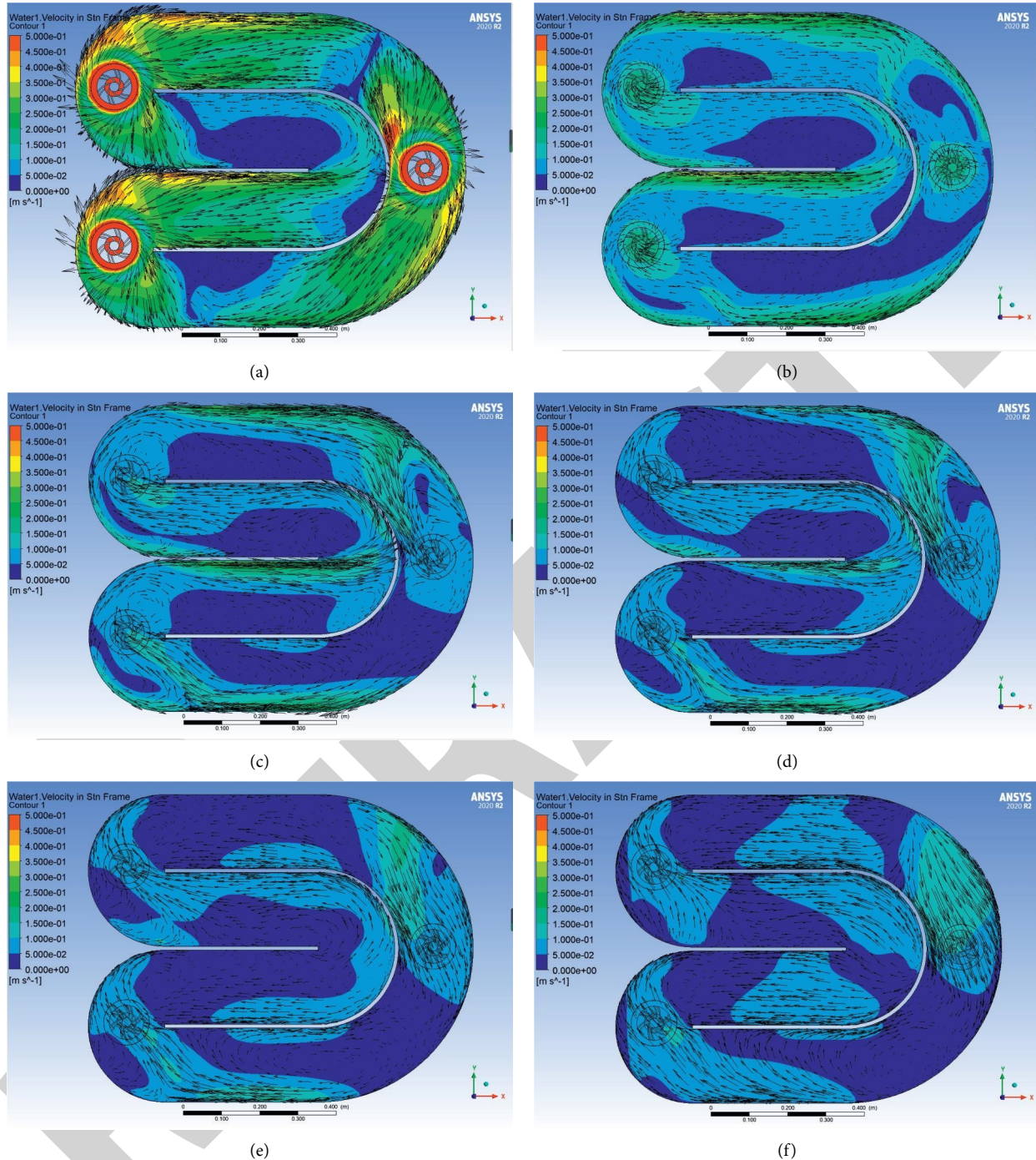


FIGURE 8: Vector and velocity cloud maps at different depths (a) $H = 300$ mm, (b) $H = 250$ mm, (c) $H = 200$ mm, (d) $H = 150$ mm, (e) $H = 100$ mm, and (f) $H = 50$ mm.

to be higher than that of the lower part and the turbulent kinetic energy to be higher than the lower part. For the deep water area below the blade, the red area with high turbulent energy does not appear in the deep flow field, most of the area is cyan, the intensity of turbulence kinetic energy decreases gradually with the increase of depth, especially the area of deep water near the wall (Figures 9(e) and 9(f)). The area with high turbulent kinetic energy is concentrated in the upper layer of the oxidation ditch flow field, in which the fluid will continue to

be pushed by the blade, maintaining the state of high turbulent kinetic energy, and where the oxygen transfer efficiency is high, it appears in the area with strong turbulent dynamic energy.

3. Airbag Characteristic Test

3.1. Experimental Materials and Platforms. In order to study the distribution of airbags during high-speed motion, the flow field near the aerator is photographed by high-speed

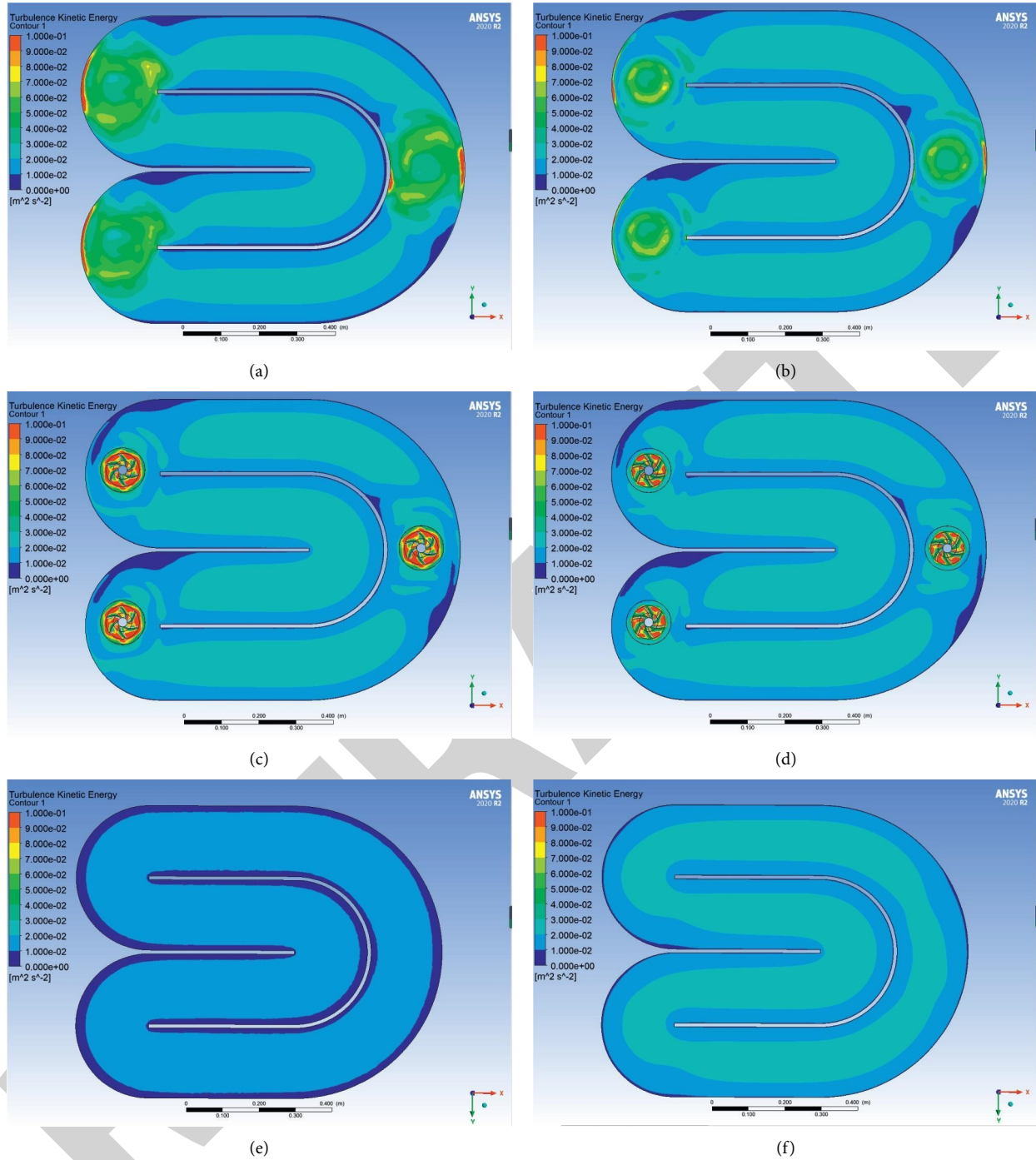


FIGURE 9: Turbulent kinetic energy cloud map at different depths (a) $H = 330$ mm, (b) $H = 310$ mm, (c) $H = 290$ mm, (d) $H = 280$ mm, (e) $H = 200$ mm, and (f) $H = 100$ mm.

camera to observe the situation of bubbles. The equipments used for shooting are Carousel oxidation ditch, curved blade aerator, LED lights, high-speed camera, computer, etc.

The model of the high-speed camera is 5f01. The shooting range selected in the experiment is a square area with a resolution of 840×840 . The set shooting rate is 1000 frames per second and the time of single shooting is 1 second. The high-speed camera and the LED light are shown in Figure 10. A position diagram of the camera and the LED

light at the time of shooting is shown in Figure 11. In Figure 10(a), 1 is an LED lamp, 2 is a high-speed camera, and 3 is a computer for storing data.

In this article, an image processing technique based on distance transformation and watershed algorithm is adopted [18–20]. This technique can be very good at improving noise, background, and bubble adhesion in noninvasive experiments, in order to understand the size distribution of different depth bubbles. The photographed

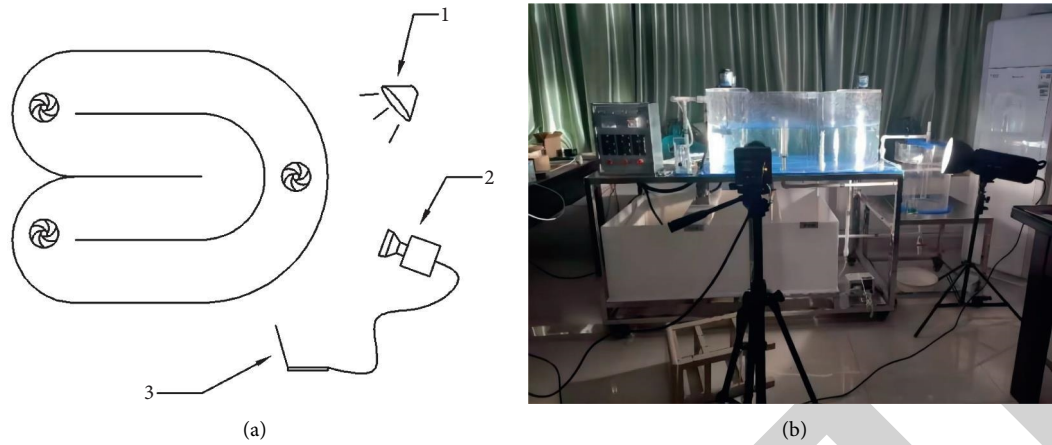


FIGURE 10: High-speed camera with LED lights.

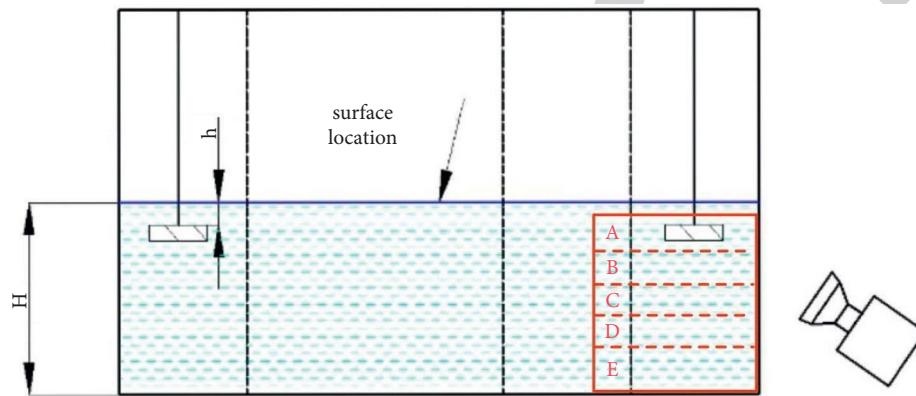


FIGURE 11: High-speed camera with LED and map of the shooting area.

areas are divided into five groups: area A (depth 0 to 60 mm), area B (depth 60 to 120 mm), area C (depth 120 to 180 mm), area D (depth 180 to 240 mm), and area E (depth 240 to 300 mm), and the size distribution of bubbles in each area was identified by image processing technology when the rotational speed was 400 rpm, and the position of the bubbles was photographed as shown in Figure 11. At the same time, for the A-region with the largest number of bubbles, the speed of the aerator is set to 250, 300, 350, 400, and 450 rpm, and the immersion depth is 5, 0, -5, -10, and -15 mm. The size distribution of bubbles in different parameters is observed.

The photos taken are shown in Figure 12. From the figure, we can intuitively see that the shape change of bubbles in the photos is very huge and irregular. This is because the bubbles in the water will collide under the stirring and propulsion of the impeller, resulting in the overlap of bubbles, and the rupture of bubbles is caused by the shear flow effect of eddy current and the instability of bubbles in the water. Due to the above effects, most of the bubbles taken are not spherical or elliptical, and the shape and size change greatly, so we need to deal with the photos.

Through the mean of shift filtering, image binarization, and distance transformation, watershed segmentation is

performed on the image. After watershed segmentation, as can be seen from Figure 13, the phenomena of noise, uneven background, and bubble sticking in the original image have been greatly improved. In the later image analysis, the size, shape, and distribution of bubbles under different rotating speeds and immersion depths should be analyzed.

Next, this article uses the method of equal area circle, and calculates the various dimension parameters of bubbles by the following formula:

$$d_m = \frac{\sum n_L d_L}{\sum n_L}, \quad (2)$$

where d_L is the diameter of the bubble (μm), n_L is the number of bubbles with a d_L diameter, and d_m is the average diameter of the bubble.

Since this experiment uses noninvasive measurements and cannot estimate the volume size of the shooting area, the local gas content is calculated using the picture after the watershed segmentation, as follows:

$$\alpha_g = \frac{S_{\text{bubbles}}}{S_A}, \quad (3)$$



FIGURE 12: Photos taken by high-speed camera.



FIGURE 13: Final result of processing.

where α_g is the local gas rate, S_{bubbles} is the total area of the bubble, and S_A is the total area of the shooting area.

3.2. Results and Analysis. Observation of experimental phenomena found that when the impeller rotates at high speed, a large amount of liquid will be thrown from the junction of the blade and the plate to form a water curtain, the water curtain moves obliquely upward, contacts with the air, and finally under the action of gravity falls into the water, called the water leap phenomenon.

Under the pushing action of the blade, the liquid thrown out has a high initial velocity. Under the influence of resistance and gravity, the liquid velocity decreases and begins to fall. At the same time, the liquid disperses from the water curtain into water droplets in the air and finally falls into the water surface. In the process of leaping, the liquid is in full contact with the air and after dispersing into water droplets, the contact area is further expanded. When it falls into the water, it will hit the water surface and wrap a large number of bubbles.

As the impeller rotates at high speed, air enters the airbag behind the blade through the middle opening and perimeter

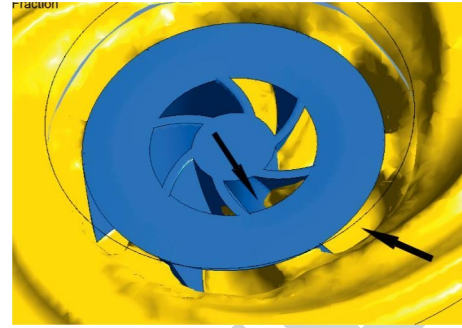


FIGURE 14: Air enters position.

of the impeller, as shown by the black arrow in Figure 14. Airbags increase the area of air–water contact, thereby increasing the rate of oxygen transfer in the aeration machine. Through simulation and high-speed photography, the free surface of the aerator blade from the bottom view is obtained, as shown in Figure 15(a) and 15(b). The distribution of airbags in the two cases in the figure is similar, which shows that the results obtained by numerical simulation have certain accuracy and reference value.

For this purpose, the distribution of airbags on the XY cross section was made, as shown in the flow and velocity vectors of Figure 16. The image shows that the shape of the airbag approximates a trapezoid, naming the surface of the airbag in contact with the rear of the blade as the side of the airbag, and the interface between the airbag and the blade push flow liquid is the back of the airbag. The velocity direction of the liquid and the air entering the air bag are shown in Figure 16(a), and the two phases are in the same speed direction at the back of the airbag, so the turbulent energy here is low. As can be seen from Figure 16(a), water on the side of the airbag is in the opposite direction to air, faster relative to the back, and more frequently exchanged. Observations of high-speed photography show that when the air on the side of the airbag comes into contact with the liquid, bubbles are thrown out of the airbags, which break in the water to form a large number of small bubbles dissolved into the water. This is due to the high-speed movement of the airbags with the blades, the side of the airbags relative to the liquid, as shown in the red area of Figure 17, where the turbulence strength is highest, resulting in more vortex and reflux. As shown by the white arrow in Figure 16(b), 16(a) small vortex forms on the side air–liquid interface of the airbag, and under the action of the vortex, a portion of the air is drawn into the water, forming bubbles of varying sizes. According to the double membrane theory, in the process of oxygen transfer, resistance mainly comes from the membrane of the liquid phase, and the greater turbulence strength can reduce the thickness of the membrane, where the turbulence is strong, the thinner the thickness of the membrane, the higher the efficiency of oxygen transfer.

3.2.1. Distribution of Bubble Size in Different Regions.

The results of watershed treatment show that the maximum size of the bubble is 7 pixels, because each pixel corresponds

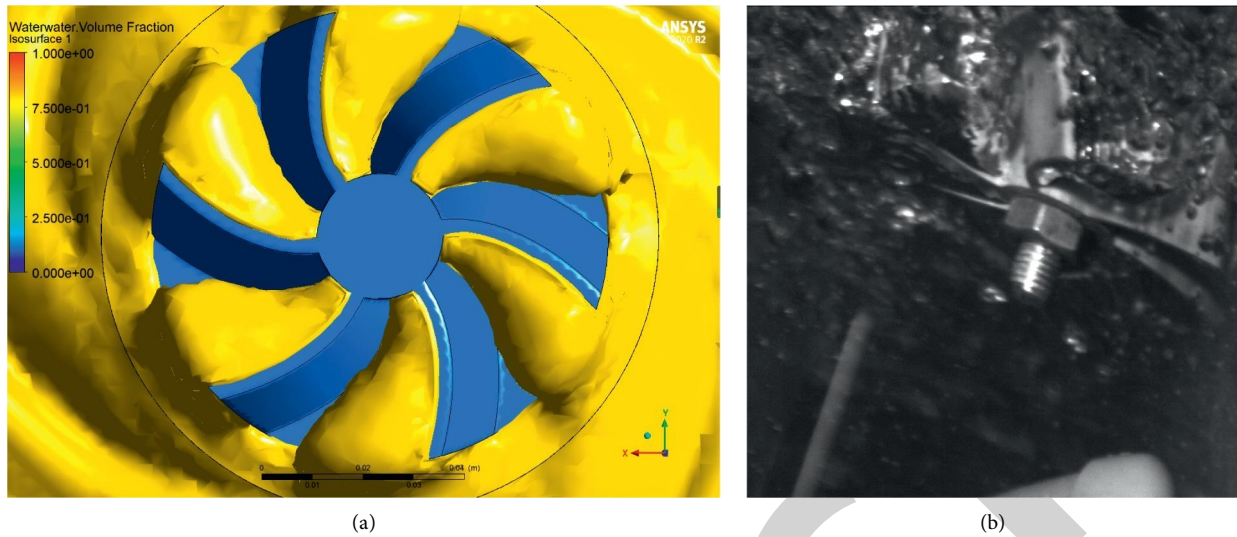


FIGURE 15: Air enters the airbag behind the blade. (a) Air enters position in simulated level. (b) Air enters position in experimental level.

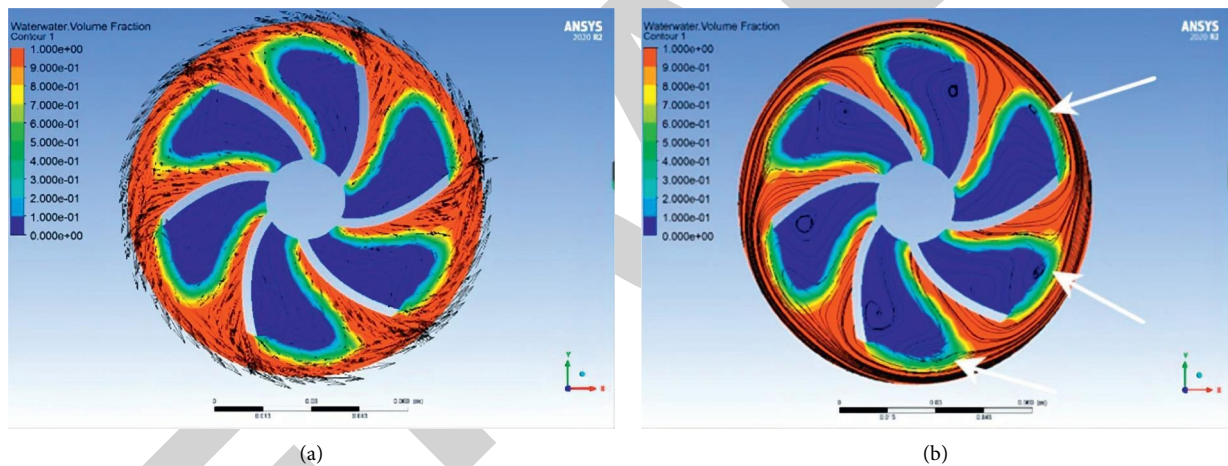


FIGURE 16: Gas-liquid distribution map: (a) Velocity vector and (b) flow chart.

to the size of 0.31 mm, the maximum bubble diameter is 2.17 mm. Bubbles range in size from 0 to 2.17 mm. The size range of bubbles is subdivided into four areas: 0–1.75 pixels, 1.75–3.5 pixels, 3.5–5.25 pixels, and 5.25–7 pixels. The corresponding dimensions are 0–0.54 mm, 0.55–1.09 mm, 1.1–1.63 mm, and 1.64–2.17 mm. The following image (Figure 18) shows the number and size distribution of bubbles in five areas at a speed of 400 rpm and a blade immersion depth of -10 mm.

From Figure 18, it can be seen that from area A to area E, as the depth increases, the number of bubbles decreases gradually, the blade's push flow capacity on the surface of the water body is significantly stronger, and the water leap phenomenon on the surface of the water body will also increase the number of bubbles.

To examine the average bubble size, combined with the results of the high-speed camera, 100 photos were taken in each area to calculate the average bubble size. As can be seen

from Table 1, with the increase of depth, the average size of bubbles gradually decreases, the maximum average size of bubbles is A, and then we set the speed of the aerator to 250, 300, 350, 400, and 450 rpm. The following two situations are then analyzed.

3.2.2. The Size Distribution of Bubbles at Different Speeds and Immersion Depths. The size distribution of bubbles in different parameters is observed. First, immersion depth is set to -10 mm. As can be seen from Figure 19, with the increase of speed, the average size of bubbles gradually increases, when the speed increases from 250 rpm to 350 rpm, the average size of bubbles increases the most. The proportion of bubbles of different sizes at different speeds is: 0–0.54 mm accounting for 26%–67%, 0.55–1.09 mm accounting for 20%–54%, 1.1–1.63 mm accounted for 11%–19%, and 1.64–2.17 mm accounted for 5%–9%. As the speed increases,

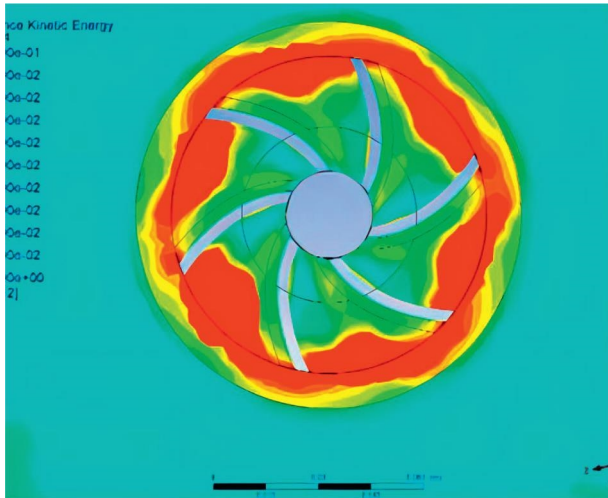


FIGURE 17: Turbulent kinetic energy cloud map.

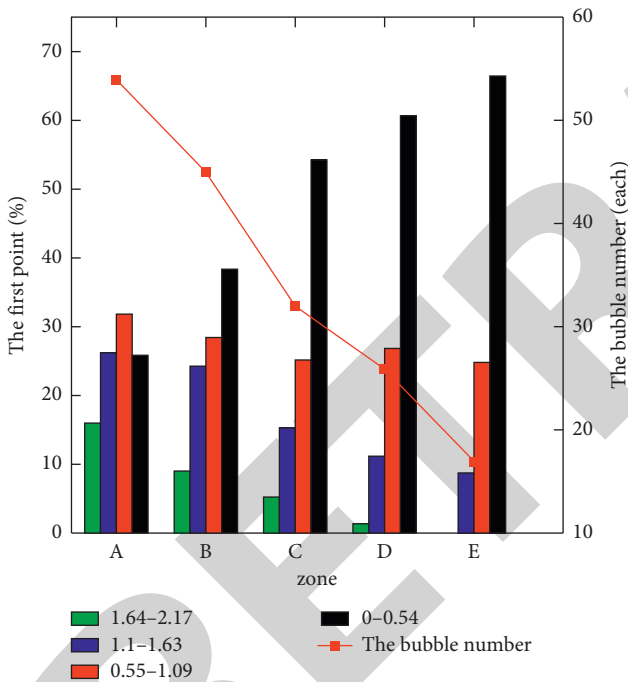


FIGURE 18: Distribution of the number and size of bubbles in each region.

TABLE 1: The size distribution of bubbles in different regions.

Region	Bubble average size/mm	Number of bubbles/each
A	1.56	67
B	1.23	53
C	0.82	32
D	0.76	26
E	0.43	12

the percentage of large bubbles increases gradually, but at speed above 400 rpm, the percentage of large bubbles above 1.1 mm decreases slightly because the atmospheric bubbles break faster due to intense agitation at ultra-high speeds.

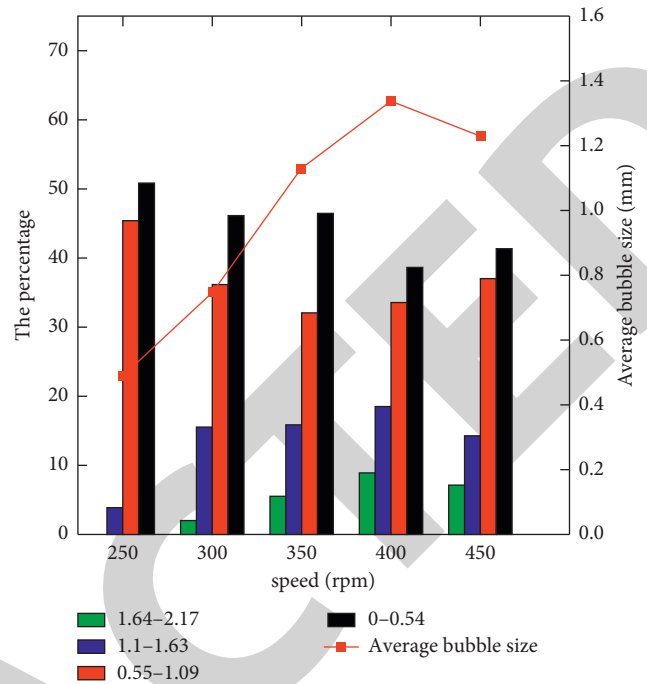


FIGURE 19: The size distribution of bubbles at different speeds.

Next, according to the experimental results of the single-factor experiment, the aerator speed is set to an optimum value of 400 rpm. As can be seen from Table 2, as the depth of immersion increases, the average diameter of the bubbles increases and decreases, reaching a maximum value of -10 mm.

3.2.3. Effect of Different Speeds and Immersion Depth on Local Gas Content. The local gas content of the whole viewfinder range is measured, and the change in local gas content under different environmental parameters is observed. It can be seen from Figure 20 that with the increase of the speed of the aerator, the local gas holdup in area A increases significantly. The reason is that the increase of rotating speed will increase the turbulence intensity at the liquid level and more air will be sucked into the opening of the aerator, and the increase of liquid level flow velocity caused by the increase of rotating speed will also make more bubbles moving to deeper positions and increase the overall gas holdup. With the increase of the immersion depth of the aerator blade, the local gas content of the A area increases first and decreases, with a peak of 0.41% at -10 mm.

3.2.4. Effects of Different Rotating Speed and Immersion Depth on Oxygenation Performance. By adjusting the amount of water in the oxidation ditch, the experimental water surface is selected to be 15 mm, 10 mm, and 5 mm higher than the impeller (record as -15 mm, -10 mm, -5 mm), level with the impeller (0 mm), and 5 mm lower than the impeller. By controlling the motor, the aeration performance of the aerator at 250r/min, 300r/min, 350r/min, 400r/min, and 450r/min was measured. The

TABLE 2: Distribution of bubble size at different immersion depths.

Blade immersion depth/mm	Average bubble diameter/mm	Number of bubbles/each
5	1.19	179
0	1.25	176
-5	1.38	203
-10	1.43	214
-15	1.32	197

TABLE 3: Standard dynamic efficiency SAE under different motion parameters.

Rotation rate(r/min)	Immersion depth(mm)				
	-5	0	5	10	15
250	8.358741	9.903545	10.08076	6.224943	4.407669
300	11.52945	15.61059	19.26355	18.94075	15.92139
350	17.97342	24.30924	30.77573	39.48686	29.99074
400	18.96033	28.60427	37.00992	43.84839	37.47218
450	19.07107	29.24774	36.60363	42.97512	40.83162

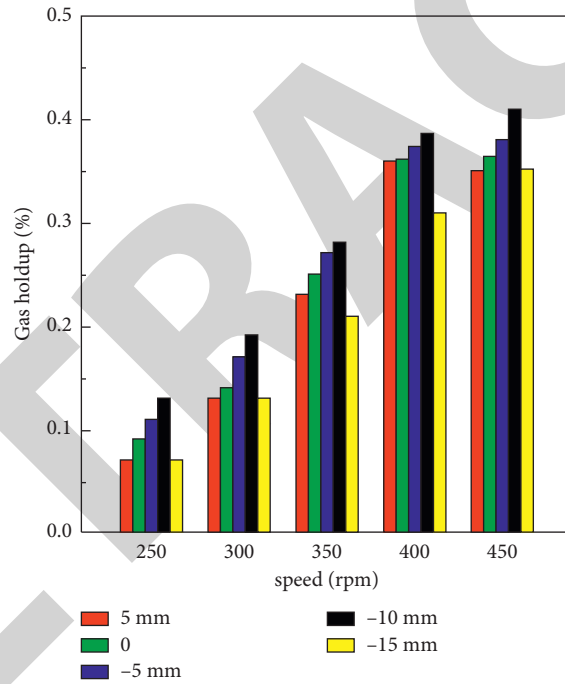


FIGURE 20: Comparison of local gas content at different speeds and immersion depths.

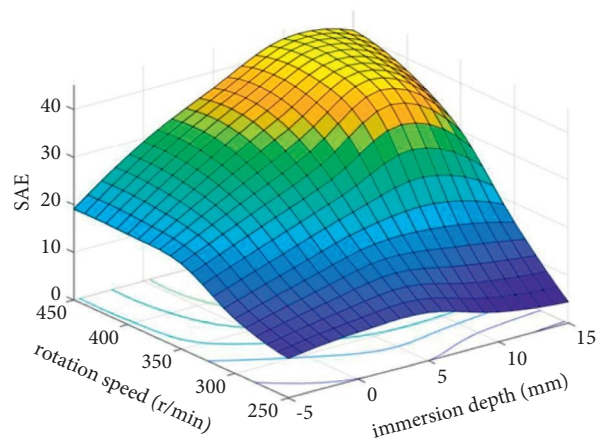


FIGURE 21: Standard power efficiency SAE.

experimental data eliminate the influence caused by the temperature difference in different experiments, and fit the aeration capacity of the aerator under different immersion depth and rotating speed. The standard dynamic efficiency SAE obtained is shown in Table 3. According to Table 3, the curved surface diagram of standard dynamic efficiency SAE under different motion parameters is drawn, as shown in Figure 21.

In Figure 21, the x -axis represents the immersion depth, the y -axis represents the speed, and the z -axis represents the standard dynamic efficiency (mg/min-w). As can be seen from the three-dimensional curved surface diagram, the standard dynamic efficiency of the aerator mainly presents a peak shape. When the immersion depth is 15 mm and the rotating speed is 250r/min, the standard dynamic efficiency of the aerator is the lowest. When the speed of the aerator is lower than 300r/min, the standard dynamic efficiency of the aerator and the dynamic efficiency of the aerator are always at a low level. At this time, changing the immersion depth has no great impact on the standard dynamic efficiency of the aerator. When the speed of the aerator is 400R/min and the immersion depth is about 10 mm, the standard dynamic efficiency of the aerator is the highest.

4. Conclusion

In this article, the motion of the high-speed rotation of the aerator impeller in the oxidation ditch is observed and simulated by fluent simulation and high-speed photography experiments. The flow of liquid after the stabilization of the flow field in the oxidation ditch was analyzed by the VOF free liquid surface model and the Euler multiphase flow model:

- (i) The flow rate and turbulent kinetic energy intensity of the liquid near the surface of the water is higher than that of the water surface, and the horizontal effect of the blade push flow on the inner flow field of the oxidation ditch is greater than the vertical effect. Where turbulence is high, it is around the blade, and where the liquid is flowing fast, it is mainly near the blade.
- (ii) The upper flow field of the flow channel has the highest flow rate near the wall. The liquid of the upper layer of the oxidation ditch flows in the direction of the main push flow of the blade, and the flow rate gap between the upper and lower stratospheres in the main push flow area is large, which will produce circulation in the vertical direction. Most of the liquid in the lower layer of the oxidation ditch flows towards the nearest impeller. At the same time, when the flow rate gap between the two walls of each channel is too large, a return flow is generated in the horizontal direction.
- (iii) The aeration turbine will have a certain lifting ability and push flow ability of the liquid, the liquid under the action of lifting force from the liquid under the blade will move in the direction of the impeller.

After entering the impeller, under the push of the blade, with the blade line movement, a part of the liquid under the combined force of the blade side along the slope, forming a water leap.

- (iv) High-speed rotation around the blade will produce a certain amount of negative pressure, so that the oxidation ditch center fluid facing the depression, air into the rear of the blade to form an air bag, the liquid around the blade flow rate is very fast, forming a turbulent vortex on the contact surface between the liquid and the air bag, and the air will form bubbles and be drawn into the water under the action of turbulence.
- (v) By observing the bubble size, it can be seen that when the rotating speed is 400 rmp and the immersion depth is -10 mm, the bubble size is the largest, and at this depth, the local gas holdup in area A is the largest. In conclusion, the new curved blade aerator has the best oxygenation performance when the rotating speed is 400 rmp, and the immersion depth is -10 mm.

Data Availability

Data sharing is not applicable to this article as no datasets were generated or analyzed during the current study.

Conflicts of Interest

The authors declare that they have no conflicts of interest.

Acknowledgments

The research work of this article was supposed by the China national founding of 51768045, and Technology Plan key R and D Project of Jiangxi province, China (nos. 20181ACG70024 and 20202BBF63010).

References

- [1] A. Zhao and X. Shi, "Comparative analysis and regulation of process design between surface aeration oxidation ditch and bottom aeration biological tank," *Journal of Jiaozuo University*, vol. 35, no. 2, pp. 102–105, 2021.
- [2] S. Fu, X. Lu, and T. Yang, "Development and practice of integrated oxidation ditch a \sim 2/O process water treatment experimental device," *Comprehensive utilization of resources in China*, vol. 39, no. 10, pp. 70–73, 2021.
- [3] Z. Han, S. Li, G. Zhu, Y. Lu, G. Yan, and Z. Li, "Study on the influence factors of oxygen transfer in aeration tanks in highland areas," *Water treatment technology*, vol. 47, no. 6, pp. 34–38, 2021.
- [4] K. Wang, L. Guo, H. Yu, and B. Liu, "Engineering application research of the improved carousel oxidation groove process in PTA wastewater treatment," *Chemical Engineering and Equipment*, vol. 92, no. 11, pp. 255–257, 2017.
- [5] H. Liu, H. Shang, X. Tang et al., "Study on the effect of the number of blades on the aeration performance of the parachute aerator," *Journal of Drainage and Irrigation Mechanical Engineering*, vol. 38, no. 9, pp. 922–927, 2020.

Retraction

Retracted: Deformation Analysis of Surrounding Rock of Deep Roadway by the Fluid Structure Coupling Model with MIDAS-GTS

Advances in Materials Science and Engineering

Received 26 December 2023; Accepted 26 December 2023; Published 29 December 2023

Copyright © 2023 Advances in Materials Science and Engineering. This is an open access article distributed under the Creative Commons Attribution License, which permits unrestricted use, distribution, and reproduction in any medium, provided the original work is properly cited.

This article has been retracted by Hindawi, as publisher, following an investigation undertaken by the publisher [1]. This investigation has uncovered evidence of systematic manipulation of the publication and peer-review process. We cannot, therefore, vouch for the reliability or integrity of this article.

Please note that this notice is intended solely to alert readers that the peer-review process of this article has been compromised.

Wiley and Hindawi regret that the usual quality checks did not identify these issues before publication and have since put additional measures in place to safeguard research integrity.

We wish to credit our Research Integrity and Research Publishing teams and anonymous and named external researchers and research integrity experts for contributing to this investigation.

The corresponding author, as the representative of all authors, has been given the opportunity to register their agreement or disagreement to this retraction. We have kept a record of any response received.

References

- [1] J. Jiang, Z. Hou, K. Hou, Y. Lu, H. Sun, and X. Niu, "Deformation Analysis of Surrounding Rock of Deep Roadway by the Fluid Structure Coupling Model with MIDAS-GTS," *Advances in Materials Science and Engineering*, vol. 2022, Article ID 9945383, 6 pages, 2022.

Research Article

Deformation Analysis of Surrounding Rock of Deep Roadway by the Fluid Structure Coupling Model with MIDAS-GTS

Jun Jiang ^{1,2}, Zhengmeng Hou ^{1,2,3}, Kepeng Hou,^{1,2} Yongfeng Lu ^{1,2}, Huafen Sun,^{1,2} and Xiangdong Niu^{1,2}

¹Faculty of Land and Resources Engineering, Kunming University of Science and Technology, Kunming 650093, China

²Yunnan Key Laboratory of Sino-German Blue Mining and Utilization of Special Underground Space, Kunming 650093, China

³Institute of Subsurface Energy Systems, Clausthal University of Technology, Clausthal-Zellerfeld 38678, Germany

Correspondence should be addressed to Zhengmeng Hou; houzm4199@126.com

Received 24 November 2021; Accepted 30 December 2021; Published 16 March 2022

Academic Editor: Palanivel Velmurugan

Copyright © 2022 Jun Jiang et al. This is an open access article distributed under the Creative Commons Attribution License, which permits unrestricted use, distribution, and reproduction in any medium, provided the original work is properly cited.

In order to verify the universal applicability of the fluid structure coupling model to the analysis requirements of deep tunnels under the MIDAS-GTS geotechnical simulation environment, the study, together with several mining enterprises, carried out verification and analysis on the measured data of 107 deep tunnels in recent years. The reference group selects the mean value of the analysis results generated by the analysis model using the preferred nonfluid structure coupling model in the MIDAS-GTS environment. Finally, it is confirmed that the fluid structure coupling model group data have significant advantages over the reference group data within the buried depth of 550 ~ 1450 m and the tunnel cross-sectional area of 45 ~ 102 m². Finally, it is considered that the fluid structure coupling model has universal applicability within the analysis range. It is suggested that, in the future work, for example, when the tunnel construction project within the above analysis scope needs to carry out the simulation analysis of roof displacement and anchor bolt tension, the fluid structure coupling model should be directly selected as the analysis model.

1. Introduction

The surrounding rock pressure distribution of deep roadway is relatively complex. In the current ground pressure theory, there is no calculation formula to fully control the deep surrounding rock pressure. Therefore, relevant research records the actual ground pressure data in the process of adjacent roadway excavation and selects the ground pressure model in line with the actual ground pressure performance for subsequent simulation according to the actual data, so as to determine the ground pressure control strategy [1]. The mine pressure control strategy includes active support schemes such as anchor bolt, anchor cable and grouting, and passive support schemes such as steel beam and arch. The combined technical scheme has a more reliable support control effect in the deep roadway with the current buried depth of less than 1600 meters [2].

In this study, MIDAS-GTS (geotechnical and tunnel analysis system) is a finite element analysis control for geotechnical mechanics, which runs on MIDAS CIVIL 2021 software platform. In the study, the fluid structure coupling model is used to analyze the measured data of deep roadway in different mine types and compare the coupling and difference between the simulation analysis results and the measured results, so as to demonstrate whether the fluid structure coupling model has universal adaptability in deep roadway.

2. Data Sources and Research Methods

Thirty five tunnels in Xinjiang, Inner Mongolia, Gansu, and Shaanxi in Northwest China, 15 tunnels in Guizhou and Sichuan in Southwest China, 12 tunnels in Heilongjiang and Liaoning in Northeast China, and 45 tunnels in Shanxi,

Henan, Shandong, and Anhui in Central Plains of China were selected. A total of 107 tunnels were investigated. The main data source related to the tunnel is the channel obtained by contacting the technical department of relevant mining companies for the research, and the secondary data source is the data sharing channel in public reports, papers, and conference documents. The buried depth of the tunnel selected into the research database is 550 ~ 1450 m, and the tunnel section is 45 ~ 102 m². The specific distribution is shown in Figure 1:

In Figure 1, there are 51 tunnels with a buried depth of 800 ~ 1000 m, accounting for 47.66%, 96 tunnels with a buried depth of 550 ~ 1200 m, accounting for 89.72%, 63 tunnels with a cross-sectional area of 55 ~ 75 m², accounting for 58.88%, and 96 tunnels with a cross-sectional area of 45 ~ 95 m², accounting for 89.72%. That is, the core data in the research database are buried depth 550 ~ 1200 m and cross-sectional area 45 ~ 95 m².

In this study, MIDAS-GTS control is loaded in MIDAS CIVIL 2021 software to conduct finite element analysis of tunnel data in the database. Because all data are historical data from 2016 to 2020, the analysis results can be certified in time. Analyze the data before date t to judge the difference and correlation between the ground pressure simulation results and the actual ground pressure records on date t and date $t + n$. The comparison data include roof displacement and bolt tension.

3. Model Design and Experimental Record

The deep roadway involved in this study has different buried depths, cross-sectional area, geological environment, and support scheme. In the support scheme, the length and density of anchor rod and anchor cable are different, the composition of anchoring agent and grouting fluid are also different, and the schemes of passive support are also different (such as steel beam, steel strip, shotcrete, and arch building), so the construction principle of the three-dimensional model of different support schemes should be determined [3], as shown in Figure 2.

In Figure 2, all tunnels are built with three-dimensional models according to the four-layer model, of which the innermost layer is the passive support structure layer, including the support structure other than the metal support structure. The metal passive support structure is built in the passive support structure layer, and the metal passive support structure layer is modeled according to the actual size of metal support structures such as steel beam and steel strip. The surrounding rock part is divided into the anchor layer and the surrounding rock layer. The anchor layer is designed according to 1.2 times of the anchor length or 0.7 times of the anchor cable structure. After determining the thickness of the anchor layer, the surrounding rock layer model with 6 times of the thickness of the anchor layer is designed. The differences of different tunnels due to geological conditions, buried depth, cross-sectional area, and other influencing factors are modeled from the weight of surrounding rock, external stress, and the design parameters of elastic modulus, compressive strength, and shear strength of each layer.

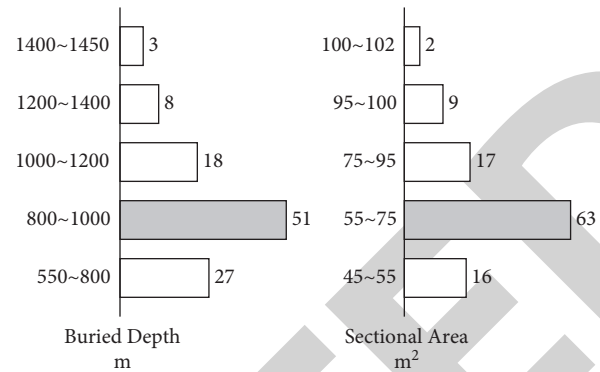


FIGURE 1: Distribution of tunnel characteristics in the research database (data source: collected by the study).

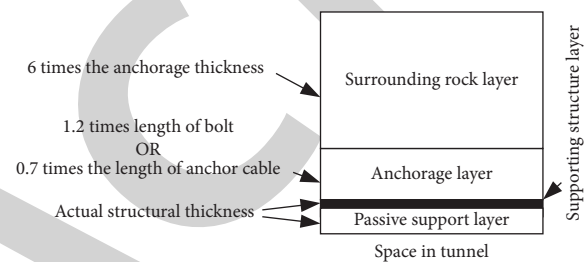


FIGURE 2: Design principle of the finite element three-dimensional model (local of roof section).

Deep tunnels are divided into development tunnels and mining area tunnels. The development tunnel is generally excavated in the whole rock in the stable rock stratum, the tunnel section is large, the tunnel is far from the coal seam and soft rock stratum, its service time is long, and the pressure environment is relatively stable. Mining area tunnels are generally excavated near or in coal seams, with short service time and complex pressure environment [4]. The mining area tunnel in this study is subject to the pressure control technology of deep tunnel, and less all coal or all soft rock tunnel is selected. It is generally arranged along the coal seam roof. When the coal seam roof is soft rock, it is generally arranged along the soft rock stratum roof, so as to ensure the stability of the tunnel roof first. Therefore, the cross-section strata of 107 deep tunnels involved in the research database include 85 whole rock structures, accounting for 79.44%. In the actual development scheme, all tunnels are arch sections or circular arch sections, as shown in Figure 3:

In Figure 3, H is the full height of the tunnel, B is the full width of the tunnel, R_L and R_R are the radius of the two shoulder circular arch structure of the arched tunnel, R_M is the radius of the central arch structure of the arched tunnel, O_L and O_R are the center of the two shoulder circular arch structure of the arched tunnel, O_M is the center of the central arch structure of the arched tunnel, R is the radius of the circular arch structure of the arched tunnel, O is the center of the circular arch structure of the arched tunnel, H_A is the height of the side wall of the arched tunnel, and H_C is the height of side wall of the circular arch tunnel. Because the excavation maintenance period of most deep tunnels is

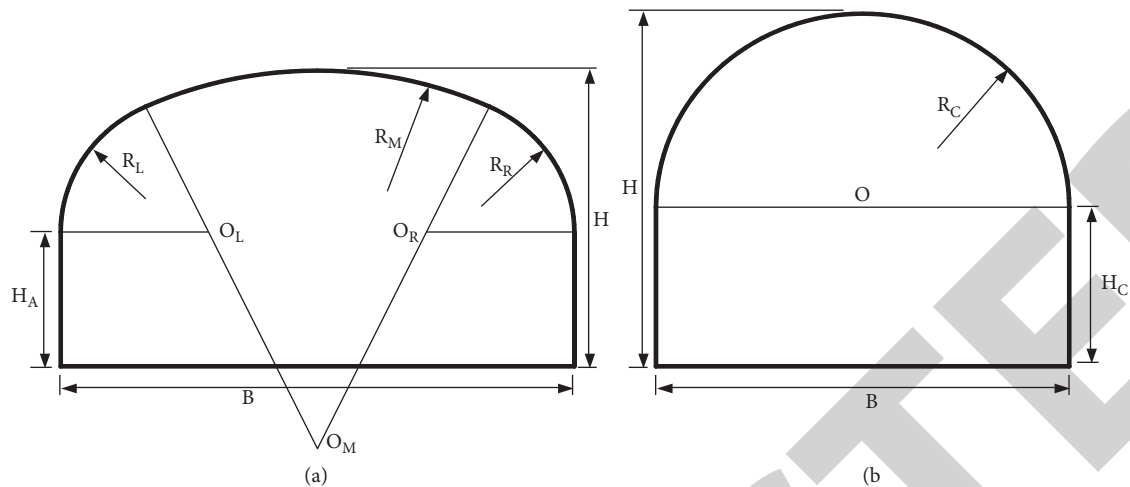


FIGURE 3: Section composition of two tunnel sections. (a) An arched section and (b) a circular arched section.

about 15 days, the excavation depth per day under the current process conditions is about 4 ~ 7 m, and a three-dimensional finite element model with a length of 105 m is constructed along the section in the figure.

The excavation process of large section deep tunnel is mostly divided into steps and the multistep excavation method. Generally, one step is set every 3 ~ 5 m height to form the top, side wall, and bottom plate in turn. The tunnel with height less than 7 m adopts the one-time smooth blasting forming method. Advance support is generally adopted within the 8-hour construction period (2 ~ 3M), which is generally the construction process of predrilling beam and pregrouting [5]. The preanchor cable method will be used to strengthen the support in the soft rock fracture zone, the active support will be completed within the 24-hour construction period (4 ~ 7M), and the passive support will be completed within the 48-hour construction period (8 ~ 14 m), which is generally anchor bolt, anchor cable, permanent grouting, and steel beam. For shotcrete and other support schemes, the arch filling layer will be arranged in the shotcrete layer in the development tunnel. Therefore, the structure of the front end of the tunnel in the model design is more complex, and the structure of the rear section is basically the same [6].

Because the working face structure of the full face tunneling method is relatively simple and limited by space, the modeling method of working face structure of the full face tunneling method is not analyzed in [7]. The 2-step bench excavation method for developing the tunnel with a net height of more than 7 m is shown in Figure 4.

In Figure 4, A_1 is the roof advance support section, A_2 is the roof active support construction section, A_3 is the roof passive support construction section, B_1 is the sidewall advance support section, B_2 is the sidewall active support construction section, B_3 is the sidewall passive support construction section, and C (including the subsequent parts in the model not drawn in the figure) is the action section of complete support [8].

According to the tunnel design drawing data in the research database and the model design standards shown in

Figures 2, 3, and 4, after designing the three-dimensional finite element model for the tunnel, run the simulation calculation process in the finite element simulation system with the help of the fluid structure coupling model and MIDAS-GTS control and compare the simulation results with the real data, so as to evaluate the universal applicability and value of the fluid structure coupling model and MIDAS-GTS control.

4. Simulation Results and Research Conclusions

All simulations are performed in MIDAS-GTS environment. Group A is the simulation analysis directly using fluid structure coupling model, and group B is the simulation analysis closest to the model after comparing multiple available models according to the actual collected data in the traditional mode. In the traditional concept, group B can obtain simulation results closer to the actual analysis requirements. In this study, the actual effects of the two groups of simulation are compared with the simulation results of roof displacement and bolt tension.

First, the results of the two groups are compared from the perspective of overall statistics, and Table 1 is obtained.

In Table 1, the concept of deviation is the difference between the simulation result and the measured value and the ratio of the absolute value to the measured value:

$$D_i = \frac{|S_i - A_i|}{A_i} \times 100\%, \quad (1)$$

where D_i is the output value of the deviation corresponding to the i th input variable, S_i is the simulation result value in the i th input variable, and A_i is the measured value in the i th input variable.

Maximum deviation is the maximum value in all deviation result sets within the statistical range, and average deviation is the arithmetic average of all deviation result sets within the statistical range. The average calculation method is

$$\text{Arg}(D) = \frac{1}{N} \sum_{i \leq N} D_i, \quad (2)$$

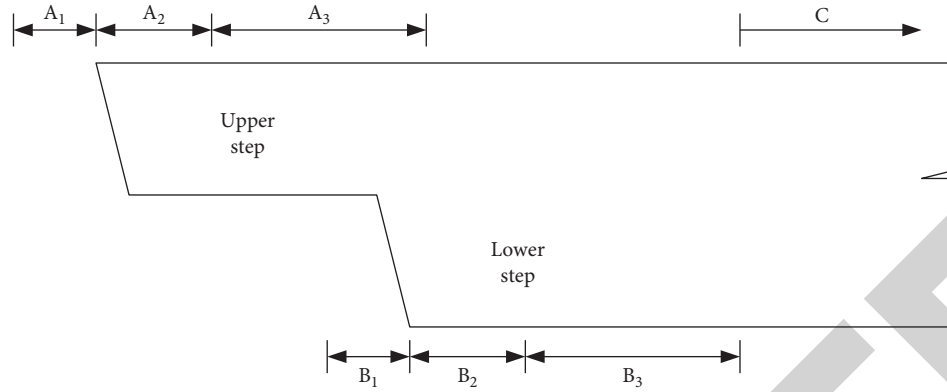


FIGURE 4: Modeling scheme of two-step bench method heading face (side view).

TABLE 1: Comparison of overall statistical results (data source: collected by the study).

Grouping	Roof displacement			Bolt tension		
	Maximum deviation %	Average deviation %	STD	Maximum deviation %	Average deviation %	STD
Group A	2.569	1.392	0.854	4.692	2.373	1.037
Group B	2.736	1.438	0.863	5.059	2.527	1.159
Leadership of group A	6.50%	3.30%	—	7.82%	6.49%	—

where $\text{Arg}(D)$ is the average output result, D_i is the output value of the deviation corresponding to the i th input variable, and N is the number of data pointers within the statistical range. The meanings of other mathematical symbols are the same as those above.

STD is the standard deviation rate of data, and the statistical method is as

$$\text{STD} = \sqrt{\frac{\sum_{i \leq N} (D_i - \text{Arg}(D))^2}{N - 1}}, \quad (3)$$

where STD is the output result of the standard deviation rate. The meanings of other mathematical symbols are the same as those above;

In Table 1, group A, using the fluid structure coupling model, has certain data advantages over group B. In terms of roof display, maximum deviation increased by 6.50%, average deviation increased by 3.30%, bolt tension and maximum deviation increased by 7.82%, and average deviation increased by 6.49%. Analyze the reasons for the statistical results, select the model with high predata coupling rate among many analysis models, and do not use fluid structure coupling model, and the analysis accuracy of this model (group B) is lower than that of the analysis model (group A) using the fluid structure coupling model. The representative fluid structure coupling model has general advantages over the common geotechnical analysis models. At least in the geotechnical analysis of deep tunnel, the fluid structure coupling model shows significant advantages.

In order to further verify the above point of view, the analysis error distribution is analyzed from different statistical control variables, and the data statistical grouping method is the same as the above. For example, the error rate

distribution of simulation results obtained under different tunnel depths is shown in Figure 5:

In Figure 5, although the mean deviation rate of the simulation analysis of the fluid structure coupling model is always less than that of other models, the slope of the linear regression function within the buried depth of 550 ~ 1450 m analyzed by the fluid structure coupling model in this study is also significantly greater than that of other models, that is, with the increase of the buried depth of the tunnel. The deviation rate of simulation results of the fluid structure coupling model increases faster than the average value of other models. When the future deep tunnel construction demand reaches the buried depth of more than 1450 m, the applicability of the fluid structure coupling model is likely to be lower than that of other models. That is, the research results show that the fluid structure coupling model is generally applicable to tunnels with a buried depth of 550 ~ 1450 m, but it does not mean that it is applicable to the geotechnical simulation of tunnels with a buried depth of more than 1450 m in inland rivers.

Under the same grouping mode and statistical mode, compare the deviation rate of simulation data driven by tunnel section data, as shown in Figure 6.

In Figure 6, the data analysis results further verify the analysis results of the data in Figure 5. The data analysis scope of the study is the deep tunnel with a tunnel cross-sectional area of 45 ~ 102 m² and a tunnel buried depth of 550 ~ 1450 m. The analysis results of the fluid structure coupling model in this range are better than the average values of other models in terms of the deviation rate of simulation data, indicating that the fluid structure coupling model has universal applicability in this analysis range. This study does not mean that the fluid structure coupling model still has universal applicability in a wider range of tunnel

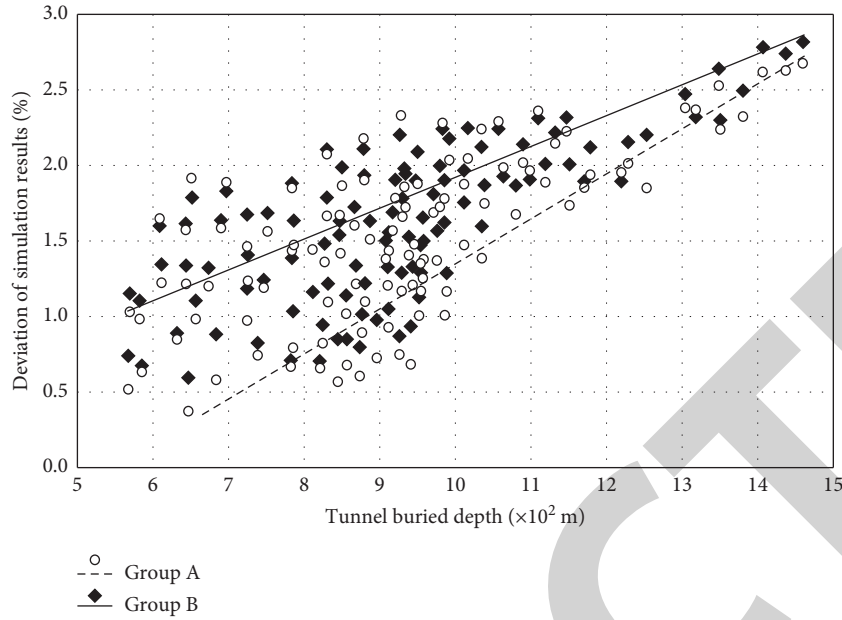


FIGURE 5: Linear regression relationship between simulation results and measured results (based on tunnel buried depth) (data source: collected by the study).

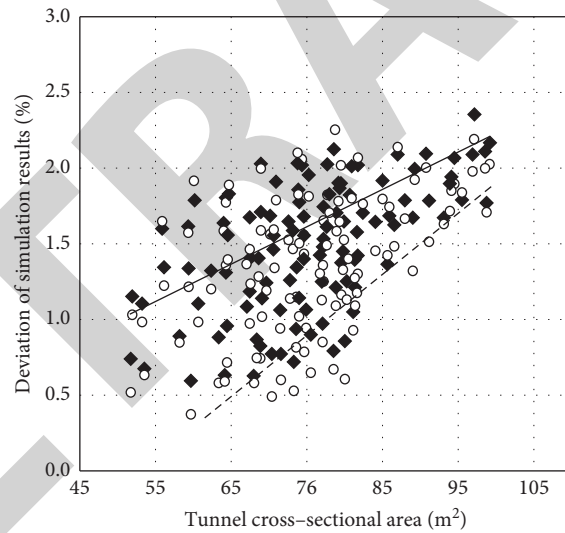


FIGURE 6: Linear regression relationship between simulation results and measured results (based on tunnel cross-sectional area) (data source: collected by the study).

geotechnical simulation. In particular, according to the linear regression results of the deviation rate of the simulation data, when the tunnel depth is larger or the tunnel cross-sectional area is larger, the deviation rate of the simulation results of the fluid structure coupling model may exceed the average value of other models. However, in the actual construction, under the design specifications for deep underground mining of coal mines and iron mines, the vast majority of deep tunnels are within the scope of this analysis, so the fluid structure coupling model has universal applicability in the actual construction.

Comprehensively, compare the analysis results of the deviation rate of the above simulation results. Under the

grouping conditions set in the study, compared with group A using the fluid structure coupling model and group B using the preferred model, the comprehensive advantages of the model are shown in Table 2.

In Table 2, linear regression R^2 value represents the reliability of linear regression. The statistical method is shown as

$$R^2 = \frac{SSR}{SST} = 1 - \frac{SSE}{SST}, \quad (4)$$

where SSR is the sum of regression squares and the sum of longitudinal axis squares of projection points on the regression line, SSE is the sum of squares of residuals, that is,

Retraction

Retracted: Development of Quality Information Management System for Alumina Ceramic Tube Manufacturing Process

Advances in Materials Science and Engineering

Received 26 December 2023; Accepted 26 December 2023; Published 29 December 2023

Copyright © 2023 Advances in Materials Science and Engineering. This is an open access article distributed under the Creative Commons Attribution License, which permits unrestricted use, distribution, and reproduction in any medium, provided the original work is properly cited.

This article has been retracted by Hindawi, as publisher, following an investigation undertaken by the publisher [1]. This investigation has uncovered evidence of systematic manipulation of the publication and peer-review process. We cannot, therefore, vouch for the reliability or integrity of this article.

Please note that this notice is intended solely to alert readers that the peer-review process of this article has been compromised.

Wiley and Hindawi regret that the usual quality checks did not identify these issues before publication and have since put additional measures in place to safeguard research integrity.

We wish to credit our Research Integrity and Research Publishing teams and anonymous and named external researchers and research integrity experts for contributing to this investigation.

The corresponding author, as the representative of all authors, has been given the opportunity to register their agreement or disagreement to this retraction. We have kept a record of any response received.

References

- [1] Y. Huang, "Development of Quality Information Management System for Alumina Ceramic Tube Manufacturing Process," *Advances in Materials Science and Engineering*, vol. 2022, Article ID 5816221, 13 pages, 2022.

Research Article

Development of Quality Information Management System for Alumina Ceramic Tube Manufacturing Process

Yulong Huang 

Business School, Southwest Minzu University, Chengdu 610041, Sichuan, China

Correspondence should be addressed to Yulong Huang; yluang@swun.edu.cn

Received 29 December 2021; Revised 26 January 2022; Accepted 19 February 2022; Published 11 March 2022

Academic Editor: Palanivel Velmurugan

Copyright © 2022 Yulong Huang. This is an open access article distributed under the Creative Commons Attribution License, which permits unrestricted use, distribution, and reproduction in any medium, provided the original work is properly cited.

This paper is based on the alumina ceramic manufacturing process and its quality to build a quality information management system to study alumina ceramics and its quality factors such as physical properties, chemical properties, and other pieces of related information to find a kind of alumina ceramics. The management of quality management brings efficiency and guarantee to the management system. Obviously, this research is based on the two parts of alumina ceramic tube and quality management information system for data acquisition and analysis. One part is based on the production and performance analysis of alumina ceramic tube and summarizes the quality problems that occurred in this process. This paper constructs an information management system to count these issues and conducts research on information dominance and management; among them, exponential smoothing calculation methods, linear trends, convolutional neural algorithms, and so on are applied for methodological analysis. The experimental results show that the lack of corners and uneven corners in alumina production has been greatly reduced, and the maximum probability of uneven corners has been reduced from 9.27 to 5.27. The scrap rate of ceramic tube quality decreased from the highest value of 5.82 to 3.17, and the maximum value of unqualified quality was changed from 5.76 to 3.03.

1. Introduction

With the rapid development of the national economy, the demand for bauxite resources is increasing, especially for high-altitude bauxite [1]. My country's bauxite resources are increasingly scarce, the resource reserves are declining, the contradiction between the supply of high-alumina-rich ore is becoming increasingly prominent, and the bauxite resources restrict the development of the aluminum processing industry. Alumina ceramic material is one of the ceramic materials with the largest production scale and the largest consumption in the world [2]. Alumina ceramics is a kind of ideal heat dissipation and packaging material with excellent performance and is suitable for large-scale integrated circuits and high-power electronic devices. However, its application and development are affected by problems such as difficulty in sintering and easy oxidation. Alumina ceramic material is the best type of material currently developed and used, which have good chemical stability, wear resistance, heat resistance, and excellent mechanical

properties, and are used in machinery, wind power, electrical, and construction-electrical engineering. There are many toolkit applications, which have great development and practical value. The preparation of aluminum alloy is one of the first developments in the future [3, 4]. On the one hand, it is to find low-cost raw materials, reduce product costs, improve manufacturing processes increase output, and shorten metabolism; on the other hand, it is to improve its efficiency and high-temperature equipment [5]. Oxide ceramic materials have excellent strength, hard breaking, absolute dimensionality, heat conduction, high temperature, carving oxidation, and financial loss. The characteristics of Mu Peng and Gao Group are strong. Under the environmental conditions of Yan Meng, F has good high temperature stability and mechanical properties. It attracts attention at the Murake Industrial Building. Oxide ceramic materials mainly include binary oxides, glass ceramics, titanate ceramics, and hydroxyapatite ceramic materials. Binary oxide ceramic materials mainly include silicon oxide, oxide drink, alumina, zinc oxide, and barrel oxide. These

ceramic materials are widely used as ordinary daily ceramics and high-tech water ceramics.

Information is the main component of the quality management system documents. The technology-based quality information management system also covers the entire life cycle of the product and can effectively use quality information to meet customer needs and expectations for products in a timely manner [6]. The development process of the manufacturing and information industry is an important development process formulated by the 18th National Congress of the Communist Party of China. Information construction mainly serves the medium and long-term development process of enterprises, screening and identifying macro and microdata, regularly understanding market opportunities, and using relevant competitive actions [7]. Under normal business development conditions, informatization management will become the first choice for the main indicators of the enterprise in the long-term competition [8].

Alumina ceramics is a ceramic material that has been widely developed and used at present, and it has good chemical stability. In the process of Shukla M's research, X-ray diffraction analysis confirmed the formation of Ti-based compounds at the interface of the base material-filler alloy of the microwave and traditional brazing joints. The basic shape of the joint cross section is determined by X-ray energy analysis. The Vickers microhardness measurement shows that the microwave-assisted brazing joint has a reliable joint function in the practical application of electric tubes. The brazing force measurement and helium leak test provide evidence for the alignment of the alumina-alumina joint [9, 10]. Since there is no universal standard to evaluate the quality of process information, it is necessary for document producers to design appropriate process descriptions to provide practical solutions. In order to achieve the main purpose, Grudzien and Hamrol created a method to examine the characteristics of the influence of the process on the user's information needs of the process documentation and introduced the results of the survey conducted in the enterprise process, aiming at finding the relationship between the attributes of the description information and the process characteristics [11]. Khalilpourazary and Salehi aimed to study the effect of using alumina nanoparticles on the final surface characteristics of Al7175 cylindrical specimens manufactured by the tumbling process. In order to compare the results, the input parameters of the two groups, including workpiece diameter, speed, feed rate, and polishing tool, are all selected the same. In addition, dry and nanofluid polishing, number of passes, and penetration depth are considered as variable parameters in this study [12]. Ryabchikov discussed the organization-related issues of sintering quality management by rationed fuel in a full-cycle steel plant. This work considers the model structure for calculating agglomerate quality index values and shows that one of the most important interference factors that interfere with the effective management of agglomerate quality is the low authenticity of the genotype and chemical composition information of iron currently used. The work gives the possible reasons for this situation, which are related to the consistency of the mine base of the metallurgical plant, the characteristics of the material supply, and their preparation for aggregation

[13]. Current methods for modeling such information manufacturing systems (IMS) lack the ability to systematically represent the dynamic changes involved in manufacturing (or creating) IP. Thi and Helfert aim to solve these limitations and propose a modeling method, the IASDO model. It represents a framework for evaluating the quality of the IMS modeling metamodel, comparing the IASDO model with current methods [14]. Shrivastava research explored the current status of Indian cement company green manufacturing (GM) strategy and provided industrial ecology, methods to reduce energy consumption, environmental impact data collection, manufacturing system design and control, and product and manufacturing system integration. It also reveals the problems in the decision-making system due to the influence of green product design [15]. Waple et al.'s response to NCA3's information management challenges means balancing relevance and authority, complexity and accessibility, and inclusiveness and rigor. Improving the traceability of the data behind the numbers and graphics, designing the public-facing website, managing the hundreds of technical inputs to the NCA, and developing IAQA-compliant guidelines for the 300+ participants were all well thought out, which in many ways embodies a strategic information management approach [16]. Although these studies have certain research significance and value in terms of experimental data and experimental process, from the data point of view, the experimental methods are too simplistic, resulting in the fact that the practicality of the experimental data is still worth discussing; in addition, for alumina ceramic tubes, there are few researches on the quality information management system of the manufacturing process.

Observe the appearance of each sample of high-content alumina ceramic material after 20 cycles of freeze-thaw experiments, and start production; collect, store, and analyze the quality information circulating in the process network and the execution information of each process. Supervise and manage the operation of the quality system to provide information support for the effective operation and continuous improvement of the quality system; on the basis of system identification, quality information entry, storage, requirements, and services are combined to develop a process-based information management system. The basis of institutional changes lies in the analysis and extraction of basic services and related components that are part of the company's system quality. The system administrator should form a detailed change plan. The director of the information center shall approve the change—boutique-boutique—scheme according to the change proposal. The implementation process shall be carried out in accordance with the provisions of the software development process. Establish a basic production team in a standardized way; role-based role management and modeling are used to design role-based safety management systems.

2. Alumina Ceramic Tube and Its Quality Information Processing

2.1. Alumina Ceramic Tube. The content of each oxide in the ceramic material will affect the comprehensive performance of the ceramic material [17]. With the deepening of scientific

research and the gradual maturity of the preparation process of alumina ceramics, people can prepare denser and higher-strength alumina ceramics and use them as structural materials. By the end of the high growth period of ceramics, the commercial status of ceramic material production has changed from traditional manuscripts or automated services to linear and automated manufacturing processes. With the successful preparation of transparent ceramics, General Electric successfully used alumina ceramics to manufacture high-pressure sodium lamps. Alumina ceramic lamps are more resistant to high temperatures than traditional quartz tubes and have much better performance. They are widely used in medical, engine wear parts, tool cutting, and other fields [18]. It is limited to the promotion and application of ceramic alumina. Therefore, solving the brittleness problem of ceramic alumina materials is one of the important ways to promote the application of ceramic alumina materials and solve the brittleness problem of ceramic alumina materials [19]. The alumina ceramic structure is shown in Figure 1.

The microscopic morphology of ceramics has undergone tremendous changes, from the accumulation of small disordered grains to a large ordered oriented sheet-like stacked structure. When the texture degree is low, ceramics are mainly composed of closely coupled fine-grained matrix grains, in which some oriented large flaky grains are embedded. The particles are tightly combined, and there are no defects such as delamination and large pores. In the fine-grained matrix, the existence of large-size, parallel, and uniformly arranged flake-shaped microcrystalline templates can be clearly observed, indicating that the template has good orientation, which can lay a solid foundation for obtaining high-quality alumina textured ceramics [20, 21]. Although the general isostatic press is equipped with a pressure gauge or pressure sensor, it can only observe each pressure process and cannot collect continuous pressure change data and the highest pressure and pressure holding time of each pressure process. The pressure of the medium (liquid or gas) in a closed container can be transmitted equally in all directions. Information feedback lags behind, quality problems are not easy to find, and there are other shortcomings. Through the measurement of porosity, bulk density, and water absorption, the compactness and sinterability of ceramic materials can be roughly reflected. Density is not only the basic characteristic of ceramic materials but also an important parameter of the microstructure of ceramic materials. Effectively preventing or reducing the quality problems of unqualified product compactness and providing an effective guarantee for the smooth production of products is a problem that needs to be solved urgently. During the preparation of ceramic materials, due to the presence of moisture and air in the blank, some pores will inevitably be generated during sintering. The location of the pores has a significant impact on the performance of the ceramic material. It is very brittle and very sensitive to blemishes and has strong elasticity [22]. This determines its reliability and poor destructive resistance and restricts its further development and high-tech applications. Increase the material strength σ , reduce the elastic modulus E , and increase σ/E . In the isostatic pressing process, the highest

pressure value and the holding time during the pressing process become the key parameters. The holding time is set as a constant sequence, and the exponential smoothing calculation is performed on it:

$$\begin{aligned} Q_t^i &= ul_1 Q_{t-1}^i, \quad 0 < u < 1, \quad 1 \leq t \leq k, \\ Q_t^i &= ul_1 + (1-u)[ul_{t-1} + (1-u)Q_{t-1}^i], \end{aligned} \quad (1)$$

where Q_t^i is the exponential smoothing value at t and u is the smoothing coefficient. This series of exponential smoothing values include the weight of the data during the preparation of the alumina ceramic tube, which decreases with the increase of i and finally becomes 1; that is,

$$\sum_{i=1}^i u(1-u) + (1-u)^i = 1, \quad (2)$$

$$l_{i+1}^{\bullet} = \frac{Q_i}{ul_i} (1-u) \sum_{i=1}^i l_{i+1}^{\bullet},$$

where l_{i+1}^{\bullet} is the predicted average value and the recursive formula for correcting the linear trend of time series $l_1, l_2, l_3, l_4, \dots, l_n$ is

$$Q_t^1 = ul_1 + (1-u)Q_{t-1}^1. \quad (3)$$

A time series refers to a series of numerical values of the same statistical indicator arranged in the chronological order of their occurrence. The main purpose of time series analysis is to predict the future based on existing historical data.

$$Q_t^2 = uQ_t^1 + (1-u)Q_{t-1}^2, \quad a < u < 1, \quad 1 < t < m, \quad (4)$$

where Q_t^2 is the prediction made on the basis of Q_t^1 , m is the number of time points for forward prediction, and the establishment of the initial value can be calculated using a formula

$$\begin{aligned} l_{a+B}^{\bullet} &= a_i + u_i \bullet B + l_i \bullet B^2, \\ u_i &= \frac{u}{2(1-u)^2} [(2-u)Q_t^i - (4-3u)Q_t^3], \end{aligned} \quad (5)$$

$$l_i = \frac{u^2}{2(1-u)^2} (Q_i^1 - 2Q_i^2 + Q_i^3),$$

where a_i is the level value, u_i is the increase in the predicted vector value, l_i is the increase in the complexity, and the comparison basis for the initial value is

$$Q_{\mu} = \sum_{i=1}^v \frac{2i}{v(v+1)} (u_i - v_i)^2, \quad (6)$$

$$Q_o^{\mu} = \frac{\alpha}{1 - (1-\alpha)} \sum_{i=1}^{\mu} (1-\alpha)^i Q_o^{\mu-1},$$

where μ represents a fully adaptive value, Q_o^{μ} is a dynamic index, where v is the convergence speed of the data, and α here is the best smoothing coefficient value.

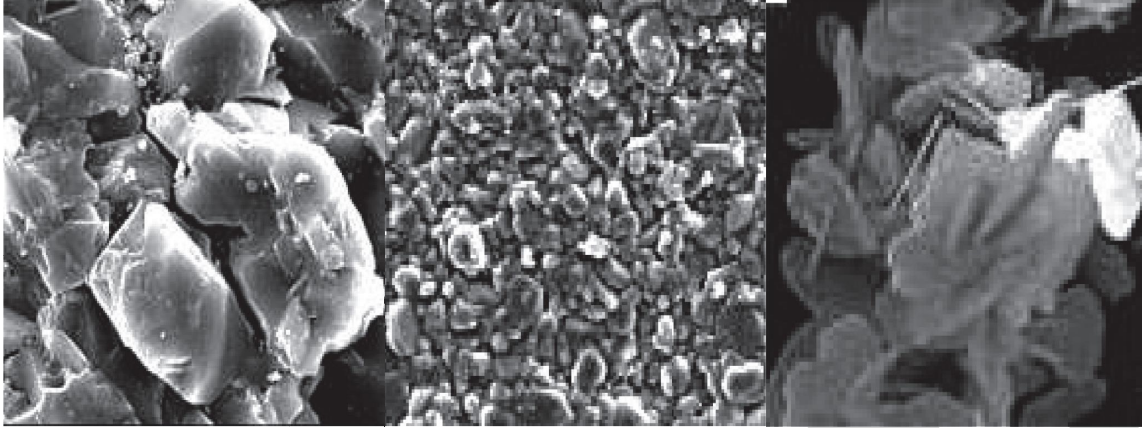


FIGURE 1: Alumina ceramics.

The exponential smoothing method further strengthens the role of recent observations in the observation period on the predicted value and gives different weights to the observations at different times so as to increase the weight of recent observations so that the predicted value can quickly reflect the actual changes of the market.

2.2. Quality Information Management System. Manufacturer quality control plays an important role in chain supply chain management. The quality control stage determines the determination, cost, and delivery date of the purchased product [23]. Therefore, it determines the competitiveness of industrial products in the market. After continuous research and update on quality management, its ideas and methods are also constantly upgraded and gradually developed to a higher level. In the enterprise, the original production management and quality management have not existed. It is the original situation, but these two situations have now been upgraded to the management level. With the widespread application of information management systems, its quality problems have become increasingly prominent [24]. In fact, in the construction of a management information system, its quality is an important content throughout the whole process of life information system development. The management information system model is shown in Figure 2. The quality of the management information system depends on the quality of development and maintenance of the management information system. People improve the efficiency of software design and the quality of software development through the development and update of technology. People continue to research and develop technology and at the same time transfer the focus of software quality control to the field of control and manage software products and software through effective control of software products. The concept of total quality control has led to a broader definition of quality, that is, the combination of product quality and service quality [25]. Work quality refers to many quality-related activities, that is, methods to ensure product quality and a wide

range of quality-related activities to demonstrate product quality metrics [26]. To obtain good product quality, we must focus on quality work and use traditional manual and automatic asset loading to collect quality information through sensors or test equipment, usually represented by descriptive clauses or intellectual property rules, which are difficult to quantify and have low reliability and efficiency. Service is the foundation of service marketing, and service quality is the core of service marketing. Whether it is a production enterprise of tangible products or a service industry, service quality is the magic weapon for an enterprise to win in the competition.

Product process information is mainly recorded in process cards and other documents, and enterprises can trace back to the specific content of each process of the product, process developers, and reviewers through inquiries on these documents [27]. The accuracy and attractiveness of the information automatically collected by search tools have been greatly improved. It can be described by specific numbers to help people roughly understand the quality situation. This is the development of knowledge-quality information machines. Based on mathematical statistics and control charts as tools, monitor the status of the manufacturing process, analyze abnormal changes that occur, help staff understand the production process, take timely measures to solve problems, and keep the product under continuous and stable control during the process to achieve continuous improvement of quality [28]. According to the logistics interface relationship between the manufacturing logistics network nodes, it can be classified, and the information features are processed through convolutional nerves; then, there are

$$a_i^e + d_i^e = f(d)_{ie} \bullet \sum_{i \in m_{ie}} a_i^{i-1} * h_{ie}^i + d_i^e, \quad (7)$$

$$d_i^e = \delta_i^e \min(a_i^{i-1} + d_{i-1}(a-d)),$$

where d_i^e is the feature value extracted from a_i^e , $f(d)_{ie}$ represents the form of sampling and weighting processing, h is a constant, and half of it is calculated by probability; that is, δ_i^e is used to form image classification, and the linear

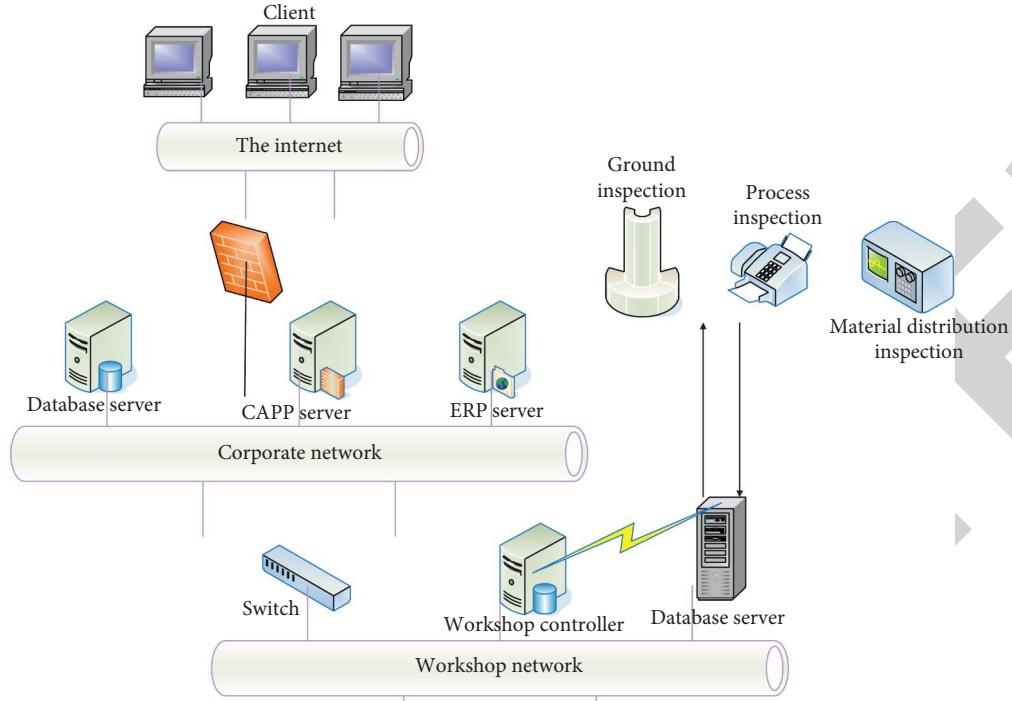


FIGURE 2: Management information system.

relationship between each quality measurement index can be expressed as

$$R(x, y, p, q) = \frac{1}{2} \sum_{i=1}^I \|t_i - a_i\|^2, \chi^i = y_e^{i+1} (g'(a_i^e) \bullet \max(\chi_e^{i+1})), \quad (8)$$

where a_i represents the vector value input for the i -th sample information, $R(x, y, p, q)$ is the loss function, χ^i is the calculation of the sensitivity, g' is the partial derivative trend of the process, and the degree of freedom of the classification process can be calculated by the formula

$$\chi_i^e = g'(a_i^e) * V^2(\chi_i^{e+1} \varepsilon(b_{i+1}^e), all'),$$

$$all' = \frac{(\alpha_{ie} x_i + \beta y_i + \chi)}{i} + 1, \quad (9)$$

$$r_{a,b} = \frac{\sum_{i=1}^m (A_i - \bar{A})(B_i - \bar{B})}{\sqrt{\sum_{i=1}^m (A_i - \bar{A})^2 \sum_{i=1}^m (B_i - \bar{B})^2}} \rightarrow [-1, 1].$$

The correlation of degrees of freedom is calculated by $r_{a,b}$, \bar{A}, \bar{B} are the average value of samples a and b , respectively, α is the minimum value that the quality factor must reach, and x_i, y_i are the input sample, which is optimized for processing:

$$P = \sum_{i=1}^m \sum_{e=1}^n y_e x_{ie} + p_1 + \dots + p_n, \quad (10)$$

$$P_n = \sum_{e=1}^n y_e x_{1e} + \phi_{12} p_2 + \dots + \phi_{n-1,n} p_n,$$

where p_n is the cost budget for quantification of quality, ϕ is the limiting condition for it, and the impact of the cost and time investment of each stage on the system quality is determined by n .

3. Experiment Related Work and Data Analysis

3.1. Relevant Data for the Production of Alumina Ceramic Tubes. With the rapid development of social science and technology, the efficiency and load of machinery used in industrial production are getting higher and higher, and many parts and components fail faster and faster due to wear. Ceramic has excellent mechanical properties, good corrosion resistance, and excellent chemical stability, but its thermal shock resistance is often poor, which limits its application in the preparation of ceramic/s metal elements through casting and inlay systems. Weigh dichloromethane and pour it into a clean beaker, then weigh a dose of anhydrous aluminum chloride and pour it into the beaker, then weigh a dose of isopropyl ether and pour it into the beaker, stir well, and put it in the oven for coagulation. After gelation treatment, an alumina xerogel is obtained, as shown in Figure 3.

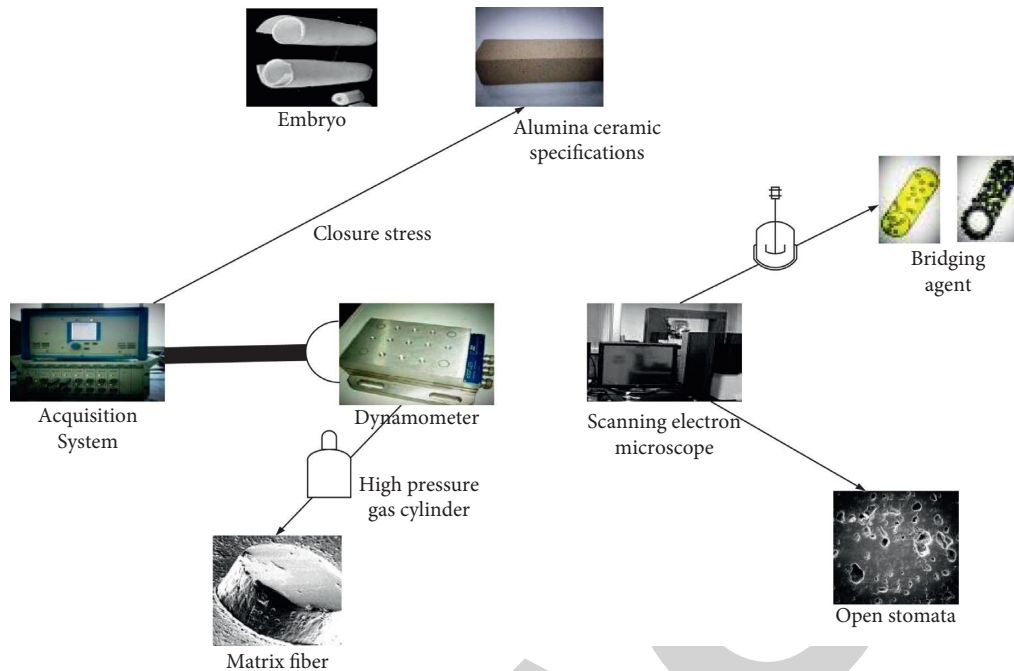


FIGURE 3: Preparation of alumina ceramics.

Alumina ceramic materials are widely used as ceramic casings in vacuum capacitors in electric power and power plants. The casting methods of alumina ceramic tube include grouting, molding, gel injection molding, isostatic pressing, and other molding methods. The product density of isostatic pressing is high, generally 5–15 higher than that of one-way and two-way pressing. The density of the compact is uniform. Because the density is uniform, the length-diameter ratio can be made unlimited, which is beneficial to the production of rod-shaped and tubular thin and long products. Through the technological advantages of informatization construction, change the traditional control position, improve the key competitiveness, and maintain a good development culture. Therefore, the structural problem of the ceramic tube in the manufacturing process is raised. The structure and performance of alumina ceramics are shown in Table 1, and the dimensions of some alumina ceramic tubes are shown in Table 2. The volume measurement value of alumina ceramics increases with the increase of the erosion angle, reaching the maximum value at 90° and the minimum value at 30° , reflecting the characteristics of typical brittle materials. At small angles, cutting wear is the main cause. The energy of the abrasive is sufficient to cause the alumina ceramic to fracture in the grain boundary area, which makes the small alumina grains easy to fall off and cause volume loss. Due to the different expansion coefficients of the embedded whiskers/strings and the matrix, when the welding wire is encountered during the crack propagation process, the propagation direction of the crack is blocked, rotation or bifurcation occurs, and the extension of the welding process increases the rigidity.

Alumina injection molding provides powdery materials according to different product requirements and different brewing processes. The particle size of the powder is below

TABLE 1: Composition and properties of alumina ceramics.

Chemical composition	Parameter (%)	Physical properties	Parameter
Aluminum	>94	Density	3.42
Silica	<2.4	Apparent porosity	0.31
Iron trioxide	<1.9	Compressive strength	277
Monovalent oxide	<0.6	Refractoriness	1721–1810

$1 \mu\text{m}$. If high-alumina ceramic products are manufactured, in addition to 99.99% alumina matrix, ultrafine coating and uniform particle size distribution are also required. During extrusion or injection molding, clay and plasticizer must be injected into the powder, usually a thermoplastic or resin with a density ratio of 10–30%. The organic mixture should be at a temperature of 150–200 degrees, and the mixed mixture is at the bottom to facilitate work. The oxidation of alumina at different temperatures varies with time, as shown in Figure 4. The applied pressure will vary with the amount of filling powder, which can easily cause the difference in shrinkage after softening, which will affect the quality of the product. Generally speaking, the smaller the particle size of the mineral, the better the mechanical properties of the filler material. For example, for the particle added to the rubber, the smaller the particle size, the greater the tear strength. But at the same time, the smaller the particle size is, the more difficult it is to achieve its uniform dispersion. In addition, the smaller the particles, the greater the oil absorption value, the more the additives required, and the higher the processing cost. The filling of the mold is uniform during the dry pressing process. The normal sintering amount of ceramic alumina has a great influence on the size control. Although the alumina ceramic tube has met the requirements in

TABLE 2: Dimensions of some alumina ceramic tubes.

Model	Inside diameter of	Length	Wall thickness	Maximum outer diameter
NC240	6.29 ± 0.1	89.7 ± 1	0.69 ± 0.05	7.13
NG390	7.27 ± 0.1	105.3 ± 1	0.70 ± 0.05	8.12
NG600-3	8.13 ± 0.1	176.2 ± 2	0.74 ± 0.04	9.01
NG600-4	7.08 ± 0.1	181.2 ± 2	0.74 ± 0.04	7.96
NG999	10.24 ± 0.1	186.9 ± 2	0.74 ± 0.04	11.12

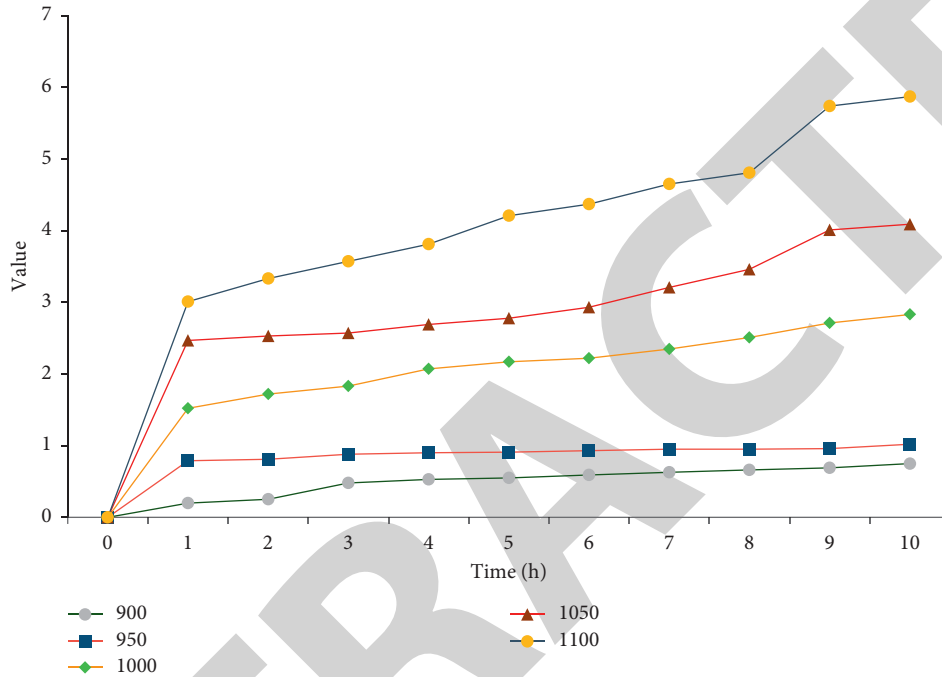


FIGURE 4: Oxidation of alumina at different temperatures.

structure after sintering, it still does not meet the application requirements. It needs to be processed by size correction, polishing, and so on to make the surface of the ceramic tube more dense and smooth and further enhance the performance. The final product is formed. The relevant data of general alumina ceramic formulations are shown in Table 3.

The ceramic alumina body is decomposed at 600°C and then sintered at different temperatures (1200°C to 1500°C) to allow the ceramic bone to pass through. The higher the temperature, the lower the porosity of the ceramic process and the larger the average grain size. In addition to relying on electrostatic precipitation between particles to prevent particles from approaching and invading, it can also build a material barrier around the particles to increase the space between the particles to achieve stable dispersion.

The increase in porosity will increase the overall flux, which corresponds to the increase in suction capacity, but its flexural strength will decrease, which will affect the service life of the support. In addition, due to the high cost of raw materials and the high cost of high-temperature firing, the price of ceramic supports has been high, which has led more and more researchers to pay attention to the research on the preparation process of high-performance and low-cost ceramic supports. To this end, this study tested four types of

alumina ceramic samples, the basic conditions of which are shown in Table 4.

Through the detailed analysis of the above-mentioned formula of ordinary alumina ceramics and the four formulas of the test alumina ceramic samples, we can make an inference about the specific formula components so as to improve the actual formula ratio. As the ceramic particles approach each other, the polymer molecules distributed on the surface of the particles will also be distributed. This distribution is unstable in terms of force, and the two particles must overcome the potential barrier to achieve perfect stability. The mechanical method of granular ceramic body weight and solid material casting is called sintering. Sintering is the process of removing the gaps between the particles in the green body, removing a small amount of gas and impurities, and making the particles grow and combine with each other to form a new substance. The data on the interoperability, correctness, reliability, efficiency, and completeness of the alumina ceramic tubes made by these four formulas are shown in Figure 5.

The traditional grinding process is difficult to process ceramic structural parts with high efficiency. With the increase of ball milling time and the smashing of large-size particles, there is a better particle gradation between ceramic

TABLE 3: Formulation of general alumina ceramics.

Aluminous rock (%)	Kaolin (%)	Quartz sand (%)	Alumina (%)	Water content (%)	Resting time (day)
52.14	13.67	23.47	11.24	0	1-4
58.37	33.24	31.98	1.39	0	1-4
58.91	30.29	317.4	1.47	6.55	1-4
66.29	27.01	41.53	1.54	18.24	1-4

TABLE 4: Four formulations of alumina ceramic samples for testing.

Sample	Dry weight	Wet weight	Bulk density	Porosity	Water absorption
A	321.67	322.57	2.37	0.59	0.23
B	358.24	360.17	2.57	0.88	0.48
C	311.29	322.87	2.05	3.74	2.36
D	317.89	333.39	1.78	5.92	3.94

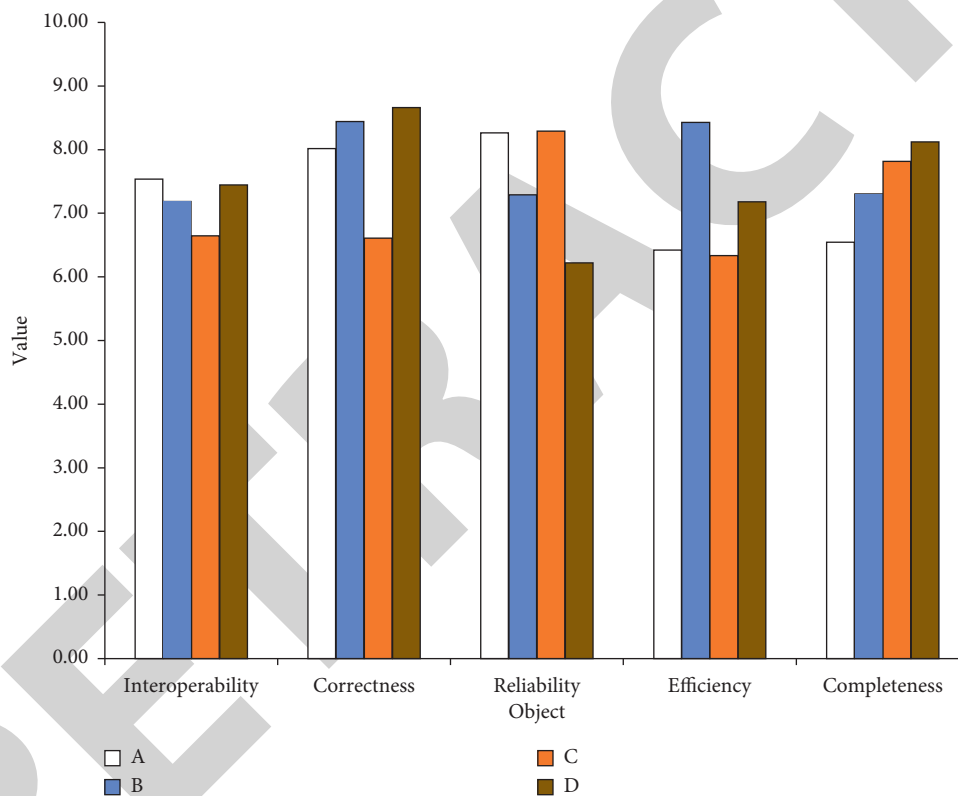


FIGURE 5: The performance of the four formulations.

particles, which reduces internal friction and viscosity when the slurry flows; in addition, another main function of ball milling is to mix materials. As the milling time increases, the components of the slurry become more uniform, and the viscosity decreases. Therefore, research on stone grinding wheels with good performance is of great significance for improving the quality and efficiency of ceramic materials and promoting the reputation and application of this technology. Use big data regression technology to analyze the performance of 20 alumina ceramic tube samples from a factory, as shown in Figure 6.

The data in the above figure is mainly for the maintainability, adaptability, usability, testability, and so on of alumina ceramics, showing that it can still maintain good

stability, wear resistance, high temperature resistance, high hardness, and so on, and when cutting, there will be no chemical reaction with the workpiece.

3.2. Construction and Application of Quality Information Management System. The quality chain has been further developed under the integrated environment of the global technology system and the rapid development of information technology. With the increasing promotion of the concept of total quality control and the implementation of ISO9000 standards, traditional quality control will surely pass regulations. Due to globalization, different regions, cultures, companies, and companies around the

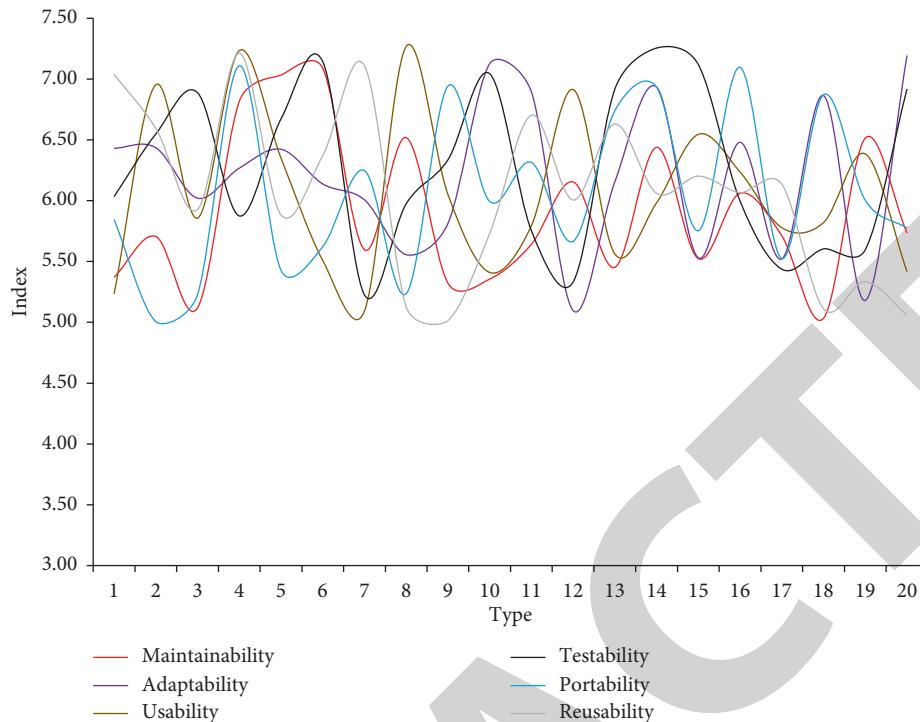


FIGURE 6: Performance of alumina ceramic tube.

world can establish partnerships to improve progress and speed response to customer needs. The plan for arranging improvement standards is mainly to adopt a development perspective to deal with the obtained test results, that is, to preserve the experience that can achieve good results and to form a standardized guidebook to set a benchmark for future work. The statistical data is to aim at the satisfaction of major customers, product sales, market share, and so on, with the help of this information to obtain good product quality judgments. Before starting a new business, you first need to judge whether to use project management well. After the project is launched, organization, planning, and project management can only follow the basic and basic methods of project management in order to achieve the success of the project. Quality assurance is the basis for all the concepts and performance of the implementation plan to meet the requirements of the quality plan. It is a reliable guarantee for the normal operation of the project quality system and should run through the entire process of project implementation. There is a causal relationship between quality and cost. Quality is one of the life elements of an enterprise, and continuous improvement of product quality is the eternal theme that most enterprises strive for. There is a price to be paid for improving quality, whether it is improving tangible products (physical products) or intangible products (services or jobs). The frequency of product replacement is accelerated, and the continuous investment in quality cost is inevitable. Quality cost exists objectively in all aspects of production and operation of an enterprise. The input of quality cost should not only meet the relative needs of customers but

also meet the internal requirements of enterprises to increase profits. These two factors restrict each other and constitute the basic contradiction of the development and change of quality cost. The data before and after the application of the constructed information management system are compared and analyzed. First, statistics are made on the production overview of alumina ceramic tubes, such as missing corners, size differences, and uneven corners, as shown in Figure 7.

The data in the above figure shows that the lack of corners and uneven corners in the production of alumina has been greatly reduced. The maximum probability of uneven corners has been reduced from 9.27 to 5.27; the key to preparing high-purity alumina ceramics is to control the number of impurities introduced, and the grinding media is one of the main sources of pollution of the raw materials; therefore, how to overcome the brittleness of the material and improve the toughness has become the main issue in the production of alumina materials. During the sintering process, the number of grain boundaries and the area of grain boundaries will gradually decrease, resulting in a relative increase in the impurity composition at the grain boundaries, resulting in a decrease in the eutectic temperature of the microdomains, and liquid phases are prone to appear. The liquid phase enters the particles to provide lubrication for the reconstitution of the particles in the initial stage of dissolution. However, during the production process, process-related information also needs to be studied, such as furnace plate collapse and unreasonable process. The comparison of data before and after is shown in Figure 8.

A large number of studies have shown that adding Ni as a binder phase will increase the plasticity of ceramic materials,

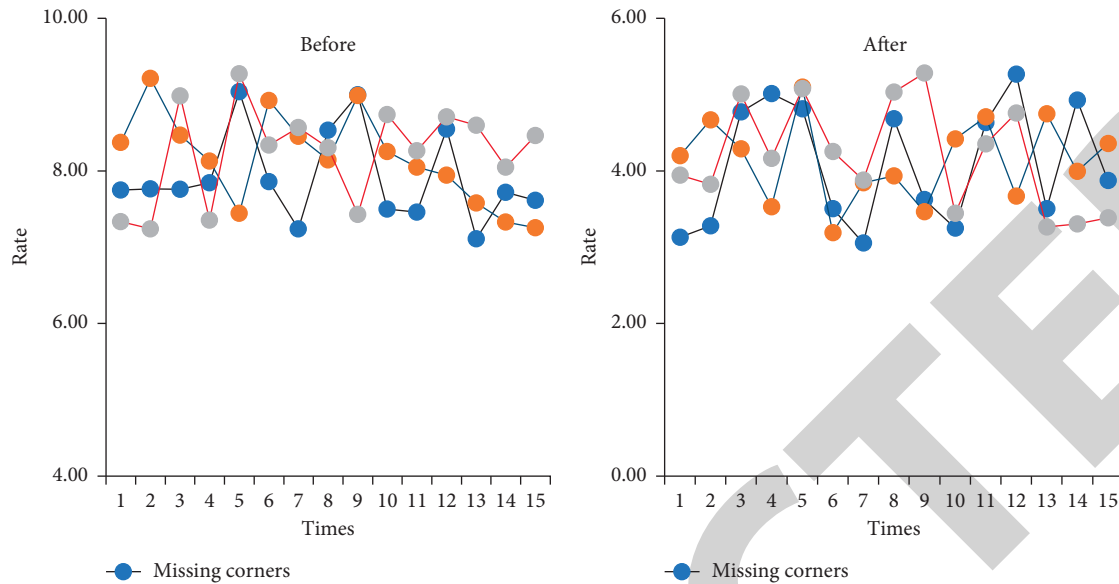


FIGURE 7: Overview of alumina production.

and the flexibility of ceramic materials has a great relationship with the added value. As the amount of Ni increases, the tensile strength of ceramic materials will also increase. At the same time, the hardness of the ceramic material will gradually decrease. However, if the content of Ni is excessive, brittle phases will be formed in the ceramic material. Therefore, after the experiment is carried out on this basis, the quality of the alumina ceramic tube will be counted for cracks, intercalation, and so on, as shown in Figure 9.

The generally constructed quality system framework is based on the life cycle of the product, from the material entering the factory, production, leaving the factory, and delivery links, and lacks the construction of information system for quality management activities. In addition, the construction of a systematic quality system is mainly based on the use of products. Because the existing quality records of the factory have not been fully electronically managed, it is difficult to process paper record information. If you want to count the quality information, you need to manually check a large number of paper files. The quality information on the file data also needs to be manually entered into the computer system to facilitate analysis and statistics, and these tasks will cost a lot of manpower and material resources. The main method of management information quality technology is control. Only when accurate and complete information is grasped in time, project management and decision-making personnel have a reliable basis to implement effective control and management of the project. From the data of reject rate and unqualified quality, the application of quality information management system is generally effective, as shown in Figure 10.

European and American countries are in a leading position in terms of quality information management systems. Research started early, and practical applications are relatively extensive. Since China's reform and opening up,

the western advanced management experience has been gradually applied, and the term information system has also begun to appear in China. With the deployment of computers and the establishment of local corporate networks, a central application platform for quality inspection information is provided. In order to meet the needs of rapid growth of enterprises and the pursuit of product quality, the quality inspection information system has become an important part of the rapid growth of enterprises. From these 15 tests, the scrap rate of alumina ceramic tubes has decreased from the highest value of 5.82 to 3.17, and the maximum value of unqualified quality has changed from 5.76 to 3.03.

4. Discussion

For quality management, it is a large-scale, complex, and systematic project. At present, there is still a big gap between the alumina ceramic tube production technology and foreign advanced technology. It is on the eve of continuous exploration, improvement, and breakthroughs, and the problems faced are more and more complicated. At the same time, with the rapid development of information technology, the application of computers in the field of quality control has received widespread attention in the world, and it is an important way to improve the efficiency of enterprise quality control. Due to the rapid development of technology and craftsmanship, products have become more and more complex and multiplied. The failures and failures of these products always bring huge losses to users and society. Speed is needed to improve quality and reduce failure rates. Quality improvement is the foundation for the growth and stability of corporate strategic interests. For enterprises, improving product quality can increase product share and form a virtuous circle. The main areas of project quality control include quality, time, and cost.

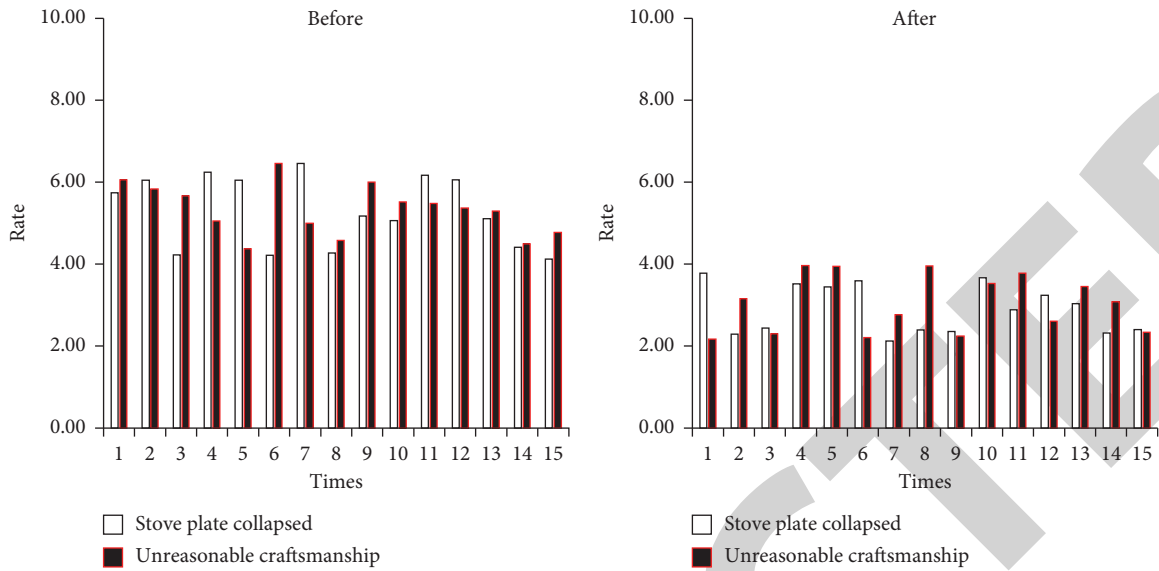


FIGURE 8: Alumina ceramic tube process.

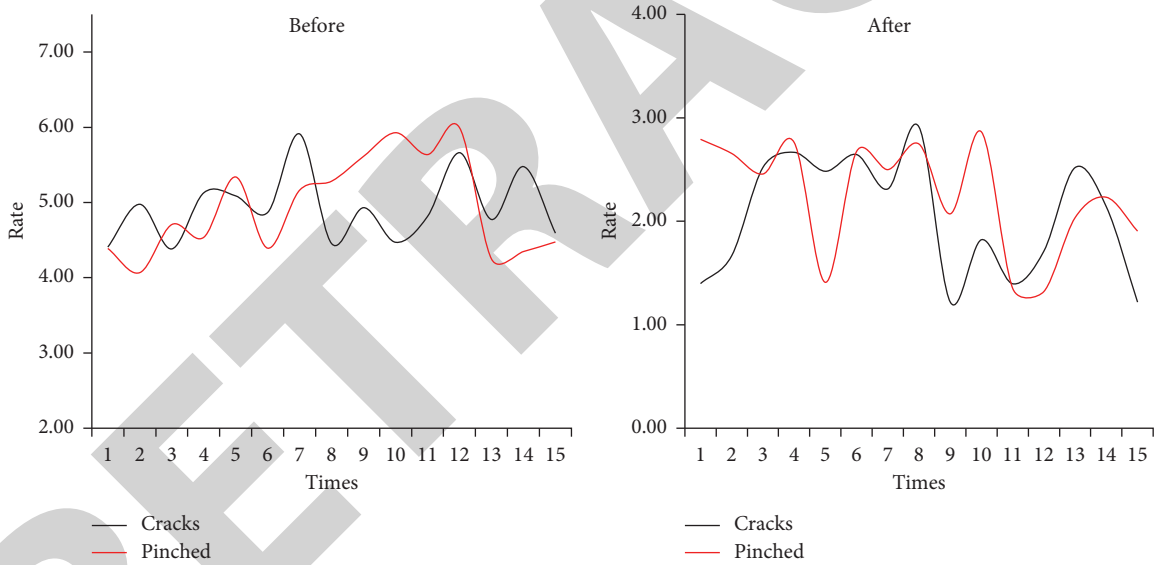


FIGURE 9: Finished alumina ceramic tube.

Project quality assurance is one of the main areas of project management. The quality control of the project is very important to ensure the successful completion of the project in accordance with the requirements set by the model and to enable all tasks of the project to be carried

out in accordance with the original quality and quality requirements. Quality management is based on quality and quality control. Quality assurance and quality improvement are the success of the quality assurance system.

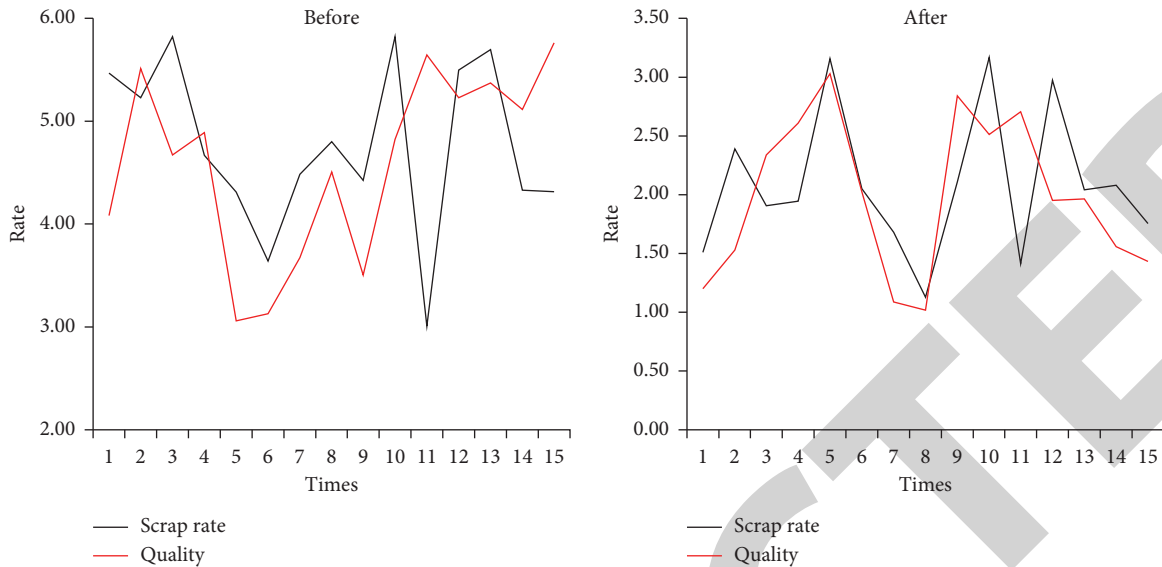


FIGURE 10: The quality of alumina ceramic tube.

5. Conclusion

With the development of information technology, computers and networks are slowly used in factories to automatically store process information, and it can be promoted and applied. With the rapid development and progress of science and technology, especially computer and network technology, people continue to adopt more advanced methods to improve work performance, to obtain or maintain competitive opportunities in order to maintain sustainable survival and development capabilities. The development of the global economy is a transition from growth to growth. The quality control function of the current system is very weak, and it can only manage and analyze the quality after the fact, and it is difficult to prevent the quality beforehand. It is impossible to achieve continuous improvement of the quality system. The information provided by the quality control system can be used to adjust and manage the production process to ensure that the production meets the required product quality. In general, the most fundamental reason why oxide ceramics are difficult to sinter is that the oxide itself has large lattice energy and a relatively stable structure, so the high activation energy barrier must be overcome during the sintering process. The combination of information technology and the operation of ceramic enterprises has itself become an important part of the improvement of ceramic enterprises' technical capabilities. A degree of sharing, transparency, openness, and exchanging distinguishes the traditional departmental function management structure.

Data Availability

The data that support the findings of this study are available from the corresponding author upon reasonable request.

Conflicts of Interest

The author declares that they have no conflicts of interest.

References

- [1] B.-J. Jin, "The study on improvement plan of FTA origin information management system," *International Commerce and Information Review*, vol. 18, no. 2, pp. 107–127, 2016.
- [2] S. Raskova, "Information about quality management system requirements from heat treatment processes. HTM," *Zeitschrift für Werkstoffe Wärmebehandlung Fertigung*, vol. 71, no. 6, pp. 272–277, 2016.
- [3] M. Shukla and S. Ghosh, "Analysis of interfacial joint strength of microwave and conventionally brazed alumina ceramic joints using scratch test method," *Materials Today: Proceedings*, vol. 5, no. 1, pp. 2010–2015, 2018.
- [4] Y. Zhang, Y. Li, and C. Bai, "Microstructure and oxidation behavior of Si-MoSi₂ functionally graded coating on Mo substrate," *Ceramics International*, vol. 43, no. 8, pp. 6250–6256, 2017.
- [5] A. K. Fellenberg, C. L. Luchese, and N. R. Marcilio, "Supported carbon membranes using poly(ether sulfone) precursor," *Korean Journal of Chemical Engineering*, vol. 38, no. 3, pp. 565–575, 2021.
- [6] A. Sarina, J. Antony, Z. He, and N. Arshed, "Critical observations on the statistical process control implementation in the UK food industry: a survey," *International Journal of Quality & Reliability Management*, vol. 34, no. 5, pp. 684–700, 2017.
- [7] L. Sharma, A. Chandrasekaran, K. K. Boyer, and C. M. McDermott, "The impact of Health Information Technology bundles on Hospital performance: an econometric study - ScienceDirect," *Journal of Operations Management*, vol. 41, no. 1, pp. 25–41, 2016.
- [8] H. Rodrigues, F. Silva, L. G. Morgado, and J. C. Sá, "A novel computer application for scrap reporting and data management in the manufacturing of components for the automotive industry," *Procedia Manufacturing*, vol. 51, no. 9–12, pp. 1319–1326, 2020.
- [9] M. Shukla, S. Ghosh, N. Dandapat, A. K. Mandal, and V. K. Balla, "Microwave-assisted brazing of alumina ceramics for electron tube applications," *Bulletin of Materials Science*, vol. 39, no. 2, pp. 587–591, 2016.

Retraction

Retracted: Investigation of Mechanical and Physical Behaviours of Polyester Resin Matrix from Recycled Polyethylene Terephthalate with Bamboo Fibre

Advances in Materials Science and Engineering

Received 26 December 2023; Accepted 26 December 2023; Published 29 December 2023

Copyright © 2023 Advances in Materials Science and Engineering. This is an open access article distributed under the Creative Commons Attribution License, which permits unrestricted use, distribution, and reproduction in any medium, provided the original work is properly cited.

This article has been retracted by Hindawi, as publisher, following an investigation undertaken by the publisher [1]. This investigation has uncovered evidence of systematic manipulation of the publication and peer-review process. We cannot, therefore, vouch for the reliability or integrity of this article.

Please note that this notice is intended solely to alert readers that the peer-review process of this article has been compromised.

Wiley and Hindawi regret that the usual quality checks did not identify these issues before publication and have since put additional measures in place to safeguard research integrity.

We wish to credit our Research Integrity and Research Publishing teams and anonymous and named external researchers and research integrity experts for contributing to this investigation.

The corresponding author, as the representative of all authors, has been given the opportunity to register their agreement or disagreement to this retraction. We have kept a record of any response received.

References

- [1] N. Kaliappan, V. Govindarajan, T. C. Anil Kumar et al., "Investigation of Mechanical and Physical Behaviours of Polyester Resin Matrix from Recycled Polyethylene Terephthalate with Bamboo Fibre," *Advances in Materials Science and Engineering*, vol. 2022, Article ID 4233302, 8 pages, 2022.

Research Article

Investigation of Mechanical and Physical Behaviours of Polyester Resin Matrix from Recycled Polyethylene Terephthalate with Bamboo Fibre

Nandagopal Kaliappan,¹ Venkatesan Govindarajan,¹ T CH Anil Kumar ,²
R. Vishnu Kumar,³ S. Muthukumar,⁴ Maqusood Ahamed ,⁵ Mahadeo A. Mahadik,⁶
and Mebratu Markos ⁷

¹Department of Mechanical Engineering, Haramaya Institute of Technology, Haramaya University, Dire Dawa, Ethiopia

²Department of Mechanical Engineering, VFSTR, Vadlamudi, Andhra Pradesh, India

³Department of Mechanical Engineering, Panimalar Engineering College, Chennai 600123, Tamil Nadu, India

⁴Department of Mechanical Engineering, University College of Engineering Panruti, Panruti, Tamil Nadu, India

⁵Department of Physics and Astronomy, College of Science, King Saud University, Riyadh 11451, Saudi Arabia

⁶College of Environmental & Bioresource Sciences, Chonbuk National University, Iksan 570752, Republic of Korea

⁷Department of Mechanical Engineering, College of Engineering, Wolaita Sodo University, Wolaita Sodo, Ethiopia

Correspondence should be addressed to Mebratu Markos; mebratumarkos@wsu.edu.et

Received 26 December 2021; Accepted 22 January 2022; Published 10 March 2022

Academic Editor: Palanivel Velmurugan

Copyright © 2022 Nandagopal Kaliappan et al. This is an open access article distributed under the Creative Commons Attribution License, which permits unrestricted use, distribution, and reproduction in any medium, provided the original work is properly cited.

In this research article, we investigate the physical and mechanical properties of composites comprised of unsaturated polyester resin (UPR) and recycled polyethylene terephthalate (PET) with 10% to 40% volume of bamboo fibre (BF). Chemical evaluation of BF revealed that BF has a cellulose content of 49.86%, hemicellulose content of 25.17%, and lignin content of 7.14%. As the UPR's different connections, FTIR identified an interconnecting framework between the styrene monomer (ST) and the unsaturated polyester (UP). It was found by TGA-DTG that there were two breakdown phases. UPR's physical and mechanical properties were found to be affected by increasing the amount of fibre in the material, with the water absorption rising from 0.7% to 2.81% and the density (1214.38 to 1168.83 kg/m³), flexural strength (51.81 to 28.92 MPa), flexural modulus (2.78 to 2.83 GPa), and tensile strength (9.71 to 3.86 MPa) all decreasing at the same time. On the other hand, the hardness increased from 82.4 Shore D to 67.9 Shore D. Fibre distribution flaws in the UPR were found, affecting the composites' mechanical characteristics. By repurposing two waste products, this study helps create new materials that are better for the surroundings.

1. Introduction

There are several advantages of using agricultural waste instead of reinforced plastic composites, including its biodegradability, non-toxicity, and ease of supply [1]. Polymeric composites might benefit from employing this waste since it includes cellulose, hemicelluloses, lignins, pectins, and waxes, which can be used to strengthen polymeric fibres [2, 3]. Because of its high mechanical resilience, cellulose is the most significant polymer in the creation of composites

from plant fibres. Table 1 illustrates the chemical makeup of several plant fibres which have good thermal and mechanical qualities [4].

Polyester resins are the most cost-effective resin systems utilized in engineering, but they have limited applicability in more excellent composites. They may be made to have a wide range of qualities, including soft and malleable to rigid and brittle. PET is the most recycled plastic on the planet, yet it still accounts for a large portion of landfill waste. PET is a terephthalic acid (TPA) and ethylene glycol (EG)-based

TABLE 1: Composition of certain plant fibres.

S.No.	Fibre type	Percentage of cellulose	Percentage of hemicellulose	Percentage of lignin
1	Jute fibre	61 to 71.6	13.6 to 20.4	12 to 13
2	Flax fibre	71.0	18.6 to 20.7	2.3
3	Hemp fibre	70.3 to 74.5	18.0 to 22.5	3.8 to 5.8
4	Ramie fibre	68.7 to 76.3	13.2 to 16.8	0.7 to 0.8
5	Kenaf fibre	31 to 39	21.6	16 to 19
6	Sisal fibre	67.1 to 78.2	10.1 to 14.3	8.1 to 11.1

synthetic polyester (EG). Because of its low weight, durability, and chemical resistance, it is widely utilized in manufacturing textile fibres and packaging materials across the globe. Bottles made of PET, a crystalline thermoplastic polyester, are used in the production of water and beverage containers and other products such as fibres for use in textiles and engineering plastic. PET is a widely discarded substance, despite the fact that it poses no direct environmental concern [5–8]. This is due to PET's large volume and strong resistance to breakdown by applying ecological and environmental components. It is possible to recycle PET chemically in a variety of ways depending on the depolymerization of PET, such as hydrolysis, methanolysis, or by employing excess glycol and zinc acetate as catalysts under pressure and heat, all of which are extensively utilized in the production of UPR [9, 10]. Ammonolysis, glycation, and carbonyls, the type of glycol used in the PET depolymerization technique, all directly impact the physical and mechanical qualities of UPR. Glycolic solution based on ethylene glycol (EG) exhibits lower elasticity, higher fracture toughness, and lower humidity resistance in the UPR synthesis [11].

Composite materials made from UPR and natural fibres such as pineapple leaves, coconuts, and sugarcane bagasse were tested for their mechanical and physical qualities. Composites made from post-consumer PET strengthened with natural fibres, like rice husk, coconut, kenaf, and acacia, have been developed recently [12, 13]. The impact of fibre content, fibre surface handling, and fibre length on composite characteristics was examined. Although pieces of bamboo have been utilized in the creation of composite materials, such as husks and stalk, they have not been employed as a whole, which is necessary to maximize the utilization of this waste [14]. PG-based UPR is used solely for the production of polymer concrete and polymer mortar. An unsaturated polyester resin generated from polyethylene terephthalate garbage by glycolysis and bleaching was investigated for its physical and mechanical properties in this research endeavour, together with all of its components (stalk/husk/leaf/cob) [15, 16].

2. Experimental Procedure

2.1. Material Selection. The chemical treatment changed the superficial of BF with sodium hydroxide (NaOH). A variety of chemicals were employed to determine the chemical composition of the sample: EDTA, sodium dihydrogen phosphate, sodium tetraborate decahydrate, cetyltrimethylammonium bromide, and sulfuric acid. The flakes were made by collecting and cutting PET debris from soft

drink bottles [17, 18]. Pre-polymerization of UPR was carried out using the following materials: PG; zinc anhydride; MA; ST; BPO; DMA; and AZn, the latter of which was employed in the synthesis of UPR. The purity of all reagents was more than 99.99%.

2.2. Fibre Treatment. BF was soaked in a NaOH solution of 5% for two hours at room temperature, rinsed three times, and dehydrated in an oven at 110°C for 5 h with distilled water to remove excess alkali to remove waxes and pectins.

2.3. Pre-Polymerization of UPR. Glycolysis was employed to synthesise pre-polymerized UPR, as has been done in prior studies. Soft drink bottle PET flakes and a 4-stage procedure were used to produce this product [17–20]. To begin with, PET flakes were depolymerized using the glycolysis process in a Syria Vessel type reactor, which was combined with mechanical stirrer for two hours at 200°C to produce bis (2-hydroxy propyl terephthalate) (BHPT). The proportion of molecular weights of 1:1.6 BHPT: AM was used in the second stage, which was held at 200°C for 2 h with 2 h of stirring [21]. At this point, UP, ST, and PBO were all added to ST and stirred for 30 minutes at different weight ratios of 100:35:0.25 each. Final step: the ST-benzoyl peroxide combination was added to the unsaturated polyester and the composite was continuously stirred until the mixture was homogeneous. After that, 100:0.2 UP:DMA weight proportion was added as a catalyst and remixed the mixture.

2.4. Preparation of UPR-BF Composites. Nomenclature and formulation of unsaturated polyester resin-BF mixtures are shown in Table 2. Polymerization was carried out in an oven at 55°C for one hour after the mixtures were dissolved in a mechanical stirrer and compressed in steel moulds conferring to ASTM specifications [22].

2.5. Characterization. Bamboo fibre is a bamboo-derived renewed cellulose fibre. The starchy pulp is created from bamboo stems and leaves through alkaline hydrolysis and multi-phase bleaching. In order to determine the BF's chemical composition, three methods were used. In order to make a neutral detergent solution for neutral detergent fibre (NDF), NaOH, EDTA, Na₂HPO₄, and Na₂B₄O₇·10H₂O were used (ISO 16472:2005 standard). Acerbic cleansing fibre was determined by preparing a cleaning solution with an acidic content containing CTAB and H₂SO₄ (ISO 13906:2008 standard). ADL, a 72% solution of H₂SO₄, was used in

TABLE 2: Nomenclature and formulation of UPR-BF composites.

S.No.	Composite nomenclature	UPR-bamboo fibre formulation based on volume percentage	
		Percentage of bamboo fibre content	Percentage of UPR content
1	UPR	0	100
2	Bamboo fibre-10	10	90
3	Bamboo fibre-20	20	80
4	Bamboo fibre-30	30	70
5	Bamboo fibre-40	40	60

this (ISO 13906:2008 standard). FTIR study of BHPT, UP, and UPR was conducted to determine the functional groups present. Testing for thermal stability following polymerization was carried out using thermogravimetric equipment from TA Instruments, which scanned 5 mg samples at 10 °C/min up to 800 °C in an environment of air. An ASTM D 570 water absorption test was performed using three rectangular specimens that were weighed dry and saturated with water for 24 hours at 23 °C. The samples were then roughly dried before being weighed again. According to ASTM D 792, compactness was determined by a change in capacity utilizing purified water at 23 °C. Conferring to ASTM D 790 standards, the flexural stiffness and compressive strength of the material were restrained utilizing a universal testing machine as shown in Figure 1 at 1 mm/min and a length ratio of 16:1. Conferring to ASTM D 638, mechanical properties were restrained using the similar kit used in the flexural test, at 5 mm/min, the rate at which the specimen moves [23]. Figure 2 reveals the impact tester. Conferring to ASTM D 2240, a Shore D durometer was used to measure the hardness of the material. Figure 3 reveals the flexural testing setup.

3. Results and Discussion

3.1. Chemical Characterization of BF. Chemical examination of BF yielded cellulose, hemicellulose, and lignin concentrations of 48.97%, 24.06%, and 6.59%, respectively. When compared to other kinds of vegetable fibre, these were shown to be chemically similar (Table 1). BF has a higher cellulose content than kenaf. All fibres have hemicellulose concentration that is close to that of hemp. BF's lignin level is lower than that of sisal, jute, and kenaf.

3.2. Characteristics of the UPR

3.2.1. FTIR. The transmittance axis was randomly shifted for these spectra. Bands at 3400 cm^{-1} , 2973 cm^{-1} , and 2884 cm^{-1} correlate to frequency band of CH₃, CH₂, and CH in BHPT's FTIR spectrum. Frequency ranges at 1720 cm^{-1} are indicative of bending of C-O and C-O-C bonds, accordingly. The aliphatic ring's C-H bonds vibrate in the 875–525 cm^{-1} range. BHPT's frequency band does not include the O-H bond band at 3520 cm^{-1} , the CH₃, CH₂, and C bond elongating harmonic resonance band at 2982 cm^{-1} , the C-O bond straining peak at 1720 cm^{-1} , the C-C bond resonance frequency integrated by MA peak at 1645 cm^{-1} , and the C-O-C bond straining peak at 979 cm^{-1} . The C-O-C bond straining peak is excluded from the BHPT spectrum. There



FIGURE 1: Universal testing machine.

was no band at 1645 cm^{-1} correlated with the UP's C-C bond at 1645 cm^{-1} in UPR spectrum, and thus it indicates that crosslinking happened via unsaturated fatty acid of the polyester in UP.

3.2.2. Thermogravimetric Analysis. The thermogravimetric curves have exhibited the effect of DTG, weight % of fiber, and temperature in polymerized UPR based PG. It is revealed that the two pounds of fatty acid were detected in TGA, with the first being 78 percent from 35 to 445 °C and the second being 22 percent from 445 to 575 °C, which is attributable to the random, more manageable pieces of the constant sequences that may be freely connected generated during the first disintegration. Each peak in the DTG curve corresponds to one of the mass losses in TGA curves. At 363 and 547 °C, the highest degradations are seen on the curve, and it is shown in Figure 4.

3.3. Fibre Content's Significant Impact on the Physical and Mechanical Qualities

3.3.1. Water Absorption. As shown in Figure 5, the water absorption of unsaturated polyester resin and the BF-10 to BF-40 samples ranged from 0.7% to 2.8% depending on the concentration of BF. Due to its hydrophobic nature, unsaturated polyester resin had a less value than UPR-BF mixtures, and when BF concentration grew, absorption of water increased in UPR-BF mixtures, as BF has a hydrophilic character. When combined with the UPR's superior

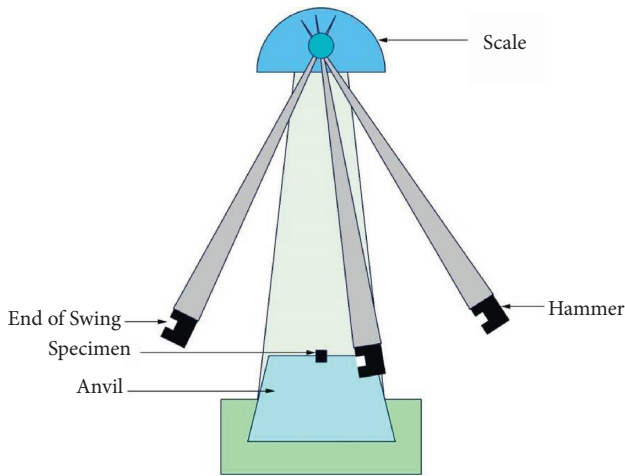


FIGURE 2: Impact tester.

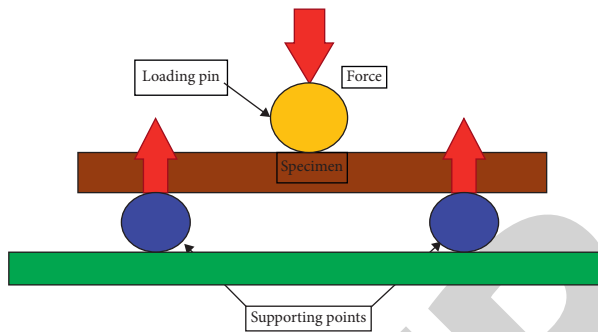


FIGURE 3: Flexural testing setup.

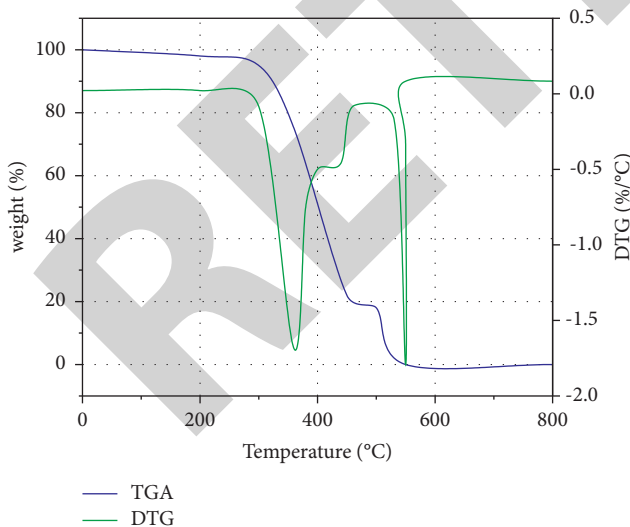


FIGURE 4: Thermogram of polymerized UPR-based PG.

absorption and mechanical interlock, it becomes more effective; the fibre was treated with NaOH, removing impurities like waxes, oils, and other hydrophilic substances, and this reduced the fibre's hydrophilicity. Additionally, unsaturated polyester resin-based PG was utilized, which

offered water absorption ability (hydrophobic composites) by protecting ester bonds from the p-ester.

3.3.2. Density. According to the curve in Figure 6, from 1214.23 kg/m^3 to 1168.31 kg/m^3 , there is an increase in the percentage of beryllium (BF) in UPR and BF-10 through BF-40. Unsaturated polyester resin had a high density than the unsaturated polyester resin-BF content, according to the results [24, 25]. BF-UPR composites had less density than the polymeric matrix, which was attributable due to the lower rate of natural fibres' density than the polymeric matrix. On the other hand, a low void content is desirable because it allows for excellent interaction between the UPR and the BF. Post-consumer PET UPR and acacia sawdust have both been shown to have similar densities.

3.3.3. Flexural Strength and Flexural Modulus. Flexural strength (MPa) and flexural modulus (GPa) are plotted in Figure 7 for UPR, and the range is from 10% to 40% of the total content of BF. The flexural strength (50.58 MPa) was near to that of an actual marketable UPR, and it dropped significantly in BF-10 (67.42% less than UPR) to 16.48 MPa. BF-10 had increases in fibre content of 21.43 MPa (30.03%), 25.43 MPa (18.67%), and 26.98 MPa that were all less than the previous increases from BF-10 (6.1%), respectively, for BF-20, BF-30, and CF-40. The flexural modulus of UPR was greater than that of the UPR-BF composites (2.66 GPa) in comparison. With an increase in fibre content, the value increased to 2.26 GPa (33.73%) for BF-10, 2.56 GPa (13.27%) for BF-20, and 2.29 GPa (10.55%) for BF-40 before decreasing to 2.29 GPa again for BF-40. In the case of BF-10, this translates to a 36.47 percent decrease in pressure from UPR to 1.69 GPa. We may deduce from these findings that the decrease in toughness and elasticity from UPR to BF-10 could be due to the BF content not being sufficient to strengthen the unsaturated polyester resin and the random distribution of the BF inside the UPR matrix [26]. Because of the difficulty of wetting it, the increase in flexural strength was smaller than expected from BF-30 to 40, which might be related to an interaction between the material and the UPR. The flexural modulus exhibited a similar pattern of development; however, the BF-40 value declined in this instance.

3.3.4. Tensile Strength and Tensile Modulus. A BF content (percentage) vs. tensile property graph is shown in Figure 8 for UPR and BF-10 to BF-40, respectively. Another work that synthesised base PG for the UPR showed similar tensile strength values for the UPR (7.93 MPa). From BF-10 to BF-20, 7.42 MPa (14.86 percent) dropped, 7.53 MPa (14.82 percent) dropped from BF-20 to BF-30, and 3.84 MPa (35.69 percent) dropped from BF-40. UPR had a tensile modulus of 1.18 GPa, BF-10 had a tensile modulus of 1.008 GPa, and BF-20, 30, and 40 had values of 0.87, 1.72, and 0.43 GPa, respectively. Compounds made with UPR and cotton-kapok fibres showed similar tensile properties which were ascribed to three features. By increasing the amount of BF content in composites to an unacceptable level, it causes poor fibre

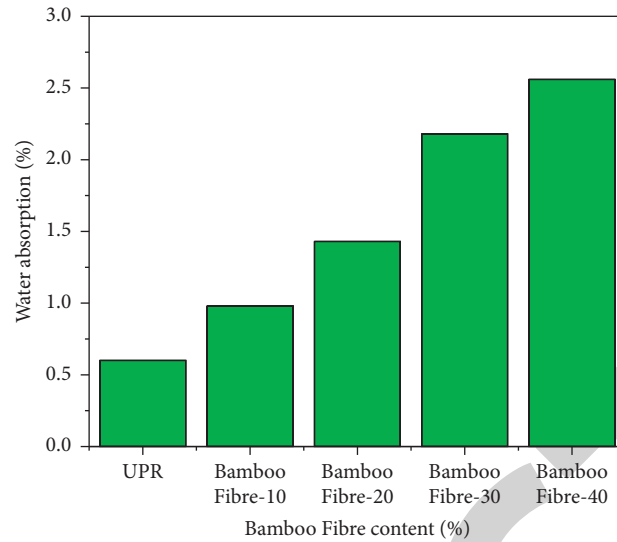


FIGURE 5: Water absorption in unsaturated polyester resin-bamboo fibre composites is influenced by the amount of bamboo fibre present.

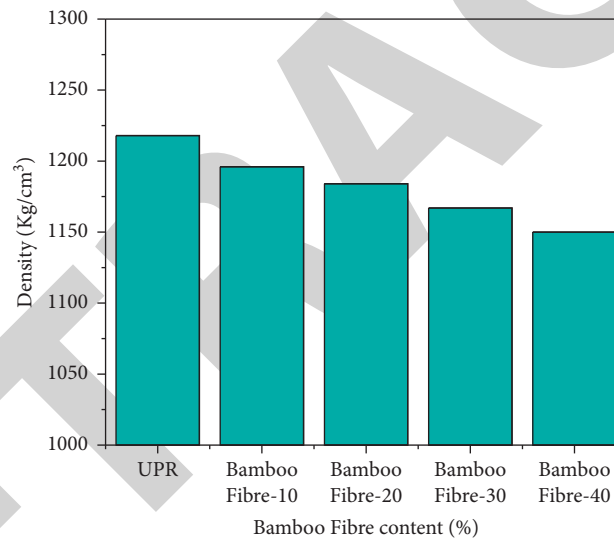


FIGURE 6: Effect of bamboo fibre content on density in UPR-bamboo fibre composites.

wettability and adhesion, hence the production of voids at the unsaturated polyester resin and beryllium impact, which reduces the transmission of loads among these two materials [27, 28]. Increases in the BF specimens in mixtures result in less fibre hydrophilicity and adherence to the UPR, which leads to the creation of voids at the unsaturated polyester resin and bonding fibre interface. There may be gaps and unreinforced areas in the UPR due to an uncontrolled distribution of bonding fibres (BF), and when the BF content in the UPR matrix grew, fibre agglomerations formed in the UPR matrix, creating stress concentrations that encourage fracture propagation.

3.3.5. Hardness Test. Hardness (Shore D) ranges from 81.67 to 65.67 Shore D for the UPR and BF-40, with BF concentration (percentage) shown in Figure 9. The hardness of UPR composites was found to be greater than that of

UPR-BF composites. To account for this, jute-based composites with commercial UPR showed a similar decrease in hardness as they increased in BF content. The apparent decrease in hardness from BF-30 to BF-40 may be due to the fact that the maximum allowable BF content has been exceeded and there is no good interfacial relationship with UPR.

To get BF with longitudinal rupture, the alignment and homogeneous dispersion of the fibres are critical, as they are placed in different positions. Superior mechanical properties of composite materials have the high adherence of the fiber to the UPR was blamed for its fracture, which resulted in an uneven BF cross-section. Mechanical testing revealed smooth grooves in the matrix created by fibres that had been pulled out, indicating that the BF and UPR's connection is weak in some regions [29–31]. The fatigue caused tyre tracks (striations) to appear in the UPR matrix, which were spotted.

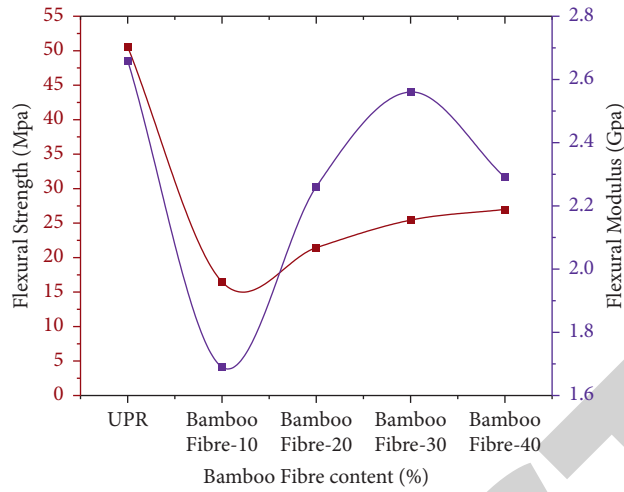


FIGURE 7: Flexural strength and modulus of UPR-bamboo fibre composites may be improved by increasing the bamboo fibre content.

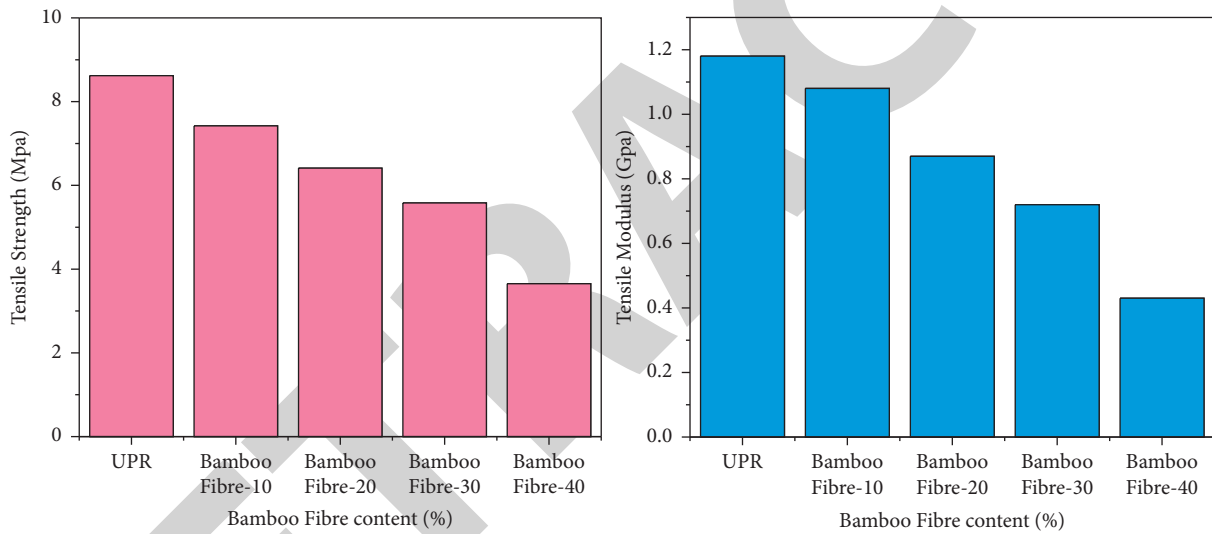


FIGURE 8: Impact of bamboo fibre content on tensile strength and tensile modulus in unsaturated polyester resin-bamboo fibre composites.

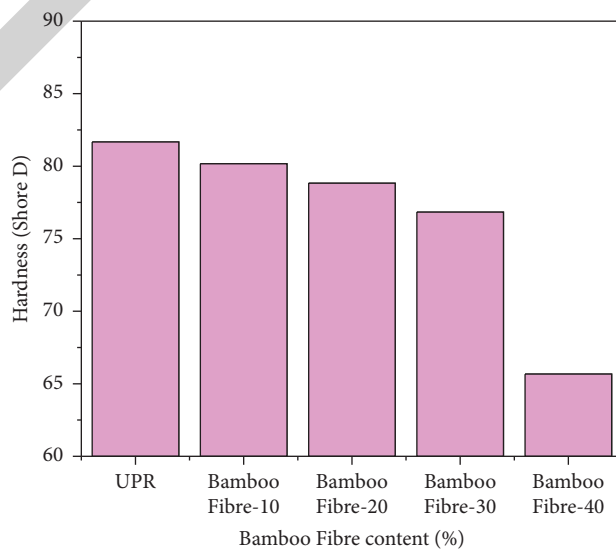


FIGURE 9: Impact of bamboo fibre content on hardness in unsaturated polyester resin-bamboo fibre composites.

The fibres of the UPR were found to have uneven ruptured surfaces as a result of crack arrest. Fibre dispersion in the UPR was found to be ineffective in some areas where the fibres did not entirely disseminate. This means that there is a low BF content and its dispersion is not uniform, which encourages crack propagation and so does nothing to strengthen the UPR [32]. It is clear from the results that the BF dispersion is generally homogeneous throughout the UPR, but some agglomerations were found, and stress concentration in composite materials and a decrease in flexural and tensile strength were connected to these changes. As a result, the presence of these agglomerations did not help reinforce the composite material in the zones where they were present.

4. Conclusions

Recycled polyethylene terephthalate depolymerization with excess PG yielded UPR-BF composites with BF (10%–40%), which were effectively developed. The degradation of UPR was discovered to have two separate stages. The first was attributed to the breaking of RPI bonds and the second to unrestrained continuous chains (TGA-DTG analysis). Though hydrophilic, BF had a lower density than its polymeric matrix, and hence the composites' water absorption ranged from 0.7% to 2.81%. Natural fibres were blamed for this since they were less dense than the polymeric matrix, which is why the density fell. A loss in mechanical qualities such as hardness and toughness might be due to random dispersion and aggregates of BBF as well as the lack of reinforcement provided by the mixture of stalks, husks, leaves, and bamboo.

When force was applied to the BF, it cracked, but the remnants of BF remained interlocked in the UPR both longitudinally and transversely. This indicates a strong interfacial connection between the BF and the UPR. However, certain places had low concentrations of BF, while others had high concentrations, albeit with agglomerations in between. There was no benefit to the UPR from the BF in either case. It was unable to improve UPR-BF composite strength because of the defects in the unsaturated polyester resin matrix, and the distributed occurrences of the BF were found to be the reason for their low mechanical characteristics. Due to its great availability, cheap cost, and non-toxicity, the UPR-BF produced represents an ecological option.

Data Availability

The data used to support the findings of this study are included within the article. Further data or information is available from the corresponding author upon request.

Conflicts of Interest

The authors declare that there are no conflicts of interest regarding the publication of this article.

Acknowledgments

The authors appreciate the support from Haramaya University, Ethiopia. The authors would also like to thank Panimalar Engineering College, Chennai, and King Saud University, Saudi Arabia, for providing technical assistance to complete this experimental work. The authors thank to Researchers Supporting Project (RSP-2021/129), King Saud University, Riyadh, Saudi Arabia.

References

- [1] N. Saravanan, V. Yamunadevi, V. Mohanavel et al., "Effects of the interfacial bonding behavior on the mechanical properties of E-glass fiber/nanographite reinforced hybrid composites," *Advances in Polymer Technology*, vol. 2021, Article ID 6651896, 9 pages, 2021.
- [2] R. Rangaraj, S. Sathish, T. L. D. Mansadevi et al., "Investigation of weight fraction and alkaline treatment on *catechu linnaeus/Hibiscus cannabinus/sansevieria ehrenbergii* plant fibers-reinforced epoxy hybrid composites," *Advances in Materials Science and Engineering*, vol. 2022, Article ID 4940531, 9 pages, 2022.
- [3] A. R. Lara-Vázquez, A. Sánchez, and I. Valdez-Vazquez, "Hydration treatments increase the biodegradability of native wheat straw for hydrogen production by a microbial consortium," *International Journal of Hydrogen Energy*, vol. 39, no. 35, pp. 19899–19904, 2014.
- [4] Y. Ma, S. Wu, J. Zhuang, J. Tong, Y. Xiao, and H. Qi, "The evaluation of physio-mechanical and tribological characterization of friction composites reinforced by waste corn stalk," *Materials*, vol. 11, no. 6, p. 901, 2018.
- [5] H. Ye, Y. Zhang, Z. Yu, and J. Mu, "Effects of cellulose, hemicellulose, and lignin on the morphology and mechanical properties of metakaolin-based geopolymer," *Construction and Building Materials*, vol. 173, pp. 10–16, 2018.
- [6] L. Y. Mwaikambo and M. P. Ansell, "Chemical modification of hemp, sisal, jute, and kapok fibers by alkalization," *Journal of Applied Polymer Science*, vol. 84, no. 12, pp. 2222–2234, 2002.
- [7] A. K. Mohanty, M. Misra, and L. T. Drzal, "Surface modifications of natural fibers and performance of the resulting biocomposites: an overview," *Composite Interfaces*, vol. 8, no. 5, pp. 313–343, 2001.
- [8] A. K. Mohanty, M. Misra, and G. Hinrichsen, "Macromolecular mater," *Engineering Times*, vol. 276, no. 277, p. 1, 2000.
- [9] C. Pudack, M. Stepanski, and P. Fässler, "PET recycling - contributions of crystallization to sustainability," *Chemie Ingenieur Technik*, vol. 92, no. 4, pp. 452–458, 2020.
- [10] M. M. Lubna, K. S. Salem, M. Sarker, and M. A. Khan, "Modification of thermo-mechanical properties of recycled PET by vinyl acetate (VAc) monomer grafting using gamma irradiation," *Journal of Polymers and the Environment*, vol. 26, no. 1, pp. 83–90, 2018.
- [11] M. E. Çınar and F. Kar, "Characterization of composite produced from waste PET and marble dust," *Construction and Building Materials*, vol. 163, pp. 734–741, 2018.
- [12] R. Park, V. Sridhar, and H. Park, "Taguchi method for optimization of reaction conditions in microwave glycolysis of waste PET," *Journal of Material Cycles and Waste Management*, vol. 22, no. 3, pp. 664–672, 2020.

Retraction

Retracted: Effect of Using Modern Banking Services on Customer Inspiration: Statistical Analysis

Advances in Materials Science and Engineering

Received 26 December 2023; Accepted 26 December 2023; Published 29 December 2023

Copyright © 2023 Advances in Materials Science and Engineering. This is an open access article distributed under the Creative Commons Attribution License, which permits unrestricted use, distribution, and reproduction in any medium, provided the original work is properly cited.

This article has been retracted by Hindawi, as publisher, following an investigation undertaken by the publisher [1]. This investigation has uncovered evidence of systematic manipulation of the publication and peer-review process. We cannot, therefore, vouch for the reliability or integrity of this article.

Please note that this notice is intended solely to alert readers that the peer-review process of this article has been compromised.

Wiley and Hindawi regret that the usual quality checks did not identify these issues before publication and have since put additional measures in place to safeguard research integrity.

We wish to credit our Research Integrity and Research Publishing teams and anonymous and named external researchers and research integrity experts for contributing to this investigation.

The corresponding author, as the representative of all authors, has been given the opportunity to register their agreement or disagreement to this retraction. We have kept a record of any response received.

References

- [1] M. I. Jassem, R. A. Rahman, and A. M. Ibrahim, "Effect of Using Modern Banking Services on Customer Inspiration: Statistical Analysis," *Advances in Materials Science and Engineering*, vol. 2022, Article ID 7130559, 6 pages, 2022.

Research Article

Effect of Using Modern Banking Services on Customer Inspiration: Statistical Analysis

Moqdad Ibrahim Jassem,¹ Rafiduraida Abdul Rahman,¹
and Abdelrahman Mohamed Ibrahim ²

¹Department of Business Management, Faculty of Management and Economics, University Pendidikan Sultan Idris (UPSI),
Tanjong Malim, Malaysia

²Accounting and Financial Management School of Management Studies, University of Khartoum, Khartoum, Sudan

Correspondence should be addressed to Abdelrahman Mohamed Ibrahim; amibrahim@uofk.edu

Received 7 January 2022; Revised 19 January 2022; Accepted 31 January 2022; Published 17 February 2022

Academic Editor: Palanivel Velmurugan

Copyright © 2022 Moqdad Ibrahim Jassem et al. This is an open access article distributed under the Creative Commons Attribution License, which permits unrestricted use, distribution, and reproduction in any medium, provided the original work is properly cited.

Customer inspiration has recently gained much interest in marketing theory due to its consistent results as a customer management technique. Herein, the relationship between banking services and customer inspiration through the role of gender moderation is presented. Structural equation modelling through partial least squares modelling (PLS-SEM) has been employed to determine the nature of relationships between variables. Six hundred and forty questionnaires are distributed to branches of ten banks distributed in nine major cities in Iraq, including the capital, Baghdad. Data collection took 62 days; 394 complete answers (i.e., 61.56%) are collected. The approximate viability was evaluated by analyzing the average values of the extracted AVE contrast, where the average AVE was greater than 0.5 for all formulations. The findings show that banking services have a significant positive effect on inspiration and that gender has a positive role in mediating the relationship as a moderation variable.

1. Introduction

The world is changing in terms of doing work in institutions and businesses. Internet, smartphones, and applications and social media provided organizations with the opportunity to easily communicate directly with their clients and establish a close relationship with them [1]. Most of the banks in recent years have become providing their services via the Internet, where their transactions are completed with one click on the mobile application, which led to the development of these banks and the growth of their revenues [2]. Modern banking services have changed the work of banks in a very large and accelerated manner, as communication and relations between customers led and financial institutions to understand and know the ideas and aspirations of customers, which imposed a great competition between financial institutions in innovation, development, and service provision [3].

Since our study on Iraq, we must talk about the poor services that bank customers suffer in Iraq and the delay in

keeping pace with the development taking place in the world, which made it difficult to compete and maintain customers [4]. It has become necessary to evaluate the performance of these banks through their customers and to know their strengths and weaknesses in order to improve their performance, survival, continuity, and innovation. Some research has dealt with the concept of inspiration and its impact on the marketing of services in institutions, as the study of Oleynick.

Oleynick et al. [5] indicated that inspiration is a motivational state for customers through which ideas are transformed into products and solutions that benefit organizations and societies. Böttger et al. [6] confirmed through field experience and experimentation the role of inspiration in influencing service marketing as a form of individual marketing through the analysis of individual lifestyle marketing on click rates and customer buying behavior. In addition, patriarchy and gender inequality in the socio-economic framework are still evident in the Middle

East, where it has a significant impact on clients and their interaction with services [7, 8]. Therefore, it may be interesting to analyze the effects of a moderate gender variant, to provide additional understanding of how the model fits in with male and female clients for adopting banking services.

However, during the past decades that have passed, some studies and empirical research on marketing, customer relations, and management have introduced the concept of gender in several ways leading to a better understanding of the subjective reflection of the nature of gender in interaction with services [9]. Although previous studies on adoption of banking services received substantial empirical validation, most studies did not take into account the moderate variables that were discovered mainly in gender, age, and qualifications. On another aspect, Venkatesh et al. [10] showed that there is a significant influence of the gender variable in the use of banking services, including in particular electronic services, where customer satisfaction with services is necessary in the interrelated exchanges between stakeholders.

Van Tonder and Petzer [11] have shown that individual and renewed customer needs are met by new ideas that often derive from customer inspiration, and inspiration is an important factor in the innovation process. Oleynick et al. [5] and Buheji et al. [12] reported similar results about customer inspiration and stressed that inspiration is an important factor in the innovation process.

According to the above survey, a lot of studies employed the inspiration effect on the customer, but available data of the role of using modern banking services tests are very limited. Therefore, the main objective of this study is to investigate the role of using modern banking services. On customer inspiration and the role of gender as a broker in the Commercial Bank of Iraq, it is hoped that the results of this study will serve as a guide for financial institutions intending to develop a similar solution.

2. Theoretical Background

2.1. Customer Inspiration. Inspiration simply means the feeling of excitement and drive that you get from a person or thing that gives you new and original ideas. Clients are introduced to new and innovative ideas through the banking system at the heart of marketing, but surprisingly little is known about the state of customer inspiration and drive [6]. Therefore, customer inspiration as a temporary motivational condition, which is given to inspire a client, plays a role in capturing and harnessing ideas.

Therefore, different authors believe that inspiration is a motivational state that forces individuals to bring ideas to fruition and that this inspiration is important to the creative process, and the goal is to achieve a goal related to the consumption of a specific product or service. The use of inspiration has an important role in personal development and professional development for individuals. Inspiration plays a major role in changing or improving the individual characteristics and characteristics of people that lead to stability [12]. Customer inspiration is a temporary, motivational state that facilitates acceptance of market-stimulated ideas for the innate pursuit of a consumption goal.

2.2. Electronic Banking. Electronic banking services perform a bank transfer or any online service or transaction as if you did it personally within a bank branch [13]. For the success and effectiveness of the process of providing services to customers, banks have been able to use the Internet, as banks have created a ready-to-use banking system and created a customer database [14]. Electronic banking services have many important advantages, such as lower costs and ease of use through mobile devices and other electronic devices, and it is also possible to communicate easily with customers, motivate them, and find out what ideas they bring to help build new services that satisfy their desires. Internet banking is an integral part of the new development in information and communication technology, as the financial sector seizes the opportunity to grow beyond reasonable doubts, and the wave of transformation in information and communication technology has led to accurately providing banking services to customers in terms of ease and cost of transactions through banking services online [15].

By understanding the basic elements of online banking, scholars in the field of management emphasized the need to investigate the factors that encourage and discourage sponsorship of online banking service evaluation [16]. The banking sector in Iraq was developed and dealt with as an essential aspect of the advanced economy, as it provides electronic banking services to customers, and uses fast communications, information network security, and comprehensiveness, but it still suffers from many problems, for example, the need to be reviewed and communicated with customers to know their needs and aspirations to stimulate their ideas so that these banks can provide better services for continuity and success.

2.3. Mobile Banking Services. Banks have recognized the importance of financial applications in gaining a competitive advantage and establishing effective relationship and communication management with customers [17]. When banks started offering services via mobile phone, customer usage rates were very low, which led to administrative and technical changes which aimed at encouraging customers to switch to this technology.

Efforts to enhance transaction processing along with the development of mobile devices as well as the international economic transformations that have occurred are among the factors that have led to the rapid adoption of this important technology in the banking sector [18]. After the development of these services, it became possible for customers to access their financial resources remotely with the help of mobile devices [19]. Mobile/phone use in large numbers has become a beloved treasure for many users who are encouraging innovation in mobile banking. When banks introduce new services through mobile banking, they are able to attract new customers as well as retain existing ones [20]. The ability to communicate instantly with customers helps solve complaints and reduce them in general. Four factors play a vital role when it comes to mobile banking: ease of navigation, level of personalization, quality of information, and rewards.

Gender constitutes most of the widely recognized and investigated individual difference variables [21]. Some recent studies indicated the important role that gender plays in choosing the use of modern technology, and this is to find differences in decision-making between men and women [22]. Also, Chen and Macredie [23], conducted on online services, found that they differ in terms of usage patterns and preferring specific applications different behaviors and patterns, as well as different perceptions and attitudes towards web-based interaction. It can be argued that individual motivations in using technology are dependent on gender. In addition, men and women have different structures of needs, and their ratio varies according to the desired needs, while satisfying these needs can lead to positive psychological responses such as a feeling of contentment, which leads to gender playing a large role in the relationship between different needs and thus will reflect users' perceptions of benefits [24]. The results of some studies on the use of technology around gender show that men have more perceptions of the benefit in decisions to use technology.

Scientists always indicate, when studying gender, that men are more pragmatic [10]. They are task-oriented and highly motivated by productivity or task-related factors (such as utility) of women; hence, it must be verified which many of the traditional techniques used in the workplace are designed to be "practical" and task-oriented. They are useful if they help enhance user productivity. Zhou et al. [25] have also provided some evidence that men are less motivated by expediency and tendencies to use the Internet and interact with them than women. This required an expansion of the literature on gender in the use of the Internet.

3. Research Model and Hypotheses

Based on the literature review, it can propose hypotheses intended to validate our study, as shown in Figure 1. Accordingly, these Hypothesis are as follows:

H1 : there is a significant and positive impact of mobile banking on customer inspiration in Iraqi commercial banks

H2 : there is an important and positive impact of electronic banking services on inspiring customers in Iraqi commercial banks

H3 : gender moderates the impact of mobile banking on customer inspiration in Iraqi commercial banks

H4 : gender moderates the effect of electronic banking services on inspiring customers in Iraqi commercial banks

4. Research Methods

This study analyzes an individual who is a customer who has received service from Iraqi commercial banks through mobile banking and electronic banking services. Six hundred and forty questionnaires were distributed to branches of ten banks distributed in nine major cities, including the capital, Baghdad. With permission taken from bank directors, the questionnaire was distributed at bank branch offices and

then collected after answering it from clients. Data collection took 62 days. On completion, 394 complete answers (61.56%) were collected. All variables were measured using a Likert scale from 1 to 5, where 1 = very dissatisfied up to 5 = very satisfied. Hypothesis testing was performed using the partial least squares structural equation model (PLS-SEM), chosen for its ability to analyze on small sample sizes Wang and Yang (2016) [29]. It can also work better if it has a predictive goal, for easy navigation and features offered.

5. Analysis and Results

The number of forms distributed is 640 forms to the branches of ten banks distributed in nine major cities, including the capital, Baghdad. With permission taken from bank directors, the questionnaire was distributed to the bank's branch offices and was collected after answering it from customers. Data collection took 62 days. Upon completion, 394 full responses (61.56%) were collected. One case was deleted using box graph analysis and 6 additional cases were deleted using the Mahalanobis test, see Table 1. Of the 394 surveys, this resulted in 387 cases.

The analysis also showed the demographic characteristics of the gender variable to a difference between the numbers of male and female respondents, where the percentage of males was 56.33% more than the percentage of females 43.67%, as shown in Table 2.

5.1. Analyze the Measurement Model. The analysis of the measurement model will be a confirmatory assessment of reliability as well as convergence of validity and discriminatory validity [26]. The load factor value for the model variables was verified by measuring the model, where we can see through the analysis that the Cronbach Alpha CA values for the bank variable MB were 0.855, the value of EB0.757, and the CI variable was 0.811, where all the values were achieved and the lowest value was 0.7 according to Nounally and Bernstein [27]. The reliability of the individual component was also assessed by a process of examining the loading factors of both variables with their respective groups. All variants ranged from 0.715 for CI3 to MB2 versus 0.911, combined with a minimum value of 0.7 [26]. The reliability of the compound was checked. As for the final measure of model reliability, the result showed that all installations met the requirements of 0.7 [28]. Based on Table 2, the result showed that all installations met the requirements of 0.7 [28]. Thus, the reliability of the search model is acceptable, see Table 2. Table 2 shows the measurement of model reliability.

The other measure that should be taken is the convergent validity, which indicates the degree of agreement on measuring the same concept [29]. In this study, the approximate viability was evaluated by examining the average values of the extracted AVE contrast, where the average AVE for all formulations was higher than 0.5, as shown in Table 3. Thus, it fulfilled the required conditions, and this indicates a good sign of convergence in the scale. As for the final measurement of the research model, the discriminatory validity was

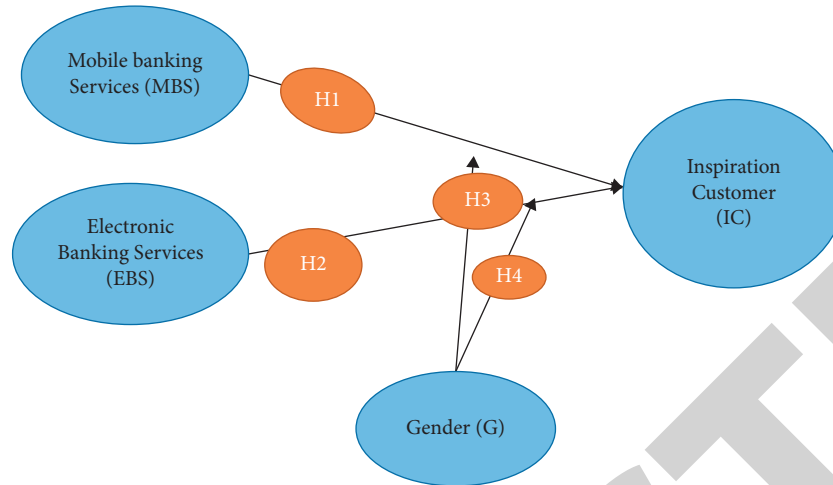


FIGURE 1: Research model.

TABLE 1: Mahalanobis outlier analysis.

Case	<i>p</i> value
1	0.0000034
2	0.0001115
3	0.0000554
4	0.0001466
5	0.0000647
6	0.0001459

TABLE 2: Demographic gender of respondents.

Variables	Categories	Frequency	Percent
Gender	Male	218	56.33
	Female	169	43.67

TABLE 3: Measurement model analysis.

Construct	Item	Loadings	AVE	CA	Cr
MB	MB1	0.905	0.654	0.855	0.924
	MB2	0.911			
	MB3	0.896			
EB	EB1	0.820	0.686	0.757	0.845
	EB2	0.771			
	EB3	0.735			
CI	CI1	0.856	0.683	0.811	0.843
	CI2	0.840			
	CI3	0.715			
	CI4	0.892			
	CI5	0.896			

TABLE 4: Fornell–Larckers criterion.

Construct	Mobile banking services	Electronic banking services	Customer inspiration
Mobile banking services	0.773	0.457	0.368
Electronic banking services	-	0.843	0.437
Customer inspiration	-	-	0.724

Bold values represent AVE (average variance extracted) validity and discriminant validity.

evaluated, and this is done by measuring the common variance between the structure and other combinations [30]. The calculation results also appeared in Table 3.

From Table 4, it was found that all square roots of the AVE are greater than the corresponding correlation coefficients with the other factors. These results indicate that all formulations satisfy the discriminant validity test. From these results, the results of the analysis indicate that our analyses satisfied both convergent validity and discriminant validity.

5.2. Structural Model Results. In this step, the structural model is evaluated where analyses are made on the hypotheses and the relationship of the structures based on the standard pathways examination, as shown in Table 5.

From Table 5 and Figure 2, the positive correlation of mobile bank services with inspired customers is shown with average effect size ($\beta = 0.456$, t -value = 6.763, and Cohen $f^2 = 0.546$). Hence, hypothesis 1 is supported. Electronic banking correlates very positively with customer inspiration with a small approximate effect size ($\beta = 0.321$, t -value = 3.756, and Cohen $f^2 = 0.179$). Therefore, hypothesis 2 is

supported. Mobile bank services have a high positive correlation with inspiring clients who engage in moderate intermediary gender with a small effect size ($\beta = 0.199$, t -value = 2.467, and Cohen $f^2 = 0.109$). Hence, hypothesis 3 is supported. Males were more satisfied with their money management services and more inspired than the females at their banks. There is no positive statistically significant relationship between electronic banking and customer inspiration in the presence of gender as a moderator with a very small effect size ($\beta = 0.067$, t -value = 1.001, and Cohen $f^2 = 0.001$). Therefore, hypothesis 4 is supported.

TABLE 5: Hypotheses testing results.

Hypothesis	Relationship	Std. beta	Cohen f2	t-value	Decision
H1	MBS -> IC	0.456	0.546	6.763	Supported
H1	EBS -> IC	0.321	0.179	3.756	Supported
Moderation (gender: male to female)					
H3	MBS * G -> IC	0.199	0.209	2.467	Supported
H4	EBS * G -> IC	0.067	0.001	0.001	Supported

The value 0.209 represents the effect size to measure the strength of the relationship between two structures on a numerical scale. MBS ->IC represents the relationship between mobile banking services and customer inspiration, where there is a relationship with an average effect size ($\beta = 0.456$, t-value = 6.763, Cohen $f^2 = 0.546$)

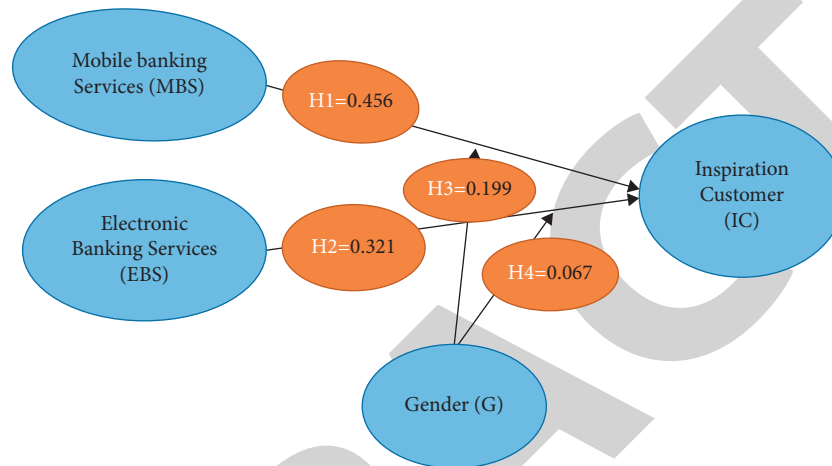


FIGURE 2: Structural model results.

6. Conclusion

In this study, it draws attention to inspiration as a new building in marketing services, enhancing customer behavior, strengthening customer loyalty, and an important factor for innovation. This paper illustrates the importance of inspiring customers through their communication to obtain information and new ideas that could be innovations in the development of banking services. The research dealt with a strategic model in the subject of inspiration and banking services, which integrates many variables that the researchers did not address before. The study concluded that there is a positive role for banking services in inspiring customers and a positive role for services with the presence of the influence of gender. On the contrary, the study indicates the role of inspiration in knowing the ideas and trends of customers which have a significant impact on innovation and the development of banking services.

Data Availability

The data underlying the results presented in the study are available within the article.

Conflicts of Interest

The authors declare that they have no conflicts of interest regarding the publication of this paper.

References

- [1] X. Yan, A. M. Shah, L. Zhai, S. Khan, and S. A. A. Shah, "Impact of mobile electronic word of mouth (EWOM) on consumers purchase intentions in the fast-causal restaurant industry in Indonesia," in *Proceedings of the 51st Hawaii International Conference on System Sciences*, Hilton Waikoloa Village, HA, USA, 2018 January.
- [2] E. Basci, "Which types of Internet banking service effects bank's income statement? an empirical study for Turkey between 2006 – 2013," *The Macrotheme Review a Multidisciplinary Journal of Global Macro Trends*, vol. 7, 2014.
- [3] B. B.-H. Chai, P. S. Tan, and T. S. Goh, "Banking services that influence the bank performance," *Procedia - Social and Behavioral Sciences*, vol. 224, pp. 401–407, 2016.
- [4] J. M. Leimeister, H. Österle, and S. Alter, "Digital services for consumers," *Electronic Markets*, vol. 24, no. 4, pp. 255–258, 2014.
- [5] V. C. Oleynick, T. M. Thrash, M. C. LeFew, E. G. Moldovan, and P. D. Kieffaber, "The scientific study of inspiration in the creative process: challenges and opportunities," *Frontiers in Human Neuroscience*, vol. 8, p. 436, 2014.
- [6] T. Böttger, T. Rudolph, H. Evanschitzky, and T. Pfrang, "Customer inspiration: conceptualization, scale development, and validation," *Journal of Marketing*, vol. 81, no. 6, pp. 116–131, 2017.
- [7] S. Glas, N. Spierings, M. Lubbers, and P. Scheepers, "How politics shape support for gender equality and religiosity's impact in arab countries," *European Sociological Review*, vol. 35, no. 3, pp. 299–315, 2019.
- [8] A. M. Ghouri, T. M. Kin, N. K. b. Y. Yunus, and P. Akhtar, "The dataset for validation of customer inspiration construct

Retraction

Retracted: Optimization of Process Parameters for Friction Stir Welding of Different Aluminum Alloys AA2618 to AA5086 by Taguchi Method

Advances in Materials Science and Engineering

Received 26 December 2023; Accepted 26 December 2023; Published 29 December 2023

Copyright © 2023 Advances in Materials Science and Engineering. This is an open access article distributed under the Creative Commons Attribution License, which permits unrestricted use, distribution, and reproduction in any medium, provided the original work is properly cited.

This article has been retracted by Hindawi, as publisher, following an investigation undertaken by the publisher [1]. This investigation has uncovered evidence of systematic manipulation of the publication and peer-review process. We cannot, therefore, vouch for the reliability or integrity of this article.

Please note that this notice is intended solely to alert readers that the peer-review process of this article has been compromised.

Wiley and Hindawi regret that the usual quality checks did not identify these issues before publication and have since put additional measures in place to safeguard research integrity.

We wish to credit our Research Integrity and Research Publishing teams and anonymous and named external researchers and research integrity experts for contributing to this investigation.



The corresponding author, as the representative of all authors, has been given the opportunity to register their agreement or disagreement to this retraction. We have kept a record of any response received.

References

- [1] G. Sasikala, V. M. Jothiprakash, B. Pant et al., "Optimization of Process Parameters for Friction Stir Welding of Different Aluminum Alloys AA2618 to AA5086 by Taguchi Method," *Advances in Materials Science and Engineering*, vol. 2022, Article ID 3808605, 9 pages, 2022.

Research Article

Optimization of Process Parameters for Friction Stir Welding of Different Aluminum Alloys AA2618 to AA5086 by Taguchi Method

G. Sasikala,¹ V. M. Jothiprakash,² Bhasker Pant,³ R. Subalakshmi,⁴ M. Thirumal Azhagan,⁵ K. Arul ,⁶ Wadi B. Alonazi,⁷ M. Karnan,⁸ and S. Praveen Kumar ⁹

¹Department of Mathematics, SRM Valliammai Engineering College, Kattankulathur, Chennai 603202, Tamil Nadu, India

²Department of Mechanical Engineering, Easwari Engineering College (Autonomous), Ramapuram, Chennai 600 089, Tamil Nadu, India

³Department of Computer Science & Engineering, Graphic Era Deemed to be University, Dehradun, Uttarakhand 248002, India

⁴Department of Civil Engineering, Sri Sairam Engineering College, Chennai, Tamil Nadu 600044, India

⁵Department of Production Technology, Madras Institute of Technology, Anna University, Chennai, Tamil Nadu 600044, India

⁶Department of Mechanical Engineering, Agni College of Technology, Chennai 603 103, Tamil Nadu, India

⁷Health Administration Department, College of Business Administration, King Saud University, PO Box 71115, Riyadh 11587, Saudi Arabia

⁸Grassland and Forage Division, National Institute of Animal Science, Cheonan-si, Chungcheongnam-do 31000, Republic of Korea

⁹Department of Mechanical Engineering, Faculty of Mechanical Engineering, Arba Minch Institute of Technology (AMIT), Arba Minch University, Arba Minch, Ethiopia

Correspondence should be addressed to S. Praveen Kumar; praveen.kumar@amu.edu.et

Received 3 December 2021; Accepted 3 January 2022; Published 15 February 2022

Academic Editor: Palanivel Velmurugan

Copyright © 2022 G. Sasikala et al. This is an open access article distributed under the Creative Commons Attribution License, which permits unrestricted use, distribution, and reproduction in any medium, provided the original work is properly cited.

Friction stir welding (FSW) was used to combine two different Al–Cu alloys, AA2618-T87 and Al–Mg alloy AA5086-H321 plates, and the characteristics of the procedure were adjusted using Taguchi L16 orthogonal experiments planned in advance. Consideration was given to a variety of factors including rotational and cross-sectional speeds, geometry, and the tool-to-pin-diameter ratio. The tensile strength of the joint was used to identify the best procedure parameters. Runs with the ideal settings confirmed the projected optimal tensile strength value. A wide range of process parameters can be used to generate high-quality joints, according to this study. According to the results of an analysis of variance, the most important factor in determining the soundness of a joint is the fraction of tool contact area to pin diameter, although pin shape and welding speed also have a major impact. During this examination, it was observed that the nugget region is dominated by material on the forward-moving side. Heat-affected zones with tensile failures occurred on the alloy 5086 side of the weldment.

1. Introduction

There are many difficulties associated with welding dissimilar aluminium alloys, mainly because the constituent elements create low melting eutectics (hot cracking) [1]. Weld metal composition is highly dependent on the filler metal, base metal, and quantity of dilution when it comes to solidification cracking in aluminum alloys [2, 3]. For the weld connection to be free of solidification cracks, the filler composition and/or

welding parameters must be carefully selected. This may be done easily using fusion welding aluminum alloys. Depending on the aluminum alloy, filler metals can be selected in a variety of ways [4]. Fusion welding of different aluminum alloys presents a challenge in terms of dealing with solidification cracking. There are no filler metals that can create crack-free welding for many aluminum alloy combinations [5–7]. When filler metal is available, joint efficiency can not be achieved even if the metal is of adequate quality. Fusion welding of different

aluminum alloys is often discouraged in the industry because of these reasons [8].

Welding different aluminum alloys is best done using solid-state welding methods. There is no need to worry about weld solidification cracking because these methods do not require melting [9–11]. Using solid-state welding procedures, these problems with pores, dispersion, fragile intermetallic creation, and heat influenced zone liquation cracking in aluminum alloy fusion welding can be avoided [12]. Welding dissimilar aluminum alloys can be done via friction stir welding to create butt joints and other custom-designed weld joint types. As a result of its engineering importance and challenges connected with traditional welding, FSW has been the subject of a lot of academic studies [13, 14]. Friction stir welding (FSW) is a type of solid-state welding. It is frequently referred to as a sort of friction welding, but it is regarded as a different welding technique due to its many uses. There is no external heat in this welding process, and the joint formation occurs due to diffusion at interface surfaces under high pressure and friction force. Because there is no molten or plastic state involved in this process, it is classified as a solid-state welding technique.

Welding a range of aluminum alloys combined with FSW has been done before, with outstanding results. As in most of these studies, the Stir Zone (SZ) or Weld Nugget Zone (WZ) showed substantial mechanical mixing with a complicated vortex of two alloys [15]. The position of two different alloys has been found to have a significant impact on the flow of material and the quality of welds [16]. In many studies, experts have shown that it is better to place one of the two materials on the side that is moving forward. Cast aluminum alloy A356 was discovered to have a much higher SZ than wrought aluminum alloy AA6061 when compared to the FSW of the two alloys [17]. In the SZ during the FSW of the transition from AA2618 to AA6061, the material on the advancing side was most common. Aside from material flow visualization, there was no optimal FSW parameter or tool geometry found in these systems in these investigations [18, 19].

1.1. FSW Parameters. With a quasiroller, pins and shoulders are intertwined with each other at their opposite ends, in which the joint line is traveled along the lateral aspect. The tool is used to manipulate the material and heat it to create the joint [20–22]. It is used to heat the workpiece by using friction and plastic deformation between the instrument and the object being worked on. Heating around the pin softens the surrounding material while a mix of tool rotation and translation is used [23]. This technique results in a strong joint. Because of the instrument's multiple geometrical features, the flow of material around the pin might be somewhat difficult. Due to FSW, fine and equiaxed recrystallized grains are formed in the material because of plastic deformation at high temperatures [24, 25]. FSW have good mechanical properties because of their fine microstructure. Listed below is a complete breakdown of the various factors that go into the FSW process:

(1) The tool's speed of rotation (rpm).

- (2) Welding speed in the transverse direction. (mm/min).
- (3) A piece of equipment's form.
 - (a) Pin profile.
 - (b) Size of the tool's shoulder, D (mm).
 - (c) Size of the pin, d (mm).
 - (d) D/d ratio of the tool.
 - (e) The length of the pin (mm).
 - (f) inclination of the tool

Equipment geometry, speed of rotation, and other factors have been studied and found to have a substantial impact on the quality of welds in FSW. A perfectly executed weld between the dissimilar metals AA5052 and AA2017 has been reported to be possible at transverse speeds of 60 mm/min and rotation speeds of 1000 rpm, according to the available information. Furthermore, the fracture toughness of the material increases directly to the welding speed. Then it starts to fall. Due to the rare, irregularly created voids along the base metal/weld zone boundary on the advancing side. Weld flaws are common at high rotating speeds. On the advancing side, there are irregularly formed voids along the base metal/weld zone border. At high rotational speeds, weld defects are also typical.

To compare rotational speeds for friction, stir welding of AA8009, [26]observed at 1200 revolutions per minute, the fracture toughness was 60–70% that of the basic metal and 90% at 428 rpm, in their investigations. Elangovan et al. [18] found that when the more durable foundation was positioned on the forward-moving side, the nugget region was properly mixed. When welding with poorer material, the weld nugget was much thinner and there was insufficient mixing. According to the information shown above, successful dissimilar friction stir welding necessitates using good judgement when deciding where to position the materials, developing the tools, and adjusting the process parameters according to on the joining materials' qualities.

Figure 1 reveals the schematic diagram of Friction stir welding. Aluminum alloys with copper and magnesium, such as AA2618 and AA5086, are common in the aircraft sector. When Cu and Mg are combined in a liquid state, a low melting eutectic is formed, resulting in solidification cracking. Using fusion welding on these alloys is not an option. When it comes to combining different metals and alloys, friction stir welding has been examined by scientists in the past few years. With good joint efficiency, FSW has effectively combined a variety of options of aluminum alloys. A significant amount of magnesium is used in the 5000 series alloys. Strength and corrosion resistance in seawater can be achieved with a magnesium content of 5% or more. FSW is almost unexplored for this particular set of materials. AA5086 is weldable with FSW because of this. Data for the four factors studied, the transversal speed in addition to the speed of rotation, the shape of a tool pin, and the D/d ratio are tabulated in Table 1. Table 2 reveals the alloys' chemical composition (weight percent). Figure 2 reveals the welded sample.

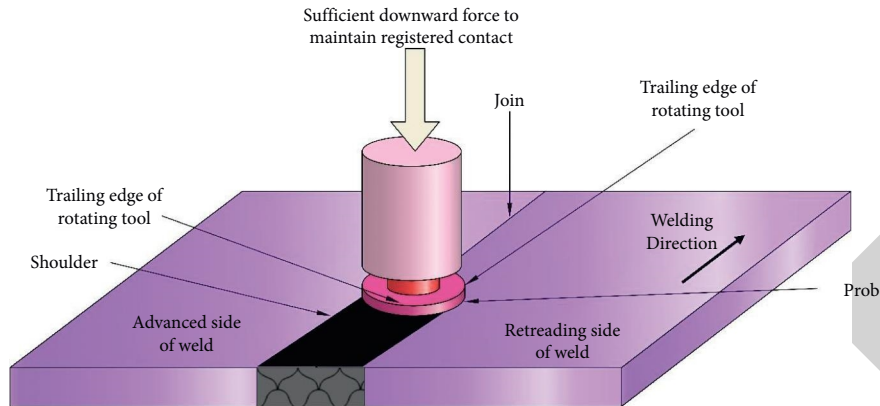


FIGURE 1: Schematic Diagram of Friction stir welding.

TABLE 1: The values and levels of each of the four performance characteristics.

Levels	Tool pin geometry	Rotational speed	Transverse speed	Ratio
1	Straight cylinder	450	15	2
2	Tapered cylinder	600	35	2.5
3	Cylindrical threaded	750	50	2.75
4	Tapered threaded	850	65	3

TABLE 2: The alloys chemical composition (weight percent).

Material	Mg	Mn	Fe	Si	Cu
AA5086	4.5	0.7	0.31	0.4	0.1
AA2618	1.5	1	0.13	0.01	4.0

1.2. *Taguchi Method.* Quality assurance, both on and off-line, is two of Taguchi’s main areas of focus. A typical experimental design focuses primarily solely on the average quality of the data, but Taguchi is considered as the core design, the minimizing of the characteristic of interest’s variation. However, despite its many flaws, the Taguchi approach now has an excellent job of solving single response issues. The purpose of robust design is to create a product that never fails to perform its intended function during its useful life. The Taguchi technique, widely known as robust design methodology, provides a method for developing requirements for complete design utilizing the design of experiments theory. Using the Taguchi approach, a process or product design can be improved through the three stages:

- (1) Designing a concept or a system.
- (2) Design of parameters.
- (3) Design with a degree of slack.

The following enumerated items are measures that must be taken in order to optimize the process parameters.

Step 1: The quality attribute to be optimized must be determined.

Step 2: Remain aware of the noise components and test conditions that could influence the results.

Step 3: Determine the variables under control and the range of possible values for each.

Step 4: The data analysis technique should be defined in conjunction with the matrix experiment design.

Step 5: Perform the matrices test.

Step 6: Data analysis is necessary to identify optimal levels for control parameters.

Step 7: At these criteria, estimate the outcomes.

1.3. *The Decision of an Orthogonal Array (OA).* These factors are listed in ascending order of importance when deciding which orthogonal array to utilize:

- (1) Quantity of products and interconnections that are relevant
- (2) Factors of interest that have a certain number of levels
- (3) Cost constraints or the required experimental resolution

L16 OA is chosen in this study because four levels and four components are taken into account. The interactions between factors are not taken into account. In order to get a total of 12 degrees of freedom (Dof), each aspect has a degree of freedom of 3 (No. Of levels 1, i.e., $4 \times 1 = 3$). A good rule of thumb is that the OA’s dof should be bigger than all other factor dofs combined on average. L16’s dof is 15, which makes it eligible for the study. Table 3 detail the plate’s mechanical characteristics.

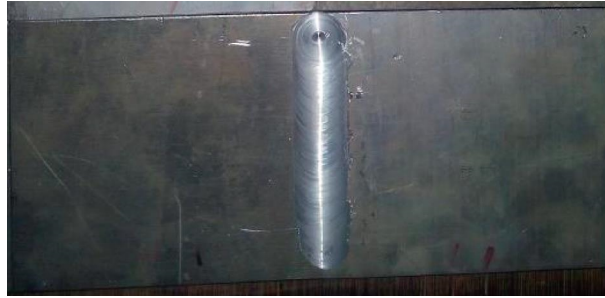


FIGURE 2: Welded sample.

TABLE 3: Materials' mechanical characteristics.

Metal	Proof strength at 0.2% (MPa)	Ultimate tensile strength (MPa)	Percentage of elongation
AA5086	268	320	31
AA2618	400	488	22

2. Experimental Procedure

In this project, Al-Cu alloy AA2618-T87 and Al-Mg alloy AA5086-H321 sheets with a thickness of 6 mm were utilized. It was cut into rectangular coupons (160 mm in length and 70 in width) for friction stir welding from rolled plates. Using a FSW process, the butt joints were welded. The butt joints were constructed in the same direction as the rolling. The trials were carried out utilizing the design parameters, L16 OA. A better approach with process parameters is with rotor velocity, spindle speed, pin profile, and D/d ratio. These are all good starting points. For friction stir welding, H13 grade tool steel (5.7 mm pin span and 12 mm pin radius) was employed. Joint lines were aligned, and a little pin was placed in each one. Figure 3 reveals the tensile specimen's dimensions. Samples were made welding coupons in their final, as-welded state, each with an overall length of 100 millimetres (25 mm gauge length \times 6 mm width). Universal tensile testing equipment was used to conduct tensile tests on three materials at room temperature in accordance with ASTM E8 [32]. The smooth profile tensile specimens were cut using a wire cut EDM. Three specimens were made for each level of the planned matrix in order to minimize the machining error (noise). These samples were tested for their tensile strength, and the results were published. It is shown in Table 4 that the experiment was successful. As-welded welds were examined for microstructure. For 15 seconds, a force of 100 g was applied to the weldment to measure Vickers microhardness data.

3. Results and Discussion

The quality of the intended qualities is calculated as a percentage of the SN ratio. As structural rigidity is the primary objective, the higher the SN ratio, the better the outcomes. The method of computing the SN ratio is presented as follows:

$$\frac{S}{N \text{ ratio}} (\eta) = -10 \log_{10} \frac{1}{n} \sum_{i=1}^n \frac{1}{y_i^2} \quad (1)$$

FSW joint tensile strength is measured in order to better understand the FSW process. Experimental data is used in order to compute both mean and standard deviation (SN) as shown in Table 4. For each level, the average mean and SN ratio are shown in Tables 5 and 6. Higher SN Ratios indicate better quality. A3, B3, C1, and D4 are the best choices based on mean and SN ratios.

3.1. Analysis of Variance (ANOVA). Analysis of Variance is a technique that identifies which variables are statistically significant. So you can see just how much the process parameter influences your reaction and how significant it is. There are ANOVA tables in Tables 7 and 8 for the mean and the noise to signal ratio. In terms of the mean and SN ratio, the results are shown in Figures 4 and 5. The F test is being used to determine the performance parameters that are of immense value in this study. An F value that is higher indicates that the factor has a greater impact on the outcome of the process. We discovered that the D/d ratio had a substantial impact on the tensile strength of the weld throughout our investigation.

3.2. Toughness Estimation of Tensile Strength. A_3, B_3, C_1, D_4 are the best settings for the experiment. According to the literature, we use a tensile strength prediction using an additive modelling approach. Table 4 displays the average values for each of the components at the various levels.

Based on the mean, these are the best parameters to use. $A_3 B_3 C_1 D_4$.

Based on the SN ratio, these are the best parameters to use. $A_3 B_3 C_1 D_4$.

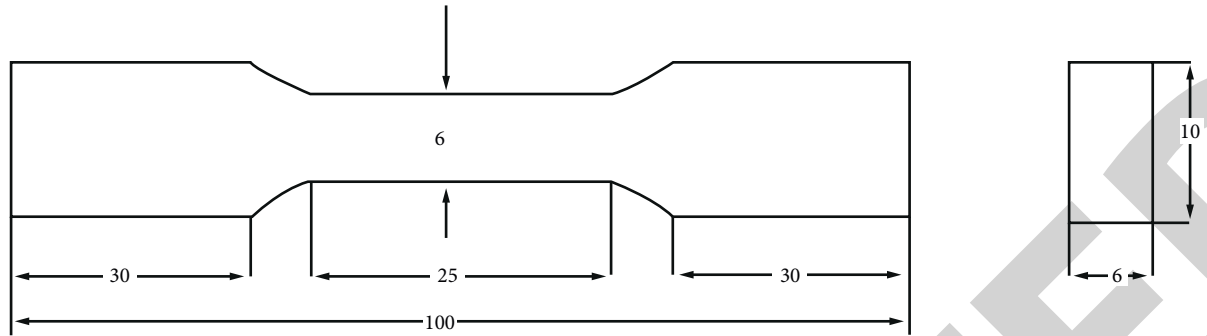


FIGURE 3: Tensile specimen's dimensions.

TABLE 4: L16 orthogonal array with a mean value and SN ratio measurement.

S.No	A tool pin geometry	B rotational speed	C transverse speed	D D/d ratio	Mean tensile strength (MPa)	SN ratio
1	1	1	1	1	105	40.4750
2	1	2	2	2	240	47.5798
3	1	3	3	3	248	47.8815
4	1	4	4	4	159	43.9851
5	2	1	2	3	204	46.1941
6	2	2	1	4	263	48.3926
7	2	3	4	1	105	40.3889
8	2	4	3	2	116	41.2504
9	3	1	3	4	289	49.2144
10	3	2	4	3	279	48.9159
11	3	3	1	2	277	48.8549
12	3	4	2	1	127	42.0312
13	4	1	4	2	299	49.4958
14	4	2	3	1	102	40.1050
15	4	3	2	4	291	49.2625
16	4	4	1	3	247	47.8358

TABLE 5: Means values.

Level	A	B	C	D
1	192	231	231	110
2	178.6	228	229	241
3	251	240	196	252
4	246	178	219	259
Delta	82	76.3	35.4	149
Rank	2	3	4	1

TABLE 6: SNR (signal to noise ratio).

Level	A	B	C	D
1	47.8	47.4	48	41
2	45.2	49.2	48.1	48.1
3	49.6	48	46	47.4
4	47.4	46.2	44	4.6
Delta	4.1	3.1	2.1	7.2
Rank	2	3	4	1

3.3. *Confirmation Run.* The cylindrically threaded pin profile was used in the confirmation studies. Other parameters were set to their optimum values as well. The spinning speed was set to 750 rpm, the transversal speed to 15 mm/min, and the D/d ratio was adjusted to 3. It was

found that the average compressive strength of the FSW specimens AA2618 and AA5086 was 301 MPa.

Particles of second-phase intermetallic were found in both of the materials used in the research. Iron/manganese aluminides were found in alloy 5086's second-phase

TABLE 7: Means-variance analysis.

Source	Degrees of freedom	Seq SS	Adj MS		% Contribution
A	3	14428.6	4812.124	0.81	15.81
B	3	12168.2	4128.41	0.51	14.12
C	3	26.41.2	861.1312	0.22	2.16
D	3	52471.6	17817.34	4.71	61.50
Residual error	3	5681.3	1871.7		6.1284
Total	15	81342.1			100

TABLE 8: Statistical ANOVA for the correlation between signal and noise.

Source	Degrees of freedom	Sequential sum of squares	Adjusted mean square	Fisher ratio	Contribution percentage
A	3	21.28	7.6829	0.51	13.142
B	3	19.81	6.91284	0.39	9.9582
C	3	6.82	2.4283	0.41	4.186124
D	3	128.546	41.2838	7.16	69.5428
Residual error	3	11.812	3.9426		5.4823
Total	15	201.428			100

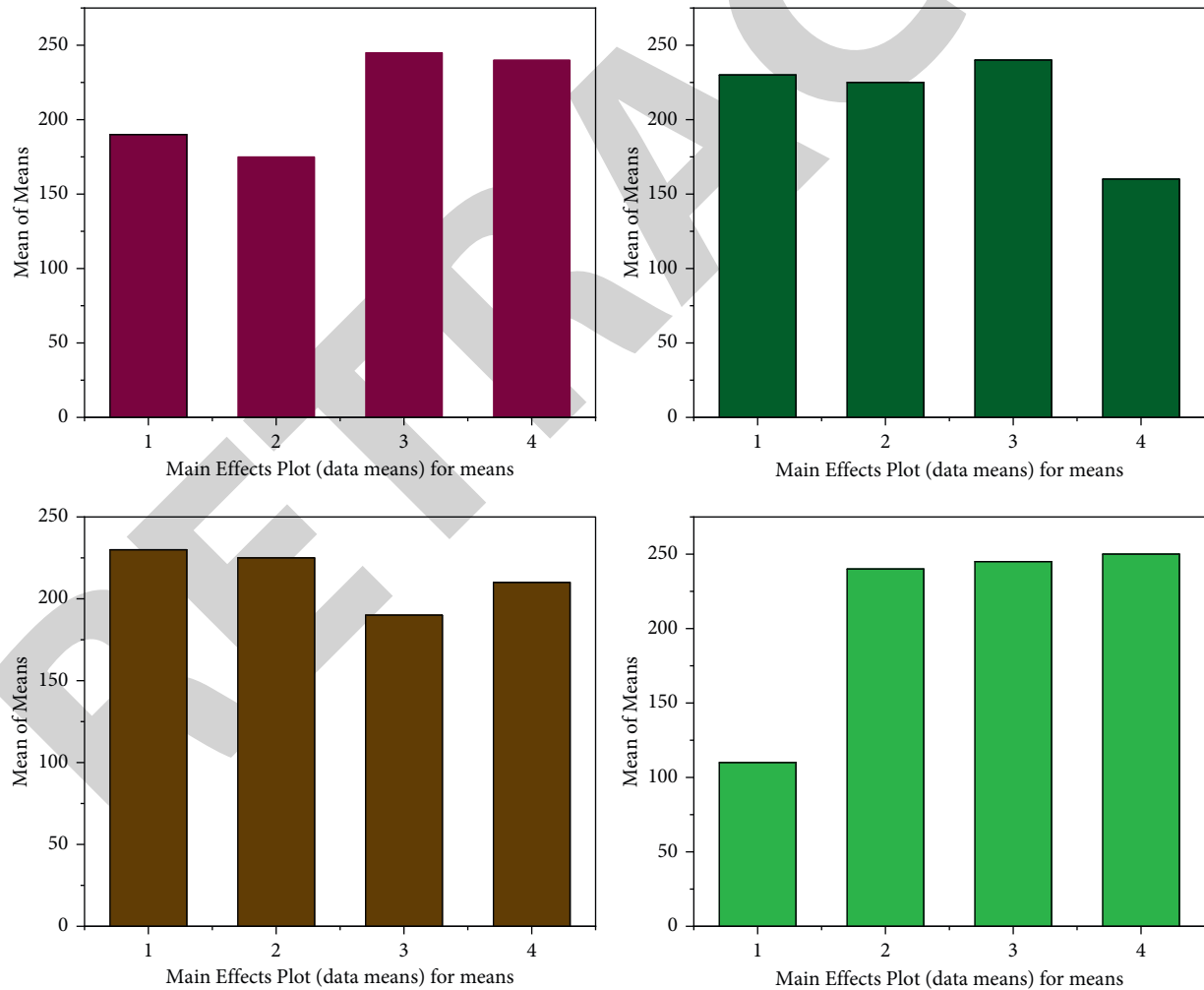


FIGURE 4: Main effects of the plot for mean.

particles, while eutectic Al-2Cu (θ) particles were found in alloy 2618. Particles in the alloy's second phase 5086 were smaller and finer than those in alloy 2618. The weld

contained three unique microstructural zones: SZ, TMAZ, and HAZ. There was a clearly defined SZ/TMAZ and TMAZ/HAZ boundary on the forward-moving side of the

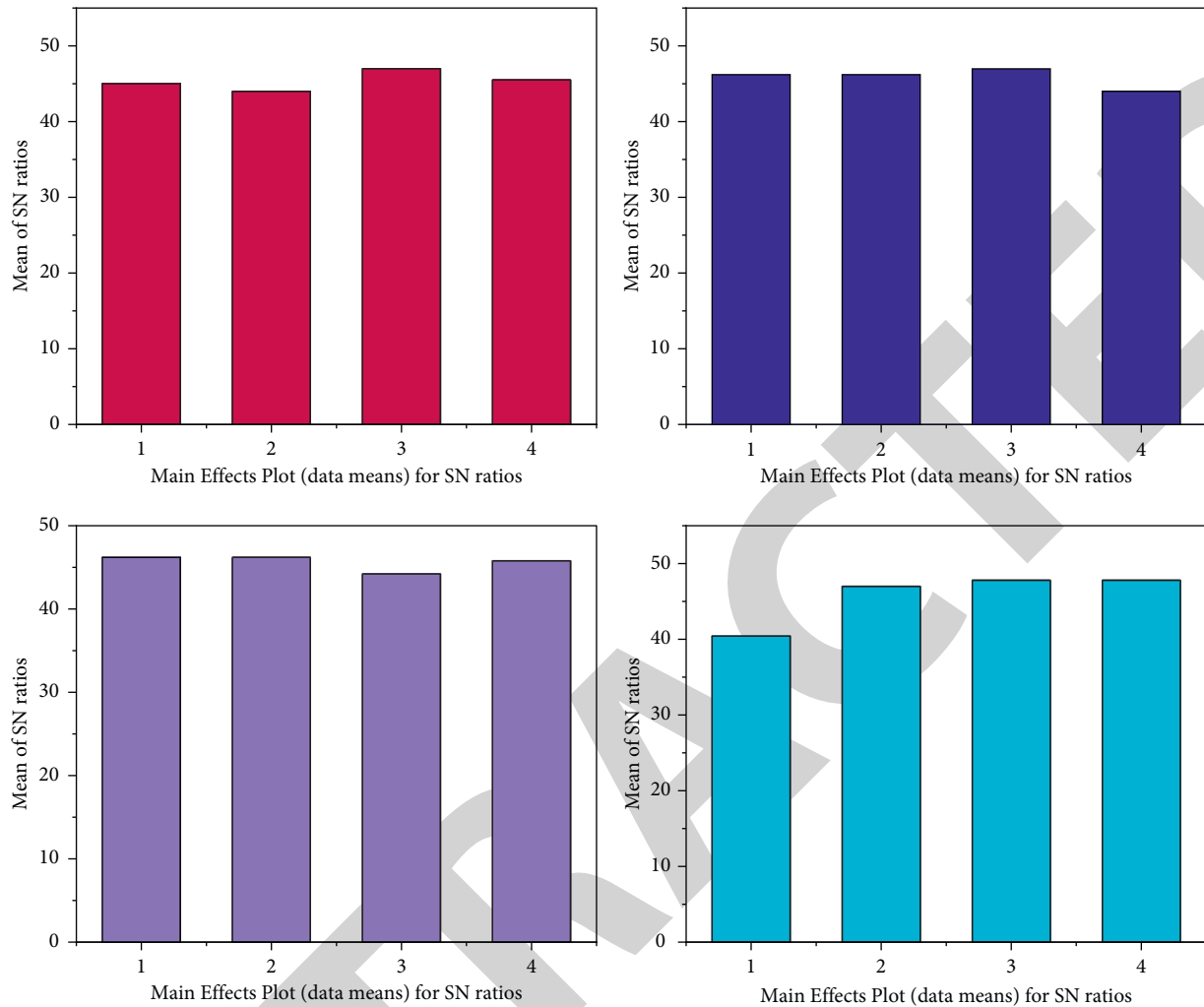


FIGURE 5: Main effects of the plot for SN ratio.

TMAZ. Dispersion of these contacts was greater on the retreating side. Compared to the foundation materials that were not affected, the grain structure of the weld nugget did not appear to have changed significantly in the HAZ. For the purpose of identifying any differences in properties between the various areas of the weld, Vickers microhardness tests were performed at 0.25 mm intervals across the weld. Using unmodified 2618, the hardness of the weld nugget boundaries was reduced considerably. Because the weld nugget was softer than the 2618 base material, its hardness was significantly lower. Relative to the 5086 base material, the hardness of the weld nugget retreating side was just marginally reduced. A 5086 basic material is compared, the weld nugget had a higher hardness. Base material 2618 had a much greater hardness rating than 2618 base material, which is predicted.

On the 5086-side HAZ, all three weld specimens failed. Figure 6 depicts the welding microhardness profile. Compared to alloy 5086, alloy 2618 has a much higher strength. Welded specimens were significantly stronger than those made of the 5086 basic material.

FSW was discovered to be the case to make acceptable butt welds between the two aluminum alloys studied, proving its ability to weld incompatible aluminum alloys. Even though FSW of aluminum alloys from different families has been established in several previous studies, one unique element of the welds formed in this work is insufficient metal mixing to cause significant corrosion. Similarly, friction stir welds between alloys 5086 and 6061 had comparable findings. "Chaotic mixing" welding two different metals together was reported in numerous earlier experiments. In addition, it was found that the onion rings had alternating layers of the two metals. Materials positioned closer to the nuggets are more likely to be dragged into them. Friction Stir On the substrate surface of a weld, temperatures rise, and deformations are more significant than on the receding side. Based on what we have learned so far, further investigation is needed to explain this observation fully. Positioning the more robust base material forward increases joint efficiency in any case.

To determine whether a weld qualifies for dissimilar welding, the lower one base material should fail out of the

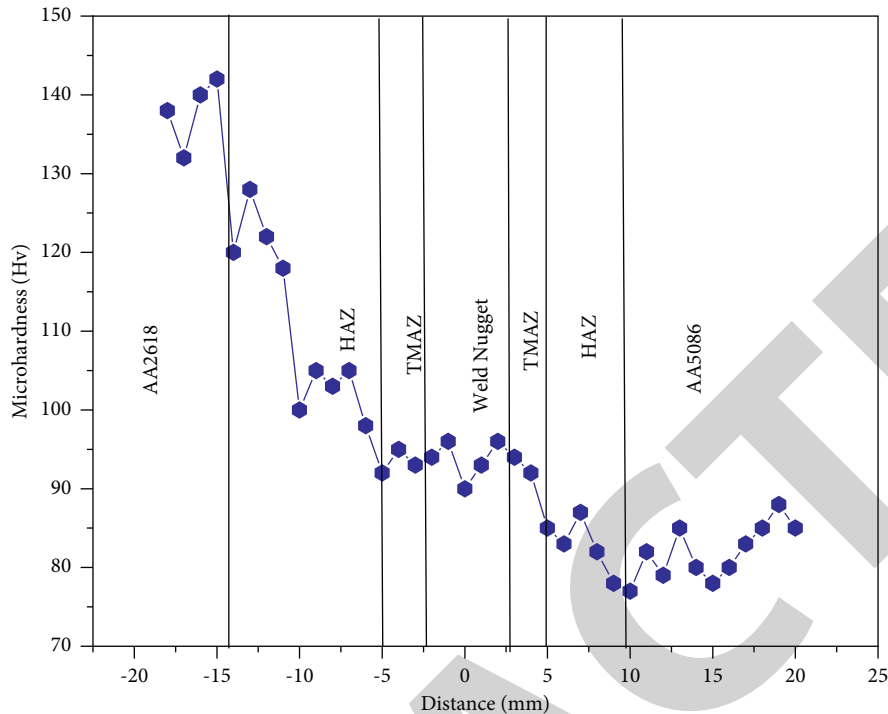


FIGURE 6: Welding microhardness profile.

way of the joint. All of the failures occurred on the 5086-side of the weldment, which has the lowest hardness ratings, due to friction stir welding. Only significantly less intense than 5086-H321 base material specimens were weld specimens. Due to annealing effects, cold work in the HAZ may have been lost. FSW achieves a junction efficiency of over 90% (based on alloy AA5086), significantly more significant than the standard fusion welding procedure can accomplish.

4. Conclusions

The ultimate tensile strength was taken into account for optimizing FSW process parameters. The spindle speed is 700 rpm, the transversal speed is 15 mm/min, and the D/d ratio is 3. When tool profiles were compared, the cylindrical threaded pin tool profile won. The D/d ratio accounts for 60% of the overall contribution, essential. FSW has a connection effectiveness of 90% and may be used to join AA2618-T87 and AA5086-H321 sheets, 5086 Alloy (based on AA5086). This material combination occurs in the heat-affected zone of Alloy 5086. The best parameters are tool pin geometry (A)–15.81 percent, rotational speed (B)–14.12 percent, transverse speed (C)–2.16 percent, D/d ratio (D)–61.50 percent, and the best parameters are $A_3B_3C_1D_4$.

Data Availability

The data used to support the findings of this study are included in the article. Should further data or information be required, these are available from the corresponding author upon request.

Conflicts of Interest

The authors declare that there are no conflicts of interest regarding the publication of this paper.

Acknowledgments

The authors thank Sri Sairam Engineering College, Chennai, and SRM Valliammai Engineering College, Chennai, for providing technical assistance to complete this experimental work. This project was supported by Researchers Supporting Project number (RSP-2021/332) King Saud University, Riyadh, Saudi Arabia.

References

- [1] S. T. Amancio-Filho, S. Sheikhi, J. F. Dos Santos, and C. Bolfarini, "Preliminary study on the microstructure and mechanical properties of dissimilar friction stir welds in aircraft aluminium alloys 2024-T351 and 6056-T4," *Journal of Materials Processing Technology*, vol. 206, no. 1–3, pp. 132–142, 2008.
- [2] K. S. A. Ali, V. Mohanavel, S. A. Vendan et al., "Mechanical and microstructural characterization of friction stir welded SiC and B4C reinforced aluminium alloy AA6061 metal matrix composites," *Materials*, vol. 14, no. 11, Article ID 3110, 2021.
- [3] R. Priya, V. Subramanya Sarma, and K. Prasad Rao, "Effect of post weld heat treatment on the microstructure and tensile properties of dissimilar friction stir welded AA 2219 and AA 6061 alloys," *Transactions of the Indian Institute of Metals*, vol. 62, no. 1, pp. 11–19, 2009.
- [4] R. S. Mishra and Z. Y. Ma, "Friction stir welding and processing," *Materials Science and Engineering: R: Reports*, vol. 50, no. 1–2, pp. 1–78, 2005.

Retraction

Retracted: Thermal Analysis of the Solar Dish Array Concentrator System

Advances in Materials Science and Engineering

Received 26 December 2023; Accepted 26 December 2023; Published 29 December 2023

Copyright © 2023 Advances in Materials Science and Engineering. This is an open access article distributed under the Creative Commons Attribution License, which permits unrestricted use, distribution, and reproduction in any medium, provided the original work is properly cited.

This article has been retracted by Hindawi, as publisher, following an investigation undertaken by the publisher [1]. This investigation has uncovered evidence of systematic manipulation of the publication and peer-review process. We cannot, therefore, vouch for the reliability or integrity of this article.

Please note that this notice is intended solely to alert readers that the peer-review process of this article has been compromised.

Wiley and Hindawi regret that the usual quality checks did not identify these issues before publication and have since put additional measures in place to safeguard research integrity.

We wish to credit our Research Integrity and Research Publishing teams and anonymous and named external researchers and research integrity experts for contributing to this investigation.

The corresponding author, as the representative of all authors, has been given the opportunity to register their agreement or disagreement to this retraction. We have kept a record of any response received.

References

- [1] Y. H. Mahmood, R. Y. J. Al-Salih, S. Amer Mahdi, and A. Mohamed Ibrahim, "Thermal Analysis of the Solar Dish Array Concentrator System," *Advances in Materials Science and Engineering*, vol. 2022, Article ID 1823630, 8 pages, 2022.

Research Article

Thermal Analysis of the Solar Dish Array Concentrator System

**Yaseen H. Mahmood,¹ R. Y. J. Al-Salih,¹ Saif Amer Mahdi,¹
and Abdelrahman Mohamed Ibrahim²**

¹Department of Physics, College of Sciences, University of Tikrit, Tikrit, Iraq

²Accounting and Financial Management, School of Management Studies, University of Khartoum, Khartoum, Sudan

Correspondence should be addressed to Abdelrahman Mohamed Ibrahim; amibrahim@uofk.edu

Received 22 December 2021; Accepted 13 January 2022; Published 1 February 2022

Academic Editor: Palanivel Velmurugan

Copyright © 2022 Yaseen H. Mahmood et al. This is an open access article distributed under the Creative Commons Attribution License, which permits unrestricted use, distribution, and reproduction in any medium, provided the original work is properly cited.

This research aimed at fabricating solar array concentrator. It is one of the best options for solar energy concentration. Compared with other systems, because of the higher concentration ratios and high control focal length, good accept angles, higher efficiency, rigid with high wind, and low cost, the system has been locally designed and fabricated to produce steam. The dimensions of the active aperture area of 3.25 m² were studied. The absorber receiver, which conveyed water as heat in a closed cycle with an appropriate pump, produced steam at a higher temperature and with more efficiency. The best characterizations of the system are the focal length 1.25 m, concentration ratio 103, optical power 1.2 kW, losses 0.2 kW, and efficiency 60–70%.

1. Introduction

Man is looking for new sources of energy to cover his growing needs in the applications of advanced life. But some sources of energy are known for their depletion and the cost of their high exploitation and the negative impact of their use in modern times. Man has been alerted to the possibility of taking advantage of the heat of the Sun, which is characterized as renewable energy. It is as sustainable as energy that can be obtained from wind, flowing water, or other natural phenomena from which energy can be produced. The world is clearly aware of the great danger it is causing. The use of other common sources of energy (especially oil and natural gas) to pollute and destroy the environment, which makes renewable energy, is the best option for some countries. Several research has been carried out in solar energy to develop the main components and parts of energy uses [1–5]. A parabolic dish with reflector is used for melting snow to produce water. The receiver arrangement focuses to melt the snow and store the water in the tank [6] with the help of dynamic simulation, a small solar concentrator. With the aid of a Computational Fluid Dynamics simulation, a solar trough concentrator and a pipe with flowing water are set in the concentrator focus. This work aims to investigate

the feasibility of generating steam from such a system as well as analyzing the generated steam quantitatively and qualitatively. Effects of variation of solar radiation intensity, ambient temperature, water flow rate, and pipe diameter on the quantity and quality of the generated steam have been investigated. A 130 kg of “steam could be generated per day with a 0.01 m diameter with 0.0042 kg/s flowing water” [7] privatize development of the new solar receiver (DSG) provides a solution to get rid of the difficult operating situations in that time [8]. Design and fabrication of three low-cost solar concentrators are with diameter 5, 10, and 20 m, and the focal length is 0.3 m. The result of this study is high reflective facets and increases the rib angle and applies full stress [9]. Recently designing diameter of 1.4 m and receiver diameter of 0.3 m the surface area of 1.53 m² from this component, has been done diameter Solar bifocal design by low-cost material which contains fabricating solar array concentrators, such that the receiver work on a thermosiphon 650 kJ where these materials are sufficient for Solar bifocal design It is one of the best options for solar energy concentration [10]. Two concentrators for solar water heating design used metal dish with reflectivity of 95% because the efficiency is 73% covered by mirror, output energy is 1853 W, and the second with reflectivity up to 80%,

result by covered with a layer of 60% efficiency and output energy of 1551 W, [11]. In Tunisia, a (3.8) meter solar dish is designed to decrease the heat losses and steam production, and many experimental tests were conducted [12]. The tracking system is added to produce steam generation [13]. PDSC is a solar dish with aperture area of 16 m², the diameter of the solar boiler is 0.126 m². The system is analyzed by using Taguchi method analysis to find heat transfer. The change flow rate between inlet and out let temperature is one of more influencing factors[14]. Two types of solar collector are discussed with non-concentrating and high concentrating with application and studied the optical heat loss and tracking system such as different heat transfer and thermal storage for system [15].(Table 1)

2. Theoretical Analysis of System

2.1. Mirrors. When a surface reflects light incident in some ranges of wavelengths, the reflected light conserves most of physical features of the original light.

There are three types of mirror.

- (i) 1- plane
- (ii) 2- concave
- (iii) 3- convex

The surface that has the ability to reflect the light must be greatly smooth. The features of the picture in plane mirror must be steady and in the same size and dimension as the original body that is behind the mirror. The reflected picture must not only be steady from up and down but must also be reversed from the sides (left and right) [16].

“ Concentration ratio (CR) is defined as the area of collector (Ac) to area of receiver (Ar):

$$CR = \frac{A_c}{A_r} \quad (1)$$

” The greatest value of the concentration ratio in three dimensions for the collector is given by the following equation [17, 18]:

$$CR_{\max} = \frac{1}{\sin^2 \theta} \quad (2)$$

The incident ray on the surface of a mirror will be truckled according to the two laws given below:

The first law: the incident beam and the reflected beam and the column from the point of incident fall are all located in one level perpendicular to the point of incident

The second law: the angle of incident equals the angle of reflection

2.2. Heat Transfer. We can calculate the characterization of the system and heat transfer from equations (3)–(13) as follows [17, 18]:

$$Q_{\text{out}} = \eta_0 I_b A_a - U_L (T_r - T_{\text{amb}}) A_r \quad (3)$$

Efficiency of collector:

$$\eta_{\text{collector}} = \frac{Q_{\text{out}}}{A_a I_b} = \eta_0 - \frac{A_r}{A_{\text{amb}}} \frac{U_L (T_r - T_a)}{I_b} \quad (4)$$

$$Q_{\text{out}} = Q_{\text{opt}} - Q_{\text{loss}} \quad (5)$$

$$Q_{\text{opt}} = A_a \rho_{s-m} \tau_g \alpha_\gamma S I_b \quad (6)$$

$$Q_{\text{loss}} = A_r U_L (T_r - T_{\text{amb}}) \quad (7)$$

$$T_r = \frac{T_{\text{out}} + T_{\text{in}}}{2} \quad (8)$$

$$U_L = \left(\frac{1}{h_w + h_r} \right)^{-1} \quad (9)$$

$$h_r = 4\sigma\epsilon T^3 \quad (10)$$

$$N_U = 0.3 \text{Re}^{0.6} \quad (11)$$

$$R_e = \frac{V \cdot D_{\text{out}}}{\nu} \quad (12)$$

$$h_w = \frac{K_{\text{air}} N_u}{D_{\text{out}}} \quad (13)$$

[16].

3. Experimental Work

3.1. Concentration. The solar dish array, as shown in Figure 1, consists of 52 square shaped plane mirrors with reflectivity (95%) and area (25 × 25) Cm². Figure 2 shows that the mirror is fixed on a metal frame, and moved up, down, left, and right by four screws to add the spot of solar radiation at one location focus. It is one of the best options for solar energy concentration. Compared with other systems, because of the higher concentration ratios and high control focal length, well accept angles, higher efficiency, rigid with high wind, and low cost, the system has been locally designed and fabricated to produce steam such that the dimensions of the active aperture area of 3.25 m and the active area 3.14 m² such that the incident beam, the reflected beam, and the column from the point of incident fall are all located in one level perpendicular to the point of incident.

3.2. Receiver. Receiver is most important to convert solar radiation to heat energy. We used 4 mm cylindrical steel with dimensions of 20 cm in length and 25 cm in diameter, and two disc metals was used, one fixed at the front and the other behind by three screws, Figure 3. It consisted of 10 rolls of copper pipe with a diameter of 6 mm which we fixed at the focus.

3.3. Water Pump. A pump was used to push water, which is used in houses to circulate between the metal tank through the pipes and the solar receiver.

TABLE 1: Nomenclature.

Simple	Abbreviations
A_a	Aperture area of the collector
A_r	Aperture area of the receiver
Q_{opt}	The rate of the optical energy absorbed by the receiver
Q_{out}	Useful energy delivered to the total incoming solar energy
Q_{Loss}	The rate of the energy lost from the receiver to the ambience
$\rho_{s,m}$	Specular reflectance of the concentrator
τ_g	Transmittance of the glass
α_y	Absorbance of the receiver
I_b	Beam insolation incident on the collector aperture
S	Receiver shading factor
T	Averaged receiver temperature
T_{amb}	Ambient temperature
UL	The overall heat loss coefficient
T_{out}	Temperature of the fluid exiting the receiver
T_{in}	Temperature of the fluid entering the receiver
H_w	Convective coefficient
H_r	Radiation coefficient between the receiver (or glass cover) and the ambient
Σ	Stefan-Boltzmann constant
E	Emittance of the absorbing surface
Nu	Nusselt number
Re	Reynolds numbers
V	Wind speed
D_{outer}	Diameter of the receiver
N	Viscosity



FIGURE 1: Concentrator before mirror is fixed and after mirror is fixed.

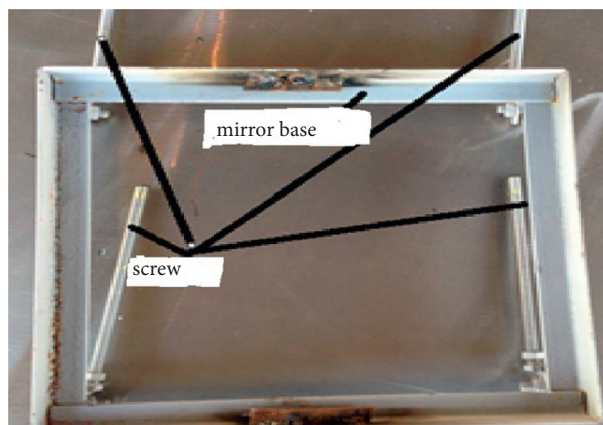


FIGURE 2: Mirror frame.

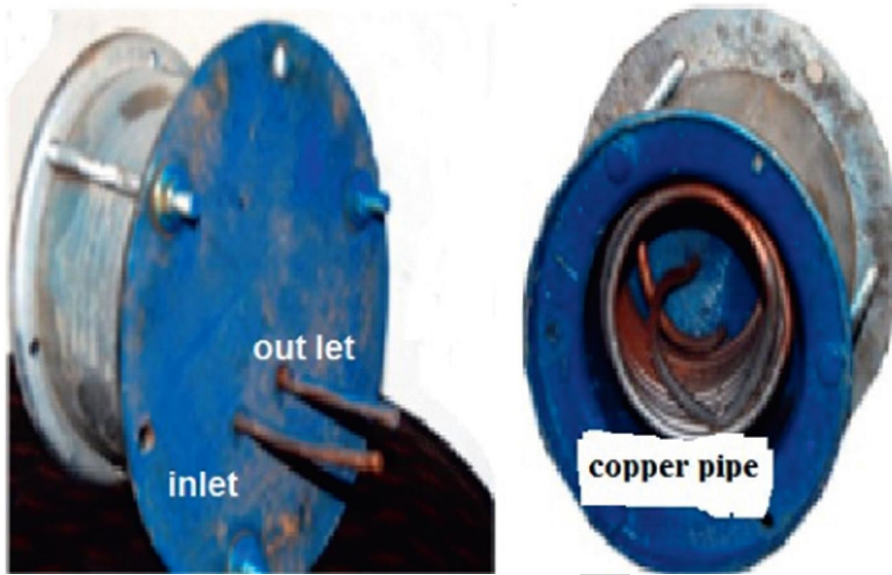


FIGURE 3: The receiver, from rear and front.

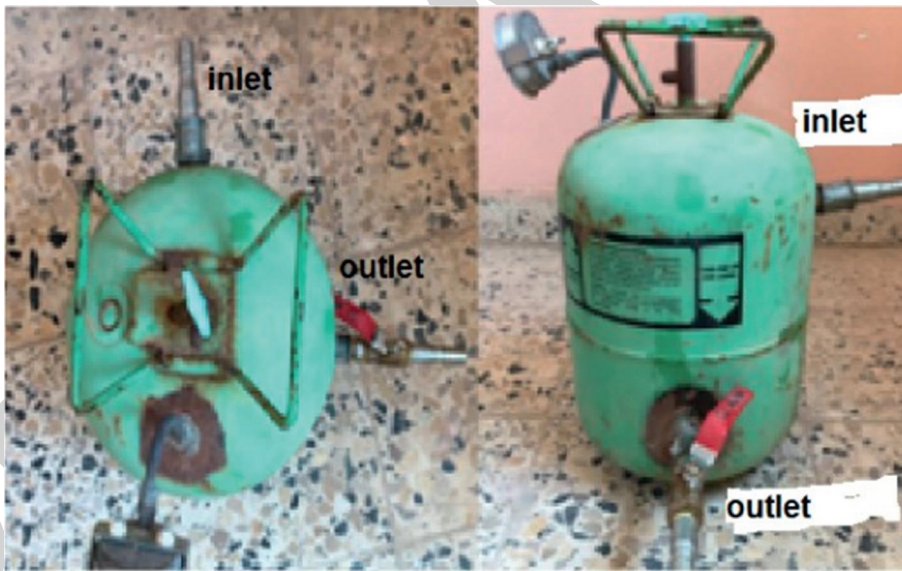


FIGURE 4: Storage tank.

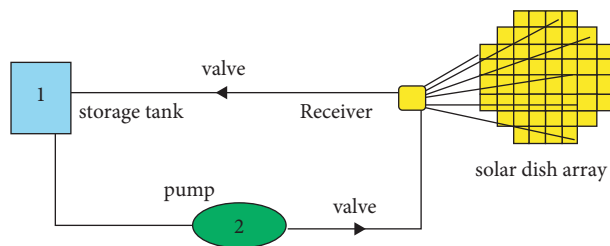


FIGURE 5: Schematic connection of system.



FIGURE 6: Solar dish component system.

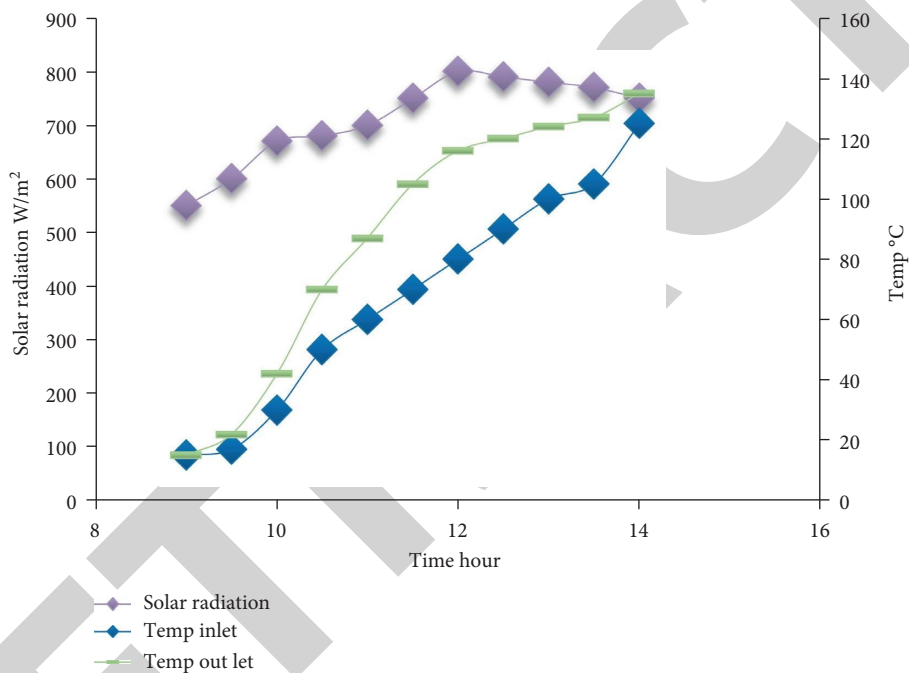


FIGURE 7: Relation between Solar radiation with time and temperature.

3.4. *Storage Tank.* We used a cylindrical steel tank Figure 4 with diameter 0.3 m, and capacity 20 L, and added two valves.

E-piping connections: we used a plastic pipe to connect all components for more isolation of all piping enfold by heat wool with aluminum cover. Figure 5 shows the scheme explicates, how to connect storage tank with pump, and a one-way valve to the receiver and another valve with storage tank. Figure 6 demonstrates the experiential connected all parts of the system fabricating, which is solar array concentrators by the pump worked to push the water from the storage tank to pump steam, which conveyed water as heat in a closed cycle with an appropriate pump produced steam at a higher temperature and with more efficiency.

System tested: after connecting all parts of the system, we fixed the concentrator to the south of the solar radiation incident directed on the mirror and fixed by the screws in the rear mirror to reflect the radiation on the receiver; after 10 mins, the

temperature of the receiver will reach up to 350°C; at this time; the pump works to push water from the storage tank to pump and to receiver and return to the storage tank and measure the temperature from inlet and outlet from the receiver with time and other parameters of the system.

4. Results and Discussion

Solar radiation and temperature with time have been studied in Iraq-Tikrit with longitude (43.68) and altitude (34.59).The recording time was in March 2018 as described in Figure 7. In this zone, the maximum solar radiation was found between 9: 00 AM to 2:00 PM; after this time, the solar radiation begins to decrease between 1:00AM to sun set; the relation between the temperature and time is increased because the system is a closed cycle (the inlet and out let temperature) when solar radiation increase (Figure 7). It is compatible with [10, 11].

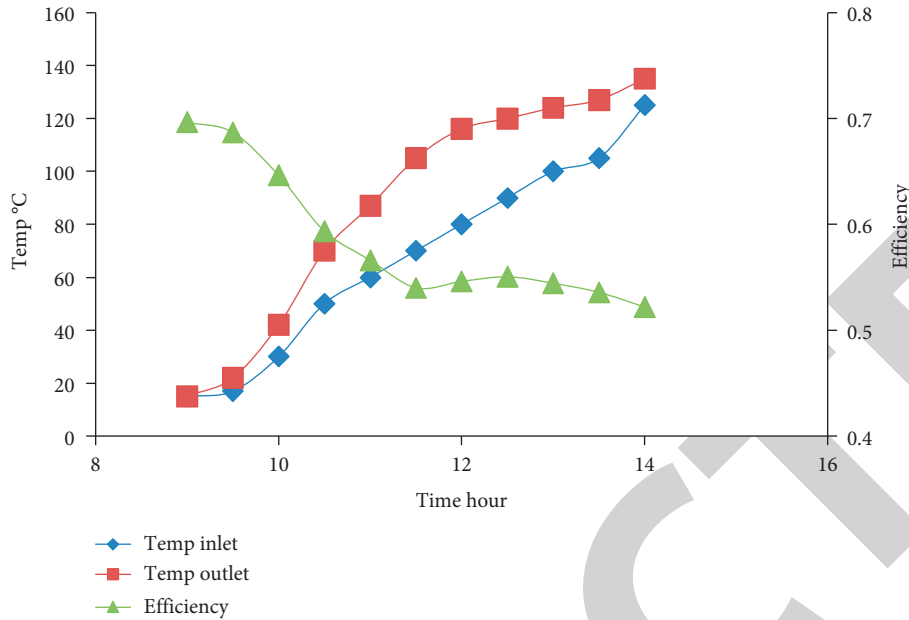


FIGURE 8: Relation between efficiency with time and temperature.

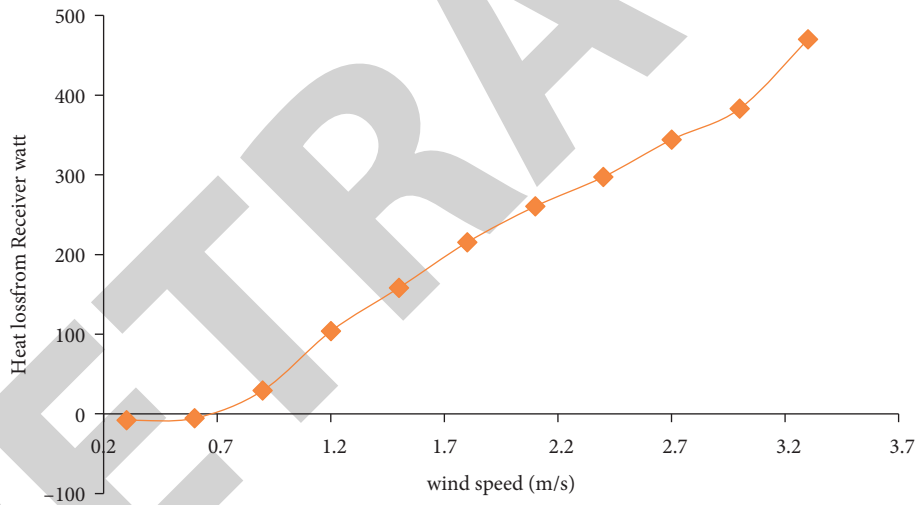


FIGURE 9: Heat loss from receiver for wind speeds.

Also, by using equation (3)–(13) and writing in Microsoft Excel, another characterization of the system is found as shown in Figure 8. It shows the variation of temperature and efficiency with time for the receiver. The higher the solar radiation is for the period between nine and one o'clock at noon; the water temperature increased in the circulating between the tank and the receiver so as the water continues to circulate several times due to the closed cycle with the water pump; this behavior is similar to the fabricated solar array [16]. It was observed that efficiency decreased related with receiver temperature because of the loss of the radiation which is proportional to the fourth power of receiver temperature as mentioned before. Also, the results of the

efficiency for the receiver are decreasing to higher temperature difference and reduced due to loss to continuous exposure to ambient air, as well as loss by convection [19].

The heat loss of the receiver increases as the temperature increases. Figure 9 with the wind speed increases due to contact between the liquid and the tubes with the surrounding air. The loss should reduce the size of the receiver and packaging with thermal wool [18].

In a clear day, when the wind speed is low, the loss is low and the optical energy increases. As a result, the system becomes more efficient as seen in Figure 10 and compatible with the source [18, 19].

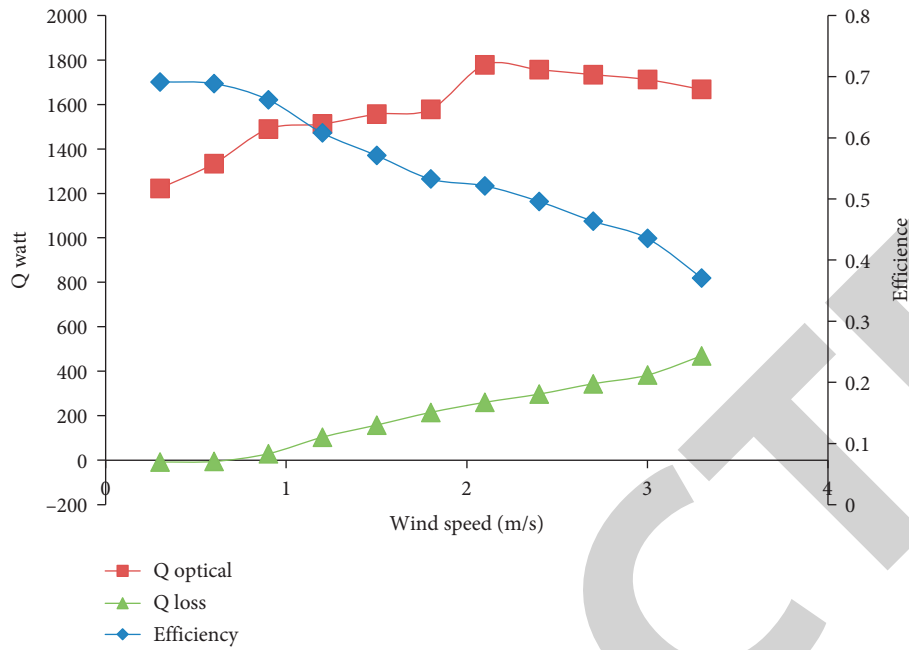


FIGURE 10: Relation between efficiency with wind speed.

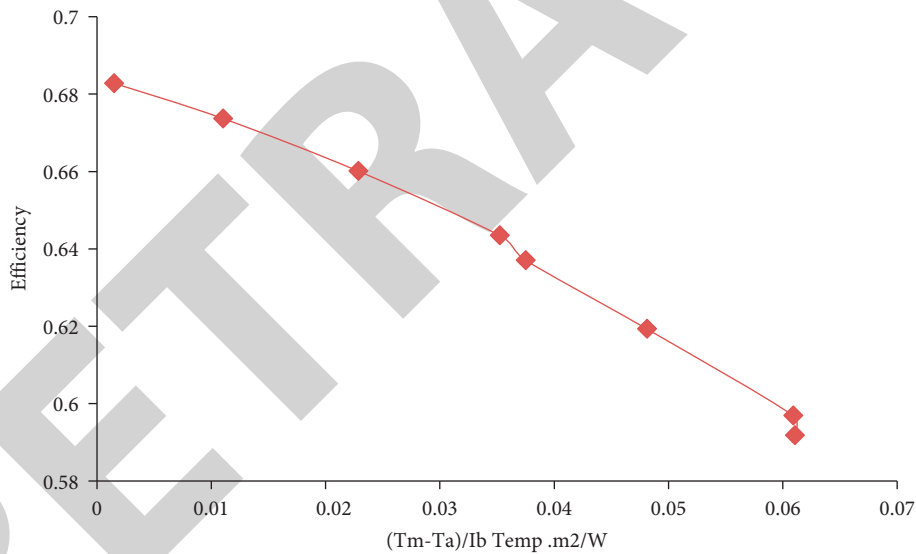


FIGURE 11: Relation between efficiency with work temperature divided to solar radiation.

From equation (5), the thermal output value was being transferred from the concentrator to the boiler. This results a collector with high efficiency. Figure 11 shows the efficiency of the system due to the work temperature divided to solar insulation. The system is suitable with these parameters and the same with the source [19, 20].

5. Conclusion

The solar dish array concentrator has been produced according to the matching theoretical equation data, based on the theoretical and experimental examination of a closed cycle solar array collector system. The reflectivity of the array concentrator is high (up to 90 percent). The closed cycle with

pump raises the temperature of the output water in the receiver cavity, increasing system operating efficiency, and making it an excellent system for solar thermal to make steam. In Iraq, it is feasible to utilize it for solar thermal.

Data Availability

The data underlying the results presented in the study are available within the manuscript.

Conflicts of Interest

The authors declare that they have no conflicts of interest regarding the publication of this paper.

Retraction

Retracted: Anti-Quorum Sensing in Pathogenic Microbes Using Plant-Based Bioactive Phytochemicals

Advances in Materials Science and Engineering

Received 26 December 2023; Accepted 26 December 2023; Published 29 December 2023

Copyright © 2023 Advances in Materials Science and Engineering. This is an open access article distributed under the Creative Commons Attribution License, which permits unrestricted use, distribution, and reproduction in any medium, provided the original work is properly cited.

This article has been retracted by Hindawi, as publisher, following an investigation undertaken by the publisher [1]. This investigation has uncovered evidence of systematic manipulation of the publication and peer-review process. We cannot, therefore, vouch for the reliability or integrity of this article.

Please note that this notice is intended solely to alert readers that the peer-review process of this article has been compromised.

Wiley and Hindawi regret that the usual quality checks did not identify these issues before publication and have since put additional measures in place to safeguard research integrity.

We wish to credit our Research Integrity and Research Publishing teams and anonymous and named external researchers and research integrity experts for contributing to this investigation.

The corresponding author, as the representative of all authors, has been given the opportunity to register their agreement or disagreement to this retraction. We have kept a record of any response received.

References

- [1] K. Subramanian, H. Selvaraj, B. K. P. Sampath Renuga, V. S. and W. Aruni, "Anti-Quorum Sensing in Pathogenic Microbes Using Plant-Based Bioactive Phytochemicals," *Advances in Materials Science and Engineering*, vol. 2022, Article ID 7532086, 7 pages, 2022.

Review Article

Anti-Quorum Sensing in Pathogenic Microbes Using Plant-Based Bioactive Phytochemicals

Kumaran Subramanian,^{1,2} Harshni Selvaraj ,^{2,3} Balakrishnan K,⁴
Pugazhvendan Sampath Renuga,^{5,6} Velmurugan S ,⁷ and Wilson Aruni⁸

¹Centre for Drug Discovery and Development, Sathyabama Institute of Science and Technology, Chennai, Tamil Nadu, India

²Department of Biotechnology, School of Bio and Chemical Engineering, Sathyabama Institute of Science and Technology, Chennai, Tamil Nadu, India

³Department of Mechanical and Process Engineering, Offenburg University of Applied Sciences, Offenburg 77652, Germany

⁴Department of Zoology, Government Art's College (A), Karur, Tamil Nadu, India

⁵Department of Zoology, Annamalai University, Chidambaram, Tamil Nadu 608002, India

⁶Department of Zoology, Arignar Anna Government Arts College, Cheyyar, Tamil Nadu, India

⁷Department of Biology, School of Natural Science, Madawalabu University, Oromiya Region, Ethiopia

⁸Loma Linda Veteran Affairs, Loma Linda University, Loma Linda, California 92350, USA

Correspondence should be addressed to Velmurugan S; velkas.cas@gmail.com

Received 12 November 2021; Accepted 19 December 2021; Published 28 January 2022

Academic Editor: Palanivel Velmurugan

Copyright © 2022 Kumaran Subramanian et al. This is an open access article distributed under the Creative Commons Attribution License, which permits unrestricted use, distribution, and reproduction in any medium, provided the original work is properly cited.

Infectious disease-causing pathogenic microorganisms grow rapidly within quorum sensing mediated biofilms. Attempts are made to restrict quorum sensing in pathogens, and the formation of biofilms has paved the way for the identification of bioactive phytochemicals. Anti-QS compounds have been proven to reduce bacterial pathogenicity in the past. Medicinal plants provide an enticing repertoire of phytochemicals with distinct microbial disease-controlling potential due to the vast spectrum of secondary metabolites included in extracts such as phenolics, quinones, flavonoids, alkaloids, terpenoids, and polyacetylenes. This review makes a specialty of the bioactive molecules produced using vegetation which have a target closer to quorum sensing accompanied via biofilm formation in pathogenic microbes.

1. Introduction

The communication between cells allows the pathogenic microorganisms to exchange information about cell density and adjust gene expression is termed quorum sensing. This enables the bacterial pathogens to create an impact on the environment or the host [1]. The microorganisms attach on a surface and proliferate which also produces extracellular polymers that consolidation the attachment and form a matrix of biofilm which leads to a change in phenotype. The formation of biofilm also involves the attachment to a substrate, microcolonies formation, and also the complex channels that form new planktonic cells are formed. The methods which consist of biofilm formation, virulence issue expression, production of secondary

metabolites, strain adaption mechanisms are regulated with the aid of quorum sensing. It is far a key regulator of the virulence factors and biofilm formation in pathogens especially in gram-negative microorganism. The study is carried out to test the bacterial culture extract of a particular strain for its inhibitory effects on virulence factors and biofilm formation of the bacterial culture are regulated by quorum sensing, both in vitro and in vivo [2]. Often, quorum sensing is loosely correlated with the number of cells. The aggregation of a compound called an autoinducer requires the induction of a quorum-sensing gene. The more the cells in a given room, the faster the autoinducer builds up and more likely it can reenter the cells after a cell produces an autoinducer, and the molecule easily diffuses out of the cell.

Quorum sensing has been involved within the developmental tolerance to and the law of many antimicrobial remedies in the immune device. Blocking quorum sensing by a drug increases the liability of the organism that infects the host acquires a defense mechanism. Much bacterial pathogenicity is regulated by quorum sensing, regulation of this kind of mechanism may suppress the virulence [3]. Quorum sensing inhibitors are useful in attenuating the pathogenicity of bacteria regarding the boom of multi antibiotic-resistant bacteria. The intervention of quorum sensing had been an innovative approach to control infections in bacteria, as it manages the spanned words as you want, the pathogens depend on quorum sensing [4]. The arena health employer (WHO) record states that 80% of the arena's population is the usage of herbal medication for healthcare.

Many other studies that are focused on phytochemicals play an important role in the prevention, treatment, and management of various illnesses as it has reduced side effects, for their efficacy and affordability [5]. Phytochemicals that acquire medicinal values are used as a novel drug by increasing the potential of a plant by ayurveda to improve human health with its medicinal properties.

Quorum sensing plays a crucial role in the improvement of novel anti-infectives. Pathogenic for virulence, microbes depend on the quorum sensing mechanism to regulate the expression of the gene. The molecules that are responsible for quorum sensing inhibition that tends to suppress biofilm formation and virulence factors are said to be quorum sensing inhibitors (QSIs). It engaged furanones and some of the glycosylated flavonoids, bismuth porphyrin, structural analogs, complexes, glycolmonoterpenols, and other nanomaterials. Quorum sensing inhibitory activity is carried out due to the similarity in the structure of furanones with AHL some other studies said that furanones may function by the degradation of LuxR type of protein or reducing the DNA binding activity of LuxR which is a transcriptional regulatory protein. The formation of biofilm and virulence factors so as to be managed by quorum sensing was reduced by sulphoraphane erucin [6].

2. Quorum Sensing in Gram-Negative and Gram-Positive Bacteria

Autoinducers that belong to the first class are used by Gram-negative bacteria, the second class is used for Gram-positive bacteria and the third class of biomolecules is used for both Gram-negative and Gram-positive bacteria. Quorum sensing is used by both Gram-positive and Gram-negative bacteria. Secreted oligopeptides and two-component systems, which comprise membrane-bound sensor kinase receptors and cytoplasmic transcription factors that direct gene expression changes are commonly used in gram-positive systems.

Gram-negative bacteria produce acylated homoserine lactone (AHL) as its autoinducers, that are synthesized by LuxI type of enzyme which is a signal synthase encoded by the first gene of Lux operon [1] (Figure 1)

2.1. Gram Negative Bacterial Quorum Sensing Arrangement. The complex LuxR-AHL binds to DNA promoting and activation of genes manipulates through the quorum sensing. The LuxR/3-oxo-C6-HSL complex turns on the transcription by the promotor lux operon promotor, which suggested the rise to different genes by the side of Lux AB genes that encode luciferase and Lux CDE, encoding the enzymes producing the substrate for luciferase observed via bioluminescence. The molecules diffuse passively through the bacterial membrane and get gathered each intracellular and extracellularly with respect to the cell density. Quorum sensing circuits are observed in above 25 species of Gram-negative bacteria.

The LasR-autoinducer complex activates the expression of every other *P. aeruginosa* quorum-sensing machine by triggering unique target genes of 2d magnificence that encode the sigma factor rhamnosyl transferase stationary portion, which involves the synthesis of biosurfactant/hemolysin rhamnolipid and also the genes that include pyocyanin antibiotic and pyocyanin synthesis. A Gram-negative microbe that can be contained in water and soil, like *Chromobacterium violaceum*, a number of things that include antibiotics, cyanide hydrogen, proteases, chitinase, and especially violacein, a purple pigment that is water-insoluble with a purple pigment involvement of phenotypic response to AHLs [7].

2.2. Quorum Sensing System in Gram Positive Bacteria. Numerous techniques that respond to the increase in mobile density are controlled by Gram-positive microorganisms, but in contradiction to Gram-negative microorganisms using HSL autoinducers. These high-quality gram-bacteria use peptides that are processed from precursors that can be used for quorum sensing as autoinducers. Indicators are actively transported outside the cell, where they interact with external domains of membrane-bound sensor proteins. The transduction of the sign that could be created by phosphorylation cascade ends the activation of DNA binding protein by affecting the transcription of precise genes so that each sensor protein is selective to its peptide signal. In the case of Gram-positive bacteria, the peptide signal precursor locus is being translated to precursor protein which is cleaved to form a processed peptide autoinducer signal.

Further, many different Gram-positive bacteria show off oligopeptides signaling systems alongside AI-2. Developing and responding to the mixture of these signals permit bacteria to note their own populace nitrogen tiers and also the density of population of others in its locality. A properly-defined response to indicators or response that is based on the combinatorial sampling of various kinds of signals may want to permit microorganisms to constantly regulate the behavior depending on the institution of species [1].

3. Phytochemicals against Quorum Sensing

The possible inhibitors of quorum sensing are phytochemicals present in plant extracts that include quercetin, myricetin, kaempferol, baicalin, eugenol, and 6-gingerol.

QUORUM SENSING

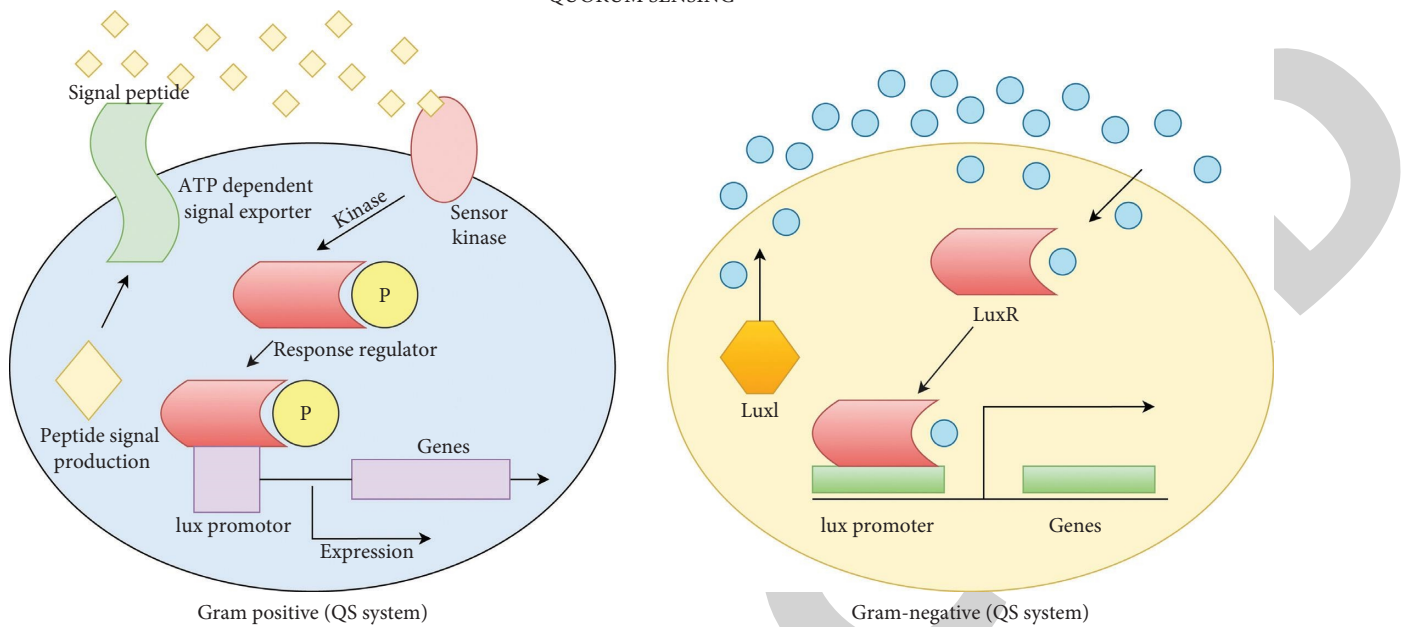


FIGURE 1: Quorum sensing arrangement in gram-positive and gram-negative bacteria.

Notable substitutes for synthetic antibacterial drugs are bioactive compounds from plant extracts with anti-quorum sensing activities, especially among multidrug resistant (MDR) pathogens, flavanones such as naringenin, eriodictyol, and taxifolin [8, 9], flavonoids such as quercetin, myricetin, kaempferol [10], eugenol [11], are some of the big quorum sensing inhibitors [12], and baicalin [13].

Most of the flavonoids exhibit inhibitory interest with quorum sensing. Cumarin, is a phenolic compound observed by using cinnamon, includes numerous naturally acquired compounds [14, 15]. *Dalbergia trichocarpa* bark [16], 6-gingerol, a stinky oil received from fresh ginger and rosmarinic acid, includes a new bioactive compound, oleonic aldehyde coumarate (OLAC), an effective quorum sensing inhibitor [17, 18].

The administration of flavonoids to the pathogen suppresses the production of virulence elements. A note on structure-interest courting is essential to inhibit LasR/RhlR and hydroxyl moieties present in flavone-a ring spine [19]. A few extracts exhibit fine end result quorum sensor inhibitor screening which includes extracts of cauliflower, celery salt, lawn cress, chervil, lemongrass, radish, thyme, and watercress. The aqueous extract of *Conocarpus erectus*, *Callistemon viminalis*, *Bucida buceras* inhibit the mortality of *C. elegans*. A few different essential oils together with cinnamon, lavender, and peppermint showed anti-quorum sensing hobby [20].

Studies show that some natural products' phytochemical extracts interfered with AHL pastime. Better inhibitory activity against the development of violacein mediated by AHL was expressed in raspberry, blueberry, and grape extracts. A number of herbs and spices expressed an effective reaction in reducing the inhibition of production of violacein mediated by the AHL concern. Basil, thyme, and brassica oleracea had the strongest pastime and decreased

formation of pigments, followed by rosemary, ginger, and turmeric with a decreased formation of violacein. Figure 2 shows numerous virulence factors in bacteria that include motility swarming for its quorum sensing gene expression, which is regulated. The extracts were also investigated for the inhibitory activity on quorum sensing [21].

Recent studies are carried out for the investigation of the aspect of food ecology quorum sensing. Signaling compounds are including autoinducers 1 and 2 existing in foods especially in milk, meat, and vegetables. Food matrices are of solid environment except liquid food. The food matrices are mostly of the solid environment with the exception of liquid foods that give rise to pathogens that get trapped and localized at high densities where there is increased growth rates and biofilm formation. The pathogenic activity and formation of biofilm are affected by the presence or growth of microbial species as well as the cell-cell interactions that occur in the solid food matrix, by determining the capability of a pathogen to produce quorum sensing. Various reports had suggested that the target to quorum sensing would be a novel strategy for the inhibition of biofilm infections [22]. On this controversy, researchers are increasingly investigating the herbal products for the novel therapeutic and antimicrobial agents that act as nontoxic inhibitors of quorum sensing by controlling infectious microbes that appear to resist the bacterial strains. In recent times it is assessed that 10% of terrestrial flowering plants of various communities are being used as therapeutic agents but only 1% have been recognized and validated [1].

3.1. Anti-Quorum Sensing. Thereby, phytochemicals are the richest reservoir that is available for therapeutics. The antimicrobial activity of some phytochemicals is not well known for its exact mechanism of antimicrobial functions.

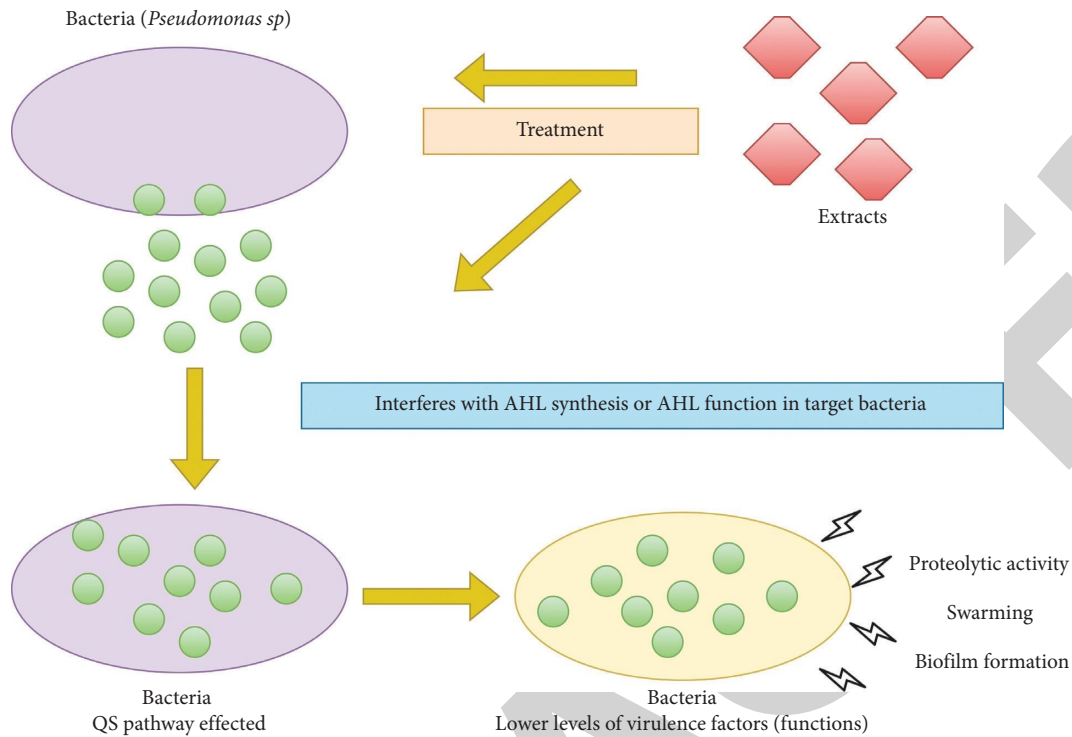


FIGURE 2: Representation of quorum sensing, modulates the pathogenic virulence on phytochemicals.

Various types of phytochemicals that inhibit quorum sensing such as polyphenols have the ability to affect the formation of biofilm in some pathogens [23].

Selectivity, virulence decrease, and lack of resistance to quorum sensing are all advantages of anti-quorum sensing drugs. The anti-quorum sensing activity of phytochemicals is not well defined and is found to contain antimicrobial efficacy that is mediated by quorum sensing inhibition. Most of the flora contribute to being the source for medicines and the development of pharmaceutical products. Quorum quenching molecules are also identified in plants are also being reported. Many plants have been established which are constricted symbiotic or syntrophic associations with pathogens. The phytochemical molecules or the extracts of various fruits, herbs, and spices are noted for their ability against quorum sensing. One of the best examples includes a eukaryotic organism such as Australian red alga *Delisea pulchra* [1], which produces metabolites interfering with bacterial communication known as halogenated furanones. These compounds show various biological activities such as the display of antifouling and antimicrobial properties. Some furanones particularly hinder the process of N-acylated l-homoserine lactone (AHL) regulation by the acceleration of degrading AHL receptor protein. The detection of phytochemicals against pathogens inhibits the regulation of quorum sensing of bacterial colonization and virulence factors provide an alternative for anti-infective agents [24].

The extracts of plants acted as quorum sensing inhibitors when there is a similarity in the chemical structure of AHL or quorum sensing signals or the capability of degradation of signal receptors (LuxR/LasR) [21]. Some plants produce GABA (γ -aminobutyric acid), which acts as the promotor

for which the N-acylated l-homoserine lactone (AHL) signal is degraded by lactonase in *A. tumefaciens*, thereby limiting the process of quorum sensing-infection. The extracts of *Curcuma longa* produce curcumin and act as the inhibitor for genes expressing virulence factors in *P. aeruginosa* PA01. Various diversities of apples and their derivative extracts like cider exhibit quorum sensing inhibiting activity which is probably it is due to the polyphenol present in hydroxycinnamic acids, rutin, and epicatechin that behave as anti-quorum sensing agents against *C. violaceum* in a synergistic manner [25, 26]. Anti-quorum sensing activities are reported for *L. nobilis*, *S. oleraceus*, *R. officinalis*, *T. capensis*, *J. sambac*, *P. alba*, and *P. nigra* extracts, which have the ability to decrease the production of violacein. Cinnamaldehyde and its derivatives contain an extensive quorum sensing regulation which includes the formation of biofilm and quorum sensing mediated by AI-2 in various other pathogens such as *P. aeruginosa* and *Vibrio* sp. Furocoumarins that are present in grapefruit inhibit those activities of autoinducers 1 and 2 in *V. harveyi* and also the formation of biofilm in some pathogenic organisms. Isolimonic acid and deacetyl nomilinic acid 17 β -D-glucopyranoside which are the limonoids, that are present in orange seeds may cause more than 90% inhibition of autoinducer 2 in *V. harveyi* at 100 $\mu\text{g/ml}$ concentration shows AI mediated bioluminescence [7].

The production of naringenin which is driven by the LasI and RhlI genes reduces the production of acyl homoserine lactones N-(3-oxododecanoyl)-l-homoserine lactone (3-oxo-C12-HSL) and N-butanoyl-l-homoserine lactone (C4-HSL). Flavan-3-ol catechin reduces the quorum sensing production that mediates virulence factors that include

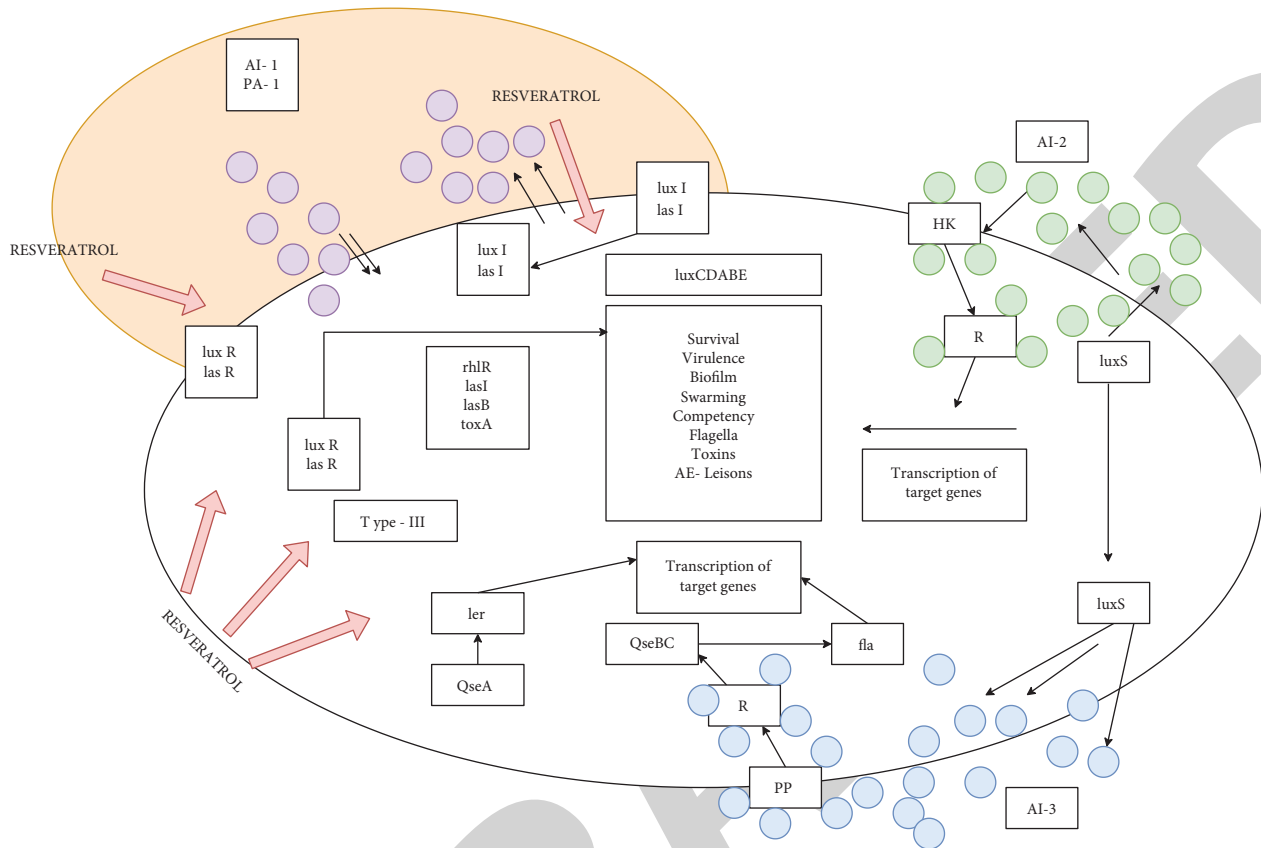


FIGURE 3: Representation of phytochemicals that inhibit quorum sensing.

pyocyanin, elastase, and also the formation of biofilm in *P. aeruginosa* PAO1 [27]. Varieties of legumes that include clover, peas, and yam beans are reported to have the ability of AHL degradation [28]. The roots of *Ocimum basilicum* commonly known as sweet basil which produce rosmarinic acid have the ability to disrupt the biofilm formed by *E. coli* [21]. AHL-lactonase enzyme expression is stimulated by salicylic acid which is a phenolic plant secondary metabolite. Ursolic acid at $10 \mu\text{g/ml}$ has the capability to reduce the formation of biofilm by 79% formed by *E. coli* and 57–95% in *V. harveyi* and *P. aeruginosa* PAO1. Quorum sensing associated gene expressions can be inhibited by the extracts of broccoli and its constituents which then downregulates the virulence attributes of *E. coli* O157 : H7 both in-vitro and in-vivo, vegetal like Brassicaceae possess the potential to get developed as an anti-infective agent. Some other extracts such as ethanol and ethyl acetate from *Hypericum conatum*, express quorum sensing inhibition activity on *C. violaceum* which limits the violacein production [29].

Polyphenol compounds that contain the moiety present in gallic acid which includes ellagic acid and tannic acid that are induced by several plant species acquiring the capability of specifically interfering AHL mediated signaling which in turn by blocking the communication of pathogens [23]. For example, ellagitannins which include punicalagin and ellagic acid which are abundant in pomegranates and berries exhibit in concentration that is higher than $300 \text{ mg}/100 \text{ g}$. The gut microbiota hydrolyses ellagitannins to ellagic acid which

are eventually metabolized to create urolithin-A and B, by which these metabolites are accumulated in the gut where predominant activities are performed. For example, Urolithin-A has the capability of regulating the bacterial growth in the intestines of rats before and after the induction of inflammation chemically. Both urolithin-A and urolithin-B also have the ability to inhibit the quorum sensing associated processes up to 40% and there could be a decrease in the levels of AHL that is initiated by Enteropathogen *Y. enterocolitica* up to 45%. Some examples include chestnut honey with high inhibitory activity on the other hand orange and rosemary honey was inefficient [1]. Truchado et al. hypothesized that one of the main factors that affect inhibition is that floral origin irrespective of its geographic location.

Many phytochemical extracts inhibit the quorum sensing activity by hindering the AHL activity by the competence with them for their structural similarity and also by the acceleration to degrade LuxR/LasR receptors of AHL inhibitors. It was experimentally reported that fruits, herbs, and spice extracts had a better quorum sensing inhibitory activity at sublethal concentrations. Although there are various inhibition processes carried out it was also observed that two different mechanisms in combination have the capability of phytochemicals to restrict the AHL activity and by regulating the synthesis of AHL by the pathogens [30]. The natural phytochemical extracts have the ability to regulate quorum sensing by the inhibition of signal

molecules that had never been indicated. Various extracts that act as quorum sensing inhibitors decreased the accumulation of two pathogenic bacteria PAO1 and *E. coli*. The results were reported on the ability of phytochemicals to regulate quorum sensing at multiple levels as shown in Figure 3 [21]. Many plant extracts have been described as effective alternatives to conventional pesticides, and their ingredients have been employed in food preservation due to their promising anti-QS action against a number of food pathogenic bacteria.

Also, it was found that phytochemical extract from *Camellia sinensis* significantly declined and the conjugative R plasmid in *E. coli* is transferred which is related to quorum sensing [31]. Therefore, phytochemicals have the ability to inhibit quorum sensing followed by its virulence factors and formation of biofilm in the pathogenic microorganisms revealed the strategy of antimicrobial chemotherapy. This method may lead to the novel identification of safe anti-pathogenic drug from the phytochemicals which has no risk of antibiotic resistance and contains low toxic levels.

Potential anti-quorum sensing properties are proved to be present in traditional medicinal plants against pathogens. Different phytochemical extracts, extracted from plants include flavonoids which are more potent in decreasing the effect of quorum sensing in various pathogens. Some extracts of plants that exhibit potential quorum sensing include *Cassia alata*, *Camellia nitidissima*, *Parkia javanica*, *Nepenthes alata*, *Brassica oleracea*, *Terminalia bellirica*, *Pistacia atlantica*, and *Laserpitium ochridanum*. The upcoming medicines prefer plant as its genesis, in which the phytochemical extracts are being explored further to flourish as an effective substitute to reduce the misconsumption and excessive use of antibiotics on the health of humans. Some phytochemicals such as essential oils obtained from cinnamon, norfloxacin, chrysin, and curcumin revealed the least MIC value [7].

4. Conclusion

The use of extracts from vegetative sources or pure compounds of plants for biocontrol approaches when in contrast with other conventional treatments express some advantages in particular comparatively. Certainly, such foods that are conventionally treated are regarded to be green and natural. Even though, there is no biocontrol approach that has the perspective of the issue entirely, such kinds of approaches altogether initiate a tool to act in a combined and compatible way through various implementations either applied individually or in combination. A better understanding of the phytochemical for the potential diffidence of quorum sensing is of eminent significance to research which aimed for the discovery and progression of new anti-quorum sensing phytochemicals that have the ability to prevent infectious human pathogens. Such antipathogenic compounds in contradiction to antibacterial compounds may not kill the bacteria or inhibit the entire growth and would likely prevent the resistant strain development. Eventually, in recent years, plant bioengineering, in particular, may influence the bacterial association; for example, quorum

sensing strategies suppress the influence of pathogenic microorganisms. Phytochemistry, with the use of inhibitors for various targets or quorum sensing activities, could be a major benefit in the confront against multiantibiotic bacterial diseases.

Data Availability

The data used to support the findings of this study are included in the article.

Conflicts of Interest

The authors declare that they have no conflicts of interest.

Acknowledgments

The authors thank to Madawalabu University, Oromiya Region, Ethiopia. The authors would like to thank the management of Sathyabama Institute of Science and Technology, Chennai for their constant support to this work.

References

- [1] F. Nazzaro, F. Fratianni, and R. Coppola, "Quorum sensing and phytochemicals," *International Journal of Molecular Sciences*, vol. 14, no. 6, pp. 12607–12619, 2013.
- [2] S. M. Alasil, R. Omar, S. Ismail, and M. Y. Yusof, "Inhibition of quorum sensing-controlled virulence factors and biofilm formation in *Pseudomonas aeruginosa* by culture extract from novel bacterial species of *Paenibacillus* using a rat model of chronic lung infection," *International journal of bacteriology*, vol. 2015, 2015.
- [3] K. Bacha, Y. Tariku, F. Gebreyesus et al., "Antimicrobial and anti-quorum sensing activities of selected medicinal plants of Ethiopia: implication for development of potent antimicrobial agents," *BMC Microbiology*, vol. 16, no. 1, pp. 139–9, 2016.
- [4] Q. Jiang, J. Chen, C. Yang, Y. Yin, and K. Yao, "Quorum sensing: a prospective therapeutic target for bacterial diseases," *BioMed Research International*, vol. 2019, Article ID 2015978, 15 pages, 2019.
- [5] J. Xie, A.-h. Zhang, H. Sun, X.-j. Yan, and X. J. Wang, "Recent advances and effective strategies in the discovery and applications of natural products," *RSC Advances*, vol. 8, no. 2, pp. 812–824, 2018.
- [6] A. Borges, P. Sousa, A. Gaspar, S. Vilar, F. Borges, and M. Simões, "Furvina inhibits the 3-oxo-C12-HSL-based quorum sensing system of *Pseudomonas aeruginosa* and QS-dependent phenotypes," *Biofouling*, vol. 33, no. 2, pp. 156–168, 2017.
- [7] M. I. A. El-Hamid, "A new promising target for plant extracts: inhibition of bacterial quorum sensing," *Journal of Molecular Biology and Biotechnology*, vol. 1, no. 1, pp. 1–3, 2016.
- [8] O. M. Vandeputte, M. Kiendrebeogo, T. Rasamiravaka et al., "The flavanone naringenin reduces the production of quorum sensing-controlled virulence factors in *Pseudomonas aeruginosa* PAO1," *Microbiology*, vol. 157, no. 8, pp. 2120–2132, 2011.
- [9] A. Omanakuttan, N. Pandurangan, V. S. Vargis, M. Maneesh, B. G. Nair, and G. B. Kumar, "Clove bud oil reduces kynurenine and inhibits pqs A gene expression in *P. aeruginosa*," *Applied Microbiology and Biotechnology*, vol. 100, no. 8, pp. 3681–3692, 2016.

Retraction

Retracted: Ternary Complexation Process for New Spectrophotometric Assay of Levodopa using Ni(II) and 2,3-Diaminopyridine

Advances in Materials Science and Engineering

Received 26 December 2023; Accepted 26 December 2023; Published 29 December 2023

Copyright © 2023 Advances in Materials Science and Engineering. This is an open access article distributed under the Creative Commons Attribution License, which permits unrestricted use, distribution, and reproduction in any medium, provided the original work is properly cited.

This article has been retracted by Hindawi, as publisher, following an investigation undertaken by the publisher [1]. This investigation has uncovered evidence of systematic manipulation of the publication and peer-review process. We cannot, therefore, vouch for the reliability or integrity of this article.

Please note that this notice is intended solely to alert readers that the peer-review process of this article has been compromised.

Wiley and Hindawi regret that the usual quality checks did not identify these issues before publication and have since put additional measures in place to safeguard research integrity.

We wish to credit our Research Integrity and Research Publishing teams and anonymous and named external researchers and research integrity experts for contributing to this investigation.

The corresponding author, as the representative of all authors, has been given the opportunity to register their agreement or disagreement to this retraction. We have kept a record of any response received.

References

- [1] F. Abdoon, M. J. Bichan, A. Mohamed Ibrahim, A. Mundher Tayyeh, M. Kishore, and A. Abdelhakeem Khalid, "Ternary Complexation Process for New Spectrophotometric Assay of Levodopa using Ni(II) and 2,3-Diaminopyridine," *Advances in Materials Science and Engineering*, vol. 2022, Article ID 4915162, 8 pages, 2022.

Research Article

Ternary Complexation Process for New Spectrophotometric Assay of Levodopa using Ni(II) and 2,3-Diaminopyridine

Fadam Abdoon , Mustafa J. Bichan, Abdelrahman Mohamed Ibrahim ,
Alnoman Mundher Tayyeh, Medikundu Kishore , and Azam Abdelhakeem Khalid 

¹Department of Chemistry, College of Science, Tikrit University, Tikrit, Iraq

²Ministry of Education, Diyala Education Directorate, Baqubah, Diyala, Iraq

³Accounting and Financial Management, School of Management Studies, University of Khartoum, Khartoum, Sudan

⁴Mangalore University, Department of Biology, Mangalore, India

⁵Department of Chemistry, SVRM (Aut) College, Acharya Nagarjuna University, Guntur, A.P, India

⁶Department of Accounting and Finance, Faculty of Management and Economics, Sultan Idris Education University, Tanjung Malim, Perak, Malaysia

Correspondence should be addressed to Abdelrahman Mohamed Ibrahim; amibrahim@uofk.edu

Received 15 December 2021; Revised 5 January 2022; Accepted 11 January 2022; Published 25 January 2022

Academic Editor: Palanivel Velmurugan

Copyright © 2022 Fadam Abdoon et al. This is an open access article distributed under the Creative Commons Attribution License, which permits unrestricted use, distribution, and reproduction in any medium, provided the original work is properly cited.

A novel, accurate, precise, inexpensive, and sensitive spectrophotometric approach is established to assay levodopa (LD) in both bulk drug and its pharmaceutical formulations. The method depends on the reaction of the ternary complex of a mixed-ligand type among LD, nickel(II) (Ni(II)), and 2,3-diaminopyridine (DAP) to form a stable complex of Ni-LD-DAP which is not extractable. The complex showed maximum absorption at 478 nm, with the apparent molar absorptivity of $4.93 \times 10^3 \text{ L}\cdot\text{mol}^{-1}\cdot\text{cm}^{-1}$ and Sandell's sensitivity of $0.04 \mu\text{g}\cdot\text{cm}^{-2}$. Beer's law is obeyed within the concentration range of $2\text{--}58 \mu\text{g}\cdot\text{mL}^{-1}$, and the regression line equation is as follows: $Y = 0.0251X + 0.0045$ ($R^2 = 0.9990$; $n = 5$). The detection limit and quantitation limit are found to be $0.1388 \mu\text{g}\cdot\text{mL}^{-1}$ and $0.4207 \mu\text{g}\cdot\text{mL}^{-1}$, respectively. The present study achieved reasonable accuracy (average recovery of 100.17%) and good precision (RSD did not exceed 1.71%). The developed method has been validated according to the current ICH guidelines (2013). The results of pure LD and pharmaceutical preparations using the recommended spectrophotometry are promising.

1. Introduction

Parkinson's disease (PD) is a neurodegenerative disorder of the extrapyramidal neuronal system, and the pathogenesis of the disease is due to deterioration of the cerebral dopaminergic pathways and the graduated degradation of dopamine (DA) in the black substance (substantia nigra). Mobility and control of the skeletal muscle system will be affected and major symptoms in people with PD are shown in the form of tremor, muscle stiffness, bradykinesia, and postural instability. Levodopa (L-3,4-dihydroxyphenylalanine, LD) (Figure 1) is a direct chemical precursor of DA and neurotransmitter modulator and is used as an effective drug

to treat PD, it penetrates the blood-brain barrier unlike DA, and it will metabolize as soon as it enters and undergoes a rapid decarboxylation by aromatic L-amino acid decarboxylase (AADC) to give DA [1–4].

However, not more than 1% of LD can be reached to the central nervous system because the metabolism of LD to DA by peripheral AADC will be outside the brain that releases amounts of DA in the circulatory system, which will exhibit undesirable side effects including vomiting, nausea, and hypotension, so it is necessitated that LD is combined with AADC inhibitors such as carbidopa, which reduces the effects of DA and increases the abundance of LD to the brain, hence increasing the kinetic benefit of the doses given of LD

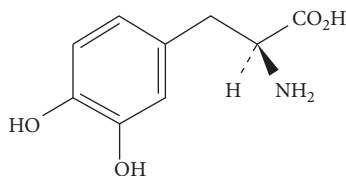


FIGURE 1: Chemical structure of levodopa.

[5–8]. Several methods such as HPLC, electrochemistry [9, 10], and spectrophotometry [11, 12] are used to determine LD, despite the diversity of techniques used in the determination, but there are many obstacles (Table 1), for example, the chromatography and techniques connected with it are of high cost in terms of materials and tools used, need to experience in the operation system, sample preparation, and specific conditions in separation, and on the other hand, electrochemical methods are quick to accomplish the analysis, but it displays some errors in the analysis unless it provides a special environment such as the need to clean or polish the electrodes. Therefore, spectroscopic methods were used for ease, speed, accuracy, and low cost [13–18].

The investigated study characterizes the color reaction of LD by utilizing a mixed-ligand complex formation in an aqueous media, where there is no need for solvents or surfactants for its extraction. In previous works, dyes were exploited in the ternary complexes for the spectrophotometric analytical field, such as drugs [19], metals [20], biological molecules [21], and surfactants [22]. With the current pharmaceutical compound, the reagent phenyl-fluorone [23–28] was previously used. But herein, 2,3-diaminopyridine (DAP) is used as a chelating ligand, and Ni(II) is represented as the central metal. We noticed no previous work that used the same method of determining the LD in our literature review.

2. Experimental

2.1. Apparatus. All spectrophotometric measurements were carried out by using a Shimadzu UV-Vis Spectrometer (Model UV-1800, Tokyo, Japan) double beam and E-Chrom Tech single beam (Taipei, Taiwan), and Balance Kern Abs 120-4N four-digit balance (North Lincolnshire, United Kingdom) was used.

2.2. Reagents. All chemicals and reagents used were of analytical grade and the deionized water was used to guarantee the absence of foreign ions. The pure LD compound was kindly donated by Pioneer Pharmaceutical (Iraq-Sulaymaniyah). A solution ($1000 \mu\text{g}\cdot\text{mL}^{-1}$, $4.21 \times 10^{-3} \text{mol}\cdot\text{L}^{-1}$) of Ni(II) chloride hexahydrate (BDH, Pool, UK) and a solution ($0.1 \text{mol}\cdot\text{L}^{-1}$) of DAP (Merck, Darmstadt, Germany) were prepared. Approximate concentrations ($0.1 \text{mol}\cdot\text{L}^{-1}$) for both NaOH (BDH, Pool, UK) and HCl (37%) (Fluka, Switzerland) were also prepared. Pharmaceutical tablet Dopal Forte® labeled 100 mg of LD per tablet (Ibn Hayyan Pharmaceuticals, Syria) was purchased from local drug stores.

2.3. Preparation of Analytical Solutions

2.3.1. Standard Solution of Levodopa. A stock solution ($100 \mu\text{g}\cdot\text{mL}^{-1}$, $5.05 \times 10^{-4} \text{mol}\cdot\text{L}^{-1}$) of LD standard was prepared by dissolving 10 mg of pure LD powder in 100 mL of deionized water.

2.3.2. Preparation of Tablet Solution. Ten tablets were weighed and finely pulverized, and then a quantity equivalent to 10 mg was dissolved for preparing a solution of $100 \mu\text{g}\cdot\text{mL}^{-1}$ in a 100 mL volumetric flask and then made up to mark with water. The obtained solution was filtered and then further diluted according to its linearity range.

2.4. General Procedure for Levodopa Analysis

2.4.1. Calibration Curve. The color reaction is based on the chelation of both LD and DAP with Ni(II), aliquots of stock solution ($100 \mu\text{g}\cdot\text{mL}^{-1}$) measured accurately were transferred ($0.5\text{--}14.5 \text{mL}$ of $100 \mu\text{g}\cdot\text{mL}^{-1}$) into separate 25 mL volumetric flasks so that the final concentrations were in the range $2\text{--}58 \mu\text{g}\cdot\text{mL}^{-1}$ of LD, and then, 1.0 mL of Ni(II) solution was added to each flask followed by 1.2 mL of DAP solution; the contents of each flask were shaken thoroughly, each mixture was diluted to 25 mL with water and placed in a water bath for 30 min at 65 C and then immediately cooled under the tap to room temperature, and the resultant absorbance of the colored complex was determined at 478 nm against a reagent blank prepared similarly without the addition of the analyzed drug.

2.4.2. Procedure for Determination of the Levodopa in Pharmaceutical Tablet. Aliquots of drug solution equivalent to $2\text{--}58 \mu\text{g}\cdot\text{mL}^{-1}$ were transferred into a 25 mL volumetric flask and the assay was applied using the same procedure described above.

3. Results and Discussion

3.1. Optimization of Analytical Conditions. Various experimental parameters affecting the absorbance intensity were optimized (Figure 2) by changing each parameter while keeping all others constant. And the constant amount of LD, 2.5 mL of stock solution ($100 \mu\text{g}\cdot\text{mL}^{-1}$), was transferred into a 25 mL volumetric flask (to become $10 \mu\text{g}\cdot\text{mL}^{-1}$ as final concentration), and then, the absorbance was measured at 478 nm.

TABLE 1: Comparative analytical results of the proposed approach with various previously described methods for determining levodopa.

Method of analysis	Principle	Linearity	Limitation
Spectrophotometry	The method was based on the reaction of levodopa with vanadium(V) which was reduced to vanadium(IV) and the formed complex with eriochrome cyanine R to give the product has λ_{\max} at 565 nm [11].	0.028–0.84 $\mu\text{g}\cdot\text{mL}^{-1}$	Nonselective among catecholamines
	The method was based on the reaction of alizarin red with the primary amino group present in the levodopa in basic medium; a purple color product has λ_{\max} at 588 nm [12].	10–60 $\mu\text{g}\cdot\text{mL}^{-1}$	Also, nonselective among catecholamines
HPLC coupled with chemiluminescence	The method depends on the improved chemiluminescence (CL) signal of the online gold particle-catalyzed luminol- H_2O_2 system by levodopa, and the HPLC-CL detection system consists of an HPLC system and a CL detection system. The sample separation was achieved on an ODS column at 40°C with gradient elution at a flow rate of 1.0 $\text{mL}\cdot\text{min}^{-1}$. The mobile phase was composed of a mixture of methanol and 0.2% aqueous phosphoric acid (5:95, V/V) [7].	10–1000 $\text{ng}\cdot\text{mL}^{-1}$	Expensive method
HPLC coupled with mass spectrometry	Separation is achieved on a C_8 column set at 30°C, with a mobile phase consisting of a gradient of water and acetonitrile: methanol (90:10 v/v), both containing 0.1% formic acid, eluted at 700 $\mu\text{L}\cdot\text{min}^{-1}$ [8].	20–1000 $\text{ng}\cdot\text{mL}^{-1}$	Expensive method
Voltammetry	This electrochemical method is based on chloranil(CA) modified carbon paste electrode (CAMCPE) in the voltammetric determination of levodopa in an aqueous solution [9].	3–500 $\mu\text{mol}\cdot\text{L}^{-1}$	Lack of reproducibility because the electrochemical activity of CAMCPE decreased during successive scans due to the removal of the mediator by dissolving it into an aqueous solution, so the surface of the electrode must be renewed before each determination
	This method is based on adsorption stripping voltammetry by using a multiwalled carbon nanotubes-Nafion modified glassy carbon electrode [10].	3.5×10^{-7} - 1.5×10^{-5} $\text{mol}\cdot\text{L}^{-1}$	Some cations may have effect on the analysis of levodopa because they interact with anion sites SO_3^- in the Nafion film, which will reduce the signal of levodopa, so it needs certain conditions to get rid of this interfering as in Fe(III) which needs to add 1.0×10^{-3} $\text{mol}\cdot\text{L}^{-1}$ oxalic acid to eliminate it

3.1.1. *Effect of First Ligand Amount (Ni(II)).* Different amounts of 4.21×10^{-3} $\text{mol}\cdot\text{L}^{-1}$ Ni(II) solution in the range of 0.2–2.0 mL were added to a fixed mixture for 10 $\mu\text{g}\cdot\text{mL}^{-1}$ of LD and 1.0 mL of 0.1 $\text{mol}\cdot\text{L}^{-1}$ of DAP solution to predict the effect of Ni(II) amount on the absorbance. It was noted that 1.0 mL of 4.21×10^{-3} $\text{mol}\cdot\text{L}^{-1}$ of Ni(II) was used to produce a maximum absorbance, and this volume was chosen as the optimum value to examine other variables (Figure 3).

3.1.2. *Effect of Second Ligand Amount (DAP).* After the optimum quantity of the central metal was selected, the effect of the second ligand (DAP) was investigated. Different amounts of 0.1 $\text{mol}\cdot\text{L}^{-1}$ DAP solution in the range of 0.2–2.0 mL were added to the previous order (10 $\mu\text{g}\cdot\text{mL}^{-1}$ of LD + 1.0 mL of 4.21×10^{-3} $\text{mol}\cdot\text{L}^{-1}$ of Ni(II)). It was noted

that 1.2 mL of 0.1 $\text{mol}\cdot\text{L}^{-1}$ of DAP was used to produce a maximum absorbance, and this volume was chosen as the optimum value to check other variables (Figure 4).

3.1.3. *Effect of Order of Addition.* All sequence addition of reactants were studied to determine the order with the highest absorption, where it was at LD + Ni(II) + DAP (order III) as shown in (Table 2).

3.1.4. *Effect of pH.* A simple increase of acid or base into the solution makes the color of the solution disappear or turbid, and this negatively affects the shape and absorption of the ternary complex, so throughout all the experiments, the addition of acid or base to the solution was excluded.

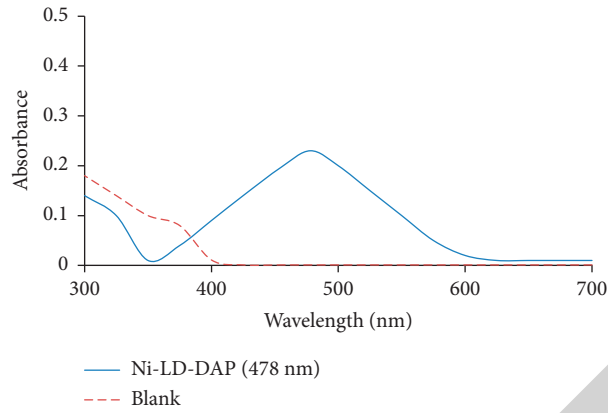


FIGURE 2: Absorption spectrum at 487 nm of LD using the suggested procedure.

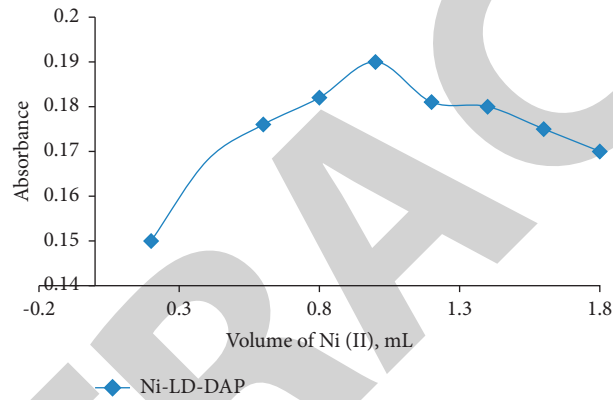


FIGURE 3: Effect of Ni(II) volume on the maximum absorbance signal of LD.

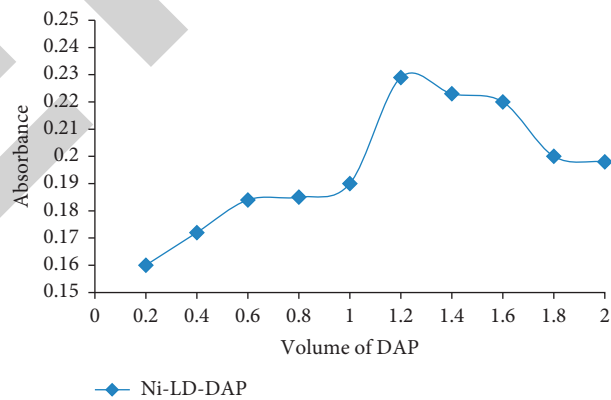


FIGURE 4: Effect of DAP volume on the maximum absorbance signal of LD.

TABLE 2: Order of addition.

Order number	Order of addition	Absorbance
I	LD + DAP + Ni(II)	0.187
II	DAP + Ni(II) + LD	0.193
III	LD + Ni(II) + DAP	0.231

3.1.5. Effect of Temperature. The effect of temperature on the absorption of the solution was studied and it has been observed that increasing the heat increases the absorption of the solution, as shown in Figure 5.

3.1.6. Effect of Reaction Time. The color of the complex does not settle immediately but continues to increase its intensity until the end of the reaction, and the process takes more than 80 minutes (Figure 6). Therefore, time and temperature variables were taken into consideration to facilitate the recording of absorbance value. A mixture was heated at 55, 60, 65, and 70 C for 20–50 min where it was observed that the greatest and most stable absorbance was at 65 C for 30 minutes, and the color of the solution remained stable for the next day after cooling.

3.2. Validity of the Method. The validity of the analytical method has been verified according to the ICH guidelines [24], with relating to the accuracy, precision, and others as follows.

3.2.1. Linearity Range. The calibration curve was drawn (Figure 7) using the optimum conditions mentioned above, and the linearity of the proposed method was evaluated by measuring the absorbance of fifteen concentrations covering the range $2\text{--}58\ \mu\text{g}\cdot\text{mL}^{-1}$.

The analytical parameters for the determination of LD were collected statistically (Table 3), the regression equation was $A = 0.0251^\circ\text{C} + 0.0045$ ($n = 5$; $R^2 = 0.9990$). The mean recovery percentage of twelve LD standard solutions within the range of $14\text{--}58\ \mu\text{g}\cdot\text{mL}^{-1}$ was calculated for the proposed spectrophotometric method to ensure accuracy. Each solution was measured for three replicates (Table 4).

3.2.2. Limit of Detection (LOD) and Limit of Quantitation (LOQ). The proposed spectroscopic system displayed high sensitivity to the studied analyte with LOD ($3.3\sigma/s$) and LOQ ($10\sigma/s$) of 0.1388 and $0.4207\ \mu\text{g}\cdot\text{mL}^{-1}$, respectively. The obtained analytical data revealed high sensitivity for the determination of LD using a ternary complexation procedure with Ni(II) and DAP.

3.2.3. Precision and Accuracy. The accuracy of the recommended spectrophotometric method was evaluated by calculating the average recovery (%) of nine LD solutions in the range of 2 to $58\ \mu\text{g}\cdot\text{mL}^{-1}$. The final result is $99.6 \pm 0.4\%$, which shows that the accuracy of the proposed method is very high (Table 4). In addition, to study the precision of the proposed method, intraday precision and interday precision were applied, and three different concentrations of LD were determined in pure form through three consecutive occasions or repeated analyses over three consecutive days (Table 5). The estimated RSD percentage is between 0.2 and 0.7% in the interday test and between 0.2 and 0.8% in the

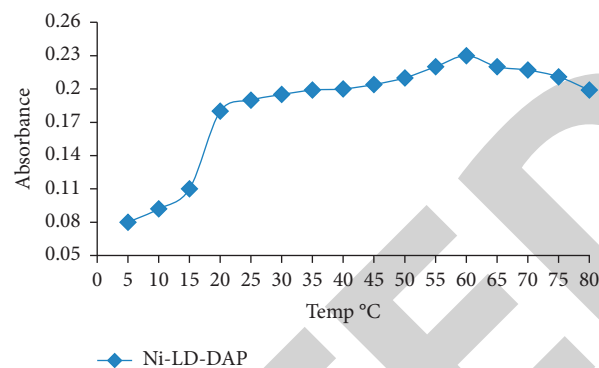


FIGURE 5: Effect of temperature for the maximum absorbance signal on the determination of LD.

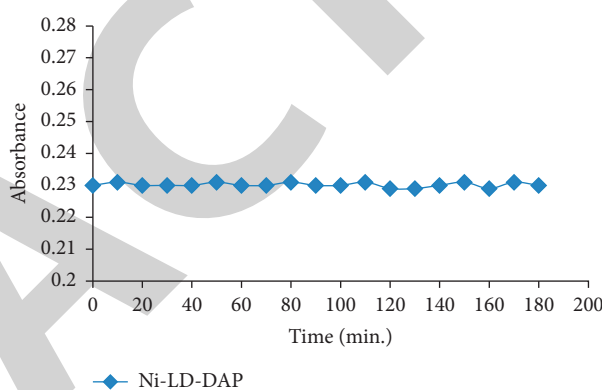


FIGURE 6: Effect of time per min on the maximum absorbance signal of LD.

intraday test, which indicates that the proposed method has good accuracy in the determination of LD.

3.2.4. Selectivity. The selectivity of the suggested method against the assay of LD was measured by the determination of LD in the presence of some possible interfering substances. Among these, cations, anions, and other additive substances are K^+ , Na^+ , Mg^{2+} , Ca^{2+} , and $\text{SO}_4^{=}$, glucose, starch, lactose, citric acid, and magnesium stearate. Under optimal conditions, the detection of $10\ \mu\text{g}\cdot\text{mL}^{-1}$ LD in the presence of $1.0\ \mu\text{g}\cdot\text{mL}^{-1}$ of each interfering substance was studied using the recommended method. Table 6 shows that no significant interference was found. Therefore, the recommended procedure can be considered as an alternative method to determine LD.

3.2.5. Reaction's Stoichiometry. The reaction ratio of LD with Ni(II) and DAP was measured using the method of continuous variations (Job's method). Several equimolar ($5 \times 10^{-3}\ \text{mol}\cdot\text{L}^{-1}$) solutions, including varying quantities of LD ($0.1\text{--}0.9\ \text{mL}$) and the DAP reagent ($0.9\text{--}0.1\ \text{mL}$) in volumetric flasks of $10\ \text{mL}$, are utilized in this technique. The extra solutions are added according to the optimum working procedure, and the absorbance is measured at $478\ \text{nm}$

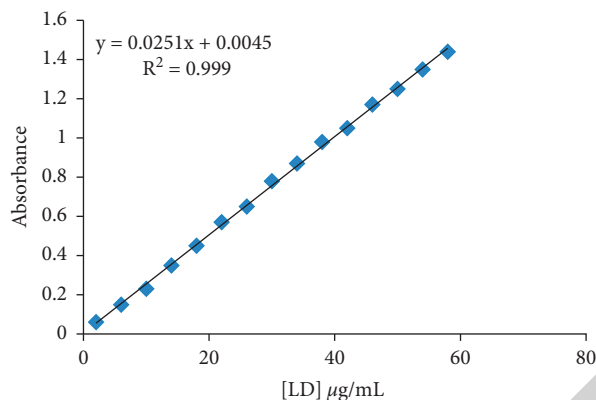


FIGURE 7: Calibration graph of LD determination using the proposed procedure.

TABLE 3: Analytical parameters for the determination of LD (Ni-LD-DAP).

Parameter	Values
Linearity, $\mu\text{g}\cdot\text{mL}^{-1}$	2–58
Calibration curve equation	$A = 0.0251^{\circ}\text{C} + 0.0045$
Slope	0.0251
Intercept	0.0045
Correlation coefficient, R	0.9995
Molar absorptivity, $\text{L}\cdot\text{mol}^{-1}\cdot\text{cm}^{-1}$	4.93×10^3
Sandell's sensitivity, $\mu\text{g}\cdot\text{cm}^{-2}$	0.04
LOD, $\mu\text{g}\cdot\text{mL}^{-1}$	0.1388
LOQ, $\mu\text{g}\cdot\text{mL}^{-1}$	0.4207
RSD, %	1.71
Accuracy (rec% \pm SD)	100.17 ± 1.71

TABLE 4: Analytical parameters for the determination of LD.

Sample	Taken, $\mu\text{g}\cdot\text{mL}^{-1}$	Found, $\mu\text{g}\cdot\text{mL}^{-1}$	% recovery
1	14	13.76	98.29
2	18	17.75	98.61
3	22	22.53	102.41
4	26	25.72	98.92
5	30	30.89	102.97
6	34	34.48	101.41
7	38	38.86	102.26
8	42	41.65	99.17
9	46	46.43	100.93
10	50	49.62	99.24
11	54	53.61	99.28
12	58	57.19	98.6
Mean \pm SD		$100.17 \pm 1.71\%$	
n		12	
Variance		2.91	
SE%		0.17	
%RSD		1.71	

TABLE 5: Evaluation of the proposed method using intraday and interday assay.

Sample	LD determination using the proposed method			% RSD
	Taken, $\mu\text{g}\cdot\text{mL}^{-1}$	Found, $\mu\text{g}\cdot\text{mL}^{-1}$	% recovery \pm SD, ($n = 3$)	
Intraday assay	81218	8.0111.9318.09	$100.13 \pm 0.899.42 \pm 0.3100.50 \pm 0.6$	0.80.30.2
Interday assay	81218	7.9611.9517.93	$99.50 \pm 0.799.58 \pm 0.299.61 \pm 0.3$	0.7
				0.2
				0.3

TABLE 6: Tolerable limits of $10 \mu\text{g}\cdot\text{mL}^{-1}$ LD using the proposed procedure.

Interferences	Tolerable values
Glucose, lactose, starch	280
Zn^{2+} , Mg^{2+} , Ca^{2+} , Na^+ , and K^+	850
Citric acid, magnesium stearate	160

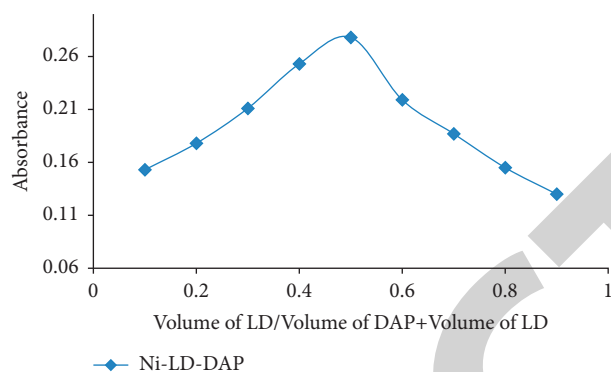


FIGURE 8: Stoichiometry of the reaction of the proposed method of LD determination using the ternary complexation procedure.

TABLE 7: Analytical results of LD in pure form and pharmaceutical preparations determined by spectrophotometry using the ternary complexation procedure.

Sample	Taken, $\mu\text{g}\cdot\text{mL}^{-1}$	Found, $\mu\text{g}\cdot\text{mL}^{-1}$	% recovery \pm SD, ($n = 6$)	% SE	Present method	t -test	F-test
Pure drug	51015	4.9210.0214.84	$99.4 \pm 0.6100.2 \pm 0.78.9 \pm 0.3$	0.240.290.12	100.01 ± 0.7	$1.78(2.228)^*$	$3.01(5.05)^*$
Tablets	51015	4.919.9714.95	$98.2 \pm 0.399.7 \pm 0.499.7 \pm 0.9$	0.120.160.37	$SE = 0.29$ $n = 6$	$1.91(2.228)^*$	$2.18(5.05)^*$

*Figures in parentheses are the tabulated values of t -test and F-test at 95% confidence limit.

against a blank. The ratio of the LD to the DAP is 1 : 1, as illustrated in Figure 8.

3.3. Analytical Application. The developed spectrophotometric approach was used for the assay of LD in the drug substance, with a recovery average of 100.01 ± 0.7 . In addition, an established approach was used to estimate the LD of its drug form. The data obtained (Table 7) were statistically evaluated and then compared with the data obtained in another previously published spectrophotometric article [25].

4. Conclusion

The present study introduced a low-cost, accurate, and precise spectrophotometric method based on a ternary complexation procedure to determine LD using Ni(II) and DAP as first and second ligands. The proposed method provided promising results for the assay of LD in its bulk drug and pharmaceutical formulations. The developed method exhibited a linear relationship over a concentration range of $2\text{--}58 \mu\text{g}\cdot\text{mL}^{-1}$. Also, the acquired results indicated that the present procedure is simpler and more flexible to determine LD without significant interference from other coformulated species or possible interfering compounds.

Data Availability

The data underlying the results presented in the study are available within the manuscript.

Conflicts of Interest

The authors declare that they have no conflicts of interest regarding the publication of this study.

Acknowledgments

The authors express their gratitude and thanks to the Department of Chemistry, College of Science, Tikrit University, Iraq, for using their equipment and facilities.

References

- [1] M. Karimi, J. L. Carl, S. Loftin, and J. S. Perlmutter, "Modified high-performance liquid chromatography with electrochemical detection method for plasma measurement of levodopa, 3-O-methyldopa, dopamine, carbidopa and 3,4-dihydroxyphenyl acetic acid," *Journal of chromatography. B, Analytical technologies in the biomedical and life sciences*, vol. 836, no. 1-2, pp. 120-123, 2006.
- [2] T. H. Kim, K. H. Cho, W. S. Jung, and M. S. Lee, "Herbal medicines for Parkinson's disease: a systematic review of randomized controlled trials," *PLoS One*, vol. 7, no. 5, Article ID e35695, 2012.

Retraction

Retracted: Enhancement Modelling Based on Electrical Discharge Machining Successive Discharges

Advances in Materials Science and Engineering

Received 26 December 2023; Accepted 26 December 2023; Published 29 December 2023

Copyright © 2023 Advances in Materials Science and Engineering. This is an open access article distributed under the Creative Commons Attribution License, which permits unrestricted use, distribution, and reproduction in any medium, provided the original work is properly cited.

This article has been retracted by Hindawi, as publisher, following an investigation undertaken by the publisher [1]. This investigation has uncovered evidence of systematic manipulation of the publication and peer-review process. We cannot, therefore, vouch for the reliability or integrity of this article.

Please note that this notice is intended solely to alert readers that the peer-review process of this article has been compromised.

Wiley and Hindawi regret that the usual quality checks did not identify these issues before publication and have since put additional measures in place to safeguard research integrity.

We wish to credit our Research Integrity and Research Publishing teams and anonymous and named external researchers and research integrity experts for contributing to this investigation.

The corresponding author, as the representative of all authors, has been given the opportunity to register their agreement or disagreement to this retraction. We have kept a record of any response received.

References

- [1] F. N. Abed, V. Ramesh, M. Fadhil Jwaid, N. Agarwal, D. Koundal, and A. Mohamed Ibrahim, "Enhancement Modelling Based on Electrical Discharge Machining Successive Discharges," *Advances in Materials Science and Engineering*, vol. 2022, Article ID 8017375, 7 pages, 2022.

Research Article

Enhancement Modelling Based on Electrical Discharge Machining Successive Discharges

Farook Nehad Abed ¹, **V. Ramesh** ², **Mohanad Fadhil Jwaid**,³ **Nidhi Agarwal**,⁴
Deepika Koundal,⁵ and **Abdelrahman Mohamed Ibrahim** ⁶

¹Faculty of Mechanical, Manufacturing Engineering, Imamaladham University College, Baghdad, Iraq

²Research Department of Mathematics, Kandaswami Kandari's College, Velur, Namakkal, Tamilnadu, India

³Al-Imam University College, Riyadh, Saudi Arabia

⁴Department of Information Technology, KIET Group of Institutions, Delhi-NCR, Ghaziabad, India

⁵Department of Systemics, University of Petroleum & Energy Studies, Dehradun, India

⁶Accounting and Financial Management School of Management Studies, University of Khartoum, Khartoum, Sudan

Correspondence should be addressed to Abdelrahman Mohamed Ibrahim; amibrahim@uofk.edu

Received 11 December 2021; Revised 28 December 2021; Accepted 4 January 2022; Published 15 January 2022

Academic Editor: Palanivel Velmurugan

Copyright © 2022 Farook Nehad Abed et al. This is an open access article distributed under the Creative Commons Attribution License, which permits unrestricted use, distribution, and reproduction in any medium, provided the original work is properly cited.

The surface roughness of Inconel 718 is predicted using a sequential discharge model for electrical discharge machining (EDM). To begin with, the EDM single pulse discharge machining process was accurately simulated using the finite-element method (FEM). The surface topography under various discharge settings, the size, and the characteristic parameters of a single-pulse crater are simulated. Second, the material defines the discharge position as the minimum gap width between the work piece's starting surface and the electrode in the removal model. The simulation shows that the magnitude of the single-pulse discharge energy influences the crater's form and size. A difference in discharge energy causes a divergence in the increasing crater radius, depth, and flanging height trends. On the other hand, the ultimate surface morphology of an EDM machined surface is determined by the distribution of discharge locations around the parts in the workpiece; finally, machined surfaces are inspected using the same discharge parameters. The EDM work piece's surface morphology matches the material removal. Between simulation and experiment, there is a relative error in surface roughness around 8.26%, and there is a relative error in surface roughness.

1. Introduction

EDM uses the instantaneous local high temperature generated by the pulse. Cast iron material has the characteristics of spark discharge between the workpiece and the high strength, wear resistance, and heat resistance. Electrode wire to melt and vaporize in all cast iron materials uses Inconel 718 (grey cast workpiece material, to achieve the purpose of iron) because of its corrosion resistance and shock removal. Compared with the absorption and excellent casting performance of traditional machining, EDM makes use of other characteristics often used in the electrode wire to keep a certain distance from the manufacture of machine tool bed and column workpiece, and it can achieve high-precision machining [1].

When machining cast iron materials by EDM, not only the surface deformation of the workpiece is small but also there is almost no environmental pollution in the whole machining process. These characteristics make EDM suitable for machining Inconel 718 materials [2]. However, due to the randomness and disorder in the EDM process, the surface roughness of processed materials often cannot reach the predetermined standard, and instruments and equipment cannot directly observe the processing of materials in the process of machining, so the surface roughness of processed materials cannot be accurately controlled. In the EDM process, discharge parameters play an important role in surface roughness, and many researchers control surface roughness by optimizing discharge parameters [3, 4]. The Taguchi

method is commonly used to improve the EDM process, and the best parameters can all be found through experimentation through statistical analysis. [5] conducted primary research on EDM from mechanical and electrical principles and provided fundamental insights on EDM processing. [6] studied the effects of WDEM process parameters such as the cutting radius of a workpiece, water flow, and the wire feed rate on the surface roughness of alumina particle-reinforced materials and optimized the process parameters. Chaudhary et al. [7] used the heat transfer search algorithm to conduct multiresponse optimization of process parameters for EDM machining of superelastic Ni-Ti-N shape memory alloy. At present, based on the principle of EDM, the establishment of a material removal model based on successive discharges is always considered to be a challenging job. Furthermore, there have been very few studies on the modeling of surface roughness caused by the EDM process. Various extensive mathematic models and simulation methodologies have been devised to model EDM processes. In an EDM procedure, Tao and Ni et al. [8] developed a model to mimic discharge crater formation by considering the effect of bubble pressures to obtain very good crater geometry. [3] simulated the formation of craters in EDM using the molecular dynamics method while taking into account the pressure of the medium between the electrodes. The rate of material removal is found to be faster when the medium pressure is higher. In studying final surface morphology formation, the establishment of a single-pulse discharge crater model in EDM is critical formation [9]. The EDM process, in which the workpiece surface is built by the superposition of craters formed by numerous discharges, cannot be explained by the production of a single crater [10]. [11] have carried out a numerical analysis using the finite difference method. They were able to predict the material removal rate and surface roughness with a 6 percent margin of error using inverted identification. [2, 12–19] established a surface topography prediction model under EDM continuous discharge based on FEM, and Ra simulation results were consistent with experimental results. [20–24] established a model based on 3D continuous discharge to study the relationship between workpiece surface topography and electrode wire vibration. Results: in the SV-MF composite-assisted EDM process, the surface roughness of the workpiece decreases by more than 10%, and the uniformity of the discharge position distribution is improved. Experiments back up the numerical model, and also, the simulated error for surface roughness is a little less than 5%.

A 3D material removal system is proposed in this study to simulate the removal of materials. Successive discharges machining process of EDM: the relationship between single-pulse crater morphology, discharge position, and dynamic surface morphology is established. Meanwhile, the effects of the molten vaporization of the processed material and the residual heat generated by a single spark are considered for simulation. The impact of different discharge energies in singular pulse discharge models is created by studying the

impact crater's surface form and size. Minimum gap width determines discharge position, rather than assuming a random distribution of discharge position, which is more consistent with the actual EDM machining process. Several profile lines were extracted from the 3D material removal model, and the characteristic parameters were determined through averaging to predict the surface roughness. This study used pulse width and peak current as input parameters, and surface roughness was used as the output parameter. Experiments verified the accuracy of the continuous discharge material removal model in predicting surface roughness.

2. Experimental Details

The continuous discharge material removal model was verified on the EDM (CHMER EDM) machine. The dielectric was emulsion, and the electrode was 20 mm. Figure 1 shows the experimental setup. The workpiece material is Inconel 718, and the dimensions of the specimens were $10 \times 10 \times 5$ mm. The percentage of chemical composition properties of the workpiece material is given in Table 1. Pulse width (T_{on} μ s) and peak current (I_p A) were used as independent input parameters, and surface roughness (R_a μ m) was used as output parameters. The levels of the independent parameters are shown in Table 2. The other parameters, 120 V open-circuit voltage, 1 : 3 interval ratio, 4 m/min, 5 kg/cm² dielectric flushing pressure, and 9 kg wire tension, were kept constant during the experiments.

As a first step, the surface roughness of each machined material was unified by grinding, and the original surface roughness of each machined material was controlled between 1.3 μ m and 1.5 μ m. Secondly, in the normal machining process of EDM, the discharge is continuous, and the crater is superimposed on each other, so it is almost impossible to study every single-pulse discharge crater. Therefore, to conform to the assumed conditions of the material removal model as much as possible and at the same time, to obtain a single crater, another series of experiments were designed with apparent surface morphology on the continuous electric discharge machining surface. An often overlooked but important idea is to find the distance between the molybdenum wire and the workpiece at which the spark discharge occurs in the first contact. The motion distance of the molybdenum wire can be detected by using the coordinate motion system of the EDM machine (CHMER EDM) machine. The experimental steps are shown in Figure 1. Firstly, the initial gap between the continuous discharge material removal model was verified on the EDM machine (CHMER EDM). The dielectric was emulsion, and the electrode wire was 0.18 mm molybdenum wire. Figure 1 shows the experimental setup. The workpiece material is Inconel 718, and the dimensions of the specimens were $10 \times 10 \times 5$ mm. The percentage of chemical composition properties of the workpiece material is given in Table 1. Pulse width (T_{on} μ s) and peak current (I_p A) were used as independent input parameters, and surface roughness (R_a μ m) was used as the output parameter. The levels of the independent parameters are shown in Table 3. During the



FIGURE 1: EDM machine (CHMER EDM).

TABLE 1: Chemical composition properties of Inconel 718.

Chemical composition (%)	Ni	Fe	C	Al	Ti	Si	Mn	P	S
	50	Balance	0.08	0.20	0.65	0.35	0.35	0.015	0.18

TABLE 2: Factors and levels for the experiment.

No.	1	2	3	4	5	6	7	8	9
Peak current (A)	10	10	10	14	14	14	18	18	18
Pulse width (μ s)	14	14	14	26	26	26	34	34	34

TABLE 3: Comparison of surface roughness values.

No.	Experimental Ra (μ m)	Model Ra (μ m)	Error (%)
1	4.22	3.78	5.29
2	4.34	3.89	2.27
3	4.54	3.78	2.35
4	6.33	5.87	7.53
5	6.89	6.22	7.9
6	9.12	8.89	5.18
7	10.45	9.66	9.77
8	11.76	10.87	7.86
9	12.45	11.34	15.16

experiments, the other parameters, 120 V open-circuit voltage, 1:3 interval ratio, 4 m/min, 5 kg/cm² dielectric flushing pressure, 9 kg wire tension, and 0.18 mm wire diameter, were kept constant.

As a first step, the surface roughness of each machined material was unified by grinding, and the original surface roughness of each machined material was controlled between 1.3 μ m and 1.5 μ m. Secondly, in the normal machining process of EDM, the discharge is continuous, and the crater is superimposed on each other, so it is almost impossible to study every single pulse discharge crater. Therefore, to conform to the assumed conditions of the material removal model as much as possible and at the same time, to obtain a single crater, another series of experiments were designed with apparent surface morphology on the

continuous electric discharge machining surface. An often overlooked but important idea is to find the distance between the molybdenum wire and the workpiece at which the spark discharge occurs in the first contact. The motion distance of the copper tool can be detected by using the coordinate motion system of the EDM machine (CHMER EDM). The experimental steps are shown in Figure 1. Firstly, the initial gap between the copper tool and the workpiece is controlled at 1 mm, and then, the discharge machining of the material surface is carried out. Finally, the discharge parameters were adjusted by the EDM operating panel. The comparative experiments of nine groups were carried out, and workpieces are controlled at 1 mm, and then, the discharge machining of the material surface is carried out. Finally, the discharge parameters were adjusted by the EDM operating panel, and the comparative experiments of nine groups were carried out.

White light scanning interferometry: To acquire the average roughness and three-dimensional shape image of the material machined surface, we installed the sample on the noncontact preview W1 optical 3D surface profiler. Images of 489.5 μ m \times 489.5 μ m area were acquired accordingly. Surface composition measurement: to measure the composition of the material surface after EDM, the machined surface was sampled and measured by X-ray diffraction (XRD).

3. Experimental Results and Discussion

Each experimental material's final surface morphology and crater morphology were analyzed using three-dimensional morphological images. Figure 2 shows a crater's surface topography and size metrics. It is found that the radius of the

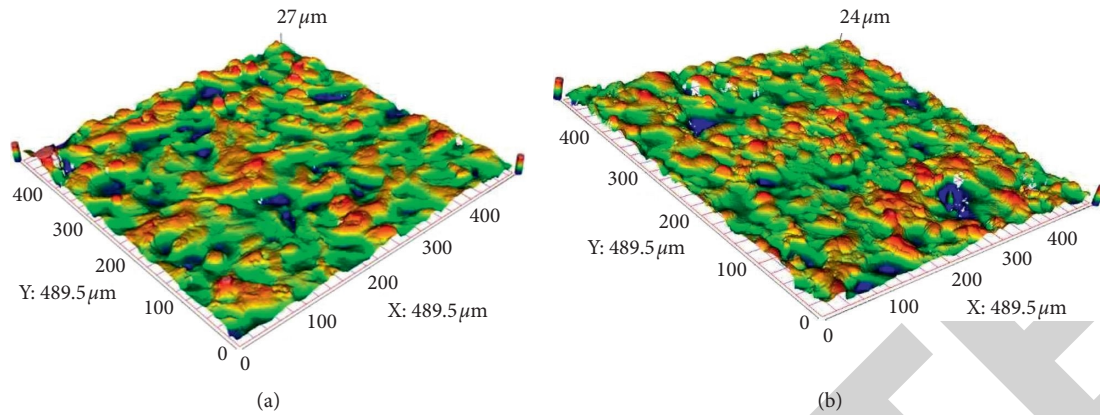


FIGURE 2: Surface topography of EDM continuous discharge: 3D view and crater shape and dimensions ($I_p = 10$ A, $T_{on} = 14$ μ s).

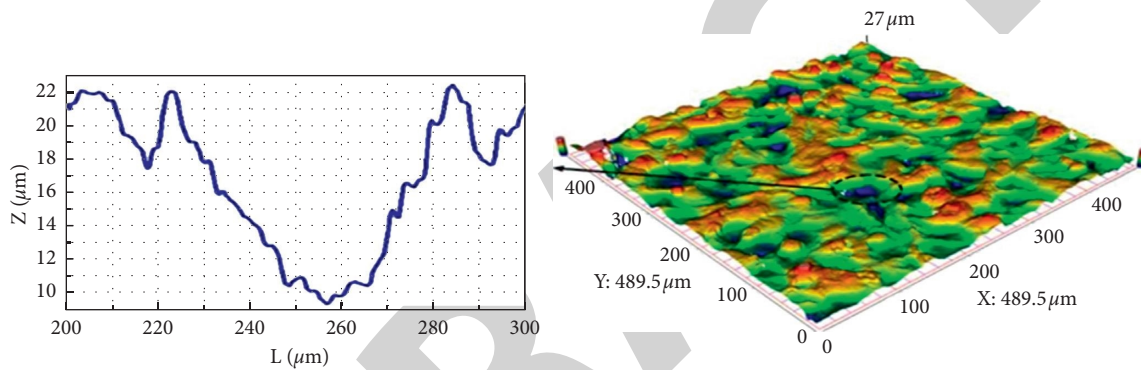


FIGURE 3: 3D micrometer surface morphology with different discharge energies: (a) $I_p = 14$ A, $T_{on} = 26$ μ s; (b) $I_p = 18$ A, $T_{on} = 34$ μ s.

crater is 50–80 μ m, the depth of the crater is 6 μ m–10 μ m, and the flanging height is 2 μ m–8 μ m. This is consistent with the characteristic parameters of the single-pulse discharge crater model obtained by the previous simulation. Figure 3 shows the machined surface topography with different discharge parameters; as the discharge energy increases as more material is taken from the workpiece, the material removed increases. The size and number of craters on the workpiece surface: at the same time, in the process of crater formation, with the rise of discharge energy, the crater size increase is not synchronized, the crater diameter increase scope is more prominent, and the growth rate is the fastest, then the indentation depth is used to achieve the stable value, and finally, because of the effect of processing waste heat of molten material flow trend, flanging height also gradually achieves the typical value. The variation trend of crater size characteristic parameters with discharge energy during simulation is verified.

After the experiment, the material's surface was observed by using a scanning electron microscope (SEM), and XRD measurements were made. The composition of the surface of the material is shown in Figure 4. The change of chemical composition and microstructure of the surface layer after EDM machining verified the phase transition of the material surface caused by heat during the simulation process of single-pulse discharge

3.1. Model Validation. Figure 5 depicts an example of a simulated and an experimental surface. To verify the accuracy of the predicted surface roughness of the material removal model, the measured surface roughness is compared with the expected surface roughness of the model. The surface roughness and average error between the experimental results and the simulation results are shown in Table 3 and Figure 6. The predicted values of the model are consistent with the experimental measurements. The average relative error of the EDM continuous discharge material removal model established in this paper to predict the surface roughness is 8.26%. There is a particular error between the measured value and the expected value of the model because there are many influencing factors in the experiment and modeling process. In the process of single-pulse discharge simulation, the grid division, the selection of energy distribution coefficient and convective heat transfer coefficient, and the measurement of thermal properties of Inconel 718 material at different temperatures have a particular influence on the accuracy of simulation results. In the actual machining process of EDM, the regular discharge, arc discharge, and short-circuit discharge states are inevitable. However, different types of discharge states have different discharge energy levels. This phenomenon makes the changes of each discharge crater inconsistent, increasing surface roughness.

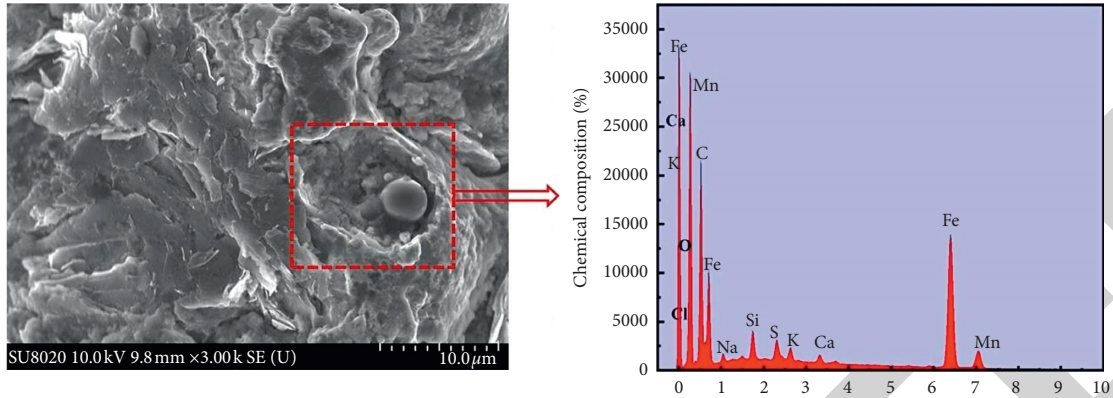


FIGURE 4: SEM micrograph and the corresponding XRD spectrum of the microcrater.

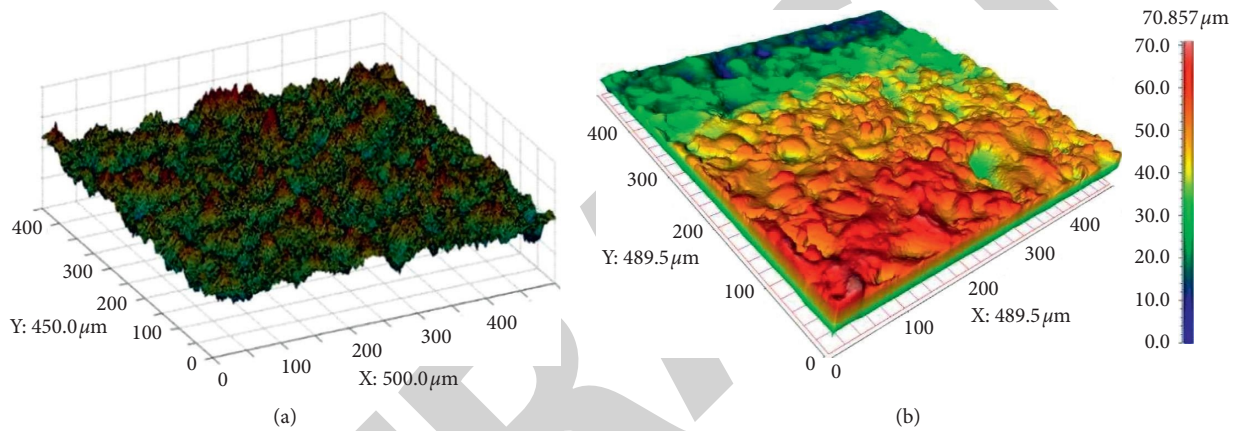


FIGURE 5: Experimental and simulated surface topographies: (a) simulated result; (b) experimental result.

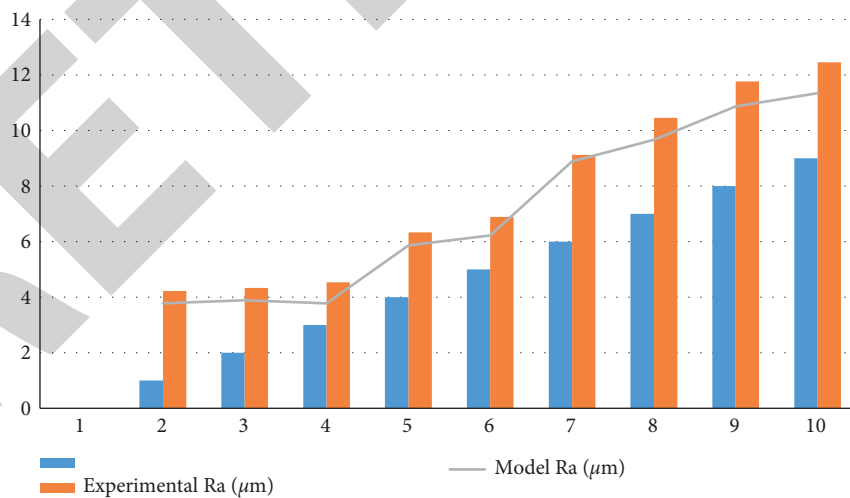


FIGURE 6: Comparison of Ra values of the simulation and experiment.

3.2. Influence of Discharge Parameters on Surface Roughness. Figure 7 shows the relationship between peak current, pulse width, and surface roughness. Surface roughness rises as peak current and pulse width increase, and the effect of peak current on surface roughness is greater than that of the pulse width. When the discharge current and the increase of pulse

width mean the addition of single-pulse discharging energy, according to the simulation result, it is shown that, in front of a single-pulse discharge energy increase, in the process of heat transfer of radial direction in the pits, the discharge rate of growth is greater than the depth direction, thus forming the discharge crater diameter growth rate greater than the

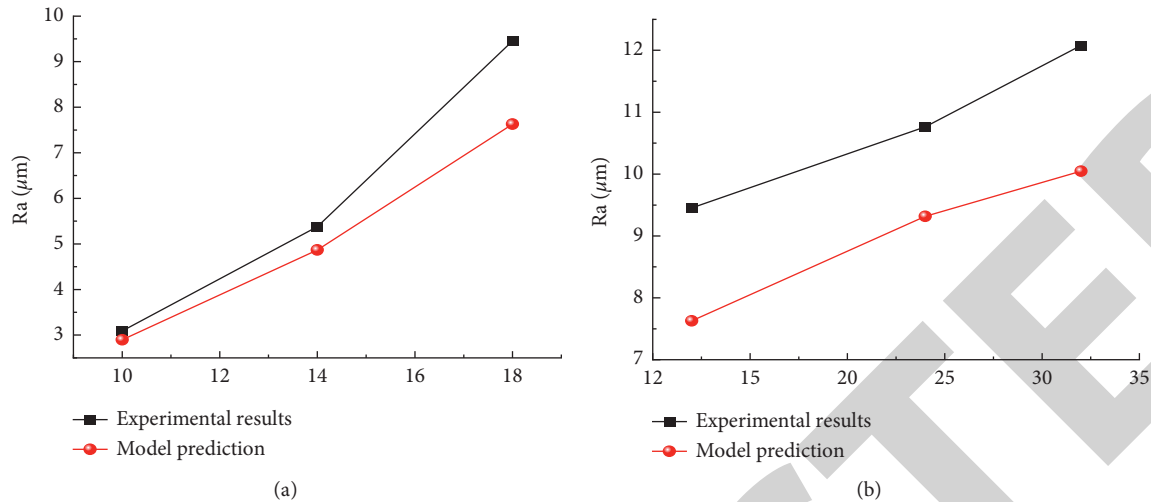


FIGURE 7: The relationship between (a) peak current and surface roughness and (b) pulse width and surface roughness. (a) Peak current (A); (b) pulse width (μs).

depth of the growth rate; finally, the surface roughness increases with the increase of discharge current and pulse width.

4. Conclusions

From the analysis as mentioned above and experiments, the following conclusions can be drawn.

According to the energy conservation theorem, different discharge parameters replicate the impact crater's characteristic size.

- (1) Peak current and pulse width impact discharge pit temperature and velocity. The increasing crater radius, depth, and deformation heights are not related to increased discharge energy, but to variable factors. The crater's radius changes in synchrony with the increasing trend. The material removal model uses EDM machining mechanism.
- (2) Continuous discharge was established to simulate the procedure of machining. Peak current and pulse width are used as inputs, and surface roughness is used as an output measure. The workpiece's initial surface topography and the electrode wire with a minimum gap width were taken as the discharge position. Then, the material removal model was tested by experiments. The results show that the prediction accuracy of the EDM continuous discharge material removal model for surface roughness is around 8.26%. The surface roughness increases with the increase of peak current and pulse width, and the effect of the peak current on surface roughness is greater than that of the pulse width.
- (3) It can also precisely estimate the eventual surface shape of materials following continuous discharge. Adjusting discharge parameters improves EDM machining accuracy and surface integrity. To better anticipate the material erosion surface created by

continuous pulse discharge, the influence of electric field was incorporated into the model continuous pulse discharge to achieve a more accurate prediction.

Data Availability

The data underlying the results presented in the study are available within the manuscript.

Conflicts of Interest

The authors declare that there are no conflicts of interest regarding the publication of this paper.

References

- [1] S. K. Gauri and S. Chakraborty, "A study on the performance of some multi-response optimisation methods for WEDM processes," *International Journal of Advanced Manufacturing Technology*, vol. 49, no. 1-4, pp. 155-166, 2010.
- [2] A. Bin Sapit, S. Kariem Shather, and F. Nehad Abed, "Enhancement of the performance surface roughness of wire cutting process by additives Nano (Al_2O_3)," *Let's Save the World and Humanity*, vol. 8, no. 2, pp. 933-941, 2020.
- [3] A. Abdullah Hamad, M. Lellis Thivagar, M. Bader Alazzam et al., "Dynamic systems enhanced by electronic circuits on 7D," *Advances in Materials Science and Engineering*, vol. 2021, Article ID 8148772, 11 pages, 2021.
- [4] V. Anand, S. Gupta, D. Koundal, S. Mahajan, and A. Kant Pandit, "Deep learning based automated diagnosis of skin diseases using dermoscopy," *CMC-Computers, Materials & Continua*, vol. 71, no. 2, pp. 3145-3160, 2022.
- [5] L. Malacrida, S. Ranjit, D. M. Jameson, and E. Gratton, "The phasor plot: a universal circle to advance fluorescence lifetime analysis and interpretation," *Annual Review of Biophysics*, vol. 50, pp. 575-593, 2021.
- [6] L. Wang, A. A. Hamad, and V. Sakthivel, "IoT assisted machine learning model for warehouse management," *Journal of Interconnection Networks*, vol. 3, Article ID 2143005, 2021.

Retraction

Retracted: Mechanics of Materials Natural Fibers Technology on Thermal Properties of Polymer

Advances in Materials Science and Engineering

Received 31 October 2023; Accepted 31 October 2023; Published 1 November 2023

Copyright © 2023 Advances in Materials Science and Engineering. This is an open access article distributed under the Creative Commons Attribution License, which permits unrestricted use, distribution, and reproduction in any medium, provided the original work is properly cited.

This article has been retracted by Hindawi following an investigation undertaken by the publisher [1]. This investigation has uncovered evidence of one or more of the following indicators of systematic manipulation of the publication process:

- (1) Discrepancies in scope
- (2) Discrepancies in the description of the research reported
- (3) Discrepancies between the availability of data and the research described
- (4) Inappropriate citations
- (5) Incoherent, meaningless and/or irrelevant content included in the article
- (6) Peer-review manipulation

The presence of these indicators undermines our confidence in the integrity of the article's content and we cannot, therefore, vouch for its reliability. Please note that this notice is intended solely to alert readers that the content of this article is unreliable. We have not investigated whether authors were aware of or involved in the systematic manipulation of the publication process.

Wiley and Hindawi regrets that the usual quality checks did not identify these issues before publication and have since put additional measures in place to safeguard research integrity.

We wish to credit our own Research Integrity and Research Publishing teams and anonymous and named external researchers and research integrity experts for contributing to this investigation.

The corresponding author, as the representative of all authors, has been given the opportunity to register their agreement or disagreement to this retraction. We have kept a record of any response received.

References

- [1] M. B. Alazzam, F. Hajje, A. S. AlGhamdi, S. Ayouni, and M. A. Rahman, "Mechanics of Materials Natural Fibers Technology on Thermal Properties of Polymer," *Advances in Materials Science and Engineering*, vol. 2022, Article ID 7774180, 5 pages, 2022.

Research Article

Mechanics of Materials Natural Fibers Technology on Thermal Properties of Polymer

Malik Bader Alazzam ¹, Fahima Hajje ², Ahmed S AlGhamdi ³, Sarra Ayouni ²
and Md Adnan Rahman ⁴

¹Faculty of Computer Science and Informatics, Amman Arab University, Amman, Jordan

²Department of Information Systems, College of Computer and Information Sciences,
Princess Nourah bint Abdulrahman University, P.O. Box 84428, Riyadh 11671, Saudi Arabia

³Department of Computer Engineering, Collage of Computers and Information Technology, Taif University, P.O. Box 11099,
Taif 21944, Saudi Arabia

⁴College of Business Administration (CBA), International University of Business Agriculture and Technology (IUBAT),
Dhaka, Bangladesh

Correspondence should be addressed to Malik Bader Alazzam; m.alazzam@aau.edu.jo and Md Adnan Rahman;
adnan.cba@iubat.edu

Received 22 November 2021; Revised 8 December 2021; Accepted 17 December 2021; Published 7 January 2022

Academic Editor: Palanivel Velmurugan

Copyright © 2022 Malik Bader Alazzam et al. This is an open access article distributed under the Creative Commons Attribution License, which permits unrestricted use, distribution, and reproduction in any medium, provided the original work is properly cited.

The thermal characteristics of polymathic methacrylate combined with unsaturated polyester were determined by numerical and experimental research. Models for numerically investigating the parameters of thermal conductivity, specific heat capacity, and thermal diffusivity were developed using COMSOL Multiphysics. The numerical data were then compared to experimental results for the same material using the same measurements to ensure that they were correct. By comparing the thermal conductivity data to two sets of theoretical data, the results were confirmed. The COMSOL models were quite close to the experimental data, with just minor differences between the three models. One set of theoretical data coincided with the mean of the other data, while the second set revealed a significant departure below the other data.

1. Introduction

Despite the fact the polymer composites have been around for a long time, novel composites have been produced in the recent few decades and used in a variety of demanding applications [1]. The synthetic apparatus of today's polymer composites relies heavily on polymer mixtures. They are often manufactured by combining two or more polymers to create a miscible mixture with much better physical qualities than the separate polymers. Polymer blends may be used in a wide spectrum of material processing and manufacturing because of their distinct properties [2, 3]. The majority of polymer blends are made by mixing molten polymers to create heterogeneous systems with an emulsion structure. The component with the smaller volume fraction is disseminated in the medium of the second piece

as particles. Thermal characteristics of polymer blends are highly prized because they can give crucial information regarding their functioning in many applications [4]. Furthermore, data on thermal characteristics can aid in identifying the best processing settings and heat transport studies of the nominated materials [5, 6]. Thermal conductivity, thermal diffusivity, and specific heat capacity are important examples of the thermal qualities that need to be understood for these materials, because this knowledge may assist designers and manufacturers make sound judgments about whether or not to employ them in the intended applications. Such investigations and methods need a thorough understanding of the heat flux profile, which is based on the creation and refinement of highly effective models that can precisely anticipate thermal behavior [7].

To anticipate the thermal characteristics of polymer composites, several theoretical and experimental studies have been undertaken [8]. However, just a few researches have attempted to simulate polymer mixes. Because it incorporates complicated geometrical and thermodynamic principles, both in terms of their reactions to thermo-mechanical stresses and with regard to the mechanics of miscibility itself, modeling polymer blends necessitates tremendous attention, thinking, and focus. Furthermore, because of their complexity, generating successful models of polymer blends needs a fast computing environment capable of handling the vast number of items in the finite element mesh. All load and boundary conditions contained in the model domains should be computed and solved using the CAD (Computer Aided Design) system.

The finite element technique is a systematic approach for converting functions in an infinite dimensional function space to finite dimensional function space and then to ordinary vectors (in a vector space) that may be solved numerically.

COMSOL Multiphysics is well-known as a reliable finite element analysis program. Its sound and user-friendly architecture, as well as its capacity to permit highly exact theoretical studies, have made it the preferred analytical program for a variety of physical issues, including thermal and structural characterizations [9]. Polyamides are among the most widely used crystalline engineering thermoplastics, owing to their outstanding performance features such as high melting temperatures, high mechanical strength, and excellent solvent resistance [10]. PMMA (polymathic methacrylate) is a transparent polymeric material with a number of desired features, including low weight, high transparency, chemical resistance, weathering corrosion resistance, and good insulating capabilities. When it comes to composites and polymer blends, unsaturated polyester (UP) is one of the most useful polymers [11–13].

The features of these blends may be easily studied and investigated using the modeling method, and it is critical that each model undergoes a highly reliable and efficient experimental validation. Estimating the characteristics of polymer blends can aid in making more accurate predictions regarding their behavior.

The several types of polymer blends explored in this study were made up of the two polymers mentioned above: UP and PMMA. In terms of polymer volume fractions and geometrical constructs, the two models differed. Their thermal characteristics were studied, including thermal conductivity (k), specific heat capacity (C), and thermal diffusivity.

1.1. Thermographic Analysis. Thermal analysis was carried out in two ways. The first included theoretical techniques based on Maxwell's theory [14, 15], which employs a unique equation to calculate the thermal conductivity of a polymer-and-distributed-filler system. The equation is used to calculate the thermal conductivity of polymer blends rather

than polymer and filler systems, in which the UP was utilized as the matrix and the PMMA was employed as the second phase material. The following is the equation:

$$k = k_{UP} \frac{2k_{UP} + k_{PMMA} - 2(k_{UP} + k_{PMMA})\phi_{PMMA}}{2k_{UP} + k_{PMMA} + 2(k_{UP} + k_{PMMA})\phi_{PMMA}} \quad (1)$$

The appropriate heat conductivities of polyester resin (UP) and polymathic methacrylate (PMMA) are k_{UP} and k_{PMMA} , respectively. In the PMMA:UP composite, PMMA is the mass fraction of PMMA.

The second way for calculating k is to utilize Bridgeman's theory, [12–15] which looks at effective thermal conductivity using a different method based on the modified equation:

$$1 - \phi = \frac{k - k_{PMMA}}{k_{UP}} \left(\frac{k_{UP}}{k} \right)^{1/2} \quad (2)$$

The second sort of study includes building and investigating three alternative models using Simulation Tool 5.3 and a range of geometric and theoretical principles. These were determined as the best models to employ for this sort of research based on relevant experimental data.

Each component was represented as a circle with a radius corresponding to its volume fraction in the initial model, which was generated using two-dimensional geometries. The volume fractions were changed using a parametric approach. The 2D model was named after it, and it is seen in Figure 1.

The third model, dubbed the 3D model, was created utilizing three-dimensional geometry. This model was created to imitate experimental measurement samples with various volume ratios and a constant thickness of 3 mm (which is consistent with the experimental test sample shape) (Figure 2).

The squared lattice model based upon that Flory–Huggins model was used to construct the third model. A lattice model has the advantage of being the best form of model for dealing with binary mixes of various structures.

The Flory–Huggins model is being utilized for the first time to investigate the thermodynamics of mixing binary systems such polymer blends and/or polymer-solvent mixtures. The lattice model's key benefit is that each material's molecules may explicitly disperse over the lattice squares, allowing each square to be occupied by only one kind of molecule.

The models were solved with the help of thermal conduction considerations using the heat transfer in solids module.

The following were the imposed boundary criteria within the context of these considerations:

- (1) For the 2D model, two distinct temperatures T_1 and T_2 were applied to each quadrant of the outer circle, with T_1 referring to ambient temperature and T_2 referring to raised temperature. To ensure that the test was as exact as feasible, the other two opposing quarters were isolated

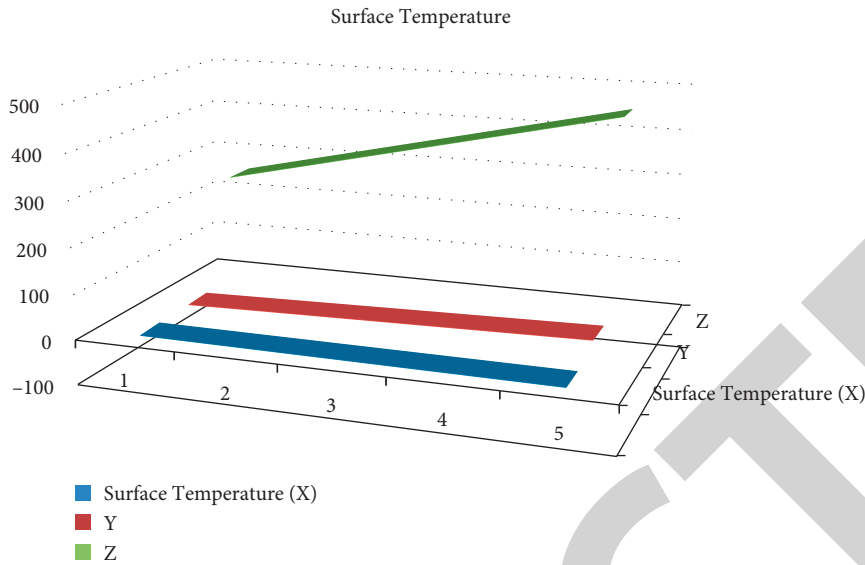


FIGURE 1: Surface temperature distribution.

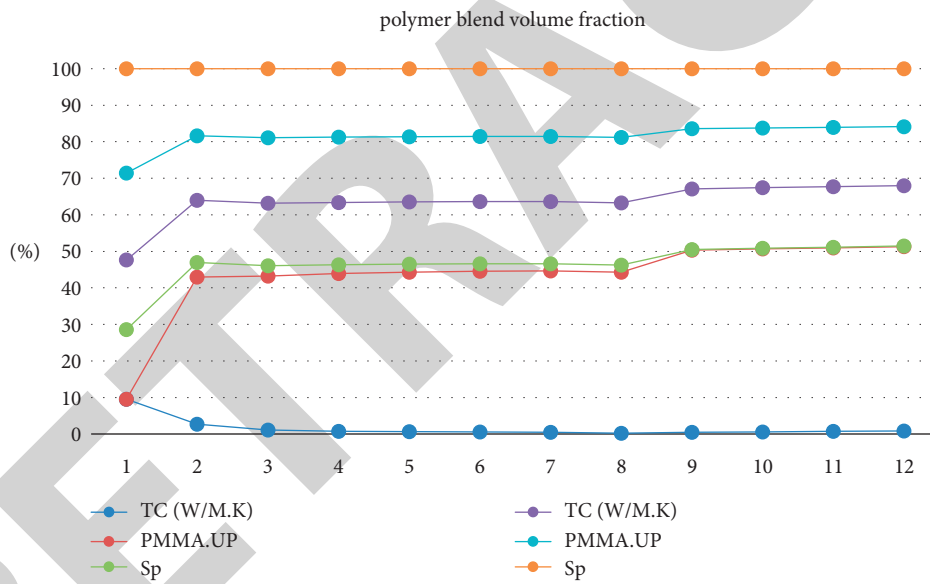


FIGURE 2: Polymer blend volume fraction.

(2) T_1 and T_2 were applied to the bottom and surfaces of the 3D model, respectively, while the cylinder's side wall was insulated

T_1 and T_2 were used on the left and right walls, respectively, in the F-H model.

The following formula was used to get the numerical value of the effective thermal conductivity:

$$k = \frac{\phi}{A} \frac{R}{(T_1 - T_2)} \tag{3}$$

Specific heat capacity, in contrast to conductivity, is a measurement of a material's ability to store thermal energy. The thermal diffusivity is the third property in the heat transfer equation, and it depends on the other two characteristics (thermal conductivity k and specific heat capacity at constant pressure C_p) and may be calculated using the following formula:

$$\alpha = \frac{k}{\rho C_p} \tag{4}$$

where ρ is the density measured in kg/m^3 .

As a result, a material's thermal diffusivity may be defined as the ratio of thermal energy conduction to thermal energy storage.

1.2. The Procedure for Testing

1.2.1. Models of Different Materials. Material models are all mathematical approximations of real-world physical behavior. Material models, on the other hand, are not usually developed from physical concepts such as mass conservation or equilibrium equations. They are phenomenological in nature and based on measurements. The mathematical frameworks of material models and the possible values of material attributes will, however, be constrained by physical laws.

Even in ordinary life, it is commonly understood that different materials behave in radically different ways. A material can be extremely brittle, such as glass, or extremely elastic, such as rubber. The operating conditions, as well as the material itself, play a role in selecting a material model. A typical instructional experiment is to soak a piece of rubber in liquid nitrogen until it becomes as brittle as glass. Additionally, when glass is heated, it begins to creep and exhibit viscoelastic behavior.

The translucent, viscous unsaturated polypropylene resin (UP) from (SIR) employed as one of the study's polymers has a density of 1200 kg/m^3 at ambient temperature. When a hardener (methyl-ethyl ketone peroxide (MEKP)) made by the same business is added to UP, it solidifies (SIR). This polymer, together with methacrylate (PMMA) from Castavaria, was combined for 1-2 minutes in an electrical blender to achieve the ratios specified in the modeling. The hardener was then added to the reaction mixture and let to set for 24 hours. The solid composite was then placed in a furnace at 55 degrees Celsius to finish the solidification processes.

The hot disc technique was used to test thermal conductivity, thermal diffusivity, and specific heat capacity. Discussion of the findings agrees with the actual data (as shown in Table 1 and Figure 2). The experimental data differed only little from the COMSOL models, which differed less from one another.

The surface temperature pattern for the three numerical models is shown in Figure 1. In contrast to the 3D sample, where the hot zone prevailed over the model's other regions, the hot region did not dominate the whole model in the 2D sample. The temperature distribution in the F-H model was more uniform. The 2D model had the biggest height fluctuations in temperature, with a rate of 71 percent, while the F-H model had the lowest, with a rate of just 12 percent.

In contrast to the anticipated data from Maxwell's theory, Table 2 which showed substantial variation from the others, all COMSOL models, as well as Bruggeman's theoretical data, showed complete.

This behavior differs in terms of specific heat and thermal diffusivity, where modeling data demonstrate substantial variation for various blend proportions, as

TABLE 1: Surface temperature.

Surface temperature (X)	Y	Z
-0.03	5	250
-0.06	10	300
0	15	350
0.03	20	400
0.06	25	450

TABLE 2: Substantial variation.

TC (W/M.K)	PMMA.UP	Value
0.1	0	0.2
0.2	3	0.3
0.15	6	0.4
0.16	9	0.5
0.17	12	0.6
0.18	15	0.7
0.19	18	0.8
0.1	21	0.9
0.2	22	0.10
0.3	25	0.11
0.4	28	0.12
0.5	29	0.12

illustrated in Figures 1 and 2. However, when it comes to the thermal diffusivity data, both the model and the experimental data exhibit a similar pattern of change.

A comparison of numerical and experimental data for specific heat data as a function of polymer blend volume fraction combines the statistical validation of calculated and measured data from several modeling setups.

The validation evaluations suggest that the COMSOL models and experimental work are generally in excellent agreement and that the differences between the two types of analysis are within acceptable ranges. For each attribute, however, the data deviation is different.

When just one of the two polymers is maintained in the polymer blend, the biggest deviations occur, and when the polymer blend is at the intermediate concentration, the deviations are minimized. At the 15 percent and 20 percent PMMA:UP volume fractions, the Flory-Huggins configuration displays less variation than the others.

Unlike thermal conductivity, the attribute of specific heat follows a distinct pattern. The equilibrium concentration of 15% causes the biggest variation in specific heat, whereas the PMMA content with the lowest PMMA content offers the best agreement between the models and experimental results. The F-H configuration, notably at the 15% and 20% PMMA volume fractions, exhibits the highest agreement with the experimental results.

The deviations for diffusivity and thermal conductivity and specific heat reveal considerable differences. At 20% PMMA:UP, the maximum deviation of the F-H model, the greatest variance in diffusivity arises. As the PMMA concentration climbs from 5% to 15%, the two other models indicate a progressive increase in their departure from the experimental data, before dropping to a lower value at 20% PMMA:UP. The deviation of the F-H model climbs with the

Retraction

Retracted: Implementation of TQM and the Integration of BIM in the Construction Management Sector in Saudi Arabia

Advances in Materials Science and Engineering

Received 26 December 2023; Accepted 26 December 2023; Published 29 December 2023

Copyright © 2023 Advances in Materials Science and Engineering. This is an open access article distributed under the Creative Commons Attribution License, which permits unrestricted use, distribution, and reproduction in any medium, provided the original work is properly cited.

This article has been retracted by Hindawi, as publisher, following an investigation undertaken by the publisher [1]. This investigation has uncovered evidence of systematic manipulation of the publication and peer-review process. We cannot, therefore, vouch for the reliability or integrity of this article.

Please note that this notice is intended solely to alert readers that the peer-review process of this article has been compromised.

Wiley and Hindawi regret that the usual quality checks did not identify these issues before publication and have since put additional measures in place to safeguard research integrity.

We wish to credit our Research Integrity and Research Publishing teams and anonymous and named external researchers and research integrity experts for contributing to this investigation.

The corresponding author, as the representative of all authors, has been given the opportunity to register their agreement or disagreement to this retraction. We have kept a record of any response received.

References

- [1] M. Abazid, H. Gökçekuş, and T. Çelik, "Implementation of TQM and the Integration of BIM in the Construction Management Sector in Saudi Arabia," *Advances in Materials Science and Engineering*, vol. 2021, Article ID 1232620, 9 pages, 2021.

Research Article

Implementation of TQM and the Integration of BIM in the Construction Management Sector in Saudi Arabia

Mohammad Abazid ¹, Hüseyin Gökçekuş,¹ and Tahir Çelik²

¹Faculty of Civil and Environmental Engineering, Near East University TRNC, Mersin 10, Turkey

²Faculty of Engineering, Cyprus International University TRNC, Mersin 10, Turkey

Correspondence should be addressed to Mohammad Abazid; abazmohammad997@gmail.com

Received 14 November 2021; Revised 3 December 2021; Accepted 9 December 2021; Published 26 December 2021

Academic Editor: Palanivel Velmurugan

Copyright © 2021 Mohammad Abazid et al. This is an open access article distributed under the Creative Commons Attribution License, which permits unrestricted use, distribution, and reproduction in any medium, provided the original work is properly cited.

Total Quality Management (TQM) is based on the conceptions of managing and enhancing the success of construction projects. When applied, TQM improves execution of time management of project, satisfies clients' needs, minimizes the expenses and increases the profit of contractor, and fulfils safety regulations on the construction site. This research is aimed at evaluating the impacts of employing the concepts of TQM to the construction projects in Saudi Arabia. The results of the study were obtained through utilization of a descriptive analytical approach, where 300 questionnaires were distributed to engineering firms and companies with a response rate of 200 questionnaires, hence achieving the study sample for this research. The data gathered was analyzed by applying the Statistical Package for Social Science (SPSS) program and calculating the relative importance index (RII) and the mean values. From the research conducted, the outcomes showed that the management's ability to commit using TQM while applying BIM obtained a relative importance of (0.717), while the relative importance for the management's ability to commit using TQM without the application of BIM is (0.552). The results showed that construction projects in Saudi Arabia still sustain setbacks from applying TQM concepts and suffer from the lack of administrative, scientific, and technical applications.

1. Introduction

For the past ten years, the construction industry in Saudi Arabia has endorsed a significant development. Construction developments are globally considered the most productive venture phases of any nation. Aside from the focus of construction projects on traditional endowments, currently, the focus has been extended into quality, cost-efficiency, cutback in cost, time management, and investment [1, 2].

Presently, construction projects face many developments and enhancements, which makes maintaining the projects more difficult and incomprehensible. This is particularly true for the construction projects in Saudi Arabia [3]. Contractors encounter several conflicts when planning and executing construction works such as uncoordinated drawings, specifications, absent pertinent information, and overdue delivery of design material. As a result, the majority of the regions, in Saudi Arabia, were required to apply and implement innovative techniques and principles in project

management and execution. Additionally, they needed to increase the qualifications, requirements such as skills and highly developed technology, and properties of the projects. The application of such approaches enhances production that is more accurate, offering simpler implementing tactics and eases operations. In turn, contractors will become more attentive and contribute to the application of quality insights throughout the entire duration of the projects construction [4, 5].

The growing complications of projects have resulted in many developments within the construction industry. Information and Communication Technology (ICT) is one of the few matters that has developed and evolved at a rapid rate. Over the past decade, the construction industry observed a significant transformation in ICT, which is the initiation of Building Information Modeling (BIM). BIM was developed as a modern prototype for Computer Aided Design (CAD) to be implemented within industrial and academic services [6]. Currently, BIM is recognized to be the

ultimate general compellation for an innovative approach in managing the design, construction, and maintenance of a project/structure. One definition of BIM is “an array of interrelating guidelines, developments, and tools creating an approach to administer the fundamental structure design and project information in a digital system throughout the structure’s life-cycle” [6].

Generally, theoretical progressions within BIM implies that, besides its assistance in geometric display of the structures’ implementation, it also aids the management and functional quality employment of a construction project.

Depending on research in several fields, it revealed that TQM and BIM convey association in execution and productivity of institutions, which also speculated that advanced information would eventually lead to advanced outcomes of quality throughout the construction works [7, 8] (Wheaton et al.).

Accordingly, to determine whether the implementation of TQM concepts within the construction projects in Saudi Arabia can be accomplished, this research will study the evaluation of tangible BIM application. A comparison of the TQM will also be made regarding the outcomes of the project when BIM is applied or disregarded. The results will be obtained by conducting researches, applying evaluation/assessment utilities, and the method used to comprehend the outcomes while acknowledging the primary features of the project that is represented by time and cost is incorporated to acquire the vital quality.

2. Literature Review

The application of Building Information Methodology (BIM) in the construction industry can be viewed as a method in employing Information Technology (IT) [9], which represents the analyzation, enhancement, structuring, maintenance, and processing computer-based data systems. The concept of BIM was initially publicized in 2003 by Autodesk. It was developed as an innovative and sophisticated approach for structure design, building, and management. All over the world, the BIM has been able to transform the method followed by the industrial professionals in anticipating the impact of employing technology for structure design, building and management [8].

Ever since BIM has appeared, the modeling and documentation of structure projects have endorsed exploitation of a modern approach (Lee et al.). Building Information Modeling (BIM), as a term, was originally formulated to disengage the customary Computer Aided Design (CAD) that has been primarily focused on the drawing production of structures from the previous IT and CAD generations. BIM can be identified as the enhancement and processing of structural statistics by an interoperable and viable method. Therefore, BIM is recognized as a systematic process or a set of systematic processes that lets operators integrate and retrieve structural information and domain data throughout the structures life cycle [10].

Many definitions have been associated to the Building Information Modeling (BIM) approach. The American Institute of Architects (AIA) defined BIM as a “model-based

machinery associated with a databank of project statistics” [11]. The National Building Information Model Standard (NBIMS) stated that the BIM is viewed as an “automated interpretation of substantial and efficient aspects of a facility” [12]. They also claimed that BIM is “a communal information source for data on the facility, establishing a dependable foundation for assessments during the facilities life-cycle; or in other terms from the initial origin up to the demolition of the facility” [12].

BIM has been implemented in the execution of large and high-scale projects. An example of such projects includes the recently constructed [13] Olympic, 6,000 seating, Velodrome cycle track and the 225 meters high, 48 floors, Leadenhall Building “The cheese grater.” BIM is not only implemented within massive projects, but also processed in smaller scale projects on particular components throughout the project. One example of smaller scale projects with BIM application is the new bus post located in Slough, UK. It was opened in 2011 of June, in which BIM was utilized to model and install the modular stairs [14]. Due to the anticipated compensations from BIM employment, with respect to the cutbacks of operation costs and smaller chances of error, the UK government declared that all contracts as of 2014 will compel source chain partners to work jointly by utilizing the “fully collaborative 3D” BIM [15]. The three-dimensional BIM insinuates all resource information, data, and records of all projects in a programmed method. In the United States, both the public and private sectors are collaborating to validate the application of the BIM method [16].

On the contrary, there have been several evaluations that claim that the application of BIM has not yet proven or justified it to be completely effective [17]. Succar provided a definition on BIM that emphasizes its entire aspect, which consists of a software that involves arithmetical modelling and input of information, as well as the utensils and procedures coupled with Project Management (PM). Hence, observing BIM in its complete complexion undeniably classifies it within the structure of the Project Management domain. Structural project managers are capable of employing BIM to develop the involvement among investors, in which the duration needed for documentation is reduced, resulting in profitable project results. From previous literature works on BIM features, some incorporated the detailed record of BIM application on specific project conditions such as the Heathrow Terminal 5 [13] and the Walt Disney Concert Hall [18].

3. Research Methodology

The objective of this research was obtained by manipulating the descriptive and analytical method to analyze the data collected. The data was collected through the distribution of 100 questionnaires to engineering organizations and construction companies that apply BIM concepts, and another 100 questionnaires were sent to firms and companies that do not apply BIM in their work, which totals 200 questionnaires. The sample size was determined by using a sample size calculator found online. The mathematical equation to determine the sample size is as follows:

$$n = N * \frac{Z^2 * p * (1 - p) / e^2}{[N - 1 + (Z^2 * p * (1 - p)) / e^2]} \quad (1)$$

In which n signifies the sample size, N represents the population size, Z is the confidence level, p denotes the sample proportion, and e represents the margin of error. For the following study, the population size is 412, the confidence level is 95%, the margin of error is 5%, and the sample proportion is 50%, which resulted in the sample size of 200. This census was acquired from the Saudi Engineers Association, which was based on the targeted research sample.

To assess the information gathered from the questionnaires, the SPSS program, the relative importance index, and mean values methodologies were employed.

3.1. Statistical Analysis Tools of SPSS. To analyze the data, both qualitative and quantitative data analysis techniques were utilized. The data analysis obtained was collected from the application of the SPSS 23 software. To test the normality of the data, Kolmogorov-Smirnov test of normality was applied. As for the validity, Pearson correlation coefficient for validity was used as well as Cronbach's alpha to obtain the reliability of the statistics. The following statistical tools were also applied: frequency and descriptive analysis, stepwise regression, and one-sample T -test.

The T -test was applied to verify that the mean of an item differs significantly from a theoretical value of three (middle value of the Likert scale). In situations where the P value (Sig.) is less than or equal to the significance level, then the mean of the item is substantially distinctive from the theoretical value of three. The calculated sign from the test value specifies whether the mean is considerably larger or smaller than the theoretical value. Alternatively, when the P value (Sig.) is larger than the significance level, the mean of the item is slightly different from the theoretical three value.

3.2. Relative Importance Index (RII). The assessment was manipulated to determine the most effective factors based on the relative importance integers and the Mean Relative Importance Index (RII) figures. For all the responses obtained from the questionnaire, especially those from the multisection questions, they were categorized in order. This helps in verifying the significance of the respondent's opinion on the placement of the outcomes. By utilizing this weight/ranking tactic, which is the most dependent and precise system, the Relative Importance Index (RII) will be applied to determine the significance of the response selection received from the respondents. [19]. The equation used to determine the RII is shown below:

$$RII = \frac{(\sum w)}{w_{highest} * n} \quad (2)$$

where W : Weight/rank of each response. n : the total amount of responses gathered. W highest: the highest rank/weight that can be acquired.

From the equation, the value of the RII will always be equal to or smaller than one but greater than zero.

Considering this a reference for acceptance, if the value of RII is 0.7 or higher, then it is reliable.

3.3. Data Measurement. The questionnaire was developed in order for the respondents to determine the weights of the factors by using the Likert scale as a rating system. The Likert scale is believed to be the most appropriate method for analyzing data. The ordinal scales (Likert) that were used are shown in Table 1.

3.4. Questionnaire Model. For this research, the questions used for the questionnaire were developed and selected by intensive understanding of previous studies and the perceptions of various experts. The information collected determined that the ten questions applied in the questionnaire are adequate to cover the entire research scope. The questionnaire was thoroughly structured to clarify the gathering process and to enhance the reliability and validity of the gathered information from the respondents. The questionnaire was sectioned into various divisions. The first part was targeted at gathering information on the respondents' details such as place of work, scientific qualification, experience, and employment position. The following sections were established to comprehend the evaluation responses on the higher management's ability to confide in applying the TQM concepts.

3.5. Validity of the Questionnaire. The term validity is applied when referring to the extent that a tool quantifies the item being measured. Validity is comprised of various aspects and assessment methods. Moreover, statistical validity is applied to evaluate the system validity, which encompasses internal and structural validity.

3.6. Internal Validity. The first statistical assessment was implemented to evaluate the validity of the questionnaire, known as the internal validity. A surveying example, composed of 30 questionnaires, was utilized for the measurement procedure. They calculated the correspondence coefficients of each element within a particular subject as well as the whole subject.

The corresponding coefficients of the items and the field total of the questionnaire, "the higher management's ability to commit to applying TQM concepts when the organization does not use BIM," are listed in Table 2. From the table, the p values (sig.) calculated are less than 0.05. For this field, the corresponding elements of the subject are deemed to be important at $\alpha = 0.05$. Therefore, it may be established that all the items of this subject are valid and consistent and can be used as a measuring tool.

Correspondingly, Table 3 illustrates the corresponding coefficient of each item and the field total of the questionnaire: "the higher management's ability to commit to applying TQM concepts when the organization uses BIM." The results depicted that the p values were less than 0.05, which means that the corresponding coefficients of the subjects for this field are significant at $\alpha = 0.05$. As a result, the items presented in this field are highly valid and consistent to be utilized for measurement.

TABLE 1: Likert scale.

Statement	Completely agree	Mostly agree	Slightly agree	Mostly disagree	Completely disagree
Scale	5	4	3	2	1

TABLE 2: Corresponding coefficient and field total of “the higher management’s ability to commit to applying TQM concepts when the organization does not use BIM.”

No.	Item	Pearson correlation coefficient	<i>p</i> value (sig.)
1.	What is your assessment on the performance of the higher management of engineering projects in Saudi Arabia in applying the concepts of TQM?	0.678	≤0.001
2.	What is your assessment on the performance of the higher management of engineering projects in adhering to time schedule for engineering projects?	0.669	≤0.001
3.	What is your assessment on the performance of the higher management of engineering projects in seeking to enhance project implementation?	0.590	≤0.001
4.	What is your assessment on the performance of the higher management of engineering projects in seeking to cut back on expenses?	0.676	≤0.001
5.	What is your assessment on the performance of the higher management of engineering projects in seeking to satisfy the client?	0.588	≤0.001

TABLE 3: Corresponding coefficient for each item and the field total for “the higher management’s ability to commit to applying TQM concepts when the organization uses BIM.”

No.	Item	Pearson correlation coefficient	<i>p</i> value (sig.)
6.	What is your assessment that BIM application assists the higher management of engineering projects in Saudi Arabia by applying TQM?	0.967	≤0.001
7.	What is your assessment that BIM application assists the higher management of engineering projects to commit to projects schedule?	0.973	≤0.001
8.	What is your assessment on BIM application in assisting the higher management of engineering projects to improve project performance?	0.960	≤0.001
9.	What is your assessment on BIM application in assisting the higher management of engineering projects in seeking to cut back on expenses?	0.964	≤0.001
10.	What is your assessment on BIM application in assisting the higher management of engineering projects in pursuing customer satisfaction?	0.984	≤0.001

3.7. *Structural Validity of the Survey/Questionnaire.* To guarantee the validity of the structure of the second questionnaire, the second statistical assessment is conducted and is referred to as the structure validity. This is obtained by analyzing each field’s validity as well as the validity of the whole questionnaire. This assessment is also able to identify the corresponding coefficient that has the same ranking as the Likert scale, between the one subject and all the subjects of the questionnaire.

The corresponding coefficient for each field and the entire questionnaire is illustrated in Table 4. From the table, the *p* values (sig.) are all less than 0.05, denoting that the corresponding coefficients are significant at $\alpha = 0.05$. This signifies that the fields are consistent and valid and can be manipulated as a measuring tool, which is utilized to attain the main research objective.

4. Cronbach’s Alpha Coefficient

For the internal consistency to be calculated, the Cronbach alpha was developed, which is also known as the coefficient of reliability. To rephrase, all the elements present and incorporated in the instrument quantify the equivalent entity.

In general, the average range of Cronbach alpha coefficient may vary from any value between 0.0 and +1.0, where the larger the integer, the larger the extent of internal consistency [20]. For this research, the Cronbach alpha for each field in the questionnaire was calculated.

The Cronbach alpha values calculated for the individual subject of the questionnaire and the entire questionnaire are illustrated in Table 5. The results showed that the Cronbach alpha for the fields ranged from 0.970 and 0.988, and as for the entire questionnaire, the Cronbach alpha value was 0.979. This concludes that the outcomes of the fields are highly valid and consistent and that the questionnaire is highly reliable.

4.1. *Normality Test.* The One-Sample Kolmogorov-Smirnov test procedure is manipulated to compare the identified accumulative allocation function for a variable with the quantified theoretical allocation. This test procedure should be applied in cases where the results may be standard, Poisson, or exponential. The vital difference among the identified and theoretical variables is the absolute value calculated by the Kolmogorov-Smirnov Z-value. Moreover,

TABLE 4: Corresponding coefficient of each subject and the total of both questionnaires.

No.	Subject	Pearson correlation coefficient	<i>p</i> value (sig.)
1.	The higher management's ability to commit to applying TQM concepts when the organization uses BIM	0.640	≤0.001
2.	The higher management's ability to commit to applying TQM concepts when the organization does not use BIM	0.970	≤0.001

this assessment looks into the probability that the specific allocation is able to compute such observations rationally. Normal allocated variables are fundamental necessities for the majority of the parametric assessments. Additionally, this form of assessment may be implemented to identify if a particular variable is standardly allocated or not [21].

The results of the normality assessment, other known as Kolmogorov-Smirnov, are shown in Table 6. From the table, the outcomes prove that the *p* value for a particular element is greater than the significance level of 0.05, which signifies that the allocations of these elements are normal. Hence, parametric assessments should be manipulated to perform the statistical data analysis.

5. Results and Discussion

5.1. Occupation of the Participants in the Questionnaire. From the responses gathered, 35% of the participants are site engineers with a frequency of 69, 29% are site managers with a 58 frequency, and 37% of the participants are company managers with a frequency of 73. Table 7 illustrates the results.

Figure 1 further illustrates the results obtained in a pie chart. From the graph shown, it can be concluded that the participants who are company managers have the higher percentage, followed by the site engineers and site managers.

5.2. Experience of Participants in the Questionnaire. The questionnaires showed that the participants have a 26% of "1–5 years" with a frequency of 52, 34% have "5–10" years of experience and a frequency of 67, and 41% of the participants have more than "10" years of experience with a frequency of 81. The results are shown in Table 8 and Figure 2 illustrates the results in a pie chart.

From the graph, it can be seen that the participants with more than ten years of experience are the highest percentage at 41%, followed by participants with "5–10" years at 34%, and the lowest percentage are those participants with "1–4 years" experience at 26%.

5.3. Organization of Participants in the Questionnaire. From the responses collected, 22% of the respondents are employed in government organizations, and the frequency is 43, 33% are employed in consultant organizations with a frequency of 66, and 46% of the respondents are employed in contractor organizations with a frequency of 91. The results are shown in Table 9 and Figure 3 illustrates the results in a pie graph.

From the graph shown, the participants who are part of a contractor organization had the highest rate at 46%, 33% were part of consultant organizations, and only 21% were part of government organizations.

5.4. Results of "The Higher Management's Ability to Commit to Applying TQM Concepts When the Organization Does Not Use BIM". Table 10 illustrates the mean of the field "the higher management's ability to commit to applying TQM concepts when the organization does not use BIM." It can be seen that the mean of all the items in this field has a total value of (2.76). Moreover, the proportional mean is found to be 55.16%; the relative importance is equal to 0.552; the test value is -2.404 ; and the *p* value was found to be 0.201, wherein the value is greater than the significance level $\alpha = 0.05$. When compared to the theoretical value of (3), the mean value calculated for this field is insignificantly different, including the relative importance value that is less than 0.7. From the questionnaires, the responses showed that the participants were either uncertain or neutral in their judgements for this field.

Figure 4 indicates that the questions obtained the highest mean and relative importance values, which resulted in question 2 with a mean value of 2.79 and relative importance of 0.558. It also shows that the higher management's ability to commit to utilizing the conceptions of total quality management is extensively smaller than the theoretical value (3) for the mean and smaller than 0.7 for relative importance.

5.5. Discussion of the Higher Management's Ability to Commit Utilizing the Conceptions of Total Quality Management When the Company Not Using BIM. From the research conducted and based on the majority of the respondent's judgements, the results prove that there is weak implementation of Total Quality Management concepts for delivering construction projects. The results showed that the higher management's ability to commit to utilizing the conceptions of total quality management is extensively smaller than the theoretical value (3) for the mean, which was calculated at 2.76, and smaller than 0.7 for relative importance, which was calculated to be 0.552.

This reflects on how much of an influential factor TQM concepts can be on the duration, cost, and customer satisfaction in construction projects in Saudi Arabia, wherein not applying TQM concepts can negatively affect a project. Furthermore, this research advocates that when enhancing the activities of the company's quality systems, the administrative work displays inadequacy. The presence of

TABLE 5: Cronbach alpha value for the individual field of the survey.

No.	Subject	Cronbach's alpha
1.	The higher management's ability to commit to applying TQM concepts when the organization uses BIM	0.988
2.	The higher management's ability to commit to applying TQM concepts when the organization does not use BIM	0.970
All items of the questionnaire		0.979

TABLE 6: Kolmogorov-Smirnov assessment.

Subject	Kolmogorov-Smirnov	
	Statistic	p value
The higher management's ability to commit to applying TQM concepts when the organization does not use BIM	0.224	0.897
The higher management's ability to commit to applying TQM concepts when the organization uses BIM	0.250	0.849

TABLE 7: Frequency and percentage of participants occupation.

Job	Frequency	Percent (%)
Company manager	73	37
Site manager	58	29
Site engineer	69	35
Total	200	100

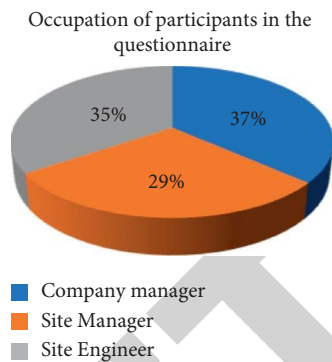


FIGURE 1: Occupation of Participants in the questionnaire.

TABLE 8: Frequency and percentage of experience of participants.

Experience	Frequency	Percent (%)
1-5 years	52	26
5-10 years	67	34
More than 10 years	81	41
Total	200	100

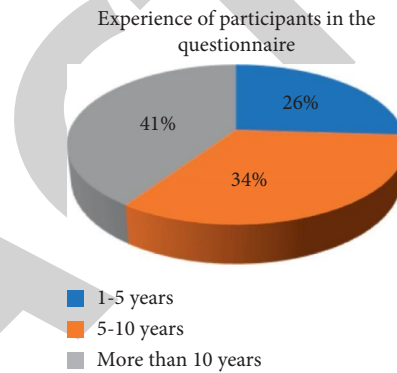


FIGURE 2: Frequency and percentage of experience of participants.

TABLE 9: Frequency and percentage of organization of participants.

Organization	Frequency	Percent (%)
Government	43	22
Consultant	66	33
Contractor	91	46
Total	200	100

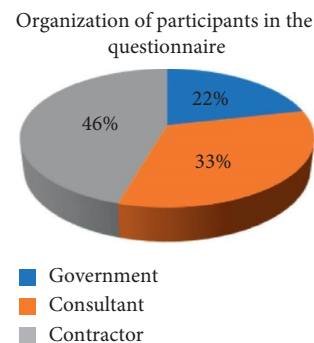


FIGURE 3: Percentage of organization of participants.

inefficiency in setting methods and techniques for reaching a critical observation could assist in guaranteeing that TQM is manipulated in construction projects. All of the aforementioned results prove that the higher management is unable to commit to manipulating the conceptions of total quality management when they do not utilize BIM in construction projects.

5.6. Results of "The Higher Management's Ability to Commit Applying TQM Concepts When the Organization Uses BIM". Table 11 illustrates the mean of the field "the higher management's ability to commit to applying TQM concepts

when the organization uses BIM." The results in the table show that the mean of all the items in this field has a total value of 3.59. Additionally, the proportional mean is calculated to be 71.71%; the relative importance is found to be 0.717; the test value is 0.860; and the p value was calculated to be 0.402, wherein the value is greater than the significance

TABLE 10: The values of the means and test quantity for “the higher management’s ability to commit to applying TQM concepts when the organization does not use BIM.”

No.	Item	Mean	Proportional mean (%)	Relative importance	Test value	<i>p</i> value (sig.)	Rank
1	What is your assessment on the performance of the higher management of engineering projects in Saudi Arabia in applying the concepts of TQM?	2.76	55.16	0.552	-2.537	0.105	3
2	What is your assessment on the performance of the higher management of engineering projects in adhering to time schedule for engineering projects?	2.79	55.81	0.558	-2.031	0.125	1
3	What is your assessment on the performance of the higher management of engineering projects in seeking to enhance project implementation?	2.75	55.00	0.550	-2.544	0.355	4
4	What is your assessment on the performance of the higher management of engineering projects in seeking to cut back on expenses?	2.72	54.35	0.544	-2.781	0.322	5
5	What is your assessment on the performance of the higher management of engineering projects in seeking to satisfy the client?	2.77	55.48	0.555	-2.128	0.098	2
All items of the field		2.76	55.16	0.552	-2.404	0.201	

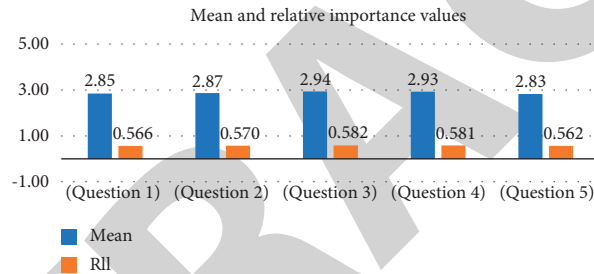


FIGURE 4: Mean and relative importance values of “the higher management’s ability to commit to applying TQM concepts when the organization does not use BIM.”

TABLE 11: The values of the means and test quantity for “the higher management’s ability to commit to applying TQM concepts when the organization uses BIM.”

No.	Item	Mean	Proportional mean (%)	Relative importance	Test value	<i>p</i> value (sig.)	Rank
6.	What is your assessment that BIM application assists the higher management of engineering projects in Saudi Arabia by applying TQM?	3.56	71.13	0.711	0.568	0.571	5
7.	What is your assessment that BIM application assists the higher management of engineering projects to commit to projects schedule?	3.60	72.10	0.721	1.080	0.282	2
8.	What is your assessment on BIM application in assisting the higher management of engineering projects to improve project performance?	3.57	71.45	0.715	0.736	0.463	4
9.	What is your assessment on BIM application in assisting the higher management of engineering projects in seeking to cut back on expenses?	3.61	72.26	0.723	1.126	0.262	1
10.	What is your assessment on BIM application in assisting the higher management of engineering projects in pursuing customer satisfaction?	3.58	71.61	0.716	0.792	0.430	3
All items of the field		3.59	71.71	0.717	0.860	0.402	

level $\alpha = 0.05$. By observing the test value, it is seen that the value was a positive integer, which means that the average of this field is significantly greater than the theoretical value (3) and is larger than the relative importance value. From the questionnaires, the responses showed that the participants

were fond of and accepted the field “the higher management’s ability to commit to applying TQM concepts when the organization uses BIM.”

Moreover, Figure 5 illustrates the questions that obtained the highest and lowest values of mean and relative

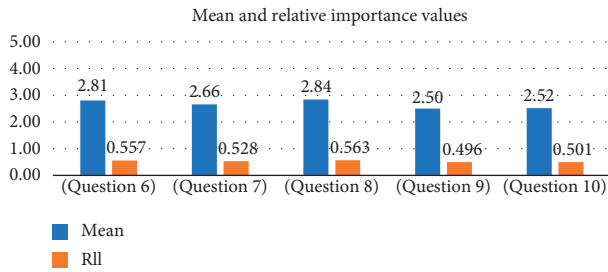


FIGURE 5: Mean and relative importance values of “the higher management’s ability to commit to applying TQM concepts when the organization uses BIM.”

importance. Based on the figure, it is concluded that the question with the largest values is question 9 with a mean of 3.61 and relative importance of 0.723. The question that has the lowest values is question 6, with a mean value of 3.56 and relative importance value of 0.711. Furthermore, it depicts that the mean and relative importance of “the higher management’s ability to commit to applying TQM concepts when the organization uses BIM” is significantly greater than the theoretical value (3) for mean and greater than 0.7 for relative importance.

5.7. Discussion of the Higher Management’s Ability to Commit to Utilizing the Conceptions of Total Quality Management When the Company Uses BIM. The results showed that a large part of the respondents support the question of the engineering departments’ ability to apply the concepts of TQM when utilizing BIM in their companies. The question with the highest value is question 9, “What is your assessment on BIM application in assisting the higher management of engineering projects in seeking to cut back on expenses?” which acquired a mean of 3.61 and relative importance of 0.723.

In addition, the results proved that the companies that applied BIM were capable of adhering to project schedule, cost, and customer satisfaction unlike those companies that do not apply BIM in their projects. Moreover, all the results gathered from this study prove that the higher management is unable to commit to applying TQM concepts when BIM is not used in the construction projects. Hence, the mean and relative importance of “the higher management’s ability to commit to applying TQM concepts when the organization uses BIM” is considerably higher than the theoretical value (3) for the mean that is 3.59 and higher than 0.7 for the relative importance, which is 0.717.

6. Conclusion

Total Quality Management (TQM) represents the management method for continuous success through client satisfaction. By applying the concepts of TQM, operators or project owners are able to adhere to time schedule, meet all the clients’ demands, increase revenues, minimize expenses, and accomplish safety protocols. Moreover, they are able to maintain management and reliability within the

fundamental constraints, which are time, cost, and quality of a project.

The results collected were dependent on the dominance of the respondent’s judgements and showed that applying the TQM concepts when implementing construction projects is inadequate and incomplete, and the higher management cannot commit to applying TQM concepts within projects. The majority of the respondents judged that, within the construction divisions, accomplishing the administrative, scientific, and technical abilities while applying TQM is weak and insufficient. This study proposes that the organizations lack a sufficient committee to manipulate the TQM concept.

The aim of this research was to focus on the significance and assess the influence of TQM application within the construction industry. This was completed by using descriptive and analytical approaches, as well as the SPSS program, the relative importance, and the mean values. The results were gathered by distributing questionnaires to engineering organizations and companies, which discussed the significance of TQM concepts on construction projects in Saudi Arabia [22–24].

Data Availability

The data are available upon request to the corresponding author.

Disclosure

The authors acknowledge that this paper has been submitted as a preprint in Research Square (NOT PEER-REVIEWED) on 17th March 2021.

Conflicts of Interest

The authors declare that they have no conflicts of interest.

References

- [1] M. Abazid, H. Gökçekus, and T. Çelik, “Study of the quality concepts implementation in the construction of projects in Saudi Arabia by using building information modelling (BIM),” *International Journal of Innovative Technology and Exploring Engineering*, vol. 8, no. 3, pp. 84–87, 2019.
- [2] M. Malik, R. Banerjee, and S. Ahmad, “A review paper on implementation of total quality management (TQM) in construction industry,” *International Journal of Recent Scientific Research*, vol. 5, no. 2, pp. 26515–26517, 2018.
- [3] A. Albogamy, D. Scott, and N. Dawood, “Dilemma of Saudi arabian construction industry,” *Journal of Construction Engineering and Project Management*, vol. 3, no. 4, pp. 35–40, 2013.
- [4] S. Nyoman, A. B. Mohammed, Z. Yuri, and S. Isti, “Enhancing the quality of products and projects through better designs and modeling,” *International Journal of Technology*, vol. 6, no. 5, pp. 718–721, 2015.
- [5] M. A. Berawi, “Managing technology towards sustainable products and services,” *International Journal of Technology*, vol. 6, no. 2, pp. 105–108, 2015.

Retraction

Retracted: Graphene: A Multifunctional Nanomaterial with Versatile Applications

Advances in Materials Science and Engineering

Received 26 December 2023; Accepted 26 December 2023; Published 29 December 2023

Copyright © 2023 Advances in Materials Science and Engineering. This is an open access article distributed under the Creative Commons Attribution License, which permits unrestricted use, distribution, and reproduction in any medium, provided the original work is properly cited.

This article has been retracted by Hindawi, as publisher, following an investigation undertaken by the publisher [1]. This investigation has uncovered evidence of systematic manipulation of the publication and peer-review process. We cannot, therefore, vouch for the reliability or integrity of this article.

Please note that this notice is intended solely to alert readers that the peer-review process of this article has been compromised.

Wiley and Hindawi regret that the usual quality checks did not identify these issues before publication and have since put additional measures in place to safeguard research integrity.

We wish to credit our Research Integrity and Research Publishing teams and anonymous and named external researchers and research integrity experts for contributing to this investigation.

The corresponding author, as the representative of all authors, has been given the opportunity to register their agreement or disagreement to this retraction. We have kept a record of any response received.

References

- [1] H. C. A. Murthy, S. Ghotekar, B. Vinay Kumar, and A. Roy, "Graphene: A Multifunctional Nanomaterial with Versatile Applications," *Advances in Materials Science and Engineering*, vol. 2021, Article ID 2418149, 8 pages, 2021.

Review Article

Graphene: A Multifunctional Nanomaterial with Versatile Applications

H. C. Ananda Murthy ¹, Suresh Ghotekar ², B. Vinay Kumar ³, and Arpita Roy ⁴

¹Department of Applied Chemistry, School of Applied Natural Science, Adama Science and Technology University, Adama, P.O. Box. 1888, Ethiopia

²Department of Chemistry, Smt. Devkiba Mohansinhji Chauhan College of Commerce and Science College, Silvassa 396 230, Dadra and Nagar Haveli (UT), India

³Department of Chemistry, RNS Institute of Technology, Uttarahalli-Kengeri Main Road, Channasandra, Bengaluru 560098, Karnataka, India

⁴Department of Biotechnology, School of Engineering & Technology, Sharda University, Greater Noida, India

Correspondence should be addressed to H. C. Ananda Murthy; anandkps350@gmail.com

Received 12 November 2021; Accepted 7 December 2021; Published 24 December 2021

Academic Editor: Palanivel Velmurugan

Copyright © 2021 H. C. Ananda Murthy et al. This is an open access article distributed under the Creative Commons Attribution License, which permits unrestricted use, distribution, and reproduction in any medium, provided the original work is properly cited.

Graphene is a 2D material of high quality obtained from a single atom with unique electronic properties. Graphene has the potential to improve the efficiency, versatility, and durability of a wide range of materials and their applications, but its commercial exploitation will require further study. Due to its flatness and semiconductivity in addition to its high surface area, high mechanical rigidity, high thermal stability, superior thermal conductivity, and electrical conductivity, good biocompatibility, and easy functionalization, graphene is the best candidate for multifunctional applications which opened up new possibilities for potential devices and systems. Every type of graphene material is found to exhibit different and unique tunable properties. Graphene is the best candidate in making nanocomposite-based electrochemical sensors. Graphene is among the best electronic materials, but synthesizing a single sheet of graphene has received less attention. The objective of this chapter is to bring awareness to readers on the synthesis, properties, and applications of graphene. The limitations of the current knowledge base and prospective research directions related to graphene materials have also been illustrated.

1. Introduction

Graphene has received a lot of attention as a multifunctional material in the recent years which is possibly due to its extraordinary properties such as high current density, chemical stability, ballistic transport, optical property, high thermal conductivity, and superior hydrophobicity at the nanoscale. A method known as micromechanical cleavage was used to remove the first graphene from graphite. This method appears to be very simple and made it possible to make superior quality graphene crystallites, which led to a slew of new experiments [1–4]. Intrinsic graphene material is a semimetal or zero gap semiconductor with excellent opacity for an atomic monolayer low absorption ratio of

2.3% of visible light due to its peculiar electronic properties. It has also been explored that the resistivity of the graphene sheet is superior to that of platinum, the lowest resistivity material known at room temperature. The electrical properties of graphene nanoribbons (GNRs) with zigzag or armchair configurations differ; zigzag GNRs exhibit metallic nature, whereas armchairs behave as either metallic or semiconductor. The energy band gap of armchair GNRs' was found to vary inversely with their width [5, 6].

The unique electrical properties possessed by graphene have been utilized in applications related to electronics such as transistors, field emitters, integrated circuit modules, transparent conducting electrodes, and electrochemical and biosensors. Many types of graphene materials such as single

and multilayer graphene, graphene oxide (GO), reduced graphene oxide (rGO), and graphene quantum dots (GQDs) have been applied for the fabrication of varieties of electrochemical and biosensor applications. Since graphene exhibits a high electron (or hole) mobility and low Johnson noise, it can be used as a field effect transistor tube (FET). Because of its 2D structure, its entire volume is exposed to the environment, making it very effective at detecting adsorbed molecules. In addition, graphene also finds applications in touch screens, displays, organic photovoltaic cells, and organic light-emitting diodes (OLEDs) [6]. The majority of the abovementioned intriguing applications have created a great demand for a single-layer graphene decorated on a suitable substrate, which is extremely difficult to monitor and has yet to be achieved. Many reports on graphene synthesis are available, with the majority of them relying on mechanical exfoliation from graphite, thermal graphitization of a SiC surface, and more recently, chemical vapor deposition [7–13]. This chapter starts with a brief description of the significant properties of graphene, followed by a review on the synthesis technologies, as well as their feasibility and possible applications in fields such as field emission, energy, electronics, photocatalysis, and sensors. The superior properties of modified graphene materials, such as higher surface area and availability of functional groups at the surface compared to CNTs, make them apply for enormous electrochemical sensor arrays.

2. Properties of Graphene

Graphene is a type of carbon nanomaterial that is considered advanced. It is a two-dimensional solitary carbon atom sheet. Figure 1 shows how carbon atoms are arranged in a hexagonal network. This historical material was synthesised in the year 2004 using the scotch tape peeling method [14]. Graphene can also be visualized as a single layer of carbon atoms arranged in the form of a hexagonal 3D lattice, as previously described. The versatile atomic structure of graphene can be used to create other carbon-based materials/nanomaterials. The sheet can also be twisted into fullerenes, nanotubes, and graphite by stacking it [15].

The conducting properties of graphene are also significantly influenced by the symmetry orientation of $2p_z$ orbitals [16–18]. Acoustic phonons are the reason for the thermal conductivity of solitary layer graphene under ambient conditions [19]. This thermal conductivity occurs due to the absence of a crystal defect and the suppression of the Umklapp processes [20]. These factors contribute to the future importance of graphene in the production of nano-electric devices [21]. At the microscopic level, graphene crystals are normally well preserved and very stable [22]. These properties of graphene lead to its excellent heat conduction (Figure 2). They are regarded as a high-strength material in terms of mechanical properties. The yield power of graphene is 42 N/m. They have a mechanical strain of about 25% [24]. Mechanical stress measurements can also be used to monitor their mechanical thickness [21, 25]. As previously mentioned, graphene is made of one atom thick two-dimensional layer of carbon. These features, along with

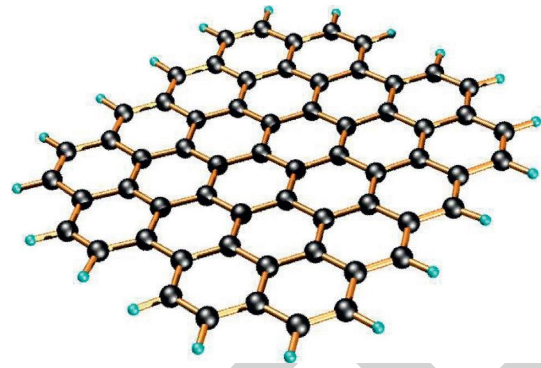


FIGURE 1: The structure of graphene.

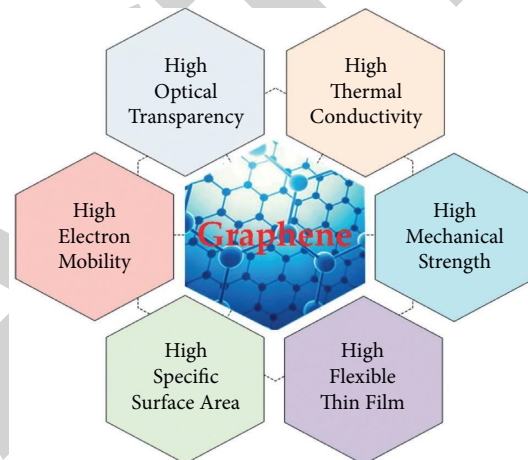


FIGURE 2: Properties of graphene [23].

the fact that they are a component of sp^2 , distinguish them from carbon materials. The presence of a large surface area is one of these properties [26–28]. Graphene is also fully transparent; in terms of physical properties, it is thinner million times than a sheet of paper. In terms of thickness, it can be understood that a million sheets of paper are equal to 1 mm of graphene.

3. Synthesis of Graphene

The graphene synthesis process is determined by the size and purity of the final product. Until the end of 1970s, several methods for synthesizing thin graphitic films were used [29–31] (Figure 3). In 1975, chemical deposition was used to create smaller graphite layers. However, since it was difficult to classify the material at the time and it was not needed for many applications, this material was not classified as graphene. Other aspects of the materials, such as their electronic properties, were not studied at the time [32]. Ruoff et al. investigated the possibility of isolating thin graphite flakes on SiO_2 substrates in 1990s. In this work, researchers used highly oriented pyrolytic graphite to rub the patterned island [33]. The inquiry was unable to obtain detailed information on the material's electrical property characterization. Kim et al. used the same approach in their investigation in the year 2005, and the electrical characteristics of graphene was

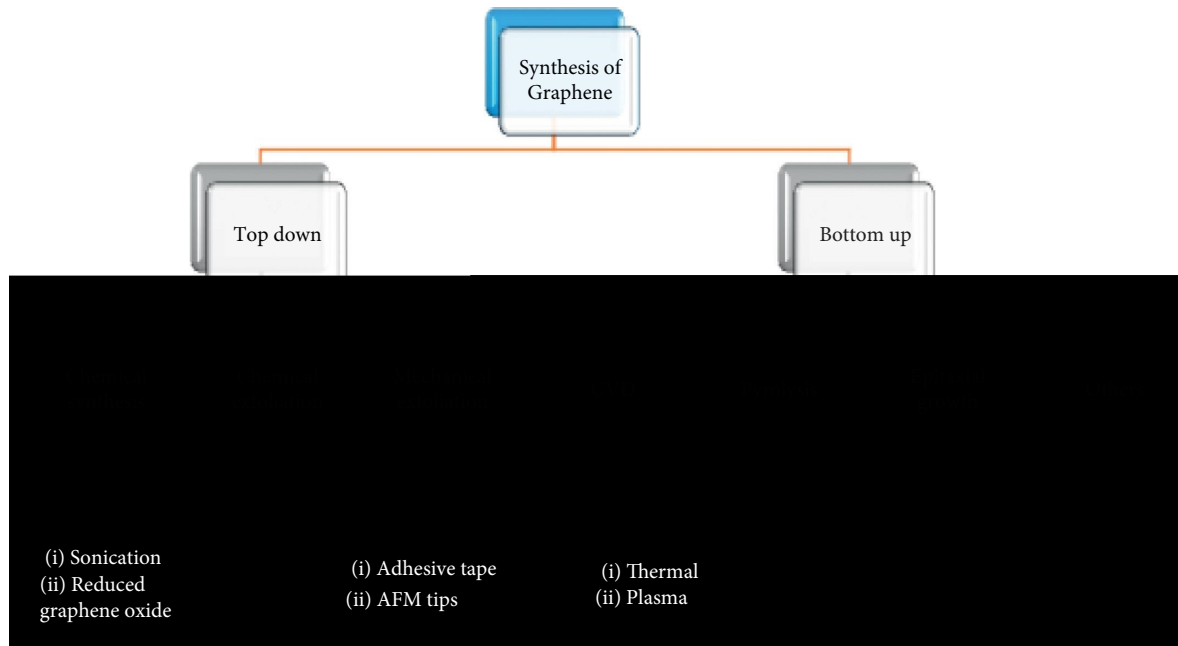


FIGURE 3: A schematic on various synthetic methods for graphene.

captured in their findings [32]. Geim et al. [34] conducted an investigation that resulted in a ground-breaking finding. Their research focused on the decoration of graphene on a SiO_2 substrate as well as the measurement of electrical properties. Since 2015, a variety of methods for producing graphitic films and graphene layers have been used. Graphene was discovered to be a two-dimensional crystal in an experiment performed in 2004. A decade ago, mechanical exfoliation of graphite produced the first type of graphene in the form of flakes [35]. Although the graphene generated using these methods is of superior quality, there are practical challenges in scaling up the mass production due to the need for a fabrication process to break down wafer scale graphene. Mechanical exfoliation, chemical exfoliation [36], chemical synthesis [8, 12], and thermal chemical vapor deposition (CVD) [37–40] are all methods that have been used in the past. Other techniques include unzipping nanotubes [41, 42] and microwave synthesis. Mechanical exfoliation with a cantilever has been shown to produce layered graphene in recent studies [43–48]. The graphene thickness ranged from 10 nm to 30 nm, which is comparable to a 30-layer graphene. In the chemical exfoliation process, solution dispersed graphite is exfoliated by introducing strong alkali ions into the layers of the graphite [49]. Breakdown of graphite oxide, diffusion in a solution, and the use of hydrazine are all part of the chemical synthesis of graphene. Separate processes are also involved in the amalgamation of nanotubes. The thermal CVD method has been shown to be the best method for producing graphene. PECVD or enhanced CVD is a process that involves plasma-assisted development. Many of these approaches have advantages and disadvantages. The use of a mechanical exfoliation technique will aid in the fabrication of single and fewer layers of graphene. The generation of same structure of graphene with this technique would be the key challenge [50–54].

The chemical synthesis technique is carried out at low temperatures, making it easier to fabricate graphene on various substrates at room temperatures; however, most of the times, the graphene formed under these conditions is not uniform and dispersed. Graphene synthesis can also be achieved by reduced graphene oxides (RGOs) which results in a graphite oxide reduction process that is inadequate. This raises more concerns about its electrical properties. Thermal chemical vapor deposition is also suitable for fabricating large-area devices [55–58]. The thermal graphitization of SiC results in the development of epitaxial graphene, which is another method for graphene synthesis. However, the main disadvantage of this method is that it is carried out at high temperatures. This distinguishes the thermal CVD method because it creates a constant layer of catalyzed carbon atoms. After that, the atoms can be fixed to the metal surface. Graphene is made using a variety of techniques (Table 1).

Table 1 presents the synthetic methods for various forms of graphene such as nanosheets, aerogel, quantum dots [69], and nanoribbons.

4. Applications of Graphene

Graphene has been applied for multifunctional applications in the recent years (Figure 4). The following sections details the various applications of graphene, with an emphasis on its use in energy storage and conversion devices.

4.1. Electrochemical Sensors. The qualitative and quantitative detection of trace targets is possible with graphene. Because of the large pores, analyte transport is increased, which aids in the identification of binding targets. As graphene can be functionalized for the direct sensing systems and useful biological moieties can be detected at lower concentrations,

TABLE 1: Diverse approaches for the synthesis of graphene with their applications.

Methods	Precursor	Morphology	Applications	Reference
Chemical vapor deposition (CVD)	Cu foil	Monolayer	Hydrogen sensing	[59]
Ultrasonic synthesis	Graphene oxide	Quantum dots	Sensing of alkaline phosphatase	[60]
Electrochemical reduction	Graphene oxide	Nanosheet	Electrocatalysis of dopamine	[61]
Electron-beam irradiation	1,3,6-Trinitropyrene	Quantum dots	Cell imaging	[62]
Suzuki coupling reaction	Polymers	Nanoribbons	Thin-film transistor	[23]
Green synthesis	Corn powder	Quantum dots	Photocatalysis	[63]
Sol-gel	Graphene oxide	Aerogel	Electrical conductivity	[64]
Exfoliation approach	Graphite	Nanosheet	Electrochemical sensing of H ₂ O ₂	[65]
CVD	Cu foil	Quantum dots	Phototransistor application	[66]
Lithography	Graphite	Nanoribbons	Field effect transistor	[67]
Arc discharge method	Graphite	Nanosheet	Electrical properties	[68]

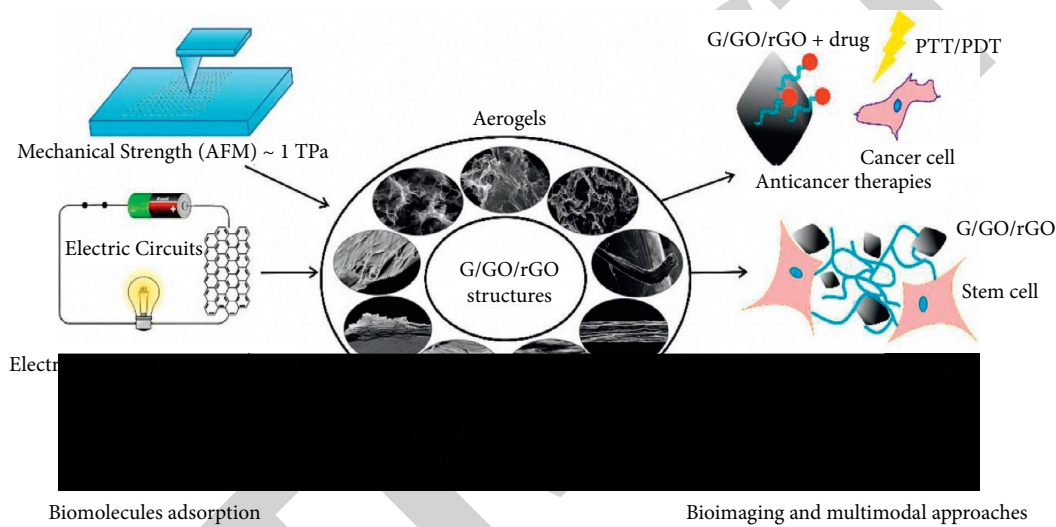


FIGURE 4: Multifunctional applications of graphene/graphene structure [62].

to improve the efficiency of graphene in making better electrochemical sensor in terms of functionality and applicability, surface modification with suitable functional groups, molecules, biomolecules, or nanomaterials necessary in the fabrication of different electrochemical sensors, it was shown in some reports that the functionalization of graphene oxide can be accomplished via the formation of amide linkage between GO sheet edges and organic molecules, for example, *p*-amino thiophenol, polyethyleneimine, or imidazole under mild conditions [69].

4.2. Composite Materials. In composites, graphene is used as a functional element, which improves the composite's properties and efficiency. When graphene is mixed with composites that have strong elasticity, strength, and porosity, it has a positive effect. Compression increases the power of certain graphene. Under cross-linked conditions, this type of graphene exhibits high compression. These graphene materials are suitable for reinforcing polymer matrices because of their spongy composition. It means that graphene matrices have a high strength, hydrophobicity, and conductivity [70].

4.3. Energy Storage Devices. Graphene is really a great material for making energy storage systems. This is particularly true when they have been treated with metal oxide, resulting in minimal sheet restacking. The fact that graphene's interconnected networks are highly conductive adds to the appeal of graphene as an energy storage material. Other advantages of graphene as energy storage devices include their porous microstructure, electrochemical stability, and mechanical stability. These devices can be used in fuel cells, solar cells, batteries, and supercapacitors, among other applications. Graphene is commonly used as anodic and cathodic material in proton exchange membrane (PEM) fuel cells, in batteries such as Li batteries. Graphene finds application as electrode material in both double layer capacitors and pseudocapacitors in supercapacitors. It is also used as dye sensitizers in fuel cells [71].

4.4. Adsorbents. The surface area of three-dimensional graphene is very large. They are suitable for absorption events due to their characteristics. In contrast to other materials, graphene has a strong take-up for organic liquids and is also reusable. Graphene sheets have been shown to adsorb certain gases at the lower concentrations once again.

Also in the industry, graphene's functional group is also capable of reducing gas exposure for trapping and converting unwanted gases [72].

4.5. Drug Delivery. In the last few years, graphene has been widely investigated as a unique drug nanocarrier for the loading of a variety of treatments, including anticancer medications, antibiotics, poorly soluble pharmaceuticals, antibodies, genes, DNA, RNA, and peptides [73, 74]. Selected examples from this study will be provided to demonstrate the use of graphene for targeted, controlled, and stimulated drug delivery, including certain anticancer and gene therapy applications. Conjugating drug carriers with particular ligands that can recognize molecular markers on the cancer cell surface is a well-known technique for achieving effective tumor targeting. Peptides, folic acid, polysaccharides, transferrin, and monoclonal antibodies are examples of targeting ligands that are being investigated using graphene as drug nanocarriers for cancer therapy [75, 76].

Wang et al. [77] synthesized a gold nanocluster and graphene nanocomposite and showed that it could inhibit HepG2 cells at high concentrations, transport DOX inside the cells, and induce karyopyknosis in a synergistic manner.

Iannazzo et al. proposed combining graphene quantum dots with biotin (GQD-BTN) to boost the anticancer effect of graphene quantum dots (GQD) [78]. DOX loaded on GQD-BTN was found to suppress A549 cell growth more effectively than DOX or GQD-BTN alone. GQD-BTN appears to transfer DOX more efficiently into cells than free DOX.

Under low-power NIR laser irradiation, Yang et al. [79] observed that the PEGylated graphene nanosheets (GNS) themselves had ultrahigh *in vivo* tumor uptake and efficient photothermal treatment capabilities in mice. Following that, Markovic et al. [80] compared the photothermal anticancer activity of graphene nanoparticles and carbon nanotubes (CNT) and revealed that, despite its lower NIR-absorbing capacity, a suspension of polyvinylpyrrolidone-coated graphene sheets exposed to NIR radiation generated more heat than DNA or sodium dodecylbenzenesulfonate-solubilized single-wall CNTs under the same.

Pan et al. [81] used click chemistry to functionalize graphene sheets (GS) with poly (N-isopropylacrylamide) (PNIPAM). After 72 h at 37°C in water and PBS, the PNIPAM-GS had a greater ability to bind CPT with a high loading ratio of CPT.

Improved surface chemistry and graphene functionalization are necessary to accomplish effective goals. Furthermore, the unique features of graphene-based materials and their hybrids are likely to provide resources for enhanced gene delivery vector design in the future.

5. Future Perspective

Graphene's benefits are among the core merits of its use in a variety of energy storage and conversion applications. The recent technical advancements in the synthesis,

characterization, and modern-day applications of these advanced materials were extensively investigated in this investigation. Today, 3D graphene structures have been developed that have shown to be as good as 2D graphene in terms of efficiency. The aim of this study was to find new ways to synthesize graphene in order to improve its quality and efficiency. CVD is one of these methods, and it often results in the formation of larger pore structures with good conductivity. Using this technique, the material's consistency is greatly improved. There are also increasing questions about the approach's scalability. The size and consistency of the precursor have an equal impact on the characteristics and efficiency of graphene. The quality and size of the precursor, the type of reducing agent, cross linkers, and pH, all of them play a role in the sponges' strength. Again, the strength of graphene sponges must be greatly enhanced in order to manufacture them on a large scale. Another interesting path for research in this field is to investigate the adoption of new techniques aimed at improving intersheet binding. These characteristics can be achieved by combining graphene sponges with elastic polymers.

Many research activities are currently being conducted to explore the futuristic application of graphene materials in a variety of multifunctional systems. This chapter looked at graphene's suitability for electrochemical and non-electrochemical applications. The advantages of graphene over other carbon allotropes were also discussed. Some of these advantages include a large surface area, ease of synthesis, high conductivity, solubility, and a low-cost material source. There has been a lot of technical progress, but there is still space for development in both electroanalytical and electrochemical sensors. Some of the material's problems, such as its ease of synthesis, must be tackled. The design and methodology used in the manufacture of graphene-based devices are also important for the material's potential advancement. Despite the challenges listed, graphene applications in electrochemical sensors remain the most promising future development of graphene.

6. Conclusions

The multifunctional graphene exhibits many numbers of benefits, even though it has several drawbacks. Further modification of graphene material is inevitable to explore its commercialization and compete with other prominent materials already on the market. Most of the graphene sponges considered in this study are still on a small scale, and despite being flexible and elastic, these sponges are easily damaged, leading researchers to label them as fragile when not treated properly. The future research on graphene materials should focus on the methods that can produce improved intersheet binding and composites that are flexible and tear resistant. This can be accomplished by using elastic polymers, as well as changing the fibrous material or optimizing the structure's crosslink agents. The size of the furnace, as well as defects in the sheets, reduces the scale of template growth techniques. More research can be done in order to create a furnace design that can support more

layers. For commercial applications, graphene sponges made by dry and self-assembly methods need a freeze-drying process. Other factors may also prevent the sponge structure from adhering. In future studies, the characterization of graphene precursors must be looked into further to make it easier to detect changes in binding forces, especially during compositing and sponge formation. The use of concentrated acid, as well as variable sheet sizes and functionality, limits the commercial processing of graphene. In the quest to commercialize graphene, regulated surface functionalization of graphene sheets obtained from the exfoliation of graphite must also be considered as an advanced research path. It is also necessary to look into the need for template support. In order to overcome the challenges, above-described features in terms of graphene sponge, further research will be needed. The use of three-dimensional graphene and graphene oxide in many applications is the future, so it must be critically considered in the future study.

Data Availability

The data used to support the findings of this study are included within the article.

Conflicts of Interest

The authors declare that they have no conflicts of interest.

Acknowledgments

The authors are grateful to the support rendered by Adama Science and Technology University, Ethiopia.

References

- [1] J.-H. Chen, C. Jang, S. Xiao, M. Ishigami, and M. S. Fuhrer, "Intrinsic and extrinsic performance limits of graphene devices on SiO₂," *Nature Nanotechnology*, vol. 3, no. 4, pp. 206–209, 2008.
- [2] A. K. Geim and P. Kim, "Carbon wonderland," *Scientific American*, vol. 298, no. 4, pp. 90–97, 2008.
- [3] K. S. Novoselov, A. K. Geim, S. V. Morozov et al., "Electric field effect in atomically thin carbon films," *Science*, vol. 306, no. 5696, pp. 666–669, 2004.
- [4] M. I. Katsnelson, "Graphene: carbon in two dimensions," *Materials Today*, vol. 10, no. 1-2, pp. 20–27, 2007.
- [5] A. B. Kuzmenko, E. Van Heumen, F. Carbone, and D. Van Der Marel, "Universal optical conductance of graphite," *Physical Review Letters*, vol. 100, no. 11, Article ID 117401, 2008.
- [6] A. K. Geim and K. S. Novoselov, "The rise of graphene," *Nature Materials*, vol. 6, pp. 183–191, 2010.
- [7] H. Shioyama, H. Sakakihara, N. Iwashita, K. Tatsumi, and Y. Sawada, "On the generation of fine metallic particles in graphite matrix," *Journal of Materials Science Letters*, vol. 13, no. 14, pp. 1056–1057, 1994.
- [8] L. M. Viculis, J. J. Mack, and R. B. Kaner, "A chemical route to carbon n," *Science*, vol. 299, no. 5611, p. 1361, 2003.
- [9] C. Berger, Z. Song, T. Li et al., "Ultrathin epitaxial graphite: 2D electron gas properties and a route toward graphene-based nanoelectronics," *The Journal of Physical Chemistry B*, vol. 108, no. 52, pp. 19912–19916, 2004.
- [10] T. A. Land, T. Michely, R. J. Behm, J. C. Hemminger, and G. Comsa, "STM investigation of single layer graphite structures produced on Pt(111) by hydrocarbon decomposition," *Surface Science*, vol. 264, no. 3, pp. 261–270, 1992.
- [11] A. Nagashima, K. Nuka, H. Itoh, T. Ichinokawa, C. Oshima, and S. Otani, "Electronic states of monolayer graphite formed on TiC (111) surface," *Surface Science*, vol. 291, no. 1-2, pp. 93–98, 1993.
- [12] A. Reina, X. Jia, J. Ho et al., "Large area, few-layer graphene films on arbitrary substrates by chemical vapor deposition," *Nano Letters*, vol. 9, no. 1, pp. 30–35, 2009.
- [13] C. N. R. Rao, K. Biswas, K. S. Subrahmanyam, and A. Govindaraj, "Graphene, the new nanocarbon," *Journal of Materials Chemistry*, vol. 19, no. 17, pp. 2457–2469, 2009.
- [14] A. H. Castro Neto, F. Guinea, N. M. R. Peres, K. S. Novoselov, and A. K. Geim, "The electronic properties of graphene," *Reviews of Modern Physics*, vol. 81, no. 1, pp. 109–162, 2009.
- [15] J. Hass, W. A. De Heer, and E. H. Conrad, "The growth and morphology of epitaxial multilayer graphene," *Journal of Physics: Condensed Matter*, vol. 20, no. 32, Article ID 323202, 2008.
- [16] Z. H. Ni, H. M. Wang, J. Kasim et al., "Graphene thickness determination using reflection and contrast spectroscopy," *Nano Letters*, vol. 7, no. 9, pp. 2758–2763, 2007.
- [17] K. S. Kim, Y. Zhao, H. Jang et al., "Large-scale pattern growth of graphene films for stretchable transparent electrodes," *Nature*, vol. 457, no. 7230, pp. 706–710, 2009.
- [18] M. I. Katsnelson, K. S. Novoselov, and A. K. Geim, "Chiral tunnelling and the Klein paradox in graphene," *Nature Physics*, vol. 2, no. 9, pp. 620–625, 2006.
- [19] J. S. Bunch, A. M. Van Der Zande, S. S. Verbridge et al., "Electromechanical resonators from graphene sheets," *Science*, vol. 315, no. 5811, pp. 490–493, 2007.
- [20] C. Lee, X. Wei, J. W. Kysar, and J. Hone, "Measurement of the elastic properties and intrinsic strength of monolayer graphene," *Science*, vol. 321, no. 5887, pp. 385–388, 2008.
- [21] A. Sakhaee-Pour, "Elastic properties of single-layered graphene sheet," *Solid State Communications*, vol. 149, no. 1-2, pp. 91–95, 2009.
- [22] H. Chen, M. B. Müller, K. J. Gilmore, G. G. Wallace, and D. Li, "Mechanically strong, electrically conductive, and biocompatible graphene paper," *Advanced Materials*, vol. 20, no. 18, pp. 3557–3561, 2008.
- [23] K. T. Kim, J. W. Jung, and W. H. Jo, "Synthesis of graphene nanoribbons with various widths and its application to thin-film transistor," *Carbon*, vol. 63, pp. 202–209, 2013.
- [24] K. S. Novoselov, E. McCann, S. V. Morozov et al., "Unconventional quantum Hall effect and Berry's phase of 2π in bilayer graphene," *Nature Physics*, vol. 2, no. 3, pp. 177–180, 2006.
- [25] E. McCann, "Asymmetry gap in the electronic band structure of bilayer graphene," *Physical Review B*, vol. 74, no. 16, Article ID 161403, 2006.
- [26] S. Y. Zhou, G.-H. Gweon, A. V. Fedorov et al., "Substrate-induced bandgap opening in epitaxial graphene," *Nature Materials*, vol. 6, no. 10, pp. 770–775, 2007.
- [27] J. Hass, F. Varchon, J. E. Millán-Otoya et al., "Why multilayer graphene on 4H-SiC(0001) behaves like a single sheet of graphene," *Physical Review Letters*, vol. 100, no. 12, Article ID 125504, 2008.
- [28] D. C. Elias, R. R. Nair, T. M. G. Mohiuddin et al., "Control of graphene's properties by reversible hydrogenation: evidence for graphane," *Science*, vol. 323, no. 5914, pp. 610–613, 2009.

- [29] R. R. Nair, P. Blake, A. N. Grigorenko et al., "Fine structure constant defines visual transparency of graphene," *Science*, vol. 320, no. 5881, p. 1308, 2008.
- [30] M. Nayfeh, Ed., *Fundamentals and Applications of Nano Silicon in Plasmonics and Fullerenes*, pp. 287–309, Elsevier, 2008.
- [31] M. Eisenberg and J. Blakely, "Carbon interaction with nickel surfaces—monolayer formation and structure stability," *The Journal of Chemical Physics*, vol. 71, pp. 3467–3477, 1979.
- [32] Y. Zhang, J. P. Small, W. V. Pontius, and P. Kim, "Fabrication and electric-field-dependent transport measurements of mesoscopic graphite devices," *Applied Physics Letters*, vol. 86, no. 7, Article ID 073104, 2005.
- [33] X. Lu, M. Yu, H. Huang, and R. S. Ruoff, "Tailoring graphite with the goal of achieving single sheets," *Nanotechnology*, vol. 10, no. 3, pp. 269–272, 1999.
- [34] K. S. Novoselov, D. Jiang, F. Schedin et al., "Two-dimensional atomic crystals," *Proceedings of the National Academy of Sciences*, vol. 102, no. 30, pp. 10451–10453, 2005.
- [35] H. P. Boehm, R. Setton, and E. Stumpp, "Nomenclature and terminology of graphite intercalation compounds (IUPAC Recommendations 1994)," *Pure and Applied Chemistry*, vol. 66, no. 9, pp. 1893–1901, 1994.
- [36] M. J. Allen, V. C. Tung, and R. B. Kaner, "Honeycomb carbon: a review of graphene," *Chemical Reviews*, vol. 110, no. 1, pp. 132–145, 2010.
- [37] H. C. Ananda Murthy, K. Gebremedhn Kelele, C. R. Ravikumar, H. P. Nagaswarupa, A. Tadesse, and T. Desalegn, "Graphene-supported nanomaterials as electrochemical sensors: a mini review," *Results in Chemistry*, vol. 3, Article ID 100131, 2021.
- [38] X. Wang, H. You, F. Liu et al., "Large-scale synthesis of few-layered graphene using CVD," *Chemical Vapor Deposition*, vol. 15, no. 1-3, pp. 53–56, 2009.
- [39] Y. Wang, X. Chen, Y. Zhong, F. Zhu, and K. P. Loh, "Large area, continuous, few-layered graphene as anodes in organic photovoltaic devices," *Applied Physics Letters*, vol. 95, p. 209, 2009.
- [40] S. J. Chae, K. K. Kim, E. S. Kim et al., "Synthesis of large-area graphene layers on poly-nickel substrate by chemical vapor deposition: wrinkle formation," *Advanced Materials*, vol. 21, no. 22, pp. 2328–2333, 2009.
- [41] D. V. Kosynkin, A. L. Higginbotham, A. Sinitskii et al., "Longitudinal unzipping of carbon nanotubes to form graphene nanoribbons," *Nature*, vol. 458, no. 7240, pp. 872–876, 2009.
- [42] P. Sutter, "How silicon leaves the scene," *Nature Materials*, vol. 8, no. 3, pp. 171–172, 2009.
- [43] W. Zhang, J. Cui, C.-A. Tao et al., "A strategy for producing pure single-layer graphene sheets based on a confined self-assembly approach," *Angewandte Chemie*, vol. 121, no. 32, pp. 5978–5982, 2009.
- [44] E. Dervishi, Z. Li, F. Watanabe et al., "Large-scale graphene production by RF-cCVD method," *Chemical Communications*, no. 27, pp. 4061–4063, 2009.
- [45] C.-a. Di, D. Wei, G. Yu, Y. Liu, Y. Guo, and D. Zhu, "Patterned graphene as source/drain electrodes for bottom-contact organic field-effect transistors," *Advanced Materials*, vol. 20, no. 17, pp. 3289–3293, 2008.
- [46] N. Li, Z. Wang, K. Zhao, Z. Shi, Z. Gu, and S. Xu, "Large scale synthesis of N-doped multi-layered graphene sheets by simple arc-discharge method," *Carbon*, vol. 48, no. 1, pp. 255–259, 2010.
- [47] S. Karmakar, N. V. Kulkarni, A. B. Nawale et al., "A novel approach towards selective bulk synthesis of few-layer graphenes in an electric arc," *Journal of Physics D: Applied Physics*, vol. 42, no. 11, Article ID 115201, 2009.
- [48] M. C. Bayisa and H. C. Ananda Murthy, "Effect of reinforcement of reduced graphene oxide on Mechanical Properties of Concrete nanocomposite," *Journal of Materials and Environmental Science*, vol. 11, no. 6, pp. 844–855, 2020.
- [49] W. A. De Heer, C. Berger, X. Wu et al., "Epitaxial graphene," *Solid State Communications*, vol. 143, no. 1-2, pp. 92–100, 2007.
- [50] A. Mattausch and O. Pankratov, "Density functional study of graphene overlayers on SiC," *Physica Status Solidi (B)*, vol. 245, no. 7, pp. 1425–1435, 2008.
- [51] Z. H. Ni, W. Chen, X. F. Fan et al., "Raman spectroscopy of epitaxial graphene on a SiC substrate," *Physical Review B*, vol. 77, no. 11, Article ID 115416, 2008.
- [52] P. W. Sutter, J.-I. Flege, and E. A. Sutter, "Epitaxial graphene on ruthenium," *Nature Materials*, vol. 7, no. 5, pp. 406–411, 2008.
- [53] T. Seyller, A. Bostwick, K. V. Emtsev et al., "Epitaxial graphene: a new material," *Physica Status Solidi (B)*, vol. 245, no. 7, pp. 1436–1446, 2008.
- [54] M. Sprinkle, P. Soukiassian, W. A. De Heer, C. Berger, and E. H. Conrad, "Epitaxial graphene: the material for graphene electronics," *Physica Status Solidi (RRL) - Rapid Research Letters*, vol. 3, no. 6, pp. A91–A94, 2009.
- [55] A. Hirsch, "Unzipping carbon nanotubes: a peeling method for the formation of graphene nanoribbons," *Angewandte Chemie International Edition*, vol. 48, no. 36, pp. 6594–6596, 2009.
- [56] C.-D. Kim, B.-K. Min, and W.-S. Jung, "Preparation of graphene sheets by the reduction of carbon monoxide," *Carbon*, vol. 47, no. 6, pp. 1610–1612, 2009.
- [57] A. B. Bourlinos, V. Georgakilas, R. Zboril, T. A. Steriotis, and A. K. Stubos, "Liquid-phase exfoliation of graphite towards solubilized graphenes," *Small*, vol. 5, no. 16, pp. 1841–1845, 2009.
- [58] Y. Hernandez, V. Nicolosi, M. Lotya et al., "High-yield production of graphene by liquid-phase exfoliation of graphite," *Nature Nanotechnology*, vol. 3, no. 9, pp. 563–568, 2008.
- [59] M. Li, D. Liu, D. Wei, X. Song, D. Wei, and A. T. S. Wee, "Controllable synthesis of graphene by plasma-enhanced chemical vapor deposition and its related applications," *Advanced Science*, vol. 3, no. 11, Article ID 1600003, 2016.
- [60] Y. Zhu, G. Wang, H. Jiang, L. Chen, and X. Zhang, "One-step ultrasonic synthesis of graphene quantum dots with high quantum yield and their application in sensing alkaline phosphatase," *Chemical Communications*, vol. 51, no. 5, pp. 948–951, 2015.
- [61] H.-L. Guo, X.-F. Wang, Q.-Y. Qian, F.-B. Wang, and X.-H. Xia, "A green approach to the synthesis of graphene nanosheets," *ACS Nano*, vol. 3, no. 9, pp. 2653–2659, 2009.
- [62] L. Wang, W. Li, B. Wu, Z. Li, D. Pan, and M. Wu, "Room-temperature synthesis of graphene quantum dots via electron-beam irradiation and their application in cell imaging," *Chemical Engineering Journal*, vol. 309, pp. 374–380, 2017.
- [63] H. Teymourinia, M. Salavati-Niasari, O. Amiri, and H. Safardoust-Hojaghan, "Synthesis of graphene quantum dots from corn powder and their application in reduce charge recombination and increase free charge carriers," *Journal of Molecular Liquids*, vol. 242, pp. 447–455, 2017.

Retraction

Retracted: Using Depth Cameras for Recognition and Segmentation of Hand Gestures

Advances in Materials Science and Engineering

Received 26 December 2023; Accepted 26 December 2023; Published 29 December 2023

Copyright © 2023 Advances in Materials Science and Engineering. This is an open access article distributed under the Creative Commons Attribution License, which permits unrestricted use, distribution, and reproduction in any medium, provided the original work is properly cited.

This article has been retracted by Hindawi, as publisher, following an investigation undertaken by the publisher [1]. This investigation has uncovered evidence of systematic manipulation of the publication and peer-review process. We cannot, therefore, vouch for the reliability or integrity of this article.

Please note that this notice is intended solely to alert readers that the peer-review process of this article has been compromised.

Wiley and Hindawi regret that the usual quality checks did not identify these issues before publication and have since put additional measures in place to safeguard research integrity.

We wish to credit our Research Integrity and Research Publishing teams and anonymous and named external researchers and research integrity experts for contributing to this investigation.

The corresponding author, as the representative of all authors, has been given the opportunity to register their agreement or disagreement to this retraction. We have kept a record of any response received.

References

- [1] K. T. Alhamazani, J. Alshudukhi, T. S. Alharbi, S. Aljaloud, and Z. Meraf, "Using Depth Cameras for Recognition and Segmentation of Hand Gestures," *Advances in Materials Science and Engineering*, vol. 2021, Article ID 7100727, 6 pages, 2021.

Research Article

Using Depth Cameras for Recognition and Segmentation of Hand Gestures

Khalid Twarish Alhamazani ¹, Jalawi Alshudukhi ¹, Talal Saad Alharbi ¹,
Saud Aljaloud ¹ and Zelalem Meraf ²

¹University of Ha'il College of Computer Science and Engineering, Department of Computer Science, Hail, Saudi Arabia

²Department of Statistics, Injibara University, Injibara, Ethiopia

Correspondence should be addressed to Zelalem Meraf; zelalemmeraf@inu.edu.et

Received 21 November 2021; Accepted 8 December 2021; Published 18 December 2021

Academic Editor: Palanivel Velmurugan

Copyright © 2021 Khalid Twarish Alhamazani et al. This is an open access article distributed under the Creative Commons Attribution License, which permits unrestricted use, distribution, and reproduction in any medium, provided the original work is properly cited.

In recent years, in combination with technological advances, new paradigms of interaction with the user have emerged. This has motivated the industry to create increasingly powerful and accessible natural user interface devices. In particular, depth cameras have achieved high levels of user adoption. These devices include the Microsoft Kinect, the Intel RealSense, and the Leap Motion Controller. This type of device facilitates the acquisition of data in human activity recognition. Hand gestures can be static or dynamic, depending on whether they present movement in the image sequences. Hand gesture recognition enables human-computer interaction (HCI) system developers to create more immersive, natural, and intuitive experiences and interactions. However, this task is not easy. That is why, in the academy, this problem has been addressed using machine learning techniques. The experiments carried out have shown very encouraging results indicating that the choice of this type of architecture allows obtaining an excellent efficiency of parameters and prediction times. It should be noted that the tests are carried out on a set of relevant data from the area. Based on this, the performance of this proposal is analysed about different scenarios such as lighting variation or camera movement, different types of gestures, and sensitivity or bias by people, among others. In this article, we will look at how infrared camera images can be used to segment, classify, and recognise one-handed gestures in a variety of lighting conditions. A standard webcam was modified, and an infrared filter was added to the lens to create the infrared camera. The scene was illuminated by additional infrared LED structures, allowing it to be used in various lighting conditions.

1. Introduction

The effectiveness of the human-computer interaction is directly influenced by the way the interface is designed. With the rise of personal computers in the 1980s, HCI arose. Computers were no longer being created just for professionals, and HCI's purpose was to make all computer interactions simple and efficient for a wide range of users with varying skill levels.

Human-computer interaction (HCI for its acronym in English) is a prevalent concept among large companies. A more intuitive relationship between man and computer is sought to apply it in different technological devices. It is considering end-user satisfaction by reducing their effort to perform tasks. Projects have been worked on where communication is carried

out through body gestures; Microsoft is one of the companies that made this possible with one of its projects called Kinect; another case is that of Nintendo with the Wii console. That is why, contributing to the improvement of HCI and the new trends of creating interaction with body gestures, the search for interaction with the user is proposed where it is required to identify a hand using infrared light as a critical tool [1].

Infrared light provides information that cannot be obtained from visible light. All bodies tend to emit infrared radiation, which depends directly on the temperature in which the body is located, and this is one of the advantages that are taken advantage of within the developments of computer vision since the image capture provides clear images, with really striking lighting that allows identifying bodies in the scene. An infrared camera is a device that, from the middle infrared emissions of

the electromagnetic spectrum of the detected bodies, forms luminous images visible to the human eye. The risk of common eye illnesses has been linked to high ambient temperatures. This type of infrared shot is associated with night shots or the possibility of seeing in very dark situations [2].

1.1. Review of Literature. Hameed et al. [3] proposed developing a gesture recognition system to communicate through a more natural human-computer interaction. The main objective is to create a robust and efficient segmentation algorithm based on colour spaces and morphological processing necessary for skin colour detection, image background removal, and variable lighting conditions. In work, the OpenCV library was used for monitoring and a perimeter travel algorithm to detect the hand contour.

According to [4], detection of gestures is one of the important parts of HCI, which is why he proposes a work in which the detection of gestures is done through pre-processing of images to reduce noise in addition to using support vector machines (SVM) for the detection and extraction of the region where the hands are located using prominent characteristics with an appearance-based approach.

This segmentation technique is based on combining two unsupervised clustering approaches such as K -means and expectation maximization. The experimental results showed that this technique succeeds in correctly segmenting the hand from the body, the face, the arm of a person, and other elements found in the image, which was taken with variable lighting conditions in real-time.

Ito et al. [5] developed a method of obtaining hand characteristics from image sequences, specifically when a person performs the signs of the Japanese sign language to recognise the words of a said language in a complex background. For recognition, the hidden Markov model (HMM) technique is used using six features of the face and hands. The results presented indicate that the objective of monitoring the face and hands is met.

On the other hand, in [6], a method of predicting the poses of an articulated hand is presented in real-time with a depth camera to carry out the interaction in an environment of mixed reality and to study the effects of models of real and virtual articulated hands in a simulator. Random decision forests were used to carry out the recognition, which proved to have better results in real-time applications, avoiding the typical errors in the use of these technologies and showing low consumption of computational resources and high precision.

In this work, an infrared camera is built from small modifications at the hardware level of a conventional webcam, achieving a clean image, and through the segmentation of the scene, the hand is identified, finally leading to a gesture recognition process. The contribution of this work can be determined as obtaining a device that allows images to be captured with the characteristics mentioned earlier and with which the possibility of being used in projects that require capturing scenes. It should be noted that the tests are carried out on a set of relevant data from the area. Based on this, the

performance of this proposal is analyzed about different scenarios such as lighting variation or camera movement, different types of gestures, sensitivity, or bias by people, among others.

2. Methodology

For the development of this work, it was decided to adopt the improved cascade methodology used in software development [6] because this methodology establishes the stages of the software life cycle so that the beginning of each phase must wait. However, the end of the previous one allows the improvement of prior stages, if necessary. In Figure 1, the scheme of the methodology that includes three steps is shown.

The first stage, named “hardware adaptation,” refers to all the activities to obtain the camera with the necessary modifications and the best alternative for capturing the desired image to continue with the process. In the second stage, “image processing and feature extraction,” essential aspects are defined for the features to be compared and the structure of the library to be built. The third stage, “gesture recognition and implementation,” refers to how the training is achieved to detect gestures and implement the library in an application.

2.1. Hardware Adaptation. This section presents the hardware structure and its modifications to obtain an infrared camera with the necessary characteristics for the project. Figure 2 shows a diagram of the camera and the essential additions to convert it into an infrared camera.

First, the web camera (Figure 2(a)) model COM-105 with a 480-pixel CMOS sensor is modified so that the ICR filter is eliminated following the procedure explained in (WANG 2013). Subsequently, to make adequate lighting of the scene that would be evaluated during the tests, building an array of LEDs (Figure 2(c)) is necessary.

In a second phase, this structure is built using an arrangement of 10 LEDs model TN130BF, whose greater illumination amplitude angle allows the objects to be segmented more completely, unlike other diode models.

Finally, some materials that allow filtering the infrared light are used to determine the elements present in the image (Figures 2(a) and 2(b)). The materials used were selected considering the wavelength captured by each of the materials, carrying out experimental tests to determine the one that offered the appropriate capture of the hand and the gestures performed. At the end of these tests, the negative of a roll photographic film was selected as the material (Figure 3), allowing observing elements with a wavelength between 800 nm and 1000 nm.

2.2. Image Processing and Feature Extraction. The term “digital image processing” refers to the use of a computer to process digital images. We can also call it the application of computer algorithms in order to obtain a better image or extract useful information. After the camera had been modified, it had to be checked to see whether the acquired pictures had enough information to recognise one-handed

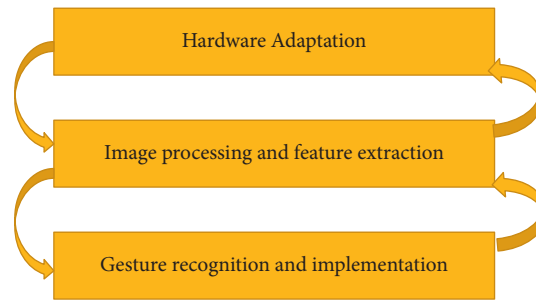


FIGURE 1: Scheme of the proposed methodology.

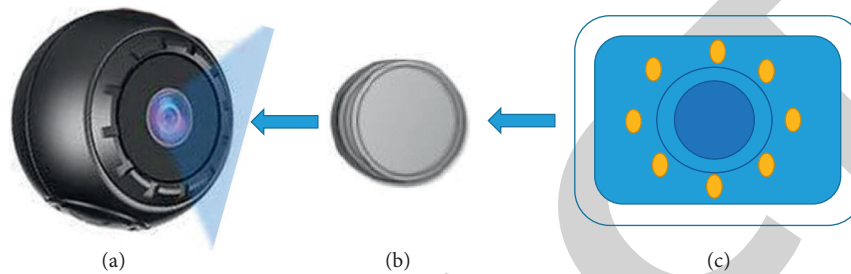


FIGURE 2: Chamber schematic and additions.

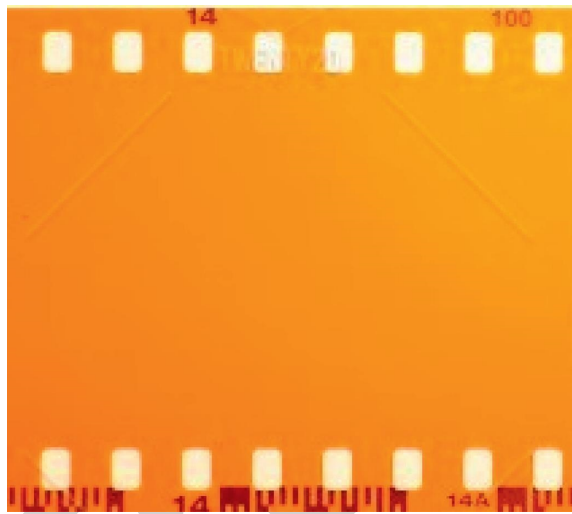


FIGURE 3: Photographic film negative strip.

motions. A library of functions based on the C++ language and the OpenCV library [7] were created to carry out the verification.

The first step to carry out is the hand segmentation in the foreground from the rest or background of the captured image. The way selected to perform this segmentation is based on threshold segmentation where, based on values established by a person, a colour image was obtained by the camera constructed through a mask that verifies pixel by pixel, if the numerical value of each one of these pixels is in the range that defines a hand. Otherwise, it is determined that that pixel does not belong to the hand. Figure 4 shows the process for establishing the threshold for a colour channel found in the images.

Because one of the characteristics of the images captured by an infrared camera is that the objects reflect this type of light, the use of this channel was analysed for a program to transform the information in it into another image at a scale of greys to support better segmentation of the hand in the image. This transformation offered an improvement in segmentation, which is why it was selected to continue using the grayscale. In image five, you can see the image resulting from this process.

Since the hand has been segmented, the defining characteristics must be extracted. These characteristics will be obtained from the analysis of the contour of the hand and the location of the centroid of the hand.

The hand contour is obtained as a sequence of points using the algorithm developed by Satoshi in [7] and is implemented in the OpenCV library. Once received, the convex envelope (larger polygon that surrounds a figure in the image) and its defects (deep points between the convex envelopes) must be found [8–14]. This allows determining the space occupied by the hand and locating the fingertips, as shown in Figure 5. In the figure, you can see the beginning and end of a defect that corresponds to the union of the space between the fingers of the hand and their tip.

After the location of the largest polygon, which corresponds to the hand with the fingers included, the centroid of the hand is determined using the detected polygon (Figure 6).

With the above, it is determined that the characteristics to be used to identify the gestures would be defined by a defect and the centroid, as defined in Table 1.

With the above, it is established that 20 characteristics are used to represent an extended hand to which the width and height of the hand are added to make a total of 22 elements to analyse (Figure 7).



FIGURE 4: Assignment of the threshold for the channel with the colour red and segmented with that information.



FIGURE 5: Threshold assignment for grayscale and segmented with such information.

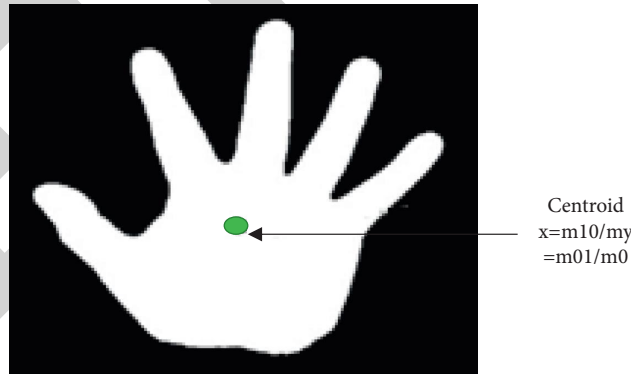


FIGURE 6: Location and description of the convex envelope and its defects.

TABLE 1: Description of extracted characteristics.

Feature in the picture	Feature extracted from the image
Default	Distance from start to finish Starting distance to the deepest point Distance from the end to the deepest point
Centroid	Distance from start to the centroid Distance from end to the centroid

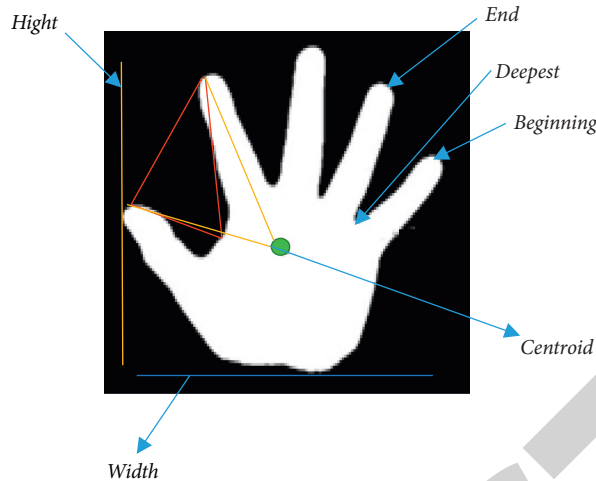


FIGURE 7: Description of extracted features.

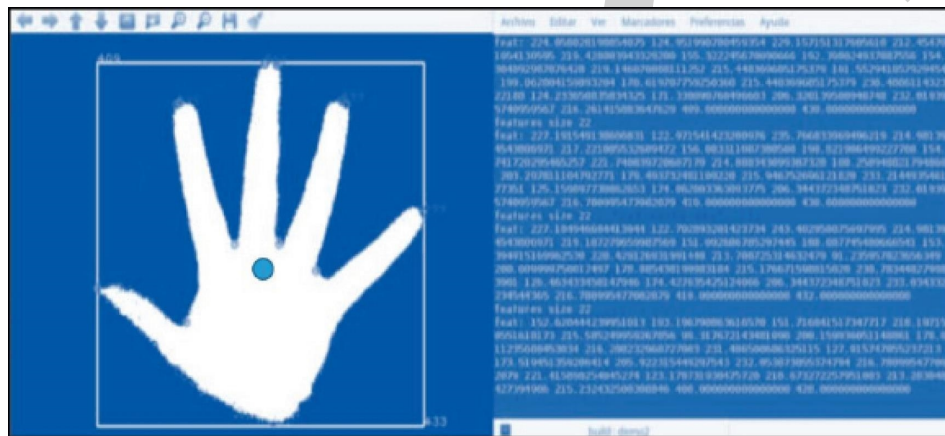


FIGURE 8: Hand identification with five sides extended and features removed.

3. Results

It can be concluded that both the built camera and the implemented library can support the detection and recognition of hand gestures. This was achieved using the technique of vector support machines (SVM) [15], which learns to classify data into two different classes. An implementation of SVM is included in the OpenCV library with which it was possible to use it.

To perform the training of the machines, the extraction of characteristics of various shots taken with the developed library was executed, and each gesture shot was labelled as five fingers and four fingers. Examples of the parts are presented in Figure 8.

For each gesture of extended fingers, 55 samples were used, with which the machines were trained to later verify with images captured directly from the camera turned on. Each gesture is checked separately with another motion where the fingers are not separated, as shown in Figure 8.

The results obtained allowed us to observe that the development carried out identifies in a better way the gesture of five fingers against the motion without extended fingers than the gesture of four fingers against that of.

4. Conclusions and Future Work

With the project's development, it can be concluded that both the built camera and the implemented library can support the detection and recognition of hand gestures. It should be noted that the technologies developed are relatively inexpensive. Based on this, the performance of this proposal is evaluated in a variety of circumstances, including illumination changes or camera movement, various sorts of gestures, and people's sensitivity or prejudice, among others. We will look at how infrared camera pictures may be utilized to segment, categorize, and recognise one-handed movements in various illumination circumstances in this post, which could be part of the consideration when compared with some of the works previously carried out and analysed in the related works section. However, the results obtained open the possibility of improving the technologies developed after reviewing the negative aspects that were found. One of them, for example, is the affectation of the identification of gestures due to the distance between the camera and the hand that makes the gestures, since when training vector support machines with a characteristic such as height and width, the samples used in training may not have been

Retraction

Retracted: Dynamic Systems Enhanced by Electronic Circuits on 7D

Advances in Materials Science and Engineering

Received 31 October 2023; Accepted 31 October 2023; Published 1 November 2023

Copyright © 2023 Advances in Materials Science and Engineering. This is an open access article distributed under the Creative Commons Attribution License, which permits unrestricted use, distribution, and reproduction in any medium, provided the original work is properly cited.

This article has been retracted by Hindawi following an investigation undertaken by the publisher [1]. This investigation has uncovered evidence of one or more of the following indicators of systematic manipulation of the publication process:

- (1) Discrepancies in scope
- (2) Discrepancies in the description of the research reported
- (3) Discrepancies between the availability of data and the research described
- (4) Inappropriate citations
- (5) Incoherent, meaningless and/or irrelevant content included in the article
- (6) Peer-review manipulation

The presence of these indicators undermines our confidence in the integrity of the article's content and we cannot, therefore, vouch for its reliability. Please note that this notice is intended solely to alert readers that the content of this article is unreliable. We have not investigated whether authors were aware of or involved in the systematic manipulation of the publication process.

Wiley and Hindawi regrets that the usual quality checks did not identify these issues before publication and have since put additional measures in place to safeguard research integrity.

We wish to credit our own Research Integrity and Research Publishing teams and anonymous and named external researchers and research integrity experts for contributing to this investigation.

The corresponding author, as the representative of all authors, has been given the opportunity to register their agreement or disagreement to this retraction. We have kept a record of any response received.

References

- [1] A. Abdullah Hamad, M. Lellis Thivagar, M. Bader Alazzam et al., "Dynamic Systems Enhanced by Electronic Circuits on 7D," *Advances in Materials Science and Engineering*, vol. 2021, Article ID 8148772, 11 pages, 2021.

Research Article

Dynamic Systems Enhanced by Electronic Circuits on 7D

Abdulsattar Abdullah Hamad ¹, M. Lellis Thivagar ², Malik Bader Alazzam ³,
Fawaz Alassery ⁴, Muayyad Mahmood Khalil⁵, V. Ramesh,⁶
Zelalem Meraf ⁷, and Vishal Kumar ⁸

¹Tikrit University, College of Sciences, Tikrit, Iraq

²School of Mathematics, Madurai Kamaraj University, Madurai, India

³Faculty of Computer Science and Informatics, Amman Arab University, Amman, Jordan

⁴Department of Computer Engineering, College of Computers and Information Technology, Taif University, Taif, Saudi Arabia

⁵Department of Mathematics, College of Education for Pure Sciences, Tikrit University, Tikrit, Iraq

⁶Dept of Mathematics, Kandaswami Kandar's College, Velur Namakkal, Tamilnadu, India

⁷Department of Statistics, Injibara University, Injibara, Ethiopia

⁸Department of Computer Science & Engineering Bipin Tripathi Kumaon, Institute of Technology, Dwarahat, India

Correspondence should be addressed to Zelalem Meraf; zelalemmeraf@inu.edu.et

Received 10 November 2021; Accepted 30 November 2021; Published 15 December 2021

Academic Editor: Palanivel Velmurugan

Copyright © 2021 Abdulsattar Abdullah Hamad et al. This is an open access article distributed under the Creative Commons Attribution License, which permits unrestricted use, distribution, and reproduction in any medium, provided the original work is properly cited.

Hybrid synchronization is one of the most significant aspects of a dynamic system. We achieve nonlinear control unit results to synchronize two comparable 7D structures in this study. Many dynamic systems are directly connected to health care and directly enhance health. We employed linearization and Lyapunov as analytical methods, and since the linearization method does not need updating the Lyapunov function, it is more successful in achieving synchronization phenomena with better outcomes than the Lyapunov method. The two methods were combined, and the result was a striking resemblance to the dynamic system's mistake. The mathematical system with control and error of the dynamic system was subjected to digital emulation. The digital good outcomes were comparable to the two methods previously stated. We compared the outcomes of three hybrid synchronizations based on Lyapunov and linearization methods. Finally, we used the existing system, presenting it in a new attractor and comparing the findings to those of other similar systems.

1. Introduction

Real-world turbulent dynamics are studied and analyzed with greater importance in many aspects of nonlinear dynamic systems. The Lorenz system, which includes only true variables and was uncovered in 1963, is the first physical and mathematical model of a chaotic system, opening new pathways to other chaos systems such as the Chen system, Liu system, Lu's system, and Pan system. In each system, there are 3D differential equations and a positive exponent of Lyapunov [1–5].

In the complete synchronization scheme, we focused on the nonlinear control strategy, and another method was suggested, namely, linearization; in addition, we used the

Lyapunov method which is adopted in all previous works in order to compare and verify between the two methods. The results show that the linearization method is the best for achieving the synchronization; because the stability Lyapunov method needs, the Lyapunov exponent and the nonlinear dynamic system attractor are the base. Encryption [6–9], engineering [10–13], and nonlinear trunks [14] have generated greater interest in computer technology and other science applications. Safe networking is one of the leading engineering technologies. Messages made nuts by simple dysfunction mechanisms are not inherently stable. To solve this problem, the idea is higher dimensions, hyperchaotic systems, eradicate randomness, and unpredictability from the equation [15–17].

Rössler found the first 7D hyperchaotic system in 1979, containing real variables and two positive exponents for Lyapunov, as well as alternative 7D and 5D systems, with three positive exponents for Lyapunov [18]. Complex structures in higher dimensions are more efficient than low-dimensional systems [19–21].

Most papers deal with the contemporary hyperchaotic systems in higher dimensions (5D). The majority of experiments are focused on 7D and 5D systems and some studies are carried out in 6D nonlinear dynamic systems [20]. The equilibrium and equilibrium exponents from Lyapunov include the characteristics of 7D, which include ten operators with seven parameters and different functions. The exciting attractor is one of the latest dynamic systems with recent studies which differentiate between autonomous and secret types of attractors. In the following paragraphs, the results of this review are outlined.

- (i) The coordination between related 7D hyperchaotic structures is therefore explored, and a computational engineering application is suggested to distinguish dynamics errors for each and their secure contact
- (ii) Nonlinear control is based on Lyapunov stability techniques, and linearization creates a large number of controllers for various synchronization phenomena
- (iii) The right controllers are calculated by comparing the effects of the Lyapunov and linearization processes

2. The Description of the Problem and Our Solution

This research provides the second Lyapunov approach and linearization methods in which it shows that Lyapunov serves as a specific building tool:

$$V(e) = \frac{1}{2} \sum_{i=1}^n e_i^2 = e^T P e, \quad (1)$$

$$P = \text{diag}\left(\frac{1}{2}, \frac{1}{2}, \dots, \frac{1}{2}\right),$$

where P denotes a normal function and R denotes a random function.

Derivatives of the Lyapunov function:

$$\dot{V}(e) = \sum_{i=1}^n e_i \dot{e}_i = -e^T Q e. \quad (2)$$

This is clearly a negative result since Q is a positive matrix of the cube. In the case of negative Q matrix, however, the P matrix must be modified, in order to achieve the optimal Q matrix.

In the last two decades, extensive studies have been conducted on the properties of nonlinear dynamical systems. The most important characteristic of nonlinear dynamical systems is chaos. This phenomenon is an important topic in nonlinear sciences and has been extensively investigated in mathematics, physics, engineering sciences, and communications secrecy.

In a nutshell, this final point clarifies three key questions. Is the Lyapunov method always successful? Is the linearization method, on the contrary, superior? And, finally, how can we tell the difference between these two approaches? This paper establishes the preceding questions and, in the end, provides a clear answer to them.

3. System Portrayal

The Lorenz method is the most common 3D chaotic system and is widely applied. Using a linear feedback control system, the original architecture is converted into a 5D and 7D hyperchaotic configuration. The built 7D hyperchaotic frame is made up of $LE_1 = 0.94613$, $LE_2 = 0.28714$, $LE_3 = 0.0047625$, and $LE_5 = -0.19386$, $LE_6 = -0.79691$, and $LE_7 = -12.701$. The system is mathematically explained as follows:

$$\begin{cases} x = a(y - x) + u, \\ y = cx - xz + w - y + hs, \\ z = xy - bz, \\ u = -xz + hu - v, \\ v = qy - pv - rx, \\ w = rv + qs - px, \\ s = ry - qw. \end{cases} \quad (3)$$

The variables $x_1, x_2, x_3, x_4, x_5, x_6, x_7$, as well as the parameters a, b, c, h, p, q , and r , all have positive real values equal to (10, 8/3, 28, 1, 0.2, 8, 0.5), and this 7D device is filled with dynamical properties. Figures 1 and 2 depict the system's 3D attractor (3), while Figures 3 and 4 depict the structure's 2D attractor (3).

3.1. Lyapunov Exponents and Dimensions. A numerical emulation of $a = 10, b = 8/3, c = 28, h = 1, p = 0.2, q = 8$, and $r = 0.5$ was proved using MATLAB and Wolf algorithm. $LE_1 = 0.9461$, $LE_2 = 0.2871$, $LE_3 = 0.0048$, $LE_4 = 0.0007$, $LE_5 = -0.19386$, $LE_6 = -0.7969$, and $LE_7 = -12.702$, with three positive Lyapunov exponents, $LE_1 = 0.9461$, $LE_2 = 0.2871$, $LE_3 = 0.0048$, $LE_4 = 0.0007$, $LE_5 = -0.19386$, and $LE_6 = -0.7969$, $LE_7 = -12.702$.

Figure 5 depicts the exponents of the Lyapunov diagram. Lyapunov's proportions are as follows:

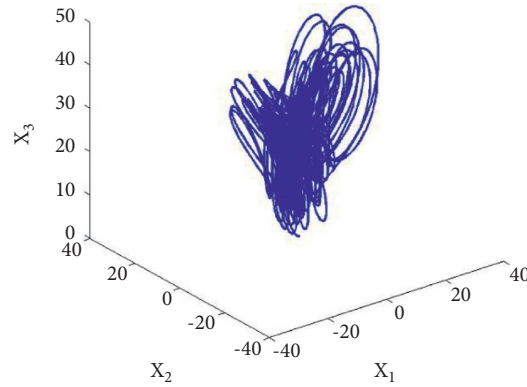


FIGURE 1: Three-dimensional attractor of system (3) in the (x_1, x_2, x_3) space.

$$D_{LE} = j + \frac{1}{|LE_{j+1}|} \sum_{i=1}^j LE_i = 6 + \frac{LE_1 + LE_2 + LE_3 + LE_4 + LE_5 + LE_6}{|LE_7|} = -0.012798. \quad (4)$$

3.2. *Hybrid Synchronization.* Theoretically, this section establishes with its numerical emulation which is one of the main applications of protected information engineering. The first device (known as the drive system) thus represents the message information to be communicated, while the second system displays the sound preceding this information to keep it from being violated. Suppose the computer (3) is a drive and the second method is written (called response system).

Hybrid synchronization, where one part of the system is synchronized with another part of asynchrony so that full synchronization and asynchrony coexist in the system mathematically; the phenomenon of hybrid synchronization of the two systems is achieved when $\lim_{t \rightarrow \infty} Y - \alpha X = 0$, where Y and X are the state vectors of the drive-response system, respectively, and $(\alpha = \mp 1)$:

$$\begin{cases} x = a(y - x) + u, \\ y = cx - xz + w - y + hs, \\ z = xy - bz, \\ u = -xz + hu - v, \\ v = qy - pv - rx, \\ w = rv + qs - px, \\ s = ry - qw. \end{cases} \quad (5)$$

While the response system is as follows:

$$\begin{cases} x' = a(y' - x') + u' + u_1, \\ y' = cx' - x'z' + w' - y' + hs' + u_2, \\ z' = x'y' - bz' + u_3, \\ u' = -x'z' + hu' - v' + u_4, \\ v' = qy' - pv' - rx' + u_5, \\ w' = rv' + qs' - px' + u_6, \\ s' = ry' - qw' + u_7, \end{cases} \quad (6)$$

and let $U = [u_1, u_2, u_3, u_4, u_5, u_6, u_7]^T$ be the nonlinear controller to be designed.

The 7D hyperchaotic system (4) and system (5) synchronization error dynamics are known as

$$e_i = x' \pm \alpha_i x, \quad i = 1, 2, 3, 4, 5, 6, 7, \quad (7)$$

$$\lim_{t \rightarrow \infty} e_i = 0.$$

Response system and hybrid synchronization are satisfied. The following is a description of the error's dynamics:

$$\begin{cases} \dot{e}_1 = ae_2 = ae_1 + e_4 - 2u + u_1, \\ \dot{e}_2 = ce_1 + 2cx - e_2 - x'e_3 + ze_1 = 2x'z + e_6 + he_7, \\ \dot{e}_3 = -be_3 + e_1e_2 - ye_1 + xe_2 - 2xy + u_3, \\ \dot{e}_4 = he_4 - x'e_3 + ze_1 - 2x'z - e_5 - 2v + u_4, \\ \dot{e}_5 = qe_2 - 2qy - pe_5 - ge_1 + u_5, \\ \dot{e}_6 = ge_5 + 2v - qe_7 + 2s + pe_1 + u_6, \\ \dot{e}_7 = -qe_6 - 2w + ge_2 - 2y + u_6. \end{cases} \quad (8)$$

System (7) of error dynamics is unpredictable based on linearization approach and legislation $|\lambda I_6 - J_{E_1}| = 0$.

The characteristic equation and eigenvalues are, respectively, as

$$-x^7 - \frac{193}{15}x^6 + \frac{3163}{10}x^5 + \frac{13661}{10}x^4 - \frac{505483}{30}x^3 - \frac{411241}{12}x^2 + \frac{816488}{15}x + 46576,$$

$$\left\{ \begin{array}{l} \lambda_1 = -8, \\ \lambda_2 = -\frac{8}{3}, \\ \lambda_3 = 11.8983, \\ \lambda_4 = 7.8681, \\ \lambda_5 = 1.5246, \\ \lambda_6 = -0.6703, \\ \lambda_7 = -22.8207. \end{array} \right. \quad (9)$$

After many controller systems have been developed using Lyapunov and linearization approach, we can calculate the power of the error mechanism (6). The concern arises as to which of these two tactics is superior. Our questions are answered by the following theorems.

Theorem 1. *If the regulator U of structure (6) is the scheme as*

$$\left\{ \begin{array}{l} u_1 = -ae_2 - e_4 + 2u, \\ u_2 = -ce_1 - 2cx + x'e_3 - ze_1 + 2x'z - e_6 - he_7 - 2s, \\ u_3 = -e_1e_2 + ye_1 - xe_2 + 2xy, \\ u_4 = -2he_4 + x'e_3 - ze_1 + 2x'z + e_5 + 2v, \\ u_5 = -qe_2 + 2qy + ge_1, \\ u_6 = -ge_5 - +2v + qe_7 - 2s - pe_1 - e_6, \\ u_7 = qe_6 + 2w - ge_2 + 2y - e_7. \end{array} \right. \quad (10)$$

Machine (6) can then be monitored using two different methods (5).

Proof. If we replace the error dynamics (6) mechanism with control,

$$\left\{ \begin{array}{l} \dot{e}_1 = -ae_1, \\ \dot{e}_2 = -e_2, \\ \dot{e}_3 = -be_3, \\ \dot{e}_4 = -he_4, \\ \dot{e}_5 = -pe_5, \\ \dot{e}_6 = -e_6, \\ \dot{e}_7 = -e_7, \end{array} \right. \quad (11)$$

positively defined Lyapunovs are successfully built and elected, depending on the rules of Lyapunov method:

$$V(e) = e^T P e = \frac{1}{2}e_1^2 + \frac{1}{2}e_2^2 + \frac{1}{2}e_3^2 + \frac{1}{2}e_4^2 + \frac{1}{2}e_5^2 + \frac{1}{2}e_6^2 + \frac{1}{2}e_7^2, \quad (12)$$

where P is defined in formula (1); the derivative function of Lyapunov $V(e)$ is related to time:

$$\begin{aligned} \dot{V} &= e_1\dot{e}_1 + e_2\dot{e}_2 + e_3\dot{e}_3 + e_4\dot{e}_4 + e_5\dot{e}_5 + e_6\dot{e}_6 + e_7\dot{e}_7, \\ \dot{V} &= e_1(-ae_1) + e_2(-e_2) + e_3(-be_3) + e_4(-he_4) + e_5(-pe_5) + e_6(-e_6) + e_7(-e_7), \\ \dot{V} &= -ae_1^2 - e_2^2 - be_3^2 - he_4^2 - pe_5^2 - e_6^2 - e_7^2 = -e^T Q e, \end{aligned} \quad (13)$$

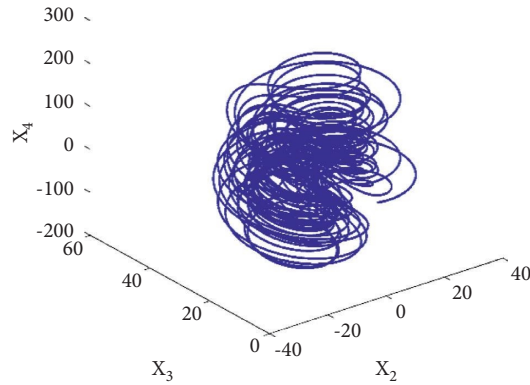


FIGURE 2: Three-dimensional attractor of system (3) in the (x_2, x_3, x_4) space.

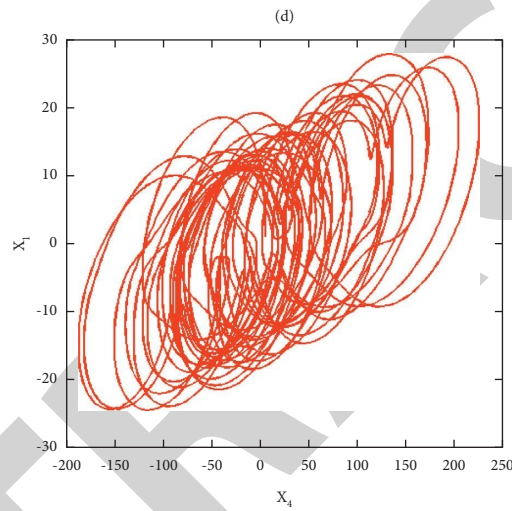


FIGURE 3: Two-dimensional attractor of system (3) in the (x_4, x_1) plane.

where $Q = \text{diag}(a, 1, b, h, p, 1, 1)$, so $Q > 0$. Consequently, $\dot{V}(e_i)$ is negative definite on \mathbb{R}^4 . The nonlinear controller works and eventually the syncing is complete.

In the second method (linearization method), the law $|\lambda I_6 - J_{E_1}| = 0$ on system (11) is applied; then, the given equations and eigenvalues are shown as follows:

$$x^7 + \frac{253}{15}x^6 + \frac{260}{3}x^5 + \frac{610}{3}x^4 + 249x^3 + \frac{485}{3}x^2 + \frac{758}{15}x + \frac{16}{3},$$

$$\left\{ \begin{array}{l} \lambda_1 = -1, \\ \lambda_2 = -1, \\ \lambda_3 = -1, \\ \lambda_4 = -1, \\ \lambda_5 = -10, \\ \lambda_6 = -1/5, \\ \lambda_7 = -8/5. \end{array} \right. \tag{14}$$

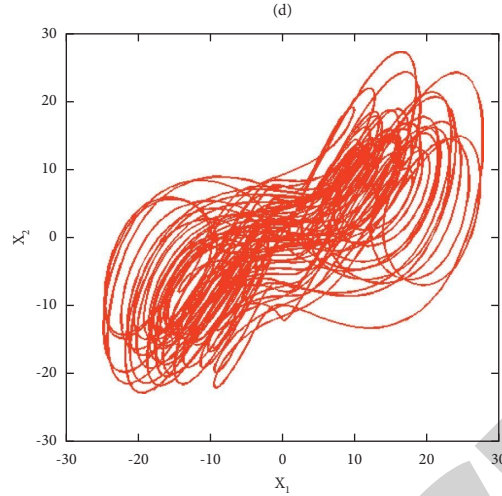


FIGURE 4: Two-dimensional attractor of system (3) in the (x_1, x_2) plane.

Naturally, linearization is done with unit (5) to machine hybrid synchronization (6).

Of course, in all roots with negative real components, the linearization process successfully synchronizes system (6) and system (5). Figure 6 shows the numerical inspections of those steps. Figure 7 contains the eigenvalues during the

response of driving processes and drive systems for controlling the convergence of the system. \square

4. Circuit Experiment

Utilizing Kirchhoff's law, the corresponding circuit equations can be written as

$$\begin{cases}
 \dot{X} = \frac{1}{C_1 R_1} (X) + \frac{1}{C_1 R_2} \frac{R_5}{R_4} (-Y) + \frac{1}{C_1 R_2} \frac{R_7}{R_6} (-U), \\
 \dot{Y} = \frac{1}{C_2 R_{10}} \frac{R_9}{R_8} (-X) + \frac{1}{C_2 R_{11}} (X * Z) + \frac{1}{C_2 R_{12}} \frac{R_{16}}{R_{15}} (-W) + \frac{1}{C_2 R_{13}} (Y) + \frac{1}{C_2 R_{14}} \frac{R_7}{R_6} (-S), \\
 \dot{Z} = \frac{1}{C_3 R_{21}} \frac{R_{22}}{R_{21}} (-X * Y) + \frac{1}{C_3 R_{24}} (Z), \\
 \dot{U} = \frac{1}{C_4 R_{27}} (X * Z) + \frac{1}{C_4 R_{28}} \frac{R_{31}}{R_{30}} (-U) + \frac{1}{C_4 R_{29}} (V), \\
 \dot{V} = \frac{1}{C_5 R_{34}} \frac{R_{33}}{R_{32}} (-Y) + \frac{1}{C_5 R_{35}} (V) + \frac{1}{C_5 R_{36}} (X), \\
 \dot{W} = \frac{1}{C_6 R_{39}} \frac{R_{38}}{R_{37}} (-V) + \frac{1}{C_6 R_{40}} \frac{R_{43}}{R_{42}} (-S) + \frac{1}{C_6 R_{41}} (X), \\
 \dot{S} = \frac{1}{C_7 R_{46}} \frac{R_{45}}{R_{44}} (-Y) + \frac{1}{C_7 R_{47}} (X),
 \end{cases} \quad (15)$$

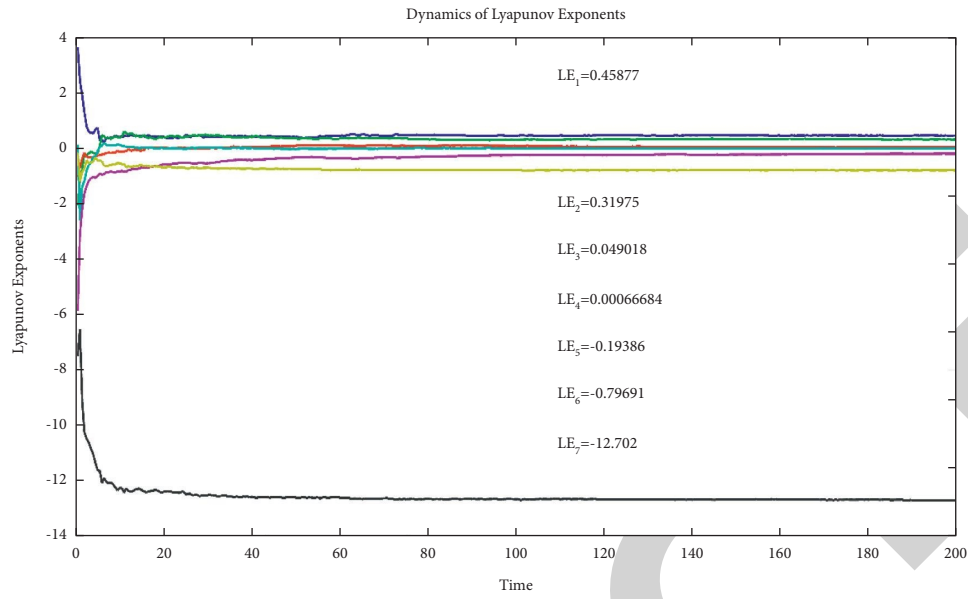


FIGURE 5: Seven-dimensional hyperchaotic system exponents of Lyapunov.

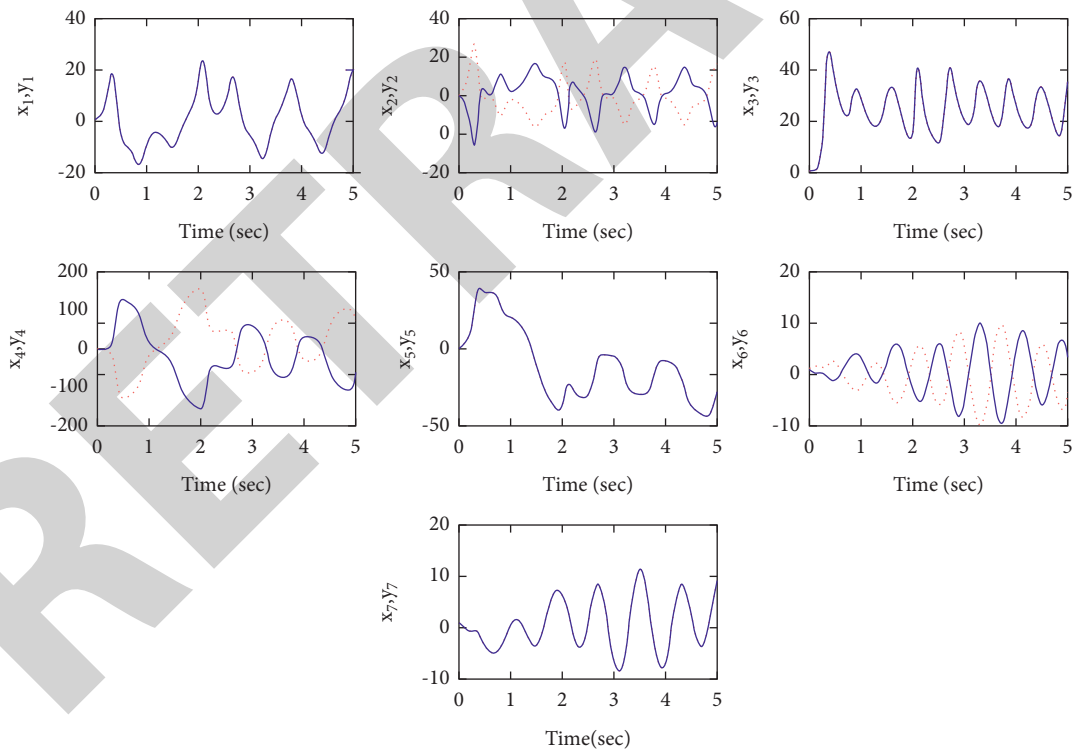


FIGURE 6: Hybrid synchronization between systems (6) and (5) with control (7).

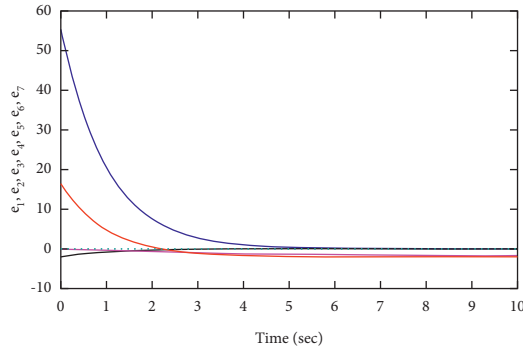
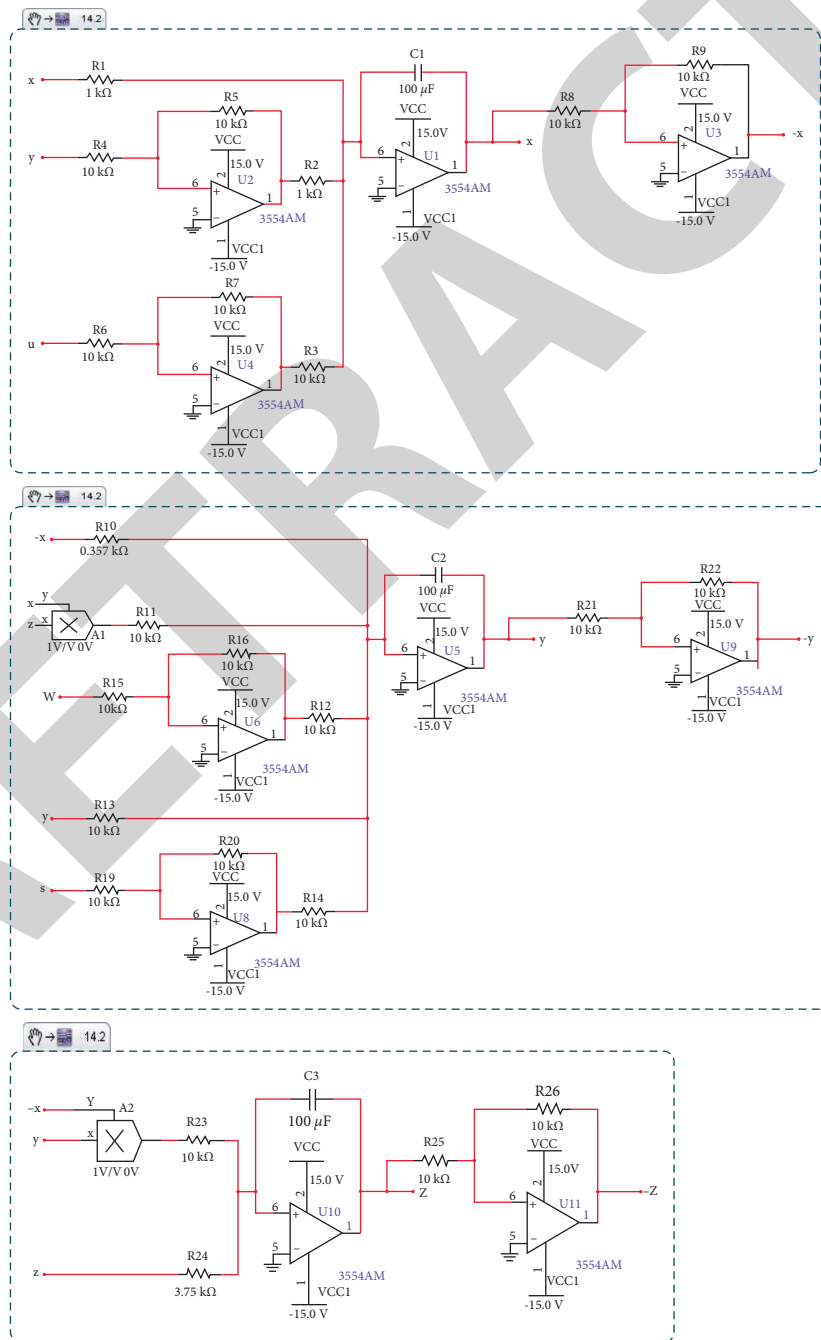


FIGURE 7: The convergence of system (8) with controller (7).



(a)

FIGURE 8: Continued.

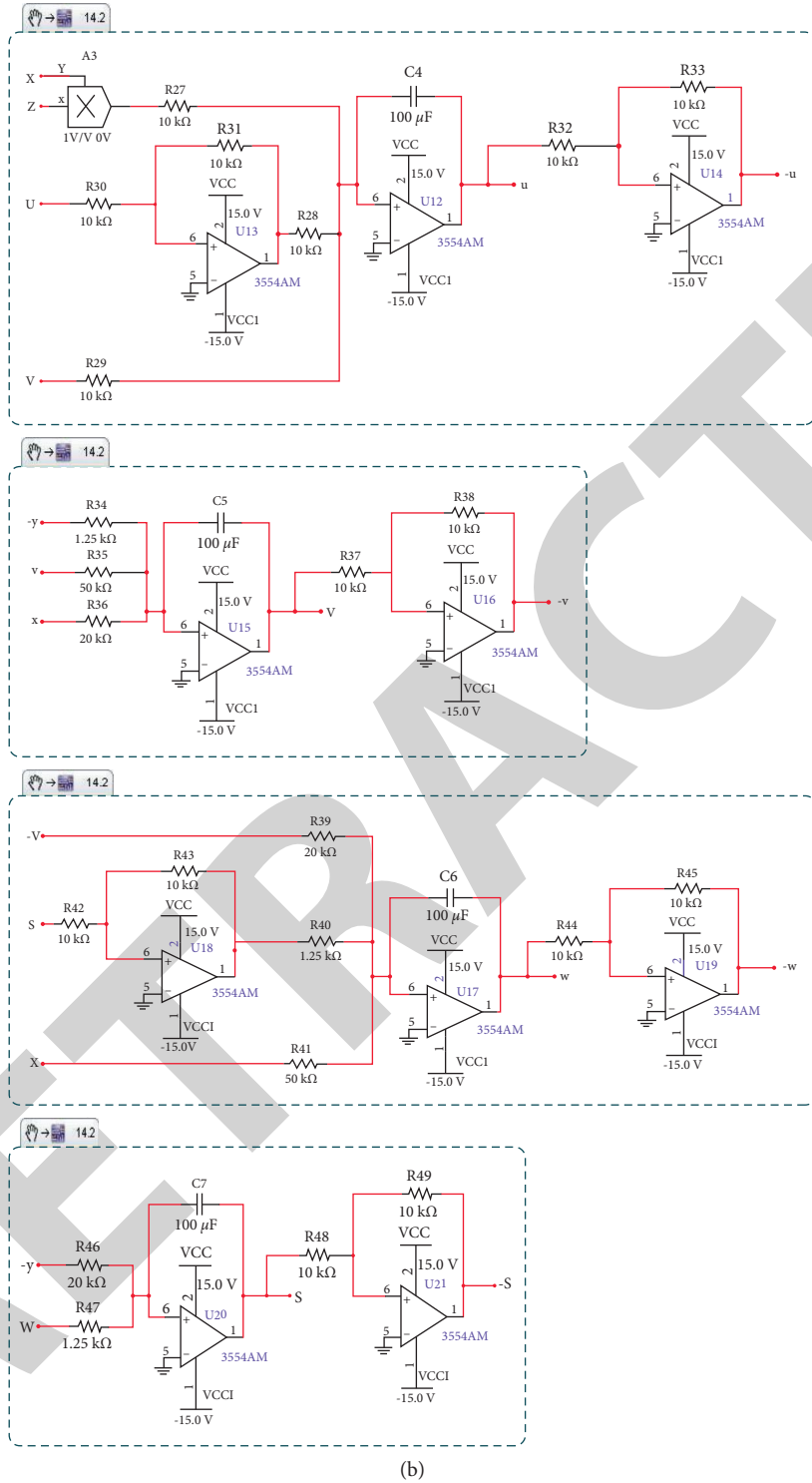


FIGURE 8: Circuit diagram of system (1).

where x' , y' , z' , u' , v' , w' , and s' represent voltages on capacitors C_1 , C_2 , C_3 , C_4 , C_5 , C_6 , and C_7 , respectively. The implement circuit is shown in Figure 8.

5. Conclusions

By Lyapunov and linearization techniques, we have been attempting to comprehend the inconsistencies in each step and how to achieve synchronization. To achieve hybrid synchronization, two identical 7D hyperchaotic systems are employed in this article. What is the most effective method? This study uses the linearization technique to answer such problems based on the outcomes and comparisons conducted between the two processes. It is important to note that the Lyapunov method should not be changed or constructed as a supporting function. The linearization method is superior to the Lyapunov way. The same results were explained using a computer simulation.

Data Availability

The data underlying the results presented in the study are available within the article.

Conflicts of Interest

The authors declare that they have no conflicts of interest.

Acknowledgments

The authors deeply acknowledge Taif University for supporting this study through Taif University researchers' supporting project no. TURSP-2020/150, Taif University, Taif, Saudi Arabia.

References

- [1] I. Lee and K. Lee, "The internet of things (IoT): applications, investments, and challenges for enterprises," *Business Horizons*, vol. 58, no. 4, pp. 431–440, 2015.
- [2] M. L. Thivagar and A. Abdullah Hamad, "A theoretical implementation for a proposed hyper-complex chaotic system," *Journal of Intelligent and Fuzzy Systems*, vol. 38, no. 3, pp. 2585–2595, 2020.
- [3] D. L. Lukes, "Optimal regulation of nonlinear dynamical systems," *SIAM Journal on Control*, vol. 7, no. 1, pp. 75–100, 1969, p.
- [4] H. Abdullah, S. Ahmed, A. S. Al-Obeid, H. Enas, and E. H. Al-Taiy, "Synchronization phenomena investigation of a new nonlinear dynamical system 4D by gardano's and lyapunov's methods," *Computers, Materials & Continua*, vol. 66, no. No.3, pp. 3311–3327, 2020.
- [5] S. Jha, S. Ahmad, H. A. Abdeljaber, A. A. Hamad, and M. B. Alazzam, "A post COVID Machine Learning approach in Teaching and Learning methodology to alleviate drawbacks of the e-whiteboards," *Journal of Applied Science and Engineering*, vol. 25, no. 2, pp. 285–294, 2021.
- [6] E. L. Ionides, C. Breto, and A. A. King, "Inference for nonlinear dynamical systems," *Proceedings of the National Academy of Sciences*, vol. 103, no. 49, pp. 18438–18443, 2006.
- [7] K. S. Okour, M. A. Alharbi, and M. B. Alazzam, "Identify factors that influence healthcare quality by adoption mobile health application in KSA E-health," *Indian Journal of Public Health Research & Development*, vol. 10, no. 11, pp. 2409–2413, 2019.
- [8] S. Sengan, O. I. Khalaf, S. Priyadarsini, D. K. Sharma, and K. Amarendra, "Smart healthcare security device on medical IoT using raspberry pi," *International Journal of Reliable and Quality E-Healthcare*, vol. 11, no. 3, pp. 1–11, 2022.
- [9] K. A. Abed and A. A. Ahmad, "The best parameters selection using peso Algorithm to solving for ito system by new iterative technique," *Indonesian Journal of Electrical Engineering and Computer Science*, vol. 18, no. 3, pp. 1638–1645, 2020.
- [10] A. H. Hameed, E. A. Mousa, and A. A. Hamad, "Upper limit superior and lower limit inferior of soft sequences," *International Journal of Engineering & Technology*, vol. 7, no. 47, pp. 306–310, p, 2018.
- [11] F. M. Abdoon, A. I. Khaleel, and M. F. El-Tohamy, "Utility of electrochemical sensors for direct determination of nicotinamide (B3): comparative studies using modified carbon nanotubes and modified β -cyclodextrin sensors," *Sensor Letters*, vol. 13, no. 6, pp. 462–470, 2015.
- [12] M. L. Thivagar, A. A. Hamad, and S. G. Ahmed, "Conforming dynamics in the metric spaces," *Journal of Information Science and Engineering*, vol. 36, no. 2, pp. 279–291, 2020.
- [13] H. D. Chiang and J. S. Thorp, "Stability regions of nonlinear dynamical systems: a constructive methodology," *IEEE Transactions on Automatic Control*, vol. 34, no. 12, pp. 1229–1241, 1989, S.
- [14] M. K. Al-Azzam, M. B. Alazzam, and M. K. Al-Manasra, "Health for decision making support: a case study of EHealth in the public sector," *International Journal of Advanced Computer Science and Applications*, vol. 10, no. 5, pp. 381–387, 2019.
- [15] A. A. Mohammed and Y. F. Al-Irhayim, "An overview for assessing a number of systems for estimating age and gender of speakers," *Tikrit Journal of Pure Science*, vol. 26, no. 1, pp. 101–107, 2021.
- [16] F. M. Abdoon and H. M. Atawy, "Prospective of microwave-assisted and hydrothermal synthesis of carbon quantum dots/silver nanoparticles for spectrophotometric determination of losartan potassium in pure form and pharmaceutical formulations," *Materials Today: Proceedings*, vol. 42, no. 7, pp. 2141–2149, 2021.
- [17] M. Mohammadi, A. Al-Fuqaha, S. Sorour, and M. Guizani, "Deep learning for IoT big data and streaming analytics: a survey," *IEEE Communications Surveys & Tutorials*, vol. 20, no. 4, pp. 2923–2960, 2018.
- [18] F. M. Abdoon and S. Y. Yahyaa, "Validated spectrophotometric approach for determination of salbutamol sulfate in pure and pharmaceutical dosage forms using oxidative coupling reaction," *Journal of King Saud University Science*, vol. 32, no. 1, pp. 709–715, 2020.
- [19] K. Y. Jhad and B. N. Shahab, "Characterizations of weakly approximately primary submodules in some types of modules," *Tikrit Journal of Pure Science*, vol. 26, no. 4, pp. 85–90, 2021.